GEOCHRONOLOGY OF IRON OXIDES AND DEVELOPMENT OF MATRIX-MATCHED REFERENCE MATERIAL FOR ROUTINE U-PB DATING

Liam Courtney-Davies

This thesis is submitted for the degree of Doctor of Philosophy

in the

School of Chemical Engineering and Advanced Materials,

Faculty of Engineering, Computer and Mathematical Sciences

at

The University of Adelaide



October 2019

TABLE OF CONTENTS

ABSTRACT ..... **xiii**

DECLARATION ..... **xv**

ACKNOWLEDGEMENTS ..... **xvi**

PREFACE ..... **xviii**

CHAPTER 1: INTRODUCTION **1**

1.1 Research objectives and thesis structure 7

1.2 References 13

CHAPTER 2: MATRIX-MATCHED IRON-OXIDE LASER ABLATION ICP-MS U–PB GEOCHRONOLOGY USING MIXED SOLUTION STANDARDS **18**

Abstract 22

2.1 Introduction 23

2.2 Experimental Methodology 23

2.2.1 Instrumentation 23

2.2.2 Experimental Procedure 24

2.2.3 Reagents and Standard Material 25

2.2.4 Stability and Precision of the Mass Spectrometer 25

2.2.5 Calibration Process 26

2.3 Sample Selection 26

2.4 U/Pb Geochronology Results 28

2.5 Discussion 34

2.5.1 Advantages of the Mixed-Solution Method and Comparison of Data with GJ-1 Zircon 34

2.5.2 Geologic Meaning of the Hematite Ages 35

2.6 Implications and Outlook 36

2.7 Acknowledgements 36

2.8 References 36

CHAPTER 3: A MULTI-TECHNIQUE EVALUATION OF HYDROTHERMAL HEMATITE U-PB ISOTOPE SYSTEMATICS: IMPLICATIONS FOR ORE DEPOSIT GEOCHRONOLOGY 39

Abstract 43

3.1 Introduction 44

3.2 Background 45

3.2.1 Samples 45

3.2.2 Oscillatory-zoned hematite 45

3.3 Methodology 45

3.3.1 LA-ICP-MS spot analyses 45

3.3.2 LA-ICP-MS U-Pb isotope mapping 46

3.3.3 SHRIMP spot analysis 46

3.3.4 ID-TIMS 47

3.4 Results 48

3.4.1 Sample LCD4 48

3.4.1.1 Petrography 48

3.4.1.2 LA-ICP-MS mapping 48

3.4.1.3 LA-ICP-MS 49

3.4.1.4 ID-TIMS 49
3.4.2 Sample MV005A 51
3.4.2.1 Petrography 51
3.4.2.2 LA-ICP-MS mapping 51
3.4.2.3 LA-ICP-MS 51
3.4.2.4 ID-TIMS 51
3.4.3 Sample RX6607 51
3.4.3.1 Petrography 51
3.4.3.2 LA-ICP-MS 53
3.4.3.3 ID-TIMS 53
3.4.4 Sample MV095 53
3.4.4.1 Petrography 53
3.4.4.2 LA-ICP-MS 54
3.4.4.3 ID-TIMS 54
3.4.5 Sample 7295GM 54
3.4.5.1 Petrography 54
3.4.5.2 LA-ICP-MS 55
3.4.5.3 SHRIMP 55
3.4.5.4 ID-TIMS 55
3.5 Discussion 55
3.5.1 Evaluating the U-Pb and Pb-Pb systematics of hematite 55
3.5.1.1 Common Pb in hematite 55
3.5.1.2 Evaluating the causes of reverse discordancy within hematite dates 57
3.5.1.3 Pb-loss within hematite 58

3.5.2 The effectiveness of hematite as a U-Pb mineral geochronometer and implications for future hematite U-Pb geochronology 58

3.5.2.1 Effects of $^{238/235}$U variation on external interpretation of U-Pb ages ... 58

3.5.2.2 Evaluating the geological accuracy of hematite U-Pb dates and analytical methods 59

3.6 Conclusions 59

3.7 Acknowledgements 60

3.8 References 60

CHAPTER 4: OPENING THE MAGMATIC-HYDROTHERMAL WINDOW: HIGH-PRECISION U-PB GEOCHRONOLOGY OF THE MESOPROTEROZOIC OLYMPIC DAM CU-U-AU-AG DEPOSIT, SOUTH AUSTRALIA 63

Abstract 67

4.1 Introduction 68

4.2 Background 70

4.3 Rationale and Samples 74

4.4 Methodology 77

4.5 Results: Petrography and Geochronology 79

4.5.1 Zircon 79

4.5.1.1 Gawler Range Volcanics 79

4.5.1.2 Roxby Downs Granite 80

4.5.2 Hematite 83

4.5.2.1 SE-lobe hematite-rich breccias 83

4.5.2.2 High-grade bornite ore 84

4.5.2.3 Deep bedded lithologies 84

4.5.2.4 Volcanic and ‘barren’ deposit center breccias 85

4.5.2.5 ‘Outer shell’, northern deposit margin 86
4.6 Discussion 86
4.6.1 Formation of the Olympic Dam IOCG deposit: constraints on the magmatic-hydrothermal window 86
4.7 Implications 92
4.8 Conclusions 95
4.9 Acknowledgements 96
4.10 References 96

CHAPTER 5: HEMATITE GEOCHEMISTRY AND GEOCHRONOLOGY RESOLVE GENETIC AND TEMPORAL LINKS AMONG IRON-OXIDE COPPER GOLD SYSTEMS, OLYMPIC DAM DISTRICT, SOUTH AUSTRALIA 102

Abstract 106
5.1 Introduction 106
5.2 Geological background 108
5.3 Methodology 110
5.4 Results 110
5.4.1 Sampling 110
5.4.2 Iron oxide petrography 111
5.4.2.1 Magnetite 111
5.4.2.2 Uranium-bearing hematite 112
5.4.2.3 Iron oxides in the Wirrda Well shear zone 113
5.4.3 Iron oxide geochemistry – LA-ICP-MS data 113
5.4.3.1 Trace element concentrations 114
5.4.3.2 Trace element correlation trends 114

5.4.3.3 REY partitioning trends in iron oxides 115

5.4.3.4 Hematite U-Pb geochronology 115

5.5 Discussion 116

5.5.1 Formation and evolution of iron-oxides at Wirrda Well and Acropolis 116

5.5.2 Geological significance of the U-Pb hematite geochronology 120

5.5.3 Timing and evolution of IOCG metallogeny across the Olympic Dam district 120

5.6 Conclusions and outlook 122

5.7 Acknowledgements 122

5.8 References 122

CHAPTER 6: ~1760 MA MAGNETITE-BEARING PROTOLITHS IN THE OLYMPIC DAM DEPOSIT: IMPLICATIONS FOR ORE GENESIS AND REGIONAL METALLOGENY 125

Abstract 129

6.1 Introduction 129

6.2 Samples and Methodology 131

6.2.1 Samples 131

6.2.2 Analytical methodology 132

6.2.2.1 Electron microprobe analysis 132

6.2.2.2 Fe-oxide U-Pb geochronology 132

6.2.2.3 Fe-oxide trace element analysis 133

6.3. Results 133

6.3.1 Petrography and geochemistry 133

6.3.2 Iron oxide U-Pb geochronology 134

6.4 Discussion 135

6.4.1 Generations of iron oxides 135

6.4.2 Timing of U-rich iron-oxide protoliths and their incorporation in the Olympic Dam deposit 136

6.5 Implications and Conclusions 137

6.6 Acknowledgements 139

6.7 References 139

CHAPTER 7: ZIRCON AT THE NANOSCALE RECORDS METASOMATIC PROCESSES LEADING TO LARGE MAGMATIC–HYDROTHERMAL ORE SYSTEMS 143

Abstract 148

7.1 Introduction 149

7.2 Background and rationale 149

7.2.1 Zircon Chemistry and Structure 149

7.2.2 The Olympic Cu–Au Province 150

7.3 Sample Suite 152

7.4 Methodology 152

7.5 Results 154

7.5.1 Zircon Petrography, U–Pb Dating, and Selection of Grains for Nanoscale Study 154

7.5.2 Trace and Minor Element Concentration 156

7.5.3 Assessment of Zircon Stoichiometry and Substitution Model 157

7.5.4 Distribution of Minor Elements: Micron- to Nanoscale Patterns 161

7.5.5 Mottled Areas: Nanoparticles to Fine Particles of Chloro–Hydroxy–Zircon . 163

7.5.6 Atomic-Scale HAADF STEM Imaging—Zircon Crystallinity and Lattice-Scale Defects 166

7.6 Discussion 174

7.6.1 Zircon Metasomatism Down to the Nanoscale: Are Iron and Chlorine of Magmatic or Hydrothermal Origin? 174

7.6.2 Timing of Zircon Alteration: Is Metasomatism Pre- or Post-Metamictization? 174

7.6.3 Zircon Alteration Model and Magma "Fertility" 176

7.7 Conclusions and Implications 178

7.8 Acknowledgements 178

7.9 References 179

CHAPTER 8: SYNTHESIS OF U-PB DOPED HEMATITE USING A HYDRATED FERRIC OXIDE APPROACH 184

Abstract 188

8.1 Introduction 188

8.2 Methods and results 189

8.2.1 Doping experiments 189

8.2.2 Characterization methods 192

8.2.3 Morphology and appearance 193

8.2.4 X-ray powder diffraction 194

8.2.5 Geochemistry and U/Pb isotopic composition 194

8.2.6 Grain-scale distributions and homogeneity 196

8.3 Discussion and conclusions 196

8.4 Acknowledgements 196

8.5 References 196

CHAPTER 9: EVALUATION AND APPLICATION OF A SYNTHETIC HEMATITE REFERENCE MATERIAL FOR U-PB GEOCHRONOLOGY 199

Abstract 204

9.1 Introduction 205
9.2 Methodology 206
9.2.1 Imaging 206
9.2.2 Laser ablation ICP-MS 206
9.2.3 Isotope dilution TIMS 206
9.3 Samples 211
9.3.1 Synthetic hematite reference material (HFO) 211
9.3.2 Natural hematite 212
9.4 Results and Discussion 214
9.4.1 Characterization of HFO reference material 214
9.4.2 U/Pb measurement of HFO reference material 217
9.4.3 Application of HFO reference material 222
9.5 Conclusions and outlook 224
9.6 Acknowledgements 225
9.7 References 226

CHAPTER 10: SUMMARY, RECOMMENDATIONS AND CONCLUDING REMARKS 229

10.1 Summary and recommendations 231
10.1.1 Geochronology of the Olympic Dam Cu-U-Au-Ag Deposit 232
10.1.2 Zircon evolution in U-rich IOCG systems 235
10.1.3 Development of hematite U-Pb reference material 241
10.2 Concluding remarks 243
10.3 References 245

CHAPTER 11: SUPPLEMENTARY AND ADDITIONAL MATERIAL 251

SUPPLEMENTARY MATERIAL A: For Chapter 2 253

Electronic Appendix A for Chapter 2 254

SUPPLEMENTARY MATERIAL B: For Chapter 3 256

Electronic Appendix A for Chapter 3 257

Electronic Appendix B for Chapter 3 259

Electronic Appendix C for Chapter 3 260

Electronic Appendix D for Chapter 3 262

SUPPLEMENTARY MATERIAL C: For Chapter 4 263

Electronic Appendix A for Chapter 4 264

Electronic Appendix B for Chapter 4 270

SUPPLEMENTARY MATERIAL D: For Chapter 5 271

Electronic Appendix A for Chapter 5 272

Electronic Appendix B for Chapter 5 276

Electronic Appendix C for Chapter 5 278

SUPPLEMENTARY MATERIAL E: For Chapter 6 279

Electronic Appendix A for Chapter 6 280

Electronic Appendix B for Chapter 6 281

SUPPLEMENTARY MATERIAL F: For Chapter 7 283

Electronic Appendix A for Chapter 7 284

Electronic Appendix B for Chapter 7 297

Electronic Appendix C for Chapter 7 303

SUPPLEMENTARY MATERIAL G: For Chapter 8 311

Electronic Appendix A for Chapter 8 312

Electronic Appendix B for Chapter 8 314

Electronic Appendix C for Chapter 8 315

SUPPLEMENTARY MATERIAL H: For Chapter 9 316

Electronic Appendix A for Chapter 9 317

ADDITIONAL MATERIAL I: Iron-oxides constrain BIF evolution in terranes with protracted geological histories: the Iron Count prospect, Middleback Ranges, South Australia 318

ADDITIONAL MATERIAL J: Petrographic and geochronological constraints on the granitic basement to the Middleback Ranges, South Australia 320

ADDITIONAL MATERIAL K: Silician Magnetite: Si–Fe-Nanoprecipitates and Other Mineral Inclusions in Magnetite from the Olympic Dam Deposit, South Australia 322

ADDITIONAL MATERIAL L: Advances and opportunities in ore mineralogy 324

ADDITIONAL MATERIAL M: Textures and U-W-Sn-Mo signatures in hematite from the Olympic Dam Cu-U-Au-Ag deposit, South Australia: Defining the archetype for IOCG deposits. 326

ADDITIONAL MATERIAL N: Defining early stages of IOCG systems: evidence from iron-oxides in the outer shell of the Olympic Dam deposit, South Australia 328

ADDITIONAL MATERIAL O: Copper-arsenic nanoparticles in hematite: fingerprinting fluid-mineral interaction. 330

ADDITIONAL MATERIAL P: Chloro-hydroxy-zircon nanoprecipitates fingerprint fertility and mineralization potential of granitic magmas 332

ADDITIONAL MATERIAL Q: U-Pb doped synthetic reference material for in-situ hematite geochronology 336

ADDITIONAL MATERIAL R: Developing iron-oxide U-Pb geochronology for new, robust, temporal insights into IOCG and BIF mineralization 339

ADDITIONAL MATERIAL S: Uranium bearing, oscillatory-zoned hematite: assessing closed system behavior for U-Pb systematics 342

ADDITIONAL MATERIAL T: U-Pb geochronology of Fe-oxides: LA-ICP-MS and SHRIMP analysis 345

ADDITIONAL MATERIAL U: The U-Pb systematics of hydrothermal hematite: insights from the IOCG system at Olympic Dam, South Australia 348

ADDITIONAL MATERIAL V: Oscillatory-zoned hematite: a reliable U-Pb mineral geochronometer 351

ADDITIONAL MATERIAL W: Matrix-matched Fe-oxide laser ablation ICP-MS U-Pb geochronology using mixed solution standards. 353

ADDITIONAL MATERIAL X: SHRIMP U-Pb analysis of hematite 355

ADDITIONAL MATERIAL Y: A multi-platform microanalysis approach to unravelling geological problems: a case study from Olympic Dam South Australia 359

ADDITIONAL MATERIAL Z: Iron-oxides: a versatile tool for geochemical fingerprinting and geochronology 362

ADDITIONAL MATERIAL AA: Towards a suitable natural standard for routine U-Pb dating of iron oxides 365

ADDITIONAL MATERIAL BB: Trace element signatures of iron-oxides in BIF-style iron deposits of the Middleback Ranges, South Australia 367

ADDITIONAL MATERIAL CC: BIF-style iron deposits of the Middleback Ranges, South Australia: Trace element signatures of Fe-oxides and implications for ore formation 369

ADDITIONAL MATERIAL DD: Links between sedimentary protoliths and IOCG-skarn alteration, Island Dam, South Australia 371

ADDITIONAL MATERIAL EE: Trace element signatures in U-W-Sn-Mo zoned hematite from the IOCG deposit at Olympic Dam, South Australia 376

ADDITIONAL MATERIAL FF: Why detailed mineralogy is important: understanding evolution of the Olympic Dam iron-oxide-copper-gold system, South Australia 381

ADDITIONAL MATERIAL GG: Nanoscale study of silician magnetite from IOCG systems: examples from the Olympic Dam district, South Australia 384

ADDITIONAL MATERIAL HH: Metal-bearing nanoparticles in hematite 387

ADDITIONAL MATERIAL II: Geological setting of BIF ores, Middleback Ranges, South Australia 390

ADDITIONAL MATERIAL JJ: A multiplatform approach to ore mineralogy: advances and future prospects 393

ADDITIONAL MATERIAL JJ: Tungsten-bearing nanoparticles in hematite: insights into open system behaviour of mineral geochronometers 412

CHAPTER 12: REFERENCES 415

ABSTRACT

Iron oxides, hematite and magnetite, are common minerals throughout rocks and ores of all types and ages. The discovery of U-bearing hematite at Olympic Dam, the largest iron oxide copper-gold (IOCG) deposit in the Gawler Craton (South Australia) prompted development of this mineral as a new U-Pb geochronometer. Unlike accessory minerals routinely used to track hydrothermal mineralisation, iron oxides are dominant components of Precambrian IOCG systems and therefore geochronology of iron oxides is pivotal to understand deposit evolution.

Iron oxide minerals are studied in terms of U-Pb systematics and reliability for dating Olympic Dam and surrounding IOCG prospects formed at ~1.6 Ga. The temporal window between crystallisation of magmatic zircon and hydrothermal Fe-oxides is investigated to define the onset and lifespan of mineralisation and assess magma fertility. A matrix-matched reference material for routine microbeam geochronology is synthesised and tested for U/Pb isotope homogeneity by ID-TIMS.

The U-Pb systematics of hematite are complex, exhibiting U-Th-Pb concentration and ratio heterogeneity at the nano- to micron-scales. Nevertheless, using a multi-instrument approach, high- precision data is routinely obtained. Reconnaissance SEM imaging in BSE mode and LA-ICP-MS isotope mapping allows pinpointing of U/Pb-homogeneous, inclusion-free grain domains. Dating of such domains via LA-ICP-MS using both mixed-(U/Pb)-solution and zircon reference materials produced successful results and a steppingstone to investigate at higher resolution and precision. The first application of both SHRIMP and ID-TIMS to hematite dating confirmed the robust U-Pb system in natural hematite, yielding $^{207}Pb/^{206}Pb$ (ID-TIMS) precision of up to ~0.05%.

Coupled with (CA-)ID-TIMS analysis of magmatic zircon, hematite sampled throughout the Olympic Dam deposit provides a well constrained magmatic-hydrothermal timeline of

events. The granite intrusion hosting Olympic Dam was emplaced rapidly at 1593.28 ± 0.28 Ma. The orebody was formed during a major mineralising event following granite uplift and during cupola collapse over a period of ~2 Ma, whereby the earliest hydrothermal activity is recorded in the early, deep 'outer shell' of the deposit at 1591.27 ± 0.89 Ma. Findings discredit a shallow origin for the deposit based on irreconcilable differences between the depth of granite emplacement and timeframes of uplift and fluid exsolution.

Recognition of U-bearing hematite with a comparable W-Mo-Sn-bearing signature and age as Olympic Dam hematite within other IOCG systems, Wirrda Well and Acropolis, links the fluid forming the wider Olympic Cu-Au Province to a common source and time period.

LA-ICP-MS U-Pb dating of U-bearing, silician magnetite from Fe-rich lithologies in the outer shell at Olympic Dan yields an age of 1761 ± 19 Ma, distinct from any other ages found within the deposit. The age is likely linked to ca. 1750 Ma intrusive/extrusive magmatism reported across the Gawler Craton. This shows the presence of older ore protoliths within Olympic Dam and represents the first successful application of U-Pb dating to magnetite.

Magmatic zircon studied down to the nanoscale from two granite suites in the Gawler Craton shows crystal zoning with respect to 'non-formulae' elements such as Fe, Ca, and Cl, and also chloro-hydroxy-zircon nanoprecipitates when associated with IOCG mineralisation. This is indicative of early Fe-Cl-metasomatism prior to metamictisation, a diagnostic tool for assessing 'fertility' of granitic magmas. In contrast, metamict zircon from high-grade bornite ores shows patchy amorphisation throughout domains with pervasive enrichment in U-, Y- and non-formula elements.

Hydrated ferric oxide doped with U-Pb solutions was converted to Fe-oxide and assessed by SEM imaging, XRD and LA-ICP-MS indicating the presence of homogenous U-Pb domains in cm-sized chips of hematite. Micro-sampled domains were measured by ID-TIMS confirming U-Pb isotope homogeneity at high precision.

Hematite is a remarkably robust U-Pb geochronometer for dating hydrothermal ore deposits. Dissemination of the synthesized reference material to the wider community will allow routine LA-ICP-MS dating.

DECLARATION

I certify that this work contains no material which has been accepted for the award of any other degree or diploma in my name, in any university or other tertiary institution and, to the best of my knowledge and belief, contains no material previously published or written by another person, except where due reference has been made in the text. In addition, I certify that no part of this work will, in the future, be used in a submission in my name, for any other degree or diploma in any university or other tertiary institution without the prior approval of the University of Adelaide and where applicable, any partner institution responsible for the joint-award of this degree.

I acknowledge that copyright of published works contained within this thesis resides with the copyright holder(s) of those works.

I also give permission for the digital version of my thesis to be made available on the web, via the University's digital research repository, the Library Search and also through web search engines, unless permission has been granted by the University to restrict access for a period of time.

Signed _ __ Date __29/10/2019__

ACKNOWLEDGEMENTS

First and foremost, I would like to acknowledge my principal supervisor Dr. Cristiana L. Ciobanu. It has been a privilege to be her PhD student over the last four years. The selfless contributions of time and energy, coupled with stimulating company made my doctoral candidature challenging, exhausting and incredibly rewarding. The immense enthusiasm she has for her research was infectious and motivational for myself and so many others. Thank you for taking me on as your student, and teaching me how to contemplate, debate and communicate geology, you have been an extraordinary mentor. This sentiment extends to Professor Nigel J. Cook, who shows remarkable perseverance towards his student's success, and without whom, we would not be able to accomplish anywhere near as much. The continuous encouragement, dissemination of ideas and diligent editing of manuscripts day and night facilitates everyone within the research group's significant productivity.

I would like to thank my co-supervisors, Dr Daniel J. Condon and Dr Allen K. Kennedy, for offering many insights into the world of U-Pb geochronology, particularly at the beginning of my candidature; I was very fortunate to be under the tutelage of two pioneers in the field. Much of the work presented in this thesis would not have been possible without the expertise and patience of Dr. Simon R. Tapster, a meticulous and innovative geochronologist, from whom I learnt so much.

Special thanks must go to Dr. Kathy Ehrig, whose unrelenting appetite to learn more about Olympic Dam enabled myself and colleagues to come to Australia to study this enigmatic deposit. The encouragement of us to peruse diverse topics was pivotal for the work presented here; we were truly lucky to have such a communicative, driven and funny person coordinating our research.

All the staff at Adelaide Microscopy are thanked for their training and support over the years, particularly Dr. Benjamin P. Wade and Dr. Sarah E. Gilbert, for providing so much time, insight and putting up with us during innumerable analytical sessions.

Dr. Marcus W. Richardson made an exceptional contribution to this thesis, and cannot be thanked enough for his determination in finding novel methods to synthesise reference materials. His hunger and persuasion to keep on going until the very end is unparalleled.

Thank you to all my current and former student colleagues who supported and assisted me throughout the Ph.D: Dr. William M. Keyser, Miss. Marija Dmitrijeva, Dr. Danielle S. Schmandt, Mr. Nicholas D. Owen, Mr. Mark Rollog, Dr. Wenyuan Gao and Mr. Urs Domnick. Special mention goes to Dr. Zhiyong-Zhu, who really helped me to understand new concepts when I first arrived, and Dr. Jing Xu, for your comedic value and comradery during two visits to Adelaide. The last colleague but certainly not the least I must thank is the selfless Mr. Max R. Verdugo-Ihl, for his major contribution towards this and others theses, but mostly for the countless shared pilgrimages for Hofbräu Weisse after work, whatever the weather.

Finally, I would like to recognise my family, particularly my mother, and friends for their support from the U.K. over the years, and for not forgetting about me whilst down-under.

PREFACE

This thesis comprises of a portfolio of articles and manuscripts which are either published or under review in international peer-reviewed journals, and one abridged thesis chapter to be submitted for publication. The journals in which these papers are published or have been submitted to are *'Minerals'* (Chapter 2, published), *'Chemical Geology'* (Chapter 3, published), *'Economic Geology'* (Chapter 4, revision submitted), *'Precambrian Research'* Chapter 5, published) *'Ore Geology Reviews'* (Chapter 6, published), *'Minerals'* (Chapter 7, published), *'Journal of Crystal Growth'* (Chapter 8, published), *'Geostandards and Geoanalytical Research'* (Chapter 9, intended submission). All eight chapters are closely related and summarize key findings and interpretations, to be read as standalone contributions. Recommendations have been made in Chapter 10, as a direct result of the key findings of this research, with the aim to explore certain aspects at a later date.

The six published articles, one revised and resubmitted manuscript and one thesis chapter which form the basis of this thesis are:

1. Courtney-Davies, L., Zhu, Z., Ciobanu, C.L., Wade, B.P., Cook, N.J., Ehrig, K., Cabral, A.R., Kennedy, A., 2016. Matrix-matched iron-oxide laser ablation ICP-MS U-Pb geochronology using mixed solution standards. Minerals 6(3), 85.

2. Courtney-Davies, L., Tapster, S.R., Ciobanu, C.L., Cook, N.J., Verdugo-Ihl, M.R., Ehrig, K.J., Kennedy, A.K., Gilbert, S.E., Condon, D.J., Wade, B.P., 2019. A multi-technique evaluation of hydrothermal hematite U-Pb isotope systematics: Implications for ore deposit geochronology. Chemical Geology 513, 54-72.
3. Courtney-Davies, L., Ciobanu, C.L., Tapster, S.R., Cook, N.J., Ehrig, K.J., Crowley, J.L., Verdugo-Ihl, M.R., S.E., Wade, B.P., Condon, D.J., revision submitted. Opening

the Magmatic-Hydrothermal Window: High-Precision U-Pb Geochronology of the Mesoproterozoic Olympic Dam Cu-U-Au-Ag Deposit, South Australia. Economic Geology.

4. Courtney-Davies, L., Ciobanu, C.L., Verdugo-Ihl, M.R., Dmitrijeva, M., Cook, N.J., Ehrig, K., Wade, B.P., 2019. Hematite geochemistry and geochronology resolve genetic and temporal links among iron-oxide copper gold systems, Olympic Dam district, South Australia. Precambrian Research 335, 105480.
5. Courtney-Davies, L., Ciobanu, C.L., Verdugo-Ihl, M.R., Cook, N.J., Ehrig, K., Wade, B.P., Zhu, Z-Y., Kamenetsky, V.S., 2020. ~1760 Ma magnetite-bearing protoliths in the Olympic Dam deposit: Implications for ore genesis and regional metallogeny. Ore Geology Reviews. 118, 103337
6. Courtney-Davies, L., Ciobanu, C.L., Verdugo-Ihl, M.R., Slattery, A., Cook, N.J., Dmitrijeva, M., Keyser, W., Wade, B.P., Dominick, U.I., Ehrig, K., Xu, J., Kontonikas-Charos, A., 2019. Zircon at the nanoscale records metasomatic processes leading to large magmatic-hydrothermal ore deposits. Minerals 9(6), 364.
7. Courtney-Davies, L., Ciobanu, C.L., Richardson, M.W., Prosser, N., Verdugo-Ihl, M.R., Wade, B.P., Gilbert, S.E., Ehrig, K., Cook, N.J., 2019. Synthesis of U-Pb doped hematite using a hydrated ferric oxide approach. Journal of Crystal Growth 513, p. 48-57.
8. Courtney-Davies, L., Gilbert, S.E., Ciobanu, C.L., Tapster, S.R., Richardson, M.W., Wade, B.P., Cook, N.J., Ehrig, K., Verdugo-Ihl, M.R., Kennedy, A.K., Condon, D.J., Maas, R. (thesis chapter intended for later submission). Appraisal and implementation of a synthetic hematite reference material for microbeam U-Pb geochronology.

Chapter 11 contains supplementary material for all chapters outlined above, as well as co-authored publication abstracts, conference abstracts and posters and co-authored conference abstracts that have been generated during PhD candidature.

The additional material is as follows:

A. Supplementary material for Chapter 2 (Minerals).

B. Supplementary material for Chapter 3 (Chemical Geology).

C. Supplementary material for Chapter 4 (Economic Geology, in review).

D. Supplementary material for Chapter 5 (Precambrian Research).

E. Supplementary material for Chapter 6 (Ore Geology Reviews, in review).

F. Supplementary material for Chapter 7 (Minerals).

G. Supplementary material for Chapter 8 (Journal of Crystal Growth).

H. Supplementary material for Chapter 9 (Thesis chapter).

Co-authored article abstracts

I. Keyser, W., Ciobanu, C.L., Cook, N.J., Dmitrijeva, M., **Courtney-Davies, L.**, Feltus, H., Gilbert, S., Johnson, G., Ehrig, K., 2019. Iron-oxides constrain BIF evolution in terranes with protracted geological histories: the Iron Count prospect, Middleback Ranges, South Australia. Lithos. 324- 325, 20-38.

J. Keyser, W., Ciobanu, C.L., Cook, N.J., **Courtney-Davies, L.**, Kennedy, A., Wade, B.P., Ehrig, K., Dmitrijeva, M., Kontonikas-Charos, A., Feltus, H., Johnson, G., 2019.

Petrographic and geochronological constraints on the granitic basement to the Middleback Ranges, South Australia. Precambrian Research. 324, 170-193.

K. Ciobanu, C.L., Verdugo-Ihl, M.R., Slattery, A., Cook, N.J., Ehrig, K., **Courtney-Davies, L.**, Wade, B.P., 2019. Silician Magnetite: Si–Fe-Nanoprecipitates and Other Mineral Inclusions in Magnetite from the Olympic Dam Deposit, South Australia. Minerals. 9(5), 311.

L. Cook, N.J., Ciobnau, C.L., Ehrig, K.J., Slattery, A., Verdugo-Ihl, M.R., **Courtney-Davies, L.**, Gao, W., 2017. Advances and opportunities in ore mineralogy. Minerals, 7, 23.

M. Verdugo-Ihl, M.R., Ciobanu, C.L., Cook, N.J., Ehrig, K.J., **Courtney-Davies, L.**, Gilbert, S., 2017. Textures and U-W-Sn-Mo signatures in hematite from the Olympic Dam Cu-U-Au-Ag deposit, South Australia: Defining the archetype for IOCG deposits. Ore Geology Reviews. 91, 173–195.

N. Verdugo-Ihl, M.R., Ciobanu, C.L., Cook, N.J., Ehrig, K., **Courtney-Davies, L., 2019**. Defining early stages of IOCG systems: evidence from iron-oxides in the outer shell of the Olympic Dam deposit, South Australia. Mineralium Deposita, in press, DOI: 10.1007/s00126-019-00896-2.

O. Verdugo-Ihl, M.R., Ciobnau, C.L., Slattery, A., Cook, N.J., Ehrig, K.J., **Courtney-Davies, L.**, 2019. Copper-arsenic nanoparticles in hematite: fingerprinting fluid-mineral interaction. Minerals. 9:388, https://doi.org/10.3390/min9070388.

First author conference abstracts (poster presentations)

P. **Liam Courtney-Davies**, Cristiana L. Ciobanu, Max Verdugo-Ihl, Ashley Slattery, Nigel J. Cook, Kathy Ehrig, 2019. Chloro-hydroxy-zircon nanoprecipitates fingerprint fertility and mineralization potential of granitic magmas. TIGeR Conference 2019, Curtin University, Perth, W.A., Australia, September 11th-13th.

Q. **Liam Courtney-Davies**, Marcus W. Richardson, Sarah E. Gilbert, Cristiana L. Ciobanu, Max Verdugo-Ihl, Nigel J. Cook, Kathy Ehrig, Benjamin P. Wade, 2018. U-Pb doped synthetic reference material for in-situ hematite geochronology. Geoanalysis 2018 Conference, Sydney, N.S.W., Australia, July 10th–14th.

R. **Liam Courtney-Davies**, Cristiana L. Ciobanu, Simon R. Tapster, Daniel J. Condon, Allen K. Kennedy, Nigel J. Cook, Kathy Ehrig, Benjamin P. Wade, Marcus W. Richardson, 2017. Developing iron-oxide U-Pb geochronology for new, robust, temporal insights into IOCG and BIF mineralization. MDSG Conference 2017, Bristol, U.K., December 19th–21st.

S. **Liam Courtney-Davies**, Cristiana L. Ciobanu, Nigel J. Cook, Simon R. Tapster, Daniel J. Condon, Allen K. Kennedy, Kathy Ehrig, 2017. Uranium bearing, oscillatory-zoned hematite: assessing closed system behavior for U-Pb systematics. Goldschmidt Conference 2018, Boston, U.S.A, August 12th–17th.

T. **Liam Courtney-Davies**, Allen K. Kennedy, Cristiana L. Ciobanu, Nigel J. Cook, Kathy Ehrig, Benjamin P. Wade, Daniel J. Condon, Simon R. Tapster, 2016. U-Pb geochronology of Fe-oxides: LA-ICP-MS and SHRIMP analysis. Goldschmidt Conference 2016, Yokohama, Japan, June 26th-1st July.

First author conference abstracts (oral presentation)

U. **Liam Courtney-Davies**, Cristiana L. Ciobanu, Simon R. Tapster, Nigel J. Cook, Kathy Ehrig, Allen K. Kennedy, Daniel J. Condon, Max Verdugo-Ihl, Benjamin P. Wade, Sarah E. Gilbert, 2018. The U-Pb systematics of hydrothermal hematite: insights from the IOCG system at Olympic Dam, South Australia. 15th Quadrennial IAGOD Symposium 2018, Salta, Argentina, August 28th-31st.

V. **Liam Courtney-Davies**, Cristiana L. Ciobanu, Nigel J. Cook, Max Verdugo-Ihl, Simon R. Tapster, Daniel J. Condon, Allen K. Kennedy, Kathy Ehrig, Benjamin P. Wade, Sarah E. Gilbert, 2017. Oscillatory-zoned hematite: a reliable U-Pb mineral geochronometer. Goldschmidt Conference 2017. Goldschmidt Conference 2017, Paris, France, August 13th-18th.

W. **Liam Courtney-Davies**, Zhi-Yong Zhu, Cristiana L. Ciobanu, Benjamin P. Wade, Nigel J. Cook, Kathy Ehrig, 2016. Matrix-matched Fe-oxide laser ablation ICP-MS U-Pb geochronology using mixed solution standards. CHEMECA, Adelaide, Australia, 25-28 September, 2016.

Co-authored conference abstracts

X. Allen K. Kennedy, **Liam Courtney-Davies**, Cristiana L. Ciobanu, Benjamin P. Wade, Nigel J. Cook, Kathy Ehrig, C. Talavera, Daniel J. Condon, Simon R. Tapster, 2016. SHRIMP U-Pb analysis of hematite. Conference abstract and oral presentation (presented by Allen K. Kennedy), VIII International SHRIMP Workshop, Granada, Spain, 6-10 September, 2016.

Y. Angus K.O. Netting, Benjamin P. Wade, Max R. Verdugo-Ihl, **Liam Courtney-Davies**, Cristiana L. Ciobanu, Nigel. J Cook, Kathy Ehrig, Ashley Slattery, Sarah E. Gilbert, Ken Neubauer, 2019. A multi-platform microanalysis approach to unravelling

geological problems: a case study from Olympic Dam South Australia. Microscopy and Microanalysis 2019, Portland, U.S.A, 4-8 August, 2019.

Z. Cristiana L. Ciobanu, Nigel J. Cook, Kathy Ehrig, William M. Keyser, **Liam Courtney-Davies**, Benjamin P. Wade, Vadim S. Kamenetsky, Christian Maunders, 2016. Iron-oxides: a versatile tool for geochemical fingerprinting and geochronology. 35th International Geological Congress, Cape Town, South Africa, August 25th – September 4th.

AA. Cristiana L. Ciobanu, Nigel J. Cook, Kathy Ehrig, **Liam Courtney-Davies**, William M. Keyser, Benjamin P. Wade, Christian Maunders, Vadim S. Kamenetsky, 2016. Towards a suitable natural standard for routine U-Pb dating of iron oxides. Australian Earth Science Convention 2016, 'Uncover Earth's Past to Discover Our Future', Adelaide, Australia, June 26th–30th.

BB. William M. Keyser, Cristiana L. Ciobanu, Nigel J. Cook, Geoff Johnson, Holly Feltus, Steve Johnson, Kathy Ehrig, **Liam Courtney-Davies**, Vadim S. Kamenetsky, 2016. Trace element signatures of iron-oxides in BIF-style iron deposits of the Middleback Ranges, South Australia. 35th International Geological Congress, Cape Town, South Africa, August 25th–September

CC. William M. Keyser, Cristiana L. Ciobanu, Nigel J. Cook, Geoff Johnson, Holly Feltus2, Steve Johnson, Kathy Ehrig, **Liam Courtney-Davies**, Vadim S. Kamenetsky, 2016. BIF-style iron deposits of the Middleback Ranges, South Australia: Trace element signatures of Fe-oxides and implications for ore formation. Australian Earth Science Convention 2016, 'Uncover Earth's Past to Discover Our Future', Adelaide, Australia, June 26th–30th.

DD. William M. Keyser, Cristiana L. Ciobanu, Nigel J. Cook, **Liam Courtney-Davies**, Kathy Ehrig, Sarah Gilbert, Jocelyn McPhie, 2017. Links between sedimentary protoliths and IOCG-skarn alteration, Island Dam, South Australia. Proceedings of the 14th SGA Biennial Meeting, Québec, Canada, August 20-23rd.

EE. Max R. Verdugo-Ihl, Cristiana L. Ciobanu, Nigel J. Cook, Kathy Ehrig, **Liam Courtney-Davies**, Sarah E. Gilbert, 2017. Trace element signatures in U-W-Sn-Mo zoned hematite from the IOCG deposit at Olympic Dam, South Australia. Proceedings of the 14th SGA Biennial Meeting, Québec, Canada, August 20-23rd.

FF. Nigel J. Cook, Kathy Ehrig, Cristiana L. Ciobanu, **Liam Courtney-Davies**, Max R. Verdugo-Ihl, Mark Rollog, Danielle S. Schmandt, Nicholas D. Owen, Edeltraud Macmillan, Alkiviadis Kontonikas-Charos, Sasha Krneta, Marija Dmitrijeva, 2018. Why detailed mineralogy is important: understanding evolution of the Olympic Dam iron-oxide-copper-gold system, South Australia. 15th Quadrennial IAGOD Symposium, Salta, Argentina, August 28th - 31st.

GG. Cristiana L. Ciobanu, Max R. Verdugo-Ihl, Ashley Slattery, Nigel J. Cook, Kathy Ehrig, **Liam Courtney-Davies**, 2018. Nanoscale study of silician magnetite from IOCG systems: examples from the Olympic Dam district, South Australia. 15th Quadrennial IAGOD Symposium, Salta, Argentina, August 28th – 31st.

HH. Max R. Verdugo-Ihl, Cristiana L. Ciobanu, Nigel J. Cook, Ashley Slattery, Kathy Ehrig, **Liam Courtney-Davies**, 2018. Metal-bearing nanoparticles in hematite. 15th Quadrennial IAGOD Symposium, Salta, Argentina, August 28th - 31st.

II. William M. Keyser, Cristiana L. Ciobanu, Nigel J. Cook, **Liam Courtney-Davies**, Holly Feltus, Geoff Johnson, Allen Kennedy, Kathy Ehrig, 2018. Geological setting of

BIF ores, Middleback Ranges, South Australia. 15th Quadrennial IAGOD Symposium, Salta, Argentina, August 28th–31st.

JJ. Netting, A.K.O, Wade, B.P., Verdugo-Ihl, M.R., **Courtney-Davies, L**., Ciobanu, C.L., Cook, N.J., Ehrig, K., Slattery, A., Gilbert, S., Neubauer, K., 2019. A Multiplatform approach to unravelling geological problems: a case study from Olympic Dam, South Australia, 2019. 16th European Workshop on Modern Developments and Applications in Microbeam Analysis (EMAS 2019), Norwegian University of Technology and Science, Trondheim, Norway, 19-23 May 2019. Microscopy and Microanalysis 25 (Suppl. 2), 2432-2433.

KK. Max R. Verdugo-Ihl, Cristiana L. Ciobanu, Nigel J. Cook, **Liam Courtney-Davies**, Kathy Ehrig, Ashley Slattery, 2019. Tungsten-bearing nanoparticles in hematite: insights into open system behaviour of mineral geochronometers. TIGeR 2019, Perth, Australia, September 11th-13th.

The final chapter of this thesis consists of a complete reference list of all publications cited within any of the manuscripts, chapters, supplementary and additional material submitted as a component of this thesis.

CHAPTER 1

INTRODUCTION

CHAPTER 1: INTRODUCTION

Iron constitutes 5% of Earth's crust, readily bonding with oxygen to form the iron-oxide minerals hematite (α-Fe_2O_3) and magnetite ($Fe^{2+}Fe^{3+}{}_2O_4$) in most geological environments (Deer et al., 2013). Combinations of magmatic, hydrothermal, detrital and biochemical processes have concentrated these minerals in economic quantities throughout Earth history. The Gawler Craton, South Australia, contains two genetically and temporally distinct types of iron-oxide accumulation: (1) chemically precipitated, banded iron formation (BIF); and (2) magmatic-hydrothermal iron-oxide copper gold (IOCG) systems (Drexel et al., 1993). Such iron-rich deposits contribute a significant value share of the mineral resources in South Australia.

Extensive accumulations of BIF were deposited in the Middleback Ranges, northeastern Eyre Peninsula, in the period straddling the Archean-Paleoproterozoic boundary (Szpunar at al., 2011), and currently represents the major iron-ore producing region in South Australia. The complex evolution from BIF to Fe-ore spans multiple tectonothermal events and hydrothermal fluids over more than ~1 Ga (Keyser et al., 2019). These events are recorded in the textures preserved in iron-oxides, their geochemical signatures and geochronology (Keyser et al., 2018, 2019; Dmitrijeva et al., 2018). Iron-rich (meta)sedimentary rocks of BIF-type affiliation are found throughout the late Paleoproterozoic Wallaroo Group, which can be spatially associated with IOCG systems (Keyser et al., 2017). Superposition between Fe-rich protoliths and IOCG mineralisation is well documented (e.g., Carajás district, Brazil; Grainger et al., 2008), however, evidence for direct genetic links between BIFs and IOCG systems remain tenuous within the Gawler Craton.

The eastern Gawler Craton hosts a ~700 km long belt of temporally and mineralogically correlated Mesoproterozoic IOCG deposits and prospects, collectively termed the 'Olympic

Cu-Au province' (Skirrow et al., 2007; Reid, 2019). This belt hosts the eponymous Olympic Dam IOCG deposit. The timing of Cu-(U)-Au mineralisation across the province is considered broadly coeval with emplacement of the Gawler Silicic Large Igneous Province (Allen et al., 2008) at ~1.6 Ga (e.g. Skirrow et al., 2002; 2007; Reid et al., 2013), however, the tempo and lifespan of mineralisation remains contentious. This is largely due to four factors: (1) the timescales of geological processes in question are often shorter than achievable levels of analytical precision required to resolve them; (2) few minerals precipitating at the conditions of ore formation can homogeneously incorporate radioactive elements and preserve unperturbed isotopic decay-chains throughout geological time and superimposed tectonothermal events; (3) uncertainty regarding which event(s) a given mineral is isotopically recording; and (4) IOCG systems are hosted within at least six temporally and mineralogically distinct lithologies. Such challenges are amplified in Precambrian IOCG *sensu stricto* deposits, in which brecciation, pervasive alteration and geological timescales combine to limit accurate and precise dating.

Although the phenomenon has been known since the work of Oreskes (1990), the first detailed characterisation of U-bearing hematite at Olympic Dam, the largest IOCG deposit in the Gawler Craton, propelled development of this mineral as a potential U-Pb geochronometer (Ciobanu et al., 2013). Although often considered as an archetypal IOCG deposit, Olympic Dam differs from other IOCG deposits in the region, and worldwide, in that the U content is high – sufficiently high for the element to be recovered economically.

More than 90 % of this U is contained within uraninite, coffinite and brannerite (Ehrig et al., 2012), but is commonly measurable in hematite (which makes up ~30 % of modal mineralogy) at minor to trace concentrations , and may reach wt. % concentrations within high-U zones in some zoned hematite grains (Ciobanu et al., 2013; Verdugo-Ihl et al., 2017). A distinct, primary generation of hematite, which typically displays oscillatory (±sectorial)

zoning with respect to U,W, Sn, and Mo (a characteristic signature hereafter referred to as 'granitophile elements'), and variably enriched in REE and HFSE, is ubiquitous within all ore zones and major lithologies found throughout the 6 km-strike and 2 km-deep vertical extent of the Olympic Dam Breccia Complex (Verdugo-Ihl et al., 2017). Such hematite is also recognised within the early, deep 'outer shell' of the deposit, at the contact to granite hosting the breccia complex (Verdugo-Ihl et al., in press).

Although some of the zoned hematite grains record evidence of repeated episodes of reworking, overprinting, brecciation, fluid-mineral reaction and element remobilisation (Ciobanu et al., 2013; Verdugo-Ihl et al., 2017), primary zonation patterns are commonly preserved and the isotopic systems are retained unmodified (Courtney-Davies et al., 2019a). Nanoscale imaging of primary zoned hematite using transmission electron microscopy (TEM) reveals that the measured U and radiogenic Pb are present within the crystal lattice, rather than as discrete micro- to nano- scale inclusions (Ciobanu et al., 2013). The notion that hematite can incorporate U is supported by experimental studies, whereby synthetic hematite was successfully doped with up to several wt.% UO_2 (Duff et al., 2002). The proposed substitution mechanism in U-rich hematite from Olympic Dam (up to 0.013 atoms per formula unit, assuming U^{6+}; Verdugo-Ihl et al., 2017), is based on vacancy-induced crystal-structure modifications (long-range superstructures) following the proposed substitution: $2Fe^{3+} \leftrightarrow Me^{6+} + \square$ (Me: U, W, Mo; Ciobanu et al., 2013, 2018). Likewise, evidence exists for the incorporation of Pb in hematite (e.g., Vu et al., 2010).

Reconnaissance U-Pb dating of zoned hematite from Olympic Dam by laser ablation-inductively coupled plasma-mass spectrometry (LA-ICP-MS) established that ~1590 Ma dates could be obtained (Ciobanu et al., 2013). Such dates were later replicated (e.g., Apukhtina et al., 2017). At this stage, calibration of unknowns involved the use of zircon reference materials, predicated based on comparable U/Pb downhole fractionation trends between the two materials

(Ciobanu et al., 2013). Subsequent studies overseas have tested the applicability of low-U hematite to LA-ICP-MS U-Pb geochronology within other minerals systems (e.g., young gold-porphyries; Zhou et al., 2017). Calibration strategies involved line rastering across grains, minimising matrix sensitivity and down-hole fractionation, however, uncertainties of acquired $^{206}Pb/^{238}U$ weighted average dates were typically high (~10 %). All previous studies nevertheless provide geologically meaningful data within a given context. The accuracy of data cannot, however, be comprehensively assessed and corrected without matrix-matched reference materials.

Identifying natural hematite suitable as a U-Pb reference material, as with any other mineral, is not a trivial process. The search was compounded by the fact that high-U hematite has been reported solely from Olympic Dam, where grain sizes are generally too small to yield sufficient material to support multiple bulk chemical analyses, while retaining enough material for extensive calibration of unknowns and distribution to the wider community. Therefore, development of synthetic reference materials is required, however, synthesis of U/Pb reference materials is generally not perused, due to either exclusion of dopants during crystal growth (e.g. exceptionally low partition coefficient of Pb in zircon), or to a difficulty in homogeneously distributing U-Pb isotopes within synthetic crystals (e.g. Nasdala et al., 2018).

An alternative to microbeam dating methods is 'standardless' bulk chemical techniques, such as isotope dilution – thermal ionisation mass spectrometry (ID-TIMS), capable of generating <0.2 % analytical precision (U/Pb), compared to >2 % uncertainties for LA-ICP-MS (Schoene et al., 2016). However, ID-TIMS is far more time consuming, costly and requires sample volumes that are many orders of magnitude greater than for *in-situ* analyses (e.g., LA-ICP-MS), thus significantly increasing the potential for U/Pb heterogeneity at the grain-scale (Schaltegger et al., 2015).

Accurately constraining the timing of mineralisation requires dateable minerals to form coeval with ore minerals, however linking formation of the two is not always clear-cut. Long-lived or protracted hydrothermal events will inherently dissolve and re-precipitate minerals (e.g., uraninite from Olympic Dam; Macmillan et al., 2016a, b), resetting isotopic systems and/or incorporating common-Pb (e.g., apatite; Chew et al., 2011), while dateable minerals may be absent altogether. Iron-oxides are key minerals for tracking hydrothermal activity associated with BIF and IOCG deposits, because they are the dominant ore- and gangue-minerals, and hence pivotal for understanding deposit evolution. Although Fe-oxides formed during BIF deposition will not represent the timing of ore formation, Fe-oxides can fingerprint upgrading to Fe-ores by superimposed events, allowing dating if U is introduced to the system at a particular stage (Keyser et al., 2019). Within IOCG systems *sensu-stricto*, pervasive metasomatism of host-rocks or earlier alteration-products can form hematite pseudomorphs, facilitating study of the onset and evolution of a hydrothermal system. At Olympic Dam, Fe-metasomatism can be traced from the deposit edges, to the deposit centre, where constituent breccias gradationally increase in intensity of alteration, brecciation and Fe-content (Ehrig et al., 2012; Mauger et al., 2016; Kontonikas-Charos et al., 2017). Although relationships between hematite and Cu-minerals are rarely explicit at Olympic Dam, Cu–(Fe)-sulphides infill hematite breccias, hematite forms overgrowths on Cu-sulphides, and commonly contains inclusions of Cu-(Fe)-sulphides, suggesting that Fe-metasomatism and Cu-mineralisation were synchronous (Ciobanu et al., 2013). Although highly contested, the source of IOCG mineralising fluids has, in part, been attributed to hydrothermal fluids origination from Hiltaba Suite granitoids across the province, through a combination of studies applying geochemical modelling, isotopic fingerprinting, geochronology and mineralogical observations (e.g., Kirchenbaur et al., 2016; Schlegel et al., 2017; Courtney-Davies et al., 2019b; Dmitrijeva et al., 2019).

The application and significance of hematite geochronology in IOCG systems is founded on its utility as a proxy for Cu-(U)-Au mineralisation, the high lattice-bound concentrations of U (and Pb), and its ubiquity throughout Olympic Dam and adjacent satellite prospects (e.g., Acropolis, Wirrda Well; Courtney-Davies et al., 2019c). Hematite geochronology thus represents a game-changer for constraining geochronological frameworks within such deposits, where accurate and high-precision measurements of ore-forming events are either lacking or poorly defined. This is in contrast to other magmatic-hydrothermal ore deposit classes, notably porphyry Cu deposits, in which discrete ore-forming events spanning <100 ka are routinely constrained (e.g., Li et al., 2018).

This thesis aims to address key geochronological questions regarding the formation of the Olympic Dam deposit using a multi-mineral geochronological and geochemical approach. Outstanding research gaps, relevant to both Olympic Dam and the wider Cu-Au province include: (i) constraining the timing between the magmatic and onset of the hydrothermal systems; (ii) the lifespan of mineralising event(s); and (iii) the age of conspicuous Fe-rich protoliths within the deposit. Development of hematite U-Pb reference material unlocks the potential to routinely date all iron-oxide-bearing ore deposits, including U-bearing BIF, which, along with IOCG, have proven notoriously challenging types of deposit to confidently and unambiguously date until now.

1.1. Research objectives and thesis structure

This thesis is a contribution to the research project, 'Trace elements in iron-oxides: deportment, distribution and application in ore genesis, geochronology, exploration and mineral processing'. One broad objective of this overarching project was to ascertain the formation and evolution of IOCG systems in South Australia using both iron-oxide and accessory mineral geochronology, focusing on the development of hematite geochronology

and fabrication of hematite reference materials in order to streamline IOCG and related iron-oxide bearing mineral system geochronology in the future. The datasets and interpretation generated during the course of this study expand upon the current knowledge of IOCG system formation, in turn contributing to a better understanding of regional-scale processes that impact on the Gawler Craton. Nano-scale studies of zircon have shed new light on early, metasomatic processes leading to large magmatic-hydrothermal ore systems, whereby the features imaged can assist in the development of exploration models for 'fertile' granitic intrusions. The successful synthesis and appraisal of a homogeneous matrix-matched, hematite reference material, presented in this thesis, will facilitate widespread, reliable hematite dating.

This main body of this thesis comprises eight chapters (Chapters 2-9), each of which is either published, submitted for peer review, or written as a standalone chapter in the form of a manuscript for future submission. Each chapter represents a publication to be read independently, in which the individual samples and analytical methodologies are explained in detail, or are provided in the appendices compiled as Chapter 11.

Chapter 2 (Courtney-Davies et al., 2016) takes an exploratory look at an analytical method which may circumvent the necessity for matrix-matched hematite reference materials. This involved simultaneous mixing between a U–Pb solution of independently measured composition, and ablated, pure synthetic hematite within a nebuliser chamber, subsequently introduced to an ICP-MS. The mixture of these components formed the basis of a 'standard' analyses. One advantage of this method was the capability to adjust U/Pb values of 'standard' analyses to that of the unknown, particularly significant for low-U BIF samples. Despite the benefits of the method, downhole fractionation quantification and correction remained unconstrained, and is dealt with further in the following chapter. Recommendations for future

studies (e.g. application of line rasters for low U-hematite), was subsequently implemented by Zhou et al. (2017).

Chapter 3 (Courtney-Davies et al., 2019a) presents a large body of zoned hematite geochronological data, acquired via LA-ICP-MS, sensitive high-resolution ion microprobe and ID-TIMS, highlighting a new method for hematite dissolution and bulk chemical analysis. The U-Pb systematics of compositionally and morphologically distinct samples from Olympic Dam are assessed, and their suitability to the different dating methods evaluated. Through pinpointing of U/Pb homogeneous grain domains via LA-ICP-MS isotope mapping, coupled with a new *in-situ* laser ablation grain extraction technique, we demonstrate that up to ~ 0.1 % ID-TIMS precision is achievable, and that in some cases, hematite can retain a near-closed U-Pb system over ~1.6 Ga. The accuracy of acquired microbeam data when compared to ID-TIMS data (all within ~2 %), signals the suitability of hematite to all dating methods, however, data-features such as non-zero age Pb loss, reverse discordance and common Pb are recognised, and treatment strategies for such data are explored and advised.

Subsequent to refinement of hematite dating techniques, **Chapter 4** (Courtney-Davies et al., in review, a) draws upon a high-precision dataset obtained from several locations throughout the Olympic Dam breccia complex, coupled with chemical abrasion-ID-TIMS zircon dates from the deposits host granite, and volcanic breccias. For the first time, a confident temporal 'window' between the magmatic (1593.28 ± 0.28 Ma) and hydrothermal (1591.27 ± 0.89 Ma) systems is defined. Integrating zircon and hematite ages underpins a model involving a single, major mineralising event, hinting at a temporal evolution of zoned hematite within distinct locations and lithologies, ~1 Ma after granite emplacement. Data is presented in the context of generic crustal continuum models for IOCG formation, refuting earlier models of shallow maar-diatreme formation (e.g. Reeve et al., 1990), based upon irreconcilable differences

between the deep emplacement of host granite (Kontonikas-Charos et al., 2017), and timeframe between the magmatic, and activation of the hydrothermal systems.

Discovery of granitophile element-rich zoned hematite outside of Olympic Dam, provides a single, traceable mineral which can be used to compare IOCG genesis in terms of age and hydrothermal fluid signatures at the district scale. In **Chapter 5** (Courtney-Davies et al., 2019c), the Wirrda Well and Acropolis prospects are addressed with respect to Fe-oxide mineralogy and geochronology. The two prospects are distinct from one another, and from Olympic Dam, in terms of host lithologies, iron-oxide mineral associations, intensity of brecciation and grade of Cu-(U)-Au mineralisation. Textures and compositions of zoned hematite vary significantly between the three IOCG systems with different relationships between earlier generations of titaniferous or silician magnetite. A common U-Pb LA-ICP-MS age of ~1590 Ma is nevertheless obtained from both prospects, indistinguishable from zoned hematite at Olympic Dam. The hematite U-Pb mineral geochronometer is demonstrated to be radio-isotopically reliable within both magnetite- and hematite-dominant IOCG systems displaying different stages of evolution, and further relates formation of the Olympic Cu-Au province to a common fluid source and ore forming event.

Chapter 6 (Courtney-Davies et al., in review, b) switches attention to magnetite, in this case, a conspicuous coarse-grained generation, characterised by high U-content, siliceous chemistry and zoning textures, that is found within drillholes intersecting the early, deep 'outer shell' at Olympic Dam. Dating of this magnetite generation via LA-ICP-MS using both zircon reference materials and the 'mixed U-Pb solution standard' method during separate analytical session generated reproducible dates at ~1760 Ma, the first documented occurrence of a pre-1.6 Ga protolith within the deposit. This older, Fe-rich crustal material is likely sourced from the ~1.76-1.74 Ga (meta)sedimentary Wallaroo Group, host to Fe-rich horizons across the

Gawler Craton. A generation of granitoid rocks, which intruded bedrock at ~1750 Ma are present ~30 km NE of Olympic Dam, and likely exsolved hydrothermal fluids, enriching pre-existing magnetite-bearing protoliths in U. Such material was mechanically incorporated into the 'outer shell' at Olympic Dam some ~150 Ma later, during granite uplift along faults. The coincidence between Fe-rich horizons/BIF and ~1750 Ma granitoids may have provided Olympic Dam with an additional source of both Fe and U and additionally gives a new genetic link between BIF-type lithologies and IOCG mineralisation in the region.

A multi-mineral approach is required to fingerprint the genesis of ore deposits at different stages of evolution. **Chapter 7** (Courtney-Davies et al., 2019b) details trace element chemistry and micro- to nano- scale features of magmatic zircon within both mineralised and unmineralised granitoids from the Olympic Cu-Au Province and adjacent Eyre Peninsula. Electron probe microanalysis, LA-ICP-MS, high-angle annular dark-field scanning transmission electron microscopy (HAADF-STEM) imaging, and energy-dispersive X-ray spectrometry STEM mapping/spot analysis were combined to identify and classify superimposed textures and chemistries, formed during early Fe-Cl-metasomatism, immediately prior to ore deposition. A major finding of this research was the observation of crystal zones within zircon that are enriched in non-formulae elements, notably Fe and Cl, and host to chloro–hydroxy–zircon nanoprecipitates. These features are interpreted as a direct record of fluid interaction during the magmatic-hydrothermal transition shortly after granite emplacement and well prior to alteration mediated by alpha-decay damage. Such features markedly increase in abundance in zircons from granites hosting IOCG deposits and prospects, and thus represent a new, potentially valuable pathfinder for the location of fertile granites hosting IOCG mineralisation.

In order to accurately date iron-oxides routinely via microbeam methods, suitable matrix-matched reference materials are required. **Chapter 8** (Courtney-Davies et al., 2019d) presents a novel method for fabrication of U-Pb doped synthetic hematite. Hydrated ferric oxide absorbed U and Pb nitrates from a doped solution, which was followed by drying and heating to the material to 700 °C, converting doped hydrated ferric oxide to 'chips' of α-Fe_2O_3, as confirmed by X-ray powder diffraction. Consistent concentrations and ratios of U/Pb were measured inter- and intra-chip by LA-ICP-MS spot analysis and isotope mapping. The material represents a potential reference material for hematite U-Pb geochronology but still required high-precision U-Pb analysis.

Following on from the successful fabrication, an appraisal and implementation of the potential synthetic hematite U-Pb reference material is presented in **Chapter 9**. Four chips were micro-sampled for ID-TIMS analysis via laser ablation-extraction, returning high-precision, reproducible data across all chips. Averaged reference values measured by ID-TIMS for $^{206}Pb/^{238}U$, $^{207}Pb/^{235}U$ and $^{207}Pb/^{206}Pb$ were assigned to the reference material within data reduction software packages. LA-ICP-MS spot analyses were collected adjacent to Olympic Dam zoned hematite grain domains, independently dated by ID-TIMS, providing a baseline to assess data accuracy between microbeam data calibrated using zircon and hematite reference material. In all cases, the hematite reference material calibrated data generates marginally more accurate $^{207}Pb/^{206}Pb$ dates when compared to zircon. Hematite reference material calibrated data plotted on a Wetherill diagram is however considerably more concordant, accurate and higher precision (upper intercept) than zircon-calibrated analyses. This is noteworthy, as intercepts are often the most suitable form of date used in hematite geochronology, particularly for samples of BIF derivation, where Pb loss and common Pb-components can be substantial, and concentrations of U are typically low.

A summary of the key findings and implications of this research are provided in **Chapter 10**. This chapter also identifies a number of open questions and areas for potential future investigation. Additional material, including supplementary materials associated with **Chapters 2-9**, co-authored publications and conference contributions are compiled in **Chapter 11**. A complete reference list for all chapters is provided in **Chapter 12**.

1.2 References

Allen, S., McPhie, J., Ferris, G., Simpson, C., 2008. Evolution and architecture of a large felsic igneous province in western Laurentia: the 1.6 Ga Gawler Range Volcanics, South Australia. Journal of Volcanology and Geothermal Research 172, 132-147.

Apukhtina, O.B., Kamenetsky, V.S., Ehrig, K., Kamenetsky, M.B., Maas, R., Thompson, J., McPhie, J., Ciobanu, C.L., Cook, N.J., 2017. Early, deep magnetite-fluorapatite mineralization at the Olympic Dam Cu-U-Au-Ag deposit, South Australia. Economic Geology 112, 1531–1542.

Chew, P.J., Sylvester, M.N., Tubrett, M.N., 2011. U-Pb and Th-Pb dating of apatite by LAICPMS. Chemical Geology 280, 200–216.

Ciobanu, C.L., Wade, B.P., Cook, N.J., Mumm, A.S. Giles, D., 2013. Uranium-bearing hematite from the Olympic Dam Cu–U–Au deposit, South Australia: A geochemical tracer and reconnaissance Pb–Pb geochronometer. Precambrian Research 238, 129-147.

Ciobanu, C.L., Slattery, A., Verdugo-Ihl, M., Courtney-Davies, L., Cook, N.J., Ehrig, K., 2018. Crystal structural modifications in U-rich, oscillatory-zoned hematite. Abstract, Goldschmidt Conference, Boston, MA, USA, 12-17 August 2018.

Courtney-Davies, L., Zhu, Z., Ciobanu, C.L., Wade, B.P., Cook, N.J., Ehrig, K., Cabral, A.R., Kennedy, A., 2016. Matrix-matched iron-oxide laser ablation ICP-MS U-Pb geochronology using mixed solution standards: Minerals 6, 85.

Courtney-Davies, L., Tapster, S.R., Ciobanu, C.L., Cook, N.J., Verdugo-Ihl, M.R., Ehrig, K.J., Kennedy, A.K., Gilbert, S.E., Condon, D.J., Wade, B.P., 2019a. A multi-technique evaluation of hydrothermal hematite U-Pb isotope systematics: Implications for ore deposit geochronology. Chemical Geology 513, 54-72.

Courtney-Davies, L., Ciobanu, C.L., Verdugo-Ihl, M.R., Slattery, A., Cook, N.J., Dmitrijeva, M., Keyser, W., Wade, B.P., Dominick, U.I., Ehrig, K., Xu, J., Kontonikas-Charos, A., 2019b, Zircon at the nanoscale records metasomatic processes leading to large magmatic-hydrothermal ore deposits: Minerals 9, 364, doi:10.3390/min9060364.

Courtney-Davies, L., Ciobanu, C.L., Verdugo-Ihl, M.R., Dmitrijeva, M., Cook, N.J., Ehrig, K., Wade, B.P., 2019c. Hematite geochemistry and geochronology resolve genetic and temporal links among iron-oxide copper gold systems, Olympic Dam district, South Australia. Precambrian Research 335, 105480.

Courtney-Davies, L., Ciobanu, C.L., Richardson, M.W., Prosser, N., Verdugo-Ihl MR, Wade, B.P., Gilbert, S.E., Ehrig, K., Cook., N.J., 2019d. Synthesis of U-Pb doped hematite using a hydrated ferric oxide approach. Journal of Crystal Growth. 513, 48-57.

Courtney-Davies, L., Ciobanu, C.L., Tapster, S.R., Cook, N.J., Ehrig, K., Crowley, J.L., Verdugo-Ihl, M.R., Condon, D.J., in review, a. Opening the Magmatic-Hydrothermal Window: High-Resolution Geochronology of the Olympic Dam Iron Oxide-Cu-U-Au-Ag Deposit, South Australia. Economic Geology.

Courtney-Davies, L., Ciobanu, C.L., Verdugo-Ihl, M.R., Cook, N.J., Ehrig, K., Benjamin P. Wade, Z.-Y. Zhu., in review, b. ~1760 Ma magnetite-bearing protoliths in the Olympic Dam deposit, South Australia: Implications for ore genesis and regional metallogeny. Ore Geology Reviews.

Deer, W.A., Howie, R.A., Zussman, J., 2013. An Introduction to the Rock-Forming Minerals. Mineralogical Society of Great Britain and Ireland. https://doi.org/10.1180/DHZ.

Dmitrijeva, M., Metcalfe, A.V., Ciobanu, C.L., Cook, N.J., Frenzel, M., Keyser, W.M., Johnson, G., Ehrig, K., 2018. Discrimination and variance structure of trace element signatures in hematite: a case study of BIF-mineralization from the Middleback Ranges, South Australia. Mathematical Geosciences 50, 381-415.

Dmitrijeva, M., Ciobanu, C.L., Ehrig, K., Cook, N.J., Metcalfe, A., Verdugo-Ihl, M.R., and McPhie, J., 2019, Defining IOCG signatures through compositional data analysis: A case study of lithogeochemical zoning from the Olympic Dam deposit, South Australia: Ore Geology Reviews 105, 86–101.

Drexel, J.F., Preiss, W.V., Parker, A.J., 1993. The Geology of South Australia. Vol. 1, the Precambrian. Geological Survey of South Australia Bulletin 54.

Duff, M.C., Coughlin, J.U., Hunter, D.B., 2002. Uranium co-precipitation with iron oxide minerals. Geochimica et Cosmochimica Acta 66, 3533–3547.

Ehrig, K., McPhie, J., Kamenetsky, V., 2012, Geology and mineralogical zonation of the Olympic Dam iron oxide Cu-U-Au-Ag deposit, South Australia: Society of Economic Geologists, Special Publication 16, 237-268.

Grainger, C.J., Groves, D.I., Tallarico, F.H.B., Fletcher, I.R., 2008. Metallogenesis of the Carajás mineral province, southern amazon craton, Brazil: Varying styles of Archean through Paleoproterozoic to Neoproterozoic base and precious-metal mineralisation. Ore Geology Reviews 33, 451–489.

Groves, D.I., Bierlein, F.P., Meinert, L.D., Hitzman, M.W., 2010. Iron oxide copper-gold (IOCG) deposits through Earth history: Implications for origin, lithospheric setting, and distinction from other epigenetic iron oxide deposits: Economic Geology 105, 641–654.

Keyser, W.M., Ciobanu, C.L., Cook, N.J., Courtney-Davies, L., Ehrig, K., Gilbert, S., McPhie, J., 2017. Links between sedimentary protoliths and IOCG-skarn alteration, Island Dam, South Australia, Extended abstract, 14th Biennial SGA Conference, Québec, Canada, 3, 935-938.

Keyser, W.M., Ciobanu, C.L., Cook, N.J., Johnson, G., Feltus, F., Johnson, S., Dmitrijeva, M., Ehrig, K., Nguyen, P., 2018. Petrography and trace element signatures of iron-oxides in deposits from the Middleback Ranges, South Australia: from banded iron formation to ore. Ore Geology Reviews 93, 337-360.

Keyser, W., Ciobanu, C.L., Cook, N.J., Johnson, G., Dmitrijeva, M., Courtney-Davies, L., Feltus, H., Gilbert, S., Johnson, G., Ehrig, K., 2019. Iron-oxides constrain BIF evolution in terranes with protracted geological histories: the Iron Count prospect, Middleback Ranges, South Australia. Lithos 324-325, 20-38.

Kirchenbaur, M., Maas, R., Ehrig, K., Kamenetsky, V.S., Strub, E., Ballhaus, C., Münker, C., 2016, Uranium and Sm isotope studies of the supergiant Olympic Dam Cu–Au–U–Ag deposit, South Australia: Geochimica et Cosmochimica Acta 180, 15–32.

Kontonikas-Charos, A., Ciobanu, C.L., Cook, N.J., Ehrig, K., Krneta, S., and Kamenetsky, V.S., 2017, Feldspar evolution in the Roxby Downs Granite, host to Fe-oxide Cu-Au-(U) mineralisation at Olympic Dam, South Australia: Ore Geology Reviews 80, 838–859.

Li, Y., Selby, D., Condon, D., Tapster, S., 2017, Cyclic Magmatic-Hydrothermal Evolution in Porphyry Systems: High-Precision U-Pb and Re-Os Geochronology Constraints on the Tibetan Qulong Porphyry Cu-Mo Deposit: Economic Geology 112, 1419-1440.

Macmillan, E., Cook, N.J., Ehrig, K., Ciobanu, C.L., Pring, A., 2016a. Uraninite from the Olympic Dam IOCG-U-Ag deposit: linking textural and compositional variation to temporal evolution. American Mineralogist 101, 1295–1320.

Macmillan, E., Ciobanu, C.L., Ehrig, K., Cook, N.J., Pring, A., 2016b. Replacement of uraninite by bornite via coupled dissolution-reprecipitation: evidence from texture and microstructure. Canadian Mineralogist 54, 1369–1383.

Mauger, A.J., Ehrig, K., Kontonikas-Charos, A., Ciobanu, C.L., Cook, N.J., Kamenetsky, V.S., 2016. Alteration at the Olympic Dam IOCG–U deposit: insights into distal to proximal feldspar and phyllosilicate chemistry from infrared reflectance spectroscopy. Australian Journal of Earth Sciences 63, 959-972.

Nasdala, L., Corfu, F., Schoene, B., Tapster, S.R., Wall, C.J., Schmitz, M.D., Ovtcharova, M., Schaltegger, U., Kennedy, A.K., Kronz, A., Reiners, P.W., Yang, Y., Wu, F., Gain, S.E., Griffin, W.L., Szymanowski, D., Chanmuang N.,C., Ende, M., Valley, J.W., Spicuzza, M.J.,

Wanthanachaisaeng, B. Giester, G., 2018. GZ7 and GZ8 – Two Zircon Reference Materials for SIMS U-Pb Geochronology. Geostandards and Geoanalytical Research 42, 431-457.

Oreskes, N., 1990. Uranium content of Olympic Dam hematite: Implications for fluid chemistry and ore depositional mechanisms. Program with Abstracts, 8th Quadrennial IAGOD Conference, Ottawa, Canada, p. A137.

Reeve, J.S., Cross, K.C., Smith, R.N., Oreskes, N., 1990, Olympic Dam copper-uranium-gold-silver deposit. in Hughes, F.E., ed., Geology of the Mineral Deposits of Australia and Papua New Guinea: Australasian Institute of Mining and Metallurgy, Monograph 14, 1009–1035.

Reid, A., 2019. The Olympic Cu-Au Province, Gawler Craton: A Review of the Lithospheric Architecture, Geodynamic Setting, Alteration Systems, Cover Successions and Prospectivity. Minerals 9, 371.

Reid, A., Smith, R.N., Baker, T., Jagodzinski, E.A., Selby, D., Gregory, C.J., Skirrow, R.G., 2013. Re-Os dating of molybdenite within hematite breccias from the Vulcan Cu-Au prospect, Olympic Cu-Au province, South Australia. Economic Geology 108, 883–894.

Schaltegger, U., Schmitt, A.K., Horstwood, M.S.A., 2015. U–Th–Pb zircon geochronology by ID-TIMS, SIMS, and laser ablation ICP-MS: Recipes, interpretations, and opportunities. Chemical Geology 402 89-110.

Schlegel, T.U., Wagner, T., Boyce, A., and Heinrich, C.A., 2017, A magmatic source of hydrothermal sulfur for the Prominent Hill deposit and associated prospects in the Olympic iron oxide copper-gold (IOCG) province of South Australia. Ore Geology Reviews 89, 1058–1090.

Skirrow, R., Bastrakov, E., Davidson, G., Raymond, O., Heithersay, P., 2002. The geological framework, distribution and controls of Fe-oxide Cu-Au mineralisation in the Gawler Craton, South Australia. Part II-alteration and mineralisation. In Porter, T.M. (Ed.), Hydrothermal Iron Oxide Copper-Gold and Related Deposits: A Global Perspective, PGC Publishing, Adelaide, 33-47.

Skirrow, R.G., Bastrakov, E.N., Barovich, K., Fraser, G.L., Creaser, R.A., Fanning, C.M., Raymond, O.L., Davidson, G.J., 2007. Timing of iron oxide Cu-Au-(U) hydrothermal activity and Nd isotope constraints on metal sources in the Gawler Craton, South Australia. Economic Geology 102, 1441-1470.

Szpunar, M., Hand, M., Barovich, K., Schwarz, M., Jagodzinski, E., Belousova, E., 2011. Isotopic and geochemical constraints on the Paleoproterozoic Hutchison Group, southern Australia: Implications for Paleoproterozoic continental reconstructions. Precambrian Research 187, 99-126.

Schoene, B., Condon, D.J., Morgan, L.N., McLean, N., 2013. Precision and Accuracy in Geochronology. Elements 9, 19-24.

Skirrow, R.G., Bastrakov, E.N., Barovich, K., Fraser, G.L., Creaser, R.A., Fanning, C.M., Raymond, O.L., Davidson, G.J., 2007. Timing of iron oxide Cu-Au-(U) hydrothermal activity and Nd isotope constraints on metal sources in the Gawler Craton, South Australia. Economic Geology 102, 1441-1470.

Verdugo-Ihl, M.R., Ciobanu, C.L., Cook, N.J., Ehrig, K.J., Courtney-Davies, L., Gilbert, S., 2017. Textures and U-W-Sn-Mo signatures in hematite from the Olympic Dam Cu-U-Au-Ag deposit, South Australia: Defining the archetype for IOCG deposits. Ore Geology Reviews 91, 173-195.

Verdugo-Ihl, M.R., Ciobanu, C.L., Cook, N.J., Ehrig, K., Courtney-Davies, L., in press. Defining early stages of IOCG systems: Evidence from iron-oxides in the outer shell of the Olympic Dam deposit, South Australia. Mineralium Deposita. http/doi:10.1007/s00126-019-00896-2.

Vu, H.P., Shaw, S., Brinza, L., Benning, L.G., 2010. Crystallization of hematite (α-Fe_2O_3) under alkaline condition: The effects of Pb, Crystal Growth & Design 10, 1544-1551.

Zhou, H., Sun, X., Wu, Z., Liao, J., Fu, Y., Li, D., Hollings, P., Liu, Y., Lin, H., Lin, Z., 2017. Hematite U-Pb geochronometer: insights from monazite and hematite integrated chronology of the Yaoan gold deposit, Southwest China. Economic Geology 112, 2023–2039.

CHAPTER 2

MATRIX-MATCHED IRON-OXIDE LASER ABLATION ICP-MS U–PB GEOCHRONOLOGY USING MIXED SOLUTION STANDARDS

Liam Courtney-Davies [1], Zhiyong Zhu [1,2], Cristiana L. Ciobanu [1], Benjamin P. Wade [3], Nigel J. Cook [1], Kathy Ehrig [4], Alexandre R. Cabral [5] and Allen Kennedy [6]

[1]*School of Chemical Engineering, The University of Adelaide, Adelaide, SA 5005, Australia;*

[2]*State Key Laboratory for Mineral Deposits Research, Department of Earth Sciences, Nanjing University, Nanjing 210093, China*

[3]*Adelaide Microscopy, The University of Adelaide, Adelaide, SA 5005, Australia;*

[4]*BHP Billiton Olympic Dam, Adelaide, SA 5000, Australia; Kathy.J.Ehrig@bhpbilliton.com*

[5]*Lagerstätten und Rohstoffe, Technische Universität Clausthal, Adolph-Roemer-Str. 2A, Clausthal-Zellerfeld D-38678, Germany*

[6]*John de Laeter Centre, Curtin University of Technology, Bentley, WA 6102, Australia;*

Article published in Minerals (2016), 6(3), 85.

Statement of Authorship

Title of Paper	Matrix-Matched Iron-Oxide Laser Ablation ICP-MS U–Pb Geochronology Using Mixed Solution Standards
Publication Status	☑ Published ☐ Accepted for Publication ☐ Submitted for Publication ☐ Unpublished and Unsubmitted w ork w ritten in manuscript style
Publication Details	Courtney-Davies, L., Zhu, Z., Ciobanu, C.L., Wade, B.P., Cook, N.J., Ehrig, K., Cabral, A.R., Kennedy, A., 2016. Matrix-matched iron-oxide laser ablation ICP-MS U-Pb geochronology using mixed solution standards. Minerals 6 (3), 85. https://doi.org/10.3390/min603008.

Principal Author

Name of Principal Author (Candidate)	Liam Courtney-Davies		
Contribution to the Paper	Performed lab work, analytical work, carried out data processing and interpretation, oversaw development of work and wrote the manuscript and oversaw revisions.		
Overall percentage (%)	55		
Certification:	This paper reports on original research I conducted during the period of my Higher Degree by Research candidature and is not subject to any obligations or contractual agreements with a third party that would constrain its inclusion in this thesis. I am the primary author of this paper.		
Signature		Date	29/10/2019

Co-Author Contributions

By signing the Statement of Authorship, each author certifies that:

i. the candidate's stated contribution to the publication is accurate (as detailed above);

ii. permission is granted for the candidate in include the publication in the thesis; and

iii. the sum of all co-author contributions is equal to 100% less the candidate's stated contribution.

Name of Co-Author	Zhiyong Zhu		
Contribution to the Paper	Performed analytical work, carried out data processing and data interpretation, assisted in writing the manuscript and its revision.		
Overall percentage (%)	20		
Signature		Date	29/10/2019

Name of Co-Author	Cristiana L. Ciobanu		
Contribution to the Paper	Helped define direction of research, supervised development of work, assisted with data interpretation and contributed to manuscript preparation.		
Overall percentage (%)	15		
Signature		Date	29 Oct 2019

Name of Co-Author	Benjamin P. Wade		
Contribution to the Paper	Assisted with lab work, data interpretation, and evaluation of manuscript.		
Overall percentage (%)	2		
Signature		Date	~~30/10/2019~~ 29/10/2019

Name of Co-Author	Nigel J. Cook		
Contribution to the Paper	Assisted with analytical instrumentation, data processing and evaluation of manuscript.		
Overall percentage (%)	2		
Signature		Date	29/10/2019

Name of Co-Author	Kathy Ehrig		
Contribution to the Paper	Helped coordinate sample collection and evaluation of manuscript.		
Overall percentage (%)	2		
Signature		Date	29/10/2019

Name of Co-Author	Alexandre R. Cabral		
Contribution to the Paper	Helped define research direction and assisted with evaluation of manuscript.		
Overall percentage (%)	2		
Signature		Date	29/10/2019

Name of Co-Author	Allen Kennedy		
Contribution to the Paper	Assisted with construction of figures and evaluation of manuscript.		
Overall percentage (%)	2		
Signature		Date	29/10/2019

minerals

MDPI

Article

Matrix-Matched Iron-Oxide Laser Ablation ICP-MS U–Pb Geochronology Using Mixed Solution Standards

Liam Courtney-Davies [1,*], Zhiyong Zhu [1,2], Cristiana L. Ciobanu [1], Benjamin P. Wade [3], Nigel J. Cook [1], Kathy Ehrig [4], Alexandre R. Cabral [5] and Allen Kennedy [6]

1 School of Chemical Engineering, The University of Adelaide, Adelaide, SA 5005, Australia; zhiyong.zhu@adelaide.edu.au (Z.Z); cristiana.ciobanu@adelaide.edu.au (C.L.C.); nigel.cook@adelaide.edu.au (N.J.C.)

2 State Key Laboratory for Mineral Deposits Research, Department of Earth Sciences, Nanjing University, Nanjing 210093, China

3 Adelaide Microscopy, The University of Adelaide, Adelaide, SA 5005, Australia; Benjamin.wade@adelaide.edu.au

4 BHP Billiton Olympic Dam, Adelaide, SA 5000, Australia; Kathy.J.Ehrig@bhpbilliton.com

5 Lagerstätten und Rohstoffe, Technische Universität Clausthal, Adolph-Roemer-Str. 2A, Clausthal-Zellerfeld D-38678, Germany; alexandre.cabral@tu-clausthal.de

6 John de Laeter Centre, Curtin University of Technology, Bentley, WA 6102, Australia; A.Kennedy@exchange.curtin.edu.au

* Correspondence: liam.courtney-davies@adelaide.edu.au; Tel.: +61-8-8313-4645

Academic Editor: Antonio Simonetti

Received: 18 May 2016; Accepted: 16 August 2016; Published: 23 August 2016

Abstract: U–Pb dating of the common iron-oxide hematite (α-Fe_2O_3), using laser-ablation inductively-coupled-plasma mass-spectrometry (LA-ICP-MS), provides unparalleled insight into the timing and processes of mineral deposit formation. Until now, the full potential of this method has been negatively impacted by the lack of suitable matrix-matched standards. To achieve matrix-matching, we report an approach in which a U–Pb solution and ablated material from 99.99% synthetic hematite are simultaneously mixed in a nebulizer chamber and introduced to the ICP-MS. The standard solution contains fixed U- and Pb-isotope ratios, calibrated independently, and aspiration of the isotopically homogeneous solution negates the need for a matrix-matched, isotopically homogenous natural iron-oxide standard. An additional advantage of using the solution is that the individual U–Pb concentrations and isotope ratios can be adjusted to approximate that in the unknown, making the method efficient for dating hematite containing low (~10 ppm) to high (>1 wt %) U concentrations. The above-mentioned advantage to this solution method results in reliable datasets, with arguably-better accuracy in measuring U–Pb ratios than using GJ-1 Zircon as the primary standard, which cannot be employed for such low U concentrations. Statistical overlaps between $^{207}Pb/^{206}Pb$ weighted average ages (using GJ-1 Zircon) and U–Pb upper intercept ages (using the U–Pb mixed solution method) of two samples from iron-oxide copper-gold (IOCG) deposits in South Australia demonstrate that, although fractionation associated with a non-matrix matched standard does occur when using GJ-1 Zircon as the primary standard, it does not impact the $^{207}Pb/^{206}Pb$ or upper intercept age. Thus, GJ-1 Zircon can be considered reliable for dating hematite using LA-ICP-MS. Downhole fractionation of $^{206}Pb/^{238}U$ is observed to occur in spot analyses of hematite. The use of rasters in future studies will hopefully minimize this problem, allowing for matrix-matched data. Using the mixed-solution method in this study, we have validated a published hematite Pb–Pb age for Olympic Dam, and provide a new age (1604 $\pm$ 11 Ma) for a second deposit in the same province. These ages are further evidence that the IOCG mineralizing event is tied to large igneous province (LIP) magmatism in the region at ~1.6 Ga.

Keywords: iron-oxide; U–Pb geochronology; matrix-matched standard; LA-ICP-MS

1. Introduction

Laser-ablation inductively-coupled plasma mass-spectrometry (LA-ICP-MS allows the user to rapidly obtain accurate geochronological data [1,2]. The caveat to this is the requirement of certified matrix-matched reference materials, which do not exist for a large number of potentially dateable minerals (unless it can be demonstrated that the effects of using a non-matrix-matched standard are smaller than the propagated errors). This includes the common iron-oxide, hematite (α-Fe_2O_3), which, until now, has only been dated by the U–Pb method using the reference material GJ-1 Zircon [1] as the primary external standard [3]. Analysis of uranium-bearing (up to several wt % U) hematite from Olympic Dam (OD), South Australia, returned dates for hematite mineralization in two samples (1577 $\pm$ 5 and 1590 $\pm$ 8 Ma) [3]. These are in good agreement with U/Pb zircon ages from OD [4,5]. Ciobanu et al. (2013) [3], thus, argued that the utilization of the GJ-1 Zircon standard is sufficiently reliable for exploratory Fe-oxide geochronological applications.

The analytical approach used by Ciobanu et al. (2013) [3] did not employ a matrix-matched standard, and, thus, only $^{207}Pb/^{206}Pb$ dates could be considered reliable due to the relatively low matrix-dependent fractionation effects on Pb–Pb ratios. Accurate U/Pb ages could not be well constrained, as the matrix effects on the measured U/Pb ratios in hematite were largely unknown when standardizing to a non-matrix-matched standard, such as zircon. These matrix effects include phenomena such as laser-induced elemental fractionation, resultant plasma loading and ionization [5–7]. The present study aims at circumventing this problem by using an alternative, mixed solution–solid type of standard for U/Pb dating using LA-ICP-MS. This concept has been tested successfully for U/Pb dating of zircon and baddeleyite [8–10], and non-matrix-matched trace element determination [11,12], and is here applied to dating of U-bearing hematite for the first time. The aims of this study were to: Evaluate the potential of hematite as a U–Pb geochronometer; to assess the effect of "matrix effects" when using a non-matrix matched standard, such as zircon, by comparison with the data of Ciobanu et al. (2013) [3]; to test whether the method gives reliable ages for hematite with low U concentrations; and to provide an "easy-and-ready to use" method for U/Pb dating of hematite.

2. Experimental Methodology

2.1. Instrumentation

Isotope measurements were determined using a Resonetics 193 ArF M-50 Excimer laser ablation system coupled to an Agilent 7700s ICP-MS, housed at Adelaide Microscopy, University of Adelaide. Analysis parameters included a constant repetition rate of 5 Hz, laser fluence of 4.3–9.4 J/cm^2, and a beam diameter set between 18 and 60 µm (spot analyses) depending on the size of the analyzed U-bearing zones within the hematite grains and their U concentrations. Spot analyses were chosen due to the small size of the hematite grains, which do not have large enough areas of high U zonation to use line rastering. Data were collected using time-resolved acquisition in fast peak-jumping mode and calculations were carried out using the data reduction software GLITTER [13]. Isotope ratios are presented uncorrected for common lead, with concordia plots generated using Isoplot/Ex 3.75 [14]. Instrument optimization and calibration was performed using NIST-610 standard glass (National Institute of Standards and Technology, U.S. Department of Commerce). Table 1 provides instrument and analysis parameters.

Table 1. Instrument and analysis parameters.

Laser Ablation System		***ICP-MS***	
Type	ArF Excimer	Type	Agilent 7700
Wavelength	193 nm	Makeup gas	Argon
Repetition Rate	5 Hz	Peltier chamber temperature	2 C
Spot diameter	18–60 µm	Plasma RF power	1550 W
Solution standard	U–Pb	Acquisition mode	TRA
He gas flow	0.55 L·min^{-1}	Detector mode	Dual Range
Laser Fluence	4.3–9.4 J/cm^2	***Dwell Time***	
Solution Nebulization		^{204}Pb	10 ms
Nebulizer	Quartz 250 uL/min	^{206}Pb	50 ms
Ar carrier gas flow	0.5 L·min^{-1}	^{207}Pb	40 ms
Spray chamber	Custom Cyclonic	^{208}Pb	30 ms
		^{238}U	30 ms

2.2. Experimental Procedure

A typical measurement of the "standard" in this experiment comprises aspiration of a liquid, represented by a U–Pb solution with known isotopic ratios in 2% HNO_3, combined with the ablated aerosol of a pure hematite sample, mounted in a 1-inch diameter epoxy block. Mixing was carried out in a spray chamber, in which the ablated hematite aerosol was fed and mixed with the aspirated and nebulized U–Pb solution. Analysis of unknowns comprised mixing of the ablated unknown aerosol with a pure 2% HNO_3 solution to ensure the same liquid plasma loading between the standard and unknown. Between analysis of standards and unknowns, the solution line was washed with aspirated 5% HNO_3 solution. Figure 1 shows the LA-ICP-MS system setup.

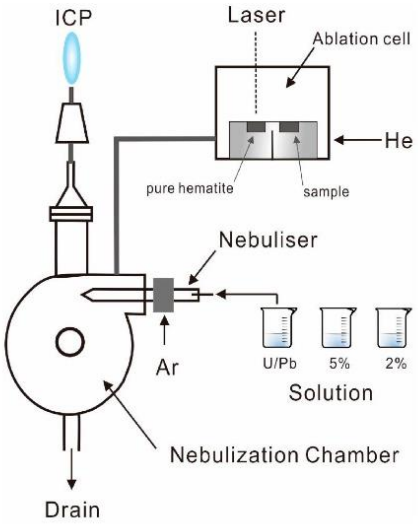


Figure 1. Schematic of the sample introduction system displaying the laser-ablation inductively-coupled plasma-mass spectrometry (LA-ICP-MS) system connected to the U–Pb solution and blank HNO_3 solutions.

2.3. Reagents and Standard Material

The pure hematite analyzed as part of the standard analysis comprised a laboratory-grade synthetic hematite (3–12 mm in size, ≥99.98% trace metals basis; Sigma Aldrich Pty. Ltd., St. Louis, MO, USA). The U–Pb calibration solution was made via mixing individual U and Pb single element standard solutions in 2% HNO_3 diluted with Milli-Q water. The Pb isotope ratios of the resultant solution were measured by MC-ICP-MS at Nanjing University, China (Table S1), using added thallium as an internal isotopic standard [15] to correct for mass-dependent isotopic fractionation. Absolute U/Pb concentrations were calibrated via solution ICP-MS on an Agilent 7500cs instrument at Adelaide Microscopy (Table S2). Depending on the U concentration of the sample being analyzed, a stronger or weaker U–Pb solution was made by dilution with 2% HNO_3. The criteria for using different solution strengths were based on the counts-per-second (CPS) registered by the LA-ICP-MS when optimizing the machine parameters.

2.4. Stability and Precision of the Mass Spectrometer

U–Pb mixed standard solutions avoid the potential heterogeneity problems encountered by solid standards. The measured $^{206}Pb/^{238}U$ ratio of our solution standard is shown in Figure 2A. To ensure the ^{238}U sensitivity of the unknowns is matched to the standard, pre-ablation of the sample was carried out to assess the ^{238}U CPS. The ^{238}U concentration of the standard was then adjusted appropriately. In our experiment, two concentrations of U–Pb solution (1 and 12 ppb) were employed. The 12-ppb U–Pb mixed solution was used for hematite containing hundreds of ppm U, and the 1-ppb solution was used to calibrate samples that were lower in U (tens of ppm). Each analytical run of 15 unknowns was bracketed by two solution standards.

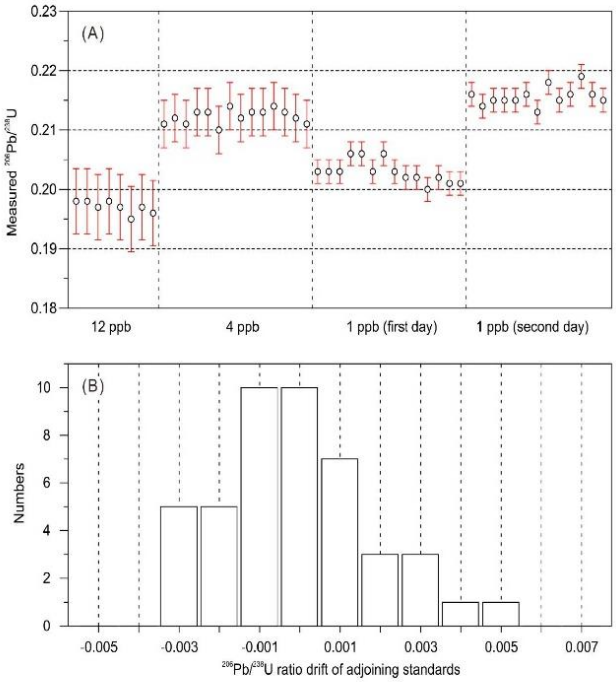


Figure 2. (**A**) Measured $^{206}Pb/^{238}U$ ratios of solution standards with different concentrations; (**B**) $^{206}Pb/^{238}U$ drifts of adjoining standards. The error bars represent 1 sigma standard error.

The total integration time was 60 s, which incorporated 25 s for background collection followed by 35 s for laser firing. This was followed by 40 s for washing. The measured $^{206}Pb/^{238}U$ drift over the 23-min period of each run sequence is less than ±0.003, which accounts for only 1.5% of the measured ratio (Figure 2B). Although the measured $^{206}Pb/^{238}U$ ratio for the same solution can vary day-to-day, the variation within one run is minimal (Figure 2B), allowing the acquisition of high-precision data. In particular, the stability of the 1-ppb mixing solution was still very efficient, even for especially low U samples. Fifteen spots were analyzed on NIST610, immediately following analysis of OD10-4 using just the solution standard calibration method, which gave a 1σ error for the $^{206}Pb/^{238}U$ age of 3–4 Ma (<1%), testifying to the stability of the measured signals and instrument at the time of analysis.

2.5. Calibration Process

The $^{207}Pb/^{206}Pb$ ratio (0.866312) of the solution standard was measured using MC-ICP-MS with uncertainties of ~0.12%. The $^{206}Pb/^{238}U$ ratios (0.286356) were calculated from Q-ICP-MS U/Pb concentration data and MC-ICP-MS Pb isotope ratios; this is expanded upon in Supplementary Text File S1. We assume that the uncertainties of ^{206}Pb and ^{238}U concentrations are 1%; and the propagated 1 sigma deviation of $^{206}Pb/^{238}U$ was 1.4%. The uncertainties are then defined in GLITTER (GEMOC Laser ICPMS Total Trace Element Reduction software, Macquarie University, Sydney, Australia) to calibrate the samples. The two ratios from the solution standard were used to calibrate the $^{207}Pb/^{206}Pb$ and the $^{206}Pb/^{238}U$ ratios of the samples respectively, while the final $^{207}Pb/^{235}U$ ratios of the samples were calculated from the calibrated $^{207}Pb/^{206}Pb$ and $^{206}Pb/^{238}U$.

3. Sample Selection

Hematite samples used in this study are from iron-oxide copper gold (IOCG) deposits in South Australia (Figure 3), and an analogous IOCG province, the Carajás mineral province, Brazil. The Australian samples (i.e., OD10-4 from Olympic Dam and PH-93 from a potentially different tectonic setting within the Olympic Cu-Au Province) contain thousands of ppm to a few wt % U, while the Brazilian sample (CUR-002) has orders of magnitude lower U, but is higher in W (hundreds ppm). Prior to LA-ICP-MS analysis, polished blocks were imaged on an FEI Quanta 450 FEG ESEM, using a back-scattered electron detector optimized to reveal the presence of elevated U and grain-scale zonation in hematite. The samples are all compositionally zoned in uranium (Figure 4), and it is such zones that were targeted for dating.

Sample OD10-4 represents a high-grade ore where the high-U hematite is embedded in bornite (Figure 4A). This is one of ten polished blocks prepared from the same hand specimen, petrographically characterized and analyzed by Ciobanu et al. (2013) [3], who obtained a $^{207}Pb/^{206}Pb$ weighted average age of 1577 ± 5 Ma. Sample PH-93 represents hematite breccia cemented with chalcopyrite, and is sourced from an IOCG deposit to the north-nest of Olympic Dam. Although similar in terms of hematite textures to the Olympic Dam material, the high-U zones in PH-93 are coarser (Figure 4B). This sample was also analyzed in this study using GJ-1 Zircon as the primary standard to allow comparison between the two methods. Sample CUR-002 was dated to test the reliability of the mixed solution method with a provincially non-related sample. The sample is from a vein filled with aggregates of coarse lamellar hematite, displaying similar but weaker zoning compared to the two Australian specimens (Figure 4C,D). The vein from which sample CUR-002 was taken crosscuts quartzite and is located some 30 km east north-east of the 1.88 Ga Cigano granite [16], in the ridge that marks the Cinzento strike-slip system of the Carajás mineral province [17].

In addition to providing direct comparison between analysis using GJ-1 Zircon and mixed solution standards, the samples were chosen to assess the age obtained for high-grade ore at OD, to provide a hematite age for associated mineralization elsewhere in the Olympic Cu-Au Province, and to test the application of the method on low-U samples. Ultimately, the choice of samples was designed to illustrate how the method introduced here might find broad application throughout the IOCG province in South Australia and elsewhere.

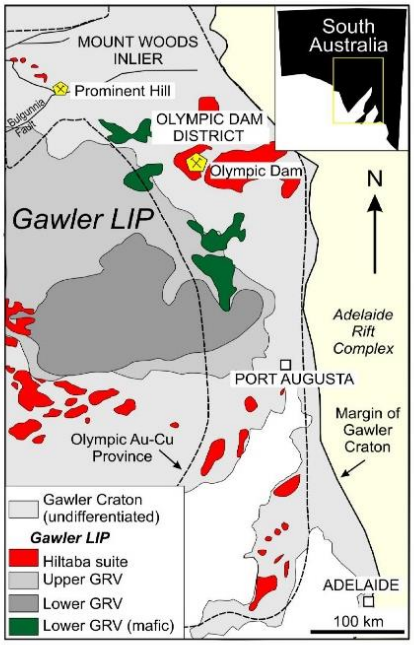


Figure 3. Sketch map showing the location of the Olympic Cu-Au Province within South Australia, as well as exposed Gawler Range Volcanics and Hiltaba Suite intrusive rocks.

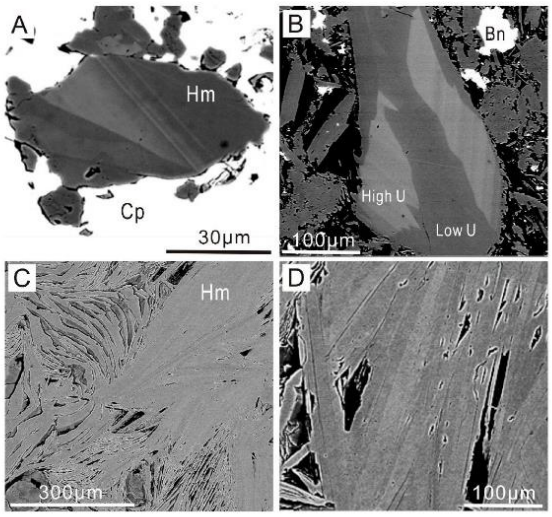


Figure 4. Back scattered electron images of U-bearing zoned hematite. (**A**,**B**) Hematite (Hm) displaying oscillatory and sectorial zoning expressed as high-U from Olympic Dam (**A**) and a second sample from another IOCG deposit in the Olympic Cu-Au Province (**B**) note differences in size, and coarser zones for the latter. Additionally note association with sulphides, bornite (Bn) and chalcopyrite (Cp), respectively; (**C**,**D**) low-U hematite from Carajás (CUR-002) showing aggregates of hematite with zones containing U and W in the centers of the lamellae (brighter on BSE images).

4. U/Pb Geochronology Results

Sample OD10-4 (Table 2, Figure 5) produced a U/Pb upper intercept date of 1595 ± 18 Ma and was anchored to a lower intercept of 0 ± 40 Ma using an 18 µm spot size and a 12-ppb mixed solution. None of the spots analyzed in this sample have been excluded from the processed dataset. The data ranges from 100% to 112% concordance, with the discordancy either due to recent Pb loss, or, more likely, due to laser induced elemental fractionation; points plotting above the concordia relate to U loss. Although the error is relatively high, the low amount of points analyzed and inclusion of all points attests to the reliability of the method to generate coherent ages.

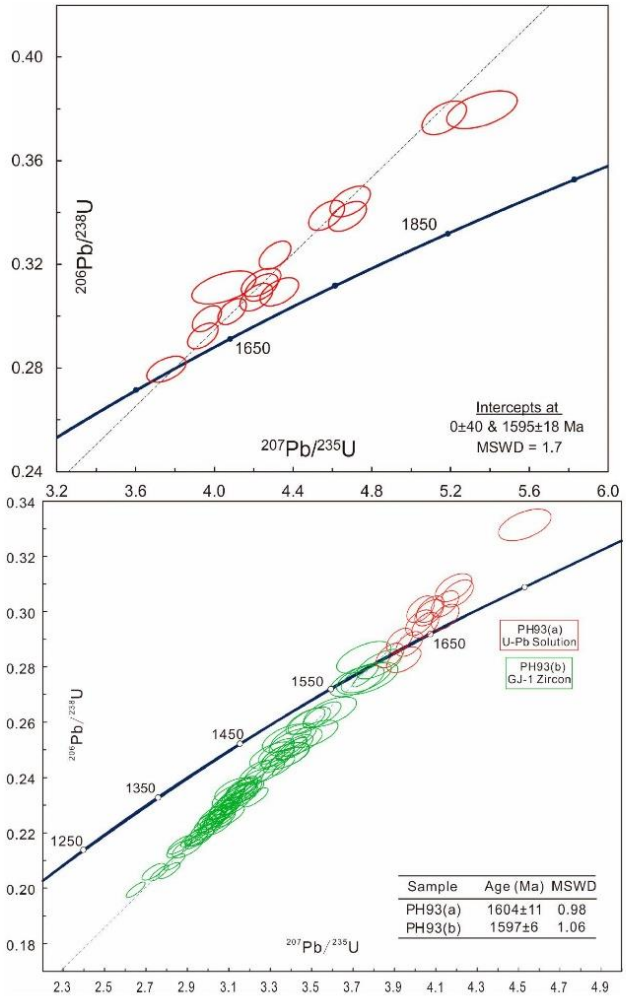


Figure 5. Conventional concordia plots displaying analyzed grains of high-U hematite from the Olympic Province. The first concordia displays sample OD10-4 analyzed through the U–Pb solution method. The second concordia overlays data from sample PH93 collected through the U–Pb solution method (a) and GJ-1 Zircon (b). Data are given in Tables 2–4. Note, all U–Pb solution data plots on or above concordia, whereas all GJ-1 Zircon data plots on or below concordia.

Table 2. Geochronological data for zoned hematite (sample OD10-4) using mixed-solution method.

Spot No.	$^{207}Pb/^{206}Pb$	1σ	$^{206}Pb/^{238}U$	1σ	$^{207}Pb/^{235}U$	1σ	$^{207}Pb/^{206}Pb$	1σ	$^{206}Pb/^{238}U$	1σ	$^{207}Pb/^{235}U$	1σ	Concordancy (%)	^{204}Pb	^{206}Pb	^{207}Pb	^{208}Pb	^{238}U	$^{204}Pb/^{207}Pb$	Inc/Exc
1	0.0975	0.0019	0.2795	0.0033	3.7565	0.0662	1577	35	1589	17	1584	16	100	5	33,155	3283	137	171,602	0.0015	Inc
2	0.0978	0.0013	0.2923	0.0033	3.9418	0.0510	1582	24	1653	17	1622	12	102	3	76,344	7580	91	377,715	0.0004	Inc
3	0.0966	0.0012	0.3235	0.0036	4.3083	0.0533	1560	23	1807	18	1695	11	107	0	91,744	8999	52	410,380	0.0000	Inc
4	0.0944	0.0029	0.3111	0.0042	4.0485	0.1076	1516	56	1746	21	1644	24	106	14	12,125	1161	176	56,402	0.0121	Inc
5	0.0961	0.0012	0.2990	0.0033	3.9618	0.0489	1550	23	1686	17	1626	11	104	17	98,322	9589	119	475,862	0.0018	Inc
6	0.1002	0.0014	0.3385	0.0038	4.6762	0.0635	1628	25	1879	19	1763	13	107	0	57,251	5819	169	244,735	0.0000	Inc
7	0.1024	0.0025	0.3796	0.0048	5.3595	0.1186	1668	45	2075	23	1878	21	110	0	10,321	1072	185	39,352	0.0000	Inc
8	0.0988	0.0013	0.3111	0.0035	4.2398	0.0554	1602	24	1746	18	1682	12	104	0	68,567	6873	202	319,022	0.0000	Inc
9	0.0995	0.0013	0.3073	0.0035	4.2137	0.0550	1614	24	1727	18	1677	12	103	5	62,854	6338	539	296,105	0.0008	Inc
10	0.0982	0.0016	0.3130	0.0036	4.2370	0.0666	1590	31	1755	18	1681	14	104	3	31,642	3148	243	146,337	0.0010	Inc
11	0.0983	0.0011	0.3017	0.0033	4.0906	0.0478	1593	21	1700	17	1652	11	103	7	205,525	20,481	174	986,231	0.0003	Inc
12	0.0988	0.0015	0.3442	0.0039	4.6900	0.0679	1602	28	1907	20	1765	14	108	11	44,410	4447	305	186,834	0.0025	Inc
13	0.0996	0.0015	0.3765	0.0043	5.1679	0.0747	1616	28	2060	21	1847	14	112	0	42,844	4321	79	164,804	0.0000	Inc
14	0.1015	0.0016	0.3093	0.0036	4.3303	0.0647	1652	29	1737	18	1699	14	102	0	30,706	3158	229	143,785	0.0000	Inc
15	0.0978	0.0013	0.3389	0.0038	4.5702	0.0602	1583	25	1881	19	1744	12	108	23	51,642	5115	1491	220,769	0.0045	Inc

Table 3. Geochronological data for zoned hematite (sample PH-93) using mixed-solution method.

Spot No.	$^{207}Pb/^{206}Pb$	1σ	$^{206}Pb/^{238}U$	1σ	$^{207}Pb/^{235}U$	1σ	$^{207}Pb/^{206}Pb$	1σ	$^{206}Pb/^{238}U$	1σ	$^{207}Pb/^{235}U$	1σ	Concordancy (%)	^{204}Pb	^{206}Pb	^{207}Pb	^{208}Pb	^{238}U	$^{204}Pb/^{207}Pb$	Inc/Exc
1	0.0969	0.0011	0.3013	0.0032	4.0267	0.0444	1566	20	1698	16	1640	10	104	0	115,237	11,217	2	524,174	0.00000	Inc
2	0.1008	0.0011	0.2984	0.0031	4.1449	0.0446	1638	19	1683	16	1663	10	101	0	183,960	18,611	1	845,094	0.00000	Inc
3	0.0991	0.0010	0.3032	0.0032	4.1430	0.0443	1607	19	1707	16	1663	10	103	6	213,122	21,209	8	963,706	0.00028	Inc
4	0.0994	0.0010	0.2954	0.0031	4.0487	0.0431	1613	19	1669	16	1644	10	101	0	265,097	26,461	5	1,230,702	0.00000	Inc
5	0.0980	0.0011	0.3013	0.0032	4.0726	0.0443	1587	20	1698	16	1649	10	103	0	130,179	12,815	0	592,727	0.00000	Inc
6	0.0984	0.0011	0.2964	0.0031	4.0208	0.0443	1594	20	1673	16	1638	10	102	6	141,507	13,980	4	655,082	0.00043	Inc
7	0.0998	0.0011	0.2885	0.0030	3.9717	0.0427	1621	19	1634	16	1628	10	100	0	167,315	16,772	0	795,856	0.00000	Inc
8	0.0982	0.0015	0.3092	0.0034	4.1860	0.0581	1590	27	1737	17	1671	13	104	9	19,282	1900	4	85,593	0.00474	Inc
9	0.0982	0.0010	0.2898	0.0030	3.9241	0.0417	1590	19	1641	16	1619	10	101	0	326,254	32,167	18	1,545,714	0.00000	Inc
10	0.0990	0.0011	0.2843	0.0030	3.8787	0.0443	1605	21	1613	15	1609	10	100	13	134,769	13,391	2	651,199	0.00097	Inc
11	0.0983	0.0011	0.3000	0.0032	4.0680	0.0463	1593	21	1691	16	1648	10	103	6	133,301	13,161	0	610,394	0.00046	Inc
12	0.0993	0.0012	0.3070	0.0033	4.2042	0.0508	1611	23	1726	17	1675	11	103	11	107,235	10,692	21	479,948	0.00103	Inc
13	0.0989	0.0020	0.3322	0.0038	4.5293	0.0839	1604	38	1849	19	1736	17	106	0	20,203	2006	6	83,611	0.00000	Inc
14	0.1012	0.0015	0.2828	0.0031	3.9446	0.0549	1646	27	1605	16	1623	13	99	6	35,223	3578	19	171,296	0.00168	Inc

Table 4. Geochronological data for zoned hematite (sample PH-93) using GJ-1 Zircon as standard, U units are in net integrated counts/s.

Spot No.	$^{207}Pb/^{206}Pb$	1σ	$^{206}Pb/^{238}U$	1σ	$^{207}Pb/^{235}U$	1σ	$^{207}Pb/^{206}Pb$	1σ	$^{206}Pb/^{238}U$	1σ	$^{207}Pb/^{235}U$	1σ	Concordancy (%)	^{204}Pb	^{206}Pb	^{207}Pb	^{208}Pb	^{238}U	$^{204}Pb/^{207}Pb$	Inc/Exc	Notes
1	0.0974	0.0016	0.2491	0.0030	3.3457	0.0563	1575.6	31	1434	15	1492	13	91	0	358,124	35,083	0	1,571,490	0.0000	Inc	
2	0.0983	0.0015	0.2288	0.0025	3.1016	0.0457	1592.9	28	1328	13	1433	11	83	34	1,679,299	165,047	57	7,631,865	0.0002	Inc	
3	0.0993	0.0017	0.2507	0.0030	3.4310	0.0585	1611.0	31	1442	15	1512	13	90	47	4,388,089	436,897	1904	19,018,996	0.0001	Inc	
4	0.0991	0.0012	0.2761	0.0025	3.7704	0.0405	1606.6	22	1572	13	1587	9	98	26	641,549	63,493	119	2,066,412	0.0004	Inc	
5	0.0994	0.0015	0.2301	0.0026	3.1542	0.0462	1613.5	27	1335	13	1446	11	83	15	3,612,039	359,811	311	16,437,574	0.0000	Inc	
6	0.0977	0.0016	0.2363	0.0026	3.1819	0.0508	1580.2	31	1367	14	1453	12	87	26	626,242	61,641	34	2,629,886	0.0004	Inc	
7	0.0988	0.0016	0.2268	0.0026	3.0890	0.0491	1601.8	29	1318	14	1430	12	82	12	1,057,774	105,597	246	5,011,429	0.0001	Inc	
8	0.0994	0.0015	0.2347	0.0026	3.2155	0.0464	1612.7	27	1359	13	1461	11	84	13	686,076	68,084	317	2,983,425	0.0002	Inc	
9	0.0983	0.0012	0.2317	0.0021	3.1384	0.0343	1591.3	23	1343	11	1442	8	84	36	481,616	47,324	27	1,806,129	0.0008	Inc	
10	0.0991	0.0013	0.2452	0.0025	3.3499	0.0422	1607.3	25	1414	13	1493	10	88	21	897,793	88,769	126	3,483,487	0.0002	Inc	
11	0.0992	0.0014	0.2500	0.0027	3.4188	0.0485	1609.3	27	1438	14	1509	11	89	43	1,236,666	122,600	265	5,024,110	0.0004	Inc	
12	0.0985	0.0014	0.2311	0.0024	3.1389	0.0411	1596.7	25	1340	12	1442	10	84	11	1,373,742	134,877	23	5,764,943	0.0001	Inc	
13	0.0981	0.0016	0.2241	0.0025	3.0302	0.0492	1588.7	31	1303	13	1415	12	82	29	2,621,084	257,454	521	12,092,409	0.0001	Inc	
14	0.0978	0.0017	0.2462	0.0029	3.3195	0.0566	1582.5	32	1419	15	1486	13	90	34	88,275	8696	9	377,705	0.0039	Exc	a
15	0.0993	0.0019	0.2804	0.0035	3.8364	0.0724	1610.5	35	1594	18	1600	15	99	19	397,112	40,162	164	1,571,576	0.0005	Inc	
16	0.0972	0.0018	0.2600	0.0031	3.4847	0.0620	1571.8	34	1490	16	1524	14	95	0	150,286	14,739	45	614,635	0.0000	Inc	
17	0.0991	0.0012	0.2471	0.0023	3.3736	0.0385	1606.3	23	1423	12	1498	9	89	53	1,036,758	102,851	278	3,725,470	0.0005	Inc	
18	0.0983	0.0017	0.2288	0.0026	3.1005	0.0525	1592.3	32	1328	14	1433	13	83	1	2,603,502	256,726	61	11,838,008	0.0000	Inc	
19	0.0991	0.0013	0.2094	0.0019	2.8612	0.0332	1607.3	24	1226	10	1372	9	76	24	990,138	98,206	53	4,177,061	0.0002	Inc	
20	0.0986	0.0019	0.2421	0.0030	3.2912	0.0623	1598.1	36	1398	15	1479	15	87	60	2,274,552	225,982	215	10,140,658	0.0003	Inc	
21	0.0993	0.0014	0.2208	0.0022	3.0221	0.0403	1610.6	26	1286	12	1413	10	80	25	1,242,696	123,093	74	5,310,694	0.0002	Inc	
22	0.0997	0.0013	0.2064	0.0019	2.8359	0.0339	1618.0	24	1210	10	1365	9	75	11	686,332	68,503	27	2,888,126	0.0002	Inc	
23	0.1004	0.0013	0.2224	0.0020	3.0771	0.0370	1630.6	25	1295	11	1427	9	79	16	1,329,609	133,557	307	5,178,292	0.0001	Inc	
24	0.0995	0.0013	0.2182	0.0020	2.9923	0.0361	1614.6	24	1272	11	1406	9	79	14	1,841,114	183,403	135	7,458,065	0.0001	Inc	
25	0.0980	0.0013	0.2217	0.0021	2.9930	0.0365	1585.4	25	1291	11	1406	9	81	15	1,573,534	154,374	80	6,220,637	0.0001	Inc	
26	0.0990	0.0017	0.2254	0.0025	3.0762	0.0500	1605.1	31	1311	13	1427	12	82	9	1,181,199	116,969	18	5,122,869	0.0001	Inc	
27	0.1029	0.0014	0.2496	0.0024	3.5399	0.0445	1676.4	25	1437	12	1536	10	86	13	209,668	21,612	11	745,289	0.0006	Exc	b
28	0.0993	0.0023	0.2475	0.0032	3.3886	0.0761	1610.9	42	1426	17	1502	18	89	19	1,609,400	162,276	10	7,066,943	0.0001	Inc	
29	0.1002	0.0022	0.2555	0.0032	3.5266	0.0743	1626.8	40	1467	17	1533	17	90	47	1,071,385	108,255	60	4,488,290	0.0004	Inc	
30	0.0988	0.0025	0.2525	0.0035	3.4378	0.0833	1601.6	46	1451	18	1513	19	91	14	1,946,683	195,519	68	8,610,834	0.0001	Inc	
31	0.1006	0.0012	0.2438	0.0022	3.3800	0.0359	1634.5	22	1407	11	1500	8	86	32	562,421	56,764	322	2,025,558	0.0006	Inc	
32	0.0989	0.0012	0.2367	0.0022	3.2255	0.0342	1602.5	22	1370	11	1463	8	85	4	960,716	95,346	13	3,570,458	0.0000	Inc	
33	0.0981	0.0012	0.2273	0.0021	3.0728	0.0328	1587.9	22	1320	11	1426	8	83	18	759,636	74,830	179	2,937,270	0.0002	Inc	
34	0.0988	0.0014	0.2231	0.0023	3.0405	0.0422	1602.4	27	1298	12	1418	11	81	10	444,428	44,200	46	1,912,461	0.0002	Inc	
35	0.1158	0.0014	0.2723	0.0026	4.3452	0.0491	1891.7	22	1552	13	1702	9	82	104	87,658	10,202	5406	286,152	0.0102	Exc	c
36	0.1207	0.0015	0.3719	0.0035	6.1896	0.0706	1966.9	22	2038	16	2003	10	104	202	82,870	10,054	8583	199,203	0.0201	Exc	c
37	0.0997	0.0014	0.3164	0.0027	4.3477	0.0536	1618.2	26	1772	13	1703	10	109	39	360,353	36,098	1705	888,545	0.0011	Exc	c
38	0.0976	0.0015	0.2263	0.0025	3.0452	0.0461	1579.1	28	1315	13	1419	12	83	42	2,915,401	287,873	68	13,379,398	0.0001	Inc	
39	0.0973	0.0015	0.2418	0.0027	3.2435	0.0495	1572.9	29	1396	14	1468	12	89	24	1,084,105	106,636	81	4,645,543	0.0002	Inc	
40	0.0970	0.0016	0.2333	0.0027	3.1184	0.0522	1566.7	31	1352	14	1437	13	86	20	1,166,921	115,101	97	5,317,064	0.0002	Inc	
41	0.0977	0.0015	0.2303	0.0026	3.1028	0.0479	1581.0	29	1336	14	1433	12	85	65	3,206,861	317,610	271	14,493,242	0.0002	Inc	
42	0.0985	0.0016	0.2251	0.0026	3.0580	0.0485	1596.1	30	1309	13	1422	12	82	25	3,258,201	325,873	16	15,085,051	0.0001	Inc	
43	0.0979	0.0016	0.2355	0.0027	3.1780	0.0524	1584.1	31	1363	14	1452	13	86	34	2,438,001	242,741	219	10,914,086	0.0001	Inc	
44	0.0984	0.0018	0.2337	0.0027	3.1695	0.0562	1593.6	34	1354	14	1450	14	85	15	993,572	99,903	83	4,366,896	0.0002	Inc	
45	0.0976	0.0019	0.2602	0.0032	3.5019	0.0669	1579.2	36	1491	17	1528	15	94	15	1,812,700	182,136	143	7,664,977	0.0001	Inc	
46	0.1001	0.0013	0.2242	0.0021	3.0947	0.0365	1626.4	24	1304	11	1431	9	80	29	302,131	30,514	202	1,200,461	0.0010	Inc	
47	0.0993	0.0021	0.2756	0.0036	3.7739	0.0789	1611.3	39	1569	18	1587	17	97	34	1,198,725	122,333	61	4,828,669	0.0003	Inc	
48	0.0982	0.0013	0.2188	0.0020	2.9622	0.0352	1589.9	24	1276	11	1398	9	80	23	1,668,670	165,554	22	6,676,239	0.0001	Inc	
49	0.0990	0.0013	0.2173	0.0020	2.9663	0.0355	1605.7	24	1268	11	1399	9	79	7	1,855,607	185,626	43	7,550,038	0.0000	Inc	
50	0.0989	0.0013	0.2221	0.0021	3.0278	0.0366	1603.2	24	1293	11	1415	9	81	20	1,805,412	180,401	10	7,238,337	0.0001	Inc	

Table 4. *Cont.*

Spot No.	$^{207}Pb/^{206}Pb$	1σ	$^{206}Pb/^{238}U$	1σ	$^{207}Pb/^{235}U$	1σ	$^{207}Pb/^{206}Pb$	1σ	$^{206}Pb/^{238}U$	1σ	$^{207}Pb/^{235}U$	1σ	Concordancy (%)	^{204}Pb	^{206}Pb	^{207}Pb	^{208}Pb	^{238}U	$^{204}Pb/^{207}Pb$	Inc/Exc	Notes
51	0.0989	0.0013	0.2260	0.0021	3.0802	0.0376	1602.9	25	1313	11	1428	9	82	22	1,366,690	136,630	12	5,394,476	0.0002	Inc	
52	0.0981	0.0013	0.2263	0.0021	3.0593	0.0377	1587.8	25	1315	11	1423	9	83	13	1,403,969	139,309	31	5,542,698	0.0001	Inc	
53	0.0987	0.0013	0.2182	0.0021	2.9691	0.0371	1599.5	25	1272	11	1400	9	80	22	1,619,038	161,606	44	6,603,413	0.0001	Inc	
54	0.0982	0.0016	0.2343	0.0026	3.1730	0.0511	1590.4	31	1357	14	1451	12	85	11	1,610,758	161,574	29	6,854,733	0.0001	Inc	
55	0.0976	0.0014	0.2250	0.0022	3.0270	0.0387	1578.4	26	1308	11	1415	10	83	18	457,802	45,280	177	1,824,297	0.0004	Inc	
56	0.0970	0.0022	0.2539	0.0034	3.3953	0.0773	1567.3	43	1459	17	1503	18	93	36	4,452,099	443,120	34	19,586,568	0.0001	Inc	
57	0.0972	0.0014	0.2060	0.0020	2.7602	0.0360	1571.2	26	1207	11	1345	10	77	14	959,312	94,476	14	4,158,679	0.0001	Inc	
58	0.0976	0.0014	0.2142	0.0021	2.8808	0.0380	1577.8	26	1251	11	1377	10	79	20	1,450,919	143,445	34	6,049,981	0.0001	Inc	
59	0.0986	0.0014	0.2261	0.0022	3.0741	0.0411	1598.2	27	1314	12	1426	10	82	15	571,895	57,181	82	2,260,135	0.0003	Inc	
60	0.0967	0.0018	0.2356	0.0027	3.1402	0.0582	1560.9	35	1364	14	1443	14	87	19	956,335	95,287	35	4,086,355	0.0002	Inc	
61	0.1052	0.0015	0.2473	0.0027	3.5852	0.0494	1718.0	26	1425	14	1546	11	83	16	254,148	26,922	29	1,046,269	0.0006	Exc	b
62	0.1041	0.0012	0.2105	0.0020	3.0188	0.0328	1697.5	22	1232	10	1412	8	73	6	184,596	19,297	61	782,648	0.0003	Exc	d
63	0.0990	0.0016	0.2346	0.0027	3.1989	0.0513	1605.2	30	1358	14	1457	12	85	4	1,925,329	192,516	55	8,914,925	0.0000	Inc	
64	0.0989	0.0017	0.2147	0.0025	2.9234	0.0484	1602.8	31	1254	13	1388	13	78	9	792,921	79,559	35	3,850,466	0.0001	Inc	
65	0.0976	0.0013	0.2318	0.0025	3.1167	0.0421	1579.0	25	1344	13	1437	10	85	3	1,765,155	173,074	216	7,785,311	0.0000	Inc	
66	0.0997	0.0014	0.2364	0.0026	3.2466	0.0451	1618.1	26	1368	13	1468	11	85	101	1,098,693	110,264	287	4,758,180	0.0009	Exc	c
67	0.0980	0.0014	0.2388	0.0025	3.2225	0.0437	1585.5	26	1380	13	1463	11	87	3	933,955	92,136	299	3,898,835	0.0000	Inc	
68	0.1143	0.0015	0.2331	0.0022	3.6724	0.0423	1868.7	23	1351	11	1565	9	72	17	79,178	9127	999	295,491	0.0019	Exc	a
69	0.0985	0.0012	0.2054	0.0019	2.7877	0.0299	1595.0	22	1204	10	1352	8	76	22	1,439,121	142,793	43	6,191,064	0.0002	Inc	
70	0.0973	0.0012	0.2362	0.0023	3.1664	0.0380	1572.5	23	1367	12	1449	9	87	12	1,175,148	115,582	47	4,740,360	0.0001	Inc	
71	0.0980	0.0013	0.2282	0.0023	3.0837	0.0392	1587.2	25	1325	12	1429	10	83	10	1,054,676	104,286	9	4,487,131	0.0001	Inc	
72	0.0986	0.0017	0.2622	0.0031	3.5627	0.0600	1598.5	31	1501	16	1541	13	94	19	642,983	63,740	115	2,647,484	0.0003	Inc	
73	0.0996	0.0014	0.2243	0.0021	3.0788	0.0396	1616.1	26	1305	11	1427	10	81	23	29,009	2923	59	110,735	0.0079	Exc	a
74	0.0993	0.0022	0.1845	0.0022	2.5247	0.0509	1610.1	40	1092	12	1279	15	68	22	4875	488	19	22,920	0.0451	Exc	a
75	0.0988	0.0016	0.2190	0.0025	2.9815	0.0482	1601.3	30	1277	13	1403	12	80	8	1,979,677	196,785	49	9,503,796	0.0000	Inc	
76	0.0973	0.0012	0.1995	0.0018	2.6761	0.0298	1573.2	23	1173	10	1322	8	75	21	399,834	39,344	144	1,748,439	0.0005	Inc	
77	0.0987	0.0014	0.2291	0.0024	3.1165	0.0439	1599.4	27	1330	13	1437	11	83	0	1,078,987	107,212	210	4,628,883	0.0000	Inc	
78	0.1001	0.0017	0.2259	0.0026	3.1157	0.0518	1626.2	31	1313	14	1437	13	81	16	2,587,938	260,008	462	12,235,322	0.0001	Inc	
79	0.0981	0.0012	0.2321	0.0021	3.1378	0.0353	1587.7	23	1346	11	1442	9	85	14	620,074	61,490	192	2,342,069	0.0002	Inc	
80	0.0992	0.0012	0.2509	0.0023	3.4306	0.0390	1608.8	23	1443	12	1511	9	90	22	455,461	45,655	30	1,607,845	0.0005	Inc	
81	0.0990	0.0013	0.2408	0.0022	3.2874	0.0374	1605.6	23	1391	11	1478	9	87	15	834,712	83,678	19	3,004,981	0.0002	Inc	
82	0.0979	0.0012	0.2179	0.0020	2.9404	0.0336	1583.9	23	1271	11	1392	9	80	20	886,685	87,861	31	3,560,567	0.0002	Inc	
83	0.1012	0.0014	0.2326	0.0023	3.2455	0.0406	1646.0	25	1348	12	1468	10	82	0	476,332	48,675	12	1,865,476	0.0000	Inc	
84	0.0981	0.0013	0.2461	0.0023	3.3268	0.0389	1587.5	24	1418	12	1487	9	89	24	303,591	30,129	12	1,090,386	0.0008	Inc	
85	0.0976	0.0014	0.2102	0.0020	2.8297	0.0361	1579.3	26	1230	11	1363	10	78	14	43,652	4317	7	184,217	0.0032	Exc	a
86	0.0971	0.0014	0.2156	0.0022	2.8871	0.0384	1569.6	26	1259	11	1379	10	80	20	856,148	83,793	50	3,731,805	0.0002	Inc	
87	0.0979	0.0021	0.2542	0.0033	3.4275	0.0721	1584.5	39	1460	17	1511	17	92	23	1,736,866	171,672	17	7,714,529	0.0001	Inc	
88	0.0986	0.0020	0.2328	0.0029	3.1632	0.0640	1598.5	38	1349	15	1448	16	84	21	2,302,525	227,831	27	10,881,509	0.0001	Inc	
89	0.0994	0.0022	0.2475	0.0032	3.3875	0.0744	1612.1	41	1425	16	1502	17	88	5	2,176,639	214,810	625	9,634,952	0.0000	Inc	
90	0.0966	0.0022	0.2829	0.0038	3.7626	0.0857	1558.5	43	1606	19	1585	18	103	22	1,157,825	112,175	4	4,575,889	0.0002	Inc	
91	0.0987	0.0023	0.2744	0.0037	3.7291	0.0859	1599.1	43	1563	19	1578	18	98	35	935,888	93,406	143	3,881,266	0.0004	Inc	
92	0.0993	0.0023	0.2634	0.0036	3.6021	0.0825	1610.9	43	1507	18	1550	18	94	21	273,655	27,538	108	1,172,947	0.0008	Inc	
93	0.0997	0.0026	0.2754	0.0039	3.7788	0.0965	1617.5	48	1568	20	1588	21	97	11	1,194,297	118,707	124	4,905,337	0.0001	Inc	
94	0.0974	0.0021	0.2478	0.0032	3.3247	0.0702	1574.5	40	1427	16	1487	16	91	27	303,011	29,789	168	1,328,016	0.0009	Inc	
95	0.1971	0.0028	0.4371	0.0042	11.8798	0.1518	2802.5	23	2338	19	2595	12	83	548	73,261	14,660	30,042	147,870	0.0374	Exc	c

Notes: a: High $^{204/207}$ ratio; b: Low ^{207}Pb cts.; c: High ^{204}Pb cts.; d: Low ^{238}U cts.

Table 5. Geochronological data for zoned hematite (sample CUR-002) using mixed-solution method.

Spot No.	$^{207}Pb/^{206}Pb$	1σ	$^{206}Pb/^{238}U$	1σ	$^{207}Pb/^{235}U$	1σ	$^{207}Pb/^{206}Pb$	1σ	$^{206}Pb/^{238}U$	1σ	$^{207}Pb/^{235}U$	1σ	Concordancy (%)	^{204}Pb	^{206}Pb	^{207}Pb	^{208}Pb	^{238}U	$^{204}Pb/^{207}Pb$	Inc/Exc	Notes
1	0.5079	0.0237	0.7545	0.0227	52.8353	2.0992	4264	67	3624	88	4047	45	90	15	695	349	889	1225	0.04298	Exc	
2	0.5755	0.0197	0.7510	0.0179	59.5928	1.7618	4447	49	3611	70	4167	34	87	30	687	391	949	1217	0.07673	Exc	
3	0.7995	0.0107	2.7586	0.0389	304.0886	4.4477	4921	19	8535	74	5809	17	147	265	5445	4307	10,609	2625	0.06153	Exc	a
4	0.4339	0.0162	0.4913	0.0108	29.3881	0.9197	4031	55	2576	49	3467	35	74	30	804	345	1025	2177	0.08696	Exc	
5	0.3478	0.0198	0.5110	0.0143	24.5040	1.1702	3697	84	2661	64	3289	53	81	19	373	128	368	972	0.14844	Exc	
6	0.5249	0.0230	0.8138	0.0237	58.8979	2.2419	4313	63	3838	89	4156	44	92	35	369	191	495	604	0.18325	Exc	
7	0.5480	0.0181	0.9369	0.0226	70.7932	2.1173	4376	48	4262	80	4340	34	98	36	778	421	1083	1105	0.08551	Exc	
8	0.3938	0.0187	0.5880	0.0152	31.9254	1.2866	3886	70	2981	65	3548	45	84	19	416	162	429	941	0.11728	Exc	
9	0.6101	0.0222	0.7556	0.0194	63.5579	1.9968	4532	52	3628	75	4232	36	86	37	562	339	870	989	0.10914	Exc	
10	0.4062	0.0120	0.4921	0.0088	27.5560	0.6905	3932	43	2580	40	3403	28	76	8	1217	488	1594	3289	0.01639	Exc	
11	0.5650	0.0162	0.6452	0.0128	50.2601	1.2436	4420	41	3209	53	3997	28	80	38	1003	560	1500	2068	0.06786	Exc	
12	0.4724	0.0195	0.6368	0.0160	41.4764	1.4602	4157	60	3176	66	3807	40	83	13	455	212	545	951	0.06132	Inc	
13	0.4312	0.0239	0.5323	0.0160	31.6463	1.4703	4022	80	2751	70	3539	52	78	8	342	146	367	856	0.05479	Inc	
14	0.4377	0.0196	0.5959	0.0151	35.9663	1.3620	4044	65	3013	64	3666	43	82	13	398	172	430	888	0.07558	Exc	
15	0.5415	0.0091	0.7428	0.0100	55.4611	0.8533	4358	24	3581	39	4096	18	87	141	4477	2394	5560	8013	0.05890	Inc	
16	0.5260	0.0092	0.6350	0.0085	46.0560	0.7213	4316	25	3169	35	3911	18	81	82	2763	1435	3412	5785	0.05714	Exc	
17	0.6219	0.0175	1.0434	0.0234	89.4817	2.3285	4560	40	4607	79	4574	30	101	31	816	507	1251	1028	0.06114	Inc	
18	0.6026	0.0128	0.9530	0.0161	79.1910	1.5412	4514	30	4315	57	4452	22	97	39	1436	865	2136	1982	0.04509	Inc	
19	0.5659	0.0162	0.8979	0.0191	70.0616	1.8009	4423	41	4131	69	4329	30	95	15	953	539	1332	1397	0.02783	Inc	
20	0.4046	0.0134	0.5231	0.0103	29.1756	0.8171	3926	49	2712	46	3459	31	78	22	1246	504	1187	3135	0.04365	Inc	
21	0.4512	0.0169	0.6666	0.0156	41.4718	1.3298	4089	54	3293	64	3807	36	86	36	706	318	837	1393	0.11321	Exc	
22	0.4556	0.0079	0.5857	0.0076	36.7934	0.5699	4104	26	2972	33	3688	18	81	85	3205	1458	3389	7199	0.05830	Inc	
23	0.4090	0.0059	0.5192	0.0060	29.2778	0.3877	3942	22	2696	27	3463	15	78	113	5986	2444	5153	15,168	0.04624	Inc	
24	0.4637	0.0061	0.5731	0.0064	36.6418	0.4497	4130	19	2920	28	3684	14	79	228	8706	4031	9108	19,990	0.05656	Inc	
25	0.4704	0.0062	0.6199	0.0070	40.2129	0.4940	4151	19	3110	29	3776	14	82	207	8683	4077	9156	18,431	0.05077	Inc	
26	0.4395	0.0057	0.5672	0.0063	34.3697	0.4176	4050	19	2896	27	3621	14	80	185	9174	4023	8902	21,285	0.04599	Inc	
27	0.3975	0.0073	0.5024	0.0065	27.5376	0.4435	3900	27	2624	29	3403	18	77	90	4110	1630	3469	10,768	0.05521	Inc	
28	0.4998	0.0075	0.7029	0.0086	48.4418	0.6644	4241	22	3431	34	3961	16	87	110	4804	2395	5666	8995	0.04593	Exc	
29	0.4129	0.0109	0.6638	0.0112	37.7835	0.8694	3957	39	3282	46	3714	26	88	29	1052	433	1124	2086	0.06697	Exc	
30	0.4790	0.0071	0.6511	0.0079	42.9972	0.5849	4178	22	3232	32	3842	15	84	140	4823	2303	5181	9752	0.06079	Inc	
31	0.5911	0.0081	0.8230	0.0098	67.0843	0.8588	4486	20	3871	37	4286	15	90	244	6976	4110	9492	11,159	0.05937	Exc	
32	0.4414	0.0129	0.5088	0.0093	30.9697	0.7696	4056	43	2652	42	3518	28	75	36	1206	530	1572	3121	0.06792	Exc	
33	0.4970	0.0064	0.6938	0.0082	47.5389	0.6026	4232	19	3397	33	3942	14	86	257	9016	4565	10,418	18,473	0.05630	Inc	
34	0.5287	0.0072	0.7490	0.0092	54.5962	0.7268	4323	20	3604	36	4080	15	88	174	7320	3942	9031	13,891	0.04414	Inc	
35	0.5094	0.0085	0.6856	0.0091	48.1500	0.7354	4269	24	3366	37	3955	17	85	36	3437	1783	4112	7126	0.02019	Inc	
36	0.4075	0.0052	0.5208	0.0061	29.2629	0.3683	3937	19	2703	27	3462	14	78	259	11,938	4954	10,495	32,573	0.05228	Inc	
37	0.4097	0.0065	0.5319	0.0068	30.0497	0.4415	3945	23	2750	30	3488	17	79	115	4992	2082	4365	13,336	0.05524	Inc	
38	0.4434	0.0059	0.5706	0.0069	34.8889	0.4528	4063	20	2910	30	3636	15	80	248	10,188	4598	10,140	25,363	0.05394	Inc	
39	0.4438	0.0086	0.6720	0.0098	41.1226	0.7212	4065	28	3313	40	3798	20	87	72	3388	1530	3761	7163	0.04706	Exc	
40	0.3807	0.0051	0.4800	0.0057	25.1978	0.3247	3835	20	2527	26	3316	14	76	208	10,362	4014	8264	30,661	0.05182	Inc	
41	0.5439	0.0077	0.7781	0.0099	58.3534	0.7965	4365	21	3710	38	4146	16	89	211	6461	3575	8414	11,794	0.05902	Inc	
42	0.4461	0.0061	0.5755	0.0070	35.3955	0.4646	4072	20	2930	30	3650	15	80	215	9036	4100	9398	22,298	0.05244	Inc	
43	0.3909	0.0055	0.5083	0.0062	27.3917	0.3676	3874	21	2649	27	3398	15	78	224	9642	3832	8136	26,937	0.05846	Inc	
44	0.4289	0.0064	0.5484	0.0069	32.4251	0.4558	4014	22	2818	30	3563	16	79	161	6409	2795	6425	16,595	0.05760	Inc	
45	0.4938	0.0064	0.6516	0.0078	44.3641	0.5614	4223	19	3235	32	3873	14	84	325	11,453	5750	13,157	24,955	0.05652	Inc	

Table 5. *Cont.*

Spot No.	$^{207}Pb/^{206}Pb$	1σ	$^{206}Pb/^{238}U$	1σ	$^{207}Pb/^{235}U$	1σ	$^{207}Pb/^{206}Pb$	1σ	$^{206}Pb/^{238}U$	1σ	$^{207}Pb/^{235}U$	1σ	Concordancy (%)	^{204}Pb	^{206}Pb	^{207}Pb	^{208}Pb	^{238}U	$^{204}Pb/^{207}Pb$	Inc/Exc	Notes
46	0.4894	0.0065	0.6799	0.0082	45.8711	0.5930	4210	19	3344	33	3907	15	86	279	10,540	5243	11,951	22,008	0.05321	Exc	
47	0.8669	0.0088	0.2860	0.0031	34.1905	0.3687	5036	14	1622	16	3616	12	45	777	13,952	12,306	30,244	69,651	0.06314	Exc	b
48	0.4972	0.0072	0.6791	0.0086	46.5568	0.6617	4233	21	3341	35	3921	16	85	313	9793	4954	11,138	20,592	0.06318	Inc	
49	0.5108	0.0072	0.7374	0.0093	51.9359	0.7105	4273	21	3561	37	4030	16	88	197	7059	3669	8418	13,670	0.05369	Exc	
50	0.5035	0.0068	0.6961	0.0086	48.3154	0.6385	4251	20	3406	34	3958	15	86	233	8236	4219	9461	16,898	0.05523	Inc	
51	0.4086	0.0052	0.5346	0.0063	30.1152	0.3762	3941	19	2761	27	3491	14	79	235	12,837	5336	11,538	34,294	0.04404	Inc	
52	0.4116	0.0064	0.5463	0.0070	31.0008	0.4509	3952	23	2810	30	3519	16	80	131	5235	2192	4653	13,684	0.05976	Inc	
53	0.4689	0.0061	0.6022	0.0072	38.9287	0.4980	4146	19	3039	30	3744	14	81	221	9413	4490	10,079	22,322	0.04922	Inc	
54	0.5037	0.0070	0.6836	0.0085	47.4700	0.6426	4252	20	3358	35	3941	15	85	185	6693	3430	7921	13,983	0.05394	Inc	
55	0.4660	0.0062	0.5967	0.0072	38.3383	0.4977	4137	20	3017	31	3729	15	81	228	9452	4481	10,003	22,618	0.05088	Inc	
56	0.4682	0.0068	0.6175	0.0077	39.8614	0.5506	4144	21	3100	32	3767	16	82	169	6028	2871	6551	13,941	0.05886	Inc	
57	0.5054	0.0081	0.6809	0.0092	47.4539	0.7169	4257	23	3348	37	3940	17	85	128	5101	2623	6203	10,697	0.04880	Inc	
58	0.4745	0.0062	0.6141	0.0074	40.1715	0.5132	4164	19	3086	31	3775	14	82	271	10,198	4922	11,044	23,715	0.05506	Inc	
59	0.4109	0.0053	0.5469	0.0064	30.9847	0.3917	3950	19	2812	28	3519	14	80	207	11,033	4612	9957	28,810	0.04488	Inc	
60	0.4873	0.0063	0.6545	0.0078	43.9712	0.5584	4203	19	3246	32	3865	14	84	276	9859	4887	11,148	21,511	0.05648	Inc	
61	0.5060	0.0064	0.6879	0.0082	47.9915	0.6050	4259	19	3375	33	3952	14	85	312	11,239	5786	13,189	23,331	0.05392	Inc	
62	0.4921	0.0061	0.6461	0.0076	43.8357	0.5412	4218	18	3213	31	3862	14	83	289	12,589	6302	14,254	27,823	0.04586	Inc	
63	0.8656	0.0088	0.2867	0.0031	34.2216	0.3698	5034	14	1625	16	3616	12	45	759	13,760	12,118	29,798	68,525	0.06263	Exc	b

Notes: a: Age ratios too high; b: High ^{204}Pb cts.

5. Discussion

5.1. Advantages of the Mixed-Solution Method and Comparison of Data with GJ-1 Zircon

Dating of the same hematite sample from the Olympic Dam high-grade ore (OD-10), using the GJ-1 Zircon calibration and the U–Pb solution method, produced ages that are statistically identical (1577 ± 5 Ma and 1595 ± 18 Ma). The larger error using the mixed-solution method is most likely attributable to the reduced size of the dataset (all 15 data points obtained are displayed in Figure 5, whereas 116 spots were included, and 97 rejected by Ciobanu et al. (2013)) [3]. Statistical overlaps between $^{207}Pb/^{206}Pb$ weighted average ages (using GJ-1 Zircon) and U/Pb upper intercept ages (using the U–Pb mixed solution method) demonstrate that, although fractionation associated with a non-matrix matched standard does occur when using zircon as the primary standard, it does not impact the $^{207}Pb/^{206}Pb$ or intercept age. GJ-1 Zircon can thus be considered reliable for dating hematite by LA-ICP-MS. The data acquired in this study via the mixed solution method minimises these matrix effects and is considered more reliable since all analyzed points could be included.

The dates obtained for sample PH93 also overlap statistically (1597.2 ± 6.1 Ma vs. 1604 ± 11 Ma when using GJ-1 Zircon and mixed solution standards, respectively). The larger error for the mixed-solution method can again be attributed to the smaller dataset. Of importance here is the fact that, unlike the U–Pb mixed-solution date, the $^{207}Pb/^{206}Pb$ GJ-1 Zircon age features data points that plot very far along the discordia (Figure 5). This clearly highlights the reduction in matrix effects by using the mixed-solution method. Both examples of high-U hematite show that the mixed-solution method used here can give higher quality data from the majority of analyzed points.

An important result of this study is that when using either the GJ-1 Zircon calibration or the solution method for the same samples (high-U, Olympic Cu-Au Province hematite), the majority of data plot either below or above the concordia. In both cases, however, data points that intercept the concordia are also obtained. Data points above concordia can be attributed to an increase in the $^{206}Pb/^{238}U$ ratio due to downhole fractionation effects (Figure 7), a phenomenon also observed in zircon spot analysis by Paton et al. (2010) [19]. In this study, such an effect cannot be corrected for via modeling of the downhole fractionation whilst ablating the standard, as the U and Pb analyzed is not contained within the pure α-Fe_2O_3 matrix ablated, but rather introduced as a solution, and thus the U/Pb ratio remains unaffected by laser induced fractionation during ablation (Figure 7). The results here also place further constraints on the GJ-1 Zircon calibration method, where data points plotting below concordia can be mostly attributed to effects of matrix mismatch (different levels of U fractionation between zircon and hematite). In both cases, however, there is uncertainty about the relative loss or addition of U (open system behavior), which cannot be solved by either method.

By including the low-U concentration Brazilian sample (6 ppm) in our study (CUR-002), we have shown that the solution method has advantages over the GJ-1 Zircon calibration method, and has wide application to analysis of samples containing low concentrations of U (tens of ppm or less). Following this, it is reasonable to assume that samples of comparable U concentration can be dated by this method, opening up considerable scope for very low U age determinations elsewhere.

Although downhole fractionation was likely occurring during analysis of the CUR-002 sample, the large spread through the discordia (Figure 6) is predominantly due to the high amount of common Pb contained within these grains, as attested to by the high ^{204}Pb measured during analysis. Of importance here, is that we have shown how samples of such low U concentration, can only be considered suitable for dating through the U–Pb solution method, which can be tailored to accommodate the significantly lower U concentrations. This is because GJ-1 Zircon and other zircon standards have much higher U concentrations, relative to this sample, or others with similarly low-U concentrations, creating potential matrix effects when employed as the primary standard.

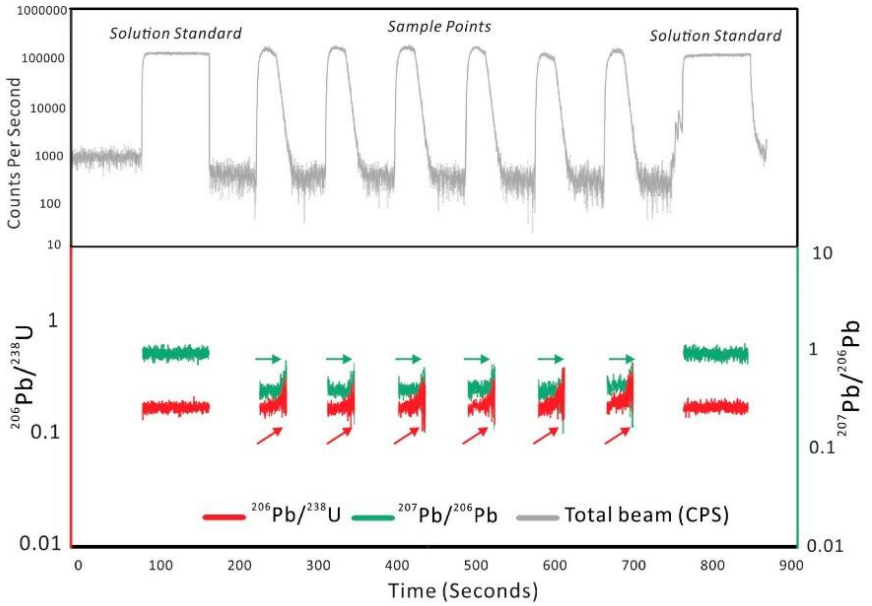


Figure 7. Time-resolved spectra data produced using IOLITE from data obtained from hematite in Olympic Cu-Au Province samples. Note no downhole fractionation within the solution standard, but significant fractionation of the $^{206}Pb/^{238}U$ ratio (red), which increases with time during the duration of the spot analysis. The $^{207}Pb/^{206}Pb$ ratio (green) remains relatively constant throughout analysis, showing the robustness of the $^{207}Pb/^{206}Pb$ ages. This represents a minor disadvantage of the method but may be overcome in the future through linear rastering rather than spot analysis, if the homogeneity of the analyzed grain allows this.

5.2. Geologic Meaning of the Hematite Ages

The geological significance of the Olympic Dam hematite ages has been amply discussed in [3] and references therein, and supports formation of IOCG systems in South Australia coeval with LIP magmatism (Hiltaba Intrusive Suite and Gawler Range Volcanics) at ~1.6 Ga.

In contrast to relatively abundant data for the Olympic Dam District, supportive geochronological data for other deposits in the Olympic Cu-Au Province deposit remains sparse. The 1597.2 + 6.1 Ma hematite date obtained using GJ-1 Zircon as the primary standard does not overlap with a published U/Pb zircon crystallization ages of 1586 ± 3 Ma for an associated granite from the central Mount Woods Inlier [20], but does statistically overlap with the of 1587 ± 4 Ma date obtained for a cumulate gabbronorite [20]. Although the mixed-solution U–Pb hematite date (1604 ± 11 Ma) is statistically different to published ages, it is nonetheless very close. Minor differences in absolute age could be attributed to a non-direct relationship between the hematite associated with mineralization and LIP magmatism in the area. Most importantly, the present data for PH93 is further argument for the importance of the ~1.6 Ga IOCG event throughout the Olympic Cu-Au Province.

The date obtained for the Brazilian sample (1707 ± 39 Ma) is within the range of geological events associated with the Carajás mineral province (1.80 Ga U/Pb zircon ages from A-type magmatism at the Carajás Granite [16], and 1.61 Ga U/Pb zircon ages from rift-related granitic magmatism [17]). The hematite dated here could represent a vein-related mineralizing event, but needs to be corroborated by data on samples with less common Pb or by using dating methods, such as ID-TIMS, for more accurate age determination. Regardless, the date obtained in this study is similar to the other ages considered for the protracted tectono-magmatic history of the Carajás mineral province [21].

6. Implications and Outlook

This study has successfully established a new matrix-matched dating method for hematite using a U–Pb mixed solution/pure hematite standard. Through the decreased matrix effects, homogeneity of the solution and tailoring of U concentration differences between the sample and standard, a set of reliable dates have been obtained. The Fe-oxide hematite can now be dated using a U–Pb mixed solution/pure hematite standard method that provides high signal stability and has broad application to low-U samples. The samples will be further evaluated by ID-TIMS, to show whether the apparent discordance is due to the problems associated with the analytical methods used so far (e.g., Matrix-effects and downhole fractionation) or open system behavior. Although the zircon standardized data does show increased U/Pb fractionation, most likely due to matrix effects, the upper intercept ages are still statistically the same as that of the solution method, making the GJ-1 Zircon standard reliable for obtaining upper intercept and ^{207}Pb-^{206}Pb weighted average ages. Using the mixed solution method, we have also validated the original age obtained for OD-10 [3]. We have demonstrated that although the use of GJ-1 Zircon as the primary standard does create more "apparent" fractionation with greater spreading of analytical points down the discordia, the upper intercept and weighted average ^{207}Pb-^{206}Pb dates obtained are still geologically meaningful. To eliminate downhole fractionation associated with the solution method, we will analyze samples using a line raster. This was not carried out in the analytical session described in this paper because of the lack of current samples exhibiting the same high U zonation patterns with large enough grains to carry out this type of analysis.

Further research includes finding suitable material for a solid hematite standard so that other more-precise microbeam methods, including SHRIMP, can be routinely used for dating. The mixed solution standard method presented here will also be applied to U-bearing magnetite following similar procedures. The petrographic and genetic link between Fe-oxides and hydrothermal mineralization is one that can be directly correlated when compared to other mineral geochronometers, such as monazite and zircon, making this study an important step towards establishing U–Pb iron-oxide geochronology as a valuable tool that can be routinely used to constrain the genesis of mineral deposits.

Supplementary Materials: The following are available online at www.mdpi.com/2075-163X/6/3/85/s1, Supplementary Text File S1: Additional analytical procedures for calculating and certifying the Pb/U ratios; Table S1: Pb isotope ratios of Pb standard solution; Table S2: U and Pb concentrations in standard solutions; Table S3: Correlation coefficient of the regression line.

Acknowledgments: This work is a contribution to the "FOX" project (Trace elements in iron oxides: deportment, distribution and application in ore genesis, geochronology, exploration and mineral processing), supported by BHP Billiton Olympic Dam and the S.A. Mining and Petroleum Services Centre of Excellence. Alexandre R. Cabral gratefully acknowledges VALE S.A. for financing his research position at the Technische Universität Clausthal and for logistically supporting his fieldwork in Carajás. We also gratefully acknowledge Yang Tao and Yan Xiong for their assistance with lead isotope analysis at the State Key Laboratory for Mineral Deposits Research, Department of Earth Sciences, Nanjing University, China.

Author Contributions: Zhiyong Zhu conceived and designed the experiments; Liam Courtney-Davies, Zhiyong Zhu and Cristiana L. Ciobanu performed the experiments under the guidance of Benjamin P. Wade. Liam Courtney-Davies, Zhiyong Zhu and Benjamin P. Wade processed the data; Kathy Ehrig and Alexandre R. Cabral contributed samples and information; Liam Courtney-Davies, Zhiyong Zhu, Cristiana L. Ciobanu and Nigel J. Cook wrote the paper, assisted by Benjamin P. Wade, Allen Kennedy and Kathy Ehrig. The work is part of the PhD project of Liam Courtney-Davies. We would also like to thank two anonymous reviewers for their detailed thoughts and important amendments, which helped us to clarify our interpretations, along with Matthew Horstwood with whom conversations further aided this study.

Conflicts of Interest: The authors declare no conflict of interest. The project sponsors approve publication of the manuscript.

References

1. Jackson, S.E.; Pearson, N.J.; Griffin, W.L.; Belousova, E.A. The application of laser ablation inductively coupled plasma-mass spectrometry to in-situ U–Pb zircon geochronology. *Chem. Geol.* **2004**, *211*, 47–69. [CrossRef]

2. McFarlane, C.R.M.; Luo, Y. U–Pb Geochronology Using 193 nm Excimer LA-ICP-MS Optimized for In-Situ Accessory Mineral Dating in Thin Sections. *Geosci. Can. Anal. Tech. Ser.* **2012**, *39*, 158–172.
3. Ciobanu, C.L.; Wade, B.P.; Cook, N.J.; Schmidt Mumm, A.; Giles, D. Uranium-bearing hematite from the Olympic Dam Cu-U-Au deposit, South Australia; a geochemical tracer and reconnaissance Pb-Pb geochronometer. *Precambr. Res.* **2013**, *238*, 129–147. [CrossRef]
4. Johnson, J.P.; Cross, K.C. U–Pb geochronological constraints on the genesis of the Olympic Dam Cu-U-Au-Ag deposit, South Australia. *Econ. Geol.* **1995**, *90*, 1046–1063. [CrossRef]
5. Günther, D.; Heinrich, C.A. Enhanced sensitivity in laser ablation-ICP mass spectrometry using helium-argon mixtures as aerosol carrier. *J. Anal. At. Spectrom.* **1999**, *14*, 1363–1368. [CrossRef]
6. Becker, J.S. State-of-the-art and progress in precise and accurate isotope ratio measurements by ICP-MS and LA-ICP-MS. *Plenary Lecture. Anal. At. Spectrom.* **2002**, *17*, 1172–1185. [CrossRef]
7. Günther, D. Laser Ablation-Inductively Coupled Plasma Mass Spectrometry Trends. *Anal. Bioanal. Chem.* **2002**, *372*, 31–32. [CrossRef]
8. Horn, I.; Rudnick, R.L.; McDonough, W.F. Precise elemental and isotope ratio determination by simultaneous solution nebulization and laser ablation-ICP-MS: application to U–Pb geochronology. *Chem. Geol.* **2000**, *164*, 281–301. [CrossRef]
9. Košler, J.; Fonneland, H.; Sylvester, P.; Tubrett, M.; Pedersen, R.-B. U–Pb dating of detrital zircons for sediment provenance studies—A comparison of laser ablation ICPMS and SIMS techniques. *Chem. Geol.* **2002**, *182*, 605–618. [CrossRef]
10. Simonetti, A.; Heaman, L.M.; Hartlaub, R.P.; Creaser, R.A.; MacHattie, T.G.; Böhm, C. U-Pb zircon dating by laser ablation MC-ICP-MS using a new multiple ion counting Faraday collector array. *J. Anal. At. Spectrom.* **2005**, *20*, 677–686. [CrossRef]
11. Leach, J.J.; Allen, L.A.; Aeschliman, D.B.; Houk, R.S. Calibration of Laser Ablation ICP-MS Using Standard Additions with Dried Solution Aerosols. *Anal. Chem.* **1999**, *71*, 440–445. [CrossRef]
12. Pickhardt, C.; Becker, J.S.; Dietze, H.J. A new strategy of solution calibration in laser ablation inductively coupled plasma mass spectrometry for multi element trace analysis of geological samples. *J. Anal. Chem.* **2000**, *368*, 173–181. [CrossRef]
13. Van Achterbergh, E.; Ryan, C.; Jackson, S.; Griffin, W. Appendix 3 Data reduction software for LA-ICP-MS. In *Laser-Ablation-ICPMS in the Earth Sciences*; Sylvester, P., Ed.; Mineralogical Association of Canada: Quebec City, QC, Canada, 2001; Volume 29, pp. 239–243.
14. Ludwig, K.R. *A User's Manual for Isoplot 3.75: A Geochronological Toolkit for Microsoft Excel*; Berkeley Geochronology Centre Special Publication No.5; Berkeley Geochronology Centre: Berkeley, CA, USA, 2012.
15. White, W.M.; Albarède, F.; Télouk, P. High-precision analysis of Pb isotope ratios by multi-collector ICP-MS. *Chem. Geol.* **2000**, *167*, 257–270. [CrossRef]
16. Machado, N.; Lindenmayer, Z.; Krogh, T.E.; Lindenmayer, D. U–Pb geochronology of Archean magmatism and basement reactivation in the Carajás area, Amazon Shield, Brazil. *Precambr. Res.* **1991**, *49*, 329–354. [CrossRef]
17. Pimentel, M.M.; Heaman, L.; Fuck, R.A.; Marini, O.J. U–Pb zircon geochronology of Precambrian tin-bearing continental-type acid magmatism in central Brazil. *Precambr. Res.* **1991**, *52*, 321–335. [CrossRef]
18. York, D. Least-squares fitting of a straight line with correlated errors. *Earth Plan. Sci. Lett.* **1969**, *5*, 320–324. [CrossRef]
19. Paton, C.; Woodhead, J.D.; Hellstrom, J.C.; Hergt, J.J.; Greig, A.; Maas, R. Improved laser ablation U-Pb zircon geochronology through robust downhole fractionation correction. *Geochem. Geophys. Geosyst.* **2010**, *11*, 1–36. [CrossRef]
20. Jagodzinski, E.A. Compilation of SHRIMP U–Pb geochronological data, Olympic Domain, Gawler Craton, South Australia, 2001–2003. *Geosci. Aust. Rec.* **2005**, *20*, 211.
21. Pinheiro, R.V.L.; Holdsworth, R.E. Reactivation of Archaean strike-slip fault systems, Amazon region, Brazil. *J. Geol. Soc.* **1997**, *154*, 99–103. [CrossRef]

© 2016 by the authors; licensee MDPI, Basel, Switzerland. This article is an open access article distributed under the terms and conditions of the Creative Commons Attribution (CC-BY) license (http://creativecommons.org/licenses/by/4.0/).

CHAPTER 3

A MULTI-TECHNIQUE EVALUATION OF HYDROTHERMAL HEMATITE U-PB ISOTOPE SYSTEMATICS: IMPLICATIONS FOR ORE DEPOSIT GEOCHRONOLOGY

Liam Courtney-Davies [1], Simon R. Tapster [2], Cristiana L. Ciobanu [1], Nigel J. Cook [1], Max R. Verdugo-Ihl [1], Kathy J. Ehrig [3], Allen K. Kennedy [4], Sarah E. Gilbert [5], Daniel J. Condon [2] and Benjamin P. Wade [5]

[1]*School of Chemical Engineering and Advanced Materials, The University of Adelaide, Adelaide, SA 5005, Australia*

[2] *NIGL, British Geological Survey, Keyworth, Nottingham, NG12 5GG, UK*

[3] *BHP Billiton Olympic Dam, Adelaide, SA, 5000, Australia*

[4]*John de Laeter Centre, Curtin University of Technology, Bentley, WA 6102, Australia*

[5]*Adelaide Microscopy, The University of Adelaide, Adelaide, SA 5005, Australia*

Article published in Chemical Geology (2019), 513, 54-72.

Statement of Authorship

Title of Paper	A multi-technique evaluation of hydrothermal hematite U-Pb isotope systematics: Implications for ore deposit geochronology
Publication Status	☑ Published ☐ Accepted for Publication ☐ Submitted for Publication ☐ Unpublished and Unsubmitted w ork w ritten in manuscript style
Publication Details	Courtney-Davies, L., Tapster, S.R., Ciobanu, C.L., Cook, N.J., Verdugo-Ihl, M.R., Ehrig, K.J., Kennedy, A.K., Gilbert, S.E., Condon, D.J., Wade, B.P., 2019. A multi-technique evaluation of hydrothermal hematite U-Pb isotope systematics: Implications for ore deposit geochronology. Chemical Geology 513, 54-72.

Principal Author

Name of Principal Author (Candidate)	Liam Courtney-Davies		
Contribution to the Paper	Performed lab work, analytical work, carried out data processing and interpretation, oversaw development of work and wrote manuscript and oversaw revisions.		
Overall percentage (%)	65		
Certification:	This paper reports on original research I conducted during the period of my Higher Degree by Research candidature and is not subject to any obligations or contractual agreements with a third party that would constrain its inclusion in this thesis. I am the primary author of this paper.		
Signature		Date	29/10/2019

Co-Author Contributions

By signing the Statement of Authorship, each author certifies that:

i. the candidate's stated contribution to the publication is accurate (as detailed above);

ii. permission is granted for the candidate in include the publication in the thesis; and

iii. the sum of all co-author contributions is equal to 100% less the candidate's stated contribution.

Name of Co-Author	Simon R. Tapster		
Contribution to the Paper	Performed lab work, analytical work, carried out data processing and data interpretation, assisted in writing the manuscript and its revision.		
Overall percentage (%)	20		
Signature		Date	29.Oct 2019

Name of Co-Author	Cristiana L. Ciobanu		
Contribution to the Paper	Helped define direction of research, supervised development of work, assisted with data interpretation and contributed to manuscript preparation.		
Overall percentage (%)	5		
Signature		Date	29. Oct. 2019

Name of Co-Author	Nigel J. Cook		
Contribution to the Paper	Assisted with data interpretation, and evaluation of manuscript.		
Overall percentage (%)	2		
Signature		Date	~~30/4/2019~~ 29/10/2019

Name of Co-Author	Max R. Verdugo-Ihl		
Contribution to the Paper	Assisted with analytical instrumentation, data processing and evaluation of manuscript.		
Overall percentage (%)	2		
Signature		Date	29/10/2019

Name of Co-Author	Kathy Ehrig		
Contribution to the Paper	Helped coordinate sample collection and evaluation of manuscript.		
Overall percentage (%)	2		
Signature		Date	29/10/2019

Name of Co-Author	Allen Kennedy		
Contribution to the Paper	Helped define research direction and assisted with evaluation of manuscript.		
Overall percentage (%)	1		
Signature		Date	29/10/2019

Name of Co-Author	Sarah E. Gilbert		
Contribution to the Paper	Assisted with construction of figures and evaluation of manuscript.		
Overall percentage (%)	1		
Signature		Date	29/10/19

Name of Co-Author	Daniel J. Condon		
Contribution to the Paper	Assisted with analytical work and manuscript evaluation.		
Overall percentage (%)	1		
Signature		Date	29.Oct 2019

Name of Co-Author	Benjamin P. Wade		
Contribution to the Paper	Assisted with analytical instrumentation, data processing and evaluation of manuscript.		
Overall percentage (%)	1		
Signature		Date	29/10/2019

Chemical Geology 513 (2019) 54–72

Contents lists available at ScienceDirect

Chemical Geology

journal homepage: www.elsevier.com/locate/chemgeo

A multi-technique evaluation of hydrothermal hematite U—Pb isotope systematics: Implications for ore deposit geochronology

Liam Courtney-Davies[a,*], Simon R. Tapster[b], Cristiana L. Ciobanu[a], Nigel J. Cook[a], Max R. Verdugo-Ihl[a], Kathy J. Ehrig[c], Allen K. Kennedy[d], Sarah E. Gilbert[e], Daniel J. Condon[b], Benjamin P. Wade[e]

[a] School of Chemical Engineering, The University of Adelaide, Adelaide, SA 5005, Australia
[b] NIGL, British Geological Survey, Keyworth, Nottingham, NG12 5GG, UK
[c] BHP Olympic Dam, Adelaide, SA 5000, Australia
[d] John de Laeter Centre, Curtin University of Technology, Bentley, WA 6102, Australia
[e] Adelaide Microscopy, The University of Adelaide, Adelaide, SA 5005, Australia

ARTICLE INFO

Editor: Balz Kamber

Keywords:
Hematite
U-Pb
Micro-sampled ID-TIMS
LA-ICP-MS mapping
Geochronology
Olympic Dam
IOCG

ABSTRACT

Hematite (α-Fe_2O_3) is a common iron-oxide mineral known to incorporate U into its crystal lattice at up to wt% concentrations and has been previously used to date ore formation within iron-oxide copper gold and banded iron formation deposits. However, there has been no detailed evaluation of the potential challenges this novel mineral geochronometer may present for accurate temporal interpretation. We report a multi-technique U—Pb geochronological study comprising laser ablation-inductively coupled plasma-mass spectrometry (LA-ICP-MS), sensitive high-resolution ion microprobe (SHRIMP) and the first isotope dilution-thermal ionization mass spectrometry (ID-TIMS) procedure and analyses using an in-situ grain micro-sampling technique. We assess intra- and inter-sample data reproducibility, and examine the compatibility of spatial and analytical resolutions to texturally and compositionally diverse samples.

Five samples of hydrothermal, primary, oscillatory-zoned hematite were analysed from distinct lithologies throughout the ~1.59 Ga Olympic Dam Cu-U-Au-Ag deposit, with typical U concentrations ranging between ~20 and 1000 ppm. LA-ICP-MS mapping of isotope distributions across mm-sized grains allows pinpointing of U-rich and relatively U/Pb isotopically 'homogeneous' domains. Micro-domains were extracted via laser-cut square shaped trenches (100 × 100 μm). U—Pb datum range in complexity, with concordant age domains measured by ID-TIMS indicating that hematite can retain a near-closed U—Pb system over ~1.6 Ga, while also demonstrating that younger Pb-loss events may be recorded. Significant reverse discordance is common in the data, likely to be a real feature due to both internal decoupling and mobility of Pb within a single grain and U—Pb fractionation during microbeam analysis. These effects will obscure the interpretation of real ages for Proterozoic samples where non-zero age Pb-loss events occur, and restricts the evaluation of common Pb mixing components. As a result, microbeam analyses may be biased younger or older in terms of $^{207}Pb/^{206}Pb$ dates in samples with complex histories. Microbeam datum compare favourably with high precision ID-TIMS ages. Although reproducible ID-TIMS U—Pb dates were generally not obtained, in the best-case example, a $^{207}Pb/^{206}Pb$ weighted mean age of 1589.91 ± 0.91 Ma (MSWD = 1.3, n = 5), within 0.2% of the Olympic Dam granite host rock age (1593.87 ± 0.21 Ma) was generated. All five hematite samples dated by LA-ICP-MS and SHRIMP yield weighted mean $^{207}Pb/^{206}Pb$ dates within 2% of the host granite age after small degrees of data rejection. The results demonstrate that with careful sample petrography, screening and data interpretation, hematite can be considered a very useful U—Pb mineral geochronometer, with potential application to all U-bearing Fe-oxide rich mineral systems.

Editor: Balz Kamber

* Corresponding author.
E-mail address: liam.courtney-davies@adelaide.edu.au (L. Courtney-Davies).

https://doi.org/10.1016/j.chemgeo.2019.03.005
Received 8 October 2018; Received in revised form 28 February 2019; Accepted 4 March 2019
Available online 07 March 2019
0009-2541/ © 2019 Elsevier B.V. All rights reserved.

Table 1
Sample list, location and key characteristics.

Sample ID[a]	Drillhole ID	Coordinates		Drillhole dip	Azimuth	Downhole depth (m)	-RL Depth (m)	Deposit location	Orezone	Key characteristics
		East	North							
MV005A	RD2366	683140.5	6629045.9	−88.4	−70.1	1017	916	SE-Lobe deposit margin	Cp-Py	Heterolithic, granite-rich breccia with laminated sedimentary clasts, hematite occurs predominantly as mm-sized aggregates
LCD4	RD2786A	681902.7	6629375.0	−44.8	1.8	1802	1562	SE-Lobe		Hematite-rich breccia with grains up to 1000 μm in diameter, often as aggregates with well-preserved zonation
7295GM	RD1988	681960.6	6629460.5	−87.3	68.8	1810	1720			Hematite-rich breccia at depth containing coarse oscillatory-zoned hematite laths co-existing with minor magnetite
RX6607	RD2852A	682086.3	6629394	−62.5	42.3	658	495		Bn-Cc	Fine-grained hematite within a matrix of a fluorite-rich, hematite breccia, but coarse-grained, zoned hematite up to ~2 mm occurs
MV095	RU36-9867W1	681168.9	6630045.8	−33.4	−27.2	119	417	Centre	No sulphide	Hematite-quartz rich breccia of predominantly fine (~10 μm) grains of zoned hematite, which are porous and inclusion-rich

Abbreviations: Bn-bornite; Cc-chalcocite; Cp-chalcopyrite; Py-pyrite.
[a] Sample ID's are kept in their original format for correlation with other published studies.

1. Introduction

Ore deposits originate from complex geological processes, often requiring a range of minerals to temporally constrain their initial formation age, mineralization lifespan, and post-mineralization processes. Multi-mineral U–Pb data-sets promote refinement of geological and mineralization models, and are complimented by ever-increasing speed of data acquisition, analytical precision and spatial resolution (Horstwood et al., 2016). However, ore deposits that have formed via cumulative hydrothermal processes, over time-scales that may extend to events tens to even hundreds of millions of years apart, can prove challenging to derive robust ages from. The U–Pb systematics of a mineral, that in an idealized scenario should document the timing of a specific geological event such as crystallisation, can be altered through various pathways that mobilise parent and daughter isotopes, commonly by fluid interaction, metamorphism and diffusion (e.g., zircon; Ewing et al., 1988; apatite; Chew et al., 2011; monazite; Cherniak et al., 2004).

Hematite (α-Fe_2O_3) is a common Fe-oxide in many ore systems, most abundant in iron-oxide-copper-gold (IOCG) and banded iron formation deposits. Uranium-bearing hematite in such deposits potentially provides a well-constrained radiogenic-system within an abundant hydrothermal mineral. Preceding studies have acquired U–Pb hematite data (Ciobanu et al., 2013; Courtney-Davies et al., 2016; Apukhtina et al., 2017; Zhou et al., 2017). The ca. 1.59 Ga Olympic Dam Cu-U-Au-Ag deposit (Ehrig et al., 2012), as well as other IOCG systems within the Gawler Craton, South Australia, contains abundant U-bearing hematite that provided the first reconnaissance laser-ablation inductively-coupled plasma mass spectrometry LA-ICP-MS U–Pb hematite dating (Ciobanu et al., 2013; Courtney-Davies et al., 2016; Cook et al., 2016; Verdugo-Ihl et al., 2017 Apukhtina et al. (2017). Samples yielded comparable dates at ~1.6 Ga, which are geologically meaningful in the context of IOCG systems from the Gawler Craton (Skirrow et al., 2007). Beyond Olympic Dam, there is a growing body of literature documenting and dating U-bearing hematite from a diverse range of environments and time periods. These include Proterozoic IOCG-systems from Carajás, Brazil (Courtney-Davies et al., 2016), as well as hematite ores derived from banded iron formations in the Middleback Ranges, South Australia (Keyser et al., 2019). Younger examples include U-bearing hematite from a Cenozoic porphyry Au deposit in China (Zhou et al., 2017). To negate the issues associated with U–Pb hematite dating, due to the lack of relatively homogeneous, well characterised reference material, previous hematite U–Pb studies have used non-matrix matched zircon reference materials (GJ-1 and Plešovice; Ciobanu et al., 2013) and mixed U/Pb solution standards (Courtney-Davies et al., 2016). However, use of such reference materials may not accurately correct for U–Pb fractionation (Eggins et al., 1998; Kuhn et al., 2009). This in-turn inhibits accurate interpretation of the effects of common Pb (hereafter referred to as Pb_c) and open system behavior within mineral grains. However, the paucity of matrix-matched reference materials restricts the evaluation of possible analytical biases (e.g. U–Pb fractionation) and obscures interpretation of open system features.

To derive accurate geochronological interpretations from hematite U–Pb data, there is a need to understand the competing natural and analytical effects that can occur, and how these issues relate to sample petrography. To address this, we present the first systematic study of hematite U–Pb data conducted over a range of scales and analytical techniques. We utilize high spatial resolution techniques (LA-ICP-MS spot-analysis, U–Pb isotope mapping and SHRIMP) in tandem with a novel method of micro-sampling hematite domains to analyse by ID-TIMS. The combination of techniques allows evaluation of the issues and limitations, as well as benefits of utilizing hematite U–Pb geochronology. We report on hematite samples from Olympic Dam which are oscillatory-zoned and strongly enriched in the granitophile elements, U, W, Sn and Mo (individually up to wt% concentrations). This

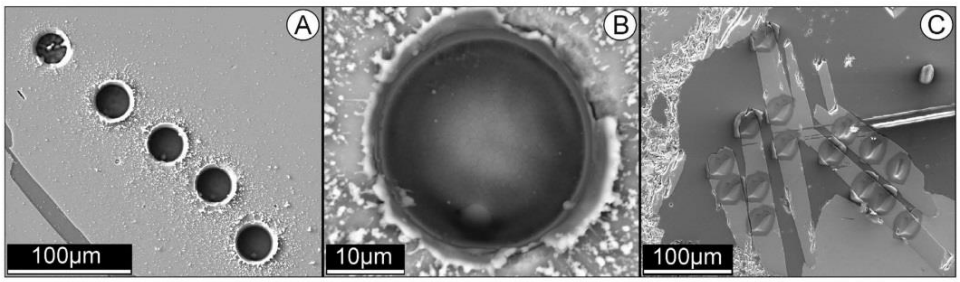


Fig. 1. (A) BSE image of 29 µm-diameter laser-ablation craters in zoned hematite with a selected fluence of 1 J cm^{-2} in the top left of the image, ascending to 5 J cm^{-2} in the bottom right; (B) BSE image of the LA-ICP-MS crater for a fluence of 4 J cm^{-2} used in this study. Laser ablation pits are all morphologically alike with smooth crater walls and flat crater floors; average crater depths were ~15 µm; (C) BSE image of typical elliptical ~25 µm-diameter SHRIMP craters with an average depth of ~5 µm.

type of hematite has been documented throughout the 6 km-strike and 2 km-vertical extent of the deposit (Verdugo-Ihl et al., 2017).

2. Background

2.1. Samples

The U concentrations of sampled hematite typically range from ~10 ppm to ~2000 ppm, while Th concentrations are largely below < 1 ppm (LA-ICP-MS). Hematite grains containing wt% levels of U were not considered for this study due to generally small grain sizes, which cannot be micro-sampled for ID-TIMS without potential contamination from surrounding minerals. The zoned hematite in each sample is documented in terms of both location, petrography and U–Pb composition in the results and Tables 1, A1-3.

2.2. Oscillatory-zoned hematite

Hematite incorporates elements in octahedral-coordination, allowing accommodation of a wide range of foreign cations at concentrations from ppm up to wt% (e.g., Barkov et al., 2008; Ciobanu et al., 2013). Substituting cations can include those with higher oxidation states, notably U, W, Mo and Sn, as shown by X-ray absorption near-edge spectroscopy (XANES), suggesting the presence of U^{6+} in the distorted lattice of synthetic hematite (Duff et al., 2002). Incorporation of U (up to 0.013 atoms per formula unit assuming U^{6+}) and radiogenic Pb in zoned hematite at Olympic Dam was interpreted as being due to vacancy-induced crystal structure modifications producing long-range superstructures, following the proposed substitution: $2Fe^{3+} \leftrightarrow Me^{6+}$ + vacancy (Me: U, W and Mo; Ciobanu et al., 2013). A contemporary literature overview of substitution mechanisms in hematite is provided in Verdugo-Ihl et al. (2017).

Oscillatory- and sector-zoned hydrothermal hematite is a ubiquitous and primary hydrothermal mineral at Olympic Dam. The zoned hematite contains granitophile elements at a range of concentrations from < 10 ppm to wt%, while the size of individual grains ranges from microns to millimetres. A significant amount of hematite in the orebody occurs as pseudomorphic replacements after the zoned type, which partially preserve pre-existing trace element signatures and, in many cases, comparable oscillatory and sector-zoning textures (Verdugo-Ihl et al., 2017). Furthermore, at the nano-scale, zoned hematite shows no signs of alpha decay damage (Ciobanu et al., 2013), as would be common in comparably U-rich zircon of Proterozoic age. Therefore, the composition, relatively large grain size (compared to other datable minerals) and prevalence throughout Olympic Dam makes this textural variety of hematite suitable for a detailed inter-sample and multi-instrumental comparison.

3. Methodology

One-inch diameter polished blocks were prepared from Olympic Dam core samples. These were examined for zoned hematite grains via reflected light microscopy and scanning electron microscopy (SEM) using an FEI Quanta 450 equipped with a back-scattered electron (BSE) detector and an energy dispersive X-ray spectrometer at Adelaide Microscopy, The University of Adelaide.

3.1. LA-ICP-MS spot analyses

All reported LA-ICP-MS data were obtained from grains within one-inch-diameter polished blocks. Data were collected at Adelaide Microscopy, The University of Adelaide, using a 193 nm RESOlution-LR excimer laser microprobe (Australian Scientific Instruments) coupled to an Agilent 7900x Quadrupole ICP-MS. This combination of laser and ICP-MS offers good spatial resolution (~29 µm) coupled with sub-ppm sensitivity for most trace elements. The laser has a large format S155 two-volume ablation cell designed by Laurin Technic Pty. Laser ablation was performed in an atmosphere of UHP He (0.38 l/min). The aerosol was mixed with Ar carrier gas (1.05 l/min) immediately above the ablation site before being transported to the ICP-MS via a 'squid' pulse-homogenizing device (Laurin Technic Pty). Acquisition protocols followed a similar methodology as outlined in Ciobanu et al. (2013), with the exception of a fluence of 4 J cm^{-2}, and spot diameter of 29 µm, resulting in crater depths generally between 10 and 15 µm over the 30 s ablation time (Fig. 1A, B). The ICP-MS was tuned daily using the NIST612 reference glass to maximize sensitivity on isotopes of the mass range of interest, while keeping production of molecular oxide species (i.e., $^{232}Th^{16}O/^{232}Th$) and doubly charged ion species (i.e., $^{140}Ce^{2+}/^{140}Ce^{+}$) as low as possible, and generally at < 0.2%. The plasma conditions were tuned for a robust plasma with U/Th ratio of 1.00–1.05. The GJ-1 zircon (Jackson et al., 2004) was used as the primary reference material, while 91,500 (Wiedenbeck et al., 1995) and Plešovice (Sláma et al., 2008) were analysed as secondary reference materials. Data collection consisted of a 30 s gas blank followed by 30 s of data acquisition with the laser firing. Isotopes measured were ^{57}Fe, ^{204}Pb, ^{206}Pb, ^{207}Pb, ^{208}Pb, ^{232}Th, and ^{238}U with dwell times of 5, 20, 50, 50, 10, 10, and 50 ms, respectively; U decay constants are from Jaffey et al. (1971) and ^{235}U was calculated here (and in all other analytical methods) using the $^{238}U/^{235}U$ ratio of 137.88 (Steiger and Jäger, 1977). Mass ^{204}Pb was measured for fast assessment of Pb_c-rich samples, but due to the unresolvable isobaric interference of ^{204}Hg on ^{204}Pb, Pb_c corrections were not considered or conducted using ^{204}Pb. All data reduction was performed and presented using Iolite™ (Paton et al., 2011) in combination with Isoplot 3.75 (Ludwig, 2012), with uncertainties calculated from internal errors unless stated otherwise.

Table 2
LA-ICP-MS parameters.

Laboratory and sample preparation	
Laboratory name	Adelaide Microscopy
Sample type/mineral	In-situ hematite grains within 1-inch polished block
Imaging	FEI Quanta 450 scanning electron microscope
Laser ablation system	
Make, Model and type	RESOlution-LR excimer laser microprobe (Australian Scientific Instruments)
Ablation cell and volume	Large format S155 two-volume ablation cell designed by Laurin Technic Pty
Laser wavelength (nm)	193 nm
Pulse width (ns)	20 ns
Fluence (J cm^{-2})	Zircon reference material 2 5 J cm^{-2}; Hematite 4 J cm^{-2}
Repetition rate (Hz)	5 Hz
Ablation duration (s)	30 s
Ablation pit depth	10–15 μm
Spot diameter (um)	29 μm
Sampling mode/pattern	Static spot ablation
Carrier gas	100% He in the cell, Ar make-up gas combined within the funnel of the two-volume ablation cell, immediately after ablation
Cell carrier gas flow (l/min)	0.38 l/min (He); 1.05 l/min (Ar)
ICP-MS instrument	
Make, Model and type	Agilent 7900x Quadrupole ICP-MS
Sample introduction	Direct aerosol injection into the plasma
RF power (W)	1350 W
Make-up gas flow (l/min)	n/a
Detection system	Electron Multiplier, Pulse mode
Masses measured	^{57}Fe, ^{204}Pb, ^{206}Pb, ^{207}Pb, ^{208}Pb, ^{232}Th, and ^{238}U
Integration time per peak/dwell times (ms)	5, 20, 50, 50, 10, 10, 50 ms, respectively
Settling time between mass jumps	2.8 ms
Total integration time per output data point (s)	0.233 s
IC Dead time (ns)	3.6 × 10–8 s
Data processing	
Gas blank	30 s gas background
Calibration strategy	GJ-1 used as primary reference material, Plešovice and 91,500 as secondary
Reference material information	Plešovice (Sláma et al., 2008); 91,500 (Wiedenbeck et al., 1995); GJ-1 (Jackson et al., 2004)
Data processing package used	Iolite™ (Paton et al., 2011); DRS scheme: U_Pb_Geochronology3
Common-Pb correction	No common-Pb correction applied to the data
Uncertainty level and propagation	2 sigma level uncertainty, basic error propagation through Iolite
^{238}U/^{235}U data reduction value	137.88 (Steiger and Jäger, 1977)

Further LA-ICP-MS analytical details and methodology are summarized in Table 2.

3.2. LA-ICP-MS U—Pb isotope mapping

Isotope mapping was conducted using the same instrumentation as described for spot analysis. Data acquisition involved ablating sets of parallel line rasters in a rectangular grid across the area of interest with a beam size of 11 μm (square profile) and a scan speed of 11 μm/s. Line spacing was kept at a constant 11 μm to match the size of the laser beam used. The effect of redeposition during mapping was minimized by pre-ablating each line immediately prior to its analysis. A laser repetition rate of 10 Hz was combined with a fluence of ~3.5 J cm^{-2}. Isotopes measured were ^{57}Fe, ^{204}Pb, ^{206}Pb, ^{207}Pb, ^{232}Th, ^{235}U and ^{238}U, with corresponding dwell times of 30 ms for U, Th and Pb isotopes and 5 ms for ^{57}Fe. A 30 s background was acquired at the start of every raster, and a delay of 15 s was applied after each line to allow for sample washout.

Images were compiled and processed with Iolite™ using the VizualAge data reduction scheme (Petrus and Kamber, 2012). A typical mapping run was analysed over a 6 to 8-hour session, in which significant instrument drift could occur. To correct for this, the average background was subtracted from its corresponding signal from the ablated area for each raster and element. Zircon reference materials (GJ-1; Plešovice; 91500) were analysed immediately before and after the run to assess drift, and if present, this was corrected by applying a linear fit between the two sets of reference materials. The rasters were then compiled into a 2-D image displaying combined background and drift corrected intensities for each element. Regions of interest within zoned hematite grains were interrogated using the Iolite add-on 'Monocle' (Petrus et al., 2017) based on a criterion of different ^{207}Pb/^{206}Pb ranges (Data shown in Appendix A5).

3.3. SHRIMP spot analysis

Ion microprobe data were obtained using a SHRIMP II at the John De Laerter Centre, Curtin University (Perth, Australia), with analytical methods following those described by Compston et al. (1984), Claoué-Long et al. (1995) and Williams (1998). The beam diameter was set around ~15–25 μm with a crater depths of ~5 μm (Fig. 1C). During initial testing, 14 points in 7 grains within a single polished block from Olympic Dam were analysed. Data were collected during 6 cycles through 9 magnetic field values, corresponding to $^{56}Fe_3{}^{16}O_2{}^+$, $^{204}Pb^+$, background, $^{206}Pb^+$, $^{207}Pb^+$, $^{208}Pb^+$, $^{238}U^{16}O^+$, $^{232}Th^{16}O^+$, and $^{238}U^{16}O_2{}^+$, with respective dwell times of 4, 10, 10, 30, 30, 20, 5, 5 and 5 s. Ion yields were in the thousands of counts-per-second (cps) for UO^+ and $UO_2{}^+$. The $^{238}U^+$ peak had exceptionally low counts and therefore was not measured. Pb_c was present in variable amounts and small corrections were needed, but these were relatively minor corrections for many points, as the ^{204}Pb intensities were close to the background levels. The distribution of U is highly variable between and within grains; e.g., for the fourth grain analysed, the UO^+ count rate varied from 116 to 4793 cps. The consistently low Th content of the single hematite sample measured by SHRIMP allowed a correction for Pb_c using the ^{208}Pb method.

Isotopic measurements were reduced with the SQUID software package (Ludwig, 2009). In the absence of a homogeneous and well-characterised hematite reference material, the reported U/Pb ages are relative, as the U/Pb ages have been normalized to a value of 1593 Ma for selected hematite grains within the polished block used as the

reference material. Such grains were chosen as reference material because of the high U counts and large grain size allowing multiple spots within the same grains. SHRIMP was undertaken prior to ID-TIMS analysis, preventing the more accurately measured grains being used as reference material. This excludes robust comparison of external precision with other dating techniques, but does allow internal comparison within the SHRIMP data-set. Hematite reference material was preferred to zircon reference material in a separate polished block, as movement between two blocks would add to the uncertainties of results. For SHRIMP analyses the calculation of $^{206}Pb/^{238}U$ and $^{207}Pb/^{235}U$ ages requires correction for Pb_c and then normalization to the mean of the ratio of $^{206}Pb/^{238}U$ measured on the reference material. The correction formula for Pb/U fractionation is $^{206}Pb^{+}/^{238}U^{+} = a(^{238}U^{16}O^{+}/^{238}U^{+})^{b}$ (Claoué-Long et al., 1995) using the parameter values of Black et al., 2003). Uncertainties cited for individual analyses include uncertainties from counting statistics, the Pb_c correction, and the U–Pb calibration error based on the reproducibility of U–Pb measurements of the standard. The $^{207}Pb/^{206}Pb$ ages given in this report are independent of the standard used, as the $^{207}Pb/^{206}Pb$ ratio bias in SHRIMP measurements is insignificant.

3.4. ID-TIMS

Sample preparation and analyses were conducted at the Natural Environment Research Council, Isotope Geosciences Laboratory, British Geological Survey. Hematite was extracted in-situ from one-inch polished blocks by ablating trenches with an ESI NWR213 solid state laser ablation system (3 line raster passes at 10 Hz, 1 μm/s, 20–80 μm beam diameter) to form ~100 × 100 μm squares within zoned-grains (Fig. 2A). Following ultra-sonic cleaning of the polished blocks, the target hematite material (area contained within the square) was manually extracted (Fig. 2B, C) under a microscope with tweezers and transferred to PTFE Savillex beakers in 1 ml of ultra-pure H_2O and rinsed in an ultrasonic bath. The largest remaining fragment(s) of the micro-sampled regions were then transferred to a new clean PTFE beaker, ensuring that no additional material fragmented during the extraction. The mixed ^{205}Pb-^{233}U-^{235}U U–Pb tracer (NIGL-2) and 400 μl of 6N HCl were added to each sample and fluxed for ≥2 days at 120 °C in closed beakers. The majority of the hematite aliquots dissolved in HCl within 2 days, however, a small number of aliquots did contain residue when examined under a microscope. Further HF and HNO_3 were applied to these aliquots, but no significant additional dissolution was achieved and therefore were not considered for further analysis.

Following dissolution and equilibration, the tracer samples were dried to chloride form, then dissolved in ~300 μl of concentrated 9M HBr, and fluxed on a hotplate overnight at 120 °C to convert to bromide form. Samples were then dried and dissolved in ~300 μl 1 M HBr to complete the conversion to bromide form. Separation of Pb from matrix elements and U was conducted using a variation of the HBr-HNO_3 AG 1-X8 anion exchange resin chemistry (Lugmair and Galer, 1992). Separation of U from the remaining matrices was achieved using an AG 1-X8 HNO_3- and HCl-based chemistry modified from Edwards et al. (1986). Lead fractions were dried down individually with ~10 μl of H_3PO_4 and then loaded onto a zone-refined Re filament in a silica gel matrix (Gerstenberger and Haase, 1997).

Isotope ratios were measured using a Thermo Triton thermal ionization mass-spectrometer. Lead was measured in peak hopping (dynamic) mode on a single MassCom secondary electron multiplier (SEM). Linearity and dead time corrections on the SEM were monitored using repeated analyses of the NBS 982, NBS 981 and U 500 reference materials (Pb = 24.5 ns; U = 22 ns). Uranium was run in oxide form (UO_2) and measured in static mode on Faraday detectors equipped with a $10^{12}\Omega$ resistor, and corrected for isobaric interferences using an $^{18}O/^{16}O$ value of 0.00205. Uranium mass fractionation was calculated in real-time based on the isotopic composition of the tracer solutions. Mass bias for Pb was corrected for using the fractionation factor of 0.14 ± 0.02% per amu (1σ). Decay constants used are from Jaffey et al. (1971) for ^{238}U and ^{235}U, and the $^{238}U/^{235}U$ ratio of Steiger and Jäger (1977) unless otherwise stated.

Isotope measurements were processed using the TRIPOLI software package (Bowring et al., 2011). Data reduction, error propagation and date calculations were carried out using the excel spreadsheet of Schmitz and Schoene (2007). Based on the analysis of 14 total procedural blanks, Pb_c of 3.598 ± 51.66% (1σ) was attributed to the laboratory blank with an isotopic composition of $^{206}Pb/^{204}Pb$ = 18.206 ± 1.97%, $^{207}Pb/^{204}Pb$ = 15.295 ± 0.657% and $^{208}Pb/^{204}Pb$ = 37.054 ± 1.289% (1σ uncertainties). Sample 7295GM, which was analysed in a separate ID-TIMS session 1 year prior to all other analyses was attributed laboratory blank of 2 ± 100% (1σ) Pb_c and an isotopic composition of $^{206}Pb/^{204}Pb$ = 18.099 ± 1.51%, $^{207}Pb/^{204}Pb$ = 15.545 ± 0.879% and $^{208}Pb/^{204}Pb$ = 37.824 ± 1.08% (1σ uncertainties). Additional Pb_c was attributed to initial Pb_c within the hematite sample and assigned a model isotopic composition of Stacey and Kramers (1975) at 1593 Ma. Data are presented using Isoplot (Ludwig, 2012).

Five samples were selected for LA-ICP-MS and ID-TIMS analyses, one for SHRIMP analysis and two for U–Pb isotope mapping (Fig. 3). All ages and intercepts are reported at the 95% confidence level unless stated otherwise. The sample locations, depths and characteristics are presented in Table 1, while U–Pb data for each sample and method are

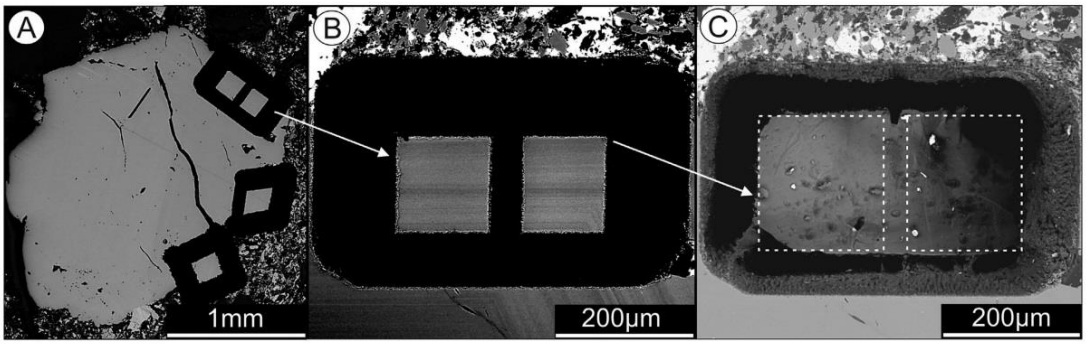


Fig. 2. (A) Reflected light photomicrograph of the largest hematite grain in sample LCD4, displaying four laser cut trenches; (B) BSE image of an enlarged area from 2A. Oscillatory zonation can clearly be seen within the 100 × 100 μm squares; (C) BSE image of the same area as 2B, after manual removal of the squares. The bottom surface is flat indicating no additional material was sampled during the extraction process. Bright flecks at the bottom of the trenched area are fragments of remnant material and dirt rather than inclusions within the hematite. The depth from the grain surface to the bottom of the extraction site was generally ~150 μm.

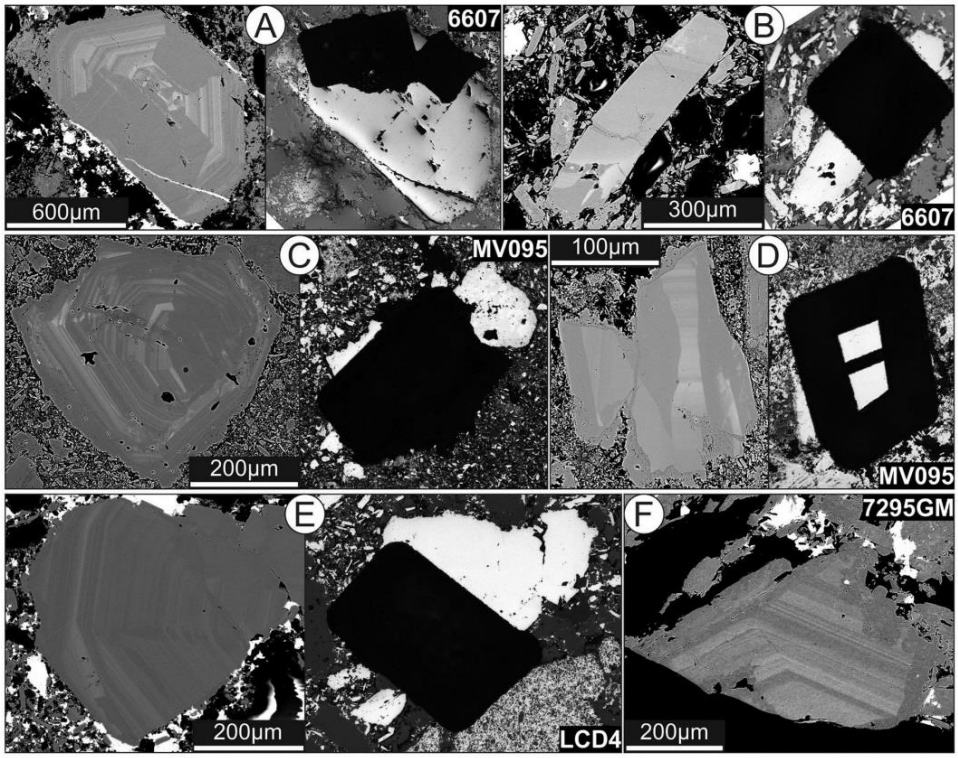


Fig. 3. Selection of BSE and optical images of hematite grains showing the range of grain sizes and oscillatory/sectorial zonation patterns which were microsampled for ID-TIMS; (A–B) Sample RX6607 grain 1 and 2; features mm size grains with strong zonation patterns as well as overprint truncating such zones. (C–D) Sample MV095; featuring the smallest average grain size of all samples. The optical photomicrograph displays the trenches prior to extraction; (E) Sample LCD4 grain 2; two aliquots were extracted from this grain, while 3 more came from a larger grain shown in Fig. 2; (F) Sample 7295GM; a very large, clearly-zoned grain on the edge of the polished block prior to laser cutting.

reported in Tables A1-3.

4. Results

Prior to LA-ICP-MS data collection, the effect of varying laser fluence was assessed (Fig. 4). A single 1 mm-sized grain of zoned hematite (spots selected randomly) was ablated at eight different fluence settings between 1.5 and 8.5 J cm^{-2}. Eight hematite spot analyses for each fluence setting were bracketed and normalized to four GJ-1 reference zircon analyses, which was ablated at a constant fluence of 2.5 J cm^{-2} while the hematite fluences were changed. Below 2.5 J cm^{-2} only reversely discordant hematite data were produced, whereas analyses above 5.5 J cm^{-2} yielded entirely discordant data (Fig. 4). The fluence yielding the most consistently concordant hematite data (3.5–4 J cm^{-2}), and mutually consistent concordance for GJ-1 (2.5 J cm^{-2}) was selected for subsequent LA-ICP-MS U—Pb spot data acquisition. However, the fluence selection here is based on assumed concordance of the unknown.

4.1. Sample LCD4

4.1.1. Petrography

Oscillatory-zoned grains are common in this sample (~15% by area) and range in size from ~20 μm to over 1000 μm in diameter, often as aggregates with well-preserved zonation. Smaller, more porous grains which are not visibly zoned make up the majority of the hematite in the sample and average ~20 μm in size. Grains across the sample average hundreds of ppm U and can reach up to ~2000 ppm, while Th is below detection limit for LA-ICP-MS. Sample LCD4 was dated by LA-ICP-MS, ID-TIMS and isotopically mapped. The largest grain in this sample (1100 × 1300 μm) displayed bright zonation on BSE images whilst being relatively clean and free of inclusions. This was ideal for assessing intra-grain heterogeneity using isotopic mapping, as well as being large enough to micro-sample 3 areas for ID-TIMS to gain high precision data from mapped areas deemed most isotopically homogeneous.

4.1.2. LA-ICP-MS mapping

Isotope ratio and concentration maps were obtained for the previously discussed and largest grain in the sample (LCD4 grain 2) prior to LA-ICP-MS and ID-TIMS dating (Fig. 5). The resultant images were acquired during an 8-hour session over a 1200 × 1400 μm area. Elemental zonation in the grain is observed in BSE images as distinct bright and darker bands (Fig. 5A). Other bright areas within the grain are attributable to sulfide infill and inclusions. Uranium concentrations reveal two distinct domains within the grain (Fig. 5B): 1) the right-hand side and remnant segments at the bottom and top left of the grain which contain much higher concentrations of U; and 2) the left-hand side, with distinctly lower U concentrations, which progressively decrease away from the high-U domain.

The two U—Pb and Pb—Pb isotope maps, like the U concentration

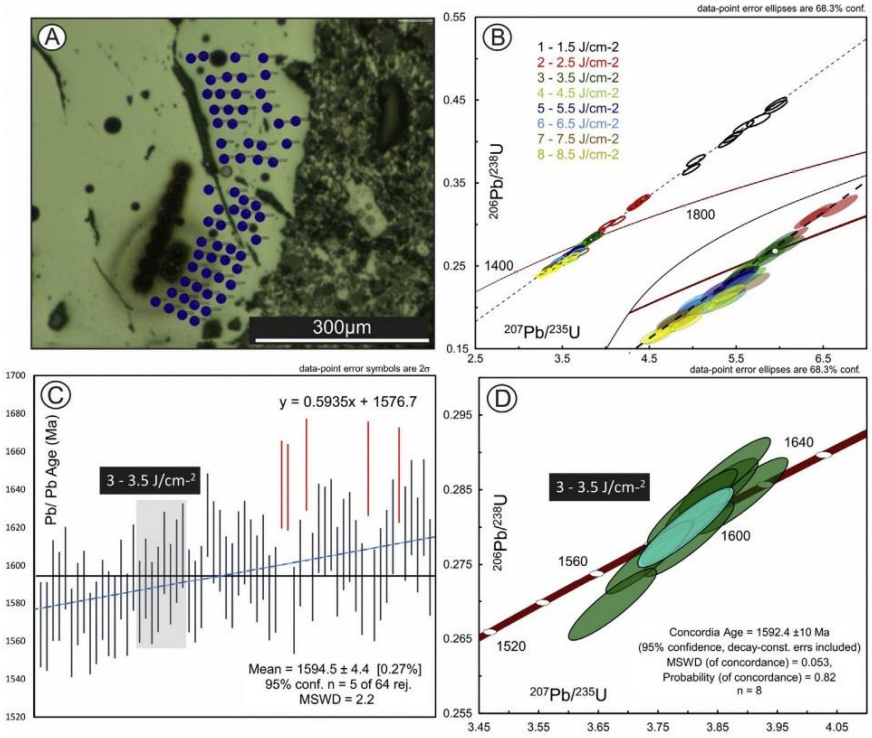


Fig. 4. Effect of different LA-ICP-MS fluences when ablating oscillatory-zoned hematite; (A) Location of spots which were picked randomly along the zonation of a grain of clean, zoned-hematite; (B) Wetherill Concordia diagram displaying the results of different fluences applied. Eight spots were ablated for each selected fluence shown on the diagram. At low fluence the data plots reversely discordant, and is discordant at higher fluences; (C) $^{207}Pb/^{206}Pb$ weighted average diagram displaying the above results. The most concordant data from (B) used a fluence of 3.5 J cm^{-2} which is highlighted in the grey rectangle; (D) Wetherill Concordia diagram showing the Concordia age of the most concordant analyses. The optimal fluence for U–Pb dating of hematite using LA-ICP-MS ranges between 3 and 4 J cm^{-2}.

map (Fig. 5C–F), show a sharp contrast between the right and left-hand sides of the grain. The U-rich side of the grain gives an apparent 'older' average age for the $^{206}Pb/^{238}U$ (equivalent to ~1.8 Ga or 0.2 ratio) compared to $^{207}Pb/^{206}Pb$ (~1.6 Ga). The yellow regions of both images indicate Pb_c, which clearly follows fractures, inclusions and sulfide infills within the hematite grain, as well in the surrounding minerals such as chalcopyrite, barite and porous hematite.

Inter-grain $^{207}Pb/^{206}Pb$ variability was evaluated using 'Monocle' (Fig. 5G). Pixels corresponding to seven ranges of $^{207}Pb/^{206}Pb$ were assigned different colors, with $^{207}Pb/^{206}Pb$ values closest representing an assumed formation age of ~1593 Ma assigned to 0.005 $^{207}Pb/^{206}Pb$ intervals. $^{207}Pb/^{206}Pb$ zonation in the U-rich side of the grain is visible, albeit with a heterogeneous distribution of ranges between 0.010 and 0.2 $^{207}Pb/^{206}Pb$, equivalent to a large spread in dates. There are however far more pixels representing dates around ~1593 Ma within the U-rich side than the U-poor side, dominated by high $^{207}Pb/^{206}Pb$ ranges. Combined U–Pb, Pb–Pb and U concentration mapping shows the interior of higher-U zones yield ~1.6 Ga while the edges of the high U zones produce high and low $^{207}Pb/^{206}Pb$ dates. Variation in $^{207}Pb/^{206}Pb$, both higher and lower than ~1593 Ma, follows oscillatory zoning shown in the BSE image. Low $^{207}Pb/^{206}Pb$ dates extracted from the 'Monocle' map (Fig. 5G) supports non-zero age Pb-loss, while older dates are attributable to Pb_c.

4.1.3. LA-ICP-MS

Data were collected from 6 grains (30 spots), with selection based on SEM imaging of inclusion free oscillatory-zoned grains larger than ~100 μm (Fig. 3E). Concentration of U ranges from 244 to 1800 ppm (mean = 657 ppm).

The associated Wetherill Concordia diagram (Fig. 6A) shows a single point plotting discordantly (1.88%) while the remaining spots plot reversely discordant (−1.4 to 10.5%). The lack of a consistent single population and a geologically meaningful weighted average date in the $^{206}Pb/^{238}U$ data at the achievable level of precision is documented by the high MSWD (MSWD = 35, n = 30) of the $^{206}Pb/^{238}U$ weighted mean date (1702 ± 16 Ma).

A Discordia line including all data yields lower and upper intercepts at 335 ± 310 and 1605 ± 15 Ma (MSWD = 6.5; n = 30) also indicating excess scatter. Including the external propagated uncertainties (95% confidence interval) without rejecting any points, a date of 1615.2 ± 8.3 Ma, with an appropriate MSWD of 0.66 was obtained.

4.1.4. ID-TIMS

Five aliquots were successfully subsampled from two grains. The first grain (250 × 200 μm, n aliquots = 2, Fig. 3E) represents the average grain size for zoned hematite in this sample. Grain two (1200 × 800 μm; n aliquots = 3, Fig. 2A) had a higher U concentration.

Ratios of radiogenic Pb to initial common Pb (Pb^*/Pb_c) (after laboratory blank subtraction) range between 3 and 264 (mean = 97).

The Wetherill Concordia diagram (Fig. 6B) shows three overlapping data points that also overlap with Concordia. One datum is slightly above Concordia and while another is highly reversely discordant.

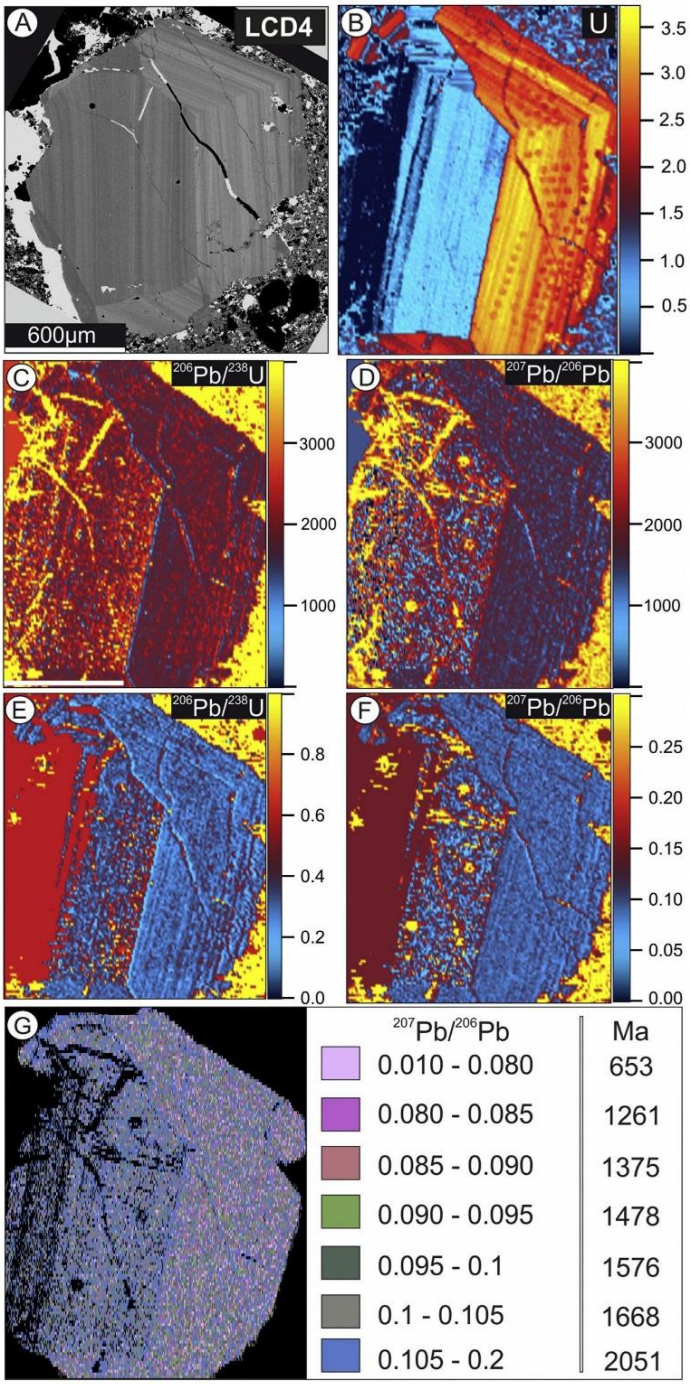


Fig. 5. (A) BSE image and (B–F) LA-ICP-MS element/isotope maps of oscillatory-zoned hematite from sample LCD4; (B) Uranium distribution map (scale: counts per second, 10^n) displaying a sharp divide in U concentrations between two domains within the grain; (C) $^{206}Pb/^{238}U$ and (D) $^{207}Pb/^{206}Pb$ age maps (scale in Ma) mirror the U concertation, clearly defining the heterogeneous domain to the left. (E–F) $^{206}Pb/^{238}U$ and $^{207}Pb/^{206}Pb$ pure isotope ratio maps. The red areas to the left of the ratio maps are due to a thresholding issue and should be ignored. (G) $^{207}Pb/^{206}Pb$ isotope range variation map constructed using 'Monocle'. Coloured boxes represent the different ranges of coloured pixels and correspond to averaged $^{207}Pb/^{206}Pb$ dates (Ma). (For interpretation of the references to colour in this figure legend, the reader is referred to the web version of this article.)

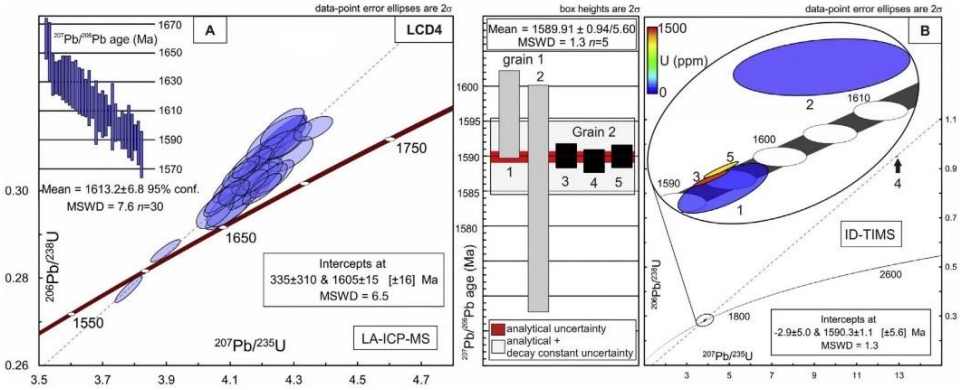


Fig. 6. (A) LA-ICP-MS and (B) ID-TIMS Wetherill Concordia and $^{207}Pb/^{206}Pb$ weighted average diagrams (Sample LCD4). The insert on the ID-TIMS Concordia diagram is of the most concordant aliquots, as aliquot LCD4-4 contains very high Pb/U. Aliquots are coloured according to U concentration with values ranging from 16 to 1326 ppm. The $^{207}Pb/^{206}Pb$ weighted average to the left of the ID-TIMS Concordia presents data compared to the purely analytical uncertainty in a red rectangle, as well as the analytical and decay constant uncertainties in a white rectangle. The numbering (1–5) matches the weighted average aliquots to the Concordia plot aliquots. The $^{207}Pb/^{206}Pb$ weighted mean date for the 3 aliquots with the lowest uncertainties (LCD 3–5) is 1589.79 ± 0.95 Ma (MSWD = 0.45). (For interpretation of the references to colour in this figure legend, the reader is referred to the web version of this article.)

However, aliquot LCD4-4 (−38% discordancy), yields a $^{207}Pb/^{206}Pb$ date of 1589.17 ± 1.6 Ma, within uncertainty of the main population indicating that while aliquots may contain excess Pb, they still yield $^{207}Pb/^{206}Pb$ dates consistent with concordant data. All data lie along a Discordia line that yields lower and upper intercepts at −2.9 ± 5.0 and 1590.3 ± 1.1 Ma (MSWD = 1.3; n = 5), respectively, in agreement with the $^{207}Pb/^{206}Pb$ age data (Fig. 6B) which yield a weighted mean date of 1589.9 ± 1.5 Ma (MSWD = 1.3, n = 5).

4.2. Sample MV005A

4.2.1. Petrography

Zoned hematite is rare in this sample, but one large grain (1000 × 500 μm) contains zonation patterns, albeit with cracks and displacements indicating intense brecciation (Fig. 7A). MV005A was obtained from just outside of the orebody at OD and contains high concentrations of Th (up to 30 ppm, and 400 ppm U by LA-ICP-MS).

4.2.2. LA-ICP-MS Mapping

Isotope ratio and concentration maps from a 1200 × 900 μm area were obtained for MV005A prior to LA-ICP-MS and ID-TIMS dating. The BSE image reveals faint zonation patterns (Fig. 7A). Domains extracted for ID-TIMS are numbered in the photomicrograph (Fig. 7B), and correspond to numbering within the ID-TIMS Concordia for individual aliquots (Fig. 8). The U concentration map shows a clear sectorial zoning within the grain (Fig. 7C), mirroring the light and dark zonation in Fig. 7A. Thorium concentrations (Fig. 7D) more closely mirrors the BSE image and differs from the sectorial pattern of U, suggesting decoupling between the two elements.

The two isotope ratio age maps (Fig. 7E, F) broadly show the same dates, representing ~1600 Ma. Common Pb follows and infills fractures and aggregate boundaries. This is reflected in far higher Pb^*/Pb_c in ID-TIMS aliquots from this area of the grain. The higher degree of fracturing may have also contributed to the introduction of more Pb_c to the sample (Fig. 7G, H).

Subsequent interrogation with 'Monocle' using six ranges of $^{207}Pb/^{206}Pb$ from 0.05 to 0.2 (Fig. 7I) clearly show that sector zones enriched in U (Fig. 7C) contain $^{207}Pb/^{206}Pb$ dates most consistent with ~1593 Ma. Adjacent oscillatory zones, particularly on the boundaries of high-U domains, contain sharp changes in $^{207}Pb/^{206}Pb$ dates, both older and younger than ~1593 Ma. Low U domains are dominated by older $^{207}Pb/^{206}Pb$ dates corresponding to high proportions of Pb_c, most evident within fractures and voids matching the BSE image. LA-ICP-MS spot data for this grain ranged from a cluster at ~1600 Ma up to ~2000 Ma ($^{207}Pb/^{206}Pb$), mirroring the high $^{207}Pb/^{206}Pb$ dates within the maps and their corresponding spot locations in Fig. 7B.

4.2.3. LA-ICP-MS

Concentration of U ranges from 26 to ~2300 ppm (mean = 482 ppm) for 20 spots from across the same grain reported for ID-TIMS and isotope mapping (Figs. 7 and 8).

The Wetherill Concordia diagram (Fig. 8A) shows that most of the data plot around Concordia, although only 6 out of 20 overlap with the curve, while two data are noticeably discordant and older, suggesting a significant component of Pb_c. A coherent $^{207}Pb/^{206}Pb$ population at 1600.6 ± 7.3 Ma (MSWD = 1.5, n = 13) is obtained by excluding 7 low U analyses.

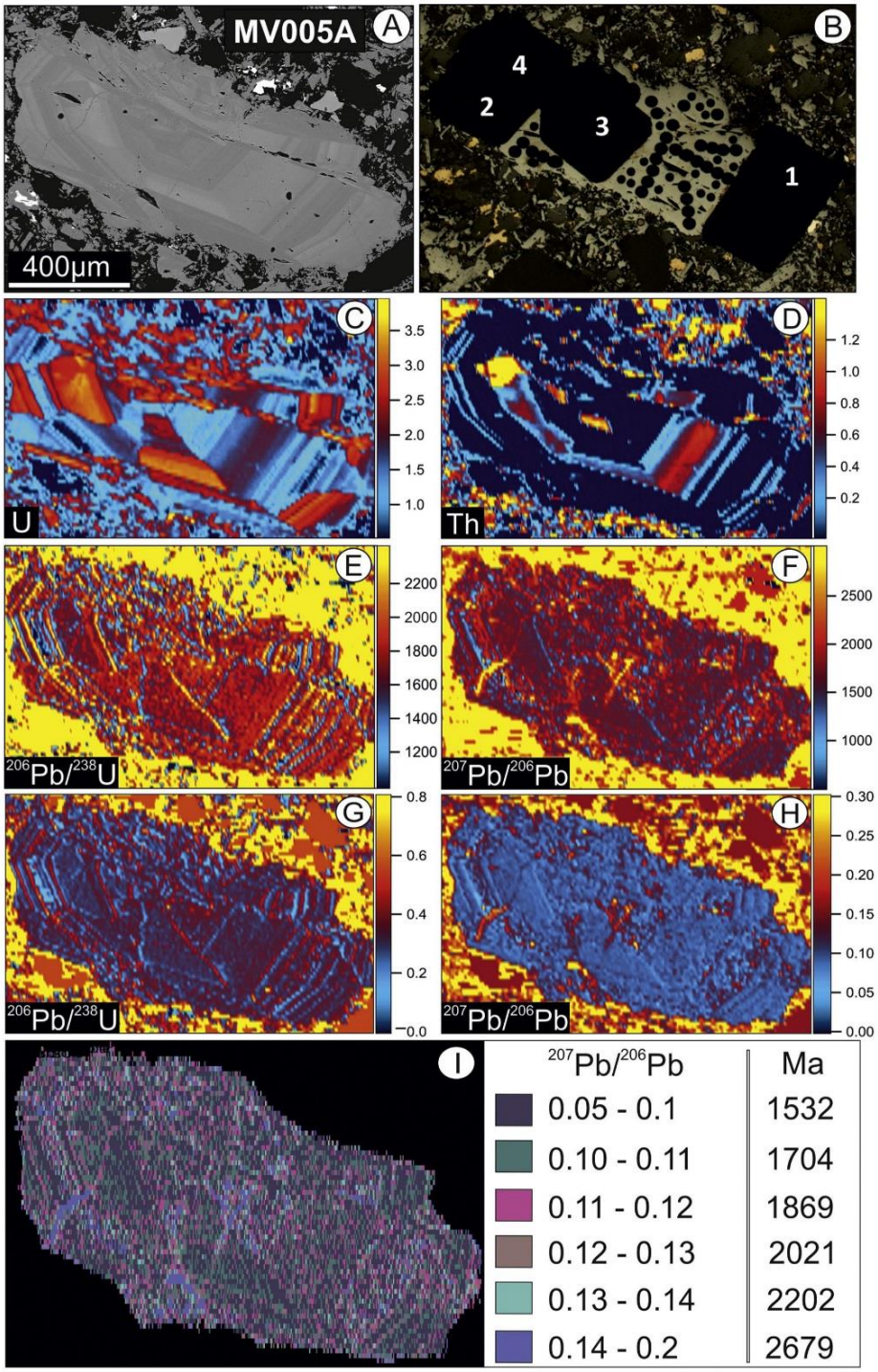
4.2.4. ID-TIMS

Four aliquots were sampled from a single grain. The positions of the sampled material are numbered in Fig. 7B as on the ID-TIMS Concordia (Fig. 8B). Pb^*/Pb_c ranges between 2 and 56 (mean = 18). The Wetherill Concordia diagram (Fig. 8B) shows only one precise data point overlapping Concordia, with a $^{207}Pb/^{206}Pb$ date of 1584.7 ± 2.4 Ma. Other aliquots plot both discordantly (13.3%) and reversely discordant (−0.61 and −1.49%). All data lie along a Discordia line which yields lower and upper intercepts at 160 ± 120 and 1587 ± 15 Ma (MSWD = 8.4; n = 4), respectively. Exclusion of the most discordant datum (aliquot MV005-2), intercepts at 722 ± 230 and 1587.6 ± 3.2 Ma with an MSWD of 0.001 (n = 3).

4.3. Sample RX6607

4.3.1. Petrography

Hematite is predominantly fine-grained within the matrix of a fluorite-rich, hematite breccia (Fig. 3A, B), but coarse-grained, zoned hematite grains up to ~2 mm are also found. One such grain, preserves oscillatory/sectorial zoning despite being locally heavily overprinted, as indicated by the darker regions cross cutting the brighter oscillatory zonation (Fig. 3A). This grain shows decoupling between granitophile elements, e.g., selective depletion of W yet retention of Sn zonation, in the overprinted parts (Verdugo-Ihl et al., 2017). Such overprint most



(caption on next page)

Fig. 7. Oscillatory-zoned hematite from sample MV005A; (A) BSE image prior to ID-TIMS extraction and LA-ICP-MS spot analysis; (B) Optical reflected light photomicrograph displays the removed areas and LA-ICP-MS spots, the smaller spots (29 μm) are U–Pb analyses while the larger (51 μm) spots were for trace element analysis; (C–D) Uranium and Th concentration maps (scale: counts-per-second 10^n); (E–F) $^{206}Pb/^{238}U$ and $^{207}Pb/^{206}Pb$ isotope ratio maps (scale in Ma). (G–H) $^{206}Pb/^{238}U$ and $^{207}Pb/^{206}Pb$ pure isotope map ratios. (I) $^{207}Pb/^{206}Pb$ isotope variation map interrogated using 'Monocle'.

likely contributes to lower concentrations of U (average ~ 20 ppm) and the lower precision of obtained U–Pb data.

4.3.2. LA-ICP-MS

Data comprise 19 spots from 7 grains. All analyses plot reversely discordant (−7.7 to −23.6%). The $^{207}Pb/^{206}Pb$ age data (Fig. 9A) ranges between 1502 and 1662 Ma and yield a weighted mean date of 1597 ± 12 Ma (MSWD = 1.6; n = 19).

4.3.3. ID-TIMS

Four aliquots were prepared from two grains (Fig. 3A, B). All 4 dates (Fig. 9B) plot reversely discordant (−15 to −31%). $^{207}Pb/^{206}Pb$ age data ranges between 1204 and 1541 Ma, measured Pb_c was the highest of all samples, ranging from 40 to 320 pg ($^{238}U/^{204}Pb$ ranges from 93 to 584).

4.4. Sample MV095

4.4.1. Petrography

Hematite-quartz rich breccia containing grains ranging from 300 μm at their largest to predominantly fine (~10 μm) grains of zoned hematite, which are considerably more porous and inclusion-rich than previously described samples (Fig. 3C, D). This sample contains low U concentrations, generally below 10 ppm, and was included to test its reliability for dating. The grain size is not ideal for ID-TIMS, since a majority of grains were too small for extraction, pointing towards a

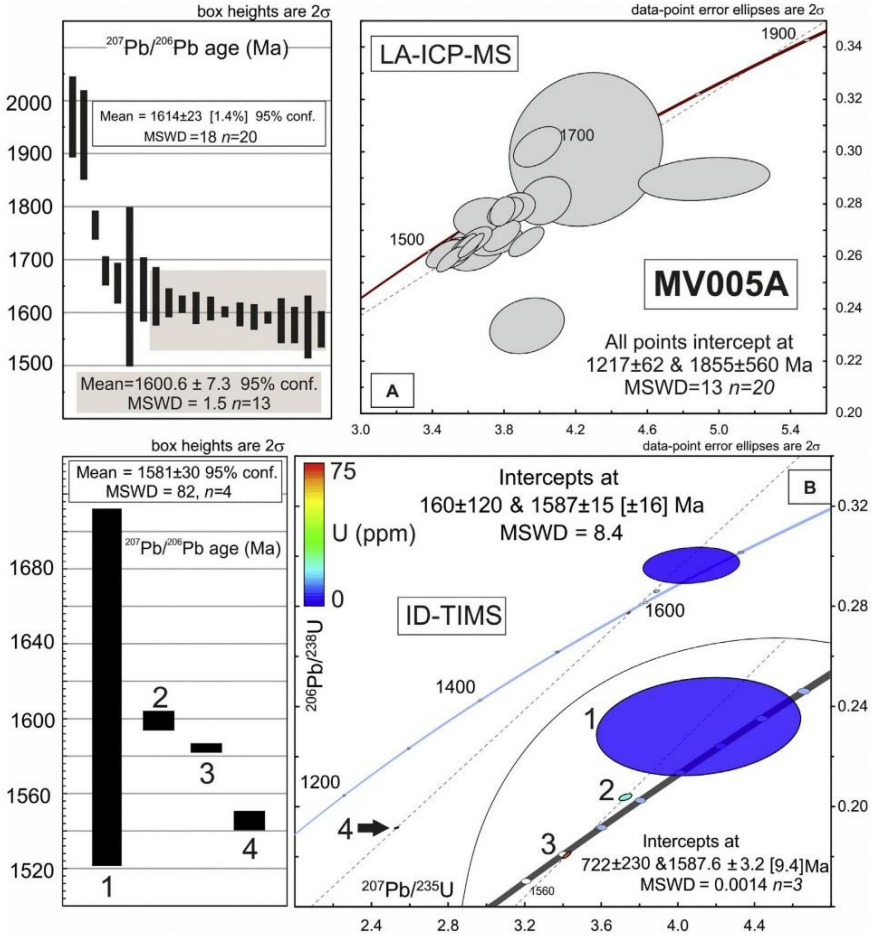


Fig. 8. LA-ICP-MS (A) and ID-TIMS (B) Wetherill Concordia and corresponding $^{207}Pb/^{206}Pb$ weighted average diagrams for sample MV005A. The ID-TIMS aliquots are numbered to link the data on the Concordia diagram with the $^{207}Pb/^{206}Pb$ weighted average. The aliquots with the lowest uncertainties also contain the highest U concentrations (U ranges from 2 to 75 ppm).

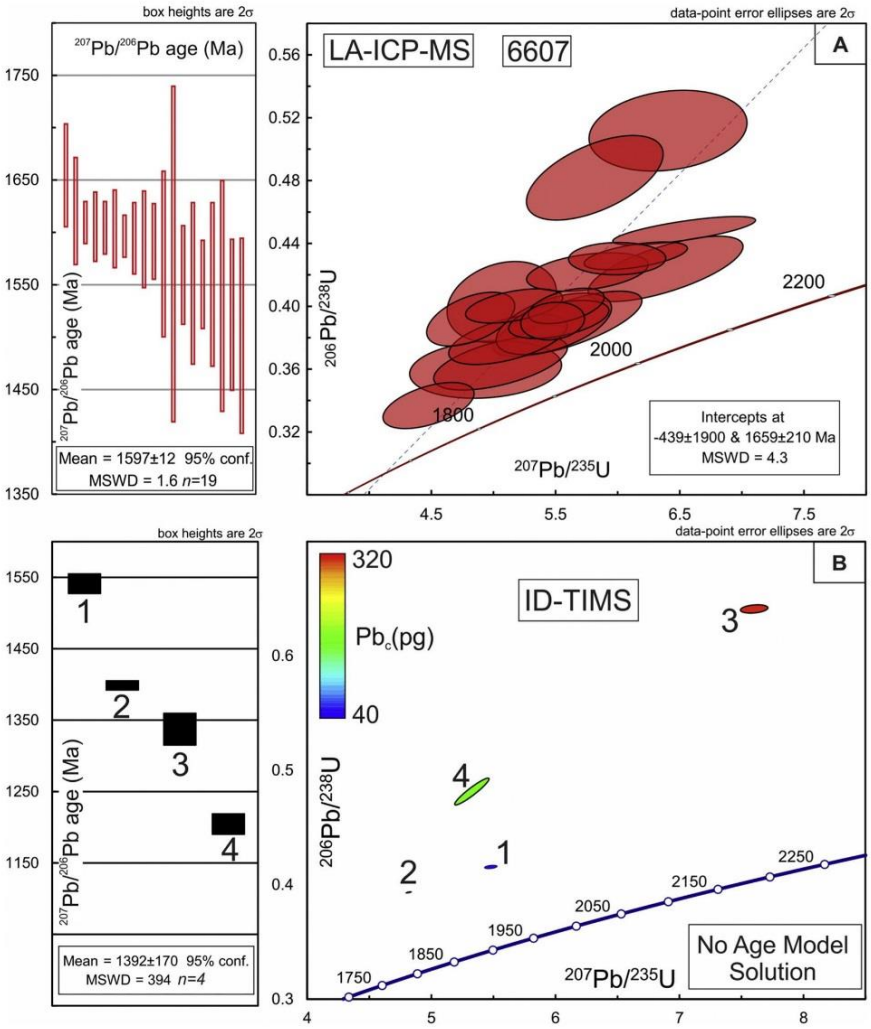


Fig. 9. Sample RX6607 (A) LA-ICP-MS and (B) ID-TIMS $^{207}Pb/^{206}Pb$ weighted average and Wetherill Concordia diagrams. The ID-TIMS data points are colour coded according to their Pb_c components ranging from 40 to 320 pg.

greater suitability for microbeam examination.

4.4.2. LA-ICP-MS

Data comprise 19 spots from 5 grains. Of the 19 spot analyses (Fig. 10A), 3 are discordant (2.5 to 10.2%) while the remaining spots plotting reversely discordant (−1.3 to −51%). The normally discordant data clearly have a significant component of Pb_c while the other data appear to be affected by variable bias in Pb/U but show relatively consistent $^{207}Pb/^{206}Pb$. Nine data points containing the lowest U concentrations give an average $^{207}Pb/^{206}Pb$ age of 1568 ± 9 Ma with an MSWD of 2.9 (n = 9).

4.4.3. ID-TIMS

Three U–Pb data were measured on aliquots from 2 grains. All 3 dates (Fig. 10B) are highly discordantly (34 to 74%). $^{207}Pb/^{206}Pb$ ages range between 1687 and 2531 Ma. The model Th/U ratios are extremely high (average of 671 whereas most other samples are < 0.002), which suggests that the inclusions are monazite or some other REE mineral.

4.5. Sample 7295GM

4.5.1. Petrography

Hematite-rich breccia at depth (Table 1) contains coarse oscillatory-zoned hematite laths (average ~200 μm) co-existing with minor magnetite. Zoned-grains show a variable degree of overprint, featuring porosity, inclusion nucleation, and loss of primary zonation patterns, nonetheless several grains are relatively fresh compared to other samples (Fig. 3F). This sample was dated by LA-ICP-MS, SHRIMP and ID-TIMS, allowing exploratory investigations into the suitability of such

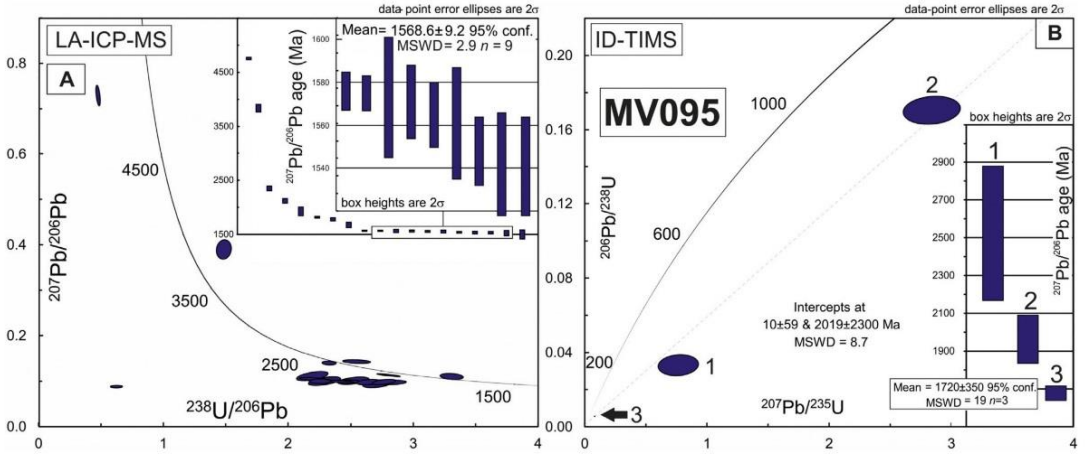


Fig. 10. Sample MV095 (A) LA-ICP-MS Terra-Wasserburg and (B) ID-TIMS Wetherill diagrams. The LA-ICP-MS contains two weighted average inserts due to the large spread in $^{207}Pb/^{206}Pb$ dates.

material to the SHRIMP method, while also allowing inter-microbeam instrument comparisons. The particularly large grain size of hematite in this sample (> 800 μm) provided the space for the multiple method comparison all within the same grains (Fig. 4F).

4.5.2. LA-ICP-MS

Data for 28 spots from 8 grains vary from concordant to 5.5% discordant (Fig. 11A), but have overlapping $^{207}Pb/^{206}Pb$ ages that yield a weighted mean date of 1597 ± 12 Ma (MSWD = 0.41; n = 28).

4.5.3. SHRIMP

Data comprise 23 spots from 6 grains. Of the 23 spots, 2 plot discordantly (6%) while the remaining spots plot concordant to reversely discordant (up to 8%). All data points lie along a Discordia line which yields lower and upper intercepts at −60 ± 290 and 1590 ± 17 Ma (MSWD = 2.3; n = 23), respectively. The $^{207}Pb/^{206}Pb$ age data (Fig. 11B) yield a weighted mean date of 1588.4 ± 8.4 Ma, (MSWD = 2.3; n = 23), rejection of 4 outliers (Fig. 11B, rejected points in yellow) reduces the MSWD to 0.66 (1588.7 ± 5.5 Ma, n = 19).

4.5.4. ID-TIMS

From sample 7295GM, five aliquots from four grains that ranged in size from 100 × 100 to 400 × 300 μm were selected and microsampled for ID-TIMS analysis. Four data points overlap or are close to Concordia while one is 57% discordant with a slightly older $^{207}Pb/^{206}Pb$ age (Fig. 11C). One concordant datum has a significantly younger $^{207}Pb/^{206}Pb$ age (1520 Ma) while the other 3 give a mean $^{207}Pb/^{206}Pb$ age of 1584 ± 5 Ma (MSWD = 0.7).

5. Discussion

5.1. Evaluating the U–Pb and Pb–Pb systematics of hematite

5.1.1. Common Pb in hematite

Incorporation of Pb_c, a mixture of initial (^{204}Pb) and unsupported radiogenic Pb, within an analysed volume of hematite presents an issue for accurate interpretation of geochronological data, as mixing with Pb_c drives data towards apparently older $^{207}Pb/^{206}Pb$ dates. The effects of Pb_c can be observed within the LA-ICP-MS data where no correction for Pb_c has been applied. Without correction, all samples demonstrate a number of $^{207}Pb/^{206}Pb$ dates that are significantly older than the ~1593 Ma age of the host granite formation (Fig. 12) and must be attributed to a component of Pb_c. Highly variable amounts of Pb_c within the analysed volumes of hematite are supported by the range of Pb_c in ID-TIMS analyses, containing concentrations comparable to the measured laboratory blank contribution (~3.6 pg), but are commonly an order of magnitude higher, and reach a maximum value of 312 pg. Corrections for Pb_c have been applied to the ID-TIMS data sets using an initial Pb composition from Stacey and Kramers (1975) two-stage Pb isotope evolution model at the nominal sample age (1593 Ma in this study), yet any inaccuracies within this correction will limit the robustness of data interpretation. Confidence in the correction can be gained from sample LCD4, whereby aliquots containing < 20 pg U and proportionally high Pb_c (e.g. LCD4-2 $^{206}Pb/^{204}Pb$ = 213) provide corrected $^{207}Pb/^{206}Pb$ dates within uncertainty of aliquots that are relatively insensitive to the Pbc correction (e.g., LCD4–4 and 5; $^{206}Pb/^{204}Pb$ = 17,010 and 8665 respectively), suggesting that the isotopic composition of Pb_c used for the correction is valid in this instance. However, $^{207}Pb/^{206}Pb$ dates well in excess of ~1593 Ma in sample MV095 infer that this may not always be the case.

The component of Pb_c associated with the hematite of this study may have been incorporated as: 1) initial Pb_c within the hematite lattice, introduced during mineral crystallisation; 2) Pb_c that may have been introduced to the crystal by diffusion from surrounding minerals or exchanged with later fluids during mineral alteration; 3) Inclusion of Pb_c–rich minerals such as sulfides within the analysed volume of hematite. Incorporation of Pb_c into the hematite lattice during crystallisation is probable, as shown for sample RX6607 that yields analyses with consistently high Pbc. Oscillatory-zones which define $^{207}Pb/^{206}Pb$ dates in excess of the ~1593 Ma host granite within isotope maps of Fig. 7 may also be invoked as evidence for this. However, the hematite did not always incorporate high enough concentrations of Pb_c during initial crystallisation to significantly affect the U–Pb systematics at the resolution of mapping, particularly in the highest-U grain domains, as for example sample LCD4, supported by the amounts of Pb_c in some ID-TIMS fractions which were indistinguishable from the laboratory blank contribution. In these instances, dates affected by Pb_c may not be distinguishable from dominant date population using low precision LA-ICP-MS analyses, presenting issues for the interpretation of microbeam data sets. This is apparent in sample 7295GM, whereby high precision older $^{207}Pb/^{206}Pb$ dates (1620 Ma) are present in the ID-TIMS dataset, while the LA-ICP-MS dates become biased to slightly older low-

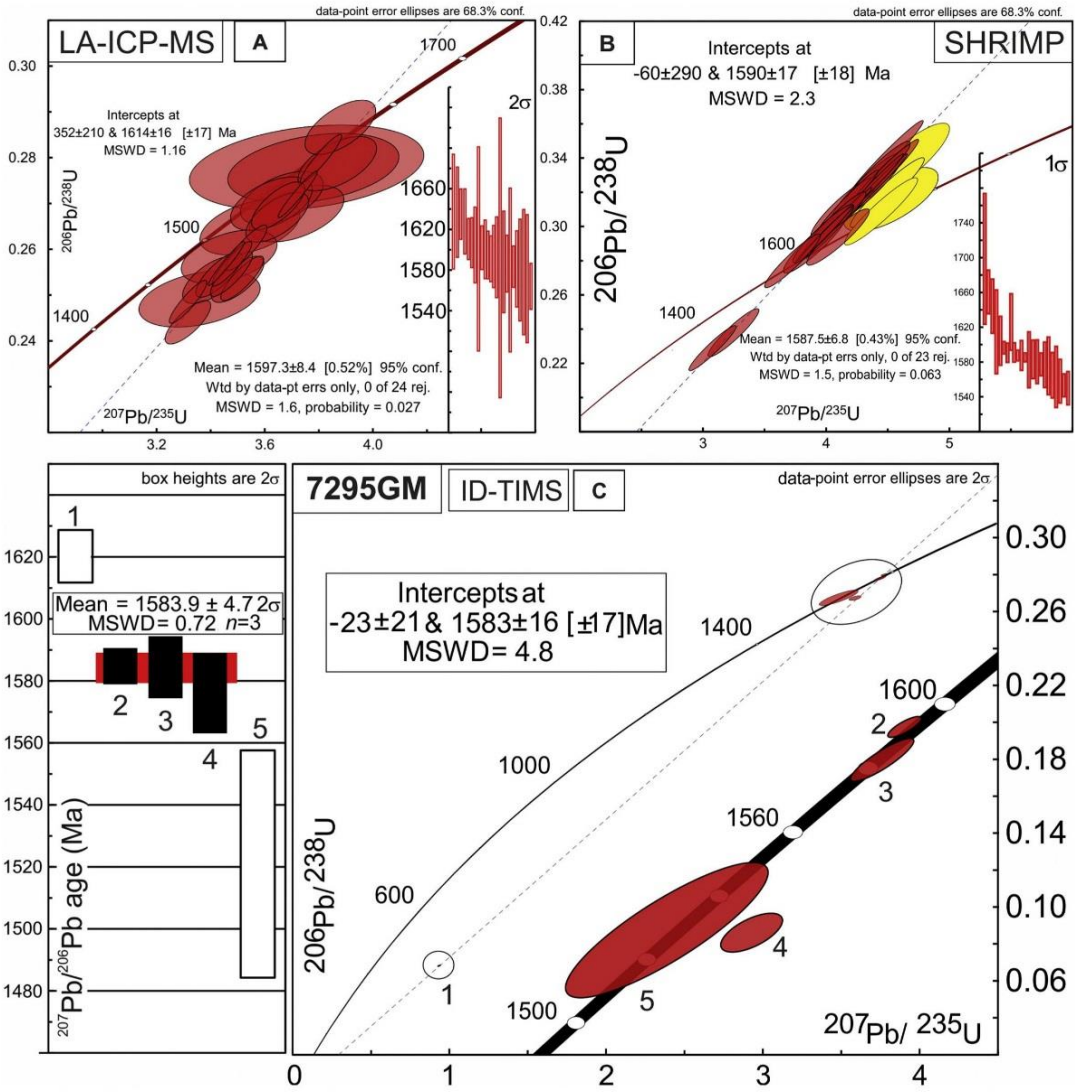


Fig. 11. (A) LA-ICP-MS, (B) SHRIMP and (C) ID-TIMS Wetherill Concordia and $^{207}Pb/^{206}Pb$ weighted average diagrams for sample 7295GM. The ID-TIMS diagram contains an insert of the most concordant data. SHRIMP spots with the lowest uncertainties are closest to the age of the magmatic Olympic Dam zircon. In general, the worse the precision in the SHRIMP analysis, the further the data (Pb—Pb) falls from this value. This implies that heterogeneity within the analysis pit is what is controlling the bias for the SHRIMP analyses. Yellow spots indicate excluded data corresponding to an optimum weighted average age. (For interpretation of the references to colour in this figure legend, the reader is referred to the web version of this article.)

precision dates, as well as potentially leveraging the freely regressed lower intercept date.

The isotopic maps highlight that the distributions of Pb_c-rich domains are predominantly associated with inclusions, fractures and veinlets that cross-cut and overprint oscillatory zonation. Extensive fracturing within the low U domain of the mapped grain of LCD4 is accompanied by elevated Pb_c. It can be inferred that post-formation processes (e.g., fluid-mineral interaction) introduced or facilitated the incorporation of Pb_c into certain grains, grain domains or zones. Whilst the lower-U concentrations may result from primary variations, it may also support a decoupling between granitophile element distributions within hematite (Verdugo-Ihl et al., 2017) resulting in high Pb_c and low U grains. Ultimately, this suggests that a single Pb_c mixing component is unlikely to be suitable for hematite within complex ore forming environments, if petrographic evidence of overprinting is observed. The addition of Pb_c bearing inclusions or fractures to the analysed volume is potentially one of the major sources in the hematite, and also presents more of an issue for the higher volume, lower spatial resolution ID-TIMS analyses, whereby the petrographic controls that can be used to avoid these features on a planar surface, become less useful with greater

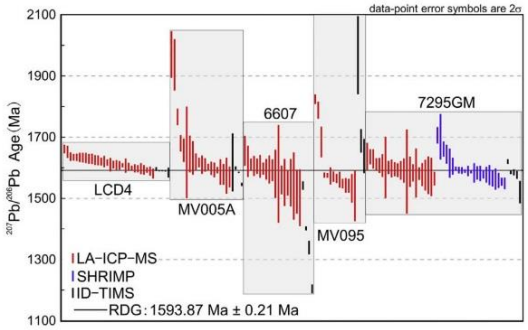


Fig. 12. Individual $^{207}Pb/^{206}Pb$ data points for each sample and analytical method. The grey line at 1593.87 Ma represents the age of magmatic zircon at Olympic Dam (Cherry et al., 2018).

sub-surface sampling. In the instances where inclusions are likely the dominant source of Pb_c, the higher spatial resolution of microbeam techniques may hold an advantage over the bulk sampling method of ID-TIMS, as is evident in sample MV095 (Fig. 10), which yields $^{207}Pb/^{206}Pb$ dates that are generally closer to the ~1593 Ma host granite age, and more precise, than the ID-TIMS U–Pb dates after the Pb_c correction has been applied. Sub-micron inclusions not visible using standard SEM techniques, but indicated by other geochemical features of U–Pb analyses such as high Th/U ratios, may also exert a control on the Pb_c component.

5.1.2. Evaluating the causes of reverse discordancy within hematite U–Pb dates

Both ID-TIMS and microbeam data-sets of all samples demonstrate significant dispersion in U–Pb dates that is induced by both normal and reverse discordance. During microbeam data acquisition, fractionation of Pb and U can occur during analysis due to the higher volatility of Pb compared to U, which cannot be accurately corrected for without matrix-matched reference materials (Jackson et al., 2004). In this study, decreasing laser fluences generate increased Pb/U fractionation when measured relative to the non-matrix matched zircon reference material, and therefore drive analyses to reverse discordancy if the fluence used is too low (relative to the zircon reference material ablated at 2.5 J cm^{-2}) and will likely underestimate the normal discordancy, or Pb-loss, within hematite data. Nevertheless, this is based on the assumption of concordance in the sample used. Variation within the hematite material that has domains containing wt% concentrations of granitophile elements also has the potential to generate fractionation as hematite may ablate differently based on chemistry.

Reverse discordance within the ID-TIMS data could be induced by laboratory artefacts such as the loss of U prior to attaining equilibrium with the tracer, the formation of insoluble U-rich precipitates, or the incomplete dissolution of hematite. Hematite in this study was exposed only to water and acetone during sample preparation, making the removal of lattice bound U (Ciobanu et al., 2013) unlikely, but indicating an extreme susceptibility to disturbance of the U–Pb system if this were the case. Likewise, the apparent total dissolution of aliquots when examined using a binocular microscope and the ability to achieve concordant data using the same method, suggests that at least some of the observed reverse discordance results from a real feature of the hematite U–Pb isotopic systematics. Step-wise zircon dissolution experiments have shown that relatively low-U zones in some zircon can contain "excess" or "parentless" radiogenic Pb (Mattinson et al., 1996) that results in reverse discordance following dissolution of the high-U zones during the process of chemical abrasion. The inferred mechanisms for this include Pb diffusion and boundary ejection of Pb at the interface between high-U and low U-zones despite the extremely slow diffusion of Pb in zircon. Without constraints on Pb and U diffusion rates in hematite it is difficult to assess just how effective this mechanism is at explaining the disturbance of U–Pb systematics. However, it seems probable that a comparable process is in operation within hematite whereby the U concentrations range over greater than an order of magnitude between ~20 μm scale oscillatory zones (34 to 565 ppm; Fig. 13, data shown in Table A4) provide a large concentration gradient and large interface surface between high-U and low-U zones. Micro-sampling hematite, either by laser ablation or the protocols utilised for ID-TIMS, is likely to select unequal amounts of zones that are either enriched (low-U) or depleted (high-U) in radiogenic Pb and will correspond with normal and reverse discordancy respectively, regardless of whether a crystal has remained an externally closed system. The implications of both analytically and geologically induced U–Pb fractionation must be considered when interpreting the U–Pb data, as much of the power of Concordia plots for interpreting Pb-loss and Pb_c is lost, crucially though, the $^{207}Pb/^{206}Pb$ dates should not be changed by U–Pb fractionation.

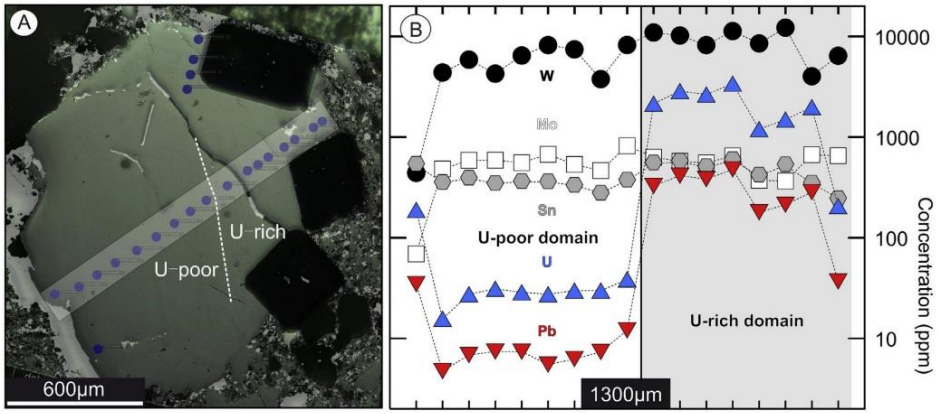


Fig. 13. LA-ICP-MS granitophile element composition transect through grain 1 in sample LCD4. The measured W, Sn and Mo remain relatively constant within both the right and left domain of the grain, shown to be markedly different in U–Pb composition by isotope mapping. The U-rich domain shows an increase in U and Pb concentrations of over an order of magnitude between individual spots placed ~20 μm from one another. LA-ICP-MS geochemical data shown in Table A4.

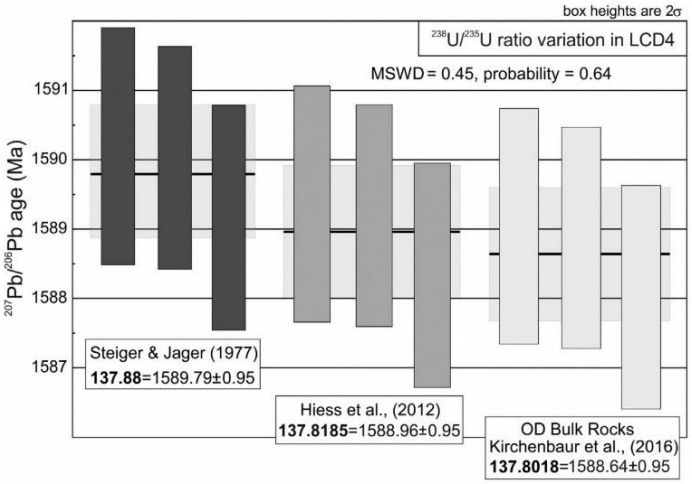


Fig. 14. $^{207}Pb/^{206}Pb$ weighted average diagram displaying the effect that variation of the assumed $^{238}U/^{235}U$ ratio can have on the calculated age for high precision data from sample LCD4. There is a ~1 Ma difference ($^{207}Pb/^{206}Pb$) between the ratio used in this study (Steiger and Jäger., 1977), and the ratio most likely to represent hematite breccias at Olympic Dam (Kirchenbaur et al., 2016).

5.1.3. Pb-loss within hematite

Despite the potential disturbance of hematite U–Pb systematics due to the analytical or sampling artefacts discussed in the previous section, the phenomena of geologically driven Pb-loss remains a probable explanation for the presence of U–Pb dates significantly younger than the ~1593 Ma age of the granite. Pb-loss that is ongoing to the present day will effectively have a zero-age intercept, and will therefore not reduce the $^{207}Pb/^{206}Pb$ date for a given aliquot. It is therefore of importance to explain why $^{207}Pb/^{206}Pb$ dates that are significantly younger than dates that cluster around the timing of granite emplacement are obtained from the same sample (Figs. 8 and 11). In order to generate the $^{207}Pb/^{206}Pb$ dates significantly younger than the ~1593 Ma clusters, either younger hematite growth must be present within the analyte volume, or, a non-zero age Pb-loss component must be invoked (as summarized in Schoene, 2014). The interpretation of younger $^{207}Pb/^{206}Pb$ dates is obscured by the variable degrees of U–Pb fractionation and reverse discordance as the system no longer adheres to binary mixing models. In turn this inhibits the ability to extract consistent or accurate lower intercept ages consistent with the timing of the younger geological event that caused the variation in dates.

Isotopically mapped hematite (Figs. 5 and 7) demonstrates that younger $^{207}Pb/^{206}Pb$ dates lie within zones that accord to the oscillatory zonation, bounded by zones that yield ~1593 Ma dates and supports that younger $^{207}Pb/^{206}Pb$ dates represent a component of non-zero age Pb-loss rather than later hematite growth. Mapping of sample LCD4 also documents younger $^{207}Pb/^{206}Pb$ dates in association with the fractured overprinted left domain of the crystal. Within the higher-U domain, evidence of younger $^{207}Pb/^{206}Pb$ dates can be extracted using 'Monocle', but are not clearly observed within the corresponding LA-ICPMS spot and ID-TIMS data, likely resulting from analyses being weighted by the high U-zones that appear to correspond to zero-age lower intercepts, rather than the volumetrically minor and lower U-zones of non-zero age Pb-loss. In contrast, both the LA-ICP-MS and ID-TIMS U–Pb data sets of sample MV005A demonstrate younger $^{207}Pb/^{206}Pb$ dates, and respectively form lower intercept dates of 1217 ± 620 and 722 ± 230. These lower intercept dates may result from tightly clustered, or low *n* data, and the incorporation of Pb_c-rich analyses that leverage the line of Discordia. However, non-zero age Pb-loss yielding a consistent lower intercept age of 927 ± 170 Ma has previously been documented by magmatic zircon from a rhyolite unit within the Olympic Dam breccia-complex, which hosts oscillatory-zoned hematite (Apukhtina et al., 2017). Whilst the intercept dates documented by the hematite must be treated with caution due to their interplay with other features such as Pb_c and fractionation of the U–Pb system, the independent evidence of non-zero age Pb-loss events at Olympic Dam indicates that $^{207}Pb/^{206}Pb$ dates can be disturbed by Pb-loss and weighted mean $^{207}Pb/^{206}Pb$ dates derived by lower precision microbeam methods, can be biased younger by components of this non-zero age Pb-loss.

5.2. The effectiveness of hematite as a U–Pb mineral geochronometer and implications for future hematite U–Pb geochronology

5.2.1. Effects of $^{238/235}U$ variation on external interpretation of U–Pb ages

The assumed $^{238}U/^{235}U$ of a dated material will exert a control on calculated $^{207}Pb/^{206}Pb$ due predefined decay rates within the coupled U–Pb decay chains (e.g., Hiess et al., 2012), and hence it is important to have an accurate estimation of the $^{238}U/^{235}U$ ratio for highly accurate age calculations. During this study the conventional value of 137.88 (Steiger and Jäger, 1977) was utilised, allowing comparison with the magmatic zircon ID-TIMS data-set of Cherry et al. (2018). Recent studies have identified natural isotopic fractionation within U-bearing accessory minerals from a wide range of lithologies and geological settings (Stirling et al., 2007; Weyer et al., 2008; Hiess et al., 2012) with a preferred value for zircon of 137.818 ± 0.045 (2σ; Hiess et al., 2012). It is thus important to consider the potential for deviation of the U isotopic composition within hematite from the assumed value of 137.88 and the resultant effect this could bear on age.

No direct measurements of U isotopes in hematite are known, but measurement of U and Sm isotopes in whole rock samples from the major lithological facies at Olympic Dam have been undertaken (Kirchenbaur et al., 2016). From the U isotope data-set, exclusion of host granite, high U/Sm and one anomalous sample yields measured $^{238}U/^{235}U = 137.7951 \pm 0.0065$ (2σ) in the bulk rocks, which is more comparable to the value of Heiss et al. (2012) than Steiger and Jäger (1977). Furthermore, a value of $^{238}U/^{235}U = 137.811 \pm 0.0073$ (2σ) was calculated from samples of the host granite, which suggests a slight overestimation in the host granites zircon ID-TIMS ages.

Modification of the $^{238}U/^{235}U$ ratio to calculate the age of sample LCD4, yields a difference in $^{207}Pb/^{206}Pb$ age of 1.15 Ma (Fig. 12) when using a value of 137.7951 ± 0.0065 (Olympic Dam bulk rock) compared to the 137.88 (Steiger and Jäger, 1977) used in the hematite data-set presented above (Fig. 14). The larger uncertainties for microbeam techniques, compared to TIMS analyses, means the $^{238}U/^{235}U$

ratio variation will produce negligible changes to age interpretation. However, the potential for U−Pb fractionation in the magmatic to hydrothermal environment, coupled with unconstrained $^{238}U/^{235}U$ in zoned hematite, limits the accuracy of high precision U−Pb data, which must be taken into account when comparing the ages of magmatism (zircon analyses) and the hydrothermal system (zoned-hematite analyses).

5.2.2. Evaluating the geological accuracy of hematite U−Pb dates and analytical methods

The U−Pb systematics of the zoned hematite examined within this study are often complex, but also demonstrate that hematite U−Pb can be a useful geochronological tool, particularly considering the complex ~1.6 Ga history of Olympic Dam. The $^{207}Pb/^{206}Pb$ weighted average results for all samples and all dating methods are combined in Fig. 12 for comparison. Of the five hematite samples, weighted average or upper intercept dates, provided by at least one dating method for that sample following reasonable data exclusion protocols, are within 1% of the Olympic Dam host granite age (zircon; 1593.87 ± 0.21 Ma; Cherry et al., 2018). The most precise data, microsampled for ID-TIMS from the largest and least heterogeneous grains (LCD-4), yielded a $^{207}Pb/^{206}Pb$ weighted mean date within 0.25% of the host granite zircon. The presented microbeam data for all samples yields $^{207}Pb/^{206}Pb$ weighted mean dates within 2% of the RDG age (1593.87 ± 0.21 Ma) and > 90% of individual data points for the Mesoproterozoic, brecciated, multi-stage hydrothermal system hosting the Olympic Dam orebody at the level of precision are within uncertainty of the host granite age. This study suggests that U−Pb geochronology of hematite can be effectively applied to gain high-resolution insights into ore deposit formation utilizing ID-TIMS methods described within this contribution, and that hematite can, in some instances retain near-primary, concordant U−Pb geochronological information at the 0.1% 2σ level. Likewise, microbeam analysis, without utilizing a matrix matched standard can obtain geologically informative $^{207}Pb/^{206}Pb$ dates, at the 2% level in this case. However, this will be dependent upon the age, nature and geological history of the sample.

The compositionally-zoned hematite demonstrates a variety of complexities within its U−Pb systematics, resulting from initial Pb_c, open system behaviour and potentially internal Pb diffusion due to high chemical gradients. To conclusively constrain Pb diffusion within hematite, mapping of fine oscillatory zones by nanoscale-secondary ion mass spectrometry (nanoSIMS) could image differences in U and Pb isotope concentration or U/Pb ratios at a much higher resolution than LA-ICP-MS (Rollog et al., 2019). Also, atom probe tomography can be used to characterize 3D nanoscale chemistry (Valley et al., 2015; Peterman et al., 2016: Saxey et al., 2018) and investigate the mechanisms and scale of possible Pb mobility.

Superimposed on these effects is analytically-induced U−Pb fractionation, and although this does not appear to affect the $^{207}Pb/^{206}Pb$ dates, the issue is inhibitive to fully interpreting complex Pb-loss histories, or interpreting issues related to Pb_c. In some instances, such as sample RX6607, the combination of these factors makes extracting a useful intercept or $^{207}Pb/^{206}Pb$ date from a low number of ID-TIMS analyses impossible.

When using lower precision micro-beam methods, these effects may be indistinguishable from dates that reflect the "true" date of hematite crystallisation and closure of the U−Pb system, and would therefore bias age interpretations derived from weighted mean statistics or intercept ages. Likewise, in younger samples where U−Pb dating is preferable or the $^{207}Pb/^{206}Pb$ dates are not accessible, fractionation effects, and potentially internal diffusion will generate scatter in the U−Pb system that is effectively parallel to Concordia and will thus yield inaccurate ages.

In order to address both geological and analytical challenges when acquiring U−Pb data from hematite to obtain geologically meaningful ages, detailed petrographic imaging needs to be undertaken. Oscillatory zoning in BSE images can be indicative of the presence of granitophile elements, but alteration can overprint these features, removing or transporting U and/or Pb from individual domains of grains or grain aggregates (e.g., Verdugo-Ihl et al., 2017). Likewise the petrography is critical for the identification of inclusion-rich zones and fractures that will introduce Pb_c. The second consideration is to identify the domains of highest U concentration, areas of greatest homogeneity and lowest Pb_c, either through LA-ICP-MS isotope mapping or systematic screening of textural features with spot analyses. High-U domains are the most effective in retrieving chronological data that is least sensitive to the effects of Pb_c. For high resolution insights into ore forming processes, targeting these domains by micro-sampling can achieve internal uncertainties of ca. ± 0.94/5.6 Ma (0.05/0.35%) for $^{207}Pb/^{206}Pb$ dates. However, until a matrix-matched reference material is characterised, the interpretive power of microbeam data is limited.

6. Conclusions

Through a multi-instrument and technique approach, a number of different oscillatory-zoned hematite crystals, containing tens to thousands of ppm U from the Mesoproterozoic Olympic Dam ore body have been evaluated for their U−Pb systematics, to assess the suitability of hematite in ore deposit geochronological studies. The first analytical procedures and data-sets for both SHRIMP and hematite micro-sampled by laser ablation for ID-TIMS U−Pb geochronology have been developed.

Results show several key features that demonstrate the potential of hematite for interpreting robust and geologically meaningful ages from U−Pb geochronology when taken in a wider context. Despite the potential for significant disturbance during alteration, in the best cases domains of hematite can yield near-concordant analyses that are evidence of its ability to remain a closed U−Pb system over ~1.6 Ga. Domains of hematite grains can contain low initial Pb_c, however, it is necessary to target high-U domains in order to reduce the sensitivity of dates to the Pb_c component, as the U concentration and Pb_c correction exert the greatest control on the precision of ID-TIMS U−Pb data-sets. These high U zones can be targeted through detailed petrography and isotopic mapping.

Fractionation of U from Pb during microbeam analysis, owing principally to the current absence of a matrix matched reference material and likely also to compositional variability within natural hematite samples, is a significant issue for interpreting complexities in the U−Pb data of hematite, which may lead to inaccurate age interpretation. Whilst preserving $^{207}Pb/^{206}Pb$ dates, fractionation limits the potential of microbeam data-sets to derive accurate dates from samples which have experienced non-zero age Pb-loss, and complicates the effects of Pb_c mixing components. Evidence of reverse discordance is also prevalent in the ID-TIMS data set, and although laboratory induced fractionation of the U−Pb system cannot be excluded, a model of internal diffusion of Pb can be invoked. Decoupling of U from Pb within hematite crystals where large concentration gradients and large surface areas of zonation are present, could explain a component of this behaviour observed in both the microbeam and ID-TIMS data. Nevertheless, this feature is not present throughout the entire sample-set and further work is required to definitively understand and link the datasets acquired over a diverse range of spatial resolutions. This phenomenon appears to preserve the $^{207}Pb/^{206}Pb$ dates obtaining a weighted mean date within 0.1% of the host-granite age, regardless of reverse discordance. As with all geological materials used within geochronology, open system behaviour is a common phenomenon. It is important to consider these factors when utilizing hematite geochronology, particularly in younger samples, where $^{207}Pb/^{206}Pb$ dates are not precise and the discordancy will drive dates parallel to Concordia, yielding inaccurate but potentially concordant U−Pb dates.

Despite this, with careful evaluation of data and the multi-technique approach, this study demonstrates hematite U−Pb ages can be used to

interpret ore forming events to 0.15% and > 1% precision by ID-TIMS and LA-ICP-MS respectively, at similar levels of accuracy relative to the age of the granite that hosts the hematite mineralization.

The key to robust temporal interpretations of complex deposits like Olympic Dam, is a well-constrained magmatic U–Pb framework combined with a sufficiently large and well-characterised sample set to decipher and interpret different processes occurring across the whole deposit. The presence of oscillatory-zoned, U-W-Sn-Mo-rich hematite is likely an intrinsic feature of IOCG-systems, where hematite is the main Fe-oxide associated with Cu-Au(−U) ores, as it is at Olympic Dam. Although we report here on a single deposit recognized as exceptionally endowed in U relative to other IOCG-systems worldwide, hematite U–Pb geochronology has potential application to all U-bearing Fe-oxide rich mineral systems if utilised in the appropriate manner.

Acknowledgements

This is a contribution to “Trace elements in iron oxides: deportment, distribution and application in ore genesis, geochronology, exploration and mineral processing” (FOX project), supported by BHP Olympic Dam and the Government of South Australia Mining and Petroleum Services Centre of Excellence. N.J.C. acknowledges additional support from the ARC Research Hub for Australian Copper-Uranium (Grant IH130200033). We thank Professor Balz Kamber for his attentive editorial handling and constructive review, Associate Professor Don Davis for his very thorough review and an anonymous reviewer, who all helped us improve this manuscript.

Appendix A. Supplementary data

Supplementary data to this article can be found online at https://doi.org/10.1016/j.chemgeo.2019.03.005.

References

Apukhtina, O., Kamenetsky, V.S., Ehrig, K., Kamenetsky, M.B., Maas, R., Thompson, J., McPhie, J., Ciobanu, C.L., Cook, N.J., 2017. Early magnetite-fluorapatite mineralization at the Olympic Dam Cu-U-Au-Ag deposit, South Australia. Econ. Geol. 112, 1531–1542.

Barkov, A.Y., Martin, R.F., Shi, L., LeBarge, W., Fedortchouk, Y., 2008. Oscillatory zoning in stanniferous hematite and associated W- and Bi-rich minerals from Canadian Creek, Yukon, Canada. Can. Mineral. 46, 59–72.

Black, L.P., Kamo, S.L., Williams, I.S., Mundil, R., Davis, D.W., Korsch, R.J., Foudoulis, C., 2003. The application of SHRIMP to Phanerozoic geochronology; a critical appraisal of four zircon standards. Chem. Geol. 200 (1–2), 171–188.

Bowring, J.F., McLean, N.M., Bowring, S.A., 2011. Engineering cyber infrastructure for U-geochronology. Tripoli and U-Pb Redux. Geochem. Geophys. Geosyst. 12, Q0AA19. https://doi.org/10.1029/2010GC003479.

Cherniak, D., Watson, E.B., Grove, M., Harrison, T.M., 2004. Pb diffusion in monazite: a combined RBS/SIMS study. Geochim. Cosmochim. Acta 68, 829–840.

Cherry, A., Ehrig, K., Kamenetsky, V., McPhie, J., Crowley, J., Kamenetsky, M., 2018. Precise geochronological constraints on the origin, setting and incorporation of ca. 1.59 Ga surficial facies into the Olympic Dam Breccia Complex, South Australia. Precambrian Res. 315, 162–178.

Chew, D.M., Sylvester, P.J., Tubrett, M.N., 2011. U–Pb and Th–Pb dating of apatite by LA–ICPMS. Chem. Geol. 280, 200–216.

Ciobanu, C.L., Wade, B.P., Cook, N.J., Schmidt Mumm, A., Giles, D., 2013. Uranium-bearing hematite from the Olympic Dam Cu-U-Au deposit, South Australia: a geochemical tracer and reconnaissance Pb-Pb geochronometer. Precambrian Res. 238, 129–147.

Claoué-Long, J.C., Compston, W., Roberts, J., Fanning, C.M., 1995. Two Carboniferous ages: a comparison of SHRIMP zircon dating with conventional zircon ages and $^{40}Ar/^{39}Ar$ analysis. In: Geochronology Time Scales and Global Stratigraphic Correlation. SEPM Spec. Publ. 54. pp. 3–21.

Compston, W., Williams, I.S., Meyer, C.E., 1984. U-Pb geochronology of zircons from lunar breccia 73217 using a sensitive high-mass resolution ion microprobe. In: Proceedings of the Fourteenth Lunar and Planetary Science Conference, Part 2: J. Geophys. Res. 89 (Supplement, B525 B534).

Cook, N.J., Ciobanu, C.L., George, L., Zhu, Z.Y., Wade, B., Ehrig, K., 2016. Trace element analysis of minerals in magmatic-hydrothermal ores by laser ablation inductively-coupled plasma mass spectrometry: approaches and opportunities. Minerals 6 (4), 111. https://doi.org/10.3390/min6040111.

Courtney-Davies, L., Zhu, Z., Ciobanu, C.L., Wade, B.P., Cook, N.J., Ehrig, K., Cabral, A.R., Kennedy, A., 2016. Matrix-matched iron-oxide laser ablation ICP-MS U-Pb geochronology using mixed solution standards. Minerals 6 (3), 85. https://doi.org/10.3390/min603008.

Duff, M.C., Urbanik-Coughlin, J., Hunter, D.B., 2002. Uranium co-precipitation with iron oxide minerals. Geochim. Cosmochim. Acta 66, 3533–3547.

Edwards, R.L., Chen, J.H., Wasserburg, G.J., 1986. ^{238}U-^{234}U-^{230}Th-^{232}Th systematics and the precise measurement of time over the past 500,000 years. Earth Planet. Sci. Lett. 81, 175–192.

Eggins, S.M., Kinsley, L.P.J., Shelley, J.M.G., 1998. Deposition and element fractionation processes during atmospheric pressure laser sampling for analysis by ICP-MS. Appl. Surf. Sci. 127–129, 278–286.

Ehrig, K., McPhie, J., Kamenetsky, V., 2012. Geology and mineralogical zonation of the Olympic Dam Iron Oxide Cu-U-Au-Ag deposit, South Australia. In: Hedenquist, J.W., Harris, M., Camus, F. (Eds.), Geology and Genesis of Major Copper Deposits and Districts of the World: A Tribute to Richard H. Sillitoe. Society of Econ. Geol. Inc, pp. 237–267.

Ewing, R.C., Chakoumakos, B.C., Lumpkin, G.R., Murakami, T., Greegor, R.B., Lytle, F.W., 1988. Metamict minerals: Natural analogues for radiation damage effects in ceramic nuclear waste forms. Nucl. Instrum. Methods Phys. Res., Sect. B 32, 487–497.

Gerstenberger, H., Haase, G., 1997. A highly effective emitter substance for mass spectrometric Pb isotope ratio determinations. Chem. Geol. 136, 309–312.

Hiess, J., Condon, D.J., McLean, N., Noble, S.R., 2012. $^{238}U/^{235}U$ systematics in terrestrial uranium-bearing minerals. Science 335, 1610–1614.

Horstwood, M.S., Košler, J., Gehrels, G., Jackson, S.E., McLean, N.M., Paton, C., Pearson, N.J., Sircombe, K., Sylvester, P., Vermeesch, P., Bowring, J.F., Condon, D.J., Schoene, B., 2016. Community-derived standards for LA-ICP-MS U-(Th)-Pb geochronology–uncertainty propagation, age interpretation and data reporting. Geostand. Geoanal. Res. 40, 311–332.

Jackson, S.E., Pearson, N.J., Belousova, E.A., Griffin, W.L., 2004. The application of laser ablation-inductively coupled plasma-mass spectrometry (LA-ICP-MS) to in situ U-Pb geochronology. Chem. Geol. 211, 47–69.

Jaffey, A.H., Flynn, K.F., Glendenin, L.E., Bentley, W.C., Essling, A.M., 1971. Precision measurement of half-lives and specific activities of ^{235}U and ^{238}U. Phys. Rev. C: Nucl. Phys. 4, 1889–1906.

Keyser, W., Ciobanu, C.L., Cook, N.J., Dmitrijeva, M., Courtney-Davies, L., Feltus, H., Gilbert, S., Johnson, G., Ehrig, K., 2019. Iron-oxides constrain BIF evolution in terranes with protracted geological histories: the Iron Count prospect, Middleback Ranges, South Australia. Lithos. 324–325, 20–38.

Kirchenbaur, M., Maas, R., Ehrig, K., Kamenetsky, V.S., Strub, E., Ballhaus, C., Münker, C., 2016. Uranium and Sm isotope studies of the supergiant Olympic Dam Cu–Au–U–Ag deposit, South Australia. Geochim. Cosmochim. Acta 180, 15–32.

Kuhn, B.K., Birbaum, K., Luoc, Y., Günther, D., 2009. Fundamental studies on the ablation behaviour of Pb/U in NIST 610 and zircon 91500 using laser ablation inductively coupled plasma mass spectrometry with respect to geochronology. J. Anal. At. Spectrom. 25, 21–27.

Ludwig, K.R.A., 2009. SQUID 2.50: A User's Manual: Berkeley Geochronology Center, Special Publication No. 5, 110, Berkeley, California.

Ludwig, K.R.A., 2012. Isoplot/Ex rev. 4.1: A Geochronological Toolkit for Microsoft Excel; Berkeley Geochronology Centre Special Publication No.5, 75; Berkeley Geochronology Centre: Berkeley, California.

Lugmair, G.W., Galer, S.J.G., 1992. Age and isotopic relationships among the angrites Lewis Cliff 86010 and Angra dos Reis. Geochim. Cosmochim. Acta 56, 1673–1694.

Mattinson, J.M., Graubard, C.M., Parkinson, D.L., McClelland, W.C., 1996. U-Pb reverse discordance in zircons: the role of fine-scale oscillatory zoning and sub-micron transport of Pb. In: Basu, A.R., Hart, S.R. (Eds.), Earth Processes: Reading the Isotopic Code, Geophysical Monograph Series. Am. Geophys. Union 95. pp. 355–370.

Paton, C., Hellstrom, J., Paul, P., Woodhead, J., Hergt, J., 2011. Iolite: Freeware for the visualisation and processing of mass spectrometric data. J. Anal. Atom. Spectrom. 26, 2508–2518.

Peterman, E.M., Reddy, S.M., Saxey, D.W., Snoeyenbos, D.R., Rickard, W.D., Fougerouse, D., Kylander-Clark, A.R., 2016. Nanogeochronology of discordant zircon measured by atom probe microscopy of Pb enriched dislocation loops. Sci. Adv. 2, e1601318.

Petrus, J., Kamber, B., 2012. VizualAge: A Novel Approach to Laser Ablation ICP-MS U-Pb Geochronology Data Reduction. Geostand. Geoanal. Res. 36, 247–270.

Petrus, J., Chew, D., Leybourne, M., Kamber, B., 2017. A new approach to laser-ablation inductively-coupled-plasma mass-spectrometry (LA-ICP-MS) using the flexible map interrogation tool 'Monocle'. Chem. Geol. 463, 76–93.

Rollog, M., Cook, N.J., Guagliardo, P., Ehrig, K., Kilburn, M., 2019. In situ spatial distribution mapping of radionuclides in minerals by nanoSIMS. In: Geochemistry: Exploration, Environment, Analysis, https://doi.org/10.1144/geochem2018-038. (in press).

Saxey, D.W., Moser, D.E., Piazolo, S., Reddy, S.M., Valley, J.W., 2018. Atomic worlds: current state and future of atom probe tomography in geoscience. Scr. Mater. 148, 115–121.

Schmitz, M.D., Schoene, B., 2007. Derivation of isotope ratios, errors, and error correlations for U-Pb geochronology using ^{205}Pb-^{235}U-(^{233}U)-spiked isotope dilution thermal ionization mass spectrometric data. Geochem. Geophys. Geosyst. 8, Q08006. https://doi.org/10.1029/2006GC001492.

Schoene, B., 2014. U-Th-Pb geochronology. In: The Crust (Ed.), Treatise on Geochemistry, 2nd edn. 4. Elsevier Ltd, pp. 341–378.

Skirrow, R.G., Bastrakov, E.N., Barovich, K., Fraser, G.L., Creaser, R., Fanning, M.C., Raymond, O.L., Davidson, G.J., 2007. Timing of iron oxide Cu–Au–(U) hydrothermal activity and Nd isotope constraints on metal sources in the Gawler Craton, South Australia. Econ. Geol. 102, 1441–1470.

Sláma, J., Košler, J., Condon, D.J., Crowley, J.L., Gerdes, A., Hanchar, J.M., Horstwood, M.S.A., Morris, G.A., Nasdala, L., Norberg, N., Schaltegger, U., Schoene, B., Tubrett, M.N., Whitehouse, M.J., 2008. Plešovice zircon - a new natural reference material for U–Pb and Hf isotopic microanalysis. Chem. Geol. 249, 1–35.

Stacey, J.S., Kramers, J.D., 1975. Approximation of terrestrial lead isotope evolution by a 2-Stage Model. Earth Planet. Sci. Lett. 26, 207–221.
Steiger, R.H., Jäger, E., 1977. Subcommission on geochronology: convention on the use of decay constants in geo- and cosmochronology. Earth Planet. Sci. Lett. 36, 359–362.
Stirling, C.H., Andersen, M.B., Potter, E.K., Halliday, A.N., 2007. Low-temperature isotopic fractionation of uranium. Earth Planet. Sci. Lett. 264, 208–225.
Valley, J.W., Reinhard, D.A., Cavosie, A.J., Ushikubo, T., Lawrence, D.F., Larson, D.J., Kelly, T.F., Snoeyenbos, D.R., Strickland, A., 2015. Nano- and micro-geochronology in Hadean and Archean zircons by atom-probe tomography and SIMS: New tools for old minerals. Am. Mineral. 100, 1355–1377.
Verdugo-Ihl, M.R., Ciobanu, C.L., Cook, N.J., Ehrig, K., Courtney-Davies, L., Gilbert, S., 2017. Textures and U-W-Sn-Mo signatures in hematite from the Olympic Dam Cu-U-Au-Ag deposit, South Australia: Defining the archetype for IOCG deposits. Ore Geol. Rev. 91, 173–195.
Weyer, S., Anbar, A.D., Gerdes, A., Gordon, G.W., Algeo, T.J., Boyle, E.A., 2008. Natural fractionation of $^{238}U/^{235}U$. Geochim. Cosmochim. Acta 72, 345–359.
Wiedenbeck, M., Alle, P., Corfu, F., Griffin, W.L., Meier, M., Oberli, F., von Quadt, A., Roddick, J.C., Spiegel, W., 1995. 3 natural zircon standards for U-Th-Pb, Lu-Hf, trace-element and REE analyses. Geostand. Newslett. 19, 1–23.
Williams, I.S., 1998. U-Th-Pb geochronology by ion microprobe. Applications of microanalytical techniques to understanding mineralizing processes. Rev. Econ. Geol. 7, 1–35.
Zhou, H., Sun, X., Wu, Z., Liao, J., Fu, Y., Li, D., Hollings, P., Liu, Y., Lin, H., Lin, Z., 2017. Hematite U-Pb geochronometer: insights from monazite and hematite integrated chronology of the Yaoan gold deposit, Southwest China. Econ. Geol. 112, 2023–2039.

CHAPTER 4

OPENING THE MAGMATIC-HYDROTHERMAL WINDOW: HIGH-PRECISION U-PB GEOCHRONOLOGY OF THE MESOPROTEROZOIC OLYMPIC DAM CU-U-AU-AG DEPOSIT, SOUTH AUSTRALIA

Liam Courtney-Davies [1], Cristiana L. Ciobanu [1], Simon R. Tapster [2], Nigel J. Cook [1], Kathy Ehrig [3], James L. Crowley [4], Max R. Verdugo-Ihl [1], Benjamin. P. Wade [5] and Daniel J. Condon [2]

[1]School of Chemical Engineering and Advanced Materials, The University of Adelaide, Adelaide, S.A. 5005, Australia

[2]NIGL, British Geological Survey, Keyworth, Nottinghamshire, NG12 5GG, U.K.

[3]BHP Olympic Dam, Adelaide, S.A. 5000, Australia

[4]Department of Geosciences, Boise State University, Boise, ID 83725, U.S.A.

[5]Adelaide Microscopy, The University of Adelaide, Adelaide, S.A. 5005, Australia

Revised version submitted for publication in Economic Geology as a Scientific Communication 28 January 2020.

Statement of Authorship

Title of Paper	Opening The Magmatic-Hydrothermal Window: High-Precision U-Pb Geochronology Of The Mesoproterozoic Olympic Dam Cu-U-Au-Ag Deposit, South Australia
Publication Status	☐ Published ☐ Accepted for Publication ☑ Submitted for Publication ☐ Unpublished and Unsubmitted w ork w ritten in manuscript style
Publication Details	Courtney-Davies, L., Ciobanu, C.L., Tapster, S.R., Cook, N.J., Ehrig, K., Crowley, J.L., Verdugo-Ihl, M., Wade, B.P., Condon, D.J., in review. Opening The Magmatic-Hydrothermal Window: High-Precision U-Pb Geochronology Of The Mesoproterozoic Olympic Dam Cu-U-Au-Ag Deposit, South Australia. Economic Geology.

Principal Author

Name of Principal Author (Candidate)	Liam Courtney-Davies		
Contribution to the Paper	Performed analytical work, carried out data processing and interpretation, oversaw development of work and wrote manuscript.		
Overall percentage (%)	60		
Certification:	This paper reports on original research I conducted during the period of my Higher Degree by Research candidature and is not subject to any obligations or contractual agreements with a third party that would constrain its inclusion in this thesis. I am the primary author of this paper.		
Signature		Date	29/10/2019

Co-Author Contributions

By signing the Statement of Authorship, each author certifies that:

i. the candidate's stated contribution to the publication is accurate (as detailed above);

ii. permission is granted for the candidate in include the publication in the thesis; and

iii. the sum of all co-author contributions is equal to 100% less the candidate's stated contribution.

Name of Co-Author	Cristiana L. Ciobanu		
Contribution to the Paper	Define direction of research, supervised development of work, assisted with data interpretation and contributed to manuscript preparation.		
Overall percentage (%)	10		
Signature		Date	29.Oct 2019

Name of Co-Author	Simon R. Tapster		
Contribution to the Paper	Performed ID-TIMS, carried out data processing and interpretation, helped define direction of research, supervised development of work and contributed to manuscript preparation.		
Overall percentage (%)	10		
Signature		Date	29. Oct 2019

Name of Co-Author	Nigel J. Cook		
Contribution to the Paper	Contributed to manuscript preparation.		
Overall percentage (%)	5		
Signature		Date	29/10/2019

Name of Co-Author	Kathy Ehrig		
Contribution to the Paper	Helped coordinate sample collection, defined research direction and assisted with evaluation of manuscript.		
Overall percentage (%)	5		
Signature		Date	29/10/2019

Name of Co-Author	James L. Crowley		
Contribution to the Paper	Performed ID-TIMS, carried out data processing and interpretation.		
Overall percentage (%)	5		
Signature		Date	29/10/2019

Name of Co-Author	Max R. Verdugo-Ihl		
Contribution to the Paper	Performed analytical work, evaluated manuscript.		
Overall percentage (%)	2		
Signature		Date	29/10/2019

Name of Co-Author	Benjamin. P. Wade		
Contribution to the Paper	Evaluated manuscript.		
Overall percentage (%)	2		
Signature		Date	29/10/2019

Name of Co-Author	Daniel J. Condon		
Contribution to the Paper	Helped define research direction and assisted with evaluation of manuscript.		
Overall percentage (%)	1		
Signature		Date	29. Oct. 2019

Abstract

Establishing robust timescales for iron-oxide copper gold (IOCG) deposit formation and the temporal relationships between ores and the magmatic rocks from which hydrothermal, metal-rich fluids are sourced, is often reliant on low-precision data and assumptions, particularly for deposits that formed during the Precambrian. Unlike accessory minerals routinely used to track hydrothermal mineralization, iron-oxides are dominant components of IOCG systems and are therefore pivotal to understand deposit evolution. The presence of ubiquitous, magmatic-hydrothermal U-(Pb)-W-Sn-Mo-bearing zoned hematite resolves a range of geochronological issues concerning formation of the ~1.6 Ga Olympic Dam IOCG deposit, South Australia, at up to ~0.05% precision ($^{207}Pb/^{206}Pb$ weighted mean; 2σ) using isotope dilution-thermal ionization mass spectrometry (ID-TIMS). Coupled with chemical abrasion-ID-TIMS zircon dates from host granite and volcanic rocks within and enclosing the orebody, a confident magmatic-hydrothermal chronology is defined. The youngest obtained zircon date from the granite intrusion hosting Olympic Dam indicate magmatism was occurring up until 1593.28 ± 0.26 Ma. The orebody was principally formed during major mineralizing event following granite uplift and during cupola collapse, whereby the hematite with the oldest age is recorded in the 'outer shell' of the deposit at 1591.27 ± 0.89 Ma, ~2 Ma later than the youngest documented magmatic zircon. Hematite dates captured throughout major lithologies, different orezones, and throughout the ~2 km vertical extent of the deposit support hydrothermal activity for ~2 Ma. New age constraints on the spatial-temporal evolution of the formation of Olympic Dam are considered with respect to a mantle to crustal continuum model.

4.1 Introduction

Constraining the onset and lifespan of mineralizing events is critical for understanding the genesis of ore deposits, and for the development of prospecting strategies within metallogenic provinces. However, identifying cases where mineralization can be accurately dated and bracketed by causative intrusions or events can prove challenging. The duration and periodicity of intrusion-related mineralization events are commonly controlled by the tectono-magmatic settings in which they occur. Timescales required for such processes have been proposed to range from near instantaneous (Weatherley and Henley, 2013) to millions of years (Sillitoe and Mortenson, 2010). Advances in radioisotopic dating techniques, notably chemical abrasion-isotope dilution-(negative)-thermal ionization mass spectrometry CA-ID-TIMS and ID-N-TIMS, has permitted routine high-precision dating of discrete magmatic pulses and hydrothermal phases, proving invaluable for dating deposits formed in Phanerozoic volcanic arcs on subduction or collision zones (Chiaradia et al., 2013, and references therein). For example, the combination of U-Pb zircon and Re-Os molybdenite data has enabled mineralizing intervals to be temporally resolved at both high analytical precision and spatial resolution, in the range of tens of thousands of years to a few millions of years for porphyry systems, where distinct ore-causative intrusions and alteration-mineralization stages can be bracketed by crosscutting vein networks (e.g., von Quadt et al., 2011; Chiaradia et al., 2014; Zimmerman et al., 2014; Li et al., 2017).

Difficulties occur when dating Precambrian deposits due to increasingly larger absolute uncertainties with increasing absolute ages. Such uncertainties may conceal discrete mineralizing events, or overestimate the duration of individual events. Furthermore, minerals which can confidently record a mineralization date relative to magmatic activity are often elusive, either due to modification of primary isotope systematics, or simply because they do not form at the conditions of mineralization. Development of the hematite U-Pb mineral

geochronometer has allowed direct dating of ores derived from iron-oxide copper gold (IOCG), porphyry-related Au, unconformity-related and banded iron formation deposits (Ciobanu et al., 2013; Courtney-Davies et al., 2016; 2019a, b; Zhou et al., 2017; Walter et al., 2018; Keyser et al., 2019). Such a tool is significant due to the conspicuous lack of dateable crosscutting features within breccia-hosted IOCG systems.

The archetypal example of an IOCG system *sensu stricto* is the Mesoproterozoic Olympic Dam deposit, South Australia (Ehrig et al., 2012), containing a total resource of 10,892 Mt at 0.73% Cu, 0.24 kg/t U_3O_8, 0.31 g/t Au and 1.2 g/t Ag (BHP, 2019). Located within one of the richest Precambrian metallogenic provinces on Earth, Olympic Dam hosts U-bearing, oscillatory-zoned hematite as a ubiquitous component of ores throughout the 6 km-strike and 2 km-depth of the deposit (Verdugo-Ihl et al., 2017). Moreover, U-bearing hematite is found within all major lithologies, including weakly mineralized granite forming the 'outer shell' of the deposit (Verdugo-Ihl et al., 2020).

The presence of an abundant U-(Pb)-bearing phase, that can be demonstrated to be radioisotopically robust throughout the deposit (Courtney-Davies et al., 2019a), makes Olympic Dam particularly well suited for temporally constraining the magmatic-hydrothermal window (the relative ages of the two systems), by integrating hydrothermal hematite and magmatic zircon (CA-)ID-TIMS U-Pb geochronology.

Data presented below are interpreted with respect to the evolving genetic model for the deposit. Early concepts involving shallow granite emplacement with diatreme-maar development (Reeve et al., 1990; Haynes et al., 1995; Johnson and Cross, 1995) have been superseded by deep granite crystallization (Kontonikas-Charos et al., 2017), whereby hydrothermal fluids accumulate and form ores during uplift, brecciation and cupola collapse of the host granite (Verdugo-Ihl et al., 2020). The absolute and inferred timing of such processes are investigated.

4.2 Background

The eastern Gawler Craton hosts the Mesoproterozoic *Olympic Cu-Au Province* (Skirrow et al., 2007; Reid, 2019), a metallogenic belt which strikes roughly N-S for 700 km and encompasses several dozen IOCG-style deposits and prospects (Fig. 1). At the center of the province (the Olympic Dam district), the geology is concealed under thick Neoproterozoic cover and includes a sequence of gneissic rocks (the Mulgathing Metamorphic Complex, ~3.2 Ga), intruded by Donington Suite granitoids (~1.85 Ga), all unconformably overlain by metavolcanic-sedimentary rocks of the Wallaroo Group (~1.75 Ga; Fig. 1). Breakup of the Columbia/Nuna supercontinent triggered a craton-scale tectono-magmatic event at ~1.6 Ga, forming the >25,000 km^2 (Blissett et al., 1993) Gawler Silicic Large Igneous Province (SLIP; Allen et al., 2008). The SLIP is composed of the intrusive/extrusive Gawler Range Volcanics (GRV) and comagmatic Hiltaba Suite granitoids. Although highly debated, the source of IOCG mineralizing fluids has been largely attributed to Hiltaba Suite granitoids across the province through a combination of studies applying geochemical modelling, geochronology and mineralogical observations (e.g., Kirchenbaur et al., 2016; Schlegel et al., 2017; Courtney-Davies et al., 2019c; Dmitrijeva et al., 2019).

The Olympic Dam deposit is entirely contained within the Olympic Dam breccia complex (ODBC; Reeve et al., 1990). Breccias are hosted and largely derived from the Roxby Downs Granite (RDG), an evolved Hiltaba Suite pluton of the Burgoyne Batholith (Fig. 2). Emplacement of the RDG occurred at depths of 6-8 km (plagioclase-amphibole thermobarometry; Kontonikas-Charos et al., 2017), with equivalent estimates obtained for a quartz monzonite of the Burgoyne Batholith distal from Olympic Dam (Creaser 1996). A temporal range in Hiltaba Suite plutons (up to ~30 Ma) has been reported across the Gawler Craton (Fanning et al., 2007) Five samples of 'shallow' (<681 m) RDG from three drillholes ~2 km south of the ODBC were previously dated, by zircon CA-ID-TIMS (Boise State

University; Cherry et al., 2018), yielding a pooled weighted mean of 1593.03 ± 0.21 Ma (*n*=36, MSWD=1.08), suggesting the RDG was not emplaced incrementally.

Several issues of debate remain concerning formation of the ODBC and, implicitly, the contained mineralization. Concentric zoning of sulfides (deeper, outer chalcopyrite-pyrite, to bornite-chalcopyrite and shallow, inner bornite-chalcocite; Fig. 3), relative to a 'barren', high-Fe breccia center suggest fluids were supplied from a central diatreme (Reeve et al., 1990). However, this model was redefined with the discovery of mineralization across a ~2 km-thick interval in the deposits southeastern-lobe (Fig. 3; Ehrig et al., 2012). This suggests there could have been deeper centers offset to the zoning, or alternatively, that the concentric ore distribution results from superposition of primary (upwards zonation preserves high-T species in Cu-(Fe)-sulfides; Ciobanu et al., 2017) and secondary (replacement) processes.

Defining a temporal timeframe for the deposit is complicated by the extensive, multistage brecciation within a voluminous and heterogeneous breccia complex (Reeve et al., 1990; 6 × 8 km in plan; Oreskes and Einaudi, 1990; and at least ~1.9 km in vertical extent, Ehrig et al., 2012), which underwent pervasive, hematite-sericite alteration (Ehrig et al., 2012). The deposit also straddles intersections between regional fault zones (Hayward and Skirrow, 2010), where long-lived reactivated faults have dismembered large segments of the orebody (Clark et al., 2018). High-precision dating of magmatic zircon distal to the orebody (drillhole RD2488; Fig. 2A) provides a maximum age constraint for hydrothermal activity. Historically, a major, broad mineralizing event occurring at ~1.6 Ga has been recognized at Olympic Dam using a variety of minerals and dating techniques (Reeve et al., 1990; Creaser and Cooper, 1993; Johnson and Cross, 1995).

There is now a growing body of laser ablation-inductively coupled plasma-mass spectrometry (LA-ICP-MS) U-Pb data, which broadly constrains the hydrothermal system to ~1590 Ma. Hematite dates were first acquired by Ciobanu et al. (2013) and corroborated by

samples from different areas of the deposit generating comparable data (Courtney-Davies et al., 2016; Apukhtina et al., 2017). Additional constraints at ~1590 Ma were obtained from fluorapatite and uraninite in altered RDG and from volcanic rocks outside the orebody, respectively (Apukhtina et al., 2017). Irrespective of the accuracy of LA-ICP-MS methods used, data produced thus far support hydrothermal activity commencing broadly coeval with RDG crystallization as determined via ID-TIMS, with analytical uncertainties of ~5 to 25 Ma for individual dates.

Primary, oscillatory-zoned, U-(Pb)-W-Sn-Mo-bearing hematite is present throughout all ore zones and all major lithologies at Olympic Dam (Verdugo-Ihl et al., 2017). The majority of hematite in the orebody occurs either as replacements or as overprinted variants of the zoned-type via coupled-dissolution-(re)precipitation-reactions, which can allow partial preservation of pre-existing trace element signatures (Verdugo-Ihl et al., 2017).

There is an intimate association between Fe-metasomatism and Cu mineralization, displayed by the outline of the Cu resource mirroring the >5 wt% Fe boundary within the breccia complex (Fig. 2; Ehrig et al., 2012). The ubiquitous presence of U-bearing zoned hematite and the secondary hematite textures, which can be tied to replacement of the primary zoned type (Verdugo-Ihl et al., 2017, 2020), clearly indicate that U was an integral component of the magmatic-hydrothermal IOCG system. Therefore, high-precision dating of primary, zoned hematite from the aforementioned lithologies and ore zones, may provide a temporal framework for the hydrothermal system.

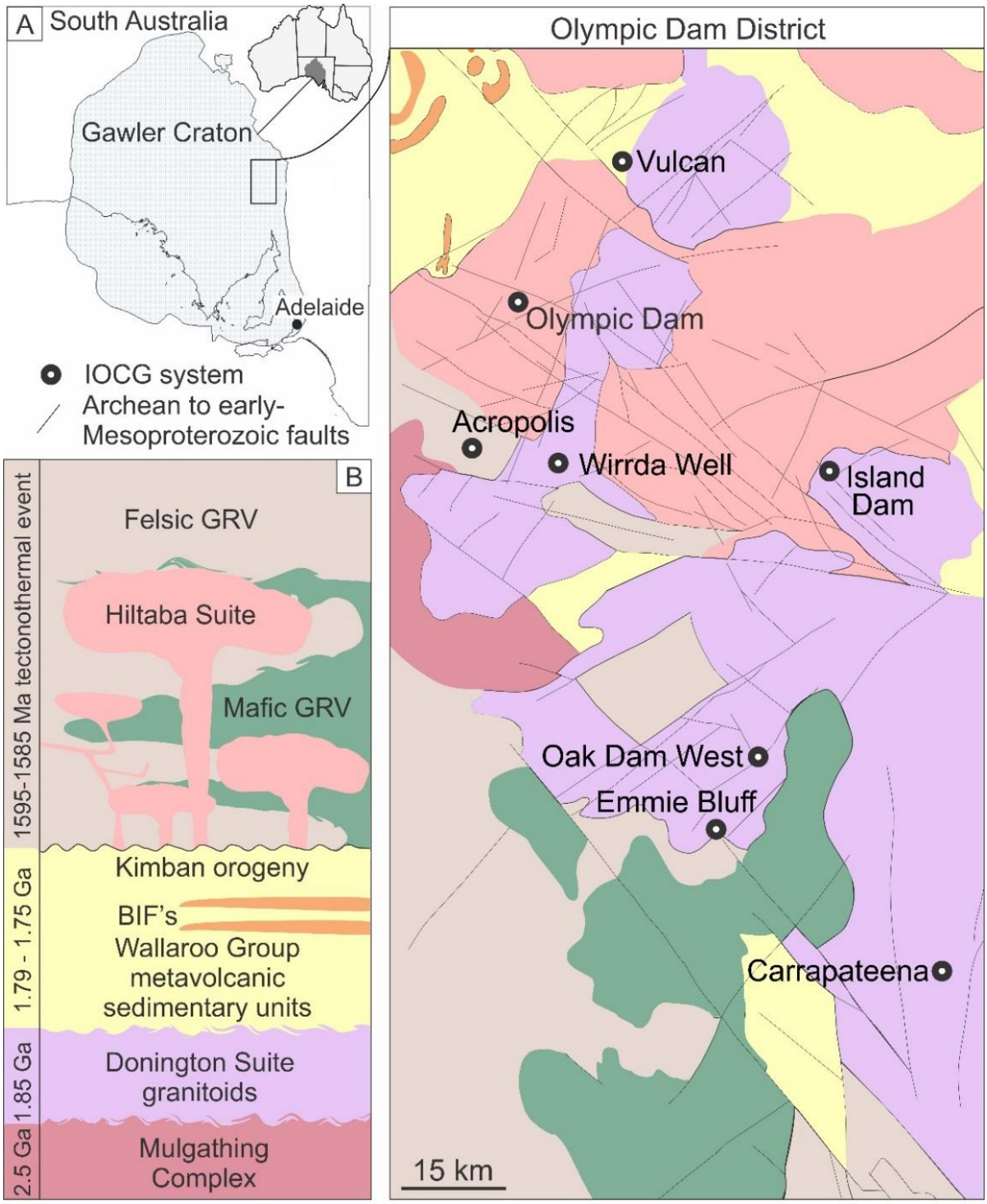


Figure 1: (A) Map of South Australia overlain by the outline of the Gawler Craton, with the location of the Olympic Dam district boxed, and enlarged displaying a geological map of the region (right). The location of selected IOCG systems and major faults are marked. (B) Generalized diagram depicting relationships between the different country rocks and IOCG host lithologies within the Olympic Dam district.

4.3 Rationale and Samples

Although there is widespread evidence for multiple tectonothermal events impacting on Olympic Dam, likely contributing to cycles of U and Cu remobilization and new mineral growth (e.g., 820 Ma dike swarms; Huang et al., 2015), this does not necessarily imply multiple, major episodes of metal introduction. Previous studies of U, Pb and Sm isotopes have suggested that post ~1590 Ma events contributed to and upgraded the large U resource within the deposit (e.g., Trueman et al., 1988; Johnson, 1993, Meffre et al., 2010; Maas et al., 2011; Kirchenbaur et al., 2016; Cherry et al., 2017). At present, however, there are no geochronological constraints to confirm or refute this.

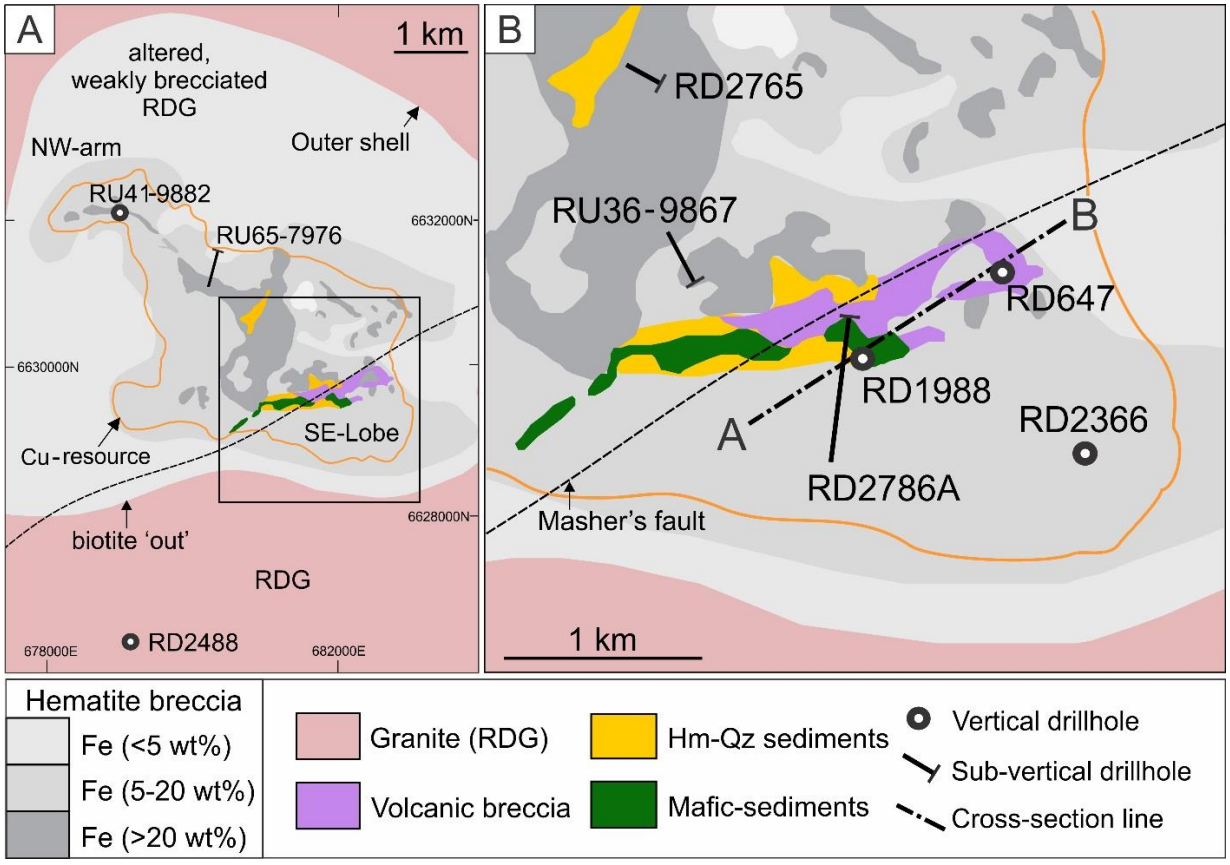


Figure 2: (A) Sketch of the Olympic Dam deposit including major lithologies and sampled/discussed drillholes and drillhole projections. (B) Expanded map of the SE-lobe, marking the cross-section A-B shown in Fig. 3.

The absence of evidence for extensive mineralizing events post-1590 Ma, prompted this study to define and refine the timing and extent of the major, initial ore-forming event, using a single mineral with a traceable geochemical signature. Spanning all ore-zones and major lithologies, zoned hematite from the deposit center to 'outer shell' (nine samples) was selected for ID-TIMS dating (no chemical abrasion; Fig. 2A, B; Table 1). To provide further constraints on the maximum timing of mineralization from samples spatially associated with zoned hematite, volcanic zircons within the breccia complex and magmatic zircon located within ~50 m of sampled hematite were dated by CA-ID-TIMS (Fig. 3; Table 1).

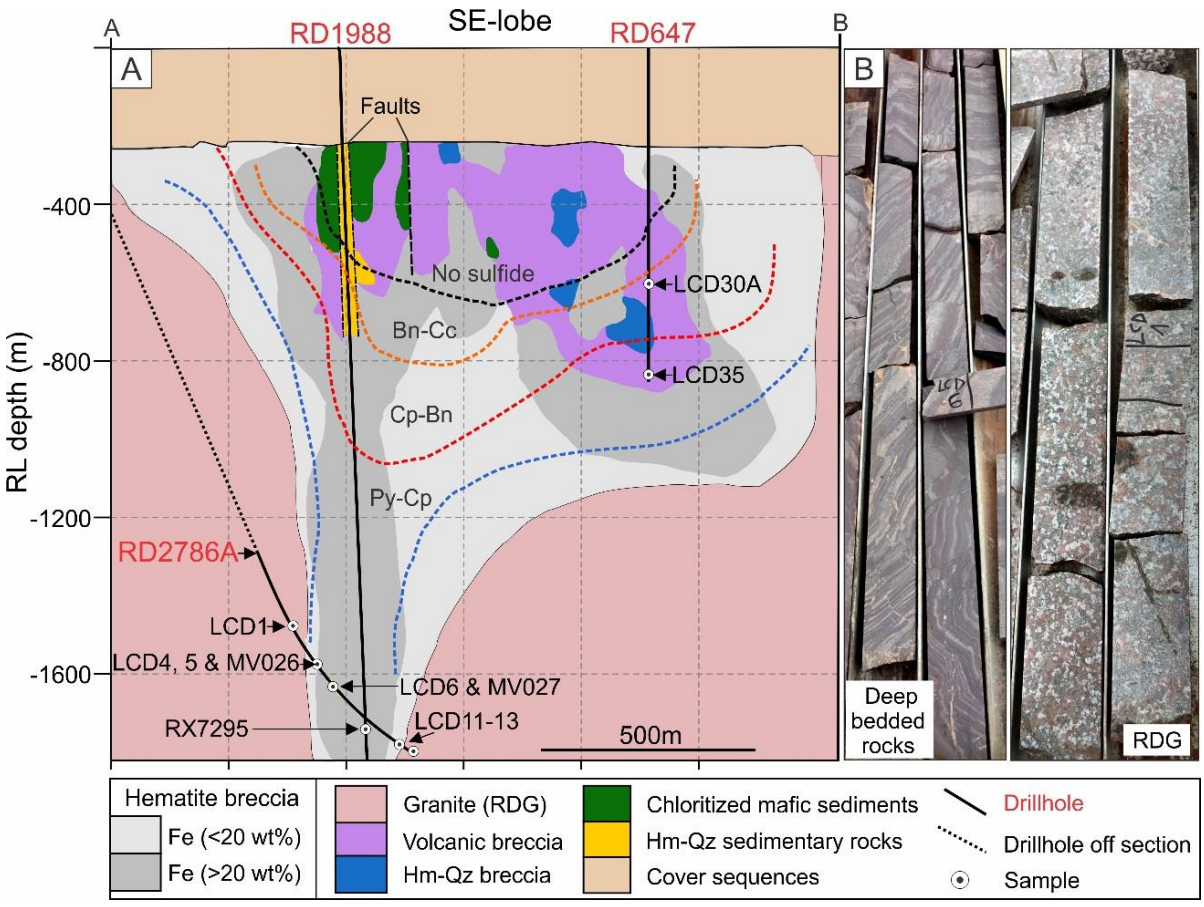


Figure 3: (A) Cross-section (A to B; marked of Fig. 2) through the SE-lobe, with lithologies, drillholes, sample locations and orezones marked. (B) Photographs of sampled bedded packages (left) and RDG (right). Abbreviations: Py-Cp: pyrite-chalcopyrite; Cp-Bn: chalcopyrite-bornite; Bn-Cc: bornite-chalcocite.

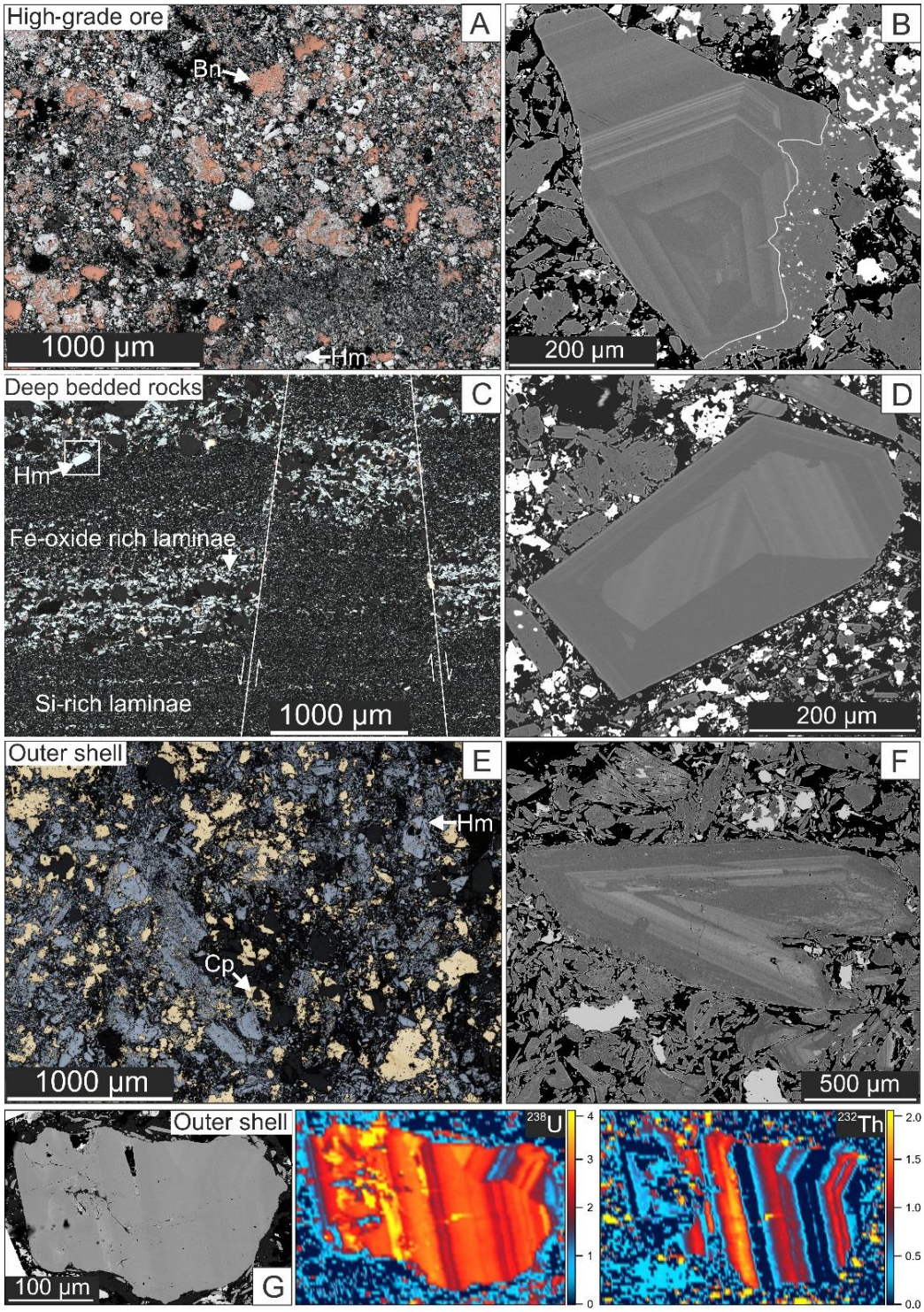


Figure 4: (A-F) Representative coarse scale photomicrographs of zoned hematite bearing samples (left) and magnified BSE images (right) of dated zoned hematite grains. (B) The white arrow and line marks the corroded grain boundary, populated by a dense field of uraninite inclusions. (G) Isotopic LA-ICP-MS maps of a zoned hematite grain in sample CLC10, displaying strong zonation in both U and Th (scale: n·105). Abbreviations: Bn-bornite; Cp-chalcopyrite; Hm-hematite.

We assess whether hematite can capture discrete ore-forming stages from geochemically diverse locations across the deposit. For example, zoned hematite contains distinct signatures with respect to HFSE (e.g., Ti, Th) in specimens from the deposits 'outer shell', but not in the orebody (Verdugo-Ihl et al., 2020; Fig. 4). Such a signature is indicative of an early hydrothermal origin since these elements are attributable to the magmatic stage. Changes in the REE signatures of fluorapatite (Krneta et al., 2017, 2018) and previous dating of a younger hematite in high-grade bornite ores (Ciobanu et al., 2013; Fig. 4A, B) suggest protracted fluid introduction, which may be reflected in high-precision dating. Packages of bedded, hematite and quartz are present at depth (up to ~1.6 km) can be used to constrain a geodynamic model for the deposit, whereby the timing of their introduction into the ODBC can be understood through dating of *in-situ* hydrothermal hematite (Fig. 3 and Fig. 4C, D). More broadly, the resolution at which Proterozoic IOCG ore deposits can be accurately dated is examined.

4.4 Methodology

One-inch diameter polished blocks were prepared from drill cores. Zoned hematite grains were identified by scanning electron microscopy (SEM) using an FEI Quanta 450 equipped with a back-scattered electron (BSE) detector and an energy-dispersive X-ray spectrometer at Adelaide Microscopy, The University of Adelaide.

Hematite dating was conducted at the Natural Environment Research Council, Isotope Geoscience Laboratory, British Geological Survey (BGS). Full details of the *in-situ* grain extraction method, extensive hematite ID-TIMS methodology and assessment of hematite U-Pb isotope systematics can be found in Appendix A and Courtney-Davies et al. (2019a). Hematite fractions were spiked with the NIGL-2 tracer solution. Zircon separated from core samples were selected for CA-ID-TIMS at both the BGS and the Isotope Geology Laboratory, Boise State University. Grains were imaged at Boise in cathodoluminescence (CL) mode using a scanning electron microscope. Analyses were composed of single zircon grains or grain

fragments, using a method modified after Mattinson (2005). All zircon analyzed at the BGS was spiked with the ET235 tracer solution, while zircon at Boise was spiked with either BSU1B or ET2535 (Table A1). Broader laboratory and analytical details for hematite and zircon CA-ID-TIMS can be found in Appendix A.

All hematite and zircon U-Pb data are presented at the 2σ level and reduced using the U decay constants recommended by Jaffey et al. (1971), with a preferred $^{238}U/^{235}U$ value of 137.8185 ± 0.045 (2σ; Heiss et al., 2012). This value was selected due to its close comparability with direct U isotope studies of Olympic Dam, where a value of 137.801 was obtained from whole rock samples (Kirchenbaur et al., 2016). It should be noted that previous studies dating the RDG (Cherry et al., 2018) and Olympic Dam hematite (Courtney-Davies et al., 2019a), used a $^{238}U/^{235}U$ value of 137.88 (Steiger and Jäger, 1977), therefore, when age data from previously published studies is cited, it has been modified using the same $^{238}U/^{235}U$ value applied in this study. Isotope measurements were processed using the 'TRIPOLI' software package (Bowring et al., 2011). Data reduction, error propagation and date calculations were generated using the excel spreadsheet of Schmitz and Schoene (2007) for hematite and zircon at Boise, ET REDUX was used for zircon at the BGS. Concordia and weighted average diagrams were constructed using the Excel add-in 'ISOPLOT 3.75' (Ludwig, 2012). Only analytical uncertainties are presented, uncertainties arising from the $^{238}U/^{235}U$ value uncertainty, different tracer solution systematics, comparing hematite to zircon and data reduction methods are not included due to the negligible additional uncertainty and low relative uncertainty compared to the decay constant uncertainty for a sample of ~1.6 Ga ($^{207}Pb/^{206}Pb$ uncertainty is ~5.6 Ma).

Isotope maps of hematite were acquired using a RESOlution-LR 193 nm ArF excimer laser microprobe (Australian Scientific Instruments) coupled to an Agilent 7900cx quadrupole ICP-MS. The maps, scaled in counts-per-second (cps), were compiled and processed into 2-D

images displaying the combined background-subtracted intensities using 'IOLITE' (Paton et al., 2011; see Verdugo-Ihl et al., 2017 for further details).

4.5 Results: Petrography and Geochronology

Sample locations, drillhole ID's and depths relative to sea-level (RL) are summarized in Table 1 and displayed in Fig. 2 and 3, with corresponding geochronological data (isotopic ratios, dates and U-Th-Pb contents) provided in Tables A1 to A2.

4.5.1 Zircon

Concordia diagrams and weighted average dates for zircon are presented in Fig. 5. Cathodoluminescence images of whole and fragmented magmatic RDG zircon highlight typical magmatic oscillatory zonation patterns (Fig. 5A; sample LCD12). These are invariably crosscut by swelling cracks induced by time and actinide-dependent metamictization. Grains average ~150 μm in length, smaller than zircon found within the ODBC (Ciobanu et al., 2013). Extended CL images are displayed in Fig. A1.

4.5.1.1 Gawler Range Volcanics

Polymictic volcanic clast-rich breccia in a fine-grained matrix was sampled from the SE-lobe of the deposit (604 m), interpreted as belonging to the GRV (sample LCD30A; Fig. 3; Fig. A2). One large porphyritic clast was isolated from the breccia and crushed, with eight separated zircons analyzed at the BGS (Fig. 5B). Analyses are largely concordant (apart from one highly discordant datapoint) defining a zero-age lower and upper intercept at 1594.55 ± 0.8 Ma, in good agreement with the $^{207}Pb/^{206}Pb$ weighted average (1594.63 ± 0.71 Ma; n=8, MSWD=0.77).

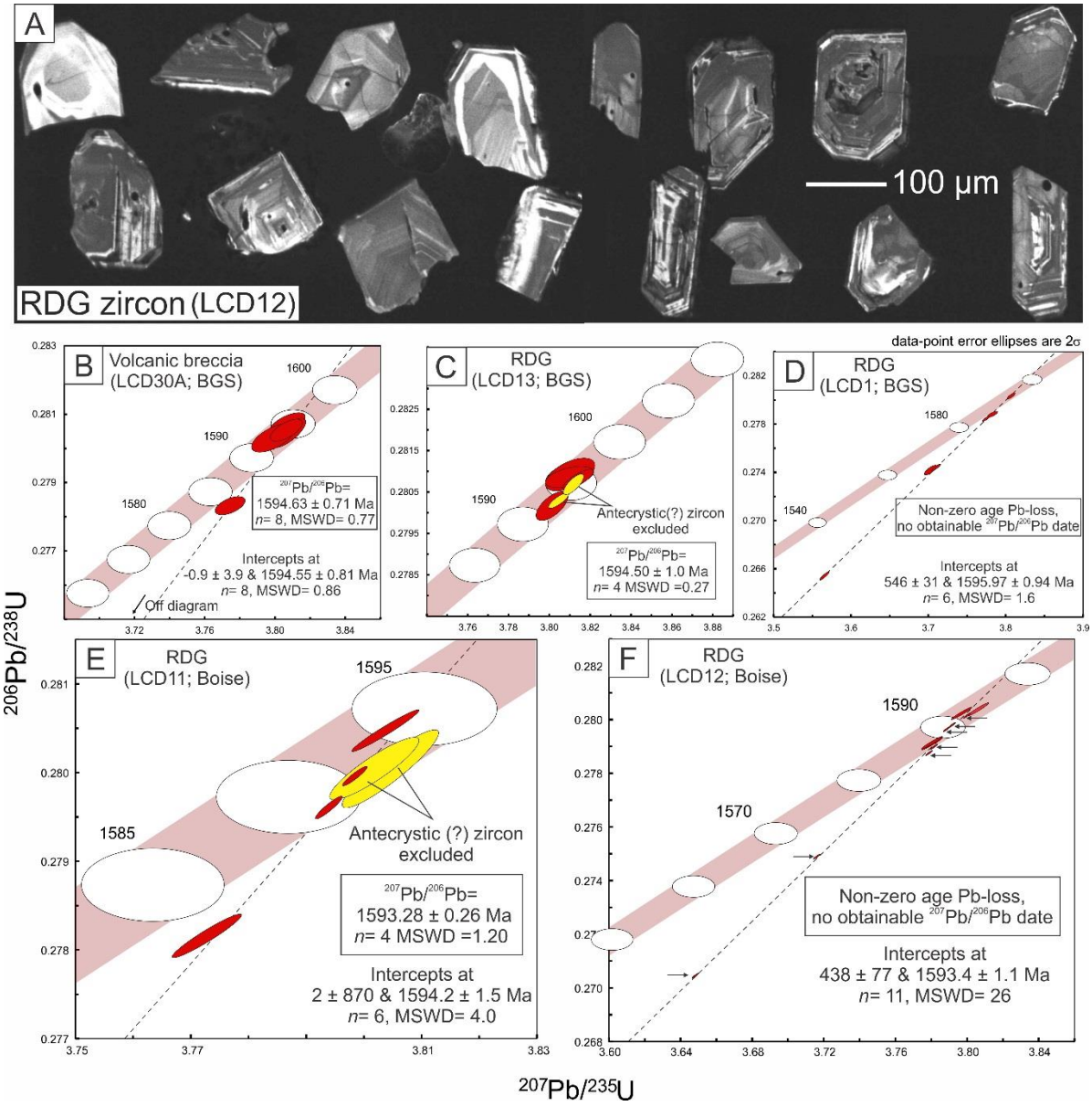


Figure 5: Representative CL images of RDG zircon (sample LCD12). Grains are fragmented due to the separation process and are invariably metamict and overprinted. (B-F) Wetherill concordia diagrams (CA-ID-TIMS) for GRV zircon (B) and RDG zircon (C-F). Intercept and weighted average ($^{207}Pb/^{206}Pb$) dates are provided on the diagrams if obtainable.

4.5.1.2 Roxby Downs Granite

Granite hand specimens display macroscopic alteration at varying degrees but retain granitoid textures and some relict magmatic minerals (Fig. 3B; see Kontonikas-Charos et al.,

2017 for further detail). Zircon dated here underwent pervasive Fe-Cl-metasomatism shortly after crystallization, during initiation of the hydrothermal system at Olympic Dam (Courtney-Davies et al., 2019c), possibly influencing the U-Pb data presented.

Zircon separated from two samples of RDG from the same drillhole (samples LCD13 and LCD1; Fig. 3) were analyzed at the BGS (Fig. 5C, D). Six zircons were separated from the deeper sample (LCD13). The intercept date is poorly constrained due to concordance of the data. As with the previous sample, two $^{207}Pb/^{206}Pb$ populations can be extracted at 1595.9 ± 1.10 Ma (n=2) and 1594.50 ± 1 Ma (n=4, MSWD=0.27). The two older grains, of likely antecrystic origin are plotted in yellow (Fig. 5C).

From the shallower sample (LCD1), six zircons with varying degrees of Pb loss define a lower intercept at 546 Ma (Delamerian orogeny), and upper intercept at 1595.97 ± 0.94 Ma. (Fig. 5D).

Two populations can be extracted in $^{207}Pb/^{206}Pb$ space at 1595.10 ± 1.10 Ma (n=2,) and 1593.28 ± 0.26 Ma (n=4, MSWD=1.20), with the former likely representing antecrystic material, exerting influence on the upper intercept date

Two further samples of RDG from the same drillhole (sampled within 40 m) were prepared for CA- ID-TIMS at Boise University (Fig. 5 E, F). Five grains were analyzed from sample LCD11 (using either ET2535 or BSUB1 tracer solutions, Table A2), with one grain broken into two fragments that were analyzed separately (fraction z4a, b). The poorly defined intercept line forms a date at 1594.2 ± 1.5 Ma (n=6, MSWD=4). Two dates from the broken grain yield a $^{207}Pb/^{206}Pb$ weighted mean of 1595.10 ± 1.10 Ma (MSWD=1.6; BSU1B tracer solution). This grain has much lower U and higher Th concentrations than the other grains, inferring a different fractionation history and potentially being antecrystic in origin (Table A2). The dates from the

other four grains yield a weighted mean of 1593.28 ± 0.26 Ma (MSWD=1.2; ET2535 tracer solution).

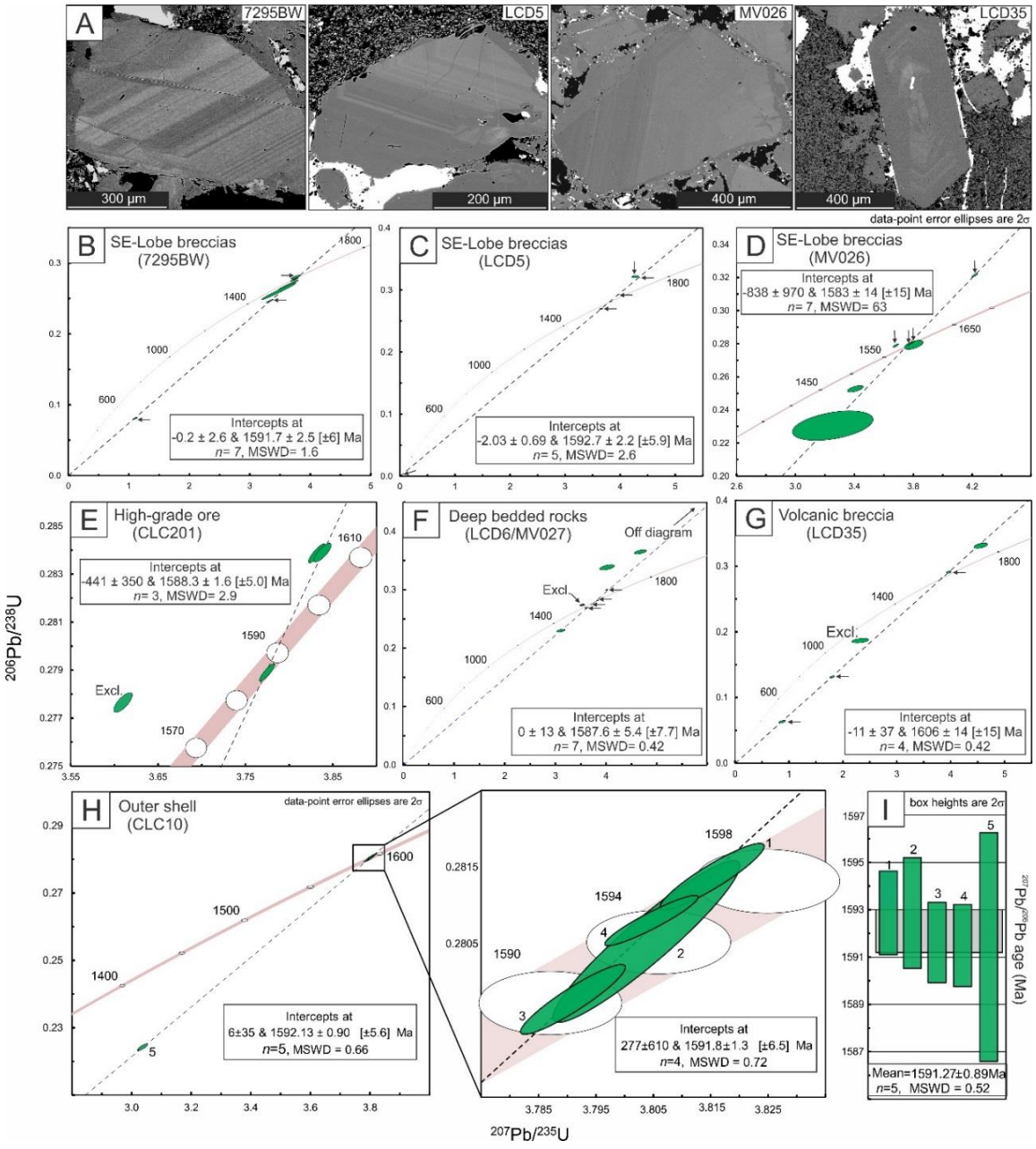


Figure 6: (A) Selection of BSE images showing zoned hematite grains which were micro-sampled for ID-TIMS. (B-H) Wetherill concordia diagrams for zoned hematite and corresponding intercept dates. Data marked Excl. is excluded from the intercept calculations due to low U or high common Pb. Small error ellipses are arrowed. (I) $^{207}Pb/^{206}Pb$ weighted average diagram for sample CLC10 from the deposits outer shell.

From sample LCD12, eleven grains spiked with BSU1B or ET2535 (Fig. 5F) generated poorly defined intercept dates with high degrees of Pb loss. This inhibits calculation of an acceptable weighted mean when including all data. When considering only the most precise datapoints which have not been (likely) leveraged by ancient Pb-loss or contaminated by antecrystic material, a $^{207}Pb/^{206}Pb$ date of 1593.06 ± 2.0 (n=2; ET2535 tracer solution) is defined.

4.5.2 Hematite

Concordia diagrams are presented in Fig. 6, with a selection of BSE images of grains micro-sampled for ID-TIMS presented in Fig. 6A. Plots of $^{207}Pb/^{206}Pb$ age versus Th/U and $^{206}Pb/^{204}Pb$ are used to discriminate data, defining the most reliable data with fewest inclusions and highest radiogenic versus common Pb at ~1590 Ma (Fig. 7).

4.5.2.1 SE-lobe hematite-rich breccias

The deepest zoned hematite was sampled at 1720 m (pyrite-chalcopyrite zone) from drillhole RD1988 (sample 7295BW). Seven aliquots obtained from four grains returned a zero-age lower intercept and upper intercept at 1591.7 ± 2.5 Ma (MSWD=1.6) (Fig. 6B). Individual $^{207}Pb/^{206}Pb$ dates range from 1606 to 1565 Ma precluding calculation of an acceptable weighted mean date.

Hematite-rich breccias from two locations in drillhole RD2786A show a similar spread in data, with highly variable U concentrations, Pb loss, and common Pb components. Sample LCD 5 forms a zero-age lower and upper intercept at 1592.7 ± 2.2 Ma (n=5, MSWD=2.6) (Fig. 6C). Removal of the highly discordant and common-Pb rich data points defines an upper intercept of 1588.8 ± 4.4 Ma (MSWD=0.95). Sample MV026, yields highly scattered analyses, with high common Pb and Th/U, returning an unconstrained lower intercept and upper intercept

at 1583 ± 14 Ma (n=7, MSWD=63) (Fig. 6D). Individual $^{207}Pb/^{206}Pb$ dates taken alone can provide informative data, however the spread precludes confident weighted mean calculations.

4.5.2.2 High-grade bornite ore

Sample CLC201, from the NW-arm of the deposit, represents an example of high-grade Cu mineralization (Fig. 4A), with abundant bornite and minor chalcopyrite. Four aliquots were prepared from two zoned hematite grains, both displaying corrosion to grain margins with nucleation of uraninite inclusions in marginal domains (Fig. 4B). Three concordant to reversely discordant datapoints form an upper intercept at 1588.3 ± 1.6 Ma (MSWD=2.9; Fig. 6E), while the fourth is reversely discordant and shifted to the left of all other data. The anomalous datapoint contains similar Th/U to other analyses (0.020), but the lowest U concentration and highest common Pb. Individual $^{207}Pb/^{206}Pb$ dates yield low relative uncertainties, however a weighted average with an acceptable MSWD cannot be generated due to high scatter from ~1589 to ~1584 Ma.

4.5.2.3 Deep bedded lithologies

Bedded, fine-grained rocks are found at depths of at least 1.7 km (pyrite-chalcopyrite zone). The sampled rocks occur as a 44 m-thick interval, composed of rhythmic bands of alternating hematite or quartz dominance. Zoned hematite is found along, but also crosscutting, bedding, i.e., along trails of sulfides, with oblique orientation to bedding. These packages were sampled in two locations one meter apart (LCD6 and MV027; Fig. 3B and 4G, H). Nine aliquots from four grains were prepared, with eight analyses forming a zero-age lower and upper intercept at 1587.6 ± 5.4 Ma (MSWD= 0.42; Fig. 6F). All analyses are either discordant, or reversely discordant and individual $^{207}Pb/^{206}Pb$ dates spread from 1594 to 1581 Ma, precluding an acceptable weighted mean calculation.

4.5.2.4 Volcanic and 'barren' deposit center breccias

The volcanic (GRV) breccia (sample LCD35) is hematite-rich, with zoned grains up to 600 µm in length (Fig. 6A). Hematite aliquots (5) sampled from two grains are characterized by very low U contents (mean 15 ppm), low $^{206}Pb/^{204}Pb$ and high Th/U. Despite this, with exclusion of one datapoint containing highest Th/U, a zero-age lower and upper intercept at 1606 ± 14 Ma (MSWD=0.42) is obtainable (Fig. 6G). Hematite sampled from the deposit core (sample MV101) is not shown in Fig. 6 as an intercept cannot be formed from the scattered data.

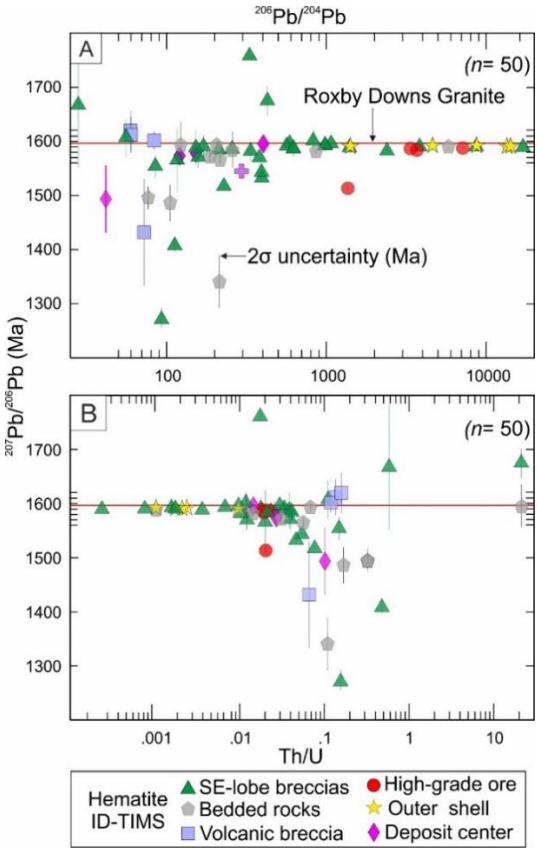


Figure 7: (A-B) Plots of $^{207}Pb/^{206}Pb$ (Ma) versus $^{206}Pb/^{204}Pb$ and Th/U, used to discriminate hematite data from different lithologies, in terms of its common Pb content (A), and presence of inclusions (B). The most geochronologically reliable data clusters at ~1.59 Ga, with 2σ uncertainty bars increasing and datapoints becoming more scattered when $^{206}Pb/^{204}Pb$ drops below ~1000 and Th/U exceeds 0.1. Presented data can be found in tables A1.

4.5.2.5 'Outer shell', northern deposit margin

Zoned hematite grains are not pristine, with inclusion nucleation and porosity developing on grain boundaries, however the cores remain clean, and retain oscillatory zonation patterns. Compared to those within the orebody, grains are unusually rich in HFSE, particularly Ti and Th, of which the latter mirrors U within zonation patterns (Fig. 4G). Further petrographic and geochemical data for hematite in this sample and the 'outer shell' was given by Verdugo-Ihl et al. (2019). Data are collected from five aliquots (Fig. 6H), micro-sampled in the center of two grains shown in Fig. 4F, G. Uranium concentrations ranged from 527 to 135 ppm (average 331 ppm), with high radiogenic versus common Pb components for each aliquot (average $^{206}Pb/^{204}Pb$= 8505; Fig. 7). Of the five aliquots, four are concordant and one is highly discordant. The $^{207}Pb/^{206}Pb$ values for each aliquot are within uncertainty of one another, with individual dates ranging from 1592.1 to 1590.6. Including all data, a confident $^{207}Pb/^{206}Pb$ weighted average of 1591.27 ± 0.89 Ma (n=5, MSWD=0.52) is generated (Fig. 6I).

4.6 Discussion

4.6.1 Formation of the Olympic Dam IOCG deposit: constraints on the magmatic-hydrothermal window

Considering the new geochronological data in the context of generic crustal continuum models for IOCG formation (Groves et al., 2010), and reconstructions of lithospheric architecture for the eastern Gawler Craton (Skirrow et al., 2018), we suggest the following spatial-temporal evolution for formation of the Olympic Dam deposit (Fig. 8). Intracontinental extension during the Gawler SLIP event induced crustal thinning and emplacement of large, felsic bodies of magma such as the Burgoyne Batholith at upper crustal levels, below active GRV volcanoes (Fig. 8A). Bimodal magmatism is evident from mafic lava flows and

dikes/sills, including olivine-phyric basalts and dikes intersected throughout the Olympic Dam district (Huang et al., 2016), thus supporting the hypothesis of deep-rooted magmatism derived from a heterogeneous mantle source (Wade et al., 2019). Central to magma fertility in the region is magma mingling at the sub continental lithospheric mantle/crustal boundary, for which evidence of such phenomena have been inferred by the presence of mafic enclaves in the RDG (Krneta et al., 2016; Kontonikas-Charos et al., 2017).

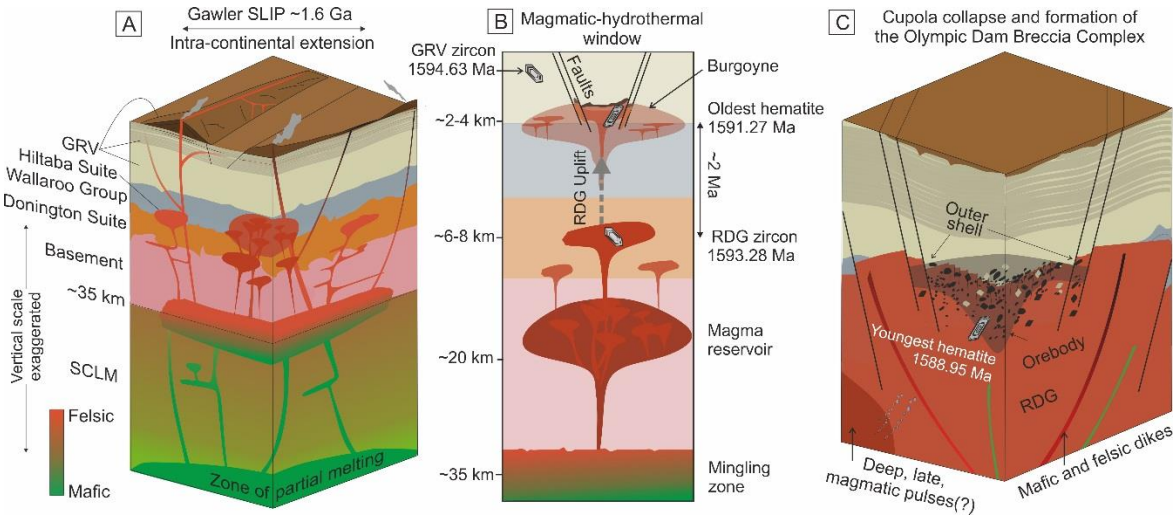


Figure 8: Schematic diagrams illustrating the evolution of the Olympic Dam deposit from mantle to crust. (A) Generalized regional scale model for the Olympic Dam district at ~1.6 Ga from the upper mantle to surface. (B) Cross-section through the mid- to upper crust illustrating the timing of the magmatic-hydrothermal systems, with respect to RDG intrusion, uplift and cupola collapse at different depths. (C) Enlargement showing the collapsed granite cupola and Olympic Dam orebody. Mafic and felsic dikes intrude the RDG/ODBC, while volcanic activity ceases based on the GRV zircon ages presented.

The ~2 Ma age difference between magmatic RDG zircon (1593.28 ± 0.23 Ma) and earliest hydrothermal hematite (1591.27 ± 0.89 Ma; Fig. 9) implies a scenario analogous to that invoked by stochastic models for large porphyry system formation (Chiaradia and Caricchi, 2017). In such models, magma that accumulated in the lower to middle crust (~20 km)

during an interval of ~2-3 Ma is transferred and degassed in the upper crust over timespans of up to 2 Ma. High-precision dating of most porphyry systems, however, indicates timespans of no more than 1 Ma between magmatic zircon and hydrothermal minerals (e.g. Chiaradia et al., 2013; Li et al., 2017).

If we assume that the Olympic Dam mineralization is sourced from hydrothermal fluids exsolved from the RDG during ascent, the ~2 Ma age difference suggests that rates of exhumation/uplift must have been in the range of 1 to 2.5 mm/year. This allows for accumulation of fluids in a supercritical state (e.g., Candela, 1991; Candela and Blevin, 1995) and their release at shallower depths (2-4 km) via decompression of a partially crystallized granite mush.

The plutons that form the Burgoyne Batholith (Creaser and Cooper, 1993) must have been fed by a deep undifferentiated magma reservoir lying at a crustal depth of ~20 km (Fig. 8B). Despite compositional differences among intrusive rocks of the Burgoyne Batholith, all individual granitic sub-suites and plutons dated so far yield zircon ages within uncertainty of one another (Creaser and Cooper, 1993; Jagodzinski, 2005). A first magmatic crystallization stage in RDG is recognized at a depth of ~6-8 km from feldspar+amphibole thermobarometry (Kontonikas-Charos et al., 2017). This stage and depth are constrained from zircon crystallization at ~1593.2 Ma. However, co-existing antecrystic zircon with an age of ~1595 Ma is likely recycled from the deeper magmatic plumbing system (Fig. 8B).

Magnetite formation in an early, ‘outer shell’ at Olympic Dam predates a sudden depressurization that leads to cupola collapse, hydraulic brecciation of both the granite and country rocks and deposition of hematite-dominant ore (Fig. 8C; Verdugo-Ihl et al., 2020). The latter event is constrained by the hematite age of 1591.27 ± 0.89 Ma. Assuming uplift rates as above, this would correspond to a depth of 2-4 km and could have been triggered by catastrophic, destabilizing tectonic events (e.g., mega-earthquakes) as considered for large

porphyry systems (Richards, 2018). Hematite from deposit center is characteristically fine-grained and intensely brecciated, demonstrating highly variable U-Pb systematics, likely due to formation directly within the collapsing cupola (Figs. 8C and 10).

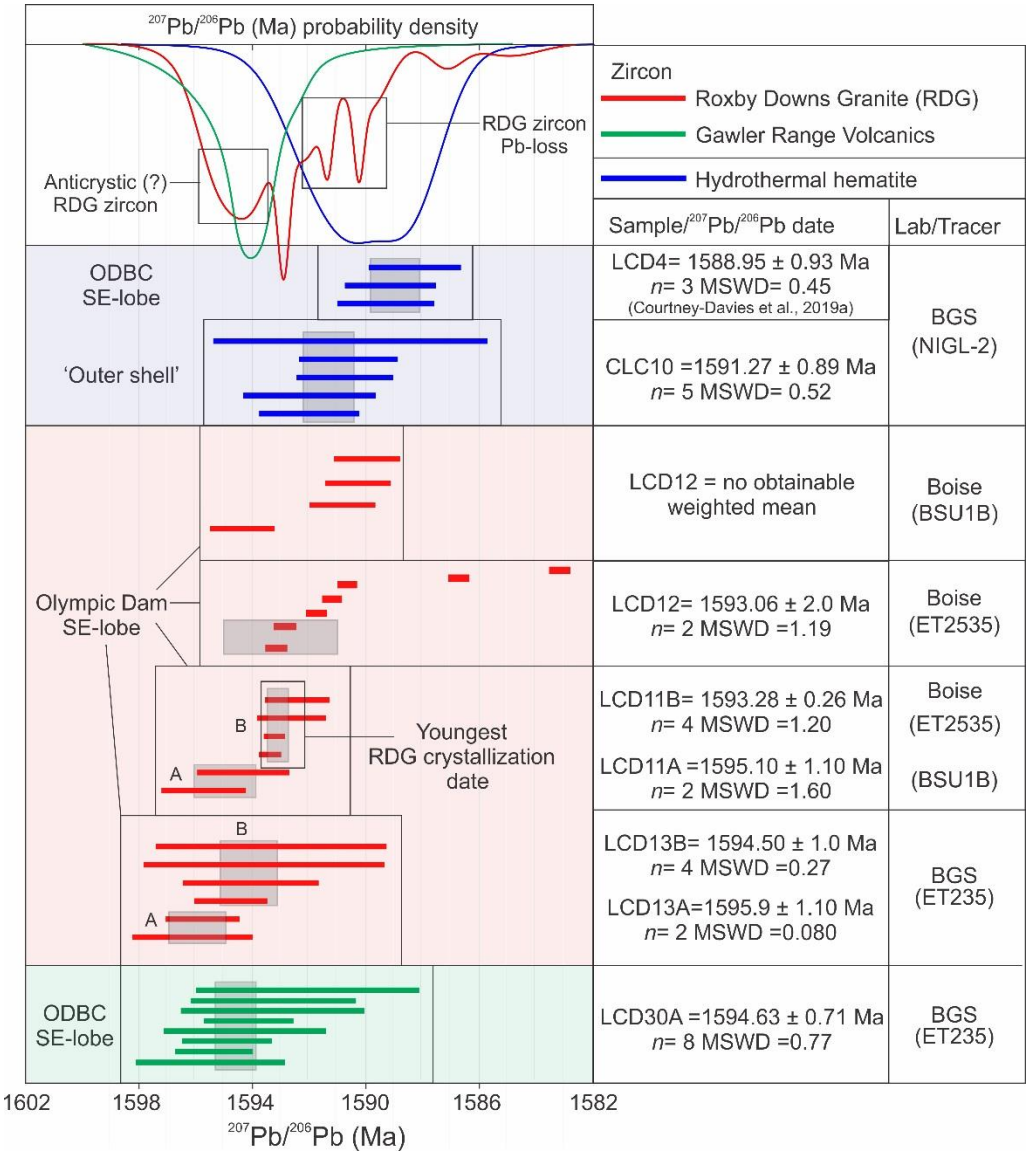


Figure 9: ^{207}Pb/^{206}Pb weighted average diagram for individual GRV/RDG zircon and highest-precision hematite samples (color marked in key). The corresponding ^{207}Pb/^{206}Pb probability density plot for combined weighted averages is presented (upper) and grouped by GRV (1 sample), RDG (4 samples) and hematite (2 samples; sample LCD4 included from Courtney-Davies et al. (2019a). The ^{207}Pb/^{206}Pb dates for the weighted averages are presented to the right, with the laboratory they were analyzed at and the tracer samples were spiked with.

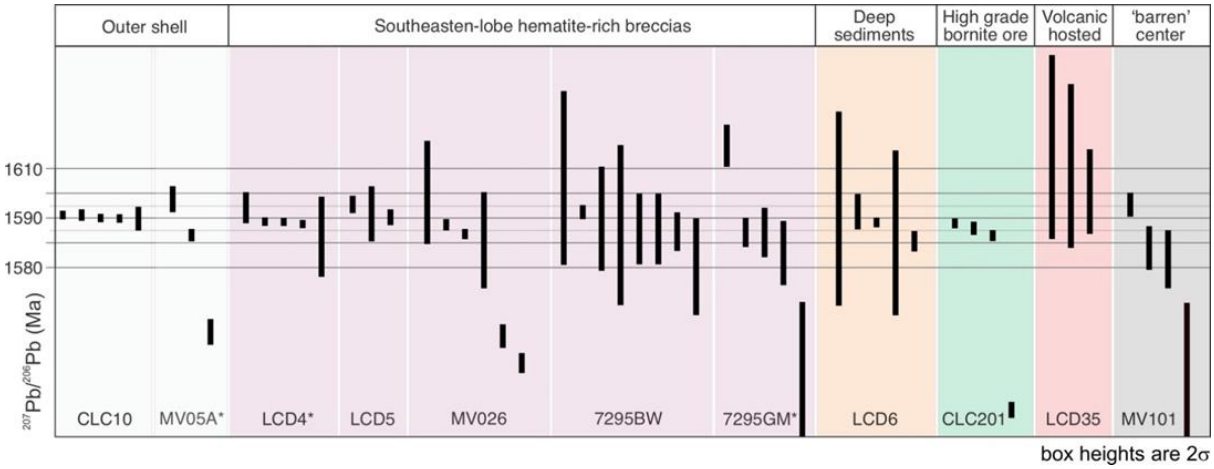


Figure 10: $^{207}Pb/^{206}Pb$ weighted average diagram displaying every zoned hematite ID-TIMS aliquot for each sample within this study. Colors indicate the location/lithology of each sample. Samples labelled with an asterisk are included from Courtney-Davies et al. (2019a).

Zoned hematite from deep (~1.6 km) in the SE-lobe records a confident ($^{207}Pb/^{206}Pb$) population at 1588.95 ± 0.93 (sample LCD4), i.e., ~4 Ma after RDG zircon crystallization. Such younger ages could possibly result from fault (re)activation, augmenting the orebody, and (re)opening fluid pathways or episodic magmatic pulses feeding magmatic-hydrothermal fluids for an additional ~2 Ma interval after the RDG uplift. High-grade bornite ores from the NW-arm, sampled at a shallower level (425 m), yielded young, but highly scattered individual $^{207}Pb/^{206}Pb$ dates. The high Cu-grade of these samples may be the result of younger fluid pulses, introduced late into the hydrothermal system (Krneta et al., 2017, 2018), rather than fault reactivation which has not offset the NW of the deposit as seen in the SE, however, the poorly constrained and non-zero lower intercept likely leverage the date. Continued circulation of primary ore-forming fluids dissolved, reprecipitated, and/or overprinted mineral assemblages, including zoned hematite (Verdugo-Ihl et al., 2017). Variably altered mafic (Huang et al., 2016) and felsic (Johnson and Cross, 1995) dikes tied to the GRV/Hiltaba Suite event have been interpreted to intrude the RDG and ODBC, although mineral assemblages dated so far provide only low-precision constraints at ~1590 Ma. Bedded, silica- and hematite-rich rocks

found at depths of ~1.6 km yield a ~1590 Ma hematite population. This indicates that either pre-existing rocks (Wallaroo Group?) were entrapped within the RDG during uplift/brecciation and subsequently altered, or these units were incorporated into the breccia complex from above via faults, post-deposit formation. Entrapment of Fe-rich lithologies from the Wallaroo Group in the outer shell at Olympic Dam was also documented from U-Pb dating of ~1760 Ma magnetite (Courtney-Davies et al., 2020).

The only published fluid inclusion and stable isotope study invokes a magmatic signature for magnetite (~400 °C, 10 ‰ $\delta^{18}O$) but suggests mixing with seawater or basinal groundwaters during the hematite stage (~200–400 °C, 9‰ $\delta^{18}O$; Oreskes and Einaudi, 1992). This interpretation is, however, based upon an earlier scenario in which the deposit formed close to the paleosurface rather than at depth, as presented here. The fluid source for hematite can only be magmatic-hydrothermal in origin when considering the 'granitophile' signature of dated, zoned hematite found throughout the deposit (Verdugo-Ihl et al., 2017). This signature, comprising a U-W-Sn-Mo element association, is typically enriched in granite-derived fluids (e.g., Kozlov, 2011), and extends and overlaps with mineralization throughout the ODBC, down to >2 km, based on principal component analysis of large whole rock datasets (Dmitrijeva et al., 2019).

We can test this hypothesis by simplified mass balance calculations (Appendix B) assuming fluid exsolution from a parent melt to produce a mineralization mass comparable to that in the Olympic Dam deposit. We select Cu rather than Fe since the latter can be influenced by incorporation of older, pre-existing, Fe-rich lithologies (~1.75 Ga; Courtney-Davies et al., 2020). The reported resource at OD is 79.45 Mt Cu (10,892 Mt @ 0.73 wt.% Cu; BHP 2019). Choosing a range of parameters for average granite composition, including Cu contents of 20 to 120 ppm measured in RDG, water estimate for a typical granitic melt (e.g., 2.5 wt.% H_2O; Clemens, 1984; Holtz et al., 2001), copper partitioning coefficients between a granitic melt and

fluid, $D_{Cu}^{f/m}$, of 2 to 80 (Keppler and Wyllie, 1991; Bai and Koster van Groos, 1999), we can calculate the amount of Cu produced from a volume of parent melt, assuming a total fluid exsolution percentage of 95% after crystallization of hydrous minerals (biotite, amphibole). This assumption is consistent with the calculated H_2O requirement to produce 5% hydrous minerals in RDG (Ehrig et al., 2012), based on H_2O values for the two minerals given by Cline and Bodnar (1991).

Good fits between the resource and calculated Cu produced by the model are obtained (Table B1, Appendix) if we assume a melt volume (15x10x3 = 450 km^3) that is of similar order of magnitude to a realistic estimated volume for the RDG. For example, using $D_{Cu}^{f/m}$, of 80, 2.5 wt.% H_2O, melt density of 2,320 kg/m^3, and Cu content of 120 ppm in the initial melt, we obtain 82.8 Mt Cu extracted to fluid. The volume of the RDG is, in reality, unconstrained and may be significantly larger than estimated from available data.

This model does not, however, explain why this particular intrusion appears to have been so efficient in generating mineralization compared to others of similar composition elsewhere in the same region, including in the same batholith. One intriguing possibility is the role of abundant volatiles within the hydrothermal fluids (as evidenced, for example, by the presence of Cl in zircon; Courtney-Davies et al., 2019c). Equally likely is that a confluence of events (tectonics, cupola collapse) led to the fluids being captured, precipitated and concentrated as an orebody rather than lost.

4.7 Implications

Considering the maximum and minimum hematite dates yielding statistically acceptable MSWD at the 95% confidence interval, a single, major mineralizing event lasted at least ~2 Ma (Fig. 9). When considering the size of the Olympic Dam orebody and large magma flux

during the Gawler SLIP event, a long-lived magmatic-hydrothermal event is plausible, resulting in metallogenesis at the regional-scale. Such a timeframe supports flow of magmatic-hydrothermal fluids for another ~2 Ma post-RDG uplift. In this scenario, a suite of nested, deeper magmatic bodies, intruding below the RDG, as part of the Burgoyne Batholith, can be invoked, which were not captured in the presented sample set, containing zircon of the same age as earliest dated hematite. The oldest hematite age from the 'outer shell' may capture the timing of this event, with 'younger', discordant dates resulting from post-crystallization isotopic modification, or alternatively, attributable to variation in $^{238}U/^{235}U$ upon crystallization, as discussed in (Courtney-Davies et al., 2019a). The accepted $^{238}U/^{235}U$ value for zircon (137.818; Heiss et al., 2012) is well constrained, although there are no direct measurements for this value in hematite, imposing a limiting factor on the accuracy of hematite U-Pb data. However, Kirchenbaur et al. (2016) observed negligible variation from an average $^{238}U/^{235}U$ value of 137.801 determined from analysis of forty whole rock samples in the ODBC, suggesting a common, narrow range of initial $^{238}U/^{235}U$ in all major lithologies, and implicitly in constituent minerals. Therefore, considering the highest-precision, concordant hematite data, and likely narrow range in the $^{238}U/^{235}U$ values for hematite, a ~2 Ma mineralizing timeframe is suggested (Fig. 9). If sampled hematite does contain a $^{238}U/^{235}U$ value akin to that reported by Kirchenbaur et al. (2016), the difference in calculated dates compared to the zircon data reduced with the value of Heiss et al. (2012) would be negligible at the presented resolution. Concordant datapoints confirm that some hematite grains have remained near closed-system and are therefore unaffected by post-crystallization isotope modification

The zircon and oldest captured hematite ages presented above discriminate a temporal difference between the magmatic and magmatic-hydrothermal systems, whereby the earliest zoned hematite crystallizes ~2 Ma after youngest recorded magmatic zircon (Fig. 9), however, unconstrained closure temperatures between zircon and hematite create additional uncertainty.

The relatively low measured difference in age compared to previous estimates (e.g., Johnson and Cross, 1995) supports involvement of magmatic-hydrothermal fluids derived from the parent melts of Hiltaba Suite granites, the geochemical signature of which is recorded within U-W-Sn-Mo-bearing zoned hematite. The ~2 Ma age difference between the magmatic and magmatic-hydrothermal systems further supports a deep, rather than near surface diatreme-maar origin for the deposit, as such sudden uplift from depths of 6-8 km is irreconcilable with the measured window. Diagrams showing Olympic Dam as a 'maar' type of IOCG deposit (e.g., Groves et al., 2010; in press) should be abandoned based on such evidence.

The timescales discussed here emphasize the analytical resolving power required to capture and distinguish between magmatic and magmatic-hydrothermal events, a level of precision that is currently beyond the capabilities of microbeam methods. Uranium-bearing hematite demonstrates that relative precisions of ± 0.1% and ± 0.05% (and interpreted ages) for individual crystal-fragments and $^{207}Pb/^{206}Pb$ grouped weighted means, respectively, is achievable using Mesoproterozoic samples. Despite this, temporal differences between ore zones within the deposit have not been resolved and may not exist (Fig. 10). However, if such a difference does exist, it is likely that the timescales cannot be accurately resolved by the methods and samples used in this study. The data presented here highlights how individual plutons and their associated hydrothermal fluids can be very difficult to date, especially when the largest orebody is hosted within a breccia complex largely composed from the enclosing host granite. Without access to a much wider set of samples from multiple depths across the batholith, requiring substantial drilling of holes almost certain to be barren, the true extent of magmatic-hydrothermal activity may never be fully constrained. Overall, combined zircon-hematite ages represent the highest-precision geochronological study of a Proterozoic IOCG deposit, underpinning the growing value of hematite to accurately date ore forming events at

levels of precision equal to or higher than more conventional methods (e.g., Re-Os dating of molybdenite; Chiaradia et al., 2013).

Geochronological understanding of the Olympic Dam deposit, as well as the larger Olympic IOCG province would benefit from future studies encompassing high-precision dating of mafic dikes within the ODBC, Hiltaba Suite granite from different areas of the Burgoyne Batholith and U-bearing magnetite in the deposits 'outer shell'. Furthermore, future CA-ID-TIMS dating in the region should preferably be undertaken using the same tracer calibration solutions and data reduction methods for transparency in data comparison.

4.8 Conclusions

Three key geochronological constraints on the magmatic-hydrothermal genesis of the Olympic Dam deposit are demonstrated here with confidence for the first time. Integrating zircon and hematite ages underpins a model involving a single, major mineralizing event, hinting at a temporal evolution of zoned hematite within distinct locations and lithologies throughout the deposit, ~2 Ma after zircon crystallization. Furthermore, Olympic Dam hematite (U-Pb) ID-TIMS geochronology has generated a date with the highest (current) analytical precision for a hydrothermal mineral reported within any Proterozoic IOCG deposit. Hematite and zircon should therefore be considered a key mineral pair to constrain the timeframes of U-rich, intrusion-hosted ore systems of any age.

- The magmatic-hydrothermal system at Olympic Dam became active ~2 Ma after the youngest recorded zircon in the granite hosting Olympic Dam at 1593.28 ± 0.26 (2σ).
- The orebody was principally formed during a single, major mineralizing event, whereby the earliest magmatic-hydrothermal activity is recorded in hematite from the 'outer shell' of the deposit at 1591.27 ± 0.89 Ma (2σ).

- Hematite ages constrained throughout all lithologies and orezones within the deposit suggest the magmatic-hydrothermal system was active over a period of ~2 Ma.
- Mesoproterozoic (~1.6 Ga) magmatic-hydrothermal events can be accurately constrained at up to ~0.05 % uncertainty ($^{207}Pb/^{206}Pb$) using the hematite U-Pb mineral geochronometer.

4.9 Acknowledgements

This work is a contribution to the 'FOX' project (Trace elements in iron oxides: deportment, distribution and application in ore genesis, geochronology, exploration and mineral processing), supported by BHP Olympic Dam and the South Australian Government Mining and Petroleum Services Centre of Excellence. N.J.C. and K.E. acknowledge support from the ARC Research Hub for Australian Copper-Uranium (Grant IH130200033). We gratefully acknowledge the constructive comments from Massimo Chiaradia and Adam Simon which helped us improve this manuscript.

4.10 References

Allen, S., McPhie, J., Ferris, G., and Simpson, C., 2008, Evolution and architecture of a large felsic igneous province in western Laurentia: The 1.6 Ga Gawler Range Volcanics, South Australia: Journal of Volcanology and Geothermal Research, v. 172, p. 132–147.

Apukhtina, O., Kamenetsky, V.S., Ehrig, K., Kamenetsky, M.B., Maas, R., Thompson, J., McPhie, J., Ciobanu, C.L., and Cook, N.J., 2017, Early magnetite-fluorapatite mineralization at the Olympic Dam Cu-U-Au-Ag deposit, South Australia: Economic Geology, v. 112, p. 1531-1542.

Bai, T., Koster van Groos, A., 1999, The distribution of Na, K, Rb, Sr, Al, Ge, Cu, W, Mo, La, and Ce between granitic melts and coexisting aqueous fluids: Geochimica et Cosmochimica Acta, v. 63, p. 1117–1131. https://doi.org/10.1016/S0016-7037(98)00284-1

BHP, 2019, BHP Annual report 2019 316 pp: https://www.bhp.com/investor-centre/annual-report-2019/.

Blissett, A.H., Creaser, R.A., Daly, S.J., Flint, R.B., and Parker, A.J., 1993, Gawler Range Volcanics. In: Drexel, J.F., Preiss, W.V., Parker, A.J. (Eds.), The Geology of South Australia. vol. 1, The Precambrian: Geological Survey of South Australia, Bulletin, v. 54, p. 107-131.

Bowring, J.F., McLean, N.M., and Bowring, S.A., 2011, Engineering cyber infrastructure for U-geochronology: Tripoli and U-Pb Redux: Geochemistry, Geophysics, Geosystems, v. 12, Q0AA19.

Candela, P.A., 1991, Physics of aqueous phase evolution in plutonic environment: American Mineralogist, v. 76, p. 1081-1091.

Candela, P.A., Blevin, P.L., 1995, Do some miarolitic granites preserve evidence of magmatic volatile phase permeability?: Economic Geology, v. 90 (8), p. 2310–2316.

Cherry, A.R., McPhie, J., Kamenetsky, V.S., Ehrig, K., Keeling, J.L., Kamenetsky, M.B., Meffre, S., and Apukhtina, O.B., 2017, Linking Olympic Dam and the Cariewerloo Basin: was a sedimentary basin involved in formation of the world's largest uranium deposit?: Precambrian Research, v. 300, p. 168–180.

Cherry, A., Ehrig, K., Kamenetsky, V., McPhie, J., Crowley, J., and Kamenetsky, M., 2018, Precise geochronological constraints on the origin, setting and incorporation of ca. 1.59 Ga surficial facies into the Olympic Dam Breccia Complex, South Australia: Precambrian Research, v. 315, p. 162-178.

Chiaradia, M., Caricchi, L., 2017, Stochastic modelling of deep magmatic controls on porphyry copper deposit endowment: Scientific Repots, 7, 44523.

Chiaradia, M., Schaltegger, U., Spikings, R.A., Wotzlaw, J.F., and Ovtcharova, M., 2013, How accurately can we date the duration of magmatic-hydrothermal events in porphyry systems?: Economic Geology, v. 108, p. 565–584.

Chiaradia, M., Schaltegger, U., and Spikings, R.A., 2014, Time scales of mineral systems – advances in understanding over the past decade: Society of Economic Geologists, Special Publication, v. 18, p. 37–58.

Ciobanu, C.L., Wade, B.P., Cook, N.J., Schmidt Mumm, A., and Giles, D., 2013, Uranium-bearing hematite from the Olympic Dam Cu-U-Au deposit, South Australia: a geochemical tracer and reconnaissance Pb-Pb geochronometer: Precambrian Research, v. 238, p. 129-147.

Ciobanu C.L., Cook, N.J., and Ehrig, K., 2017, Ore minerals down to the nanoscale: Cu-(Fe)-sulphides from the iron oxide copper gold deposit at Olympic Dam, South Australia: Ore Geology Reviews, v. 81, p. 1218–1235.

Clark, J.M., Poznik, N., Ehrig, K., Cherry, A., McPhie, J., and Kamenetsky, V.S., 2018, Syn- to Post-mineralization Structural Dismemberment of the Olympic Dam Fe-Cu-U-Au-Ag Deposit, Gawler Craton: SEG 2018 Conference Abstract, Keystone, Colorado, USA.

Clemens, J.D., 1984, Water contents of silicic to intermediate magmas: Lithos, v. 17, p. 273–287.

Cline, J.S., and Bodnar, R.J., 1991, Can economic porphyry copper mineralization be generated by a typical calc-alkaline melt?: Journal of Geophysical Research, v. 96, p. 8113.

Courtney-Davies, L., Zhu, Z., Ciobanu, C.L., Wade, B.P., Cook, N.J., Ehrig, K., Cabral, A.R., and Kennedy, A., 2016, Matrix-matched iron-oxide laser ablation ICP-MS U-Pb geochronology using mixed solution standards: Minerals, v. 6, 85, doi:10.3390/min603008.

Courtney-Davies, L., Tapster, S.R., Ciobanu, C.L., Cook, N.J., Verdugo-Ihl, M.R., Ehrig, K.J., Kennedy, A.K., Gilbert, S.E., Condon, D.J., and Wade, B.P., 2019a, A multi-technique evaluation of hydrothermal hematite U-Pb isotope systematics: Implications for ore deposit geochronology: Chemical Geology, v. 513, p. 54-72.

Courtney-Davies, L., Ciobanu, C.L., Verdugo-Ihl, M.R., Dmitrijeva, M., Cook, N.J., Ehrig, K., and Wade, B.P., 2019b, Hematite geochemistry and geochronology resolve genetic and temporal links among iron-oxide copper gold systems, Olympic Dam district, South Australia: Precambrian Research, 335, 105480.

Courtney-Davies, L., Ciobanu, C.L., Verdugo-Ihl, M.R., Slattery, A., Cook, N.J., Dmitrijeva, M., Keyser, W., Wade, B.P., Dominick, U.I., Ehrig, K., Xu, J., and Kontonikas-Charos, A., 2019c, Zircon at the nanoscale records metasomatic processes leading to large magmatic-hydrothermal ore deposits: Minerals, v. 9, 364, doi:10.3390/min9060364.

Courtney-Davies, L., Ciobanu, C.L., Verdugo-Ihl, M.R., Cook, N.J., Ehrig, K., Wade, B.P., Zhu, Z.Y., Kamenetsky, V., 2020, ~1760 Ma magnetite-bearing protoliths in the Olympic Dam deposit, South Australia: Implications for ore genesis and regional metallogeny: Ore Geology Reviews, 118, 103337.

Creaser, R.A., 1996, Petrogenesis of a Mesoproterozoic quartz latite-granitoid suite from the Roxby Downs area, South Australia: Precambrian Research, v. 79, p. 371–394.

Creaser, R.A., and Cooper, J.A., 1993, U-Pb geochronology of Middle Proterozoic felsic magmatism surrounding the Olympic Dam Cu-U-Au-Ag and Moonta Cu-Au-Ag deposits, South Australia: Economic Geology, v. 88, p. 186-197.

Dmitrijeva, M., Ciobanu, C.L., Ehrig, K., Cook, N.J., Metcalfe, A., Verdugo-Ihl, M.R., and McPhie, J., 2019, Defining IOCG signatures through compositional data analysis: A case study of lithogeochemical zoning from the Olympic Dam deposit, South Australia: Ore Geology Reviews, v. 105, p. 86–101.

Ehrig, K., McPhie, J., and Kamenetsky, V., 2012, Geology and mineralogical zonation of the Olympic Dam iron oxide Cu-U-Au-Ag deposit, South Australia: Society of Economic Geologists, Special Publication, v. 16, p. 237-268.

Fanning, C.M., Reid, A.J., and Teale, G.S., 2007, A geochronological framework for the Gawler Craton, South Australia: Geological Survey of South Australia. Geological Society of South Australia Bulletin, v. 55, p.258.

Groves, D.I., Bierlein, F.P., Meinert, L.D., and Hitzman, M.W., 2010, Iron oxide copper-gold (IOCG) deposits through Earth history: Implications for origin, lithospheric setting, and distinction from other epigenetic iron oxide deposits: Economic Geology, v. 105, p. 641–654.

Groves, D.I., Zhang, L., and Santosh, M., in press, Subduction, mantle metasomatism, and gold: A dynamic and genetic conjunction: Geological Society of America Bulletin; https://doi.org/10.1130/B35379.1

Haynes, D.W., Cross, K.C., Bills, R.T., and Reed, M.H., 1995, Olympic Dam ore genesis: a fluid-mixing model: Economic Geology, v. 90, p. 281–307.

Hayward, N., and Skirrow, R.G., 2010, Geodynamic setting and controls on iron oxide Cu-Au (±U) ore in the Gawler Craton, South Australia. In: Porter, T.M (ed.), Hydrothermal Iron Oxide Copper-Gold & Related Deposits: A Global Perspective, PGC Publishing, Adelaide, v. 3, p. 1-27.

Hiess, J., Condon, D.J., McLean, N., and Noble, S.R., 2012, $^{238}U/^{235}U$ Systematics in Terrestrial Uranium-Bearing Minerals: Science, v. 335, p. 1610-1614.

Holtz, F., Johannes, W., Tamic, N., Behrens, H., 2001, Maximum and minimum water contents of granitic melts generated in the crust: a reevaluation and implications: Lithos, v. 56, p. 1–14.

Huang, Q., Kamenetsky, V.S., McPhie, J., Ehrig, K., Meffre, S., Maas, R., Thompson, J., Kamenetsky, M., Chambefort, I., Apukhtina, O., and Hu, Y., 2015, Neoproterozoic (ca. 820–830 Ma) mafic dykes at Olympic Dam, South Australia: Links with the Gairdner Large Igneous Province: Precambrian Research, v. 271, p. 160-172.

Huang, Q., Kamenetsky, V.S., Ehrig, K., McPhie, J., Kamenetsky, M., Cross, K., Meffre, S., Agangi, A., Chambefort, I., Direen, N.G., Maas, R., and Apukhtina, O., 2016, Olivine-phyric basalt in the Mesoproterozoic Gawler silicic large igneous province, South Australia: Examples at the Olympic Dam Iron Oxide Cu–U–Au–Ag deposit and other localities: Precambrian Research, v. 281, p. 185–199.

Jaffey, A.H., Flynn, K.F., Glendenin, L.E., Bentley, W.C., and Essling, A.M., 1971, Precision Measurement of Half-Lives and Specific Activities of ^{235}U and ^{238}U: Physical Review C, v. 4, p. 1889-1906.

Jagodzinski, E.A., 2005, Compilation of SHRIMP U-Pb geochronological data Olympic Domain, Gawler Craton, South Australia, 2001-2003: Geoscience Australia Record 2005/020.

Johnson, J.P., 1993, The geochronology and radiogenic isotope systematics of the Olympic Dam copper-uranium-gold-silver deposit, South Australia: Unpublished Ph.D. thesis, Canberra, Australia, The Australian National University.

Johnson, J.P., and Cross, K.C., 1995, U-Pb geochronological constraints on the genesis of the Olympic Dam Cu-U-Au-Ag deposit, South Australia: Economic Geology, v. 90, p. 1046–1063.

Keppler, H., Wyllie, P.J., 1991. Partitioning of Cu, Sn, Mo, W, U, and Th between melt and aqueous fluid in the systems haplogranite-H_2O-HCl and haplogranite-H_2O-HF: Contributions to Mineralogy and Petrology, v, 109, p. 139–150.

Keyser, W., Ciobanu, C.L., Cook, N.J., M., Dmitrijeva, M., Courtney-Davies, L., Feltus, H., Gilbert, S., Johnson, G., and Ehrig, K., 2019, Iron-oxides constrain BIF evolution in terranes with protracted geological histories: The Iron Count prospect, Middleback Ranges, South Australia: Lithos, v. 324-325, p. 20-38.

Kirchenbaur, M., Maas, R., Ehrig, K., Kamenetsky, V.S., Strub, E., Ballhaus, C., and Münker, C., 2016, Uranium and Sm isotope studies of the supergiant Olympic Dam Cu–Au–U–Ag deposit, South Australia: Geochimica et Cosmochimica Acta, v. 180, p. 15–32.

Kontonikas-Charos, A., Ciobanu, C.L., Cook, N.J., Ehrig, K., Krneta, S., and Kamenetsky, V.S., 2017, Feldspar evolution in the Roxby Downs Granite, host to Fe-oxide Cu-Au-(U) mineralisation at Olympic Dam, South Australia: Ore Geology Reviews, v. 80, p. 838–859.

Kozlov, V.D., 2011, Trace-element composition and origin of granitoids from the Shakhtama complex and Kukul'bei rare-metal complex (Aga zone, Transbaikalia): Russian Geology and Geophysics, vol. 52(5), p. 526–536.

Krneta, S., Ciobanu, C.L., Cook, N.J., Ehrig, K., and Kontonikas-Charos, A., 2016, Apatite at Olympic Dam, South Australia: a petrogenetic tool: Lithos, v. 262, p. 470–485.

Krneta, S., Ciobanu, C.L., Cook, N.J., Ehrig, K., and Kontonikas-Charos, A., 2017, Rare earth element behaviour in apatite from the Olympic Dam Cu–U–Au–Ag deposit, South Australia: Minerals, v. 7, 135. https://doi.org/10.3390/min7080135.

Krneta, S., Ciobanu, C., Cook, N., and Ehrig, K., 2018, Numerical modeling of REE fractionation patterns in fluorapatite from the Olympic Dam deposit (South Australia): Minerals, v. 8, 342. https://doi.org/10.3390/ min8080342.

Li, Y., Selby, D., Condon, D., and Tapster, S., 2017, Cyclic Magmatic-Hydrothermal Evolution in Porphyry Systems: High-Precision U-Pb and Re-Os Geochronology Constraints on the Tibetan Qulong Porphyry Cu-Mo Deposit: Economic Geology, v. 112, p. 1419-1440.

Ludwig, K.R.A., 2012, User's Manual for Isoplot 3.75: A Geochronological Toolkit for Microsoft Excel: Berkeley Geochronology Centre Special Publication, v. 5.

Maas, R., Kamenetsky, V.S., Ehrig, K., Meffre, S., McPhie, J., and Diemar, G., 2011, Olympic Dam U-Cu-Au deposit, Australia: New age constraints: Mineralogical Magazine, Goldschmidt Conference abstract, v. 75, p. 1375.

Mattinson, J.M., 2005, Zircon U-Pb chemical abrasion ("CA-TIMS") method: combined annealing and multi-step partial dissolution analysis for improved precision and accuracy of zircon ages: Chemical Geology, v. 220, p. 47-66.

Meffre, S., Ehrig, K., Kamenetsky, V.S., Chambefort, I., Maas, R., and McPhie, J., 2010, Pb isotopes at Olympic Dam: Constraining sulphide growth: Giant ore deposits down under: Proceedings of 13th Quadrennial International Association on the Genesis of Ore Deposits (IAGOD) Symposium, Adelaide, South Australia, p. 78–79.

Oreskes, N., and Einaudi, M.T., 1990, Origin of rare earth element-enriched hematite breccias at the Olympic Dam Cu-U-Au-Ag deposit, Roxby Downs, South Australia: Economic Geology, v. 85, p. 1–28.

Oreskes, N., and Einaudi, M.T., 1992, Origin of hydrothermal fluids at Olympic Dam: preliminary results from fluid inclusions and stable isotopes: Economic Geology, v. 87, p. 64–90.

Paton, C., Hellstrom, J., Paul, P., Woodhead, J., and Hergt, J., 2011, Iolite: Freeware for the visualisation and processing of mass spectrometric data: Journal of Analytical Atomic Spectrometry, v. 26, p. 2508.

Reeve, J.S., Cross, K.C., Smith, R.N., and Oreskes, N., 1990, Olympic Dam copper-uranium-gold-silver deposit, in Hughes, F.E., ed., Geology of the mineral deposits of Australia and Papua New Guinea: Melbourne, Australia, Australian Institute of Mining and Metallurgy, p. 1009–1035.

Reid, A., 2019, The Olympic Cu-Au Province, Gawler Craton: A Review of the Lithospheric Architecture, Geodynamic Setting, Alteration Systems, Cover Successions and Prospectivity: Minerals, v. 9(6), 371, doi:10.3390/min9060371.

Richards, J.P., 2018, A Shake-Up in the Porphyry World?: Economic Geology, v. 113 (6), p. 1225–1233.

Schlegel, T.U., Wagner, T., Boyce, A., and Heinrich, C.A., 2017, A magmatic source of hydrothermal sulfur for the Prominent Hill deposit and associated prospects in the Olympic iron oxide copper-gold (IOCG) province of South Australia: Ore Geology Reviews, v. 89, p. 1058–1090.

Schmitz, M.D., and Schoene, B., 2007, Derivation of isotope ratios, errors, and error correlations for U-Pb geochronology using ^{205}Pb-^{235}U-(^{233}U)-spiked isotope dilution thermal ionization mass spectrometric data: Geochemistry, Geophysics, Geosystems, v. 8, Q08006, doi:10.1029/2006GC001492.

Sillitoe, R.H., and Mortensen, J.K., 2010, Longevity of porphyry copper formation at Quellaveco, Peru: Economic Geology, v. 105, p. 1157–1162.

Skirrow, R.G., Bastrakov, E.N., Baroncii, K., Fraser, G.L., Creaser, R.A., Fanning, C.M., Raymond, and O.L., Davidson, G.J., 2007, Timing of iron oxide Cu-Au-(U) hydrothermal activity and Nd isotope constraints on metal sources in the Gawler craton, South Australia: Economic Geology, v. 102, p. 1441–1470.

Skirrow, R.G., Van Der Wielen, S.E., Champion, D.C., Czarnota, K., and Thiel, S., 2018, Lithospheric architecture and mantle metasomatism linked to iron oxide Cu-Au ore formation: Multidisciplinary evidence from the Olympic Dam Region, South Australia: Geochemistry, Geophysics, Geosystems, v. 19(8), p. 2673–2705.

Steiger, R.H., and Jäger, E., 1977, Subcommission on geochronology: Convention on the use of decay constants in geo- and cosmochronology: Earth and Planetary Science Letters, v. 36, p. 359-362.

Trueman, N.A., Long, J.V.P., Reed, S.J.B., and Chinner, G.A., 1988, The lead-uranium systematics, and rare earth element distributions of some Olympic Dam and Stuart shelf mineralisation: Adelaide, Australia, Western Mining Corporation, unpublished report, K/3143, p. 46.

Verdugo-Ihl, M.R., Ciobanu, C.L., Cook, N.J., Ehrig, K., Courtney-Davies, L., and Gilbert, S., 2017, Textures and U-W-Sn-Mo signatures in hematite from the Olympic Dam Cu-U-Au-Ag deposit, South Australia: Defining the archetype for IOCG deposits: Ore Geology Reviews, v. 91, p. 173-195.

Verdugo-Ihl, M.R., Ciobanu, C.L., Cook, N.J., Ehrig, K., and Courtney-Davies, L., 2020, Defining early stages of IOCG systems: evidence from iron-oxides in the outer shell of the Olympic Dam deposit, South Australia: Mineralium Deposita (in press), doi:10.1007/s00126-019-00896-2.

Von Quadt, A., Erni, M., Martinek, K., Moll, M., Peytcheva, and Heinrich, C.A., 2011, Zircon crystallization and the lifetimes of ore-forming magmatic-hydrothermal systems: Geology, v. 39, p. 731−734.

Wade C.E., Payne, J.L., Barovich, K.M., and Reid, A.J., 2019, Heterogeneity of the sub-continental lithospheric mantle and 'non-juvenile' mantle additions to a Proterozoic silicic large igneous: Lithos, v. 340–341, p. 87-107.

Walter, B.F., Gerdes, A., Kleinhanns, I.C., Dunkl, I., Von, H., Kreissl, S., and Markl, G., 2018, The connection between hydrothermal fluids, mineralization, tectonics and magmatism in a continental rift setting: fluorite Sm-Nd and hematite and carbonates U-Pb geochronology from the Rhine graben in SW Germany: Geochimica et Cosmochimica Acta, v. 240, p. 11-42

Weatherley, D.K., and Henley, R.W., 2013, Flash vaporization during earthquakes evidenced by gold deposits: Nature Geoscience, v. 6, p. 294–298.

Zhou, H., Sun, X., Wu, Z., Liao, J., Fu, Y., Li, D., Hollings, P., Liu, Y., Lin, H., and Lin, Z., 2017, Hematite U-Pb geochronometer: insights from monazite and hematite integrated chronology of the Yaoan gold deposit, Southwest China: Economic Geology, v. 112, p. 2023–2039.

Zimmerman, A., Stein, H.J., Morgan, J.W., Markey, R.J., and Watanabe, Y., 2014, Re-Os geochronology of the El Salvador porphyry Cu-Mo deposit, Chile: Tracking analytical improvements in accuracy and precision over the past decade: Geochimica et Cosmochimica Acta, v. 131, p. 13–32.

CHAPTER 5

HEMATITE GEOCHEMISTRY AND GEOCHRONOLOGY RESOLVE GENETIC AND TEMPORAL LINKS AMONG IRON-OXIDE COPPER GOLD SYSTEMS, OLYMPIC DAM DISTRICT, SOUTH AUSTRALIA

Liam Courtney-Davies[1], Cristiana L. Ciobanu[1], Max R. Verdugo-Ihl[1], Marija Dmitrijeva[1], Nigel J. Cook[1], Kathy Ehrig[2], Benjamin P. Wade[3]

[1]*School of Chemical Engineering and Advanced Materials, The University of Adelaide, Adelaide, SA 5005, Australia*

[2] *BHP Billiton Olympic Dam, Adelaide, SA, 5000, Australia*

[3] *Adelaide Microscopy, The University of Adelaide, Adelaide, SA 5005, Australia*

Article published in Precambrian Research (2019), 355, 105480.

Statement of Authorship

Title of Paper	Hematite geochemistry and geochronology resolve genetic and temporal links among iron-oxide copper gold systems, Olympic Dam district, South Australia
Publication Status	☑ Published ☐ Accepted for Publication ☐ Submitted for Publication ☐ Unpublished and Unsubmitted w ork w ritten in manuscript style
Publication Details	Courtney-Davies, L., Ciobanu, C.L., Verdugo-Ihl, M., Dmitrijeva, M., Cook, N.J., Ehrig, K., Wade, B.P., 2019. Hematite geochemistry and geochronology resolve genetic and temporal links among iron-oxide copper gold systems, Olympic Dam district, South Australia. Precambrian Research 335, 105480.

Principal Author

Name of Principal Author (Candidate)	Liam Courtney-Davies		
Contribution to the Paper	Performed analytical work, carried out data processing and interpretation, oversaw development of work and wrote manuscript.		
Overall percentage (%)	65		
Certification:	This paper reports on original research I conducted during the period of my Higher Degree by Research candidature and is not subject to any obligations or contractual agreements with a third party that would constrain its inclusion in this thesis. I am the primary author of this paper.		
Signature		Date	29/10/2019

Co-Author Contributions

By signing the Statement of Authorship, each author certifies that:

i. the candidate's stated contribution to the publication is accurate (as detailed above);

ii. permission is granted for the candidate in include the publication in the thesis; and

iii. the sum of all co-author contributions is equal to 100% less the candidate's stated contribution.

Name of Co-Author	Cristiana L. Ciobanu		
Contribution to the Paper	Helped define direction of research, supervised development of work, assisted with data interpretation and contributed to manuscript preparation.		
Overall percentage (%)	15		
Signature		Date	29 Oct 2019

Name of Co-Author	Max Verdugo-Ihl		
Contribution to the Paper	Assisted with data collection and interpretation and contributed to manuscript preparation and evaluation.		
Overall percentage (%)	10		
Signature		Date	29/10/2019

Name of Co-Author	Marija Dmitrijeva		
Contribution to the Paper	Assisted with data processing and interpretation, and evaluation of manuscript.		
Overall percentage (%)	4		
Signature		Date	~~30/4/2019~~ 29/10/2019

Name of Co-Author	Nigel J. Cook		
Contribution to the Paper	Assisted with analytical instrumentation, data processing and evaluation of manuscript.		
Overall percentage (%)	2		
Signature		Date	29/10/2019

Name of Co-Author	Kathy Ehrig		
Contribution to the Paper	Supplied samples, helped define research direction and evaluated manuscript.		
Overall percentage (%)	2		
Signature		Date	29/10/2019

Name of Co-Author	Benjamin P. Wade		
Contribution to the Paper	Assisted with data acquisition, processing, interpretation and evaluation of manuscript.		
Overall percentage (%)	2		
Signature		Date	29/10/2019

Precambrian Research 335 (2019) 105480

Contents lists available at ScienceDirect

Precambrian Research

journal homepage: www.elsevier.com/locate/precamres

Hematite geochemistry and geochronology resolve genetic and temporal links among iron-oxide copper gold systems, Olympic Dam district, South Australia

Liam Courtney-Davies[a,*], Cristiana.L. Ciobanu[a], Max R. Verdugo-Ihl[a], Marija Dmitrijeva[a], Nigel J. Cook[a], Kathy Ehrig[b], Benjamin P. Wade[c]

[a] School of Chemical Engineering and Advanced Materials, The University of Adelaide, Adelaide, SA 5005, Australia
[b] BHP Olympic Dam, Adelaide, SA 5000, Australia
[c] Adelaide Microscopy, The University of Adelaide, SA 5005, Australia

ARTICLE INFO

Keywords:
Hematite U-Pb dating
IOCG
Wirrda Well
Acropolis
Olympic Cu-Au province

ABSTRACT

The Wirrda Well and Acropolis prospects, ~25 km south from the Olympic Dam deposit, are among several dozen examples of iron-oxide copper gold (IOCG) mineralisation forming a 600 km-long province in the eastern Gawler Craton, South Australia. IOCG systems across the province differ in terms of host lithology, iron-oxide mineral associations, intensity of brecciation, and grade of Cu-(U)-Au mineralisation. Previous efforts to provide a geochronological framework for mineralisation, and correlate this with igneous activity, were inhibited by a lack of clear crosscutting features (particularly in breccia-hosted systems) and a scarcity of reliable hydrothermal mineral geochronometers. The earliest generation of hematite, characterised by enrichment in U-W-Sn-Mo and previously reported from Olympic Dam, provides confident U-Pb dates and insights into hydrothermal fluid signatures. Similar hematite is recognised from Wirrda Well and Acropolis, allowing direct comparison between the three IOCG systems. Relationships between early, silician (Wirrda Well) and titaniferous (Acropolis) magnetite and U-bearing hematite at the two prospects differ. Inferred martitisation of magnetite at Acropolis has generated zoned hematite with U-W-Mo-enrichment at constant Sn concentration, but with a marked loss of REE + Y (REY) and Ti, whereas at Wirrda Well, single-crystal zoned hematite, resembling that from Olympic Dam, retains high REY and Sn concentrations. Although morphologies, textures and compositions of U-bearing hematite at Olympic Dam, Wirrda Well and Acropolis vary significantly, a common U-Pb (laser ablation-inductively coupled plasma-mass spectrometry) age of ~1590 Ma is obtained from the most reliable data ($^{207}Pb/^{206}Pb$: 1598.9 ± 6.3 Ma at Wirrda Well and 1590.6 ± 6.5 Ma at Acropolis). The geochemical signatures of iron-oxides from the two prospects share common trends for U, W, Sn, Mo, high field strength and siderophile elements, comparable with signatures of Fe-oxides from the 'outer shell' of the Olympic Dam deposit. Given that datable iron-oxides would seem to be ubiquitous phases throughout the eastern Gawler Craton, the commonality in geochemistry and age of U-bearing hematite from the Olympic Dam district is significant, as it provides a single, traceable mineral to compare IOCG systems across the province.

1. Introduction

Mesoproterozoic magmatic-hydrothermal ore deposits and prospects occur within a Cu-Au ± U-rich metallogenic province, extending for 600 km along the eastern margin of the Gawler Craton, South Australia (Fig. 1A). Climaxing at ~1.6 Ga, a craton-scale tectonothermal event resulted in emplacement of voluminous, bi-modal intrusive and volcanic rocks of the co-magmatic Gawler Range Volcanics (GRV) and Hiltaba Suite (Drexel et al., 1993, and references therein). Together, these rocks form an intracontinental Large Igneous Province (LIP), which unlike most mantle plume derived LIP's (Ernst, 2014), is dominated by felsic rather than mafic rocks (Allen et al., 2008). The magmatism, and associated metallogenesis in the region, has been temporally correlated with the episodic breakup of the Columbia/Nuna supercontinent (Goldfarb et al., 2010; Groves et al., 2010).

Based on geophysical and geochemical data, lithospheric models for the region acknowledge the important role of mantle-derived components and, moreover, recognise delamination of metasomatised

* Corresponding author.
E-mail address: liam.courtney-davies@adelaide.edu.au (L. Courtney-Davies).

https://doi.org/10.1016/j.precamres.2019.105480
Received 12 June 2019; Received in revised form 4 October 2019; Accepted 4 October 2019
Available online 05 October 2019
0301-9268/ © 2019 Elsevier B.V. All rights reserved.

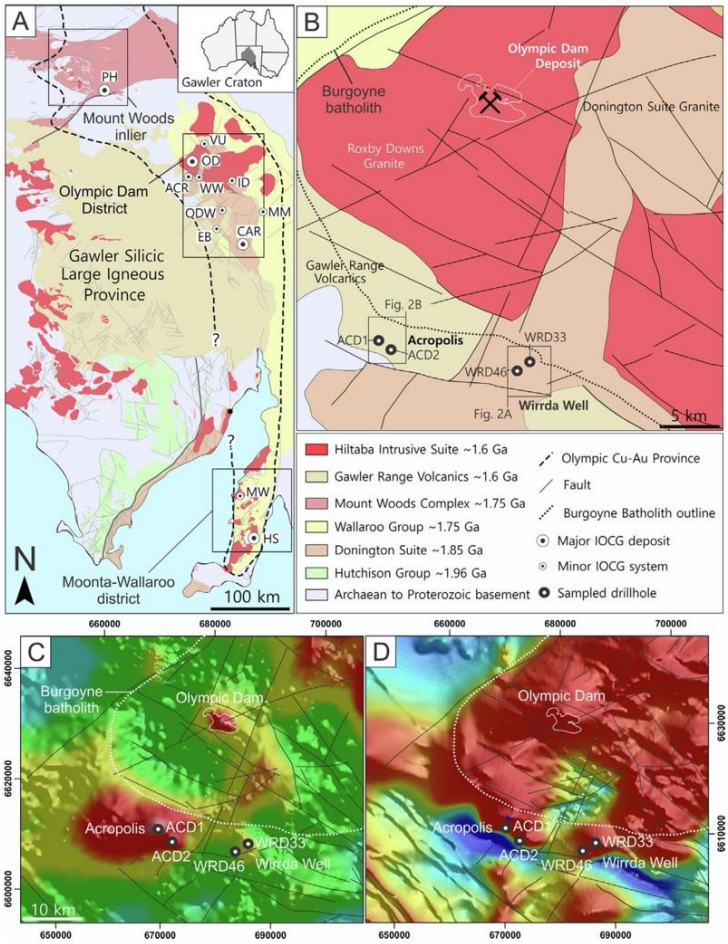


Fig. 1. (A) Geological map of the eastern Gawler Craton and (B) the Olympic Dam deposit and Wirrda Well and Acropolis prospects, with corresponding (C) Bouguer and (D) total magnetic intensity anomaly maps, displaying the geophysical expressions of the three IOCG systems. Data is sourced the Geological Survey of South Australia (https://map.sarig.sa.gov.au/). Abbreviations: ACR-Acropolis; CAR-Carrapateena; EB-Emmie Bluff; HS-Hillside; ID-Island Dam; MM-Murdie Murdie; MW-Moonta-Wallaroo; ODW-Oak Dam West; OD-Olympic Dam; PH-Prominent Hill; VU-Vulcan; WW-Wirrda Well.

subcontinental lithospheric mantle (SCLM) accompanying the LIP event (Skirrow et al., 2018; Wade et al., 2019). Such a setting, in which SCLM was fertilized with volatiles and ore elements during earlier subduction, accompanied by back-arc development, accounts for bi-modal magmatism with a high component of metals and incompatible elements typical of IOCG systems (Groves et al., 2010).

The genetic concept of a single metallogenic province along the eastern margin of the Gawler Craton has evolved through complimentary studies of structural architecture, mineralogy and geochronology across the region, leading to definition of an iron-oxide copper–gold (IOCG) belt termed the "Olympic Cu-Au province" (Reid, 2019; Skirrow et al., 2007). The province hosts the world-class Olympic Dam Cu-U-Au-Ag deposit (Ehrig et al., 2012), as well as numerous other deposits and prospects, displaying a variety of mineralisation styles (e.g., breccia, skarn, vein) and hosted within lithologies including granite, metasedimentary and volcanic rocks.

A spectrum of geochronological data has confirmed the relationship between IOCG mineralisation and alteration with the ~ 1.6 Ga magmatic event (e.g. Skirrow et al., 2007; Reid et al., 2013; Ciobanu et al., 2013; Bowden et al., 2017). The synchronicity of timing is, however, considered broad, with even the most reliable U-Pb dates for the primary Cu-Au mineralisation event spanning an interval as large as ~30 Ma (Table 1). Several factors have contributed to this given timespan: (1) there is a lithological and temporal range in the rocks hosting the IOCG systems; (2) geochronology has been based on a wide variety of minerals, capturing different stages of the same geological event, or even events that are temporally quite distinct; (3) radio-isotopic systems and instrumentation used for dating are often not directly comparable; (4) high-precision geochronological data for major breccia-hosted deposits other than Olympic Dam (e.g., Prominent Hill, Carrapateena) remains relatively limited; and (5) there is a lack of geochronological data from minerals which can only be hydrothermal in origin and therefore directly related to Cu-Au-(U) mineralisation.

Hematite, which is ubiquitous to generic schemes for IOCG

formation, can co-exist with magnetite in different proportions throughout alteration assemblages forming the broader footprints of a given mineralising system (Barton, 2013, and references therein). Advances in hematite U-Pb geochronology have shown that reproducible, < 1 Ma precision is achievable by isotope dilution thermal ionisation mass spectrometry (ID-TIMS) (Courtney-Davies et al., 2019a), as demonstrated using hydrothermal hematite from Olympic Dam, dated at 1589.94 ± 0.91 Ma ($^{207}Pb/^{206}Pb$). Datable hematite is compositionally zoned with respect to U (+radiogenic Pb), W, Sn, and Mo, (representing a primary association hereafter termed 'granitophile elements'), reaching up to wt.% concentrations. Transmission electron microscopy on thinned foils of U-richest zoned hematite at Olympic Dam, prepared *in-situ* by focused ion beam SEM methods, confirm that U and radiogenic Pb is lattice-bound and thus not present as nanometer- to micrometer-scale inclusions (Ciobanu et al., 2013). At the micron scale, LA-ICP-MS spot analysis consistently provides stable downhole ablation profiles for U and Pb, while LA-ICP-MS mapping demonstrates that concentrations of U and Pb correlate with grain-scale zoning (Ciobanu et al., 2013; Verdugo-Ihl et al., 2017). Moreover, experimental studies have successfully doped synthetic hematite with U, demonstrating that up to several wt. % can be incorporated (Duff et al., 2002; Courtney-Davies et al., 2019b).

The granitophile hematite signature is present throughout the ~6 km-strike and ~2 km-depth of the breccia complex hosting the Olympic Dam orebody (Dmitrijeva et al., 2019; Verdugo-Ihl et al., 2017). Coupled with chemical abrasion-ID-TIMS ages of magmatic zircon from granite hosting the deposit, dated at 1593.87 ± 0.21 Ma (Cherry et al., 2018a), a transitional timeframe between the magmatic and hydrothermal systems can be measured (~2–4 Ma). The accuracy of U-Pb microbeam data acquisition is also confirmed, albeit with somewhat lower analytical precision, facilitating fast and reliable hematite dating of additional representative samples via laser ablation-inductively coupled plasma-mass spectrometry (LA-ICP-MS; Ciobanu et al., 2013; Courtney-Davies et al., 2016; Courtney-Davies et al., 2019a).

High-precision magmatic-hydrothermal geochronology explicitly links the mineralising fluids forming Olympic Dam to a single, major ore-forming event, tied to the granite hosting the deposit. This conclusion is supported by other studies, e.g., (1) isotope studies and modelling, that have proposed a single magmatic sulphur source for IOCG deposits in the Cu-Au Olympic Province (Schlegel et al., 2017); (2) the overlap between, and low range of, $\delta^{238}U$ values in the Olympic Dam Breccia Complex and host granite (Kirchenbaur et al., 2016), indicating that $\delta^{238}U$ mineralisation values reflect a source from a granitoid rock; (3) chloro-hydroxy-zircon-nanoprecipitates have been imaged within magmatic zircon from the host granite and are interpreted to have formed through pervasive coupled dissolution reprecipitation reaction driven metasomatism shortly after granite crystallisation (Courtney-Davies et al., 2019c); and (4) the granitophile element signature defining IOCG mineralisation (Dmitrijeva et al., 2019a) is particularly well expressed by early-stage, oscillatory (growth)-zoned hematite (Verdugo-Ihl et al., 2017), the dominant Fe-oxide in the deposit (Ehrig et al., 2012).

If all mineralisation is genetically tied to fluids derived from deep-rooted magmas of common origin and evolution, hematite should contain a traceable geochemical signature, common to all IOCG deposits in the Olympic Cu-Au province, irrespective of its proportion relative to magnetite, or host lithology. In this contribution, we study hematite to ascertain whether the same geochemical signature defined by enrichment in granitophile elements that was identified in the Olympic Dam deposit also occurs ~25 km to the south, at the Wirrda Well and Acropolis IOCG prospects (Fig. 1B). The prospects differ from Olympic Dam, and one another, in terms of: (1) Fe-oxide association (paragenetically less evolved e.g., a dominance of magnetite over hematite); (2) major host lithologies (Donington Suite granite at Wirrda Well and GRV at Acropolis *versus* Hiltaba Suite granite at Olympic Dam); and (3) less intense Cu-Au mineralisation, alteration and brecciation. Through textural, geochemical and U-Pb analysis, hematite can be used to compare the IOCG systems in terms of both the timing of ore formation and the geochemical signatures of mineralising fluids. U-W-Sn-Mo-rich hematite can be used to underpin a robust U-Pb framework of mineralisation ages throughout the Olympic Cu-Au province, resolving the relative chronologies of IOCG systems, regardless of mineralisation style, host lithology or location.

2. Geological background

Basement rocks of the Olympic Dam District comprise the 2.5 Ga Mulgathing Metamorphic Complex, 1.85 Ga Donington Suite granitoid rocks, and 1.76–1.74 Ga Wallaroo Group (meta)sedimentary rocks, which are intruded by, and unconformably overlain by the ~1.6 Ga Hiltaba Suite and GRV, respectively (Fig. 1). Olympic Dam and two satellite prospects, Wirrda Well and Acropolis, occur close to intersections between regional NW-ENE trending structures, in association with second-order NE-ENE-striking faults, interpreted to have provided steeply plunging fluid conduits for all major IOCG deposits in the Olympic Cu-Au province (Hayward and Skirrow, 2010). At the crustal scale, Olympic Dam and the two satellite prospects are contained within a fault-bounded block, characterised by a magnetic anomaly, and host to a cluster of Hiltaba Suite plutons of the Burgoyne batholith (Hayward and Skirrow, 2010). This cluster includes the Roxby Downs Granite, host to Olympic Dam, and other Hiltaba Suite affiliated plutons, intersected by drillholes to the NE of Wirrda Well (Ehrig, 2013) and in the north-western part of Acropolis (Creaser, 1989). GRV rocks are present within all three locations, albeit in various amounts, predominantly as lavas and dikes. Felsic GRV rocks are the main host to mineralisation at Acropolis, whereas minor mafic/ultramafic dikes of both GRV-affiliation and Donington age are abundant in Wirrda Well (Ehrig et al., 2017, and references therein). The presence of alkaline picrite is noteworthy in the latter case. Acropolis is characterised by a large positive gravity coincident with a dipolar magnetic anomaly, compared to the confined potential field anomaly at Olympic Dam and the low geophysical expressions at Wirrda Well (Fig. 1C and D).

Mineralisation in both prospects comprises chalcopyrite + pyrite, an association which is typical of the deeper and outer ore zone at Olympic Dam (Ehrig et al., 2012). Hematite is the dominant Fe-oxide in both prospects, although magnetite can be locally dominant, and is volumetrically far more significant than at Olympic Dam, whilst also being more abundant at Acropolis than Wirrda Well. Magnetite increases in abundance in the outer shell at Olympic Dam relative to the orebody, where hematite is still the dominant Fe-oxide through the chalcopyrite + pyrite ore zone (Verdugo-Ihl et al., 2017, 2019). Bornite and chalcocite are nonetheless present at the upper part in Wirrda Well, but are scarce in Acropolis (Ehrig, 2013; Krneta et al., 2017). Based on such characteristics and the less intense brecciation, the two prospects are considered less evolved IOCG systems compared to Olympic Dam (Ehrig et al., 2017).

Mineralisation at Wirrda Well occurs as disseminations, patches and veinlets, dominantly hosted within sheared, weakly-brecciated Donington granite, with increased shearing and mylonitisation at depth (Ehrig, 2013). Recent petrographic studies show intensifying alteration from the margin to centre of the prospect (plagioclase completely replaced by secondary chlorite + sericite + carbonate) but with preservation of magmatic textures in K-feldspar (cryptoperthites, quartz-feldspar myrmekites; Kontonikas-Charos et al., 2017). The latter are also reported from fresh Donington granite at Cape Donington (Port Lincoln, Eyre Peninsula; Keyser et al., 2019). The host granite has been constrained as part of the Donington Suite by dating of zircon in two drillholes ~ 2 km apart (Table 1; Jagodzinski, 2005; Courtney-Davies et al., 2019c; Figs. 1 and 2).

Wirrda Well comprises two mineralised areas of which the northern area is deeper (down to ~ 2 km) and displays subvertical breccia pipes

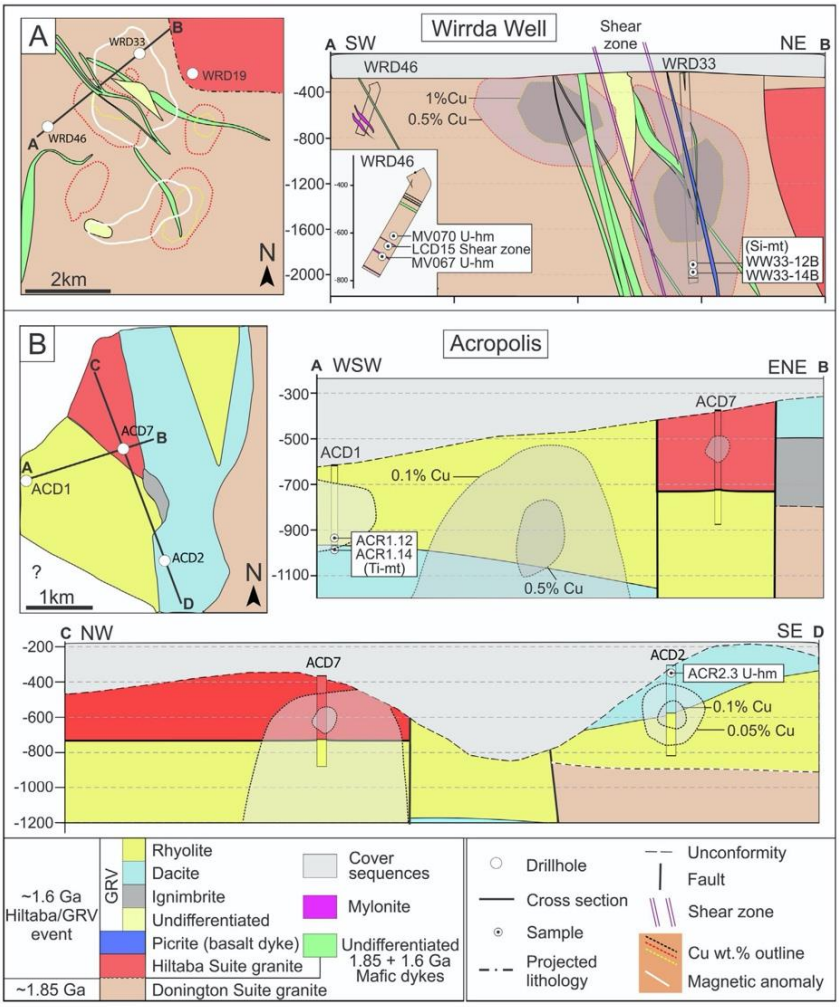


Fig. 2. Schematic maps and cross-sections projected through geological models of (A) Wirrda Well and (B) Acropolis, depicting host rock lithologies, Cu grade isosurfaces and drillhole/sample locations. A large, whole-rock data-set was utilised to construct prospect models and cross sections using Leapfrog Geo 4.4.2 implicit modelling software (See Dmitrijeva et al., 2019b for further details).

considered of hydrothermal origin, with Cu > 0.5% through the Donington granite (Ehrig, 2013). High-grade Cu-Au mineralisation (> 1% Cu) occurs along contacts between mafic dikes and Donington granite, but not at contacts to picrite which are considered to be post-mineralisation (Ehrig, 2013). A shorter mineralised interval (~800 m-thick) is present in the southern area, but with wider high-grade breccia containing chalcocite at the upper part. No direct constraints on the timing of Cu-Au mineralisation are available.

In contrast to Wirrda Well, mineralisation at Acropolis is dominantly hosted by altered GRV overlying Donington Suite granitoid rocks (Cross, 1993). The GRV sequence comprise various felsic lavas, with minor interbedded clastic facies (McPhie, 2016). Zircon from a quartz latite sample at Acropolis returned a U-Pb age of 1591 ± 10 Ma (drillhole ACD5; Creaser and Cooper, 1993). So far, granite attributable to the Hiltaba Suite are inferred based on petrography, but have not yet been dated, and appear restricted to a single area in the SW part of the prospect (Cross, 1993).

Sulphide mineralisation is associated with cm- to dm-wide magnetite-rich veins, localised stockworks and breccia matrices, locally overprinted to hematite ± sericite ± chlorite assemblages (Cross, 1993; Ehrig et al., 2017; Krneta et al., 2017). The sulphides are present as dissemination and pockets, with concentration increasing with hematite abundance (Krneta et al., 2017). Multivariate statistical analysis of whole rock data shows an IOCG-signature defined by principal component analysis overlapping with, but not coincidental with the Hiltaba granite (Dmitrijeva et al., 2019b). Nonetheless, a 'granitophile' element signature comprising W-Sn-Mo (± U) is recognised for geochemically distinct hematite (Dmitrijeva et al., 2019b). The two Fe-oxides are also considered to have formed at distinct temperatures (> 400 °C and 150–300 °C for magnetite and hematite, respectively),

Table 2
U-bearing hematite and magnetite sample details.

	Sample ID	Sample depth (-RL m)	Analysed Fe-oxide	Host lithology
Wirrda Well			Drillhole: WRD46	
	MV070	615	U-bearing hematite	Granite (Donington Suite)
	LCD15	643	Shear zone hematite	Mylonite (Donington Suite)
	MV067	709	U-bearing hematite	Granite (Donington Suite)
			Drillhole: WRD33	
	WW33-12B	1898	Silician magnetite	Granite (Donington Suite)
	WW33-14B	1951		
Acropolis			Drillhole: ACD2	
	ACR2.3	334	U-bearing hematite	Rhyolite (GRV)
			Drillhole: ACD1	
	ACR1.12	941	Titaniferous magnetite	Rhyolite (GRV)
	ACR1.15	987		Dacite (GRV)

based upon fluid inclusions studies and oxygen isotope analysis (Oreskes and Einaudi, 1992).

Locally abundant and in some cases of pegmatitic size, vein apatite in felsic volcanic rocks at Acropolis were dated at 1602 ± 7 Ma (ID-TIMS; Mortimer et al., 1988) and 1596.7 ± 7.1 (MC-ICP-MS; Thompson et al., 2016), overlapping with the GRV zircon ages of Creaser and Cooper (1993). Apatite from Olympic Dam, Wirrda Well and Acropolis shows a transition from light rare earth element to medium rare earth element (REE) enrichment and a coincident weakening of negative Eu anomalies, tracking an evolution from the magmatic to early and late hydrothermal stages (Krneta et al., 2017, 2018). Two generations of apatite from Acropolis were dated by LA-ICP-MS (Cherry et al., 2018b), but do not confirm early and late crystallisation, respectively, due to low analytical precision coupled with high common Pb yielding high uncertainties. Although robust constraints on the timing of mineralisation are unavailable at present, apatite has nevertheless been shown to crystallise broadly coeval with host GRV lithologies.

3. Methodology

One-inch polished blocks were examined for zoned hematite grains via reflected light microscopy and scanning electron microscopy (SEM) using a FEI Quanta 450 instrument equipped with a back-scattered electron (BSE) detector and an energy-dispersive X-ray spectrometer at Adelaide Microscopy, The University of Adelaide.

LA-ICP-MS U-Pb spot data were collected at Adelaide Microscopy using a 193 nm RESOlution-LR excimer laser microprobe (Applied Spectra) coupled to an Agilent 7900x Quadrupole ICP-MS. Hematite U-Pb data acquisition protocols follow the exact methodology described in Courtney-Davies et al. (2019a; see Appendix A for further details). A matrix-matched reference material was not used to calibrate U-Pb data since a fully validated hematite reference material does not currently exist. The GJ-1 zircon (Jackson et al., 2004) was used as the primary reference material, while 91,500 (Wiedenbeck et al., 1995) and Plešovice (Sláma et al., 2008) were analysed as secondary zircon reference materials, due to similar U-Pb downhole fractionation behaviour between zircon and hematite (Ciobanu et al., 2013). U decay constants are from Jaffey et al. (1971) and ^{235}U was calculated here using the $^{238}U/^{235}U$ ratio of 137.88 (Steiger and Jäger, 1977). All data reduction was performed in Iolite™ (Paton et al., 2011) using the VizualAge data reduction scheme (Petrus and Kamber, 2012), and presented using Isoplot 3.75 (Ludwig, 2012), with uncertainties calculated from internal and propagated errors (reported at 95% confidence). Mass ^{204}Pb was measured for fast assessment of samples rich in common Pb, but due to the unresolvable isobaric interference of ^{204}Hg on ^{204}Pb, common Pb corrections were not considered or conducted using ^{204}Pb.

Trace element spot analysis and isotope mapping were conducted using the same instrumentation as described above, with extended methodology given by Verdugo-Ihl et al. (2019). Isotopes measured included ^{24}Mg, ^{27}Al, ^{43}Ca, ^{45}Sc, ^{49}Ti, ^{51}V, ^{55}Mn, ^{57}Fe, ^{75}As, ^{89}Y, ^{93}Nb, ^{95}Mo, ^{118}Sn, ^{181}Ta, ^{182}W, ^{206}Pb, ^{207}Pb, ^{232}Th, ^{238}U and rare earth elements. Spot analysis (50 µm-diameter spot size) comprised measurement of background (30 s) followed by acquisition of signal during ablation (30 or 40 s). Iron, measured as ^{57}Fe, was used as the internal standard element, assuming ideal stoichiometries for hematite and magnetite. GSD-1G or BHVO-2G and NIST-610 were employed as external reference materials and used for instrument drift correction and trace element quantification. Isotope map data acquisition involved ablating sets of parallel line rasters in a rectangular grid across the area of interest with a beam size of 11 µm (square profile) and a scan speed of 11 µm/s. Images were compiled and processed with Iolite™.

4. Results

4.1. Sampling

The Fe-oxides studied here are collected from drillholes marked on cross-sections chosen to illustrate the main host lithologies, Cu grades and relationships with Hiltaba Suite granite for each prospect (Fig. 2). These samples are representative of magnetite and hematite from different parts of the mineralised domains. Magnetite is from the deepest parts of both prospects, whereas oscillatory-zoned hematite, enriched in U and granitophile elements (hereafter referred to as U-bearing hematite) is from shallower levels relative to magnetite (Table 2). At Wirrda Well, both Fe-oxides are hosted in Donington Suite granite but with different degrees of alteration and shearing, increasing with depth and proximity to mineralisation (Fig. 3A-C). Magnetite was sampled from one of the deepest drillholes (WRD33; ~2 km depth) located in the northern mineralised area, ~1 km SW of a Hiltaba Suite granitoid rock (Fig. 2A). At this depth, magnetite predominates across the ~53 m-thick sampled interval and occurs within pockets containing a Fe-oxide ± pyrite ± chalcopyrite assemblage found along contacts between Donington Suite granite and a finer-grained rock (Fig. 3D), both lithologies being strongly chloritised (+sericite + carbonates). In contrast, U-bearing hematite (drillhole WRD46) was found distal from mineralisation and Hiltaba Suite granite, towards the western side of the prospect (Fig. 2A). This type of hematite occurs at depths ~1 km shallower than magnetite, over an interval of ~100 m (Table 2). This drillhole intersects one of the freshest sequences of Donington Suite granite, albeit with shearing, alteration of plagioclase and chloritisation (Fig. 3A). Towards the lower half of the drillhole, the granite becomes increasingly sheared with development of mylonitic zones. Fine-grained hematite from a mylonite shear zone, occurring in between two dated U-bearing hematite samples was also collected for comparison (Fig. 2A and 3A–C). The U-bearing hematite is from massive, cm-sized pockets of Fe-oxides in coarse-grained Donington Suite granite (Fig. 3E and F). These show sharp contacts against the granite, or diffusely connect to crackle-breccia domains (Fig. 3E and F).

At Acropolis, deeper magnetite was sampled from a ~46 m-thick interval across a rhyolite/dacite boundary, at a depth of ~1 km in the western part of the prospect (ACD1; Fig. 2B). Uranium-bearing hematite was found in rhyolite from the south-eastern part of the prospect (ACD2; Fig. 2B), 0.6 km shallower than the sampled magnetite. The only Hiltaba Suite granite intersected by drilling (ACD7) is located ~1.5 km to the NNW from the drillhole (ACD2) containing U-bearing hematite.

Iron-oxides occur as mm- to cm-wide veins throughout the GRV sequences with selvages of carbonate or other gangue minerals, as crosscutting veinlets within stockworks, or cementing angular fragments of volcanic rock (Fig. 4A–C). Multiple vein opening is suggested

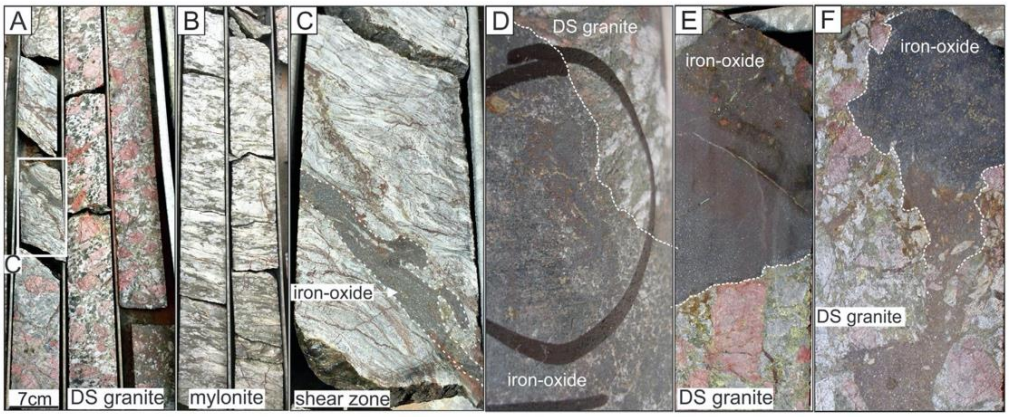


Fig. 3. Photographs of the major host lithologies at the Wirrda Well prospect. All drill cores are 7 cm in diameter. (A) An overview of sampled drill core (drillhole WRD46; ~650 m -RL depth) composed of Donington Suite (DS) granite, (B) mylonites and (C) shear zones containing iron-oxides. Studied, deep magnetite (D) forms as large pockets in contact with DS granite (drillhole WRD33) and (E-F) shallower, U-bearing hematite from drillhole WRD46.

by assemblages within veins with new selvages and patchy Fe-oxides preserved in the centre (Fig. 4D). In most cases, the vein Fe-oxide is magnetite (drillhole ACD1), ranging from cm- to sub-mm sized grains (Table 2).

Unusually coarse hematite occurs in veins in the rhyolite from shallower levels than the U-bearing hematite intersected in drillhole ACD2 (Fig. 4E and F). In detail, bladed hematite infills granular shapes suggesting this pseudomorphically replaces a pre-existing magnetite or carbonate mineral. The U-bearing hematite is from an altered dacite (Fig. 4G), which is highly brecciated, and contains angular/subrounded clast-like hematite possibly derived from brecciation of a vein (Fig. 4G).

4.2. Iron oxide petrography

4.2.1. Magnetite

Magnetite from the two prospects differ in terms of internal textures, in that oscillatory zoning is present at Wirrda Well but not at Acropolis (Fig. 5A and B). Hematite is present as the product of incipient martitisation and newly-formed grains in Wirrda Well and Acropolis, respectively. Although magnetite from both prospects is mostly euhedral, inclusions of gangue minerals associated with local grain-scale brecciation are observed. In detail, the zoning is composed of mottled bands with sub-micron-scale Si-Fe-bearing inclusions in Wirrda Well magnetite (Fig. 5C). In contrast, the Acropolis magnetite contains Ti-oxides forming trellis-like exsolutions with finer-still mottling

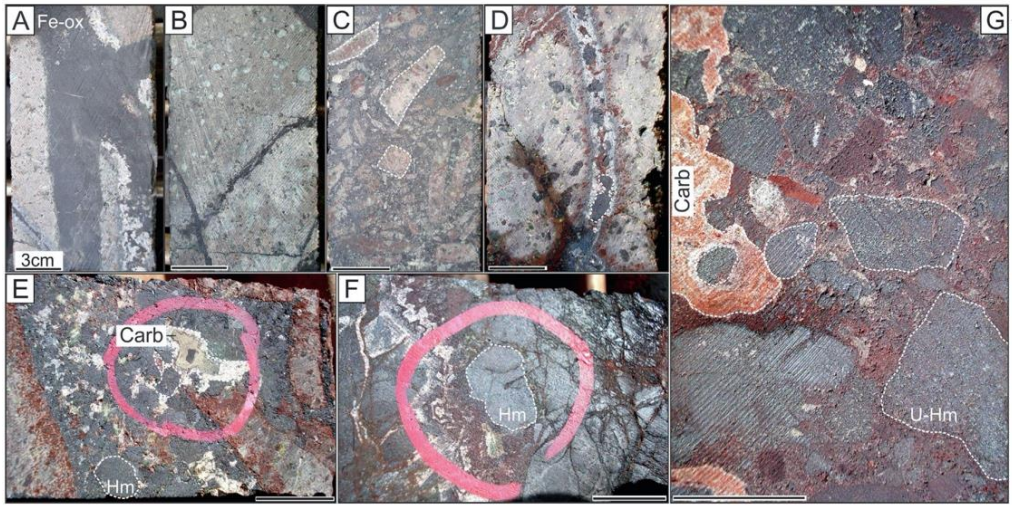


Fig. 4. Photographs of drill cores containing various styles of vein mineralisation and GRV host rocks at the Acropolis prospect, all scale bars represent 3 cm. Iron-oxides (predominantly magnetite) found throughout GRV sequences (drillhole ACD1), occurring as (A, B) crosscutting veinlets and stockworks, (C) cementing angular volcanic fragments, or (D) forming as patchy iron-oxides preserved in the centre of veins with new selvage. (E-F) Coarse hematite within veins, forming at shallower levels to the magnetite dominant veins. (E, F) The hematite (Hm) infills pre-existing granular shapes, suggesting pseudomorphic replacement of a mineral e.g., magnetite/carbonate (carb). (G) Coarse, U-bearing hematite from drillhole ACD2.

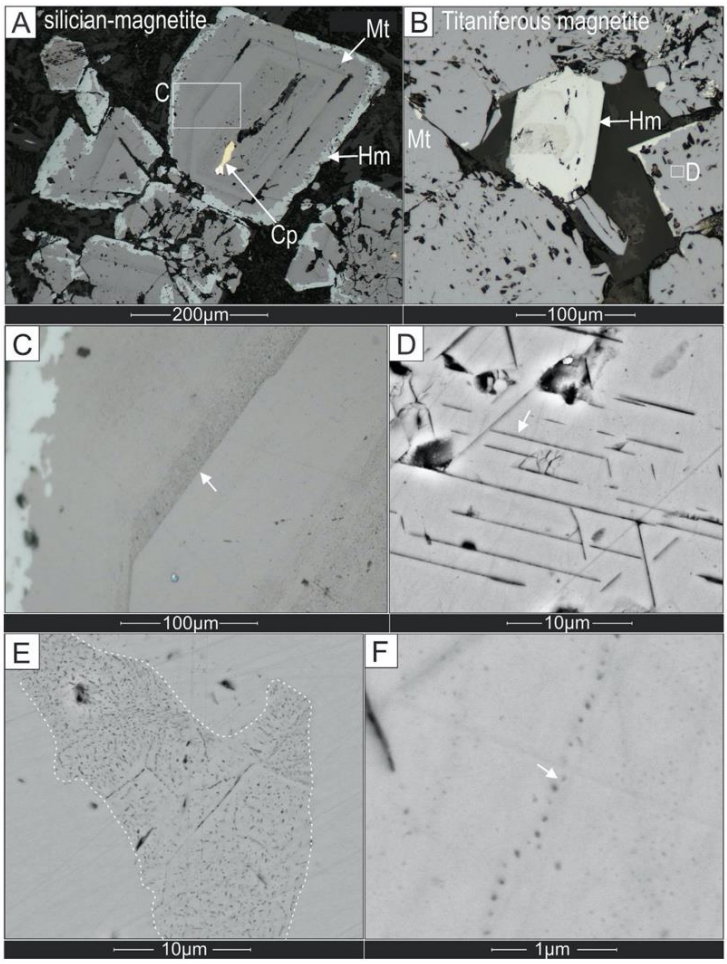


Fig. 5. (A-C) Reflected light photomicrograph and (D-F) BSE images of studied magnetite (Mt). (A) Oscillatory zoning pattern typical of silician magnetite (Si-Mt) at Wirrda Well. Note the presence of gangue minerals and sulphides (chalcopyrite-Cp) as indicated the middle or along zonation boundaries, as well as marginal replacement by hematite (Hm). (B) Titaniferous Mt (Ti-Mt) from Acropolis enclosing a grain of oscillatory-zoned, Ti-bearing Hm. (C, D) Details showing representative textures (arrowed) for the two types of magnetite shown in (A) and (B), i.e., zonation formed by inclusion mottling and {1 1 1}-trellis inclusions, respectively. (E) Mottled area (dashed line) in Si-Mt showing inclusion (re) arrangement along short trails. (F) Mottled areas with spinel + ilmenite between two trellis arrays in Ti-Mt. Coarser inclusion trail is arrowed.

textures within the trellis networks (Fig. 5D). Inclusion arrangements can locally vary within the two types of magnetite, with occurrence of small arrays and/or coarsening along trails (Fig. 5E, F). These represent two distinct types of magnetite, silician and titaniferous at Wirrda Well and Acropolis, respectively. These were previously documented in a preliminary study at the nanoscale (Ciobanu et al., 2018), showing the identity of the smallest inclusions (i.e., silicates + Si-Fe-nanoprecipitates at Wirrda Well and two-component (hercynite + ilmenite) inclusions at Acropolis.

4.2.2. Uranium-bearing hematite

Uranium-bearing zoned hematite is rare and found within hematite aggregates (Fig. 6A-C) which also contain abundant sulphides (pyrite + chalcopyrite) in the Wirrda Well samples. The studied zoned hematite occurs along the margins of the aggregates, is coarser and free of inclusion in comparison to enclosing aggregate. Hematite along the Wirrda Well shear zone is fine-grained and closely associated with sulphides (mostly chalcopyrite), siderite, and sericite + quartz (Fig. 6D).

The U-bearing, zoned hematite differs in terms of habit and internal textures in the two samples from Wirrda Well (Fig. 7A and F). The deeper sample (MV067) is intensely twinned, contains abundant inclusions of magnetite (Fig. 7A and B), and is weakly zoned on BSE images (Fig. 7C). Twinning is associated with lamellae displacement and local replacement of hematite by magnetite as well as precipitation of sulphides (Fig. 7A and B). In the shallower sample (MV070), short lamellar hematite surrounds the coarser grains with pronounced oscillatory zoning (Fig. 7D-F). Crystal zoning co-exists with more patchy zoning within larger domains, albeit with some of the highest contrast between individual bands (Fig. 7E and F). In both cases, superimposed alteration is indicated by the presence of numerous cavities, pores, and U-mineral inclusions (e.g. uraninite).

In contrast, the U-bearing hematite from Acropolis is found as euhedral, granular aggregates (Fig. 7G and J), with gangue inclusions (Fig. 7H). Magnetite inclusions and small sulphide blebs occur along trails around such pockets of granular coarse hematite (Fig. 7I and J). Uniquely, oscillatory and sectorial zoned patterns include high-contrast zones underlying aggregates with fan-like grain arrangement (Fig. 7G and H). This type of texture could result from pseudomorphic replacement of a pre-existing mineral, e.g., magnetite or carbonate.

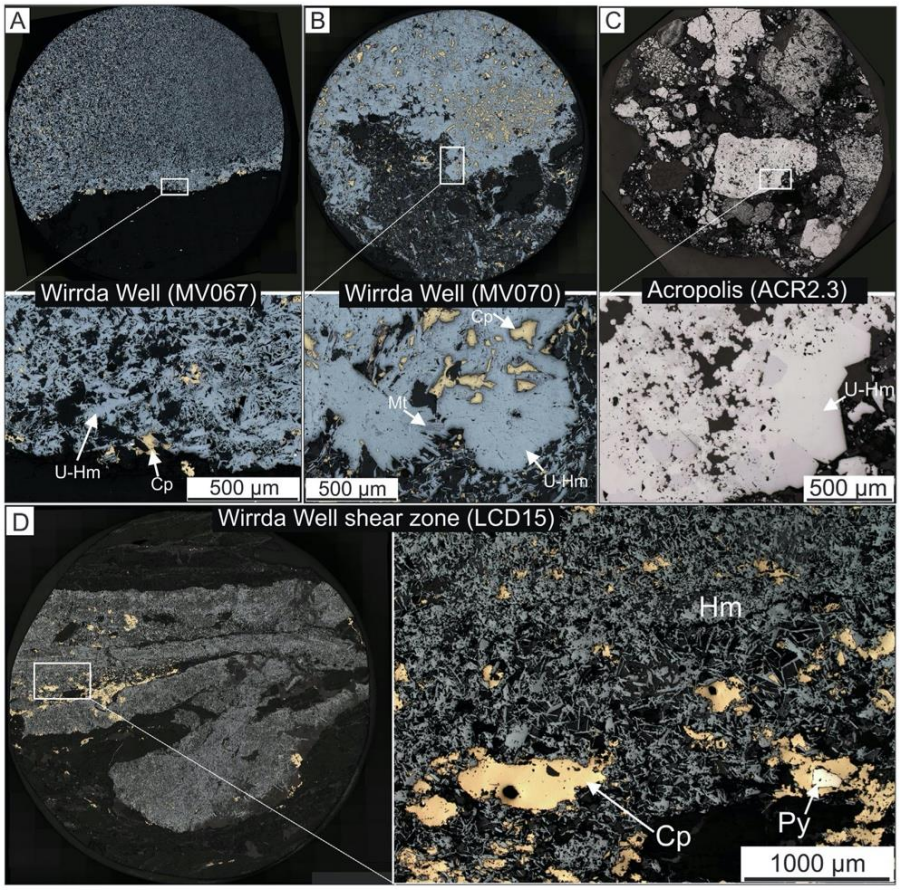


Fig. 6. (A-D) Reflected light microphotographs showing maps and aspects of the studied polished blocks (1-inch diameter). White boxes correspond to locations of studied hematite (Hm) and U-bearing hematite (U-Hm) from location as marked presented as photo micrographs either below or to the right of the polished block maps. Note presence of sulphides as disseminations/veinlets of pyrite (Py) and chalcopyrite (Cp).

However, other areas contain zoned lamellae of hematite, a more common habit of U-bearing hematite (Fig. 7H).

The zonation patterns observed in the coarsest U-bearing hematite with conspicuous, fan-like distributions were also assessed by LA-ICPMS mapping (Fig. 8). The brightest areas on the BSE image correlate with high U + Pb, and moderate Sn, but not with higher concentrations of W or Mo. Uranium and radiogenic Pb share a clear relationship in both oscillatory and sectorial patterns, in contrast to Sn, W and Mo, which most strongly correlate with each other within oscillatory patterns. Tin does, however, display weak sectorial zoning that correlates with that shown by U and Pb.

4.2.3. Iron oxides in the Wirrda Well shear zone

At least two generations of hematite: (i) lamellar; and (ii) fine-grained, porous aggregates replaced by magnetite, are recognised in the shear zone at Wirrda Well (Fig. 9A). Very weak compositional zoning, indicative of 'granitophile' element signature, is present in some of the lamellar aggregates (Fig. 9B). However, U is low, and rich in common Pb, precluding reliable U-Pb dating. The shear zone contains assemblages with siderite + monazite (Fig. 9C) and scarce fractured magmatic zircon (Donington?; Fig. 9D). In detail, zonation patterns in siderite are crosscut by hematite lamellae (late generation?) (Fig. 9E). Such relationships indicate multiple stages of shear zone (re)activation and fluid focussing leading to element remobilisation and overprint of datable minerals, including monazite (which contains abundant galena inclusions; Fig. 9F) and hematite.

4.3. Iron oxide geochemistry – LA-ICP-MS data

The trace element dataset for Fe-oxides (Table 1, Appendix A) is presented in a selection of box and scatter plots (Figs. 10, 11) and comprises 82 spot analyses of U-bearing hematite (55 from Wirrda Well, 27 from Acropolis) and 62 analyses of magnetite (22 analyses of silician magnetite from Wirrda Well, 40 of titaniferous magnetite from Acropolis). Inter- and intragrain variability in the concentrations of granitophile elements in U-bearing hematite and magnetite are evident from both prospects. Spots were selected in zones or domains identified as inclusion-free and appearing 'brightest' on BSE images. Despite their large differences in concentration within U-bearing hematite, elements integral to U-Pb geochronology showed steady signals in time-resolved ablation profiles (Appendix Fig. 1) indicating that U and Pb are lattice-bound. Granitophile elements also display consistently flat profiles in

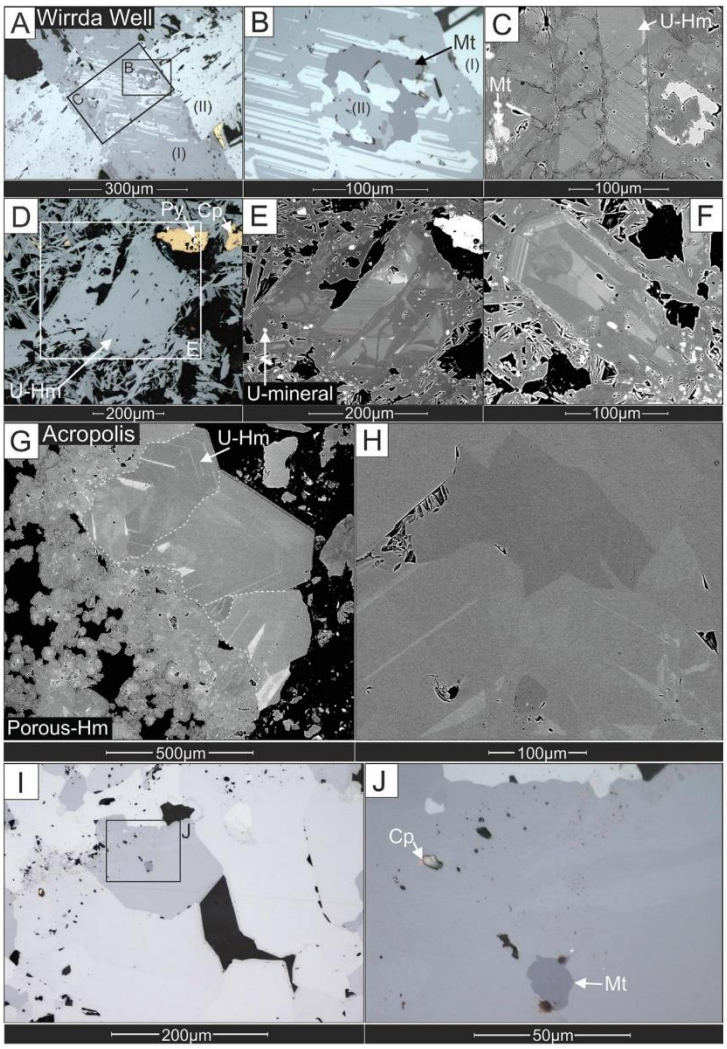


Fig. 7. Reflected light photomicrographs and BSE images of studied U-bearing hematite (U-Hm) from (A-F) Wirrda Well and (G-J) Acropolis. Note the striking difference in morphology between the two examples of U-Hm. (A) Crosscutting hematite lamellae showing different textures indicative of overprint (sample MV067). One lamella (I) displays sets of twins whereas the other lamella (II) is filled by fine-grained hematite (pseudomorphic replacement). Note presence of magnetite (Mt) inclusions throughout Hm. (B) Detail of magnetite from (A) showing multi-stage relationships between the two Fe-oxides, i.e., Mt replaces the twinned Hm (I) but is replaced by overgrowing Hm (II). (C) Zonation pattern of twinned Hm (I) showing porosity and replacement along cross-cutting veinlets with Hm-(II). (D, E) Coarse, U-Hm displaying patchy oscillatory-zoning enclosed within fine, lamellar aggregates of un-zoned Hm (sample MV070). Note presence of high-contrast areas (arrowed) as well as dissemination of sulphides (pyrite-Py and chalcopyrite-Cp). Some of the brighter inclusion on BSE image in (E) are U-bearing phases. (F) Oscillatory and sectorial zoned pattern in single grain U-Hm (sample MV070). Note partial replacement associated with darkening on the BSE image and presence of sulphides (bright). (G) Band with coarse-grained, granular U-Hm at the margin of fine-grained, porous Hm aggregate (sample ACR2.3). Note the crystal oscillatory zoning pattern in each grain with narrow high-contrast zones (U-rich). (H) Detail of zonation in U-Hm aggregate from another area showing high to low contrast domains/bands. (I, J) Aggregates of U-Hm showing overprint as trails of inclusions (sulphides and gangue minerals). Note presence of Mt as relict inclusions.

spot analyses from both prospects.

4.3.1. Trace element concentrations

Concentration ranges for the main groups of elements are shown for magnetite and U-bearing hematite in the two prospects on Fig. 10. At Wirrda Well, total granitophile element concentrations (U + Sn + W + Mo) in zoned hematite range between 71 ppm and 9,970 ppm, and from 13 ppm to 2000 ppm at Acropolis. Magnetite generally contains < 10 ppm.

High field strength elements (HFSE) such as Sc (up to 10 ppm), Th (up to 50 ppm), V (up to 80 ppm) and Ti (up to ~700 ppm) are enriched in hematite from Wirrda Well, but generally < 1 ppm at Acropolis, even though U exceeds 1000 ppm in hematite from both prospects. The inverse is seen in magnetite, with higher concentrations of HFSE at Acropolis, by an order of magnitude for both V (up to ~480 ppm) and Ti (up to 17,000 ppm).

Rare earth element and Y (REY) concentrations in hematite vary over 3 orders of magnitude, from fractions of a ppm to tens of ppm. As with the granitophile elements, REY concentrations are higher at Wirrda Well than Acropolis, although concentrations of REY are similar in magnetite at both prospects.

4.3.2. Trace element correlation trends

Uranium and radiogenic Pb (^{206}Pb) correlate strongly in hematite from both prospects, but are decoupled in magnetite, precluding U-Pb dating of the latter (Fig. 11A). A comparable discrepancy between the two Fe-oxides is also shown in terms of U *vs*. Sn + W + Mo on Fig. 11B. On this plot the magnetite from each prospect forms distinct clusters, whereby the silician magnetite from Wirrda Well is the lowest in granitophile element concentration. Titaniferous magnetite from Acropolis shows a wide, four-order-of-magnitude spread in U values but at constant Sn + W + Mo. Points with the upper part of this cluster on the

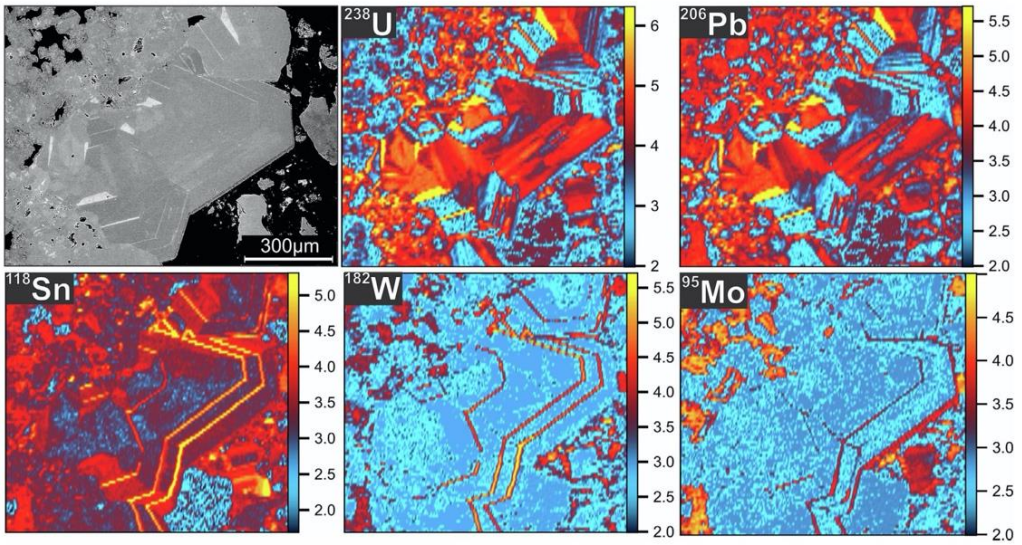


Fig. 8. BSE image and LA-ICP-MS isotope maps (scale: counts per second, 10^n) of U-bearing hematite aggregate from Acropolis, imaged in Fig. 7G (sample ACR2.3). Note sectorial zoning with inverse correlation between U + Pb and Sn, whereas thin bands within the oscillatory zoning are rich in Sn, W and Mo.

diagram are overlapped by the Acropolis hematite, whereas Wirrda Well hematite plots at the upper end of the diagram, with overlap between the two analysed samples (Fig. 11B). Comparison between different pairs of granitophile elements shows a strong correlation ($r^2 = 0.91$) for Mo *vs*. W across the entire dataset, where the magnetite has the lowest concentration of either element, whereas Wirrda Well hematite is highest (Fig. 11C). In contrast, different fields for Fe-oxides within each prospect can be discriminated in terms of Sn *vs*. W (Fig. 11D). The lowest and highest parts of the diagram are occupied by silician magnetite and the hematite from Wirrda Well, respectively, whereas the middle part is represented by Acropolis Fe-oxides with constant Sn but with increasing W in hematite relative to magnetite (Fig. 11D). Both types of magnetite are clustered relative to hematites from the two prospects on ΣREY *vs*. U plots (Fig. 11E). The two magnetites have comparably high ΣREY and with Wirrda Well hematite, whereas Acropolis hematite is the lowest in ΣREY despite the large spread in U content (Fig. 11E). Very good correlations between Ti and Al, Sc and V are observed across all Fe-oxides (Fig. 11F–H). Evidently, titaniferous magnetite plots at the upper end on both the Al *vs*. Ti and the Sc and V *vs*. Ti diagrams. Silician magnetite also plots along the same trends on these diagrams, whereas Acropolis hematite plots in the lower corner with a spread in Al and V at relatively constant Ti (Fig. 11F and H). Diagrams for pairs of elements that have geochemical affinity show very distinct trend and/or clusters for each Fe-oxide or prospect (Fig. 11I–K). A strong positive correlation between V and Nb is obtained for hematite, whereas magnetite shows a spread of Nb content at relatively constant, high V (Fig. 11I). In contrast, the dataset plots as clusters on the Ni *vs*. Co plot (Fig. 11J), where highest values are typical of magnetite rather than hematite. In the latter, the highest Ni and lowest Co concentrations are recorded from Acropolis (Fig. 11J). Titaniferous magnetite from Acropolis shows a spread in Cr concentration up to 200 ppm at relatively constant Ni, whereas silician magnetite contains less Cr (Fig. 11K). Hematite contains the least Cr (between 0.1 and 1 ppm).

4.3.3. REY partitioning trends in iron oxides

Chondrite-normalised REY-fractionation trends for the Fe-oxides show distinct patterns for hematite but a very scattered, poorly defined trend for magnetite in both prospects (Fig. 12). The best-defined trend is a slightly concave, upwards-sloping HREE segment for Wirrda Well hematite, high in ΣREY (Fig. 12a). Weak, negative Eu and Y anomalies are noted. In contrast, Acropolis hematite, with the least ΣREY, shows a flat trend but with a LREE to MREE-depleted segment and a pronounced negative Y anomaly (Fig. 12B). The REY fractionation trends for magnetite are comparable with one another in terms of variability within each prospect (Fig. 12C and D). Nonetheless, magnetite from Wirrda Well generally shows a flat trend with a marked negative Eu-anomaly (Fig. 12C). Magnetite from Acropolis, higher in terms of ΣREY than hematite in the same locality, is comparable with the flat trend of hematite but with an upwards-sloping LREE segment and less pronounced negative Y anomaly (Fig. 12C).

4.4. Hematite U-Pb geochronology

Intercept and weighted average $^{207}Pb/^{206}Pb$ dates are calculated with internal and propagated uncertainties at the 2σ level (Fig. 13). Accompanying U-Pb data is presented in Appendix A. Criteria for grain selection was based on SEM imaging of inclusion free oscillatory-zoned grains larger than ~100 µm.

Uranium-Pb data from Wirrda Well hematite (sample MV070) were collected across 10 grains (18 spots). Concentrations of U ranged from 133 to 3570 ppm (mean, 1371 ppm), and Th from 1 to 28 ppm (mean, 16 ppm). A Wetherill Concordia diagram (Fig. 13) including all analyses was constructed, forming upper and lower intercept at 1620 ± 13 (± 14) and 38 ± 320 Ma, respectively (MSWD = 4). Data define an intercept line, but generally cluster around concordia at ~1.6 Ga, although five data points are reversely discordant. A $^{207}Pb/^{206}Pb$ weighted mean of all the data yields an unacceptable MSWD of 3.1. Exclusion of grain 1, which contributes to the high MSWD of the intercept date, produce a younger date of 1598.9 ± 6.3 Ma (MSWD = 0.25, n = 15).

From Acropolis, 26 spots in 11 grains were analysed (sample ACR2.3), yielding U concentrations ranging from 1 to 4040 ppm (mean 1729 ppm). Analyses yielding < 100 ppm U (12 spots) are excluded

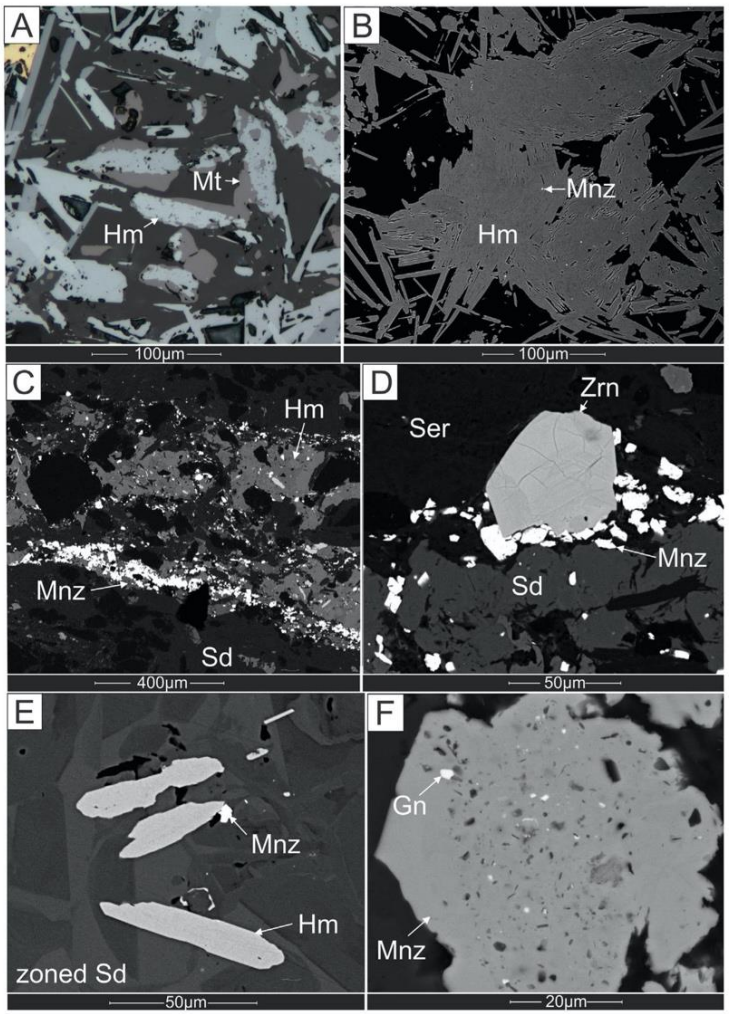


Fig. 9. (A) Reflected light photomicrograph (a) and BSE images (B-F) showing mineral association within the Wirrda Well shear zone (sample LCD15). (A) Iron-oxide association showing two generations of hematite (Hm) as lamellar aggregates and fine-grained Hm replacing magnetite (Mt). (B) Faint, patchy zoning (low-U, high common Pb) in lamellar aggregate of Hm. Note bright inclusion of monazite (Mnz). (C) Edge of Hm veinlet showing selvage with Mnz. (D) Detail of the vein selvage showing metamict zircon (Zrn) of likely Donington Suite granite origin. (E) Zoned siderite (Sd) along the edges of the hematite in (C) containing later Hm (crosscutting the zoning) and Mnz Hematite lamellae crosscutting zoned siderite (Sd). (F) The monazite grains all contain inclusions of galena (Gn) which precluded U-(Th)-Pb dating. Other abbreviations Ser-sericite.

from age interpretations as they contain higher common Pb components, returning meaningless data. An intercept line (Fig. 13) encompassing all other data points (14) forms upper and lower intercepts at 1590.5 ± 3.9 (± 7.2) and 195 ± 200 Ma, respectively (MSWD = 1.6). The $^{207}Pb/^{206}Pb$ weighted average is in good agreement with the intercept date at 1590.6 ± 6.5 Ma (MSWD = 0.34, n = 14). Lower U data points are reversely discordant, while higher U points plot on or just below concordia.

5. Discussion

5.1. Formation and evolution of iron-oxides at Wirrda Well and Acropolis

The present study, although not a comprehensive assessment of all generations of Fe-oxides, highlights textural-geochemical characteristics that are suitable for comparison between the two prospects and with the Olympic Dam deposit.

Silician magnetite from Wirrda Well is directly comparable with the earliest hydrothermal magnetite found in the outer shell at Olympic Dam (based on the presence of Si-Fe nanoprecipitates and nanoparticles of silicates; Verdugo-Ihl et al., 2019; Ciobanu et al., 2019). In contrast, vein titaniferous magnetite from Acropolis is very similar to magmatic magnetite from the Roxby Downs Granite, host to the Olympic Dam deposit, based on the presence of preferentially-oriented ilmenite + rutile inclusions − trellis textures (Krneta et al., 2017) and nm-scale spinels (authors unpublished data) responsible for the high-Ti (+V) content. Despite this, magnetite from the two prospects show comparable signatures, being highest in HFSE (Sc, V) and siderophile elements (Ni, Co). The high V also recorded by magmatic magnetite at Olympic Dam (Verdugo-Ihl et al., 2019), suggests fluids of magmatic affiliation in the two prospects. Measurable elements of mafic affiliation, Ni and Cr, in magnetite from the two prospects relative to hydrothermal magnetite in the outer shell at Olympic Dam, could indicate differences in the local environment among the three localities. Considering that host lithologies are all felsic igneous rocks, Ti-rich vein magnetite at Acropolis can be considered to precipitate from high-T

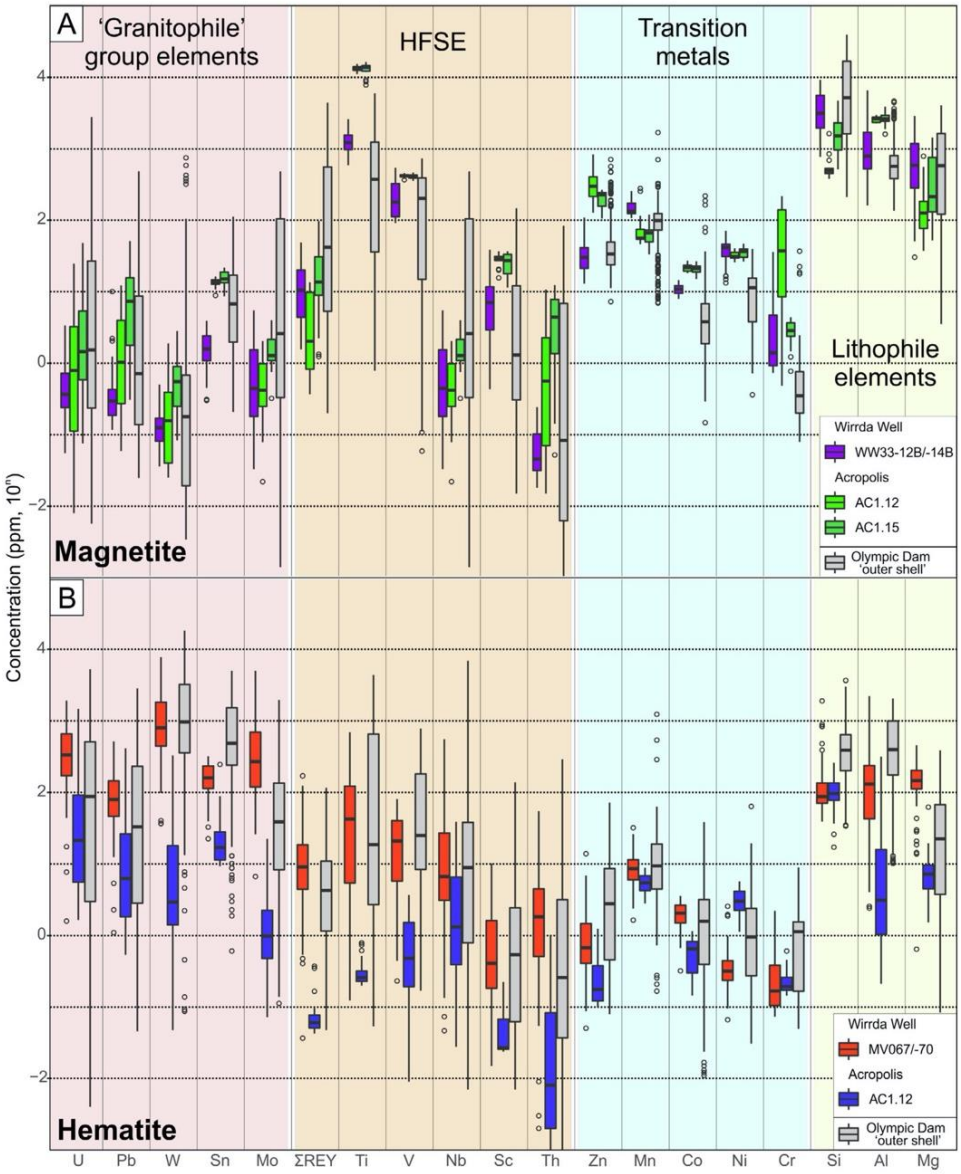


Fig. 10. Box plots for magnetite (A) and hematite (B) from Wirrda Well and Acropolis showing ranges of trace element concentration for groups of elements as indicate. Published data for silician magnetite and high- U-W-Sn-Mo, oscillatory-zoned hematite from the outer shell at Olympic Dam is shown for comparison (Verdugo-Ihl et al., 2019).

(> 600 °C, as indicated by the presence of spinel + Ti-Fe-phases; Buddington and Lindsley, 1964) fluids that were focussed upwards along fractures (high fluid/rock ratio). The large alteration footprint at Acropolis (relative to either Olympic Dam or Wirrda Well; Fig. 1C; Dmitrijeva et al., 2019b) supports the focussing of fluid along open fractures connecting with surficial fracture network. Formation of such veins would, however, have been sufficiently deep to account for the high-T recorded by magnetite. Porphyry Cu systems recording similar high-T during the potassic alteration stage are known to form down to depths of 5 km (e.g., Murakami et al., 2010).

High-T crystallisation of Acropolis magnetite is also inferred from fluid inclusions and stable isotope studies (Oreskes and Einaudi, 1992). However, if we assume a magmatically-derived hydrothermal fluid, the Ni-Cr-bearing signature of this magnetite cannot be easily reconciled with granitic magmas alone. It could, however, be indicative of mafic + felsic magma mingling at deeper levels – or even leaching of

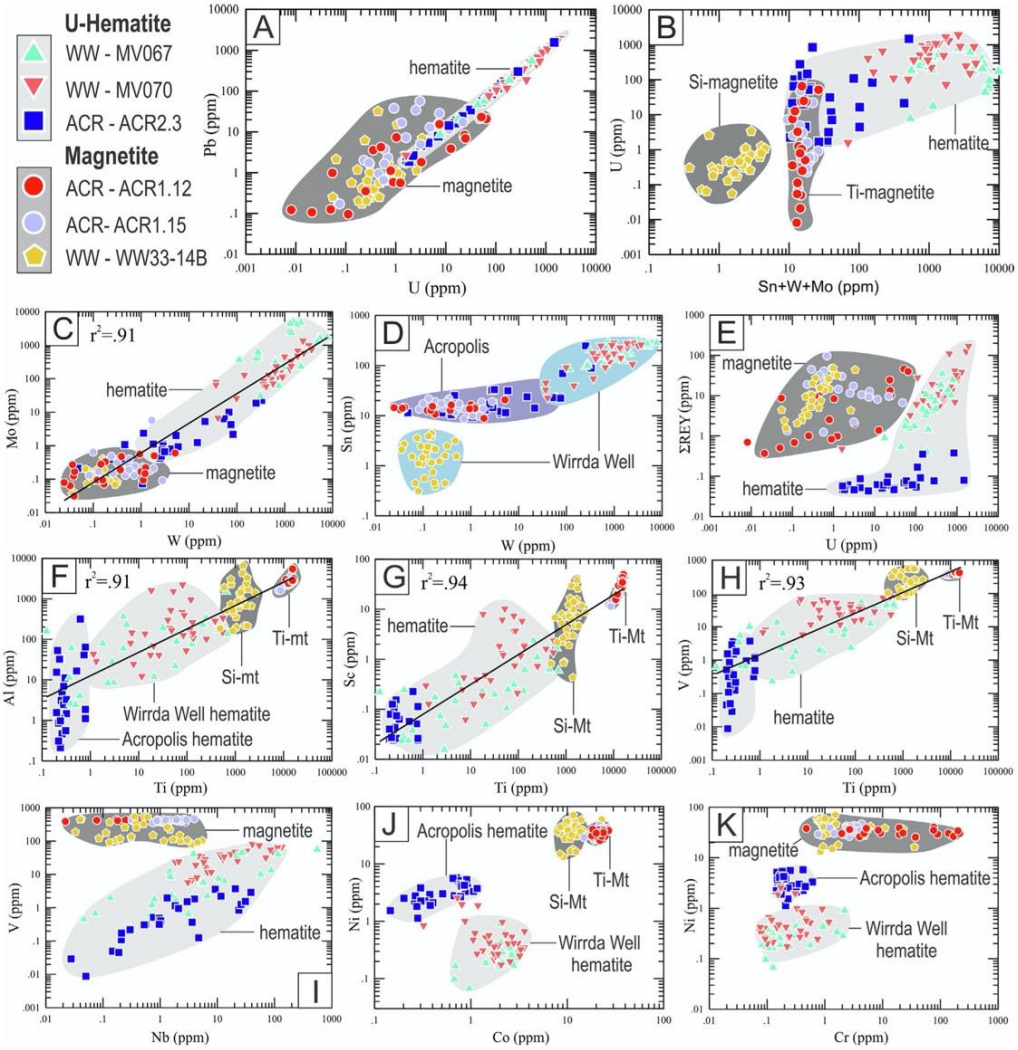


Fig. 11. LA-ICP-MS scatter plots of selected element (-groups)-pairs to compare hematite and magnetite from Wirrda Well and Acropolis as marked by coloured shading. (A) Pb *vs.* U; (B) U *vs.* Mo + Sn + W; (C) Mo *vs.* W; (D) Sn *vs.* W; (E) ΣREY *vs.* U; (F) Al *vs.* Ti; (G) Sc *vs.* Ti; (H) V *vs.* Ti; (I) V *vs.* Nb; (J) Ni *vs.* Co; (K) Ni *vs.* Cr. See text for further explanations.

unexposed mafic/ultramafic lithologies.

In contrast, the ~2 km-deep silician magnetite at Wirrda Well, host to comparable silicate inclusions as the silician magnetite from the southeast side of Olympic Dam (Ciobanu et al., 2018; 2019), could be considered as having been formed during host granite alteration by replacement reactions with low fluid-rate ratio, such as those considered for coupled dissolution reprecipitation reactions. However, the host Donington Suite granite cannot explain the marked enrichment in Ni, and particularly Cr, at Wirrda Well relative to Acropolis or Olympic Dam (Fig. 10A). The high Cr could be associated with presence of abundant mafic/ultramafic dikes which could have been leached by the same fluids that alter Donington Suite granite.

The oscillatory-zoned, U-bearing hematite reported here for the first time from the two prospects, (and outside the Olympic Dam deposit), is directly comparable with Olympic Dam hematite. Contents of W + Sn + Mo are orders of magnitude higher at Wirrda Well than Acropolis, at comparable U content, whereas the Mo concentration in Wirrda Well hematite (average ~ 832 ppm) is highest and stands out on Fig. 10B, even compared to Olympic Dam hematite. Despite varying concentrations, the 'granitophile' signature indicates a potential common metal source relating to Hiltaba Suite plutons. Such plutons, known at distances of 2–3 km from the sample locations (Fig. 2) should be present underneath and/or nearby to U-bearing hematite. Based upon higher W + Sn + Mo at Wirrda Well hematite may suggest a closer proximity to a Hiltaba Suite source than Acropolis hematite. Fault (re)activation along shear zones at Wirrda Well could explain the

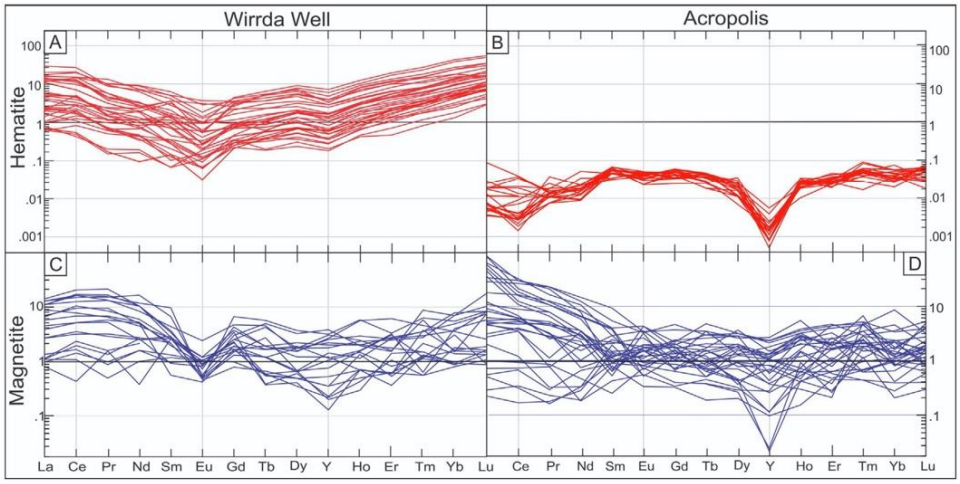


Fig. 12. LA-ICP-MS chondrite-normalised REY fractionation trends for (A, B) hematite and (C, D) magnetite at Wirrda Well and Acropolis. Note the similarities between the hematite and magnetite trends at Acropolis.

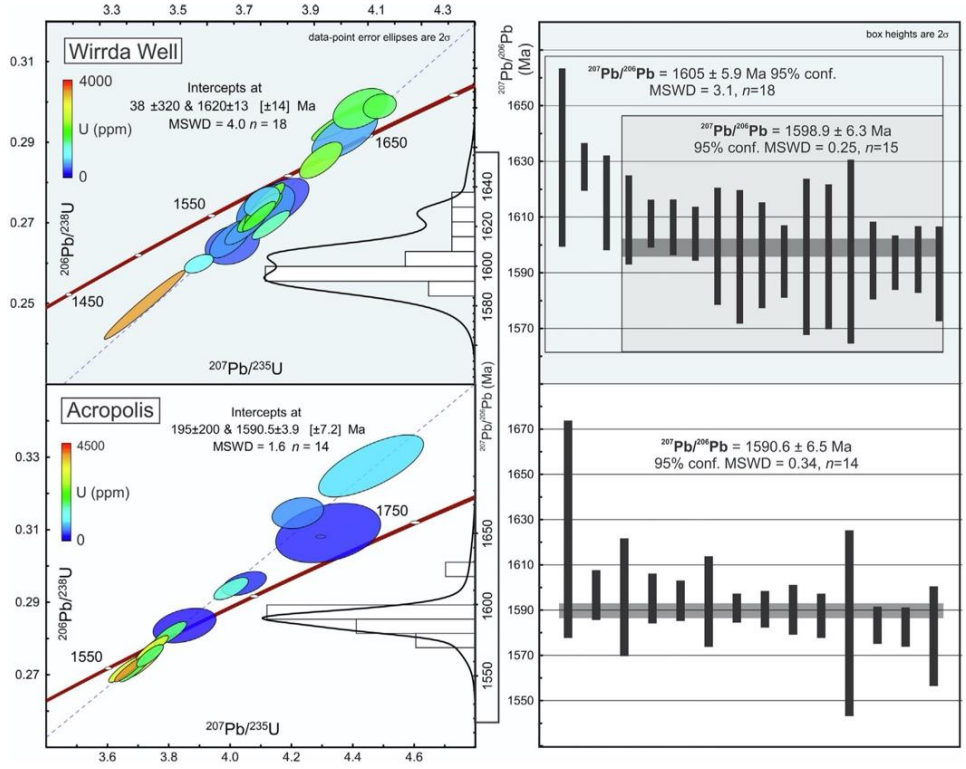


Fig. 13. $^{206}Pb/^{238}U/^{207}Pb/^{235}U$ Wetherill concordia diagrams and corresponding $^{207}Pb/^{206}Pb$ weighted average diagrams for Wirrda Well (top, blue) and Acropolis (bottom, white). Age errors in the concordia diagrams are shown both with [in brackets] and without incorporation of the uranium decay-constant errors. The grey boxed inset to the Wirrda Well weighted average diagram includes only analyses yielding an acceptable MSWD. Data point error ellipses are coloured according to their corresponding U-content (ppm). The bottom right insets of the concordia diagrams are probability density diagrams scaled by $^{207}Pb/^{206}Pb$ (Ma).

more pronounced open system behaviour of U-Pb in hematite (see below). The high-ΣREY concentrations and chondrite-normalised fractionation trends showing upwards sloping HREE in hematite from Wirrda Well (Fig. 11) resemble those observed in early hematite from the outer shell at Olympic Dam (Verdugo-Ihl et al., 2019).

The comparable chondrite-normalised REY fractionation trends for magnetite and hematite from Acropolis, albeit at lower ΣREY in hematite, together with their textures (Fig. 7G), can be considered as evidence for pseudomorphic replacement of one by another (Fig. 12). If true, and assuming that Ti is completely removed during the replacement event, the selective enrichment in some granitophile elements relative to others (U, Mo, W *vs.* constant Sn; Fig. 11) may indicate preferential metal discharge, considering a common hexavalent oxidation state for U, W, and Mo, but not Sn (4 +) within hydrothermal fluids. This can be explained by the greater capacity of the hematite crystal structure to incorporate the larger hexavalent metal cations in comparison with magnetite. More precipitation of metals from the same fluid can be invoked during the mineral-buffered stage of replacement of magnetite by hematite than during the faster, open-fracture fluid infiltration (magnetite deposition). The preferential incorporation of REY into carbonates along vein selvages may account for the apparent loss of REY during pseudomorphic replacement of magnetite by hematite (martitisation).

The Fe-oxides along the shear zone may be associated with trace element remobilisation from the host lithology (Donington Suite granite?), or to variation in pH or redox conditions (magnetite-hematite conversion). Particularly notable is the REE enrichment in mylonites containing monazite-siderite-veins (Fig. 9). A second overprint relates to fluids that would account for Pb (re)mobilisation and precipitation within pores in minerals that are otherwise datable (monazite and hematite). The latest, post-siderite, generation of hematite does not carry U (Fig. 9E).

In summary, mineralisation from both prospects and from Olympic Dam can be linked together to the same U-W-Sn-Mo-bearing fluids derived from Hiltaba Suite granitoid rocks, despite differences in host lithology, the hybrid character of the magma and/or deeper lithologies, and depth of formation, shallow (< 5 km) at Acropolis, and deeper at Olympic Dam and Wirrda Well (> 5 km). Although magnetite is the dominant Fe-oxide at both prospects, hematite is present and often telescoped with magnetite in a comparable way as seen from the outer shell at Olympic Dam (Verdugo-Ihl et al., 2019).

In order to confirm a common fluid source derived from Hiltaba Suite granitoid rocks in the Olympic Dam district, the U-W-Sn-Mo signature of oscillatory zoned hematite must be reconciled with geochronological evidence.

5.2. Geological significance of the U-Pb hematite geochronology

Samples from Wirrda Well and Acropolis returned $^{207}Pb/^{206}Pb$ weighted averages that are statistically different, but within the uncertainty (2σ) of each weighted average uncertainty (1598.9 ± 6.3 Ma and 1590.6 ± 6.5 Ma, respectively). This discrepancy may be attributable to varying components of common Pb, relative U-Th concentrations, leveraging of weighted means via non-zero age Pb loss and analytical artefacts associated with calibration against non-matrix matched reference materials. Another possibility exists that this is a real temporal difference in crystallisation age. At Wirrda Well, the spot analysis with the highest U and high $^{206}Pb/^{204}Pb$ returned a $^{207}Pb/^{206}Pb$ date of 1594 Ma, while the lowest, returned a much older date of 1631 Ma. A similar trend is seen at Acropolis, with higher U and higher $^{206}Pb/^{204}Pb$ analyses returning ages at ~1590 Ma. This supports the notion that common Pb and U-Th contents are limiting the accuracy of individual $^{207}Pb/^{206}Pb$ dates. However, common Pb is not noticeably higher at Wirrda Well than Acropolis, which returned an older $^{207}Pb/^{206}Pb$ weighted average. The younger weighted average at Acropolis may have been due to data leveraging by a Pb-loss event forming a non-zero lower intercept, although lower intercept uncertainties are high. As discussed in Courtney-Davies et al. (2019a), the relative roles and interplay between such effects must be treated with caution, particularly with relatively lower precision methods such as LA-ICP-MS.

Therefore, without further evidence, the discrepancy in age between the two prospects should not be treated as a real temporal difference, as the analytical resolution of the method, coupled with fractionation of U from Pb during analysis, and calibration against non-matrix-matched reference material, can significantly impact on accurate interpretation U-Pb hematite data. We are confident, however, that the highest precision, lowest common Pb and highest U analyses, yielding dates at 1590 Ma, can be considered the crystallisation age of U-bearing hematite at both prospects. There is no clear divergence in age between any grains, indicating that all grains crystallised in a single event. Uranium-Pb data here is further supported by an ID-TIMS baseline for U-bearing hematite from Olympic Dam at 1589.94 ± 0.88 (Courtney-Davies et al., 2019a). Interestingly, Th, which is commonly below the detection in the LA-ICP-MS analyses of U-bearing hematite from Acropolis, was consistently measured at Wirrda Well, as it also was in the outer shell at Olympic Dam (Verdugo-Ihl et al., 2019).

5.3. Timing and evolution of IOCG metallogeny across the Olympic Dam district

There is currently no reliable evidence for multiple, major episodes of Cu-Au-(U) mineralisation within any of the IOCG systems in the Olympic Dam district. All evidence points to formation during a ~1.59 Ga magmatic-hydrothermal event irrespective of host rocks or local geological setting. Studies have, however, shown geochronological evidence suggestive of later superimposed events that have impacted on the deposits as seen today (e.g., the ~825 Ma Gairdner dyke swarm; Huang et al., 2015; Apukhtina et al., 2016). This is supported by mineralogical studies of IOCG systems, mostly at Olympic Dam, that have documented cycles of replacement, remobilisation and recrystallisation among disparate mineral groups (oxides, sulphides, REE-minerals etc.; Ciobanu et al., 2013; Krneta et al., 2018; Verdugo-Ihl et al., 2017; Owen et al., 2018; Schmandt et al., 2019). Notably, remobilisation of U has been documented from Olympic Dam, with U redeposited as flooding, veinlets and pockets (Macmillan et al., 2016) clearly long after crystallisation of early disseminated uraninite. This evidence has been taken to infer (probably multiple) stages of dissolution and re-precipitation, or, possible upgrading via secondary enrichment.

Identifying the principal source(s) and timing of metal introduction relative to the ~1.6 Ga magmatic-hydrothermal event is significant for constraining province-scale IOCG metallogeny, since element remobilisation or isotopic resetting, even when induced by relatively minor hydro- or tectonothermal events may lead to misinterpretation of 'new' metal influxes or protracted mineralising events. The realistic limit of analytical precision when dating hydrothermal minerals of Proterozoic age (e.g., ~1 Ma for U-bearing hematite), restricts measurement of mineralisation lifespans and may preclude individual stages of mineralising events to be distinguished. For example, Cenozoic magmatic-hydrothermal porphyry Cu deposits are known to form in discrete fluid pulses over just tens to hundreds of thousands of years (e.g., Li et al., 2017), timescales currently unresolvable for Proterozoic IOCG systems. Nonetheless, there is an apparent measurable variation within the ~1.6 Ga GRV/Hiltaba Suite magmatic event across the Olympic Cu-Au province, within which temporally distinct intrusions likely control the timing of associated Cu-Au mineralisation (Skirrow et al., 2007; Reid et al., 2013). On this basis, it should be possible to obtain an accurate measure of the variation in mineralisation/alteration ages from each IOCG system, bracketed by high-precision zircon ages of either the host, or nearby Hiltaba Suite intrusions. Nevertheless, it must be considered that zircons from Hiltaba Suite

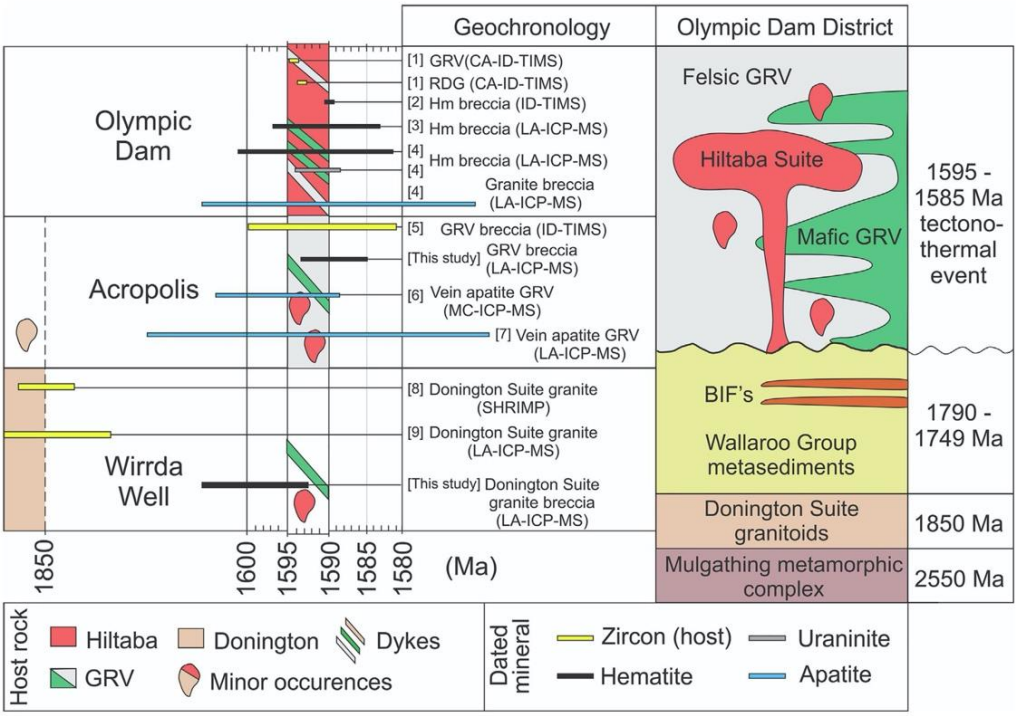


Fig. 14. Schematic representation of published dates for host lithologies and hydrothermal minerals at Olympic Dam, Acropolis and Wirrda Well (deposits and prospects that are closely spatially related), and (right) a diagram displaying the general relationships between the different major host lithologies and basement rocks of the Olympic Dam district. Coloured units relate to individual rock types and coloured age uncertainty bars relate do the different dated mineral, as marked. The numbered age uncertainty bars indicate their published reference (1-Cherry et al., 2018a; 2- Courtney-Davies et al., 2019a; 3-Ciobanu et al., 2013; 4-Apukhtina et al., 2017; 5-Creaser and Cooper, 1993; 6-Thompson et al., 2016; 7-Cherry et al., 2018b; 8-Jagodzinski, 2005; 9-Courtney-Davies et al., 2019b). Abbreviations: Hm (hematite); MC-ICP-MS (multiple collector-inductively coupled plasma-mass spectrometry).

granite are generally U-Th-rich and invariably affected by α-decay damage, whereby Pb-loss can result in spuriously young dates. Interpretation may be further compromised by comparing datasets with wide-ranging levels of precision for different intrusions.

The Hiltaba Suite/GRV rocks were likely emplaced during a tectonic switch from compressional to extensional regimes in a post-subduction setting at ~1594 Ma, supported by seismic reflection evidence for GRV-filled half-grabens (Carr et al., 2010). The development of major IOCG systems during this tectonic switch was guided by prior trans-lithospheric weaknesses (Skirrow et al., 2018).

In summary, there is a broad discrepancy in alteration and mineralisation dates in the region, possibly due to real temporal differences in crystallisation, the dating of different events (e.g. hematite *vs.* sericite alteration), open system behaviour in dated minerals and low accuracy of some methods or instruments used (Fig. 14). Any synthesis of relatively large geochronological data sets that have used a spectrum of minerals, radiogenic systems, and instrumentation is therefore challenging and ultimately, may not be particularly helpful for accurately defining the timing or duration of IOCG mineralisation.

Currently, no examples of high-precision geochronological data are available for monazite, uraninite, baddeleyite, rutile, allanite, xenotime or Ca-Fe-Mg-Mn carbonates from deposits in the Olympic Dam district or their host rocks. Several studies of these minerals have, however, contributed important data to broadly bracket the timing of mineralisation. These have, in general, clarified the relationship between the ~1.6 Ga magmatic and crystallisation of accessory minerals (e.g. Skirrow et al., 2007; Apukhtina et al., 2017; Cherry et al., 2018b).

The presence of hydrothermal zircon at Olympic Dam has been claimed, which if such an origin could be validated, would provide a benchmark for hydrothermal mineral dating in the Olympic Cu-Au province. However, such grains contain unusually high U-contents resulting in intense metamictization and subsequent Pb-loss (1598 ± 12 Ma; n = 5; SHRIMP; Jagodzinski, 2014). Furthermore, due to a lack of discriminatory geochemical data, unequivocal evidence for the existence of a distinct generation of hydrothermal zircon remains lacking. A more likely scenario involves magmatic zircon from granite hosting the deposit is incorporated into the orebody during brecciation. Interaction with hydrothermal/metasomatic fluids has been shown to impact on grain morphology and chemical composition (e.g. Courtney-Davies et al., 2019c).

Three minerals (apatite, molybdenite and hematite), which are hydrothermal in the reported cases, have returned reliable data that can be used to directly date primary IOCG mineralisation. Apatite has been dated in several locations, but due to (i) the tendency to incorporate common Pb during (re-) crystallisation (Chew et al., 2011) and (ii) medium range closure temperature (Schoene and Bowring, 2007), most examples have produced often accurate, but rather imprecise data (Apukhtina et al., 2018; Cherry et al., 2018), which in some cases may not date the primary ore-forming event. One example of a reliable U-Pb apatite age from a sample containing relatively low common Pb was obtained at Acropolis (1596.7 ± 7.1; Thompson et al., 2016), within uncertainty of U-bearing hematite presented here (1589.1 ± 5.6).

Rhenium-Os negative-TIMS provided a molybdenite age at the Vulcan prospect (~25 km NE of Olympic Dam) of 1586 ± 8 Ma (Reid et al. 2013). The ages of hematite and molybdenite from prospects and deposits within or bordering the Burgoyne batholith (Fig. 1) have yielded dates within narrow analytical uncertainty of one another (Table 1).

Uranium-Pb ages of hematite at Olympic Dam and Acropolis (1589.98 ± 0.89 Ma and 1590.6 ± 6.5 Ma, respectively) underpin the timing of Cu-Au mineralisation in the Olympic Dam district, further supported by apatite and molybdenite dates. We expect to find U-bearing hematite ages indistinguishable from ~1590 Ma in all IOCG systems of the Olympic Dam district (e.g., Carrapateena, Oak Dam West, Vulcan and Emmie Bluff).

The variation in age between Hiltaba Suite plutons across the Olympic Cu-Au province, is the most likely factor controlling the timing of IOCG-style mineralisation. High-precision hematite dating from deposits such as Prominent Hill in the north, and from Hillside or Moonta in the south (Fig. 1), will provide a temporal record of mineralisation at the province-scale, clarifying major or rather more subtle differences in the timing of Cu-Au mineralisation between the three districts.

6. Conclusions and outlook

1. Silician and titaniferous magnetite are typical for the early-stage mineralisation at Wirrda Well and Acropolis, respectively. Late-stage, U-W-Sn-Mo-bearing, oscillatory-zoned hematite is characterised from both prospects, but with discrepant relationships to early magnetite. At Acropolis, martitisation of magnetite results in U-W-Mo-enrichment at constant Sn concentration, and loss of REY, whereas at Wirrda Well single-crystal zoned hematite, resembling those from Olympic Dam occurs.
2. Geochemical signatures of Fe-oxides from the two prospects share common trends for HFSE, granitophile elements and siderophile elements. Whereas these are comparable with signatures of Fe-oxides from the outer shell at Olympic Dam, the presence of measurable Ni and Cr is a distinctive feature of both prospects. High Mo content (mean ~ 860 ppm) is characteristic for Wirrda Well hematite. Chondrite-normalised REY-trends for magnetite are comparable with each other but distinct for hematite from each prospect. Wirrda Well hematite is highest in ΣREY and comparable with hematite from the outer shell at Olympic Dam.
3. U-Pb geochronology of the two textural types of hematite provides dates at 1598.9 ± 6.3 Ma and 1590.6 ± 6.5 Ma for Wirrda Well and Acropolis, respectively. These ages are consistent with, and within uncertainty of, those found at Olympic Dam.
4. Vein-hosted titaniferous magnetite replaced by U-bearing hematite at Acropolis is formed in a shallower environment than the silician magnetite and U-bearing hematite at Wirrda Well. U-W-Sn-Mo enriched oscillatory-zoned hematite found in the Olympic Dam district is likely a common feature of IOCG systems throughout the eastern Gawler Craton. Such evidence can underpin models for the timing and evolution of IOCG systems in South Australia and will contribute to the resolution of long-standing debates often based on speculation or incompatible datasets. As shown here for the Olympic Dam district, host rock lithology would not appear to be a significant factor controlling IOCG mineralisation, and this should be valid also outside the Olympic Dam district (e.g. Prominent Hill). However, common to Olympic Dam, Wirrda Well and Acropolis is the presence of Hiltaba Suite granite, either hosting the ores, or intersected in drillholes close to mineralisation. The W-Mo-Sn signature recorded in hydrothermal U-bearing hematite, and deposition of that hematite shortly after crystallisation of zircon in host Roxby Downs Granite at Olympic Dam, strongly indicates that the magmas that generated Hiltaba Suite granite are the major source of metals found throughout the Olympic Cu-Au Province.

The hematite U-Pb mineral geochronometer is radio-isotopically reliable within both magnetite- and hematite-dominant IOCG systems displaying different stages of evolution. Due to formation under differing conditions, the morphology and chemistry of U-bearing hematite at Olympic Dam, Wirrda Well and Acropolis varies significantly, however, a confident, common age can still be obtained. U-bearing hematite represents a critical phase to identify in order to constrain the chronology of IOCG systems within and outside the eastern Gawler Craton. High precision ID-TIMS dating of U-bearing hematite from several deposits along the 700 km-strike of the Olympic Cu-Au province (from the Mount Woods Inlier to the Yorke Peninsula), can unequivocally define the onset of Fe-metasomatism and the potential lifespan of each IOCG mineralisation event. Coupled with a robust framework of U-Pb zircon ages for magmatic rocks across the region, the transition from magmatic crystallisation to establishment of hydrothermal systems can be temporally calibrated using a single hydrothermal mineral at high-resolution.

Acknowledgements

This work is a contribution to the 'FOX' project (Trace elements in iron oxides: deportment, distribution and application in ore genesis, geochronology, exploration and mineral processing), supported by BHP Olympic Dam and the South Australian Government Mining and Petroleum Services Centre of Excellence. N.J.C. acknowledges additional support from the ARC Research Hub for Australian Copper-Uranium (Grant IH130200033). We acknowledge the valuable comments of John Hanchar, an anonymous reviewer, Associate Editor Natasha Wodicka and Chief Editor Victoria Pease, which helped us improve and clarify our presentation and interpretations.

Appendix A. Supplementary data

Supplementary data to this article can be found online at https://doi.org/10.1016/j.precamres.2019.105480.

References

Allen, S., McPhie, J., Ferris, G., Simpson, C., 2008. Evolution and architecture of a large felsic igneous province in western Laurentia: the 1.6 Ga Gawler Range Volcanics, South Australia. J. Volcanol. Geotherm. Res. 172, 132–147.

Apukhtina, O.B., Kamenetsky, V.S., Ehrig, K., Kamenetsky, M.B., Maas, R., Thompson, J., McPhie, J., Ciobanu, C.L., Cook, N.J., 2017. Early, deep magnetite-fluorapatite mineralization at the Olympic Dam Cu-U-Au-Ag deposit, South Australia. Econ. Geol. 112, 1531–1542.

Apukhtina, O.B., Kamenetsky, V.S., Ehrig, K., Kamenetsky, M.B., McPhie, J., Maas, R., Meffre, S., Goemann, K., Rodemann, T., Cook, N.J., Ciobanu, C.L., 2016. Postmagmatic magnetite–apatite assemblage in mafic intrusions: a case study of dolerite at Olympic Dam, South Australia. Contrib. Mineral. Petrol. 171, 15.

Barton, M.D., 2013. Treatise on Geochemistry, second ed. 13. Elsevier, pp. 515–541.

Bowden, B., Fraser, G., Davidson, G.J., Meffre, S., Skirrow, R.G., Bull, S., Thompson, J., 2017. Age constraints on the hydrothermal history of the Prominent Hill iron oxide copper-gold deposit, South Australia. Miner. Deposita. 52 (6), 863–881.

Buddington, A.F., Lindsley, D.H., 1964. Iron-titanium oxide minerals and synthetic equivalents. J. Petrol. 5, 310–357.

Carr, L.K., Korsch, R.J., Holzschuh, J., Costelloe, R.D., Meixner, A.J., Matthews, C., Godsmark, B., 2010. Geological interpretation of seismic reflection lines 08GA-C1 and 09TE-01: Arrowie Basin, South Australia. In: Korsch, R.J. and Kositcin, N., South Australian Seismic and MT Workshop 2010, Extended Abstracts. Geoscience Australia Record 2010/10, 54–65.

Cherry, A.R., Ehrig, K., Kamenetsky, V.S., McPhie, J., Crowley, J.L., Kamenetsky, M.B., 2018a. Precise geochronological constraints on the origin, setting and incorporation of ca. 1.59 Ga surficial facies into the Olympic Dam Breccia Complex, South Australia. Precambr. Res. 315, 162–178.

Cherry, A.R., Kamenetsky, V.S., McPhie, J., Thompson, J.M., Ehrig, K.J., Meffre, S., Kamenetsky, M.B., Krneta, S., 2018b. Tectonothermal events in the Olympic IOCG Province constrained by apatite and REE-phosphate geochronology. Austral. J. Earth. Sci. 65, 643–659.

Chew, P.J., Sylvester, M.N., Tubrett, M.N., 2011. U-Pb and Th-Pb dating of apatite by LA-ICPMS. Chem. Geol. 280, 200–216.

Ciobanu, C.L., Wade, B.P., Cook, N.J., Schmidt, Mumm A., Giles, D., 2013. Uranium-bearing hematite from the Olympic Dam Cu–U–Au deposit, South Australia: A geochemical tracer and reconnaissance Pb–Pb geochronometer. Precambr. Res. 238, 129–147.

Ciobanu, C.L., Verdugo-Ihl, M.R., Slattery, A., Cook, N.J., Ehrig, K.J., Courtney-Davies, L., 2018. Nanoscale study of silician magnetite from IOCG systems: Examples from the

Olympic Dam District (South Australia). In: Proceedings of the 15th Quadrennial IAGOD Symposium, Salta, Argentina. pp. 185-186.
Ciobanu, C.L., Verdugo-Ihl, M.R., Slattery, A., Cook, N.J., Ehrig, K., Courtney-Davies, L., Wade, B.P., 2019. Silician magnetite: Si–Fe-nanoprecipitates and other mineral inclusions in magnetite from the Olympic dam deposit, South Australia. Minerals 9 (5), 311. https://doi.org/10.3390/min9050311.
Courtney-Davies, L., Zhu, Z., Ciobanu, C.L., Wade, B.P., Cook, N.J., Ehrig, K., Cabral, A.R., Kennedy, A., 2016. Matrix-matched iron-oxide laser ablation ICP-MS U-Pb geochronology using mixed solution standards. Minerals 6 (3), 85. https://doi.org/10.3390/min603008.
Courtney-Davies, L., Tapster, S.R., Ciobanu, C.L., Cook, N.J., Verdugo-Ihl, M.R., Ehrig, K.J., Kennedy, A.K., Gilbert, S.E., Condon, D.J., Wade, B.P., 2019a. A multi-technique evaluation of hydrothermal hematite U-Pb isotope systematics: implications for ore deposit geochronology. Chem. Geol. 513, 54–72.
Courtney-Davies, L., Ciobanu, C.L., Richardson, M.W., Prosser, N., Verdugo-Ihl, M.R., Wade, B.P., Gilbert, S.E., Ehrig, K., Cook, N.J., 2019b. Synthesis of U-Pb doped hematite using a hydrated ferric oxide approach. J. Crst. Growth. 513, 48–57.
Courtney-Davies, L., Ciobanu, C.L., Verdugo-Ihl, M.R., Slattery, A., Cook, N.J., Dmitrijeva, M., Keyser, W., Wade, B.P., Dominick, U.I., Ehrig, K., Xu, J., Kontonikas-Charos, A., 2019c. Zircon at the nanoscale records metasomatic processes leading to large magmatic-hydrothermal ore deposits. Minerals 9 (6), 364. https://doi.org/10.3390/min9060364.
Creaser, R.A., 1989. The geology and petrology of Middle Proterozoic felsic magmatism of the Stuart shelf, South Australia. La Trobe University.
Creaser, R.A., Cooper, J.A., 1993. U-Pb geochronology of middle Proterozoic felsic magmatism surrounding the Olympic Dam Cu-Au-U-Ag and Moonta Cu-Au-Ag deposits, South Australia. Econ. Geol. 88, 186–197.
Cross, K.C., 1993. Acropolis and Wirrda Well. In: Drexel, J.F., Preiss, W.V., Parker, A.J. (Eds.), The geology of South Australia. vol. 1, The Precambrian. Geological Survey of South Australia, South Australia, pp. 138.
Davidson, G.J., Paterson, H., Meffre, S., Berry, R.F., 2007. Characteristics and origin of the oak dam east breccia-hosted, iron oxide Cu-U-(Au) deposit: Olympic Dam Region, Gawler Craton, South Australia. Econ. Geol. 102 (8), 1471–1498.
Duff, M.C., Coughlin, J.U., Hunter, D.B., 2002. Uranium co-precipitation with iron oxide minerals. Geochim. Cosmochim. Acta 66, 3533–3547.
Dmitrijeva, M., Ciobanu, C.L., Ehrig, K., Cook, N.J., Metcalfe, A., Verdugo-Ihl, M.R., McPhie, J., 2019a. Defining IOCG signatures through compositional data analysis: a case study of lithogeochemical zoning from the Olympic Dam deposit, South Australia. Ore. Geol. Rev. 105, 86–101.
Dmitrijeva, M., Ehrig, K., Ciobanu, C.L., Cook, N.J., Verdugo-Ihl, M.R., Metcalfe, A., 2019b. Mineralization-alteration footprints in the Olympic Dam IOCG district, South Australia: the Acropolis prospect. J. Geochem. Explor. 205 106333.
Drexel, J.F., Preiss, W.V., Parker, A.J., 1993. The Geology of South Australia, Vol. 1, The Precambrian. Geol. Surv South Austra. Bull. 54, 170–203.
Ehrig, K., McPhie, J., Kamenetsky, V., 2012. Geology and mineralogical zonation of the olympic dam iron oxide Cu-U-Au-Ag deposit, South Australia. Econ. Geol. 16, 237–267 Special Publication.
Ehrig, K., 2013. Geology of the Wirrda Well IOCG Deposit. 10th Annual SA Exploration and Mining Conference. http://www.saexplorers.com.au/archive/2013/.
Ehrig, K., Kamenetsky, V.S., McPhie, J., Apukhtina, O., Ciobanu, C., Cook, N., Kontonikas-Charos, A., Krneta, S., 2017. The IOCG-IOA Olympic Dam Cu-U-Au-Ag deposit and nearby prospects, South Australia. Proceedings, 14th Biennial SGA Meeting 'Mineral Resources to Discover' Québec City, Canada. 3, pp. 823–826.
Ernst, R., 2014. Large Igneous Provinces. Cambridge University Press, Cambridge.
Goldfarb, R.J., Bradley, D., Leach, D.L., 2010. Secular variation in economic geology. Econ. Geol. 105, 459–465.
Groves, D.I., Bierlein, F.P., Meinert, L.D., Hitzman, M.W., 2010. Iron oxide copper-gold (IOCG) deposits through Earth history: Implications for origin, lithospheric setting, and distinction from other epigenetic iron oxide deposits. Econ. Geol. 105, 641–654.
Hayward, N., Skirrow, R.G., 2010. Geodynamic setting and controls on iron oxide Cu-Au (± U) ore in the Gawler Craton, South Australia. In: Porter, T.M. (Ed.), Hydrothermal Iron Oxide Copper-Gold & Related Deposits: A Global Perspective. PGC Publishing, Adelaide, pp. 1–27.
Huang, Q., Kamenetsky, V.S., McPhie, J., Ehrig, K., Meffre, S., Maas, R., Thompson, J., Kamenetsky, M., Chambefort, I., Apukhtina, O., Hu, Y., 2015. Neoproterozoic (ca. 820–830 Ma) mafic dykes at Olympic Dam, South Australia: Links with the Gairdner Large Igneous Province. Precambr. Res. 271, 160–172.
Huang, Q., Kamenetsky, V.S., Ehrig, K., McPhie, J., Kamenetsky, M., Cross, K., Meffre, S., Agangi, A., Chambefort, I., Direen, N.G., Maas, R., Apukhtina, O., 2016. Olivine-phyric basalt in the Mesoproterozoic Gawler silicic large igneous province, South Australia: examples at the Olympic dam iron oxide Cu–U–Au–Ag deposit and other localities. Precambr. Res. 281, 185–199.
Jackson, S.E., Pearson, N.J., Belousova, E.A., Griffin, W.L., 2004. The application of laser ablation-inductively coupled plasma-mass spectrometry (LA-ICP-MS) to in situ U-Pb geochronology. Chem. Geol. 211, 47–69.
Jaffey, A.H., Flynn, K.F., Glendenin, L.E., Bentley, W.C., Essling, A.M., 1971. Precision measurement of half-lives and specific activities of ^{235}U and ^{238}U. Phys. Rev. C. Nucl. Phys. 4, 1889–1906.
Jagodzinski, E.A., 2005. Compilation of SHRIMP U-Pb geochronological data Olympic Domain, Gawler Craton, South Australia, 2001-2003. Geoscience Australia Record 2005/020.
Jagodzinski, E.A. The age of magmatic and hydrothermal zircon at Olympic Dam. In: Proceedings of the 2014 Australian Earth Sciences Convention, Sustainable Australia, Newcastle, Australia. 110, 260.
Keyser, W., Ciobanu, C.L., Cook, N.J.M., Courtney-Davies, L., Kennedy, A., Wade, B.P., Ehrig, K., Dmitrijeva, M., Kontonikas-Charos, A., Feltus, H., Johnson, G., 2019. Petrographic and geochronological constraints on the granitic basement to the Middleback Ranges, South Australia. Precambr. Res. 324, 170–193.
Kirchenbaur, M., Maas, R., Ehrig, K., Kamenetsky, V.S., Strub, E., Ballhaus, C., Münker, C., 2016. Uranium and Sm isotope studies of the supergiant Olympic Dam Cu–Au–U–Ag deposit, South Australia. Geochim. Cosmochim. Acta. 180, 15–32.
Krneta, S., Cook, N.J., Ciobanu, C.L., Ehrig, K.J., Kontonikas-Charos, A., 2017. The Wirrda well and Acropolis prospects, Gawler Craton, South Australia: insights into evolving fluid conditions through apatite chemistry. J. Geochem. Explor. 181, 276–291.
Kontonikas-Charos, A., Ciobanu, C.L., Cook, N.J., Ehrig, K., Krneta, S., Kamenetsky, V.S., 2017. Rare earth element geochemistry of feldspars: Examples from Fe-oxide Cu-Au systems in the olympic Cu-Au Province, South Australia. Mineral. Petrol. 112, 145–172.
Krneta, S., Ciobanu, C.L., Cook, N.J., Ehrig, K.J., 2018. Numerical modeling of REE fractionation patterns in fluorapatite from the Olympic Dam deposit (South Australia). Minerals 8, 342. https://doi.org/10.3390/min8080342.
Li, Y., Selby, D., Condon, D., Tapster, S., 2017. Cyclic magmatic-hydrothermal evolution in porphyry systems: High-precision U-Pb and Re-Os geochronology constraints from the Tibetan Qulong porphyry Cu-Mo deposit. Econ. Geol. 112, 1419–1440.
Ludwig, K.R.A., 2012. Isoplot/Ex rev. 4.1: A Geochronological Toolkit for Microsoft Excel; Berkeley Geochronology Centre Special Publication No.5, 75. Berkeley Geochronology Centre, Berkeley, California.
Macmillan, E., Cook, N.J., Ehrig, K., Ciobanu, C.L., Pring, A., 2016. Uraninite from the Olympic Dam IOCG-U-Ag deposit: linking textural and compositional variation to temporal evolution 2016. Am. Mineral. 101, 1295–1320.
McPhie, J., 2016. Acropolis Report. BHP Olympic Dam (unpublished).
Mortimer, G.E., Cooper, J.A., Paterson, H.L., Cross, K., Hudson, G.R.T., Uppill, R.K., 1988. Zircon U-Pb dating in the vicinity of the olympic dam Cu–U–Au deposit, roxby downs, South-Australia. Econ. Geol. 83, 694–709.
Murakami, H., Seo, J.H., Heinrich, C.A., 2010. The relation between Cu/Au ratio and formation depth of porphyry-style Cu–Au ± Mo deposits. Mineral. Deposita. 45 (1), 11–21.
Oreskes, N., Einaudi, M.T., 1992. Origin of hydrothermal fluids at Olympic Dam; preliminary results from fluid inclusions and stable isotopes. Econ. Geol. 87, 64–90.
Owen, N.D., Ciobanu, C.L., Cook, N.J., Slattery, A., Basak, A., 2018. Nanoscale study of clausthalite-bearing symplectites in Cu-Au-(U) ores: Implications for ore genesis. Minerals 8, 67. https://doi.org/10.3390/min8020067.
Paton, C., Hellstrom, J., Paul, B., Woodhead, J., Hergt, J., 2011. Iolite: Freeware for the visualisation and processing of mass spectrometric data. J. Anal. At. Spectrom. 26, 2508–2518.
Petrus, J., Kamber, B., 2012. VizualAge: a novel approach to laser ablation ICP-MS U-Pb geochronology data reduction. Geostand. Geoanal. Res. 36, 247–270.
Reid, A., Smith, R.N., Baker, T., Jagodzinski, E.A., Selby, D., Gregory, C.J., Skirrow, R.G., 2013. Re-Os dating of molybdenite within hematite breccias from the Vulcan prospect, Olympic Dam Cu-Au province, South Australia. Econ. Geol. 108, 883–894.
Reid, A., 2019. The olympic Cu-Au province, Gawler craton: a review of the lithospheric architecture, geodynamic setting, alteration systems, cover successions and prospectivity. Minerals 9 (6), 371. https://doi.org/10.3390/min9060371.
Schlegel, T.U., Wagner, T., Boyce, A., Heinrich, C.A., 2017. A magmatic source of hydrothermal sulfur for the Prominent Hill deposit and associated prospects in the Olympic iron oxide copper-gold (IOCG) province of South Australia. Ore Geol. Rev. 89, 1058–1090.
Schoene, B., Bowring, S.A., 2007. Determining accurate temperature–time paths from U-Pb thermochronology: an example from the Kaapvaal craton, southern Africa. Geochim. Cosmochim. Acta 71, 165–185.
Schmandt, D.S., Cook, N.J., Ciobanu, C.L., Ehrig, K., Wade, B.P., Gilbert, S., Kametetsky, V.S., 2019. Rare earth element phosphate minerals from the Olympic Dam Cu-U-Au-Ag deposit, South Australia: recognizing temporal-spatial controls on REE mineralogy in an evolved IOCG systems. Can. Mineral. 57, 3–24.
Skirrow, R.G., Bastrakov, E.N., Baroncii, K., Fraser, G.L., Creaser, R.A., Fanning, C.M., Raymond, O.L., Davidson, G.J., 2007. Timing of iron oxide Cu-Au-(U) hydrothermal activity and Nd isotope constraints on metal sources in the Gawler craton, South Australia. Econ. Geol. 102, 1441–1470.
Skirrow, R.G., Van Der Wielen, S.E., Champion, D.C., Czarnota, K., Thiel, S., 2018. Lithospheric architecture and mantle metasomatism linked to iron oxide Cu-Au ore formation: multidisciplinary evidence from the Olympic Dam Region, South Australia. Geochem. Geophys. Geosys. 19 (8), 2673–2705.
Sláma, J., Košler, J., Condon, D.J., Crowley, J.L., Gerdes, A., Hanchar, J.M., Horstwood, M.S.A., Morris, G.A., Nasdala, L., Norberg, N., Schaltegger, U., Schoene, B., Tubrett, M.N., Whitehouse, M.J., 2008. Plešovice zircon - a new natural reference material for U-Pb and Hf isotopic microanalysis. Chem. Geol. 249, 1–35.
Steiger, R.H., Jäger, E., 1977. Subcommission on geochronology: convention on the use of decay constants in geo- and cosmochronology. Earth. Planet. Sci. Lett. 36, 359–362.
Thompson, J., Meffre, S., Maas, R., Kamenetsky, V., Kamenetsky, M., Goemann, K., Danyushevsky, L., 2016. Matrix effects in Pb/U measurements during LA-ICP-MS analysis of the mineral apatite. J. Anal. At. Spectrom. 31, 1206–1215.
Verdugo-Ihl, M.R., Ciobanu, C.L., Cook, N.J., Ehrig, K.J., Courtney-Davies, L., Gilbert, S., 2017. Textures and U-W-Sn-Mo signatures in hematite from the Olympic Dam Cu-U-Au-Ag deposit, South Australia: defining the archetype for IOCG deposits. Ore. Geol. Rev. 91, 173–195.
Verdugo-Ihl, M.R., Ciobanu, C.L., Cook, N.J., Ehrig, K., Courtney-Davies, L., 2019. Defining early stages of IOCG systems: evidence from iron-oxides in the outer shell of the Olympic Dam deposit, South Australia. Mineral. Deposita. https://doi.org/10.1007/s00126-019-00896-2.
Wade, C.E., Payne, J.L., Barovich, K.M., Reid, A.J., 2019. Heterogeneity of the sub-continental lithospheric mantle and 'non-juvenile' mantle additions to a Proterozoic silicic large igneous province. Lithos 340–341 87–107.
Wiedenbeck, M., Alle, P., Corfu, F., Griffin, W.L., Meier, M., Oberli, F., von Quadt, A., Roddick, J.C., Spiegel, W., 1995. 3 natural zircon standards for U-Th-Pb, Lu-Hf, trace element and REE analyses. Geostand. Newslett. 19, 1–23.

CHAPTER 6

~1760 MA MAGNETITE-BEARING PROTOLITHS IN THE OLYMPIC DAM DEPOSIT, SOUTH AUSTRALIA: IMPLICATIONS FOR ORE GENESIS AND REGIONAL METALLOGENY

Liam Courtney-Davies [1], Cristiana L. Ciobanu [1], Max R. Verdugo-Ihl [1], Nigel J. Cook [1], Kathy J. Ehrig [2], Benjamin P. Wade [3], Zhi-Yong Zhu [4], Vadim S. Kamenetsky [5]

[1] School of Chemical Engineering and Advanced Materials, The University of Adelaide, SA 5005, Australia

[2] BHP Olympic Dam, Adelaide, SA 5000, Australia

[3] Adelaide Microscopy, The University of Adelaide, SA 5005, Australia

[4] MNR Key Laboratory of Isotope Geology and Deep-Earth Dynamics, Institute of Geology, Chinese Academy of Geological Sciences, China

[5]ARC Centre of Excellence in Ore Deposits (CODES), School of Natural Sciences, University of Tasmania, Hobart, Tasmania 7001, Australia

Article published in Ore Geology Reviews 118 (2020) 103337

Statement of Authorship

Title of Paper	~1760 Ma magnetite-bearing protoliths in the Olympic Dam deposit, South Australia: Implications for ore genesis and regional metallogeny
Publication Status	☐ Published ☐ Accepted for Publication ☑ Submitted for Publication ☐ Unpublished and Unsubmitted w ork w ritten in manuscript style
Publication Details	Courtney-Davies, L., Ciobanu, C.L., Verdugo-Ihl, M., Cook, N.J., Ehrig, K., Wade, B.P., Zhu, Z.Y., Kamenetsky, V.S., (in review). ~1760 Ma magnetite-bearing protoliths in the Olympic Dam deposit, South Australia: Implications for ore genesis and regional metallogeny. Ore Geology Reviews.

Principal Author

Name of Principal Author (Candidate)	Liam Courtney-Davies		
Contribution to the Paper	Performed analytical work, carried out data processing and interpretation, oversaw development of work and wrote manuscript.		
Overall percentage (%)	50		
Certification:	This paper reports on original research I conducted during the period of my Higher Degree by Research candidature and is not subject to any obligations or contractual agreements with a third party that would constrain its inclusion in this thesis. I am the primary author of this paper.		
Signature		Date	29/10/2019

Co-Author Contributions

By signing the Statement of Authorship, each author certifies that:

i. the candidate's stated contribution to the publication is accurate (as detailed above);

ii. permission is granted for the candidate in include the publication in the thesis; and

iii. the sum of all co-author contributions is equal to 100% less the candidate's stated contribution.

Name of Co-Author	Cristiana L. Ciobanu		
Contribution to the Paper	Defined direction of research, supervised development of work, carried out data collection and processing and contributed to manuscript preparation.		
Overall percentage (%)	10		
Signature		Date	29 Oct 2019

Name of Co-Author	Max R. Verdugo-Ihl		
Contribution to the Paper	Performed analytical work, carried out data processing and interpretation, contributed to manuscript preparation.		
Overall percentage (%)	10		
Signature		Date	29/10/2019

Name of Co-Author	Nigel J. Cook		
Contribution to the Paper	Contributed to data interpretation, manuscript preparation and evaluation		
Overall percentage (%)	10		
Signature		Date	29/10/2019

Name of Co-Author	Kathy Ehrig		
Contribution to the Paper	Coordinated sample collection, defined research direction and assisted with evaluation of manuscript.		
Overall percentage (%)	10		
Signature		Date	29/10/2019

Name of Co-Author	Benjamin P. Wade		
Contribution to the Paper	Performed analytical work, carried out data processing and interpretation. Evaluation of manuscript.		
Overall percentage (%)	5		
Signature		Date	29/10/2019

Name of Co-Author	Zhi-Yong Zhu		
Contribution to the Paper	Performed analytical work, carried out data processing and interpretation.		
Overall percentage (%)	2.5		
Signature		Date	29/09/2019

Name of Co-Author	Vadim S. Kamenetsky		
Contribution to the Paper	Helped define research direction.		
Overall percentage (%)	2.5		
Signature		Date	29.Oct 2019

Ore Geology Reviews 118 (2020) 103337

Contents lists available at ScienceDirect

Ore Geology Reviews

journal homepage: www.elsevier.com/locate/oregeorev

~1760 Ma magnetite-bearing protoliths in the Olympic Dam deposit, South Australia: Implications for ore genesis and regional metallogeny

Liam Courtney-Davies[a,*], Cristiana L. Ciobanu[a], Max R. Verdugo-Ihl[a], Nigel J. Cook[a], Kathy J. Ehrig[b], Benjamin P. Wade[c], Zhi-Yong Zhu[d], Vadim S. Kamenetsky[e]

[a] School of Chemical Engineering and Advanced Materials, The University of Adelaide, SA 5005, Australia
[b] BHP Olympic Dam, Adelaide, SA 5000, Australia
[c] Adelaide Microscopy, The University of Adelaide, SA 5005, Australia
[d] MNR Key Laboratory of Isotope Geology and Deep-Earth Dynamics, Institute of Geology, Chinese Academy of Geological Sciences, Beijing, China
[e] ARC Centre of Excellence in Ore Deposits (CODES), School of Natural Sciences, University of Tasmania, Hobart, Tasmania 7001, Australia

ARTICLE INFO

Keywords:
Olympic Dam
Magnetite U-Pb dating
IOCG
Gawler Craton

ABSTRACT

Spatial associations between banded iron formation and iron-oxide Cu-Au (IOCG) style mineralization are well documented in the Gawler Craton (South Australia), but the possible genetic relationships between these two distinct types of mineralization are hitherto unclear. A texturally conspicuous generation of coarse-grained silician magnetite, intergrown with carbonates and quartz, is observed in drillholes intersecting the 'outer shell' of the Olympic Dam IOCG-type deposit. This magnetite is characterised by high U-content (~50 ppm), siliceous chemistry, and unusual zonal textures with respect to Si-Fe-nanoprecipitates. Direct dating of this magnetite by laser ablation inductively coupled plasma mass spectrometry yields reproducible $^{207}Pb/^{206}Pb$ dates (1761 ± 16 Ma) that are significantly older than the granite hosting the deposit (1593 Ma), or the mineralized breccias constituting the Cu-U-Au-Ag resource (~1592–1589 Ma). The older, Fe-rich crustal material can be correlated with the ~1.76–1.74 Ga (meta)sedimentary Wallaroo Group, host to Fe-rich horizons across the Gawler Craton, including locations ~15 km NW of Olympic Dam. A generation of granitic rocks, which intruded bedrock at ~1.75 Ga are present ~30 km NE of Olympic Dam, and likely exsolved hydrothermal fluids that enriched pre-existing magnetite-bearing protoliths in both U and REE. Such material was physically, and likely chemically, incorporated into the 'outer shell' at Olympic Dam some ~150 Ma later, during granite uplift along faults. The coincidence between Fe-rich horizons/BIF and ~1750 Ma granitoids may have provided IOCG systems with an additional source of both Fe and U that predates the ~1.59 Ga craton-scale metallogenic event. The uranium concentrations in some South Australian IOCG systems represent major global anomalies in the element. A combination of the fortuitous geological circumstances outlined here, may help explain the highly anomalous accumulation of uranium found at Olympic Dam.

1. Introduction

Olympic Dam is by far the largest iron-oxide copper gold (IOCG) system within a N-S-striking, 500 km-long belt defined as the Olympic Cu-Au Province (e.g., Skirrow et al., 2007; Reid, 2019), located on the eastern margin of the Gawler Craton, South Australia. The IOCG mineralization is associated with bimodal intrusive rocks of the Hiltaba Suite (Fanning et al., 1988) and subaerial Gawler Range Volcanics (GRV; Blissett et al., 1993), which together comprise the ~1.6 Ga Gawler Silicic Large Igneous Province (SLIP; Fig. 1A; Allen et al., 2008). The Olympic Dam district contains numerous IOCG-style deposits and prospects which are concealed by post-mineralization sedimentary cover (Reid, 2019), making the area highly prospective and the current focus of exploration (Wise, 2019).

Basement rocks of the district comprise the 2.5 Ga Mulgathing Metamorphic Complex, ~1.85 Ga Donington Suite granitoid rocks, and the 1.76–1.74 Ga Wallaroo Group (meta)sedimentary rocks, which are intruded, and unconformably overlain by, the Hiltaba Suite granitoids and GRV, respectively (Fig. 1B). The Wallaroo Group is a diverse suite of siltstone-dominated metasedimentary, felsic and mafic metavolcanic rock packages, including the Wandearah and Weetulta Formations (Cowley et al., 2003; Conor et al., 2010), which comprise metasedimentary units, including a range of feldspathic, carbonaceous and calc-silicate-bearing members. Iron-rich horizons attributed to Banded Iron

* Corresponding author.
E-mail address: liam.courtney-davies@adelaide.edu.au (L. Courtney-Davies).

https://doi.org/10.1016/j.oregeorev.2020.103337
Received 25 October 2019; Received in revised form 10 January 2020; Accepted 13 January 2020
Available online 17 January 2020
0169-1368/ © 2020 Elsevier B.V. All rights reserved.

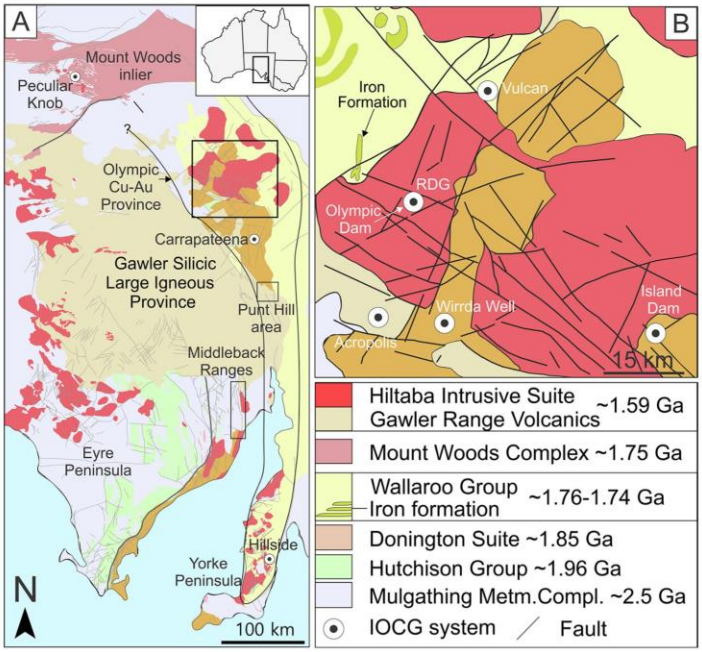


Fig. 1. (A) Geological map of the Eastern Gawler Craton depicting locations of IOCG deposits and prospects within the Olympic Cu-Au Province. (B) Detailed geological map of a 60 × 60 km area containing Olympic Dam and satellite prospects. Iron-rich horizons within the Wallaroo Group occur in the NW of the map.

Formations (BIF) are known within Wallaroo Group metasedimentary rocks from at least several locations, including 15 km NW of the Olympic Dam deposit (Geological Survey of South Australia, 2019, https://map.sarig.sa.gov.au/; Fig. 1B). Impure limestone, dolostone and thin, Fe-rich horizons of BIF affiliation have also been inferred at the Island Dam prospect, 90 km SE of Olympic Dam, where IOCG mineralization is associated with skarn assemblages (Keyser et al., 2017). There are no direct constraints on the genesis of such Fe-rich horizons, however, their stratigraphic position restricts their stratigraphic age to the Wallaroo Group. The Wallaroo Group sequences are traceable from the Mt. Woods Inlier in the north to the Yorke Peninsula in the south, albeit with some difficulties in paleo-reconstruction and stratigraphic correlation from district to district (Cowley et al., 2003).

The lithologies hosting IOCG mineralization either formed prior to, or contemporaneously with, the widespread ~1.59 Ga mineralizing event. Notable host rocks include ~1.85 Ga Donington Suite granites (Carrapateena deposit and Wirrda Well prospect), (meta)sedimentary rocks of the ~1.76–1.74 Wallaroo Group (Island Dam prospect), ~1.75 Ga Wallaroo Group intrusive rocks (Vulcan prospect), ~1.59 Ga GRV (Acropolis prospect), and Hiltaba Suite granites (Olympic Dam deposit) (Fig. 1).

Mineralization across the province also differs in terms of style, ore grade and structural features. For example, vein-style mineralization is dominant in the Acropolis prospect (Krneta et al., 2017; Courtney-Davies et al., 2019a; Dmitrijeva et al., 2019a) whereas the Wirrda Well prospect features structurally-controlled breccia pipe mineralization (Krneta et al., 2017; Courtney-Davies et al., 2019a). Calcic skarns are observed in the Punt Hill area (e.g., in the Groundhog Zn-Cu skarn; Reid et al., 2011), and Cu-Au skarns are present at Hillside, Yorke Peninsula (Conor et al., 2010; Ismail et al., 2014). One example of a hematite breccia-hosted system is the Vulcan Cu-Au prospect, 30 km NE of the Olympic Dam deposit (Fig. 1B). A Re-Os molybdenite age of 1586 ± 8 Ma was obtained by Reid et al. (2013), consistent with other ages for IOCG mineralization across the province. What is noteworthy about the Vulcan prospect, however, is a SHRIMP zircon U-Pb age for the host hematite-sericite-chlorite–altered and brecciated granite (1743 ± 7 Ma), firmly within the 1750–1740 Ma timeframe for a post-Donington, pre-Hiltaba intrusive and extrusive magmatic event in the Gawler Craton (Reid et al., 2013, and references therein). Importantly, volcanic rocks of the same age are known to be intercalated with sediments of the Wallaroo Group (Fanning et al., 1988; 2007; Fraser and Neumann, 2010).

The Olympic Dam deposit (Ehrig et al., 2012, 2017, and references therein) is a giant breccia-hosted hydrothermal ore system hosted by the Roxby Downs Granite, affiliated to the Hiltaba Suite (HS). Although long recognized as having formed during the major ~1590 Ma magmatic event termed the Gawler SLIP, significant progress has been made recently towards establishing a more precise age for both the host rocks and mineralization at Olympic Dam (Cherry et al., 2018a; Courtney-Davies et al., 2019b). The latest geochronological data, combining isotope dilution-thermal ionization mass spectrometry (ID-TIMS) U-Pb ages for hydrothermal U-(Pb)-W-Sn-Mo-bearing zoned hematite and chemical abrasion-ID-TIMS zircon ages from host granite and volcanic rocks within and enclosing the orebody, suggests the granite intrusion hosting the Olympic Dam Breccia Complex was emplaced rapidly at 1593.28 ± 0.28 Ma (Courtney-Davies et al., in revision). The orebody was principally formed during a single, major mineralizing event following granite uplift and during cupola collapse, whereby the earliest hydrothermal activity is recorded in the early, deep 'outer shell' of the deposit (1591.27 ± 0.89 Ma), ~1–2 Ma after crystallization of magmatic zircon. Hematite dates, captured throughout major lithologies, different orezones, and throughout the ~2 km vertical extent of the

deposit, support prolonged hydrothermal activity for ~2 m.y. (Courtney-Davies et al., in revision). Contemporary genetic models consider deep granite crystallization (Kontonikas-Charos et al., 2017), and accumulation of hydrothermal fluids during uplift, brecciation and cupola collapse of the host granite (Verdugo-Ihl et al., 2020).

Obtained using various isotopic systems and methods, a plethora of younger, post-1590 Ma mineral ages have been generated in recent years. These have been largely acquired for Olympic Dam, with some from other IOCG systems across the region, clearly demonstrating that multiple tectonothermal events have impacted on mineralization since initial formation (e.g., Apukhtina et al., 2016; Cherry et al., 2017, 2018; Ciobanu et al., 2013; Davidson et al., 2007; Huang et al., 2015; Maas et al., 2011; McInnes et al., 2008). Incorporation of post-1590 Ma sedimentary material into the deposit has also been reported (McPhie et al., 2016; Cherry et al., 2017b), including quartz-rich sandstones that can be correlated with lithologies from the ~1.4 Ga Cariewerloo Basin. There is, however, no record of older (pre-1590 Ma) ages in rocks from Olympic Dam.

Iron oxides in the outer shell at Olympic Dam are represented by both hematite and magnetite, whereby some magnetite displays a distinctly siliceous character (Ciobanu et al., 2019; Verdugo-Ihl et al., 2020). Although hematite ages obtained also approximate to ~1590 Ma, the mineralogy and geochemistry of some magnetite in two drillholes (RU65-7976 and RD2336; Fig. 1A) is conspicuously different. A preliminary description was given by Ciobanu et al. (2014), noting that this magnetite contained particularly high U, featured textures reminiscent of a sedimentary origin, and coexisted with typical (1590 Ma) hematite. Reconnaissance dating of this magnetite by laser ablation-inductively coupled plasma-mass spectrometry (LA-ICP-MS) provided an unexpectedly old $^{207}Pb/^{206}Pb$ date, predating assumed deposit formation by ~170 Ma (Ciobanu et al., 2014). An imperfect fit between the anomalous (metasomatic) enrichment in Fe and IOCG-element signatures is also reported from principal component analysis of whole-rock datasets from Olympic Dam (Dmitrijeva et al., 2019).

The aim of the present study was to confirm and better constrain the age of this apparently older magnetite within the outer shell at Olympic Dam, and secondly, to discuss the implications which the presence of older, Fe-rich crustal material, potentially affiliated to the Wallaroo Group and contained felsic intrusives, may have for the generation of major iron anomalies represented by large IOCG systems. The fact that the older protolith material is also uraniferous, and thus dateable, carries implications for regional geology and for Proterozoic metallogeny across the region.

2. Samples and methodology

2.1. Samples

Investigated samples are derived from drillhole RU65-7976, which intersects the outer shell of the deposit on its northern margin (location 1; Fig. 2A). This drillhole comprises variably altered granite breccias with more massive intervals of Fe-oxide minerals changing from hematite to magnetite-dominant towards the lower third of the 255 m-thick interval (Fig. 2B). Massive magnetite occurs at a depth of ~869 m (Fig. 2C). Polished blocks were prepared from the drillcore shown in Fig. 2D. The mounted block used for geochronology is illustrated in Fig. 2E.

The samples are from one of the five drillholes from the outer shell at Olympic Dam documented in previous publications (Ciobanu et al., 2019; Verdugo-Ihl et al., 2020). Common to all these drillholes, irrespective of location around the deposit margin, is the presence of hydrothermal magnetite within weakly mineralised (pyrite + chalcopyrite), brecciated granite. An exception is the least altered granite in drillhole RD2494, where only magmatic magnetite is present. Magnetite from locations 1–4 (Fig. 2A) is silician in composition (up to several wt.% SiO_2). At the nanoscale, Si-Fe-nanoprecipitates are ubiquitous (Ciobanu et al., 2019) but the speciation of other mineral inclusions differs along the E transect, i.e., U-, As-, Y-bearing nanoparticles in location 1, and predominant calc-silicate inclusions in locations 2–4 (Fig. 2A).

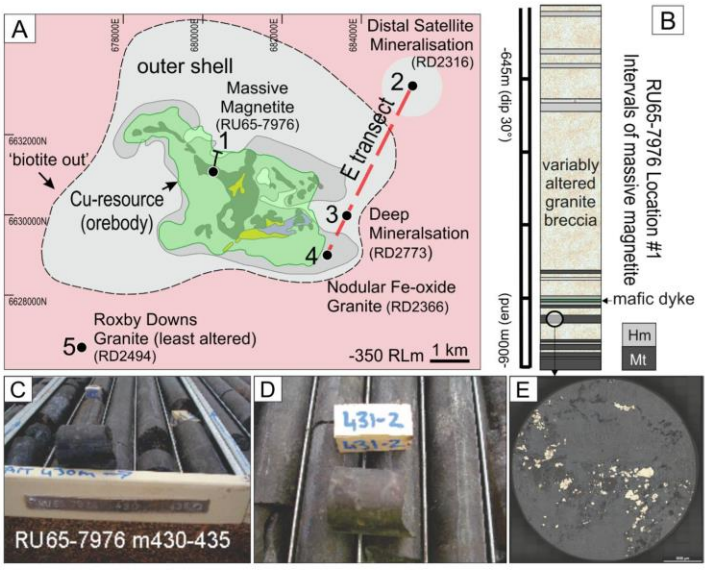


Fig. 2. (A) Geological map of the Olympic Dam deposit, highlighting contacts between the orebody, 'outer shell' and Roxby Downs Granite. Locations 1–5 indicate drillholes discussed in this contribution. Location 1 contains the dated magnetite. (B) Simplified drillhole log for RU65-7976, showing the location of dated magnetite within an interval of massive magnetite. (C-D) photographs of drillcore tray and sampled drillcore. (E) Reflected light micrograph of a one-inch polished block, obtained from the drillcore in (D).

2.2. Analytical methodology

All instrumentation used is housed at Adelaide Microscopy, The University of Adelaide. Magnetite grains studied here were characterised using reflected light optical microscopy and scanning electron microscopy, using a FEI Quanta 450 instrument operated at 20 or 25 kV in back-scattered electron (BSE) mode.

2.2.1. Electron microprobe analysis

Element mapping was obtained using a Cameca SX-Five electron probe microanalyzer (EPMA), running PeakSite Version 6.2 software for microscope operation, and 'Probe for EPMA' software (Donovan et al., 2016). X-ray maps were acquired using a focussed electron beam (20 kV and 100nA), with dwell times of 100 ms. Mapped x-ray lines were Fe-Kα, Si-Kα and U-Mα, which were peaked prior to acquisition using appropriate standards.

2.2.2. Fe-oxide U-Pb geochronology

A magnetite reference material for U-Pb geochronology is currently unavailable. We therefore undertook calibration with materials of known composition – in this case both widely reported zircon reference materials and 'mixed U-Pb solution standards' (approach given by Courtney-Davies et al., 2016). Geochronology was performed during two analytical sessions using grains from the same polished block (after careful repolishing of the sample to remove laser ablation pits), to compare consistency between two datasets obtained in separate sessions using the two different methods. Isotope measurements were determined using an Applied Spectra 193 ArF M − 50 Excimer laser ablation system coupled to an Agilent 7700 s ICP-MS. Analysis parameters for unknowns included a constant repetition rate of 5 Hz, laser fluence of 4 J/cm^{-2} and a beam diameter set at 60 μm (spot analyses). Individual dwell times for measured isotopes were; ^{204}Pb, 10 ms; ^{206}Pb, 50 ms; ^{207}Pb, 40 ms; ^{208}Pb, 30 ms and ^{238}U, 30 ms.

During the first LA-ICP-MS session, GJ-1 zircon (Jackson et al., 2004) was implemented as the primary reference material, with Plešovice (Sláma et al., 2008) and Temora (Black et al., 2003) zircon reference materials used as secondary standards. Downhole U/Pb fractionation profiles between Fe-oxide minerals and zircon have previously been shown to match closely (Ciobanu et al., 2013; Courtney-Davies et al., 2019b). The 'mixed U-Pb solution standard' technique follows the methodology described in Courtney-Davies et al. (2016) for hematite dating, which provides results within analytical precision of data calibrated using zircon reference materials, and bulk methods such as ID-TIMS when applied to the same sample sets (Courtney-Davies et al., 2019b). The solid, pure hematite employed by Courtney-Davies et al. (2016), was replaced in this study with a pure, homogeneous, synthetic magnetite sample mounted in a 1-inch polished block (Fig. 1 Appendix). The calibration solution was made via mixing individual U and Pb single element standard solutions in 2% HNO_3 diluted with Milli-Q water. Ablated magnetite aerosol was fed and mixed with the aspirated and nebulized U–Pb solution in the spray chamber, representing a typical measurement of the 'standard'.

Data were collected using time-resolved acquisition in fast peak-jumping mode and calculations were carried out using the data reduction software 'Glitter' (Van Achterbergh et al., 2001). Isotope ratios are presented uncorrected for common lead, with concordia and weighted average plots generated using the Excel add-on Isoplot 3.75 (Ludwig, 2012). Instrument optimization and calibration was

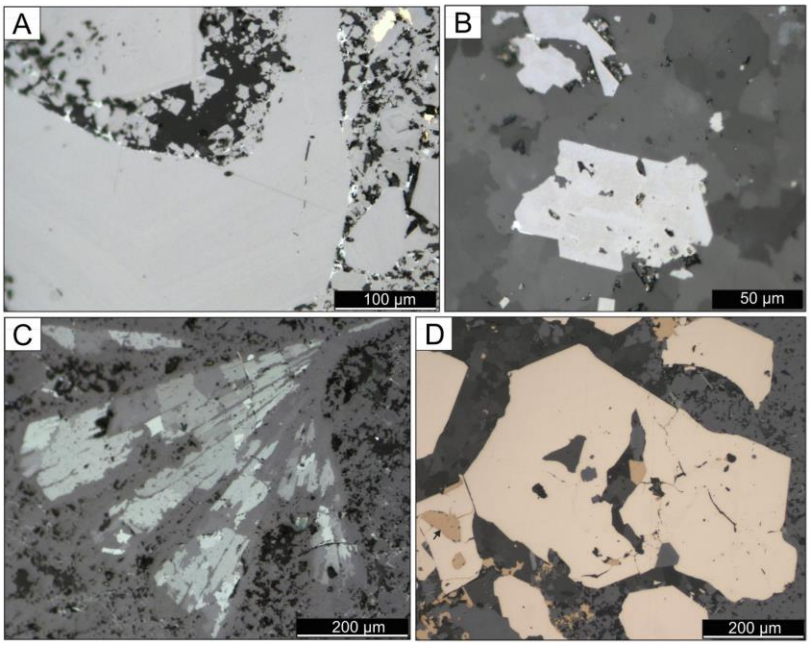


Fig. 3. Optical photomicrographs of Fe-oxide and sulfide minerals within the one-inch polished block displayed in Fig. 2E. (A) Typical coarse-grained, faintly zoned and clean magnetite which was dated, and (B) fine-grained, inclusion rich magnetite in carbonate gangue. (C) Dated, fan like hematite lath aggregates replacing magnetite and (D) weakly-zoned and brecciated pyrite containing darker chalcopyrite within a matrix of fine-grained magnetite and carbonates.

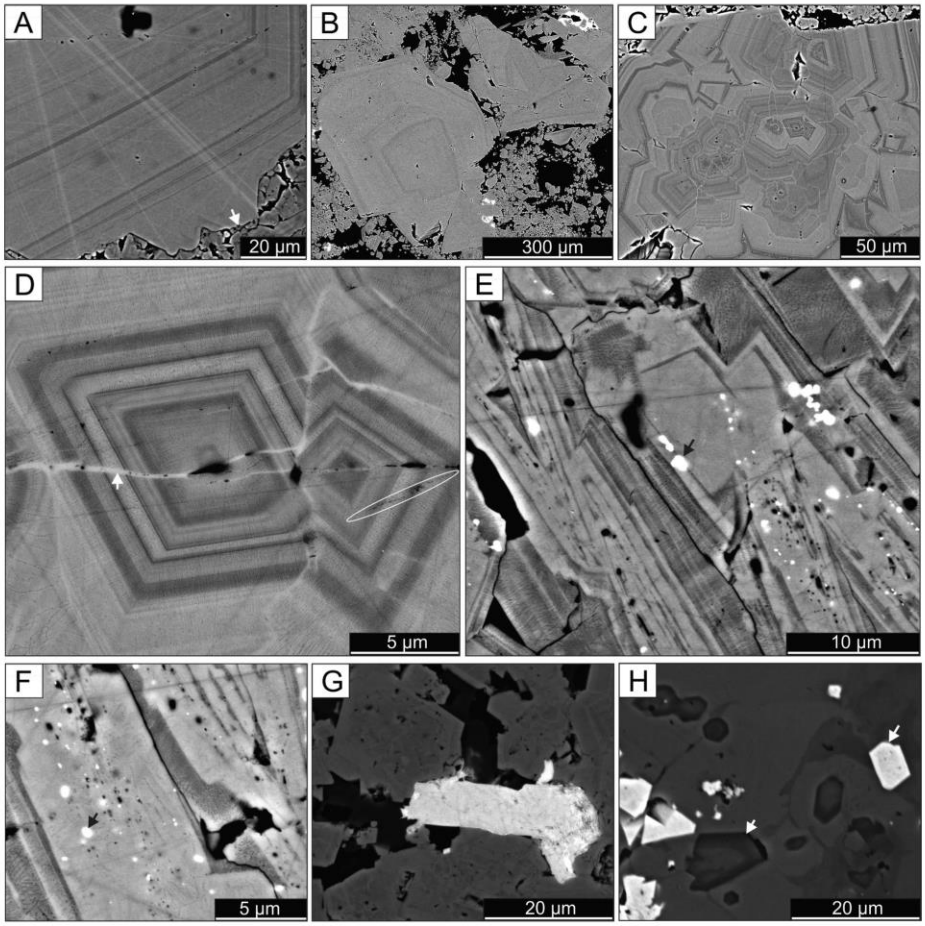


Fig. 4. Selection of BSE images comprising (A, B) dated, coarse, faintly-zoned single-grains of U-bearing magnetite, displaying corrosional interfaces (arrowed) with finer-grained, porous magnetite. (C) Aggregates of magnetite, strongly zoned and mottled with respect to sub-micron-scale inclusions. (D) In detail, this magnetite grain contains dark, inclusion-rich trails (circled) and lighter fractures that crosscut zonation patterns (arrowed). (E, F) Interconversions between hematite (darker) and magnetite (lighter), containing micron- to sub-micron scale inclusions of U-minerals (arrowed), forming either along intergrowth margins, or as fields across grain lamellae. (G) Molybdenite (bright) intergrown with the fine-grained magnetite matrix. (H) Finest, 'dirty' grains of bright magnetite (arrowed) and dark apatite (arrowed) within carbonate gangue dominated by siderite.

performed using the NIST-610 reference glass. Uranium-lead sample and reference material data is presented in Table 1A at the 1 sigma level.

2.2.3. Fe-oxide trace element analysis

Data were acquired using the same LA-ICP-MS instrument described above. Spot analysis comprised measurement of background (30 s) followed by acquisition of signal during ablation (30 s). Assuming ideal stoichiometries for hematite and magnetite, iron measured as ^{57}Fe was used as the internal standard element. GSD-1G or BHVO-2G and NIST-610 were utilized as external reference materials and used for instrument drift correction and trace element quantification. Off-line data reduction was performed in 'Glitter'. Reported Pb contents correspond to total Pb concentrations calculated from the individual abundances of ^{206}Pb, ^{207}Pb and ^{208}Pb.

3. Results

3.1. Petrography and geochemistry

The studied samples comprise massive magnetite (~80%) within a gangue consisting of carbonates + quartz (Fig. 2E) and minor pyrite, present as disseminations throughout the magnetite. Two types of magnetite are present: (i) clean, subhedral, coarser single grains (several hundred μm in diameter), with faint crystal zonation (Fig. 3A); and (ii) 'dirty', small (a few to some tens of microns) grains or aggregates characterised by zoning with respect to the distribution of sub- μm-scale inclusions (Fig. 3B). The latter type of magnetite is dominant and is intergrown with zoned carbonates in the matrix. Volumetrically minor, fan-like aggregates of hematite replacing magnetite are also present (Fig. 3C). Pyrite with a faint compositional/growth zoning is brecciated

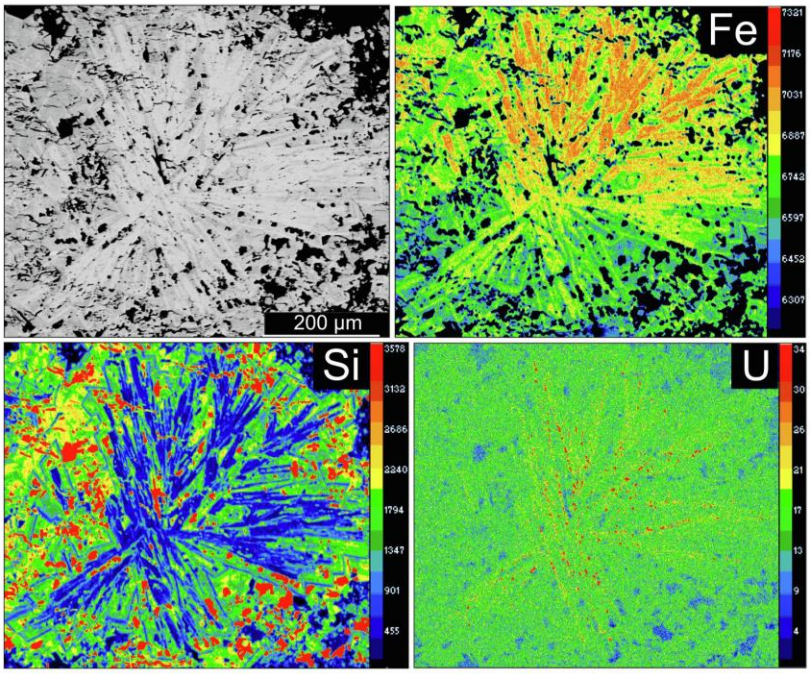


Fig. 5. BSE image of magnetite-hematite interconversions and corresponding EPMA element maps. Note the nucleation of micron-scale U-bearing inclusions towards the centre of the aggregates and along lamellae.

and infilled by chalcopyrite and gangue minerals (Fig. 3D).

Coarse, clean grains of magnetite show scalloped boundaries against the finer grains (Fig. 4A, B). Zonation patterns within single grains are expressed as alternating µm-scale Si-rich bands and Si-poor bands (the former appear darker on BSE images). There are also coarser aggregates displaying Si-rich cores marked by nucleation of euhedral, mottled grains (Fig. 4C, D). These are similar to the finer-grained magnetite matrix in that they display oscillatory zoning and crosscutting trails that run perpendicular to the zoning, both consisting of Si-Fe-nanoprecipitates (see Ciobanu et al., 2019). Lastly, fractures of brighter contrast on BSE images crosscut grains in random orientations (Fig. 4D). Further textural complexity is observed in aggregates of hematite and magnetite displaying micron-scale interconversion (Fig. 4E, F). In this case, fine particles of U-minerals occur along the margins of such intergrowths (Fig. 4E), or form fields of micron- to sub-micron inclusions within lamellae that are also marked by porosity (Fig. 4F). Minor molybdenite is present within the fine-grained magnetite (Fig. 4G). Apatite grains occur throughout siderite-dominant carbonate gangue (Fig. 4H). Smallest 'dirty' magnetite is present throughout the same area. A variety of other minerals, including U- and REE-bearing species, are observed in areas of magnetite displaying porosity and micro-fractures. Importantly, no zircon was observed.

EPMA maps of the aggregates displaying magnetite-hematite interconversion show the presence of µm-scale U-bearing mineral inclusions along the laths, particularly in the centres of the aggregate (Fig. 5). The laths are, however, free of Si-bearing inclusions.

Trace element data for magnetite and hematite obtained by LA-ICP-MS spot analysis are provided in Table A1 (Appendix). Compositional differences between the two types of magnetite and hematite are seen on Fig. 6A. The boxplot shows that coarse magnetite has a narrower range of U and Pb concentration if compared with the fine-grained type. Hematite, however, displays higher U-concentrations relative to the two types of magnetite. All Fe-oxides show geochemical signatures containing W, Sn and Mo. Coarser magnetite is enriched in ΣREY relative to fine-grained magnetite and hematite, although hematite is comparatively enriched in HFSE (Nb, V, Th). The Fe-oxides are comparable in terms of transition metal concentrations, with relatively high Mn and low Cr observed in all categories. Among the lithophile elements, Si-enrichment is highest in magnetite relative to hematite.

Chondrite-normalised REY fractionation trends show concave patterns for the coarse magnetite with flatter HREE segments for the finer-grained type (Fig. 6B, C). Both types of magnetite display pronounced negative Eu anomalies. Hematite shows comparable trends to the fine-grained magnetite, but with a much less pronounced Eu anomaly (Fig. 6D).

Time-resolved LA-ICP-MS downhole profiles obtained from the coarse-grained, clean (dated) magnetite (Fig. 7A) show flat signals for measured isotopes, including U and Pb (Fig. 7A). In contrast, the fine-grained, dirty magnetite shows signal irregularities indicative of sub-surface mineral inclusions (Fig. 7B).

3.2. Iron-oxide U-Pb geochronology

The first U-Pb dataset was obtained using zircon reference materials to calibrate unknowns (Table A2 Appendix. A selection of analysed grains is presented in Fig. 8A, B. All data (n = 34) forms intercepts at 172 ± 180 Ma and 1769 ± 58 Ma (MSWD = 1; Fig. 8C). Data are discordant (92 – 62%) and yields a younger $^{207}Pb/^{206}Pb$ weighted average (1727 ± 16 Ma, n = 34, MSWD = 2.5). The high MSWD does however indicate excess scatter; removal of the 6 youngest analyses

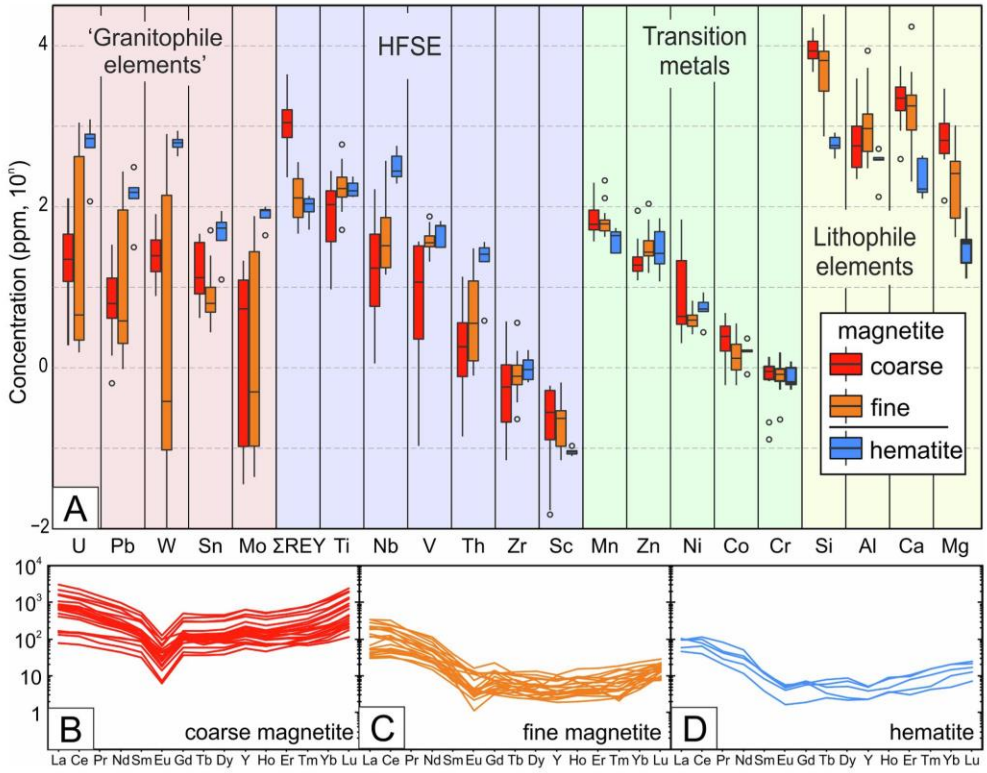


Fig. 6. (A) Box plots of LA-ICP-MS trace element data for coarse- and fine-grained magnetite and hematite, displaying ranges of trace element concentration for different elements groups. Importantly, coarse-grained magnetite has a narrower range of U and Pb concentration when compared to the fine-grained type and the highest REY concentrations. All Fe-oxides contain a marked granitophile signature. (B-D) LA-ICP-MS chondrite-normalised REY fractionation trends for coarse magnetite (B), fine-grained magnetite (C) and hematite (D).

(possibly affected by Pb-loss), yields a date with an acceptable MSWD (1749 ± 11 Ma, n = 27, MSWD = 1.09; Fig. 8D), within uncertainty of the intercept date.

Uranium-lead data acquired by the 'mixed U-Pb solution standard dating' technique comprises 44 spot analyses across 6 grains, with 25 spots selected on the largest grain (500 × 300 µm; Fig. 9A–C; Table A2 Appendix). Of the 44 analyses, 41 form an intercept line defining lower and upper intercepts of −79 ± 330 Ma and 1766 ± 24 Ma, respectively (MSWD = 0.13; Fig. 9D). Three analyses plot far off the intercept and are likely contaminated by common Pb (excluded grey error ellipses; Fig. 9D). Data points range from slightly discordant to reversely discordant. All datapoints forming the intercept line yields a $^{207}Pb/^{206}Pb$ weighted average of 1761 ± 19 Ma (n = 41, MSWD = 0.109), in good agreement with the intercept date, and data acquired using zircon reference materials. There is no statistical difference in $^{207}Pb/^{206}Pb$ between individual grains.

Fine-grained magnetite containing silica-rich inclusions was dated using the 'mixed U-Pb solution standard dating' method (Fig. 10A). Datapoints are largely reversely discordant (n = 13), due to high common Pb components (low $^{206}Pb/^{204}Pb$; Table A2 Appendix), from which a meaningful intercept cannot be obtained.

Uranium-bearing hematite was analysed using only the 'mixed U-Pb solution standard' method (Fig. 10B). Datapoints are reversely discordant, (n = 18), and no reasonable intercept date can be derived, likely due to matrix effects pushing data 'up' the Wetherill diagram. A $^{207}Pb/^{206}Pb$ weighted average of 1562 ± 37 Ma can be formed from all the datapoints, however, there is large scatter in the data (MSWD = 12), and little ground for data rejection to attain an acceptable MSWD value.

4. Discussion

4.1. Generations of iron oxides

The heterogeneous magnetite textures observed within the same sample (Fig. 4) are attributable to variable degrees of interaction with later fluids during a protracted geological history, thus producing at least two distinct generations of magnetite. The coarser grains are least affected and typically retain primary U-Pb systematics. In contrast, the finer-grained magnetite is rich in common Pb, indicating an overprinting event during which abundant U-bearing nanoparticles formed along trails crosscutting the primary zonation patterns (Ciobanu et al., 2019). Obliteration of primary signatures in the finer-grained magnetite is due to fluid percolation along grain boundaries preferentially affecting the fine-grained matrix relatively to coarse grains. Further reworking of the Fe-oxides displaying interconversion leads to nucleation

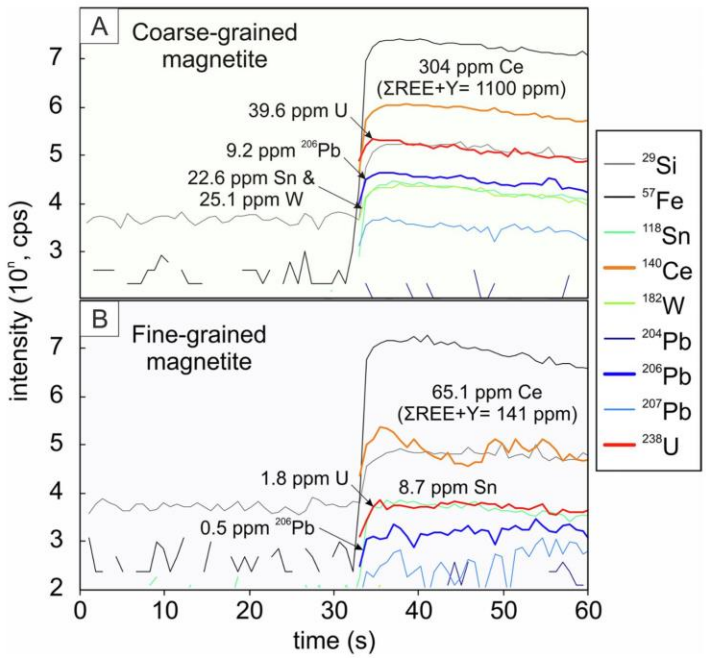


Fig. 7. Time-resolved, downhole LA-ICP-MS profiles obtained for (A) the coarse-grained, dated magnetite, displaying flat signals for U and Pb isotopes and (B) the fine-grained magnetite, showing heterogeneous isotope signals at lower concentrations, particularly for Ce, indicating the presence of REE bearing inclusions.

of micron-scale U-mineral inclusions (Fig. 4E, F; 5). Growth of other minor and accessory minerals, e.g., molybdenite, apatite and monazite), either at grain boundaries or within fractures in brecciated domains, can be ascribed to an event that introduced S-bearing fluids from which pyrite and chalcopyrite were precipitated (Figs. 3D, 4F–H).

The wider ranges of trace element concentrations in the finer-grained magnetite, relative to the low, generally consistent ranges of the same elements in the coarser magnetite (Fig. 6A) are concordant with the heterogeneous magnetite overprint. Geochemically, the magnetite signatures are comparable with those recorded in magnetite from drillhole RD2336 in the SE lobe of the deposit, particularly with respect to U and REE (location 4; Fig. 2A; see Verdugo-Ihl et al., 2020). The latter is however affected by fault reactivation (Verdugo-Ihl et al., 2020), which induced a strong overprint on the U-Pb systematics, thus precluding reliable U-Pb dating. The studied magnetite, although comparable with the silician magnetite at Wirrda Well, has much higher concentrations of both U and REE (Courtney-Davies et al., 2019a), implying that Donington granitoid cannot be the source for these elements. The youngest generation of Fe-oxides is represented by the hematite, which displays elevated HFSE and a characteristic U + W + Sn + Mo (granitophile) signature. Such a trace element signature is directly comparable with the early hematite from the outer shell at Olympic Dam described by Verdugo-Ihl et al. (2020).

Previous dating studies based on the U-Pb system in magnetite have employed bulk, stepwise leaching techniques, to produce imprecise U/Pb and Pb/Pb isochrons (e.g. Erel et al., 1997; Frei et al., 1999). Here, we date magnetite directly via U-Pb LA-ICP-MS spot analysis, due to the requirement of high-spatial resolution *in-situ,* using two independent calibration strategies. Hematite has previously been demonstrated as a reliable mineral geochronometer in hydrothermal environments, due to high concentrations of lattice-bound U (Ciobanu et al., 2013; Verdugo-Ihl et al., 2017) and demonstrated retention of radiogenic Pb (Courtney-Davies et al., 2019b). The LA-ICP-MS U-Pb magnetite data calibrated using zircon reference materials displays purely discordant data, indicating geological Pb-loss (Fig. 8C). In contrast, data calibrated using the 'mixed U-Pb solution standard' displays a spread in datapoints intersecting concordia trending towards reverse discordance (Fig. 9D). This implies that the apparent Pb-loss is analytical rather than geological, as demonstrated by the effects of different fluences applied when collecting LA-ICP-MS hematite data, and the inferred, but negligible differences in downhole fractionation between unknowns and reference materials (Courtney-Davies et al., 2019b). Nevertheless, $^{207}Pb/^{206}Pb$ is not affected by downhole fractionation, and the weighted means provided by the two calibration methods agree well with one another. The magnetite age, ~1750–1740 Ma, is in the range of granite intrusions as previously dated from Vulcan prospect (Reid et al., 2013). Such an age is also within the timeframe of ~1.76–1.74 Ga Wallaroo Group sedimentation (Cowley et al., 2003).

4.2. Timing of U-rich iron-oxide protoliths and their incorporation in the Olympic Dam deposit

Since the presented ~1760 Ma iron-oxide ages lie firmly within the range of Wallaroo Group deposition, we assume that the dated magnetite originated within that stratigraphic unit. Based upon massive magnetite textures, the dominance of carbonate + quartz gangue, and lack of detrital zircon, we can consider the protolith containing the dated magnetite to be an iron formation of possible BIF-derived origin. Uranium contents in the dated, coarse magnetite are comparable with the concentrations reported from hematite within ores derived from BIFs that have been affected by interaction with hydrothermal fluids associated with granites or surficial waters in the Middleback Ranges

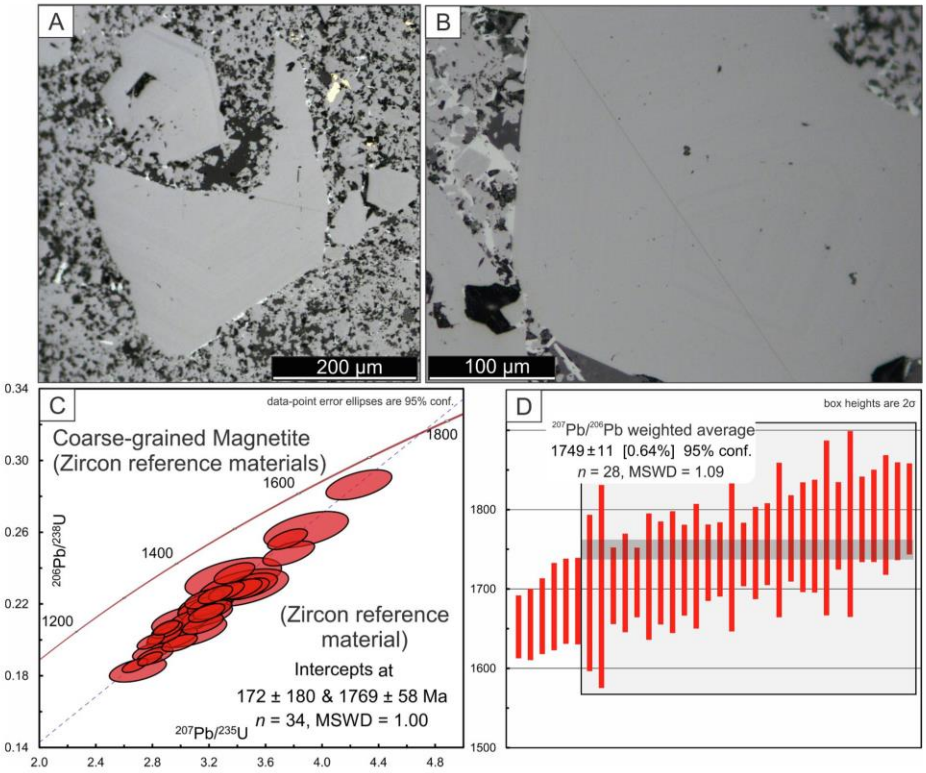


Fig. 8. (A-B) Optical photomicrographs in reflected light showing coarse-grained magnetite, prior to U-Pb dating. (C) LA-ICP-MS conventional Wetherill concordia diagram, containing magnetite U-Pb data, calibrated using zircon reference materials. (D) $^{207}Pb/^{206}Pb$ weighted average diagram for 28 of the datapoints shown in the Wetherill diagram.

southwest of the Olympic Cu-Au Province (Fig. 1A; Keyser et al., 2019a, 2019b, 2020).

The data presented above can be interpreted within a geological model shown schematically in Fig. 11. Considering the Wallaroo Group age, the massive magnetite intervals likely originate from Fe-rich sediments deposited in a basin active prior to 1760 ± 20 Ma (Fig. 11A). Magnetite is likely formed via diagenesis, at a depth of ~1–2 km upon burial (Fig. 11B). At this stage, formation of Si-Fe-nanoprecipitates can occur, as described from weakly metamorphosed BIF deposits from the Hamersley Group, Western Australia (Huberty et al., 2012; Xu et al., 2014). The relative enrichment in U and REE can be attributed to interaction with post-magmatic fluids derived from a ~1760–1740 Ma granitoid (Fig. 11C) belonging to the same magmatic affiliation as that dated from the Vulcan prospect (1743 ± 7 Ma; Reid et al., 2013). This granite, however, cannot be emplaced proximal to the magnetite-rich horizons as associated thermal gradients would have produced abundant calc-silicate inclusions, which are not observed (Ciobanu et al., 2019). Instead, granite-derived fluids migrated upwards, becoming focused along graben faults (Fig. 11C).

Some ~150 Ma later, emplacement of the Gawler SLIP introduced granites which were fertile sources of hydrothermal fluids (Courtney-Davies et al., 2019c), generating IOCG mineralization that could be hosted within the causative Hiltaba-aged granite. Interpreted to have been emplaced at depths of 6–8 km (Kontonikas-Charos et al., 2017), the Roxby Downs Granite which hosts the Olympic Dam deposit, came into contact with blocks of (meta)sedimentary rocks of the Wallaroo Group which were faulted into the RDG during uplift at 1593 Ma along faults (Fig. 11D).

Collapse of the granite cupola along faults released the main phase of hydrothermal fluids, forming the Olympic Dam orebody (Verdugo-Ihl et al., 2020). Protoliths derived from sequences intruded by granite could have readily been entrapped as blocks during uplift, thus potentially explaining the presence of massive, old (~1760 Ma) magnetite in the outer shell (at the boundary with the orebody; Fig. 11E). Reworking of fine-grained magnetite (crosscutting trails with numerous U-bearing nanoparticles; Ciobanu et al., 2019) and interconversion with younger, ~1.59 Ga hematite, are attributable to interaction with the late RDG-derived fluids.

5. Implications and conclusions

The proposed model readily explains the presence of older, Fe-rich, U-bearing protoliths in the outer shell at Olympic Dam. Furthermore, this opens the possibility of additional pre-Hiltaba Suite sources of both Fe and U within the deposit, and, potentially at least, regionally across the eastern Gawler Craton, representing a partial resolution of the long-standing question of the source of these metals. Interaction between hydrothermal fluids originating from Hiltaba Suite granitoid magmas and older iron formations, whether of BIF or detrital origin, was raised for Fe deposits in the Mt. Woods Inlier (e.g., Peculiar Knob; Keyser

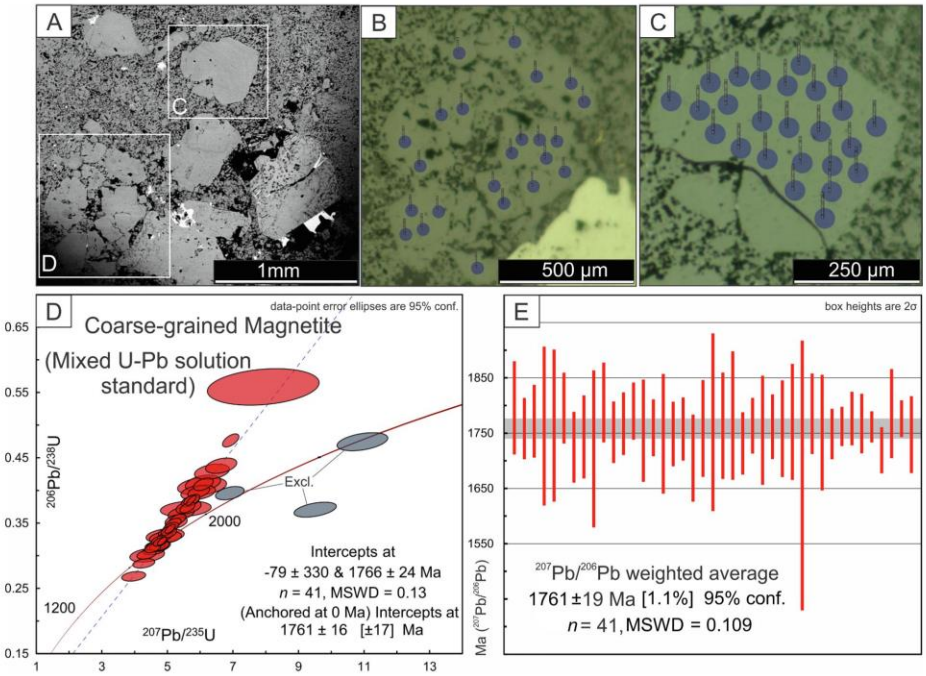


Fig. 9. (A) BSE image of a polished block region containing dated magnetite grains using 'mixed U-Pb solution standard' calibration. (B, C) Optical photographs of dated grains and location of LA-ICP-MS spot analyses. (D) Conventional Wetherill concordia diagram for magnetite U-Pb data. Grey error ellipses represent rejected datapoints. (E) Corresponding $^{207}Pb/^{206}Pb$ weighted average diagram for all data points included in the Wetherill diagram.

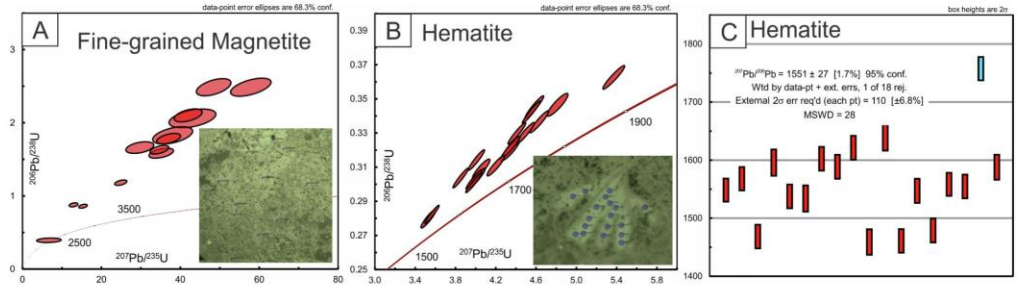


Fig. 10. Other Fe-oxide U-Pb data, calibrated using the 'mixed U-Pb solution standard' method. (A) Conventional Wetherill concordia diagram for fine-grained magnetite, displaying highly-reversely discordant data, and optical image (top left) of dated grains. (B) Conventional Wetherill concordia diagram showing data for hematite lathes and an optical image of dated grains (top left). (C) $^{207}Pb/^{206}Pb$ weighted average diagram for all data from the hematite laths.

et al., 2019c). Geochemical signatures coincident with IOCG mineralization are also identified in the alteration style displayed by some basement granites adjacent to BIF-derived deposits in the Middleback Ranges, Eyre Peninsula (Keyser et al., 2019b). Researchers have mused over possible connections between the two styles of mineralization in South Australia, but direct evidence for a genetic relationship has been sparse until now, although such relationships have been proposed (e.g., Keyser et al., 2017). Additional evidence should be sought to further substantiate the concept but it is tempting to suggest the presence of U-bearing Fe-rich protoliths into crust into which Hiltaba-aged granites have intruded as an illustrative example of "étagement temporal" (Routhier, 1967). If true, the presence of such protoliths is more than a combination of fortuitous geological circumstances but an essential contributing component to IOCG metallogeny in the region.

From a global perspective, superposition of BIF- and IOCG-type mineralization is also recognized in other Proterozoic terranes, notably in the Carajás district of Brazil (e.g., Grainger et al., 2008). Other analogous terranes, such as the Bergslagen and Kiruna districts (Fennoscandian Shield, Sweden) display co-existence of BIF-, IOCG- and kin IOA-type mineralization (Jonsson et al., 2013; Troll et al., 2019).

As discussed here, the coincidence between iron formations and ~1750 Ma granitoids provides additional sources of Fe and U predating

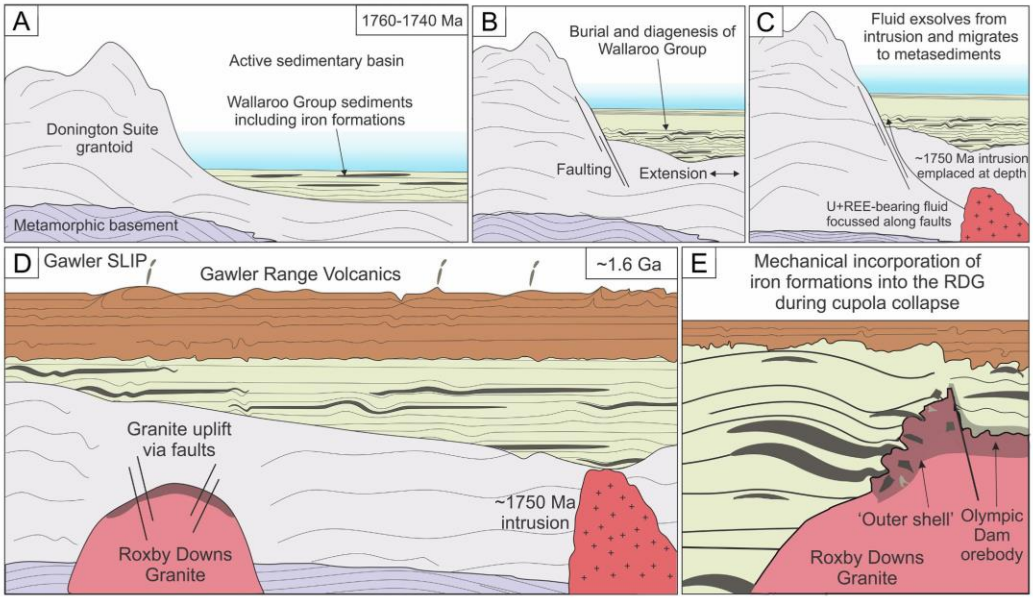


Fig. 11. Geological model for the formation, U-enrichment and incorporation of iron formations into the 'outer shell' at Olympic Dam. (A) Wallaroo Group sediments, including iron formations were deposited in an active sedimentary basin between ~1760 and ~1740 Ma, undergoing burial and diagenesis, forming coarse grains of magnetite (B). (C) At ~1750 Ma, granitic magmas were emplaced at depth across the region. Hydrothermal fluids escaping from such granitoids migrated to, and heterogeneously interacted with coarse grained magnetite within buried Wallaroo Group (meta)sediments. (D) During the ~1.6 Ga Gawler SLIP event, Hiltaba Suite granites intruded country rock. The RDG was emplaced at a depth of 6–8 km, accumulating hydrothermal fluids within an 'outer shell'. (E) The granite was uplifted via faults, facilitating mechanical incorporation of pre-existing Fe-rich horizons during granite cupola collapse.

~1.6 Ga, and thus could be a contributing factor in the formation of U-rich IOCG mineralization in the Olympic Cu-Au Province. For example, this may explain why some IOCG systems within a 60 × 60 km area (Fig. 1B) containing fertile Hiltaba Suite granitoids are relatively U-poor (Wirrda Well, Acropolis), whereas others contain greater U contents (Vulcan, Island Dam, and in particular, Olympic Dam). Therefore, proximity to Fe-rich source rocks, such as the Wallaroo Group, may be a positive indicator for IOCG system exploration.

To the best of our knowledge, the conventional (non-isochron) U-Pb geochronological data reported here is the first presented for magnetite LA-ICP-MS. Together with advances in constraining the advantages and limitations of hematite geochronology (Courtney-Davies et al., 2019b), the use of magnetite to obtain geologically meaningful ages represents a further step towards establishing iron-oxide geochronology as a valuable tool in ore deposit studies. Evaluation of data accuracy remains challenging in the absence of matrix-matched reference material or independent bulk chemical analysis. Nevertheless, confidence can be taken from this novel mineral geochronometer, considering the likely derivation of the dated magnetite from ~1.76–1.74 Ga Wallaroo Group (meta)sediments and the ~1.76–1.75 dates obtained when calibrating unknowns with both zircon reference materials and mixed U-Pb solution standards, during separate analytical sessions. The homogeneous downhole distributions of both U and radiogenic Pb reinforce the potential reliability of magnetite as a mineral geochronometer.

Declaration of Competing Interest

The authors declare that they have no known competing financial interests or personal relationships that could have appeared to influence the work reported in this paper.

Acknowledgements

This is a contribution to the 'FOX' project (Trace elements in iron oxides: deportment, distribution and application in ore genesis, geochronology, exploration and mineral processing), supported by BHP Olympic Dam and the South Australian Government Mining and Petroleum Services Centre of Excellence. N.J.C. acknowledges additional support from the ARC Research Hub for Australian Copper-Uranium (Grant IH130200033). We acknowledge the valuable comments of two anonymous reviewers, and *Ore Geology Reviews* Editor-in-Chief Franco Pirajno for his attentive editorial handling.

Appendix A. Supplementary data

Supplementary data to this article can be found online at https://doi.org/10.1016/j.oregeorev.2020.103337.

References

Allen, S., McPhie, J., Ferris, G., Simpson, C., 2008. Evolution and architecture of a large felsic igneous province in western Laurentia: the 1.6 Ga Gawler Range Volcanics, South Australia. J. Volcanol. Geoth. Res. 172, 132–147.

Apukhtina, O.B., Kamenetsky, V.S., Ehrig, K., Kamenetsky, M.B., McPhie, J., Maas, R., Meffre, S., Goemann, K., Rodemann, T., Cook, N.J., Ciobanu, C.L., 2016. Postmagmatic magnetite–apatite assemblage in mafic intrusions: a case study of dolerite at Olympic Dam, South Australia. Contrib. Miner. Petrol. 171 (2). https://doi.org/10.1007/s00410-015-1215-7.

Black, L.P., Kamo, S.L., Allen, C.M., Aleinikoff, J.N., Davis, D.W., Krosch, R.J., Foundoulis, C., 2003. TEMORA 1: a new zircon standard for Phanerozoic U-Pb geochronology. Chem. Geol. 200, 155–170.

Blissett, A.H., Creaser, R.A., Daly, S.J, Flint, D.J., Parker, A.J., 1993. Gawler Range Volcanics. In: Drexel, J.F., Preiss, W.V., Parker, A.J. (eds.), The Geology of South Australia. Volume 1, The Precambrian: Adelaide, Geological Survey of South Australia, Bulletin 54, 107–131.

Cherry, A.R., McPhie, J., Kamenetsky, V.S., Ehrig, K., Keeling, J.L., Kamenetsky, M.B., Meffre, S., Apukhtina, O.B., 2017a. Linking Olympic Dam and the Cariewerloo Basin: was a sedimentary basin involved in formation of the world's largest uranium deposit? Precambr. Res. 300, 168–180.
Cherry, A.R., Kamenetsky, V.S., McPhie, J., Kamenetsky, M., Ehrig, K., Keeling, J.L., 2017b. Post-1590 Ma modification of the supergiant Olympic Dam deposit: links with regional tectonothermal events. Proceedings, 14th SGA Biennial Meeting 'Mineral Resources to Discover', Québec City, QC, Canada, 20–23 August 2017, p. 847-850.
Cherry, A.R., Ehrig, K., Kamenetsky, V.S., Ehrig, K., McPhie, J., Crowley, J.L., Kamenetsky, M.B., 2018a. Precise geochronological constraints on the origin, setting and incorporation of ca. 1.59 Ga surficial facies into the Olympic Dam Breccia Complex, South Australia. Precambrian Res. 315, 162–178.
Cherry, A.R., Kamenetsky, V.S., McPhie, J., Thompson, J.M., Ehrig, K., Meffre, S., Kamenetsky, M.B., Krneta, S., 2018b. Tectonothermal events in the Olympic IOCG Province constrained by apatite and REE-phosphate geochronology. Aust. J. Earth Sci. 65, 643–659.
Ciobanu, C.L., Wade, B.P., Cook, N.J., Schmidt Mumm, A., Giles, D., 2013. Uranium-bearing hematite from the Olympic Dam Cu-U-Au deposit, South Australia: a geochemical tracer and reconnaissance Pb-Pb geochronometer. Precambr. Res. 238, 129–147.
Ciobanu, C.L., Cook, N.J., Wade, B.P., Ehrig, K., 2014. Ore Minerals Down to Nanoscale: Petrogenetic Implications. Acta Geologica Sinica (English Edition) 88, 1441–1443.
Ciobanu, C.L., Verdugo-Ihl, M.R., Slattery, A., Cook, N.J., Ehrig, K., Courtney-Davies, L., Wade, B.P., 2019. Silician Magnetite: Si–Fe-Nanoprecipitates and Other Mineral Inclusions in Magnetite from the Olympic Dam Deposit, South Australia. Minerals 9 (5), 311. https://doi.org/10.3390/min9050311.
Conor, C., Raymond, O., Baker, T., Teale, G., Say, P., Lowe, G., 2010. Alteration and Mineralisation in the Moonta-Wallaroo Cu-Au Mining Field Region, Olympic Domain, South Australia. In: Porter, T.M. (Ed.), Hydrothermal Iron Oxide Copper-Gold and Related Deposits: A Global Perspective 3. PGC Publishing, Adelaide, pp. 1–24.
Courtney-Davies, L., Zhu, Z., Ciobanu, C.L., Wade, B.P., Cook, N.J., Ehrig, K., Cabral, A.R., Kennedy, A., 2016. Matrix-matched iron-oxide laser ablation ICP-MS U-Pb geochronology using mixed solution standards. Minerals 6 (3), 85. https://doi.org/10.3390/min603008.
Courtney-Davies, L., Ciobanu, C.L., Verdugo-Ihl, M.R., Dmitrijeva, M., Cook, N.J., Ehrig, K., Wade, B.P., 2019a. Hematite geochemistry and geochronology resolve genetic and temporal links among iron-oxide copper gold systems, Olympic Dam district, South Australia. Precambrian Res. 335, 105480.
Courtney-Davies, L., Tapster, S.R., Ciobanu, C.L., Cook, N.J., Verdugo-Ihl, M.R., Ehrig, K.J., Kennedy, A.K., Gilbert, S.E., Condon, D.J., Wade, B.P., 2019b. A multi-technique evaluation of hydrothermal hematite U-Pb isotope systematics: Implications for ore deposit geochronology. Chem. Geol. 513, 54–72.
Courtney-Davies, L., Ciobanu, C.L., Verdudo-Ihl, M.R., Slattery, A., Cook, N.J., Dmitrijeva, M., Keyser, W., Wade, B.P., Domnick, U.I., Ehrig, K., Xu, J., Kontonikas-Charos, A., 2019c. Zircon at the nanoscale records metasomatic processes leading to large magmatic-hydrothermal ore systems. Minerals 9, 364. https://doi.org/10.3390/min9060364.
Courtney-Davies, L., Ciobanu, C.L., Tapster, S.R., Cook, N.J., Ehrig, K., Crowley, J.L., Verdugo-Ihl, M.R., Condon, D.J., in revision. Opening the Magmatic-Hydrothermal Window: High-Resolution Geochronology of the Olympic Dam Iron Oxide-Cu-U-Au-Ag Deposit, South Australia. Econ. Geol.
Cowley, W., Conor, C., Zang, W., 2003. New and revised Proterozoic stratigraphic units on northern Yorke Peninsula. MESA J. 29, 46–58.
Davidson, G.J., Paterson, H.L., Meffre, S., Berry, R.F., 2007. Characteristics and origin of the Oak Dam East breccia-hosted, iron oxide Cu-U-(Au) deposit: Olympic Dam region, Gawler Craton, South Australia. Econ. Geol. 102, 1471–1498.
Dmitrijeva, M., Ciobanu, C.L., Ehrig, K.J., Cook, N.J., Metcalfe, A., Verdugo-Ihl, M.R., McPhie, J., 2019a. Mineralization-alteration footprints in the Olympic Dam IOCG district, South Australia: The Acropolis prospect. J. Geochem. Explor. 205, 106333.
Dmitrijeva, M., Ehrig, K.J., Ciobanu, C.L., Cook, N.J., Verdugo-Ihl, M.R., Metcalfe, A.V., 2019b. Defining IOCG signatures through compositional data analysis: a case study of lithogeochemical zoning at Olympic Dam, South Australia. Ore Geol. Rev. 105, 86–101.
Donovan, J.J., Singer, J.W., Armstrong, J.T., 2016. A new EPMA method for fast trace element analysis in simple matrices. Am. Mineral. 101, 1839–1853. https://doi.org/10.2138/am-2016-5628.
Ehrig, K., McPhie, J., Kamenetsky, V., 2012. Geology and mineralogical zonation of the Olympic Dam iron oxide Cu-U-Au-Ag deposit, South Australia. In: Hedenquist, J.W., Harris, M., Camus, F. (Eds), Geology and Genesis of Major Copper Deposits and Districts of the World, a Tribute to Richard Sillitoe. SEG Special Publication 16, p. 237-268.
Ehrig, K., Kamenetsky, V., Mc'Phie, J., Cook, N.J., Ciobanu, C.L., 2017. Olympic Dam iron-oxide Cu-U-Au-Ag deposit. In: Phillips, G.N. (Ed.), Australian Ore Deposits. AusIMM, Melbourne, pp. 601–610.
Erel, Y., Harlavan, Y., Stein, M., Blum, J.D., 1997. U-Pb dating of Fe-rich phases using a sequential leaching method. Geochim. Cosmochim. Acta 61, 1697–1703.
Fanning, C.M., Flint, R.B., Parker, A.J., Ludwig, K.R., Blisset, A.H., 1988. Refined Proterozoic evolution of the Gawler craton, South Australia, through U-Pb zircon geochronology. Precambr. Res. 40, 363–386.
Fanning, C.M., Reid, A.J., Teale, G.S., 2007. A geochronological framework for the Gawler Craton, South Australia: Geological Survey of South Australia. Geological Society of South Australia Bulletin 55, 258.
Fraser, G.L., Neumann, N., 2010, New SHRIMP U-Pb zircon ages from the Gawler craton and Curnamona province, South Australia, 2008–2010: Geoscience Australia Record 2010/16, p. 256.
Frei, R., Bridgwater, D., Rosing, M., Sletcher, O., 1999. Controversial Pb-Pb and Sm-Nd isotope results in the early Archean Isua (West Greenland) oxide iron formation: Preservation of primary signatures versus secondary disturbances. Geochim. Cosmochim. Acta 63, 476–488.
Geological Survey of South Australia, 2019. SARIG Database. https://map.sarig.sa.gov.au/.
Grainger, C.J., Groves, D.I., Tallarico, F.H.B., Fletcher, I.R., 2008. Metallogenesis of the Carajás mineral province, southern amazon craton, Brazil: Varying styles of Archean through Paleoproterozoic to Neoproterozoic base and precious-metal mineralisation. Ore Geol. Rev. 33, 451–489.
Huang, Q., Kamenetsky, V.S., McPhie, J., Ehrig, K., Meffre, S., Maas, R., Thompson, J., Kamenetsky, M., Chambefort, I., Apukhtina, O., Hu, Y., 2015. Neoproterozoic (ca. 820–830 Ma) mafic dykes at Olympic Dam, South Australia: links with the Gairdner Large Igneous Province. Precambr. Res. 271, 160–172.
Huberty, J.M., Konish, H., Heck, P.R., Fournelle, J.H., Valley, J.W., Xu, H., 2012. Silician magnetite from the Dales Gorge member of the Brockman iron formation, Hamersley Group, Western Australia. Am. Mineral. 97, 26–37.
Ismail, R., Ciobanu, C.L., Cook, N.J., Teale, G.S., Giles, D., Mumm, A.S., Wade, B., 2014. Rare earths and other trace elements in minerals from skarn assemblages, Hillside iron oxide-copper-gold deposit, Yorke Peninsula, South Australia. Lithos 184–187, 456–477.
Jackson, S.E., Pearson, N.J., Belousova, E.A., Griffin, W.L., 2004. The application of laser ablation-inductively coupled plasma-mass spectrometry (LA-ICP-MS) to in situ U-Pb geochronology. Chem. Geol. 211, 47–69.
Jonsson, E., Troll, V.R., Högdahl, K., Harris, C., Weis, F., Nilsson, K.P., Skelton, A., 2013. Magmatic origin of giant 'Kiruna-type' apatite-iron-oxide ores in Central Sweden. Sci. Rep. 3, 1644.
Keyser, W.M., Ciobanu, C.L., Cook, N.J., Courtney-Davies, L., Ehrig, K., Gilbert, S., McPhie, J., 2017. Links between sedimentary protoliths and IOCG Links between sedimentary protoliths and IOCG-skarn skarn alteration, Island Dam, South Australia. Proceedings, 14th SGA Biennial Meeting 'Mineral Resources to Discover', Québec City, QC, Canada, 20–23 August 2017, p. 935–938.
Keyser, W.M., Ciobanu, C.L., Cook, N.J., Johnson, G., Dmitrijeva, M., Courtney-Davies, L., Feltus, F., Gilbert, S., Johnson, G., Ehrig, K., 2019a. Iron-oxides constrain BIF evolution in terranes with protracted geological histories: the Iron Count prospect, Middleback Ranges, South Australia. Lithos 324–325, 20–38.
Keyser, W., Ciobanu, C.L., Cook, N.J., Courtney-Davies, L., Kennedy, A., Wade, B.P., Ehrig, K., Dmitrijeva, M., Kontonikas-Charos, A., Feltus, H., Johnson, G., 2019b. Petrographic and geochronological constraints on the granitic basement to the Middleback Ranges, South Australia. Precambr. Res. 324, 170–193.
Keyser, W., Ciobanu, C.L., Cook, N.J., Feltus, H., Johnson, G., Slattery, A., Wade, B.P., Ehrig, K., 2019c. Mineralogy of zirconium in iron-oxides: A micron- to nanoscale study of hematite ore from Peculiar Knob. Minerals 9, 244.
Keyser, W., Ciobanu, C.L., Cook, N.J., Wade, B.P., Wade, B.P., Kennedy, A., Kontonikas-Charos, A., Ehrig, K., Feltus, H., Johnson, G., 2020. Episodic mafic magmatism in the Eyre Peninsula: defining syn- and post-depositional BIF environments for iron deposits in the Middleback Ranges, South Australia. Precambr. Res. 337, 105535.
Kontonikas-Charos, A., Ciobanu, C.L., Cook, N.J., Ehrig, K., Krneta, S., Kamenetsky, V.S., 2017. Feldspar evolution in the Roxby Downs Granite, host to Fe-oxide Cu-Au-(U) mineralisation at Olympic Dam, South Australia. Ore Geol. Rev. 80, 838–859.
Krneta, S., Ciobanu, C.L., Cook, N.J., Ehrig, K., Kontonikas-Charos, A., 2017. The Wirrda Well and Acropolis prospects Gawler Craton, South Australia: insights into evolving fluid conditions through apatite chemistry. J. Geochem. Explor. 181, 276–291.
Ludwig, K.R., 2012. A User's Manual for Isoplot 3.75: A Geochronological Toolkit for Microsoft Excel. Berkeley Geochronology Centre Special Publication No.5; Berkeley Geochronology Centre: Berkeley, CA, USA.
Maas, R., Kamenetsky, V.S., Ehrig, K., Meffre, S., McPhie, J., Diemar, G., 2011. Olympic Dam U-Cu-Au deposit, Australia: New age constraints. Mineral. Mag. 75, 1375.
McInnes, B.I.A., Keays, R.R., Lambert, D.D., Hellstrom, J., Allwood, J.S., 2008. Re-Os geochronology and isotope systematics of the Tanami, Tennant Creek and Olympic Dam Cu-Au deposits. Aust. J. Earth Sci. 55, 967–981.
McPhie, J., Orth, K., Kamenetsky, V., Kamenetsky, M., Ehrig, K., 2016. Characteristics, origin and significance of Mesoproterozoic bedded clastic facies at the Olympic Dam Cu-U-Au-Ag deposit, South Australia. Precambr. Res. 276, 85–100.
Reid, A., 2019. The Olympic Cu-Au Province, Gawler Craton: A Review of the Lithospheric Architecture, Geodynamic Setting, Alteration Systems, Cover Successions and Prospectivity. Minerals 9 (6), 371. https://doi.org/10.3390/min9060371.
Reid, A.J., Swain, G.S., Mason, D., Maas, R., 2011. Nature and timing of Cu-Au-Zn-Pb mineralisation at Punt Hill, eastern Gawler Craton. MESA J. 60, 7–17.
Reid, A., Smith, R.N., Baker, T., Jagodzinski, E.A., Selby, D., Gregory, C.J., Skirrow, R.G., 2013. Re-Os dating of molybdenite within hematite breccias from the Vulcan Cu-Au prospect, Olympic Cu-Au province, South Australia. Econ. Geol. 108, 883–894.
Routhier, P., 1967. Le modèle de la genèse. Quelques concepts fondamentaux en pétrologie et en métallogénie. Modèles des théories métallogénétiques. Chron Min 363, 177–190.
Skirrow, R.G., Bastrakov, E.N., Baroncii, K., Fraser, G.L., Creaser, R.A., Fanning, C.M., Raymond, O.L., Davidson, G.J., 2007. Timing of iron oxide Cu-Au-(U) hydrothermal activity and Nd isotope constraints on metal sources in the Gawler craton, South Australia. Econ. Geol. 102, 1441–1470.
Sláma, J., Košler, J., Condon, D.J., Crowley, J.L., Gerdes, A., Hanchar, J.M., Horstwood, M.S.A., Morris, G.A., Nasdala, L., Norberg, N., Schaltegger, U., Schoene, B., Tubrett, M.N., Whitehouse, M.J., 2008. Plešovice zircon - a new natural reference material for U-Pb and Hf isotopic microanalysis. Chem. Geol. 249, 1–35.
Troll, V.R., Weis, F.A., Jonsson, E., Andresson, U.B., Majidi, S.A., Högdahl, K., Harris, C., Millet, M.-A., Chinnasamy, S.S., Kooijman, E., Nilsson, K.P., 2019. Global Fe–O isotope correlation reveals magmatic origin of Kiruna-type apatite-iron-oxide ores. Nat.

Commun. https://doi.org/10.1038/s41467-019-09244-4.
Van Achterbergh, E., Ryan, C., Jackson, S., Griffin, W., 2001. Appendix 3 Data reduction software for LA-ICP-MS. In: Laser-Ablation-ICPMS in the Earth Sciences (Sylvester, P., Ed.), Short Course Volume, Mineralogical Association of Canada: Quebec City, QC, Volume 29, p. 239–243.
Verdugo-Ihl, M.R., Ciobanu, C.L., Cook, N.J., Ehrig, K.J., Courtney-Davies, L., Gilbert, S., 2017. Textures and U-W-Sn-Mo signatures in hematite from the Olympic Dam Cu-U-Au-Ag deposit, South Australia: Defining the archetype for IOCG deposits. Ore Geol. Rev. 91, 173–195. https://doi.org/10.1016/j.oregeorev.2017.10.007.
Verdugo-Ihl, M.R., Ciobanu, C.L., Cook, N.J., Ehrig, K.J., Courtney-Davies, L., 2020. Defining early stages of IOCG systems: evidence from iron-oxides in the outer shell of the Olympic Dam deposit, South Australia. Mineralium Deposita, in press, doi:10.1007/s00126-019-00896-2.
Wise, T., 2019. Prospectivity modelling of the Olympic Cu–Au Province. MESA J. 90, 36–41.
Xu, H., Shen, Z., Konishi, H., 2014. Si-magnetite nano-precipitates in silician magnetite from banded iron formation: Z-contrast imaging and ab initio study. Am. Mineral. 99, 2196–2202.

CHAPTER 7

ZIRCON AT THE NANOSCALE RECORDS METASOMATIC PROCESSES LEADING TO LARGE MAGMATIC–HYDROTHERMAL ORE SYSTEMS

Liam Courtney-Davies [1], Cristiana L. Ciobanu [1], Max R. Verdugo-Ihl [1], Ashley Slattery [2], Nigel J. Cook [1], Marija Dmitrijeva [1], William Keyser [1], Benjamin P. Wade [2], Urs I. Domnick[1], Kathy Ehrig [3], Jing Xu [1,4] and Alkiviadis Kontonikas-Charos [1]

[1] *School of Chemical Engineering and Advanced Materials, The University of Adelaide, Adelaide, SA 5005, Australia*

[2] *Adelaide Microscopy, The University of Adelaide, Adelaide, SA 5005, Australia*

[3] *BHP Billiton Olympic Dam, Adelaide, SA, 5000, Australia*

[4] *Key Laboratory of Mineral Resources, Institute of Geology and Geophysics, Chinese Academy of Sciences, Beijing 100029, China*

Article published in Minerals (2019), 9(6), 364.

Statement of Authorship

Title of Paper	Zircon At The Nanoscale Records Metasomatic Processes Leading To Large Magmatic–Hydrothermal Ore Systems
Publication Status	☑ Published ☐ Accepted for Publication ☐ Submitted for Publication ☐ Unpublished and Unsubmitted w ork w ritten in manuscript style
Publication Details	Courtney-Davies, L., Ciobanu, C.L., Verdugo-Ihl, M.R., Slattery, A., Cook, N.J., Dmitrijeva, M., Keyser, W., Wade, B.P., Dominick, U.I., Ehrig, K., Xu, J., and Kontonikas-Charos, A., 2019c, Zircon at the nanoscale records metasomatic processes leading to large magmatic-hydrothermal ore deposits: Minerals, 9(6), 364.

Principal Author

Name of Principal Author (Candidate)	Liam Courtney-Davies		
Contribution to the Paper	Performed analytical work, carried out data processing and interpretation, oversaw development of work and wrote manuscript.		
Overall percentage (%)	50		
Certification:	This paper reports on original research I conducted during the period of my Higher Degree by Research candidature and is not subject to any obligations or contractual agreements with a third party that would constrain its inclusion in this thesis. I am the primary author of this paper.		
Signature		Date	29/10/2019

Co-Author Contributions

By signing the Statement of Authorship, each author certifies that:

i. the candidate's stated contribution to the publication is accurate (as detailed above);

ii. permission is granted for the candidate in include the publication in the thesis; and

iii. the sum of all co-author contributions is equal to 100% less the candidate's stated contribution.

Name of Co-Author	Cristiana L. Ciobanu		
Contribution to the Paper	Performed analytical work, carried out data processing and data interpretation and wrote manuscript.		
Overall percentage (%)	20		
Signature		Date	29 Oct 2019

Name of Co-Author	Max R. Verdugo-Ihl		
Contribution to the Paper	Performed analytical work, carried out data processing and data interpretation and contributed to manuscript preparation.		
Overall percentage (%)	10		
Signature		Date	29/10/2019

Name of Co-Author	Ashley Slattery		
Contribution to the Paper	Operated the TEM and contributed to manuscript preparation.		
Overall percentage (%)	10		
Signature		Date	29/10/2019

Name of Co-Author	Nigel J. Cook		
Contribution to the Paper	Assisted with data processing and contributed to manuscript preparation.		
Overall percentage (%)	2.5		
Signature		Date	29/10/2019

Name of Co-Author	Marija Dmitrijeva		
Contribution to the Paper	Assisted with analytical instrumentation, data processing and evaluation of manuscript.		
Overall percentage (%)	2.5		
Signature		Date	29/10/2019

Name of Co-Author	William Keyser		
Contribution to the Paper	Assisted with analytical instrumentation		
Overall percentage (%)	1		
Signature		Date	29/10/2019

Name of Co-Author	Benjamin P. Wade		
Contribution to the Paper	Assisted with analytical instrumentation and contributed to manuscript preparation.		
Overall percentage (%)	1		
Signature		Date	29/10/2019

Name of Co-Author	Urs I. Domnick		
Contribution to the Paper	Assisted with analytical work.		
Overall percentage (%)	1		
Signature		Date	29/10/2019

Name of Co-Author	Kathy Ehrig		
Contribution to the Paper	Helped coordinate sample collection and evaluation of manuscript.		
Overall percentage (%)	1		
Signature		Date	29/10/2019

Name of Co-Author	Jing Xu		
Contribution to the Paper	Assisted with analytical instrumentation and data processing		
Overall percentage (%)	0.5		
Signature		Date	~~30/9/2019~~ 29/10/2019

Name of Co-Author	Kontonikas-Charos		
Contribution to the Paper	Assisted with evaluation of manuscript.		
Overall percentage (%)	0.5		
Signature		Date	~~30/9/2019~~ 29/10/2019

minerals

MDPI

Article

Zircon at the Nanoscale Records Metasomatic Processes Leading to Large Magmatic–Hydrothermal Ore Systems

Liam Courtney-Davies [1,*], Cristiana L. Ciobanu [1], Max R. Verdugo-Ihl [1], Ashley Slattery [2], Nigel J. Cook [1], Marija Dmitrijeva [1], William Keyser [1], Benjamin P. Wade [2], Urs I. Domnick [1], Kathy Ehrig [3], Jing Xu [1,4] and Alkiviadis Kontonikas-Charos [1]

1 School of Chemical Engineering and Advanced Materials, The University of Adelaide, Adelaide, SA 5005, Australia; cristiana.ciobanu@adelaide.edu.au (C.L.C.); max.verdugoihl@adelaide.edu.au (M.R.V.-I.); nigel.cook@adelaide.edu.au (N.J.C.); marija.dmitrijeva@adelaide.edu.au (M.D.); william.keyser@adelaide.edu.au (W.K.); urs.domnick@adelaide.edu.au (U.I.D.); j.xu@adelaide.edu.au (J.X.); alkiviadis.kontonikas-charos@adelaide.edu.au (A.K.-C.)

2 Adelaide Microscopy, The University of Adelaide, Adelaide, SA 5005, Australia; ashley.slattery@adelaide.edu.au (A.S.); benjamin.wade@adelaide.edu.au (B.P.W.)

3 BHP Olympic Dam, Adelaide, SA 5000, Australia; kathy.ehrig@bhp.com

4 Key Laboratory of Mineral Resources, Institute of Geology and Geophysics, Chinese Academy of Sciences, Beijing 100029, China; xujing3800@126.com

* Correspondence: liam.courtney-davies@adelaide.edu.au

Received: 30 April 2019; Accepted: 13 June 2019; Published: 16 June 2019

check for updates

Abstract: The petrography and geochemistry of zircon offers an exciting opportunity to better understand the genesis of, as well as identify pathfinders for, large magmatic–hydrothermal ore systems. Electron probe microanalysis, laser ablation inductively coupled plasma mass spectrometry, high-angle annular dark-field scanning transmission electron microscopy (HAADF-STEM) imaging, and energy-dispersive X-ray spectrometry STEM mapping/spot analysis were combined to characterize Proterozoic granitic zircon in the eastern Gawler Craton, South Australia. Granites from the ~1.85 Ga Donington Suite and ~1.6 Ga Hiltaba Suite were selected from locations that are either mineralized or not, with the same style of iron-oxide copper gold (IOCG) mineralization. Although Donington Suite granites are host to mineralization in several prospects, only Hiltaba Suite granites are considered "fertile" in that their emplacement at ~1.6 Ga is associated with generation of one of the best metal-endowed IOCG provinces on Earth. Crystal oscillatory zoning with respect to non-formula elements, notably Fe and Cl, are textural and chemical features preserved in zircon, with no evidence for U or Pb accumulation relating to amorphization effects. Bands with Fe and Ca show mottling with respect to chloro–hydroxy–zircon nanoprecipitates. Lattice defects occur along fractures crosscutting such nanoprecipitates indicating fluid infiltration post-mottling. Lattice stretching and screw dislocations leading to expansion of the zircon structure are the only nanoscale structures attributable to self-induced irradiation damage. These features increase in abundance in zircons from granites hosting IOCG mineralization, including from the world-class Olympic Dam Cu–U–Au–Ag deposit. The nano- to micron-scale features documented reflect interaction between magmatic zircon and corrosive Fe–Cl-bearing fluids in an initial metasomatic event that follows magmatic crystallization and immediately precedes deposition of IOCG mineralization. Quantification of α-decay damage that could relate zircon alteration to the first percolation point in zircon gives ~100 Ma, a time interval that cannot be reconciled with the 2–4 Ma period between magmatic crystallization and onset of hydrothermal fluid flow. Crystal oscillatory zoning and nanoprecipitate mottling in zircon intensify with proximity to mineralization and represent a potential pathfinder to locate fertile granites associated with Cu–Au mineralization.

Keywords: zircon; IOCG deposits; Olympic Cu–Au Province; HAADF STEM; Fe–Cl-metasomatism; chloro–hydroxy–zircon nanoprecipitates; granite fertility

1. Introduction

Ore deposits falling within the broad iron-oxide-Cu–Au (IOCG) clan are a fascinating, and in some cases, poorly understood, family of magmatic–hydrothermal ore systems (References [1,2] and references therein). Debate on their genesis includes the relative timing and evolution of fluids during transition from the magmatic to hydrothermal stage. Detailed investigation of magmatic accessory minerals at appropriate scales of observation has enabled fluid–mineral interaction to be fingerprinted (e.g., using apatite [3,4]).

Zircon ($ZrSiO_4$) is a common accessory mineral and has been pivotal for the evolution of U–(Th)–Pb geochronology (References [5] and references therein). Aside from actinides, magmatic zircon will incorporate a range of trace elements (lanthanides, Y, Hf, and Ti) which are valuable tracers for mantle versus crustal origin of melts and for underpinning plate tectonic models during Earth cycles (e.g., [6–8]). Contemporary consensus views the incorporation of other, "non-formula" components in zircon, including Ca, Fe, Al, and H_2O, as being unrelated to primary magmatic processes (Reference [9], and references therein). These are most often measured within altered zircon (e.g., [10]) and are attributed to metamictization-related effects.

In this contribution, we bridge micron- to nanoscale observations to comprehensively characterize magmatic zircon from Proterozoic granites in the eastern Gawler Craton, South Australia (Figure 1A). Iron-oxide copper gold systems of various sizes are found within granites of different ages in the Olympic Cu–Au Province [11], for example, the Olympic Dam deposit [12] and Wirrda Well prospect, hosted by ~1.6 Ga (Hiltaba Suite) and ~1.85 Ga (Donington Suite) granitoids, respectively. The U–Pb age of hydrothermal hematite from Olympic Dam, a product of Fe-metasomatism, has been constrained by isotope dilution-thermal ionization mass spectrometry (ID-TIMS) to 1589.91 ± 0.94 Ma [13], crystallizing roughly 2–4 Ma after zircon within the granite hosting the deposit (chemical abrasion ID-TIMS; 1593.87 ± 0.21 Ma) [14].

The overarching aims of the present work were two-fold. Firstly, we aimed to document metasomatic, fluid-assisted alteration of zircon that occurs in a magmatic–hydrothermal environment prior to structural damage induced by alpha-decay. Secondly, we tested this hypothesis and its implications using samples from metallogenetically productive and unproductive granites of the same suites across the Gawler Craton. We set out to show that micron- to nanoscale observations of zircon geochemistry and crystal structure can, in combination, be used to trace early mineralizing fluids. Furthermore, we provide atomic-scale resolution images of zircon, offering insights into metasomatic processes and products, such as the formation of zircon nanoprecipitates and structural defects.

Such an approach provides potential qualitative indicators of magma fertility (the ability of a magma to generate hydrothermal fluids that are sufficiently well-endowed with Cu, etc., to form a sizable ore deposit). Such an idea is validated by geochemical analysis of known productive and unproductive granites, with a broad application in IOCG exploration across the Gawler Craton and elsewhere.

2. Background and Rationale

2.1. Zircon Chemistry and Structure

Magmatic zircon has a crystal structure resistant to physical and chemical degradation during secondary processes, properties which have motivated research into its usage as a durable host for nuclear waste storage [15]. However, zircon undergoes self-irradiation damage during U–(Th)–Pb decay, ultimately transitioning from crystalline to an amorphous (metamict) state [10], which can be

followed by partial to complete recrystallization. The amorphous domains begin to interconnect due to the radiation damage (α-decay), over a time period determined by U/Th concentrations and annealing rates [16]. The time dependency of structural damage is highly relevant for geochronology, as it can result in discordance of the U–Pb system, most commonly through Pb-loss. Disturbances to zircon U–Pb systematics via metamictization can, however, be selectively eliminated by chemical abrasion of damaged zones, prior to ID-TIMS, permitting high-precision geochronological constraints [17].

The secondary textures commonly observed to crosscut growth zones in magmatic zircon are attributed to re-equilibration of zircon in aqueous fluids and melts (Reference [18] and references therein). Primary oscillatory zoning in zircon can, however, be locally preserved, even in cases when the superimposed reaction temperature exceeds ~600 °C [19]. Structural damage can also create pathways for fluids to enter and precipitate minerals as inclusions within zircon displaying secondary microstructures. For example, Fe–Ti oxides and ZrO_2 observed along dislocation and pores in Hadean zircons (Jack Hills, Western Australia) are considered to postdate primary crystallization [20].

Elemental abundance and isotope ratios in zircon, including rare earth element (REE) fractionation patterns and Eu/Eu*, Sr/Y, and V/Sc anomalies, all readily determined by microbeam analysis, can be used to define magma fertility and track its evolution (Reference [21] and references therein). These geochemical pathfinders have been extensively applied to target metallogenically productive ("fertile") and non-productive ("infertile") granitic intrusions [22]. Despite the potential for identifying geochemical changes in zircon as a response to metasomatism, the commonly used microanalytical instrumentation, such as laser-ablation inductively-coupled plasma mass-spectrometry (LA-ICP-MS), cannot accurately spatially resolve compositions smaller than a few microns at best, a high threshold relative to typical internal textures and structures commonly found in zircon.

Z-contrast techniques such as high-angle annular dark-field scanning transmission electron microscopy (HAADF STEM; e.g., [23]) allows processes of metamictization and alteration to be addressed down to the nanoscale. For example, fission tracks relating to radiation damage, the nanoscale occurrence of Pb, and evidence for nanoscale U-mobility have been revealed by this technique [24–27]. Increasing levels of spatial resolution and analytical precision combined with in situ micro-sampling techniques have permitted HAADF STEM study of foils prepared by focused ion beam (FIB)-scanning electron microscopy (SEM) to visualize atomic structure and defects in minerals (e.g., [28,29]).

2.2. *The Olympic Cu–Au Province*

The Olympic Cu–Au Province, South Australia (Figure 1A) hosts IOCG-style mineralization attributed to hydrothermal activity associated with emplacement of the Gawler Silicic Large Igneous Province at ~1.6 Ga [11], accompanying the onset of Columbia/Nuna supercontinent breakup [30]. Magmatic activity is represented by the Hiltaba Suite and contemporaneous Gawler Range Volcanics [31]. The ~700 km long Olympic Cu–Au Province strikes roughly N–S along the eastern margin of the Gawler Craton from the Mount Woods Inlier in the north, which hosts the Prominent Hill deposit, through Olympic Dam and Carrapateena, to the Moonta and Hillside deposits in the south (Figure 1A). Each major deposit is surrounded by numerous smaller, less explored prospects. Host lithologies range from Gawler Range Volcanics (e.g., Acropolis prospect; Figure 1B), granites of Hiltaba Suite affiliation (e.g., Olympic Dam within Roxby Downs Granite; RDG), or older granitoids (e.g., ~1.85 Ga Donington Suite granites at Wirrda Well and Carrapateena; Figure 1A,B).

Several other styles of mineralization occur on the Eyre Peninsula to the immediate west of the Olympic Province. These include older banded iron formations [32] and younger U-mineralization within cover rocks suprajacent to granites belonging to the Samphire Pluton of Hiltaba Suite affiliation [33]. A further Hiltaba Suite granitoid is the Charleston Granite (Figure 1A). No IOCG-style mineralization has yet been discovered associated with either the Charleston Granite or the Samphire Pluton. Donington Suite granitoids are present throughout the Eyre Peninsula and outcrop as far south as Cape Donington, south of Port Lincoln. Although the potential for an extension of the Olympic Cu–Au Province westwards into the Eyre Peninsula remains largely untested, we note that

several of the aforementioned banded iron formation ores feature geochemical signatures suggestive of overprinting by hydrothermal fluids of granitic affiliation [32,34,35].

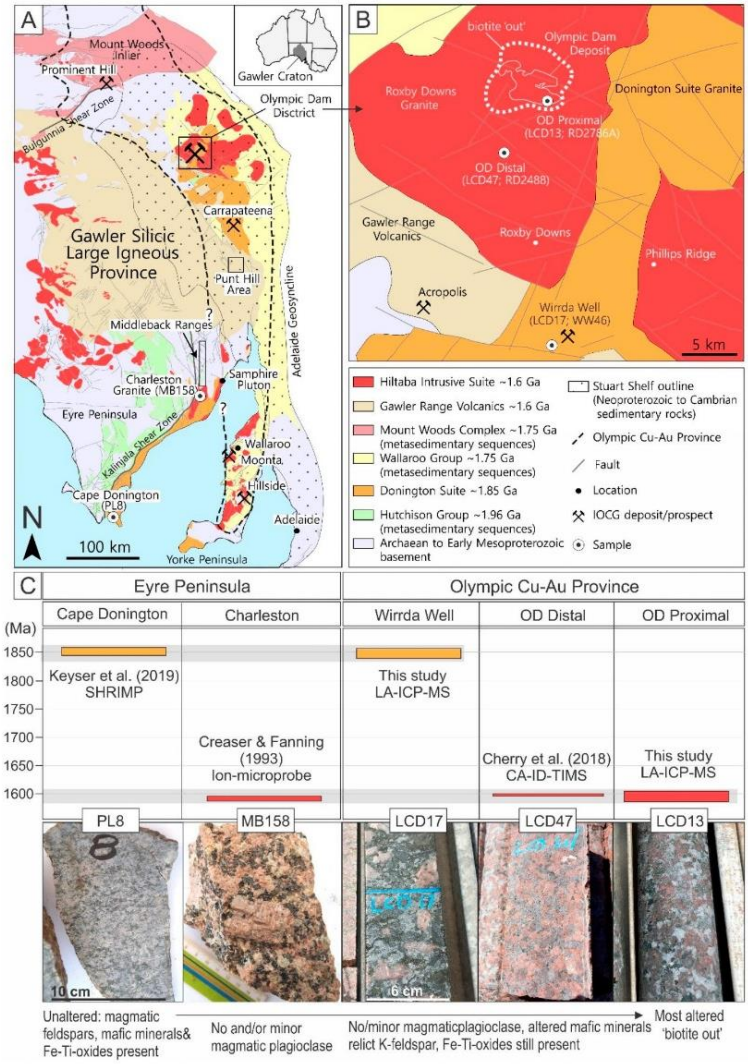


Figure 1. (**A**) Geological map of the eastern Gawler Craton and (**B**) the Olympic Dam district; data were taken from the Geological Survey of South Australia (https://map.sarig.sa.gov.au/). Locations of the five granite samples addressed in this study and the outline of the Olympic Cu–Au district are marked. (**C**) Table of ages and corresponding uncertainties (colored bars) for each granite sample studied here, with geochronology conducted either in this study (LA-ICP-MS) or in previous published work as indicated. The orange and red uncertainty bars represent the Donington Suite and Hiltaba Intrusive Suite, respectively, and their location within either the Eyre Peninsula or Olympic Cu–Au Province. Corresponding hand specimen photographs of each sample are shown below the age diagram, indicating degree of granite alteration. References: Keyser et al. (2019) [34]; Creaser and Fanning (1993) [36]; Cherry et al. (2018) [14].

Formation of IOCG deposits remains highly contested, particularly with respect to sources and timing of fluids and contained metals (References [1,2], and references therein). In the Gawler Craton,

lithospheric architecture, mantle metasomatism, and cratonic metallogeny [37,38] have been linked to generic models for IOCG genesis with global applicability [1]. The large volumes of Fe required to form IOCG deposits associated with granitoid-derived fluids or felsic magmatism have recently been proposed to be derived from underplating mafic magma in deeper reservoirs allowing for volatile- and metal-transfer via magma mingling and magnetite flotation [39]. If Fe is sourced from a deep magma reservoir, then zircon, as a ubiquitous magmatic accessory mineral, should record this, either in the magmatic growth stage or as an overprint following interaction with early, low pH hydrothermal fluids released from the locally Fe-enriched magma. Zircon from fertile and barren granitoids should, therefore, differ from one another, both in terms of their geochemical signatures and textures at the micron- to nanoscale.

3. Sample Suite

For this study, we used magmatic zircon from five granitoids of Donington- (~1.85 Ga) and Hiltaba-affiliation (~1.6 Ga) from within and outside the Olympic Cu–Au Province (Figure 1C; Table 1). Except for the example from Cape Donington, all granites considered here displayed macroscopic alteration, albeit to varying degrees, while still retaining granitoid textures and some relict magmatic minerals. The sample suite is summarized in Table 1 with respect to rock type, location, key features, and types of analysis reported in the present contribution.

Zircon from all five case studies were temporally well-constrained by U–Pb methods, either previously published, or given in this study (Figure 1C). We included zircon from RDG samples, collected at locations distal and proximal to the Olympic Dam deposit (Figure 1B), to evaluate whether metasomatic processes analogous to those reported for feldspars [40] and apatite [3] could be tracked. Secondly, we sought to identify whether such processes are recognizable in older zircon from Donington Suite granite hosting the Wirrda Well prospect [41], 25 km SSE of Olympic Dam. Zircon from the Charleston and Cape Donington granites are included to assess the potential of zircon as an indicator of the metallogenic fertility of plutons in the Eyre Peninsula bordering the Olympic Cu–Au Province, where IOCG-style mineralization has not thus far been discovered.

4. Methodology

Four granite samples (3 one-inch polished blocks and one thin-section) and one polished block containing separated zircon (sample PL8) were studied in backscattered electron (BSE) and secondary electron (SE) modes using an FEI Quanta 450 SEM. Cathodoluminescence imaging was undertaken using an FEI Quanta 600 SEM equipped with a tungsten filament electron source. The purpose was to identify zircon grains with representative characteristics, particularly primary growth with oscillatory zoning textures and overprinting thereof. Such grains were analyzed by electron probe microanalysis (EPMA; Cameca SX-Five) and LA-ICP-MS (RESOlution-LR excimer laser microprobe coupled to an Agilent 7900x Quadrupole ICP-MS) for minor to trace element and U–Pb compositions using both spot analysis and mapping. All instruments are housed at Adelaide Microscopy, University of Adelaide. Extended details of instrumentation and analytical parameters are provided in Supplementary Materials A. All geochemical data are tabulated in Supplementary Materials B.

For subsequent S/TEM study, seven foils (Table 1; Figure 2A–E, Figure 3B,C, and Supplementary Materials C, Figure S1) were extracted in-situ, thinned to <100 nm by ion beam (Ga^+) milling and attached to Cu grids on an FEI Helios Nanolab 600 FIB-SEM platform. Of the seven foils, five were cut across oscillatory zonation observed on grain surfaces in zircon to target their development at depth, allowing correlation between micron- and nanoscale characteristics. In the case of the Wirrda Well Donington sample (LCD17), foil preparation targeted areas that yielded concordant (Foil #5) and discordant (Foil #4) U/Pb data points. In the Olympic Dam (OD) distal sample (LCD47), two zircon grains were cut, one with primary oscillatory zoning (Foil #1) and a second grain (Foil #2) displaying secondary, highly altered domains lacking oscillatory zoning.

Table 1. Summary of the samples and foils investigated in this study.

Region	Sample ID	Granite Petrography and Age(s), References	Locality (Drill Hole)	Micron-scale Analysis				Nanoscale Analysis: HAADF STEM Imaging and EDS Spot/Mapping					Figures Showing Zircon Images and Maps
				Analytical Methods					Key Zircon Features			Main Zone Axes Imaged (See Figures 12 and 13)	
				LA-ICP-MS			EPMA Map	Foil No. (#)	NF Element Zoning (STEM Maps)	Mottling/ CHZ-Nano-precipitates	Others		
				U–Pb Dating	Spot Analysis	Map							
Olympic Cu–Au Province	LCD47	HS-Roxby Downs granite [14,40,42], this study	Distal from OD (RD2488)		x			#1	Fe, Ca, Cl	X	screw dislocation	$(1\bar{1}1]$)	Figures 2, 8, 10, 11, 14, 15, Supplementary C, Figures S1 and S3
								#2 *	Fe, Ca, Al, <Cl, Y	x	Xtm veinlet, pores	(001])	Figure 2, Supplementary Figure S3
	LCD13		Proximal to OD (RD2786A)	x	x		Fe, Cl	#3	Fe, Cl, <Ca	x	Hm inclusions	(001])	Figures 3, 5, 9, Supplementary Figure S3
	LCD17	DS granite [42,43], this study	Wirrda Well (WW46)	x	x		Fe, Cl	#4	Fe, Ca	x	Xtm veinlet, screw dislocation	(001])	Figures 3, 5, 6, 15, Supplementary Figure S3
								#5 **	Not mapped	x	Fe detected from spot analysis	[100]; $[1\bar{1}0]$	Figures 3 and 5
Eyre Peninsula	MB158	HS-Charleston granite [36,44]	South of Middleback Ranges					#6	Fe, Ca, Ti, Al, Y, Th		2-D screw dislocation, fracture U-NP	[001]	Figures 7, 15, Supplementary Figure S1
	PL8	DS granite [44]	Cape Donington		x	x		#7	None—primary magmatic		stretching defects	[100]; $[1\bar{1}0]$	Figures 2, 15, Supplementary Figure S2

All samples were characterized by EPMA spot analysis. Sample MB158 for Charleston granite was not analyzed by LA-ICP-MS due to the small size of zircon grains, and particularly the grain from which Foil #6 was extracted (see Figure S1). U–Pb dating was carried out for two samples (including the grains from which the foils were extracted) from locations that were not previously dated. * Foil #2 differs from Foil #1 in containing secondary rather than primary textures. ** Foils #4 and #5 were cut perpendicular and parallel to grain elongation (c-axis), respectively. Upper case X represents the most intense mottling/nanoprecipitates. Abbreviations: CHZ—chloro–hydroxy–zircon; NF—non-formula elements; Hm—hematite; Xtm—xenotime; OD—Olympic Dam; HS—Hiltaba Suite; DS—Donington Suite; U-NP—uranium-bearing nanoparticles.

Nanoscale study, HAADF STEM imaging, and EDS spot analysis/mapping were performed using an ultra-high-resolution, probe-corrected, FEI Titan Themis S/TEM operated at 200 kV. This instrument is equipped with the X-FEG Schottky source and Super-X EDS geometry. The Super-X EDS detector provides geometrically symmetric EDS detection with an effective solid angle of 0.8 Sr. Probe correction delivered sub-Ångstrom spatial resolution and an inner collection angle greater than 50 mrad was used for HAADF experiments using the Fischione HAADF detector.

Diffraction indexing was performed using Winwulff© 1.5.2 software and publicly available data from the American Mineralogist Crystal Structure Database. Crystal structure models were obtained using CrystalMaker®version 10.1.1 and STEM for xHREM^{TM} version 4.1 software.

5. Results

5.1. Zircon Petrography, U–Pb Dating, and Selection of Grains for Nanoscale Study

Screening of zircon populations in each sample shows a range of grain sizes from 30 to ~300 μm, displaying both primary and secondary overprinting textures (Figure 2A–D). Zircons in two samples of unknown age but with assumed affiliation were dated by LA-ICP-MS to confirm their Hiltaba and Donington Suite ages.

Uranium–Pb dating of Wirrda Well zircon (LCD17) produced an upper intercept age of 1848 ± 10 Ma with concordant and highly discordant data points (Figure 3A), corresponding to published Donington Suite ages [43,44]. Dating of the OD proximal zircon (LCD13) gives an upper intercept age of 1572 ± 37 Ma, with analyses displaying both a high degree of concordance and discordancy. Full U–Pb data for analyzed zircons and reference material is tabulated in Supplementary Materials B, Table S3.

Selection of grains for nanoscale study was based upon several criteria: (i) well-constrained U–Pb ages in which case the FIB cut was placed next to a LA-ICP-MS crater (Figure 3); (ii) euhedral morphology with elongation along the *c*-axis; and (iii) large, least-fractured, inclusion-free grains. Subhedral zircon with marginal dissolution was also included to assess the most intense alteration observed within the sample suite (e.g., OD distal zircon; Figure 2B,D). In all five samples, zircon displays crystal oscillatory zoning expressed as bright and dark bands on BSE images (Figures 2 and 3 and Supplementary Materials C, Figure S1A). The intensity contrast of the banding ranged from subtle in zircon in granites from the Eyre Peninsula (PL8 and Charleston; Figure 2E and Supplementary Materials C, Figure S1A) to strong in granites from the Olympic Cu–Au Province. Furthermore, the dark bands could display mottled textures with respect to what appears to be inclusions, varying from sub-micron (in the banding) to ~1–2 μm (in the domains obliterating the zoning) (Figure 2C,D).

Spot EDS-SEM analysis does not show any compositional difference between the "inclusions" and host band/domain suggesting these could instead be pores. However, secondary electron imaging only rarely shows the presence of pores, generally in the scalloped areas with coarser mottled textures. Otherwise, the nature of the sub-micron "inclusions" cannot be resolved with SEM imaging alone.

Except for the Cape Donington sample (PL8; Figure 2E), all grains were fractured to varying degrees and were associated with marginal corrosion and occurrence of darker still domains with irregular and/or scalloped morphologies superimposed on crystal zoning (Figure 2D). Radial fractures, typically interpreted as accompanying metamictization, were present in such cases, notably in the OD distal zircon (Figure 2B,D). Additionally, veinlets and overgrowths of xenotime (Figure 3B), as well as tiny U-bearing phases, were also present in the RDG samples.

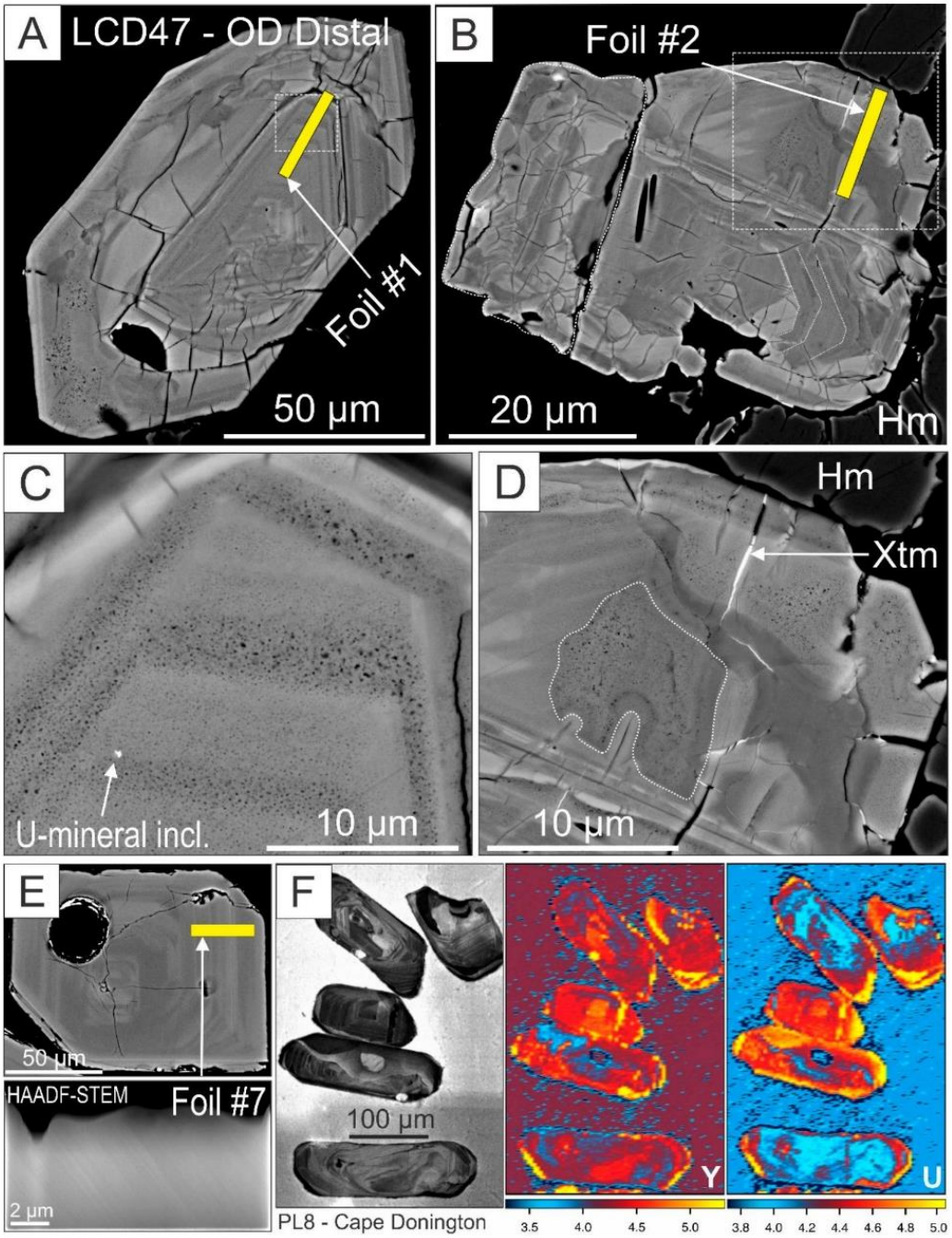


Figure 2. BSE images of grains #1 (**A** and **C**) and #2 (**B** and **D**) from OD distal zircon (sample LCD47). Note the mottled dark areas were either bands within crystal oscillatory zoning (**C**) or scalloped domains superimposed onto crystal zoning (**D**). (**E**) BSE (top) and HAADF STEM image (bottom) showing crystal oscillatory zoning for Cape Donington zircon (PL8). (**F**) Cathodoluminescence image (left) and LA-ICP-MS element maps (right) showing oscillatory zoned patterns for Y and U in coarser zircon grains from PL8. Scale in 10^n counts per second (extended maps are given in Supplementary Materials C, Figure S2).

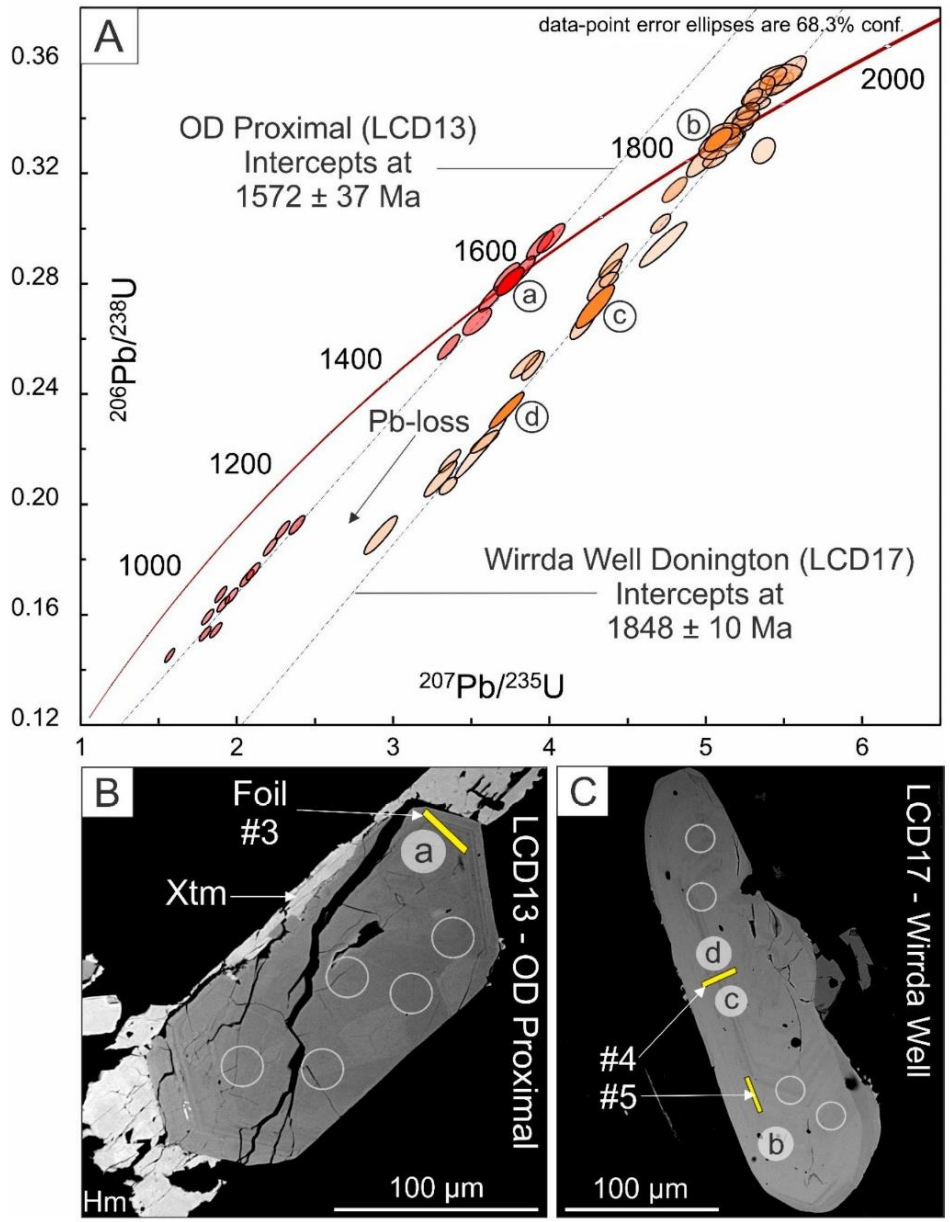


Figure 3. Concordia diagram (**A**) for OD proximal zircon (LCD13, red ellipses) and Wirrda Well zircon (LCD17, orange ellipses; U–Pb data are presented in Supplementary Materials B, Table S3). Circled letters correspond to LA-ICP-MS craters in BSE images of the dated grains (**B** and **C**).

5.2. *Trace and Minor Element Concentrations*

Electron microprobe datasets for analyzed zircon (Table 2 and Supplementary Materials B, Table S4) showed steady, consistent concentrations of HfO_2 (1.5–2.0 wt.%), Y_2O_3, $(HREE)_2O_3$ and P_2O_5, minor UO_2, PbO, and ThO_2 in most but not all analyses, and sporadic concentrations of Na_2O, K_2O, CaO, MgO, MnO, and Al_2O_3 above the minimum detection limit (mdl) values across the sample suite. TiO_2

was measured consistently (up to 0.06 wt.%) in the Charleston Granite sample only. Sc_2O_3 was below mdl in most analyses.

"Bright" and "dark" bands in zircon from Cape Donington zircon (PL8) were indistinguishable in terms of composition but the latter had lower analytical totals before recalculation. "Dark" bands in zircon from the Wirrda Well Donington Suite and Charleston Granite samples (LCD17 and MB158) also had totals ~1 wt.% lower than the "bright" bands, generally higher Fe_2O_3 and minor but measurable Cl. Analogous trends were seen in samples the two OD samples (LCD47 and LCD13), in which the "dark" bands contained 1.0–1.9 wt.% Fe_2O_3 and ~0.1 wt.% Cl. Analytical totals were 1–2 wt.% lower than for "bright" bands. Additionally, fluorine was measurable (up to 0.15 wt.%) in a minority of analytical spots from the "dark" bands. Variability of concentrations within each sample, and between "bright" and "dark" bands in the same zircon grain, was a feature of the dataset; the degree of intra-grain variability increased with the total of non-formula elements. Importantly, measured concentrations of Y_2O_3, $(HREE)_2O_3$, P_2O_5, UO_2, and ThO_2 were statistically identical in "bright" and "dark" bands across the dataset.

Laser ablation inductively coupled plasma mass spectrometry datasets (Supplementary Materials B, Table S5) corroborated and confirmed the accuracy and inherent variability of the EPMA data. Zircon from the Charleston granite was not considered due to the small grain sizes. Other elements (e.g., Sn, Nb, Ta) were not present at concentrations exceeding (at most) a few tens of ppm. Even using a small diameter spot (19 μm), the LA-ICP-MS method did not permit selective analysis of "bright" and "dark" bands.

Cape Donington zircon showed oscillatory patterns correlating with U, Pb, REE, and Y in LA-ICP-MS maps (Figure 2F; Supplementary Materials C, Figure S2). Chondrite-normalized fractionation trends constructed from LA-ICP-MS data (Figure 4A) showed reproducible patterns for zircon in each granite, although with systematic differences in the LREE portion between Donington and Hiltaba Suite samples.

Principal component analysis (PCA) applied to the centered logratio-transformed LA-ICP-MS dataset provided additional insights. A projection of PC1 versus PC2 (Figure 4B,C) showed two distinct groupings: (1) Y, REE (except Eu and Pr) and P; and (2) Hf, U, Pb, Th, Ti, Nb, Eu, and Pr. On both plots, these groupings are distinct from a third group comprising Fe, Mn, Al, and Ca. These patterns underscore interpretation of the EPMA data in which the geochemical signature associated with the metasomatic overprint was defined by Fe, Mn, Al, and Ca, and is independent of any magmatic signature or pattern of distribution at the grain-scale involving element groups (1) and (2). A ternary Fe–Al–Hf diagram (Figure 4D) allows a visual expression of chemical change from least-altered zircon (sample PL8), effectively without Fe or Al, through moderately altered zircon in sample LCD17, to the sub-populations of zircon in samples LCD13 and LCD17 from Olympic Dam, which contained the highest amounts of substituting non-formula (NF) elements.

5.3. Assessment of Zircon Stoichiometry and Substitution Model

Recalculation of EPMA data was undertaken following a template used for hydrogarnet and underlying assumptions/substitutions as provided by Supplementary Materials A. A key objective was an estimation of H_2O content based on allocation of all minor elements (Fe, Al, Mn, and Ca) to structural sites, bringing analytical totals close to 100 wt.% (from ~99.2). The data (Supplementary Materials B, Table S4) showed a correlation between atom per formula unit (apfu) values for $(REY + Sc)^{3+}$ and P^{5+} on the plot of these two variables (Figure 4E), albeit with a deficiency in the latter—a feature widely described in several publications (see Supplementary Materials A) and taken to indicate more complex substitution mechanisms. Electron microprobe datasets implicitly carry a margin of analytical error, which in the case of the zircon analyzed here were compounded by concentrations of many elements around or below mdl, and by assumptions in the formula calculation that were in turn based on equivocal evidence given in the literature (see Supplementary Materials A). As such, derived stoichiometries and calculated OH contents represent only a best-possible estimation based on the data available.

Nonetheless, using mean compositions and a simplified formulation in which Zr* + REE* + Fe + NF = 1, where Zr * = Zr + Hf + Th + U; REE* = Sc + Y + (La to Lu); NF = Mg + Ca + Mn + Nb + Pb + Al, B = Si + Al + P + Ti = 1, and I = Na + K (interstitial), mean compositions (Table 3) can be defined for zircon from the bright and dark bands within each sample.

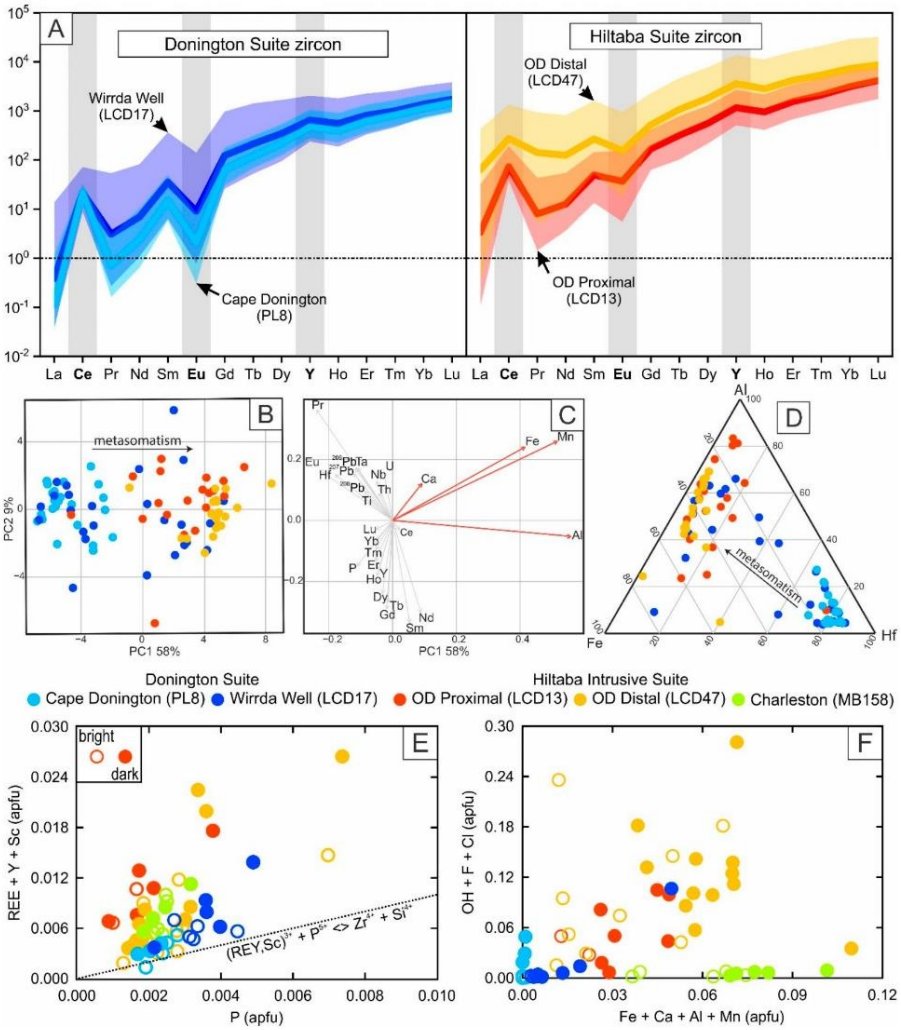


Figure 4. (**A**) LA-ICP-MS chondrite-normalized REY (REE + Y) fractionation trends for Donington Suite (light and dark blue) and Hiltaba Intrusive Suite (red and orange) samples. (**B** and **C**) PCA of LA-ICP-MS data, used to distinguish associated element signatures, and (**D**) a ternary Fe–Al–Hf diagram demonstrating the degree of zircon metasomatism (LA-ICP-MS data; Supplementary Materials B, Table S5). (**E**) Plot of $(REY+Sc)^{3+}$ versus P^{5+} (EPMA data). (**F**) Plot of "non-formula" components $\Sigma(Fe_2O_3 + Al_2O_3 + MnO + CaO)$ versus apfu $\Sigma(OH + Cl + F)$, respectively. The EPMA diagrams illustrate the relationship between substitution of both non-formulae elements and OH in zircon. Open and closed data points represent bright and dark bands in zircon, respectively; color codes correspond to samples in **A**–**D** (EPMA data; Supplementary Materials B, Table S4). See main text and Supplementary Materials A for additional explanation.

Table 2. EPMA zircon spot analyses. Gr1: grain 1; Gr2; grain2.

LCD13 (OD Proximal)		Na_2O	MgO	Al_2O_3	SiO_2	P_2O_5	K_2O	CaO	TiO_2	MnO	Fe_2O_3	Y_2O_3	ZrO_2	HfO_2	PbO	ThO_2	UO_2	Cl	Sum	H_2O *	Sum *
Bright		0.046	0.016	<mdl	32.57	0.039	0.011	0.076	0.01	0.035	0.822	0.023	63.834	2.355	0.036	<mdl	0.163	0.116	100.60	0.11	100.69
Bright		0.03	0.011	<mdl	32.165	0.064	<mdl	0.042	0.01	0.037	0.46	0.145	64.104	1.454	0.089	0.08	0.332	0.048	99.640	0.23	99.86
Mean	$n = 2$	0.038	0.014	<mdl	32.368	0.052	<mdl	0.059	0.01	0.036	0.641	0.084	63.969	1.905	0.063	<mdl	0.248	0.082	100.12	0.17	100.275
Dark		0.083	0.047	0.011	32.291	0.063	0.011	0.153	0.015	0.029	0.972	0.085	62.507	1.532	0.032	0.078	0.178	0.119	98.599	0.002	98.574
Dark		0.123	0.028	0.41	31.637	0.565	0.031	0.138	0.036	0.117	1.152	1.051	60.714	2.818	0.083	0.09	0.888	0.075	101.254	0.197	101.434
Dark		0.197	0.019	0.186	31.056	0.39	0.017	0.211	0.024	0.11	1.386	0.868	59.613	2.485	0.097	0.073	0.827	0.066	98.842	0.465	99.292
Dark		0.058	0.022	0.008	32.46	0.145	0.007	0.123	0.012	0.049	0.9	0.484	62.749	1.148	0.048	0.196	0.25	0.156	99.547	0.049	99.561
Dark		<mdl	0.021	0.021	32.218	0.082	0.011	0.185	0.008	0.071	0.956	0.12	63.205	1.385	0.048	0.122	0.21	0.379	99.705	0.149	99.769
Dark		0.067	0.013	0.007	31.601	0.034	0.016	0.085	0.008	0.068	0.912	0.029	62.204	2.855	0.048	<mdl	0.203	0.163	98.780	0.353	99.096
Dark		0.064	0.021	0.056	31.239	0.066	0.01	0.381	0.007	0.114	1.161	0.166	60.557	2.049	0.07	0.092	0.742	0.086	97.675	0.438	98.052
Mean	$n = 7$	0.099	0.024	0.1	31.786	0.192	0.015	0.182	0.016	0.08	1.063	0.4	61.65	2.039	0.061	0.109	0.471	0.149	99.20	0.236	99.397
LCD47 (OD Distal)		**Na_2O**	**MgO**	**Al_2O_3**	**SiO_2**	**P_2O_5**	**K_2O**	**CaO**	**TiO_2**	**MnO**	**Fe_2O_3**	**Y_2O_3**	**ZrO_2**	**HfO_2**	**PbO**	**ThO_2**	**UO_2**	**Cl**	**Sum**	**H_2O ***	**Sum ***
Bright (Gr2)		<mdl	0.017	0.132	31.645	0.113	0.006	0.032	0.043	0.059	0.227	0.317	67.091	1.379	0.03	0.103	0.145	0.008	101.963	1.194	103.156
Bright (Gr2)		0.074	0.023	0.122	31.294	0.072	0.008	0.535	0.024	0.153	1.807	0.211	61.755	1.399	0.042	0.117	0.219	0.076	98.399	0.877	99.259
Mean	$n = 2$	<mdl	0.02	0.127	31.47	0.093	0.007	0.284	0.034	0.106	1.017	0.264	64.423	1.389	0.036	0.11	0.182	0.042	100.181	1.036	101.208
Dark (Gr2)		0.036	0.027	0.18	30.965	0.115	0.006	0.427	0.009	0.143	1.44	0.167	61.61	1.402	0.03	0.051	0.111	0.147	97.233	0.651	97.851
Dark (Gr2)		0.046	0.03	0.196	31.273	0.054	0.006	0.435	0.038	0.174	1.333	0.043	61.692	1.736	0.037	0.023	0.12	0.089	97.565	0.467	98.012
Dark (Gr2)		0.059	0.033	0.838	30.827	0.136	0.012	0.792	0.018	0.262	1.948	0.553	58.456	1.225	<mdl	0.089	0.125	0.111	96.520	0.086	96.532
Mean	$n = 3$	0.047	0.03	0.405	31.022	0.102	0.008	0.551	0.022	0.193	1.574	0.254	60.586	1.454	0.034	0.054	0.119	0.116	97.106	0.401	97.465
Bright (Gr1)		<mdl	0.011	0.009	33.017	0.11	<mdl	0.01	0.011	<mdl	0.91	0.116	65.951	1.263	0.036	0.036	0.048	0.008	101.641	0.143	101.783
Bright (Gr1)		0.053	0.023	0.09	30.846	0.073	0.006	0.47	<mdl	0.138	1.177	0.113	61.442	1.618	0.04	0.058	0.188	0.099	96.740	0.645	97.335
Bright (Gr1)		0.111	0.032	0.143	31.561	0.266	0.011	0.329	0.007	0.202	1.348	0.486	60.903	1.602	0.042	0.042	0.286	0.066	98.095	0.149	98.193
Bright (Gr1)		<mdl	0.016	0.034	31.791	0.05	0.006	0.015	0.037	0.012	0.496	0.017	65.21	1.247	0.03	0.017	0.051	<mdl	99.214	0.465	99.679
Bright (Gr1)		<mdl	0.012	0.035	32.376	0.086	<mdl	0.024	0.007	0.019	0.381	0.057	65.094	1.416	0.025	0.024	0.037	0.009	99.780	0.072	99.850
Bright (Gr1)		<mdl	0.4	0.447	32.714	0.118	0.006	0.03	0.035	0.03	0.69	0.165	65.902	1.477	0.041	0.027	0.061	0.012	102.467	0.375	102.839
Bright (Gr1)		<mdl	0.02	0.1	32.199	0.108	<mdl	0.033	0.017	0.06	0.4	0.15	65.179	1.394	0.029	0.041	0.052	0.012	100.099	0.253	100.349
Mean	$n = 5$	<mdl	0.073	0.123	32.072	0.116	0.007	0.13	0.019	0.077	0.772	0.158	64.24	1.431	0.035	0.035	0.103	0.034	99.719	0.3	100.004
Dark (Gr1)		0.034	0.029	0.467	30.897	0.129	0.014	0.429	0.013	0.214	1.45	0.764	60.699	1.358	0.037	0.074	0.147	0.09	97.673	0.648	98.301
Dark (Gr1)		0.038	0.019	0.027	31.119	0.071	0.007	0.244	0.021	0.132	1.239	0.06	62.206	1.414	0.023	0.035	0.082	0.098	97.233	0.613	97.823
Dark (Gr1)		0.023	0.027	0.214	31.359	0.072	0.006	0.455	0.048	0.163	1.175	0.159	61.716	1.448	0.029	0.053	0.116	0.122	97.660	0.386	98.018
Dark (Gr1)		0.028	0.02	0.228	31.43	0.067	0.008	0.434	0.01	0.145	1.909	0.138	61.736	1.232	0.019	0.055	0.094	0.125	98.030	0.58	98.582
Dark (Gr1)		0.032	0.03	0.216	31.454	0.064	0.008	0.374	0.077	0.186	1.666	0.081	61.894	1.405	0.017	0.035	0.105	0.085	98.014	0.462	98.457
Dark (Gr1)		0.067	0.021	0.159	31.781	0.069	<mdl	0.442	0.006	0.171	1.413	0.087	62.024	1.258	0.025	0.042	0.085	0.065	98.042	0.232	98.233
Dark (Gr1)		0.098	0.028	0.262	31.635	0.288	0.014	0.512	0.029	0.189	1.74	0.937	60.734	1.349	0.032	0.101	0.276	0.067	99.357	0.468	99.748
Dark (Gr1)		0.06	0.039	0.335	30.747	0.061	0.009	0.478	0.083	0.191	1.774	0.094	63.446	1.476	0.038	0.03	0.134	0.069	99.311	1.397	100.692
Dark (Gr1)		0.094	0.023	0.073	30.481	0.12	<mdl	0.28	0.008	0.143	0.968	0.252	62.081	1.27	0.035	0.059	0.082	0.124	96.452	0.843	97.267
Mean	$n = 9$	0.053	0.026	0.22	31.211	0.105	0.009	0.405	0.033	0.17	1.482	0.286	61.837	1.357	0.028	0.054	0.125	0.094	97.975	0.625	98.569

Table 2. *Cont.*

MB158 (Charleston)		Na_2O	MgO	Al_2O_3	SiO_2	P_2O_5	K_2O	CaO	TiO_2	MnO	Fe_2O_3	Y_2O_3	ZrO_2	HfO_2	PbO	ThO_2	UO_2	Cl	Sum	H_2O	Sum *
Bright		<mdl	<mdl	0.036	33.001	0.099	0.008	0.175	0.04	0.129	1.292	0.224	65.185	1.353	0.051	0.148	0.13	0.016	102.381	0.032	102.41
Bright		0.032	0.016	<mdl	31.708	0.092	<mdl	0.674	0.052	0.188	2.082	0.147	63.283	1.32	0.049	0.081	0.12	0.046	100.153	0.005	100.147
Bright		0.058	0.007	0.02	31.93	0.087	0.007	0.66	0.06	0.087	1.704	0.108	63.229	1.393	0.046	0.042	0.107	0.034	99.980	0	99.973
Bright		0.048	0.053	0.164	32.152	0.096	0.005	0.933	0.031	0.144	1.224	0.273	62.378	1.536	0.038	0.038	0.154	0.063	99.842	0.022	99.85
Bright		0.033	0.012	0.013	32.399	0.083	0.007	0.253	0.027	0.175	1.02	0.114	64.156	1.524	0.036	0.038	0.148	0.016	100.366	0.005	100.368
Mean	$n = 5$	0.043	0.022	0.058	32.238	0.091	0.007	0.539	0.042	0.145	1.464	0.173	63.646	1.425	0.044	0.069	0.132	0.035	100.544	0.013	100.55
Dark		0.044	0.019	0.035	31.646	0.095	0.007	1.115	0.029	0.133	1.784	0.206	62.498	1.21	0.057	0.124	0.143	0.06	99.657	0.016	99.659
Dark		0.04	0.016	0.073	32.077	0.124	<mdl	1.399	0.055	0.153	2.203	0.355	61.528	1.16	0.045	0.232	0.147	0.064	100.175	0.029	100.189
Dark		<mdl	0.016	0.013	31.92	0.082	<mdl	0.677	0.064	0.176	2.211	0.19	62.89	1.375	0.032	0.121	0.16	0.047	100.293	0.024	100.306
Dark		0.062	0.012	0.01	31.372	0.07	<mdl	0.981	0.014	0.219	1.306	0.102	61.879	1.397	0.036	0.046	0.15	0.052	98.0480	0	98.037
Dark		0.033	0.017	0.083	31.403	0.081	0.007	1.033	0.014	0.163	1.281	0.113	61.841	1.523	<mdl	0.084	0.154	0.049	98.317	0.014	98.32
Mean	$n = 5$	0.045	0.016	0.043	31.684	0.09	<mdl	1.041	0.035	0.169	1.757	0.193	62.127	1.333	0.043	0.121	0.151	0.054	99.298	0.017	99.302
PL8 (Cape. Don)		Na_2O	MgO	Al_2O_3	SiO_2	P_2O_5	K_2O	CaO	TiO_2	MnO	Fe_2O_3	Y_2O_3	ZrO_2	HfO_2	PbO	ThO_2	UO_2	Cl	Sum	H_2O *	Sum *
Bright		<mdl	0.008	<mdl	32.518	0.107	<mdl	<mdl	0.005	<mdl	<mdl	0.15	65.716	1.233	0.023	0.027	0.035	<mdl	100.06	0.012	100.071
Bright		<mdl	0.01	0.008	32.801	0.092	<mdl	<mdl	0.007	0.012	0.026	0.039	65.94	1.392	0.019	0.015	0.021	<mdl	100.589	0.003	100.592
Bright		<mdl	<mdl	<mdl	32.646	0.097	<mdl	0.01	<mdl	<mdl	<mdl	0.075	65.891	1.275	0.038	0.03	0.064	<mdl	100.396	0.009	100.405
Bright		<mdl	<mdl	<mdl	32.759	0.074	<mdl	<mdl	0.012	<mdl	<mdl	0.034	65.863	1.334	0.026	0.02	0.045	<mdl	100.249	0	100.249
Mean	$n = 4$	<mdl	<mdl	<mdl	32.681	0.093	<mdl	<mdl	0.008	<mdl	<mdl	0.075	65.853	1.309	0.027	0.023	0.041	<mdl	100.324	0.006	100.329
Dark		<mdl	0.009	<mdl	31.997	0.077	<mdl	<mdl	0.01	<mdl	0.032	0.028	65.14	1.326	0.03	<mdl	0.012	<mdl	98.907	0.142	99.049
Dark		<mdl	0.008	<mdl	32.423	0.09	<mdl	<mdl	0.006	<mdl	<mdl	0.038	65.806	1.41	<mdl	<mdl	0.016	<mdl	100.114	0.092	100.206
Dark		<mdl	<mdl	<mdl	32.005	0.065	<mdl	<mdl	0.008	<mdl	0.041	0.025	65.502	1.326	0.023	<mdl	0.015	<mdl	99.233	0.239	99.472
Mean	$n = 3$	<mdl	0.009	<mdl	32.142	0.077	<mdl	<mdl	0.008	<mdl	0.037	0.03	65.483	1.354	0.027	<mdl	0.014	<mdl	99.418	0.158	99.576
LCD17 (Wirrda Well)		Na_2O	MgO	Al_2O_3	SiO_2	P_2O_5	K_2O	CaO	TiO_2	MnO	Fe_2O_3	Y_2O_3	ZrO_2	HfO_2	PbO	ThO_2	UO_2	Cl	Sum	H_2O *	Sum *
Bright		<mdl	0.011	<mdl	32.758	0.104	<mdl	0.018	0.006	<mdl	0.197	0.093	64.529	1.288	0.031	0.026	0.051	<mdl	99.548	0.021	99.568
Bright		<mdl	0.013	<mdl	32.77	0.172	<mdl	<mdl	0.009	<mdl	0.161	0.108	64.598	1.265	0.028	0.027	0.048	<mdl	99.515	0.006	99.521
Bright		<mdl	0.012	<mdl	32.874	0.125	<mdl	<mdl	0.008	<mdl	0.128	0.092	65.057	1.343	0.034	0.027	0.045	0.009	99.970	0.007	99.975
Bright		<mdl	<mdl	<mdl	32.789	0.121	<mdl	<mdl	0.01	<mdl	0.236	0.083	65.159	1.389	0.034	0.025	0.047	<mdl	100.179	0.009	100.188
Bright		<mdl	0.015	<mdl	32.735	0.129	0.007	0.012	0.006	<mdl	0.105	0.089	65.159	1.31	0.019	0.031	0.059	<mdl	100.028	0.013	100.041
Mean	$n = 5$	<mdl	0.013	<mdl	32.785	0.13	<mdl	<mdl	0.008	<mdl	0.165	0.093	64.9	1.319	0.029	0.027	0.05	<mdl	99.848	0.011	99.859
Dark		0.027	0.031	0.22	31.317	0.188	0.008	0.26	0.014	0.085	1.338	0.368	62.109	1.282	0.038	0.066	0.108	0.081	98.193	0.498	98.673
Dark		0.036	0.017	<mdl	32.724	0.138	0.006	0.046	0.006	0.038	0.471	0.202	63.7	1.383	<mdl	0.05	0.077	0.052	99.383	0.016	99.388
Dark		0.035	0.013	<mdl	32.421	0.139	0.007	0.029	0.008	0.042	0.743	0.112	64.242	1.334	0.03	0.033	0.081	0.027	99.775	0.062	99.831
Dark		<mdl	0.010	<mdl	33.089	0.084	0.007	0.01	0.009	<mdl	0.272	0.053	65.846	1.245	0.026	<mdl	0.037	<mdl	100.893	0.006	100.9
Dark		<mdl	0.008	<mdl	32.259	0.152	<mdl	0.011	0.006	0.012	0.162	0.116	64.684	1.204	0.034	0.016	0.054	<mdl	99.062	0.011	99.072
Mean	$n = 5$	0.033	0.016	<mdl	32.362	0.140	0.007	0.071	0.009	0.044	0.597	0.17	64.116	1.29	0.032	0.041	0.071	0.053	99.461	0.119	99.573
average mdl		0.023	0.007	0.006	0.021	0.010	0.005	0.009	0.004	0.011	0.024	0.008	0.049	0.101	0.014	0.010	0.011	0.007			

Sum *: Sum of element totals including calculated H_2O (H_2O*) and corrected for F and Cl. Sc, Nb, and F were measured but are generally below the mdl. Full values for these elements and REY elements are included in Supplementary Materials B, Table S4. Formulae calculation values and α-decays/mg values are in Supplementary Materials B, Table S4.

Table 3. Mean zircon compositions in bright and dark bands in each studied sample.

Lithology and Location	Sample ID	Zircon Composition
Cape Donington, Donington Suite	PL8	Bright: $(Zr^*_{0.994}REE^*_{0.001})_{\sum=0.995}(Si_{1.002}P_{0.002}O_4)$;
		Dark: $(Zr^*_{0.996}Fe_{0.001}REE^*_{0.003})_{\sum=1}(Si_{0.986}P_{0.002}O_{3.95})(OH)_{0.049}$.
Wirrda Well, Donington Suite	LCD17	Bright: $Zr^*_{0.979}Fe_{0.004}REE^*_{0.006}NF_{0.001})_{\sum=0.989}(Si_{1.006}P_{0.005}O_{3.966})(OH)_{0.001}$;
		Dark: $i_{0.002}(Zr^*_{0.943}Fe_{0.031}REE^*_{0.014}NF_{0.013})_{\sum=1}(Si_{0.962}Al_{0.008}P_{0.005}O_{3.862})(OH,Cl)_{0.106}$.
OD-distal Hiltaba Suite	LCD47	Bright: $(Zr^*_{0.986}Fe_{0.009}REE^*_{0.003}NF_{0.002})_{\sum=1}(Si_{0.993}Al_{0.001}P_{0.002}O_{3.978})(OH,Cl)_{0.015}$;
		Dark: $i_{0.004}(Zr^*_{0.934}Fe_{0.04}REE^*_{0.004}NF_{0.022})_{\sum=1}(Si_{0.915}Al_{0.012}P_{0.002}Ti_{0.002}O_{3.672})(OH,Cl)_{0.281}$.
OD-proximal Hiltaba Suite	LCD13	Bright: $i_{0.003}(Zr^*_{0.97}Fe_{0.019}REE^*_{0.007}NF_{0.004})_{\sum=1}(Si_{0.993}P_{0.001}O_{3.959})(OH,Cl)_{0.028}$;
		Dark: $i_{0.004}(Zr^*_{0.942}Fe_{0.027}REE^*_{0.013}NF_{0.018})_{\sum=1}(Si_{0.972}Al_{0.002}P_{0.002}O_{3.864})(OH,F,Cl)_{0.105}$.
Charleston Granite, Hiltaba Suite	MB158	Bright:$(Zr^*_{0.962}Fe_{0.019}REE^*_{0.009}NF_{0.009})_{\sum=0.999}(Si_{0.985}Al_{0.001}P_{0.003}Ti_{0.001}Fe_{0.01}O_{3.969})(OH,Cl)_{0.007}$;
		Dark: $i_{0.003}(Zr^*_{0.941}Fe_{0.009}REE^*_{0.009}NF_{0.041})_{\sum=1}(Si_{0.964}Al_{0.001}P_{0.003}Fe_{0.031}O_{3.933})(OH,Cl)_{0.006}$.

Note: All granite samples, with the exception of PL8, show various degrees of alteration (see above). The presented compositions are for grains that were micro-sampled for S/TEM analysis. * To obtain a good stoichiometry between the A and B sites, we used a slightly modified procedure for calculating the formulae of the Charleston zircon, in which Fe was allocated in both A and B sites.

The lack of Fe or other non-formula elements and Cl is of note in the Cape Donington zircon, implying these elements were not of magmatic origin. The relatively high OH content in these otherwise less altered zircons may be an artefact of the calculation rather than real and lies within analytical precision of the EPMA method. Critical for the narrative of this contribution, zircon from all three altered granites from the Olympic Cu–Au Province (two of Hiltaba age, one of Donington age) display concomitant enrichment in Fe and other NF elements and in (OH, Cl, F) in the darker bands and over those in unaltered zircon (PL8), in full agreement with the nanoscale observations. Concentrations of other minor (magmatic) elements remain unchanged (within analytical error).

A plot of the main "non-formula" components, and Fe versus OH + Cl + F (Figure 4F) showed a strong correlation for all altered zircon, except Charleston. Mean compositions and empirical formulae for each sub-population are given in Supplementary Materials B, Table S4.

5.4. Distribution of Minor Elements: Micron- to Nanoscale Patterns

The presence of Fe and Cl in zircon was also assessed by EPMA mapping of zircon in two samples: Wirrda Well (LCD17) and OD-proximal (LCD 13). The maps show excellent positive correlation between the two elements in the crystal zoning of Wirrda Well zircon (Figure 5A,B) but antipathetic patterns for OD proximal zircon (Figure 5C,D). The OD proximal zircon displays a combination of primary and overprinting textures in which the oscillatory zoning is only preserved on the rims, whereas the middle part of the grain is affected by fractures and re-crystallization obliterating primary zoning (Figures 3B and 5C,D).

Imaging in HAADF STEM mode depicts oscillatory zoning as bright and dark bands relating to non-formula elements in all foils shown in this study (Table 1), except the Cape Donington zircon (Foil #6). Superimposed mottled textures in the darker bands were only observed in zircon from the Olympic Cu–Au Province. Mapping using STEM EDS showed Fe banding in all zircons except Cape Donington. In the latter, the oscillatory zoning was related to trace elements typical of magmatic zircon (REY, actinides), the concentrations of which were below the detection limits of the EDS STEM method but readily mappable by LA-ICP-MS (Figure 2F; Supplementary Materials C, Figure S2). In contrast, the Wirrda Well–Donington zircon displayed an excellent correlation between micron and nanoscale oscillatory zoning patterns with respect to Fe, as shown by both EPMA and STEM EDS mapping (Figure 5A,B and Figure 6). The Fe distribution, however, did not reveal the mottled texture in the darker Fe-rich bands or veinlets crosscutting the brighter bands, as observed in the HAADF STEM images (Figure 6C).

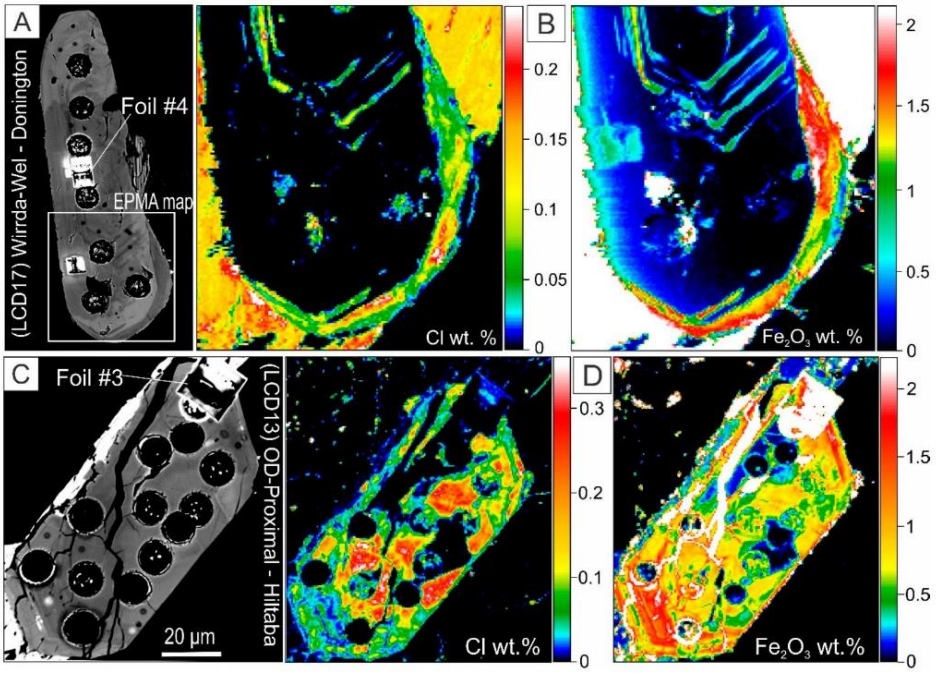


Figure 5. (**A**) BSE image of oscillatory-zoned Wirrda Well–Donington Suite zircon (sample LCD17) that was dated (LA-ICP-MS craters) and used for nanoscale study (foil location as marked). (**B**). EPMA maps for Cl and Fe_2O_3 (in wt.%), showing that both elements appear homogeneously enriched and positively correlated with one another within oscillatory bands. (**C**,**D**) BSE image and EPMA maps for Cl and Fe_2O_3 (wt.%) of OD proximal zircon (sample LCD 13; foil marked at the top). Note the high concentrations of both elements within the middle part which was affected by fractures and re-crystallization. In contrast, crystal zoning on the rim shows inverse correlation between the two elements (e.g., banding intersecting the FIB cut).

The most varied chemistry mapped at the nanoscale was observed in zircon from the Charleston Granite (Figure 7A). Banding with respect to Fe, Ca, Ti, Al, Y, and Th was recorded outside of a magmatic domain, itself defined by faint oscillatory banding expressed by variation in major element concentration as shown by O, Si, and Zr maps. No mottled textures were present throughout such chemically complex bands. The EDS STEM maps also showed that Fe displayed a sharp boundary against the magmatic domain, contrasting with the diffuse boundaries shown by the other trace elements. All these elements, including U (but not Pb), were enriched within a fracture around the magmatic domain, and within a fine particle inclusion hosted at the diffuse boundary (Figure 7A). The fracture, leading towards this U-bearing fine particle, was represented by a rectangular network of dark nanodomains that hosted pores (Figure 7B–D). These domains were nonetheless crystalline, albeit disordered and with slightly different orientation relative to one another and to host zircon.

The best example of mottled textures throughout oscillatory banding with respect to Fe (Ca, Cl) was shown by the least altered grain in OD distal zircon (Foil #1; Figure 8A). The HAADF STEM image of the foil mimics the BSE image (Figure 2A,C) with respect to the mottled textures throughout the banding. Relative to the generally homogenous distribution of Fe and Ca throughout a given band, the Cl map shows distinct spots of higher concentration. This was exemplified by the signals for Ca and Cl along a profile (Figure 8B). Likewise, variable correlations were seen between the high Cl areas and concentration of major elements, O and Zr, as shown on the EDS STEM maps obtained from mottled areas (Figure 8C). The highly altered zircon grain (Foil #2) showed two distinct domains:

(i) weakly-banded and mottled and (ii) cleaner domains that were strongly enriched in Ca, Fe, and Al. The latter surrounds veinlets of xenotime displaying enrichment in HREE and U (Supplementary Materials C, Figure S3).

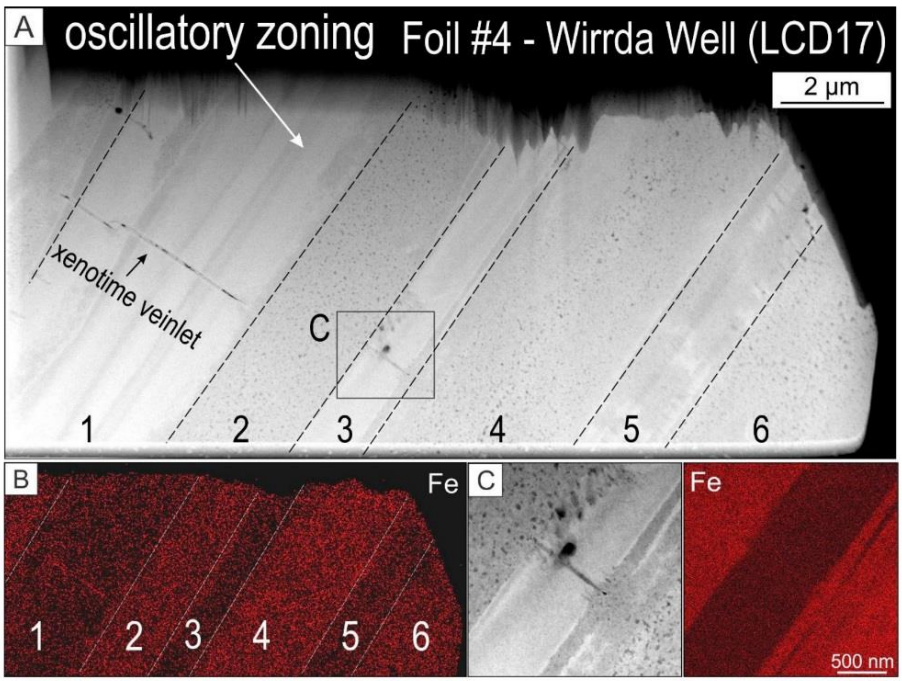


Figure 6. (**A**) HAADF STEM images (**A** and **C**) and EDS STEM maps for Fe (**B** and **D**) for Wirrda Well-Donington zircon showing crystal oscillatory zoning (**A** and **B**). The dark bands (even numbers) were enriched in Fe and show mottled texture in the image, but not on the Fe map (**B**). Note that the oscillatory banding was crosscut by a xenotime-bearing veinlet (extended map shown in Supplementary Materials C, Figure S3). (**C**,**D**) Higher resolution maps showing the interface between light and dark bands confirmed that the mottled texture (**C**) was not reflected in the Fe distribution (**D**).

Olympic Dam proximal zircon (Foil #3) displayed a combination of primary and overprinting textures correlating with minor trace element patterns (Figure 9). In depth, the foil revealed a subsurface 5 µm-diameter inclusion of hematite (Figure 9B–D), as well as oscillatory banding with mottled textures of variable density. As in the OD distal zircon, Fe was evenly distributed throughout the bands, whereas Cl appeared more heterogeneous (Figure 9E,F). In detail, the Fe-poor bands were crosscut by Fe-rich veinlets (Figure 9F). The largest areas of Cl-enrichment were observed in parts of the Fe-rich bands but typically did not correspond to the crosscutting Fe-rich trails. Such patterns of Fe and Cl explain the inverse trends mapped at the micron-scale in the same grain (Figure 5C,D).

5.5. Mottled Areas: Nanoparticles to Fine Particles of Chloro–Hydroxy–Zircon

The nature of the mottled areas (identified in foils as listed in Table 1) relative to Cl-enrichment and substitution mechanisms for zircon was addressed by EDS spot analysis and mapping at various resolutions (Figures 10 and 11). Higher resolution maps of one Cl-rich area selected from Figure 8C reproduced the same variability between major elements and Cl (and remarkably little variation in terms of minor elements) in the particles observed as dark nanodomains on HAADF STEM image (Figure 10A). An inverse correlation between O and Zr corresponded to either diffuse or stronger Cl concentration, whereas the strongest Cl concentrations were not reflected by major element variation.

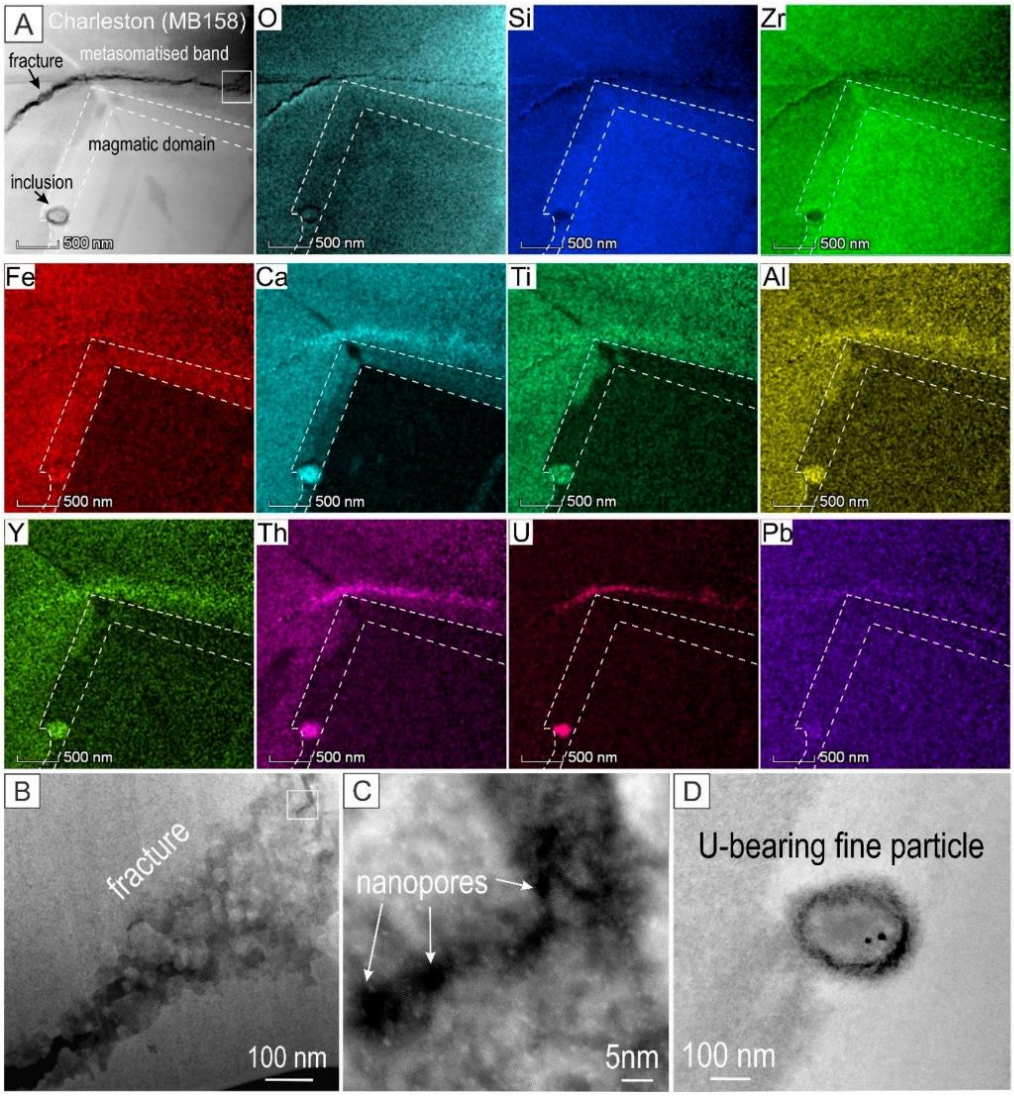


Figure 7. (**A**) HAADF STEM image and EDS STEM element maps of Charleston zircon (Foil #6) showing enrichment in trace elements outside of a magmatic domain as marked. Note the sharp boundary (dashed lines) for Fe but not the other elements, which instead display a diffuse boundary. Trace element (re)mobilization (all elements except Fe) along this boundary was observed along the adjacent fracture and the U-bearing fine particle. (**B**–**D**) HAADF STEM images showing zircon details along the fracture as marked. The U-bearing fine particle (**D**) displayed a dark rim and was beam-sensitive, indicating that it was most likely amorphous (it could not be imaged at high-resolution due to the thickness of the foil at this location). The image in (**B**) is the inset box indicated on (**A**), and image (**C**) shows the inset box indicated on (**B**). Image (**D**) shows detail of the inclusion from image (**A**).

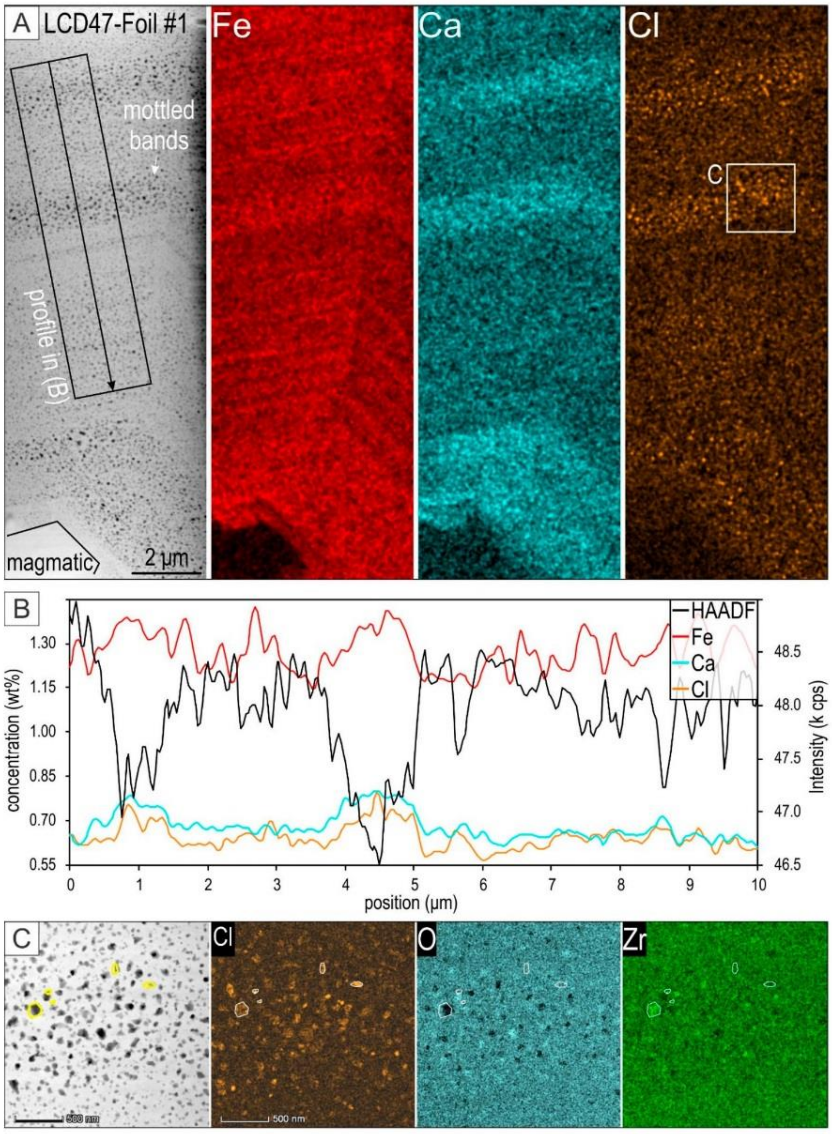


Figure 8. Trace element distributions in OD distal zircon from Foil #1. (**A**) HAADF STEM image and EDS STEM maps for Fe, Ca, and Cl showing oscillatory zoning and mottled textures. Enrichment in Ca and Cl occurred throughout the mottled bands. (**B**) Profile across the oscillatory zoning displayed positive correlation between Ca and Cl across the most intensively mottled bands. Iron distributions broadly correlated with Ca and Cl across the same bands but showed small-amplitude variation reflecting the finest-scale oscillatory banding. The HAADF intensity signal showed a negative correlation with the Ca- and Cl-enriched bands. (**C**) Image and EDS STEM maps (extended maps in Supplementary Materials C, Figure S3) of a Cl-rich area as marked in (**A**). Note the inconsistency in correlation between Cl with O and Zr (compare the areas outlined on the figure), e.g., high Zr and low-O where Cl-enrichment is moderate, but no changes for O and Zr for nanodomains with the highest Cl content.

The highest Cl concentration was recorded from the smallest particles (10–30 nm-diameter) of grey color, (Foil #1; Figure 10B). A profile across one of the darker particles shows that Cl was concentrated

at the edge of the particle (Figure 10C). The HAADF signal intensity and O decreased across the boundary of the particle, whereas major and minor elements displayed a slight increase. These results can also be associated with variable particle thickness, their position relative to the plane of imaging, or the presence of voids/pores, particularly for the coarser and darkest domains. Comparative imaging of the same area in both HAADF and bright-field STEM modes illustrates these features (Supplementary Materials C, Figure S1). Such voids could, however, also have been produced via the plucking out of coarser particles during ion milling.

The morphology and size of the particles throughout samples with mottled textures (Foils #1–5) varies from several nm up to 100 nm (nanoparticles) to hundreds of nm (fine particles) (Figure 11A). The largest particles, with well-defined geometrical shapes, can include pores, whereas cross-cutting darker veins will show numerous defects when imaged at high resolution (see below). Energy-dispersive X-ray maps of one medium-sized particle showed strong (lower and higher) variation in O and Zr concentrations relative to host zircon; no variation in Si was recorded (Foil #1; Figure 11B). Weak enrichment in Cl and U was present whereas Ca-rich nanoparticles occurred just outside, along the edge of the mapped particle. Overall, these results suggest that the main substitution involved replacement of O by OH^- and/or Cl leading to chloro–hydroxy–zircon formation. Although substitution of $(SiO_4)^{4-}$ tetrahedra by $4(OH,Cl)^-$ can also be invoked, such a relationship is not obvious from the EDS mapping.

5.6. Atomic-Scale HAADF STEM Imaging—Zircon Crystallinity and Lattice-Scale Defects

Four main zone axes in zircon were imaged throughout the seven foils (Table 1; Figure 12A–D). In each case, imaging showed the same overall orientation across zircon in any given foil, indicating that the chemically heterogenous domains were an integral part of the same single crystal. Despite observing evidence of lattice disorder, zircon in all samples was found to be crystalline with no amorphous areas identified. This absence of amorphous domains was observed in both the brighter bands of magmatic zircon from Cape Donington, throughout the darker or mottled bands in all other samples, and in the proximity of fractures containing newly formed phases such as xenotime.

Atomic arrangements on HAADF STEM images for the four zone axes shown in Figure 12 were interpreted using crystal structure models obtained after indexing of the Fast Fourier Transform (FFT) obtained for each image and also STEM simulations (Figure 13). These show that the brightest spots represent an overlap between Zr and Si atoms on (001) and $(1\bar{1}0)$ zone axes (Figure 13A,B), whereas both Zr (brightest, with dumbbell arrangement) and Si (darker) atoms can be resolved on the (100) and $(1\bar{1}1)$ zone axes (Figure 13C,D). There was a relatively good fit between the HAADF STEM images and simulations in each case. Such image assessment of individual zone axes by HAADF STEM was necessary to identify the presence of lattice-scale defects.

Lattice-scale defects on $(1\bar{1}1)$ zone axis in zircon were observed along a veinlet crosscutting a fine particle in Foil #1 (darker color on HAADF STEM images; Figure 14A–D). One of the defects had a hexagonal shape (Figure 14D) and showed clear modifications in both size and intensity of individual atoms relative to "normal" zircon on this zone axis (Figures 12D and 13D). An intensity profile showed changes across this defect which were interpretable as substitutions of individual Zr and Si atoms along the (011) direction (Figure 14E). Signals for Zr decrease within the defect suggesting substitution by lighter cations (e.g., Ca, Al) in variable proportions. One of the Si sites in the defect showed a higher signal relatively to host zircon, whereas the other was barely visible (correlating with darkest areas on the image). Substitution within the $(SiO_4)^{4-}$ tetrahedra can be invoked in which Me^{5+} (e.g., P^{5+}) replaces Si^{4+}, necessitating charge balance via substitution of $(OH,Cl)^-$ for O^{2-}.

Lattice-scale defects were imaged on all zone axes in zircon except $(1\bar{1}0)$ (Figure 15). In magmatic zircon from Cape Donington (Foil #7), lattice disorder was found in the brighter U-richer bands (Supplementary Materials B, Table S4; Figure 2F). Square-shaped defects on the $(100)_{zircon}$ zone axis appear darker and showed arrays of single Zr (and Si—although these were less well resolved on the image) columns along the c-axis, which were doubled in the b direction leading to a smaller, squarish arrangement (outlined in Figure 15A).

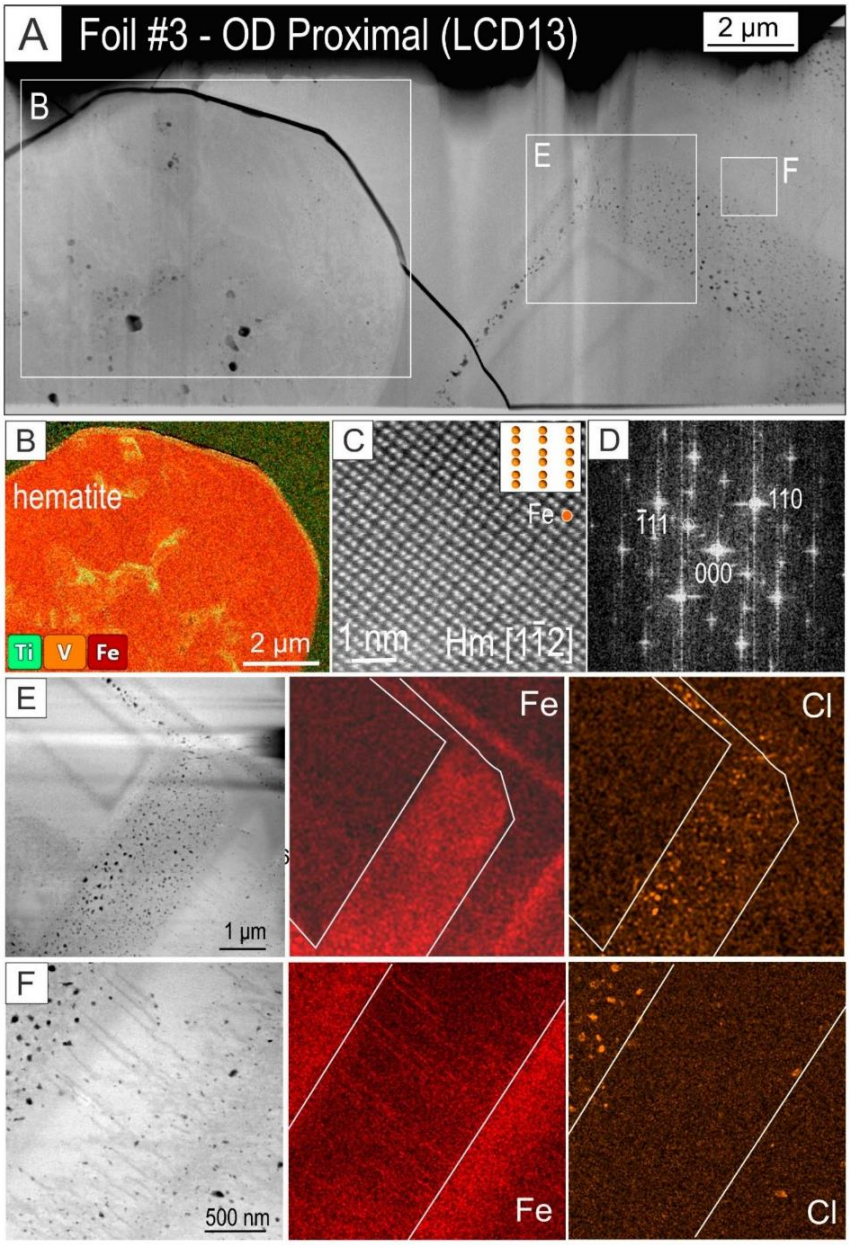


Figure 9. Trace element distributions in OD proximal zircon (Foil #3). (**A**) HAADF STEM image showing oscillatory banding, mottled textures, and an inclusion of hematite in zircon. High field strength element (HFSE) enrichment in hematite shown on the EDS STEM map in (**B**). Identification of hematite from the atomic-scale resolution image in (**C**) and Fast Fourier Transform (FFT) in (**D**) as marked. (**E**,**F**) HAADF STEM images and EDS STEM maps obtained from areas as marked on (**A**) (rotated 90 degrees clockwise) showing Fe and Cl enrichment throughout the mottled bands. Note the irregular distribution of Cl relative to Fe in both (**E**) and (**F**). Importantly, the Fe map in (**F**) shows Fe-rich veinlets crosscutting brighter bands.

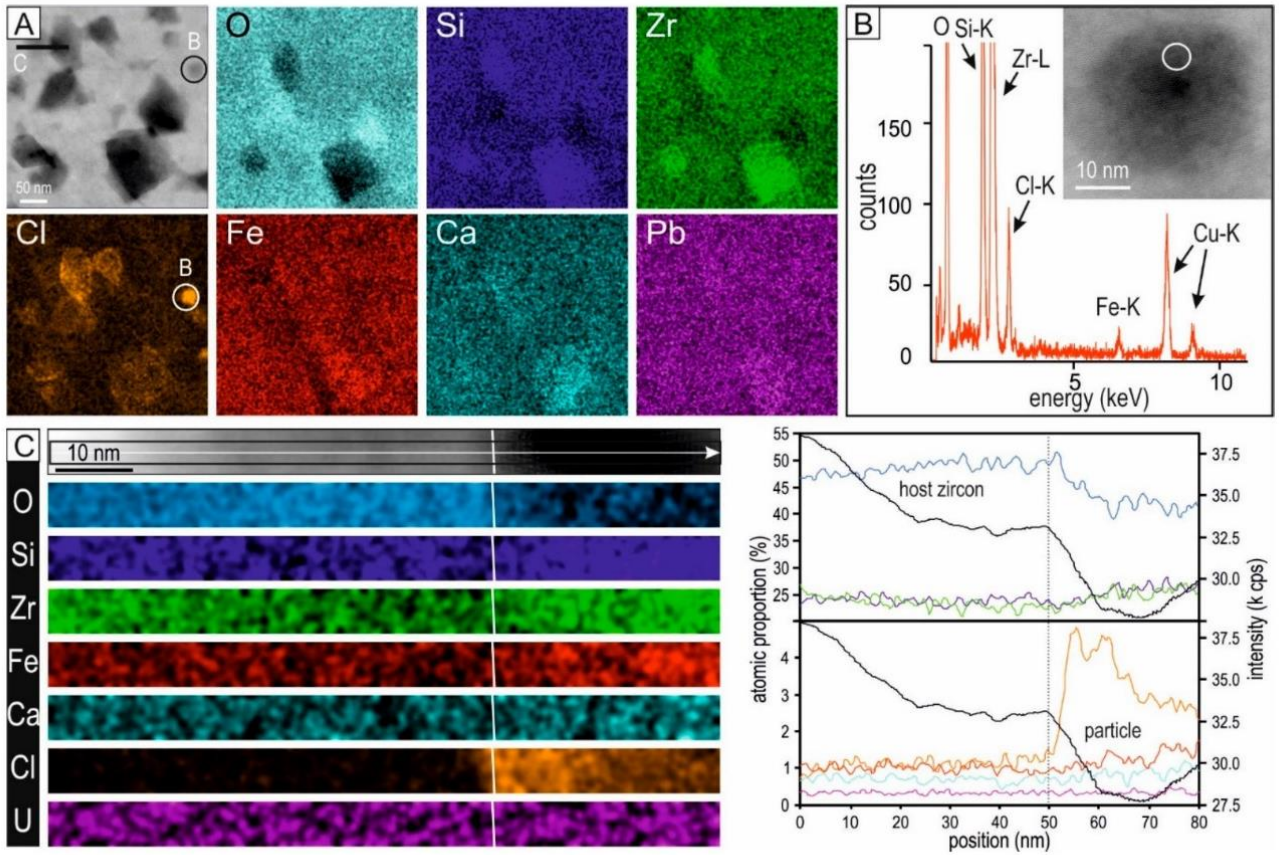


Figure 10. Aspects of nanoscale inclusions + pores throughout the mottled bands in the OD distal zircon (Foil #1). (**A**) Image and EDS STEM maps for a Cl-rich area selected from Figure 8C showing that the highest Cl was recorded in the smallest particles with no differences on the major or trace elements maps. Inverse correlation between O and Zr was recorded for the coarser, darkest inclusions with moderate enrichment in Cl. Note the weak variation in Fe and Ca, but not in Pb. (**B**) EDS spectrum for Cl-richest nanoparticle circled in (**A**). (**C**) EDS STEM maps (left) and profiles (right) across a particle with medium Cl-enrichment in (**A**). Profiles show high concentrations of Cl at the particle margin with increases in both major and minor elements but a strong HAADF signal decrease.

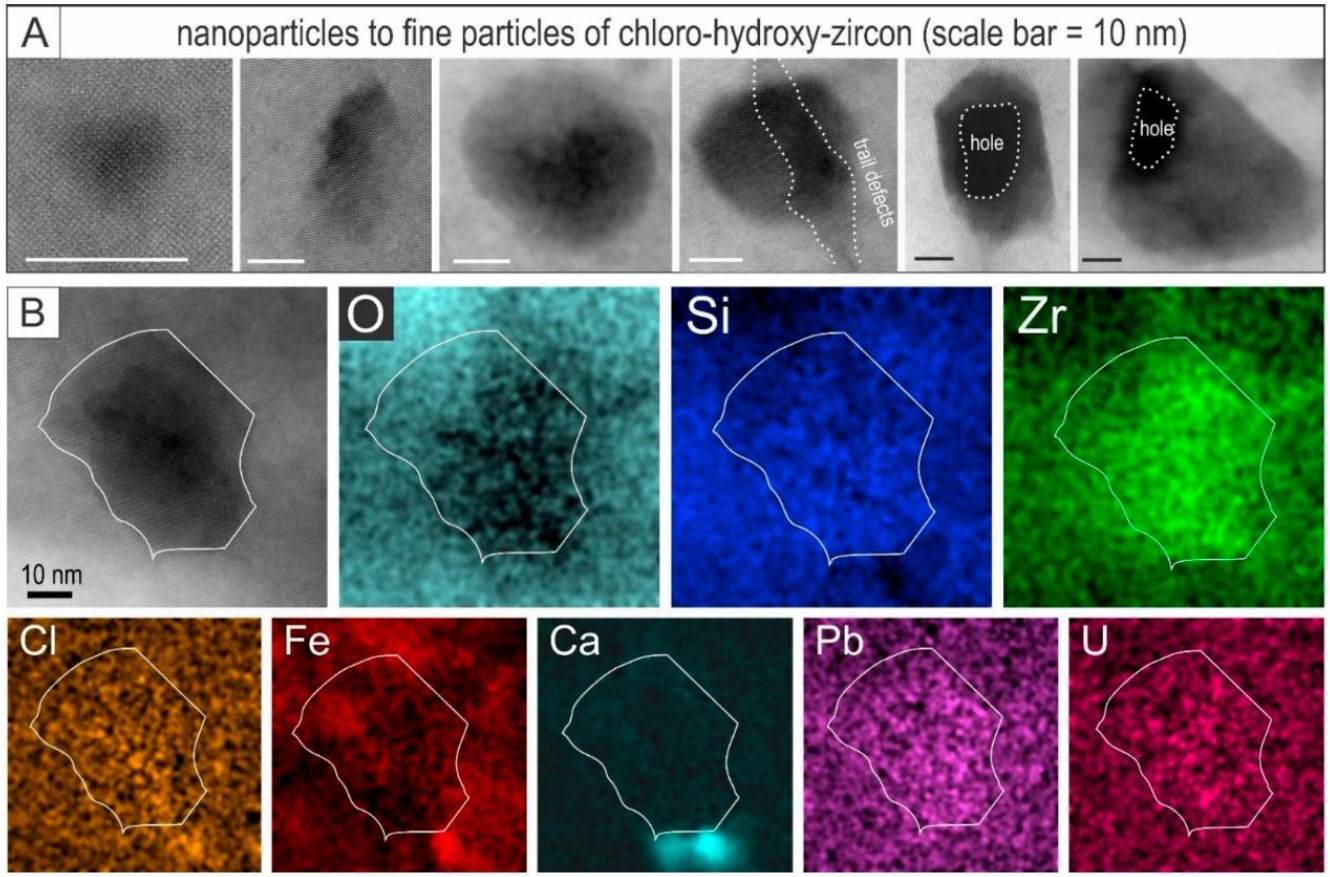


Figure 11. (**A**) HAADF STEM images of inclusions representative of all samples with mottled textures showing their variation in size and morphology as marked. Note the presence of rounded pores in the coarsest particles. (**B**) Image and EDS STEM maps of a single particle from the OD distal zircon (Foil #1). Note the strong variation in O and Zr concentration but not Si relative to host zircon and the weak relative enrichment in Cl, U, and Pb. Ca-rich nanoparticles occur just outside, at the lower edge of the mapped particle.

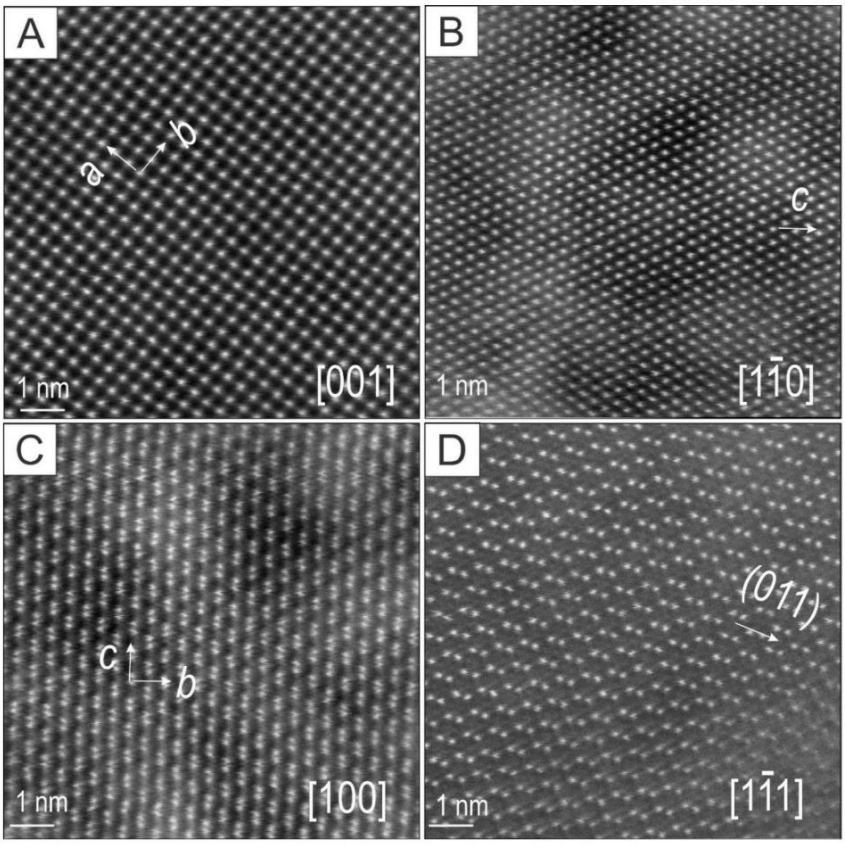


Figure 12. (**A**–**D**) High-resolution HAADF STEM images of zircon on four main zone axes as marked.

Linear defects were observed along the edge of xenotime veinlets (e.g., Wirrda Well–Donington zircon; Figure 15B). Atom displacement across the two sides of the defect can be interpreted as resulting from a simple screw dislocation considering the "atom loop" observed on the defect plane. The "loop" is illustrated by the atoms placed between the two planes with different heights relative to one another across the defect (smaller size atoms highlighted in Figure 15B). Linear defects along kink faults were imaged on (001) zone axis in Charleston zircon (Figure 15C). In this case, the fault steps/widths changed irregularly, as shown by the presence or absence of "atom loops" on the defect plane (overlays on Figure 15C). Wider planar defects, tens of nm in width, also occurred in the Charleston zircon (Figure 15D). This image can also be interpreted as a simple screw dislocation (yellow lines in Figure 15D). Interstitial atoms were inferred within the defect area only. Their size and brightness changed relative to the Zr and Si atoms on the (001) zone axis in zircon outside the defect area. Such changes could reflect differences in atom heights between the two planes on either side of the defect, or more speculatively, could be attributed to the presence of foreign atoms occurring interstitially in the zircon lattice (mixed site Ti, Ca, Th, Y, etc.). The latter supposition can be correlated with the presence of mixed sites of Ti, Ca, Th, Y, etc., as is known from zirconolite ($CaZrTi_2O_7$).

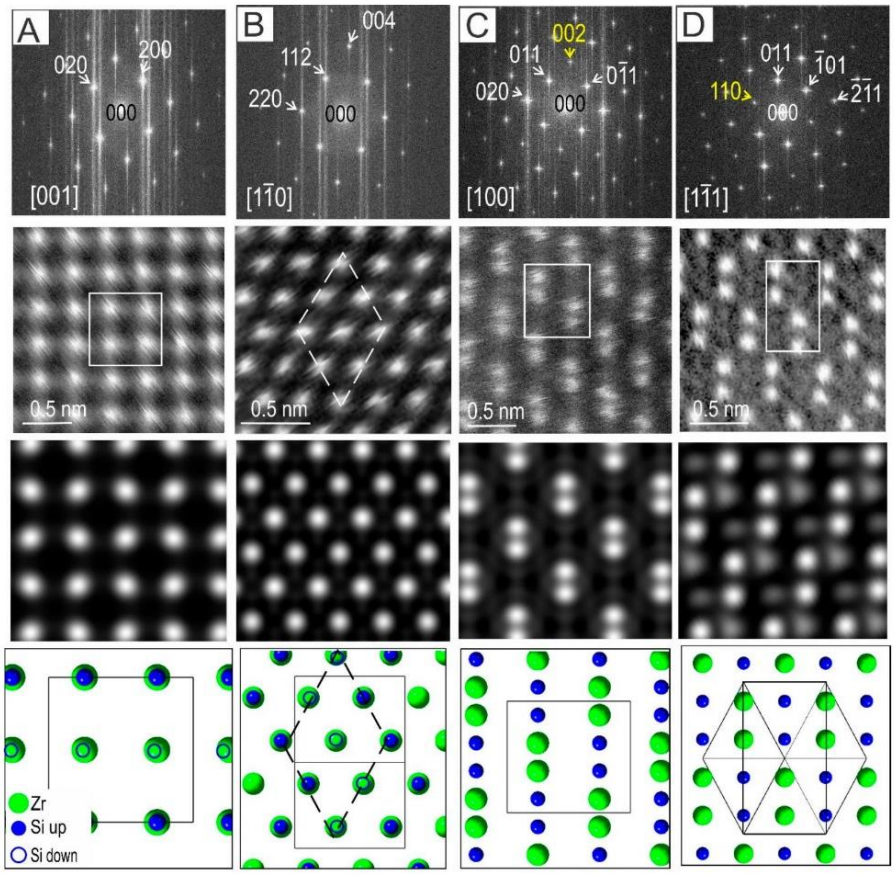


Figure 13. From top to bottom, FFT, HAADF image, STEM simulation, and crystal structure model for each of the main zone axes (**A–D**, as marked) imaged in zircon (Figure 12). The images and simulations were interpreted in agreement with crystal structure models on zone axes as obtained from indexing FFTs obtained from images in Figure 11. The two zone axes with dumbbell atomic arrangements (**C**,**D**) cannot be resolved using the ideal space group for zircon, $I4_1/amd$, due to the presence of forbidden reflections ($00l$; $l \neq 4n$ and $hh0$; $l \neq 4n$; marked in yellow). Indexing, crystal models, and STEM simulations were obtained using the $I2_12_12_1$ space group. The models and simulations did not change when using the $I4_1/amd$ space group.

The most complex defects were imaged in Fe-rich bands from OD distal zircon in the $[1\bar{1}1]$ zone axis (Foil #1; Figure 15E). In this case, changes in the atomic arrangement along the (011) can be interpreted as displacements with anti-phase modulation along fault planes (yellow lines in Figure 15E. In contrast, the defect within the fine particle described above (Figures 14D and 15F) can be interpreted as the result of local fluid–mineral interaction leading to an increase in OH/halogen content in the nanoparticles/fine particles.

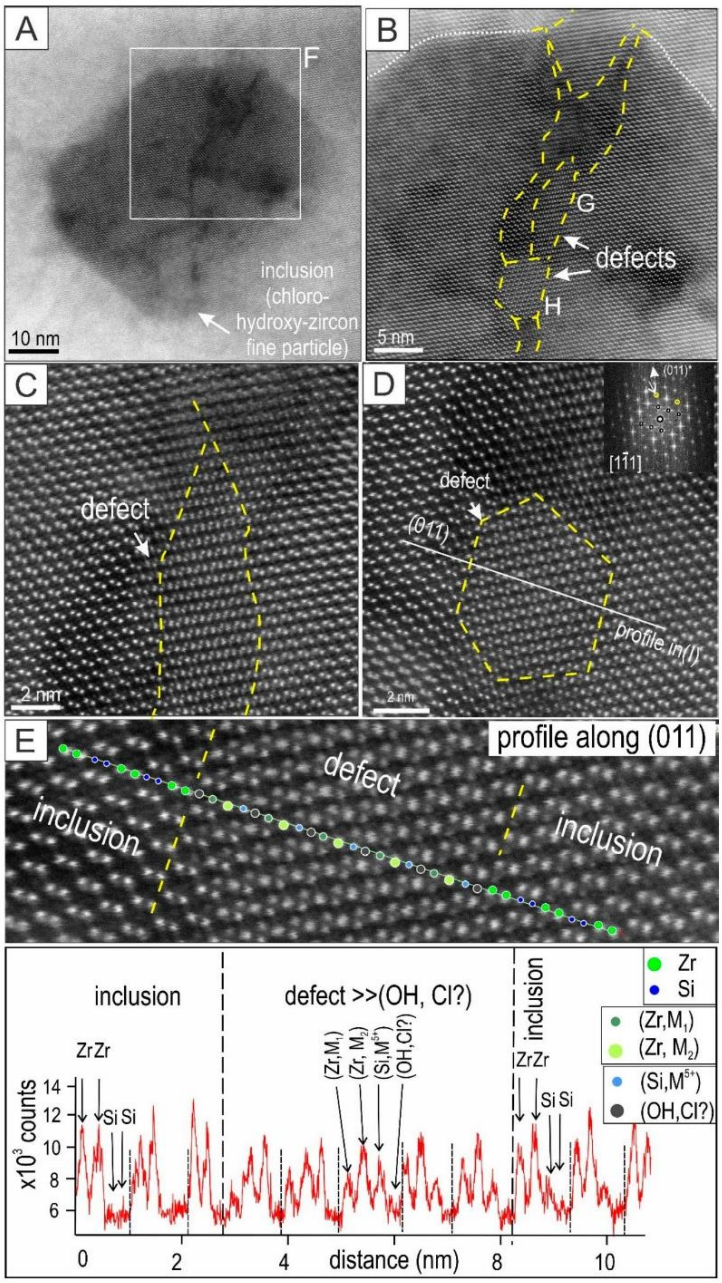


Figure 14. (**A**–**D**) Images showing defects along a fracture crosscutting one of the fine particles (Foil #1). The FFT pattern obtained from the image (inset **D**) shows a square sub-pattern with weaker reflections superimposed onto the main reflections. Yellow, dashed lines mark the defect shape. (**E**) Intensity profile across the defect in (**D**) showing modifications in the Zr and Si signals as marked.

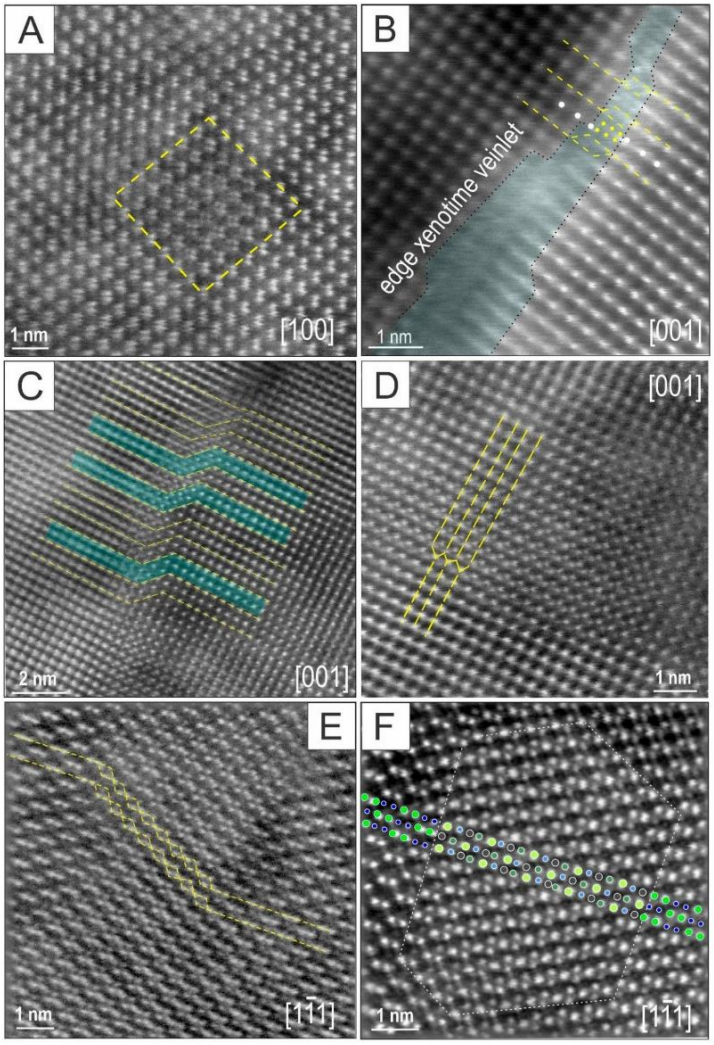


Figure 15. Atomic-scale resolution HAADF STEM images of defects in zircon. (**A**) Square-shaped defect (yellow outline) in U-richer bands from Cape Donington (Foil #7), tilted on the (100) zone axis. The doubling of Zr atoms observed along the *c*-axis suggests atom "stretching) along b induced by strain, attributable to α-recoil damage during U-decay. (**B**) Simple linear defect in Wirrda Well–Donington zircon (Foil #4) observed at the edge of a xenotime veinlet (blue overlay); sample tilted on the (001) zone axis in zircon. Screw dislocations (dashed lines) are marked by atom loops in the defect plane (yellow dots) relative to Zr atoms (white dots) outside the defect. (**C**–**D**) Screw dislocations (dashed lines) along a fault or at the edge of a planar defect on the (001) zone axis in Charleston zircon (Foil #6). Note irregular atom loops along the fault plane (blue overlays). (**E**–**F**) Defects in the Fe-rich, mottled bands from OD distal zircon (Foil #1) with sample tilted on the $[1\bar{1}1]$ zone axis in zircon. Antiphase atom displacement (dashed line) suggesting lattice stretching along (011) directions in (**E**). (**F**) Details of the defect (dotted line) in Figure 14D showing the size and intensity modifications in Zr and Si atoms along the (011) direction (colors as in Figure 14E). The image shows the inferred missing Si atoms as dark, regular spots along this direction.

6. Discussion

6.1. Zircon Metasomatism Down to the Nanoscale: Are Iron and Chlorine of Magmatic or Hydrothermal Origin?

It is difficult to unequivocally distinguish magmatic (primary) from secondary patterns in zircon displaying crystal oscillatory zoning with respect to Fe and Cl due to the lack of crosscutting textures and because such elements could also have been components in either granitic melts or hydrothermal fluids. For example, a magmatic origin for divalent Fe was suggested by Reference [45] based on observed substitutions. In the present study, we were able to rule out a magmatic origin by analysis of zircon from a granite belonging to the same ~1.85 Ga Donington Suite which showed the presence of Fe and Cl only in parts of the craton where they are associated with or host younger (~1.6 Ga) IOCG-type mineralization (Wirrda Well). Moreover, the concentrations of Fe and Cl in the Hiltaba Suite zircons increased with proximity to more intense mineralization. Oscillatory zoning patterns can be produced via metasomatism (ion exchange between a mineral and a percolating fluid moving though pores in a rock) in the absence of open fractures. Therefore, we stipulate that Fe–Cl zoning represents a first stage of zircon alteration via metasomatism that is quite distinct from late-stage fracture-infill or textures superimposed onto the zoning (xenotime veinlets, U-bearing nanoparticles; Figures 6–8).

Metasomatism allows partial or complete pseudomorphic replacement of one mineral by another. In some cases, the new mineral may be the same species but differs from the parent in terms of minor/trace elements, as was shown for hematite from Olympic Dam [46]. Such processes are "metasomatic" in a broader sense and occur when replacement reactions couple dissolution with (re)precipitation rates (CDRR). This interpretation concurs with empirical evidence from other studies of Hiltaba Suite granites [47], showing local alteration of magmatic feldspars or accessories via CDRR. Variation among the geochemical patterns recorded by zircon (e.g., Ca and Cl, as well as Ti, Al, Th, and Y in Charleston zircon) can be attributed to local mineralogical changes in the granite during early alkali–calcic alteration, e.g., release of cations during replacement of magmatic plagioclase by sericite or biotite by chlorite [42,47].

Metasomatism was accompanied by development of nanoscale structures, such as formation of chloro–hydroxy–zircon nanoprecipitates in all samples from the Olympic Dam district, but significantly, not in those from the Eyre Peninsula (Table 1).

Defects were observed throughout the Fe-rich bands, as well as in magmatic zircon from Cape Donington, but none show amorphization. Linear defects associated with fracture opening can be attributed to structure swelling along fission tracks (Figure 15B). This allows trace element remobilization, in turn leading to formation of U-nanoparticles or xenotime like those shown in zircon in Archean granites from Jack Hills [24,25]. Likewise, lattice expansion via stretching or screw-dislocation defects (Figure 16) can be considered part of the "swelling" induced by radiation damage.

The substitution model for metasomatized zircon shows cation exchange in which loss of 0.4–2 wt.% Si can be compensated by incorporation of OH– and halogens without significant removal of primary magmatic trace elements (Supplementary Materials A). Zirconium can, however, be replaced by Fe and other non-formulae cations. Chemical changes, affecting both Zr and Si, observed in defects along fractures crosscutting fine particles (Figure 14) were concordant with chloro–hydroxy–zircon of variable chemistry, as assessed by EPMA data. However, heterogeneity was observed at the nanoscale, including localized concentrations of other elements, e.g., Ca or Cl-bearing nanoparticles (Figures 10 and 11), thus explaining much of the scatter in the geochemical data obtained at the EPMA-scale.

6.2. Timing of Zircon Alteration: Is Metasomatism Pre- or Post-Metamictization?

The incorporation of Fe and associated non-formula elements relating to metasomatism as introduced above, has been extensively discussed in terms of zircon alteration linked to self-irradiation. The overarching idea is that zircon should not be able to incorporate such elements at wt.% concentration unless it accumulates radiation damage, a process resulting in swelling and amorphization, and thus, creating pathways for fluid percolation (Reference [18] and references therein).

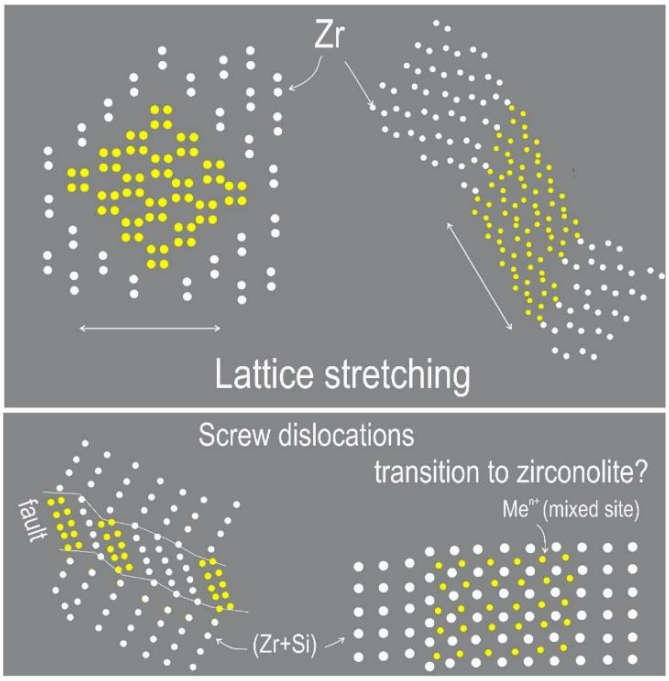


Figure 16. Schematic representation of atom arrangements in defects indicating lattice stretching and screw dislocations leading to expansion of the zircon structure. Such aspects are attributable to self-induced irradiation damage effects.

Quantification of the radiation damage necessary to facilitate major element substitution (the "First Percolation Point") was defined as a dose of ~2×10^{18} α-decays/g (hereafter, D_c), and representing ~30–40% amorphization as a network of interconnected aperiodic domains within the crystal structure [48,49]. The link between the first percolation point and a sudden increase in non-formula elements, particularly Ca, was shown for altered zircon exhibiting U–Pb discordancy [18,19]. A high-porosity-to-spongy appearance is commonly reported, leading to deficient EPMA totals and darkening on BSE images [50]. The latter authors also contend that H_2O incorporation is promoted by pores. Nanoscale Fe- or Pb-bearing inclusions were shown in Archean zircon [24], while pores with Ca- and U-rich margins have been documented from a pegmatite zircon [26].

Using molecular dynamic simulations of alpha-recoil cascades produced via actinide decay, models of self-irradiation damage in zircon show domains of disordered material as small as a few nm [18]. However, imaging of zircon in this study (Figure 12, Figure 14, and Figure 15) did not unequivocally support this model, even for samples within the D_c range required for the crystalline-to-amorphous transition. This may relate to thermal annealing following metasomatism, e.g., associated with emplacement of the Gairdner dyke swarm at ~820 Ma, the most recent major tectono-thermal event recognized throughout the Gawler Craton [51].

Nevertheless, the D_c accumulation since ~820 Ma should have produced recognizable disorder at the nanoscale. The range of defects discussed here (Figures 14–16) are the closest expression of lattice disorder, although not truly amorphization. The positive correlation reported in other studies between high non-formula elements and D_c (e.g., [19]) is not as well-defined in this dataset. Sigmoidal trendlines shown in previous studies are comparable to that shown here, although there is a large spread in the data here, with points displaying high D_c and low Fe, and vice versa (Figure 17A). Therefore, the correlation between increasing non-formula elements and D_c may not necessarily be the result of high-U zircon creating their own pathways for increased fluid interaction. Furthermore,

high-U zircon from this study indicate the D_c required to reach the first percolation point would not have been met until ~100 Ma after zircon crystallization. This postdates the measured timing of hematite crystallization, itself a result of Fe-metasomatism [13]. The presence of hematite inclusions with an HFSE signature within Olympic Dam zircon, is further evidence of Fe–Cl-metasomatism impacting on zircon (Figure 9B) occurring in the early, magmatic-to-hydrothermal transition stage [52], rather than post-metamictization. As highlighted by trace element analysis (Figure 4; Supplementary Materials Table S4), Donington Suite data plots at lower D_c and Fe_2O_3 values than Hiltaba Suite zircon (Figure 17A) reflect the lower U-contents and lesser alteration of zircon. Even in the case of zircon in Donington Suite granite from Wirrda Well, superimposed Fe–Cl-metasomatism is recognized due to the presence of adjacent Hiltaba Suite granites linked to the same batholith that generated the RDG, host to mineralization at Olympic Dam.

The D_c can affect U–Pb systematics in zircon and be manifest as discordance of data points via Pb loss (Figure 3). Accurate (CA)-ID-TIMS ages for magmatic crystallization can, nevertheless, be obtained [14], despite the presence of micron- to nanoscale domains, which in the present dataset do not appear to concentrate remobilized U or Pb. Such phenomena have been shown in previous studies [24,27], where they relate to alteration associated with highly metamict zircons.

6.3. Zircon Alteration Model and Magma "Fertility"

Concentrations of Cl within zircon containing Fe and other non-formula elements was measured and imaged for the first time in natural zircon. Electron microprobe maps show consistent distributions of Cl correlating with Fe in micron-scale banding (Figure 5). At the nanoscale, however, Cl was present as nanoparticles within Fe–Ca-metasomatized mottled bands (Figures 8–11). Such an association between Fe and Cl would be expected in early IOCG fluids exsolved after granite crystallization [52]. Cl-rich nanoparticles became volumetrically more significant in samples from the vicinity of the Olympic Dam deposit, while smaller amounts of Cl were also measured in the nearby Wirrda Well Donington zircon as well as Charleston zircon. In contrast, the Cape Donington zircon displayed a complete absence of Cl. Therefore, we concluded that Cl was inherent to hydrothermal fluids derived from the Hiltaba Suite granites. Moreover, such Fe–Cl-bearing fluids also affected nearby older granites (Donington Suite), host to ~1.6 Ga IOCG mineralization at Wirrda Well.

Zircon metasomatism can be attributed to a low-fluid, mineral-buffered diffusion-reaction process in the beginning (only crystal zoning), followed by formation of chloro–hydroxy–zircon nanoprecipitates when fluids become highly focused (Figure 17B). Iron-rich nano-veinlets begin to interconnect across crystal zones previously metasomatized during increase in the flux of Fe-rich fluids (formation of hematite inclusions; Figure 9). Comparable phenomena in which a mineral can host nanoscale inclusions of the same mineral but with subtle yet distinct chemical differences, are known from Fe oxides, notably Si–Fe nanoprecipitates within silician magnetite. These are documented both from banded iron formation deposits [53] and the Olympic Dam deposit [54].

The preservation of pre-existing crystal orientation in zircon nanoprecipitates and host zircon is characteristic of reactions via a sharp interface, typical of CDRR replacement. Moreover, transient porosity developed during CDRR progression provides sites for deposition of nanoprecipitates, as suggested here and elsewhere (e.g., [55–57]). Hydrothermal fluids interacting with zircon can be considered acidic based on the hydrated-substitution model for zircon (Supplementary Materials A and B, Table S4). Fluid transport of Fe, from the granite-derived fluid and Ca + Al from breakdown of minerals in the granite via alkali–calcic alteration is likely to occur as chloride complexes and can lead to Si and/or Zr loss, according to the reactions:

$$ZrSiO_4 + 4xH^+ \leftrightarrow Zr(SiO_4)_{1-x}(OH)_{4x} + xSi^{4+} \quad (1)$$

$$ZrSiO_4 + x\left(Fe^{n+} + nCl^-\right) \leftrightarrow Fe_xZr_{1-x}SiO_{4-xn}Cl_{xn} + xZrO_2 + x(n-2)O^{2-}, \quad (2)$$

where n = 2 or 3, and x = 0 to 1.

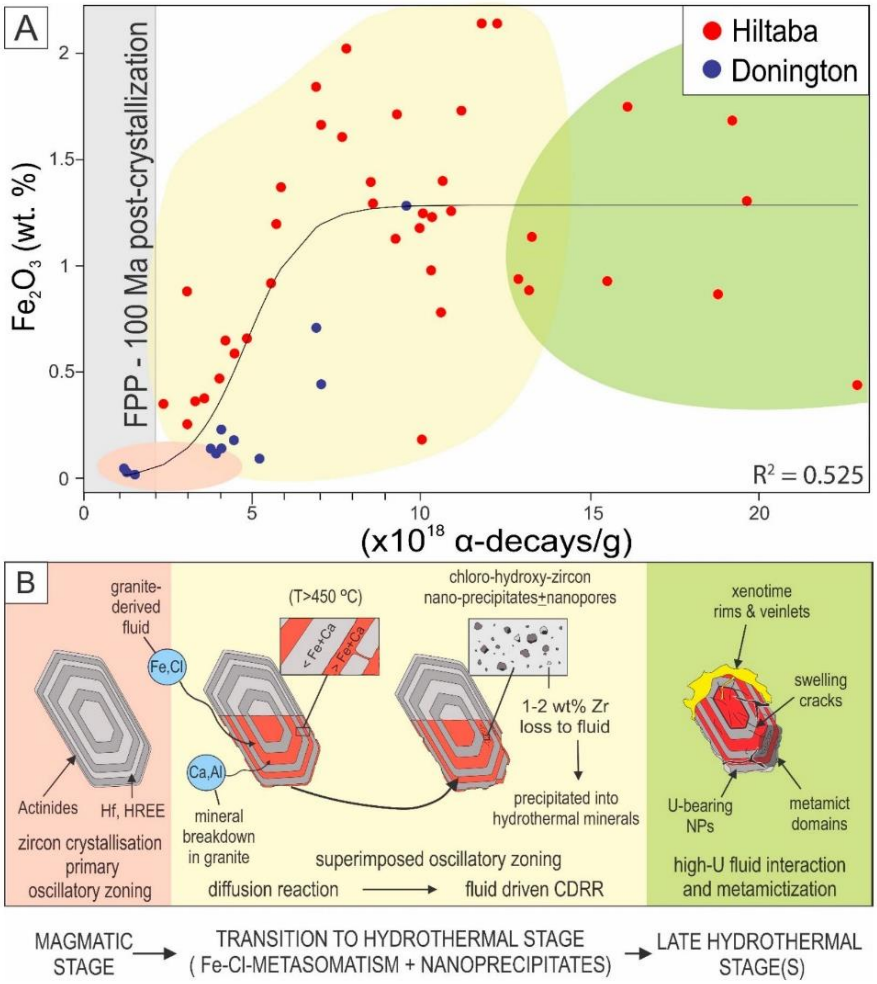


Figure 17. (**A**) Plot of Fe_2O_3 (wt.%) versus D_c (×10^{18} α-decays/g) for all zircon samples as marked and using EPMA data from Supplementary Materials B, Table S4 (four analyses with D_c > 25 were excluded). A sigmoid through the data was fit by non-linear least squares regression using the software "R". Although the first percolation point (FPP) for zircon was marked at D_c = 2 (as defined by Salje et al. [48]), a sharp increase in wt.% Fe_2O_3 was seen only at D_c = ~3. The FPP in Olympic Dam zircon was only reached at least 100 Ma after crystallization, using the dose concentration calculation of Meldrum et al. [58]. Also, note the scatter in the dataset concordant with the weak correlation between the highest measured non-formula element (Fe) and D_c. (**B**) Schematic diagram illustrating evolution of magmatic zircon from granites in the Olympic Cu–Au Province. Colored areas in (**A**) correspond to the main evolutionary stages in (**B**). Note that Cape Donington zircon, with the lowest non-formula elements, plots in a magmatic domain that straddles the FPP line. In contrast, analyses with high U concentration corresponded to intensively altered stages (green), featuring superimposed textures with all the characteristic of metamict zircon, possibly resulting from interaction with late-stage, U-rich hydrothermal fluids. Metasomatic textures and association with abundant, Cl-rich nanoprecipitates are typical features of fertile granites. The association between Fe and Cl recorded in metasomatized zircon during magmatic-to-hydrothermal transition is a diagnostic signature of fertile IOCG systems.

The Fe–Cl-rich signature of post-magmatic fluids is recorded within the mottled textures of zircon and represents the onset of IOCG mineralization during the magmatic-to-hydrothermal transition. From ID-TIMS dating of hematite, iron metasomatism is known to have occurred at Olympic Dam shortly after granite crystallization (~2–4 Ma later) [13]. The present data support early, as well as prolonged, zircon alteration, illustrated here from areas that are overprinting primary growth (Figure 2B,D). The Fe–Cl-rich metasomatized zones within zircon were also imaged directly adjacent to magmatic relict domains (Figure 8A). Recrystallization of zircon surrounding xenotime veinlets was observed down to the nanoscale (Supplementary Materials C, Figure S3). Whereas zircon metasomatism overprinting primary growth zoning can be related to the earliest hydrothermal fluids exsolved at the depth of granite emplacement, later cycles of zircon alteration could happen during and/or after granite uplift as the IOCG mineralizing system evolved.

Overall, the increase in Cl associated with abundant chloro–hydroxy–zircon nanoprecipitates correlates with proximity to the Olympic Dam orebody. Such features can, thus, be considered a direct indicator of magma "fertility" (the ability of a magma to generate hydrothermal fluids that are sufficiently well-endowed with Cu, U, etc., to form a sizable ore deposit) in Hiltaba Suite granites. Furthermore, the presence of Cl in zircon from other Hiltaba Suite granites such as Charleston, indicates potential undiscovered IOCG mineralization using the zircon pathfinder.

7. Conclusions and Implications

1. From the case studies presented and comparison between them, zircon may be substituted with non-formula elements, notably Fe and Cl, released ~2–4 Ma after magmatic crystallization, during a widespread metasomatic event, prior to fluid pathway development during metamictization.

2. Chloro–hydroxy–zircon nanoprecipitates record the Fe–Cl-signature of fluids released during the magmatic-to-hydrothermal transition in IOCG systems, which volumetrically increase in granites of different age with proximity to Olympic Dam. Such nanoprecipitates represent a potential pathfinder to mineralization associated with fertile granites. Although we recommend that the data should initially be tested in other IOCG terranes, there exists potential for similar features to be identified within zircon from other deposit types involving penetrative metasomatic alteration.

3. Relationships between micron- and nanoscale observations in zircon are a largely untapped research field. With ever increasing instrumental resolution and analytical precision, nanoscale studies can provide new insights into processes carrying implications for geochronology, ore deposit genesis and mineral exploration.

4. In summary, this study has shown that early metasomatic alteration can be recorded in magmatic zircon and that these patterns can be preserved over geological time, even when superimposed by the effects of metamictization. This implies that nanoscale studies of magmatic zircon, when coupled with careful micron-scale characterization of textures and compositions, could represent a valuable new tool in mineral exploration.

Supplementary Materials: The following are available online at http://www.mdpi.com/2075-163X/9/6/364/s1, Supplementary Materials A: Extended details of methodology (Tables S1 and S2); Supplementary Materials B: Expanded data tables (Tables S3–S5); Supplementary Materials C: Additional figures (Figures S1, S2, and S3A–S3E).

Author Contributions: L.C.-D. and C.L.C. conceived this contribution. Analytical work was conducted L.C-.D., C.L.C., M.R.V.-I., M.D., W.K., J.X. and U.I.D., with A.S. operating the Titan Themis instrument and B.P.W. assisting with EPMA set-up. The manuscript was written by L.C.-D., C.L.C., M.R.V.-I. and N.J.C., with contributions from K.E., A.K.-C. and B.P.W.

Funding: This research was funded from the project "Trace elements in iron-oxides: deportment, distribution and application in ore genesis, geochronology, exploration and mineral processing", supported by BHP Olympic Dam and the South Australian Government Mining and Petroleum Services Centre of Excellence. N.J.C. and K.E. acknowledge funding from the ARC Research Hub for Australian Copper–Uranium (Grant IH130200033).

Acknowledgments: We acknowledge the AMMRF for instrument access. Sarah Gilbert assisted with LA-ICP-MS analysis and Animesh Basak assisted with FIB-SEM operation. Chris Kalnins is thanked for preparing two of the TEM foils presented. We kindly thank two anonymous reviewers for comments that helped improve this manuscript.

Conflicts of Interest: The authors declare no conflicts of interest.

References

1. Groves, D.I.; Bierlein, F.P.; Meinert, L.D.; Hitzman, M.W. Iron oxide copper-gold (IOCG) deposits through Earth history: Implications for origin, lithospheric setting, and distinction from other epigenetic iron oxide deposits. *Econ. Geol.* **2010**, *105*, 641–654. [CrossRef]
2. Barton, M.D. Iron oxide (-Cu-Au-REE-P-Ag-U-Co) systems. In *Treatise on Geochemistry*, 2nd ed.; Elsevier: Amsterdam, The Netherlands, 2014; Volume 13, pp. 515–541.
3. Krneta, S.; Ciobanu, C.L.; Cook, N.J.; Ehrig, K.; Kontonikas-Charos, A. Apatite at Olympic Dam, South Australia: A petrogenetic tool. *Lithos* **2016**, *262*, 470–485. [CrossRef]
4. Krneta, S.; Ciobanu, C.L.; Cook, N.J.; Ehrig, K.J. Numerical modeling of REE fractionation patterns in fluorapatite from the Olympic Dam deposit (South Australia). *Minerals* **2018**, *8*, 342. [CrossRef]
5. Condon, D.J.; Schmitz, M.D. One hundred years of geochronology. *Elements* **2013**, *9*, 3–80. [CrossRef]
6. Harley, S.L.; Kelly, N.M. Zircon Tiny but Timely. *Elements* **2007**, *3*, 13–18. [CrossRef]
7. Rubatto, D.; Hermann, J. Zircon behaviour in deeply subducted rocks. *Elements* **2007**, *3*, 31–35. [CrossRef]
8. Scherer, E.E.; Whitehouse, M.J.; Munker, C. Zircon as a Monitor of Crustal Growth. *Elements* **2007**, *3*, 19–24. [CrossRef]
9. Hoskin, P.W.O.; Schaltegger, U. The composition of zircon and igneous and metamorphic petrogenesis. *Rev. Mineral. Geochem.* **2003**, *53*, 27–62. [CrossRef]
10. Ewing, R.C.; Meldrum, A.; Wang, L.M.; Weber, W.J.; Corrales, L.R. Radiation damage in zircon. *Rev. Mineral. Geochem.* **2003**, *53*, 387–425. [CrossRef]
11. Skirrow, R.G.; Bastrakov, E.N.; Barovich, K.; Fraser, G.L.; Creaser, R.A.; Fanning, C.M. Timing of iron oxide Cu-Au-(U) hydrothermal activity and Nd isotope constraints on metal sources in the Gawler craton, South Australia. *Econ Geol.* **2007**, *102*, 1441–1470. [CrossRef]
12. Ehrig, K.; McPhie, J.; Kamenetsky, V. Geology and Mineralogical Zonation of the Olympic Dam Iron Oxide Cu-U-Au-Ag Deposit, South Australia. In *Geology and Genesis of Major Copper Deposits and Districts of the World: A Tribute to Richard H. Sillitoe*; Hedenquist, J.W., Harris, M., Camus, F., Eds.; Society of Economic Geologists Special Publication 16; Society of Economic Geologists: Littleton, CO, USA, 2012; pp. 237–267.
13. Courtney-Davies, L.; Tapster, S.; Ciobanu, C.; Cook, N.J.; Verdugo-Ihl, M.R.; Ehrig, K.J.; Kennedy, A.K.; Gilbert, S.E.; Condon, D.J.; Wade, B.P. A multi-technique evaluation of hydrothermal hematite U-Pb isotope systematics: Implications for ore deposit geochronology. *Chem. Geol.* **2019**, *513*, 54–72. [CrossRef]
14. Cherry, A.R.; Ehrig, K.; Kamenetsky, V.S.; McPhie, J.; Crowley, J.L.; Kamenetsky, M.B. Precise geochronological constraints on the origin, setting and incorporation of ca. 1.59 Ga surficial facies into the Olympic Dam Breccia Complex, South Australia. *Precambr. Res.* **2018**, *315*, 162–178. [CrossRef]
15. Ewing, R.C.; Lutze, W.; Weber, W.J. Zircon—A Host-Phase for the Disposal of Weapons Plutonium. *J. Mater. Res.* **1995**, *10*, 243–246. [CrossRef]
16. Holland, H.D.; Gottfried, D. The effect of nuclear radiation on the structure of zircon. *Acta Cryst.* **1955**, *8*, 291–300. [CrossRef]
17. Mattinson, J. Zircon U–Pb chemical abrasion ("CA-TIMS") method: Combined annealing and multi-step partial dissolution analysis for improved precision and accuracy of zircon ages. *Chem. Geol.* **2005**, *220*, 47–66. [CrossRef]
18. Geisler, T.; Schaltegger, U.; Tomaschek, F. Re-equilibration of zircon in aqueous fluids and melts. *Elements* **2007**, *3*, 43–50. [CrossRef]
19. Geisler, T.; Rashwan, A.A.; Rahn, M.K.W.; Poller, U.; Zwingmann, H.; Pidgeon, R.T.; Schleicher, H.; Tomaschek, F. Low temperature hydrothermal alteration of natural metamict zircons from the Eastern Desert, Egypt. *Mineral. Mag.* **2003**, *67*, 485–508. [CrossRef]
20. Tang, F.; Taylor, J.M.; Einsle, J.F.; Borlina, C.S.; Fu, R.R.; Weiss, B.P.; Williams, H.M.; Williams, W.; Nagy, L.; Midgley, P.; et al. Secondary magnetite in ancient zircon precludes analysis of a Hadean geodynamo. *Proc. Natl. Acad. Sci. USA* **2019**, *116*, 407–412. [CrossRef]
21. Lu, Y.J.; Loucks, R.R.; Fiorentini, M.L.; McCuaig, T.C.; Evans, N.J.; Yang, Z.M.; Hou, Z.Q.; Kirkland, C.L.; Parra-Avila, L.A.; Kobussen, A. Zircon compositions as a pathfinder for porphyry Cu ± Mo ± Au deposits. *Econ. Geol.* **2016**, *19*, 329–347.

22. Belousova, E.A.; Griffin, W.L.; O'Reilly, S.Y.; Fisher, N.I. Igneous zircon: Trace element composition as an indicator of source rock type. *Contrib. Mineral. Petrol.* **2002**, *143*, 602–622. [CrossRef]
23. Utsunomiya, S.; Ewing, R.C. Application of high-angle annular dark field scanning transmission electron microscopy—Energy dispersive X-ray spectrometry, and energy-filtered transmission electron microscopy to the characterization of nanoparticles in the environment. *Environ. Sci. Technol.* **2003**, *37*, 786–791. [CrossRef]
24. Utsunomiya, S.; Palenik, C.S.; Valley, J.W.; Cavosie, A.J.; Wilde, S.A.; Ewing, R.C. Nanoscale occurrence of Pb in an Archean zircon. *Geochim. Cosmochim. Acta* **2004**, *68*, 4679–4686. [CrossRef]
25. Utsunomiya, S.; Valley, J.W.; Cavosie, A.J.; Wilde, S.A.; Ewing, R.C. Radiation damage and alteration of zircon from a 3.3 Ga porphyritic granite from the Jack Hills, Western Australia. *Chem. Geol.* **2007**, *236*, 92–111. [CrossRef]
26. Seydoux-Guillaume, A.M.; Bingen, B.; Paquette, J.L.; Bosse, V. Nanoscale evidence for uranium mobility in zircon and the discordance of U-Pb chronometers. *Earth Plan. Sci. Lett.* **2015**, *409*, 43–48. [CrossRef]
27. Kusiak, M.A.; Dunkley, D.J.; Wirth, R.; Whitehouse, M.J.; Wilde, S.A.; Marquardtd, K. Metallic lead nanospheres discovered in ancient zircons. *Proc. Natl. Acad. Sci. USA* **2015**, *112*, 4958–4963. [CrossRef]
28. Ciobanu, C.L.; Cook, N.J.; Maunders, C.; Wade, B.P.; Ehrig, K. Focused Ion Beam and Advanced Electron Microscopy for Minerals: Insights and Outlook from Bismuth Sulphosalts. *Minerals* **2016**, *6*, 112. [CrossRef]
29. Cook, N.J.; Ciobanu, C.L.; Ehrig, K.; Slattery, A.; Verdugo-Ihl, M.R.; Courtney-Davies, L.; Gao, W. Advances and opportunities in ore mineralogy. *Minerals* **2017**, *7*, 233. [CrossRef]
30. Goldfarb, R.J.; Bradley, D.; Leach, D.L. Secular variation in economic geology. *Econ. Geol.* **2010**, *105*, 459–465. [CrossRef]
31. Allen, S.R.; McPhie, J.; Ferris, G.; Simpson, C. Evolution and architecture of a large felsic igneous province in western Laurentia: The 1.6 Ga Gawler Range Volcanics, South Australia. *J. Volcanol. Geotherm. Res.* **2008**, *172*, 132–147. [CrossRef]
32. Keyser, W.M.; Ciobanu, C.L.; Cook, N.J.; Johnson, G.; Feltus, F.; Johnson, S.; Dmitrijeva, M.; Ehrig, K.; Nguyen, P. Petrography and trace element signatures of iron-oxides in deposits from the Middleback Ranges, South Australia: From banded iron formation to ore. *Ore Geol. Rev.* **2018**, *93*, 337–360. [CrossRef]
33. Domnick, U.; Cook, N.J.; Bluck, R.; Brown, C.; Ciobanu, C.L. Petrography of granitoids from the Samphire Pluton, South Australia: Implications for uranium mineralization in overlying sediments. *Lithos* **2018**, *300–301*, 1–19. [CrossRef]
34. Keyser, W.; Ciobanu, C.L.; Cook, N.J.; Dmitrijeva, M.; Courtney-Davies, L.; Feltus, H.; Gilbert, S.; Johnson, G.; Ehrig, K. Iron-oxides constrain BIF evolution in terranes with protracted geological histories: The Iron Count prospect, Middleback Ranges, South Australia. *Lithos* **2019**, *324*, 20–38. [CrossRef]
35. Dmitrijeva, M.; Metcalfe, A.V.; Ciobanu, C.L.; Cook, N.J.; Frenzel, M.; Keyser, W.M.; Johnson, G.; Ehrig, K. Discrimination and variance structure of trace element signatures in hematite: A case study of BIF-mineralization from the Middleback Ranges, South Australia. *Math. Geosci.* **2018**, *50*, 381–415. [CrossRef]
36. Creaser, R.A.; Fanning, C.M. A U-Pb zircon study of the Mesoproterozoic Charleston Granite, Gawler Craton, South Australia. *Aust. J. Earth Sci.* **1993**, *40*, 519–526. [CrossRef]
37. Skirrow, R.G.; van der Wielen, S.E.; Champion, D.C.; Czarnota, K.; Thiel, S. Lithospheric architecture and mantle metasomatism linked to iron oxide Cu-Au ore formation: Multidisciplinary evidence from the Olympic Dam Region, South Australia. *Geochem. Geophys. Geosyst.* **2018**, *19*, 2673–2705. [CrossRef]
38. Wade, C.E.; Payne, J.L.; Barovich, K.M.; Reid, A.J. Heterogeneity of the sub-continental lithospheric mantle and 'non-juvenile' mantle additions to a Proterozoic silicic large igneous province. *Lithos* **2019**, *340–341*, 87–107. [CrossRef]
39. Ovalle, J.T.; La Cruz, N.L.; Reich, M.; Barra, F.; Simon, A.C.; Konecke, B.A.; Rodriguez-Mustafa, M.A.; Deditius, A.P.; Childress, T.M.; Morata, D. Formation of massive iron deposits linked to explosive volcanic eruptions. *Sci. Rep.* **2018**, *8*, 14855. [CrossRef]
40. Kontonikas-Charos, A.; Ciobanu, C.L.; Cook, N.J.; Ehrig, K.; Krneta, S.; Kamenetsky, V.S. Feldspar evolution in the Roxby Downs Granite, host to Fe-oxide Cu-Au-(U) mineralisation at Olympic Dam, South Australia. *Ore Geol. Rev.* **2017**, *80*, 838–859. [CrossRef]
41. Krneta, S.; Cook, N.J.; Ciobanu, C.L.; Ehrig, K.; Kontonikas-Charos, A. The Wirrda Well and Acropolis prospects Gawler Craton, South Australia: Insights into evolving fluid conditions through apatite chemistry. *J. Geochem. Explor.* **2017**, *181*, 276–291. [CrossRef]

42. Kontonikas-Charos, A.; Ciobanu, C.L.; Cook, N.J.; Ehrig, K.; Krneta, S.; Kamenetsky, V.S. Rare earth element geochemistry of feldspars: Examples from Fe-oxide Cu-Au systems in the Olympic Cu-Au Province, South Australia. *Mineral. Petrol.* **2018**, *112*, 145–172. [CrossRef]
43. Jagodzinski, E.A. Compilation of SHRIMP U-Pb geochronological data Olympic Domain, Gawler Craton, South Australia, 2001–2003. *Geosci. Aust. Rec.* **2005**, *20*, 2005.
44. Keyser, W.; Ciobanu, C.L.; Cook, N.J.; Courtney-Davies, L.; Kennedy, A.; Wade, B.P.; Ehrig, K.; Dmitrijeva, M.; Kontonikas-Charos, A.; Feltus, H.; et al. Petrographic and geochronological constraints on the granitic basement to the Middleback Ranges, South Australia. *Precambr. Res.* **2019**, *324*, 170–193. [CrossRef]
45. Pérez-Soba, C.; Villaseca, C.; Gonzáles del Tánago, J.; Nasdala, L. The composition of zircon in the peraluminous Hercynian granites of the Spanish Central System batholith. *Can. Mineral.* **2007**, *45*, 509–527. [CrossRef]
46. Verdugo-Ihl, M.R.; Ciobanu, C.L.; Cook, N.J.; Ehrig, K.; Courtney-Davies, L.; Gilbert, S. Textures and U-W-Sn-Mo signatures in hematite from the Cu-U-Au-Ag orebody at Olympic Dam, South Australia: Defining the archetype for IOCG deposits. *Ore Geol. Rev.* **2017**, *91*, 173–195. [CrossRef]
47. Kontonikas-Charos, A.; Ciobanu, C.L.; Cook, N.J.; Ehrig, K.; Ismail, R.; Krneta, S.; Basak, A. Feldspar mineralogy and rare earth element (re)mobilization in iron-oxide copper gold systems from South Australia: A nanoscale study. *Mineral. Mag.* **2018**, *82*, S173–S197. [CrossRef]
48. Salje, E.K.H.; Chrosch, J.; Ewing, R.C. Is "metamictization" of zircon a phase transition? *Am. Mineral.* **1999**, *84*, 1107–1116. [CrossRef]
49. Ríos, S.; Malcherek, T.; Salje, E.K.H.; Domeneghetti, C. Localized defects in radiation-damaged zircon. *Acta Cryst.* **2000**, *56*, 947–952. [CrossRef]
50. Nasdala, L.; Kronz, A.; Wirth, R.; Váczi, T.; Pérez-Soba, C.; Willner, A.; Kennedy, A.K. Alteration of radiation-damaged zircon and the related phenomenon of deficient electron microprobe totals. *Geochim. Cosmochim. Acta* **2009**, *73*, 1637–1650. [CrossRef]
51. Wingate, M.T.D.; Campbell, I.H.; Compston, W.; Gibson, G.M. Ion microprobe U–Pb ages for Neoproterozoic basaltic magmatism in south-central Australia and implications for the breakup of Rodinia. *Precambr. Res.* **1998**, *87*, 135–159. [CrossRef]
52. Verdugo-Ihl, M.R.; Ciobanu, C.L.; Cook, N.J.; Ehrig, K.; Courtney-Davies, L. Defining early stages of IOCG systems: Evidence from iron-oxides in the outer shell of the Olympic Dam deposit, South Australia. *Mineral. Depos.* **2019**. [CrossRef]
53. Xu, H.; Shen, Z.; Konishi, H. Si-magnetite nano-precipitates in silician magnetite from banded iron formation: Z-contrast imaging and ab initio study. *Am. Mineral.* **2014**, *99*, 2196–2202. [CrossRef]
54. Ciobanu, C.L.; Verdugo-Ihl, M.R.; Slattery, A.; Cook, N.J.; Ehrig, K.; Courtney-Davies, L.; Wade, B.P. Silician magnetite: Si-Fe-nanoprecipitates and other mineral inclusions in magnetite from the Olympic Dam deposit, South Australia. *Minerals* **2019**, *9*, 311. [CrossRef]
55. Tooth, B.; Ciobanu, C.L.; Green, L.; O'Neill, B.; Brugger, J. Bi-melt formation and gold scavenging from hydrothermal fluids: An experimental study. *Geochim. Cosmochim. Acta* **2011**, *75*, 5423–5443. [CrossRef]
56. Verdugo-Ihl, M.R.; Ciobanu, C.L.; Cook, N.J.; Slattery, A.; Ehrig, K. Copper nanoparticles along fluid inclusion trails in hematite. In Proceedings of the Goldschmidt 2018, Boston, MA, USA, 12–17 August 2018.
57. Owen, N.D.; Ciobanu, C.L.; Cook, N.J.; Slattery, A.; Basak, A. Nanoscale study of clausthalite-bearing symplectites in Cu-Au-(U) ores: Implications for ore genesis. *Minerals* **2018**, *8*, 67. [CrossRef]
58. Meldrum, A.; Boatner, L.A.; Weber, W.J.; Ewing, R.C. Radiation damage in zircon and monazite. *Geochim. Cosmochim. Acta* **1988**, *62*, 2509–2520. [CrossRef]



© 2019 by the authors. Licensee MDPI, Basel, Switzerland. This article is an open access article distributed under the terms and conditions of the Creative Commons Attribution (CC BY) license (http://creativecommons.org/licenses/by/4.0/).

CHAPTER 8

SYNTHESIS OF U-PB DOPED HEMATITE USING A HYDRATED FERRIC OXIDE APPROACH

Liam Courtney-Davies [1], Cristiana L. Ciobanu [1], Marcus W. Richardson [2], Ned Prosser [1], Max Verdugo-Ihl [1], Benjamin P. Wade [3], Sarah E. Gilbert [3], Kathy Ehrig [4] and Nigel J. Cook[1]

[1]School of Chemical Engineering and Advanced Materials, The University of Adelaide, Adelaide, SA 5005, Australia;

[2] 6 Ophir Street, Goodwood, S.A. 5034, Australia

[3]Adelaide Microscopy, The University of Adelaide, Adelaide, SA 5005, Australia;

[4]BHP Olympic Dam, Adelaide, SA 5000, Australia; Kathy.J.Ehrig@bhpbilliton.com

Article published in The Journal of Crystal Growth (2019), 513, 48-57

Statement of Authorship

Title of Paper	Synthesis of U-Pb doped hematite using a hydrated ferric oxide approach.
Publication Status	☑ Published ☐ Accepted for Publication ☐ Submitted for Publication ☐ Unpublished and Unsubmitted w ork w ritten in manuscript style
Publication Details	Courtney-Davies L, Ciobanu C.L., Richardson, M.W., Prosser, N., Verdugo-Ihl, M.R., Wade, B.P., Gilbert, S.E., Ehrig, K., Cook, N.J.,2019. Synthesis of U-Pb doped hematite using a hydrated ferric oxide approach. Journal of Crystal Growth. 513, 48-57.

Principal Author

Name of Principal Author (Candidate)	Liam Courtney-Davies		
Contribution to the Paper	Performed lab work, analytical work, carried out data processing and interpretation, oversaw development of work and wrote manuscript and oversaw manuscript revision.		
Overall percentage (%)	50		
Certification:	This paper reports on original research I conducted during the period of my Higher Degree by Research candidature and is not subject to any obligations or contractual agreements with a third party that would constrain its inclusion in this thesis. I am the primary author of this paper.		
Signature		Date	29/10/2019

Co-Author Contributions

By signing the Statement of Authorship, each author certifies that:

i. the candidate's stated contribution to the publication is accurate (as detailed above);

ii. permission is granted for the candidate in include the publication in the thesis; and

iii. the sum of all co-author contributions is equal to 100% less the candidate's stated contribution.

Name of Co-Author	Cristiana L. Ciobanu		
Contribution to the Paper	Defined the direction of research. Performed analytical work, and data interpretation, assisted in writing the manuscript and its revision.		
Overall percentage (%)	20		
Signature	(	Date	29 Oct 2019

Name of Co-Author	Marcus W. Richardson		
Contribution to the Paper	Helped define direction of research, synthesised the reference material, supervised development of work, assisted with data interpretation and contributed to manuscript preparation.		
Overall percentage (%)	20		
Signature		ate	29/10/2019

Name of Co-Author	Ned Prosser		
Contribution to the Paper	Assisted with data interpretation, and evaluation of manuscript.		
Overall percentage (%)	2		
Signature		Date	30/4/2019

Name of Co-Author	Max Verdugo-Ihl		
Contribution to the Paper	Assisted with analytical instrumentation, data processing and evaluation of manuscript.		
Overall percentage (%)	2		
Signature		Date	29/10/2019

Name of Co-Author	Benjamin P. Wade		
Contribution to the Paper	Helped define research direction, assisted with analytical work and evaluated of manuscript.		
Overall percentage (%)	2		
Signature		Date	29/10/2019

Name of Co-Author	Sarah E. Gilbert		
Contribution to the Paper	Helped define research direction, assisted with analytical work and evaluated of manuscript.		
Overall percentage (%)	2		
Signature		Date	29/10/19

Name of Co-Author	Kathy Ehrig		
Contribution to the Paper	Coordinate sample collection, defined research direction and evaluated the manuscript.		
Overall percentage (%)	1		
Signature		Date	29/10/2019

Name of Co-Author	Nigel J. Cook		
Contribution to the Paper	Helped define research direction, and evaluated the manuscript and revision.		
Overall percentage (%)	1		
Signature		Date	29/10/2019

Journal of Crystal Growth 513 (2019) 48–57

Contents lists available at ScienceDirect

Journal of Crystal Growth

journal homepage: www.elsevier.com/locate/jcrysgro

Synthesis of U-Pb doped hematite using a hydrated ferric oxide approach

Liam Courtney-Davies[a,*], Cristiana L. Ciobanu[a], Marcus W. Richardson[b], Ned Prosser[a], Max Verdugo-Ihl[a], Benjamin P. Wade[c], Sarah E. Gilbert[c], Kathy J. Ehrig[d], Nigel J. Cook[a]

[a] School of Chemical Engineering, The University of Adelaide, Adelaide, S.A. 5005, Australia
[b] 6 Ophir Street, Goodwood, S.A. 5034, Australia
[c] Adelaide Microscopy, The University of Adelaide, Adelaide, S.A. 5005, Australia
[d] BHP Olympic Dam, Adelaide, S.A. 5000, Australia

ARTICLE INFO

Communicated by T. Nishinaga

Keywords:
U-Pb geochronology
Hematite
Reference material
Hydrated ferric oxide
Doping experiments

ABSTRACT

Hematite (α-Fe_2O_3) has been successfully co-doped with uranium and lead using hydrated ferric oxide (HFO) as an intermediary, precipitated by ammonia from a ferric nitrate solution. A novel synthesis approach has been developed, involving a wet stage of doping colloidal HFO by absorption from nitrate solution containing U and Pb nitrates, followed by drying and heating to 700 °C to convert HFO to Fe_2O_3. The crystal phase present in the sample was confirmed as hematite by X-ray powder diffraction. Scanning electron microscopy was used to determine sample morphology and U/Pb isotope homogeneity was assessed using laser-ablation inductively-coupled-plasma mass spectrometry (LA-ICP-MS). Although reasonably homogeneous at the scale of a LA-ICP-MS ablation analysis spot, conspicuous domains are recognized that appear 'bright' or 'dark' on backscatter electron images. These domains display distinctly different element concentrations and U/Pb ratios on LA-ICP-MS isotope maps. Nevertheless, this synthetic U-Pb-doped hematite represents a potential reference material for use in microbeam U-Pb geochronology and the results show that the preparation methods and doping conditions are effective. The observed chemical and isotopic heterogeneity between bright and dark domains may, however, inhibit widespread use of the synthesized hematite as a reference material. U/Pb heterogeneity may be controlled by the heating and cooling regimes of the method. Assuming the 'bright and dark domains' can be analytically or mechanically separated through refinement of the preparation method, then a suitable reference material may be produced. Subject to validation via high-precision chemical analysis, this reference material can be used to date uranium-bearing hematite from various types of deposits. The high speed and precision of LA-ICP-MS analyses will allow measurement of geological ages in a very common mineral, providing new insights for mineral exploration worldwide.

1. Introduction

Iron-oxide minerals such as magnetite (Fe_3O_4) and hematite (α-Fe_2O_3) are ubiquitous in many types of ore deposits. The recognition that Fe-oxides can contain measurable concentrations of uranium and radiogenic lead [1] has raised the potential of developing new U-Pb mineral geochronometers that can be widely applied to establish the age of mineral systems that may not otherwise be accurately dated. This is because conventionally dated (hydrothermal) minerals can be either absent, U-poor, or represent isotopically open systems. Zircon ($ZrSiO_4$) is the most commonly used mineral for U-Pb geochronology but has limited applicability in many hydrothermal ore bodies, due to open system behavior originating from mineral/fluid interaction and metamictization due to high U contents producing large alpha decay doses [2].

Geochronology represents a powerful tool for mineral exploration research, whereby constraints on the relative timing of magmatic and hydrothermal events can underpin models for regional-scale metallogeny and the genesis of individual ore deposits. Radiometric dating of minerals is achieved by observing a known decay of a parent isotope which was substituted into the crystal lattice of the mineral during crystallization (e.g. [3]). The uranium-to-lead decay series provides dates that can be calculated from two uranium decay chains (^{238}U and ^{235}U).

Critical for routine application of U-Pb geochronology is a suitable reference material (RM) that contains known concentrations of U and Pb isotopes, and ratios that can be accurately measured [4,5]. If this material is to be used for analysis by microbeam techniques, such as

* Corresponding author.
E-mail address: liam.courtney-davies@adelaide.edu.au (L. Courtney-Davies).

https://doi.org/10.1016/j.jcrysgro.2019.02.053
Received 8 January 2019; Received in revised form 14 February 2019; Accepted 21 February 2019
Available online 22 February 2019
0022-0248/ © 2019 Elsevier B.V. All rights reserved.

Table 1
Experimental details of U-Pb dopant concentrations, HFO to hematite conversion temperatures, and LA-ICP-MS measured U and Pb concentrations and ratios. Sample 11 represents the sample synthesized under optimized conditions. Sample C represents the least successful synthesis.

Sample ID	No of spots	Dopant concentration (mg/L)		Heating rate (°C/hour)	Temp (°C)	Mean concentrations (mg/L ± uncertainty)				Mean ratio and uncertainty	
						U		Pb		$^{206}Pb/^{238}U$	
		U	Pb			Mean	±	Mean	±	Mean	±
4.1	30	125	50	50	700	111	8	53	3.2	0.1202	0.0066
4.3	29	125	50	200	700	-	-	-	-	0.1192	0.0041
4.2	28	125	50	100	700	127	3.8	64	4.5	0.1355	0.0055
9	10	1000	500	200	700	135	22	854	46	0.1667	0.0069
11	30	125	50	200	700	129	13	61	6.4	0.1206	0.0038
A	30	250	100	200	450	-	-	-	-	0.1197	0.0058
B	15	250	100	200	600	-	-	-	-	0.1218	0.0047
C	13	250	100	200	900	-	-	-	-	0.2663	0.0098

laser-ablation inductively-coupled-plasma mass spectrometry (LA-ICP-MS) or sensitive high-resolution ion microprobe (SHRIMP), the reference material (RM) needs to be sufficiently homogeneous, and as large as possible such that it can be used multiple times by users in different laboratories.

The speed, and the relatively low cost and accessibility of LA-ICP-MS has led to it being widely used for geochronology [4,5], however several factors impact on the robustness of the technique. These include how accurately common lead can be measured and if uncertainties induced by down-hole laser induced elemental fractionation can be corrected for [5]. Common Pb refers to the fraction of Pb in a sample, which is not derived from natural radioactive decay of U and Th, most commonly present as ^{204}Pb. Down-hole fractionation occurs when the measured elemental ratio changes during ablation due to differences in element volatility [6]. Matrix-matched RMs are used to calculate correction factors to account for this fractionation effect.

Ciobanu et al. [1] showed that hematite from the Olympic Dam Cu-U-Au-Ag deposit, South Australia, can contain up to several wt.% of lattice-bound U. The first attempt at applying U-Pb hematite geochronology at the University of Adelaide used a commercially available zircon RM to obtain meaningful U-Pb ages [1]. In a subsequent study, U/Pb dates obtained using a U–Pb reference solution, Courtney-Davies et al. [7] agreed with and validated the previous ages. These data nevertheless were biased, likely due to analytical matrix effects (e.g. downhole fractionation). Although the two studies showed that geologically meaningful results could be obtained, uncertainties about the fractionation effect led to efforts to fabricate a matrix-matched RM for routine U-Pb dating of Fe-oxides. Despite being abundant, naturally occurring U-bearing hematite from the Olympic Dam deposit, and deposits of similar type elsewhere, were found not to be suitable as RM as their U/Pb ratios are too heterogeneous at the grain scale [8].

In order to maximize the chance of a successful outcome, multiple approaches to RM fabrication have been followed. Alongside pressed pellets, chemical vapor transport and flux experiments, one of the most promising methods has proven to be doping of amorphous hydrated ferric oxide (HFO), [$Fe_2O_3{\cdot}n(H_2O)$]. This has proven an efficient starting material for doping of α-Fe_2O_3 with uranium [9]. The successful crystallization of Pb-doped hematite was documented by [10], and it is also well known that U readily adsorbs onto colloidal HFO, as discussed by [11].

The present contribution describes the fabrication and subsequent characterization of synthetic, doped, compact and microcrystalline hematite samples. We assess their potential as RMs for U-Pb dating of natural U-bearing hematite. A range of microanalytical techniques are used to confirm the material as hematite and demonstrate the homogeneity of composition and U/Pb isotope ratios at the micron-scale.

2. Methods and results

2.1. Doping experiments

Materials used in these experiments consisted of: (1) ferric nitrate nonahydrate, $Fe(NO_3)_3{\cdot}9H_2O$, (FNN; Chem Supply Co., Analytical Reagent grade); and (2) doping solution containing 0.253 mg/mL U and 0.101 mg/mL Pb (for the best sample). Pb/U ratios introduced in solution varied slightly between experiments. The FNN was analytical reagent grade, conforming to ACS specifications. Maximum impurity levels (in ppm) are given as: Cl 5; PO_4 50; SO_4 100; As 2; Cd 10; Ca 50; Cu 10; Pb 20; Mg 10; Mn 50; K 50; Na 50 and Zn 10. If the 40 g of FNN that was used to make the iron nitrate solution was stoichiometric it would correspond to 7.9 g hematite after heating the precipitated HFO. The doping solution contains 0.253 mg/mL U and 0.101 mg/mL Pb for the ideal sample but varied between experiments. It was made from 1000 mg/L uranium standard solution (High-Purity Standards of Charleston SC) prepared from natural U_3O_8 in 2% nitric acid, and a Pb solution made in our laboratory by dissolving non-radiogenic lead metal in hot nitric acid.

A novel approach to RM fabrication has been developed, involving a wet stage of doping colloidal HFO by absorption from a dissolved U and Pb nitrate solution, followed by drying and heating to 700 °C to convert the HFO to Fe_2O_3. Synthesis parameters given below correspond to those used for sample 11, highlighted in Table 1 alongside other samples. The basis of the method is shown schematically in Fig. 1. The reaction that produces the colloidal HFO can be written:

$$2Fe(NO_3)_3 + 6NH_4OH = Fe_2O_3{\cdot}nH_2O + 6NH_4NO_3 + (3\text{-}n)H_2O,$$

where $Fe_2O_3{\cdot}nH_2O$ represents the precipitated HFO [11].

HFO was precipitated from a solution containing 40.0 g of analytical reagent grade ferric nitrate nonahydrate [$Fe(NO_3)_3{\cdot}9H_2O$], dissolved in 500 ml of pure H_2O in a 1 L beaker (Fig. 1). Approximately 380 ml of 2 M ammonia solution was added dropwise with stirring to this initially acidic solution of approximately pH 0.5 until pH 7.7 was reached, and the volume was then topped up to 900 ml with additional H_2O. The result was a brown, gelatinous suspension of HFO that settled in several hours to a volume of 300 ml with a clear supernatant once stirring was stopped.

The supernatant was then decanted using a siphon arrangement after which 600 ml of pure H_2O was added. The solution was stirred for several hours, allowed to settle, and decanted once more, to wash the HFO suspension and remove much of the ammonium nitrate from the initial precipitation. This washing procedure was repeated four times until the washing had removed enough of the ions in solution to cause the flocculent HFO suspension to peptise. This was seen by the supernatant no longer being clear, and the settling of HFO taking days to

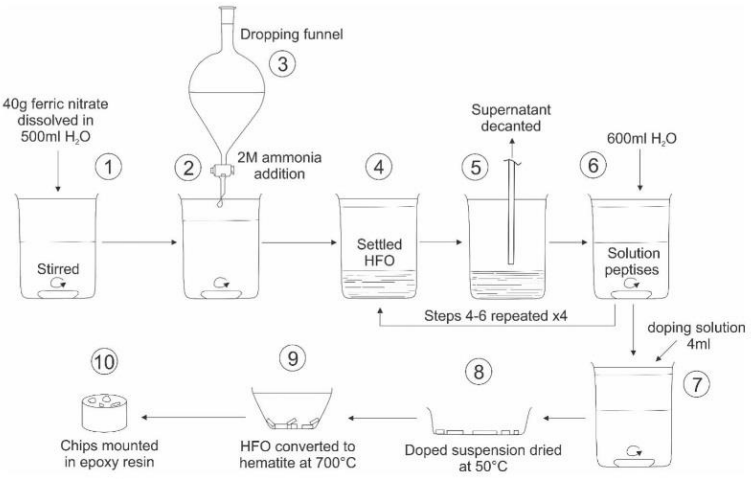


Fig. 1. Schematic diagram of the current optimal RM synthesis conditions. (1) 1000 ml beaker with ferric nitrate dissolved in 500 ml water. Stirred. (2) Beaker with slow addition of 2 M ammonia to pH 7.7 dropwise from – (3) Dropping funnel. Precipitated HFO colloid stirred for several hours. (4) Settled HFO (300 ml) with clear supernatant (600 ml). (5) Supernatant decanted by aspiration through a tube. (6) 600 ml water added, and the suspension washed by stirring for several hours. Washing steps 4–6 repeated 3–4 times until the sol peptises (as seen by the when a clear supernatant is no longer formed). (7) While stirring, 4.0 ml of the doping solution, containing U and Pb nitrates is slowly added to the peptised sol using a calibrated syringe pump. (8) The doped suspension is dried slowly in a 140 mm square stainless-steel Baine Marie dish at 50 °C on a hotplate to form chips of dried HFO. These are several mm in size and about 1 mm-thick. (9) The chips are put into a 50 ml porcelain crucible and heated to 700 °C at a rate of 200 °C/h and kept at 700 °C for one or two hours before furnace cooling back to ambient. This process converts the doped HFO to doped hematite. (10) The chips are mounted in epoxy resin and the surfaces polished for further examination. Note that the circular arrow in some of the beakers denotes a magnetic stir bar in use.

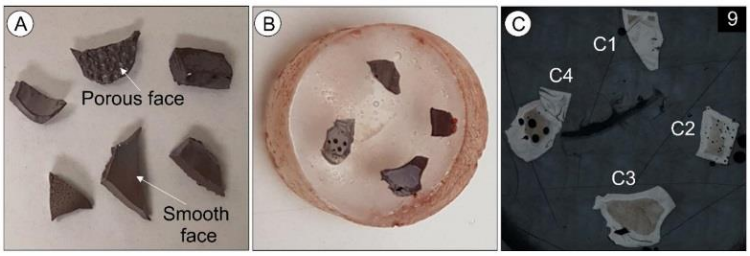


Fig. 2. (A) Chips of hematite (samples 4.1 and 4.3) showing opposite sides with differing smoothness or porosity. (B) Polished block prepared from sample 9. (C) Reflected light image of the four chips in sample 9.

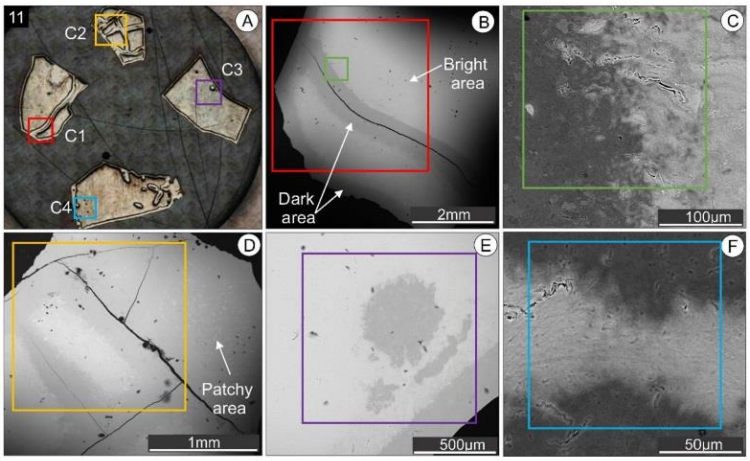


Fig. 3. (A) Low-magnification reflected light photograph of sample 11. (B–F) BSE images showing relationships between bright and dark domains.

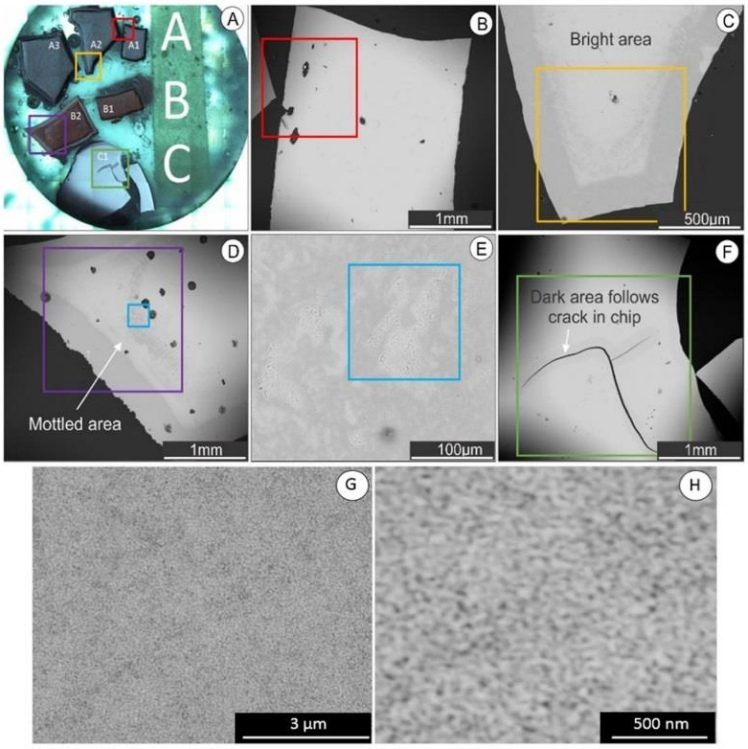


Fig. 4. (A) Reflected light photograph of polished block containing chips of samples A–C. (B–H) BSE images showing relationships between bright and dark domains. (G–H) In detail, the material in both dark and bright domains consists of sub-micron sized, randomly oriented grains of hematite.

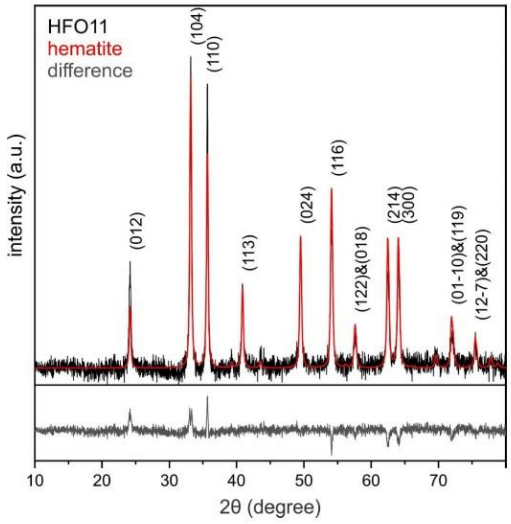


Fig. 5. Diffraction pattern of sample 11 and modelled intensity for hematite (JCPDS 04-003-2900), with the background subtracted and main peaks indexed. The difference between observed and modelled intensities is inherent to the sample preparation method.

Table 2a
Summary of U and Pb LA-ICP-MS data for 'bright' areas of the chips (concentrations in mg/L) at the 95% confidence interval.

Sample ID	U		Pb		$^{207}Pb/^{235}U$		$^{206}Pb/^{238}U$	
	Mean	±	Mean	±	Mean	±	Mean	±
4.1	112	8.29	55.5	3.56	18.44	0.66	0.1451	0.0053
4.3	–	–	–	–	16.49	0.54	0.1299	0.0043
4.2	128	4.59	83.2	5.19	19.47	0.76	0.1528	0.0058
9	1352	48.0	899	38.5	22.67	0.41	0.1776	0.0030
11	146	7.83	74.2	5.33	15.88	0.50	0.1254	0.0039
A	–	–	–	–	18.59	0.74	0.1467	0.0059
B	–	–	–	–	16.37	0.33	0.1281	0.0025
C	–	–	–	–	34.31	0.53	0.2674	0.0040

occur, even then only incompletely. The pure water used to make up solutions and wash the precipitated HFO had a conductivity of less than 1 microsiemens/cm at 20 °C, or slightly more when air-saturated. The specifications for this water were also less than 1 ppm of dissolved solids.

At this stage, 4.0 ml of the doping solution containing U and Pb was added, which would give the final hematite a dopant concentration of 125 mg/L U and 50 mg/L Pb, if quantitatively absorbed by the HFO. This addition resulted in the re-coagulation of the HFO, which was left settled once again and then aspirated to obtain 300 ml of suspended and doped colloidal HFO.

This was poured into a stainless steel, 120 × 100 mm Marie dish that was heated on a hotplate at 50 °C to remove water and produce

Table 2b
Summary of U and Pb LA-ICP-MS data for 'dark' areas of the chips (concentrations in mg/L) at the 95% confidence interval.

Sample ID	U		Pb		$^{207}Pb/^{235}U$		$^{206}Pb/^{238}U$	
	Mean	±	Mean	±	Mean	±	Mean	±
4.1	112	8.31	52.6	3.24	15.35	0.37	0.1209	0.0029
4.3	–	–	–	–	15.51	0.33	0.1221	0.0028
4.2	122.20	3.94	59.6	1.99	19.74	0.72	0.1555	0.0056
9	1336	31.0	818	24.5	20.49	0.22	0.1612	0.0017
11	136	5.63	65.2	3.13	16.16	0.47	0.1268	0.0037
A	–	–	–	–	14.20	0.27	0.1108	0.0023
B	–	–	–	–	14.06	0.19	0.1099	0.0016
C	–	–	–	–	34.83	0.65	0.2726	0.0051

dried HFO chips. These chips averaged several mm in width and roughly 1 mm in thickness. The HFO chips were then collected in a porcelain crucible and heated to 700 °C at variable heating rates (Table 1) in a laboratory furnace, and held at that temperature for 10 h, after which they were furnace-cooled to ambient temperature.

The mass loss on heating was 10%, and the resultant doped hematite chips were dark purple in colour. In most cases, additional cracks had formed during the heating. The fact that no further mass loss occurred on heating part of the material to 800 °C shows that the heating process at 700 °C was sufficient to dehydrate the HFO to Fe_2O_3, as well as to decompose any residual ammonium nitrate in the dried HFO and convert the dopant U and Pb to oxides. This establishes that hydroxides are not present within the HFO. The doped Fe_2O_3 chips were then subject of the investigations reported below to characterise them.

2.2. Characterization methods

Analysis of the resultant hematite material was conducted using a combination of optical microscopy in reflected light, scanning electron microscopy (SEM), LA-ICP-MS and X-ray powder diffraction (XRD). Except for the XRD (School of Chemical Engineering), all instrumentation used are housed at Adelaide Microscopy, University of Adelaide. This sequence of analysis allowed us to characterize domains displaying heterogeneity with respect to U and Pb isotopes.

Mounted chips representing the 8 samples analyzed here (Fig. 2; Table 1) were imaged using a FEI QUANTA 450 SEM equipped with an energy-dispersive X-ray spectrometry (EDS) detector in backscattered electron (BSE) mode. Five polished blocks containing eight different HFO samples were imaged and documented with respect to their morphology, textural and compositional heterogeneity, and the potential presence of included phases. EDS analysis facilitated a semi-quantitative, preliminary assessment of compositional differences between visually otherwise heterogeneous areas.

LA-ICP-MS was used for *in-situ* analysis of U and Pb isotopes in several samples using an ASI Resolution 193 nm excimer laser ablation instrument coupled to an Agilent 7900x ICP-MS. Analysis was performed using a consistent 29 μm-diameter laser spot size, a fluence of 4 J/cm^2 and 10 Hz repetition rate. Measured isotopes consisted of ^{57}Fe, ^{204}Pb, ^{206}Pb, ^{207}Pb, ^{208}Pb, ^{232}Th and ^{238}U. The number of data points collected on each sample was dependent on the size of the material. GJ-1 [4], Plešovice [12] and 91500 [13] were used as the primary and secondary RM's respectively. Data was reduced using the Iolite software package [14], to calculate element concentrations and isotopic ratios. Wetherill Concordia diagrams [15] were plotted from the U-Pb data using the Excel add-in ISOPLOT [16]. Such diagrams are used to display geochronological data, where the x-axis displays $^{207}Pb/^{235}U$ and the y-$^{206}Pb/^{238}U$.

Isotope mapping of selected areas of the samples was conducted using the same instrumentation (see also [7]). Data acquisition involved ablating sets of parallel line rasters in a rectangular grid across the area of interest using a beam size of 11 μm, a scan speed of 11 μm/s, a laser repetition rate of 10 Hz was used with a fluence of ~3.5 J cm^{-2}. Line spacing was kept at a constant 11 μm to match the size of the laser beam used. The effect of redeposition during mapping was minimized by pre-ablating each line immediately prior to its analysis. The depth of ablation during mapping was around ~3 μm.

XRD was used to confirm the mineralogy of the obtained samples

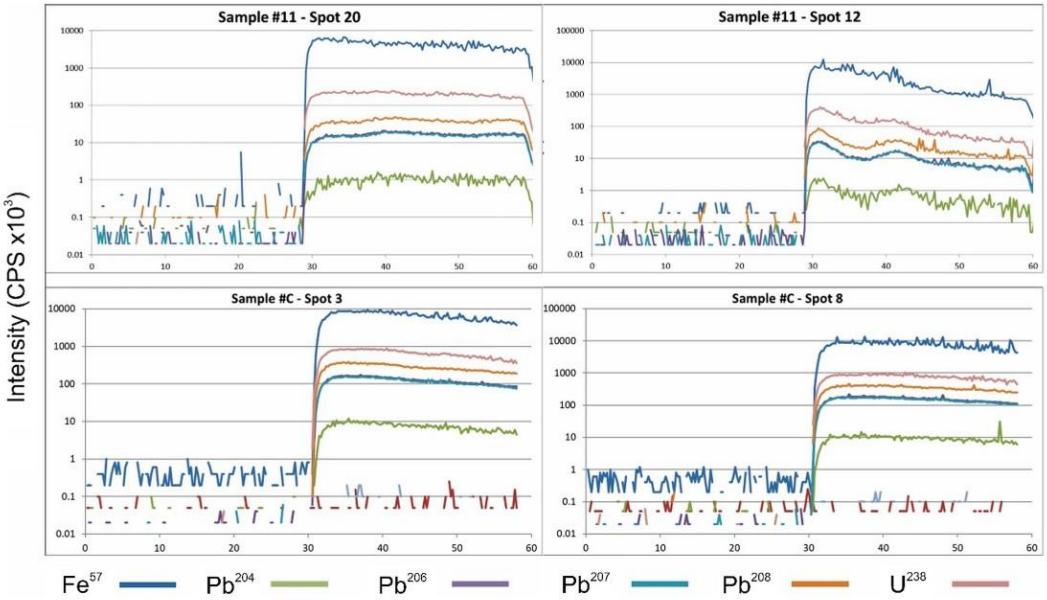


Fig. 6. Representative downhole LA-ICP-MS depth profiles for the isotopes ^{57}Fe, ^{204}Pb, ^{206}Pb, ^{207}Pb ^{208}Pb and ^{238}U.

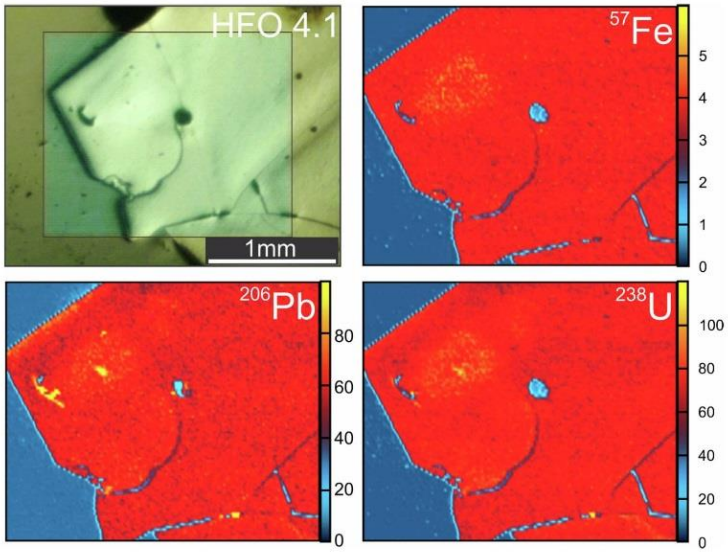


Fig. 7. Reflected light image (upper left) and LA-ICP-MS element maps of hematite (HFO 4.1), showing homogeneity across large parts of the grain, but with anomalous relative enrichment in Fe, Pb and U in the top left corner of the chip. Scales in counts-per-second $\times 10^6$ for Fe, and $\times 10^3$ for U and Pb.

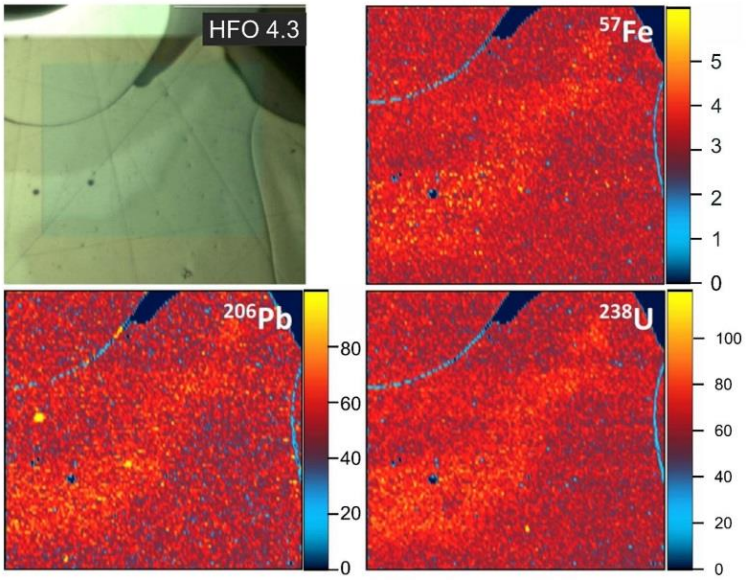


Fig. 8. Reflected light image (upper left) and LA-ICP-MS element maps of hematite (HFO 4.3) showing a good correspondence between the bright domain and higher concentrations of Fe, Pb and U. Scales in counts-per-second $\times 10^6$ for Fe and $\times 10^3$ for U and Pb.

and identify whether any oxyhydroxide phases were still present. This was done using a Rigaku MiniFlex 600 diffractometer equipped with a MiniFlex 300/600 goniometer, using X-Ray Cu-K_α radiation at 40 kV and 15 mA, scanning mode of 2Θ continuous between 10 and 80°, with steps set at 0.02°. Material from each sample was ground into a fine powder, mounted on a glass slide, and installed within the instrument holder.

2.3. Morphology and appearance

Analysis of the eight products showed that the synthetic hematite chips were polycrystalline and very fine grained (grain size < 1 μm). Compositional zoning could be recognized by optical microscopy and confirmed by BSE imaging (Figs. 2C, 3 and 4). This is expressed as contrasting bright and dark domains. No visible inclusions were

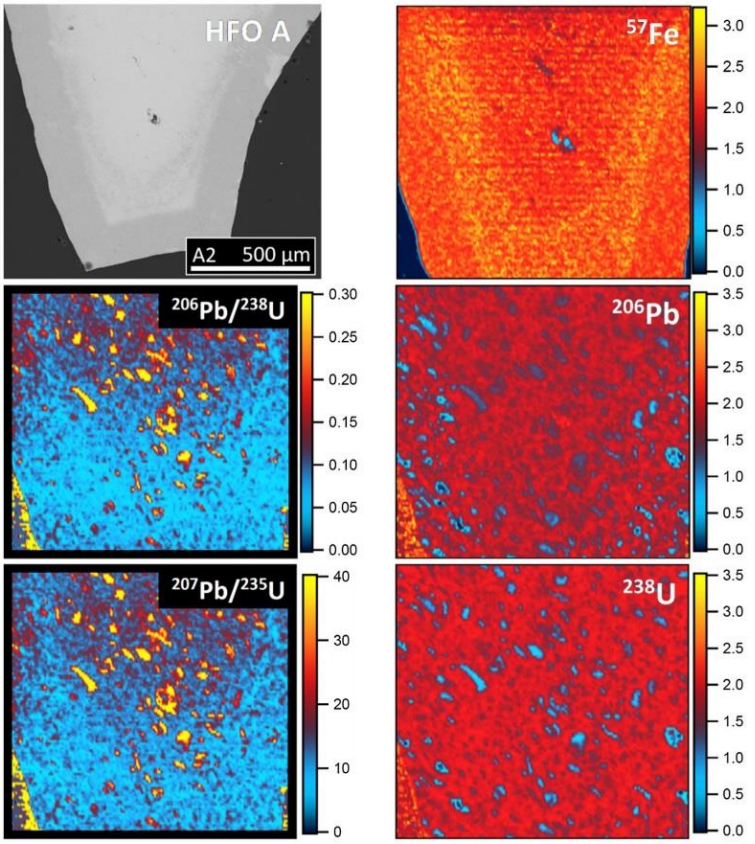


Fig. 9. BSE Image (upper left) and LA-ICP-MS element and isotope ratio maps of hematite (HFO A) as marked. Note that the brighter area in the BSE image correlates with higher Fe in the mottled light and dark transitional region. in contrast the U/Pb ratio maps fluctuate between the bright and dark zones indicating areas of heterogeneity in the central domain of the chip. Isotope scales in counts-per-second $\times 10^6$ for Fe and $\times 10^3$ for U and Pb.

identified but all chips displayed some degree of heterogeneity (Figs. 3 and 4). The chips show dark areas that are spatially related to fractures, margins or internal domains (Figs. 3 and 4). Upon closer inspection of the boundaries between bright and dark domains, a transitional color change with patchy appearance (e.g., sample 11; Fig. 3C–F) is observed on BSE images. Less common are areas with a patchy distribution of a darker domains within the brighter area (Fig. 3E). The bright and dark domains can also show a concentric distribution with respect to the outline of the chip (samples A–C; Fig. 4B–D). Moreover, mottled areas are encountered within bands (Fig. 4D and E), but the dark areas are found predominantly along fractures (Fig. 4F). The centre of chips are predominantly bright, encompassing on average ~80% of the total surface area, however, it can be as low as ~60%. Dark domains, most commonly found around the edge of chips range in width from hundreds of µm to ~1 mm, while mottled areas, generally found at the boundary between bright and dark domains, spread over a few hundred µm. Nonetheless, relationships between bright and dark domains are dominated by patterns showing zoning and mottled textures. Irrespective of the domain type, the material consists of random, sub-µm-sized grains of hematite (Fig. 4G and H).

2.4. X-ray powder diffraction

To further understand the composition of samples and how that may relate to the observation of bright and dark domains within each sample, five of the eight samples were analyzed via XRD. Full pattern deconvolution of the obtained diffractograms using Profex [17] clearly confirm the presence of hematite in all cases. No Fe-hydroxide minerals such as goethite [α-FeO(OH)] can be inferred from the difference between measured and modelled intensities (Fig. 5).

2.5. Geochemistry and U/Pb isotopic composition

Characterization of the HFO samples was primarily focused on identifying the chemical and isotopic differences between the bright and dark areas within the hematite chips and whether chips fabricated under different conditions showed any particular geochemical patterns. LA-ICP-MS spot analysis data are given in Tables 1 and 2a and 2b for each sample, and each LA-ICP-MS spot in Appendix A2-3. The bright areas consistently contain higher measured concentrations of both U and Pb, with concentrations averaging 146.4 and 74.2 mg/L in sample 11, which was the most homogeneous sample, with the error on the mean generally < 5%. Domain heterogeneity is reflected in the subtly different Pb/U isotope ratios. Measured isotopic ratios in sample 11

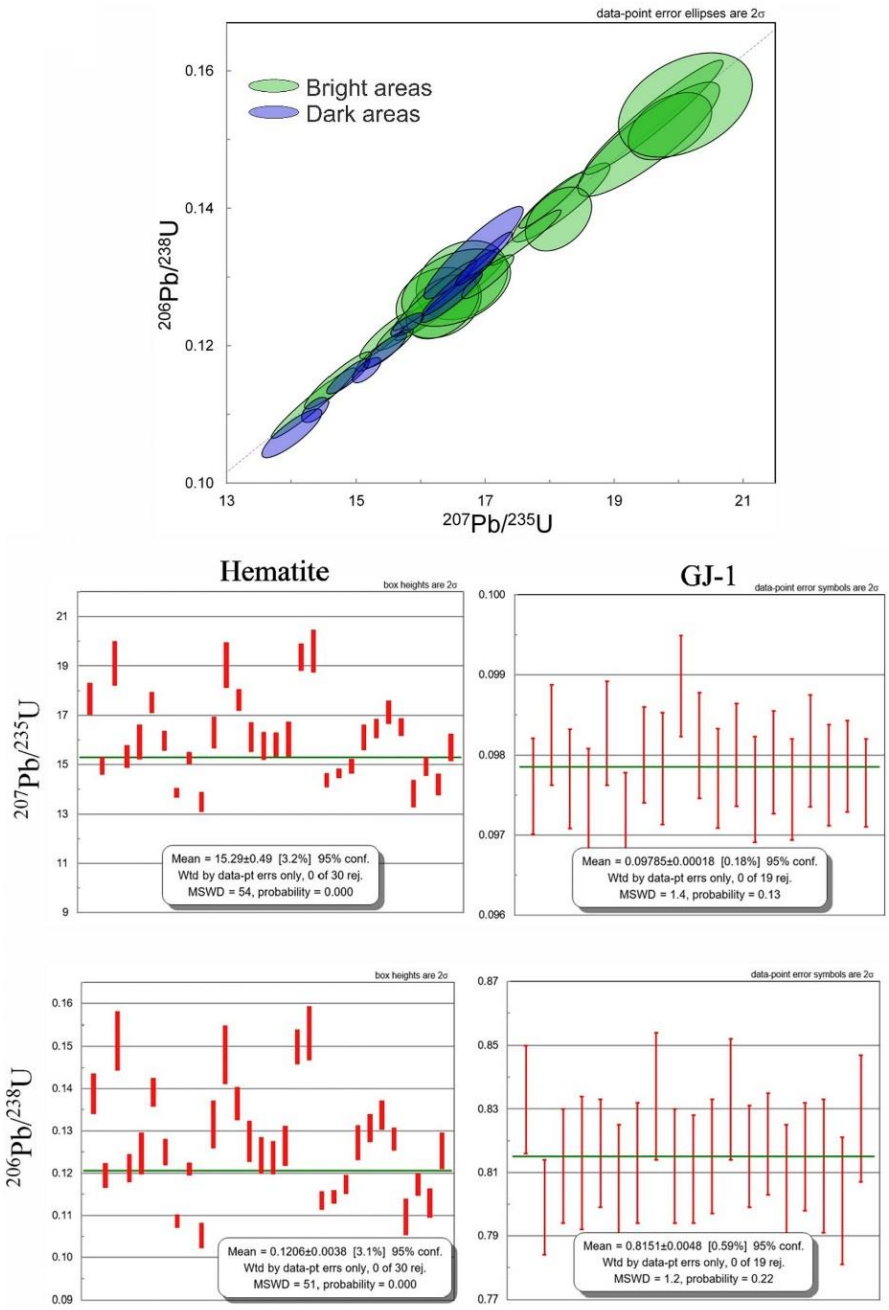


Fig. 10. Wetherill Concordia (above) for sample 11 bright and dark domains and weighted average diagrams (below) comparing $^{207}Pb/^{235}U$ and $^{206}Pb/^{238}U$ for sample 11 and the reference material GJ-1 zircon from the same analytical run.

were marginally lower in the bright area than in the dark regions. Across all samples, it was observed that the bright areas typically contain on average slightly higher U/Pb ratios. Sample 11 was found to be the most homogeneous in terms of Pb/U ratios, yielding the lowest uncertainties of all samples at ~3% for both $^{207}Pb/^{235}U$ and $^{206}Pb/^{238}U$. Conversely, sample C showed significantly higher mean ratios (twice that of most other samples). Uncertainties for $^{207}Pb/^{235}U$ and $^{206}Pb/^{238}U$ ratios in sample C were also the highest amongst the samples (~3.7%), making it the least homogeneous. These two samples are highlighted in green and red respectively in Table 1A.

2.6. Grain-scale distributions and homogeneity

Homogeneity can be assessed from the downhole intensity signals produced from LA-ICP-MS spot analysis. Fig. 6 shows signals for ^{57}Fe, ^{204}Pb, ^{206}Pb, ^{207}Pb ^{208}Pb and ^{238}U in four representative spot analyses (two from sample 11, two from sample C). These demonstrate that there exist areas of homogeneity within the chips, even within sample C, as evidenced by the smoothness of the measured LA-ICP-MS signals collected over a 60 s period. Nonetheless, the spot shown as Fig. 6B (spot 12, sample 11) shows a degree of heterogeneity with respect to all measured isotopes.

The correlation between the bright and dark areas was characterized by LA-ICP-MS maps (Figs. 7–9). The mapping targeted homogeneous regions throughout the two types of domains both in terms of composition and U/Pb isotopic ratios. Areas that show no distinct bright and dark domains can still feature a degree of heterogeneity with respect to the concentrations of Fe, Pb and U (Fig. 7, sample 4.1). In a second case (sample 3), maps show that the distribution of U and Pb clearly varies between the light and dark domains seen in reflected light and BSE images (Fig. 8). This is exemplified in Fig. 9, with grain from sample A, which is one the most heterogeneous samples. Here, variation in U and Pb is due to concentration differences, which are seen to be scattered within domains that are otherwise bright and 'speckled' where U-Pb counts per second a low (Fig. 9).

3. Discussion and conclusions

Since the samples are synthetic, they cannot have a 'natural' age, so in all cases, data points plot far from the Concordia curve i.e. natural samples which have remained a closed U-Pb system since formation, will plot on the Concordia curve as the decay of $^{206}Pb/^{238}U$ and $^{207}Pb/^{235}$ U is coupled. The trend, scatter and size of the data-point ellipses are nonetheless a useful tool for assessing sample homogeneity. Spot analyses, from both dark and bright domains in sample 11 are plotted in Fig. 10. This shows a good overlap of the more homogenous dark area (plotted blue ellipses) and a larger spread in the bright areas (green ellipses).

Weighted average diagrams for isotopic ratios ($^{207}Pb/^{235}U$ and $^{206}Pb/^{238}U$) are also shown in Fig. 10, measured in both hematite and the GJ-1 zircon RM. As expected, the hematite showed lower precision than the analyzed zircon RM at 3.2% and 0.18% respectively, but still yields acceptable homogeneity. The mean square weighted deviation value was acceptable for many of the samples e.g. sample #11 with an MSWD of 2.3; compared to 1.4 for GJ-1 zircon. Overall the sample which had similar mean isotopic ratios of ~15 for $^{207}Pb/^{235}U$, showed good data point overlap and small data point uncertainties when plotted on the same Concordia diagram (Fig. 10). These results support the potential for producing a homogeneous RM via the doping of synthetic HFO, with further refinement of the method. Although sample 11 yields the most homogeneous data, the doping concentrations and fabrication process were similar for samples 4.1–3, and therefore shows a consistency between the experiments, a slightly lower homogeneity in samples 4.1–3 can be attributed to the lower analyses *n*.

The experiments outlined here were successful in co-doping an iron-oxide with U and Pb. This synthetic hematite represents a potential RM for use in U-Pb geochronology. Results show that the preparation methods and doping conditions are valid and that synthetic hematite can be produced that contains domains sufficiently homogeneous to be suitable for *in-situ* microbeam dating.

The chemical and isotopic heterogeneity between the bright and dark domains is however real and may prevent widespread use of the synthesized material as RM. The recognized differences in U/Pb ratios, although minor, may be spatially controlled by the heating and cooling regimes of the HFO.

Assuming the 'bright and dark domains' can be analytically or mechanically separated through refinement of the preparation method, then a suitable RM for *in-situ* hematite microbeam dating may be produced. The RM would then require high-precision chemical analysis via isotope dilution-thermal ionization mass spectrometry before it could be implemented as a useable RM for geological applications [18]. Such a RM could be used for microbeam dating of uranium-bearing hematite, in deposits of various types, including world-class hematite-dominant Cu-U-Au-Ag deposits such as Olympic Dam, Australia. The RM will enable the LA-ICP-MS technique to obtain accurate geological ages in a very common mineral, providing new insights for mineral exploration worldwide.

Acknowledgements

This work is a contribution to the 'FOX' project (Trace elements in iron oxides: deportment, distribution and application in ore genesis, geochronology, exploration and mineral processing), supported by BHP Olympic Dam and the South Australian Government Mining and Petroleum Services Centre of Excellence. We extend our thanks to Quihong Hu for training and assistance with XRD determinations. Comments from two anonymous reviewers and Editor T. Nishinaga, are deeply appreciated.

Appendix A. Supplementary material

Supplementary data to this article can be found online at https://doi.org/10.1016/j.jcrysgro.2019.02.053.

References

[1] C.L. Ciobanu, B.P. Wade, N.J. Cook, A. Schmidt Mumm, D. Giles, Uranium-bearing hematite from the Olympic Dam Cu–U–Au deposit, South Australia: a geochemical tracer and reconnaissance Pb–Pb geochronometer, Precambr. Res. 238 (2013) 129–147.
[2] R.C. Ewing, A. Meldrum, L. Wang, W.J. Weber, L.R. Corrales, Radiation effects in zircon. In: J.M. Hanchar, P.W.O. Hoskin (Eds.) Zircon. Mineralogical Society of America Rev. Mineral. Geochem. 53 (2003), 387–425.
[3] P.W. Reiners, P.R. Renne, R.W. Carlson, K.M. Cooper, D.E. Granger, N.M. McLean, B. Schoene, Geochronology and Thermochronology, John Wiley & Sons, 2017.
[4] S.E. Jackson, N.J. Pearson, W.L. Griffin, E.A. Belousova, The application of laser ablation inductively coupled plasma-mass spectrometry to in-situ U-Pb zircon geochronology, Chem. Geol. 211 (2004) 47–69.
[5] U. Schaltegger, A. Schmitt, M. Horstwood, U-Th–Pb zircon geochronology by ID-TIMS, SIMS, and laser ablation ICP-MS: recipes, interpretations, and opportunities, Chem. Geol. 402 (2015) 89–110.
[6] M. Horstwood, Data reduction strategies, uncertainty assessment and resolution of LA-(MC-) ICP-MS isotope data. In: P. Sylvester (ed.), Laser Ablation ICP–MS in the Earth Sciences, Mineralogical Association of Canada Short Course. 40 (2008) 283–303.
[7] L. Courtney-Davies, Z. Zhu, C.L. Ciobanu, B.P. Wade, N.J. Cook, K. Ehrig, A.R. Cabral, A. Kennedy, Matrix-matched iron-oxide laser ablation ICP-MS U-Pb geochronology using mixed solution standards, Minerals 6 (2016) 85, https://doi.org/10.3390/min603008.
[8] L. Courtney-Davies, S. Tapster, C.L. Ciobanu, N.J. Cook, M.R. Verdugo-Ihl, K.J. Ehrig, A.K. Kennedy, S.E. Gilbert, D.J. Condon, B.P. Wade, A multi-technique evaluation of hydrothermal hematite U-Pb isotope systematics: Implications for ore deposit geochronology, Chem. Geol. (2019), https://doi.org/10.1016/j.chemgeo.2019.03.005 https://www.sciencedirect.com/science/article/pii/S0009254119301032 (in press).
[9] T.A. Marshall, K. Morris, G.T.W. Law, F.R. Livens, J.F.W. Mosselmans, P. Bots, S. Shaw, Incorporation of uranium into hematite during crystallization from ferrihydrite, Environ. Sci. Technol. 48 (2014) 3724–3731.
[10] H.P. Vu, S. Shaw, L. Brinza, L.G. Benning, Crystallization of hematite (α-Fe_2O_3)

under alkaline condition: the effects of Pb, Cryst. Growth Des. 10 (2010) 1544–1551.
[11] D. Langmuir, Aqueous Environmental Geochemistry, Prentice Hall, Pearson, 1997.
[12] J. Sláma, J. Košler, D.J. Condon, J.L. Crowley, A. Gerdes, J.M. Hanchar, M.S.A. Horstwood, G.A. Morris, L. Nasdala, N. Norberg, U. Schaltegger, B. Schoene, M.N. Tubrett, M.J. Whitehouse, Plešovice zircon – a new natural reference material for U-Pb and Hf isotopic microanalysis, Chem. Geol. 249 (2008) 1–35.
[13] M. Wiedenbeck, P. Alle, F. Corfu, W.L. Griffin, M. Meier, F. Oberli, A. Von Quadt, J.C. Roddick, W. Spiegel, 3 natural zircon standards for U-Th-Pb, Lu-Hf, trace-element and REE analyses, Geostandards Newsletter. 19 (1995) 1–23.
[14] C. Paton, J. Hellstrom, B. Paul, J. Woodhead, J. Hergt, Iolite: freeware for the visualisation and processing of mass spectrometric data, J. Anal. Atom. Spectrom. 26 (2011) 2508–2518.
[15] G.W. Wetherill, Discordant U-Pb ages, Transactions, Amer. Geophys. Union 37 (1956) 3.
[16] K.R.A. Ludwig, Isoplot/Ex rev. 4.1: A Geochronological Toolkit for Microsoft Excel; Berkeley Geochronology Centre Special Publication; Berkeley Geochronology Centre: Berkeley, CA. 5, (2012) 75.
[17] N. Doebelin, R. Kleeberg, Profex: a graphical user interface for the Rietveld refinement program BGMN, J. Appl. Crystallogr. 48 (2015) 1573–1580.
[18] L. Courtney-Davies, M. Richardson, S.E. Gilbert, C.L. Ciobanu, M.R. Verdugo-Ihl, N. J. Cook, K. Ehrig, B.P. Wade, U-Pb doped synthetic reference material for in-situ hematite geochronology. Geoanalysis 2018, Sydney, Conference Abstract (2018).

CHAPTER 9

APPRAISAL AND IMPLEMENTATION OF A SYNTHETIC HEMATITE REFERENCE MATERIAL FOR MICROBEAM U-PB GEOCHRONOLOGY

Liam Courtney-Davies [1], Sarah E. Gilbert [2], Cristiana L. Ciobanu [1], Simon R. Tapster [3], Marcus W. Richardson [4], Benjamin. P. Wade [2], Nigel J. Cook [1], Kathy Ehrig [5], Max R. Verdugo-Ihl [1], Allen K. Kennedy [6], Daniel J. Condon [3] and Roland Maas [7]

[1]*School of Chemical Engineering and Advanced Materials, The University of Adelaide, Adelaide, SA 5005, Australia*

[2]*Adelaide Microscopy, The University of Adelaide, Adelaide, SA 5005, Australia*

[3]*NIGL, British Geological Survey, Keyworth, Nottinghamshire, NG12 5GG, U.K.*

[4]*6 Ophir Street, Goodwood, SA 5034, Australia*

[5]*BHP Olympic Dam, Adelaide, SA 5000, Australia*

[6]*John de Laeter Centre, Curtin University of Technology, Bentley, WA 6102, Australia*

[7]*School of Earth Sciences, University of Melbourne, Melbourne, VIC 3010, Australia*

Statement of Authorship

Title of Paper	Assessment And Appraisal Of A Synthetic Hematite Reference Material For Microbeam U-Pb Geochronology
Publication Status	☐ Published ☐ Accepted for Publication ☐ Submitted for Publication ☑ Unpublished and unsubmitted work written in manuscript style
Publication Details	Unpublished thesis chapter intended to be submitted in a revised form to Geostandards and Geoanalytical Research in December 2019.

Principal Author

Name of Principal Author (Candidate)	Liam Courtney-Davies		
Contribution to the Paper	Oversaw development of the work, performed analytical work, carried out data processing, interpretation and wrote the manuscript.		
Overall percentage (%)	50		
Certification:	This paper reports on original research I conducted during the period of my Higher Degree by Research candidature and is not subject to any obligations or contractual agreements with a third party that would constrain its inclusion in this thesis. I am the primary author of this paper.		
Signature		Date	29/10/2019

Co-Author Contributions

By signing the Statement of Authorship, each author certifies that:

i. the candidate's stated contribution to the publication is accurate (as detailed above);

ii. permission is granted for the candidate in include the publication in the thesis; and

iii. the sum of all co-author contributions is equal to 100% less the candidate's stated contribution.

Name of Co-Author	Sarah E. Gilbert		
Contribution to the Paper	Helped define the direction of research, supervised development of work, assisted with data collection, interpretation and manuscript preparation.		
Overall percentage (%)	10		
Signature		Date	29/10/19

Name of Co-Author	Cristiana L. Ciobanu		
Contribution to the Paper	Defined the direction of research, supervised development of work and contributed to analytical work and evaluation of the manuscript.		
Overall percentage (%)	10		
Signature		Date	29 Oct 2019

Name of Co-Author	Simon R. Tapster		
Contribution to the Paper	Conducted ID-TIMS data collection and development of research direction.		
Overall percentage (%)			
Signature		Date	29 Oct 2019

Name of Co-Author	Marcus W. Richardson		
Contribution to the Paper	Helped to define research direction and synthesized the reference material.		
Overall percentage (%)	10		
Signature		Date	29/10/2019

Name of Co-Author	Benjamin. P. Wade		
Contribution to the Paper	Assisted in analytical work, assisted in data processing and interpretation.		
Overall percentage (%)	2		
Signature		Date	29/10/2019

Name of Co-Author	Nigel J. Cook		
Contribution to the Paper	Helped define the research direction and evaluation of manuscript.		
Overall percentage (%)	2		
Signature		Date	29/10/2019

Name of Co-Author	Kathy Ehrig		
Contribution to the Paper	Helped define research direction and coordinated sample collection.		
Overall percentage (%)	2		
Signature		Date	29/10/2019

Name of Co-Author	Max R. Verdugo-Ihl		
Contribution to the Paper	Assisted in LA-ICP-MS data collection, interpretation and evaluation of manuscript.		
Overall percentage (%)	1		
Signature		Date	29/10/2019

Name of Co-Author	Allen K. Kennedy		
Contribution to the Paper	Helped define research direction.		
Overall percentage (%)	1		
Signature		Date	29/10/2019

Name of Co-Author	Daniel J. Condon		
Contribution to the Paper	Helped define research direction.		
Overall percentage (%)	4		
Signature		Date	29 Oct 2019

Name of Co-Author	Roland Maas		
Contribution to the Paper	Undertook solution-ICP-MS work		
Overall percentage (%)	1		
Signature		Date	29 Oct 2019

Abstract

The common iron-oxide hematite (α-Fe_2O_3) can incorporate significant concentrations of U into its crystal structure and retain radiogenic Pb produced *in-situ* over geological time. This capacity to host both U and Pb has been confirmed in laboratory experiments. Hematite is a ubiquitous component of banded iron formation and iron-oxide copper gold (IOCG) deposits and therefore a useful hydrothermal mineral geochronometer for constraining the timing of ore formation and superimposed geological events in such environments; however, no suitable natural hematite reference material has been identified to date. Here, we characterize the first matrix-matched synthetic hematite U-Pb reference material (HFO), using bulk chemical analysis and *in-situ* microbeam techniques. Subsequently, a reconnaissance appraisal of the materials application to *in-situ* U-Pb geochronology is presented. Centimeter-scale chips of hydrated ferric oxide doped with U and Pb were converted into α-Fe_2O_3 and mounted within one-inch diameter polished blocks. Downhole depth profiles generated by laser ablation-inductively coupled plasma-mass spectrometry (LA-ICP-MS) confirm U and Pb is homogeneously distributed, not present as inclusions, and that U/Pb downhole fractionation is comparable to that observed in natural hematite specimens. Spot analyses demonstrate consistent concentrations and ratios of U and Pb within a HFO chip and across multiple HFO chips. Material was randomly microsampled via laser ablation-extraction in twelve locations across four HFO chips for isotope dilution-thermal ionization mass spectrometry (ID-TIMS). Reproducible U/Pb and Pb/Pb measurements were obtained (n=13), although three outliers are present in the dataset, either resulting from heterogeneity within the microsampled material, or due to incomplete equilibration between the sample and spike during dissolution steps. When excluding the outliers, our preferred weighted average calibration values for HFO are: $^{207}Pb/^{206}Pb = 0.9175 \pm 0.0013$, $^{206}Pb/^{238}U = 0.12213 \pm 0.00074$ and $^{207}Pb/^{235}U = 15.439 \pm 0.088$

(2σ; n = 10/13). Millimeter-scale grains of natural hematite from different locations within the Olympic Dam IOCG deposit (South Australia), were previously microsampled and analyzed by ID-TIMS, yielding reproducible and high-precision U/Pb measurements. LA-ICP-MS spot analyses were collected adjacent to the material subsampled for ID-TIMS, and calibrated separately using both the GJ-1 zircon and HFO reference materials as primary standards, employing Plešovice and 91500 as secondary standards. In both cases, LA-ICP-MS $^{207}Pb/^{206}Pb$ dates generated via calibration with HFO are marginally more accurate than those calibrated with the GJ-1 zircon, when compared to the independent ID-TIMS measurements of the grains. HFO calibrated data plotted on a Wetherill diagram is however considerably more concordant, accurate and higher precision (upper intercept) than GJ-1 calibrated analyses. This is significant, as intercepts are often the most suitable form of date to use in hematite age interpretation, particularly for banded iron formation samples where Pb loss and common Pb-components are substantial, and concentrations of U are typically low.

9.1 Introduction

Uranium-Pb dating of hematite is a fledgling field of geochronology, with applications in a range of geological environments spanning the entire geological history of the Earth. Most notably, the hematite U-Pb mineral geochronometer has been used to resolve and support the timing of ore formation within iron-oxide copper gold (IOCG), porphyry-related Au and banded iron formation deposits (Ciobanu et al., 2013; Courtney-Davies et al., 2016; 2019a, b; Zhou et al., 2017; Keyser et al., 2019).

The three fundamental caveats for accurate radioisotopic dating are: (1) incorporation of U during crystallization; (2) quasi-exclusion of common Pb during crystallization; and (3) preservation of a near-closed U-Pb system from the point of primary crystallization. Concentrations of U measured in natural hematite vary significantly, between geological

settings and often also within single systems and grains. U-bearing hematite is volumetrically abundant in uranium-rich ore systems, such as the Olympic Dam IOCG deposit (South Australia) and has, in some cases, been documented to attain several wt.% U, and likely higher within sub-microscopic domains (Ciobanu et al., 2013; Verdugo-Ihl et al., 2017). The proposed substitution mechanism for U in such hematite could involve: $2Fe^{3+} \leftrightarrow U^{6+} + \square$ (; up to 0.013 atoms per formula unit assuming U^{6+}; Verdugo-Ihl et al., 2017), based on vacancy-induced crystal-structure modifications (long-range superstructures; Ciobanu et al., 2013). Experimental studies have reproduced observations in nature, whereby Duff et al. (2002) established that U^{6+} is incorporated in Fe-oxides as the uncommon uranate species (without axial O atoms) until saturation is reached. Common Pb (primordial ^{204}Pb and/or unsupported radiogenic Pb) contents, like U, can vary by several orders of magnitude intra-grain. This feature is common within hematite that has been exposed to hydrothermal overprinting, whereby trace elements are preferentially substituted and micron- to nanoscale inclusions containing elements released from hematite nucleate along reaction fronts, modifying primary U-Pb systematics (Verdugo-Ihl et al., 2017, 2019). However, hematite has proven remarkably durable within such hydrothermal systems (Courtney-Davies et al., 2019a). Isotope dilution-thermal ionization mass spectrometry (ID-TIMS) measurements of microsampled compositionally zoned hematite grains from the ~1590 Ma Olympic Dam deposit, in some cases, yield concordant data points, where the largest contribution of common Pb is inherited from the laboratory blank (Courtney-Davies et al., 2019a). This demonstrates that hematite can retain a near-closed U-Pb system over geological time within complex magmatic-hydrothermal ore deposits. Furthermore, hematite does not appear to accumulate significant alpha-decay damage, despite high U contents (Courtney-Davies et al., 2019a).

Due to the large costs and timeframes of ID-TIMS analysis and sample preparation, development of a hematite reference material is critical for use in microbeam analytical

techniques e.g. fast and cost-effective laser ablation-inductively coupled plasma-mass spectrometry (LA-ICP-MS). Accurate LA-ICP-MS data requires analyses of unknowns to be calibrated against equivalent analyses of a well-characterized reference material. Such materials need to be exceptionally homogeneous in isotopic composition at the micron scale, structurally homogeneous, sufficiently matched to the matrix of the unknowns and not contain internal fractures, cracks or inclusions (Nasdala et al., 2018). No natural hematite grains that are sufficiently large or isotopically homogeneous to be implemented widely as reference material have been identified thus far.

Consequently, we set out to fabricate a synthetic hematite U-Pb reference material. 'Chips' of hematite were successfully co-doped with U and Pb following the methodology described in Courtney-Davies et al. (2019c), with some minor modifications to the production process (see below).

The hematite reference material, hereafter named 'HFO', underwent a sequence of characterization steps, which we present in this study: This initially involved imaging to ascertain the nature of the material from the chip to micron scales. Uranium and Pb distribution at depth was evaluated by LA-ICP-MS downhole profiles and the degree of U/Pb fractionation in the HFO *versus* natural samples assessed. Four HFO chips were microsampled for ID-TIMS, providing high precision U/Pb data. Lastly, samples of hematite from the Olympic Dam IOCG deposit were analyzed using the HFO as the reference material and compared to data using calibrations based on zircon reference material.

9.2 Methodology

9.2.1 Imaging

Mounted HFO chips were imaged via optical microscopy in reflected light and using a FEI QUANTA 450 scanning electron microscope equipped with energy-dispersive X-ray spectrometry (EDS) and backscattered electron (BSE) detectors. Laser ablation crater shape and depths were measured in 3D using an optical Olympus LEXT OLS5000 laser confocal microscope. All instruments are housed at Adelaide Microscopy, the University of Adelaide.

9.2.2 Laser ablation ICP-MS

All reported LA-ICP-MS data were collected using a 193 nm RESOlution-LR excimer laser microprobe (Australian Scientific Instruments) coupled to an Agilent 7900x Quadrupole ICP-MS during a single analytical session. Acquisition protocols followed the same methodology as outlined in Courtney-Davies et al. (2019a) for natural hematite as well as for HFO analyses (Table 1). The GJ-1 zircon (Jackson et al., 2004) was the primary zircon reference material used to calibrate unknowns, while Plešovice (Sláma et al., 2008) and 91500 (Wiedenbeck et al., 1995) were run as secondary standards. Data was processed in using Iolite data reduction software (Paton et al., 2011). Data presented was not filtered or manipulated through signal selection in order to assess unbiased values. All geochronological data is presented using Isoplot 4.1 (Ludwig, 2012). Further analytical and data processing details can be found in Table 1. LA-ICP-MS data acquisition involved a sequence of four spots on HFO, three on GJ-1, two on Plešovice, one spot on 91500, and twenty spots on unknowns, repeated.

9.2.3 Isotope dilution TIMS

Procedures follow a slightly modified methodology to that presented in Courtney-Davies et al. (2019a; see for extended details). Sample preparation for ID-TIMS was conducted at

Adelaide Microscopy. HFO was extracted *in-situ* by ablating 50 to 100 µm wide trenches using an ESI NWR213 solid state laser ablation system (three line raster passes at 10 Hz, 1 µm/s, 20–80 µm beam diameter) to form squares, ~100 × 100 µm in size, within HFO chips (Figure 1).

Table 1. LA-ICP-MS data collection and processing parameters.

Laboratory and Sample Preparation	
Laboratory name	Adelaide Microscopy
Sample type/mineral	Hematite grains within 1-inch round polished block
Imaging	FEI Quanta 450 scanning electron microscope
Laser ablation system	
Make, Model and type	RESOlution-LR excimer laser microprobe (Australian Scientific Instruments)
Ablation cell and volume	Large format S155 two-volume ablation cell (Laurin Technic Pty)
Laser wavelength (nm)	193 nm
Pulse width (ns)	20 ns
Fluence (J cm^{-2})	Zircon = 2.5 J.cm^{-2}; Hematite and HFO = 4 J.cm^{-2}
Repetition rate (Hz)	5 Hz
Ablation duration (s)	40 s
Ablation pit depth	25 µm hematite; 45 µm HFO
Spot diameter (um)	29 µm
Sampling mode/pattern	Static spot ablation
Carrier gas	0.38 L/min He in the cell; 1.05 L/min Ar carrier gas combined within the funnel of the two-volume ablation cell, after ablation
ICP-MS Instrument	
Make, Model and type	Agilent 7900x Quadrupole ICP-MS
Sample introduction	Direct aerosol injection into the lasma
RF power (W)	1350 W
Detection system	Electron Multiplier, Pulse mode
Masses measured	^{57}Fe, ^{204}Pb, ^{206}Pb, ^{207}Pb, ^{208}Pb, ^{232}Th, and ^{238}U
Integration time per peak/dwell times (ms)	5, 20, 50, 50, 10, 10, 50 ms, respectively
Settling time between mass jumps	2.8 ms
Total integration time per output data point	0.233 s
Data Processing	
Gas blank	30 s gas background
Data processing package used	Iolite™ (Paton et al., 2011); DRS scheme: U_Pb_Geochronology3
Common-Pb correction	No common-Pb correction applied to the data
Uncertainty level and propagation	2 sigma level uncertainty, internal error propagation through Iolite
^{238}U/^{235}U data reduction value	137.818 (Heiss et al., 2012)

Following ultrasonic cleaning of the polished blocks, the target material (area contained within the square) was manually extracted under a microscope with tweezers and transferred to separate vials. Each sample weighted ~0.1 mg, containing an average of 15 ng U and 6.6 ng of Pb. Analyses were conducted at the Natural Environment Research Council, Isotope

Geosciences Laboratory, British Geological Survey. The mixed ^{205}Pb-^{233}U-^{235}U U-Pb tracer (NIGL-2) and 400 µl of 6N HCl were added to each HFO aliquot and fluxed for ≥2 days at 120 °C in closed beakers. The HFO aliquots dissolved in HCl within 2 days. Following dissolution and equilibration, the tracer samples were dried to chloride form, then dissolved in ~300 µl of concentrated 9M HBr, and lastly, fluxed on a hotplate overnight at 120 °C to convert to bromide form. Samples were then dried and dissolved in ~300 µl 1 M HBr to complete the conversion to bromide form. Separation of Pb from matrix elements and U was conducted using a variation of the HBr-HNO3 AG 1-X8 anion exchange resin chemistry (Lugmair and Galer, 1992). Separation of U from the remaining matrices was achieved using an AG 1-X8 HNO_3 and HCl-based chemistry modified from Edwards et al. (1986). Lead fractions were dried down individually with ~10 µl of H_3PO_4 and then loaded onto a zone-refined Re filament in a silica gel matrix (Gerstenberger and Haase, 1997). Isotope ratios were measured using a Thermo Triton thermal ionization mass-spectrometer. Lead was measured in peak hopping (dynamic) mode on a single MassCom secondary electron multiplier. Linearity and dead time corrections on the SEM were monitored using repeated analyses of the NBS 982, NBS 981 and U 500 reference materials (Pb = 24.5 ns; U = 22 ns). Uranium was run in oxide form (UO_2) and measured in static mode on Faraday detectors equipped with a 1012 Ω resistor and corrected for isobaric interferences using an $^{18}O/^{16}O$ value of 0.00205. Uranium mass fractionation was calculated in real-time based on the isotopic composition of the tracer solutions. Mass bias for Pb was corrected using the fractionation factor of 0.14 ± 0.02% per amu (1σ). Decay constants used are from Jaffey et al. (1971) for ^{238}U and ^{235}U. Isotope measurements were processed using the TRIPOLI software package (Bowring et al., 2011). Data reduction, error propagation and date calculations were carried out using the excel spreadsheet of Schmitz and Schoene (2007) using a $^{238}U/^{235}U$ value of 137.818 (Heiss et al., 2012). Isotope ratios have been corrected for lab blanks only at this stage of the study.

9.3 Samples

9.3.1 Synthetic hematite reference material (HFO)

Synthetic hematite co-doped with U and Pb was prepared from a solution of ferric nitrate precipitated with ammonia solution. This reaction produced a suspension of colloidal hydrated ferric oxide that was washed with water several times by decantation until it peptised. A doping solution of uranyl and lead nitrates was then added to adsorb the U and Pb onto the colloidal hydrated ferric oxide particles. Ultrasonication with a powerful 200W horn subdivided the colloidal particles and increased the surface area for dopant adsorption. After settling, the doped material was dried at 50 °C to produce solid chips, each several millimeters in thickness, followed by heating to 700 °C. The material was held at 700 °C for 10 h, after which it was furnace-cooled to ambient temperatures, resulting in conversion of doped hydrated ferric oxide to α-Fe_2O_3. The doping solution contained 0.253 mg/mL U and 0.101 mg/mL Pb, obtained from 1000 mg/L U standard solution (High-Purity Standards of Charleston SC), prepared from natural U_3O_8 in 2% nitric acid, and a Pb solution made in our laboratory by dissolving non-radiogenic Pb metal in hot nitric acid. The crystal phase present in the samples were repeatedly confirmed as α-Fe_2O_3 by X-ray powder diffraction.

As described in Courtney-Davies et al. (2019c), the HFO synthesis method produces distinct domains of ‘lighter’ and ‘darker’ material within individual chips. The domains contain minor differences in U-Pb concentrations and a larger U/Pb heterogeneity in the ‘brighter’ domains, phenomena which are likely spatially controlled by the heating and cooling regimes during synthesis. Despite this, the more homogeneous ‘darker’ domains encompass sufficiently large portions of the chips (up to 8 x 4 mm), and brighter to darker domain boundaries are adequately sharp for them to be confidently assessed separately (Figure 1 A-D). Four chips of HFO within a single polished block were microsampled via laser ablation-extraction (Figure 1C) in thirteen

locations within the 'darker' domains (chips AG1-4), and three locations with a single 'brighter' domain (chip BG2; Figure 1B, D).

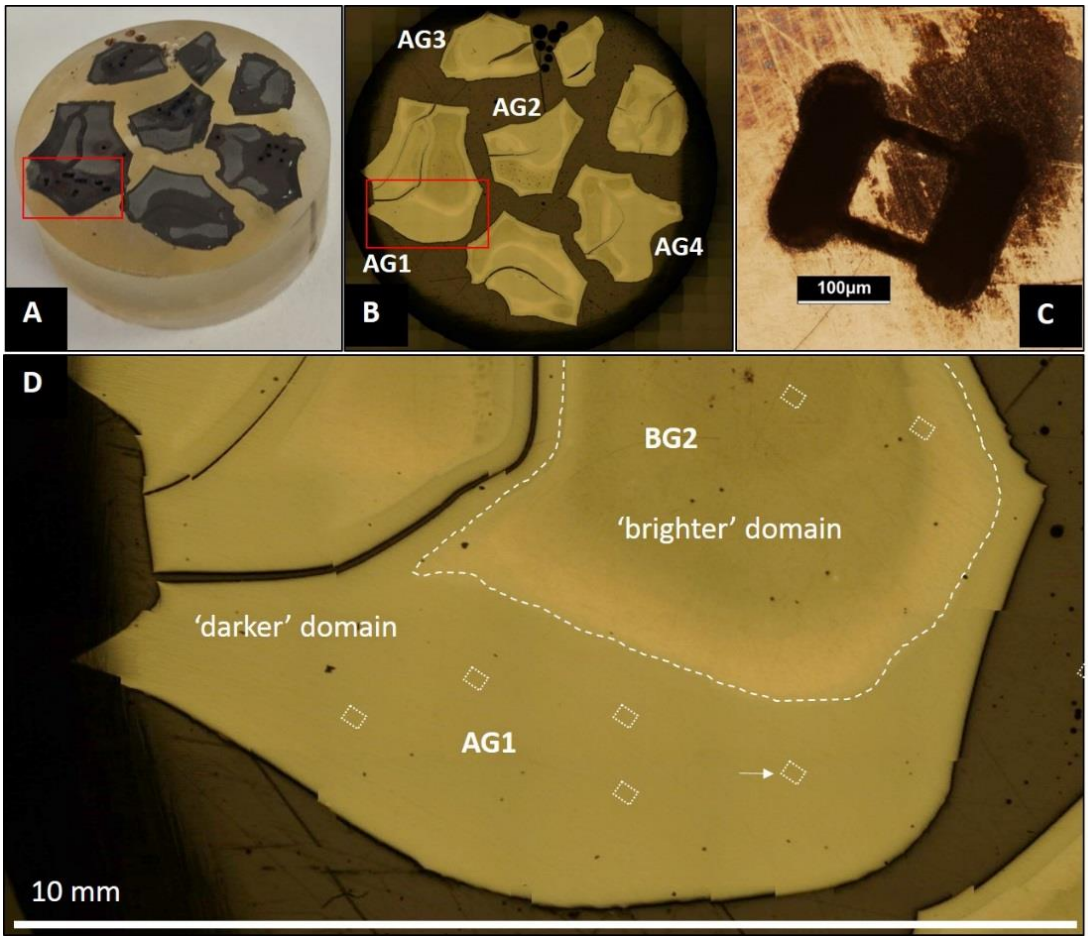


Figure 1. (A) Photograph of characterized HFO chips mounted in a 1-inch polished block. (B) Optical reflected light scan of the polished block surface. (C) Optical photomicrograph of a laser ablation cut trench, used to extract domains of the HFO for ID-TIMS. (D) Magnification of marked red box in (A, B), displaying the locations of microsampled material (arrowed).

9.3.2 Natural hematite

Two natural grains of oscillatory zoned-hematite, obtained from the Olympic Dam IOCG deposit and previously microsampled and dated by ID-TIMS (Courtney-Davies et al., 2019a) are used as 'unknowns' (of known age), to assess and compare the accuracy of LA-ICP-MS spot analysis between data calibrated on HFO and GJ-1 zircon. The natural hematite is zoned

with respect to U, W, Sn and Mo (highest concentrations in the brightest zones on BSE images), with U concentrations ranging from hundreds to thousands of ppm across the grains (Figure 2) and negligible common Pb components.

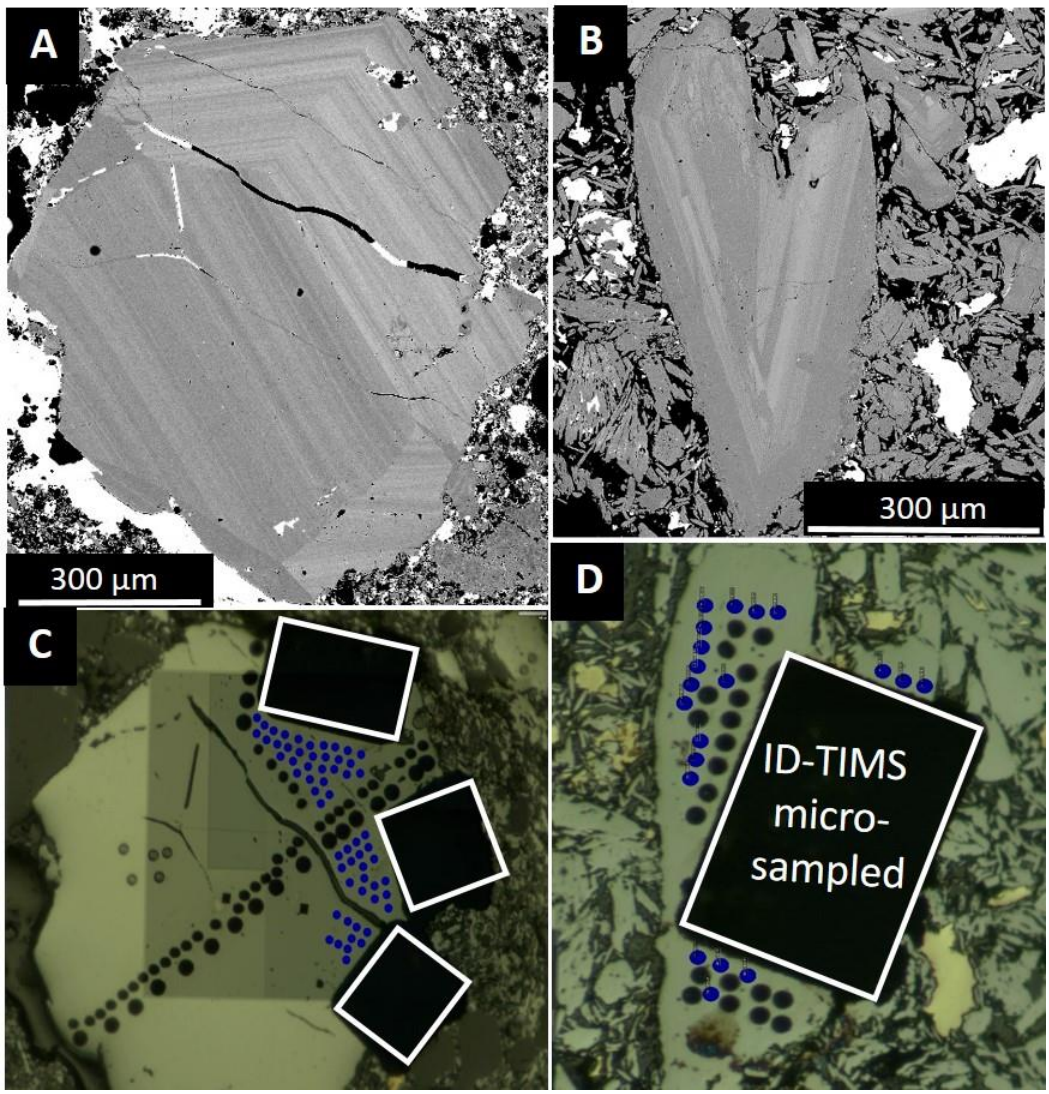


Figure 2. (A-B) Back scattered electron images of natural, oscillatory-zoned hematite from the Olympic Dam IOCG deposit and (C-B) optical reflected light images of the same grains displaying the locations of LA-ICP-MS spot analyses from this study (blue spots) compared to locations microsampled for ID-TIMS. (A) Grain LCD4, sampled from the deposits 'SE-lobe', drillhole RD27986A, 1550 m RL depth; (B) grain CLC10, sampled from the deposits 'outer shell', drillhole RU65-7976, 750 m RL depth. White boxes indicate the locations of microsampled material for ID-TIMS.

Isotope dilution-TIMS U/Pb and concentration data for grain LCD4 can be found in Courtney-Davies et al. (2019a) and grain CLC10 in Courtney-Davies et al. (2019d); $^{207}Pb/^{206}$ Pb weighted averages for the two microsampled grains are 1588.95 ± 0.93 Ma (*n*=3; MSWD=0.45) and 1591.27 ± 0.89 Ma (*n*=5; MSWD=0.52), respectively.

9.4 Results and Discussion

9.4.1 Characterization of HFO reference material

Initial LA-ICP-MS spot analyses were acquired to assess the downhole distribution of U and Pb isotopes. Time resolved ablation profiles display flat, steady signals over the analysed period for all measured isotopes (Figure 3).

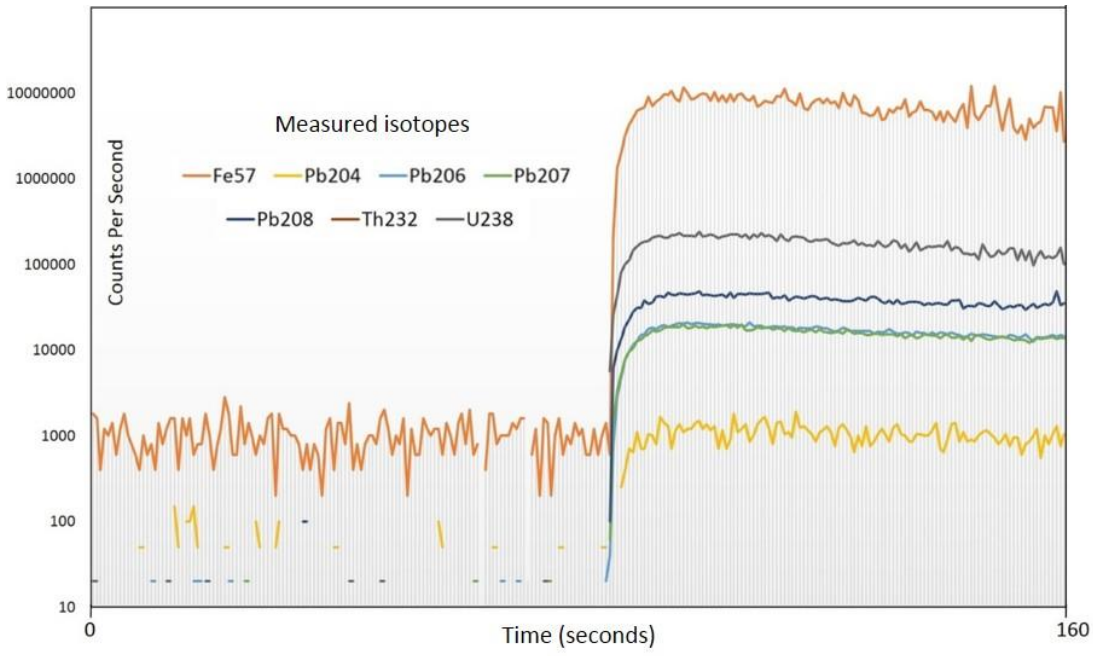


Figure 3. Downhole LA-ICP-MS profiles for Fe, U and Pb isotopes. Note the steady signals from the beginning to the end of the ablation sequence.

Averaged $^{206}Pb/^{238}U$ downhole fractionation profiles for natural hematite (LCD4; 60 spots), HFO (24 spots) and GJ-1 zircon (18 spots) over a 40 second period of data acquisition reveal three different fractionation trends (Figure 4; Appendix Tables LA 1-3). It should be noted that

LCD4 and HFO data was acquired using a fluence of 4 J cm^{-2}, compared to 2.5 J cm^{-2} for GJ-1 zircon, at a constant repetition rate of 5 Hz. The different fluences were selected to better match the downhole fractionation profiles between hematite and zircon (Courtney-Davies et al., 2019a). Both the LCD4 hematite and HFO fractionation trends begin to rise after 50 seconds, although the slope for HFO is much steeper.

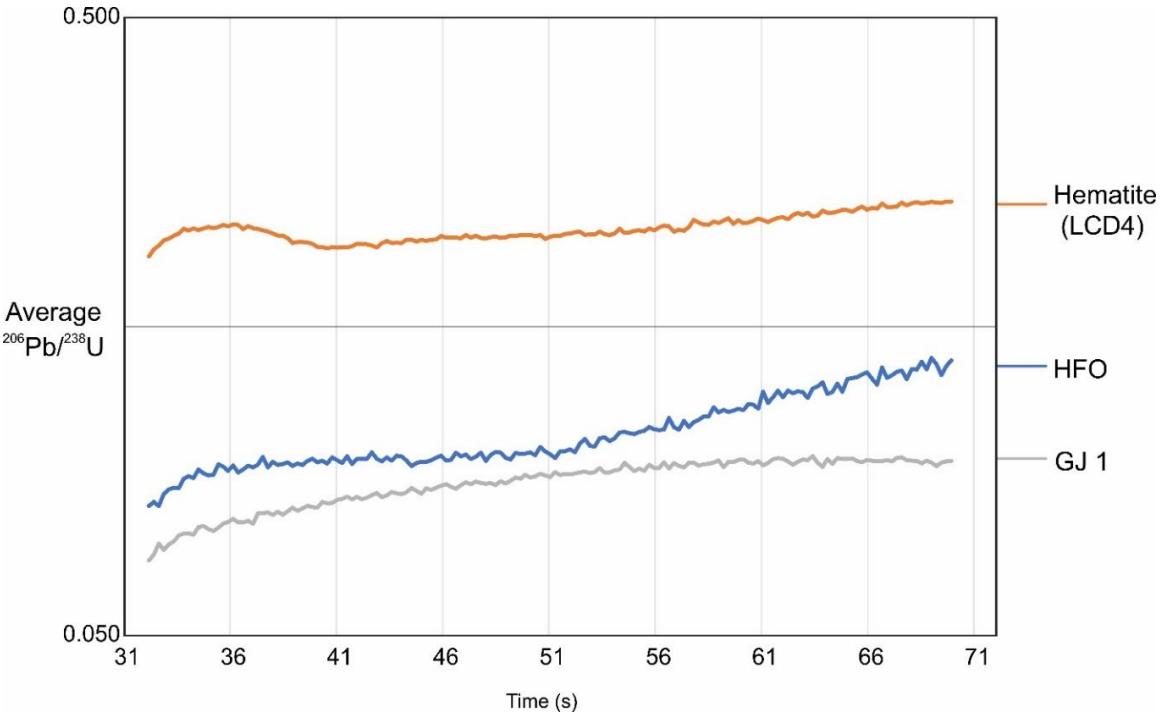


Figure 4. LA-ICP-MS $^{206}Pb/^{238}U$ downhole fractionation profiles for natural hematite, HFO and GJ-1 zircon, generated as an average from multiple spot ablations. Data were collected in a single analytical session.

HFO and LCD4 hematite laser ablation craters were examined using a laser confocal microscope to examine their shape and depth in 3D (Figure 5). LCD4 hematite crater depths ranged from 31 to 24 µm within single pits, and averaged 25 µm. In contrast, the depth of HFO craters measured 45 µm on average although the morphology of crater pits and edges are comparable between the two samples. The disproportionate volume of material being ablated between LCD4 and HFO is a plausible explanation for the late, steep increase in HFO $^{206}Pb/^{238}U$ downhole fractionation (Figure 4). The greater volume of ablated material under the

same analytical conditions can be attributed to the greater porosity in the HFO, and/or to differences in trace element chemistry (e.g. high W, Sn, Mo in natural hematite). Adjusting the laser conditions (e.g. reducing fluence) for future analyses, could reduce the ablation rate of the HFO and hence give more comparable ablated volumes and downhole fractionation profiles.

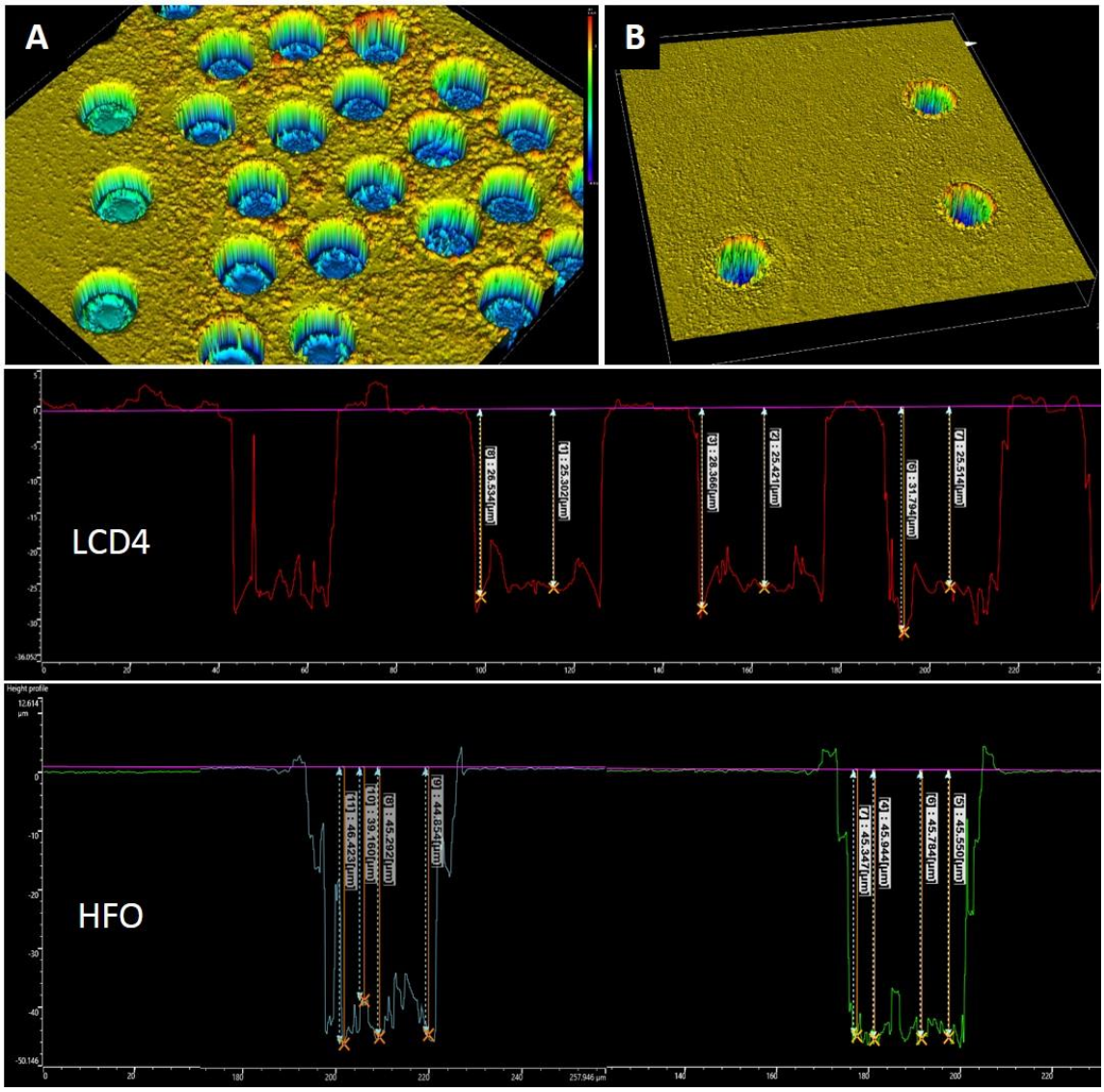


Figure 5. Representative 3D images and cross-section profiles taken across laser ablation pits in sample LCD4 hematite (A) and HFO (B).

9.4.2 U/Pb measurement of HFO reference material

Bulk chemical analysis of microsampled HFO was undertaken using both solution ICP-MS at the University of Melbourne and ID-TIMS at the British Geological Survey. Data obtained via solution Q-ICP-MS is not discussed due to a spread in U/Pb data derived from the analysis rather than intra-sample heterogeneity. This U/Pb spread is due to the microsampled HFO and the spike not equilibrating during dissolution steps. Isotope dilution-TIMS data for thirteen microsampled domains across four HFO chips is presented in Figure 6 and Table 2.

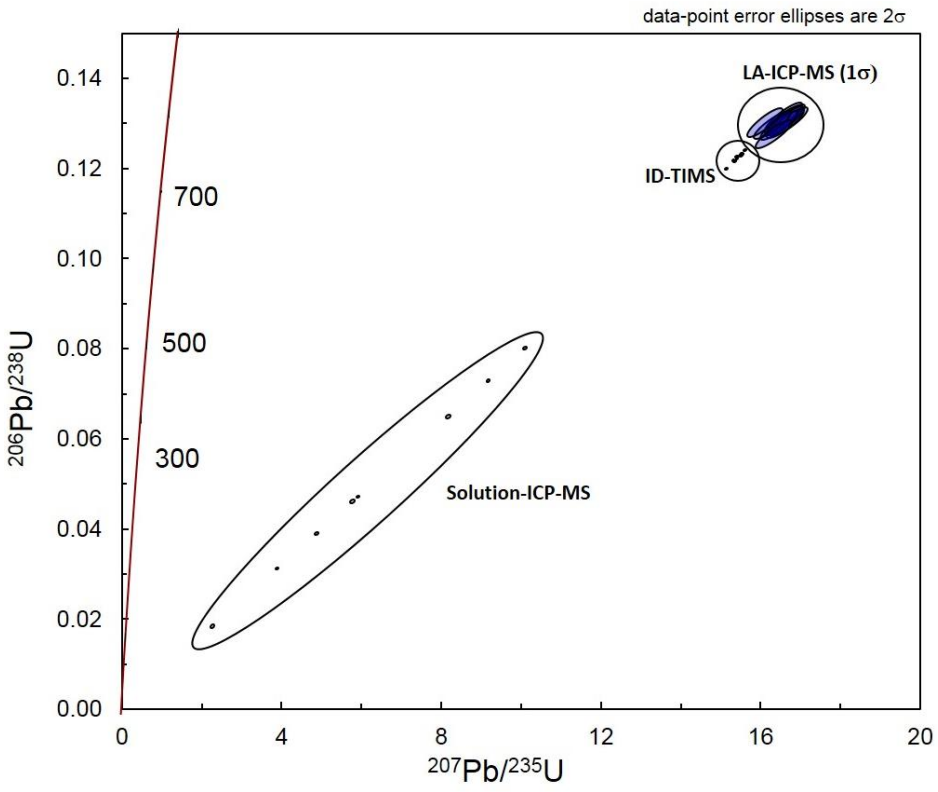


Figure 6. Conventional Wetherill concordia diagram for HFO analyses via three dating methods. Note that all error ellipses are 2σ apart from the LA-ICP-MS analyses. All thirteen ID-TIMS analyses from the 'darker' domains are plotted.

Due to the non-radiogenic isotopic composition of the Pb solution used in the HFO doping procedure, the data plots highly discordantly and is reflected in the common Pb composition ($^{206}Pb/^{204}Pb$ = 16.8). All data lie along a single intercept line forming a zero-age lower, and

upper intercept towards common Pb. The non-concordance and common Pb composition of the data is not a factor that controls the robustness of the HFO as a reference material, as long as $^{206}Pb/^{238}U$, $^{207}Pb/^{235}U$ and $^{207}Pb/^{206}Pb$ ratios can be measured repeatedly at high precision. Isotope dilution-TIMS data are clustered, although data points are not all within analytical uncertainty of one another. The small spread in data is reflected in weighted average diagrams (Figure 7) where three clear outliers are visible.

ID-TIMS Sample (Radiogenic + Initial Pb) Isotope Ratios															
HFO Chip	Aliquot	$\frac{^{207}Pb}{^{235}U}$	% err	$\frac{^{206}Pb}{^{238}U}$	% err	$\frac{^{238}U}{^{206}Pb}$	% err	$\frac{^{207}Pb}{^{206}Pb}$	% err	$\frac{^{206}Pb}{^{204}Pb}$	% err	$\frac{^{204}Pb}{^{206}Pb}$	% err	corr. coef. 238/206-207/206	corr. coef. 238/206-204/206	corr. coef. 207/206-204/206
AG1	1	15.424	0.14	0.122	0.12	8.171	0.12	0.914	0.08	16.727	0.14	0.060	0.14	-0.67	0.76	-1.15
	2	15.323	0.13	0.122	0.10	8.172	0.10	**0.909**	0.08	17.058	0.17	0.059	0.17	-0.76	0.74	-0.94
	3	15.337	0.12	0.121	0.09	8.232	0.09	0.916	0.08	16.904	0.16	0.059	0.16	-0.85	0.86	-1.02
	4	**14.336**	0.35	0.113	0.29	8.866	0.29	0.922	0.20	16.765	0.31	0.060	0.31	-0.11	0.14	-0.20
	5	**13.147**	0.12	0.104	0.09	9.643	0.09	0.920	0.08	16.834	0.16	0.059	0.16	-0.86	0.85	-0.98
AG2	1	15.446	0.16	0.122	0.14	8.173	0.14	0.916	0.08	16.840	0.16	0.059	0.16	-0.46	0.63	-0.99
	2	15.532	0.21	0.123	0.19	8.155	0.19	0.919	0.08	16.789	0.16	0.060	0.16	-0.21	0.52	-0.96
	3	15.554	0.14	0.123	0.11	8.128	0.11	0.917	0.08	16.844	0.16	0.059	0.16	-0.68	0.77	-1.00
AG3	1	15.435	0.14	0.122	0.12	8.205	0.12	0.919	0.08	16.788	0.16	0.060	0.16	-0.62	0.73	-1.00
	2	15.548	0.23	0.123	0.21	8.135	0.21	0.918	0.07	16.679	0.16	0.060	0.16	-0.22	0.46	-1.09
AG4	1	15.631	0.16	0.124	0.14	8.074	0.14	0.916	0.08	16.786	0.15	0.060	0.15	-0.49	0.65	-1.03
	2	15.366	0.17	0.121	0.15	8.250	0.15	0.920	0.08	16.786	0.16	0.060	0.16	-0.47	0.57	-1.00
	3	15.168	0.19	0.120	0.17	8.358	0.17	0.920	0.08	16.793	0.15	0.060	0.15	-0.32	0.56	-1.04
BG2	1	14.808	0.17	0.117	0.15	8.559	0.15	0.920	0.09	16.809	0.16	0.059	0.16	-0.36	0.58	-0.88
	2	14.713	0.18	0.116	0.16	8.618	0.16	0.920	0.09	16.829	0.16	0.059	0.16	-0.32	0.55	-0.85
	3	15.424	0.17	0.125	0.15	7.988	0.15	0.894	0.08	16.786	0.14	0.060	0.14	-0.44	0.64	-1.11

Table 2. Isotope dilution-TIMS data for the HFO reference material. HFO chips AG1-4 were microsampled in 'darker' domains, while chip BG2 derives from a 'brighter' domain. The individual U/Pb analyses highlighted in bold represent excluded outliers, depicted in Figure 7 weighted average diagrams. See appendix table ID HFO for an extended ID-TIMS data table. Data in bold represent excluded analyses.

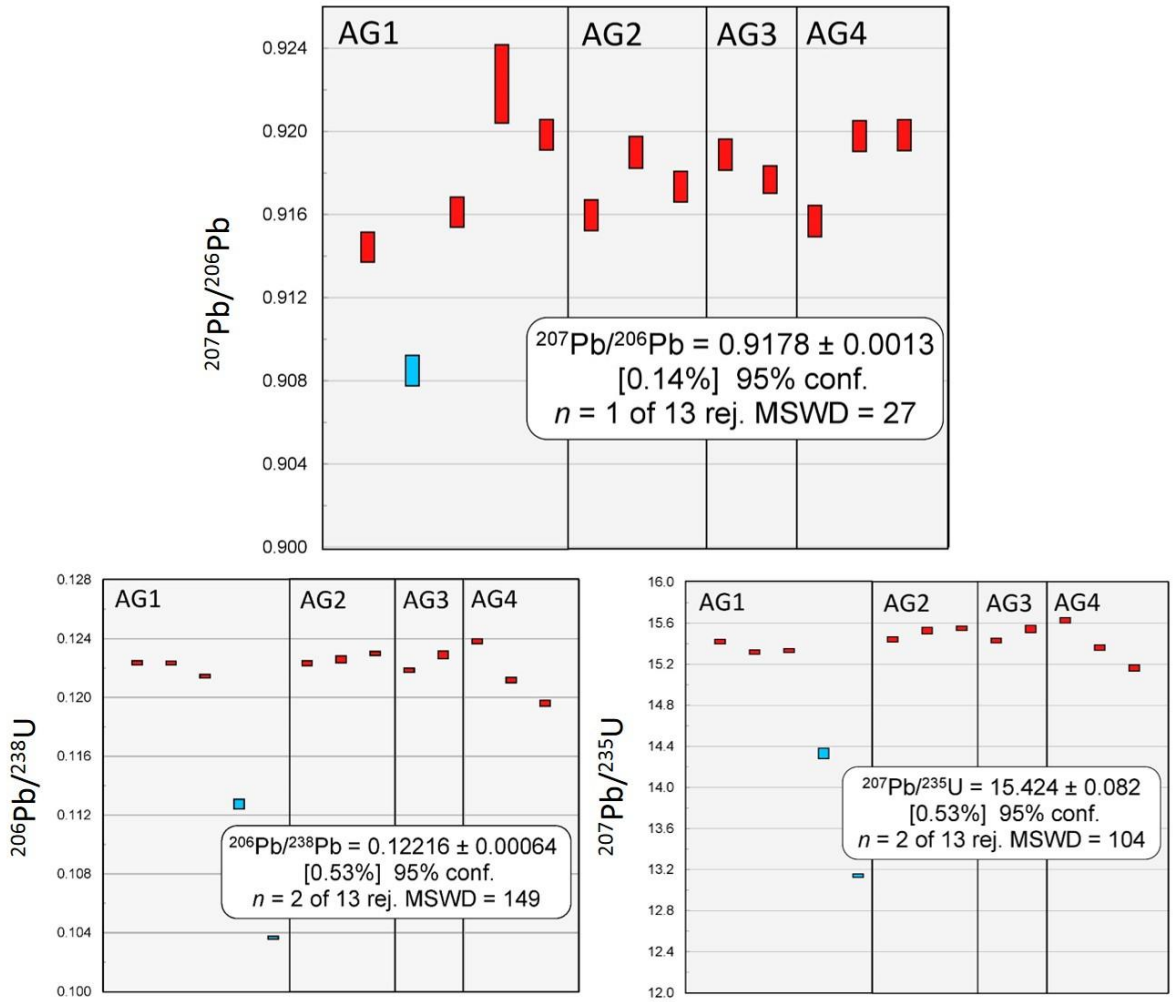


Figure 7. Weighted average diagrams for thirteen ID-TIMS analyses from four HFO chips ($^{207}Pb/^{206}Pb$, $^{206}Pb/^{238}U$ and $^{207}Pb/^{235}U$). Blue error bars (2σ) represent excluded analyses.

All three measured outliers were microsampled from the same chip of HFO (AG1; Table 2). Analysis AG1-2 yields the lowest $^{207}Pb/^{206}Pb$, while analyses AG1-4 and AG1-5 both yielded low U/Pb and slightly high $^{207}Pb/^{206}Pb$. There are two possibilities to explain the outliers. Firstly, the microsampled material and spike did not equilibrate during dissolution. This is, however, unlikely considering that the majority of analyses are consistent, and no residue was observed within any of the aliquots prepared for ID-TIMS. Therefore, it is more likely that U/Pb heterogeneity must exist within individual analyzed volumes of HFO. However, only chip AG1 yields outliers, which can be attributed to the proximity of these analyses to the 'brighter', more heterogeneous chip domains when compared with all other analyses. There is

little control over depth when employing the laser-extraction technique, and trenches commonly exceed 150 μm in depth. Therefore, the diffusional nature of the heterogeneous chip domains may continue at depth, under the visible, more homogeneous domain observed at the chip surface, and sampling a mixture of the two domains resulted in spurious U/Pb measurements. Three analyses from the 'brighter' domain (BG2; Figure 1) yielded high-precision, but highly scattered U/Pb, whereby two aliquots provide low U/Pb, equivalent to the lower U/Pb outliers in the 'darker' domains, supporting that a mixture of domains was analyzed in chip AG1.

Excess 2σ scatter is present in the U/Pb weighted means (0.53 %). When applying the quadrature to convert this mean to a single population, over-dispersion rises to 1.7 %. There is much lower scatter in Pb/Pb as expected (0.14 % internal and 0.38 % external) although it appears that two components of common Pb are present. At this stage, the source of the second component, which is unrelated to the starting material, cannot be traced, but could have been introduced at a different stage of material synthesis or during microsampling. Exclusion of all three outliers for all calculated ratios, based on the sole presence within one chip, and microsampled locations proximal to chip boundaries, yields preferred HFO values of: $^{207}Pb/^{206}Pb = 0.9175 \pm 0.0013$, $^{206}Pb/^{238}U = 0.12213 \pm 0.00074$ and $^{207}Pb/^{235}U = 15.439 \pm 0.088$ (2σ; n = 10/13). Despite a slight over-dispersion in U/Pb, the measured HFO is sufficiently homogeneous to merit application as a primary reference material for natural hematite calibration, especially for LA-ICP-MS where the TIMS results are within the precision of the technique.

9.4.3 Application of HFO reference material

Two grains of natural hematite from the Olympic Dam deposit (Figure 2) were selected for reconnaissance implementation tests using the HFO reference material. The sequence of LA-ICP-MS data acquisition for the first hematite grain (LCD4), comprised sixteen HFO, twelve GJ-1 zircon, and sixty unknown spot analyses (plus secondary zircon reference material analyses). The unknowns are plotted on a Terra-Wasserburg diagram (Figure 8), either calibrated using HFO (green error ellipses), or using GJ-1 zircon (red error ellipses). HFO calibrated unknowns are the generally concordant to slightly discordant, compared with only discordant analyses calibrated using GJ-1.

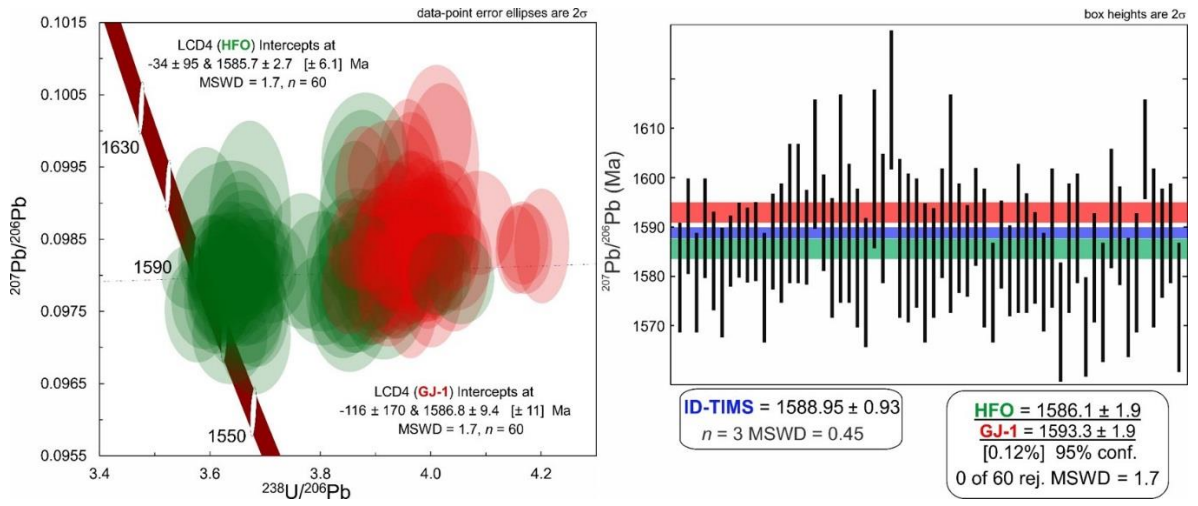


Figure 8. Terra-Wasserburg concordia diagram (left) and $^{207}Pb/^{206}Pb$ weighted average diagram (right) for HFO calibrated (green) and GJ-1 zircon calibrated (red) analyses of LCD4 natural hematite. The blue weighted average bar represents the overlain age and uncertainty of the ID-TIMS analysis of the natural hematite sample.

This demonstrates that previously interpreted Pb-loss within such samples when calibrated with GJ-1 zircon (e.g. Ciobanu et al., 2013; Courtney-Davies et al., 2019a), is likely an analytical, rather than geological feature, controlled by the interplay between analysis conditions and non-matrix matched standardization. These effects are still present to a lesser

extent when using the HFO for calibration. It is likely that this can be improved further by adjusting the laser fluence to reduce the ablation rate for HFO and provide a closer match for the downhole fractionation of natural hematite.

In addition to the U/Pb data, a $^{207}Pb/^{206}Pb$ weighted average diagram was constructed to compare the accuracy of HFO and GJ-1 calibrated unknowns *versus* ID-TIMS data from the same grain domains (Figure 8). When ignoring uncertainties, a divergence from the 'true' ID-TIMS hematite $^{207}Pb/^{206}Pb$ age of -0.18 % (HFO) *versus* 0.27 % (GJ-1) is obtained, indicating marginally higher accuracy for data calibrated using HFO. There is excess scatter in the MSWD, which may be improved when excluding analyses based on lowest U contents or $^{206}Pb/^{204}Pb$, but for the purposes described here it is unnecessary, as we are comparing whole datasets rather than deriving dates. When comparing the Terra-Wasserburg intercept and $^{207}Pb/^{206}Pb$ weighted average dates, HFO calibrated data are in good agreement, whereas data calibrated using GJ-1 does not overlap within analytical uncertainty.

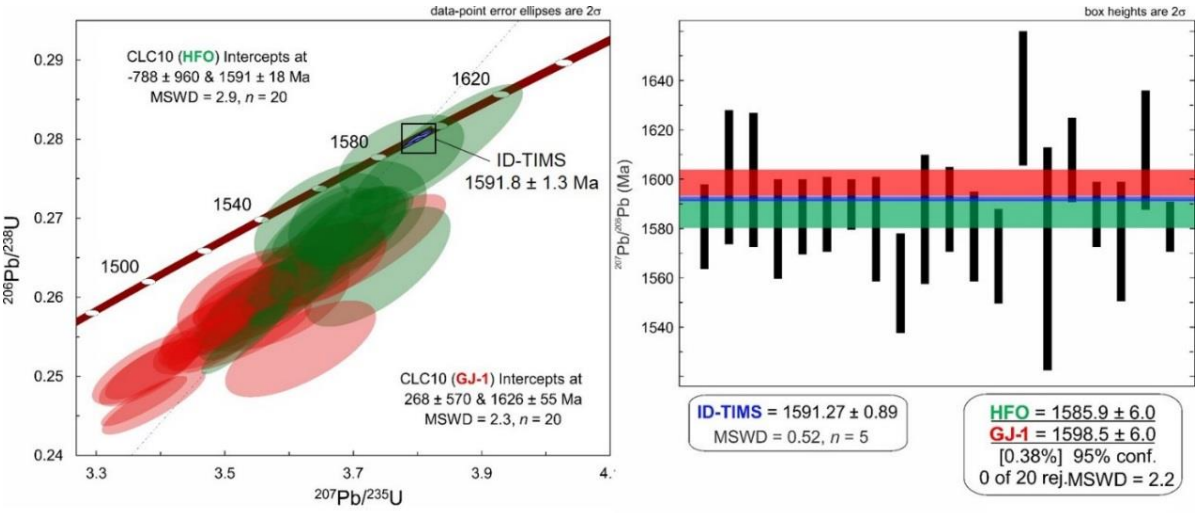


Figure 9. Wetherill concordia diagram (left) and $^{207}Pb/^{206}Pb$ weighted average diagram (right) for HFO calibrated (green) and GJ-1 zircon calibrated (red) analyses of natural hematite (sample CLC10). ID-TIMS data is also plotted in blue on the Wetherill diagram. Black error bars on the weighted average diagram relate to hematite data calibrated using HFO. The blue weighted average bar represents the overlain age and uncertainty of the ID-TIMS analysis of the natural hematite sample.

The second hematite grain (CLC10) followed the same analysis sequence as discussed above but with a lower number of analyses (20 unknowns). Data is presented on a Wetherill concordia diagram, to better assess the data in U/Pb space (Figure 9). Analogous to sample LCD4, data for sample CLC10 is more concordant, and marginally more accurate in $^{207}Pb/^{206}Pb$ when calibrated using HFO, whereas GJ-1 calibrated upper intercept and $^{207}Pb/^{206}Pb$ dates are in poor agreement with one another. Interestingly, the GJ-1 calibrated upper intercept is unrealistically old, and remains old even after exclusion of outliers, whereas the HFO calibrated upper intercept date overlaps exactly with the ID-TIMS intercept for the data (1591 ± 18 Ma *versus* 1591.8 ± 1.3 Ma). This suggests that hematite samples that require age interpretation using intercept dates, due to Pb-loss, low U or high common Pb components, are more suited to calibration with the HFO reference material. It should be noted that calibration using both reference materials produces poorly constrained lower intercepts for sample CLC10, however, anchoring of the GJ-1 calibrated data to a zero age lower intercept still produces an unrealistically old upper intercept. Discrepancies in U/Pb data calibrated using GJ-1 zircon may be related to lower concentrations of Pb (~20 ppm) in the zircon which gives lower accuracy for the $^{207}Pb/^{206}Pb$ weighted averages.

9.5 Conclusions and outlook

Preliminary implementation of the HFO reference material indicate advantages over zircon reference material calibration of hematite unknowns, as demonstrated by higher accuracy U/Pb upper intercept dates. Future work will aim to refine laser ablation analysis conditions, propagate appropriate uncertainties and compare accuracy and precision of HFO calibrated data using a range of hematite samples with varying U-Pb systematics.

Analysis parameters will be modified to better match the HFO downhole U/Pb fractionation profiles to natural hematite. This can be achieved by reducing the fluence applied during

analysis of HFO and matching the volume of material that is ablated. Reduction in $^{206}Pb/^{238}U$ downhole fractionation will result in more accurate LA-ICP-MS data when compared to ID-TIMS results for natural hematite. Addition of systematic uncertainties and error propagation strategies will need to be developed and applied to the initial ID-TIMS HFO data, and to data obtained using HFO as the reference material (e.g. calibration of ID-TIMS tracer, uncertainties applied when using bulk *versus* microbeam methods). This will ensure transparency and comparability of data between analysis methods. Since we can be confident that HFO calibrated data is more accurate than that calibrated using GJ-1, we will apply the HFO reference material to date a range of samples which have not been previously dated by ID-TIMS. This will enable: (1) comparison of results between GJ-1 and HFO for lower U, more open system and common Pb-rich samples e.g. low-U banded iron formation hematite from the Middleback Ranges (South Australia) that has been previously dated by LA-ICP-MS using GJ-1 as the reference material (Keyser et al., 2019), and (2) obtain new, higher accuracy and precision age data for such rocks, to better inform models for ore deposit genesis and later events impacting on ore systems.

Supplementary Materials

Appendix tables LA 1-3: U/Pb downhole fractionation trends for hematite, HFO and GJ1-Zircon.

Appendix tables LA 4-5: HFO and GJ-1 calibrated natural hematite U/Pb data.

Appendix table ID HFO: Extended ID-TIMS HFO tables.

9.6 Acknowledgements

This work is a contribution to the ‘FOX’ project (Trace elements in iron oxides: deportment, distribution and application in ore genesis, geochronology, exploration and mineral

processing), supported by BHP Olympic Dam and the South Australian Government Mining and Petroleum Services Centre of Excellence. N.J.C. acknowledges additional support from the ARC Research Hub for Australian Copper-Uranium (Grant IH130200033).

9.7 References

Bowring, J.F., McLean, N.M., Bowring, S.A., 2011. Engineering cyber infrastructure for U-Pb geochronology. Tripoli and U-Pb Redux. Geochem. Geophys. Geosyst. 12, Q0AA19. https://doi.org/10.1029/2010GC003479.

Ciobanu, C.L., Wade, B.P., Cook, N.J., Schmidt Mumm A., Giles, D., 2013. Uranium-bearing hematite from the Olympic Dam Cu–U–Au deposit, South Australia: A geochemical tracer and reconnaissance Pb–Pb geochronometer. Precambrian. Res. 238, 129–147.

Courtney-Davies, L., Zhu, Z., Ciobanu, C.L., Wade, B.P., Cook, N.J., Ehrig, K., Cabral, A.R., Kennedy, A., 2016. Matrix-matched iron-oxide laser ablation ICP-MS U-Pb geochronology using mixed solution standards. Minerals. 6(3), 85. DOI: 10.3390/min603008

Courtney-Davies, L., Tapster, S.R., Ciobanu, C.L., Cook, N.J., Verdugo-Ihl, M.R., Ehrig, K.J., Kennedy, A.K., Gilbert, S.E., Condon, D.J., Wade, B.P., 2019a. A multi-technique evaluation of hydrothermal hematite U-Pb isotope systematics: Implications for ore deposit geochronology. Chem. Geol. 513, 54-72.

Courtney-Davies, L., Ciobanu, C.L., Verdugo-Ihl, M.R., Dmitrijeva, M., Cook, N.J., Ehrig, K., Wade, B.P., 2019c. Hematite geochemistry and geochronology resolve genetic and temporal links among iron-oxide copper gold systems, Olympic Dam district, South Australia. Precambrian Research 335, 105480.

Courtney-Davies, L., Ciobanu, C.L., Richardson, M.W., Prosser, N., Verdugo-Ihl MR, Wade, B.P., Gilbert, S.E., Ehrig, K., Cook, N.J., 2019c. Synthesis of U-Pb doped hematite using a hydrated ferric oxide approach. J. Cryst. Growth. 513, 48-57.

Duff, M.C., Coughlin, J.U., Hunter, D.B., 2002. Uranium co-precipitation with iron oxide minerals. Geochim. Cosmochim. Acta 66, 3533–3547.

Edwards, R.L., Chen, J.H., Wasserburg, G.J., 1986. ^{238}U-^{234}U-^{230}Th-^{232}Th systematics and the precise measurement of time over the past 500,000 years. Earth Planet. Sci. Lett. 81, 175–192.

Gerstenberger, H., Haase, G., 1997. A highly effective emitter substance for mass spectrometric Pb isotope ratio determinations. Chem. Geol. 136, 309–312.

Hiess, J., Condon, D.J., McLean, N., Noble, S.R., 2012, $^{238}U/^{235}U$ Systematics in Terrestrial Uranium-Bearing Minerals. Science 335, 1610-1614.

Jackson, S.E., Pearson, N.J., Belousova, E.A., Griffin, W.L., 2004. The application of laser ablation-inductively coupled plasma-mass spectrometry (LA-ICP-MS) to in situ U-Pb geochronology. Chem. Geol. 211, 47–69.

Jaffey, A.H., Flynn, K.F., Glendenin, L.E., Bentley, W.C., Essling, A.M., 1971. Precision measurement of half-lives and specific activities of ^{235}U and ^{238}U. Phys. Rev. C: Nucl. Phys. 4, 1889–1906.

Keyser, W., Ciobanu, C.L., Cook, N.J., M., Dmitrijeva, M., Courtney-Davies, L., Feltus, H., Gilbert, S., Johnson, G., Ehrig, K., 2019. Iron-oxides constrain BIF evolution in terranes with protracted geological histories. The Iron Count prospect, Middleback Ranges, South Australia. Lithos 324-325, 20-38.

Ludwig, K.R.A., 2012. Isoplot/Ex rev. 4.1: A Geochronological Toolkit for Microsoft Excel; Berkeley Geochronology Centre Special Publication No.5, 75; Berkeley Geochronology Centre: Berkeley, California.

Lugmair, G.W., Galer, S.J.G., 1992. Age and isotopic relationships among the angrites Lewis Cliff 86010 and Angra dos Reis. Geochim. Cosmochim. Acta 56, 1673–1694

Nasdala, L., Corfu, F., Schoene, B., Tapster, S.R., Wall, C.J., Schmitz, M.D., Ovtcharova, M., Schaltegger, U., Kennedy, A.K., Kronz, A., Reiners, P.W., Yang, Y., Wu, F., Gain, S.E., Griffin, W.L., Szymanowski, D., Chanmuang N.C., Ende, M., Valley, J.W., Spicuzza, M.J., Wanthanachaisaeng, B., Giester, G., 2018. GZ7 and GZ8 – Two Zircon Reference Materials for SIMS U-Pb Geochronology. Geostand. Geoanal. Res. 42, 431-457.

Paton, C., Hellstrom, J., Paul, B., Woodhead, J., Hergt, J., 2011. Iolite: Freeware for the visualisation and processing of mass spectrometric data. J. Anal. At. Spectrom. 26, 2508–2518.

Schmitz, M.D., Schoene, B., 2007. Derivation of isotope ratios, errors, and error correlations for U-Pb geochronology using ^{205}Pb-^{235}U-(^{233}U)-spiked isotope dilution thermal ionization mass spectrometric data. Geochem. Geophys. Geosyst. 8, Q08006.

Sláma, J., Košler, J., Condon, D.J., Crowley, J.L., Gerdes, A., Hanchar, J.M., Horstwood, M.S.A., Morris, G.A., Nasdala, L., Norberg, N., Schaltegger, U., Schoene, B., Tubrett, M.N., Whitehouse, M.J., 2008. Plešovice zircon - a new natural reference material for U–Pb and Hf isotopic microanalysis. Chem. Geol. 249, 1–35.

Verdugo-Ihl, M.R., Ciobanu, C.L., Cook, N.J., Ehrig, K.J., Courtney-Davies, L., Gilbert, S., 2017. Textures and U-W-Sn-Mo signatures in hematite from the Olympic Dam Cu-U-Au-Ag deposit, South Australia: Defining the archetype for IOCG deposits. Ore. Geol. Rev. 91, 173–195.

Verdugo-Ihl, M.R., Ciobanu, C.L., Slattery, A., Cook, N.J., Ehrig, K., Courtney-Davies, L., 2019. Copper-Arsenic Nanoparticles in Hematite: Fingerprinting Fluid-Mineral Interaction. Minerals. 9(7), 388, https://doi.org/10.3390/min9070388.

Walter, B.F., Gerdes, A., Kleinhanns, I.C., Dunkl, I., Von, H., Kreissl, S., Markl, G., 2018. The connection between hydrothermal fluids, mineralization, tectonics and magmatism in a continental rift setting: fluorite Sm-Nd and hematite and carbonates U-Pb geochronology from the Rhine graben in SW Germany. Geochim. Cosmochim. Acta 240, 11-42.

Wiedenbeck, M., Alle, P., Corfu, F., Griffin, W.L., Meier, M., Oberli, F., von Quadt, A., Roddick, J.C., Spiegel, W., 1995. 3 natural zircon standards for U-Th-Pb, Lu-Hf, trace element and REE analyses. Geostand. Newslett. 19, 1–23.

Zhou, H., Sun, X., Wu, Z., Liao, J., Fu, Y., Li, D., Hollings, P., Liu, Y., Lin, H., Lin, Z., 2017. Hematite U-Pb geochronometer: insights from monazite and hematite integrated chronology of the Yaoan gold deposit, Southwest China. Econ. Geol. 112, 2023–2039.

CHAPTER 10

SUMMARY, RECOMMENDATIONS AND CONCLUDING REMARKS

CHAPTER 10: SUMMARY, RECOMMENDATIONS AND CONCLUDING REMARKS

10.1 Summary and recommendations

Recognising and reconstructing the events and processes culminating in ore deposit formation demands systematic study of the major, minor and trace minerals present. The advent of high-precision geochronology and ultra-high resolution transmission electron microscopy has shed new light on such processes, the latter technique able to make or break a deposit-scale interpretation at the smallest scale of observation. The Olympic Dam Cu-U-Au-Ag deposit, considered one of the 'archetypes' for IOCG mineralisation (Hitzman et al., 1992), is a natural laboratory for understanding complex ore-forming processes, and particularly how geochronology, if applied to mineral geochronometers studied at micron- to nanoscales of observation, can constrain deposit formation (Courtney-Davies et al., 2019a, b, c, in review a, b). Defining when, and over what timescales the Olympic Dam deposit formed has been periodically proposed and reinterpreted, however, confident, precise constraints have been elusive, inhibited by alteration, complex structural relationships and Mesoproterozoic age. Therefore, novel mineral geochronometers and innovative methods of analysis are required to accurately measure the timing of ore formation and evolutionary stages recognised within IOCG and related systems.

In this thesis and its component chapters, the composition and morphology of hydrothermal iron-oxides and magmatic zircon have been precisely measured and imaged from the scales of atoms to millimetres. The combination of studied minerals and analytical techniques applied, permits insights into events unfolding during the magmatic-hydrothermal transition of IOCG systems. Key geochronological constraints on the magmatic-hydrothermal history of the

Olympic Dam deposit and the wider Olympic Cu-Au province have been established with confidence for the first time. Presented U-Pb data elucidates a division between the magmatic and hydrothermal systems, providing insights into the timing and nature of mineralisation using a single mineral, traceable at the deposit-scale. Dissemination of an appraised, homogenous hematite reference material provides an opportunity for widespread, routine dating of iron-oxide bearing mineral systems. Achievable precision in hematite geochronology is demonstrably equivalent or superior to conventional mineral geochronometers when applicable (e.g. apatite, titanite and rutile), cementing the utility of hematite as a new, robust, target phase for ore deposit geochronology.

10.1.1 Geochronology of the Olympic Dam Cu-U-Au-Ag Deposit

The sequence of dated events presented here builds upon a succession of geochronological studies at Olympic Dam over the past thirty years (Mortimer et al., 1988; Trueman et al., 1988; Creaser and Cooper 1993; Johnson 1993; Johnson and Cross, 1995; Jagodzinski, 2014; Huang et al., 2015; Ciobanu et al., 2013; Huang et al., 2015; Apukhtina et al., 2017; Cherry et al., 2018a, and others). Coupled with dating of IOCG host rocks and hydrothermal assemblages across the eastern Gawler Craton (e.g. Jagodzinski, 2005; Skirrow et al., 2007; Davidson et al., 2007; Reid et al., 2013; Bowden et al., 2017; Cherry et al., 2008), a province scale ore-forming event has been collectively constrained at ~1600 to 1585 Ma, broadly coeval with formation of the Gawler SLIP (Allen et al., 2008)

The lifespan of mineralisation and exactly how ‘coeval’ mineralisation and crystallisation of granite hosting the Olympic Dam deposit were, was investigated through combining high-precision hematite and zircon (CA-)ID-TIMS. The sequence of events leading to formation of the Olympic Dam deposit, as discussed in Courtney-Davies et al. (in review a, b), are summarised here, with key geochronological constraints illustrated in Figure 10.1:

(**i**) Extension during the Gawler SLIP event induced crustal thinning and emplacement of large bodies of magma at upper crustal levels, below active GRV volcanoes. Incorporated clasts of GRV within the Olympic Dam breccia complex were dated at 1594.63 Ma (zircon $^{207}Pb/^{206}Pb$).

(**ii**) The Roxby Downs Granite, host to the Olympic Dam breccia complex, was emplaced at a depth of 6-8 km's (Kontonikas-Charos et al., 2017), at 1593.3-1593.0 Ma (zircon $^{207}Pb/^{206}Pb$).

(**iii**) Hydrothermal fluids accumulated in a supercritical state in the outer margins of the Roxby Downs Granite during the late stages of granite emplacement, whereby localised fluid release formed the deposits 'outer shell' and earliest zoned-hematite at 1591.27 Ma ($^{207}Pb/^{206}Pb$), ~1-2 Ma after the youngest measured Roxby Downs Granite zircon crystallised.

(**iv**) Regional-scale tectonic activity triggered uplift of the RDG via faults to shallower depths, initiating depressurisation and the main phase of hydrothermal fluid release and hydraulic brecciation. The granite cupola collapsed and the ore body formed within. Hydrothermal activity was sustained until at least 1589.95 Ma. During uplift of the granite, ~1760 Ma Fe-rich protoliths were mechanically incorporated in the deposit outer shell.

Although there is widespread evidence for post ~1590 Ma events impacting on the eastern Gawler Craton, likely contributing to cycles of U and Cu remobilisation and new mineral growth at Olympic Dam (e.g. Trueman et al., 1988; Johnson, 1993, Meffre et al., 2010; Maas et al., 2011; Kirchenbaur et al., 2016, and several others), multiple, major episodes of metal introduction have not yet been geochronologically constrained in detail. Timing of the major mineralising event at Olympic Dam has been refined here, using a hydrothermal mineral with a traceable geochemical signature (Verdugo-Ihl et al., 2017).

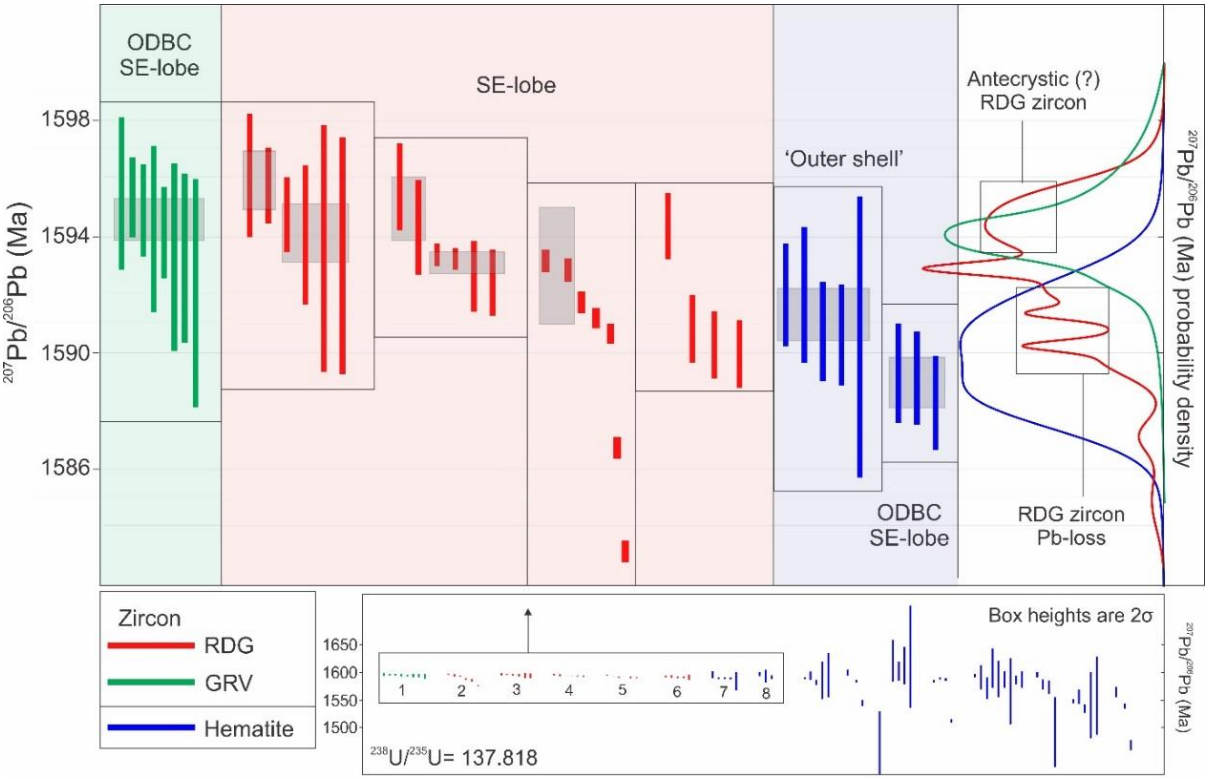


Figure 10.1: $^{207}Pb/^{206}Pb$ weighted average and probability diagram displaying key geochronological constraints between the magmatic and hydrothermal systems at Olympic Dam. The weighted average diagram at the bottom of the figure contains all data presented in the upper diagram (1 to 8), but also additional, lower precision hematite dates from Courtney-Davies et al. (2019a). Figure modified from Courtney Davies et al. (in review a).

Constraining a comprehensive high-resolution geochronological framework for multiple IOCG systems from across the Olympic Cu-Au province is unrealistic if microbeam dating methods alone (LA-ICP-MS and SHRIMP) are used, since the levels of analytical precision attainable are generally lower than the lifespan of events being measured. Granitophile element-bearing zoned hematite has been recognised outside Olympic Dam at the Wirrda Well and Acropolis IOCG prospects (Courtney-Davies et al., 2019b), and is likely a ubiquitous component of South Australian IOCG systems. To better address the timing of IOCG formation at a provincial scale, zoned hematite from several deposits and prospects should be identified and dated via ID-TIMS, coupled with CA-ID-TIMS dating of host or nearby Hiltaba Suite

intrusions. Furthermore, Hiltaba Suite intrusions are likely diachronous, even within single batholiths, potentially forming as rapidly emplaced clusters of intrusions, a common feature of porphyry Cu systems (e.g. Von Quadt et al., 2011). High-precision dating of barren, mineralised, felsic and more mafic Hiltaba Suite intrusions may uncover a timing factor controlling formation of large IOCG systems. Future CA-ID-TIMS dating in the region should preferably be undertaken using EARTHTIME tracer solutions (Condon et al., 2015; McLean et al., 2015) in order to compare U-Pb data systematically. The $^{238}U/^{235}U$ ratio within U-bearing terrestrial minerals differs, impacting on accuracy of geochronological data when all minerals are treated with the same value. It is probable that the $^{238}U/^{235}U$ value in zoned hematite from Olympic Dam diverges from the accepted value of 137.818 ± 0.045 obtained from zircon (Hiess et al., 2012), as isotopic fractionation associated with magmatic and hydrothermal crystallisation processes fluctuate. Therefore, high-precision measurements of $^{238}U/^{235}U$ should be obtained from zoned hematite, as even a slight change in the value can have large perturbations for age interpretations, as demonstrated in Courtney-Davies et al. (in review a).

10.1.2 Zircon evolution in U-rich IOCG systems

A wealth of chemical and micro-structural information recording the genesis of ore deposits can be obtained from zircon. Improved spatial resolution and Z-contrast techniques in micro-analysis has exposed atomic structures and defects in minerals by imaging of focused ion beam (FIB) prepared TEM-foils, using high-angle annular dark field scanning transmission electron microscopy (HAADF STEM; Ciobanu et al., 2016; Cook et al., 2017). Micron-to-nanoscale structures, nanoprecipitates and concentrations of non-formulae elements imaged and measured within magmatic zircon, are symptomatic of hydrothermal fluid interaction (Courtney-Davies et al., 2019c). This research is within the scope of the overarching study, as it provides a geochemical fingerprint of the magmatic-hydrothermal transition in IOCG

deposits. Chlorine, one of the main complexing ligands for hydrothermal transport of metals, is recurrently imaged within zircon-hosted nanoprecipitates, following primary magmatic zonation patterns, along with substitution of lattice-bound 'non-formulae' elements Fe and Ca, the result of early metasomatism. These features volumetrically increase in granites of different age with proximity to Olympic Dam, and represent a potential pathfinder to mineralisation associated with fertile granites. There exists potential for similar features to be identified within zircon from any other deposit types involving metasomatic alteration.

A preliminary study of zircon hosted within high-grade bornite ore from Olympic Dam opens several intriguing questions about the 'robustness' of this mineral chronometer relative to hematite in the context of a high-U environment. Studied bornite ore is intergrown with hematite (including zoned hematite, dated at 1595 ± 18 Ma; Courtney-Davies et al., 2016), with minor apatite and coarse-grained zircon. The dated hematite has some of the highest U concentrations at Olympic Dam (up to 5 wt. % UO_2) and is free of U- or Pb-mineral inclusions down to the nanoscale (Ciobanu et al., 2013). In contrast, all zircon is brecciated and metamict, retaining primary zonation patterns, but displaying radial cracks, often propagating from conspicuous 'dark domains' towards grain cores, with xenotime overgrowths forming and crosscutting the zonation patterns (Figure 10.2A).

EPMA mapping of zircon shows elevated concentrations of Th, REY, non-formulae elements and exceptionally high of UO_2 (~5 wt. %) within the dark domain crosscutting zonation (Figure 10.2B). Nanoscale study of a FIB-prepared sample across the U-rich domain shows the presence of two types of domains with strong contrast on both HAADF and BF STEM images (Fig. 10.3A, C). STEM-EDS element maps show chemical differences between the two domains, whereby the 'dark', U-rich domain is depleted in the two essential elements, Zr and Si, accounting for its darker colour on the HAADF STEM image (Fig. 10.3.B). The

brighter domain contains chloro-hydroxy-zircon nanoprecipitates and primary zoning as previously shown for magmatic zircon with early metasomatic overprint (Courtney-Davies et al., 2019c). There is no continuous overlap in distribution between any of the non-formulae elements Fe, Ca, Al, Ba and Cl, however, all are enriched within the dark, U-rich domain and interconnecting veinlets, apart from Fe, which is highest in the primary domain (Fig. 10.3D). REE and Y are enriched within the dark domain, particularly Y, where xenotime nanoparticles have nucleated across the dark domain, displaying a correlation with elevated Ca.

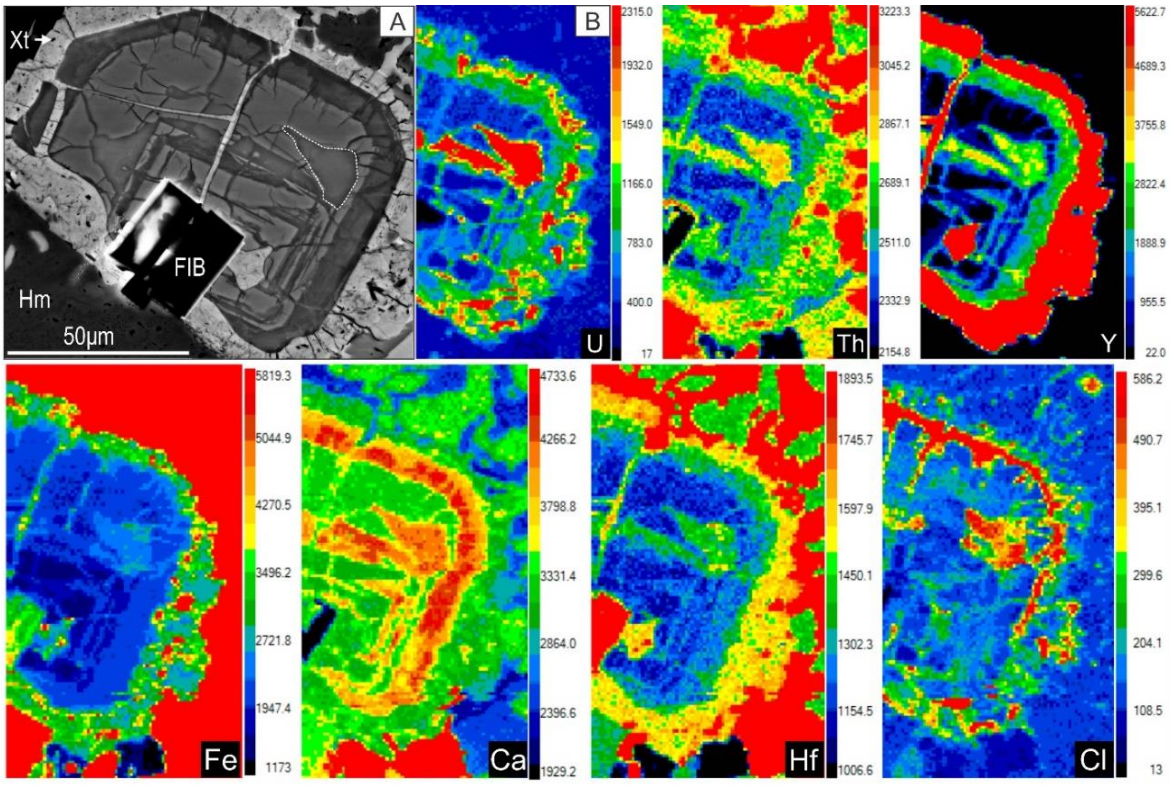


Figure 10.2. (A) BSE image of high-U zircon with a xenotime overgrowth from the Olympic Dam orebody. (B) EPMA maps displaying the distribution of minor to trace elements in zircon. Note the high-U domains within dark domains (marked by white line) crosscutting zonation patterns. Abbreviations: Hm – hematite; Xt – xenotime.

Interestingly, U and Th are both enriched within the dark domain, seemingly uniformly, albeit with U at far higher concentration, while Pb displays no apparent enrichment within the dark domain compared to the primary zoned zircon.

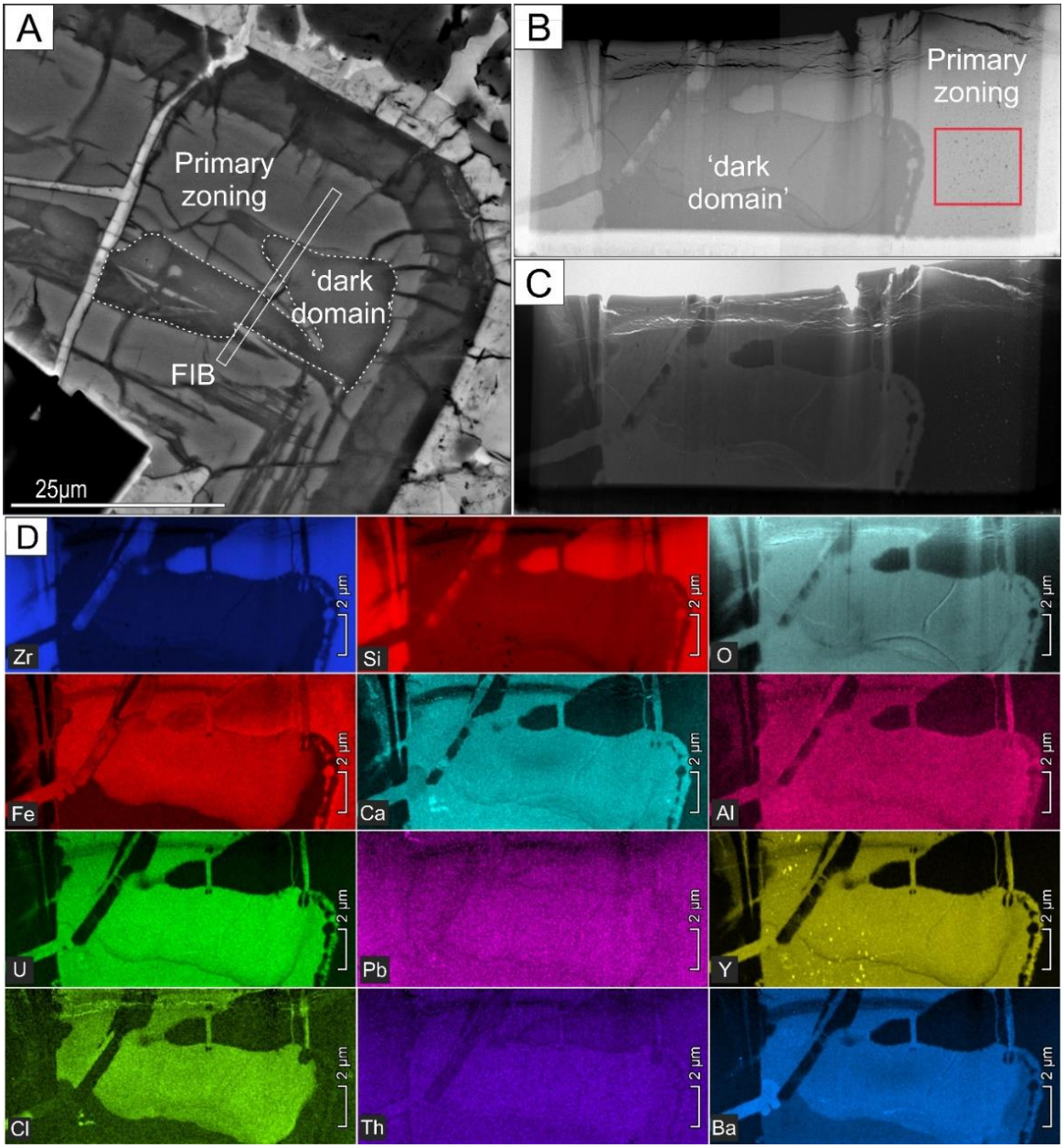


Figure 10.3: (A) BSE image showing the marked location of the FIB cut. (B) HAADF and (C) bright-field STEM images of the foil, location of chloro-hydroxy-zircon nanoprecipitates marked with red box. (D) STEM-EDS maps for selected elements displaying both positive and negative correlations between certain elements.

High-resolution imaging of the high-U, dark domain shows low crystallinity around areas of amorphisation (Fig. 10.4A, B). In contrast, material from the bright, primary-zoned domain is crystalline, however, defects are present (screw dislocations), evident from the 'splitting' of atom columns to form separate atom rows (Figure 10.4C).

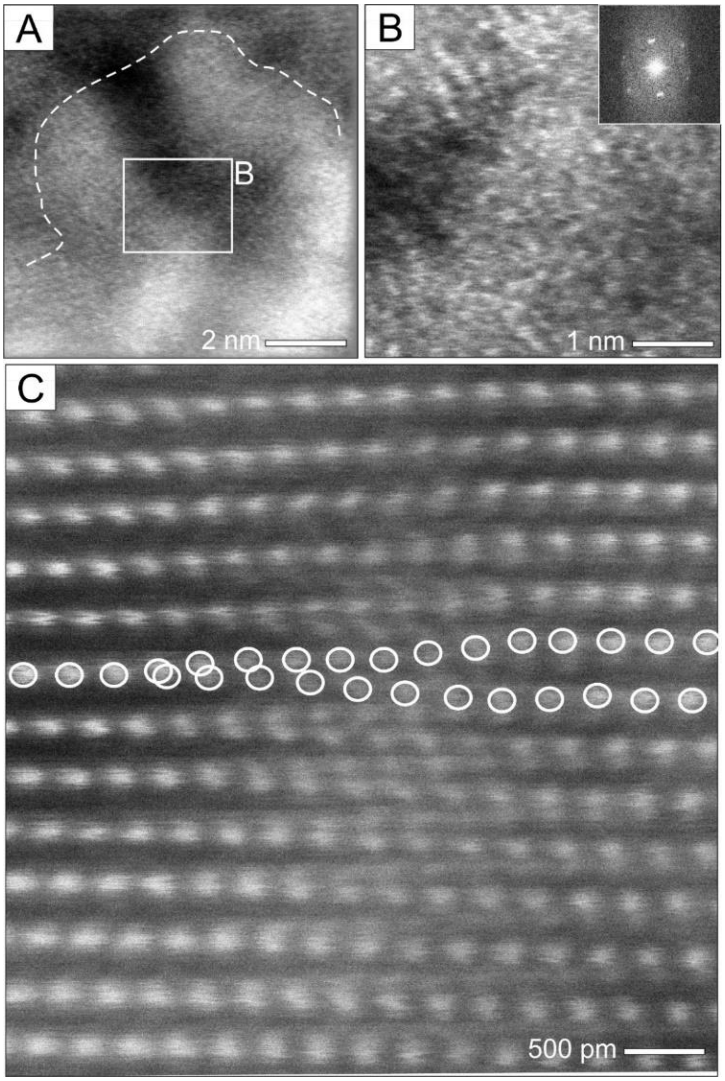


Figure 10.4: (A) HAADF STEM image of zircon showing a boundary between a low crystallinity (lower) to semi-crystalline domain (upper), marked by a white dotted line. (B) Fast Fourier Transform pattern of the poorly crystalline domain (top right) and higher resolution HAADF STEM image (location marked in A) of the low crystallinity domain. (C) HAADF STEM image of defect in the bright, primary zircon displaying screw dislocations.

The micro- to nanoscale features and composition of zircon within the Olympic Dam orebody indicate a long history of hydrothermal fluid interaction, after the principal ore-forming event at ~1590 Ma. Such zircons are not hydrothermal in origin, based upon the primary magmatic zonation patterns throughout the grains and the composition of primary zones being comparable to zircon hosted in unmineralised Roxby Downs Granite (Courtney-

Davie et al., 2019c). Zircon underwent early Fe-Cl metasomatism, forming chloro-hydroxy zircon nanoprecipitates and pores throughout zonation patterns at ~1590 Ma. Early metasomatism and brecciation of grains will inherently destabilise the zircon structure, possibly allowing high-U fluids to penetrate the zircon, dissolving and reprecipitating high-U domains within least stable areas.

Alternatively, zones or domains highest in magmatically incorporated U during primary crystallisation, accumulated high-levels of radiation damage, becoming crystalline-amorphous. At this stage, remobilised high-U fluids infiltrated the zircon along pathways opened by the swelling cracks, forming the conspicuous high-U domains. The calculated alpha-dose required for 'average' Roxby Downs Granite zircon to reach the first percolation point (Salje et al., 1999; Ríos et al., 2000), the onset of metamictisation, is ~100 Ma post-crystallisation.

The low correlation between non-formulae elements within the dark domain, indicate multiple fluid remobilisation events could have interacted with such zircon. Dating of the bright, primary zonation patterns within such zircon via LA-ICP-MS generated an unexpectedly young U/Pb upper intercept and $^{207}Pb/^{206}Pb$ date at ~1350 Ma (Ciobanu et al., 2013). Considering that this is not a late hydrothermal zircon, such a date may represent one of two possible scenarios; (1) either a thermal event at ~1350 Ma heterogeneously annealed such zircons, resetting U-Pb systematics, but failed to recover the highest-U most amorphous domains; or (2) the intercept date represents the timing of Pb-loss, during an unidentified regional scale tectono-thermal event, also recorded in monazite (Davidson et al., 2007) and apatite (Cherry et al., 2018b) within the Olympic Dam district.

Further studies are required to underpin the chemical and temporal evolution of such zircon. However, presented data demonstrates a protracted hydrothermal system at Olympic Dam, remobilising elements during multiple stages – and possibly semi-continuously given the

availability of surficial waters and heat from radioactive decay. Other nanoscale studies of zircon commonly report formation of Pb-bearing nanoparticles within altered or metamict zircon (Utsunomiya et al., 2004; Seydoux-Guillaume et al., 2015). Here, the only nanoparticles imaged comprise Y-bearing phases, without apparent Pb enrichment. This may be due to a complete loss of Pb from the zircon. When considering that Pb contents within the U-rich domain are indistinguishable from primary zones, it is likely that Pb is being continually lost until the present day. Despite prolonged hydrothermal activity post-1590 Ma, zoned hematite within the same hand specimen as the discussed zircon is dateable, retaining primary U-Pb systematics and reinforcing the refractory behaviour of hematite as a geochronometer within such environments. Due to the difficulty in imaging amorphous zircon, clear images of the metamict state are sparse, and most commonly acquired using S/TEM. Here we present HAADF STEM images representing some of the highest resolution images of metamictisation known.

Future studies would benefit from the use of nanometre-resolution secondary ion mass spectrometry (nanoSIMS; e.g. Rollog et al., 2019). This technique permits isotope mapping of pre-selected zircon grains, to better understand the grain-scale distribution of U, and how, or if, Pb and other radionuclides migrate away from the highest U domains. A systematic study of zircon composition and age throughout the Olympic Dam orebody will place better constraints on the timing and nature of element remobilisation events.

10.1.3 Development of hematite U-Pb reference material

The overarching aim of this project was identification of natural, or synthesis of, homogenous hematite U-Pb reference material, in order to calibrate U/Pb in unknowns routinely, using fast, cost-effective microbeam methods. Suitable natural material was not identified due to the nature of available samples, therefore, a novel synthesis method was developed (Courtney

Davies et al., 2019d). This involved a doping solution of uranyl and lead nitrates, added to, and absorbed by, a suspension of colloidal hydrated ferric oxide particles. The doped material was dried at 50 °C to produce solid chips several millimetres in thickness, followed by heating, and holding for several hours at 700 °C, converting the doped hydrated ferric oxide to α-Fe_2O_3, as confirmed by X-ray powder diffraction. Initial tests of inter- and intra- grain U/Pb homogeneity by LA-ICP-MS spot analysis and isotope mapping produced encouraging results, warranting higher precision measurement of the hematite reference material (HFO) by ID-TIMS. Laser ablation micro-sampling of thirteen grain domains across four chips of HFO, measured by ID-TIMS, yielded high-precision individual analyses, with a slight U/Pb over-dispersion. Measured heterogeneity was traced to a single chip, and outliers in the data were excluded on a rational basis. Representative $^{207}Pb/^{206}Pb$, $^{206}Pb/^{238}U$ and $^{207}Pb/^{235}U$ calibration value were assigned to the reference material within software data reduction packages. The material was subsequently used to calibrate U/Pb in hematite grains from Olympic Dam, independently measured by ID-TIMS, providing a high precision baseline of geochronological data, used to compare accuracy of data obtained from the same dated grains, calibrated using both HFO and zircon reference materials. Preliminary implementation of HFO indicates advantages over zircon reference material, demonstrated by the notably higher accuracy and precision of U/Pb upper intercept dates. This is significant for hematite U-Pb geochronology, as intercepts are often the most suitable form of date used in age interpretation, as demonstrated for low U, common Pb rich banded iron formation samples (Keyser et al., 2019).

Further appraisal of the reference material and refinement of analysis conditions are required prior to making the material available to the wider community. Future work will explore refinement of LA-ICP-MS analysis parameters, in order to better match the HFO downhole U/Pb fractionation profiles to natural hematite samples. This can be achieved by reducing the fluence applied during analysis of HFO and by matching the volume of material that is ablated.

Reduction in $^{206}Pb/^{238}U$ downhole fractionation will result in more accurate LA-ICP-MS data when compared to ID-TIMS results for natural hematite. Systematic uncertainties and error propagation strategies must be developed and applied initially to the ID-TIMS HFO preferred values. Importantly, they can also be applied to hematite U/Pb data obtained when using HFO as the reference material (e.g. calibration of ID-TIMS tracer, uncertainties applied when using bulk versus microbeam methods, $^{238}U/^{235}U$). This will ensure transparency and comparability of generated data-sets between analysis methods and appropriate levels of applied uncertainty. Currently, only LA-ICP-MS data obtained from high-U, relatively homogeneous samples of hematite has been calibrated using HFO. Comparison of results between HFO and zircon reference materials for lower U, more open system samples, and those characteristically rich in common Pb (e.g. low-U banded iron formation) will provide better insight into the accuracy of the reference material using a far more common variety of hematite.

10.2 Concluding remarks

The content of this thesis contributes to and compliments the extraordinary wealth of information that has been obtained from iron-oxide minerals within the Olympic Dam deposit in recent years (Ciobanu et al., 2013, 2019; Dmitrijeva et al., 2019; Verdugo-Ihl et al., 2017, 2019, in press). Collectively, these data have provided new, innovative insights into deposit mineralogy, geochronology, geochemistry and ultimately, ore genesis. Importantly, the results and methodologies described here are transferrable to ore deposit research elsewhere in the eastern Gawler Craton but also in analogous terranes worldwide, through appraisal of the hematite geochronometer and reference material, application of nanoscale techniques uncovering deposit-to-district-scale processes and characterization of mineral system pathfinders.

Key conclusions from the conducted research in this thesis include:

1. Hematite can retain a closed U-Pb system since crystallisation, generating concordant datapoints and $^{207}Pb/^{206}Pb$ ages of up to ~0.05 % precision by ID-TIMS, the highest currently reported precision for a hydrothermal mineral in any IOCG system. The iron-oxide has proven to be remarkably robust mineral geochronometer, demonstrated by the new ID-TIMS method presented. This presents an opportunity to investigate ore deposit geochronology using a new, robust tool.
2. The Olympic Dam orebody formed principally during a major, single IOCG ore-forming event, lasting at least ~2 Ma. The hydrothermal system was initiated at 1591.3 Ma, ~1-2 Ma after crystallisation of the deposits host granite at 1593.2 Ma.
3. A generation of zoned, granitophile element rich hematite, related to the same fluid source and ore forming event, is a ubiquitous component of IOCG systems across the Olympic Cu-Au province, which share a common crystallisation age of ~1590 Ma.
4. U-bearing magnetite within Fe-rich lithologies are found within the Olympic Dam 'outer shell', representing first identification of a pre-1590 Ma protolith within the deposit. A connection between BIF-type units and IOCG mineralisation is presented, which may represent an additional, hitherto unrecognised source of metals. Furthermore, the applicability of magnetite to LA-ICP-MS U-Pb geochronology is explored here for the first time.
5. Zircon within granites hosting IOCG mineralisation contain abundant chloro-hydroxy-zircon nanoprecipitates, a fingerprint of early metasomatic alteration during the magmatic-hydrothermal transition, and a potential new exploration tool for locating fertile granites hosting IOCG-style mineralisation. The capacity for zircon to undergo such pervasive, early alteration, prior to any accumulation of radiation-damage, is acknowledged here for the first time. The texture and chemistry of zircon within the Olympic Dam orebody demonstrates

the pervasive nature of the hydrothermal system and long-lived remobilisation of elements. New images of the metamict state are presented, at some of the smallest-scale resolutions ever achieved, using a state-of-the-art Titan Themis S/TEM instrument.

6. A homogeneous, U-Pb hematite reference material has been synthesised and characterised by ID-TIMS. Its application to LA-ICP-MS geochronology is confirmed, providing accurate data when compared to independent ID-TIMS analysis of unknowns. Pending further optimisation, such a hematite reference material will become available to the wider community for routine microbeam U-Pb geochronology.

References

Allen, S., McPhie, J., Ferris, G., Simpson, C., 2008. Evolution and architecture of a large felsic igneous province in western Laurentia: The 1.6 Ga Gawler Range Volcanics, South Australia. Journal of Volcanology and Geothermal Research, v. 172, p. 132–147.

Apukhtina, O., Kamenetsky, V.S., Ehrig, K., Kamenetsky, M.B., Maas, R., Thompson, J., McPhie, J., Ciobanu, C.L., Cook, N.J., 2017. Early magnetite-fluorapatite mineralisation at the Olympic Dam Cu-U-Au-Ag deposit, South Australia. Economic Geology, v. 112, p. 1531-1542.

Bowden, B., Fraser, G., Davidson, G.J., Meffre, S., Skirrow, R.G., Bull, S., Thompson, J., 2017. Age constraints on the hydrothermal history of the Prominent Hill iron oxide copper-gold deposit, South Australia. Mineralium Deposita, v. 52, p. 863–881.

Cherry, A., Ehrig, K., Kamenetsky, V., McPhie, J., Crowley, J., Kamenetsky, M., 2018a. Precise geochronological constraints on the origin, setting and incorporation of ca. 1.59 Ga surficial facies into the Olympic Dam Breccia Complex, South Australia. Precambrian Research, v. 315, p. 162-178.

Cherry, A.R., Kamenetsky, V.S., McPhie, J., Thompson, J.M., Ehrig, K.J., Meffre, S., Kamenetsky, M.B., Krneta, S., 2018b. Tectonothermal events in the Olympic IOCG Province constrained by apatite and REE-phosphate geochronology. Australian Journal of Earth Science, v. 65, p. 643–659.

Ciobanu, C.L., Wade, B.P., Cook, N.J., Mumm, A.S. Giles, D., 2013. Uranium-bearing hematite from the Olympic Dam Cu–U–Au deposit, South Australia: A geochemical tracer and reconnaissance Pb–Pb geochronometer. Precambrian Research, v. 238, p. 129-147.

Ciobanu, C.L., Cook, N.J., Maunders, C., Wade, B.P., Ehrig, K., 2016. Focused Ion Beam and Advanced Electron Microscopy for Minerals: Insights and Outlook from Bismuth Sulphosalts. Minerals, 6(4), 112, https://doi.org/10.3390/min6040112.

Ciobanu, C.L., Verdugo-Ihl, M.R., Slattery, A., Cook, N.J., Ehrig, K., Courtney-Davies, L., Wade, B.P., 2019. Silician magnetite: Si-Fe-nanoprecipitates and other mineral inclusions in magnetite from the Olympic Dam deposit, South Australia. Minerals, 9, 311, https://doi.org/10.3390/min9050311.

Condon, D.J., Schoene, B., McLean, N.M., Bowring, S.A., Parrish, R.R., 2015. Metrology and traceability of U-Pb isotope dilution geochronology (EARTHTIME tracer calibration part I). Geochimica Cosmochimica Acta, v. 164, p. 464–480.

Cook, N.J., Ciobanu, C.L., Ehrig, K., Slattery, A., Verdugo-Ihl, M.R., Courtney-Davies, L., Gao, W., 2017. Advances and opportunities in ore mineralogy. Minerals, 7(12), 233, https://doi.org/10.3390/min7120233.

Courtney-Davies, L., Zhu, Z., Ciobanu, C.L., Wade, B.P., Cook, N.J., Ehrig, K., Cabral, A.R., Kennedy, A., 2016. Matrix-matched iron-oxide laser ablation ICP-MS U-Pb geochronology using mixed solution standards. Minerals, 6, 85, https://doi.org/10.3390/min6030085.

Courtney-Davies, L., Tapster, S.R., Ciobanu, C.L., Cook, N.J., Verdugo-Ihl, M.R., Ehrig, K.J., Kennedy, A.K., Gilbert, S.E., Condon, D.J., Wade, B.P., 2019a. A multi-technique evaluation of hydrothermal hematite U-Pb isotope systematics: Implications for ore deposit geochronology. Chemical Geology, v. 513, p. 54-72.

Courtney-Davies, L., Ciobanu, C.L., Verdugo-Ihl, M.R., Dmitrijeva, M., Cook, N.J., Ehrig, K., Wade, B.P., 2019b. Hematite geochemistry and geochronology resolve genetic and temporal links among iron-oxide copper gold systems, Olympic Dam district, South Australia. Precambrian Research, v. 335, 105480.

Courtney-Davies, L., Ciobanu, C.L., Verdugo-Ihl, M.R., Slattery, A., Cook, N.J., Dmitrijeva, M., Keyser, W., Wade, B.P., Dominick, U.I., Ehrig, K., Xu, J., Kontonikas-Charos, A., 2019c. Zircon at

the nanoscale records metasomatic processes leading to large magmatic-hydrothermal ore deposits, Minerals, 9, 364, doi:10.3390/min9060364.

Courtney-Davies, L., Ciobanu, C.L., Richardson, M.W., Prosser, N., Verdugo-Ihl MR, Wade, B.P., Gilbert, S.E., Ehrig, K., Cook., N.J., 2019d. Synthesis of U-Pb doped hematite using a hydrated ferric oxide approach. Journal of Crystal Growth, v. 513, p. 48-57.

Courtney-Davies, L., Ciobanu, C.L., Tapster, S.R., Cook, N.J., Ehrig, K., Crowley, J.L., Verdugo-Ihl, M.R., Condon, D.J., in review, a. Opening the Magmatic-Hydrothermal Window: High-Resolution Geochronology of the Olympic Dam Iron Oxide-Cu-U-Au-Ag Deposit, South Australia. Economic Geology.

Courtney-Davies, L., Ciobanu, C.L., Verdugo-Ihl, M.R., Cook, N.J., Ehrig, K., Benjamin P. Wade, Zhi-yong Zhu., in review, b. ~1760 Ma magnetite-bearing protoliths in the Olympic Dam deposit, South Australia: Implications for ore genesis and regional metallogeny. Ore Geology Reviews.

Creaser, R.A., and Cooper, J.A., 1993. U-Pb geochronology of Middle Proterozoic felsic magmatism surrounding the Olympic Dam Cu-U-Au-Ag and Moonta Cu-Au-Ag deposits, South Australia. Economic Geology, v. 88, p. 186-197.

Davidson, G.J., Paterson, H., Meffre, S., Berry, R.F., 2007. Characteristics and origin of the Oak Dam east breccia-hosted, iron oxide Cu-U-(Au) deposit: Olympic Dam Region, Gawler Craton, South Australia. Economic Geology, v. 102 (8), p. 1471–1498.

Dmitrijeva, M., Ciobanu, C.L., Ehrig, K., Cook, N.J., Metcalfe, A., Verdugo-Ihl, M.R., McPhie, J., 2019. Defining IOCG signatures through compositional data analysis: A case study of lithogeochemical zoning from the Olympic Dam deposit, South Australia. Ore Geology Reviews, v. 105, p. 86–101.

Hiess, J., Condon, D.J., McLean, N., Noble, S.R., 2012. $^{238}U/^{235}U$ Systematics in Terrestrial Uranium-Bearing Minerals. Science, v. 335, p. 1610-1614.

Hitzman, M.W., Oreskes, N., Einaudi, M.T., 1992. Geological characteristics and tectonic setting of Proterozoic iron oxide (Cu-U-Au-REE) deposits. Precambrian Research, v. 58, p. 241–287.

Huang, Q., Kamenetsky, V.S., McPhie, J., Ehrig, K., Meffre, S., Maas, R., Thompson, J., Kamenetsky, M., Chambefort, I., Apukhtina, O., Hu, Y., 2015. Neoproterozoic (ca. 820–830 Ma) mafic dykes at

Olympic Dam, South Australia: Links with the Gairdner Large Igneous Province. Precambrian Research, v. 271, p. 160-172.

Jagodzinski, E.A., 2014. The age of magmatic and hydrothermal zircon at Olympic Dam. In: Proceedings of the 2014 Australian Earth Sciences Convention, Sustainable Australia, Newcastle, Australia, p. 260.

Jagodzinski, E.A., 2005. Compilation of SHRIMP U-Pb geochronological data Olympic Domain, Gawler Craton, South Australia, 2001-2003. Geoscience Australia Record 2005/020.

Johnson, J.P., 1993. The geochronology and radiogenic isotope systematics of the Olympic Dam copper-uranium-gold-silver deposit, South Australia. Unpublished Ph.D. thesis, Canberra, Australia, The Australian National University.

Johnson, J.P., and Cross, K.C., 1995. U-Pb geochronological constraints on the genesis of the Olympic Dam Cu-U-Au-Ag deposit, South Australia. Economic Geology, v. 90, p. 1046–1063.

Keyser, W., Ciobanu, C.L., Cook, N.J., M., Dmitrijeva, M., Courtney-Davies, L., Feltus, H., Gilbert, S., Johnson, G., Ehrig, K., 2019. Iron-oxides constrain BIF evolution in terranes with protracted geological histories: The Iron Count prospect, Middleback Ranges, South Australia. Lithos, v. 324-325, p. 20-38.

Kirchenbaur, M., Maas, R., Ehrig, K., Kamenetsky, V.S., Strub, E., Ballhaus, C., Münker, C., 2016. Uranium and Sm isotope studies of the supergiant Olympic Dam Cu–Au–U–Ag deposit, South Australia. Geochimica Cosmochimica Acta, v. 180, p. 15–32.

Kontonikas-Charos, A., Ciobanu, C.L., Cook, N.J., Ehrig, K., Krneta, S., Kamenetsky, V.S., 2017. Feldspar evolution in the Roxby Downs Granite, host to Fe-oxide Cu-Au-(U) mineralisation at Olympic Dam, South Australia. Ore Geology Reviews, v. 80, p. 838–859.

Maas, R., Kamenetsky, V.S., Ehrig, K., Meffre, S., McPhie, J., and Diemar, G., 2011. Olympic Dam U-Cu-Au deposit, Australia: New age constraints: Mineralogical Magazine, Goldschmidt Conference abstract, v. 75, p. 1375.

McLean, N.M., Condon, D.J., Schoene, B., Bowring, S.A., 2015. Evaluating uncertainties in the calibration of isotopic reference materials and multi-element isotopic tracers (EARTHTIME tracer calibration part II). Geochimica et Cosmochimica Acta, v. 164, p. 481–501.

Meffre, S., Ehrig, K., Kamenetsky, V.S., Chambefort, I., Maas, R., McPhie, J., 2010. Pb isotopes at Olympic Dam: Constraining sulphide growth: Giant ore deposits down under: Proceedings of 13th Quadrennial International Association on the Genesis of Ore Deposits (IAGOD) Symposium, Adelaide, South Australia, p. 78–79.

Reid, A., Smith, R.N., Baker, T., Jagodzinski, E.A., Selby, D., Gregory, C.J., Skirrow, R.G., 2013. Re-Os dating of molybdenite within hematite breccias from the Vulcan prospect, Olympic Dam Cu-Au province, South Australia. Economic Geology, v. 108, p. 883–894.

Ríos, S., Malcherek, T., Salje, E.K.H., Domeneghetti, C., 2000. Localized defects in radiation-damaged zircon. Acta Crystallographica, v. 56, p. 947–952

Rollog, M., Cook, N.J., Guagliardo, P., Ehrig, K., Kilburn, M., 2019. In situ spatial distribution mapping of radionuclides in minerals by nanoSIMS. Geochemistry: Exploration, Environment Analysis, v. 19, p. 245–254

Salje, E.K.H., Chrosch, J., Ewing, R.C., 1999. Is "metamictization" of zircon a phase transition?. American Mineralogist, v. 84, p. 1107–1116.

Seydoux-Guillaume, A.M., Bingen, B., Paquette, J.L., Bosse, V., 2015. Nanoscale evidence for uranium mobility in zircon and the discordance of U-Pb chronometers. Earth and Planetary Science Letters, v. 409, p. 43–48

Trueman, N.A., Long, J.V.P., Reed, S.J.B., Chinner, G.A., 1988. The lead-uranium systematics, and rare earth element distributions of some Olympic Dam and Stuart shelf mineralisation. Western Mining Corporation, unpublished report, K/3143, p. 46.

Utsunomiya, S., Palenik, C.S., Valley, J.W., Cavosie, A.J., Wilde, S.A., Ewing, R.C., 2004. Nanoscale occurrence of Pb in an Archean zircon. Geochimica Cosmochimica Acta, v, 68, p. 4679–4686.

Verdugo-Ihl, M.R., Ciobanu, C.L., Cook, N.J., Ehrig, K., Courtney-Davies, L., Gilbert, S., 2017. Textures and U-W-Sn-Mo signatures in hematite from the Olympic Dam Cu-U-Au-Ag deposit, South Australia: Defining the archetype for IOCG deposits. Ore Geology Reviews, v. 91, p. 173-195.

Verdugo-Ihl, M.R., Ciobanu, C.L., Cook, N.J., Ehrig, K., and Courtney-Davies, L., in press. Defining early stages of IOCG systems: evidence from iron-oxides in the outer shell of the Olympic Dam deposit, South Australia. Mineralium Deposita (in press), doi:10.1007/s00126-019-00896-2.

Verdugo-Ihl, M.R., Ciobanu, C.L., Slattery, A., Cook, N.J., Ehrig, K., Courtney-Davies, L., 2019. Copper-Arsenic Nanoparticles in Hematite: Fingerprinting Fluid-Mineral Interaction. Minerals, 9(7), 388, https://doi.org/10.3390/min9070388.

Von Quadt, A., Erni, M., Martinek, K., Moll, M., Peytcheva, Heinrich, C.A., 2011. Zircon crystallization and the lifetimes of ore-forming magmatic-hydrothermal systems. Geology, v. 39, p. 731−734.

CHAPTER 11

SUPPLEMENTARY AND ADDITIONAL MATERIAL

SUPPLEMENTARY MATERIAL A

FOR CHAPTER 2 – MATRIX-MATCHED IRON-OXIDE LASER ABLATION ICP-MS U–PB GEOCHRONOLOGY USING MIXED SOLUTION STANDARDS

APPENDIX A: METHODOLOGY

ELECTRONIC APPENDIX A FOR CHAPTER 2

Supplementary Materials: Matrix-Matched Iron-Oxide Laser Ablation ICP-MS U-Pb Geochronology Using Mixed Solution Standards

Liam Courtney-Davies, Zhiyong Zhu, Cristiana L. Ciobanu, Benjamin P. Wade, Nigel J. Cook, Kathy Ehrig, Alexandre R. Cabral and Allen Kennedy

Supplementary Text File S1. Additional analytical procedures for calculating and certifying the Pb/U ratios.

The mixed solution standard was made from single natural U and Pb solutions. The concentrations of these two solutions were calibrated using Q-ICP-MS at Adelaide Microscopy.

- Q-ICP-MS results: *Pb concentration of the mother bottle* = 9985 ppb; *U concentration of the mother bottle* = 9994 ppb.

The Pb isotope ratios were analyzed by MC-ICP-MS at Nanjing University.

- MC-ICP-MS results: $^{206}Pb/^{204}Pb$ = 17.9895 ± 0.0005; $^{207}Pb/^{204}Pb$ = 15.5847 ± 0.0005; $^{208}Pb/^{204}Pb$ = 38.0495 ± 0.0013; $^{207}Pb/^{206}Pb$ = 0.86632 ± 0.00004.

The constant $^{238}U/^{235}U$ (137.88), in combination with the Pb isotope ratio results, allows us to calculate $^{206}Pb/^{238}U$.

To achieve this, we must calculate the atomic weight of the Pb and U solution standards:

X = Proportion of isotopes; M = Mass of isotope

- Pb atomic weight = $X^{204} \times M^{204} + X^{206} \times M^{206} + X^{207} \times M^{207} + X^{208} \times M^{208}$
- U atomic weight = $X^{235} \times M^{235} + X^{238} \times M^{238}$

To then calculate the ratio of ^{206}Pb and ^{238}U, the correct amount of Pb and U standard solution to create a concentration compatible with the sample to be analyzed must be weighed.

Con = Concentration of element; W = Weight of solution

$$\frac{Pb_{206}}{U_{238}} = \frac{\frac{Con_{pb} \times W_{Pb-sol}}{Pb_{atomic\ weight}} \times X_{206}}{\frac{Con_{U} \times W_{U}}{U_{atomic\ weight}} \times X_{238}} \quad (1)$$

$$\frac{Pb_{207}}{U_{235}} = \frac{\frac{Con_{pb} \times W_{Pb-sol}}{Pb_{atomic\ weight}} \times X_{207}}{\frac{Con_{U} \times W_{U}}{U_{atomic\ weight}} \times X_{235}} \quad (2)$$

$^{207}Pb/^{206}Pb$ = 0.86632 ± 0.00004 (measured by MC-ICP-MS)

$^{206}Pb/^{238}U$ = 0.286356

The following tables contain the Pb isotope ratios and U-Pb concentrations.

Table S1. Pb isotope ratios of Pb standard solution.

Name	$Pb^{206/204}$	$Pb^{206/204}$ SE (abs)	$Pb^{207/204}$	$Pb^{207/204}$ SE (abs)	$Pb^{208/204}$	$Pb^{208/204}$ SE (abs)
NIST987-01	16.939	0.001	15.488	0.001	36.693	0.002
NIST987-02	16.937	0.001	15.487	0.001	36.690	0.002
Pb-1	17.990	0.001	15.585	0.001	38.049	0.001
Pb-2	17.991	0.001	15.586	0.001	38.052	0.001
Pb-3	17.988	0.000	15.583	0.000	38.047	0.001
NIST987-03	16.938	0.001	15.488	0.001	36.692	0.002
Average of Samples	17.990	0.001	15.585	0.001	38.050	0.001

Minerals **2016**, *6*, 85; doi:10.3390/min6030085

Table S2. U and Pb concentration of standard solutions. Conc. = Concentration.

Type	Sample Name	^{204}Pb		^{206}Pb		^{207}Pb		^{208}Pb		^{235}U		^{238}U		^{115}In (ISTD)			Average Pb		Average U		Pb/U
		Conc.	Conc. RSD	Conc.	Conc. RSD	Conc.	Conc. RSD	Conc.	Conc. RSD	Conc.	Conc. RSD	Conc.	Conc. RSD	Conc.	Conc. RSD	ISTD Recovery %	Conc.	Conc. RSD	Conc.	Conc. RSD	
CalBlk	Blank	0.00	N/A	0.00	N/A	0.00	N/A	0.00	N/A	0.00	N/A	0.00	N/A	-	-	100	-	-	-	-	-
CalStd	Standard-1 ppb	0.98	8.07	0.95	2.34	0.96	4.70	0.95	2.01	0.98	17.39	1.00	1.95	-	-	99	0.95	0.19	0.99	1.84	0.96
CalStd	Standard-2 ppb	1.97	6.05	1.97	1.74	1.96	3.03	2.00	1.88	2.04	6.45	2.02	0.84	-	-	97	1.98	1.14	2.03	0.40	0.97
CalStd	Standard-5 ppb	5.06	3.76	5.01	1.92	4.98	2.46	5.07	2.24	4.95	5.22	5.11	2.66	-	-	100	5.02	0.86	5.03	2.31	1.00
CalStd	Standard-10 ppb	9.89	4.49	9.91	3.38	9.90	3.82	10.02	3.97	9.85	4.14	9.99	3.18	-	-	103	9.94	0.65	9.92	1.02	1.00
CalStd	Standard-20 ppb	19.42	2.66	19.63	2.47	19.58	2.62	19.98	2.17	19.34	3.52	19.97	1.80	-	-	106	19.73	1.09	19.65	2.29	1.00
CalStd	Standard-50 ppb	50.25	1.82	50.17	2.09	50.19	2.63	51.55	2.91	50.30	2.23	51.82	2.48	-	-	104	50.64	1.56	51.06	2.11	0.99
Sample	Blank	<0.000	N/A	<0.000	N/A	<0.000	N/A	<0.000	N/A	<0.000	N/A	<0.000	N/A	-	-	103	-	-	-	-	-
Sample	1	1.17	12.14	1.04	5.38	1.03	4.95	1.04	5.54	1.01	14.29	0.99	5.38	-	-	105	1.03	0.78	1.00	1.98	1.04
Sample	2	4.50	4.97	4.07	2.91	3.95	2.33	4.11	2.89	3.64	4.42	3.77	1.29	-	-	115	4.04	5.95	3.71	2.50	1.09
Sample	3	11.80	2.90	11.88	2.78	11.79	1.75	12.05	2.11	11.37	4.19	11.76	2.39	-	-	111	11.91	1.09	11.56	2.41	1.03
Sample	4	43.61	1.65	44.42	2.10	44.09	2.21	44.97	2.38	38.70	3.25	40.39	2.95	-	-	108	44.50	1.00	39.54	3.01	1.13

Table S3. Relation coefficient of standards.

Tune Step	Mass	Name	Relation Coefficient	Detection Limit
2	204	Pb	0.99990	0.10246
2	206	Pb	0.99996	0.06304
2	207	Pb	0.99995	0.07154
2	208	Pb	0.99999	0.06215
2	235	U	0.99987	0.09124
2	238	U	0.99998	0.03269



© 2016 by the authors; licensee MDPI, Basel, Switzerland. This article is an open access article distributed under the terms and conditions of the Creative Commons by Attribution (CC-BY) license (http://creativecommons.org/licenses/by/4.0/).

SUPPLEMENTARY MATERIAL B

FOR CHAPTER 3 – A MULTI-TECHNIQUE EVALUATION OF HYDROTHERMAL HEMATITE U-PB ISOTOPE SYSTEMATICS: IMPLICATIONS FOR ORE DEPOSIT GEOCHRONOLOGY

APPENDIX A: ID-TIMS U-PB DATA

APPENDIX B: SHRIMP U-PB DATA

APPENDIX C: LA-ICP-MS U-PB DATA

APPENDIX C: LA-ICP-MS TRACE ELEMENT DATA

ELECTRONIC APPENDIX A FOR CHAPTER 3

	Radiogenic Isotope Ratios								Isotopic Ages													
Aliquot	$\frac{^{207}Pb}{^{206}Pb}$	% err	$\frac{^{207}Pb}{^{235}U}$	% err	$\frac{^{206}Pb}{^{238}U}$	% err	corr. coef.	$\frac{^{208}Pb}{^{206}Pb}$	$\frac{^{207}Pb}{^{206}Pb}$	±	$\frac{^{207}Pb}{^{235}U}$	±	$\frac{^{206}Pb}{^{238}U}$	±	$\frac{^{238}U}{^{206}Pb}$	% err	$\frac{^{207}Pb}{^{206}Pb}$	% err	$\frac{^{204}Pb}{^{206}Pb}$	% err	corr. coef. 8/6-7/6	corr. coef. 8/6-4/6	corr. coef. 7/6-4/6
(a)	(e)	(f)	(e)	(f)	(e)	(f)		(e)	(g)	(f)	(g)	(f)	(g)	(f)	(h)	(f)	(h)	(f)	(h)	(f)			
LCD4- 1	0.10	0.33	3.81	0.46	0.28	0.31	0.69	0.00	1595.84	6.25	1594.31	3.70	1593.15	4.43	3.54	0.97	0.10	6.52	0.00	112.85	-0.96	-0.95	1.00
LCD4-2	0.10	0.87	3.85	0.89	0.29	0.35	0.27	0.01	1584.09	16.19	1604.16	7.18	1619.48	5.03	3.30	2.24	0.15	10.48	0.00	31.74	-1.00	-1.00	1.00
LCD4-3	0.10	0.09	3.80	0.18	0.28	0.10	0.95	0.00	1590.20	1.71	1593.12	1.45	1595.32	1.40	3.55	0.10	0.10	0.23	0.00	6.54	-0.54	-0.27	0.93
LCD4-4	0.10	0.09	12.88	0.20	0.95	0.14	0.93	0.00	1589.17	1.62	2670.84	1.88	4310.83	4.37	1.05	0.16	0.10	0.55	0.00	192.02	-0.53	-0.46	0.99
LCD4-5	0.10	0.09	3.81	0.18	0.28	0.10	0.95	0.00	1590.04	1.60	1594.11	1.42	1597.20	1.44	3.55	0.11	0.10	0.28	0.00	20.59	-0.53	-0.33	0.95
MV005-1	0.10	0.13	3.75	0.23	0.28	0.15	0.84	0.00	1584.76	2.47	1581.74	1.82	1579.48	2.06	3.59	0.26	0.10	1.60	0.00	73.91	-0.85	-0.83	1.00
MV005-2	0.10	0.28	2.53	0.34	0.19	0.15	0.63	0.02	1545.55	5.18	1282.01	2.50	1130.63	1.55	4.94	0.23	0.14	1.01	0.00	3.21	-0.91	-0.87	0.99
MV005-3	0.10	0.28	3.89	0.33	0.29	0.14	0.54	0.01	1599.28	5.25	1612.32	2.68	1622.32	2.06	3.44	0.71	0.11	4.50	0.00	35.95	-0.99	-0.99	1.00
MV005-4	0.10	5.12	4.07	5.06	0.30	1.99	0.17	0.01	1617.53	95.31	1649.19	41.28	1674.16	29.33	3.37	15.39	0.10	114.31	0.00	0.00	-1.00	0.00	0.00
6607-4	0.10	0.74	5.48	0.78	0.42	0.32	0.34	0.02	1541.80	13.82	1898.16	6.68	2240.75	6.13	2.11	1.17	0.20	3.67	0.01	7.17	-0.99	-0.99	1.00
6607-3	0.09	1.16	7.61	1.19	0.64	0.46	0.26	0.08	1339.27	22.34	2185.80	10.67	3193.90	11.67	1.23	0.31	0.27	0.59	0.01	0.90	-0.91	-0.81	0.92
6607-1	0.08	0.73	5.33	2.12	0.48	1.99	0.94	0.04	1204.30	14.39	1873.98	18.13	2534.17	41.73	1.81	2.00	0.19	1.05	0.01	1.85	-0.16	-0.15	0.98
6607- 2	0.09	0.34	4.82	0.41	0.39	0.17	0.56	0.02	1401.65	6.55	1788.71	3.41	2138.81	3.03	2.38	0.22	0.15	0.91	0.00	2.38	-0.90	-0.84	0.99
MV095-1	0.17	21.18	0.77	17.59	0.03	13.90	0.11	468.87	2531.15	355.41	577.51	77.47	210.57	28.79	3.54	6.32	0.87	0.23	0.06	0.30	0.90	0.13	-0.04
MV095-2	0.12	7.16	2.84	6.72	0.17	3.59	0.14	137.67	1968.08	127.65	1366.98	50.48	1015.93	33.74	2.14	6.33	0.65	1.79	0.04	2.45	-1.00	-0.98	0.98
MV095-3	0.10	2.08	0.08	2.07	0.01	0.86	0.19	28.20	1687.83	38.43	79.03	1.57	36.46	0.31	149.59	5.18	0.24	13.30	0.01	24.43	-1.00	-1.00	1.00
7295GM- 3	0.10	0.53	3.76	0.84	0.28	0.39	0.88	0.00	1584.98	9.99	1583.69	6.77	1582.72	5.47									
7295GM- 4	0.10	0.69	3.60	0.86	0.27	0.37	0.63	0.01	1576.63	12.96	1548.84	6.85	1528.55	4.99									
7295GM- 2	0.10	0.31	3.78	0.45	0.28	0.19	0.81	0.01	1584.99	5.85	1589.54	3.58	1592.97	2.65									
7295GM-1	0.10	0.46	0.94	0.75	0.07	0.38	0.87	0.00	1620.08	8.47	673.06	3.69	426.18	1.59									
7295GM-5	0.09	1.94	3.49	2.91	0.27	1.28	0.85	0.01	1520.25	36.63	1525.54	22.99	1529.35	17.39									

(a) z1, z2 etc. are labels for single zircon grains or fragments annealed and chemically abraded after Mattinson (2005).
(b) Model Th/U ratio iteratively calculated from the radiogenic 208Pb/206Pb ratio and 206Pb/238U age.
(c) Pb* and Pbc represent radiogenic and common Pb, respectively; mol % 206Pb* with respect to radiogenic, blank and initial common Pb.
(d) Measured ratio corrected for spike and fractionation only. Fractionation estimated at 0.18 +/- 0.03 %/a.m.u. for Daly analyses, based on analysis of NBS-981 and NBS-982.
(e) Corrected for fractionation, spike, and common Pb; up to 1 pg of common Pb was assumed to be procedural blank: 206Pb/204Pb = 18.042 ± 0.61%; 207Pb/204Pb = 15.537 ± 0.52%; 208Pb/204Pb = 37.686 ± 0.63% (all uncertainties 1-sigma).
Excess over blank was assigned to initial common Pb, using the Stacey and Kramers (1975) two-stage Pb isotope evolution model at the nominal sample age.
(f) Errors are 2-sigma, propagated using the algorithms of Schmitz and Schoene (2007).
(g) Calculations are based on the decay constants of Jaffey et al. (1971). 206Pb/238U and 207Pb/206Pb ages corrected for initial disequilibrium in 230Th/238U using Th/U [magma] = 3.
(h) Corrected for fractionation, spike, and blank Pb only.
(i) Nominal fraction weights estimated from photomicrographic grain dimensions, adjusted for partial dissolution during chemical abrasion.
(j) Nominal U and total Pb concentrations subject to uncertainty in photomicrographic estimation of weight and partial dissolution during chemical abrasion.

| Sample (Radiogenic + Initial Pb) Isotope Ratios | | |

ELECTRONIC APPENDIX B FOR CHAPTER 3

	Composition			Isotopic Ages					Isotopic Ratios						
	%	U	4-corr ppm	$^{206}Pb/^{238}U$		$^{207}Pb/^{206}$ Pb		%	$\frac{^{207}Pb}{^{206}Pb}$		$\frac{^{207}Pb}{^{235}U}$		$\frac{^{206}Pb}{^{238}U}$		corr.
7295GM	Pb_c	ppm	$^{206}Pb^*$	Age	±Ma	Age	±Ma	Discordancy		±%		±%		±%	coef.
1	0.62	127	26	1375	48	1605	28	19	0.099	1.5	3.25	4.2	0.238	3.9	0.93
2	0.64	207	41	1328	46	1581	25	20	0.098	1.3	3.08	4.1	0.229	3.8	0.95
3	2	276	70	1662	55	1644	31	2	0.101	1.6	4.1	4.1	0.294	3.7	0.92
4	0.22	351	95	1764	58	1554	13	-12	0.096	0.7	4.18	3.9	0.315	3.8	0.98
5	0.91	135	34	1641	57	1583	32	-1	0.098	1.7	3.91	4.3	0.29	3.9	0.92
6	0.53	334	95	1841	61	1565	26	-17	0.097	1.4	4.42	4	0.331	3.8	0.94
7	0.24	517	135	1714	58	1592	11	-5	0.098	0.6	4.13	3.9	0.305	3.9	0.99
8	0.18	8	425	1666	55	1586	5	-2	0.098	0.3	3.98	3.8	0.295	3.7	0.99
9	0.87	2	417	1705	57	1583	22	-5	0.098	1.2	4.08	4	0.303	3.8	0.95
10	0.18	18	264	1672	55	1589	6	-3	0.098	0.3	4	3.7	0.296	3.7	0.99
11	0.99	563	159	1834	60	1578	13	-15	0.098	0.7	4.43	3.8	0.329	3.8	0.98
12	8.03	115	31	1768	60	1701	75	-1	0.104	4.1	4.53	5.6	0.316	3.9	0.69
13	0.73	137	37	1745	59	1563	35	-10	0.097	1.9	4.15	4.3	0.311	3.8	0.9
14	0.56	440	122	1808	59	1591	11	-12	0.098	0.6	4.38	3.8	0.324	3.8	0.99
15	0.79	112	31	1805	66	1576	33	-13	0.097	1.7	4.34	4.5	0.323	4.2	0.92
16	0.44	301	87	1879	73	1549	19	-21	0.096	1	4.48	4.6	0.339	4.5	0.98
17	0.24	247	70	1848	61	1589	17	-15	0.098	0.9	4.49	3.9	0.332	3.8	0.97
18	1.28	367	107	1884	68	1615	48	-15	0.099	2.6	4.66	4.9	0.339	4.2	0.85
19	0.34	403	111	1791	66	1661	25	-6	0.102	1.4	4.5	4.4	0.32	4.2	0.95
20	0.18	548	132	1592	53	1559	25	1	0.097	1.3	3.73	4	0.28	3.7	0.94
21	0.13	749	209	1812	59	1597	7	-12	0.099	0.4	4.41	3.8	0.324	3.8	0.99
22	1.25	154	41	1734	63	1706	27	1	0.105	1.5	4.45	4.4	0.309	4.2	0.94
23	0.67	223	57	1670	56	1577	26	-3	0.098	1.4	3.98	4.1	0.296	3.8	0.94

ELECTRONIC APPENDIX C FOR CHAPTER 3

	Radiogenic Isotope Ratios							Isotopic Ages					
Sample	$^{207}Pb/^{235}U$	2s err	$^{206}Pb/^{238}U$	2s err	$^{207}Pb/^{206}Pb$	2s err	err corr	$^{207}Pb/^{235}U$	± Ma	$^{206}Pb/^{238}U$	± Ma	$^{207}Pb/^{206}Pb$	± Ma
1 LCD4	4.18	0.07	0.31	0.004	0.098	0.001	0.86	1669	14	1726	21	1581	16
2 LCD4	4.13	0.04	0.30	0.003	0.098	0.001	0.71	1659	9	1710	12	1589	15
3 LCD4	4.15	0.04	0.31	0.002	0.098	0.000	0.75	1665	7	1718	10	1593	9
4 LCD4	4.27	0.06	0.31	0.004	0.098	0.001	0.75	1689	11	1763	17	1593	16
5 LCD4	4.08	0.05	0.30	0.003	0.099	0.001	0.85	1649	9	1684	15	1597	12
6 LCD4	4.25	0.08	0.31	0.005	0.099	0.001	0.87	1682	15	1747	26	1597	18
7 LCD4	4.18	0.04	0.31	0.003	0.099	0.001	0.81	1670	9	1723	14	1598	13
8 LCD4	3.90	0.04	0.29	0.002	0.099	0.000	0.89	1613	8	1623	11	1599	8
9 LCD4	4.10	0.05	0.30	0.003	0.099	0.001	0.82	1654	9	1697	16	1603	13
10 LCD4	4.25	0.08	0.31	0.005	0.099	0.001	0.72	1680	15	1748	23	1607	23
11 LCD4	3.78	0.04	0.28	0.003	0.099	0.000	0.91	1590	8	1579	13	1608	7
12 LCD4	4.20	0.06	0.31	0.004	0.099	0.001	0.84	1673	12	1722	18	1608	14
13 LCD4	4.26	0.06	0.31	0.003	0.099	0.001	0.63	1684	11	1743	13	1609	16
14 LCD4	4.15	0.07	0.30	0.004	0.100	0.001	0.56	1664	14	1697	21	1610	22
15 LCD4	4.30	0.05	0.31	0.003	0.099	0.001	0.82	1693	10	1749	16	1610	13
16 LCD4	4.07	0.05	0.30	0.003	0.100	0.001	0.81	1649	9	1680	15	1617	11
17 LCD4	4.05	0.05	0.30	0.003	0.100	0.001	0.62	1645	10	1669	15	1620	13
18 LCD4	4.29	0.06	0.31	0.003	0.100	0.001	0.66	1691	11	1734	17	1620	19
19 LCD4	4.11	0.04	0.30	0.002	0.100	0.001	0.60	1657	8	1690	12	1624	16
20 LCD4	4.10	0.06	0.30	0.004	0.100	0.001	0.68	1653	12	1671	17	1625	16
21 LCD4	4.11	0.07	0.30	0.004	0.100	0.001	0.86	1656	13	1670	19	1629	16
22 LCD4	4.19	0.06	0.30	0.003	0.100	0.001	0.71	1671	11	1706	16	1629	17
23 LCD4	4.36	0.05	0.31	0.002	0.101	0.001	0.62	1705	10	1761	11	1632	17
24 LCD4	4.16	0.05	0.30	0.002	0.101	0.001	0.63	1667	10	1701	12	1633	16
25 LCD4	4.16	0.06	0.30	0.004	0.101	0.001	0.90	1669	11	1691	18	1634	11
26 LCD4	4.20	0.05	0.30	0.003	0.101	0.001	0.81	1673	10	1694	14	1634	12
27 LCD4	4.20	0.05	0.30	0.003	0.101	0.001	0.70	1675	10	1709	15	1634	15
28 LCD4	4.24	0.05	0.30	0.003	0.101	0.001	0.77	1681	10	1709	15	1636	14
29 LCD4	4.49	0.09	0.32	0.004	0.102	0.001	0.75	1726	16	1782	19	1652	20
30 LCD4	4.22	0.05	0.30	0.003	0.102	0.001	0.77	1679	9	1704	16	1661	14
	$^{207}Pb/^{235}U$	2s err	$^{206}Pb/^{238}U$	2s err	$^{207}Pb/^{206}Pb$	2s err	U/Pb err corr	$^{207}Pb/^{235}U$	±	$^{206}Pb/^{238}U$	±	$^{207}Pb/^{206}Pb$	±
1 MV005A	3.81	0.08	0.28	0.004	0.100	0.001	0.44	1588	16	1577	21	1609	22
2 MV005A	4.26	0.35	0.30	0.024	0.105	0.009	0.10	1620	54	1647	94	1650	150
3 MV005A	3.68	0.13	0.28	0.006	0.098	0.003	0.17	1565	25	1564	31	1574	59
4 MV005A	3.93	0.17	0.23	0.009	0.124	0.005	0.22	1609	34	1349	45	1970	76
5 MV005A	3.99	0.11	0.30	0.006	0.099	0.002	0.46	1632	21	1699	31	1586	42
6 MV005A	3.76	0.12	0.27	0.004	0.101	0.002	0.44	1572	20	1518	22	1620	27
7 MV005A	3.52	0.09	0.26	0.005	0.097	0.002	0.45	1531	20	1499	25	1570	34
8 MV005A	3.47	0.09	0.26	0.004	0.098	0.002	0.59	1523	19	1495	22	1578	34
9 MV005A	3.79	0.09	0.27	0.005	0.103	0.002	0.63	1590	18	1532	24	1680	27
10 MV005A	3.57	0.06	0.26	0.004	0.098	0.001	0.87	1543	13	1508	21	1592	11
11 MV005A	3.64	0.08	0.27	0.004	0.100	0.002	0.63	1557	17	1520	22	1610	30
12 MV005A	3.50	0.06	0.26	0.004	0.099	0.001	0.77	1529	14	1484	20	1598	22
13 MV005A	3.58	0.07	0.26	0.004	0.099	0.001	0.63	1544	15	1508	22	1593	24
14 MV005A	3.87	0.09	0.28	0.005	0.102	0.002	0.21	1607	18	1584	24	1657	38
15 MV005A	3.64	0.14	0.26	0.007	0.100	0.004	0.28	1550	28	1504	36	1632	55
16 MV005A	3.62	0.06	0.26	0.004	0.099	0.001	0.86	1551	13	1513	20	1603	10
17 MV005A	3.79	0.06	0.28	0.005	0.100	0.001	0.35	1589	12	1580	22	1617	16
18 MV005A	4.92	0.30	0.29	0.007	0.122	0.007	0.21	1774	46	1649	31	1936	84
19 MV005A	4.03	0.12	0.28	0.008	0.102	0.003	0.23	1638	25	1604	36	1645	60
20 MV005A	3.93	0.08	0.27	0.005	0.108	0.002	0.69	1621	17	1518	23	1766	27

	$^{207}Pb/^{235}U$	2s err	$^{206}Pb/^{238}U$	2s err	$^{207}Pb/^{206}Pb$	2s err	U/Pb err corr	$^{207}Pb/^{235}U$	±	$^{206}Pb/^{238}U$	±	$^{207}Pb/^{206}Pb$	±
1 6607	5.60	0.49	0.39	0.017	1100.000	4740.000	0.70	2105	79	2380	490	1551	42
2 6607	4.82	0.29	0.39	0.014	44.000	7800.000	0.49	2124	66	2840	630	1592	36
3 6607	6.00	0.32	0.43	0.008	1600.000	4780.000	0.03	2309	38	2850	760	1604	37
4 6607	6.15	0.34	0.43	0.007	160.000	5230.000	0.55	2318	33	2930	780	1595	34
5 6607	5.49	0.38	0.39	0.016	990.000	1970.000	0.52	2107	74	2400	520	1560	47
6 6607	5.82	0.45	0.48	0.022	200.000	1570.000	0.56	2527	97	1620	250	1552	77
7 6607	5.76	0.40	0.42	0.010	62.000	1530.000	0.38	2266	45	2480	500	1551	78
8 6607	4.48	0.30	0.34	0.012	440.000	1050.000	0.52	1866	59	2010	410	1580	79
9 6607	5.12	0.39	0.38	0.013	630.000	2820.000	0.55	2073	61	2820	630	1594	46
10 6607	5.17	0.32	0.40	0.009	0.016	2890.000	0.48	2173	42	1490	200	1655	49
11 6607	5.06	0.44	0.36	0.014	240.000	1360.000	0.57	1998	67	2500	540	1522	72
12 6607	6.54	0.47	0.45	0.007	180.000	########	0.73	2389	33	2680	610	1605	25
13 6607	6.39	0.51	0.42	0.017	160.000	2940.000	0.68	2266	78	2210	460	1621	51
14 6607	5.48	0.21	0.39	0.010	610.000	########	0.14	2122	46	2640	580	1610	20
15 6607	6.41	0.52	0.51	0.021	150.000	652.000	0.19	2665	89	2330	470	1540	110
16 6607	5.07	0.36	0.40	0.021	200.000	920.000	0.25	2173	96	2360	500	1502	93
17 6607	5.53	0.33	0.39	0.010	460.000	7150.000	0.47	2127	46	2100	440	1606	33
18 6607	5.59	0.25	0.40	0.009	1300.000	########	0.49	2167	43	2930	810	1597	20
19 6607	4.94	0.50	0.36	0.015	860.000	222.000	0.15	1974	71	2350	500	1580	160
	$^{207}Pb/^{235}U$	2s err	$^{206}Pb/^{238}U$	2s err	$^{207}Pb/^{206}Pb$	2s err	U/Pb err corr	$^{207}Pb/^{235}U$	±	$^{206}Pb/^{238}U$	±	$^{207}Pb/^{206}Pb$	±
1 MV95	7.00	0.44	0.46	0.021	0.109	0.002	0.08	2073	56	2398	92	1788	28
2 MV95	5.49	0.31	0.40	0.015	0.098	0.001	0.92	1873	47	2160	68	1573	28
3 MV95	5.18	0.34	0.38	0.019	0.096	0.001	0.97	1810	54	2061	85	1541	23
4 MV95	5.64	0.32	0.41	0.015	0.096	0.001	0.94	1895	49	2214	68	1542	24
5 MV95	4.61	0.27	0.30	0.007	0.119	0.006	0.59	1742	46	1699	34	1932	80
6 MV95	4.81	0.33	0.37	0.013	0.094	0.004	0.08	1756	55	2011	60	1508	83
7 MV95	6.04	0.39	0.44	0.020	0.096	0.001	0.05	1934	56	2312	90	1548	16
8 MV95	4.91	0.21	0.36	0.010	0.097	0.001	0.09	1795	38	1991	48	1571	17
9 MV95	5.13	0.25	0.38	0.011	0.097	0.001	0.28	1821	41	2062	53	1565	15
10 MV95	5.58	0.27	0.36	0.010	0.112	0.001	0.97	1890	40	1959	46	1824	16
11 MV95	19.40	1.30	1.59	0.100	0.095	0.002	0.92	3045	66	6230	260	1533	47
12 MV95	4.74	0.21	0.35	0.011	0.097	0.000	0.51	1754	39	1937	55	1576	9
13 MV95	8.31	0.28	0.43	0.009	0.132	0.003	0.67	2270	32	2300	38	2126	42
14 MV95	7.76	0.37	0.39	0.014	0.151	0.004	0.89	2198	44	2125	63	2356	42
15 MV95	36.10	1.90	0.67	0.022	0.388	0.017	0.54	3628	48	3292	84	3842	68
16 MV95	6.51	0.43	0.45	0.020	0.103	0.003	0.93	2033	57	2412	92	1684	50
17 MV95	209.00	10.00	2.08	0.061	0.708	0.010	0.89	5396	49	7240	130	4757	23
18 MV95	6.12	0.31	0.44	0.014	0.097	0.001	0.61	1960	43	2356	62	1561	26
19 MV95	5.54	0.32	0.40	0.016	0.097	0.000	0.18	1870	51	2139	72	1575	8
	$^{207}Pb/^{235}U$	2s err	$^{206}Pb/^{238}U$	2s err	$^{207}Pb/^{206}Pb$	2s err	U/Pb err corr	$^{207}Pb/^{235}U$	±	$^{206}Pb/^{238}U$	±	$^{207}Pb/^{206}Pb$	±
1 7295GM	3.73	0.05	0.27	0.003	0.099	0.001	0.96	1561	14	1539	17	1591	31
2 7295GM	3.46	0.04	0.26	0.003	0.098	0.001	0.97	1608	20	1585	20	1637	44
3 7295GM	3.81	0.05	0.28	0.003	0.099	0.001	0.94	1523	12	1462	17	1608	25
4 7295GM	3.32	0.05	0.25	0.003	0.097	0.001	0.90	1610	18	1625	20	1591	40
5 7295GM	3.48	0.05	0.26	0.003	0.098	0.001	0.90	1535	11	1492	17	1595	23
6 7295GM	3.53	0.05	0.26	0.003	0.098	0.001	0.88	1506	17	1456	18	1578	37
7 7295GM	3.48	0.05	0.25	0.003	0.099	0.001	0.85	1577	10	1551	17	1611	20
8 7295GM	3.52	0.05	0.25	0.003	0.101	0.001	0.85	1560	17	1526	18	1607	37
9 7295GM	3.65	0.06	0.27	0.003	0.098	0.002	0.72	1589	44	1580	25	1601	100
10 7295GM	3.43	0.06	0.25	0.003	0.098	0.001	0.78	1523	11	1474	16	1592	22
11 7295GM	3.32	0.06	0.24	0.003	0.099	0.002	0.77	1584	61	1581	31	1588	137
12 7295GM	3.50	0.06	0.25	0.003	0.100	0.002	0.71	1564	22	1547	19	1587	50
13 7295GM	3.65	0.08	0.27	0.004	0.099	0.002	0.64	1521	27	1482	20	1575	62
14 7295GM	3.41	0.07	0.25	0.003	0.098	0.002	0.64	1538	27	1515	21	1570	63
15 7295GM	3.88	0.09	0.29	0.004	0.098	0.002	0.61	1556	22	1541	20	1576	50
16 7295GM	3.87	0.10	0.28	0.004	0.101	0.002	0.57	1486	11	1431	16	1564	23
17 7295GM	3.67	0.10	0.27	0.004	0.098	0.003	0.51	1512	13	1462	17	1583	28
18 7295GM	3.63	0.10	0.27	0.004	0.097	0.003	0.52	1485	13	1408	16	1598	29
19 7295GM	3.47	0.12	0.26	0.004	0.097	0.003	0.44	1495	34	1434	21	1583	80
20 7295GM	3.55	0.12	0.26	0.004	0.097	0.003	0.44	1518	10	1474	16	1581	20
21 7295GM	3.72	0.12	0.27	0.004	0.101	0.003	0.49	1595	11	1591	18	1601	21
22 7295GM	3.36	0.15	0.25	0.004	0.098	0.004	0.37	1528	15	1456	17	1628	32
23 7295GM	3.78	0.21	0.28	0.005	0.099	0.005	0.33	1532	12	1458	17	1635	25
24 7295GM	3.76	0.29	0.28	0.006	0.098	0.008	0.29	1576	25	1530	21	1638	56

No data points are excluded from concordia diagrams and no external propogation is applied unless stated otherwise

ELECTRONIC APPENDIX D FOR CHAPTER 3

	^{95}Mo	^{118}Sn	^{182}W	^{204}Pb	^{206}Pb	^{207}Pb	^{208}Pb	^{232}Th	^{238}U
LCD4 High U -1	685	326	6635	0	175	19	0	<0.00	155
LCD4 High U -2	699	465	4157	1	1351	142	0	<0.00	1214
LCD4 High U -3	382	708	12639	1	1013	110	0	<0.00102	937
LCD4 High U -4	390	558	8814	2	851	92	1	0	768
LCD4 High U -5	684	798	11676	1	2276	234	0	<0.00061	1981
LCD4 High U -6	580	679	8474	1	1815	187	1	<0.00085	1576
LCD4 High U -7	601	770	10560	1	1965	203	0	<0.00106	1696
LCD4 High U -8	661	737	11290	1	1554	156	0	<0.00058	1302
LCD4 High U -9	782	616	8908	1	918	97	0	<0.00059	791
LCD4 High U -10	750	379	3608	1	628	67	0	<0.00	562
LCD4 High U -11	559	634	13321	0	584	64	0	<0.00082	530
LCD4 High U -12	678	560	9835	0	625	67	0	0	565
LCD4 Low U -1	857	496	8492	<0.23	57	6	0	0	34
LCD4 Low U -2	485	368	3887	0	35	3	0	<0.00	27
LCD4 Low U -3	559	441	7667	1	30	4	0	<0.00065	27
LCD4 Low U -4	705	477	8465	1	26	5	0	<0.00	25
LCD4 Low U -5	581	479	6658	<0.22	35	3	0	0	25
LCD4 Low U -6	616	460	4396	0	35	3	0	<0.00	28
LCD4 Low U -7	614	520	6052	1	32	4	0	<0.00	25
LCD4 Low U -8	505	470	4522	<0.21	22	2	0	<0.00062	15
LCD4 Low U -9	72	715	455	1	164	18	0	<0.00053	143
LCD4 Low U -10	103	509	865	0	99	10	0	<0.00051	68

SUPPLEMENTARY MATERIAL C

FOR CHAPTER 4 – OPENING THE MAGMATIC-HYDROTHERMAL WINDOW: HIGH PRECISION U-PB GEOCHRONOLOGY OF THE MESOPROTEROZOIC OLYMPIC DAM CU-U-AU-AG DEPOSIT, SOUTH AUSTRALIA

APPENDIX A TABLE A1: ID-TIMS HEMATITE U-PB DATA

APPENDIX A TABLE A2: ID-TIMS ZIRCON U-PB DATA

APPENDIX A FIGURE A1: EXTENDED ZIRCON CL IMAGES

APPENDIX A FIGURE 2: PHOTOGRAPHS OF HAND SPECIMENS

APPENDIX B: MASS BALANCE CALCULATIONS

ELECTRONIC APPENDIX A TABLE A1 FOR CHAPTER 4

Hematite U-Th-Pb isotopic data (British Geological Survey)

		Compositional Parameters						Radiogenic Isotope Ratios								Isotopic Dates (Ma)															
Sample	Aliquot	Th/U	$^{206}Pb^*$ x10-13 mol	mol % $^{206}Pb^*$	Pb*/ Pbc	Pbc (pg)	$^{206}Pb/^{204}Pb$	$^{208}Pb/^{206}Pb$	$^{207}Pb/^{206}Pb$	% err	$^{207}Pb/^{235}U$	% err	$^{206}Pb/^{238}U$	% err	corr. coef.	$^{207}Pb/^{206}Pb$	±	$^{207}Pb/^{235}U$	±	$^{206}Pb/^{238}U$	±	$^{238}U/^{206}Pb$	% err	$^{207}Pb/^{206}Pb$	% err	$^{204}Pb/^{206}Pb$	% err	corr. coef. 8/6-7/6	corr. coef. 8/6-4/6	corr. coef. 7/6-4/6	
		(a)	(b)	(c)	(c)	(c)	(d)	(e)	(e)	(f)	(e)	(f)	(e)	(f)		(g)	(f)	(g)	(f)	(g)	(f)	(h)	(f)	(h)	(f)	(h)	(f)				
CLC10 'outer shell'	CLC 10-1	0.002	43.0	1.0	208.5	4.7	13508	0.00	0.10	0.09	3.79	0.20	0.28	0.13	0.92	1590.8	1.7	1590.5	1.6	1590.2	1.9	3.57	0.17	0.10	0.80	0.00	330.00	-0.67	-0.63	0.99	
	CLC 10-2	0.002	37.1	1.0	218.0	3.9	14239	0.00	0.10	0.09	3.80	0.17	0.28	0.10	0.93	1590.7	1.7	1593.4	1.4	1595.4	1.3	3.56	0.15	0.10	0.93	0.00	1384.49	-0.84	-0.79	1.00	
	CLC 10-3	0.001	61.9	1.0	137.8	10.2	8741	0.00	0.10	0.09	3.81	0.19	0.28	0.13	0.91	1592.0	1.8	1595.6	1.6	1598.3	1.8	3.55	0.15	0.10	0.56	0.00	53.71	-0.58	-0.51	0.99	
	CLC10-4	0.010	12.3	1.0	22.2	12.6	1413	0.00	0.10	0.26	3.04	0.46	0.22	0.37	0.83	1590.6	4.8	1417.0	3.5	1304.3	4.4	4.42	0.52	0.11	2.57	0.00	38.82	-0.71	-0.71	0.99	
	CLC 10-5	0.002	36.4	1.0	73.0	11.3	4626	0.00	0.10	0.12	3.80	0.35	0.28	0.31	0.94	1592.0	2.3	1593.2	2.8	1594.0	4.3	3.56	0.33	0.10	0.92	0.00	45.77	-0.40	-0.38	1.00	
CLC201 'high-frade ore'	CLC 201 - 1	0.019	21.4	1.0	58.0	8.4	3689	0.01	0.10	0.12	3.83	0.20	0.28	0.11	0.86	1583.7	2.2	1599.1	1.6	1610.8	1.6	3.51	0.24	0.10	1.57	0.00	73.46	-0.90	-0.89	1.00	
	CLC 201 - 2	0.018	24.9	1.0	111.1	5.1	7147	0.01	0.10	0.11	3.77	0.19	0.28	0.11	0.89	1588.7	2.0	1587.1	1.5	1585.9	1.5	3.58	0.21	0.10	1.38	0.00	236.24	-0.89	-0.87	1.00	
	CLC201- 3	0.023	14.9	1.0	52.5	6.5	3358	0.01	0.10	0.14	3.84	0.21	0.28	0.11	0.79	1586.7	2.6	1600.5	1.7	1611.0	1.6	3.51	0.32	0.10	2.26	0.00	122.48	-0.95	-0.94	1.00	
	CLC201-4	0.020	12.6	1.0	21.4	13.3	1364	0.01	0.09	0.17	3.61	0.24	0.28	0.12	0.75	1513.2	3.2	1551.4	1.9	1579.5	1.7	3.57	0.38	0.10	2.61	0.00	36.00	-0.96	-0.96	1.00	
LCD5 'SE-lobe breccia'	LCD5 - 1	0.149	2.0	0.8	1.1	41.6	85	0.04	0.10	1.15	4.27	1.18	0.32	0.47	0.25	1553.1	21.6	1688.2	9.7	1799.1	7.4	2.56	1.86	0.25	4.43	0.01	7.45	-1.00	-1.00	1.00	
	LCD5 - 2	0.030	19.5	1.0	9.3	48.2	590	0.01	0.10	0.19	4.35	0.26	0.32	0.12	0.76	1595.5	3.5	1703.0	2.2	1791.7	1.9	3.04	0.25	0.12	1.37	0.00	7.70	-0.92	-0.90	1.00	
	LCD5 - 4	0.002	2.6	1.0	14.8	4.0	983	0.00	0.10	0.59	3.66	0.62	0.27	0.27	0.32	1591.7	11.1	1562.2	5.0	1540.4	3.7	3.70	1.73	0.10	12.79	0.00	814.06	-1.00	-1.00	1.00	
	LCD5 - 5	0.034	47.6	1.0	8.9	122.4	564	0.01	0.10	0.17	3.96	0.25	0.29	0.12	0.81	1590.3	3.2	1625.9	2.0	1653.6	1.7	3.33	0.14	0.12	0.56	0.00	2.89	-0.75	-0.64	0.98	
	LCD5 - 6	21.149	0.4	1.0	45.4	1.5	428	6.81	0.10	1.48	0.05	1.47	0.00	0.60	0.18	1674.1	27.3	51.7	0.7	23.7	0.1	272.00	4.59	0.10	32.81	0.00	0.00	-1.00	0.00	0.00	
MV026 'SE-lobe breccia'	MV026-1	0.004	40.2	1.0	22.0	41.4	1394	0.00	0.10	0.12	3.80	0.31	0.28	0.25	0.92	1587.3	2.3	1592.8	2.5	1597.0	3.5	3.52	0.29	0.11	1.05	0.00	12.73	-0.53	-0.51	0.99	
	MV026-1	0.047	31.2	1.0	6.1	116.3	395	0.01	0.10	0.22	4.22	0.41	0.32	0.31	0.85	1531.3	4.1	1677.7	3.3	1797.1	4.9	2.99	0.35	0.13	1.05	0.00	4.03	-0.54	-0.51	0.99	
	MV026-3	0.054	11.7	1.0	6.1	44.1	393	0.02	0.10	0.25	3.68	0.44	0.28	0.32	0.82	1542.1	4.8	1567.3	3.5	1586.0	4.5	3.45	0.58	0.13	2.85	0.00	11.51	-0.85	-0.85	1.00	
	MV026-4	3.601	173.0	0.6	0.4	11786	37	0.14	0.10	2.84	1127	3.04	78.10	1.68	0.39	1708.6	52.3	7136.5	30.8	28175.8	107.1	0.01	1.14	0.48	0.52	0.03	0.40	-0.01	0.03	-0.06	
	MV026-5	0.021	40.9	1.0	38.0	24.5	2399	0.01	0.10	0.11	3.78	0.33	0.28	0.29	0.95	1583.5	2.0	1587.7	2.7	1590.9	4.0	3.55	0.32	0.10	1.09	0.00	23.94	-0.47	-0.45	0.99	
	MV026-6B	0.582	0.3	0.4	0.2	35.1	28	0.17	0.10	6.26	3.25	6.89	0.23	3.16	0.42	1666.4	115.9	1469.8	53.5	1337.5	38.2	2.00	9.53	0.57	4.92	0.03	6.07	-1.00	-1.00	1.00	
	MV026-6	0.010	2.9	1.0	5.0	13.1	336	0.00	0.10	1.04	3.41	1.30	0.25	0.64	0.61	1581.0	19.5	1505.9	10.2	1453.0	8.4	3.83	2.10	0.12	11.95	0.00	56.03	-0.96	-0.96	1.00	
	MV026-7	0.012	7.0	1.0	12.8	12.4	828	0.00	0.10	1.12	3.80	1.37	0.28	0.81	0.58	1600.3	20.9	1593.5	11.0	1588.4	11.4	3.54	1.14	0.11	5.91	0.00	62.43	-0.75	-0.75	0.99	
LCD6 'deep bedded rock'	LCD6. 2	0.000	34.5	1.0	89.7	8.7	5806	0.00	0.10	0.10	3.81	1.23	0.28	1.22	1.00	1589.0	1.9	1593.9	9.9	1597.6	17.3	3.55	1.23	0.10	1.34	0.00	126.29	-0.14	-0.14	1.00	
	LCD6. 3	0.146	8.2	0.9	3.1	61.2	206	0.02	0.10	0.38	91.0	0.57	6.71	0.40	0.75	1593.4	7.1	4590.9	5.7	13164.1	22.2	0.14	0.77	0.16	2.97	0.00	7.67	-0.89	-0.88	1.00	
	LCD6. 4	0.014	8.2	1.0	13.3	14.0	862	0.00	0.10	0.22	3.71	0.31	0.28	0.15	0.75	1581.4	4.1	1573.1	2.5	1567.0	2.1	3.59	0.73	0.11	5.02	0.00	51.47	-0.99	-0.99	1.00	
	LCD6. 5	0.012	0.7	0.9	3.7	4.4	260	0.00	0.10	1.78	3.11	2.15	0.23	0.94	0.58	1584.8	33.3	1434.3	16.5	1335.1	11.3	4.35	7.50	0.10	58.22	0.00	0.00	-1.00	0.00	0.00	
	LCD6.1	20.074	0.7	0.9	11.3	9.5	123	6.42	0.10	2.10	0.21	2.52	0.02	1.08	0.57	1594.6	39.2	193.3	4.4	98.9	1.1	60.29	8.11	0.16	35.93	0.00	95.57	-1.00	-1.00	1.00	
MV027 'deep sedimentary rock	MV027-2	0.324	3.6	0.8	1.1	84.3	77	0.10	0.09	1.09	3.53	1.16	0.27	0.51	0.36	1495.6	20.6	1534.3	9.2	1562.6	7.1	2.92	1.35	0.27	2.97	0.01	4.59	-0.99	-0.98	1.00	
	MV027-4	0.109	0.5	0.9	3.0	3.8	214	0.03	0.09	2.52	4.02	2.99	0.34	1.14	0.57	1340.6	48.7	1638.3	24.3	1880.0	18.6	2.95	9.23	0.09	82.74	0.00	0.00	-1.00	0.00	0.00	
	MV027-5	0.168	0.9	0.8	1.5	14.8	105	0.05	0.09	1.76	4.68	2.08	0.37	0.84	0.56	1486.3	33.3	1763.2	17.4	2006.1	14.5	2.44	5.87	0.19	21.01	0.01	41.77	-1.00	-1.00	1.00	
	MV027-6	0.031	2.9	0.9	2.7	24.1	187	0.01	0.10	0.60	3.61	0.75	0.27	0.34	0.61	1571.6	11.3	1552.5	6.0	1538.5	4.6	3.45	1.96	0.16	8.65	0.00	22.59	-1.00	-0.99	1.00	
	MV027-7	0.057	5.1	0.9	3.2	36.0	216	0.02	0.10	0.43	4.01	0.52	0.30	0.22	0.59	1565.9	8.0	1636.2	4.2	1691.5	3.3	3.12	1.12	0.15	5.13	0.00	14.01	-1.00	-0.99	1.00	
LCD35 'volcanic breccia'	LCD35. 1	0.066	0.5	0.8	0.9	13.0	72	0.02	0.09	5.17	2.33	5.57	0.19	1.52	0.39	1432.5	98.6	1220.6	39.5	1104.3	15.4	4.53	10.20	0.22	29.04	0.01	48.39	-0.99	-1.00	0.99	
	LCD35. 2	0.159	0.9	0.7	0.7	29.2	60	0.05	0.10	2.00	4.56	2.28	0.33	1.00	0.48	1620.4	37.2	1742.5	19.0	1846.0	16.0	2.30	5.19	0.30	9.47	0.01	14.16	-1.00	-1.00	1.00	
	LCD35. 3	0.120	3.9	0.8	1.1	81.4	84	0.04	0.10	0.92	3.97	0.97	0.29	0.43	0.35	1602.4	17.1	1627.3	7.9	1646.7	6.3	2.81	1.27	0.26	2.98	0.01	4.87	-1.00	-0.99	1.00	
	LCD35. 4	0.136	1.1	0.7	0.7	36.4	60	0.04	0.10	1.78	1.80	2.01	0.13	0.93	0.46	1612.7	33.1	1046.6	13.1	796.9	6.9	5.77	4.09	0.31	7.31	0.02	10.85	-1.00	-0.99	1.00	
	LCD35. 5	49.637	0.3	0.8	14.9	6.7	81	15.62	0.10	4.88	0.88	5.86	0.06	2.58	0.57	1628.2	90.7	639.7	27.8	396.9	9.9	14.78	19.77	0.15	90.90	0.00	262.92	-1.00	-1.00	1.00	
MV101 'deposit center'	MV101-1	0.027	5.9	0.9	1.7	79.9	121	0.01	0.10	0.63	3.77	0.66	0.28	0.28	0.34	1573.3	11.7	1585.6	5.3	1594.9	4.0	3.11	0.68	0.21	2.05	0.01	3.96	-0.99	-0.98	1.00	
	MV101-2	0.015	9.2	1.0	6.2	33.7	404	0.00	0.10	0.26	3.77	0.37	0.28	0.23	0.73	1595.4	4.8	1586.0	3.0	1579.0	3.3	3.47	0.52	0.13	2.62	0.00	11.25	-0.92	-0.91	1.00	
	MV101-3	0.102	4.8	0.6	0.4	263	42	0.03	0.09	3.29	3.66	3.37	0.28	1.16	0.24	1493.4	62.2	1563.2	26.9	1615.5	16.5	2.18	0.70	0.42	0.61	0.02	0.71	-0.82	-0.89	0.99	
	MV101-4	0.027	25.3	0.9	2.2	261	153	0.01	0.10	0.47	3.73	0.54	0.28	0.26	0.48	1577.8	8.8	1577.0	4.3	1576.4	3.7	3.24	0.24	0.19	0.57	0.01	1.22	-0.72	-0.63	0.96	
7295BW 'SE-lobe breccia'	SE4	0.007	9.5	1.0	15.4	14.1	982	0.00	0.10	0.15	3.78	0.28	0.28	0.17	0.88	1593.2	2.8	1587.9	2.2	1583.9	2.3	3.54	0.52	0.11	3.39	0.00	30.23	-0.96	-0.96	1.00	
	SE1	0.018	0.5	0.9	2.4	5.1	171	0.01	0.10	1.12	0.25	2.35	0.02	1.35	0.96	1590.5	20.9	223.2	4.7	116.0	1.6	51.79	8.53	0.15	39.70	0.00	112.28	-1.00	-1.00	1.00	
	SE5	0.110	0.4	0.7	0.7	15.8	56	0.05	0.10	1.88	1.10	3.06	0.08	1.63	0.85	1606.6	35.1	754.6	16.3	500.4	7.8	9.14	8.15	0.33	13.24	0.02	18.66	-1.00	-1.00	1.00	
	SE2	0.039	1.0	0.9	2.3	9.9	158	0.01	0.10	1.04	3.76	1.59	0.28	0.78	0.83	1571.0	19.5	1584.0	12.8	1593.7	11.1	3.27	4.54	0.17	18.27	0.01	42.14	-1.00	-1.00	1.00	
	SE2B	0.039	0.3	0.9	2.1	3.5	153	0.01	0.10	1.72	3.64	3.73	0.27	2.09	0.98	1587.9	32.2	1559.3	29.7	1538.2	28.6	3.52	14.20	0.14	71.22	0.00	227.09	-1.00	-1.00	1.00	
	SE11	0.000	0.9	1.0	9.1	2.2	624	0.00	0.10	0.76	3.33	1.52	0.25	0.87	0.94	1586.4	14.3	1488.9	11.9	1421.5	11.1	4.05	5.65	0.10	42.60	0.00	2413.86	-1.00	-1.00	1.00	
	SE-8	0.020	0.2	0.8	1.5	2.7	117	0.01	0.10	3.12	3.48	6.72	0.26	3.73	0.98	1565.6	58.6	1522.3	53.0	1491.4	49.6	3.67	25.62	0.13	136.60	0.00	478.62	-1.00	-1.00	1.00	
	SE-9	0.023	1.7	0.9	3.8	10.3	257	0.01	0.10	0.42	3.75	0.77	0.28	0.41	0.93	1585.3	7.8	1583.1	6.2	1581.5	5.8	3.41	2.65	0.14	13.22	0.00	41.76	-1.00	-1.00	1.00	
	SE11	0.000	0.9	1.0	9.1	2.2	624	0.00	0.10	0.76	3.74	1.48	0.28	0.81	0.95	1586.4	14.3	1580.4	11.9	1575.9	11.3	3.60	5.64	0.10	42.60	0.00	2413.86	-1.00	-1.00	1.00	

$^{238}U/^{235}U$ = 137.818 (Hiess et al., 2012)

(a) z1, z2 etc. are labels for single zircon grains or fragments annealed and chemically abraded after Mattinson (2005).

(b) Model Th/U ratio iteratively calculated from the radiogenic $^{208}Pb/^{206}Pb$ ratio and $^{206}Pb/^{238}U$ age.

(c) Pb* and Pbc represent radiogenic and common Pb, respectively; mol % $^{206}Pb^*$ with respect to radiogenic, blank and initial common Pb.

(d) Measured ratio corrected for spike and fractionation only. Fractionation estimated at 0.18 +/- 0.03 %/a.m.u. for Daly analyses, based on analysis of NBS-981 and NBS-982.

(e) Corrected for fractionation, spike, and common Pb; up to 1 pg of common Pb was assumed to be procedural blank: $^{206}Pb/^{204}Pb$ = 18.042 ± 0.61%; 207Pb/204Pb = 15.537 ± 0.52%; $^{208}Pb/^{204}Pb$ = 37.686 ± 0.63% (all uncertainties 1-sigma). Excess over blank was assigned to initial common Pb, using the Stacey and Kramers (1975) two-stage Pb isotope evolution model at the nominal sample age.

(f) Errors are 2-sigma, propagated using the algorithms of Schmitz and Schoene (2007).

(g) Calculations are based on the decay constants of Jaffey et al. (1971). $^{206}Pb/^{238}U$ and $^{207}Pb/^{206}Pb$ ages corrected for initial disequilibrium in $^{230}Th/^{238}U$ using $^{Th/U}$[magma] = 3.

(h) Corrected for fractionation, spike, and blank Pb only.

(i) Nominal fraction weights estimated from photomicrographic grain dimensions, adjusted for partial dissolution during chemical abrasion.

(j) Nominal U and total Pb concentrations subject to uncertainty in photomicrographic estimation of weight and partial dissolution during chemical abrasion.

(k) Analyses exluded from concirdia diagram age calculations, with reasoning provided.

Sample (Radiogenic + Initial Pb) Isotope Ratios																		
$^{238}U/^{204}Pb$	% err	$^{206}Pb/^{204}Pb$	% err	corr. coef. 8/4-6/4	$^{235}U/^{204}Pb$	% err	$^{207}Pb/^{204}Pb$	% err	corr. coef. 5/4-7/4	$^{206}Pb/^{204}Pb$	% err	$^{207}Pb/^{204}Pb$	% err	corr. coef. 6/4-7/4	Wt. mg	U ppm	Pb ppm	Excluded from age calculations
(h)	(f)	(h)	(f)		(h)	(f)	(h)	(f)		(h)	(f)	(h)	(f)		(i)	(j)	(j)	(k)
202181	330	56578	330	1.0	1467	330	5574	329	1.0	56578	330.0	5574.2	329.2	1.00	0.01	368.46	97.81	
728892	1385	204681	1384	1.0	5289	1385	20128	1384	1.0	204681	1384.5	20128.3	1383.6	1.00	0.01	316.69	84.37	
47132	54	13277	54	1.0	342	54	1320	53	1.0	13277	53.7	1319.5	53.2	1.00	0.01	527.26	141.10	
8587	39	1942	39	1.0	62	39	205	36	1.0	1942	38.8	204.6	36.3	1.00	0.01	131.85	29.24	
23724	46	6671	46	1.0	172	46	670	45	1.0	6671	45.8	669.8	44.8	1.00	0.01	310.99	83.54	
22154	74	6305	73	1.0	161	74	631	72	1.0	6305	73.5	631.0	71.9	1.00	0.01	180.98	49.57	
84004	236	23444	236	1.0	610	236	2315	235	1.0	23444	236.2	2315.3	234.9	1.00	0.01	213.83	57.08	
25738	123	7323	122	1.0	187	123	732	120	1.0	7323	122.5	731.9	120.2	1.00	0.01	126.15	34.66	
6560	36	1837	36	1.0	48	36	187	33	1.0	1837	36.0	187.1	33.4	1.00	0.01	108.56	29.84	x Common Pb
234	9	91	7	1.0	2	9	23	3	1.0	91	7.4	22.6	3.0	1.00	0.01	15.12	8.93	
1927	8	633	8	1.0	14	8	76	6	1.0	633	7.7	76.2	6.3	1.00	0.01	146.28	49.42	
31780	816	8594	814	1.0	231	816	859	801	1.0	8594	814.1	858.8	801.3	1.00	0.01	23.44	6.38	
1926	3	579	3	1.0	14	3	71	2	1.0	579	2.9	70.7	2.3	1.00	0.01	389.96	120.86	
0	0	0	0	0.0	0	0	0	0	0.0	0	0.0	0.0	0.0	0.00	0.01	271.87	7.00	
5532	13	1571	13	1.0	40	13	168	12	1.0	1571	12.7	167.9	11.7	1.00	0.01	343.29	95.31	
1229	4	411	4	1.0	9	4	53	3	1.0	411	4.0	53.0	3.0	1.00	0.01	232.91	82.99	
1514	12	438	12	1.0	11	12	56	9	1.0	438	11.5	55.8	8.7	1.00	0.01	100.70	31.25	
0	1	37	0	0.3	0	1	18	1	0.2	37	0.4	17.5	0.7	0.64	0.01	5.31	1622.98	x high Th/U
10563	24	2972	24	1.0	77	24	305	23	1.0	2972	23.9	304.8	22.9	1.00	0.01	350.34	95.51	
59	16	30	6	1.0	0	16	17	1	0.9	30	6.1	16.8	1.2	0.93	0.01	3.03	4.28	
1993	58	520	56	1.0	14	58	65	44	1.0	520	56.0	64.6	44.1	1.00	0.01	27.45	7.88	
4735	63	1339	62	1.0	34	63	146	57	1.0	1339	62.4	146.1	56.6	1.00	0.01	59.99	17.12	
46602	126	13121	126	1.0	338	126	1302	125	1.0	13121	126.3	1302.1	125.0	1.00	0.01	294.34	79.00	
31	8	221	8	1.0	0	8	36	5	1.0	221	7.7	35.6	4.7	1.00	0.01	2.93	25.01	
4677	52	1303	51	1.0	34	52	141	46	1.0	1303	51.5	141.2	46.5	1.00	0.01	71.58	20.05	
0	0	0	0	0.0	0	0	0	0	0.0	0	0.0	0.0	0.0	0.00	0.01	7.40	2.05	
13940	104	231	96	1.0	101	104	37	60	1.0	231	95.6	36.6	59.7	1.00	0.01	107.40	11.75	x high Th/U
235	6	80	5	1.0	2	6	21	2	1.0	80	4.6	21.4	1.6	0.99	0.01	31.72	17.32	x high Th/U
0	0	0	0	0.0	0	0	0	0	0.0	0	0.0	0.0	0.0	0.00	0.01	3.55	1.54	x Pb loss
359	48	147	42	1.0	3	48	28	21	1.0	147	41.8	27.5	20.8	1.00	0.01	6.02	3.64	
787	25	228	23	1.0	6	25	36	14	1.0	228	22.6	36.0	14.0	1.00	0.01	25.61	8.98	
767	15	246	14	1.0	6	15	38	9	1.0	246	14.0	37.7	8.9	1.00	0.01	40.50	15.23	
471	59	104	48	1.0	3	59	23	20	1.0	104	48.4	23.3	19.9	0.98	0.01	6.42	2.45	
155	19	68	14	1.0	1	19	21	5	1.0	68	14.2	20.5	4.7	1.00	0.01	6.42	5.02	
247	6	88	5	1.0	2	6	22	2	1.0	88	4.9	22.5	1.9	0.99	0.01	32.10	17.25	
382	15	66	11	1.0	3	15	20	4	1.0	66	10.8	20.4	3.6	0.99	0.01	20.48	6.29	
3823	283	259	263	1.0	28	283	40	172	1.0	259	262.9	39.7	172.1	1.00	0.01	10.80	10.60	x high Th/U
389	5	125	4	1.0	3	5	26	2	1.0	125	4.0	26.0	1.9	1.00	0.01	50.60	21.49	
1554	12	447	11	1.0	11	12	58	9	1.0	447	11.2	57.8	8.6	1.00	0.01	79.75	24.35	
92	1	42	1	1.0	1	1	18	0	1.0	42	0.7	17.8	0.1	0.84	0.01	40.36	37.35	
500	1	155	1	1.0	4	1	29	1	0.9	155	1.2	28.9	0.7	0.97	0.01	218.82	83.66	
3998	31	1130	30	1.0	29	31	125	27	1.0						0.10	8.21	2.30	
13588	121	262	112	1.0	99	121	40	73	1.0						0.10	7.10	0.17	x Pb loss
556	27	61	19	1.0	4	27	20	5	1.0						0.10	1.31	0.26	x high Th/U
623	47	191	42	1.0	5	47	32	24	1.0						0.10	0.84	0.32	
1108	241	314	227	1.0	8	241	45	156	1.0			N/A			0.10	0.29	0.11	
32145	2419	7946	2414	1.0	233	2419	793	2371	1.0						0.10	0.84	0.22	
1338	504	364	479	1.0	10	504	49	342	1.0						0.10	0.17	0.07	
1059	44	311	42	1.0	8	44	44	29	1.0						0.10	1.51	0.50	
28636	2419	7946	2414	1.0	208	2419	793	2371	1.0						0.10	0.75	0.22	

ELECTRONIC APPENDIX A TABLE A2 FOR CHAPTER 4

Zircon U-Th-Pb isotopic data (British Geological Survey)

Sample	Fraction	Composition					Isotopic Ratios								Isotopic Dates (Ma)								
		mass U (pg)	Th/U	Pb* (pg)	Pbc (pg)	Pb*/Pbc	$^{206}Pb/^{204}Pb$	$^{208}Pb/^{206}Pb$	$^{238}Pb/^{235}U$	±2σ %	$^{207}Pb/^{235}U$	±2σ %	$^{207}Pb/^{206}Pb$	±2σ %	$^{206}Pb/^{238}U$	±2σ abs	$^{208}Pb/^{232}U$	±2σ abs	$^{207}Pb/^{235}U$	±2σ abs	$^{207}Pb/^{206}Pb$	±2σ abs	Corr. coef.	% disc.
			(a)	(b)	(c)	(d)	(e)	(f)	(f)		(f)		(f)		(g)		(h)		(h)		(h)			(i)
LCD13 (RDG)	z1	821	0.58	230	0.30	844	48363	0.17	0.28	0.06	3.77	0.10	0.098	0.05	1583.7	0.9	1583.6	0.9	1587.4	0.8	1592.5	1.1	0.9	0.6
	z2	589	0.71	186	0.72	259	14461	0.21	0.28	0.07	3.81	0.11	0.099	0.06	1593.2	1.0	1593.2	1.0	1594.3	0.9	1595.9	1.2	0.8	0.2
	z3	507	0.63	156	2.02	77	4398	0.19	0.28	0.07	3.78	0.14	0.098	0.09	1585.6	1.0	1585.5	1.0	1589.2	1.2	1594.2	1.8	0.8	0.5
	z4	1661	0.62	485	0.87	556	31671	0.18	0.27	0.11	3.57	0.14	0.097	0.05	1517.6	1.4	1517.5	1.4	1542.0	1.1	1575.7	1.1	0.9	3.7
	z5	1646	0.57	492	0.45	1094	62960	0.17	0.27	0.09	3.71	0.13	0.098	0.05	1563.3	1.2	1563.2	1.2	1573.6	1.0	1587.6	1.1	0.9	1.5
	z6	490	0.65	149	0.42	352	19892	0.19	0.27	0.12	3.70	0.18	0.098	0.11	1562.2	1.7	1562.1	1.7	1572.1	1.4	1585.4	2.1	0.8	1.5
LCD1 (RDG)	z1	36	0.72	11	0.40	28	1586	0.21	0.28	0.12	3.81	0.26	0.098	0.22	1596.1	1.6	1596.0	1.6	1594.9	2.1	1593.4	4.1	0.6	-0.2
	z2	119	0.79	38	0.44	87	4774	0.23	0.28	0.10	3.80	0.17	0.098	0.12	1592.3	1.4	1592.2	1.4	1593.0	1.3	1594.1	2.4	0.6	0.1
	z3	85	0.82	27	1.09	25	1378	0.24	0.28	0.08	3.81	0.25	0.098	0.22	1595.8	1.1	1595.7	1.1	1594.8	2.0	1593.6	4.2	0.5	-0.1
	z4	174	0.75	55	0.33	170	9401	0.22	0.28	0.05	3.80	0.11	0.098	0.06	1592.9	0.8	1592.9	0.8	1593.7	0.9	1594.8	1.3	0.8	0.1
	z5	112	0.81	36	0.28	128	7016	0.24	0.28	0.07	3.81	0.16	0.099	0.11	1595.5	1.0	1595.4	1.0	1595.8	1.3	1596.2	2.1	0.8	0.0
	z6	82	0.72	26	0.15	168	9355	0.21	0.28	0.07	3.81	0.11	0.099	0.06	1594.9	1.0	1594.8	1.0	1595.3	0.9	1595.8	1.3	0.8	0.1
LCD30A (GRV)	z1	164	0.82	53	0.29	186	10112	0.24	0.28	0.07	3.81	0.12	0.099	0.07	1593.9	1.0	1595.9	1.0	1594.5	1.0	1595.4	1.4	0.8	0.1
	z2	100	0.58	31	0.40	77	4452	0.17	0.28	0.09	3.81	0.22	0.098	0.17	1595.1	1.3	1595.1	1.3	1594.3	1.7	1593.3	3.2	0.6	-0.1
	z3	162	0.68	28	0.27	104	5809	0.21	0.15	0.06	2.10	0.12	0.098	0.08	927.4	0.5	927.3	0.5	1148.8	0.9	1594.9	1.6	0.8	41.9
	z4	429	0.77	136	3.60	38	2094	0.22	0.28	0.08	3.77	0.19	0.098	0.15	1583.0	1.1	1582.9	1.1	1587.4	1.5	1593.3	2.9	0.6	0.7
	z5	88	0.71	28	0.25	112	6230	0.21	0.28	0.12	3.81	0.21	0.099	0.14	1593.7	1.8	1595.7	1.8	1594.5	1.7	1595.5	2.6	0.8	0.1
	z6	412	0.75	131	0.35	371	20503	0.22	0.28	0.08	3.80	0.14	0.098	0.08	1592.7	1.1	1592.6	1.1	1593.3	1.1	1594.2	1.6	0.9	0.1
	z7	119	0.74	38	0.41	91	5067	0.22	0.28	0.12	3.80	0.26	0.098	0.21	1593.0	1.7	1592.9	1.7	1592.6	2.1	1592.1	3.9	0.6	-0.1
	z8	51	0.76	16	0.33	49	2741	0.22	0.28	0.09	3.81	0.20	0.098	0.15	1594.1	1.3	1594.1	1.3	1594.2	1.6	1594.3	2.9	0.7	0.0

$^{238}U/^{235}U$ = 137.818 (Hess et al., 2012)

(a) Th contents calculated from radiogenic ^{208}Pb and the ^{230}Th-corrected $^{206}Pb/^{238}U$ date of the sample, assuming concordance between the U-Pb and Th-Pb systems.
(b) Total mass of radiogenic Pb.
(c) Total mass of common Pb.
(d) Ratio of radiogenic Pb (including ^{208}Pb) to common Pb.
(e) Measured ratio corrected for fractionation and spike contribution only.
(f) Measured ratios corrected for fractionation, tracer and blank.
(g) Corrected for initial Th/U disequilibrium using radiogenic ^{208}Pb and $^{Th/U}$-[magma] = 3.50000.
(h) Isotopic dates calculated using the decay constants λ^{238} = 1.55125E-10 and λ^{235} = 9.84858E-10 (Jaffey et al., 1971).
(i) % discordance = 100 - (100 * ($^{206}Pb/^{238}U$ date) / ($^{207}Pb/^{206}Pb$ date))

Zircon U-Th-Pb isotopic data (Boise)

Sample	Fraction	Composition						Isotopic Ratios								Isotopic Dates (Ma)						
		Th/U	$^{206}Pb^*$ x10^{-13} mol	mol % $^{206}Pb^*$	Pb^*/Pb_c	Pb_c (pg)	$^{206}Pb/^{204}Pb$	$^{208}Pb/^{206}Pb$	$^{207}Pb/^{206}Pb$	± 2σ %	$^{207}Pb/^{235}U$	± 2σ %	$^{206}Pb/^{238}U$	± 2σ %	corr. coef.	$^{207}Pb/^{206}Pb$	±2σ abs	$^{207}Pb/^{235}U$	±2σ abs	$^{206}Pb/^{238}U$	±2σ abs	% disc.
	(a)	(b)	(c)	(c)	(c)	(c)	(d)	(e)	(e)	(f)	(e)	(f)	(e)	(f)		(g)	(f)	(g)	(f)	(g)	(f)	(h)
LCD11 (RDG)	z4b	1.30	0.91	99.84%	226	0.12	11055	0.38	0.10	0.08	3.80	0.18	0.28	0.13	0.92	1596.6	1.5	1593.8	1.4	1591.6	1.8	0.3
	z4a	1.17	0.70	99.81%	191	0.11	9593	0.34	0.10	0.09	3.80	0.17	0.28	0.10	0.90	1595.2	1.6	1593.2	1.3	1591.6	1.5	0.2
	z5	**0.57**	**3.18**	**99.95%**	**675**	**0.12**	**38717**	**0.17**	**0.10**	**0.02**	**3.79**	**0.05**	**0.28**	**0.04**	**0.93**	**1594.3**	**0.4**	**1591.5**	**0.4**	**1589.4**	**0.5**	**0.3**
	z7	**0.72**	**4.75**	**99.96%**	**802**	**0.16**	**44474**	**0.21**	**0.10**	**0.02**	**3.80**	**0.05**	**0.28**	**0.03**	**0.93**	**1594.1**	**0.4**	**1592.4**	**0.4**	**1591.2**	**0.5**	**0.2**
	z3	0.40	4.40	99.95%	606	0.18	36176	0.12	0.10	0.07	3.77	0.13	0.28	0.07	0.95	1593.5	1.2	1587.0	1.0	1582.1	1.0	0.7
	z1	0.76	11.05	99.99%	2242	0.13	123043	0.22	0.10	0.06	3.80	0.13	0.28	0.07	0.97	1593.3	1.1	1593.6	1.0	1593.8	1.0	0.0
LCD12 (RDG)	z5	0.70	7.33	99.97%	1275	0.15	70914	0.21	0.10	0.06	3.81	0.13	0.28	0.07	0.97	1595.2	1.1	1594.2	1.0	1593.3	1.0	0.1
	z14	**0.69**	**6.32**	**99.98%**	**1831**	**0.09**	**102186**	**0.20**	**0.10**	**0.02**	**3.80**	**0.04**	**0.28**	**0.03**	**0.92**	**1594.0**	**0.4**	**1593.1**	**0.4**	**1592.4**	**0.4**	**0.1**
	z13	**0.84**	**3.43**	**99.96%**	**879**	**0.11**	**47362**	**0.25**	**0.10**	**0.02**	**3.79**	**0.06**	**0.28**	**0.04**	**0.93**	**1593.7**	**0.4**	**1590.0**	**0.4**	**1587.2**	**0.6**	**0.4**
	z8	**0.53**	**4.28**	**99.97%**	**927**	**0.12**	**53625**	**0.16**	**0.10**	**0.02**	**3.78**	**0.04**	**0.28**	**0.03**	**0.93**	**1592.6**	**0.4**	**1588.4**	**0.4**	**1585.2**	**0.4**	**0.5**
	z10	**0.87**	**8.25**	**99.98%**	**1978**	**0.12**	**106038**	**0.26**	**0.10**	**0.02**	**3.79**	**0.04**	**0.28**	**0.03**	**0.94**	**1592.0**	**0.4**	**1591.2**	**0.3**	**1590.6**	**0.4**	**0.1**
	z3	0.74	5.44	99.98%	1312	0.11	72379	0.22	0.10	0.06	3.80	0.13	0.28	0.07	0.97	1591.7	1.2	1592.2	1.0	1592.6	1.0	-0.1
	z9	**0.61**	**7.63**	**99.98%**	**1648**	**0.12**	**93541**	**0.18**	**0.10**	**0.02**	**3.79**	**0.04**	**0.28**	**0.03**	**0.94**	**1591.6**	**0.3**	**1590.5**	**0.3**	**1589.7**	**0.4**	**0.1**
	z4	0.72	5.78	99.97%	1279	0.12	70806	0.21	0.10	0.06	3.78	0.13	0.28	0.07	0.97	1591.2	1.2	1588.7	1.0	1586.9	1.0	0.3
	z2	0.98	7.00	99.98%	1527	0.13	79898	0.29	0.10	0.06	3.78	0.13	0.28	0.07	0.97	1590.9	1.2	1588.7	1.0	1587.1	1.0	0.2
	z12	**0.59**	**7.79**	**99.97%**	**938**	**0.22**	**53524**	**0.17**	**0.10**	**0.02**	**3.72**	**0.04**	**0.27**	**0.03**	**0.93**	**1587.6**	**0.4**	**1575.0**	**0.4**	**1565.7**	**0.4**	**1.4**
	z7	**0.61**	**9.95**	**99.97%**	**1021**	**0.26**	**57959**	**0.18**	**0.10**	**0.02**	**3.65**	**0.04**	**0.27**	**0.03**	**0.94**	**1583.4**	**0.4**	**1560.2**	**0.3**	**1543.2**	**0.4**	**2.5**

$^{207}Pb/^{206}Pb$ dates are younger by 0.84 Ma when using the $^{238}U/^{235}U$ of 137.818 (Hiess et al., 2012)

(a) z1, z2, etc. are labels for analyses composed of single zircon grains that were annealed and chemically abraded (Mattinson, 2005). Lables z4a and z4b are fragments from same grain.
Labels in bold denote analyses spiked with ET2535 tracer solution. Others were spiked with BSU1B tracer solution.

(b) Model Th/U ratio calculated from radiogenic $^{208}Pb/^{206}Pb$ ratio and $^{207}Pb/^{235}U$ date.

(c) Pb* and Pbc are radiogenic and common Pb, respectively. mol % $^{206}Pb^*$ is with respect to radiogenic and blank Pb.

(d) Measured ratio corrected for spike and fractionation only. Fractionation correction is 0.16 ± 0.03 (1 sigma) %/amu (atomic mass unit) for single-collector Daly analyses, based on analysis of EARTHTIME 202Pb-205Pb tracer solution.

(e) Corrected for fractionation and spike. Common Pb in zircon analyses is assigned to procedural blank with composition of 206Pb/204Pb = 18.04 ± 0.61%; 207Pb/204Pb = 15.54 ± 0.52%; 208Pb/204Pb = 37.69 ± 0.63% (1 sigma). 206Pb/238U and 207Pb/206Pb ratios corrected for initial disequilibrium in 230Th/238U using a D(Th/U) of 0.20 ± 0.05 (1 sigma).

(f) Errors are 2 sigma, propagated using algorithms of Schmitz and Schoene (2007) and Crowley et al. (2007).

(g) Calculations based on the decay constants of Jaffey et al. (1971). 206Pb/238U and 207Pb/206Pb dates corrected for initial disequilibrium in 230Th/238U using a D(Th/U) of 0.20 ± 0.05 (1 sigma).

(h) % discordance = (1 - (206Pb/238U date / 207Pb/206Pb date)) * 100.

APPENDIX A FIGURE A1: EXTENDED ZIRCON CL IMAGES FOR CHAPTER C

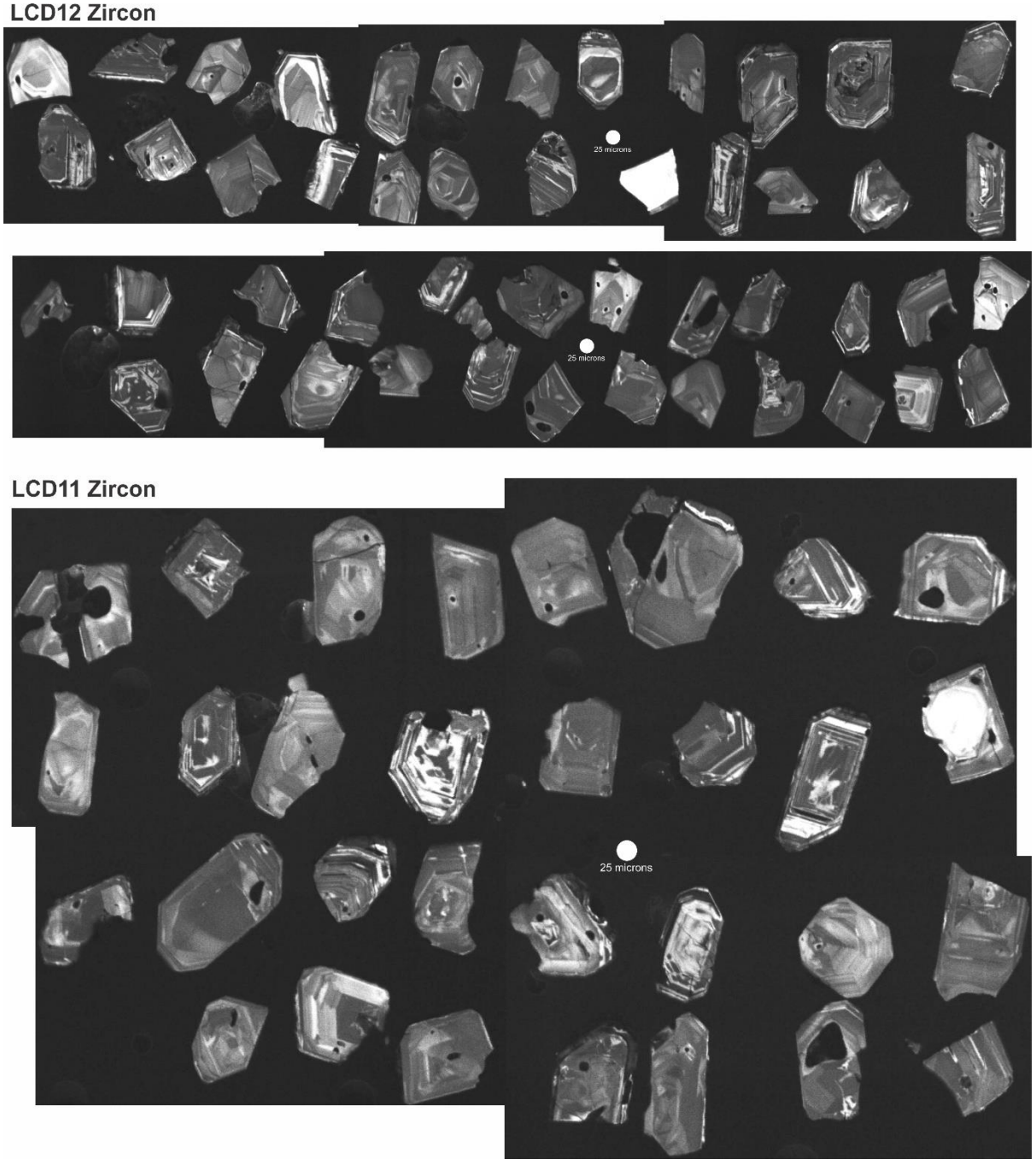


Figure A1. Extended zircon CL images taken at Boise.

APPENDIX A FIGURE B1: PHOTOGRAPH OF HAND SPECIMEN FOR CHAPTER C



Figure A2. (A) GRV breccia sampled from drillhole RD647. The isolated clast which was separated for zircon (CA-)ID-TIMS at the BGS is marked.

APPENDIX B: MASS BALANCE CALCULATIONS FOR CHAPTER C

APPENDIX B

Mass-balance calculations

Simplified mass-balance calculations were conducted assuming an initial granitic melt source at 800 °C and at 2 kbar (~8 km depth) to assess the feasibility of fluid exsolution from this source as the cause of Cu mineralisation comparable to that of the Olympic Dam copper resource. Initial melt density was estimated using data presented in Lesher and Spera (2015) and average granite composition from assay data of fresh RDG (drillhole RD2488, with K_2O/Na_2O ratios (by wt.%/wt.%) <1.6) and initial H_2O content ($C_{H_2O}^{m_0}$) of 2.5 wt.% (i.e., ρ_{m_0}= 2,320 kg/m^3). Assumed H_2O content of the initial granitic melt is within the lower range of typical granitic melts (Clemens, 1984; Holtz et al., 2001).

A melt volume (V_{m_0}) of 450 km^3 (15x10x3) is assumed, which can be considered a realistic estimate for the RDG volume. A total H_2O exsolution percentage from the initial granitic melt ($E_{m_o}^{H2O}$) of 95 % can be used, since the remaining 5% H_2O (0.15 wt.% of the 2.5 wt.% total water) can supply the necessary water to crystallize the ~5 wt.% biotite+amphibole in RDG (Ehrig et al., 2012), if this is calculated using average H_2O concentrations for the two minerals given in Cline and Bodnar (1991). The weighted average Cu content for the fresh RDG in the same drillhole is ~67 ppm Cu, with a median of 21 ppm. We assume that these values encompass the possible range of copper content in the parent RDG melt ($C_{Cu}^{m_0}$). Experimental studies have shown wide variation of copper partitioning coefficients between granitic melts and coexisting aqueous fluids ($D_{Cu}^{f/m}$) dependant upon Cl concentration among other variables (Keppler and Wyllie, 1991; Bai and Koster van Groos, 1999); $D_{Cu}^{f/m}$ can reach values >80. Different scenarios were calculated to test conditions that could reproduce the ~79.45 Mt Cu mineralisation reported for the Olympic Dam resource (10,892 Mt @ 0.73 wt% Cu; BHP, 2019) by varying:

(i) copper contents of the initial melt ($C_{Cu}^{m_0}$: 20, 60 and 120 ppm Cu), and

(ii) copper partitioning coefficient between granitic melt (RDG) and fluid ($D_{Cu}^{f/m}$: 2, 13 and 80).

The concentration of Cu in the exsolved fluid (C_{Cu}^{f}) can be calculated from the partitioning coefficient $D_{Cu}^{f/m}$ using:

(1) $D_{Cu}^{f/m} = C_{Cu}^{f}/C_{Cu}^{m}$, where C_{Cu}^{m} the concentration of Cu in RDG, considered as a 'residual melt' relative to the initial melt.

The mass fraction of the residual melt (RDG; M_m) and exsolved fluid (M_f) are calculated as:

(2) $M_m = 1 - C_{H_2O}^{m_0} \cdot E_{m_0}$,

(3) $M_f = C_{H_2O}^{m_0} \cdot E_{m_0}$.

Then, the concentration of Cu in RDG (C_{Cu}^{m}) can be calculated as:

(4) $C_{Cu}^{m} = (C_{Cu}^{m_0})/(M_m + M_f \cdot D_{Cu}^{f/m})$.

Knowing C_{Cu}^{m}, we can obtain the values of C_{Cu}^{f} for the assumed $D_{Cu}^{f/m}$ using equation (1).

The mass of deposited copper (Cu_D) can be then expressed as:

(5) $Cu_D = V_{m_0} \cdot \rho_{m_0} \cdot M_f \cdot C_{Cu}^f$.

This formula gives however a simplified estimation of the metal extracted from the melt by fluid since it ignores the effects of Cu behaviour during melt crystallisation prior to fluid saturation and exsolution (Cline and Bodnar, 1991). Nonetheless, the efficiency of Cu stripping by the fluid from the initial melt (x) calculated as a ratio between Cu_D and mass of Cu in parental melt gives values comparable (~70) as those reported in Cline and Bodnar (1991) for the porphyry Cu deposit at Yerington (Nevada, USA) when using smaller $D_{Cu}^{f/m}$ than used for the fit here (9.1 as opposed to 80).

Table B1. Summary of estimated Cu_D for Olympic Dam

V_{m_0}	ρ_{m_0}	$C_{H_2O}^{m_0}$	$C_{Cu}^{m_0}$	$E_{m_0}^{H_2O}$	$D_{Cu}^{f/m}$	M_m	M_f	C_{Cu}^m	C_{Cu}^f	Cu_D	Cu resource Olympic Dam	x
km^3	kg/m^3	wt.%	ppm	%	-	%	%	ppm	ppm	Mt	Mt	%
450	2,320	2.5	20	95	2	97.625	2.375	19.5	39.1	1.0	79.45	5
450	2,320	2.5	60	95	2	97.625	2.375	58.6	117.2	2.9	79.45	5
450	2,320	2.5	20	95	13	97.625	2.375	15.6	202.3	5.0	79.45	24
450	2,320	2.5	120	95	2	97.625	2.375	117.2	234.4	5.8	79.45	5
450	2,320	2.5	20	95	80	97.625	2.375	7.0	556.3	13.8	79.45	66
450	2,320	2.5	60	95	13	97.625	2.375	46.7	607.0	15.1	79.45	24
450	2,320	2.5	120	95	13	97.625	2.375	93.4	1214.0	30.1	79.45	24
450	2,320	2.5	60	95	80	97.625	2.375	20.9	1668.8	41.4	79.45	66
450	2,320	2.5	120	95	80	97.625	2.375	41.7	3337.7	82.8	79.45	66

Parameters and their calculations according to equations (1)-(5) above.
Best fit is highlighted in grey. Input variables in blue.

References:

Bai, T.., and Koster van Groos, A.., 1999. The distribution of Na, K, Rb, Sr, Al, Ge, Cu, W, Mo, La, and Ce between granitic melts and coexisting aqueous fluids. Geochimica et Cosmochimica Acta 63, 1117–1131. https://doi.org/10.1016/S0016-7037(98)00284-1

BHP, 2019. BHP Annual Report 2019 316 pp, https://www.bhp.com/investor-centre/annual-report-2019/.

Clemens, J.D., 1984. Water contents of silicic to intermediate magmas. Lithos 17, 273–287. https://doi.org/10.1016/0024-4937(84)90025-2

Cline, J.S., and Bodnar, R.J., 1991, Can economic porphyry copper mineralization be generated by a typical calc-alkaline melt?: Journal of Geophysical Research, v. 96, p. 8113.

Ehrig, K., McPhie, J., and Kamenetsky, V., 2012, Geology and mineralogical zonation of the Olympic Dam iron oxide Cu-U-Au-Ag deposit, South Australia: Society of Economic Geologists, Special Publication, v. 16, p. 237-268.

Holtz, F., Johannes, W., Tamic, N., and Behrens, H., 2001. Maximum and minimum water contents of granitic melts generated in the crust: a reevaluation and implications. Lithos 56, 1–14. https://doi.org/10.1016/S0024-4937(00)00056-6

Keppler, H., and Wyllie, P.J., 1991. Partitioning of Cu, Sn, Mo, W, U, and Th between melt and aqueous fluid in the systems haplogranite-H2O-HCl and haplogranite-H2O-HF. Contrib. to Mineral. Petrol. 109, 139–150. https://doi.org/10.1007/BF00306474

Lesher, C.E., and Spera, F.J., 2015. Thermodynamic and Transport Properties of Silicate Melts and Magma, in: The Encyclopedia of Volcanoes. Elsevier, pp. 113–141. https://doi.org/10.1016/B978-0-12-385938-9.00005-5

SUPPLEMENTARY MATERIAL D

FOR CHAPTER 5 – HEMATITE GEOCHEMISTRY AND GEOCHRONOLOGY RESOLVE GENETIC AND TEMPORAL LINKS AMONG IRON-OXIDE COPPER GOLD SYSTEMS, OLYMPIC DAM DISTRICT, SOUTH AUSTRALIA

APPENDIX A: LA-ICP-MS U-PB HEMATITE DATA

APPENDIX B: HEMATITE LA-ICP-MS TRACE ELEMENT DATA AND DOWNHOLE ABLATION PROFILES

APPENDIX C: MAGNETITE LA-ICP-MS TRACE ELEMENT DATA

ELECTRONIC APPENDIX A FOR CHAPTER 5

LA-ICP-MS U-Pb data for hematite.

		Isotope Ratios									
Prospect/sample ID	**Analysis ID**	**$^{207}Pb/^{235}U$**	**2σ abs**	**2σ sys***	**$^{206}Pb/^{238}U$**	**2σ abs**	**2σ sys**	**Corr. Coef.**	**$^{207}Pb/^{206}Pb$**	**2σ abs**	**2σ sys**
Wirrda Well/MV070	MV070 HmZ - 1	3.66500	0.067	0.100	0.26460	0.004	0.005	0.25	0.10040	0.002	0.002
	MV070 HmZ - 2	3.78200	0.047	0.090	0.26950	0.003	0.004	0.86	0.10022	0.000	0.001
	MV070 HmZ - 3	4.11100	0.041	0.092	0.29900	0.003	0.004	0.19	0.09953	0.001	0.001
	MV070 HmZ - 4	3.93300	0.053	0.095	0.28560	0.004	0.005	0.68	0.09920	0.001	0.001
	MV070 HmZ - 5	3.74600	0.041	0.086	0.27170	0.003	0.004	0.88	0.09913	0.000	0.001
	MV070 HmZ - 6	3.76800	0.045	0.089	0.27530	0.004	0.005	0.88	0.09906	0.001	0.001
	MV070 HmZ - 7	3.73900	0.048	0.089	0.27190	0.003	0.005	0.83	0.09894	0.001	0.001
	MV070 HmZ - 8	4.02000	0.094	0.120	0.29610	0.005	0.006	0.92	0.09870	0.001	0.002
	MV070 HmZ - 9	3.76600	0.072	0.100	0.27360	0.005	0.006	0.45	0.09850	0.001	0.002
	MV070 HmZ - 10	3.65900	0.051	0.090	0.26600	0.004	0.005	0.66	0.09853	0.001	0.001
	MV070 HmZ - 11	3.40000	0.100	0.120	0.24970	0.007	0.008	0.98	0.09841	0.001	0.001
	MV070 HmZ - 12	4.00500	0.081	0.110	0.29180	0.005	0.006	0.62	0.09850	0.002	0.002
	MV070 HmZ - 13	4.05300	0.068	0.110	0.29840	0.004	0.006	0.42	0.09850	0.001	0.002
	MV070 HmZ - 14	3.78800	0.089	0.120	0.27450	0.005	0.006	0.61	0.09860	0.002	0.002
	MV070 HmZ - 15	3.70600	0.052	0.091	0.26890	0.004	0.005	0.82	0.09843	0.001	0.001
	MV070 HmZ - 16	3.75900	0.046	0.089	0.27350	0.003	0.005	0.83	0.09839	0.001	0.001
	MV070 HmZ - 17	3.75500	0.044	0.088	0.27540	0.003	0.005	0.47	0.09818	0.001	0.001
	MV070 HmZ - 18	3.56400	0.036	0.080	0.25990	0.002	0.004	0.50	0.09845	0.001	0.001

U/Pb Dates														
$^{207}Pb/^{235}U$	**2σ abs**	**2σ sys**	**$^{206}Pb/^{238}U$**	**2σ abs**	**2σ sys**	**$^{207}Pb/^{206}Pb$**	**2σ sys**	**Grain #**	**$^{206}Pb/^{204}Pb$**	**U ppm**	**Th ppm**	**Pb ppm****	**Discrodancy (%)**	**included**
1563.8	14	21	1513.3	20	26	1631.5	38		1.20E+05	181	1	26	-10	
1588.9	10	19	1538.3	15	23	1628.2	21	1	4.60E+05	1416	17	223	6	om weighted av
1656.5	8.1	18	1686.3	13	22	1615.3	25		7.30E+05	1663	28	312	-4	
1620.5	11	20	1619.5	18	25	1609.1	25	2	5.50E+05	2074	24	175	0	
1581.3	8.7	18	1549.4	15	22	1607.8	21	3	1.11E+06	1590	27	211	4	
1586.0	9.7	19	1567.6	19	25	1606.5	22		1.11E+06	2110	24	179	2	
1579.8	10	19	1550.4	17	24	1604.2	22	4	1.24E+06	1860	28	212	4	
1638.2	19	25	1671.9	23	29	1599.7	28		1.30E+06	1923	24	192	-4	
1585.5	15	22	1559.0	25	30	1595.9	32		4.20E+06	559	17	133	2	
1562.5	11	19	1520.5	19	25	1596.5	26	5	2.90E+06	537	7	57	5	
1504.4	24	29	1436.9	37	40	1594.2	23		3.20E+06	3570	1	19	10	Yes
1635.2	16	23	1650.5	25	30	1595.9	34	6	2.50E+06	499	4	36	-3	
1644.9	14	21	1683.4	20	27	1595.9	32	7	9.30E+06	1689	22	214	-5	
1590.2	18	24	1563.6	27	32	1597.8	38		8.90E+06	233	2	20	1	
1572.7	11	20	1535.2	18	24	1594.6	23	8	2.70E+05	529	9	77	5	
1584.0	9.7	19	1558.5	16	23	1593.8	21		1.26E+06	1714	25	193	3	
1583.2	9.2	18	1568.2	15	23	1589.8	25	9	2.80E+05	727	14	117	2	
1541.6	8	18	1489.3	9.7	19	1595.0	21	10	7.90E+05	1055	11	89	6	

		Isotope Ratios									
Prospect/sample ID	**Analysis #**	**$^{207}Pb/^{235}U$**	**2σ abs**	**2σ sys**	**$^{206}Pb/^{238}U$**	**2σ abs**	**2σ sys**	**Corr. Coef.**	**$^{207}Pb/^{206}Pb$**	**2σ abs**	**2σ sys**
Acropolis/ACR2.3	ACR2.3 Hm - 1	3.73800	0.036	0.042	0.27530	0.003	0.003	0.809	0.09855	0.001	0.001
	ACR2.3 Hm - 2	4.04600	0.059	0.063	0.29520	0.003	0.003	0.476	0.09850	0.001	0.002
	ACR2.3 Hm - 3	3.80400	0.044	0.049	0.28140	0.003	0.003	0.815	0.09847	0.001	0.001
	ACR2.3 Hm - 4	3.71800	0.050	0.054	0.27370	0.004	0.004	0.864	0.09842	0.000	0.001
	ACR2.3 Hm - 5	4.22100	0.069	0.072	0.31450	0.004	0.004	0.245	0.09840	0.001	0.002
	ACR2.3 Hm - 6	3.67100	0.040	0.044	0.27150	0.003	0.003	0.914	0.09825	0.000	0.001
	ACR2.3 Hm - 7	3.65700	0.044	0.048	0.27150	0.003	0.003	0.886	0.09822	0.000	0.001
	ACR2.3 Hm - 8	4.00300	0.046	0.050	0.29380	0.003	0.003	0.693	0.09821	0.001	0.001
	ACR2.3 Hm - 9	3.73300	0.050	0.053	0.27680	0.004	0.004	0.947	0.09807	0.001	0.001
	ACR2.3 Hm - 10	3.74600	0.043	0.048	0.27740	0.003	0.003	0.886	0.09785	0.000	0.001
	ACR2.3 Hm - 11	3.69300	0.044	0.048	0.27200	0.003	0.004	0.899	0.09781	0.000	0.001
	ACR2.3 Hm - 12	3.85100	0.084	0.087	0.28360	0.004	0.004	0.355	0.09790	0.002	0.002
	ACR2.3 Hm - 13	4.32000	0.140	0.140	0.30900	0.007	0.007	0.293	0.10010	0.003	0.003
	ACR2.3 Hm - 14	4.46000	0.140	0.150	0.32750	0.007	0.007	0.702	0.09760	0.001	0.002
	ACR2.3 Hm - 15	13.6000	1.900	1.900	0.42500	0.036	0.036	0.484	0.20700	0.024	0.024
	ACR2.3 Hm - 16	5.16000	0.170	0.170	0.31470	0.008	0.008	0.640	0.12530	0.004	0.004
	ACR2.3 Hm - 17	5.68000	0.370	0.370	0.33100	0.014	0.014	0.406	0.12020	0.005	0.005
	ACR2.3 Hm - 18	6.26000	0.420	0.420	0.37100	0.015	0.015	0.320	0.12040	0.008	0.008
	ACR2.3 Hm - 19	4.75000	0.190	0.190	0.32700	0.007	0.007	0.683	0.10580	0.003	0.003
	ACR2.3 Hm - 20	5.32000	0.510	0.510	0.38200	0.018	0.018	0.182	0.10200	0.009	0.009
	ACR2.3 Hm - 21	4.27000	0.150	0.150	0.30000	0.006	0.006	0.062	0.10330	0.003	0.003
	ACR2.3 Hm - 22	5.69000	0.790	0.790	0.36100	0.032	0.033	0.210	0.11200	0.016	0.016
	ACR2.3 Hm - 23	5.61000	0.840	0.840	0.38100	0.052	0.052	0.855	0.09860	0.006	0.006
	ACR2.3 Hm - 24	4.15000	0.170	0.170	0.30700	0.005	0.006	0.257	0.09860	0.004	0.004
	ACR2.3 Hm - 25	3.96000	0.150	0.150	0.30900	0.012	0.012	0.015	0.09570	0.004	0.004
	ACR2.3 Hm - 26	4.49000	0.850	0.850	0.31500	0.035	0.035	0.020	0.10500	0.019	0.019

U/Pb Dates													
$^{207}Pb/^{235}U$	**2σ abs**	**2σ sys**	**$^{206}Pb/^{238}U$**	**2σ abs**	**2σ sys**	**$^{207}Pb/^{206}Pb$**	**2σ sys**		**$^{206}Pb/^{204}Pb$**	**U PPM**	**Th PPM**	**Pb PPM**	**Discrodancy (%)**	**age calculation**
1579.5	7.9	9.1	1567.6	13	15	1596.9	22		8.00E+05	1630	0	7	2	
1643.5	12	13	1667.5	13	16	1595.9	32	1	9.00E+06	128	0	0	-5	
1593.6	9.7	11	1598.4	13	16	1595.4	23		2.00E+05	1790	0	6	0	
1575.3	11	12	1559.6	19	20	1594.4	22		3.00E+06	3280	1	8	2	
1678.1	13	13	1762.8	17	19	1594.0	28		3.40E+06	477	1	19	-10	
1565.1	8.8	9.8	1548.4	14	16	1591.2	21	2	2.30E+05	4040	0	78	3	
1562.0	9.5	10	1548.4	15	17	1590.6	21		3.40E+04	3040	0	12	3	
1634.8	9.1	10	1660.5	13	15	1590.4	23	3	8.00E+06	1380	0	15	-4	yes
1578.5	11	12	1575.2	18	20	1587.7	22		1.20E+06	3400	1	5	1	
1581.3	9.4	10	1578.3	14	16	1583.5	21	4	2.90E+06	3270	0	2	1	
1569.9	9.4	10	1550.9	16	18	1582.8	22		4.80E+06	1727	0	22	3	
1603.5	19	19	1609.5	19	21	1584.5	46		3.00E+06	51	0	2	-3	
1697.2	27	28	1735.8	33	34	1625.9	51	5	3.06E+04	106	0	3	-11	
1723.6	21	22	1826.3	33	34	1578.8	30	6	7.00E+04	770	0	17	-15	
2722.3	140	140	2283.1	160	160	2882.2	190		2.00E+04	30	0	31	6	
1846.0	28	29	1763.8	38	39	2033.0	55	7	2.90E+04	31	0	59	12	
1928.3	57	57	1843.2	69	70	1959.2	76		1.90E+05	86	0	48	2	
2012.9	51	51	2034.1	68	69	1962.2	110		1.00E+05	85	0	159	7	
1776.1	33	33	1823.8	31	33	1728.3	54		7.00E+03	42	0	20	-8	
1872.1	96	97	2085.6	84	85	1660.8	180	8	3.00E+04	4.6	0	4	23	No - Low U
1687.6	29	29	1691.3	30	31	1684.2	64		1.70E+05	42	0	18	-4	
1929.9	120	120	1986.9	150	150	1832.1	260		2.30E+04	2.18	0	0	-30	
1917.6	150	150	2081.0	250	250	1597.8	180	9	1.10E+04	6.9	0	0	-22	
1664.2	33	34	1725.9	26	28	1597.8	76		5.90E+04	23	0	1	-13	
1626.0	32	32	1735.8	53	53	1541.9	82	10	2.60E+05	37	0	0	-18	
1729.1	180	180	1765.3	170	170	1714.3	380	11	2.20E+04	1.59	0	0	20	

Reference material data		Isotope Ratios										U/Pb Dates							
Reference Material	**Analysis #**	$^{207}Pb/^{235}U$	**2σ abs**	**2σ sys**	$^{206}Pb/^{238}U$	**2σ abs**	**2σ sys**	**Corr. Coef.**	$^{207}Pb/^{206}Pb$	**2σ abs**	**2σ sys**	$^{207}Pb/^{235}U$	**2σ abs**	**2σ sys**	$^{206}Pb/^{238}U$	**2σ abs**	**2σ sys**	$^{207}Pb/^{206}Pb$	**2σ sys**
GJ-1 Zircon	GJ - 1.d	0.82000	0.015	0.022	0.09736	0.001	0.001	0.143	0.06100	0.001	0.001	607.9	8.3	12	598.9	4.1	8	635	44
	GJ - 2.d	0.82300	0.015	0.022	0.09783	0.001	0.001	0.197	0.06080	0.001	0.001	609	8.1	12	601.6	3.7	7.8	632	44
	GJ - 3.d	0.81400	0.013	0.021	0.09847	0.001	0.001	0.142	0.05970	0.001	0.001	604.9	7.2	12	605.4	3.3	7.6	592	41
	GJ - 4.d	0.81100	0.014	0.022	0.09721	0.001	0.001	0.193	0.06000	0.001	0.001	602.8	8	12	598	3.4	7.6	610	44
	GJ - 5.d	0.80800	0.014	0.022	0.09792	0.000	0.001	0.124	0.06000	0.001	0.001	601.9	7.9	12	602.2	2.7	7.4	606	44
	GJ - 6.d	0.81600	0.014	0.022	0.09758	0.001	0.001	0.239	0.06050	0.001	0.001	605.6	7.9	12	600.2	3.5	7.7	620	44
	GJ - 7.d	0.82100	0.012	0.021	0.09872	0.001	0.001	0.071	0.05980	0.001	0.001	608.6	6.9	11	606.9	3.2	7.6	604	41
	GJ - 8.d	0.82200	0.014	0.022	0.09763	0.001	0.001	0.155	0.06060	0.001	0.001	608.1	7.9	12	600.5	3	7.5	625	43
	GJ - 9.d	0.83000	0.013	0.021	0.09896	0.001	0.001	0.107	0.06062	0.001	0.001	612.7	7.4	12	608.6	3.2	7.7	622	42
	GJ - 10.d	0.79800	0.015	0.022	0.09726	0.001	0.001	0.223	0.05940	0.001	0.001	595.7	8.3	12	598.3	3.1	7.5	574	45
	GJ - 11.d	0.82400	0.016	0.023	0.09811	0.001	0.001	0.121	0.06040	0.001	0.001	609.1	8.7	13	603.3	3.6	7.8	616	45
	GJ - 12.d	0.82700	0.018	0.024	0.09763	0.001	0.001	0.111	0.06100	0.001	0.001	612.2	9.7	13	600.5	2.9	7.5	635	50
	GJ - 13.d	0.81100	0.014	0.022	0.09825	0.001	0.001	0.053	0.05960	0.001	0.001	602.8	7.7	12	604.1	3.5	7.7	604	41
	GJ - 14.d	0.80800	0.013	0.021	0.09761	0.001	0.001	0.162	0.06008	0.001	0.001	601.6	7.3	12	600.4	3.4	7.7	606	42
	GJ - 15.d	0.80500	0.013	0.021	0.09831	0.001	0.001	0.036	0.05920	0.001	0.001	600.5	7.5	12	604.5	3.3	7.7	578	43
	GJ - 16.d	0.81700	0.015	0.022	0.09788	0.001	0.001	0.047	0.06020	0.001	0.001	605.1	8.4	12	601.9	3.8	7.9	607	46
	GJ - 17.d	0.81300	0.013	0.021	0.09700	0.000	0.001	0.057	0.06022	0.001	0.001	603.5	7.3	12	596.8	2.9	7.4	615	40
	GJ - 18.d	0.79800	0.012	0.020	0.09697	0.000	0.001	-0.114	0.05899	0.001	0.001	594.9	6.8	11	596.6	2.8	7.4	568	41
	GJ - 19.d	0.79700	0.015	0.022	0.09766	0.001	0.001	0.196	0.05900	0.001	0.001	594.1	8.6	12	600.6	3.4	7.7	561	46
	GJ - 20.d	0.81600	0.015	0.022	0.09753	0.001	0.001	0.206	0.06060	0.001	0.001	605.7	8.2	12	599.9	3.7	7.8	615	43
	GJ - 21.d	0.80500	0.013	0.021	0.09776	0.001	0.001	-0.050	0.05953	0.001	0.001	598.6	7.3	12	601.2	2.9	7.5	587	43
	GJ - 22.d	0.82400	0.014	0.022	0.09846	0.001	0.001	0.010	0.06030	0.001	0.001	609.4	7.7	12	605.3	3.4	7.7	617	45
	GJ - 23.d	0.83600	0.015	0.023	0.09857	0.000	0.001	0.236	0.06100	0.001	0.001	615.7	8.5	13	606	2.9	7.5	629	44
	GJ - 24.d	0.81200	0.014	0.022	0.09752	0.001	0.001	0.109	0.06040	0.001	0.001	604.4	7.7	12	599.8	3.1	7.5	609	45
	GJ - 25.d	0.83700	0.016	0.023	0.09872	0.001	0.001	0.278	0.06080	0.001	0.001	617.2	8.6	13	606.9	3.2	7.6	653	43
	GJ - 26.d	0.82000	0.015	0.022	0.09767	0.000	0.001	-0.001	0.06050	0.001	0.001	608	8.3	12	600.7	2.8	7.4	621	46
	GJ - 27.d	0.80800	0.013	0.021	0.09779	0.001	0.001	0.028	0.05960	0.001	0.001	601.9	7.3	12	601.8	3.3	7.5	599	43
	GJ - 28.d	0.80300	0.013	0.021	0.09678	0.001	0.001	0.015	0.06000	0.001	0.001	598	7.4	12	595.5	3.3	7.6	609	42
	GJ - 29.d	0.82500	0.014	0.022	0.09861	0.001	0.001	0.107	0.06020	0.001	0.001	610.2	7.9	12	606.2	3.1	7.6	608	42
	GJ - 30.d	0.81700	0.015	0.022	0.09731	0.001	0.001	0.056	0.06050	0.001	0.001	607	8.6	13	598.6	3.2	7.6	630	45
	GJ - 31.d	0.83400	0.013	0.021	0.09882	0.001	0.001	0.058	0.06110	0.001	0.001	615.8	7.2	12	607.4	3.4	7.7	640	44
	GJ - 32.d	0.81700	0.013	0.021	0.09838	0.001	0.001	0.005	0.06030	0.001	0.001	605.4	7.5	12	604.9	3.2	7.6	606	43
	GJ - 33.d	0.81600	0.015	0.022	0.09827	0.001	0.001	-0.049	0.05990	0.001	0.001	604.8	8.5	13	604.2	3	7.5	601	48
	GJ - 34.d	0.81300	0.014	0.021	0.09728	0.000	0.001	0.125	0.06020	0.001	0.001	603.1	7.7	12	598.4	2.8	7.4	609	44
	GJ - 35.d	0.80700	0.015	0.022	0.09906	0.001	0.001	-0.052	0.05910	0.001	0.001	600.8	8.5	13	608.9	3.4	7.7	567	49
	GJ - 36.d	0.80900	0.014	0.022	0.09639	0.001	0.001	0.169	0.06100	0.001	0.001	602.1	8.2	12	593.2	3.2	7.5	632	44
Plesovice Zircon	Plseovice - 1.d	0.39750	0.007	0.010	0.05348	0.000	0.001	0.306	0.05335	0.001	0.001	339.5	4.7	7.5	335.8	1.9	4.3	337	42
	Plseovice - 2.d	0.38870	0.006	0.010	0.05350	0.000	0.001	0.118	0.05269	0.001	0.001	333.6	4.4	7.2	335.9	1.7	4.3	305	42
	Plseovice - 3.d	0.40640	0.007	0.011	0.05357	0.000	0.001	0.161	0.05466	0.001	0.001	346.4	5	7.8	336.4	1.7	4.3	398	43
	Plseovice - 4.d	0.40020	0.006	0.010	0.05358	0.000	0.001	0.113	0.05381	0.001	0.001	342	4.4	7.4	336.5	1.4	4.2	364	41
	Plseovice - 5.d	0.40060	0.006	0.010	0.05416	0.000	0.001	0.118	0.05335	0.001	0.001	341.8	4.1	7.2	340	2	4.4	344	42
	Plseovice - 6.d	0.40180	0.006	0.010	0.05397	0.000	0.001	0.114	0.05352	0.001	0.001	342.7	4.4	7.3	338.8	1.7	4.3	356	43
	Plseovice - 7.d	0.39740	0.006	0.010	0.05351	0.000	0.001	0.117	0.05355	0.001	0.001	339.5	4.4	7.3	336	1.9	4.3	342	42
	Plseovice - 8.d	0.39130	0.006	0.010	0.05381	0.000	0.001	0.145	0.05261	0.001	0.001	335.1	4.2	7.1	337.8	1.7	4.3	303	41
	Plseovice - 9.d	0.39400	0.007	0.011	0.05345	0.000	0.001	0.198	0.05370	0.001	0.001	337.4	5.1	7.8	335.7	1.9	4.3	346	45
	Plseovice - 10.d	0.39600	0.007	0.010	0.05340	0.000	0.001	0.056	0.05358	0.001	0.001	338.4	4.7	7.5	335.4	1.7	4.3	353	46
	Plseovice - 11.d	0.39170	0.006	0.010	0.05376	0.000	0.001	0.042	0.05282	0.001	0.001	335.3	4.4	7.3	337.6	1.6	4.2	319	42
	Plseovice - 12.d	0.40460	0.007	0.011	0.05366	0.000	0.001	0.196	0.05438	0.001	0.001	344.6	5.2	7.9	337.1	1.6	4.3	382	45
	Plseovice - 13.d	0.39400	0.007	0.011	0.05380	0.000	0.001	0.136	0.05280	0.001	0.001	337.4	5.3	7.8	337.8	1.8	4.3	308	48
	Plseovice - 14.d	0.39040	0.006	0.010	0.05384	0.000	0.001	0.090	0.05254	0.001	0.001	334.4	4.1	7	338.1	1.9	4.4	309	43
	Plseovice - 15.d	0.38760	0.008	0.011	0.05391	0.000	0.001	0.115	0.05220	0.001	0.001	332.1	5.7	8.1	338.5	1.8	4.3	281	50
	Plseovice - 16.d	0.40090	0.008	0.011	0.05412	0.000	0.001	0.155	0.05400	0.001	0.001	341.8	5.9	8.3	339.8	1.5	4.2	358	50
	Plseovice - 17.d	0.39640	0.008	0.011	0.05431	0.000	0.001	0.175	0.05270	0.001	0.001	339.2	5.6	8	340.9	1.9	4.4	322	50
	Plseovice - 18.d	0.39820	0.007	0.010	0.05447	0.000	0.001	0.163	0.05293	0.001	0.001	340	4.9	7.6	341.9	1.8	4.4	326	47
91500 Zircon	91500 - 1.d	1.85500	0.043	0.057	0.17750	0.002	0.003	0.069	0.07570	0.002	0.002	1062	15	20	1053.3	8.1	14	1074	53
	91500 - 2.d	1.87000	0.041	0.056	0.17790	0.001	0.003	0.021	0.07610	0.002	0.002	1072	15	20	1055.2	6.7	13	1100	52
	91500 - 3.d	1.85200	0.042	0.056	0.17600	0.001	0.003	0.143	0.07590	0.002	0.002	1065	15	20	1045.5	7.5	14	1090	52
	91500 - 4.d	1.86000	0.044	0.058	0.17700	0.001	0.002	0.068	0.07540	0.002	0.002	1064	16	21	1050.7	6.1	13	1078	52
	91500 - 5.d	1.87800	0.045	0.059	0.18070	0.001	0.003	0.039	0.07510	0.002	0.002	1073	16	21	1070.6	6.7	14	1064	55
	91500 - 6.d	1.86000	0.045	0.059	0.17840	0.001	0.003	0.026	0.07490	0.002	0.002	1065	16	21	1058.1	7.3	14	1063	55
	91500 - 7.d	1.84400	0.052	0.064	0.17860	0.002	0.003	0.213	0.07410	0.002	0.002	1058	18	22	1059.1	8.5	14	1065	59
	91500 - 8.d	1.86200	0.043	0.057	0.18170	0.001	0.003	0.020	0.07380	0.002	0.002	1068	15	20	1076.7	6.1	13	1051	52
	91500 - 9.d	1.89000	0.047	0.060	0.17610	0.001	0.003	0.054	0.07730	0.002	0.002	1075	16	21	1045.7	7.4	14	1119	55

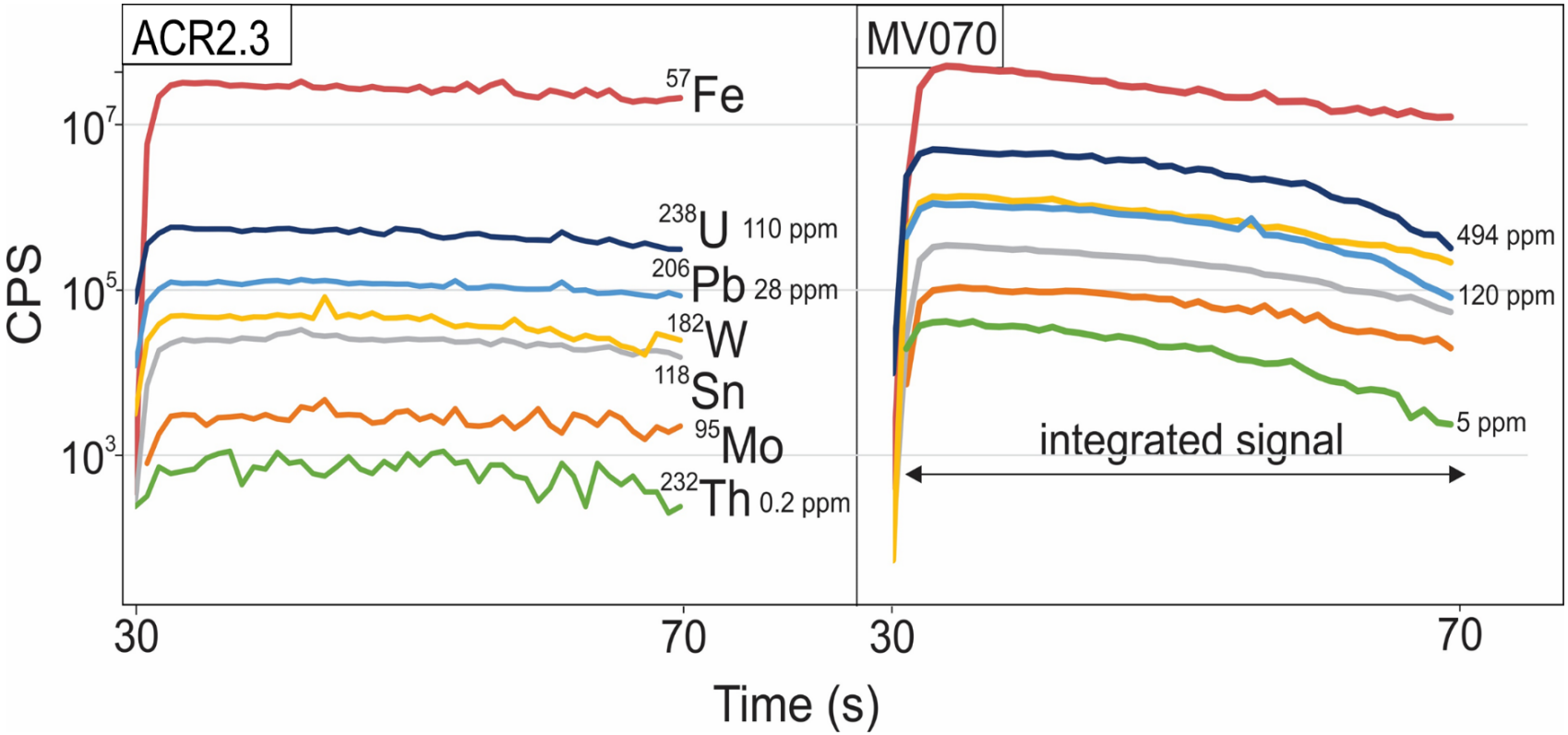
* 2σ sys refers to systematic uncertainties included within the overall ratio or age uncertainty. This is propagated uncertainty within iolite data reduction relating to scatter between analyses of the standard. Abs uncertainty refers only to analytical uncertainties.

** Pb refers to total Pb, although generally, 204 and 208 is very low

ELECTRONIC APPENDIX B FOR CHAPTER 5

LA-ICP-MS spot analyses

Prospect/sample ID	Analysis ID	Mg	Al	Si	P	Ca	Sc	Ti	V	Cr	Mn	Co	Ni	Cu	Zn	Ga	As	Sr	Y	Zr	Nb	Mo	Sn	Sb	Ba	La	Ce	Pr	Nd	Sm	Eu	Gd	Tb	Dy	Ho	Er	Tm	Yb	Lu	ΣREY	Hf	Ta	W	^{206}Pb	^{207}Pb	^{208}Pb	Th	U
Wirrda Well/MV070	MV70 - 1	78.3	394	150	6.82	<10	3.71	87.9	28.2	0.16	5.45	1.06	0.475	0.466	1.19	3.39	9.92	2.57	4.58	0.1	12.6	58.8	137	1.85	1.2	0.349	1.74	0.233	1.12	0.56	0.185	0.542	0.203	1.87	0.434	1.9	0.369	3.05	0.404	12.96	0.001	0.027	410	83.6	9.87	0.872	3.56	361
	MV70 - 2	0.647	519	97.2	7.1	<10.9	6.13	46.4	23.5	0.405	2.49	0.323	0.842	0.095	0.5	1.39	4.24	0.214	0.085	0.058	1.84	6.71	22.6	0.332	0.186	0.048	0.164	0.012	0.06	0.021	0.003	0.02	0.004	0.024	0.008	0.016	0.003	0.007	0.003	0.39	0.004	0.016	40.4	0.635	0.15	0.31	0.003	1.6
	MV70 - 3	308	137	92.8	6.9	<10.1	0.394	13.6	49.5	0.149	10.3	2.78	0.417	<0.022	0.82	3.04	2.41	0.564	8.34	0.042	92.4	112	253	5.12	0.083	0.26	1.24	0.063	0.328	0.24	0.032	0.595	0.196	2.02	0.562	2.83	0.609	6.47	1.27	16.72	<0.002	0.004	897	257	29.4	1.87	23.5	1080
	MV70 - 4	64.3	466	215	5.69	41.1	3.76	79.4	39.1	0.479	4.39	1.54	0.571	0.23	0.92	3.59	4.37	1.03	0.663	0.84	10.9	238	141	0.947	0.466	0.192	0.573	0.051	0.203	0.085	0.039	0.068	0.03	0.291	0.074	0.367	0.058	0.499	0.074	2.60	0.005	0.015	1370	18.4	2.14	0.26	0.777	72.7
	MV70 - 5	370	146	61.2	7.32	25	0.432	7.26	67.1	<0.093	11.1	3.21	0.249	0.37	0.383	3.38	1.27	0.05	10	0.033	135	122	284	5.15	0.018	0.519	3.18	0.151	0.926	0.49	0.057	0.927	0.243	2.34	0.676	3.24	0.714	7.29	1.4	22.15	0.006	0.003	989	271	31	2.63	32.7	1150
	MV70 - 6	154	43.5	39.3	7.3	<8.82	0.296	1.16	6.75	0.094	5.44	1.92	0.269	<0.019	0.174	2.12	0.19	0.035	1.34	0.005	3.6	163	180	3.38	0.001	0.012	0.08	0.004	0.008	0.014	0.003	0.046	0.018	0.224	0.103	0.545	0.139	1.9	0.432	3.53	<0.002	<0.001	625	89.8	10.2	0.303	2.64	362
	MV70 - 7	221	41.1	75.7	6.41	<8.98	0.189	17.6	31.8	<0.079	9.81	3.29	0.321	<0.023	0.543	2.48	0.465	0.318	1.88	0.029	70.6	748	263	2.6	0.208	0.622	1.41	0.108	0.575	0.151	0.017	0.166	0.046	0.488	0.157	0.747	0.163	1.59	0.36	6.60	0.001	0.004	3660	68.5	7.91	0.693	6.96	294
	MV70 - 8	187	52.5	48	9.95	<7.98	0.211	96.3	15.2	<0.1	7.72	2.55	0.199	0.097	0.492	2.12	3.87	0.984	1.97	0.018	6.41	455	173	3.05	0.288	0.147	0.523	0.048	0.211	0.032	0.006	0.097	0.038	0.444	0.17	0.794	0.208	2.41	0.494	5.62	0.018	0.01	999	122	13.5	0.439	3.71	493
	MV70 - 9	118	127	74.6	10.2	23.3	0.745	84.3	25.4	0.242	14.8	1.73	0.275	0.07	6.91	2.14	6.05	12.9	3.44	0.009	22.6	67.2	177	2.78	3.43	0.241	0.93	0.113	0.573	0.222	0.06	0.343	0.086	0.81	0.223	1.06	0.216	2.24	0.434	7.55	0.001	0.015	356	84.6	9.84	0.932	5.76	364
	MV70 - 10	87.8	141	75.9	9.14	<10.2	1.8	134	16.6	0.37	6.32	1.16	0.271	<0.018	0.99	1.82	7.4	1.96	1.42	0.058	6.08	154	91.3	2.39	1.11	1.91	3.63	0.356	1.48	0.192	0.103	0.21	0.069	0.757	0.201	1.06	0.13	1.48	0.311	11.89	0.007	0.013	649	130	15.4	0.537	1.3	755
	MV70 - 11	18.7	951	391	7.02	43.6	5.77	121	34.7	0.329	32.2	0.87	1	0.229	2.41	1.36	15.6	1.11	1.15	0.322	5.27	85.5	54.7	2.37	3.56	0.433	1.24	0.168	0.785	0.291	0.103	0.286	0.074	0.579	0.104	0.292	0.042	0.481	0.04	4.92	0.011	0.028	367	25.5	4	2.66	0.476	103
	MV70 - 12	13.8	1530	890	8.67	45.6	10.2	52.3	24.5	0.308	15.4	0.807	1.97	1.25	2.16	1.28	14.5	1.19	2	0.455	2.13	65.1	32.9	3.27	3.36	2.41	4.61	0.579	2.2	0.537	0.186	0.533	0.126	0.896	0.176	0.458	0.073	0.482	0.05	13.32	0.028	0.013	36.8	45.1	6.47	4.37	0.623	410
	MV70 - 13	14.5	1610	831	9.72	22.5	7.97	18.3	19.1	0.173	22.2	0.727	2.57	0.486	2.61	1.18	19.1	1.45	2.21	0.202	4.2	79.2	44.8	3.08	4.02	2.28	6.664	0.56	2.526	0.329	1.44	0.56	0.157	0.664	0.14	1.05	0.169	0.072	0.53	0.048	8.95	0.003	0.002	37	28	4.58	3.83	0.706	167
	MV70 - 14	124	109	65.7	6.66	<10.1	1.92	136	35.8	0.213	5.65	1.56	0.425	<0.019	0.453	1.9	2.89	0.212	1.5	0.055	4.7	118	150	3.22	0.253	0.194	0.269	0.019	0.094	0.01	0.007	0.072	0.022	0.339	0.124	0.653	0.14	1.68	0.36	3.98	<0.003	0.01	727	90.2	10.2	0.346	2.93	376
	MV70 - 15	151	102	63.3	10.7	<8.14	0.725	253	28.4	0.75	6.36	1.79	0.246	0.142	0.537	2.1	2.82	0.201	2.38	0.054	6.16	118	149	3.44	0.062	0.49	1.06	0.07	0.216	0.055	0.015	0.152	0.042	0.498	0.18	0.933	0.214	2.28	0.551	6.76	0.005	0.037	716	120	13.8	0.5	4.5	494
	MV70 - 16	290	168	95.8	9.8	18.4	1.17	113	35	<0.12	9.16	2.29	0.59	2.66	0.85	2.43	5.81	2.41	5.34	0.063	11.6	120	159	4.11	0.473	2.92	8.24	0.361	1.23	0.551	0.033	0.648	0.138	1.35	0.353	1.71	0.396	4.06	0.771	22.76	0.022	0.016	768	216	24.7	1.38	11.6	870
	MV70 - 17	312	151	172	12.5	25.6	1.35	546	81	1.18	14.1	2.67	0.538	4.19	2.72	2.57	9.11	11.3	8.6	0.099	41.2	188	226	3.37	1.87	27.6	55.5	3.55	12.3	1.75	0.169	1.33	0.257	2.29	0.617	2.68	0.554	5.83	1.19	115.62	0.009	0.094	1320	392	45.2	2.83	24.5	1680
	MV70 - 18	80.3	261	358	16.7	<9.71	1.74	131	30.7	0.56	6.27	1.43	0.52	0.283	2.15	2.19	26.6	4.04	1.48	0.018	17.1	152	117	2.37	1.42	0.238	0.788	0.094	0.407	0.141	0.056	0.242	0.061	0.528	0.103	0.392	0.092	0.835	0.193	4.17	0.02	0.02	806	54.4	8.17	5.5	0.87	224
	MV70 - 19	43.4	2230	841	7.21	200	7.37	81.2	47.3	0.155	14.9	1.18	1.88	45.6	2.34	1.32	7.33	2.31	5.09	0.576	20.4	129	39.6	2.33	2.67	1.32	5.32	0.822	3.92	1.68	0.472	1.97	0.49	3.09	0.523	1.43	0.21	1.54	0.22	23.01	0.046	0.007	144	28.2	7.15	13.4	4.07	111
	MV70 - 20	30.1	337	482	43.5	<17.4	2.35	558	23.2	0.46	13.4	1.1	0.621	1.24	1.2	1.36	12.5	3.02	3.49	0.019	5.79	26	91.2	1.09	14	24.7	50.4	4.87	18.8	2.34	0.504	1.69	0.246	1.53	0.281	0.759	0.165	0.883	0.066	107.23	0.001	0.024	99.1	112	11.5	1.32	0.527	652
	MV70 - 21	168	167	140	5.77	<8	1.21	48.3	11.7	38	5.32	1.75	0.359	0.031	0.81	2.38	2.19	0.744	4.01	0.001	6.75	233	149	3.22	0.096	2.79	9.28	0.985	4.45	0.975	0.172	0.713	0.137	1.22	0.237	1.09	0.202	2.08	0.393	24.72	<0.002	0.006	664	244	28.7	1.88	6.47	1040
	MV70 - 22	107	282	245	27.9	51.2	1.61	383	73.7	0.9	26.3	2.12	0.97	0.497	13.9	2.1	28.2	51.6	0.865	0.025	54.3	1350	106	1.73	12.6	1.22	2.48	0.221	0.891	0.07	0.02	0.144	0.029	0.249	0.085	0.346	0.079	0.747	0.184	6.77	0.001	0.037	2400	39	6.54	5.87	3.77	151
	MV70 - 23	399	41	82.3	4.57	<8.15	0.38	26.4	54	<0.076	8.67	3.09	0.419	0.045	0.55	2.91	0.62	0.113	5.45	0.052	112	334	212	4.83	0.143	4.92	12.9	0.838	3.39	0.642	0.083	0.697	0.165	1.43	0.444	2.01	0.405	4.11	0.878	32.91	0.001	0.001	1370	305	35	3.41	45.5	1300
	MV70 - 24	308	81.4	91.4	6.8	43.1	0.248	6.82	54.7	<0.107	11.9	3.6	0.667	0.268	0.614	2.88	4.18	1.19	6.72	0.036	85.5	985	249	3.44	0.062	0.49	1.06	0.07	0.216	0.055	0.015	0.152	0.042	0.498	0.18	0.933	0.473	4.6	0.89	34.53	<0.002	0.002	3170	213	24.3	2.42	30.5	882
	MV70 - 25	143	24.5	87.2	3.84	35.5	0.062	7.85	5.82	0.411	7.31	1.65	0.379	0.393	1.64	2.26	1.8	3.02	2.26	<0.002	3.06	160	155	3.09	1.61	0.651	1.85	0.137	0.472	0.111	0.056	0.166	0.904	2.02	2.26	0.497	8.13	0.001	<0.001	460	127	14.6	0.635	4.83	512
	MV70 - 26	459	69.1	161	20.4	43.3	0.481	20.4	24.2	<0.074	11.9	3.57	0.349	0.364	1.61	3.07	2.59	1.15	10.8	0.026	116	479	277	5.3	0.425	15.4	76.4	6.18	26.4	3.19	0.479	2.35	0.409	3.05	0.691	3	0.659	6.04	1.22	159.87	<0.002	0.006	1870	458	52.6	6.24	54.7	1920
	MV70 - 27	133	187	91	5.97	20.9	1.32	44.5	3.04	0.09	6.93	2.44	0.41	1	0.59	2.18	2.15	0.142	0.943	0.1	13.2	683	226	3.37	1.87	27.6	55.5	3.55	12.3	1.75	0.169	1.33	0.257	2.29	0.617	2.68	0.554	5.83	1.19	115.62	0.009	0.094	1320	392	45.2	2.83	24.5	1680
	MV70 - 28	118	301	61.2	10.8	<9.42	1.83	40.4	51.5	0.474	5.5	1.33	0.31	0.298	1.18	2.39	1.95	3.48	4.68	0.226	32.8	71.9	167	1.62	1.14	3.89	9.49	1.28	3.53	0.792	0.219	0.746	0.19	1.66	0.389	1.66	0.282	2.6	0.427	27.16	0.014	0.006	571	220	25.8	0.694	6.56	941
	MV70 - 29	151	12.2	65.2	2.04	<8	0.127	11.7	11.7	0.222	5.91	2.06	0.175	0.174	0.55	1.58	3.84	0.643	1.59	0.001	7.89	97.9	148	2.72	0.423	3.29	6.29	0.552	1.56	0.173	0.026	0.174	0.032	0.344	0.116	0.579	0.126	1.51	0.32	15.09	<0.003	0.001	524	162	18.2	0.398	3.12	693
	MV70 - 30	131	28.8	70.8	7.73	<7.79	0.127	1.32	8.08	0.127	4.92	1.75	0.214	0.223	0.315	1.4	0.341	0.35	1.17	0.001	4.4	580	285	1.6	0.143	3.94	9.54	0.548	1.25	0.202	0.033	0.161	0.035	0.346	0.092	0.466	0.096	1.13	0.239	18.08	<0.004	<0.001	2500	60.8	6.81	0.219	2.51	249
Wirrda Well/MV067	MV067 - 1	29.8	2.42	87.1	5.7	<13.7	0.023	0.5	0.643	<0.128	2.4	0.963	0.067	<0.017	0.088	1.19	<0.148	<0.002	0.004	0.001	3.13	30.5	200	0.265	0.025	0.006	0.006	<0.001	<0.006	<0.003	<0.001	<0.003	<0.001	0.001	<0.001	0.001	<0.001	<0.004	0.001	0.02	0.001	0.002	311	2.06	0.224	0.006	0.002	7.75
	MV067 - 2	20.9	27.7	99.6	5.84	37.2	0.015	2.84	2.24	<0.106	1.65	0.693	0.164	0.049	<0.051	2.28	1.05	0.165	0.021	0.001	6.7	60.2	294	0.795	0.149	0.109	0.156	0.009	0.017	<0.005	<0.002	0.004	<0.001	0.002	0.001	0.008	0.003	0.057	0.014	0.38	<0.004	0.003	753	44.5	5	0.038	0.009	188
	MV067 - 3	28.3	11.3	86.2	7.28	<11	0.023	0.37	3.35	<0.095	2.87	0.673	0.096	0.067	0.104	1.81	<0.091	0.107	0.131	0.006	19.7	155	193	0.4	0.143	0.139	0.262	0.017	0.085	0.008	0.003	0.032	0.006	0.017	0.009	0.046	0.007	0.094	0.028	0.75	<0.005	0.001	792	4.8	0.558	0.028	0.098	17.5
	MV067 - 4	153	8.28	97.9	8.72	<12.7	0.072	2.32	13.3	0.168	9.17	2.65	0.256	0.548	0.363	2.12	0.302	0.104	0.851	0.003	87.5	639	320	3.09	0.286	0.172	0.343	0.016	0.046	0.022	0.002	0.044	0.015	0.175	0.062	0.335	0.083	0.886	0.191	2.39	0.001	0.02	3270	41.7	4.74	0.108	0.848	173
	MV067 - 5	115	8.39	89.9	7.5	21.4	0.046	3.06	6.29	0.129	8.65	2.92	0.23	0.034	0.243	1.68	1.03	0.026	0.086	0.007	13.2	1260	276	2.35	0.121	0.041	0.089	0.003	0.021	0.005	<0.001	<0.003	0.001	0.013	0.009	0.051	0.014	0.148	0.052	0.45	<0.002	0.003	4820	11.1	1.27	0.085	0.101	44.1
	MV067 - 6	157	2.57	69.3	5.4	25.7	0.029	0.386	5.33	<0.092	9.67	3	0.289	0.029	0.32	1.64	<0.068	<0.002	0.377	0.003	5.33	1620	255	2.87	0.001	0.073	0.116	0.009	0.034	<0.004	<0.001	0.006	0.001	0.067	0.025	0.203	0.053	0.63	0.148	1.37	<0.003	<0.001	5470	21.8	2.44	0.014	0.125	93.6
	MV067 - 7	156	4.04	70.3	3.31	<10.1	0.037	0.61	10	0.098	10.7	2.8	0.17	<0.015	0.534	1.88	<0.058	<0.002	0.275	0.001	57	1580	240	2.59	0.017	0.071	0.105	0.01	0.02	0.012	<0.001	0.009	0.002	0.048	0.026	0.149	0.049	0.573	0.142	1.22	<0.002	0.009	5110	18.5	1.86	0.013	0.055	69.4
	MV067 - 8	195	334	141	9.3	33.6	1.06	251	35.8	0.93	11.5	2.05	0.428	0.368	6.55	2.72	8.87	0.551	0.814	0.006	21.6	306	106	4.14	1.05	0.587	1.23	0.2	0.808	0.052	0.022	0.189	0.054	0.808	0.25	0.38	0.081	1.1	0.227	4.23	<0.003	0.051	639	707	8.29	0.807	1.85	288
	MV067 - 9	251	1510	1900	6.6	38.2	1.65	647	46.2	2.22	15.3	2.01	0.896	6.9	1.68	2.54	15.2	0.621	2.41	0.058	28.9	194	127	8.73	2.01	7.24	17	0.903	3.06	0.432	0.076	0.475	0.088	0.661	0.17	0.733	0.153	1.55	0.358	32.90	0.005	0.077	781	105	12.7	2.08	4.5	442
	MV067 - 10	244	170	126	6.75	42.5	0.619	454	43.6	1.62	17.5	2.56	0.335	0.217	1.78	2.52	2.11	1.83	2.29	0.001	26.7	216	161	4.1	2.5	1.36	3.03	0.142	0.573	0.177	0.025	0.196	0.056	0.542	0.157	0.741	0.196	1.9	0.438	9.53	<0.002	0.042	984	130	14.8	0.653	4.26	526
	MV067 - 11	131	59.3	97.9	11.2	16.4	0.144	4.81	0.443	<0.083	7.09	2.5	0.359	0.077	0.574	1.52	0.83	0.072	0.285	<0.002	0.046	4390	134	2.51	<0.01	0.155	0.309	0.014	0.079	0.011	0.011	0.074	0.008	0.079	0.023	0.078	0.022	0.224	0.074	1.16	0.001	<0.001	1310	45.5	5.1	0.057	0.057	203
	MV067 - 12	201	73.3	82.2	7.15	18.1	0.226	17.7	1.98	<0.102	7.8	2.59	0.375	0.154	0.254	1.93	0.324	0.051	0.402	0.001	0.135	4140	172	2.78	0.034	1.52	2.81	0.184	0.516	0.044	0.004	0.061	0.012	0.107	0.035	0.194	0.052	0.541	0.138	6.22	0.001	0.003	1800	66.5	7.67	0.09	0.456	277
	MV067 - 13	142	230	135	8.69	16.6	2.34	211	12.3	0.313	10	2.12	0.289	0.3	1.45	2.21	4.65	0.575	0.386	0.011	1.48	2360	147	3.5	0.497	0.942	1.69	0.115	0.346	0.048	0.007	0.07	0.014	0.094	0.037	0.174	0.047	0.486	0.107	4.18	<0.002	0.015	1380	34.8	4.16	0.59	0.54	147
	MV067 - 14	242	11.9	48.4	6.83	20.8	0.049	21	1.78	<0.103	10.1	3.05	0.381	0.071	0.75	1.98	1.99	0.341	1.16	<0.004	1.89	3700	178	3.65	0.495	3.57	7.01	0.442	1.64	0.212	0.017	0.182	0.033	0.347	0.108	0.503	0.11	1.12	0.257	15.55	<0.002	0.004	1890	93.7	10.7	0.138	1.11	389
	MV067 - 15	144	136	92.6	16.2	<14.7	0.595	695	40.7	2.07	9.94	1.66	0.284	0.203	1.42	2.19	8.15	2.28	0.384	0.01	3.85	618	99.3	3.49	1.21	1.54	4.89	0.269	0.832	0.085	0.016	0.078	0.014	0.094	0.029	0.215	0.039	0.513	0.134	8.75	<0.005	0.073	278	57.6	6.77	0.605	0.75	231
	MV067 - 16	213	143	75.8	8.53	<10.7	0.31	81.7	12.38	0.154	6.64	1.9	0.24	0.064	0.42	2.48	4.68	0.593	0.541	0.001	1.58	547	107	4.04	0.315	1.24	2.99	0.142	0.379	0.043	0.007	0.062	0.015	0.137	0.054	0.294	0.08	0.921	0.235	6.60	<0.004	0.006	280	71	8.24	0.301	0.802	296
	MV067 - 17	172	191	53.1	5.86	60.6	0.195	32	7.47	<0.17	10.9	2.15	0.188	0.158	0.99	2.31	11.5	0.913	1.74	0.001	10.6	327	150	4.04	1.84	3.4	8.15	0.443	1.36	0.236	0.016	0.19	0.039	0.444	0.13	0.55	0.131	1.29	0.292	16.67	<0.004	0.01	636	99.9	11.3	1.01	2.38	406
	MV067 - 18	153	60.5	77.4	6.44	<11.3	0.242	0.408	0.664	0.108	8.28	2.82	0.253	0.043	0.501	2.08	1.99	0.099	0.254	0.001	0.074	4800	173	2.13	0.048	0.409	0.692	0.058	0.213	0.023	0.004	0.047	0.007	0.061	0.025	0.118	0.031	0.301	0.077	2.07	0.001	0.001	2170	13.6	1.64	0.177	0.1	58.1
	MV067 - 19	138	156	69	8.73	<9.96	0.218	<0.124	0.622	0.185	7.48	2.59	0.192	0.035	0.193	1.68	0.154	0.002	0.249	<0.002	0.67	5000	122	2.39	0.04	0.236	0.382	0.033	0.11	0.011	<0.001	0.007	0.008	0.07	0.019	0.126	0.026	0.342	0.081	1.45	<0.002	0.001	1530	13.3	1.44	0.022	0.092	54.6
	MV067 - 20	174	360	77.5	8.72	<10.6	0.461	4.86	1.2	0.247	5.43	1.97	0.176	0.1	0.255	2.88	2.66	0.177	0.502	<0.002	0.717	402	92.9	3.57	0.102	0.564	1.12	0.064	0.18	0.02	0.004	0.053	0.014	0.133	0.047	0.27	0.077	0.893	0.223	3.66	<0.002	0.001	251	59.8	7.04	0.561	0.684	251
	MV067 - 21	222	227	87.9	<1.63	<8.73	0.326	5.66	1.8	0.123	6.07	2.28	0.321	0.147	0.205	2.36	1.7	0.254	0.502	0.001	0.796	436	99.1	4.45	0.455	0.525	1.29	0.062	0.229	0.016	0.009	0.062	0.017	0.182	0.04	0.373	0.099	0.985	0.287	4.18	<0.005	<0.001	275	69.3	8.32	0.286	0.715	308
	MV067 - 22	143	87.3	94.5	4.73	37.8	0.247	61.1	8.3	0.56	15.8	2.39	0.184	0.857	5.08	1.9	7.98	13.3	0.707	0.006	1.51	2500	159	3.37	7.18	3.05	6.1	0.551	1.55	0.206	0.012	0.194	0.024	0.293	0.045	0.219	0.046	0.42	0.122	12.94	<0.002	0.003	1260	127	15.6	2.78	0.276	610
	MV067 - 23	117	78	49.3	4.66	21.5	0.171	1.81	0.233	<0.082	5.46	1.43	0.185	0.151	0.311	2.37	0.6	0.169	0.358	0.001	0.314	363	85.4	2.59	0.147	0.508	1.47	0.094	0.386	0.057	0.003	0.086	0.006	0.125	0.022	0.153	0.031	0.444	0.12	3.51	<0.002	<0.001	113	41.2	4.72	0.374	0.114	184
	MV067 - 24	320	103	66.3	8.82	<8.34	0.61	136	56	0.319	11.5	3.02	0.438	0.721	0.533	2.65	1.03	0.501	4.03	0.043	558	230	266	5.09	1.05	3.3	7.72	0.402	1.54	0.324	0.037	0.443	0.116	0.919	0.269	1.36	0.31	3.01	0.678	20.43	0.004	0.131	2170	185	21.5	1.47	19.1	799
	MV067 - 25	200	75.8	76.7	9.31	<8.57	0.231	185	40.5	0.326	11.5	3.29	0.283	0.407	1.54	2.67	0.87	0.244	0.69	0.062	116	1720	283	2.41	0.216	2.67	4.44	0.301	0.95	0.12	0.013	0.092	0.021	0.181	0.056	0.232	0.06	0.706	0.178	10.02	0.005	0.052	7790	39.9	4.53	0.263	2.42	176
	MV067 - 26	130	21.6	84	8.29	<9.13	0.104	57.4	5.66	0.



APPENDIX FIGURE 1. TIME-RESOLVED LA-ICP-MS DOWNHOLE PROFILES FOR HEMATITE

ELECTRONIC APPENDIX C FOR CHAPTER 5

LA-ICP-MS spot analyses

Prospect/sample ID	Analysise ID	Mg	Al	Si	P	Ca	Sc	Ti	V	Cr	Mn	Co	Ni	Cu	Zn	Ga	As	Sr	Y	Zr	Nb	Mo	Sn	Sb	Ba	La	Ce	Pr	Nd	Sm	Eu	Gd	Tb	Dy	Ho	Er	Tm	Yb	Lu	ΣREY	Hf	Ta	W	^{206}Pb	^{207}Pb	^{208}Pb	Th	U
Acropolis/ACR1.12	ACD112Mt-1	175	2830	456	37.7	1220	34.3	15400	419	201	64.2	20	34.2	<0.27	337	40.8	<0.87	0.535	0.517	0.118	0.576	0.27	14	<0.18	2.01	0.136	0.426	0.028	0.32	0.138	0.048	0.133	<0.019	0.24	<0.016	<0.035	0.131	0.3	0.034	2.5	0.092	0.042	<0.037	0.266	0.406	0.379	0.56	0.79
	ACD112Mt-2	791	2810	549	78.2	<512	36.7	15500	444	76.3	276	23.7	35	<0.21	196	59.4	<0.78	2.57	2.96	0.386	1.1	0.47	16.2	0.2	19.7	1.17	3.28	0.425	1.44	0.1	0.257	0.46	0.18	0.82	0.174	0.66	0.117	0.27	0.102	12.4	0.001	0.129	0.39	1.01	0.845	2.11	0.128	0.504
	ACD112Mt-3	94.5	2770	516	21.2	<495	31	14600	410	77.2	58.7	18.4	40.1	0.33	245	45.8	<0.75	0.077	0.07	0.267	0.327	0.094	15.2	<0.19	0.001	0.073	0.176	0.149	0.077	0.093	0.134	0.039	0.077	<0.033	0.123	0.8	0.073	0.001	0.157	0.084	0.046	0.141	0.07	0.249
	ACD112Mt-4	76.3	2400	482	25.7	<486	29.7	12700	429	8.43	86.2	21.7	35.1	<0.22	213	50.7	<0.79	<0.022	<0.021	0.164	0.249	0.079	14.4	<0.16	0.001	<0.013	0.028	<0.023	<0.077	0.001	<0.026	<0.088	<0.01	0.001	<0.013	0.001	<0.017	<0.05	0.001	0.0	0.001	0.214	<0.025	0.025	<0.018	<0.027	<0.032	<0.021
	ACD112Mt-5	125	2690	852	<16.1	<427	28.2	13000	409	216	45.8	22.8	30.4	1.27	500	38	1.56	3.5	1.66	0.472	1.5	0.56	13.7	0.36	14.9	0.766	2.51	0.261	1.1	<0.082	0.191	0.14	0.051	0.47	0.129	0.54	0.039	0.29	0.099	8.2	0.069	0.041	0.94	1.74	1.14	2.81	2.25	1.03
	ACD112Mt-6	163	2430	495	79.3	<440	27.8	13400	389	9.25	74.3	18	30.8	0.31	147	39.9	<0.65	1.44	0.096	<0.027	0.022	0.28	12.7	<0.071	0.001	3.74	3.73	0.276	0.4	<0.095	0.041	<0.045	0.001	<0.056	0.01	<0.042	<0.015	0.089	<0.007	8.4	0.22	<0.011	0.145	0.235	0.141	0.494	0.263	0.054
	ACD112Mt-7	342	2660	453	28.4	<478	34.9	13900	441	5.23	115	23.7	38.2	0.46	126	45.1	<0.77	0.077	<0.014	0.214	0.171	0.094	12.7	<0.18	5.64	0.16	0.119	0.001	<0.059	0.078	<0.024	<0.068	0.001	<0.03	0.005	0.059	<0.016	0.052	<0.01	0.5	<0.039	0.06	0.122	0.029	<0.012	0.029	<0.015	0.008
	ACD112Mt-8	560	2410	384	40.2	1140	27.6	12600	449	<0.48	252	26.9	38	0.4	141	49.5	<0.71	<0.051	0.009	0.096	0.416	0.168	14.6	<0.19	0.001	<0.021	0.024	<0.013	<0.052	<0.062	0.035	<0.103	<0.009	<0.037	<0.016	<0.047	<0.01	0.052	0.014	0.1	0.001	0.001	<0.041	0.03	<0.029	0.077	0.05	0.05
	ACD112Mt-9	65.3	2290	437	<17.3	<463	29.3	12300	411	4.79	53.9	19.3	30.5	0.59	400	40.3	1.33	0.771	0.385	0.485	0.974	0.189	12.7	<0.132	0.76	0.245	0.582	0.082	0.228	0.039	<0.044	<0.083	0.014	0.074	0.078	0.096	<0.011	<0.047	0.015	1.8	<0.068	0.001	0.37	0.431	0.141	0.458	2.05	3.24
	ACD112Mt-10	78.8	2350	434	<16.8	1500	26.9	12600	418	37.1	54.4	21.9	25.5	0.78	295	43	<0.68	0.256	0.134	0.359	0.616	0.031	13.6	0.19	0.71	0.071	0.216	0.022	0.091	<0.124	<0.02	<0.068	<0.007	<0.052	0.008	0.075	<0.012	0.066	<0.01	0.7	<0.04	0.058	<0.04	0.134	0.084	0.232	0.603	1.24
	ACD112Mt-11	1520	5460	8230	24.1	1120	43.1	15400	377	1.96	129	24.7	30.1	23.3	557	38.5	2.67	10.1	3.7	2.67	2.8	0.6	20.6	1.48	62.9	8.36	18.9	2.19	7.11	1.44	2.04	0.77	0.131	0.67	0.298	0.31	0.119	1.45	0.081	45.7	0.26	0.166	5.17	5.51	3.08	6.58	12.5	51.6
	ACD112Mt-12	182	2320	528	<16.5	1320	20	12100	407	89.7	54.7	18.2	29.2	0.26	384	41.3	1.81	4.44	2.07	0.298	0.332	0.33	10.7	<0.15	38	0.67	2.2	0.107	1.65	0.23	0.093	0.22	0.064	0.94	0.128	0.42	0.091	0.77	0.051	9.7	0.113	0.093	0.18	0.853	0.837	1.91	0.68	0.354
	ACD112Mt-13	37.1	2320	519	59.8	<478	20.6	12000	410	22.6	46.7	19.1	30.8	<0.27	406	43.7	0.91	0.628	0.16	0.244	0.18	0.071	11.9	0.12	1.61	0.178	0.461	0.074	<0.088	0.066	<0.033	<0.071	0.017	<0.082	0.023	0.047	0.03	<0.035	<0.008	1.1	0.17	0.03	0.168	0.922	0.362	1.36	5.39	12.6
	ACD112Mt-14	37.5	2770	470	<18.5	<473	35	13600	460	19.4	54.1	21.2	39.1	<0.31	292	46.6	<0.73	0.227	0.032	0.279	0.359	0.124	14.7	<0.103	0.39	0.126	0.176	0.033	<0.094	<0.079	<0.022	<0.076	0.001	0.072	<0.012	<0.024	<0.018	<0.054	<0.008	0.4	<0.063	0.096	0.039	0.139	0.088	0.176	0.411	0.89
	ACD112Mt-15	1200	3160	3280	36.2	<439	49.4	16200	424	19.6	78.7	22.2	28.8	0.7	837	44.8	2.58	6.54	3.22	6.97	1.98	0.147	13.9	0.14	18.1	7.01	16.6	2.17	6.02	0.84	0.195	0.97	0.111	0.73	0.193	0.73	0.135	0.57	0.1	39.6	0.17	0.222	1.21	4.93	2.66	7.11	33.8	65
	ACD112Mt-16	76.7	2630	695	<19.6	<504	27.2	15300	437	169	55.8	23.4	26.5	0.76	835	51.5	1.02	2.2	1.82	1	0.9	0.22	14.8	0.35	6.57	1.26	2.97	0.461	1.2	0.34	0.108	0.24	0.131	0.33	0.108	0.36	0.053	0.39	0.07	9.8	0.116	0.127	1.25	1.64	0.905	2.34	10.5	24.7
	ACD112Mt-17	63.1	2630	458	<17.8	<447	28.5	13900	424	138	58.6	21.6	30.4	<0.28	220	49.1	<0.8	<0.043	0.001	0.074	0.078	<0.064	13.2	<0.14	0.001	0.042	0.048	<0.008	0.18	<0.128	<0.021	<0.05	0.011	0.105	<0.013	<0.023	0.001	<0.036	<0.017	0.4	0.001	0.041	<0.033	<0.023	<0.015	<0.022	0.047	0.112
	ACD112Mt-18	406	2970	1640	<15.4	<421	15.5	11100	366	4.01	52.2	22	26	1.86	593	39.9	1.15	1.51	1.57	0.295	1.1	0.5	8.82	0.2	3.88	1.34	3.71	0.498	1.43	0.099	0.1	0.38	0.019	0.4	0.112	0.262	0.056	0.227	0.034	10.2	<0.074	0.039	1.88	3.67	2.25	6.23	4.78	7.47
	ACD112Mt-19	129	2330	535	<16.4	<450	30.4	14000	400	147	51.2	23.3	29.4	1.68	592	41	1.75	4.9	2.18	0.92	2.04	0.093	13.8	0.16	14.4	1.68	4.33	0.374	1.91	0.39	0.169	0.34	0.07	0.62	0.115	0.55	0.107	0.55	0.053	13.4	0.001	0.018	1.11	1.99	1.05	2.56	10.6	23.8
	ACD112Mt-20	1580	3180	3000	39.2	<444	39.5	14700	411	2.69	78.5	20.4	36.2	0.41	542	42.5	2.84	5.31	1.81	1.19	1.97	0.166	16.4	0.27	9.39	4.41	10.3	1.2	4.07	0.62	0.258	0.35	0.077	0.51	0.159	0.313	0.091	0.198	0.049	24.4	0.112	0.095	1	1.8	1	2.48	5.72	23.3
Prospect/sample ID	**Analysise ID**	**Mg**	**Al**	**Si**	**P**	**Ca**	**Sc**	**Ti**	**V**	**Cr**	**Mn**	**Co**	**Ni**	**Cu**	**Zn**	**Ga**	**As**	**Sr**	**Y**	**Zr**	**Nb**	**Mo**	**Sn**	**Sb**	**Ba**	**La**	**Ce**	**Pr**	**Nd**	**Sm**	**Eu**	**Gd**	**Tb**	**Dy**	**Ho**	**Er**	**Tm**	**Yb**	**Lu**	**ΣREY**	**Hf**	**Ta**	**W**	**^{206}Pb**	**^{207}Pb**	**^{208}Pb**	**Th**	**U**
Acropolis/ACR1.15	ACD115Mt-1	958	3510	3540	31.8	<1530	32.3	13900	389	2.53	69.5	20.8	37.5	6.51	247	31.4	2.71	4.91	0.81	1.96	2.35	0.4	17.1	1.07	16.7	12.4	9.9	1.02	2.83	0.19	0.088	0.5	0.098	0.73	0.088	0.75	0.122	0.21	0.125	29.9	0.97	0.51	0.57	1.72	1.25	2.11	4.45	1.6
	ACD115Mt-2	605	2520	1940	<32.3	<1550	22.9	13600	428	2.74	66.5	26.5	42.1	12.3	235	36.7	2.26	4.13	1.45	1.46	1.47	0.19	15.2	0.67	21	2.93	5.11	0.51	1.16	0.16	0.099	<0.16	<0.044	0.58	1.15	0.37	0.5	0.21	0.042	14.3	0.37	0.035	0.56	3.99	2.79	6.71	4.63	1.31
	ACD115Mt-3	51.9	1610	946	<35.7	<1730	11.4	8710	383	2.97	51.3	18	36.6	29.1	260	33.2	2.52	3.85	3.26	1.28	0.93	0.21	13.6	0.95	4.16	2.68	5.58	0.75	1.69	<0.15	0.105	0.41	0.113	0.81	0.207	0.78	0.076	0.6	0.135	17.2	0.31	0.074	1.81	13.5	10.6	26.6	11.8	3.04
	ACD115Mt-4	154	1890	979	<30.9	<1490	14.5	9160	356	2.12	43.5	14.9	28.8	18.2	222	34.8	3.18	3.39	2.49	0.66	0.75	0.23	9.94	0.77	<0.52	2.25	3.85	0.45	1.73	<0.177	0.117	0.43	0.04	0.34	0.146	0.35	0.175	<0.14	<0.039	12.4	<0.106	0.077	1.08	6.76	4.63	11.5	9.56	7.48
	ACD115Mt-5	266	2590	1750	100	<1740	21.6	11900	389	3.02	50.5	23.2	32.9	10.7	231	39.2	3.02	2.82	1.49	1.53	1.18	<0.13	8.57	<0.49	0.001	1.53	3.46	0.31	0.49	0.38	0.093	0.15	<0.034	0.48	0.154	0.33	<0.063	<0.147	<0.016	8.9	0.28	<0.068	0.72	3.85	2.24	5.83	7.24	7.22
	ACD115Mt-6	113	2440	1340	<35.9	<1710	18.4	13100	410	3.95	45.9	18.6	34.3	7.37	248	39.8	3.66	2.46	1.85	2.49	2.51	0.09	19	1	1.05	1.52	3.51	0.303	0.36	0.18	0.116	0.37	0.031	0.43	0.173	0.28	<0.055	0.37	<0.023	9.5	0.105	0.135	2.8	4.11	2.88	8.09	12.3	22
	ACD115Mt-7	107	2160	1000	<35.1	<1720	15.8	12300	404	3.91	32.9	19.9	27.5	8.07	228	33.4	2.85	2.11	1.46	0.93	1.15	<0.24	13.3	<0.32	4.51	2.01	3.85	0.296	0.93	0.32	0.157	<0.218	<0.029	0.32	0.04	0.44	<0.029	0.37	<0.041	10.2	0.001	0.001	0.75	3.05	2.04	5.44	5.58	4.84
	ACD115Mt-8	635	2820	2010	102	<1610	33.8	13800	393	3.6	69.8	16.7	31.7	<1.2	128	37.6	3.99	3.21	0.97	1.22	1.29	0.64	17.2	0.16	19	15.5	20.4	1.57	5.15	0.45	<0.057	0.33	<0.024	0.11	0.022	0.15	0.047	0.37	<0.021	45.1	0.46	0.29	0.1	0.417	0.375	1.14	2.73	0.29
	ACD115Mt-9	705	2690	2010	<34	<1570	33.6	13200	413	2.33	80.9	18.9	39.1	2.5	142	38.8	1.39	5.73	0.36	0.86	1.92	0.48	17.2	<0.27	15	8.75	6.83	0.63	1.34	<0.17	<0.049	0.25	<0.036	<0.118	<0.029	0.187	<0.016	<0.11	<0.036	18.3	0.001	0.078	0.24	0.482	0.188	0.636	0.88	0.23
	ACD115Mt-10	139	2750	518	87.5	<1710	35.9	16400	433	2.37	75.2	20.2	36.6	<1.39	105	38.7	<0.96	0.054	<0.03	1.39	0.321	<0.13	13.3	0.37	<0.44	0.055	0.106	<0.017	<0.137	<0.21	<0.055	<0.179	<0.026	<0.114	<0.023	<0.104	<0.025	<0.19	<0.059	0.2	<0.09	<0.036	<0.083	0.041	0.205	0.06	<0.052	0.075
	ACD115Mt-11	101	1620	930	90	<1660	12.4	7850	363	4.12	35.8	19.1	26.2	39.4	265	37.6	3.82	2.52	0.88	1.57	1.16	0.18	9.76	<0.25	3.01	2.97	4.26	0.242	1.47	<0.14	0.089	0.37	0.058	0.23	0.14	0.17	0.073	0.4	0.038	11.4	0.001	0.084	1.54	8.15	5.37	15.5	9.37	2.52
	ACD115Mt-12	565	2960	2110	186	2180	28.3	14300	444	<0.77	56	23.1	29.2	<1.46	243	42.4	1.92	4.3	1.5	1.19	2.07	0.31	19.1	<0.34	18.2	11	7.84	0.75	1.7	<0.152	<0.072	0.28	0.046	<0.094	<0.033	0.27	0.048	0.25	0.028	23.7	<0.13	0.135	0.32	0.891	0.839	1.6	1.68	0.6
	ACD115Mt-13	1240	2940	3050	63.3	<1550	36.6	14600	453	3.64	66	22.6	41.4	3.25	160	49.8	1.28	4.23	1.13	1.87	2.66	<0.17	21.6	0.36	35.5	20.2	13.5	1.16	3.21	0.61	<0.041	0.32	<0.024	0.24	0.025	0.37	<0.016	0.18	0.044	41.0	<0.082	0.08	0.13	0.395	0.32	0.636	1.34	0.59
	ACD115Mt-14	168	2590	1010	72.6	<1650	26	14700	439	2.64	68	21.4	26.3	<1.39	163	43.9	0.95	4.79	0.156	0.54	0.93	<0.15	14	<0.28	5.15	0.49	0.76	0.031	<0.16	<0.14	0.076	0.001	<0.041	<0.108	<0.035	<0.063	0.065	<0.069	<0.027	1.6	<0.121	0.136	0.26	1.19	1.1	1.91	0.77	3.12
	ACD115Mt-15	1390	3910	4750	46.3	<1730	30.9	14800	471	3.66	118	26.2	35.8	2.59	242	43.5	3.75	8.04	1.15	3.31	3.98	5.67	18.7	1.47	22	20.7	18.8	2	3.8	<0.11	<0.091	<0.15	0.059	0.2	<0.033	0.106	<0.018	0.17	0.021	47.0	0.15	0.159	1.68	9.02	6.18	19.3	3.45	0.92
	ACD115Mt-16	168	2470	1270	<33.2	<1640	15.6	11800	406	2.63	62.5	21.8	39.8	19.8	236	40.9	3.82	3.11	1.38	0.53	0.88	0.13	11.8	0.37	3.61	1.12	2.38	0.27	0.74	0.45	0.21	0.29	<0.056	0.52	0.064	0.28	0.061	0.2	<0.041	8.0	<0.086	0.063	0.47	2.7	2.75	5.89	4.77	11.7
	ACD115Mt-17	1130	3340	3440	48.1	<1530	36.2	14100	431	4.37	71.5	21.6	46.8	2.74	198	52.2	1.01	10.8	1.62	1.91	2.89	0.25	21.6	0.29	27.8	45.7	34.9	4.53	8.15	0.096	0.048	1.03	<0.031	0.2	0.046	0.3	0.087	0.14	0.035	96.9	<0.116	0.191	0.35	0.553	0.711	1.66	4.36	0.69
	ACD115Mt-18	91.2	2420	727	73.5	1770	22.4	12900	399	1.46	45.4	18.6	30.4	16.4	205	41.2	3.13	1.42	0.6	1.17	1.17	0.26	13.8	<0.35	<0.41	1.15	2.21	0.073	0.92	<0.22	0.066	0.49	0.067	0.46	0.081	0.13	0.075	<0.136	0.03	6.4	<0.12	0.093	0.55	5.03	3.46	8.89	11.1	47.7
	ACD115Mt-19	136	2710	751	59.1	2620	32.9	15000	430	1.22	74.5	21.2	39	<1.18	110	43.2	<1.04	0.223	<0.034	1.26	1.25	<0.12	14.9	<0.34	0.001	0.125	0.199	<0.015	<0.16	0.3	0.032	0.001	<0.014	0.068	0.05	<0.043	0.045	<0.15	0.001	0.8	0.001	<0.033	0.001	0.156	0.132	0.452	0.142	0.57
	ACD115Mt-20	1450	2990	3540	80	3080	28	14700	439	3.17	74.5	23.5	43.4	3.72	145	48.7	1.43	6.84	0.53	1.55	1.93	0.37	19	0.18	19.3	14.4	11.7	1.02	3.11	0.58	<0.031	0.24	0.027	<0.181	<0.039	<0.079	<0.017	<0.16	<0.048	31.6	0.089	0.33	0.18	0.228	0.188	0.636	1.36	0.45
Prospect/sample ID	**Analysise ID**	**Mg**	**Al**	**Si**	**P**	**Ca**	**Sc**	**Ti**	**V**	**Cr**	**Mn**	**Co**	**Ni**	**Cu**	**Zn**	**Ga**	**As**	**Sr**	**Y**	**Zr**	**Nb**	**Mo**	**Sn**	**Sb**	**Ba**	**La**	**Ce**	**Pr**	**Nd**	**Sm**	**Eu**	**Gd**	**Tb**	**Dy**	**Ho**	**Er**	**Tm**	**Yb**	**Lu**	**ΣREY**	**Hf**	**Ta**	**W**	**^{206}Pb**	**^{207}Pb**	**^{208}Pb**	**Th**	**U**
Wirrda Well/WW33-12B	WW3312BMt-1	1350	6610	9260	24.1	766	14	1460	223	5.56	206	13.8	36.5	20.8	109	14.7	1.33	4.26	2.53	0.181	1.48	<0.068	1.59	0.13	6.11	1.43	4.37	0.661	2.57	0.31	0.056	0.33	0.046	0.46	0.13	0.42	0.073	1.2	0.264	14.9	0.056	0.087	0.29	0.134	0.068	0.066	<0.023	0.459
	WW3312BMt-2	1390	3290	6080	<11.6	1570	25.7	1770	262	11	196	14.5	38.7	<0.23	99.9	18.6	<0.54	2.86	2.84	0.324	1.34	<0.036	2.08	0.074	3.23	2.72	10.9	1.6	5.12	0.44	0.074	0.79	0.074	0.58	0.111	0.47	0.093	1.34	0.215	27.4	<0.035	0.078	<0.036	0.093	0.02	<0.017	0.064	0.365
	WW3312BMt-3	586	1900	3470	<13.3	<384	6.77	589	323	35.7	199	12.4	16.3	2.17	49.1	8.3	<0.64	1.33	1.72	<0.027	0.51	<0.04	2.7	0.15	2.63	1.13	3.3	0.56	2.46	0.09	0.026	0.35	0.075	0.32	0.039	0.102	0.057	0.24	0.035	10.5	0.001	0.001	<0.04	0.048	<0.019	0.049	0.021	0.26
Prospect/sample ID	**Analysise ID**	**Mg**	**Al**	**Si**	**P**	**Ca**	**Sc**	**Ti**	**V**	**Cr**	**Mn**	**Co**	**Ni**	**Cu**	**Zn**	**Ga**	**As**	**Sr**	**Y**	**Zr**	**Nb**	**Mo**	**Sn**	**Sb**	**Ba**	**La**	**Ce**	**Pr**	**Nd**	**Sm**	**Eu**	**Gd**	**Tb**	**Dy**	**Ho**	**Er**	**Tm**	**Yb**	**Lu**	**ΣREY**	**Hf**	**Ta**	**W**	**^{206}Pb**	**^{207}Pb**	**^{208}Pb**	**Th**	**U**
Wirrda Well/WW33-14B	WW3314BMt-1	1190	2360	6410	<56	2700	38.4	1720	544	6.15	253	13.4	41.8	3.46	29.9	6.81	2.07	2.54	3.78	0.55	0.52	<0.089	2.15	7.05	2.88	3.51	13	2.05	5.1	0.58	<0.045	0.91	0.073	0.4	0.31	1.03	0.121	0.61	0.067	31.5	<0.091	0.001	0.18	0.23	0.053	0.084	<0.039	1.11
	WW3314BMt-2	469	1720	3710	<57.8	<2430	4.67	1850	528	20.5	127	11.1	31.8	5.44	35.4	4.41	1.58	1	0.51	<0.109	0.6	0.16	2.41	<2.86	0.001	0.67	2.04	0.312	1.35	0.35	0.001	0.36	<0.022	<0.132	0.075	<0.092	<0.035	0.17	0.001	5.8	0.001	0.001	<0.125	0.151	0.166	0.084	<0.028	0.27
	WW3314BMt-3	92.3	525	2540	90	<2300	2.65	877	334	<1.56	129	12.1	46	<1.72	39.4	4.52	2.13	0.67	1.74	18.8	0.381	0.2	0.45	<2.7	0.001	0.059	0.182	<0.024	<0.135	<0.15	<0.076	0.23	0.057	<0.09	0.024	0.34	0.074	0.94	0.195	3.8	0.63	0.001	<0.069	0.268	0.075	0.147	<0.033	2.62
	WW3314BMt-4	103	160	1230	93.8	<2280	0.84	891	120	<1.52	145	11.6	70.7	<1.84	18.7	3.35	3.37	0.349	0.51	<0.062	0.085	<0.088	1.23	<1.97	<1.01	0.286	1.51	0.155	1.06	0.001	0.028	<0.17	<0.026	<0.13	<0.028	0.107	0.015	0.31	0.042	4.0	0.001	<0.047	0.22	<0.06	0.053	0.116	0.08	0.055
	WW3314BMt-5	298	859	1960	105	4240	12.2	1140	254	4.67	127	10.2	38.8	<1.59	33.2	6.85	3.23	0.63	1.09	<0.058	0.384	0.001	2.44	<1.89	0.71	0.68	2.26	0.282	1.25	0.46	<0.029	0.28	0.047	0.18	0.086	0.52	<0.032	0.27	0.039	7.4	<0.118	0.03	<0.09	0.132	<0.033	0.113	<0.018	0.49
	WW3314BMt-6	281	214	2210	119	<2230	7.41	1800	177	<1.39	129	8.49	43.5	1.83	19.2	2.89	2.71	0.094	0.76	0.001	0.113	<0.13	1.45	3.46	0.001	0.34	1.07	0.086	0.79	<0.21	0.065	0.36	<0.021	<0.13	0.039	0.108	<0.03	<0.16	<0.023	3.6	0.37	0.07	<0.097	0.101	0.055	<0.058	0.001	0.21
	WW3314BMt-7	75.7	506	1220	<48.4	<1940	2.2	667	467	4.83	120	10.8	27.4	1.52	34.9	4.3	2.09	0.235	0.316	0.214	<0.042	<0.193	0.46	<1.22	0.001	0.276	0.7	0.049	0.5	<0.188	<0.063	0.47	<0.023	0.094	0.024	0.181	<0.015	0.14	<0.028	2.8	<0.138	0.034	<0.17	<0.048	<0.051	<0.064	<0.03	0.18
	WW3314BMt-8	975	792	4080	<53.1	<2190	1.9	1150	102	<1.34	130	8.39	14.9	<1.55	13.4	6.02	3.26	1.64	1.64	0.96	2.28	0.001	3.9	2.29	2.2	2.2	1.42	<0.065	0.54	0.065	0.5	0.088	0.54	<0.017	0.69	0.149	14.6	0.001	0.32	<0.13	0.247	<0.057	<0.05	0.111	0.79
	WW3314BMt-1	216	724	1830	<40.1	2550	2.19	811	370	4.07	118	9.1	45.5	<1.53	37.7	4.56	2.62	0.76	0.331	0.001	0.131	<0.152	1.15	<1.01	1.97	0.28	1.26	0.132	1.29	<0.147	0.05	0.73	<0.015

SUPPLEMENTARY MATERIAL E

FOR CHAPTER 6 – ~1760 MA MAGNETITE-BEARING PROTOLITHS IN THE OLYMPIC DAM DEPOSIT, SOUTH AUSTRALIA: IMPLICATIONS FOR ORE GENESIS AND REGIONAL METALLOGENY

APPENDIX A: LA-ICP-MS U-PB HEMATITE DATA

APPENDIX B: LA-ICP-MS TRACE ELEMENT DATA

ELECTRONIC APPENDIX A FOR CHAPTER 6

Mineral	Analysis	Mg	Al	Si	P	Ca	Sc	Ti	V	Cr	Mn	Co	Ni	Cu	Zn	Ga	As	Sr	Y	Zr	Nb	Mo	Sn	La	Ce	Pr	Nd	Sm	Eu	Gd	Tb	Dy	Ho	Er	Tm	Yb	Lu	Ta	W	Th	U	^{206}Pb	^{207}Pb	^{208}Pb	∑Pb	∑REE+Y
Magnetite																																														
	1	673	321	10700	46.7	1320	0.015	76.7	5.41	0.212	60	1.74	3.33	1.28	18.6	3.92	140	7.19	278	0.33	9.6	10.7	22.6	154	304	31.3	110	21.4	1.51	24.7	4.48	34.5	8.8	34.2	6.71	74	21	0.046	25.1	1.99	39.6	9.22	1.08	0.236	10.5	1108.6
	2	388	542	7200	29.7	1570	0.017	184	32.2	<0.13	44.5	1.45	4.35	0.523	12.2	2.9	83.3	8.32	219	0.76	26.8	4.03	7.57	126	252	25.7	93.4	19	1.19	21.5	3.75	27.9	6.83	22.7	3.44	34.8	8.95	0.584	15.8	1.08	20.5	4.47	0.528	0.195	5.19	866.2
	3	431	1080	11600	127	1550	<0.105	200	34.1	<0.85	199	4.8	6.57	2.95	28	5.57	571	9.27	241	0.97	40.2	18.2	9.5	169	368	33.3	110	20.3	1.95	23.9	4.18	30.5	8.07	29.7	5.85	54.4	16.7	0.529	81.2	6.85	26.6	7.12	0.753	0.983	8.86	1116.9
	4	583	260	10400	53.1	883	<0.116	31.2	0.107	<0.88	71.4	2.86	2.02	0.88	16.4	4.54	177	4.44	206	0.152	2.68	17.3	40.7	104	216	20.9	77.7	15.5	1.13	16.6	3.41	26.4	6.74	27.5	5.06	58	16.8	<0.01	23.9	1.07	22.3	5.07	0.459	0.131	5.66	801.7
	5	1510	489	16800	65.7	4330	0.132	37	6.43	<0.81	90.6	2.59	3.85	0.38	15.1	4.07	428	23.3	869	0.231	14.3	18.2	31.5	546	1090	106	363	67.2	5.54	79.9	14.7	106	27.2	104	20.3	222	62.9	0.029	74.4	3.9	128	30.1	3.17	0.452	33.8	3683.7
	6	119	222	4750	24	392	<0.11	9.42	3.01	<0.96	37.2	1.67	2.26	0.39	13.3	3.47	88.4	1.66	101	0.145	2.48	21.4	28.5	31.7	77.3	7.49	29.4	6.98	0.422	9.14	1.59	13.3	3.54	12.9	2.93	29.1	8.05	0.027	28.7	0.747	21.5	4.93	0.638	0.328	5.9	334.8
	7	1060	246	13500	58	3050	<0.142	10.4	0.111	<0.94	89.5	3.11	2.46	0.28	17.7	5.09	425	14.8	678	0.071	1.68	16.9	42	384	748	76.4	260	49.5	3.88	63.6	11	84.1	21.9	80.3	15.8	170	49.6	<0.006	67.2	1.67	97.8	24.1	2.9	0.244	27.2	2696.1
	8	1880	2280	10300	39	4270	<0.29	155	34.7	<1.07	99.3	2.33	7.14	1.03	39.1	6	284	20.8	250	1.59	51	7.33	6.98	262	604	49.1	162	26.9	3.21	27.7	5.28	36.8	7.98	26.3	4.77	40.5	10.7	1.04	44.4	1.59	42.3	10.9	1.22	0.484	12.6	1517.2
	9	404	710	8380	22.8	2550	<0.42	153	35.3	1.09	49.2	0.61	3.52	0.55	22.7	5.02	91.6	13.8	139	1.48	45.7	0.86	5.71	156	310	29.8	96	17.6	1.63	22.6	3.13	21.3	4.12	12.2	1.73	13.8	2.9	1.68	15.9	2.97	14.3	4.08	0.545	0.589	5.22	831.8
coarse-grained	10	1100	600	12600	101	5570	<0.39	138	28.9	<1.38	66.8	1.3	2.9	2.14	15.9	4.4	287	36.7	866	2.39	91.2	7.24	8.53	742	1470	141	475	82.7	7.5	102	17.3	117	28.7	103	20.5	198	52.2	1.03	63.3	13.5	96.9	25	2.7	2.71	30.4	4422.9
	11	468	382	5100	57.5	1960	<0.25	71.1	8.03	<0.69	46.1	1.95	4.34	1.65	23	2.6	191	9.59	413	0.66	12	10.9	10.2	182	415	38.2	138	26.7	1.99	34.6	6.28	48.1	12.5	46.6	9.32	108	31.1	<0.013	37	3.53	61.6	12.7	1.1	0.6	14.4	1511.4
	12	539	1050	8350	690	3150	<0.31	166	37.1	<0.97	57.8	1.04	4.06	0.69	15.6	6.11	106	15	168	3.77	50.3	2.34	4.9	215	493	42.7	137	20.8	2.72	20.7	2.71	23.5	5.28	18.2	3.03	27.5	6.8	0.96	34.3	10.8	28.6	5.7	0.737	0.526	6.96	1186.9
	13	664	990	8840	26.4	2930	<0.27	135	35	<0.7	57.8	1.04	4.1	0.59	17.5	4.36	118	15.3	177	1.54	45.7	2.4	4.16	195	402	37.7	121	20.4	2.45	22.2	3.59	24.4	5.06	17.3	2.72	23.6	5.2	1.23	24.3	2.9	22.2	5.61	0.523	0.563	6.69	1059.6
	14	489	770	6190	36	1430	<0.2	95.1	16.7	1.25	52.6	1.99	5.49	4.01	23.1	3.2	152	9.67	314	0.98	20.9	11.1	10.1	172	395	35.9	125	24.7	1.73	29	4.88	37.8	9.59	36.4	7.68	81.4	23.2	0.088	31.2	3.22	57.6	13.3	1.92	1.34	16.5	1298.3
	15	1010	3920	11300	374	2780	<0.6	280	24.8	NA	152	3.21	69.5	24.6	89.4	NA	166	18.6	113	0.88	30.4	0.052	8.82	411	813	92.1	326	44.5	5.78	32.5	3.86	19.7	3.77	12.1	2.03	16.1	4.49	1.05	15.1	3.96	3.86	1.03	0.187	0.472	1.68	1899.9
	16	2940	685	15000	<49.3	5150	<0.6	119	3.46	NA	122	3.55	38.8	<9.71	22.7	NA	358	20.3	583	0.503	8.29	0.123	46.3	209	454	51.7	199	46.4	4.22	63	11.1	78.7	18.4	67.6	13.1	117	34.2	<0.102	20.9	0.788	17.9	4.64	0.651	0.318	5.61	1950.4
	17	428	313	7290	<47.4	<1590	<0.56	36.7	0.982	NA	47.1	4.26	20.6	<9.37	14.4	NA	350	1.31	78.8	<0.152	1.13	0.067	37.7	19.3	43.8	5.37	21.4	4.96	0.367	7.53	1.4	9.95	2.54	10.2	2.03	19.4	5.73	<0.088	11.9	0.151	1.9	0.534	0.06	0.047	0.642	232.8
	18	974	3870	8320	<47	<1670	<0.56	273	25.3	NA	92.7	2.92	48.8	10.6	40.3	NA	135	4.87	114	0.429	165	0.045	17	42	93.3	11	42.1	10.1	0.854	12.1	2.17	14.9	3.57	12.9	2.57	21.8	6.57	0.821	11.8	0.204	4.36	1.36	0.161	0.09	1.61	389.9
	19	1470	295	6070	<43.7	2810	<0.51	32.9	<0.148	NA	57.5	3.6	25.6	<9.48	19	NA	71.4	4.06	190	<0.166	3.99	0.036	36.2	37.5	92.3	12	51.2	13.7	1.12	19.8	3.49	24.2	6.02	21.6	4.25	38.2	11	<0.078	7.79	0.14	4.92	1.26	0.14	0.022	1.42	526.4
	20	1080	242	6140	<47.6	<1740	<0.57	47.9	0.155	NA	61	3.99	24.2	<8.8	26	NA	114	5.45	195	0.229	6.57	0.049	35.9	39.8	97	12.1	52	13.3	1.08	19.7	3.66	25.2	6.19	22.1	4.32	37	11.5	<0.079	12.4	0.164	6.63	1.75	0.243	0.076	2.06	540.0
	1	1030	573	6600	41.6	2150	0.656	594	75.8	<0.23	60.1	1.99	4.8	0.273	28.7	2.58	1.03	5.61	3.54	1.62	15.9	0.11	8.74	34.7	65.1	7.07	22.6	2.7	0.257	1.3	0.183	0.988	0.174	0.519	0.115	1.11	0.336	0.87	0.042	1.52	1.84	0.515	0.129	0.318	0.963	140.7
	2	620	5320	16900	13.8	2000	0.18	204	44.8	1.14	128	1.1	5.69	1.66	43.1	9.02	6.54	9.59	5.4	0.79	29.7	0.38	4.87	8.99	26.2	3.29	11.7	1.52	0.204	1.52	0.134	0.66	0.182	0.73	0.111	1.36	0.453	1.47	0.27	1.22	2.43	2.06	0.426	0.726	3.21	62.5
	3	1000	8690	24600	17.4	3200	<0.138	395	64.7	<0.93	212	1.49	6.81	0.19	48.3	14.1	4.01	8.91	6.95	0.88	48.7	0.66	12	9.69	32.4	3.76	12.7	1.97	0.201	1.97	0.239	1.35	0.27	0.9	0.134	1.69	0.498	1.65	0.52	0.81	2.83	1.09	0.216	0.384	1.69	74.7
	4	158	1080	13100	23	1510	<0.103	113	38.7	<0.75	64.1	1.2	4.37	1.57	36.6	5.94	7.3	9.47	3.63	0.452	16.2	0.096	2.76	7.35	19.8	2.46	8.4	1.26	0.066	0.67	0.13	0.61	0.158	0.453	0.073	1.13	0.238	1.04	0.19	1.22	2.22	3.33	0.336	0.878	4.54	46.4
	5	294	1320	4200	21.1	1280	<0.28	171	31.8	<0.64	63.9	1.13	3.24	0.92	24	5.3	4.09	6.62	4.51	0.69	15.9	0.044	5.85	85.3	154	15.8	54.4	6.19	0.95	4.71	0.42	1.98	0.235	0.73	0.054	1.19	0.189	1.29	<0.056	12.1	2.39	0.997	0.241	1.22	2.46	330.7
	6	77.3	916	4900	13.1	1840	0.26	337	30.1	<0.56	54.6	0.71	4.41	1.05	26.9	4.4	3.75	5.13	11.7	1.48	18	10.4	3.62	16.5	70.5	7.3	27	4.04	0.71	2.4	0.413	2.75	0.47	1.85	0.395	2.27	0.415	0.533	67.3	3.84	516	112	11.6	1.59	125	148.7
	7	260	2320	7450	14.3	1780	<0.33	252	35.6	<0.82	67.5	1.96	4.21	7.33	31.7	7.26	2.82	7.8	4.38	0.63	14.4	0.17	5.16	69.5	150	16.1	48.7	5.21	0.45	2.93	0.288	0.9	0.192	0.6	0.061	0.72	0.257	1.33	0.28	3.03	1.55	0.999	0.254	0.815	2.07	300.3
	8	636	2070	8270	14.3	1810	0.39	166	35.7	0.9	82.5	0.93	3.34	0.9	29.4	7.09	3.83	7.29	5.47	0.78	22.8	0.086	4.84	10.9	28.5	3.24	11.1	1.73	0.188	0.91	0.193	0.92	0.187	0.59	0.101	1.71	0.377	1.57	0.094	0.8	2.17	1.32	0.267	0.615	2.21	66.1
	9	100	699	3110	14.6	1170	<0.3	148	32	<0.87	42.3	0.94	2.61	0.54	20.3	4.97	4.17	4.91	2.64	0.23	15.8	<0.127	2.78	27.8	80.9	5.54	17.8	1.59	0.226	1.27	0.138	0.59	0.108	0.36	0.065	0.95	0.221	0.43	0.11	1.58	1.55	0.654	0.139	0.284	1.08	140.2
	10	460	962	6560	15.9	2530	<0.29	194	31.4	<0.71	62.6	2.33	3.82	2.02	16.3	6.95	4.24	5.86	9.93	1.01	51.8	0.25	5.47	14	45.4	4.8	14.8	2.17	0.262	2.48	0.223	2.15	0.519	1.47	0.213	1.84	0.342	0.67	<0.001	4.71	15	3.66	0.879	1.09	5.62	100.6
fine-grained	11	293	1340	9510	8.65	2410	<0.29	190	45.7	0.85	58.7	1.08	3.28	<0.16	15.1	7.5	<1.74	5.53	7.43	0.93	27.3	0.051	5.39	12.3	32.5	3.64	14.3	2.89	0.216	1.6	0.301	1.35	0.33	1.14	0.163	1.53	0.394	0.69	0.074	1.19	2.09	0.865	0.097	0.153	1.11	80.1
	12	49.5	443	1160	9.87	601	<0.24	86.6	60.2	<0.73	48.3	0.607	4.07	0.46	42.4	3.29	7.43	7.07	7.15	0.76	174	69.8	17.6	83.7	203	14.3	38.8	3.46	0.78	1.59	0.186	1.47	0.346	1.11	0.264	2.52	0.503	0.622	802	20	844	165	16.9	2.6	185	359.2
	13	58.4	377	<750	10.3	354	<0.23	51.7	42.2	<0.72	46	0.94	3.42	0.94	27.6	2.39	4.46	4.46	3.18	0.372	50.2	76.8	4.93	47.2	108	7.17	17.7	1.59	0.243	0.65	0.093	0.6	0.156	0.69	0.106	1.32	0.238	0.385	580	5.75	393	73.2	8.01	0.983	82.2	188.9
	14	118	1280	4390	14	17300	<0.32	227	36.5	1.13	50.2	1.96	3.16	1.14	24	7.76	<2.07	22.2	13.7	0.41	19.6	1.72	7.52	10.1	34.4	3.93	11.5	1.66	0.156	1.11	0.136	1.12	0.364	0.7	0.104	0.79	0.319	0.79	7.72	1.01	7.25	2.3	0.249	0.268	2.82	80.1
	15	307	473	7480	<6.03	883	<0.107	149	35.6	1.47	50.2	2.72	4.93	5.25	27	3.21	3.7	4.7	4.55	0.77	373	24.2	9.42	13.1	33	3.28	11.8	1.11	0.238	0.69	0.16	0.85	0.211	0.66	0.176	1.43	0.411	3.72	110	11.9	161	35.2	3.52	2.39	41.1	71.7
	16	341	666	6590	<4.89	906	<0.092	134	35.8	0.54	48.6	1.43	5.37	1.55	26.8	2.65	3.49	4.09	4.17	0.578	139	9.84	7.24	8.14	22.3	2.23	7.06	0.9	0.131	0.77	0.108	0.78	0.187	0.71	0.212	1.42	0.211	3.06	95.4	5.84	109	24.5	2.52	0.826	27.9	49.3
	17	42	397	1870	5.29	868	<0.096	143	22	1.28	83.8	3.55	2.64	8.07	109	2.99	2.9	12.5	6.89	0.837	141	41.4	51	54.2	126	9.76	26.1	2.28	0.651	1.53	0.228	1.56	0.468	1.55	0.367	3.11	0.539	1.02	293	23	1110	247	25	3.15	275	235.2
	18	59.2	491	1590	26	4750	<0.071	126	20.8	<0.57	71.1	1.76	3.26	4.21	69.6	2.59	4.7	11	14.5	3.62	59.4	60.7	24.8	51	102	8.43	24.2	3.24	0.711	2.4	0.483	3.47	0.849	2.65	0.483	3.96	0.743	0.364	419	29.3	1070	145	13.6	0.494	159	219.1
	19	45.9	300	1250	<4.66	206	<0.086	106	32.5	1.57	54.6	1.43	3.97	1.88	24.8	1.91	3.63	4.78	5.48	1.47	236	45.7	15.9	28.9	59.3	4.34	12	1.33	0.177	0.84	0.161	1.35	0.279	1.2	0.251	2.49	0.566	1.32	277	30.4	711	141	15	3.08	159	118.7
	20	259	1680	15300	55.2	2630	0.182	393	43	0.86	64.3	0.8	3.85	0.49	25	9.48	3.69	9.56	10.5	1.31	36.4	0.08	6.81	45.9	121	11.6	32.9	4.78	0.668	2.68	0.385	2.24	0.472	1.26	0.26	1.99	0.482	1.45	<0.096	3.32	2.69	1.42	0.108	0.316	1.84	237.1
	1	36.2	409	578	14	<151	<0.093	136	31.4	<0.54	48.9	1.66	5	1.17	49	2.79	<1.17	3.73	3.21	0.714	194	44.2	12.5	23.8	70.4	7.78	25	1.83	0.285	1.37	0.127	0.64	0.198	0.504	0.11	0.84	0.183	2.47	549	3.84	117	27.9	2.87	0.626	31.4	136.3
	2	20.1	388	534	6.1	<126	<0.08	158	30.8	0.65	54.5	2.31	2.76	4.36	72.1	2.5	<1.06	5.4	3.12	1.25	573	72.7	64.2	11.1	25.4	1.92	5.67	0.6	0.097	0.39	0.096	0.572	0.189	0.69	0.134	1.68	0.332	1.97	425	36.6	543	113	11	3.06	127	52.0
Hematite	3	12.8	133	397	8.51	434	0.107	238	58.6	<0.63	26.7	1.58	6.49	2.99	19.6	3.84	18.6	11.1	6.95	0.95	278	92.3	38.2	14.7	41	2.74	10.1	1.26	0.24	1.16	0.226	1.84	0.49	1.59	0.401	3.5	0.553	2.78	624	25.7	798	154	14.7	4.74	173	86.8
	4	38.9	382	728	<4.98	399	<0.085	132	57.7	1.01	43.9	0.829	5.37	1.42	26.4	2.78	6.82	3.8	5.26	0.658	237	89.8	54.4	26.1	49.5	4.09	14.3	1.96	0.314	1.52	0.185	1.35	0.253	1.29	0.27	2.43	0.434	2.32	685	20.8	705	135	13.5	2.97	151	109.3
	5	97.8	524	834	19.2	166	<0.09	197	66.6	1.21	26.3	1.61	8.65	4.64	11.8	6.48	37	17.8	7.26	1.66	426	100	88.7	23.2	61.9	4.44	16.4	1.78	0.341	1.32	0.304	2.19	0.454	1.77	0.396	3.46	0.648	3.32	880	30.9	1220	278	26.8	6.21	311	125.9

ELECTRONIC APPENDIX B FOR CHAPTER 6

Calibrated using zircon reference materials

		Isotopic Ratios						Isotopic Dates						Isotope Concentrations					
	Analysis #	$^{207}Pb/^{235}U$	1σ	$^{206}Pb/^{238}U$	1σ	rho	Conc. %	$^{207}Pb/^{206}Pb$	1σ	$^{206}Pb/^{238}U$	1σ	$^{207}Pb/^{235}U$	1σ	^{204}Pb	^{206}Pb	^{207}Pb	^{208}Pb	^{232}Th	^{238}U
barse grained magnet	11aODMt-10	2.897	0.060	0.207	0.003	0.641	73	1653	38	1212	15	1381	16	3	26696	2694	852	6366	144930
	11aODMt-5	2.787	0.064	0.199	0.003	0.625	71	1656	44	1171	15	1352	17	7	11417	1163	348	2010	63218
	11aODMt-13	2.901	0.072	0.206	0.003	0.614	72	1666	47	1206	17	1382	19	0	13150	1358	412	2420	74547
	11aODMt-21	3.165	0.090	0.223	0.004	0.574	77	1679	54	1297	19	1449	22	6	13994	1450	657	5077	74189
	11aODMt-12	2.885	0.079	0.202	0.003	0.581	71	1685	52	1188	17	1378	21	0	9854	1023	205	2082	55457
	11aODMt-19	3.380	0.095	0.237	0.004	0.584	81	1685	53	1372	20	1500	22	2	9630	1007	467	2192	47807
	11aODMt-6	3.027	0.154	0.211	0.005	0.488	73	1696	97	1236	28	1415	39	11	1686	174	46	182	8834
	11aODMt-11	3.371	0.225	0.235	0.007	0.469	80	1704	127	1360	38	1498	52	2	1446	151	111	343	6557
	11aODMt-20	3.244	0.081	0.225	0.003	0.600	77	1705	47	1310	18	1468	19	0	9005	945	441	2866	44540
	11aODMt-11	2.793	0.089	0.194	0.003	0.546	67	1708	61	1141	18	1354	24	21	9015	938	283	1840	51407
	11aODMt-7	2.676	0.060	0.186	0.003	0.623	64	1709	43	1099	14	1322	17	6	13525	1423	231	2121	78523
	11aODMt-8	3.180	0.130	0.220	0.005	0.527	75	1716	78	1281	25	1452	32	0	5999	632	545	5190	31934
	11aODMt-16	3.067	0.103	0.211	0.004	0.553	72	1721	64	1235	21	1425	26	1	5295	562	89	151	29048
	11aODMt-8	3.168	0.125	0.218	0.004	0.518	74	1722	76	1271	24	1450	31	0	3130	329	112	487	15936
	11aODMt-22	3.189	0.095	0.219	0.004	0.573	74	1724	56	1277	20	1455	23	19	11723	1261	468	3673	64001
	11aODMt-9	2.938	0.119	0.201	0.004	0.522	68	1729	77	1183	23	1392	31	8	2643	282	123	950	14969
	11aODMt-3	3.323	0.083	0.227	0.004	0.621	76	1734	47	1319	19	1486	20	32	10290	1102	624	1665	53264
	11aODMt-9	3.756	0.093	0.256	0.004	0.598	85	1738	46	1471	19	1583	20	44	45438	4770	2529	22722	214726
	11aODMt-4	2.696	0.133	0.183	0.004	0.494	62	1743	94	1085	24	1327	37	0	2093	221	67	688	12190
	11aODMt-6	2.782	0.057	0.190	0.003	0.657	64	1744	39	1119	14	1351	15	0	16592	1779	299	1935	94435
	11aODMt-5	2.818	0.084	0.191	0.003	0.570	65	1746	57	1129	18	1360	22	26	7009	751	300	2717	41505
	11aODMt-4	3.183	0.085	0.215	0.003	0.601	71	1757	50	1256	18	1453	21	0	8216	887	119	407	43167
	11aODMt-23	3.887	0.197	0.262	0.007	0.504	85	1762	96	1498	34	1611	41	0	9673	1076	971	6109	44405
	11aODMt-8	3.225	0.090	0.217	0.004	0.582	72	1764	53	1265	19	1463	22	5	5830	631	674	3640	29654
	11aODMt-27	4.261	0.154	0.287	0.006	0.533	92	1766	68	1624	28	1686	30	45	21836	2430	1121	3303	95511
	11aODMt-2	3.188	0.117	0.214	0.004	0.537	71	1767	70	1250	22	1454	28	0	3590	384	221	407	19205
	11aODMt-2	3.059	0.175	0.205	0.006	0.498	68	1778	109	1200	31	1423	44	0	2154	234	132	1142	11920
	11aODMt-1	3.428	0.097	0.228	0.004	0.580	75	1780	54	1327	20	1511	22	1	4561	496	215	1162	21876
	11aODMt-1	3.442	0.211	0.229	0.007	0.492	75	1783	116	1330	36	1514	48	4	1810	195	159	149	9094
	11aODMt-7	2.991	0.083	0.198	0.003	0.576	65	1788	53	1167	17	1405	21	12	5650	611	175	406	31773
	11aODMt-2	3.157	0.096	0.209	0.004	0.588	68	1793	57	1223	20	1447	23	0	7770	863	336	1772	44709
	11aODMt-15	3.478	0.136	0.230	0.005	0.540	74	1794	74	1334	26	1522	31	19	7440	826	228	288	38955
	11aODMt-18	3.763	0.121	0.248	0.005	0.574	79	1799	60	1430	24	1585	26	13	8006	898	469	2132	39156
	11aODMt-7	3.469	0.104	0.229	0.004	0.586	74	1801	56	1327	21	1520	24	31	9348	1040	502	4423	48493
	Analysis #	$^{207}Pb/^{235}U$	1σ	$^{206}Pb/^{238}U$	1σ	rho	Conc. %	$^{207}Pb/^{206}Pb$	1σ	$^{206}Pb/^{238}U$	1σ	$^{207}Pb/^{235}U$	1σ	^{204}Pb	^{206}Pb	^{207}Pb	^{208}Pb	^{232}Th	^{238}U
Zircon stds's	stdGJ-1	0.794	0.011	0.097	0.001	0.719	100	594	32	595	6	594	6	9	23459	1402	238	6741	232674
	stdGJ-2	0.811	0.012	0.096	0.001	0.719	90	659	32	590	6	603	6	4	23581	1451	247	6544	233751
	stdGJ-3	0.797	0.012	0.097	0.001	0.715	103	583	34	599	6	595	7	2	25137	1496	271	7325	260858
	stdGJ-4	0.803	0.011	0.097	0.001	0.728	96	618	32	595	6	599	6	0	22812	1382	241	6445	228393
	Ples-1	0.407	0.006	0.055	0.001	0.697	96	358	36	345	4	347	5	0	35377	1898	985	50709	665097
	Ples-2	0.403	0.006	0.055	0.001	0.746	102	339	32	345	3	344	4	2	33009	1759	898	45221	580803
	Temora-1	0.508	0.012	0.066	0.001	0.516	92	449	53	413	5	417	8	14	5900	331	653	25897	87225
	Temora-2	0.496	0.009	0.065	0.001	0.619	90	447	43	403	5	409	6	0	14886	835	2354	106560	239975
	stdGJ-5	0.785	0.011	0.095	0.001	0.721	95	615	32	583	6	589	6	0	24566	1484	264	7139	254571
	stdGj-6	0.779	0.011	0.094	0.001	0.725	95	611	32	579	6	585	6	0	24073	1450	268	6931	242599
	stdGj-7	1.311	0.023	0.163	0.002	0.626	177	548	39	973	10	850	10	0	11756	689	117	2005	69304
	stdGJ-1	0.800	0.012	0.097	0.001	0.729	102	588	32	599	6	597	7	3	23413	1397	275	6812	240347
	stdGJ-2	0.816	0.012	0.098	0.001	0.731	99	610	32	604	6	606	7	0	23989	1446	244	6943	244858
	stdGJ-3	0.807	0.012	0.098	0.001	0.732	102	593	32	603	6	601	7	4	24193	1448	274	7029	246479
	stdGJ-4	0.801	0.012	0.097	0.001	0.734	99	601	32	596	6	597	7	11	23449	1409	275	6796	242198
	Ples-1	0.410	0.006	0.056	0.001	0.734	107	328	33	352	4	349	4	0	31814	1682	877	42892	558860
	Ples-2	0.410	0.006	0.056	0.001	0.736	104	339	33	351	4	349	4	0	30702	1633	789	40998	536274
	Temora-1	0.522	0.012	0.066	0.001	0.534	82	503	52	413	5	427	8	7	7117	406	1118	48436	108269
	Temora-2	0.521	0.013	0.066	0.001	0.531	82	504	56	411	5	426	9	9	8532	490	771	34393	140933
	stdGJ-5	0.840	0.014	0.097	0.001	0.660	86	696	36	599	6	619	8	0	23509	1465	196	6724	238262
	stdGJ-6	0.808	0.014	0.097	0.001	0.657	97	614	37	598	6	601	8	0	22740	1371	232	6512	235520
	stdGJ-7	0.810	0.014	0.098	0.001	0.659	101	598	37	604	6	602	8	0	22425	1343	226	6392	230337
	stdGJ-1	0.795	0.012	0.097	0.001	0.694	101	588	34	596	6	594	7	1	22066	1305	221	6343	220822
	stdGJ-2	0.780	0.012	0.096	0.001	0.695	105	564	34	591	6	585	7	8	22188	1297	214	6413	224858
	stdGJ-3	0.834	0.013	0.100	0.001	0.696	99	623	34	614	6	616	7	0	21458	1287	209	5990	209221
	stdGJ-4	0.825	0.013	0.099	0.001	0.678	99	616	35	609	6	611	7	0	21011	1256	227	5817	203586
	Ples-1	0.420	0.006	0.057	0.001	0.728	97	364	33	355	4	356	4	7	31926	1705	862	42458	555014
	Ples-2	0.413	0.006	0.056	0.001	0.741	101	348	32	352	4	351	4	0	32622	1742	953	45422	586231
	Temora-1	0.515	0.010	0.066	0.001	0.591	87	475	45	412	5	422	7	0	10388	586	1309	58507	162584
	Temora-2	0.521	0.009	0.068	0.001	0.652	97	439	38	424	4	426	6	16	15066	835	2391	96196	219689
	stdGJ-5	0.823	0.012	0.096	0.001	0.702	88	672	33	593	6	610	7	3	22143	1359	236	6318	224351
	stdGJ-6	0.812	0.014	0.097	0.001	0.638	94	635	38	595	6	603	8	0	21701	1312	229	6277	221487
	stdGJ-7	0.802	0.015	0.099	0.001	0.627	107	569	40	606	7	598	8	22	22133	1293	242	6453	226391

Calibrated using 'mixed U-Pb solution standard'

	Grain	Analysis #	$^{207}Pb/^{235}U$	1σ	$^{206}Pb/^{238}U$	1σ	rho	Conc. %	$^{207}Pb/^{206}Pb$	1σ	$^{206}Pb/^{238}U$	1σ	$^{207}Pb/^{235}U$	1σ	^{201}Hg	^{204}Pb	^{206}Pb	^{207}Pb	^{208}Pb	^{238}U
		1	6.635	0.314	0.438	0.008	0.376	130	1797	84	2342	35	2064	42	20	11	3378	366	174	9580
		2	9.504	0.426	0.371	0.008	0.455	75	2706	74	2033	36	2388	41	26	30	2180	399	518	7303
		3	5.095	0.158	0.343	0.005	0.487	108	1759	55	1903	25	1835	26	20	13	7164	760	302	25906
		4	5.949	0.220	0.398	0.006	0.418	122	1772	66	2160	28	1968	32	11	14	3987	426	188	12438
		5	6.051	0.494	0.407	0.009	0.275	125	1764	144	2201	42	1983	71	5	11	1874	199	99	5718
		6	4.923	0.384	0.331	0.007	0.275	104	1764	137	1843	34	1806	66	6	10	1885	200	47	7074
		7	5.308	0.191	0.351	0.005	0.433	108	1796	64	1938	26	1870	31	11	22	5025	543	103	17787
		8	4.545	0.162	0.312	0.005	0.425	101	1725	64	1751	23	1739	30	1	5	4881	508	139	19414
		9	4.646	0.195	0.316	0.005	0.375	101	1744	75	1769	24	1758	35	3	0	3831	402	170	15053
		10	4.375	0.350	0.301	0.007	0.285	98	1722	142	1696	34	1708	66	0	0	2527	262	113	10420
		11	4.793	0.193	0.315	0.005	0.424	98	1806	72	1765	26	1784	34	1	5	7383	802	151	29085
		12	5.167	0.161	0.350	0.005	0.482	110	1752	56	1933	25	1847	27	10	9	9038	953	343	32062
	Grain M	13	5.306	0.169	0.356	0.005	0.476	111	1768	57	1963	26	1870	27	14	25	10515	1118	335	36625
		14	5.051	0.148	0.335	0.005	0.478	104	1791	52	1861	23	1828	25	10	10	7808	840	306	28916
		15	4.272	0.222	0.289	0.005	0.319	93	1755	92	1634	24	1688	43	3	16	4243	447	136	18223
		16	4.771	0.139	0.321	0.005	0.481	102	1761	51	1796	22	1780	24	2	14	8174	865	318	31516
		17	3.964	0.241	0.269	0.005	0.298	88	1750	108	1534	25	1627	49	8	7	4050	426	109	18678
		18	4.960	0.163	0.336	0.005	0.437	107	1749	58	1868	23	1813	28	10	19	7071	743	188	26053
		19	5.692	0.183	0.384	0.005	0.445	119	1758	57	2094	26	1930	28	6	9	7441	786	372	24005
		20	4.351	0.191	0.302	0.005	0.353	100	1706	79	1701	23	1703	36	8	4	5403	554	58	22151
		21	4.586	0.225	0.309	0.005	0.331	99	1759	87	1736	25	1747	41	3	8	4567	482	23	18289
oarse grained magnet		22	5.554	0.511	0.372	0.008	0.227	115	1770	161	2039	37	1909	79	26	21	2165	230	142	7204
		23	4.694	0.254	0.316	0.005	0.310	100	1764	96	1768	26	1766	45	7	4	3882	411	279	15224
		24	4.933	0.324	0.328	0.006	0.287	103	1783	116	1830	30	1808	55	16	18	3509	375	151	13227
		25	4.732	0.150	0.324	0.005	0.454	104	1732	56	1808	23	1773	27	2	0	7599	790	181	29038
		1	5.739	0.164	0.386	0.006	0.507	119	1764	50	2103	26	1937	25	0	6	6568	696	149	21325
		2	6.352	0.352	0.429	0.008	0.329	131	1756	99	2301	35	2026	49	4	2	2535	267	66	7399
		3	6.090	0.200	0.410	0.006	0.469	126	1763	58	2214	29	1989	29	0	2	5662	599	110	17289
		5	5.413	0.264	0.365	0.007	0.369	114	1759	87	2006	31	1887	42	4	9	3905	412	152	13371
		6	5.932	0.350	0.397	0.007	0.319	122	1771	105	2156	34	1966	51	0	5	2478	263	91	7791
		7	7.918	1.125	0.559	0.018	0.232	171	1674	244	2862	76	2222	128	7	9	1187	119	7	2650
		8	6.898	0.289	0.396	0.007	0.407	105	2047	73	2151	31	2098	37	0	1	3495	433	303	11005
		9	4.746	0.194	0.315	0.005	0.388	99	1786	73	1766	24	1775	34	0	1	4175	448	374	16511
		10	6.077	0.356	0.411	0.008	0.344	127	1752	104	2221	38	1987	51	5	5	3583	377	86	10855
	Grains 5	11	4.997	0.129	0.339	0.005	0.546	107	1749	46	1880	23	1819	22	4	4	8108	852	261	29810
		12	5.077	0.104	0.341	0.005	0.659	107	1763	35	1894	22	1832	17	0	5	14926	1582	666	54396
		13	5.605	0.154	0.374	0.005	0.525	115	1777	48	2049	25	1917	24	0	2	6919	739	213	23003
		17	10.945	0.511	0.475	0.009	0.411	99	2529	77	2505	40	2519	43	6	17	2047	336	368	5359
		18	4.907	0.148	0.329	0.005	0.484	104	1768	54	1834	23	1803	26	10	10	5947	632	256	22453
		19	5.718	0.097	0.385	0.005	0.771	119	1762	28	2099	23	1934	15	1	21	24126	2556	1314	77842
		20	6.925	0.165	0.477	0.007	0.584	146	1720	42	2514	29	2102	21	11	11	9497	983	476	24713
		21	5.639	0.254	0.375	0.007	0.393	115	1786	81	2051	31	1922	39	0	12	4789	514	206	15858
		22	4.833	0.094	0.323	0.004	0.685	101	1777	33	1802	21	1791	16	0	8	19769	2112	907	75957
		23	5.227	0.202	0.354	0.006	0.423	112	1748	69	1956	28	1857	33	0	7	5706	600	212	19945
		1	12.903	0.733	0.879	0.018	0.367	234	1740	100	4066	63	2673	54	0	0	3003	315	562	4269
		2	29.693	2.335	1.663	0.052	0.400	302	2091	129	6314	127	3477	77	0	10	1486	189	437	1116
		3	48.399	2.894	2.488	0.077	0.521	359	2240	94	8054	143	3960	59	13	20	2230	310	763	1119
		4	24.869	1.020	1.182	0.024	0.500	212	2375	67	5031	72	3303	40	7	19	3110	467	2142	3283
		5	41.933	2.352	2.103	0.059	0.497	320	2283	89	7300	122	3818	56	12	26	2111	301	715	1252
		6	36.990	1.996	1.785	0.047	0.490	281	2349	86	6603	109	3693	53	5	16	2103	311	615	1469
Fine grained magnetite		7	38.015	3.343	1.830	0.078	0.484	285	2354	139	6706	177	3720	87	8	12	1907	283	907	1299
		8	6.657	2.047	0.394	0.020	0.167	108	1992	468	2143	94	2067	271	0	0	1321	159	187	4173
		9	35.110	2.045	1.586	0.045	0.489	249	2462	93	6125	113	3642	58	7	9	1816	287	709	1426
		10	15.296	0.706	0.860	0.017	0.440	192	2084	79	4001	61	2834	44	1	16	3070	390	895	4443
		11	34.651	1.580	1.633	0.039	0.524	261	2389	73	6242	96	3629	45	0	21	2926	444	1047	2229
		12	43.032	3.915	2.062	0.084	0.450	305	2362	141	7213	178	3843	90	0	11	2350	351	691	1417
		13	57.801	3.387	2.489	0.081	0.557	317	2542	88	8055	150	4137	58	3	18	1768	294	620	883
		1	3.986	0.052	0.301	0.004	0.965	109	1549	20	1696	19	1631	11	37	49	305581	28989	7667	1271916
		2	4.415	0.058	0.330	0.004	0.957	117	1569	20	1838	20	1715	11	23	88	190693	18278	6799	723760
		3	3.856	0.051	0.304	0.004	0.960	116	1469	20	1710	19	1605	11	23	29	161597	14694	2482	665850
		4	4.346	0.062	0.320	0.004	0.892	112	1596	23	1789	20	1702	12	46	49	76974	7488	3796	300963
		5	3.989	0.053	0.303	0.004	0.953	111	1538	20	1706	19	1632	11	14	47	200938	18949	5084	829391
		6	4.060	0.057	0.309	0.004	0.898	113	1535	23	1735	19	1646	12	16	35	114991	10823	3694	465340
		7	4.498	0.060	0.330	0.004	0.945	115	1603	20	1838	20	1731	11	28	54	135374	13215	5186	512583
Hematite Lathes		8	4.358	0.058	0.322	0.004	0.943	113	1589	21	1800	20	1705	11	17	42	129166	12515	3942	500844
		9	4.637	0.062	0.337	0.004	0.943	115	1622	21	1871	20	1756	11	36	56	129350	12756	4248	479553
		10	3.535	0.049	0.280	0.004	0.920	109	1460	22	1590	18	1535	11	15	55	186457	16868	3909	831471
		11	4.819	0.068	0.347	0.004	0.895	117	1639	22	1919	21	1788	12	47	55	55104	5485	2447	198268
		12	3.571	0.047	0.282	0.004	0.964	110	1462	20	1603	18	1543	10	21	49	263031	23817	4503	1161416
		13	4.019	0.054	0.304	0.004	0.942	110	1548	21	1709	19	1638	11	22	50	126868	12023	2952	520705
		14	4.013	0.053	0.314	0.004	0.951	119	1480	21	1762	19	1637	11	21	26	165414	15120	2653	655619
		15	4.559	0.059	0.342	0.004	0.968	122	1559	20	1898	21	1742	11	20	52	310741	29623	7816	1130195
		16	4.589	0.061	0.345	0.004	0.952	123	1555	20	1912	21	1747	11	22	37	160892	15307	3406	579912
		17	5.378	0.072	0.363	0.005	0.947	113	1758	20	1995	22	1881	11	21	139	140743	14938	7436	482741
		18	4.206	0.058	0.311	0.004	0.924	110	1589	22	1745	19	1675	11	10	96	165334	16010	5485	661370
		MagSTD1	34.176	0.436	0.286	0.004	0.984	32.2	5035	14	1622	18	3615	13	0	4612	83341	71150	174094	364126
		MagSTD2	34.176	0.435	0.286	0.004	0.986	32.2	5035	15	1622	18	3615	13	0	4558	82943	70952	173177	360221
		Mag STD3	34.176	0.439	0.286	0.004	0.981	32.2	5035	15	1622	18	3615	13	3	4713	85933	73141	178971	376350
		Mag STD4	34.176	0.435	0.286	0.004	0.983	32.2	5035	15	1622	18	3615	13	2	4591	83338	70998	173568	360596
	Solution std	Mag STD5	34.238	0.433	0.287	0.004	0.988	32.3	5036	14	1624	18	3617	12	0	4792	87065	74499	181624	377640
		Mag STD6	34.040	0.432	0.285	0.004	0.984	32.1	5034	15	1618	18	3611	13	0	4738	86022	73235	178954	373799
		Mag STD7	34.245	0.437	0.287	0.004	0.980	32.3	5036	15	1624	18	3617	13	0	4769	86186	73235	179672	371945
		Hm-Sol-STD1	34.176	0.436	0.286	0.004	0.986	32.2	5035	14	1622	18	3615	13	0	4698	85153	72848	178099	372902
		Hm-Sol-STD2	34.176	0.435	0.286	0.004	0.986	32.2	5035	15	1622	18	3615	13	0	4645	84315	72096	176208	366337

SUPPLEMENTARY MATERIAL F

FOR CHAPTER 7 – ZIRCON AT THE NANOSCALE RECORDS METASOMATIC PROCESSES LEADING TO LARGE MAGMATIC–HYDROTHERMAL ORE SYSTEMS

APPENDIX A: METHODOLOGY

APPENDIX B: LA-ICP-MS TRACE ELEMENT DATA

APPENDIX C: SUPPLEMENTARY FIGURES

ELECTRONIC APPENDIX A FOR CHAPTER 7

Supplementary A—Methodology

A1. LA-ICP-MS U-Pb analysis
A2. LA-ICP-MS geochemical analysis and PCA
A3. EPMA

A1. LA-ICP-MS U-Pb analysis

All reported LA-ICP-MS data was obtained from grains within one-inch-diameter polished blocks. Data was collected at Adelaide Microscopy, The University of Adelaide, using a RESOlution-LR excimer laser microprobe (Australian Scientific Instruments) coupled to an Agilent 7900x Quadrupole ICP-MS. This combination of laser and ICP-MS offers good spatial resolution (~29 µm) coupled with sub-ppm sensitivity for most trace elements. The laser has a large format S155 two-volume ablation cell designed by Laurin Technic Pty. Laser ablation was performed in an atmosphere of UHP He (0.38 l/min). The aerosol was mixed with Ar carrier gas (1.05 l/min) immediately above the ablation site before being transported to the ICP-MS via a 'squid' pulse-homogenizing device (Laurin Technic Pty). Uranium-Pb zircon analyses were undertaken using a spot diameter of 29 µm, resulting in crater depths generally between 10-15 µm over the 30 s ablation time. The ICP-MS was optimized daily using NIST612 reference glass to maximize sensitivity on isotopes of the mass range of interest, while keeping production of molecular oxide species (i.e., $^{232}Th^{16}O/^{232}Th$) and doubly charged ion species (i.e., $^{140}Ce^{2+}/^{140}Ce^{+}$) as low as possible, and generally at <0.2 %. The plasma conditions were tuned for a robust plasma with U/Th ratio of 1.00-1.05. The GJ-1 zircon (Jackson et al., 2004) was used as the primary reference material, while 91500 (Wiedenbeck et al., 1995) and Plešovice (Sláma et al., 2008) were analysed as secondary reference materials. Reference material and unknows were analyzed using a pulse repetition rate of 5 Hz and a constant fluence of 2.5 J/cm^2 within a single analytical session. Data collection consisted of a 30 second gas blank followed by 30 seconds of data acquisition with the laser firing. Isotopes measured were ^{204}Pb, ^{206}Pb, ^{207}Pb, ^{208}Pb, ^{232}Th, and ^{238}U with dwell times of 20, 50, 50, 10, 10, and 50 ms, respectively; ^{235}U was calculated using the $^{238}U/^{235}U$ ratio of 137.88 (Steiger and Jäger, 1977). Mass ^{204}Pb was measured as a monitor for Pb_c content, but due to the unresolvable isobaric interference of ^{204}Hg on ^{204}Pb, Pb_c corrections

were not considered or conducted using ^{204}Pb. Data reduction was performed and presented using Iolite™ and GLITTER in combination with Isoplot 3.75 (Ludwig, 2012).

References

Jackson, S.E., Pearson, N.J., Belousova, E.A, Griffin, W.L., 2004. The application of laser ablation-inductively coupled plasma-mass spectrometry (LA-ICP-MS) to in situ U-Pb geochronology. Chem. Geol. 211, 47-69.

Ludwig, K.R.A., 2012. Isoplot/Ex rev. 4.1: A Geochronological Toolkit for Microsoft Excel; Berkeley Geochronology Centre Special Publication No.5, 75; Berkeley Geochronology Centre: Berkeley, California.

Paton, C., Hellstrom, J., Paul, P., Woodhead, J., Hergt, J., 2011. Iolite: Freeware for the visualisation and processing of mass spectrometric data. J. Anal. Atom. Spectrom. 26, 2508-2518.

Sláma, J., Košler, J., Condon, D.J., Crowley, J.L., Gerdes, A., Hanchar, J.M., Horstwood, M.S.A., Morris, G.A., Nasdala, L., Norberg, N., Schaltegger, U., Schoene, B., Tubrett, M.N., Whitehouse, M.J., 2008. Plešovice zircon - A new natural reference material for U–Pb and Hf isotopic microanalysis. Chem. Geol. 249, 1-35.

Steiger, R.H., Jäger, E., 1977. Subcommission on geochronology: Convention on the use of decay constants in geo- and cosmochronology. Earth Plan. Sci. Lett. 36, 359-362.

Wiedenbeck, M., Alle, P., Corfu, F., Griffin W.L., Meier M., Oberli F., von Quadt A., Roddick J.C., Spiegel W., 1995. 3 natural zircon standards for U-Th-Pb, Lu-Hf, trace-element and REE analyses. Geostandards Newsletter 19, 1–23.

A2. LA-ICP-MS geochemical analysis and PCA

LA-ICP-MS spot analysis

LA-ICP-MS spot analysis of zircon was conducted using the same instrument and configurations as previously indicated in A1. A laser spot size diameter of 19 µm was employed to target areas of interest within zircon, using pulse repetition rates of 5 Hz and fluence of 3.5 J/cm^2. Prior to each spot analysis, the targeted areas were pre-ablated to avoid surface contamination. Acquisition time comprised a 30 s measurement of the background and 30 s acquisition of the signal while the laser ablates. Analytical standards were run before and after each individual set of ~25 zircon unknowns using NIST-610 as the primary standard, and GSD-1G as the secondary standard. In addition, Plesovice was also analyzed between batches for quality control.

Data reduction was performed in Glitter using stoichiometric concentrations of Si in zircon as the internal standard element. Minimum detection limits (mdl) indicated by Glitter are individually calculated for each element in each spot analysis. A suite of 33 elements, including three Pb isotopes, was measured. Depending on the required mdl, different dwell times were employed, using (i) 0.005 s for: ^{27}Al, ^{29}Si, ^{31}P and ^{91}Zr; (ii) 0.01 s for ^{43}Ca and ^{89}Y; and (iii) 0.02 s for: ^{45}Sc, ^{49}Ti, ^{55}Mn, ^{57}Fe, ^{89}Y, ^{93}Nb, ^{118}Sn, ^{139}La, ^{140}Ce, ^{141}Pr, ^{146}Nd, ^{147}Sm, ^{153}Eu, ^{157}Gd, ^{159}Tb, ^{163}Dy, ^{165}Ho, ^{166}Er, ^{169}Tm, ^{172}Yb, ^{175}Lu, ^{178}Hf, ^{181}Ta, ^{206}Pb, ^{207}Pb, ^{208}Pb, ^{232}Th and ^{238}U. Two polyatomic interferences (^{17}O^{28}Si, ^{16}O^{29}Si) on ^{45}Sc preclude its quantification at low concentrations and is therefore used qualitatively for monitoring elevated Sc contents.

LA-ICP-MS isotope mapping

Isotope mapping was conducted using the same instrumentation as described for spot analysis. Data acquisition involved ablating sets of parallel line rasters in a rectangular grid across the area of interest using a beam size of 7 µm (square profile) and a scan speed of 7 µm/s. Line spacing was kept at a constant 7 µm to match the size of the laser beam used. The effect of redeposition during mapping was minimized by pre-ablating each line immediately prior to its analysis. A laser repetition rate of 10 Hz was used with a fluence of ~3.5/Jcm^{-2}. Such conditions meant the depth of ablation during mapping was around <5 µm. Isotopes measured were ^{206}Pb, ^{208}Pb, ^{232}Th, ^{238}U and the REE'S Y, Ce, Gd, Dy, Er, Yb, with dwell times of 30 ms for U, Th and Pb isotopes and 5 ms for REE's. A 30 s background was acquired at the start of every raster, and a delay of 15 s was applied after each line to allow for sample washout.

Images were compiled and processed using Iolite™. The presented map in figure 2 ran over a ~4-hour session, in which significant instrument drift could occur. To correct for this, the average background was subtracted from its corresponding signal from the ablated area for each raster and element. NIST610 was analyzed immediately before and after the run to assess drift, and if present, was corrected for by applying a linear fit between the two sets of reference materials. The rasters were then compiled into a 2-D image displaying combined background-subtracted and drift corrected intensities for each element.

Principal component analysis

PCA was undertaken using singular value decomposition of centred logratio (clr) transformed data. Such transformation was required to respect its simplicial geometry. The above-mentioned procedures were performed in the R package 'compositions'.

A3. EPMA

Spot Analysis Methodology

Operating conditions and Processing

Quantitative compositions of zircon were determined using a Cameca SX-Five electron probe microanalyzer (EPMA), equipped with 5 tuneable wavelength-dispersive spectrometers, located at Adelaide Microscopy. The instrument is running PeakSite v6.2 software for microscope operation, and Probe for EPMA software (distributed by Probe Software Inc.) for all data acquisition and processing. Combined operating conditions were utilized in which for each individual spot, major and mobile elements were analysed first at 17 kV/20 nA, then the beam subsequently changed to 17 kV/100 nA for the remaining analysis of low-level elements. Due to the need for spatial resolution, all analyses were done with a focused beam.

The full list of elements analysed along with primary and interference standards are presented in Tables 1 and 2. Oxygen was calculated by stoichiometry, assuming that all Fe was Fe^{3+}. Matrix corrections of Armstrong-Love/Scott φ(ρz) (Armstrong, 1988) and Henke MACs were used for data reduction.

All elements were acquired using a traditional 2-point linear, excluding F Kα which was acquired using a multipoint fit. Following traditional 2-point background analysis, the "shared" background fit option in Probe for EPMA was used across the list of elements. For Nb, a traditional 2-point linear fit was used. Other elements, including those with more complex regions of the spectrum such as in the case some of the REE, multipoint or "shared" fits were used to accurately model the background continuum and/or avoid off peak interferences (Goemann et al., 2016, Goemann et al., 2017, Goemann and Donovan, 2017).

Due to the need for a focused beam, beam damage and alkali element migration (e.g., Na, F, Cl) in zircon analyses were monitored and minimized via analysis of these elements first on the detector, plus application of the Time Dependent Intensity (TDI) correction feature of Probe for EPMA (e.g., Donovan and Rowe, 2005). Using this method, the decay of x-ray counts over time is measured and modelled to return a t=0 intercept, and from this a concentration is calculated.

Mapping Methodology

Operating conditions and processing

Zircon grains were both qualitatively and quantitatively X-ray mapped utilising the same instrument at the University of Adelaide. Beam conditions were set at an accelerating voltage of 15 kV and 200 nA, utilising a focussed beam. Mapped area dimensions ranged from 100-200 µm in both

x and y axes, at a pixel resolution of 1 µm. Pixel dwell time in all maps was set to 2000 ms, and ranged in acquisition time from ~2-24 hours depending on grain size. Calibration and quantitative data reduction of maps was carried out in Probe for EPMA, distributed by Probe Software Inc. Colour images of the maps were processed in Surfer 10® distributed by Golden Software. Calibration was performed on certified natural and synthetic standards from Astimex Ltd.

Zircon grains from LCD13, and LCD17 were quantitatively mapped via measurement of Cl Kα on four separate spectrometers (3 LPET and 1 PET crystal), and Fe Kα measured on a single LLIF crystal.

Map quantification was conducted in CalcImage, a module of Probe for EPMA. Background subtraction on the maps was performed via the Mean Atomic Number (MAN) background correction (Donovan and Tingle, 1996; Donovan et al., 2016), omitting the need for a second pass "off-peak" map acquisition. Following this each pixel goes through full φ(ρz) corrected quantification identical to traditional spot analysis. Major/minor elements were not acquired in the maps, and thus for accurate ZAF correction and quantification, specified concentrations as acquired from spot analysis were entered into the map quantification procedure for elements such as Zr, Si, Hf etc.

References

Armstrong, J.T., 1988. Quantitative analysis of silicate and oxide minerals: Comparison of Monte Carlo, ZAF, and φ(ρz) procedures. Microbeam Analysis, D.E. Newbury, ed., San Francisco Press, 239-246.

Donovan, J.J., Tingle, T.N., 1996. An Improved Mean Atomic Number Background Correction for Quantitative Microanalysis. Microscopy and Microanalysis, 1, pp. 1-7.

Donovan, J.J., Rowe, M., 2005. Techniques for Improving Quantitative Analysis of Mineral Glasses. Geochimica et Cosmochimica Acta, Goldschmidt abstracts.

Donovan, J.J., Singer, J.W., Armstrong, J.T., 2016. A new EPMA method for fast trace element analysis in simple matrices. American Mineralogist, 101 (8), 1839-1853.

Goemann, K., Donovan, J.J., 2017. Electron probe microanalysis of complex natural sulphides using shared background measurements. In: AMAS 2017, 14th Biennial Australian Microbeam Analysis Symposium, 6-10 February 2017, Brisbane, Australia. *The Australian Microscopy & Micronalysis Society***,** 61-62. ISBN 978-0-9580408-6-0.

Goemann, K., Donovan, J.J., Feig, S.T., Thompson, J., 2016. "Sharing" Background Measurements in Wavelength Dispersive Electron Probe Microanalysis. In: Micronalysis Society - Topical Conference on Electron-Probe Microanalysis, Program Guide with Abstracts, 16-19 May 2016, Madison, WI, USA. *The Microanalysis Society* 28-29. ISBN 978-1-5323-0217-6.

Goemann, K., Donovan, J.J., Feig, S.T., Thompson, J., 2017. Shared backgrounds in wavelength-dispersive electron probe microanalysis. In: Book of Tutorials and Abstracts, 15th European Workshop on Modern Developments and Applications in Microbeam Analysis, 7th Meeting of the International Union of Microbeam Analysis Societies, 7-11 May 2017, Konstanz, Germany. *European Microbeam Analysis Society eV***,** 378-379. ISBN 978-90-8827-693-0.

Table S1. EPMA setup for spot analysis of zircon

Element and Line	Diffracting Crystal (Sp#)	Background type/fit	kV/nA/spot size(μm)	Peak Count Time	Bkgd Count Times		# bkgd points acquired (Lo/Hi)	Standards*		Overlapping element and order/interference correction standard			
					Lo	Hi		Primary Standard	Interference Standards	Interfering line	Int. std	Interfering line	Int. std
Zr Lα	LPET (1)	Shared	17/20/0	15	10	10	1/1	728					
Ca Kα	LPET (1)	Shared	17/20/0	20	20	20	1/1	535					
K Kα	LPET (1)	Shared	17/100/0	40	20	20	1/1	541					
P Kα	LPET (1)	Shared	17/100/0	40	20	20	1/1	504					
Y Lα	LPET (1)	Shared	17/100/0	120	60	60	1/1	1214					
U Mβ	LPET (1)	Shared	17/100/0	200	100	100	1/1	631					
Ce Lα	LPET (1)	Shared	17/100/0	100	50	50	1/1	1201					
Ti Kα	LPET (1)	Shared	17/100/0	100	50	50	1/1	540					
F Kα	PC0 (2)	Multipoint	17/20/0	20	10	10	2/2	505	502,723	Fe Lα (I)	502	Zr Lα1 (III)	723
Fe Kα	LLIF (3)	Shared	17/20/0	40	20	20	1/1	502					
Hf Lα	LLIF (3)	Shared	17/20/0	20	10	10	1/1	723					
Sc Kα	LLIF (3)	Shared	17/100/0	40	20	20	1/1	619					
Mn Kα	LLIF (3)	Shared	15/20/0	40	20	20	1/1	539					
Lu Lα	LLIF (3)	Shared	17/100/0	40	20	20	1/1	1213					
Yb Lα	LLIF (3)	Shared	17/100/0	40	20	20	1/1	1212					
Er Lα	LLIF (3)	Shared	17/100/0	40	20	20	3/2	1210					
Gd Lβ	LLIF (3)	Shared	17/100/0	40	20	20	1/1	1206					
Dy Lα	LLIF (3)	Shared	17/100/0	40	20	20	1/2	1208					
Tb Lα	LLIF (3)	Shared	17/100/0	40	20	20	1/1	1207					
Sm Lβ	LLIF (3)	Shared	17/100/0	40	20	20	1/1	1204					
Eu Lα	LLIF (3)	Shared	17/100/0	40	20	20	1/1	1205					
Nd Lβ	LLIF (3)	Shared	17/100/0	40	20	20	1/1	1203					
Pr Lβ	LLIF (3)	Shared	17/100/0	40	20	20	1/1	1202					
Tm Lα	LLIF (3)	Shared	17/100/0	40	20	20	1/2	1211					
Ho Lβ	LLIF (3)	Shared	17/100/0	40	20	20	1/1	1209					
Na Kα	TAP (4)	Shared	17/20/0	20	20	20	7/0	501					
Si Kα	TAP (4)	Shared	17/20/0	15	10	10	1/1	728					
Al Kα	TAP (4)	Shared	15/20/0	20	20	20	1/1	501					
Mg Kα	TAP (4)	Shared	15/20/0	30	20	20	1/1	502					
Cl Kα	LPET (5)	Shared	17/20/0	60	30	30	1/1	545					
La Lα	LPET (5)	Shared	17/100/0	100	50	50	1/1	1200					
Th Mα	LPET (5)	Shared	17/100/0	150	75	75	1/1	629					
Pb Mβ	LPET (5)	Shared	17/100/0	200	100	100	3/1	627					
Nb Lα	LPET (5)	2-pt	17/100/0	100	50	50	1/1	616	723	Zr Lβ4 (I)	723		

* Standard # refers to internal database. Full list of standards in Table 2

Table S2. Standard information

Reference #	Mineral composition	Natural/Synthetic	Manufacturer
501	Albite	Natural	Astimex
502	Almandine garnet	Natural	Astimex
504	Apatite	Natural	Astimex
535	Plagioclase	Natural	Astimex
539	Rhodonite	Natural	Astimex
540	Rutile	Natural	Astimex
541	Sanidine	Natural	Astimex
545	Tugtupite	Natural	Astimex
616	Niobium	Synthetic	Astimex
619	Scandium	Natural	P&H and Associates
627	K227 (Pb silicate)	Synthetic	NIST
629	Huttonite	Natural	DAS
631	UO2	Synthetic	DAS
723	Zircon	Natural	GJ Zircon standard
728	Zircon	Natural	91500 zircon standard
1200	LaPO4	Synthetic	Cherniak phosphate
1201	CePO4	Synthetic	Cherniak phosphate
1202	PrPO4	Synthetic	Cherniak phosphate
1203	NdPO4	Synthetic	Cherniak phosphate
1204	SmPO4	Synthetic	Cherniak phosphate
1205	EuPO4	Synthetic	Cherniak phosphate
1206	GdPO4	Synthetic	Cherniak phosphate
1207	TbPO4	Synthetic	Cherniak phosphate
1208	DyPO4	Synthetic	Cherniak phosphate
1209	HoPO4	Synthetic	Cherniak phosphate
1210	ErPO4	Synthetic	Cherniak phosphate
1211	TmPO4	Synthetic	Cherniak phosphate
1212	YbPO4	Synthetic	Cherniak phosphate
1213	LuPO4	Synthetic	Cherniak phosphate
1214	YPO4	Synthetic	Cherniak phosphate

Minor element substitution in zircon and formula calculation routine

Background

Aside from direct, charge-balanced substitution of Hf^{4+}, U^{4+}, Th^{4+} for Zr^{4+}, the most common minor elements in zircon are Y and HREE, which can readily substitute for Zr due to the similarity in ionic size between (Y^{3+},$HREE^{3+}$) and Zr^{4+}. Typically, this substitution correlates with incorporation of P into the Si site (so-called 'xenotime substitution'; [$(Y,REE)^{3+} + P^{5+} \leftrightarrow Zr^{4+} + Si^{4+}$]) to maintain charge balance (Hoskin and Schaltegger, 2003). Empirical observation suggests, however, that more complex substitutions may also operate (see below).

Pentavalent Nb and Ta are considered to preferentially substitute into the Zr site (Akhtar and Waseem, 2001).

Although most researchers have reached a consensus on the main mechanisms of substitution and the likely sites for each substituent, there exists some lack of equivocality, notably with respect to the potential role of interstitial sites, and even the charge of some substituted ions, e.g., Fe (Pérez-Soba et al., 2007). The routines used here are adapted from those used for hydrogarnet and are based on a logical, sequential approach but inevitably, also several of assumptions.

Volatile content in zircon is often invoked from low EPMA totals, either as substituted OH^- or molecular H_2O within amorphous domains within the zircon structure. A theoretical background and empirical evidence for OH^- substitution into zircon is well documented (Frondel, 1953; Caruba et al., 1985; Nasdala et al., 2009; Trail et al., 2011; de Hoog et al., 2014). Experimental evidence shows that $[(OH,F)_4]^{4-}$ can occupy more than half the $[SiO_4]^{4-}$ positions in zircon (Caruba et al., 1985). Unequivocal evidence for halogen substitution in natural samples remains less well documented, even if low levels of substitution are reported (e.g., Zeng et al., 2017).

Formula calculation routine

The zircon formulae, in terms of atoms-per-formula-unit (apfu), was calculated based on full occupancy of the tetrahedral ^{IV}B, *with* $\sum B \geq 1$, and variable occupancy of the dodecahedral ^{VIII}A site, with $A+B=2$. Rarely, $\sum$(Si, P, Ti) can exceed 1 apfu in the *B*-site, which is therefore compensated by <1 apfu in the *A*-site, and distribution of Al over both sites. The allocation of Fe exclusively into the *A*-site bears on the amount of water (as OH^-) incorporated by the hydrogarnet-type substitution. Based on average oxide totals (dry; no F or Cl included) across the dataset of ~99.2 wt%, the correction procedure considering hydrogarnet-type substitution and REY+Sc incorporation, as explained below, is considered to best represent our data, even if some assumptions are inevitably involved. Considering these substitutions, the corrected totals, including water moderately increase, approaching 100% (average totals of ~99.6 wt%).

Limited, monovalent cation incorporation (Me^+: Na, K) is considered within interstitial positions (*i*) in distorted octahedral coordination, or within a 4-fold coordinated site (Finch and Hanchar, 2003). Cations were assigned following the general formula $iABO_4$, although also permitting vacancies in oxygen sites and incorporation of halogens (F, Cl) or OH^--groups, with:

i: Na^+, K^+ (and potentially also Li^+);

A: Mg^{2+}, Al^{3+}*, Ca^{2+}, Sc^{3+}, Mn^{2+}, Fe^{3+}, Y^{3+}, Zr^{4+}, Nb^{5+}, REE^{3+}, Hf^{4+}, Pb^{2+}, Th^{4+} and U^{4+};

B: Al^{3+*}, Si^{4+}, P^{5+}, Ti^{4+}, Si*, with Si* representing missing Si due to hydrogarnet-type substitution: $SiO_4^{4-} \leftrightarrow 4(F, Cl, OH)^-$ (see Frondel and Collette, 1957; Botis et al., 2013).

Molecular proportions of metals were obtained by dividing the measured oxides by their molecular weights and multiplying by the number of cations per oxide molecule; molecular proportions of halogens (F, Cl) were obtained by dividing the measured concentrations by their respective atomic weights.

Titanium has been experimentally shown to substitute Si in the *B*-site (Tailby et al., 2011). Simulation modelling has indicated that Al may be preferentially present in the *B*-site (Akhtar and Waseem, 2001). The amount of Si missing by the hydrogarnet substitution is calculated from the difference between cations allocated in the *A*- and *B*-sites excluding Al; if ∑B>∑A then Al is assigned to the *A*-site so that ∑B=∑A. However, after this step, if ∑B+Al is still lower than ∑A, the difference between ∑B+Al and ∑A is considered to represent substituted Si by the hydrogarnet substitution (Si*). Following this step, a normalization factor is calculated: $f_n=2/(\sum A+\sum B)$ and applied, after which the normalized cations, in apfu, are distributed between the different sites, as indicated above.

Calculated OH^- by the hydrogarnet substitution scheme must be corrected for already-incorporated F and/or Cl, if measured, which are subtracted.

Zircon favours (H)REE-incorporation, proposed to occur by charge-balance, coupled substitution involving P, which forms isostructural compounds with REE, Y and Sc, including xenotime (YPO_4) and pretulite ($ScPO_4$) (Finch and Hanchar, 2003 and references therein): $Zr^{4+} + Si^{4+} \leftrightarrow (REEs, Y, Sc)^{3+} + P^{5+}$. In several cases, the presence of P alone cannot, however, support the observed REE concentrations, a phenomenon reflected by ∑(REEs,Y,Sc)/P ratios that deviate from unity. This is interpreted in terms of more complex substitution mechanisms:

(1) $Zr^{4+} + O^{2-} \leftrightarrow Me^{3+} + (F, Cl, OH)^-$, with Me^{3+} as a REY+Sc;

(2) $Zr^{4+} \leftrightarrow Me^{3+} + (H, Me)^+$, with Me^+ as Li, Na and/or K;

(3) $2Zr^{4+} \leftrightarrow Me^{3+} + Me^{5+}$, with Me^{5+} as Nb for example.

Uncompensated substitution of REY+Sc, is balanced by incorporation H^+ within interstitial sites. Other incorporated Me^{2+} and Me^{3+} in the *A*-site, are compensated by O-vacancies.

* In this model, Al will be distributed between the A and B site, so that B is always >=1, and if there is excess Al, this will be incorporated in the A site.

In theory, other trivalent cations might be present in dodecahedral sites, incorporated by the same type of substitution: $Zr^{4+} + O^{2-} \leftrightarrow Me^{3+} + (F, Cl, OH)^{-}$. Incorporation of, e.g., Fe and Al, in this way is, however, poorly supported in the literature.

Experimental support for Fe incorporation in zircon has been given by several authors, albeit with subtly different results and interpretations. Váczi (2009) reports the doping of zircon with Fe (0.01-0.39 wt.%). Iron, both as dominant Fe^{3+} and subordinate Fe^{2+}, was found to be "predominantly located on the six-coordinated interstitial site". Important for the present work, incorporated Fe was present within oscillatory-zoned bands within the zoned crystals. Carreto Cortés et al. (2004) have demonstrated limited solid solution, up to about 2.5 mol% Fe, may be hosted within the zircon structure, with excess Fe^{3+} forming α-Fe_2O_3 particles that become trapped in the zircon matrix. Based on synthesis at 1100-1600 °C and refinement of X-ray diffraction patterns, Herrera-Pérez (2015) proposes that Fe^{3+} is distributed into tetrahedral sites, replacing Si^{4+}.

Lanthanide concentrations

The lower abundance of lanthanides with odd atomic numbers, commonly below minimum detection limits (mdl) of the EPMA method needs to be considered for accurate assessment of zircon stoichiometry and estimation of water contents. The abundance of HREE, with odd atomic numbers, where <mdl, has been estimated from the adjacent, even atomic number HREE considering the consistent behaviour of HREE fractionation in zircon. This approach is corroborated by the LA-ICP-MS data on the same zircons. So, if Tm_2O_3 is <mdl, and Er_2O_3 = 0.071 wt% and Yb_2O_3 = 0.255 wt%, Tm_2O_3* was obtained by dividing the measured concentrations of Er_2O_3 and Yb_2O_3 by their respective molecular oxide masses and multiplied by the elemental mass of the respective REE to obtain their elemental concentration. Following this step, both elements are divided by their chondrite abundance to obtain their normalized values, from which the concentration of Tm can be interpolated. The geometric means of these two values are then multiplied by the chondrite value for Tm, and then multiplied by the oxide molecular weight of Tm_2O_3 and finally multiplied by the elemental mass of Tm, yielding Tm_2O_3*= 0.021 wt%.

Modified calculation routine for Charleston zircon

EPMA analysis of zircon from the Charleston Granite sample was undertaken simultaneously with the other samples, however recalculation of formula using the above routine does not give reasonable results in terms of A:B stoichiometry.

The main difference with the previous calculation is that substitution of Fe into the *B*-site is also considered, following a similar approach as described above. If after allocation of Al in the *B*-site, $\sum A > \sum B$ (without considering Fe), then Fe is assigned to the *B*-site so that $\sum B = \sum A$. However, if after this step $\sum B+Fe$ is lower than $\sum A$, the difference between $\sum B+Fe$ and $\sum A$ is considered to represent missing Si by the hydrogarnet substitution. In general, this approach produces lower estimates for the incorporation of OH.

References

Akhtar, M.J., Waseem, S., 2001. Atomistic simulation studies of zircon. Chem. Physics 274, 109-120.

Botis, S.M., Pan, Y., Ewing, R.C., 2013. Hydrogen incorporation in crystalline zircon: insight from ab initio calculations. Am. Mineral. 98, 745–751.

Carreto Cortés, E., Montoya de la Fuente, J.A., Moreno, J.M., Piña Pérez, C., Cordoncillo, E.C., Carda Castello, J.B., 2004. Solid-Solution Formation in the Synthesis of Fe-Zircon. J. Am. Ceram. Soc. 87, 612–16.

Caruba, R., Baumer, A., Ganteaume, M., Iacconi, P., 1985. An experimental study of hydroxyl groups and water in synthetic and natural zircons: A model of the metamict state. Am. Mineral. 70, 1224–1231.

De Hoog, J.C.M., Lissenberg, C.J., Brooker, R.A., Hinton, R., Trail, D., Hellebrand, E., EIMF, 2014. Hydrogen incorporation and charge balance in natural zircon. Geochim. Cosmochim. Acta 141, 472–486.

Finch, R.J., Hanchar, J.M., 2003. Structure and chemistry of zircon and zircon-group minerals. Rev. Miner. Geochem. 53, 1–25.

Frondel, C., 1953. Hydroxyl substitution in thorite and zircon. Am. Mineral. 38, 1007–1018.

Frondel, C., Collette, R.L., 1957. Hydrothermal synthesis of zircon, thorite and huttonite. Am. Mineral. 42, 75–765.

Herrera-Pérez, G.M., 2015. Iron Doped-$ZrSiO_4$: Structural, Microstructural and Vibrational Characterization. Mater. Res. 18, 1313-1321.

Hoskin, P.W.O, Schaltegger, U., 2003. The composition of zircon and igneous and metamorphic petrogenesis. Rev. Mineral. Geochem. 53, 27–62.

Nasdala, L., Kronz, A., Wirth, R., Váczi, T., Pérez-Soba, C., Willner, A., Kennedy, A.K., 2009. The phenomenon of deficient electron microprobe totals in radiation damaged and altered zircon. Geochim. Cosmochim. Acta 73, 1637–1650.

Pérez-Soba, C., Villaseca, C., González det Tánago, J., 2007. The composition of zircon in the peraluminous Hercynian granites of the Spanish Central System Batholith. Can. Mineral. 45, 509-527.

Tailby, N.D., Walker, A.M., Berry, A.J., Hermann, J., Evans, K.A., Mavrogenes, J.A., O'Neill, H.StC., Rodina, I.S., Soldatov, A.V., Rubatto, D., Sutton, S.R., 2011. Ti site occupancy in zircon. Geochim. Cosmochim. Acta 75, 905–921.

Trail, D., Thomas, J.B., Watson, E.B., 2011. The incorporation of hydroxyl into zircon. Am. Mineral. 96, 60–67.

Váczi, T., 2009. Mineralogical studies on zircon. Dissertation, Doktor der Naturwissenschaften, University of Vienna, Austria, 84 pp.

Zeng, L.J., Niu, H.C., Bao, Z.W., Yang, W.B., 2017. Chemical lattice expansion of natural zircon during the magmatic-hydrothermal evolution of A-type granite. Am. Mineral. 102, 655–665.

ELECTRONIC APPENDIX B FOR CHAPTER 7

Table S3. LA-ICP-MS U-Pb data for zircon.

		Isotope Ratios							U/Pb Dates					
Sample #	Analysis #	$^{207}Pb/^{235}U$	1σ uncertainty	$^{206}Pb/^{238}U$	1σ uncertainty	Error correlation	$^{207}Pb/^{206}Pb$	1σ uncertainty	$^{207}Pb/^{235}U$	1σ uncertainty	$^{206}Pb/^{238}U$	1σ uncertainty	$^{207}Pb/^{206}Pb$	1σ uncertainty
OD Proximal (LCD13)	1	2.291	0.031	0.188	0.002	0.880	0.08822	0.001	1210	9.4	1113	12.0	1387	23.1
	2	1.864	0.026	0.152	0.002	0.857	0.08885	0.001	1068	9.1	913	10.1	1401	24.1
	3	2.063	0.029	0.171	0.002	0.842	0.08754	0.001	1137	9.7	1017	11.2	1372	24.9
	4	1.568	0.021	0.143	0.002	0.871	0.07955	0.001	958	8.4	862	9.5	1186	24.2
	5	1.896	0.025	0.165	0.002	0.875	0.0833	0.001	1080	8.9	985	10.8	1276	23.9
	6	1.795	0.025	0.151	0.002	0.844	0.08631	0.001	1044	9.1	906	10.0	1345	24.8
	7	2.383	0.033	0.190	0.002	0.841	0.09085	0.001	1237	10.1	1123	12.2	1443	24.6
	8	3.354	0.047	0.255	0.003	0.849	0.09552	0.001	1494	10.9	1463	15.5	1538	24.1
	9	3.939	0.057	0.292	0.003	0.823	0.098	0.001	1622	11.7	1650	17.4	1586	25.0
	10	4.009	0.058	0.294	0.004	0.822	0.09888	0.001	1636	11.8	1662	17.5	1603	25.1
	11	3.827	0.054	0.283	0.003	0.845	0.09824	0.001	1599	11.3	1605	16.9	1591	24.1
	12	1.912	0.027	0.162	0.002	0.843	0.08581	0.001	1085	9.3	966	10.6	1334	24.9
	13	1.964	0.028	0.165	0.002	0.843	0.0866	0.001	1103	9.5	982	10.8	1352	24.9
	14	3.625	0.051	0.272	0.003	0.847	0.09654	0.001	1555	11.1	1553	16.4	1558	24.1
	15	1.812	0.025	0.157	0.002	0.850	0.08375	0.001	1050	9.1	940	10.3	1287	24.7
	16	2.213	0.030	0.182	0.002	0.873	0.08804	0.001	1185	9.5	1080	11.7	1383	23.5
	17	3.748	0.058	0.279	0.003	0.782	0.09763	0.001	1582	12.4	1584	17.0	1579	27.1
	18	3.726	0.055	0.280	0.003	0.814	0.09648	0.001	1577	11.8	1592	16.9	1557	25.5
	19	3.537	0.061	0.264	0.003	0.722	0.0972	0.002	1536	13.5	1510	16.6	1571	30.5
	20	2.103	0.030	0.173	0.002	0.844	0.08793	0.001	1150	9.7	1031	11.3	1381	24.7

		Isotope Ratios							U/Pb Dates					
Sample #	Analysis #	$^{207}Pb/^{235}U$	2σ uncertainty	$^{206}Pb/^{238}U$	2σ uncertainty	Error Correlation	$^{207}Pb/^{206}Pb$	2σ uncertainty	$^{207}Pb/^{235}U$	2σ uncertainty	$^{206}Pb/^{238}U$	2σ uncertainty	$^{207}Pb/^{206}Pb$	2σ uncertainty
Wirrda Well (LCD17)	1	5.439	0.065	0.350	0.002	0.416	0.113	0.0013	1892	10	1850	21	1850	21
	2	5.489	0.050	0.351	0.002	0.570	0.11371	0.00088	1898	7.9	1858	14	1858	14
	3	5.175	0.053	0.331	0.002	0.358	0.1135	0.0011	1848	8.8	1855	18	1855	18
	4	5.239	0.045	0.335	0.002	0.401	0.11313	0.0009	1858	7.2	1854	15	1854	15
	5	4.730	0.100	0.292	0.005	0.923	0.11712	0.00092	1771	18	1911	14	1911	14
	6	5.373	0.049	0.326	0.003	0.351	0.119	0.0013	1880	7.8	1942	20	1942	20
	7	3.560	0.110	0.218	0.008	0.969	0.11836	0.00095	1536	25	1933	15	1933	15
	8	5.137	0.048	0.330	0.002	0.460	0.1133	0.0011	1843	7.8	1851	18	1851	18
	9	5.212	0.066	0.337	0.004	0.597	0.1125	0.0013	1856	11	1843	22	1843	22
	10	5.338	0.052	0.343	0.002	0.400	0.113	0.001	1875	8.4	1846	16	1846	16
	11	5.516	0.086	0.353	0.005	0.762	0.1126	0.0011	1903	13	1843	17	1843	17
	12	5.173	0.058	0.333	0.001	0.170	0.1125	0.0013	1847	9.5	1840	21	1840	21
	13	5.487	0.088	0.353	0.003	0.286	0.1133	0.0017	1899	14	1850	28	1850	28
	14	5.144	0.053	0.329	0.002	0.294	0.1129	0.0012	1845	9.1	1846	19	1846	19
	15	3.363	0.046	0.213	0.003	0.871	0.11394	0.00077	1495	11	1862	12	1862	12
	16	2.921	0.070	0.186	0.005	0.910	0.1129	0.0011	1385	18	1848	17	1848	17
	17	4.354	0.072	0.279	0.005	0.894	0.11342	0.00088	1703	13	1853	14	1853	14
	18	5.433	0.058	0.352	0.003	0.652	0.11174	0.00091	1889	9.1	1826	15	1826	15
	19	5.261	0.057	0.338	0.002	0.469	0.1122	0.0012	1861	9.2	1833	19	1833	19
	20	5.258	0.058	0.337	0.002	0.545	0.1122	0.001	1862	9.6	1835	16	1835	16
	21	5.345	0.066	0.347	0.004	0.631	0.1119	0.0011	1875	11	1833	17	1833	17
	22	5.300	0.044	0.345	0.002	0.556	0.11143	0.00081	1869	7.1	1823	13	1823	13
	23	3.304	0.069	0.207	0.004	0.908	0.11527	0.00096	1479	16	1885	15	1885	15
	24	4.412	0.061	0.286	0.004	0.887	0.11263	0.00081	1715	12	1841	13	1841	13
	25	4.998	0.078	0.323	0.005	0.825	0.11292	0.00097	1819	13	1845	16	1845	16
	26	5.060	0.050	0.323	0.002	0.548	0.1136	0.001	1829	8.5	1855	16	1855	16
	27	3.587	0.060	0.220	0.003	0.862	0.11755	0.00099	1546	13	1919	15	1919	15
	28	4.714	0.042	0.299	0.002	0.714	0.11354	0.00077	1769	7.5	1856	12	1856	12
	29	3.728	0.073	0.232	0.004	0.926	0.1172	0.00088	1577	16	1912	13	1912	13
	30	4.294	0.081	0.269	0.005	0.872	0.1155	0.001	1689	16	1888	16	1888	16
	31	4.804	0.052	0.312	0.003	0.781	0.11207	0.00075	1786	9.2	1833	12	1833	12
	32	5.272	0.049	0.340	0.002	0.487	0.11211	0.00092	1864	7.9	1832	15	1832	15
	33	4.380	0.040	0.279	0.002	0.547	0.11365	0.00089	1709	7.7	1857	14	1857	14
	34	5.083	0.059	0.330	0.003	0.656	0.1113	0.001	1833	9.9	1822	16	1822	16
	35	3.896	0.048	0.248	0.003	0.819	0.11496	0.00086	1614	10	1878	13	1878	13
	36	3.353	0.038	0.204	0.002	0.695	0.11858	0.00099	1492	8.9	1934	15	1934	15
	37	4.218	0.055	0.263	0.004	0.797	0.11566	0.00087	1676	11	1890	14	1890	14
	38	3.847	0.063	0.248	0.003	0.873	0.11323	0.00091	1602	13	1851	15	1851	15
	39	5.096	0.093	0.328	0.004	0.527	0.1137	0.0018	1835	15	1859	27	1859	27
	40	5.133	0.064	0.333	0.002	0.214	0.1118	0.0013	1841	11	1827	22	1827	22

	Reference Material Information											
Analysis #	$^{207}Pb/^{235}U$	1σ uncertainty	$^{206}Pb/^{238}U$	1σ uncertainty		$^{207}Pb/^{206}Pb$	1σ uncertainty	$^{207}Pb/^{235}U$	uncertain	$^{206}Pb/^{238}U$	uncertain	$^{207}Pb/^{206}Pb$	1σ uncertainty
GJ1-1	0.096	0.001	0.814	0.017		0.061	0.001	652.8	43.7	591.8	7.0	604.5	9.6
GJ1-2	0.098	0.001	0.819	0.018		0.060	0.001	616.3	45.7	605.1	7.2	607.4	10.0
GJ1-3	0.099	0.001	0.807	0.018		0.059	0.001	573.7	46.2	608.2	7.3	600.8	9.9
GJ1-4	0.098	0.001	0.801	0.017		0.059	0.001	585.2	46.0	600.8	7.2	597.4	9.9
GJ1-5	0.097	0.001	0.786	0.017		0.058	0.001	547.2	46.9	599.6	7.2	588.6	9.9
GJ1-6	0.098	0.001	0.835	0.018		0.062	0.001	672.1	45.0	601.4	7.2	616.3	10.0
GJ1-7	0.098	0.001	0.782	0.017		0.058	0.001	534.0	47.8	600.4	7.2	586.7	9.9
GJ1-8	0.098	0.001	0.807	0.018		0.060	0.001	587.5	46.3	604.6	7.2	600.9	10.0
GJ1-9	0.096	0.001	0.810	0.018		0.061	0.001	636.3	46.4	593.3	7.1	602.2	10.1
GJ1-10	0.098	0.001	0.805	0.018		0.060	0.001	588.8	47.1	602.9	7.3	599.9	10.1
GJ1-11	0.098	0.001	0.814	0.018		0.061	0.001	623.6	46.3	599.8	7.2	604.7	10.1
GJ1-12	0.097	0.001	0.814	0.018		0.061	0.001	635.1	46.4	596.7	7.2	604.7	10.1
Plesovic-1	0.054	0.001	0.392	0.008		0.053	0.001	328.5	43.8	336.7	4.0	335.6	5.7
Plesovic-2	0.052	0.001	0.374	0.007		0.052	0.001	287.7	42.2	327.5	3.9	322.6	5.3
Plesovic-3	0.053	0.001	0.381	0.008		0.053	0.001	309.5	45.7	330.3	4.0	327.6	5.8
Plesovic-4	0.053	0.001	0.400	0.008		0.055	0.001	391.7	43.2	334.8	4.0	342.0	5.8
Plesovic-5	0.054	0.001	0.403	0.008		0.054	0.001	377.1	45.1	338.7	4.1	343.6	6.1
Plesovic-6	0.053	0.001	0.384	0.008		0.052	0.001	290.4	46.3	335.6	4.0	329.9	5.9
91500-1	0.177	0.002	1.773	0.050		0.073	0.002	1001.2	55.8	1052.1	13.3	1035.6	18.2
91500-2	0.177	0.002	1.818	0.051		0.074	0.002	1052.1	55.4	1052.2	13.4	1052.1	18.3
91500-3	0.182	0.003	1.792	0.051		0.071	0.002	964.8	56.8	1080.3	13.7	1042.6	18.4

	Reference Material Information											
Analysis #	$^{207}Pb/^{235}U$	2σ uncertainty	$^{206}Pb/^{238}U$	2σ uncertainty	Error Correlation	$^{207}Pb/^{206}Pb$	2σ uncertainty	$^{207}Pb/^{235}U$	uncertain	$^{206}Pb/^{238}U$	uncertain	$^{207}Pb/^{206}Pb$	2σ uncertainty
GJ1 - 1.d	0.814	0.017	0.09819	0.00057	0.14662	0.0601	0.0013	603.4	9.5	603.7	3.3	587	47
GJ1 - 2.d	0.832	0.018	0.09915	0.0006	0.23268	0.0605	0.0012	613.4	9.9	609.4	3.5	615	45
GJ1 - 3.d	0.835	0.014	0.09894	0.00055	-0.18296	0.0614	0.0012	616.3	8.1	608.2	3.2	646	41
GJ1 - 4.d	0.809	0.015	0.09829	0.00053	0.074944	0.0596	0.0011	600.8	8.4	604.3	3.1	585	40
GJ1 - 5.d	0.801	0.013	0.09772	0.00055	0.121	0.05929	0.00099	599.2	7.6	601	3.2	574	37
GJ1 - 6.d	0.815	0.015	0.09887	0.00059	0.1823	0.0599	0.0011	605	8.3	607.8	3.5	591	39
GJ1 - 7.d	0.808	0.018	0.09846	0.00049	0.034139	0.0593	0.0013	600	10	605.4	2.9	601	46
GJ1 - 8.d	0.828	0.015	0.09838	0.00048	0.10908	0.0608	0.0012	612.5	8.7	604.9	2.8	627	43
GJ1 - 9.d	0.821	0.016	0.09829	0.00057	0.17485	0.0605	0.0012	607.3	9	604.4	3.3	620	43
GJ1 - 10.d	0.803	0.016	0.09798	0.00064	0.1873	0.0594	0.0012	599.3	8.8	602.5	3.7	570	44
GJ1 - 11.d	0.802	0.017	0.09782	0.00051	0.1187	0.059	0.0012	596.6	9.7	601.6	3	578	44
GJ1 - 12.d	0.816	0.013	0.09777	0.00057	0.012343	0.0606	0.001	605.7	7.7	601.6	3.4	627	37
GJ1 - 13.d	0.806	0.018	0.09808	0.00063	0.16091	0.0595	0.0014	599	10	603.1	3.7	583	49
GJ1 - 14.d	0.81	0.017	0.09948	0.00061	0.1375	0.0592	0.0013	603.1	9.5	611.3	3.6	578	46
GJ1 - 15.d	0.792	0.016	0.09841	0.00048	-0.018446	0.0584	0.0012	593.9	9	605.1	2.8	541	46
GJ1 - 16.d	0.787	0.016	0.09809	0.00063	0.13189	0.0581	0.0012	588.6	8.8	603.2	3.7	535	44
GJ1 - 17.d	0.801	0.016	0.09904	0.00049	-0.049053	0.0586	0.0012	601.5	8.6	608.8	2.9	576	43
GJ1 - 18.d	0.8	0.017	0.09912	0.00055	-0.061183	0.0585	0.0013	596.6	9.8	609.2	3.3	543	51
GJ1 - 19.d	0.781	0.014	0.0983	0.00056	-0.10274	0.0579	0.0012	586.1	8.1	604.4	3.3	519	44
GJ1 - 20.d	0.803	0.015	0.09908	0.00055	-0.064574	0.059	0.0011	598.9	8.1	609	3.2	576	41
GJ1 - 21.d	0.801	0.015	0.09991	0.00057	-0.041088	0.0582	0.0012	597.2	8.4	613.9	3.3	535	43
Plesovic - 1.d	0.3991	0.0055	0.05505	0.00024	-0.027898	0.05251	0.00076	341.2	4	345.5	1.4	303	32
Plesovic - 2.d	0.3996	0.0062	0.05482	0.00025	0.11738	0.05278	0.00082	341.6	4.5	344	1.5	313	36
Plesovic - 3.d	0.3885	0.0068	0.05398	0.00027	0.15194	0.05198	0.00092	333	5	338.9	1.7	274	40
Plesovic - 4.d	0.3974	0.0074	0.05383	0.00028	0.1993	0.0534	0.00099	339.3	5.4	338	1.7	332	42
Plesovic - 5.d	0.383	0.0062	0.05423	0.00026	-0.03256	0.05122	0.00086	329.4	4.6	340.4	1.6	254	39
Plesovic - 6.d	0.3965	0.0063	0.05445	0.00025	0.17901	0.0527	0.00083	338.8	4.6	341.8	1.5	313	37
Plesovic - 7.d	0.39	0.0064	0.05462	0.00026	0.24847	0.05163	0.00084	334	4.7	342.8	1.6	264	37
Plesovic - 8.d	0.3932	0.0072	0.05434	0.00028	0.13326	0.05232	0.00096	336.3	5.3	341.1	1.7	288	41
Plesovic - 9.d	0.393	0.0058	0.05462	0.00025	0.20564	0.05224	0.00078	336.3	4.2	342.8	1.5	291	35
Plesovic - 10.d	0.3906	0.0074	0.05455	0.00025	0.19478	0.0519	0.00094	335	5.3	342.4	1.5	285	42
91500 - 1.d	1.859	0.047	0.1789	0.0013	0.061131	0.075	0.0019	1069	17	1061	7.1	1056	53
91500 - 2.d	1.878	0.051	0.1801	0.0014	0.078494	0.0757	0.002	1074	18	1067.5	7.5	1075	53
91500 - 3.d	1.828	0.041	0.1768	0.0016	0.28413	0.0751	0.0018	1056	15	1049.4	8.9	1073	46
91500 - 4.d	1.8	0.045	0.1807	0.0014	0.16843	0.0721	0.0018	1047	16	1070.7	7.6	999	52
91500 - 5.d	1.889	0.042	0.1786	0.0015	0.28497	0.0764	0.0017	1059	8.1	1093	45	1093	45

Table S4. Complete EPMA dataset and calculated formulae
Hiltaba Intrusive Suite Granites (~1600 Ma)

average mdl		0.023	0.007	0.006	0.021	0.01	0.005	0.009	0.012	0.004	0.011	0.024	0.008	0.049	0.018	0.008	0.009	0.041	0.043	0.023	0.046	0.024	0.025	0.05	0.027	0.027	0.028	0.029	0.101	0.014	0.01	0.011	0.054	0.007								
LCD13 OD-proximal Roxby Downs Granite		**Na_2O**	**MgO**	**Al_2O_3**	**SiO_2**	**P_2O_5**	**K_2O**	**CaO**	**Sc_2O_3**	**TiO_2**	**MnO**	**Fe_2O_3**	**Y_2O_3**	**ZrO_2**	**Nb_2O_5**	**La_2O_3**	**Ce_2O_3**	**Nd_2O_3**	**Sm_2O_3**	**Eu_2O_3**	**Gd_2O_3**	**Tb_2O_3**	**Dy_2O_3**	**Ho_2O_3**	**Er_2O_3**	**Tm_2O_3**	**Yb_2O_3**	**Lu_2O_3**	**HfO_2**	**PbO**	**ThO_2**	**UO_2**	**F**	**Cl**	**Sum**	**H_2O (c**	**-F=O**	**-Cl=O**	**Sum[A]**				
Bright		0.046	0.016	<mdl	32.57	0.039	0.011	0.076	<mdl	0.01	0.035	0.822	0.023	63.834	<mdl	<mdl	<mdl	<mdl	<mdl	<mdl	0.076	0.03	<mdl	<mdl	0.077	*0.02*	0.206	*0.043*	2.355	0.036	<mdl	0.163	<mdl	0.116	100.6	0.11	0	0.03	100.69				
Bright		0.03	0.011	<mdl	32.165	0.064	<mdl	0.042	<mdl	0.01	0.037	0.46	0.145	64.104	<mdl	<mdl	<mdl	<mdl	<mdl	<mdl	0.052	0.028	0.05	*0.015*	0.063	*0.021*	0.297	0.042	1.454	0.089	0.08	0.332	<mdl	0.048	99.64	0.23	0	0.01	99.86				
Mean	(n=2)	0.038	0.014	<mdl	32.368	0.052	<mdl	0.059	<mdl	0.01	0.036	0.641	0.084	63.969	<mdl	<mdl	<mdl	<mdl	<mdl	<mdl	0.064	0.029	<mdl	<mdl	0.07	0.021	0.252	0.043	1.905	0.063	<mdl	0.248	<mdl	0.082	100.12	0.17	0	0.02	100.275				
Dark		0.083	0.047	0.011	32.291	0.063	0.011	0.153	<mdl	0.015	0.029	0.972	0.085	62.507	<mdl	<mdl	<mdl	<mdl	<mdl	<mdl	<mdl	<mdl	<mdl	<mdl	0.066	0.038	0.251	0.038	1.532	0.032	0.078	0.178	<mdl	0.119	98.599	0	0	0.027	98.574				
Dark		0.123	0.028	0.41	31.637	0.565	0.031	0.138	<mdl	0.036	0.117	1.152	1.051	60.714	<mdl	<mdl	0.081	<mdl	<mdl	0.034	0.118	0.043	0.256	*0.063*	0.223	0.045	0.394	0.04	2.818	0.083	0.09	0.888	<mdl	0.075	101.254	0.2	0	0.017	101.434				
Dark		0.197	0.019	0.186	31.056	0.39	0.017	0.211	<mdl	0.024	0.11	1.386	0.868	59.613	<mdl	<mdl	0.07	0.059	<mdl	0.043	0.141	0.031	0.15	0.065	0.164	0.034	0.389	0.069	2.485	0.097	0.073	0.827	<mdl	0.066	98.842	0.47	0	0.015	99.292				
Dark		0.058	0.022	0.008	32.46	0.145	0.007	0.123	<mdl	0.012	0.049	0.9	0.484	62.749	0.034	<mdl	0.016	<mdl	<mdl	<mdl	0.055	*0.011*	0.08	*0.025*	0.117	0.039	0.309	0.046	1.148	0.048	0.196	0.25	<mdl	0.156	99.547	0.05	0	0.035	99.561				
Dark		<mdl	0.021	0.021	32.218	0.082	0.011	0.185	<mdl	0.008	0.071	0.956	0.12	63.205	<mdl	<mdl	0.012	<mdl	<mdl	<mdl	0.055	0.027	0.076	0.063	0.096	*0.024*	0.256	*0.053*	1.385	0.048	0.122	0.21	<mdl	0.379	99.705	0.15	0	0.086	99.769				
Dark		0.067	0.013	0.007	31.601	0.034	0.016	0.085	<mdl	0.008	0.068	0.912	0.029	62.204	0.023	<mdl	<mdl	<mdl	<mdl	<mdl	<mdl	<mdl	0.059	*0.019*	0.088	*0.021*	0.215	*0.044*	2.855	0.048	<mdl	0.203	<mdl	0.163	98.78	0.35	0	0.037	99.096				
Dark		0.064	0.021	0.056	31.239	0.066	0.01	0.381	<mdl	0.007	0.114	1.161	0.166	60.557	0.03	<mdl	0.029	<mdl	<mdl	<mdl	<mdl	<mdl	0.064	*0.021*	0.105	*0.031*	0.373	0.046	2.049	0.07	0.092	0.742	0.097	0.086	97.675	0.44	0.041	0.019	98.052				
Mean	(n=7)	0.099	0.024	0.1	31.786	0.192	0.015	0.182	<mdl	0.016	0.08	1.063	0.4	61.65	<mdl	<mdl	0.042	<mdl	<mdl	<mdl	0.092	0.028	0.114	0.043	0.123	0.033	0.312	0.048	2.039	0.061	0.109	0.471	<mdl	0.149	99.2	0.24	0.006	0.034	99.397				
LCD47 OD-distal Roxby Downs Granite																																											
Bright (Gr2)		<mdl	0.017	0.132	31.645	0.113	0.006	0.032	<mdl	0.043	0.059	0.227	0.317	67.091	<mdl	<mdl	0.087	<mdl	<mdl	<mdl	0.081	*0.015*	0.109	0.054	0.114	0.029	0.097	0.032	1.379	0.03	0.103	0.145	<mdl	0.008	101.963	1.19	0	0.002	103.156				
Bright (Gr2)		0.074	0.023	0.122	31.294	0.072	0.008	0.535	<mdl	0.024	0.153	1.807	0.211	61.755	<mdl	<mdl	0.014	<mdl	<mdl	<mdl	0.067	*0.012*	0.087	*0.024*	0.096	*0.016*	0.113	0.04	1.399	0.042	0.117	0.219	<mdl	0.076	98.399	0.88	0	0.017	99.259				
Mean	(n=2)	<mdl	0.02	0.127	31.47	0.093	0.007	0.284	<mdl	0.034	0.106	1.017	0.264	64.423	<mdl	<mdl	0.051	<mdl	<mdl	<mdl	0.074	0.014	0.098	0.039	0.105	0.023	0.105	0.036	1.389	0.036	0.11	0.182	<mdl	0.042	100.181	1.04	0	0.01	101.208				
Dark (Gr2)		0.036	0.027	0.18	30.965	0.115	0.006	0.427	<mdl	0.009	0.143	1.44	0.167	61.61	<mdl	<mdl	<mdl	<mdl	<mdl	<mdl	0.048	*0.01*	0.084	0.054	0.077	*0.012*	0.073	*0.011*	1.402	0.03	0.051	0.111	<mdl	0.147	97.233	0.65	0	0.033	97.851				
Dark (Gr2)		0.046	0.03	0.196	31.273	0.054	0.006	0.435	<mdl	0.038	0.174	1.333	0.043	61.692	<mdl	<mdl	0.014	<mdl	<mdl	<mdl	<mdl	<mdl	0.071	*0.017*	0.06	*0.009*	0.06	*0.009*	1.736	0.037	0.023	0.12	<mdl	0.089	97.565	0.47	0	0.02	98.012				
Dark (Gr2)		0.059	0.033	0.838	30.827	0.136	0.012	0.792	<mdl	0.018	0.262	1.948	0.553	58.456	<mdl	0.011	0.155	0.065	<mdl	0.034	0.089	0.04	0.182	*0.04*	0.127	0.035	0.136	*0.007*	1.225	<mdl	0.089	0.125	0.115	0.111	96.52	0.09	0.049	0.025	96.532				
Mean	(n=3)	0.047	0.03	0.405	31.022	0.102	0.008	0.551	<mdl	0.022	0.193	1.574	0.254	60.586	<mdl	<mdl	0.085	<mdl	<mdl	<mdl	0.069	0.025	0.112	0.037	0.088	0.019	0.09	0.009	1.454	0.034	0.054	0.119	<mdl	0.116	97.106	0.4	0.016	0.026	97.465				
Bright (Gr1)		<mdl	0.011	0.009	33.017	0.11	<mdl	0.01	<mdl	0.011	<mdl	0.91	0.116	65.951	<mdl	<mdl	<mdl	<mdl	<mdl	<mdl	<mdl	<mdl	0.045	*0.007*	0.046	*0.007*	1.263	0.036	0.036	0.048	<mdl	0.008	101.641	0.14	0	0.002	101.783				
Bright (Gr1)		0.053	0.023	0.09	30.846	0.073	0.006	0.47	<mdl	<mdl	0.138	1.177	0.113	61.442	0.02	<mdl	<mdl	<mdl	<mdl	<mdl	<mdl	<mdl	0.067	*0.017*	0.059	*0.009*	0.06	*0.009*	1.618	0.04	0.058	0.188	0.066	0.099	96.74	0.65	0.028	0.022	97.335				
Bright (Gr1)		0.111	0.032	0.143	31.561	0.266	0.011	0.329	<mdl	0.007	0.202	1.348	0.486	60.903	<mdl	<mdl	<mdl	<mdl	<mdl	0.024	0.083	0.036	0.146	*0.033*	0.111	0.033	0.107	<mdl	1.602	0.042	0.042	0.286	0.085	0.066	98.095	0.15	0.036	0.015	98.193				
Bright (Gr1)		<mdl	0.016	0.034	31.791	0.05	0.006	0.015	<mdl	0.037	0.012	0.496	0.017	65.21	0.031	<mdl	<mdl	0.043	0.046	<mdl	<mdl	<mdl	0.025	*0.008*	0.032	<mdl	<mdl	<mdl	1.247	0.03	0.017	0.051	<mdl	<mdl	99.214	0.47	0	0	99.679				
Bright (Gr1)		<mdl	0.012	0.035	32.376	0.086	<mdl	0.024	<mdl	0.007	0.019	0.381	0.057	65.094	<mdl	<mdl	<mdl	<mdl	<mdl	<mdl	<mdl	<mdl	0.025	0.035	*0.011*	0.05	*0.007*	0.043	*0.006*	1.416	0.025	0.024	0.037	<mdl	0.009	99.78	0.07	0	0.002	99.85				
Bright (Gr1)		<mdl	0.4	0.447	32.714	0.118	0.006	0.03	<mdl	0.035	0.03	0.69	0.165	65.902	<mdl	<mdl	<mdl	<mdl	<mdl	<mdl	0.047	*0.008*	0.055	*0.017*	0.078	*0.012*	0.082	*0.013*	1.477	0.041	0.027	0.061	<mdl	0.012	102.467	0.38	0	0.003	102.839				
Bright (Gr1)		<mdl	0.02	0.1	32.199	0.108	<mdl	0.033	<mdl	0.017	0.06	0.4	0.15	65.179	0.025	<mdl	<mdl	<mdl	<mdl	<mdl	<mdl	<mdl	0.054	*0.019*	0.093	*0.011*	0.054	*0.005*	1.394	0.029	0.041	0.052	<mdl	0.012	100.099	0.25	0	0.003	100.349				
Mean	(n=5)	<mdl	0.073	0.123	32.072	0.116	0.007	0.13	<mdl	0.019	0.077	0.772	0.158	64.24	<mdl	<mdl	<mdl	<mdl	<mdl	<mdl	<mdl	<mdl	0.064	0.018	0.067	0.013	0.065	0.008	1.431	0.035	0.035	0.103	<mdl	0.034	99.719	0.3	0.009	0.007	100.004				
Dark (Gr1)		0.034	0.029	0.467	30.897	0.129	0.014	0.429	0.016	0.013	0.214	1.45	0.764	60.699	<mdl	<mdl	0.048	<mdl	<mdl	<mdl	0.121	0.039	0.173	*0.041*	0.141	*0.024*	0.163	0.062	1.358	0.037	0.074	0.147	<mdl	0.09	97.673	0.65	0	0.02	98.301				
Dark (Gr1)		0.038	0.019	0.027	31.119	0.071	0.007	0.244	<mdl	0.021	0.132	1.239	0.06	62.206	0.031	<mdl	<mdl	0.046	0.067	<mdl	<mdl	0.031	0.062	*0.017*	0.071	*0.01*	0.055	*0.007*	1.414	0.023	0.035	0.082	<mdl	0.098	97.233	0.61	0	0.022	97.823				
Dark (Gr1)		0.023	0.027	0.214	31.359	0.072	0.006	0.455	<mdl	0.048	0.163	1.175	0.159	61.716	<mdl	<mdl	0.022	<mdl	<mdl	<mdl	0.071	*0.012*	0.075	0.067	0.087	0.044	0.096	<mdl	1.448	0.029	0.053	0.116	<mdl	0.122	97.66	0.39	0	0.028	98.018				
Dark (Gr1)		0.028	0.02	0.228	31.43	0.067	0.008	0.434	<mdl	0.01	0.145	1.909	0.138	61.736	<mdl	<mdl	0.026	<mdl	<mdl	<mdl	0.029	0.078	*0.021*	0.083	*0.013*	0.088	*0.014*	1.232	0.019	0.055	0.094	<mdl	0.125	98.03	0.58	0	0.028	98.582				
Dark (Gr1)		0.032	0.03	0.216	31.454	0.064	0.008	0.374	<mdl	0.077	0.186	1.666	0.081	61.894	<mdl	<mdl	<mdl	<mdl	<mdl	<mdl	0.058	*0.011*	0.073	*0.018*	0.065	*0.009*	0.047	*0.006*	1.405	0.017	0.035	0.105	<mdl	0.085	98.014	0.46	0	0.019	98.457				
Dark (Gr1)		0.067	0.021	0.159	31.781	0.069	<mdl	0.442	<mdl	0.006	0.171	1.413	0.087	62.024	<mdl	<mdl	<mdl	<mdl	<mdl	<mdl	0.05	*0.011*	0.086	*0.016*	0.045	*0.007*	0.044	*0.007*	1.258	0.025	0.042	0.085	0.062	0.065	98.042	0.23	0.026	0.015	98.233				
Dark (Gr1)		0.098	0.028	0.262	31.635	0.288	0.014	0.512	0.035	0.029	0.189	1.74	0.937	60.734	<mdl	<mdl	0.033	0.048	0.063	0.026	0.102	*0.02*	0.145	*0.036*	0.132	*0.025*	0.189	0.067	1.349	0.032	0.101	0.276	0.146	0.067	99.357	0.47	0.061	0.015	99.748				
Dark (Gr1)		0.06	0.039	0.335	30.747	0.061	0.009	0.478	<mdl	0.083	0.191	1.774	0.094	63.446	0.026	<mdl	0.042	<mdl	<mdl	<mdl	<mdl	<mdl	0.072	*0.016*	0.05	*0.006*	0.032	*0.004*	1.476	0.038	0.03	0.134	<mdl	0.069	99.311	1.4	0	0.016	100.692				
Dark (Gr1)		0.094	0.023	0.073	30.481	0.12	<mdl	0.28	<mdl	0.008	0.143	0.968	0.252	62.081	<mdl	<mdl	<mdl	<mdl	<mdl	<mdl	<mdl	<mdl	0.027	0.084	*0.024*	0.099	0.042	0.085	<mdl	1.27	0.035	0.059	0.082	<mdl	0.124	96.452	0.84	0	0.028	97.267				
Mean	(n=9)	0.053	0.026	0.22	31.211	0.105	0.009	0.405	<mdl	0.033	0.17	1.482	0.286	61.837	<mdl	<mdl	0.034	<mdl	<mdl	<mdl	0.08	0.023	0.094	0.028	0.086	0.02	0.089	0.024	1.357	0.028	0.054	0.125	<mdl	0.094	97.975	0.63	0.01	0.021	98.569				
MB158 Charleston Granite, Eyre Peninsula[E]																																											
Bright		<mdl	<mdl	0.036	33.001	0.099	0.008	0.175	<mdl	0.04	0.129	1.292	0.224	65.185	<mdl	<mdl	0.027	<mdl	0.044	<mdl	0.08	0.029	0.084	*0.022*	0.087	*0.014*	0.093	*0.014*	1.353	0.051	0.148	0.13	<mdl	0.016	102.381	0.03	0	0.004	102.41				
Bright		0.032	0.016	<mdl	31.708	0.092	<mdl	0.674	<mdl	0.052	0.188	2.082	0.147	63.283	<mdl	<mdl	<mdl	<mdl	<mdl	<mdl	0.029	0.079	*0.019*	0.066	0.028	0.041	<mdl	1.32	0.049	0.081	0.12	<mdl	0.046	100.153	0.01	0	0.01	100.147				
Bright		0.058	0.007	0.02	31.93	0.087	0.007	0.66	<mdl	0.06	0.087	1.704	0.108	63.229	0.026	<mdl	<mdl	<mdl	0.046	<mdl	0.077	*0.011*	0.062	*0.017*	0.071	0.035	0.054	<mdl	1.393	0.046	0.042	0.107	<mdl	0.034	99.98	0	0	0.008	99.973				
Bright		0.048	0.053	0.164	32.152	0.096	0.005	0.933	<mdl	0.031	0.144	1.224	0.273	62.378	0.027	<mdl	<mdl	0.042	0.047	0.029	<mdl	0.026	0.094	*0.025*	0.097	0.035	0.086	<mdl	1.536	0.038	0.038	0.154	<mdl	0.063	99.842	0.02	0	0.014	99.85				
Bright		0.033	0.012	0.013	32.399	0.083	0.007	0.253	<mdl	0.027	0.175	1.02	0.114	64.156	<mdl	<mdl	<mdl	<mdl	<mdl	<mdl	0.057	*0.011*	0.079	*0.019*	0.069	*0.01*	0.06	*0.008*	1.524	0.036	0.038	0.148	<mdl	0.016	100.366	0.01	0	0.004	100.368				
Mean	(n=5)	0.043	0.022	0.058	32.238	0.091	0.007	0.539	<mdl	0.042	0.145	1.464	0.173	63.646	<mdl	<mdl	<mdl	<mdl	0.046	<mdl	0.071	0.021	0.08	0.02	0.078	0.024	0.067	<mdl	1.425	0.044	0.069	0.132	<mdl	0.035	100.544	0.01	0	0.008	100.55				
Dark		0.044	0.019	0.035	31.646	0.095	0.007	1.115	<mdl	0.029	0.133	1.784	0.206	62.498	<mdl	<mdl	<mdl	<mdl	<mdl	0.04	0.051	0.047	0.082	*0.02*	0.069	0.033	0.08	0.03	1.21	0.057	0.124	0.143	<mdl	0.06	99.657	0.02	0	0.014	99.659				
Dark		0.04	0.016	0.073	32.077	0.124	<mdl	1.399	<mdl	0.055	0.153	2.203	0.355	61.528	<mdl	<mdl	0.017	0.053	<mdl	<mdl	0.084	0.026	0.112	*0.027*	0.095	*0.013*	0.069	*0.009*	1.16	0.045	0.232	0.147	<mdl	0.064	100.175	0.03	0	0.014	100.189				
Dark		<mdl	0.016	0.013	31.92	0.082	<mdl	0.677	<mdl	0.064	0.176	2.211	0.19	62.89	<mdl	<mdl	<mdl	<mdl	0.049	<mdl	<mdl	<mdl	0.095	*0.019*	0.058	*0.01*	0.076	*0.013*	1.375	0.032	0.121	0.16	<mdl	0.047	100.293	0.02	0	0.011	100.306				
Dark		0.062	0.012	0.01	31.372	0.07	<mdl	0.981	<mdl	0.014	0.219	1.306	0.102	61.879	<mdl	<mdl	<mdl	<mdl	<mdl	<mdl	0.052	0.035	0.103	*0.021*	0.06	*0.009*	0.053	*0.007*	1.397	0.036	0.046	0.15	<mdl	0.052	98.048	0	0	0.012	98.037				
Dark		0.033	0.017	0.083	31.403	0.081	0.007	1.033	<mdl	0.014	0.163	1.281	0.113	61.841	<mdl	<mdl	0.012	<mdl	<mdl	0.028	0.068	0.03	0.066	*0.019*	0.081	*0.014*	0.104	*0.017*	1.523	<mdl	0.084	0.154	<mdl	0.049	98.317	0.01	0	0.011	98.32				
Mean	(n=5)	0.045	0.016	0.043	31.684	0.09	<mdl	1.041	<mdl	0.035	0.169	1.757	0.193	62.127	<mdl	<mdl	<mdl	<mdl	<mdl	<mdl	0.064	0.035	0.092	0.021	0.073	0.016	0.076	0.015	1.333	0.043	0.121	0.151	<mdl	0.054	99.298	0.02	0	0.012	99.302				
Donington Suite Granites (~1850 Ma)																																										
PL8 Cape Donington																																										
Bright		<mdl	0.008	<mdl	32.518	0.107	<mdl	<mdl	<mdl	<mdl	0.005	<mdl	<mdl	0.15	65.716	<mdl	<mdl	<mdl	<mdl	<mdl	<mdl	0.059	0.027	0.026	*0.01*	0.057	*0.008*	0.043	*0.006*	1.233	0.023	0.027	0.035	<mdl	<mdl	100.06	0.01	0	0	100.071				
Bright		<mdl	0.01	0.008	32.801	0.092	<mdl	<mdl	<mdl	0.007	0.012	0.026	0.039	65.94	<mdl	<mdl	<mdl	<mdl	<mdl	<mdl	<mdl	<mdl	0.044	*0.012*	0.047	0.027	0.045	0.031	1.392	0.019	0.015	0.021	<mdl	<mdl	100.589	0	0	0	100.592				
Bright		<mdl	<mdl	<mdl	32.646	0.097	<mdl	0.01	<mdl	<mdl	<mdl	<mdl	0.075	65.891	<mdl	<mdl	<mdl	<mdl	<mdl	<mdl	0.071	0.027	0.037	*0.013*	0.065	*0.008*	0.044	*0.005*	1.275	0.038	0.03	0.064	<mdl	<mdl	100.396	0.01	0	0	100.405				
Bright		<mdl	<mdl	<mdl	32.759	0.074	<mdl	<mdl	<mdl	0.012	<mdl	<mdl	0.034	65.863	<mdl	<mdl	<mdl	<mdl	<mdl	<mdl	<mdl	<mdl	0.031	*0.009*	0.041	<mdl	<mdl	<mdl	1.334	0.026	0.02	0.045	<mdl	<mdl	100.249	0	0	0	100.249				
Mean	(n=4)	<mdl	<mdl	<mdl	32.681	0.093	<mdl	<mdl	<mdl	0.008	<mdl	<mdl	0.075	65.853	<mdl	<mdl	<mdl	<mdl	<mdl	<mdl	<mdl	<mdl	0.035	0.011	0.053	0.014	0.044	0.014	1.309	0.027	0.023	0.041	<mdl	<mdl	100.324	0.01	0	0	100.329				
Dark		<mdl	0.009	<mdl	31.997	0.077	<mdl	<mdl	<mdl	0.01	<mdl	0.032	0.028	65.14	<mdl	<mdl	<mdl	<mdl	<mdl	<mdl	0.046	<mdl	<mdl	0.07	0.072	*0.009*	0.044	*0.005*	1.326	0.03	<mdl	0.012	<mdl	<mdl	98.907	0.14	0	0	99.049				
Dark		<mdl	0.008	<mdl	32.423	0.09	<mdl	<mdl	<mdl	0.006	<mdl	<mdl	0.038	65.806	<mdl	<mdl	<mdl	<mdl	<mdl	0.055	<mdl	0.053	0.03	0.026	*0.01*	0.056	0.038	0.047	<mdl	1.41	<mdl	<mdl	0.016	<mdl	<mdl	100.114	0.09	0	0	100.206				
Dark		<mdl	<mdl	<mdl	32.005	0.065	<mdl	<mdl	<mdl	0.008	<mdl	0.041	0.025	65.502	<mdl	<mdl	<mdl	<mdl	<mdl	<mdl	<mdl	0.07	*0.009*	0.042	*0.011*	0.045	*0.006*	0.035	*0.004*	1.326	0.023	<mdl	0.015	<mdl	<mdl	99.233	0.24	0	0	99.472				
Mean	(n=3)	<mdl	0.009	<mdl	32.142	0.077	<mdl	<mdl	<mdl	0.008	<mdl	0.037	0.03	65.483	<mdl	<mdl	<mdl	<mdl	<mdl	<mdl	0.056	0.02	0.034	0.03	0.058	0.018	0.042	0.005	1.354	0.027	<mdl	0.014	<mdl	<mdl	99.418	0.16	0	0	99.576				
LCD17 Wirrda Well																																										
Bright		<mdl	0.011	<mdl	32.758	0.104	<mdl	0.018	<mdl	0.006	<mdl	0.197	0.093	64.529	<mdl	<mdl	<mdl	<mdl	<mdl	<mdl	0.071	0.027	0.028	0.07	0.076	0.031	0.126	*0.007*	1.288	0.031	0.026	0.051	<mdl	<mdl	99.548	0.02	0	0	99.568				
Bright		<mdl	0.013	<mdl	32.77	0.172	<mdl	<mdl	<mdl	0.009	<mdl	0.161	0.108	64.598	0.032	<mdl	<mdl	<mdl	<mdl	<mdl	<mdl	0.032	0.031	*0.011*	0.051	*0.012*	0.121	*0.024*	1.265	0.028	0.027	0.048	<mdl	<mdl	99.515	0.01	0	0	99.521				
Bright		<mdl	0.012	<mdl	32.874	0.125	<mdl	<mdl	<mdl	0.008	<mdl	0.128	0.092	65.057	<mdl	<mdl	<mdl	<mdl	<mdl	<mdl	<mdl	<mdl	<mdl	<mdl	0.056	*0.013*	0.123	*0.024*	1.343	0.034	0.027	0.045	<mdl	0.009	99.97	0.01	0	0.002	99.975				
Bright		<mdl	<mdl	<mdl	32.789	0.121	<mdl	<mdl	<mdl	0.01	<mdl	0.236	0.083	65.159	<mdl	<mdl	<mdl	<mdl	<mdl	<mdl	0.054	0.029	0.029	*0.01*	0.05	*0.01*	0.088	*0.017*	1.389	0.034	0.025	0.047	<mdl	<mdl	100.179	0.01	0	0	100.188				
Bright		<mdl	0.015	<mdl	32.735	0.129	0.007	0.012	<mdl	0.006	<mdl	0.105	0.089	65.159	<mdl	<mdl	<mdl	<mdl	<mdl	<mdl	0.051	<mdl	<mdl	<mdl	0.036	*0.012*	0.062	*0.015*	0.146	*0.03*	1.31	0.019	0.031	0.059	<mdl	<mdl	100.028	0.01	0	0	100.041				
Mean	(n=5)	<mdl	0.013	<mdl	32.785	0.13	<mdl	<mdl	<mdl	0.008	<mdl	0.165	0.093	64.9	<mdl	<mdl	<mdl	<mdl	<mdl	<mdl	<mdl	<mdl	0.029	0.031	0.026	0.059	0.016	0.121	0.02	1.319	0.029	0.027	0.05	<mdl	<mdl	99.848	0.01	0	0	99.859				
Dark		0.027	0.031	0.22	31.317	0.188	0.008	0.26	<mdl	0.014	0.085	1.338	0.368	62.109	<mdl	<mdl	0.042	<mdl	<mdl	0.078	<mdl	0.055	0.035	0.114	*0.029*	0.109	*0.02*	0.145	*0.025*	1.282	0.038	0.066	0.108	<mdl	0.081	98.193	0.5	0	0.018	98.673				
Dark		0.036	0.017	<mdl	32.724	0.138	0.006	0.046	<mdl	0.006	0.038	0.471	0.

Formulae calculation

Na	K	∑I-site	Mg	Al	Ca	Sc	Mn	Fe	Y	Zr	Nb	La	Ce	Nd	Sm	Eu	Gd	Tb	Dy	Ho	Er	Tm	Yb	Lu
0.0027	0.0004	0.0031	0.0007	0	0.0025	0	0.0009	0.0189	0.0004	0.9485	0	0	0	0	0	0	0.0008	0.0003	0	0	0.0007	0.0002	0.0039	0.0004
0.0018	0	0.0018	0.0005	0	0.0014	0	0.001	0.0106	0.0024	0.9596	0	0	0	0	0	0	0.0005	0.0003	0.0005	0.0001	0.0006	0.0002	0.0056	0.0004
0.0023	0.0002	0.0025	0.0006	0	0.002	0	0.001	0.0148	0.0014	0.9541	0	0	0	0	0	0	0.0007	0.0003	0.0003	0.0001	0.0007	0.0002	0.0048	0.0004
0.005	0.0004	0.0054	0.0022	0.0004	0.0051	0	0.0008	0.0226	0.0014	0.9438	0	0	0	0	0	0	0	0	0	0	0.0006	0.0004	0.0048	0.0004
0.0073	0.0012	0.0085	0.0013	0	0.0045	0	0.003	0.0263	0.017	0.8998	0	0	0.0009	0	0	0.0004	0.0012	0.0004	0.0025	0.0006	0.0021	0.0004	0.0074	0.0004
0.0118	0.0007	0.0125	0.0009	0	0.007	0	0.0029	0.0322	0.0143	0.898	0	0	0.0008	0.0007	0	0.0004	0.0014	0.0003	0.0015	0.0006	0.0016	0.0003	0.0074	0.0006
0.0035	0.0003	0.0038	0.001	0.0003	0.004	0	0.0013	0.0208	0.0079	0.9398	0.0005	0	0.0002	0	0	0	0.0006	0.0001	0.0008	0.0002	0.0011	0.0004	0.0059	0.0004
0	0.0004	0.0004	0.001	0	0.0061	0	0.0018	0.022	0.002	0.9436	0	0	0.0001	0	0	0	0.0006	0.0003	0.0007	0.0006	0.0009	0.0002	0.0049	0.0005
0.004	0.0006	0.0046	0.0006	0	0.0028	0	0.0018	0.0213	0.0005	0.9393	0.0003	0	0	0	0	0	0	0	0.0006	0.0002	0.0009	0.0002	0.0041	0.0004
0.0039	0.0004	0.0043	0.001	0	0.0127	0	0.003	0.0272	0.0027	0.9183	0.0004	0	0.0003	0	0	0	0	0	0.0006	0.0002	0.001	0.0003	0.0072	0.0004
0.005	0.001	0.006	0.001	0	0.006	0	0.002	0.025	0.007	0.926	0	0	0	0	0	0	0.001	0	0.001	0	0.001	0	0.006	0
0	0.0002	0.0002	0.0007	0	0.001	0	0.0015	0.005	0.005	0.9664	0	0	0.0009	0	0	0	0.0008	0.0001	0.001	0.0005	0.0011	0.0003	0.0018	0.0003
0.0043	0.0003	0.0047	0.001	0	0.0174	0	0.0039	0.0412	0.0034	0.9127	0	0	0.0002	0	0	0	0.0007	0.0001	0.0009	0.0002	0.0009	0.0002	0.0021	0.0004
0.0022	0.0003	0.0025	0.0009	0	0.0092	0	0.0027	0.0231	0.0042	0.9396	0	0	0.0006	0	0	0	0.0008	0.0001	0.001	0.0004	0.001	0.0003	0.002	0.0004
0.0022	0.0002	0.0024	0.0012	0	0.0141	0	0.0037	0.0334	0.0027	0.9267	0	0	0	0	0	0	0.0005	0.0001	0.0008	0.0005	0.0007	0.0001	0.0014	0.0003
0.0028	0.0002	0.003	0.0014	0	0.0144	0	0.0045	0.031	0.0007	0.9285	0	0	0.0002	0	0	0	0	0	0.0007	0.0002	0.0006	0.0001	0.0011	0.0003
0.0036	0.0005	0.0041	0.0015	0	0.0264	0	0.0069	0.0456	0.0092	0.8872	0	0.0001	0.0018	0.0007	0	0.0004	0.0009	0.0004	0.0018	0.0004	0.0012	0.0003	0.0026	0.0003
0.003	0	0.003	0.001	0	0.018	0	0.005	0.037	0.004	0.914	0	0	0.001	0	0	0	0	0	0.001	0	0.001	0	0.002	0
0	0	0	0.0005	0	0.0003	0	0	0.0205	0.0019	0.9637	0	0	0	0	0	0	0	0	0	0	0.0004	0.0001	0.0009	0.0003
0.0032	0.0003	0.0034	0.0011	0	0.0156	0	0.0036	0.0275	0.0019	0.9309	0.0003	0	0	0	0	0	0	0	0.0007	0.0002	0.0006	0.0001	0.0012	0.0003
0.0067	0.0004	0.0071	0.0015	0	0.0109	0	0.0053	0.0314	0.008	0.9194	0	0	0	0	0	0.0003	0.0009	0.0004	0.0015	0.0003	0.0011	0.0003	0.0021	0
0	0.0002	0.0002	0.0007	0	0.0005	0	0.0003	0.0114	0.0003	0.9731	0.0004	0	0	0.0005	0.0005	0	0	0	0.0003	0.0001	0.0003	0	0	0
0	0	0	0.0005	0	0.0008	0	0.0005	0.0088	0.0009	0.9733	0	0	0	0	0	0	0	0.0003	0.0003	0.0001	0.0005	0.0001	0.0008	0.0003
0	0.0002	0.0002	0.0176	0	0.0009	0	0.0007	0.0153	0.0026	0.9459	0	0	0	0	0	0	0.0005	0.0001	0.0005	0.0002	0.0007	0.0001	0.0015	0.0003
0	0	0	0.0009	0	0.0011	0	0.0016	0.0092	0.0024	0.9683	0.0003	0	0	0.0005	0	0	0	0	0.0005	0.0002	0.0009	0.0001	0.001	0.0003
0.001	0	0.002	0.003	0	0.004	0	0.002	0.018	0.003	0.954	0	0	0	0	0	0	0	0	0.001	0	0.001	0	0.001	0
0.002	0.0005	0.0026	0.0013	0	0.0141	0.0004	0.0056	0.0335	0.0125	0.9092	0	0	0.0005	0	0	0	0.0012	0.0004	0.0017	0.0004	0.0014	0.0002	0.0031	0.0006
0.0023	0.0003	0.0025	0.0009	0	0.0081	0	0.0035	0.0289	0.001	0.9395	0.0004	0	0	0.0005	0.0007	0	0	0.0003	0.0006	0.0002	0.0007	0.0001	0.0011	0.0003
0.0014	0.0002	0.0016	0.0012	0	0.0151	0	0.0043	0.0273	0.0026	0.9297	0	0	0.0003	0	0	0	0.0007	0.0001	0.0007	0.0007	0.0008	0.0004	0.0018	0
0.0017	0.0003	0.002	0.0009	0	0.0142	0	0.0037	0.0438	0.0022	0.9189	0	0	0.0003	0	0	0	0	0.0003	0.0008	0.0002	0.0008	0.0001	0.0017	0.0003
0.0019	0.0003	0.0022	0.0014	0	0.0123	0	0.0048	0.0384	0.0013	0.9251	0	0	0	0	0	0	0.0006	0.0001	0.0007	0.0002	0.0006	0.0001	0.0009	0.0003
0.004	0	0.004	0.001	0	0.0146	0	0.0045	0.0327	0.0014	0.9307	0	0	0	0	0	0	0.0005	0.0001	0.0009	0.0002	0.0004	0.0001	0.0008	0.0003
0.0058	0.0005	0.0063	0.0013	0	0.0166	0.0009	0.0048	0.0396	0.0151	0.8967	0	0	0.0004	0.0005	0.0007	0.0003	0.001	0.0002	0.0014	0.0003	0.0013	0.0002	0.0036	0.0006
0.0035	0.0003	0.0038	0.0017	0	0.0152	0	0.0048	0.0397	0.0015	0.9203	0.0003	0	0.0005	0	0	0	0	0	0.0007	0.0001	0.0005	0.0001	0.0006	0
0.0056	0	0.0056	0.001	0	0.0093	0	0.0038	0.0227	0.0042	0.9421	0	0	0	0	0	0	0	0.0003	0.0008	0.0002	0.001	0.0004	0.0016	0
0.003	0	0.003	0.001	0	0.013	0	0.004	0.034	0.005	0.924	0	0	0	0	0	0	0	0	0.001	0	0.001	0	0.002	0
0	0.0003	0.0003	0	0	0.0056	0	0.0033	0.0191	0.0036	0.949	0	0	0.0003	0	0.0005	0	0.0008	0.0003	0.0008	0.0002	0.0008	0.0001	0.0017	0.0003
0.0019	0	0.0019	0.0007	0	0.022	0	0.0048	0.0155	0.0024	0.9384	0	0	0	0	0	0	0	0.0003	0.0008	0.0002	0.0006	0.0003	0.0008	0
0.0034	0.0003	0.0037	0.0003	0	0.0215	0	0.0023	0.0165	0.0018	0.9396	0.0004	0	0	0	0.0005	0	0.0008	0.0001	0.0006	0.0002	0.0007	0.0003	0.001	0
0.0028	0.0002	0.003	0.0024	0	0.0304	0	0.0037	0.014	0.0044	0.9242	0.0004	0	0	0.0005	0.0005	0.0003	0	0.0003	0.0009	0.0002	0.0009	0.0003	0.0016	0
0.002	0.0003	0.0022	0.0005	0	0.0082	0	0.0045	0.0135	0.0019	0.9529	0	0	0	0	0	0	0.0006	0.0001	0.0008	0.0002	0.0007	0.0001	0.0011	0.0003
0.002	0	0.002	0.001	0	0.018	0	0.004	0.016	0.003	0.941	0	0	0	0	0	0	0	0	0.001	0	0.001	0	0.001	0
0.0026	0.0003	0.0029	0.0009	0	0.0364	0	0.0034	0.0095	0.0033	0.9285	0	0	0	0	0	0.0004	0.0005	0.0005	0.0008	0.0002	0.0007	0.0003	0.0015	0.0003
0.0023	0	0.0023	0.0007	0	0.0451	0	0.0039	0.0228	0.0057	0.9033	0	0	0.0002	0.0006	0	0	0.0008	0.0003	0.0011	0.0003	0.0009	0.0001	0.0013	0.0003
0	0	0	0.0007	0	0.022	0	0.0045	0.0222	0.0031	0.9297	0	0	0	0	0.0005	0	0	0	0.0009	0.0002	0.0006	0.0001	0.0014	0.0003
0.0037	0	0.0037	0.0006	0	0.0326	0	0.0057	0.0059	0.0017	0.9356	0	0	0	0	0	0	0.0005	0.0004	0.001	0.0002	0.0006	0.0001	0.001	0.0003
0.002	0.0003	0.0023	0.0008	0	0.0342	0	0.0043	0.0062	0.0019	0.9323	0	0	0.0001	0	0	0.0003	0.0007	0.0003	0.0007	0.0002	0.0008	0.0001	0.002	0.0002
0.002	0	0.002	0.001	0	0.034	0	0.004	0.013	0.003	0.926	0	0	0	0	0	0	0.001	0	0.001	0	0.001	0	0.001	0
0	0	0	0.0004	0	0	0	0	0	0.0025	0.9828	0	0	0	0	0	0	0.0006	0.0003	0.0003	0.0001	0.0006	0.0001	0.0008	0.0003
0	0	0	0.0005	0.0003	0	0	0.0003	0.0006	0.0006	0.9802	0	0	0	0	0	0	0	0	0.0004	0.0001	0.0005	0.0003	0.0009	0.0003
0	0	0	0	0	0.0003	0	0	0	0.0012	0.9825	0	0	0	0	0	0	0.0007	0.0003	0.0004	0.0001	0.0006	0.0001	0.0008	0
0	0	0	0	0	0	0	0	0	0.0006	0.9822	0	0	0	0	0	0	0	0	0.0003	0.0001	0.0004	0	0	0
0	0	0	0	0	0	0	0	0	0.001	0.982	0	0	0	0	0	0	0	0	0	0	0.001	0	0.001	0
0	0	0	0.0004	0	0	0	0	0.0008	0.0005	0.9835	0	0	0	0	0	0	0.0005	0	0	0.0007	0.0007	0.0001	0.0008	0
0	0	0	0.0004	0	0	0	0	0	0.0006	0.983	0	0	0	0	0.0006	0	0.0005	0.0003	0.0003	0.0001	0.0005	0.0004	0.0009	0
0	0	0	0	0	0	0	0	0.001	0.0004	0.9841	0	0	0	0	0	0	0.0007	0.0001	0.0004	0.0001	0.0004	0.0001	0.0007	0
0	0	0	0	0	0	0	0	0.001	0.001	0.984	0	0	0	0	0	0	0.001	0	0	0	0.001	0	0.001	0
0	0	0	0.0005	0	0.0006	0	0	0.0045	0.0015	0.9664	0	0	0	0	0	0	0.0007	0.0003	0.0003	0.0007	0.0007	0.0003	0.0024	0.0003
0	0	0	0.0006	0	0	0	0	0.0037	0.0018	0.967	0.0004	0	0	0	0	0	0	0.0003	0.0003	0.0001	0.0005	0.0001	0.0023	0.0002
0	0	0	0.0005	0	0	0	0	0.0029	0.0015	0.9703	0	0	0	0	0	0	0	0	0	0	0.0005	0.0001	0.0023	0.0002
0	0	0	0	0	0	0	0	0.0054	0.0014	0.9711	0	0	0	0	0	0	0.0005	0.0003	0.0003	0.0001	0.0005	0.0001	0.0017	0.0002
0	0.0003	0.0003	0.0007	0	0.0004	0	0	0.0024	0.0015	0.9725	0	0	0	0	0.0005	0	0	0	0.0004	0.0001	0.0006	0.0001	0.0028	0.0003
0	0	0	0	0	0	0	0	0.004	0.002	0.969	0	0	0	0	0	0	0	0	0	0	0.001	0	0.002	0
0.0016	0.0003	0.0019	0.0014	0	0.0086	0	0.0022	0.0309	0.006	0.9303	0	0	0.0005	0	0.0008	0	0.0006	0.0004	0.0011	0.0003	0.001	0.0002	0.0028	0.0002
0.0021	0.0002	0.0024	0.0008	0	0.0015	0	0.001	0.0109	0.0033	0.9543	0	0	0	0	0	0	0	0	0.0004	0.0005	0.0009	0.0004	0.0036	0.0002
0.0021	0.0003	0.0023	0.0006	0	0.001	0	0.0011	0.0171	0.0018	0.9596	0	0	0	0	0	0	0.0008	0.0001	0.0007	0.0002	0.0009	0.0003	0.0029	0.0002
0	0.0003	0.0003	0.0004	0	0.0003	0	0	0.0062	0.0009	0.973	0	0	0	0	0	0	0	0	0.0003	0.0001	0.0004	0.0003	0.0018	0
0	0	0	0.0004	0	0.0004	0	0.0003	0.0038	0.0019	0.9754	0.0004	0	0	0	0	0	0.0005	0.0001	0.0004	0.0001	0.0004	0.0003	0.0023	0
0.001	0	0.001	0.001	0	0.002	0	0.001	0.014	0.003	0.959	0	0	0	0	0	0	0	0	0.001	0	0.001	0	0.003	0

	Yb	Lu	REE*	Hf	Pb	Th	U	∑A-site	Al	Si	P	Ti	Fe	Si*	∑B-site	F	Cl	OH	O	age (Ga)	MW	U (pp	$^{238}U^{C}$	$^{235}U^{D}$	Th (p	α-decays/mg	
2	0.0039	0.0004	0.0067	0.0205	0.0003	0	0.0011	1	0	0.9925	0.001	0.0002	0	0.0063	1	0	0.006	0.0216	3.9586	1.59	184.7	1422	1419	2.7	0	1.06E+16	
2	0.0056	0.0004	0.0107	0.0127	0.0007	0.0006	0.0023	1	0	0.9875	0.0017	0.0002	0	0.0106	1	0	0.0025	0.0473	3.9413	1.59	184.8	2918	2913	5.6	700	2.28E+16	
2	0.0048	0.0004	0.0087	0.0166	0.0005	0.0003	0.0017	1	0	0.99	0.0014	0.0002	0	0.0085	1	0	0.0043	0.0345	3.95	1.59	184.8	2170	2166	4.2	350	1.67E+16	
4	0.0048	0.0004	0.0076	0.0135	0.0003	0.0005	0.0012	0.998	0	1	0.0017	0.0004	0	0	1.002	0	0.0062	0.0005	3.9766	1.59	183.9	1592	1589	3.1	693	1.30E+16	
4	0.0074	0.0004	0.0333	0.0245	0.0007	0.0006	0.006	1	0.0147	0.9615	0.0145	0.0008	0	0.0084	1	0	0.0038	0.04	3.9261	1.59	186.0	7683	7668	14.9	774	5.80E+16	
3	0.0074	0.0006	0.0301	0.0219	0.0008	0.0005	0.0057	1	0.0068	0.9595	0.0102	0.0006	0	0.023	1	0	0.0035	0.0959	3.8696	1.59	185.1	7315	7301	14.1	647	5.54E+16	
4	0.0059	0.0004	0.0176	0.0101	0.0004	0.0014	0.0017	0.9989	0	0.9971	0.0038	0.0003	0	0	1.0011	0	0.0081	0.0101	3.9688	1.59	184.3	2204	2199	4.3	1723	1.92E+16	
2	0.0049	0.0005	0.0108	0.0121	0.0004	0.0008	0.0014	1	0.0008	0.9864	0.0021	0.0002	0	0.0105	1	0	0.0197	0.0305	3.9291	1.59	184.0	1850	1846	3.6	1070	1.55E+16	
2	0.0041	0.0004	0.0068	0.0252	0.0004	0	0.0014	1	0.0002	0.9787	0.0009	0.0002	0	0.02	1	0	0.0085	0.0729	3.9024	1.59	184.8	1800	1796	3.5	0	1.34E+16	
3	0.0072	0.0004	0.0129	0.0182	0.0006	0.0006	0.0051	1	0.002	0.9716	0.0017	0.0002	0	0.0245	1	0.0095	0.0045	0.0908	3.8635	1.59	183.9	6644	6631	12.8	820	5.10E+16	
	0.006	0	0.017	0.018	0.001	0.001	0.003	1	0.004	0.979	0.005	0	0	0.012	1	0.001	0.008	0.049	3.919	1.59	184.6	4155	4147	8.0	818	3.22E+16	
3	0.0018	0.0003	0.0118	0.0116	0.0002	0.0007	0.001	1	0.0046	0.9349	0.0028	0.0009	0	0.0568	1	0	0.0004	0.2354	3.756	1.59	183.3	1235	1233	2.4	874	1.07E+16	
2	0.0021	0.0004	0.0091	0.0121	0.0003	0.0008	0.0015	1	0.0044	0.9486	0.0018	0.0005	0	0.0447	1	0	0.0039	0.1773	3.7733	1.59	181.0	1939	1935	3.7	1034	1.64E+16	
3	0.002	0.0004	0.0105	0.0119	0.0003	0.0008	0.0013	1	0.0045	0.9418	0.0023	0.0007	0	0.0508	1	0	0.0022	0.2064	3.7647	1.59	182.2	1587	1584	3.1	954	1.35E+16	
1	0.0014	0.0001	0.0069	0.0123	0.0003	0.0004	0.0008	1	0.0066	0.9552	0.003	0.0002	0	0.035	1	0	0.0077	0.134	3.819	1.59	181.5	996	994	1.9	460	8.29E+15	
1	0.0011	0.0001	0.0037	0.0153	0.0003	0.0002	0.0008	1	0.0071	0.9653	0.0014	0.0009	0	0.0252	1	0	0.0047	0.0963	3.8598	1.59	181.9	1080	1078	2.1	204	8.49E+15	
3	0.0026	0.0001	0.0199	0.0109	0	0.0006	0.0009	1	0.0307	0.9595	0.0036	0.0004	0	0.0057	1	0.0114	0.0058	0.0179	3.8919	1.59	180.8	1140	1138	2.2	811	9.99E+15	
	0.002	0	0.01	0.013	0	0	0.001	1	0.015	0.96	0.003	0.001	0	0.022	1	0.004	0.006	0.083	3.857	1.59	181.4	1072	1070	2.1	492	8.92E+15	
1	0.0009	0.0001	0.0034	0.0108	0.0003	0.0002	0.0003	1	0.0003	0.9895	0.0028	0.0003	0	0.0071	1	0	0.0004	0.0287	3.9594	1.59	183.4	416	416	0.8	312	3.62E+15	
1	0.0012	0.0001	0.0048	0.0144	0.0003	0.0004	0.0013	1	0.0033	0.9585	0.0019	0	0	0.0363	1	0.0065	0.0052	0.1336	3.8192	1.59	181.8	1697	1694	3.3	522	1.37E+16	
3	0.0021	0	0.0149	0.0142	0.0004	0.0003	0.002	1	0.0052	0.9772	0.007	0.0002	0	0.0105	1	0.0083	0.0034	0.0308	3.9211	1.59	182.9	2567	2562	5.0	374	1.99E+16	
	0	0	0.002	0.0109	0.0002	0.0001	0.0003	1	0.0012	0.973	0.0013	0.0008	0	0.0236	1	0	0	0.0949	3.8972	1.59	183.3	450	449	0.9	153	3.62E+15	
1	0.0008	0.0001	0.0031	0.0124	0.0002	0.0002	0.0003	1	0.0013	0.9928	0.0022	0.0002	0	0.0036	1	0	0.0004	0.0147	3.9778	1.59	184.0	328	327	0.6	213	2.79E+15	
1	0.0015	0.0001	0.0063	0.0124	0.0003	0.0002	0.0004	1	0.0155	0.963	0.0029	0.0008	0	0.0178	1	0	0.0006	0.0737	3.8908	1.59	182.0	524	523	1.0	233	4.33E+15	
1	0.001	0.0001	0.0057	0.0121	0.0002	0.0003	0.0004	1	0.0036	0.981	0.0028	0.0004	0	0.0123	1	0	0.0006	0.0514	3.938	1.59	183.8	456	455	0.9	363	3.99E+15	
	0.001	0	0.006	0.012	0	0	0.001	1	0.004	0.976	0.003	0	0	0.016	1	0.002	0.002	0.061	3.915	1.59	183.0	920	918	1.8	310	7.42E+15	
2	0.0031	0.0006	0.0224	0.0119	0.0003	0.0005	0.001	1	0.0169	0.9492	0.0034	0.0003	0	0.0302	1	0	0.0047	0.1328	3.8159	1.59	181.8	1314	1312	2.5	660	1.10E+16	
1	0.0011	0.0001	0.0053	0.0125	0.0002	0.0003	0.0006	1	0.001	0.9639	0.0019	0.0005	0	0.0327	1	0	0.0052	0.1266	3.8409	1.59	182.2	737	735	1.4	319	6.08E+15	
4	0.0018	0	0.0081	0.0128	0.0002	0.0004	0.0008	1	0.0078	0.9689	0.0019	0.0011	0	0.0203	1	0	0.0064	0.0796	3.8756	1.59	182.1	1046	1044	2.0	471	8.66E+15	
1	0.0017	0.0001	0.0065	0.0107	0.0002	0.0004	0.0006	1	0.0082	0.9594	0.0017	0.0002	0	0.0304	1	0	0.0065	0.1181	3.8304	1.59	181.0	841	839	1.6	486	7.18E+15	
1	0.0009	0.0001	0.0046	0.0123	0.0001	0.0002	0.0007	1	0.0078	0.9642	0.0017	0.0018	0	0.0245	1	0	0.0044	0.0945	3.8594	1.59	181.4	941	939	1.8	315	7.64E+15	
1	0.0008	0.0001	0.0045	0.011	0.0002	0.0003	0.0006	1	0.0058	978	0.0018	0.0001	0	0.0143	1	0.006	0.0034	0.0476	3.9042	1.59	181.7	761	759	1.5	376	6.36E+15	
2	0.0036	0.0006	0.0265	0.0117	0.0003	0.0007	0.0019	1	0.0093	0.9579	0.0074	0.0007	0	0.0248	1	0.0139	0.0034	0.0944	3.8407	1.59	181.8	2437	2433	4.7	886	1.99E+16	
1	0.0006	0	0.004	0.0125	0.0003	0.0002	0.0009	1	0.0117	0.9147	0.0015	0.0019	0	0.0702	1	0	0.0035	0.2772	3.6724	1.59	180.0	1172	1170	2.3	260	9.37E+15	
4	0.0016	0	0.0085	0.0113	0.0003	0.0004	0.0006	1	0.0027	0.9486	0.0032	0.0002	0	0.0454	1	0	0.0065	0.175	3.7915	1.59	182.0	739	738	1.4	531	6.44E+15	
	0.002	0	0.01	0.012	0	0	0.001	1	0.008	0.956	0.003	0.001	0	0.033	1	0.002	0.005	0.127	3.826	1.59	181.6	1110	1108	2.1	478	9.18E+15	
1	0.0017	0.0001	0.0092	0.0115	0.0004	0.001	0.0009	1	0.0013	0.9854	0.0025	0.0009	0.01	0	1	0	0.0008	0.0064	3.9688	1.59	183.9	1118	1116	2.2	1267	1.04E+16	
3	0.0008	0	0.0054	0.0115	0.0004	0.0006	0.0008	1	0	0.9643	0.0024	0.0012	0.0321	0	1	0	0.0024	0.001	3.946	1.59	183.1	1052	1050	2.0	714	9.05E+15	
3	0.001	0	0.006	0.0121	0.0004	0.0003	0.0007	1	0.0007	0.9731	0.0022	0.0014	0.0226	0	1	0	0.0018	0	3.9549	1.59	183.2	940	938	1.8	372	7.65E+15	
3	0.0016	0	0.0099	0.0133	0.0003	0.0003	0.001	1	0.0059	0.977	0.0025	0.0007	0.014	0	1	0	0.0033	0.0045	3.9404	1.59	182.5	1362	1359	2.6	332	1.08E+16	
1	0.0011	0.0001	0.0056	0.0133	0.0003	0.0003	0.001	1	0.0005	0.9869	0.0021	0.0006	0.0099	0	1	0	0.0008	0.0011	3.973	1.59	183.8	1295	1293	2.5	334	1.02E+16	
	0.001	0	0.007	0.012	0	0.001	0.001	1	0.002	0.977	0.002	0.001	0.018	0	1	0	0.002	0.003	3.957	1.59	183.3	1153	1151	2.2	604	9.62E+15	
3	0.0015	0.0003	0.0085	0.0105	0.0005	0.0009	0.001	1	0.0013	0.9642	0.0025	0.0007	0.0314	0	1	0	0.0031	0.0032	3.933	1.59	182.6	1263	1260	2.4	1096	1.13E+16	
1	0.0013	0.0001	0.0114	0.01	0.0004	0.0016	0.001	1	0.0026	0.9658	0.0032	0.0012	0.0272	0	1	0	0.0033	0.0058	3.9162	1.59	181.4	1292	1289	2.5	2029	1.31E+16	
1	0.0014	0.0001	0.0069	0.0119	0.0003	0.0008	0.0011	1	0.0005	0.9677	0.0021	0.0015	0.0283	0	1	0	0.0024	0.0048	3.9411	1.59	182.9	1404	1401	2.7	1059	1.23E+16	
1	0.001	0.0001	0.0056	0.0124	0.0003	0.0003	0.001	1	0.0004	0.9729	0.0018	0.0003	0.0246	0	1	0	0.0028	0	3.944	1.59	182.8	1346	1343	2.6	412	1.08E+16	
1	0.002	0.0002	0.0073	0.0134	0	0.0006	0.0011	1	0.003	0.9709	0.0021	0.0003	0.0236	0	1	0	0.0025	0.0028	3.9402	1.59	182.8	1379	1376	2.7	747	1.16E+16	
	0.001	0	0.008	0.012	0	0.001	0.001	1	0.002	0.968	0.002	0.001	0.027	0	1	0	0.003	0.003	3.935	1.59	182.5	1337	1334	2.6	1069	1.18E+16	
1	0.0008	0.0001	0.0054	0.0108	0.0002	0.0002	0.0002	0.9998	0	0.9973	0.0028	0.0001	0	0	1.0002	0	0	0.0024	3.997	1.85	184.5	310	309	0.5	237	3.18E+15	
3	0.0009	0.0003	0.0031	0.0121	0.0002	0.0001	0.0001	0.9974	0	1	0.0024	0.0002	0	0	1.0026	0	0	0.0007	3.998	1.85	184.3	181	181	0.3	131	1.85E+15	
1	0.0008	0	0.0042	0.0111	0.0003	0.0002	0.0004	0.9992	0	0.9983	0.0025	0	0	0	1.0008	0	0	0.0018	3.9976	1.85	184.6	561	560	0.9	267	5.46E+15	
	0	0	0.0014	0.0116	0.0002	0.0001	0.0003	0.9959	0	1.0019	0.0019	0.0003	0	0	1.0041	0	0	0	4.0001	1.85	184.2	400	399	0.6	179	3.88E+15	
	0.001	0	0.004	0.011	0	0	0	0.998	0	0.999	0.002	0	0	0	1.002	0	0	0.001	3.998	1.85	184.4	363	362	0.6	204	3.59E+15	
1	0.0008	0	0.0033	0.0117	0.0002	0	0.0001	1	0	0.9907	0.002	0.0002	0	0.007	1	0	0	0.0292	3.9697	1.85	184.4	103	103	0.2	0	9.15E+14	
4	0.0009	0	0.0042	0.0123	0	0	0.0001	1	0	0.9933	0.0023	0.0001	0	0.0042	1	0	0	0.0187	3.9809	1.85	184.5	142	142	0.2	0	1.26E+15	
1	0.0007	0	0.0029	0.0117	0.0002	0	0.0001	1	0	0.9862	0.0017	0.0002	0	0.012	1	0	0	0.0491	3.9502	1.85	184.2	137	137	0.2	0	1.21E+15	
	0.001	0	0.003	0.012	0	0	0	1	0	0.99	0.002	0	0	0.008	1	0	0	0.032	3.967	1.85	184.4	127	127	0.2	0	1.13E+15	
3	0.0024	0.0001	0.007	0.0113	0.0003	0.0002	0.0003	0.991	0	1.0061	0.0027	0.0001	0	0	1.009	0	0	0.0043	3.9921	1.85	184.0	450	450	0.7	232	4.43E+15	
1	0.0023	0.0002	0.0056	0.0111	0.0002	0.0002	0.0003	0.9893	0	1.0061	0.0045	0.0002	0	0	1.0107	0	0	0.0012	3.9964	1.85	183.8	427	426	0.7	241	4.24E+15	
1	0.0023	0.0002	0.0046	0.0117	0.0003	0.0002	0.0003	0.991	0	1.0056	0.0032	0.0002	0	0	1.009	0	0.0005	0.0015	3.996	1.85	184.0	396	395	0.6	240	3.96E+15	
1	0.0017	0.0002	0.0051	0.0121	0.0003	0.0002	0.0003	0.9944	0	1.0022	0.0031	0.0002	0	0	1.0056	0	0	0.0018	3.9952	1.85	184.2	416	415	0.6	215	4.08E+15	
1	0.0028	0.0003	0.0063	0.0114	0.0002	0.0002	0.0004	0.9945	0	1.002	0.0033	0.0001	0	0	1.0055	0	0	0.0026	3.9949	1.85	184.3	523	522	0.8	271	5.14E+15	
	0.002	0	0.006	0.012	0	0	0	0.992	0	1.004	0.003	0	0	0	1.008	0	0	0.002	3.995	1.85	184.1	442	442	0.7	240	4.37E+15	
2	0.0028	0.0002	0.0139	0.0112	0.0003	0.0005	0.0007	1	0.008	0.962	0.0049	0.0003	0	0.0248	1	0	0.0042	0.1021	3.8617	1.85	182.4	965	964	1.5	591	9.75E+15	
4	0.0036	0.0002	0.0093	0.0121	0	0.0003	0.0005	0.9908	0	1.0055	0.0036	0.0001	0	0	1.0092	0	0.0027	0.0034	3.9866	1.85	183.8	681	680	1.1	438	6.87E+15	
3	0.0029	0.0002	0.0079	0.0117	0.0002	0.0002	0.0005	1	0	0.9932	0.0036	0.0002	0	0.003	1	0	0.0014	0.0127	3.9744	1.85	184.0	710	709	1.1	290	6.84E+15	
3	0.0018	0	0.0038	0.0108	0.0002	0	0.0002	0.9949	0	1.0028	0.0022	0.0002	0	0	1.0051	0	0	0.0013	3.9946	1.85	183.9	320	320	0.5	0	2.84E+15	
3	0.0023	0	0.006	0.0106	0.0003	0.0001	0.0004	0.9982	0	0.9977	0.004	0.0001	0	0	1.0018	0	0	0.0022	3.9948	1.85	184.3	481	480	0.8	145	4.53E+15	
	0.003	0	0.008	0.011	0	0	0	0.997	0.002	0.992	0.004	0	0	0.006	1.003	0	0.002	0.024	3.962	1.85	183.7	631	631	1.0	293	6.17E+15	

Table S5. LA-ICP-MS data for zircon (ppm)

Affiliation	Granite	Age	Location	Sample	Grain	Al	P	Ca	Ti	Mn	Fe	Y	Nb	Sn	La	Ce	Pr	Nd	Sm	Eu	Gd	Tb	Dy	Ho	Er	Tm	Yb	Lu	Hf	Ta	^{206}Pb	^{207}Pb	^{208}Pb	∑Pb	Th	U	∑REY
DSG		1.85	Wirrda Well	LCD17	1	<0.57	377	<112	10.9	2.29	35.7	880	2.45	0.45	0.049	13.5	0.218	3.31	5.14	0.298	24.7	7.07	84.6	31	138	27	241	45.3	9450	1.04	48.1	5.34	9.04	62.5	90.9	147	1500
						927	249	<123	9.51	7.36	2820	393	1.25	0.26	0.566	9.09	0.153	1.55	1.29	0.124	6.58	2.66	33.3	13.1	64.2	12.9	125	24.5	9400	0.68	50.9	6.0	7.46	64.4	58.6	138	687
						15.8	279	531	3.29	194	4700	276	2.53	0.39	0.103	4.36	0.313	1.41	1.59	0.24	4.51	1.61	17.4	7.72	47.6	11.4	133	28.4	10200	2.56	126	15	11.7	153	81.5	646	535
						0.8	287	<101	1.51	<0.43	<23.9	444	3	0.21	0.015	10.3	0.015	1.06	0.77	0.048	6.82	2.39	35	14.1	75	16.1	153	30.8	11500	1.78	102	11.8	12.1	126	120	316	789
						4.17	331	<110	11.4	<0.42	<24.1	757	1.7	0.3	0.086	11.8	0.122	2.53	4.07	0.505	19.1	6.11	72.6	25.3	119	23.4	209	40	9660	0.87	45.6	5.28	7.48	58.4	73.2	136	1290
						323	201	<112	11.2	2.33	446	875	1.97	<0.16	0.05	14.2	0.28	3.22	5.05	0.48	25	8.26	89	33.3	143	28.3	244	46.9	10300	0.78	41.1	4.53	8.29	53.9	77	132	1510
					2	358	509	143	8.28	5.21	841	1900	1	0.22	0.335	20	1.88	13.2	22.5	3.78	82	22.3	229	66.7	277	49.5	429	79.1	10700	0.74	72.4	9.2	13.6	95.1	148	255	3200
						1.03	521	<136	5.62	0.63	94.3	1110	0.94	0.22	0.012	6.98	0.127	3.16	6.07	0.72	27.1	8.47	101	36.4	181	34.1	298	56.6	7870	0.54	57.9	6.22	11.6	75.7	100	151	1870
						7.18	239	<101	9.58	0.91	<26.4	528	2.02	0.27	0.11	9.81	0.272	2.76	2.92	0.471	13.2	4.37	53.7	17.1	82.2	16.6	150	29.2	8830	1.23	55.4	6.2	5.08	66.7	49.7	159	910
					3	2.06	414	<102	12.2	0.94	37.9	1820	2.34	0.16	0.042	18.4	0.419	6.25	12.6	0.79	52.2	16.1	187	63	277	52	421	78.7	9750	1.16	95.3	11	26	132	286	308	3010
						<0.52	253	<91.4	4.69	<0.41	<24.7	852	1.91	<0.17	<0.015	13.2	0.042	0.62	2.55	0.12	14.8	5.27	74	28.2	137	29.3	260	50.9	10700	0.998	91.9	10.9	13.4	116	138	282	1470
						<0.51	398	<105	7.41	<0.42	<24.1	1150	1.77	0.34	<0.014	13.4	0.105	1.69	3.17	0.318	26	8.31	108	39.2	176	35.6	304	57.8	10200	0.91	71.6	8.56	15	95.1	157	227	1930
						<0.65	277	169	6.87	<0.48	<28	550	1.85	0.31	0.01	10.6	0.048	0.87	2.03	0.045	11.1	3.95	44.4	17.3	88.3	18.2	172	34.4	8780	1.08	65.7	7.71	9.41	82.8	80.2	178	953
					4	402	480	197	6.22	7.19	1170	1280	2.05	<0.16	0.347	14.3	1.05	10	23	3.34	96.1	23.7	186	42.7	164	28.9	245	43.4	11600	1.53	106	12.4	11.4	130	119	347	2170
						<0.55	400	110	6.46	2.03	37.4	689	3.69	0.31	0.047	15.7	0.067	0.43	2.23	0.105	12.3	4.35	55.9	22.5	117	24.3	209	41	11700	2.12	86.9	9.84	10.9	108	115	275	1190
						70.4	852	<95.5	5.66	7.93	146	2710	3.07	0.19	1.07	24.1	3.36	32.3	56.6	8.22	191	53.8	421	91.5	273	40.4	292	48.6	11100	1.99	89.4	10	8.71	108	89.5	286	4250
						104	999	234	4.88	152	2260	3040	5.85	0.28	1.52	40.8	3.14	30.6	50.8	7.71	216	54.3	445	107	387	65.1	548	92.9	8540	2.46	153	17.6	42.3	212	422	545	5090
						426	645	530	7.98	302	4890	2170	4.75	<0.14	8.07	50.2	8.26	50.1	57.2	8.86	166	43.1	337	74	250	41	351	60.4	12700	3.7	144	17.9	14.1	176	102	723	3670
					5	1.43	548	<112	5.94	<0.48	<27.4	2590	5.48	0.5	0.099	20.9	1.01	12.9	16.1	2.08	81.5	23.7	265	88.4	372	69.5	563	105	7700	1.85	67.1	7.3	18.6	92.9	174	189	4210
						<0.55	181	305	9.85	0.84	<25.2	443	1.21	0.24	<0.009	8.17	0.07	0.9	1.78	0.105	10.2	3.48	38.6	14.9	68.9	15	133	25.3	9910	0.437	26.9	3.22	3.67	33.8	41.7	86.6	763
						25.6	268	<110	9.56	0.48	68.6	420	1.59	0.28	0.032	9.7	0.101	0.71	1.24	0.16	8.38	2.96	36.1	14.4	68.9	14.5	127	25.1	10200	0.837	38.1	4.27	5.15	47.5	52.8	119	730
						30.8	223	126	7.06	8.29	134	465	1.76	<0.18	0.792	13.4	1.46	4.87	4.76	1.17	13	3.79	40.7	14.8	71.8	14.3	132	25.5	8920	0.643	40.8	4.42	6.3	51.5	48.5	108	807
DSG		1.85	Cape Donington	PL8	1	<0.56	190	<98.2	10.4	<0.41	25.4	538	2.8	<0.14	0.202	15.3	0.087	1.17	0.75	0.096	8.83	2.9	42.6	17.3	88.3	18.6	169	32.8	11200	1.58	103	11.7	13.1	128	143	326	936
						<0.56	238	<90.7	9.58	0.41	29.8	456	2.24	0.23	<0.012	10.6	0.082	0.51	1.12	0.159	9.99	2.83	37.6	14.6	74.2	14.3	142	28.7	10600	1.23	61.4	7.34	9.3	78.1	89.4	194	792
						0.66	322	125	12.9	<0.42	<24.4	881	2.19	<0.13	<0.012	12.8	0.13	1.7	4.44	0.191	21.2	6.29	78.8	29.2	141	27.4	243	46.2	10100	1.5	83.5	10	16.2	110	154	256	1490
						1.28	349	<91.5	7.1	<0.43	<25	1730	2.49	0.27	<0.018	20.2	0.216	4.63	8.63	0.7	45.3	14.5	167	59	258	50.5	425	79.4	10200	1.14	130	15	30.9	176	330	409	2860
					2	4.86	248	244	11.4	<0.43	<24.3	399	1.55	0.2	0.021	9.65	0.023	0.51	1.36	<0.022	6.18	2.87	33.9	13	64	13.4	126	24.9	10000	0.906	50.5	5.83	7.75	64.1	74.4	158	695
						0.82	233	<104	12.3	<0.41	<24.3	656	2.61	<0.17	0.019	14	0.062	1.46	2.22	0.073	12.9	4.46	59.1	21.3	101	20.8	190	37.6	9660	1.05	70.8	7.93	12.6	91.4	131	224	1120
					3	<0.52	206	264	13.1	<0.42	<25.2	403	1.55	<0.13	<0.012	9.24	0.049	0.59	1.16	0.015	7.99	2.6	34.2	13.5	63.5	13.9	123	24.7	10000	0.715	40.1	4.34	5.49	49.9	58.6	129	698
						<0.62	324	334	11.2	<0.47	<28.4	509	2.53	0.19	0.256	14.3	0.085	0.81	1.79	0.075	9.46	3.67	43.9	16.4	79.8	17.3	152	30.3	9910	1.54	104	12.1	14.1	131	137	292	879
						<0.74	231	<133	13.8	<0.54	<32.2	371	1.31	0.31	0.01	7.91	<0.023	0.33	1.09	0.118	6.55	2.56	30.7	11.8	58.4	12.4	111	22.2	8090	0.751	43.4	4.77	6.14	54.3	51.5	108	636
					4	0.75	235	<107	12.8	<0.44	53.5	507	2.14	0.54	<0.013	11.3	0.031	0.42	1.9	0.11	10.4	3.04	42.6	16.6	82.4	16.9	154	30.7	11100	1.13	63.5	7.46	9.78	80.8	95.1	203	877
						<0.74	262	123	7.98	<0.55	<31.5	414	1.82	<0.18	0.062	10.4	0.071	0.48	1.23	0.069	7.11	2.8	32.9	13.6	65.6	13.9	124	25.3	8330	0.987	77.1	9.24	10.2	96.6	87.7	194	712
						4.6	357	<100	13.1	0.48	<25.2	1110	3.23	0.18	0.067	15.1	0.239	2.9	5.4	0.354	28.7	8.7	101	37.1	174	34.9	303	57.7	9470	1.4	88.7	10.1	18.4	117	184	266	1880
						1.94	263	<106	24	<0.44	<25.5	845	2.93	0.7	<0.01	17	0.053	1.63	4.18	0.133	19.6	5.51	77.9	28.6	134	27.7	258	48.6	10500	1.78	92.7	10.7	17.1	120	186	304	1470
					5	<0.57	325	<92.7	15.2	<0.42	<24.8	1140	2.59	0.3	0.044	18	0.143	3.46	6.9	0.368	30.4	9.07	112	37.9	176	34.6	303	55	9630	1.28	98.8	11	21.7	132	225	314	1930
						<0.54	327	<100	13.4	<0.44	<24.6	1050	2.33	0.19	<0.018	15.3	0.181	2.67	6.01	0.359	24.8	7.96	97.2	34.7	160	31.9	281	54.7	9570	1.28	89	10.2	18.8	118	189	264	1770
						1.79	293	206	12.4	<0.41	<23.1	649	3.16	0.19	<0.012	13	<0.01	1.14	1.63	0.063	10.2	4.32	53.9	20.5	105	21.9	200	38.3	10600	1.66	85.7	9.88	12.8	108	132	267	1120
						0.97	223	<85	14.1	0.42	<23.2	534	2.93	0.39	<0.008	13.6	0.075	0.29	1.6	0.11	9.29	3.34	42.2	16.8	86.1	18.5	162	31.5	10400	1.29	80.4	9.48	11.9	102	126	251	920
					6	<0.54	361	<81.3	6.32	<0.44	28.4	1300	2.41	0.39	<0.009	17.8	0.131	2.46	4.44	0.279	31	9.84	118	42.5	200	39.4	332	63.5	10300	1.32	120	13.1	26.2	159	259	369	2160
						1.04	268	<93.5	9.85	<0.43	<25	611	2.69	0.36	<0.02	15.2	0.033	1.05	1.91	0.101	12.1	3.71	50.9	19.5	97	19.6	175	35.5	10500	1.53	97.1	11.4	15.2	124	149	290	1040
						8.75	282	<105	18.2	1.57	<24.8	872	3.92	<0.16	1.08	24	1.4	8.52	6.05	0.81	23.2	6.36	82.5	30.1	138	27.6	251	46.5	10800	1.85	116	13.9	21.3	151	234	374	1520
					7	2.45	233	158	8.25	<0.42	<24.9	614	2.77	0.6	0.447	18.1	0.592	3.69	3.37	0.215	11.7	3.62	51.8	19.7	102	20.3	180	34.1	10200	1.28	75.5	8.77	12.1	96.5	134	242	1060
						0.86	356	<101	11.7	<0.43	<24.2	626	2.76	<0.16	0.03	13.9	0.027	1.18	2.16	0.058	12.5	4.14	55.3	20.6	96.8	20.4	181	35.6	9780	1.15	71.7	8.07	12.2	92	122	219	1070
						3.15	410	<109	4.27	<0.43	<26	788	3.56	0.51	0.317	21.4	0.365	5.3	2.07	0.336	17.1	6.1	66.8	25.5	119	26.2	219	44.1	10100	1.62	172	21.2	27.8	221	246	487	1340
						1.65	168	<96.6	7.48	<0.42	26.6	534	3	<0.13	0.048	13.7	0.043	1.1	1.98	0.166	7.8	2.97	42.1	17.7	89.7	18.9	176	35.7	11600	1.6	125	13.9	14.6	153	162	411	942
HIS	RDG	1.59	OD - distal	LCD47	1	275	532	861	6.04	438	3180	2120	5.43	1.07	3.78	37.1	2.85	11.3	10.9	2.6	37.8	15.1	185	63.1	277	52.1	472	91.4	12600	1.97	121	12.9	18.3	152	277	691	3380
						783	959	2060	29.7	889	5680	5470	15.1	4.78	18	116	12.8	54.9	40.3	7.54	119	44.2	529	176	797	157	1300	226	10500	4.06	130	14.3	38.1	182	950	1220	9060
						2140	1270	2530	49.9	1050	7010	7140	9.18	11	55.2	344	40.7	158	83.9	22	170	67.2	713	217	940	186	1660	271	10200	2.34	124	14.7	39	177	949	1300	12100
						2130	810	3990	37.4	1110	6950	5610	10.1	8.03	56.7	319	38.1	138	64.9	18.6	138	50.7	577	168	741	140	1180	197	11600	3.39	113	12.2	28.9	154	735	1190	9440
						1760	1380	1920	51.3	865	6230	7880	8.98	8.38	42.2	262	30.4	125	69.5	18.1	162	67.9	777	241	1150	218	1920	331	11100	2.45	144	16.5	44	205	1010	1380	13300
						318	1910	1290	31.3	155	1750	5970	8.51	7.19	9.71	88.2	8.88	44.4	40.4	8.03	123	52.5	641	194	843	154	1260	197	9170	1.81	130	16.9	38.5	185	630	868	9630
					2	1270	2070	3920	30.3	1080	8000	8890	19.1	1.42	41.6	239	22.9	84.2	58.2	13	163	66.2	729	236	1050	204	1800	323	11500	4.98	188	17.1	42.1	248	1100	2090	13900
						2290	1500	3370	40.4	1420	9790	8390	18.7	2.79	93.5	509	55.7	190	90.8	26.7	191	69.1	722	220	984	188	1680	299	10900	4.65	237	25.2	73.1	335	1730	2420	13700
						560	473	1560	26.2	890	6030	3270	11	1.42	16.4	115	10.9	46.5	27.8	6.26	64.7	24.1	291	102	483	110	1040	192	11500	2.76	159	21.9	52.3	233	672	1280	5800
						566	653	1990	22.6	805	6070	2680	13.5	1.8	15.8	134	9.57	38.7	25.5	5.01	54.1	18.8	205	73.2	377	85.7	774	156	8880	4.69	277	25.7	69.6	372	1300	1880	4660
					3	376	380	1660	20.2	651	4660	2690	7.07	0.85	12.2	106	6.4	26.6	19.3	4.26	55.8	19.5	230	83.1	391	79.8	710	137	8780	2.2	133	15	43	191	747	964	4570
						1080	739	1830	42.7	731	5290	5290	13.1	2.34	37.7	267	25.5	102	59.8	14.5	122	41.3	502	165	767	146	1380	245	11000	2.64	164	26.1	69.3	259	818	1460	9160
						754	386	2920	12.7	936	7350	2340	12.3	0.98	19.9	121	10.1	43.5	22.6	4.87	46.6	17	199	67.2	345	74.3	735	153	11400	2.99	181	19.3	41.1	242	687	1670	4200
					5	3640	508	275	1490	307	8300	2110	6.14	2.81	1.16	46.9	1.04	8.35	10.3	1.32	48	16.2	196	71.1	343	67.1	606	116	11800	2.17	112	13.7	34.4	160	427	565	3640
					6	0.62	268	<102	23.2	121	561	1780	5.5	0.23	<0.009	41.6	0.262	3.61	6.76	0.92	42.1	13.3	168	61.3	285	55.1	494	94.9	11000	2.44	122	11.8	29	163	382	510	3050
HIS	RDG	1.59	OD - proximal	LCD13	1	63.2	386	<131	7.93	44.5	751	1110	5.29	0.33	0.144	29.7	0.202	1.64	3.34	0.599	18.9	7.19	85.6	34.6	178	38.6	375	76.5	8470	2.24	182	17	38.8	238	436	649	1960
						3810	212	770	9.49	361	13200	1210	10	0.69	1.3	40.3	0.78	3.34	3.87	1.76	15.2	6.15	84	35.7	204	51.7	554	122	12100	3.44	221	19.7	42.3	283	729	1360	2340
						1370	200	1010	13.9	401	5160	1350	12	0.77	6.12	59.5	3.54	16.5	12.9	5.77	33.8	10.9	113	39.8	214	56.3	657	161	12100	3.66	216	19.4	30.8	267	479	1650	2740
						1540	326	1240	27.7	455	7310	2430	17.7	2.01	10.8	109	7.42	39.4	32.2	38.7	84	26.4	253	73.3	360	89.1	1040	253	14300	4.24	399	31.7	31.5	462	623	3620	4850
						43.4	391	334	5.8	156	1810	2060	20.3	0.46	0.536	81	0.297	4.64	5.75	1.11	35	12.3	162	63.8	327	71.7	651	133	7770	6.99	502	46.7	140	689	1930	2230	3610
						33.1	561	206	35.9	72.3	942	2020	8.86	0.51	0.362	31.7	0.545	5.44	11.2	2.71	66	21.2	218	64.4	273	53.8	522	109	10500	3.41	206	20.6	34.2	261	455	897	3400
					2	222	344	<107	11.8	6.49	624	1310	4.34	0.43	0.487	34.9	0.286	3.29	4.85	1.19	30.8	11	121	42.2	202	41.6	356	68.1	9560	1.65	75.9	8.18	18.9	103	245	306	2220
						1.46	499	<102	11.8	0.58	<29.3	1260	4.85	0.46	<0.014	36.1	0.132	1.99	5.96	0.697	25.7	8.75	108	40.9	198	38.8	352	69.6	8210	2.04	137	12.9	35	185	370	431	2140
						196	243	170	15	1.32	228	540	3.72	0.65	0.476	22.9	0.165	1.97	1.56	0.23	12.1	2.92	43.7	17.3	87.1	18.8	170	35.3	9570	1.63	63.3	6.51	10.2	80	113	249	955
					3	4720	309	288	40.5	144	7080	1640	9.99	0.96	3.38	53.6	2.84	15.1	12.4	7.63	42.7	16.9	173	55.1	278	58.5	597	118	11700	3.85	194	16.9	31	242	543	1120	3070
					4	2470	891	258	38.1	60	1060	3050	21.9	0.44	4.56	72.7	4.06	25.6	22.8	9.79	91.8	31.3	337	108	464	93.4	867	169	11600	5.46	137	12.4	21.1	170	370	1000	5350
					5	1140	461	<104	20.6	8.59	460	1540	5.36	0.21	0.474	31.4	0.562	3.92	7.59	2.29	34.7	12.5	159	52.1	258	51.6	510	96.4	10500	2.31	84.2	8.19	15.8	108	197	356	2760
					6	80	407	<127	19.8	3.2	329	1460	1.79	0.24	0.075	25.6	0.148	3.97	6.25	1.17	40.8	10.8	143	47.6	220	40.7	368	68.7	7340	0.68	70	7.67	19.8	97.6	195	209	2440
					7	881	603	572	32.7	271	5600	3710	16.4	0.4	3.62	93.8	4.2	26.9	22.2	8.51	79.4	27.2	328	121	580	123	1130	221	8790	3.4	306	27.5	95	428	1510	1790	6480
						653	512	2110	12.9	493	5690	3740	29.3	0.54	9.11	142	3.45	17.8	19.4	6.27	77.8	26.9	315	117	575	118	1090	208	7610	8.61	439	33.9	169	641	3350	3380	6460
						636	82.4	343	21.2	148	3560	913	6.86	0.67	5.02	47.4	3.37	16.3	11.6	10.8	23.3	7.74	86.2	28.4	151	38.1	408	98.6	17800	2.09	257	24.4	53.8	335	272	1330	1850
					8	242	255	714	13.6	234	3150	1770	7.53	0.32	3.78	50.3	2.35	10.2	8.43	4.33	34.8	10.5	135	52.1	280	65	665	145	10500	2.68	225	19.9	42.2	287	691	1300	3240
						225	241	174	7.99	60.3	883	1340	11.6	0.61	0.96	42.2	0.661	4.61	6.53	1.76	23.1	9.7	105	42	221	48.6	474	95.4	10300	2.84	200	18.4	38.3	256	556	958	2410

ELECTRONIC APPENDIX C FOR CHAPTER 7

Supplementary C. Figures

Figure S1. Zircon grain from the Charleston granite (A) and an example of mottled areas imaged in bright field *versus* HAADF STEM modes (B, C).

Figure S2. LA-ICP-MS element maps for Cape Donington zircon.

Figures S3 A-E. EDS-STEM extended maps for zircons.

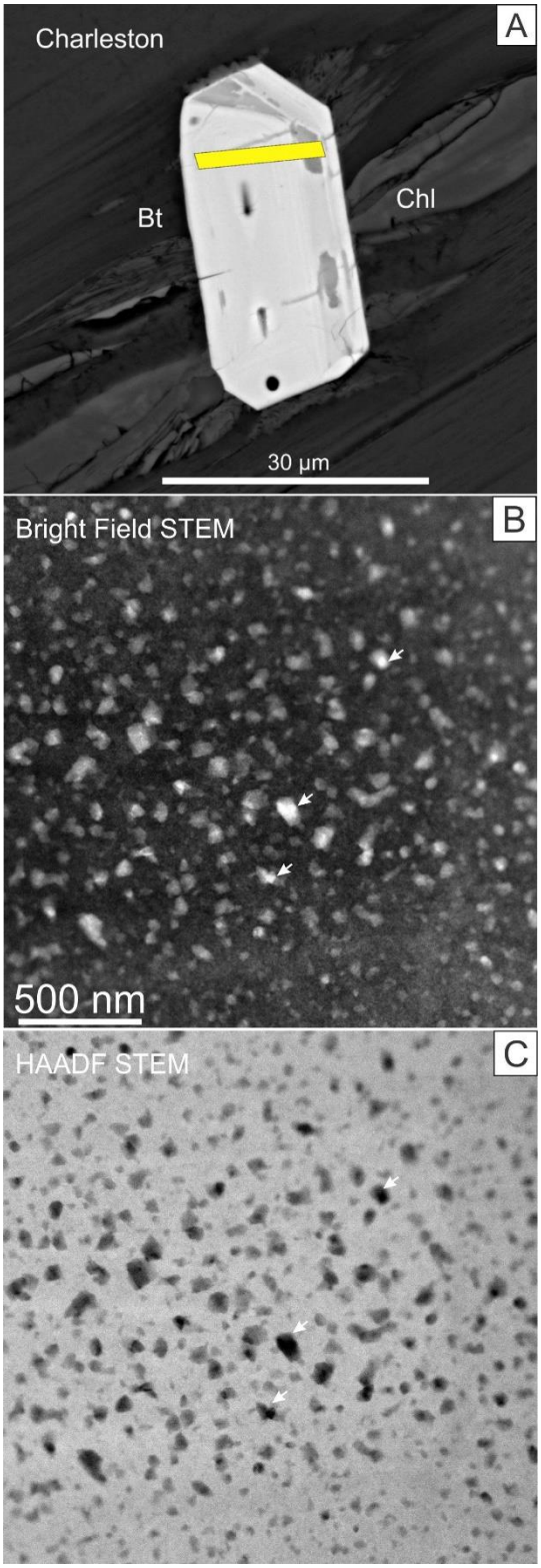


Figure S1. (A) BSE image of the Charleston zircon (Foil #6) showing the location of FIB cut (yellow rectangle). Abbreviations: Bt-biotite; Chl-chlorite. (B) Dense mottled area imaged in both bright field (BF) and (C) HAADF STEM modes (Fig. 8C) to assess presence of inclusions versus pores in OD distal zircon (Foil #1). Arrows (brightest in BF and darkest in HAADF STEM modes, respectively, shows the likelihood of holes being present.

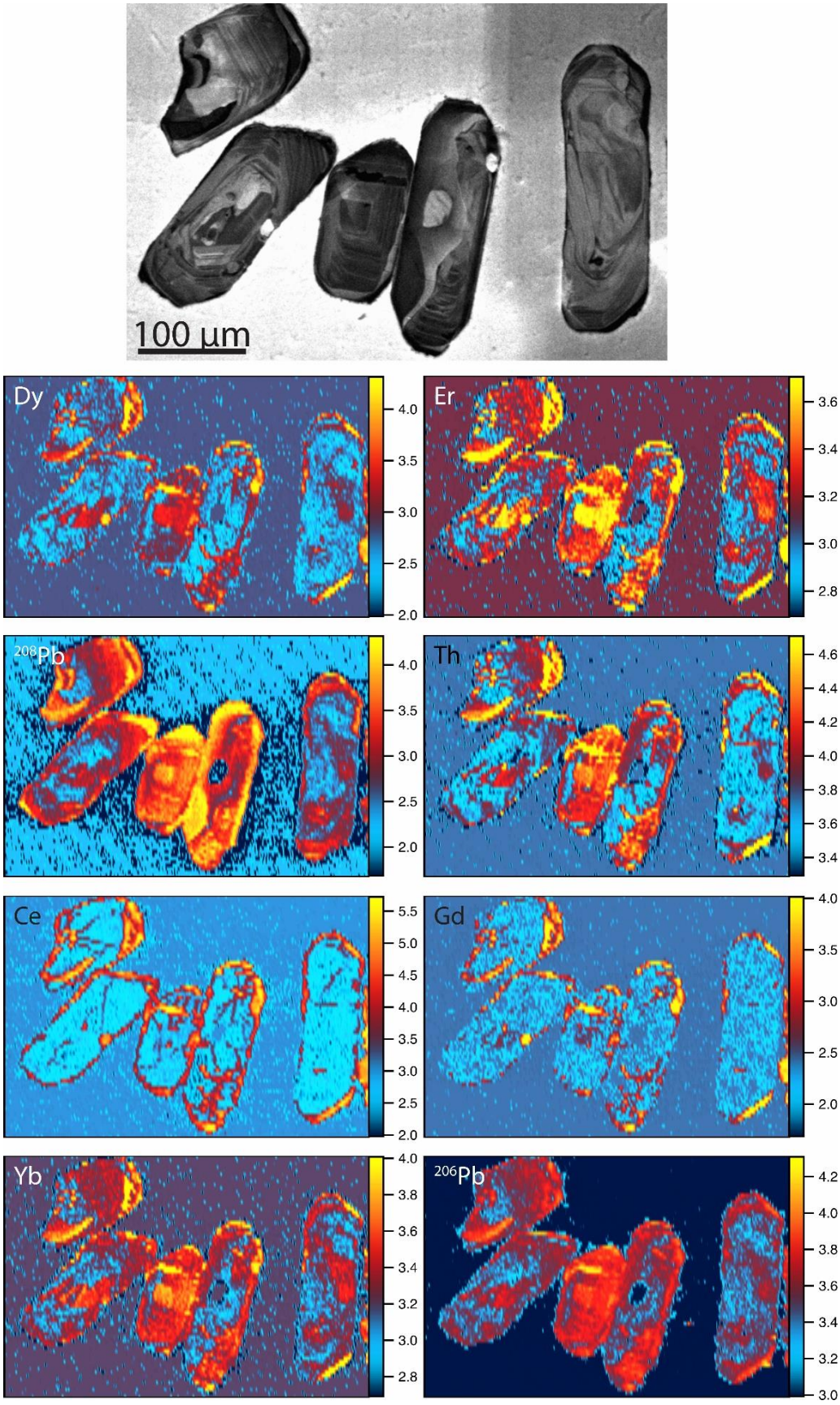


Figure S2. Extended LA-ICP-MS element maps for Cape Donington (PL8) zircon (Fig. 2F).

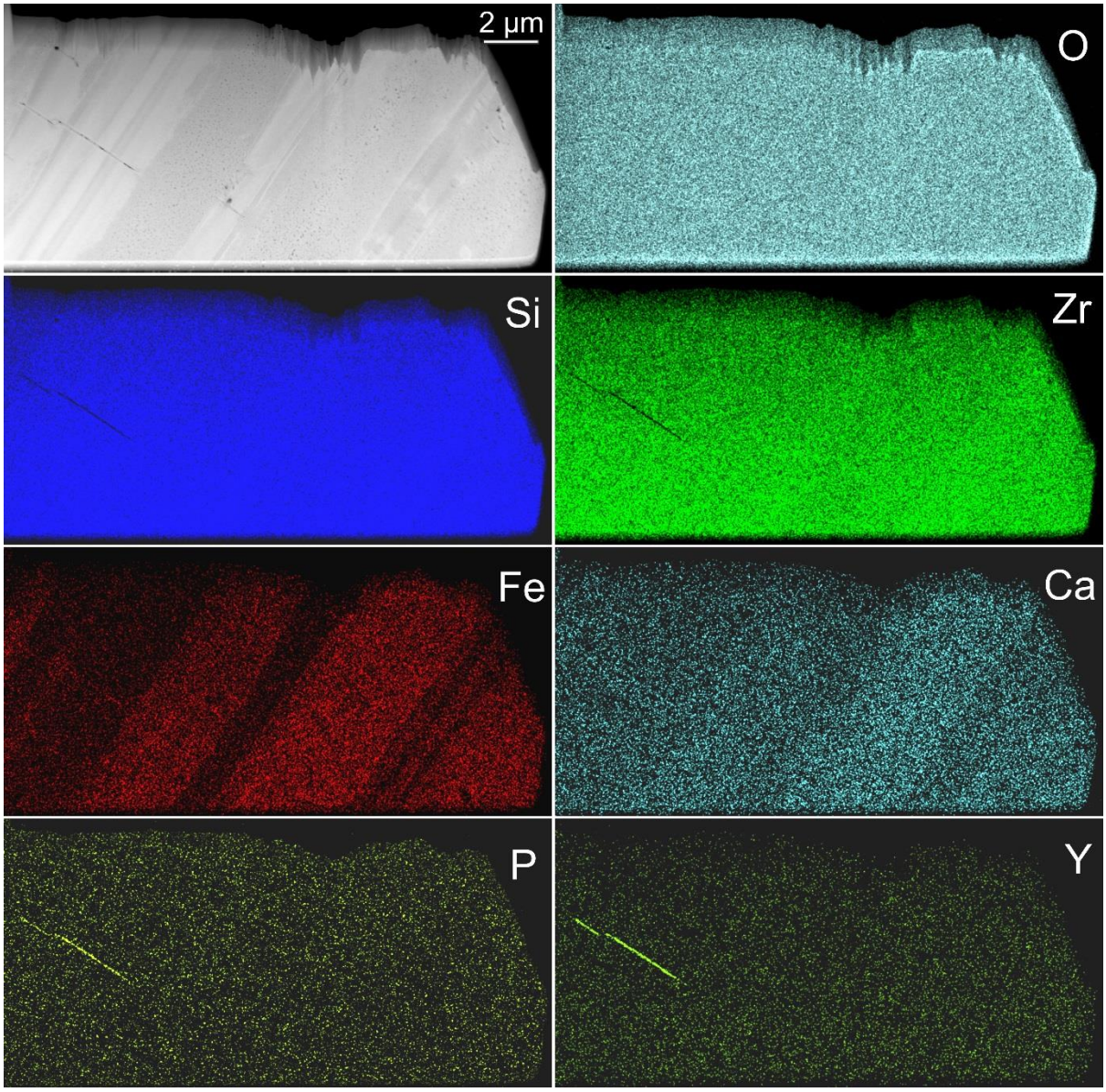


Figure S3-A. Extended EDS-STEM maps for the Wirrda Well Donington zircon (Foil #4; Fig. 6). Note weak Ca banding correlating with Fe distribution and the xenotime veinlet depicted on the P and Y maps.

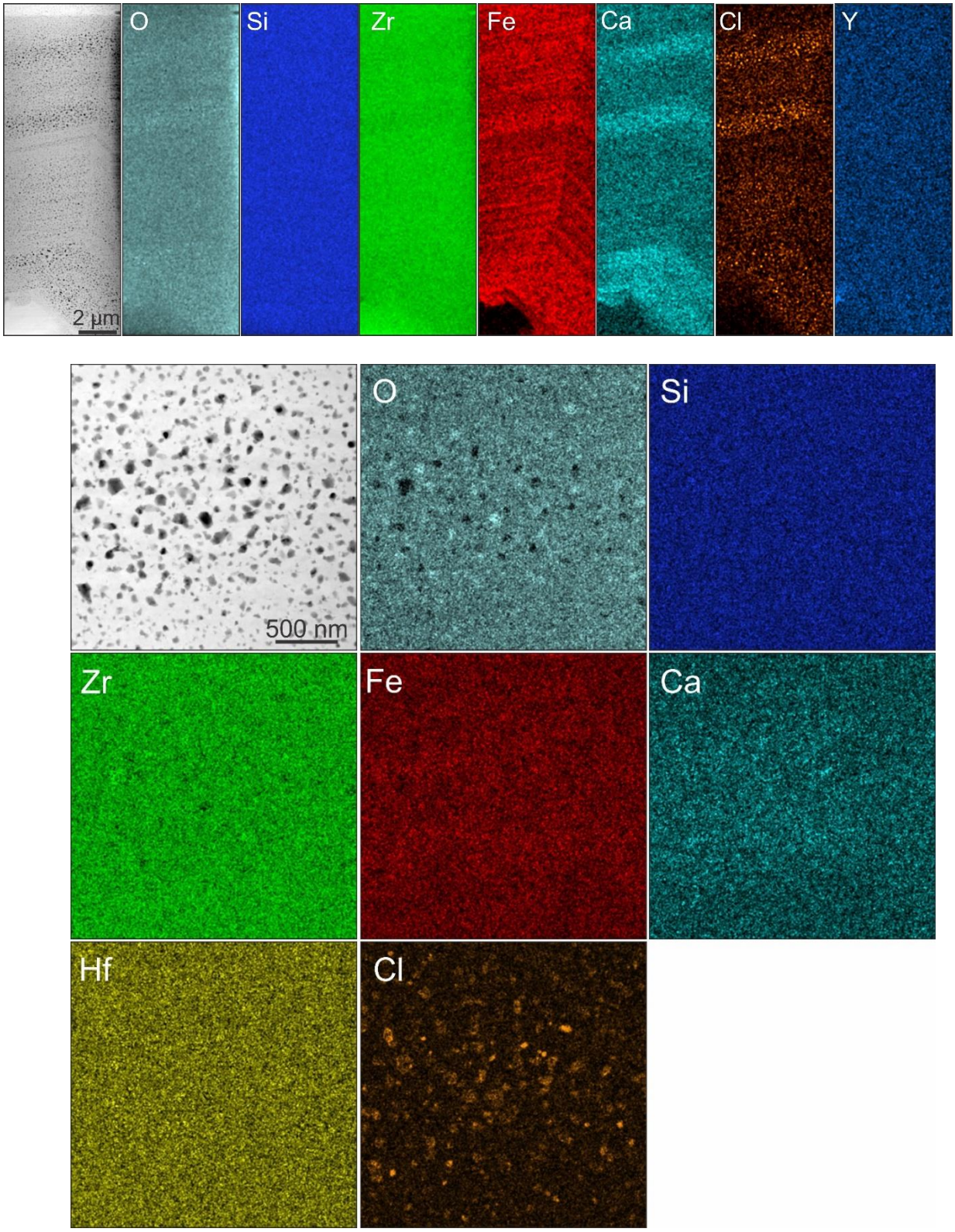


Figure S3-B. Extended EDS-STEM maps from the OD distal zircon (Foil #1; Fig. 8A and C).

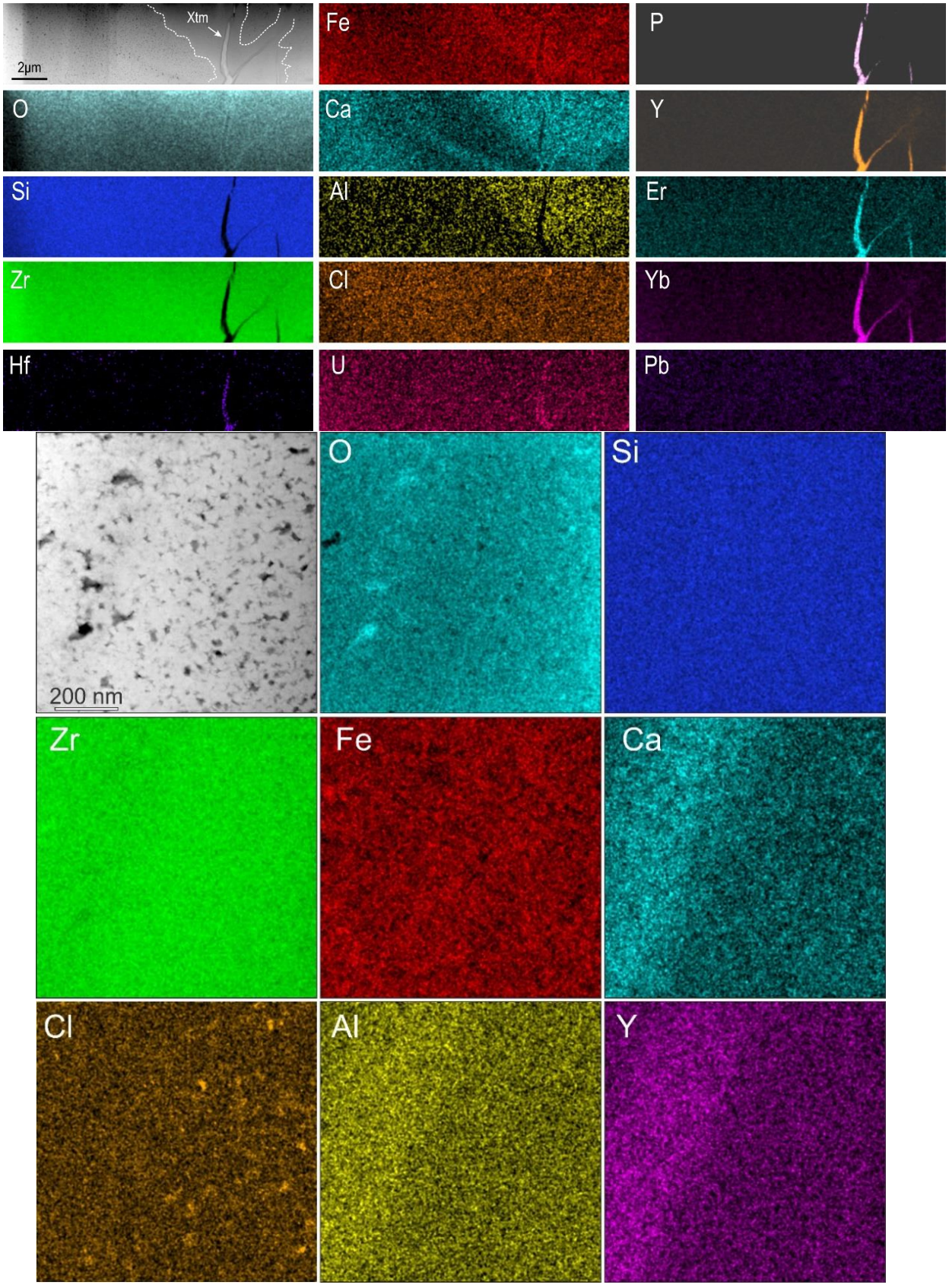


Figure S3-C. EDS-STEM maps of OD distal zircon (Foil #2). Presence of a xenotime veinlet and recrystallization of the surrounding mottled area (dashed line) is shown in the maps at the top. Chlorine is present as scattered, but nanodomains in the maps below.

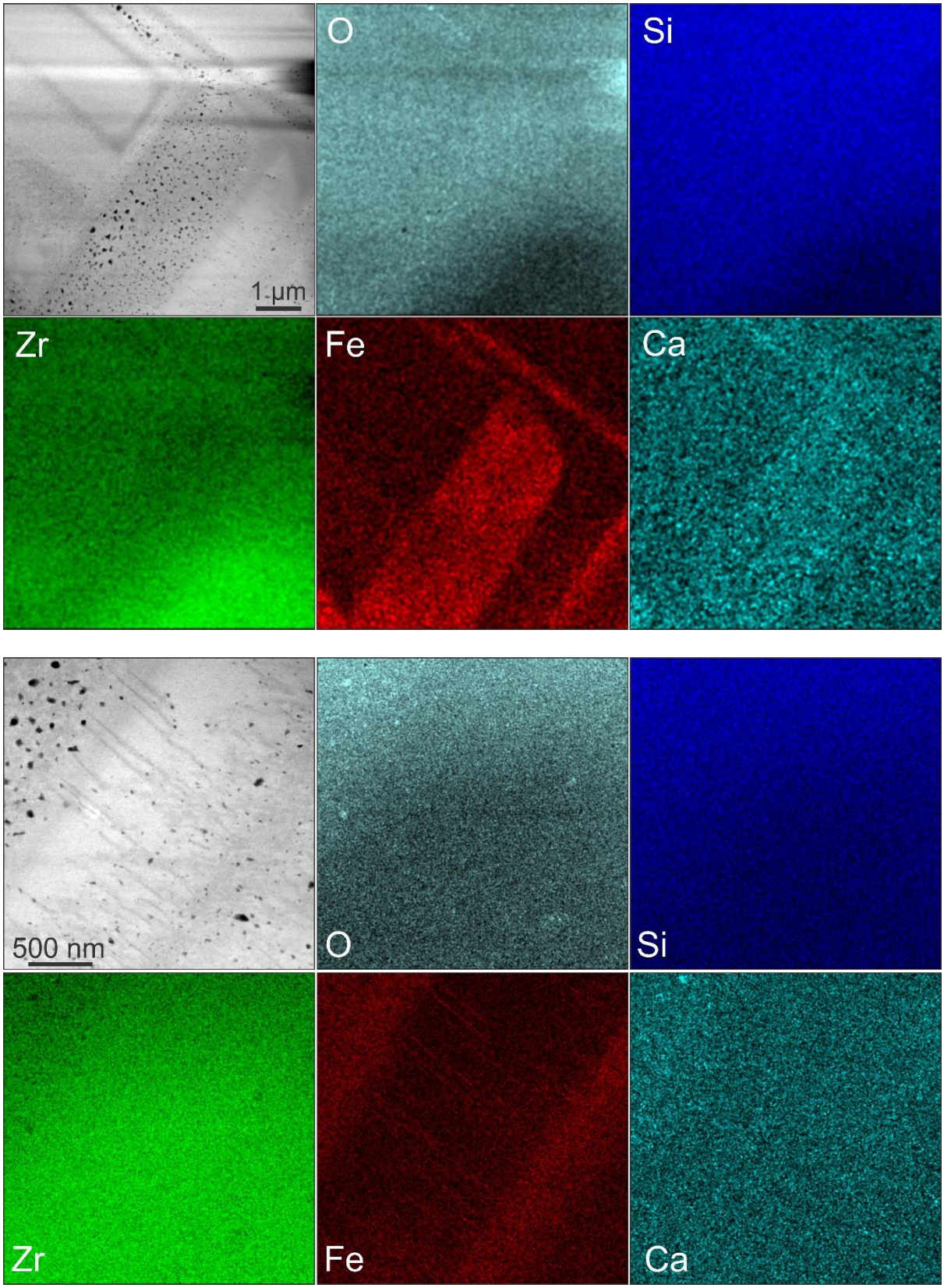


Figure S3-D. Extended EDS-STEM maps from the OD proximal zircon (Foil #3; Fig. 9E-F).

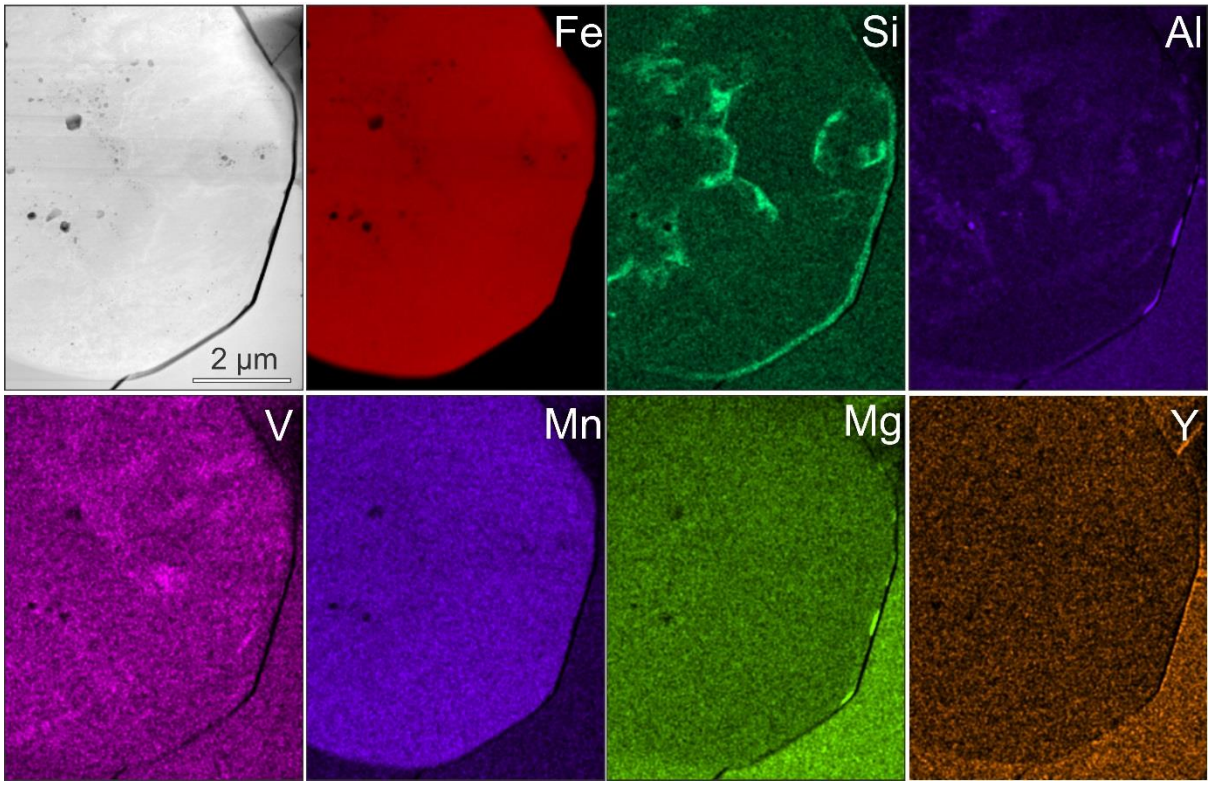


Figure S3-E. Extended EDS-STEM maps for hematite inclusion in the OD proximal zircon (Foil #3; Fig. 9B). Note presence of nanometer-sized inclusions of Mg-Al-silicates (chlorite?) along the boundary to host zircon and as inclusions in the hematite.

SUPPLEMENTARY MATERIAL G

FOR CHAPTER 8 – SYNTHESIS OF U-PB DOPED HEMATITE USING A HYDRATED FERRIC OXIDE APPROACH

APPENDIX A: XRD

APPENDIX B: LA-ICP-MS TRACE ELEMENT DATA

APPENDIX C: LA-ICP-MS TRACE U-PB DATA

ELECTRONIC APPENDIX A FOR CHAPTER 8

XRD data from samples 4.1, 4.2, 4.3 and 9

	No. Peak	2-theta (°)	d (Å)	Height(cps)	Intensity (%)
4.1	1	24.26	3.665	16325	2.8
	2	33.26	2.692	59117	10
	3	35.72	2.512	43811	7.4
	4	40.94	2.203	13869	2.3
	5	49.55	1.838	24252	4.1
	6	54.17	1.692	27579	4.7
	7	57.69	1.597	5499	0.9
	8	62.51	1.485	19556	3.3
	9	64.07	1.452	17596	3.0
	10	72.05	1.310	5420	0.9
4.2					
	1	24.33	3.656	14577	2.5
	2	33.34	2.686	58648	10
	3	35.80	2.506	44008	7.5
	4	41.03	2.198	13512	2.3
	5	49.63	1.835	23208	4.0
	6	54.23	1.690	29181	5.0
	7	57.78	1.594	5579	1.0
	8	62.59	1.483	18322	3.1
	9	64.14	1.451	18195	3.1
	10	72.11	1.309	6446	1.1
4.3					
	1	24.40	3.645	9962	2.2
	2	33.44	2.678	45948	10
	3	35.89	2.500	33121	7.2
	4	41.12	2.193	11739	2.6
	5	49.72	1.832	21610	4.7
	6	54.32	1.688	27702	6.0
	7	57.86	1.592	5276	1.1
	8	62.66	1.481	18599	4.0
	9	64.22	1.449	18228	4.0
	10	72.19	1.308	5647	1.2
9					
	1	24.19	3.677	14147	2.6
	2	33.21	2.696	54637	10
	3	35.66	2.516	39643	7.3
	4	40.89	2.205	13299	2.4
	5	49.50	1.840	21707	4.0
	6	54.11	1.694	27198	5.0
	7	57.64	1.598	5082	0.9
	8	62.46	1.486	18085	3.3
	9	64.03	1.453	17630	3.2
	10	71.99	1.311	5901	1.1

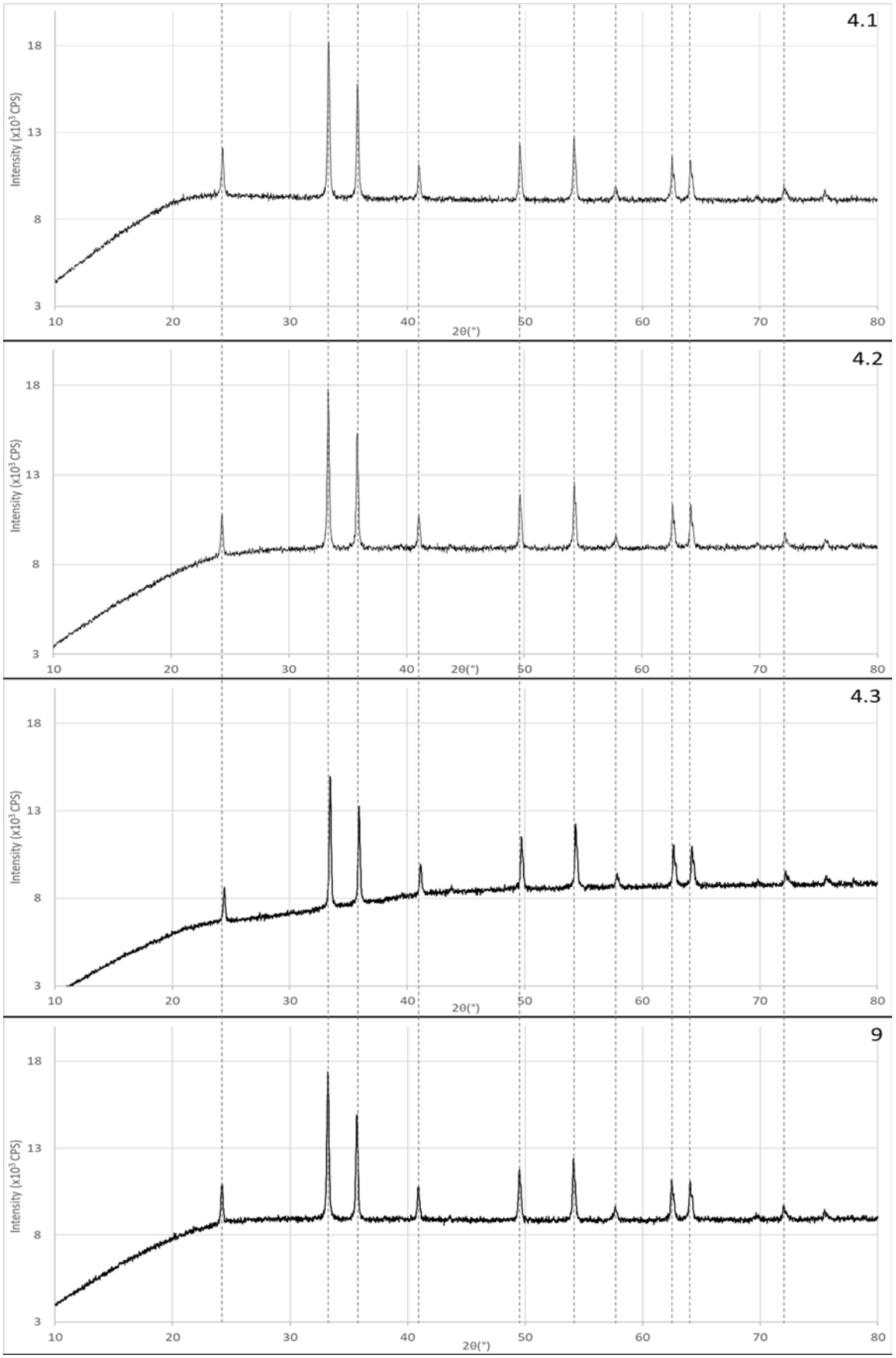


FIGURE1. X-RAY POWDER DIFFRACTION OF HFO

ELECTRONIC APPENDIX B FOR CHAPTER 8

LA-ICP-MS geochemical data for all reported samples

Sample	Spot Number	^{238}U	2SE	^{204}Pb	2SE	^{206}Pb	2SE	^{207}Pb	2SE	^{208}Pb	2SE	^{182}W	2SE	^{49}Ti	2SE	^{51}V	2SE	^{27}AL	2SE	^{24}Mg	2SE	^{55}Mn	2SE
HFO 4.1	1	123.3	9.1	64.5	6.4	56.2	4.4	62.4	5.3	59.8	5.1	0.0072	0.0082	50.4	8.3	68	5.4	505	36	2.24	0.43	16	1.8
	2	114.8	6.9	61.3	5.6	58.8	3.7	65.4	4	64.3	3.7	0.0045	0.0062	42.7	5.6	60.8	3.8	488	32	2.13	0.42	14.73	0.92
	3	116.1	5.4	64.1	4.5	54.2	2.9	61.7	2.8	59.3	2.8	0.015	0.012	49	5.8	68	4.2	481	26	2.28	0.42	17.1	1.2
	4	116	9.5	62.1	4.4	55.2	3.1	64.1	3.6	60.6	3.5	0.015	0.012	40.8	4.6	60	4.2	490	41	2.57	0.52	14.05	0.78
	5	116	6.5	66.9	5.3	59.3	2.3	67.7	3.1	64	2.5	0.021	0.015	46.9	5.5	63.6	2.8	475	27	2.35	0.34	16.5	1.1
	6	127.7	8.5	63.2	5.5	58.8	3.6	68	3.7	63.6	3.7	0.011	0.011	49.9	4	65.4	4.7	490	24	1.67	0.28	13.9	1
	7	116.7	7.6	57	5.9	56.6	3	64.1	4.1	60.7	3.6	0.0032	0.0064	42.1	4.7	66.5	4.1	497	36	2.1	0.4	14.8	1.1
	8	116.4	7.3	64.3	5.3	56.6	2.8	68.4	3.3	62.9	3.2	0	1	45.1	5.5	65.6	4.6	493	31	1.86	0.36	15.1	1.1
	9	115.1	8.8	54.4	5.4	52.3	2.9	61.1	3.7	57	3.9	0	1	44.8	4.3	62	4.7	460	26	1.83	0.37	15.2	1.5
	10	94.6	5.2	46.5	5.4	45.1	2.2	52	3	49.2	2.7	0	1	42.4	5.7	62.6	3.2	469	31	1.98	0.46	15.38	0.91
	11	109	13	54.7	7.3	47.2	3.1	53	3.9	51.9	3.7	0	1	48.3	7.7	63.4	6.6	475	42	1.59	0.4	13.96	0.95
	12	114.9	7.4	65.7	5.4	56.9	2.3	66.7	3.5	62	2.8	0.0076	0.0085	43.5	3.6	65.5	4.1	451	27	2.06	0.36	14.24	0.88
	13	116.9	7	51.2	5.9	50.4	2.9	58	3	56	3.4	0.0104	0.0097	41.5	5.5	62.7	4.8	496	38	1.82	0.3	14.6	1.5
	14	114.9	9.6	61	7.8	58.5	3.8	66.7	4.1	64.7	4.3	0.0032	0.0063	47	6	61.4	4.1	478	35	2.07	0.47	15.2	1.5
	15	113.5	7.8	59.2	4.7	50	2.6	58	3.2	55	2.7	0	1	47.1	5.3	65.7	4.2	502	36	2.12	0.4	15.14	0.93
	16	109	11	59.1	6.2	51.8	4.5	60.3	4.8	57	4.2	0.015	0.014	42.4	6.1	63.7	6.2	489	54	2.17	0.47	13.6	1.2
	17	115.1	8.6	63	6.2	58.5	4.4	65.4	4.1	62.9	4.3	0	1	41.4	5.3	56.6	4.6	477	34	1.85	0.46	13.8	1
	18	114	8.3	59.9	6.1	49.2	2.6	57.6	3.4	54.9	3.2	0	1	37.5	4.7	57.8	4.9	463	32	2.16	0.38	13.6	1.2
	19	110.5	7.9	61.4	5.3	55.6	3.3	64.6	3.5	60.6	3.5	0	1	48.6	6.9	65.3	4.2	454	34	1.78	0.34	13.6	1
	20	119.4	7.1	64.3	7	56.9	3.8	65.1	4.1	62.9	4	0.015	0.011	46.5	6.2	60	3.8	487	32	2.02	0.4	13.16	0.89
	21	113.4	5.9	58.2	5.5	50.5	3.2	57.9	3.6	55.7	3.2	0.0092	0.0087	40.5	4.2	59.5	4.3	463	41	1.72	0.23	13.4	1.1
	22	118	8.7	63.7	6.8	54.4	3.7	62.4	4.1	60.5	3.5	0	1	43.2	5.8	61.7	2.8	498	49	2.14	0.44	13.7	1.3
	23	115	10	75.9	7.7	64.8	4.6	73.7	5	71.2	5	0.0048	0.0066	45.6	6.3	65.5	4.1	485	40	2	0.37	14.7	1.1
	24	111.7	7.9	75.2	8.5	60.1	3.2	68.3	3.6	65.6	3.2	0	1	40.8	5.1	58.4	4.4	487	35	1.66	0.51	13.92	0.76
	25	69.4	6	43.9	4.4	38.6	2.3	43.3	2.5	41.9	2.4	0.0096	0.009	41.6	5.4	55.9	4.2	426	34	1.89	0.38	13.9	1.4
	26	99	13	56.2	5.6	48.8	2.7	55.1	3.2	53.2	2.9	0.011	0.01	44.4	4.8	66.2	5.2	487	37	1.5	0.37	13.5	1
	27	109.6	9.5	58.5	5.2	49.2	3.6	57.4	3.4	53.7	3.9	0.02	0.012	37.8	4.2	60.5	4.5	455	43	2.52	0.42	14	1
	28	91.8	8	49.7	5.4	45.9	3	52.4	3.3	50.1	3.3	0.0077	0.0085	38.2	4.1	53.3	3.3	460	30	1.78	0.35	14.09	0.75
	29	115.9	5.9	68.6	6.5	56.8	2.6	65.9	3	62.4	3.2	0.0056	0.0077	44.7	5.9	63.2	4.5	476	24	2.5	0.5	13.98	0.97
	30	103.9	6	59.3	6.3	50.4	2.8	57.7	3.4	56.1	2.9	0	1	47.5	6.3	66.6	5.1	521	31	2.09	0.34	15.7	1.2

ELECTRONIC APPENDIX C FOR CHAPTER 8

LA-ICP-MS geochronological data for all reported samples

Sample	Spot Number	$^{207}Pb/^{235}U$	2SE	$^{206}Pb/^{238}U$	2SE	Error Correlation
HFO 4.1	1	22.48	0.57	0.1767	0.0046	0.95148
	2	20.62	0.56	0.1635	0.0043	0.9708
	3	17.91	0.76	0.1423	0.0063	0.9688
	4	19.6	1	0.1527	0.0081	0.98364
	5	23.59	0.55	0.1849	0.0044	0.94875
	6	26.03	0.76	0.2043	0.0061	0.96446
	7	16.35	0.63	0.1283	0.005	0.97602
	8	19.67	0.59	0.1529	0.0044	0.94735
	9	14.76	0.51	0.1169	0.0041	0.96438
	10	15.29	0.23	0.1204	0.0017	0.80964
	11	15.16	0.29	0.1192	0.0022	0.90033
	12	14.7	0.29	0.1158	0.0022	0.87954
	13	14.41	0.21	0.113	0.0018	0.82468
	14	14.61	0.39	0.1142	0.0028	0.92844
	15	15.11	0.32	0.1189	0.0026	0.91622
	16	14.6	0.28	0.1148	0.0024	0.87934
	17	15.49	0.27	0.1222	0.002	0.90779
	18	14.77	0.32	0.1171	0.0023	0.86655
	19	15.1	0.25	0.1186	0.0022	0.8637
	20	20	1.4	0.161	0.011	0.98625
	21	15.04	0.25	0.1184	0.0019	0.84063
	22	15.79	0.23	0.1218	0.0019	0.86262
	23	12.57	0.47	0.1	0.0039	0.96045
	24	11.41	0.29	0.09	0.0022	0.93392
	25	14.62	0.29	0.1159	0.0021	0.88965
	26	14.1	0.3	0.1119	0.0026	0.92842
	27	19.56	0.81	0.1535	0.0063	0.97888
	28	19.02	0.87	0.1505	0.0072	0.97349
HFO 4.2	1	15.57	0.37	0.1229	0.0027	0.91575
	2	18.04	0.66	0.1396	0.0047	0.96631
	3	19.93	0.69	0.1577	0.0057	0.93644
	4	20.51	0.94	0.1601	0.0068	0.95923
	5	22.26	0.92	0.1756	0.0069	0.95587
	6	19.37	0.68	0.1505	0.0047	0.9513
	7	20.3	1.1	0.1607	0.0093	0.96385
	8	18.15	0.62	0.1414	0.0046	0.96331
	9	18.55	0.73	0.1462	0.0059	0.958
	10	15.93	0.26	0.1241	0.002	0.81863
	11	16.32	0.3	0.1288	0.0024	0.90075
	12	15.95	0.32	0.1265	0.0027	0.8894
	13	19.53	0.46	0.1545	0.0038	0.94015
	14	23.42	0.97	0.1841	0.0076	0.95487
	15	19.37	0.88	0.1532	0.0068	0.96604
	16	19.53	0.72	0.1556	0.006	0.94538
	17	19.56	0.53	0.1536	0.0038	0.89629
	18	20.36	0.81	0.1553	0.006	0.73423
	19	19.4	0.98	0.153	0.0075	0.98015
	20	16.12	0.21	0.1271	0.0017	0.73346
	21	16.31	0.31	0.1287	0.0024	0.8177
	22	17.99	0.41	0.1399	0.0029	0.90719
	23	22	1.3	0.1727	0.0095	0.97927
	24	24.1	1.3	0.1871	0.0098	0.97072
	25	20.61	0.76	0.1604	0.0058	0.95648
	26	20.9	0.95	0.1624	0.0067	0.97095
	27	19.12	0.65	0.1499	0.0051	0.93615
	28	31.3	2.7	0.247	0.021	0.99026
	29	20.13	0.86	0.1587	0.0067	0.96322
	30	15.74	0.34	0.1238	0.0025	0.91423

Sample	Spot Number	$^{207}Pb/^{235}U$	2SE	$^{206}Pb/^{238}U$	2SE	Error Correlation
HFO 4.3	1	14.54	0.55	0.1142	0.0043	0.9568
	2	15.06	0.36	0.1186	0.0029	0.88731
	3	13.4	0.38	0.1041	0.0029	0.95604
	4	15.15	0.21	0.1192	0.0017	0.82357
	5	14.54	0.25	0.1151	0.0018	0.83037
	6	15.99	0.28	0.1253	0.0021	0.86812
	7	24.67	0.93	0.1934	0.0071	0.9758
	8	16.68	0.72	0.1303	0.0054	0.97398
	9	18.91	0.74	0.1472	0.0056	0.95817
	10	14.75	0.45	0.1192	0.0045	0.96409
	11	15.62	0.46	0.1245	0.0036	0.95605
	12	16.17	0.29	0.1262	0.0025	0.90255
	13	15.37	0.23	0.1206	0.0017	0.87368
	14	16.81	0.32	0.1317	0.0028	0.90265
	15	16.81	0.49	0.1343	0.0045	0.97204
	16	15.28	0.29	0.1201	0.0022	0.85674
	17	14.92	0.61	0.1177	0.0052	0.98029
	18	14.64	0.18	0.1155	0.0015	0.82127
	19	14.73	0.21	0.1145	0.0018	0.8399
	20	16.89	0.55	0.1332	0.0045	0.96018
	21	12.37	0.3	0.1064	0.0026	0.9354
	22	16.42	0.64	0.1285	0.0048	0.94897
	23	17.71	0.82	0.1399	0.0069	0.98016
	24	18.05	0.61	0.1417	0.0048	0.94944
	25	16.97	0.34	0.132	0.0026	0.92008
	26	13.49	0.23	0.1059	0.0018	0.87079
	27	13.52	0.4	0.1065	0.0034	0.9388
	28	19.77	0.69	0.1549	0.0054	0.94291
	29	14.11	0.41	0.1107	0.0032	0.92004
HFO 9	1	20.23	0.21	0.1594	0.0016	0.94155
	2	20.74	0.22	0.163	0.0017	0.95226
	3	21.04	0.29	0.1647	0.0021	0.96793
	4	24.29	0.52	0.1904	0.0039	0.99231
	5	23.29	0.5	0.1826	0.0037	0.98755
	6	22.41	0.46	0.1755	0.0034	0.99032
	7	20.33	0.22	0.1604	0.0017	0.97267
	8	20.4	0.21	0.161	0.0018	0.9617
	9	22.42	0.35	0.1755	0.0025	0.96736
	10	23.32	0.27	0.183	0.0021	0.96882

Sample	Spot Number	$^{207}Pb/^{235}U$	2SE	$^{206}Pb/^{238}U$	2SE	Error Correlation
HFO 11	1	17.68	0.62	0.1389	0.0047	0.90036
	2	14.97	0.34	0.1196	0.0028	0.89483
	3	19.12	0.88	0.1513	0.0068	0.95656
	4	15.35	0.44	0.1213	0.0032	0.91098
	5	15.94	0.68	0.1247	0.0048	0.96946
	6	17.53	0.41	0.1392	0.0033	0.93895
	7	15.98	0.39	0.1251	0.003	0.91912
	8	13.87	0.17	0.1087	0.0015	0.59007
	9	15.29	0.21	0.1211	0.0014	0.73566
	10	13.51	0.38	0.1053	0.0029	0.84901
	11	16.32	0.63	0.1316	0.0055	0.92118
	12	19.04	0.9	0.1481	0.0068	0.86124
	13	17.64	0.42	0.1365	0.0038	0.38445
	14	16.14	0.58	0.1276	0.0047	0.26168
	15	15.78	0.54	0.1243	0.0042	0.19815
	16	15.84	0.46	0.1237	0.0038	0.42178
	17	16.05	0.69	0.1265	0.0046	0.38914
	18	19.37	0.53	0.15	0.004	0.42653
	19	19.61	0.85	0.1531	0.0062	0.38673
	20	14.38	0.27	0.1136	0.0021	0.87647
	21	14.66	0.18	0.1145	0.0015	0.70487
	22	14.95	0.27	0.1174	0.0021	0.85406
	23	16.12	0.49	0.1273	0.004	0.96105
	24	16.48	0.36	0.1307	0.0032	0.94536
	25	17.13	0.45	0.1338	0.0033	0.95037
	26	16.54	0.33	0.1281	0.0026	0.88473
	27	13.84	0.53	0.1097	0.0042	0.9639
	28	14.94	0.36	0.1174	0.0025	0.90709
	29	14.22	0.42	0.113	0.0034	0.92213
	30	15.72	0.53	0.1254	0.0042	0.96192
HFO A	1	16.19	0.43	0.1242	0.0034	0.82907
	2	15	0.34	0.1168	0.0026	0.87777
	3	24.8	1.9	0.194	0.014	0.98867
	4	16.67	0.64	0.1284	0.0048	0.903
	5	20.47	0.75	0.1622	0.0063	0.73318
	6	20.14	0.69	0.1571	0.0056	0.56105
	7	21.21	0.93	0.1658	0.0074	0.86417
	8	17.43	0.71	0.138	0.0059	0.86266
	9	19.41	0.59	0.1529	0.0044	0.73736
	10	18.82	0.48	0.1464	0.0033	0.81625
	11	16.63	0.64	0.1291	0.005	0.94682
	12	15.35	0.43	0.1217	0.0035	0.92183
	13	17.21	0.41	0.1361	0.0033	0.94136
	14	14.99	0.2	0.1189	0.0015	0.77297
	15	13.71	0.21	0.108	0.0017	0.79366
	16	14.24	0.24	0.1118	0.0021	0.85397
	17	15.2	0.3	0.1188	0.0025	0.83838
	18	15.13	0.41	0.1182	0.0035	0.92238
	19	16.91	0.68	0.1333	0.0054	0.98113
	20	14.62	0.32	0.1157	0.0024	0.91061
	21	17.34	0.75	0.1359	0.0059	0.88633
	22	19.11	0.68	0.1508	0.0057	0.8874
	23	19.53	0.53	0.1563	0.0041	0.71884
	24	26.7	2.1	0.207	0.016	0.97242
	25	19.2	1	0.1523	0.0082	0.92434
	26	15.8	0.5	0.1223	0.0042	0.91838
	27	12.17	0.44	0.1038	0.0035	0.96325
	28	16.59	0.66	0.1302	0.0052	0.97912

Sample	Spot Number	$^{207}Pb/^{235}U$	2SE	$^{206}Pb/^{238}U$	2SE	Error Correlation
HFO B	1	14.25	0.16	0.1115	0.0013	0.83628
	2	13.87	0.22	0.1083	0.0019	0.90319
	3	15.98	0.21	0.1247	0.0016	0.8674
	4	15.76	0.33	0.1227	0.0024	0.94989
	5	17.23	0.37	0.1339	0.0028	0.92751
	6	13.93	0.55	0.1192	0.0049	0.99161
	7	15.74	0.42	0.124	0.0034	0.97595
	8	15.98	0.33	0.1263	0.0026	0.94556
	9	16.13	0.33	0.1272	0.0026	0.94608
	10	15.86	0.62	0.1234	0.0047	0.98651
	11	16.79	0.26	0.1295	0.0021	0.56154
	12	16.5	0.31	0.131	0.0029	0.21176
	13	15.18	0.28	0.1181	0.0022	0.48339
	14	16.51	0.29	0.1305	0.0023	0.68734
	15	17.01	0.38	0.1323	0.0026	0.77527
HFO C	1	34.64	0.45	0.2693	0.0031	0.8842
	2	33.16	0.51	0.2592	0.0044	0.88689
	3	32.05	0.49	0.2488	0.0037	0.81799
	4	41.12	0.66	0.3226	0.0052	0.92113
	5	32.79	0.62	0.2538	0.0047	0.93336
	6	35	0.5	0.2744	0.0044	0.78853
	7	36.89	0.8	0.2898	0.0063	0.96611
	8	33.27	0.58	0.2607	0.005	0.88047
	9	34.28	0.52	0.2651	0.0036	0.8391
	10	34.89	0.69	0.2746	0.0056	0.7599
	11	33.76	0.72	0.2637	0.0055	0.83087
	12	32.49	0.5	0.2547	0.004	0.86354
	13	33.92	0.46	0.2635	0.0029	0.74253

SUPPLEMENTARY MATERIAL H

FOR CHAPTER 9 – APPRAISAL AND IMPLEMENTATION OF A SYNTHETIC HEMATITE REFERENCE MATERIAL FOR MICROBEAM U-PB GEOCHRONOLOGY

APPENDIX A: EXTENDED ID-TIMS TABLE

ELECTRONIC APPENDIX A FOR CHAPTER 9

ID-TIMS Sample (Radiogenic + Initial Pb) Isotope Ratios															
HFO Chip	Aliquot	$^{207}Pb/^{235}U$	% err	$^{206}Pb/^{238}U$	% err	$^{238}U/^{206}Pb$	% err	$^{207}Pb/^{206}Pb$	% err	$^{206}Pb/^{204}Pb$	% err	$^{204}Pb/^{206}Pb$	% err	corr. coef. 238/206-207/206	corr. coef. 238/206-204/206	corr. coef. 207/206-204/206
AG1	1	15.424	0.14	0.122	0.12	8.171	0.12	0.914	0.08	16.727	0.14	0.060	0.14	-0.67	0.76	-1.15
	2	15.323	0.13	0.122	0.10	8.172	0.10	0.909	0.08	17.058	0.17	0.059	0.17	-0.76	0.74	-0.94
	3	15.337	0.12	0.121	0.09	8.232	0.09	0.916	0.08	16.904	0.16	0.059	0.16	-0.85	0.86	-1.02
	4	14.336	0.35	0.113	0.29	8.866	0.29	0.922	0.20	16.765	0.31	0.060	0.31	-0.11	0.14	-0.20
	5	13.147	0.12	0.104	0.09	9.643	0.09	0.920	0.08	16.834	0.16	0.059	0.16	-0.86	0.85	-0.98
AG2	1	15.446	0.16	0.122	0.14	8.173	0.14	0.916	0.08	16.840	0.16	0.059	0.16	-0.46	0.63	-0.99
	2	15.532	0.21	0.123	0.19	8.155	0.19	0.919	0.08	16.789	0.16	0.060	0.16	-0.21	0.52	-0.96
	3	15.554	0.14	0.123	0.11	8.128	0.11	0.917	0.08	16.844	0.16	0.059	0.16	-0.68	0.77	-1.00
AG3	1	15.435	0.14	0.122	0.12	8.205	0.12	0.919	0.08	16.788	0.16	0.060	0.16	-0.62	0.73	-1.00
	2	15.548	0.23	0.123	0.21	8.135	0.21	0.918	0.07	16.679	0.16	0.060	0.16	-0.22	0.46	-1.09
AG4	1	15.631	0.16	0.124	0.14	8.074	0.14	0.916	0.08	16.786	0.15	0.060	0.15	-0.49	0.65	-1.03
	2	15.366	0.17	0.121	0.15	8.250	0.15	0.920	0.08	16.786	0.16	0.060	0.16	-0.47	0.57	-1.00
	3	15.168	0.19	0.120	0.17	8.358	0.17	0.920	0.08	16.793	0.15	0.060	0.15	-0.32	0.56	-1.04
BG2	1	14.808	0.17	0.117	0.15	8.559	0.15	0.920	0.09	16.809	0.16	0.059	0.16	-0.36	0.58	-0.88
	2	14.713	0.18	0.116	0.16	8.618	0.16	0.920	0.09	16.829	0.16	0.059	0.16	-0.32	0.55	-0.85
	4	15.424	0.17	0.125	0.15	7.988	0.15	0.894	0.08	16.786	0.14	0.060	0.14	-0.44	0.64	-1.11

$^{238}U/^{204}Pb$	% err	$^{206}Pb/^{204}Pb$	% err	corr. coef. 8/4-6/4	$^{235}U/^{204}Pb$	% err	$^{207}Pb/^{204}Pb$	% err	corr. coef. 5/4-7/4
136.673	0.093	16.727	0.141	0.538	0.992	0.093	15.296	0.227	0.637
139.394	0.116	17.058	0.169	0.797	1.011	0.116	15.498	0.246	0.772
139.162	0.091	16.904	0.158	0.845	1.010	0.091	15.487	0.238	0.857
148.644	0.390	16.765	0.306	0.677	1.079	0.390	15.463	0.401	0.558
162.325	0.097	16.834	0.163	0.867	1.178	0.097	15.485	0.242	0.859
137.638	0.128	16.840	0.158	0.550	0.999	0.128	15.425	0.238	0.610
136.907	0.170	16.789	0.156	0.338	0.993	0.170	15.429	0.237	0.450
136.915	0.102	16.844	0.158	0.729	0.993	0.102	15.452	0.238	0.762
137.744	0.107	16.788	0.157	0.681	0.999	0.107	15.426	0.238	0.721
135.685	0.200	16.679	0.159	0.307	0.985	0.200	15.307	0.235	0.401
135.529	0.121	16.786	0.149	0.486	0.983	0.121	15.371	0.233	0.563
138.479	0.143	16.786	0.158	0.510	1.005	0.143	15.440	0.238	0.543
140.349	0.152	16.793	0.150	0.354	1.018	0.152	15.447	0.233	0.458
143.866	0.144	16.809	0.163	0.532	1.044	0.144	15.458	0.244	0.579
145.031	0.152	16.829	0.164	0.506	1.052	0.152	15.483	0.245	0.552
134.091	0.126	16.786	0.141	0.341	0.973	0.126	15.007	0.227	0.463

ADDITIONAL MATERIAL I

CO-AUTHORED ARTICLE ABSTRACT:

IRON-OXIDES CONSTRAIN BIF EVOLUTION IN TERRANES WITH PROTRACTED GEOLOGICAL HISTORIES: THE IRON COUNT PROSPECT, MIDDLEBACK RANGES, SOUTH AUSTRALIA

William Keyser [1], Cristiana L. Ciobanu [1], Nigel J. Cook [1], Marija Dmitrijeva [1], **Liam Courtney-Davies** [1], Holly Feltus [2], Sarah Gilbert [3], Geoff Johnson [2], Kathy Ehrig [4]

[1]*School of Chemical Engineering and Advanced Materials, The University of Adelaide, Adelaide, SA 5005, Australia*

[2]*SIMEC Mining, Level 2, 169 Fullarton Road, Dulwich, SA 5065, Australia*

[3]*Adelaide Microscopy, The University of Adelaide, Adelaide, SA 5005, Australia*

[4]*BHP Olympic Dam, Adelaide, SA 5000, Australia*

Article published in Lithos (2019) *324-325*, 20-38.

Lithos 324–325 (2019) 20–38

Contents lists available at ScienceDirect

Lithos

journal homepage: www.elsevier.com/locate/lithos

Iron-oxides constrain BIF evolution in terranes with protracted geological histories: The Iron Count prospect, Middleback Ranges, South Australia

William Keyser [a,*], Cristiana L. Ciobanu [a], Nigel J. Cook [a], Marija Dmitrijeva [a], Liam Courtney-Davies [a], Holly Feltus [b], Sarah Gilbert [c], Geoff Johnson [b], Kathy Ehrig [d]

[a] School of Chemical Engineering, The University of Adelaide, Adelaide, SA 5005, Australia
[b] SIMEC Mining, Level 2, 169 Fullarton Road, Dulwich, SA 5065, Australia
[c] Adelaide Microscopy, The University of Adelaide, Adelaide, SA 5005, Australia
[d] BHP Olympic Dam, Adelaide, SA 5000, Australia

ARTICLE INFO

Article history:
Received 22 March 2018
Accepted 31 October 2018
Available online 03 November 2018

Keywords:
U—Pb hematite geochronology
Banded iron formation
Middleback Ranges
Iron-oxides
Trace element geochemistry

ABSTRACT

When studied at appropriate scales of observation and using complementary methods, the intrinsic textural and geochemical complexity of iron-oxides can provide unparalleled insights into the evolution of iron ore resources from banded iron formation deposition to ore formation. Iron Count is one of >20 deposits and prospects within the Archean Middleback Ranges iron ore belt, South Australia, in which iron-oxides from BIFs and ores display variable textural and trace element signatures. Integrated petrography, iron-oxide laser-ablation mapping and geochemistry, and in-situ dating of BIF-derived ores was undertaken to assess whether features observed in samples from this representative prospect might be attributed to localized and superimposed overprint processes. The prospect consists of a West and East ridge, each characterized by a sequence of overprints expressed as interconversions between iron-(hydr)oxides and accompanying variation in trace element concentrations. Pseudomorphic replacement of early magnetite by hematite (martite), followed by replacement by iron-hydroxides is recognized in samples from the East Ridge. Further overprints are expressed as veining, brecciation and crystallization of (micro)platy hematite rich in granitophile elements (Sn, Mo, W, U). Martitization of early magnetite in the West Ridge is accompanied by enrichment in Zn, Co and Ni in martite. Subsequent recrystallization of martite/iron-hydroxides by granoblastic hematite is marked by enrichment in Ti, Ta, Nb, REE and granitophile elements, and co-crystallization of REE-minerals. This is followed by crystallization of (micro)platy hematite, similarly rich in these elements. Enrichment in Ti and granitophile elements in granoblastic hematite is interpreted to infer crystallization from highly saline fluids generated by interaction between evaporite-bearing sedimentary rocks and granite-derived fluids. Post-Archean Australian Shale-normalized REY fractionation trends of iron-oxides from the East Ridge are consistent with precipitation of iron-rich minerals from a mixture of anoxic seawater and hydrothermal vent fluids. Analogous trends from the West Ridge lack a seawater signature. Contrasts in REY fractionation trends between the two ridges is interpreted as a combination of the loss of primary seawater signature due to severe overprinting in the West Ridge, and to lateral variation in the marine depositional environment. Results validate the hypothesis that variation in iron-oxide trace element signatures seen throughout the Middleback Ranges iron ore belt results from overprinting due to superimposed tectono-magmatic events that have locally affected each deposit. Despite undergoing different sequences of ore-forming stages, as well as possibly distinct depositional environments, the two ridges share a common overprint, dated here at ~1790 Ma using in-situ U—Pb geochronology of co-existing hematite, monazite and xenotime. This age is considered to represent the timing of interaction between granite-derived fluids with ore-hosting rock. Such interpretation is supported by the geochemical signatures of the dated iron-oxides showing enrichment in granitophile elements and coincident ages for the Wertigo Granite and Myola Volcanics, which occur proximal to the prospect and were emplaced/erupted during intracontinental rifting. The approach undertaken here, combining petrography, iron-oxide geochemistry and in-situ dating of BIF-derived ores is generically applicable to other iron resources within the Middleback Ranges or analogous terranes elsewhere.

© 2018 Published by Elsevier B.V.

* Corresponding author.
E-mail address: william.keyser@adelaide.edu.au (W. Keyser).

https://doi.org/10.1016/j.lithos.2018.10.035
0024-4937/© 2018 Published by Elsevier B.V.

ADDITIONAL MATERIAL J

CO-AUTHORED ARTICLE ABSTRACT:

PETROGRAPHIC AND GEOCHRONOLOGICAL CONSTRAINTS ON THE GRANITIC BASEMENT TO THE MIDDLEBACK RANGES, SOUTH AUSTRALIA

William Keyser [1], Cristiana L. Ciobanu [1], Nigel J. Cook [1], **Liam Courtney-Davies** [1], Allen Kennedy [2], Benjamin P. Wade [3], Kathy Ehrig [4], Marija Dmitrijeva [1], Alkiviadis Kontonikas-Charos [1], Holly Feltus [5], Geoff Johnson [5]

[1]*School of Chemical Engineering and Advanced Materials, The University of Adelaide, Adelaide, SA 5005, Australia*

[2]*John de Laeter Centre, Curtin University of Technology, Bentley, WA 6102, Australia*

[3]*Adelaide Microscopy, The University of Adelaide, Adelaide, SA 5005, Australia*

[4]*BHP Olympic Dam, Adelaide, SA 5000, Australia*

[5]*SIMEC Mining, Level 2, 169 Fullarton Road, Dulwich, SA 5065, Australia*

Article published in Precambrian Research (2019) *324*, 170-193.

Precambrian Research 324 (2019) 170–193

Contents lists available at ScienceDirect

Precambrian Research

journal homepage: www.elsevier.com/locate/precamres

Petrographic and geochronological constraints on the granitic basement to the Middleback Ranges, South Australia

William Keyser[a,*], Cristiana L. Ciobanu[a], Nigel J. Cook[a], Liam Courtney-Davies[a], Allen Kennedy[b], Benjamin P. Wade[c], Kathy Ehrig[d], Marija Dmitrijeva[a], Alkiviadis Kontonikas-Charos[a], Holly Feltus[e], Geoff Johnson[e]

[a] School of Chemical Engineering, The University of Adelaide, Adelaide, SA 5005, Australia
[b] John de Laeter Centre, Curtin University of Technology, Bentley, WA 6102, Australia
[c] Adelaide Microscopy, The University of Adelaide, Adelaide, SA 5005, Australia
[d] BHP Olympic Dam, Adelaide, SA 5000, Australia
[e] SIMEC Mining, Level 2, 169 Fullarton Road, Dulwich, SA 5065, Australia

ARTICLE INFO

Keywords:
Middleback Ranges
Archean granites
SHRIMP U-Pb zircon geochronology
Banded iron formation

ABSTRACT

The Middleback Ranges is a 60 km-long BIF-endowed iron ore belt located in the southeastern Gawler Craton and is the largest exploited iron resource in South Australia. The belt is hosted within an Archean- to Paleoproterozoic-aged granitic-gneissic basement terrane. Petrographic and geochronological constraints are given for a suite of granites associated with deposits throughout the Middleback Ranges and compared with other regional granites. Granites from the Middleback Ranges show complex mineralogical and geochemical features indicating multiple overprinting events. Sensitive high-resolution ion microprobe U-Pb zircon ages from all granites across the Middleback Ranges yield Archean ages, suggesting the existence and a more extensive distribution of Mesoarchean crust than previously recognized beneath the entire Middleback Ranges BIF sequence. Grey and pink granites from the central Middleback Ranges (Sultan prospect) produced the oldest $^{207}Pb/^{206}Pb$ weighted mean ages within the sample suite (3241 ± 6 and 3238 ± 9 Ma, respectively). Zircon in the latter granite also features overgrowths dated at ~2.6 Ga and interpreted to be metamorphic. A second group of younger granites from the Iron Monarch deposit and a sample of Cooyerdoo Granite (northern Middleback Ranges) have a minimum crystallization age of 3165 ± 8 Ma and a $^{207}Pb/^{206}Pb$ weighted mean magmatic age of 3134 ± 18 Ma, respectively. The youngest granites analyzed here derive from the Iron Baron deposit in the central part of the belt, which display strong deformation and have a minimum crystallization age of 3089 ± 9 Ma, and from the Iron Magnet deposit in the southern part of the belt ($^{207}Pb/^{206}Pb$ weighted mean age of 3023 ± 33 Ma). Petrographic and geochemical features observed within the sample suite indicate that post-Archean overprinting events led to alteration of the granitic basement and may infer that fluid-rock interaction and granite leaching were important for BIF upgrading processes and iron-oxide formation.

1. Introduction

The Middleback Ranges (MR) is a 60 km-long metallogenetic belt hosting iron ores and located in the Eyre Peninsula, South Australia (Fig. 1). These ores are associated with banded iron formation (BIF) that were initially considered as Paleoproterozoic (~2.0 Ga; Parker et al., 1988) but more recently are recognized as Late Archean (~2.5 Ga; Szpunar et al., 2011). The depositional age of the BIF with lower stratigraphic position relative to the Cook Gap Schist is thus constrained as Neoarchean ("no older than c. 2570 Ma and is likely to have been deposited before 2450 Ma"; Szpunar et al., 2011). Uncertainties nevertheless still exist with respect to the regional correlation of Fe-rich lithologies relative to this horizon along the MR, and to the origin of the basement at the time of BIF deposition.

The MR belt is part of the southeastern Gawler Craton, which comprises magmatic rocks spanning the Archean (Cooyerdoo Granite; ~3.15 Ga, Fraser et al., 2010) to Mesoproterozoic (~1.6 Ga Gawler Range Volcanics and Charleston Granite; Fanning et al., 1988; Creaser and Fanning, 1993) and is crosscut by mafic dikes inferred to be of Gairdner age (~820 Ma; Wingate et al., 1998), but as yet unconfirmed

* Corresponding author.
E-mail address: william.keyser@adelaide.edu.au (W. Keyser).

https://doi.org/10.1016/j.precamres.2019.01.024
Received 26 October 2018; Received in revised form 30 January 2019; Accepted 30 January 2019
Available online 01 February 2019
0301-9268/ © 2019 Elsevier B.V. All rights reserved.

ADDITIONAL MATERIAL K

CO-AUTHORED ARTICLE ABSTRACT:

SILICIAN MAGNETITE: SI–FE-NANOPRECIPITATES AND OTHER MINERAL INCLUSIONS IN MAGNETITE FROM THE OLYMPIC DAM DEPOSIT, SOUTH AUSTRALIA

Cristiana L. Ciobanu [1], Max R. Verdugo-Ihl [1], Ashley Slattery [2], Nigel J. Cook [1], Kathy Ehrig[3], **Liam Courtney-Davies [1],** Benjamin P. Wade [2]

[1]*School of Chemical Engineering and Advanced Materials, The University of Adelaide, Adelaide, SA 5005, Australia*

[2]*Adelaide Microscopy, The University of Adelaide, Adelaide, SA 5005, Australia*

[3]*BHP Olympic Dam, Adelaide, SA 5000, Australia*

Article published in Minerals (2019) *9*(5), 311.

minerals

MDPI

Article

Silician Magnetite: Si–Fe-Nanoprecipitates and Other Mineral Inclusions in Magnetite from the Olympic Dam Deposit, South Australia

Cristiana L. Ciobanu [1,*], Max R. Verdugo-Ihl [1], Ashley Slattery [2], Nigel J. Cook [1], Kathy Ehrig [3], Liam Courtney-Davies [1] and Benjamin P. Wade [2]

1 School of Chemical Engineering, The University of Adelaide, Adelaide, SA 5005, Australia; max.verdugoihl@adelaide.edu.au (M.R.V.-I.); nigel.cook@adelaide.edu.au (N.J.C.); liam.courtney-davies@adelaide.edu.au (L.C.-D.)

2 Adelaide Microscopy, The University of Adelaide, Adelaide, SA 5005, Australia; ashley.slattery@adelaide.edu.au (A.S.); benjamin.wade@adelaide.edu.au (B.P.W.)

3 BHP Olympic Dam, Adelaide, SA 5000, Australia; kathy.ehrig@bhp.com

* Correspondence: cristiana.ciobanu@adelaide.edu.au; Tel.: +61-432-955-000

Received: 19 April 2019; Accepted: 16 May 2019; Published: 20 May 2019

check for updates

Abstract: A comprehensive nanoscale study on magnetite from samples from the outer, weakly mineralized shell at Olympic Dam, South Australia, has been undertaken using atom-scale resolution High Angle Annular Dark Field Scanning Transmission Electron Microscopy (HAADF STEM) imaging and STEM energy-dispersive X-ray spectrometry mapping and spot analysis, supported by STEM simulations. Silician magnetite within these samples is characterized and the significance of nanoscale inclusions in hydrothermal and magmatic magnetite addressed. Silician magnetite, here containing Si–Fe-nanoprecipitates and a diverse range of nanomineral inclusions [(ferro)actinolite, diopside and epidote but also U-, W-(Mo), Y-As- and As-S-nanoparticles] appears typical for these samples. We observe both silician magnetite nanoprecipitates with spinel-type structures and a γ-$Fe_{1.5}SiO_4$ phase with maghemite structure. These are distinct from one another and occur as bleb-like and nm-wide strips along d_{111} in magnetite, respectively. Overprinting of silician magnetite during transition from K-feldspar to sericite is also expressed as abundant lattice-scale defects (twinning, faults) associated with the transformation of nanoprecipitates with spinel structure into maghemite via Fe-vacancy ordering. Such mineral associations are characteristic of early, alkali-calcic alteration in the iron-oxide copper gold (IOCG) system at Olympic Dam. Magmatic magnetite from granite hosting the deposit is quite distinct from silician magnetite and features nanomineral associations of hercynite-ulvöspinel-ilmenite. Silician magnetite has petrogenetic value in defining stages of ore deposit evolution at Olympic Dam and for IOCG systems elsewhere. The new data also add new perspectives into the definition of silician magnetite and its occurrence in ore deposits.

Keywords: silician magnetite; high angle annular dark field scanning transmission electron microscopy; Olympic Dam

ADDITIONAL MATERIAL L

CO-AUTHORED ARTICLE ABSTRACT:

ADVANCES AND OPPORTUNITIES IN ORE MINERALOGY

Nigel J. Cook [1], Cristiana L. Ciobanu [1], Kathy Ehrig [2], Ashley Slattery [3], Max R. Verdugo-Ihl [1], **Liam Courtney-Davies [1],** Wenyuan Gao [4]

[1]*School of Chemical Engineering and Advanced Materials, The University of Adelaide, Adelaide, SA 5005, Australia*

[2]*Adelaide Microscopy, The University of Adelaide, Adelaide, SA 5005, Australia*

[3]*BHP Olympic Dam, Adelaide, SA 5000, Australia*

[4]*Key Laboratory of Ministry of Education on Safe Mining of Deep Metal Mines, School of Resources and Civil Engineering, Northeastern University, Shenyang 110819, China*

Article published in Minerals (2017) 7, 233.

minerals

MDPI

Review

Advances and Opportunities in Ore Mineralogy

Nigel J. Cook [1,*], Cristiana L. Ciobanu [1], Kathy Ehrig [2], Ashley Slattery [3], Max R. Verdugo-Ihl [1], Liam Courtney-Davies [1] and Wenyuan Gao [1,4]

1 School of Chemical Engineering, The University of Adelaide, Adelaide, SA 5000, Australia; cristiana.ciobanu@adelaide.edu.au (C.L.C.); max.verdugoihl@adelaide.edu.au (M.R.V.-I.); liam.courtney-davies@adelaide.edu.au (L.C.-D.); wenyuan.gao@adelaide.edu.au (W.G.)
2 BHP Olympic Dam, Adelaide, SA 5000, Australia; Kathy.ehrig@adelaide.edu.au
3 Adelaide Microscopy, The University of Adelaide, Adelaide, SA 5000, Australia; ashley.slattery@adelaide.edu.au
4 Key Laboratory of Ministry of Education on Safe Mining of Deep Metal Mines, School of Resources and Civil Engineering, Northeastern University, Shenyang 110819, China
* Correspondence: nigel.cook@adelaide.edu.au; Tel.: +61-8-8313-1096

Received: 28 October 2017; Accepted: 22 November 2017; Published: 24 November 2017

Abstract: The study of ore minerals is rapidly transforming due to an explosion of new micro- and nano-analytical technologies. These advanced microbeam techniques can expose the physical and chemical character of ore minerals at ever-better spatial resolution and analytical precision. The insights that can be obtained from ten of today's most important, or emerging, techniques and methodologies are reviewed: laser-ablation inductively-coupled plasma mass spectrometry; focussed ion beam-scanning electron microscopy; high-angle annular dark field scanning transmission electron microscopy; electron back-scatter diffraction; synchrotron X-ray fluorescence mapping; automated mineral analysis (Quantitative Evaluation of Mineralogy via Scanning Electron Microscopy and Mineral Liberation Analysis); nanoscale secondary ion mass spectrometry; atom probe tomography; radioisotope geochronology using ore minerals; and, non-traditional stable isotopes. Many of these technical advances cut across conceptual boundaries between mineralogy and geochemistry and require an in-depth knowledge of the material that is being analysed. These technological advances are accompanied by changing approaches to ore mineralogy: the increased focus on trace element distributions; the challenges offered by nanoscale characterisation; and the recognition of the critical petrogenetic information in gangue minerals, and, thus the need to for a holistic approach to the characterization of mineral assemblages. Using original examples, with an emphasis on iron oxide-copper-gold deposits, we show how increased analytical capabilities, particularly imaging and chemical mapping at the nanoscale, offer the potential to resolve outstanding questions in ore mineralogy. Broad regional or deposit-scale genetic models can be validated or refuted by careful analysis at the smallest scales of observation. As the volume of information at different scales of observation expands, the level of complexity that is revealed will increase, in turn generating additional research questions. Topics that are likely to be a focus of breakthrough research over the coming decades include, understanding atomic-scale distributions of metals and the role of nanoparticles, as well how minerals adapt, at the lattice-scale, to changing physicochemical conditions. Most importantly, the complementary use of advanced microbeam techniques allows for information of different types and levels of quantification on the same materials to be correlated.

Keywords: ore mineralogy; microanalysis; instrumental techniques

ADDITIONAL MATERIAL M

CO-AUTHORED ARTICLE ABSTRACT:

TEXTURES AND U-W-SN-MO SIGNATURES IN HEMATITE FROM THE OLYMPIC DAM CU-U-AU-AG DEPOSIT, SOUTH AUSTRALIA: DEFINING THE ARCHETYPE FOR IOCG DEPOSITS

Max R. Verdugo-Ihl[1], Cristiana L. Ciobanu[1], Nigel J. Cook[1], Kathy Ehrig[2], **Liam Courtney-Davies[1],** Sarah E. Gilbert[3],

[1]School of Chemical Engineering and Advanced Materials, The University of Adelaide, Adelaide, SA 5005, Australia

[2] Adelaide Microscopy, The University of Adelaide, Adelaide, SA 5005, Australia

[3]BHP Olympic Dam, Adelaide, SA 5000, Australia

Article published in Ore Geology Reviews (2017) 91 173-195

Ore Geology Reviews 91 (2017) 173–195

Contents lists available at ScienceDirect

Ore Geology Reviews

journal homepage: www.elsevier.com/locate/oregeorev

Textures and U-W-Sn-Mo signatures in hematite from the Olympic Dam Cu-U-Au-Ag deposit, South Australia: Defining the archetype for IOCG deposits

Max R. Verdugo-Ihl[a,*], Cristiana L. Ciobanu[a], Nigel J. Cook[a], Kathy J. Ehrig[b], Liam Courtney-Davies[a], Sarah Gilbert[c]

[a] School of Chemical Engineering, The University of Adelaide, Adelaide, SA 5000, Australia
[b] BHP Olympic Dam, Adelaide, SA 5000, Australia
[c] Adelaide Microscopy, The University of Adelaide, Adelaide, SA 5000, Australia

ARTICLE INFO

Keywords:
Hematite
Trace elements
U-W-Sn-Mo compositional zoning
Olympic Dam
Iron-oxide copper gold deposits
Laser ablation inductively coupled plasma mass spectrometry

ABSTRACT

The textural characteristics and trace element geochemistry of hematite with U-W-Sn-Mo signatures from the Cu-U-Au-Ag orebody at Olympic Dam, South Australia, are documented. Olympic Dam is the archetype for iron-oxide copper–gold (IOCG) deposits where hematite is by far the most abundant mineral in the orebody. The deposit is located within hematite-bearing breccias (> 5% Fe) hosted by the ~1.6 Ga Roxby Downs Granite (RDG). Although such breccias are mostly derived from RDG, they also include volcanic clasts and sedimentary rocks. Samples cover the ~6 km strike length and ~2 km vertical extent of mineralisation, including hematite from the aforementioned lithologies. Hematite with U-W-Sn-Mo ('granitophile' elements) signatures is recognised throughout all lithologies and parts of the deposit. Hematite enriched in granitophile elements is represented by a variety of textures, of which zoned hematite, defined by oscillatory zonation patterns, is the most prominent and can be tied to the age of the RDG, and thus initiation of the IOCG system as confirmed by published U-Pb geochronology. Other categories of hematite with granitophile signatures include hematite resulting from replacement of pre-existing minerals (e.g., carbonates and feldspars), as well as replacement of previous oscillatory-zoned hematites. Matrix and vacuole filling hematite from volcanoclastic-dominated intervals also carry 'granitophile' signatures. In addition, some colloform types which likely post-date primary IOCG mineralisation are also rich in 'granitophile' elements. Trace element mapping and spot analysis by laser ablation inductively coupled plasma mass spectrometry (LA-ICP-MS) defines complex trace element signatures of hematite, which, in addition to the 'granitophile' elements, also comprise rare earth elements, high field strength elements, chalcogens and transition metals.

The distinct geochemical signature, characterised by enrichment in the 'granitophile' elements (up to wt% levels of U and W within individual zones, and up to thousands of ppm Mo and Sn) prevails throughout the hematite in the deposit irrespective of textures. Iron-oxides have been repeatedly formed, reworked and overprinted by subsequent cycles of brecciation, fluid-mineral reaction, remobilization, element redistribution and recrystallisation. Coupled dissolution-replacement reactions are discussed as having played a major role in the modification of textural and geochemical patterns in hematite, but also allow for widespread preservation of primary geochemical signatures. Despite its simple chemistry, the crystal-structural modularity of hematite can adapt and retain evolving fluid signatures. The reported trace element signatures are fully concordant with conceptual frameworks for the genesis of IOCG systems, and may be an inherent, albeit hitherto under-reported characteristic of other IOCG systems. Hematite is probably by far the most important W-, Sn- and Mo-bearing phase in the deposit by mass.

1. Introduction

An inherent feature of all iron-oxide copper gold (IOCG) deposits is the abundance of Fe-oxides, as either hematite (α-Fe_2O_3) and/or magnetite (Fe_3O_4), generally making the Fe-oxides by far the most dominant minerals (Hitzman et al., 1992). Iron-oxides are valuable sources of petrogenetic information, as they commonly contain trace elements at measurable concentrations, with patterns and variations among these trace elements that reflect evolving physiochemical conditions.

* Corresponding author.
E-mail address: max.verdugoihl@adelaide.edu.au (M.R. Verdugo-Ihl).

http://dx.doi.org/10.1016/j.oregeorev.2017.10.007
Received 11 August 2017; Received in revised form 8 October 2017; Accepted 10 October 2017
Available online 12 October 2017
0169-1368/ © 2017 Elsevier B.V. All rights reserved.

ADDITIONAL MATERIAL N

CO-AUTHORED ARTICLE ABSTRACT:

DEFINING EARLY STAGES OF IOCG SYSTEMS: EVIDENCE FROM IRON OXIDES IN THE OUTER SHELL OF THE OLYMPIC DAM DEPOSIT, SOUTH AUSTRALIA

Max R. Verdugo-Ihl[1], Cristiana L. Ciobanu[1], Nigel J. Cook[1], Kathy Ehrig[2], **Liam Courtney-Davies[1],**

[1]School of Chemical Engineering and Advanced Materials, The University of Adelaide, Adelaide, SA 5005, Australia

[2]BHP Olympic Dam, Adelaide, SA 5000, Australia

Article in press in Mineralium Deposita

Mineralium Deposita
https://doi.org/10.1007/s00126-019-00896-2

ARTICLE

Defining early stages of IOCG systems: evidence from iron oxides in the outer shell of the Olympic Dam deposit, South Australia

Max R. Verdugo-Ihl[1] · Cristiana L. Ciobanu[1] · Nigel J. Cook[1] · Kathy J. Ehrig[2] · Liam Courtney-Davies[1]

Received: 13 November 2018 / Accepted: 6 May 2019
© Springer-Verlag GmbH Germany, part of Springer Nature 2019

Abstract
The IOCG deposit at Olympic Dam (South Australia) is hosted within the Roxby Downs Granite, which displays a weakly mineralised contact to the orebody (hereafter 'outer shell'). In a mineralogical-geochemical characterisation of Fe-oxides from the outer shell, we show silician magnetite (Si-magnetite) and HFSE-bearing hematite define the early stages of alkali-calcic alteration. This association forms in the presence of hydrothermal K-feldspar and calc-silicates via overprinting of magmatic magnetite and ilmenite breakdown. Geochemical modelling, at ≥ 400 °C, shows such reactions occur at pH-fO_2 conditions coinciding with shifts from K-feldspar to sericite, and ilmenite to rutile stability. The subsequent Si-magnetite+siderite association forms down-T in the absence of K-feldspar. Transition from granular to bladed morphologies in Si-magnetite is part of a series of Fe-oxide interconversions, followed by formation of zoned, U-W-Sn-Mo-bearing hematite. Enrichment in REE, Y and U in Si-magnetite and the prevalence of U-W-Sn-Mo-bearing hematite support a granite-derived fluid. Combined, petrographic and geochemical evidence show a transition among Fe-oxides from the outer shell to the orebody attributable to the evolution of the same fluid. Unusual massive magnetite intervals and Fe-oxide nodules in granite are considered due to either the presence of inherited lithologies, metasomatic products, or the result of magnetite-rich, crystal mush forming in the melt. We propose a model, corroborated by recently published data including high-precision U-Pb dating of magmatic zircon and hydrothermal hematite, in which an 'outer shell' is initiated at the 6–8 km depth of granite emplacement during volatile release from fluids ponding at intrusion margins. Granite cupola collapse at shallower levels (2–3 km?) follows via uplift along faults, facilitating intense brecciation and ore formation.

Keywords IOCG · Olympic Dam · Fe-metasomatism · Silician magnetite · HFSE-bearing hematite

Introduction

Iron oxide copper gold (IOCG) deposits encompass magnetite- to hematite-rich end-members (Barton 2014 and references therein). In recent years, Cu-Au-poor, magnetite-rich system such as Kiruna (Sweden) and El Laco (Chile) have been termed 'iron oxide apatite' (IOA) deposits. We refer to them as deposits that are kin to but distinct from those of the IOCG class sensu stricto. Evolution schemes for IOCG systems consider regional-scale alteration haloes centred on fluid sources of various origins, in which Fe-oxide associations generally change from higher-temperature magnetite- to lower-temperature hematite-dominant assemblages (Barton 2014 and references therein), even if both spatially co-exist in many cases. The genetic scheme underpinning such a model stipulates that fluids change from mildly alkaline/neutral pH to more acidic, resulting in three main stages: (i) barren Na(-Ca)-alteration, (ii) K-alteration (K-feldspar and/or biotite), and (iii) hydrolytic (sericite)-alteration. However, IOCG deposits rarely preserve well-defined zonation, either due to telescoping of alteration patterns during evolution of the system, or to superimposed geological events. Olympic Dam (OD) is, however, a well-preserved, mineralogically and geochemically zoned, intrusion-hosted IOCG deposit (Ehrig et al. 2012),

Editorial handling: D. Huston

Electronic supplementary material The online version of this article (https://doi.org/10.1007/s00126-019-00896-2) contains supplementary material, which is available to authorized users.

✉ Max R. Verdugo-Ihl
max.verdugoihl@adelaide.edu.au

[1] School of Chemical Engineering, The University of Adelaide, Adelaide, SA 5005, Australia

[2] BHP Olympic Dam, Adelaide, SA 5000, Australia

Published online: 12 June 2019

ADDITIONAL MATERIAL O

CO-AUTHORED ARTICLE ABSTRACT:

COPPER-ARSENIC NANOPARTICLES IN HEMATITE: FINGERPRINTING FLUID-MINERAL INTERACTION

Max R. Verdugo-Ihl[1], Cristiana L. Ciobanu[1], Ashley Slattery[2], Nigel J. Cook[1], Kathy Ehrig [3],

Liam Courtney-Davies[1]

[1]*School of Chemical Engineering and Advanced Materials, The University of Adelaide, Adelaide, SA 5005, Australia*

[2] *Adelaide Microscopy, The University of Adelaide, Adelaide, SA 5005, Australia*

[3]*BHP Olympic Dam, Adelaide, SA 5000, Australia*

Article published in Minerals (2019) 9(7), 388.

minerals

MDPI

Article

Copper-Arsenic Nanoparticles in Hematite: Fingerprinting Fluid-Mineral Interaction

Max R. Verdugo-Ihl [1,*], Cristiana L. Ciobanu [1], Ashley Slattery [2], Nigel J. Cook [1], Kathy Ehrig [3] and Liam Courtney-Davies [1]

[1] School of Chemical Engineering and Advanced Materials, The University of Adelaide, Adelaide, SA 5005, Australia
[2] Adelaide Microscopy, The University of Adelaide, Adelaide, SA 5005, Australia
[3] BHP Olympic Dam, Adelaide, SA 5000, Australia
* Correspondence: max.verdugoihl@adelaide.edu.au; Tel.: +61-831-33093

Received: 2 June 2019; Accepted: 25 June 2019; Published: 27 June 2019



Abstract: Metal nanoparticles (NP) in minerals are an emerging field of research. Development of advanced analytical techniques such as Z-contrast imaging and mapping using high-angle annular dark field scanning transmission electron microscopy (HAADF STEM) allows unparalleled insights at the nanoscale. Moreover, the technique provides a link between micron-scale textures and chemical patterns if the sample is extracted in situ from a location of petrogenetic interest. Here we use HAADF STEM imaging and energy-dispersive X-ray spectrometry (EDX) mapping/spot analysis on focused ion beam prepared foils to characterise atypical Cu-As-zoned and weave-twinned hematite from the Olympic Dam deposit, South Australia. We aim to determine the role of solid-solution versus the presence of discrete included NPs in the observed zoning and to understand Cu-As-enrichment processes. Relative to the grain surface, the Cu-As bands extend in depth as (sub)vertical trails of opposite orientation, with Si-bearing hematite NP inclusions on one side and coarser cavities (up to hundreds of nm) on the other. The latter host Cu and Cu-As NPs, contain mappable K, Cl, and C, and display internal voids with rounded morphologies. Aside from STEM-EDX mapping, the agglomeration of native copper NPs was also assessed by high-resolution imaging. Collectively, such characteristics, corroborated with the geometrical outlines and negative crystal shapes of the cavities, infer that these are opened fluid inclusions with NPs attached to inclusion walls. Hematite along the trails features distinct nanoscale domains with lattice defects (twins, 2-fold superstructuring) relative to hematite outside the trails, indicating this is a nanoprecipitate formed during replacement processes, i.e., coupled dissolution and reprecipitation reactions (CDRR). Transient porosity intrinsically developed during CDRR can trap fluids and metals. Needle-shaped and platelet Cu-As NPs are also observed along (sub)horizontal bands along which Si, Al and K is traceable along the margins. The same signature is depicted along nm-wide planes crosscutting at 60° and offsetting (012)-twins in weave-twinned hematite. High-resolution imaging shows linear and planar defects, kink deformation along the twin planes, misorientation and lattice dilation around duplexes of Si-Al-K-planes. Such defects are evidence of strain, induced during fluid percolation along channels that become wider and host sericite platelets, as well as Cl-K-bearing inclusions, comparable with those from the Cu-As-zoned hematite, although without metal NPs. The Cu-As-bands mapped in hematite correspond to discrete NPs formed during interaction with fluids that changed in composition from alkali-silicic to Cl- and metal-bearing brines, and to fluid rates that evolved from slow infiltration to erratic inflow controlled by fault-valve mechanism pumping. This explains the presence of Cu-As NPs hosted either along Si-Al-K-planes (fluid supersaturation), or in fluid inclusions (phase separation during depressurisation) as well as the common signatures observed in hematite with variable degrees of fluid-mineral interaction. The invoked fluids are typical of hydrolytic alteration and the fluid pumping mechanism is feasible via fault (re)activation. Using a

ADDITIONAL MATERIAL P

CONFERENCE ABSTRACT AND POSTER:

CHLORO-HYDROXY-ZIRCON NANOPRECIPITATES FINGERPRINT FERTILITY AND MINERALIZATION POTENTIAL OF GRANITIC MAGMAS

Liam Courtney-Davies[1], Cristiana L. Ciobanu[1], Max Verdugo-Ihl[1], Ashley Slattery[2], Nigel J. Cook[1], Kathy Ehrig[4],

[1]School of Chemical Engineering and Advanced Materials, The University of Adelaide, Adelaide, SA 5005, Australia

[2] Adelaide Microscopy, The University of Adelaide, Adelaide, SA 5005, Australia

[3] BHP Olympic Dam, Adelaide, SA 5000, Australia

Poster presentation at TIGeR 2019, Perth, Australia, September 11th-13th.

Chloro-hydroxy-zircon nanoprecipitates fingerprint fertility and mineralization potential of granitic magmas

Liam Courtney-Davies[1], Cristiana L. Ciobanu[1], Max Verdugo-Ihl[1], Ashley Slattery[2], Nigel J. Cook[1], Kathy Ehrig[3]

[1]The School of Chemical Engineering and Advanced Materials; liam.courtney-davies@adelaide.edu.au; cristiana.ciobanu@adelaide.edu.au; max.verdugo-ihl@adelaide.edu.au; nigel.cook@adelaide.edu.au
[2]Adelaide Microscopy; Ashley.slattery@adelaide.edu.au
[3]BHP Olympic Dam; kathy.ehrig@bhp.com

Zircon micron- to nanoscale structures and trace element signatures offer an exciting opportunity to delve into the genesis of large magmatic-hydrothermal ore systems (Courtney-Davies et al., 2019a). Based on zircon within different Proterozoic granites in the Olympic Cu-Au province (Gawler Craton, South Australia), either hosting, proximal to, or distal from iron-oxide-Cu-(U)-Au (IOCG) style mineralization, we characterize and interpret features that have application as potential discriminants in exploration for IOCG deposits. This subject is of interest to igneous petrologists and mineral deposit specialists alike, since the evidence contradicts long-held consensus regarding the processes and timescales of zircon alteration in magmatic-hydrothermal environments (Geisler et al., 2007 and references therein).

Magmatic zircon was studied from two distinct granite suites: ~1.85 Ga Donington Suite and ~1.6 Ga Hiltaba Suite. Although both suites host mineralisation, only the Hiltaba Suite granites are genetically associated with IOCG mineralization. The Hiltaba Suite-affiliated Roxby Downs Granite (1593.87+0.21; Cherry et al., 2018), host to the Olympic Dam deposit, is an outstanding case of a fertile granite, whereas the Donington Suite provides examples of pristine (Cape Donington, Eyre Peninsula) to hydrothermally-altered zircon (Wirrda Well prospect), the latter impacted by the same ~1.6 Ga hydrothermal event.

Zircon grains were studied by complementary micron- and nanoscale techniques: High Angle Annular Dark Field Scanning Transmission Electron Microscopy (HAADF STEM) imaging and STEM energy-dispersive (EDS) X-ray spectrometry mapping and spot analysis, supported by STEM simulations and complemented by electron microprobe analysis (EPMA). The aims were to characterise and interpret; (1) crystal zoning with respect to 'non-formulae' elements such as Fe, Ca and Cl; (2) the nature of a characteristic inclusion mottling in zoned bands; (3) lattice defects; and (4) the relationship between metamictization and alteration. Zircon grains were selected after imaging in BSE mode. Foils for TEM study were extracted in-situ, thinned to <100 nm by ion beam (Ga+) milling, and attached to Cu grids on a FIB-SEM platform. Of seven foils, five were cut across oscillatory zoning observed on grain surfaces in zircon to target their development at depth, also allowing correlation between micron- and nanoscale characteristics. HAADF STEM imaging and EDS spot analysis and mapping, was performed using an ultra-high resolution, probe-corrected, FEI Titan Themis S/TEM operated at 200 kV.

Crystal oscillatory zoning is expressed in all zircons, but with respect to different elements. In unaltered zircon, variation is, as expected, expressed with respect to common magmatic trace elements (REE and actinides), whereas altered zircon features crystal oscillatory zoning with non-formula elements, particularly Fe, Ca and Cl. Such patterns are depicted on both EPMA and STEM-EDS maps. In zircon proximal to mineralisation dense inclusion mottling becomes typical within bands enriched in non-formula elements. At higher resolution, the mottled areas (dark nanodomains in HAADF STEM images), concentrate Cl in particles ranging in size from nanoparticles (<100 nm) to fine particles (up to hundreds of nm). The largest particles, with well-defined geometrical shapes are crosscut by veinlets with lattice-scale defects proving they are inclusions rather than pores; the latter can nonetheless be present within the inclusions. Based on EPMA data and nanoscale characterisation we define these as chloro–hydroxy–zircon nano-precipitates formed by substitution mechanisms involving replacement of O by Cl and/or OH^{-}. Remobilised U and Pb was not found to be concentrated within such precipitates.

High-resolution imaging on four main zone axes in zircon shows lattice-scale disorder expressed as screw dislocations and lattice stretching but no amorphous domains, despite a

'metamict' appearance at the micron-scale. The most complex defects were imaged in Fe-rich bands from Roxby Downs Granite zircon on $[1\bar{1}1]$ zone axis. In this case, changes in the atomic arrangement along (011) can be interpreted as displacements with anti-phase modulation along fault planes. In contrast, defects within the particles described above are interpreted as the result of local fluid–mineral interaction leading to an increase in OH/halogen content.

Overall, chloro-hydroxy-zircon nanoprecipitates in the Fe-Ca-rich zones become volumetrically more significant in close proximity to the Olympic Dam deposit. An association between Fe and Cl would be expected in early IOCG fluids exsolved after granite crystallization. We thus conclude that Cl is inherent to hydrothermal fluids derived from the Hiltaba Suite granites, which also affected and altered the older Donington Suite granites at Wirrda Well. The absence of non-formula elements in fresh Donington Suite zircon from the Eyre Peninsula rules out a magmatic origin for such elements.

Zircon metasomatism can be attributed to an initial low-fluid, mineral-buffered diffusion-reaction process, followed by formation of chloro–hydroxy–zircon nanoprecipitates when fluids become highly focused. Preservation of pre-existing crystal orientation in zircon nanoprecipitates and host zircon is characteristic of reactions via a sharp interface, typical of replacement via coupling of dissolution with reprecipitation rates (CDRR). Transient porosity developed during the progression of CDRR provides sites for deposition of such nanoprecipitates (Putnis 2002).

From high-precision dating of hematite, iron metasomatism is known to have occurred at Olympic Dam shortly after granite crystallization (~2 to 4 Ma later; Courtney-Davies et al., 2019b). The α-dose required to relate zircon alteration to metamictization is calculated at ~100 Ma after crystallization, a period that cannot be reconciled with the timing of Fe-metasomatism in the region (Courtney-Davies et al., 2019a).

These results show that early metasomatic alteration can be recorded in magmatic zircon and that these patterns can be preserved over geological time, even when superimposed by the effects of metamictization. Marked differences in the geochemistry and nanoscale features of zircon across the sample suite imply that nanoscale studies of magmatic zircon, if coupled with careful characterization of textures and compositions at the micron-scale, represent a pathfinder tool that could be used to locate mineralisation. In turn, the presence of chloro-hydroxy-zircon nanoprecipitates would represent a diagnostic tool to assess the 'fertility' of granitic magmas.

References

Cherry AR, Ehrig K, Kamenetsky VS, et al (2018) Precise geochronological constraints on the origin, setting and incorporation of ca. 1.59 Ga surficial facies into the Olympic Dam Breccia Complex, South Australia. Precambrian Research, *315*, 162–178.

Courtney-Davies, L., Ciobanu, C.L., Verdugo-Ihl, M.R., Slattery, A., Cook, N.J., Dmitrijeva, M., Keyser, W., Wade, B.P., Dominick, U.I., Ehrig, K., Xu, J., Kontonikas-Charos, A., 2019a. Zircon at the nanoscale records metasomatic processes leading to large magmatic-hydrothermal ore deposits. Minerals, *9*(6), 364.

Courtney-Davies, L. Tapster, S. Ciobanu, C. Cook, N.J. Verdugo-Ihl, M.R. Ehrig, K.J. Kennedy, A.K. Gilbert, S.E. Condon, D.J. Wade, B.P., 2019b. A multi-technique evaluation of hydrothermal hematite U-Pb isotope systematics: Implications for ore deposit geochronology. Chemical Geology, *513*, 54–72.

Geisler, T., Schaltegger, U., Tomaschek, F., 2007. Re-equilibration of zircon in aqueous fluids and melts. Elements, *3*, 43–50.

Putnis, A., 2002. Mineral replacement reactions: from macroscopic observations to microscopic mechanisms. Mineralogical Magazine, 66(5), 689-708.

Chloro-hydroxy-zircon nanoprecipitates fingerprint fertility and mineralization potential of granitic magmas

Liam Courtney-Davies[1], Cristiana L. Ciobanu[1], Max R. Verdugo-Ihl[1], Ashley Slattery[2], Nigel J. Cook[1], Kathy Ehrig[3]

THE UNIVERSITY of ADELAIDE

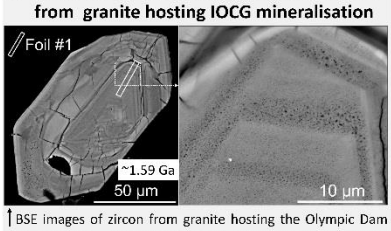
[1]*School of Chemical Engineering and Advanced Materials, The University of Adelaide*
[2]*Adelaide Microscopy, The University of Adelaide*
[3]*BHP Olympic Dam, Adelaide*

Contact: liam.courtney-davies@adelaide.edu.au

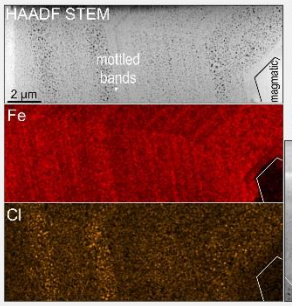
BHP

Introduction: Zircon within ~1.85 Ga Donington and ~1.59 Ga Hiltaba Suite granites from the Gawler Craton, South Australia, contain micron- to nanoscale features that have application as potential discriminants in exploration for iron-oxide Cu-(U)-Au (IOCG) deposits. A widespread metasomatic event occurred in the eastern Gawler Craton ~2-4 Ma after Hiltaba granite emplacement, resulting in several dozen IOCG-style deposits and prospects. Zircon ($ZrSiO_4$) from barren and (IOCG) mineralized granites were studied using EPMA spot/mapping, HAADF STEM imaging and STEM EDS X-ray spectrometry. **Aims:** To characterise and interpret: (1) crystal zoning with respect to 'non-formulae' elements; (2) the nature of a characteristic inclusion mottling in zonation patterns; (3) lattice defects; and (4) the temporal relationship between metamictization and metasomatism. **Questions:** (1) Zircon mottling is commonly interpreted as porosity, but is it always? - and how does it form?; (2) Physically and chemically durable zircon becomes more susceptible to alteration after accumulation of α-decay damage (metamictization), but can alteration occur prior to metamictization? How does this compare with processes and timescales of zircon alteration in magmatic-hydrothermal environments (e.g. Geisler et al. 2007)?

1. Transition to hydrothermal stage in zircon from granite hosting IOCG mineralisation



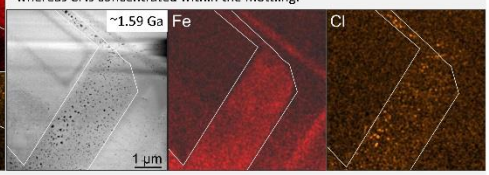
↑ BSE images of zircon from granite hosting the Olympic Dam IOCG deposit. Studied grains are characterised by crystal zonation patterns and 'mottling'. Radial cracks related to metamictization are present (Courtney-Davies et al., 2019a).

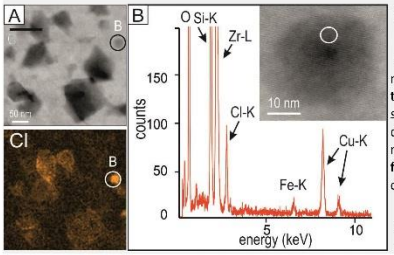


2. Non-formulae elements and mottling zonation

← **Zircon distal from Olympic Dam** (Foil #1) Fe, Ca and Al are present throughout zonation but are enriched in the mottled zones (EDS STEM maps). Primary magmatic domains are present.

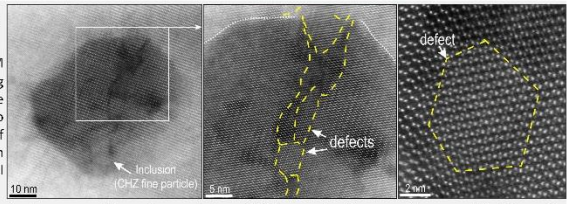
↓ **Zircon proximal to Olympic Dam** (Foil# 1a) HAADF STEM image and EDS STEM maps of a mottled bands reveal a homogeneous distribution of Fe, whereas Cl is concentrated within the mottling.





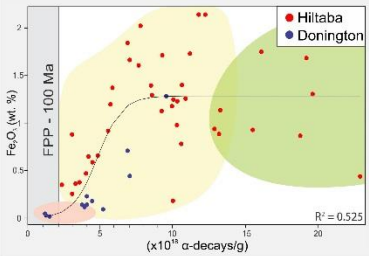
3. Chloro-hydroxy-zircon nanoprecipitates

← (A) Image and EDS STEM map of a Cl-rich area, showing that highest Cl is recorded in the smallest 'particles' with no difference in concentration of major elements. (B) EDS spectrum for the nanoparticle richest in Cl circled in (A).



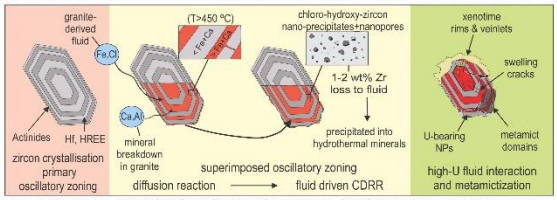
→ Lattice-scale defects along a fracture crosscutting a fine particle on [1$\bar{1}$1] zone axis. These results suggest that the main substitution involves replacement of O by OH− and/or Cl, leading to chloro–hydroxy–zircon (CHZ) formation. The zircon nanoprecipitates become volumetrically more abundant in Hiltaba and Donington granites proximal to IOCG mineralization.

4. Relative timing of non-formulae element incorporation into zircon



↙ EPMA data for zircon in Hiltaba and Donington Suite granites. The Olympic Cu-Au metallogenic event occurred ~2-4 Ma after zircon crystallization of Hiltaba granites (Courtney-Davies et al. 2019b).

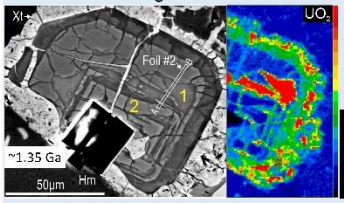
Quantification of α-decay damage that could relate zircon alteration to metamictization (FPP) is calculated to be ~100 Ma, far later than the metallogenic event recorded across the Olympic Cu-Au Province. There is also a poor correlation between alpha-decay damage and non-formulae element content.



↑ Metasomatism can be attributed to an initial low-fluid, mineral-buffered diffusion-reaction process, followed by formation of CHZ nanoprecipitates when fluids become highly focused (Courtney-Davies et al. 2019a). The preservation of pre-existing crystal orientation in zircon nanoprecipitates and host zircon is characteristic of reactions via a sharp interface, typical of CDRR replacement (Putnis 2002).

Summary: Early metasomatic alteration is recorded in magmatic zircon. Marked differences in the geochemistry and nanoscale features of zircon represent a pathfinder tool that could be used to locate mineralisation. In turn, the presence of chloro-hydroxy-zircon NPs would represent a diagnostic tool to assess the 'fertility' of granitic magmas. **What about late altered zircon?**

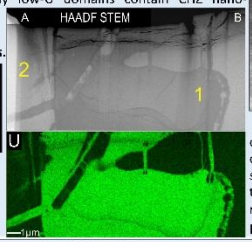
5. Late hydrothermal stage: metamict zircon in a high-U environment

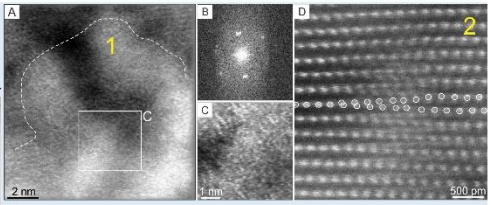


↑ EPMA map of zircon from high-grade bornite ore at Olympic Dam. The grain is highly metamict, with domains containing up to ~5 wt. % UO_2 (EPMA spot analysis). Location of Foil #2 marked. The age is ~250 Ma younger than magmatic zircon outside the orebody (Pb-loss?).

↘ (Foil #2) High-U domain continues at depth forming a dark 'pool' with inter-connecting veinlets. U is pervasively enriched in the pool and veinlets. Pb is homogeneous across high- and low-U domains. However, only low-U domains contain CHZ nano-precipitates. **No U or Pb Nanoparticles.**

1 and 2 mark domains located from micron- to nano- scales





↑ HAADF STEM images of metamict zircon (Foil #2). (A, B) Amorphous areas within crystalline zircon. Compare with simulations in Geisler et al. (2007). Note the fuzzy central area on FFT in B, typical of amorphous material. (C) Detail showing random specks/atoms – direct imaging of amorphous state(?). Note the image is in focus throughout the entire area. (D) Screw dislocation in crystalline zircon from domain 2 recording a ~250 Ma younger age than early altered magmatic zircon. **Is this healing post-amorphization of domain (1) or a relict predating amorphization?**

Acknowledgements: This is a contribution to the 'FOX project', supported by BHP Olympic Dam and the Government of South Australia Mining and Petroleum Services Centre of Excellence.
References: Courtney-Davies et al. 2019a (Minerals 9, 364); Courtney-Davies et al. 2019b (Chem Geol 513, 54-72); Putnis 2002 (Min Mag 66, 689-708); Geisler et al. 2007 (Elements 3, 43–50).

ADDITIONAL MATERIAL Q

CONFERENCE ABSTRACT AND POSTER:

U-PB DOPED SYNTHETIC REFERENCE MATERIAL FOR IN-SITU HEMATITE GEOCHRONOLOGY

Liam Courtney-Davies[1], Marcus W. Richardson[2], Sarah E. Gilbert[3], Cristiana L. Ciobanu[1], Max Verdugo-Ihl[1], Nigel J. Cook[1], Kathy Ehrig[4], Benjamin P. Wade[3]

[1]*School of Chemical Engineering and Advanced Materials, The University of Adelaide, Adelaide, SA 5005, Australia*

[2]*6 Ophir Street, Goodwood, SA 5060, Australia*

[3]*Adelaide Microscopy, The University of Adelaide, Adelaide, SA 5005, Australia*

[4] *BHP Billiton Olympic Dam, Adelaide, SA 5000, Australia*

Conference abstract and poster, Geoanalysis 2018, Sydney, Australia, July 10th-14th.

U-Pb doped synthetic reference material for *in-situ* hematite geochronology

LIAM COURTNEY-DAVIES[1], MARCUS RICHARDSON[2], SARAH E. GILBERT[3], CRISTIANA L. CIOBANU[1], MAX R. VERDUGO-IHL[1], NIGEL J. COOK[1], KATHY EHRIG[4], BENJAMIN P. WADE[3]

[1]School of Chemical Engineering, University of Adelaide, 5005 SA, Australia, Liam.Courtney-Davies@adelaide.edu.au, Cristiana.Ciobanu@adelaide.edu.au, Max.Verdugolhl @adelaide.edu.au, Nigel.Cook@adelaide.edu.au
[2]6 Ophir Street, Goodwood, 5034 SA, Australia, wcamar@internode.on.net
[3]Adelaide Microscopy, University of Adelaide, Australia, Sarah.Gilbert@adelaide.edu.au, Benjamin.Wade@adelaide.edu.au
[4]BHP Olympic Dam, Adelaide, 5000 SA, Australia, Kathy.J.Ehrig@bhpbilliton.com

Uranium-bearing hematite is widespread within iron-oxide-Cu-Au deposits and ores associated with banded iron formations of South Australia [1-4]. Valuable age data has been obtained via LA-ICP-MS applying GJ-1 Zircon and mixed U-Pb solutions as the primary reference materials [1,2,5], as well as high precision ID-TIMS U-Pb data, which is independent of the need for solid reference materials [6]. However, routine high-accuracy microbeam dating of hematite requires near-matrix-matched reference materials, of which suitable natural specimens have currently not been identified. We report a method to produce U-Pb doped hydrated ferric oxide, through slow introduction of ~150 ppm U/Pb solutions, calcinated at 700 °C to dehydrate and convert to hematite. Polycrystalline hematite fragments, up to 1 cm-long, are commonly produced through this method. The material was mounted in epoxy, polished, and imaged by SEM in backscatter electron mode (BSE) to check for potential heterogeneity or inclusions of U-Pb-bearing phases. Further characterisation by LA-ICP-MS showed that the precision of the $^{207}Pb/^{235}U$ and $^{206}Pb/^{238}U$ (50 spot analyses) was 0.2% (95% confidence interval) and with a MSWD of 0.61, compared to the zircons GJ-1 (0.5% *n*=36), Plesovice (0.6% *n*=18), and 91500 (0.6% *n*=9) analysed in the same analytical session. U concentrations are ~70 ppm, and Pb ~35 ppm. The material displays both dark and bright areas under BSE, with slightly varying U/Pb most likely formed during heating steps. Downhole U-Pb profiles for the synthetic material displayed a similar fractionation trend to natural hematite analysed within the same analytical session. To further evaluate homogeneity, the samples will be measured by ID-TIMS to define absolute U-Pb ratios, and subsequently by SHRIMP to examine U-Pb isotope homogeneity at the micron-scale. Our aspiration is that this material can be used routinely as a reference material for microbeam techniques.

[1] Ciobanu et al. (2013) *Precambr. Res.* ***238****, 129-147.* [2] Courtney-Davies et al. (2016) *Minerals.* ***6****, 3, 85.* [3] Verdugo-Ihl et al. (2017) *Ore Geol. Rev.* ***91****, 173-195.* [4] Keyser et al. (2018) *Ore Geol. Rev.* ***93****, 337-360.* [5] Apukhtina et al. (2017) *Econ. Geol.* ***112****, 1531-1542.* [6] Courtney-Davies et al. (2018) *Chem. Geol. (in review).*

U-Pb Doped Synthetic Reference Material for *In-situ* Hematite Geochronology

Liam Courtney-Davies[1]*, Marcus Richardson[2], Sarah E. Gilbert[3], Cristiana L. Ciobanu[1], Max R. Verdugo-Ihl[1], Nigel J. Cook[1], Kathy Ehrig[4] and Benjamin P. Wade[3]

[1] School of Chemical Engineering, University of Adelaide, 5005 SA; [2] 6Ophir Street, Goodwood, 5034 SA; [3] Adelaide Microscopy, University of Adelaide, SA; [4] BHP Olympic Dam, Adelaide, 5000 SA

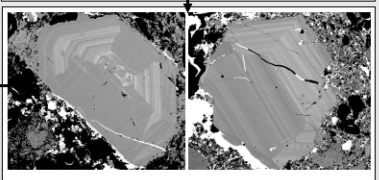
*liam.courtney-davies@adelaide.edu.au

Abstract

Uranium-bearing hematite is widespread within iron-oxide-Cu-Au deposits and ores associated with banded iron formations of South Australia. Valuable age data has been obtained via LA-ICP-MS applying GJ-1 Zircon and mixed U-Pb solutions as the primary reference materials, as well as high precision ID-TIMS U-Pb data, which is independent of the need for solid reference materials. However, routine high-accuracy microbeam dating of hematite requires near-matrix-matched reference materials, of which suitable natural specimens have currently not been identified. We report a method to produce U-Pb co-doped hydrated ferric oxide, through slow introduction of ~150 ppm U/Pb solutions, calcined at 700 °C to dehydrate and convert to hematite. Polycrystalline hematite fragments, up to 1 cm-long, are commonly produced through this method. The material was mounted in epoxy, polished, and imaged by SEM in backscatter electron mode (BSE) to check for potential heterogeneity or inclusions of U-Pb-bearing phases. Further characterization by LA-ICP-MS showed that the precision of the $^{207}Pb/^{235}U$ and $^{206}Pb/^{238}U$ (50 spot analyses) was 0.2% (95% confidence interval) and with an MSWD of 0.61, compared to the zircons GJ-1 (0.5% *n*=36), Plesovice (0.6% *n*=18), and 91500 (0.6% *n*=9) analysed in the same analytical session. Uranium concentrations are ~70 ppm, and Pb ~35 ppm. The material displays both dark and bright areas under BSE, with slightly varying U/Pb most likely formed during heating steps. Downhole U-Pb profiles for the synthetic material displayed a similar fractionation trend to natural hematite analysed within the same analytical session. To further evaluate homogeneity, the samples will be measured by ID-TIMS to define absolute U-Pb ratios, and subsequently by SHRIMP to examine U-Pb isotope homogeneity at the micron-scale. Our aspiration is that this material can be used routinely as a reference material for microbeam techniques.

1 Why Date Hematite?

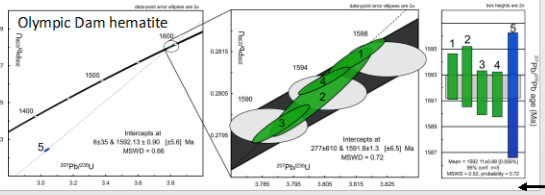
- Fe-oxides are one of the most abundant phases in Iron-oxide-Cu-Au (IOCG) and banded iron formation deposits, and can incorporate U
- Hematite can isotopically record ore forming histories in deposits where more conventional (hydrothermal) minerals are absent, U-poor or isotopically open system
- Geochronology is needed within exploration and research to understand the timing of magmatic and hydrothermal systems, the genesis of ore deposits and peaks in formation magnitude across geological time and provinces



~1.59 Ga U-bearing, oscillatory-zoned hematite from the Olympic Dam IOCG deposit, South Australia. This type of hematite has been shown to contain up to several wt% U [1] and has been dated by ID-TIMS, SHRIMP and LA-ICP-MS

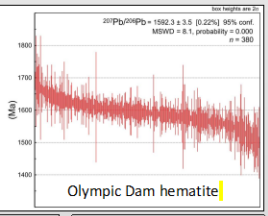
ID-TIMS

Very high precision (<0.05%) hematite ages can be obtained by isotope dilution-thermal ionization mass spectrometry [2], which is independent of solid reference materials, but is very expensive, time consuming and is not an *in-situ* technique= no spatial resolution



Microbeam

- LA-ICP-MS and SHRIMP hematite data has been obtained [1,2] using zircon as the primary and secondary reference materials (GJ-1, Plesovice, 91500).
- Dates can be extracted, but data features, accuracy and discrete generations cannot be fully assessed without near-matrix matched reference materials.
- The speed, high spatial resolution and low cost of LA-ICP-MS makes it a more viable option for routine hematite geochronology when a homogeneous reference material is fabricated

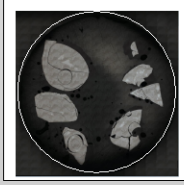


2 Reference Material Preparation

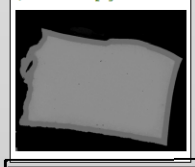
1. Synthetic hematite doped with U and Pb was prepared from a solution of ferric nitrate precipitated with ammonia solution
2. This produced a suspension of colloidal hydrated ferric oxide (HFO) that was washed with water several times by decantation until it peptised
3. A doping solution of uranyl and lead nitrates was then added to adsorb the U and Pb onto the colloidal HFO particles
4. Ultra sonication with a powerful 200W horn was used to subdivide the colloidal particles and increase the surface area for dopant adsorption
5. After settling, the doped HFO was dried at about 50°C to produce solid chips of several millimetres thickness
6. These were then heated to 700°C which converted them to U-Pb doped hematite

Imaging

Hematite chips were then mounted in epoxy in 1-inch polished blocks for optical- and SEM-imaging, to assess grain scale homogeneity



No inclusions visible in BSE images. XRD analysis confirms the only present phase is α-Fe_2O_3

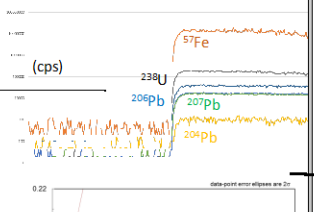


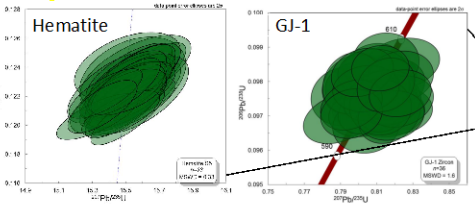
Some grains contain lighter and darker patches in optical microscope images

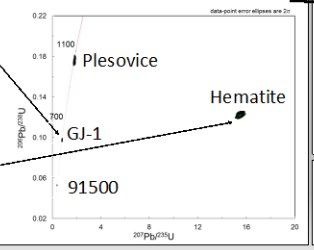


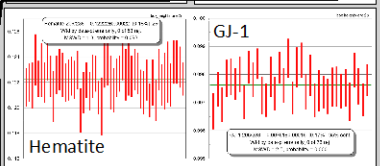
3 Assessing Reference Material (LA-ICP-MS)

- Spot analysis (32µm) yielded homogeneous U and Pb concentrations at ~70 ppm, and ~35 ppm respectively
- The downhole U-Pb profiles were flat and displayed a similar fractionation trend to natural hematite
- As the U-Pb solution used in fabrication does not have a ' real age ' the data plots far from concordia, but clusters tightly
- Weighted average precision (single session, 50 spots, 3 grains) $^{206}Pb/^{238}U$ and $^{207}Pb/^{235}U$ was 0.2% (95% conf. MSWD= 1.3 & 0.61), similar to the analysed zircon standards









Next Stages

- Although the majority of grains appear homogeneous, there are discrete patches of light material containing fractionally higher U/Pb (~0.06 $^{206}Pb/^{238}U$)
- Once these concentrated patches have been eliminated through refinement of the sample preparation method, the material will undergo higher precision analysis (e.g. solution-ICPMS and ID-TIMS)
- When characterization is completed, and if deemed homogenous enough, the reference material will be routinely implemented to date Fe-oxides from Olympic Dam and elsewhere
- This increases mineral geochronometers available to date ore deposits, BIF's and detrital assemblages

References & Acknowledgements

[1] Ciobanu, C.L. et al. (2013) Precambrian Research. **238**,129-147.
[2] Courtney-Davies, L. et al. (2018) in review.

This is a contribution to the **FOX Project** (Trace elements in Fe-oxide) sponsored by BHP Olympic Dam and the South Australian Government

ADDITIONAL MATERIAL R

CONFERENCE ABSTRACT AND POSTER:

DEVELOPING IRON-OXIDE U-PB GEOCHRONOLOGY FOR NEW, ROBUST, TEMPORAL INSIGHTS INTO IOCG AND BIF MINERALIZATION

Liam Courtney-Davies[1], Cristiana L. Ciobanu[1], Simon R. Tapster[2], Daniel J. Condon[2], Allen K. Kennedy[3], Nigel J. Cook[1], Kathy Ehrig[4], Benjamin P. Wade[5], Marcus W. Richardson[6]

[1]*School of Chemical Engineering and Advanced Materials, The University of Adelaide, Adelaide, SA 5005, Australia*

[2]*NIGL, British Geological Survey, Keyworth, U.K.*

[3]*John de Laeter Centre, Curtin University of Technology, Bentley, WA 6102, Australia*

[4] *BHP Olympic Dam, Adelaide, SA 5000, Australia*

[5]*Adelaide Microscopy, The University of Adelaide, Adelaide, SA 5005, Australia*

[6]*6 Ophir Street, Goodwood, SA 5060, Australia*

Conference abstract and poster, mineral deposit studies group (MDSG) 2017, Bristol, U.K., December 19th-21st.

APPLIED EARTH SCIENCE (TRANS. INST. MIN. METALL. B), 2017
http://dx.doi.org/10.1080/03717453.2017.1306241
The Institute of Materials, Minerals and Mining
AusIMM THE MINERALS INSTITUTE
Taylor & Francis
Check for updates

Steps to developing iron-oxide U-Pb geochronology for robust temporal insights into IOCG and BIF mineralisation

Liam Courtney-Davies[a], Cristiana Ciobanu[a], Simon Tapster[b], Daniel Condon[b], Allen Kennedy[c], Nigel Cook[a], Kathy Ehrig[d], Benjamin Wade[e] and Marcus Richardson[f]

[a]School of Chemical Engineering, University of Adelaide, Adelaide, SA, Australia; [b]NIGL, British Geological Survey, Keyworth, UK; [c]John de Laeter Centre, Curtin University of Technology, Bentley, WA, Australia; [d]BHP Billiton Olympic Dam, Adelaide, SA, Australia; [e]Adelaide Microscopy, University of Adelaide, Adelaide, SA, Australia; [f]Goodwood, SA, Australia

Direct U-Pb dating of iron-oxides, principally haematite and magnetite, is a relatively new method, which was first realised through a reconnaissance geochronological study of U-bearing oscillatory-zoned haematite from the Olympic Dam iron-oxide copper-gold deposit, South Australia (Ciobanu et al. 2013). Although successful, only $^{207/206}$Pb weighted average ages were deemed reliable due to calibration against a non-matrix-matched standard (GJ-1 Zircon).

In a push towards more robust iron-oxide geochronology, we are attempting to fabricate, characterise and evaluate natural, as well as synthetic standard material using a complimentary range of instruments and techniques. Once suitable standard material has been attained, it will be applied as a proxy to constrain the timing and potential lifespan of mineralisation in a range of complex deposits, including those in the Olympic Cu-Au province (South Australia), as well as banded iron formations (BIF) found to contain uranium. Significant steps have been taken, through characterisation of potential standard material, employing sensitive – high resolution – ion microprobes (SHRIMP) and isotope dilution–thermal ionisation mass spectrometry, both applied to iron-oxides for the first time, and which has yielded extremely positive initial results. In tandem with this, the development of a mixed U-Pb solution standard dating technique (Courtney-Davies et al. 2016) has furthered our understanding of matrix-effects and other limitations associated with haematite LA-ICPMS U-Pb geochronology, but also allowed us to date samples, including BIF haematite (Keyser et al. in review), in which U concentrations in the mineral are as low as 10 ppm. One route of fabricating synthetic haematite, using a modified chemical vapour transport method, is producing mm-sized crystals, which are now set to undergo U-Pb doping experiments.

Although numerous minerals can be dated routinely, and in many cases reliably, iron-oxides can become an important tool for directly dating mineralisation in ore deposits, in which conventional minerals like zircon and monazite are either absent, or are not necessarily representative of the ore-forming event. In turn, this can contribute to the overall genetic model of an ore deposit, and lead to potential applications in mineral exploration. The ubiquitous presence of iron-oxides in several deposit types suggests the method may have far reaching applicability.

References

Ciobanu CL, Wade BP, Cook NJ, Schmidt Mumm A, Giles D. 2013. Uranium-bearing hematite from the Olympic Dam Cu-U-Au deposit, South Australia; a geochemical tracer and reconnaissance Pb-Pb geochronometer. Precambrian Res. 238:129–147.

Courtney-Davies L, Zhu Z, Ciobanu CL, Wade BP, Cook NJ, Ehrig K, Cabral AR, Kennedy A. 2016. Matrix-matched iron-oxide laser ablation ICP-MS U-Pb geochronology using mixed solution standards. Minerals. 6(3):85. doi:10.3390/min603008.

Keyser W, Ciobanu CL, Courtney-Davies L, Wade BP, Cook NJ, Zhu Z, Feltus H, Johnson S, Ehrig K and Johnson G. In review. U-Pb dating of hematite from iron ores: examples from the Middleback Ranges banded iron formation, South Australia. Geology.

CONTACT Liam Courtney-Davies liam.courtney-davies@adelaide.edu.au
© 2017 Institute of Materials, Minerals and Mining and The AusIMM

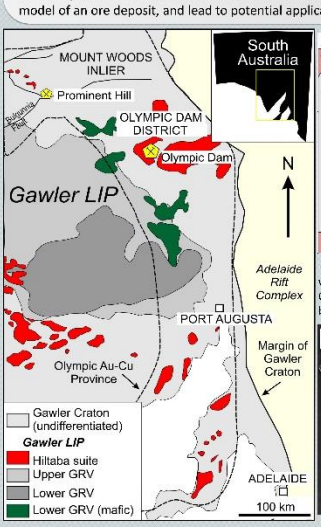
Developing iron-oxide U-Pb geochronology for new, robust, temporal insights into IOCG and BIF mineralisation

Liam Courtney-Davies[1], Cristiana L. Ciobanu[1], Simon R. Tapster[2], Daniel J. Condon[2], Allen K. Kennedy[3], Nigel J. Cook[1], Kathy Ehrig[4], Benjamin S. Wade[5] and Marcus Richardson[6]

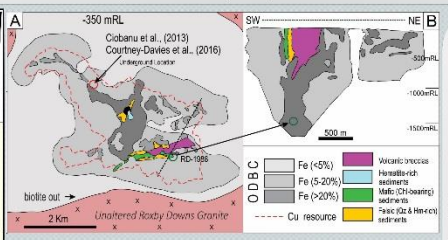
[1]School of Chemical Engineering, The University of Adelaide, South Australia; [2]NERC, British Geological Survey, Keyworth, UK; [3]John de Laeter Centre, Curtin University of Technology, Bentley, Western Australia; [4]BHP Billiton Olympic Dam, Adelaide, South Australia; [5]Adelaide Microscopy, The University of Adelaide, South Australia; [6] 6 Ophir Street, Adelaide, South Australia

Acknowledgements: This is a contribution to the **FOX Project (Trace elements in Fe-oxides)** supported by **BHP Billiton** and the **South Australian Government Department of State Development**

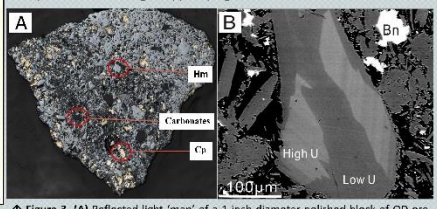
Abstract: Direct U-Pb dating of iron-oxides, principally hematite and magnetite, is a relatively new method, which was first realized through a reconnaissance geochronological study of U-bearing oscillatory-zoned hematite from the Olympic Dam iron-oxide copper-gold deposit, South Australia [1]. Although successful, only $^{207/206}$Pb weighted average ages were deemed reliable due to calibration against a non-matrix-matched standard (GJ-1 Zircon). In a push towards more robust iron-oxide geochronology, we are attempting to fabricate, characterize and evaluate natural, as well as synthetic standard material using a complimentary range of instruments and techniques. Once suitable standard material has been attained, it will be applied as a proxy to constrain the timing and potential lifespan of mineralization in a range of complex deposits, including those in the Olympic Cu-Au province (South Australia), as well as banded iron formations (BIF) found to contain uranium. Significant steps have been taken, through characterization of potential standard material, employing sensitive - high resolution - ion microprobes (SHRIMP) and isotope dilution – thermal ionization mass spectrometry (ID-TIMS), both applied to iron-oxides for the first time, and which has yielded extremely positive initial results. In tandem with this, the development of a mixed U-Pb solution standard dating technique [2] has furthered our understanding of matrix-effects and other limitations associated with hematite U-Pb geochronology, but also allowed us to date samples, including BIF hematite [3], in which U contents in the mineral are as low as 10 ppm. One route of fabricating synthetic hematite, using a modified chemical vapour transport method, is producing mm-sized crystals, which are now set to undergo U-Pb doping experiments. Although numerous minerals can be dated routinely, and in many cases reliably, iron-oxides can become an important tool for directly dating mineralization in ore deposits, in which conventional minerals like zircon and monazite are either absent, or are not necessarily representative of the ore-forming event. In turn, this can contribute to the overall genetic model of an ore deposit, and lead to potential applications in mineral exploration. The ubiquitous presence of iron-oxides in several deposit types suggests the method may have far reaching applicability.



↑ **Figure 1.** Sketch map showing location of the Olympic Dam and Prominent Hill deposits, Olympic Cu-Au Province, South Australia (after Ciobanu et al. 2013).



↑ **Figure 2. (A)** Simplified geological map of the Olympic Dam Breccia Complex (ODBC) with the locations of samples analysed by [1,2], in this study, and from the SE Lobe; **(B)** Cross-section through the SE Lobe showing the location of sample 7295 (Figure 3, below). Modified from Ehrig et al., (2012). Figure 6 data comes from RD-1988.



↑ **Figure 3. (A)** Reflected light 'map' of a 1-inch diameter polished block of OD ore comprising hematite (Hm) cemented by chalcopyrite (Cp) and pyrite. **(B)** BSE image of OD hematite displaying oscillatory and sectorial zoning expressed by varying U content. Bright zones = high U concentration.

U-Pb Methods

SHRIMP (John de Laeter Centre, Curtin University)

- Ion microprobe analytical methods follow Compston et al. (1984); Claoue-Long et al. (1995) and Williams (1998).
- All isotopic measurements were reduced by off-line computer programs using standard techniques.
- U/Pb ages were normalized to a value of 1593 Ma for the concordant hematite grain used as a standard (as measured by ID-TIMS for corresponding grains)
- The given ^{207}Pb/^{206}Pb ages are independent of our standard analyses.
- Common-Pb was corrected using the ^{204}Pb or ^{208}Pb method discussed in Williams (1998), for the standards.

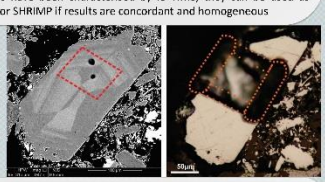
LA-ICP-MS Mixed U-Pb Solution Standard Dating (University of Adelaide)

- A homogeneous solution containing fixed U- and Pb-isotope ratios was prepared and the U/Pb ratio approximated to that of the unknown (e.g. 1, 4 and 12 ppb).
- U-Pb mixed solution and ablated material from pure synthetic hematite was mixed in the spray chamber and introduced to the ICP-MS.
- Theoretically this should reduce matrix effects compared with a non matrix-matched solid standard (e.g. GJ-1 Zircon), allowing higher precision and accuracy.

ID-TIMS (NERC, British Geological Survey)

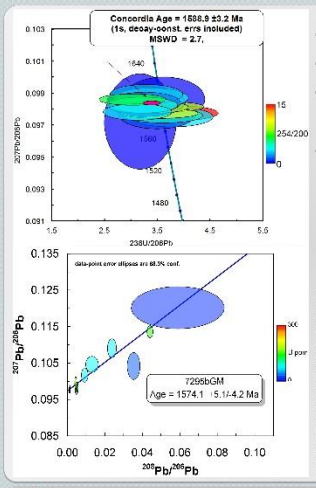
- Initial steps have been taken to develop Fe-oxides for ID-TIMS analysis.
- Considering the fine-grained nature of OD hematite, and only certain generations containing high U zonation, grains must be ablated around and then removed with tweezers for further analysis.
- Once certain grains have been characterised by ID-TIMS, they can be used as standard material for SHRIMP if results are concordant and homogeneous

Figure 4. Representative BSE and optical images of extracted grain area. This method is preferred to micro-drilling due to a lower subsequent Pb lab blank. →



SHRIMP

- Ion yields are acceptable with count rates in the 1000s of c/s for UO$^+$ and UO$_2^+$.
- The ^{238}U$^+$ peak had unacceptably low counts and should not be measured.
- Only minor variation of c/s of the molecular $Fe_3O_1^+$ reference peak, between and within analyses, suggesting that it is unlikely there is any crystallographic orientation effect on ion yields.
- ^{204}Pb is present in variable amounts and small corrections are needed



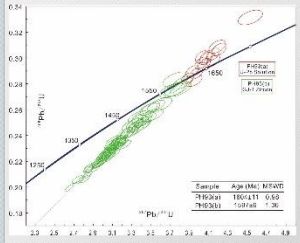
← **Figure 5.** T-W Concordia diagram for hematite (sample 10.2 OD, high-grade bornite rich ore) previously used for LA-ICP-MS ^{207}Pb-^{206}Pb dating (Ciobanu et al. 2013). Colour-coding of analyses uses the ^{238}U^{16}O/ ^{56}Fe$_2^{16}$O$_3$ peak ratio (254/200) as a proxy for U content. The U decay constants used in calculations are those of Steiger and Jager (1977).

← **Figure 6.** As a result of a wide range of U concentrations, we produced a ^{207}Pb/^{206}Pb vs ^{206} Pb/^{238}Pb isochron by treating all ^{208}Pb as common Pb. This shows that the assumptions of a single age and a single common Pb composition, are reasonable.

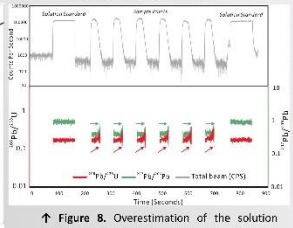
Conclusion: SHRIMP U-Pb and Pb-Pb dating of hematite produces excellent results if BSE imaging is used to identify grains with oscillatory or sector zoning, or homogeneous undisturbed cores and patches. High spatial resolution allows interrogation between different generations of hematite, and hence an estimation of mineralisation lifespan, once a matrix-matched standard is fabricated.

LA-ICP-MS – Rationale

- To further evaluate the potential of hematite as a U-Pb mineral geochronometer;
- To assess the matrix-effects when using the U-Pb solution compared to a non-matrix matched solid standard
- To test whether the method gives reliable ages for hematite with ultra low U concentrations (BIF)

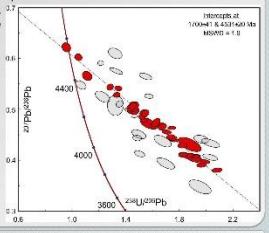


↑ **Figure 7.** Sample PH-93 **(A)** gave an upper intercept age of 1604±11 Ma anchored to 0±40 Ma, using a 27 µm spot size and a 12 ppb mixed solution. PH-93 was also dated using GJ-1 Zircon **(B)** as the primary standard, giving an age of 1597.2±6.1 Ma (82 of 95 points). Although the error is small, the range of discordance is large when compared to the solution analysis in which all data plots on, or above concordia.



↑ **Figure 8.** Overestimation of the solution dating age could be attributable to downhole fractionation of ^{206}Pb/^{238}U with time. ^{207}Pb/^{206}Pb does however remain stable. Line rastering could potentially circumvent this problem.

Figure 9. Dated sample of a BIF hematite in the Carajás Region, Brazil, containing on average 6 ppm U, with extremely high common Pb. Despite this, a meaningful age can still be derived, seen through good agreements with zircon ages from the area (grey points excluded from age regression). →



Conclusion: Solution dating results have not had any corrections applied, but nevertheless shows that ^{207}Pb/^{206}Pb ages are not greatly affected by applying different standards, and thus the GJ-1 Zircon is reliable for dating Hm and further validates the 1590±8 & 1577±5 Ma Pb-Pb ages [1]. Further refinements of the method and analyses with magnetite will now take place.

Implications

- Accurate, precise U-Pb dating of Fe-oxides allows new constraints and reassessment of the timing of ore mineralization.
- Constraining the timing of mineralization at OD is particularly important as current genetic models are associated with structural and stratigraphic interpretations combined with dating of accessory minerals associated with mineralization but not necessarily formed during the metallogenic event.
- The initial experiments open up substantial scope for refining techniques and addition of data from different instruments, thus creating momentum towards a suitable hematite standard for routine high-precision dating.

Ongoing work: Further constraints on the Olympic Cu-Au Province geochronology will take place once standard material becomes available, either using grains characterised by ID-TIMS, or via a synthetic standard currently being developed using chemical vapour transport. Bracketing of OD hematite through re-evaluation of zircon ages from in and around the deposit will be undertaken to better constrain the timing of mineralisation and build a more robust overall geochronological model.

References: [1] Ciobanu *et al.*, (2013) *Precambr. Res.* **238**,129-147; [2] Courtney-Davies *et al.*, (2016) *Minerals*, **6**(3), 80; [3] Keyser *et al.*, (in review); Claoue-Long *et al.*, (1995) *SEPM Spec. Publ.* **54**: 3-21; Compston *et al.*, (1984) *J. Geophys. Res.* **89**, Suppl. B525-B534.; Ehrig *et al.*, (2012) *SEG Spec. Publ.* 16, p. 237-267; Johnson & Cross (1995) *Econ. Geol.*, **90**, 1046–1063; Williams. (1998). *Rev. Econ. Geol.* **7**: 1-35.

ADDITIONAL MATERIAL S

CONFERENCE ABSTRACT AND POSTER:

URANIUM BEARING, OSCILLATORY-ZONED HEMATITE: ASSESSING CLOSED SYSTEM BEHAVIOR FOR U-PB SYSTEMATICS

Liam Courtney-Davies[1], Cristiana L. Ciobanu[1], Nigel J. Cook[1], Simon R. Tapster[2], Daniel J. Condon[2], Allen K. Kennedy[3], Kathy Ehrig[4]

[1]*School of Chemical Engineering and Advanced Materials, The University of Adelaide, Adelaide, SA 5005, Australia*

[2]*NIGL, British Geological Survey, Keyworth, U.K.*

[3]*John de Laeter Centre, Curtin University of Technology, Bentley, WA 6102, Australia*

[4] *BHP Olympic Dam, Adelaide, SA 5000, Australia*

Conference abstract and poster, Goldschmidt 2018, Boston, U.S.A, August 12th-17^{5h}.

Goldschmidt2018 Abstract

Uranium-bearing, oscillatory-zoned hematite: assessing closed system behaviour for U-Pb systematics

L. COURTNEY-DAVIES[1]*, C.L. CIOBANU[1], N.J. COOK[1], S.R. TAPSTER[2], D.J. CONDON[2], A.K. KENNEDY[3], K. EHRIG[4],

[1] School of Chemical Engineering, Univ. of Adelaide, Adelaide, SA 5005, Australia (correspondence*: liam.courtney-davies@adelaide.edu.au; cristiana.ciobanu@adelaide.edu.au; nigel.cook @adelaide.edu.au)

[2] NERC, British Geological Survey, Keyworth, U.K. (simont@bgs.ac.uk; dcondon@bgs.ac.uk)

[3] John de Laeter Centre, Curtin University, Bentley, WA, Australia (A.Kennedy@exchange.curtin.edu.au)

[4] BHP Olympic Dam, Adelaide, SA 5000, Australia (Kathy.J.Ehrig@bhpbilliton.com)

Oscillatory-zoning with respect to U in mineral geochronometers requires nanoscale assesesment as such patterns may reflect an overprinting event. Addition/loss of elements (open-system behaviour) disturb isotopic ratios used for U-Pb systematics. $^{207}Pb/^{206}Pb$ isotope mapping of coarse hematite from the Olympic Dam deposit, South Australia, shows ~1.6 Ga age homogeneity across oscillatory-zoned, U-bearing domains [1]. ID-TIMS analysis carried out on material micro-sampled from one such grain, up to ~1 mm apart, give approximately identical $^{207}Pb/^{206}Pb$ ages (unpubl. data). To asses open or closed system behaviour for U-Pb systematics, the same grain was chemically mapped (Fig. 1a) prior to HAADF-STEM study carried-out on a FIB-prepared foil cut across U-bands. The sample is free of inclusions (Fig. 1b) and atomic-resolution imaging shows crystallinity with no lattice damage induced by α-decay (Fig. 1c). We conclude such grains preserve a near closed system from crystallization at ~1.6 Ga.

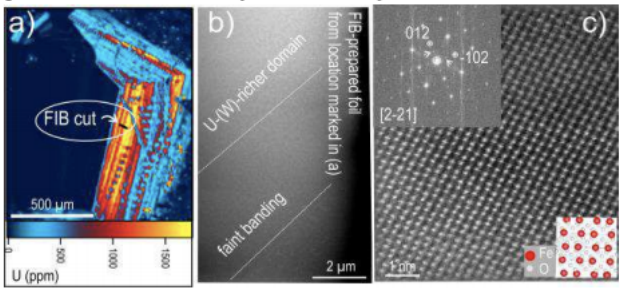


Fig. 1. (a) LA-ICP-MS map for U in hematite and location of FIB-cut. HAADF-STEM images shows a lack of inclusions (b) or α-decay induced damage. SAED for (c) in upper inset; atom model for hematite on the same [2-21] zone axis. Images at 200 Kv (Titan Themis, Adelaide Microscopy).

[1] Courtney-Davies, L. et al. (2017) Goldschmidt conference abstract

Uranium-bearing, oscillatory-zoned hematite: assessing closed system behaviour and U-Pb systematics

Liam Courtney-Davies[1]*, Cristiana L. Ciobanu[1], Nigel J. Cook[1], Simon R. Tapster[2], Daniel J. Condon[2], Allen K. Kennedy[3] and Kathy Ehrig[4]

* corresponding author e-mail: Liam.courtney-davies@adelaide.edu.au

[1]School of Chemical Engineering, The University of Adelaide, Adelaide, SA 5005, Australia

[2]NIGL, British Geological Survey, Keyworth, Nottingham, NG12 5GG, U.K

de Laerter Centre, Curtin University of Technology, Bentley, WA 6102, Australia

[3]BHP Olympic Dam, Adelaide, SA 5000, Australia

SUMMARY

Oscillatory-zoning with respect to U in mineral geochronometers requires nanoscale assessment as such patterns may reflect an overprinting event. Addition/loss of elements (open system behaviour) disturb isotopic ratios used for U-Pb systematics. $^{207}Pb/^{206}Pb$ isotope mapping of coarse hematite from the Olympic Dam deposit, South Australia, shows ~1.6 Ga age homogeneity across oscillatory-zoned, U-bearing domains. ID-TIMS analysis carried out on material microsampled from one such grain, up to ~1 mm apart, give approximately identical $^{207}Pb/^{206}Pb$ ages (unpublished data). To asses open or closed system behaviour for U-Pb systematics, the same grain was chemically mapped prior to HAAD-STEM studies carried-out on a FIB-prepared foil cut across U bands. The sample is free of inclusions and atomic resolution imaging shows crystallinity with no lattice damage induced by α-decay. We conclude such grains preserve a near closed system from crystallization at ~1.6 Ga.

BACKGROUND & METHODOLOGY

The iron-oxide-Cu-Au (IOCG) deposit at Olympic Dam (OD), South Australia, is the largest U resource under exploitation. Located within the ~1.6 Ga Gawler Silicic Large Igneous Province, the deposit is entirely contained within the Olympic Dam Breccia Complex, hosted and dominantly derived from the enclosing Roxby Downs Granite. The magmatic system at OD has been well constrained to ~1593 Ma, however, dating of hydrothermal mineralization has so far yielded low-resolution dates broadly coeval with the magmatism. Hematite (α-Fe_2O_3) is a common Fe-oxide and ubiquitous phase in IOCG deposits. U-bearing hematite at OD may provide high precision U-Pb data if the U-Pb system has remained isotopically undisturbed since crystallization.

The same grain of Olympic Dam oscillatory-zoned hematite was analysed by the following 3 methods:

1. Laser Ablation-Inductively Coupled Plasma-Mass Spectrometry (LA-ICP-MS) U-Pb Mapping 2. Isotope Dilution-Thermal Ionization Mass Spectrometry (ID-TIMS) (British Geological Survey, UK) and 3: Transmission Electron Microscopy (TEM) on a foil prepared by Focused Ion Beam (FIB) using a FEI Helios Nanolab 600 DualBeam™ platform. High-angle angular dark field scanning transmission electron microscopy (HAADF-STEM) imaging was performed on an ultra-high resolution, probe-corrected, FEI Titan Themis S/TEM operated at 200 kV. Analysis (1) and (3) were performed at Adelaide Microscopy (University of Adelaide).

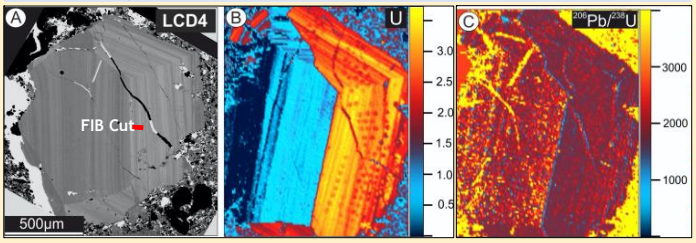


Figure 1. LA-ICP-MS U-Pb mapping. A; BSE image in high contrast revealing oscillatory zonation patterns enriched in U-Sn-W-Mo. B; U concertation map (scale: counts-per-second, 10^n).C; $^{206}Pb/^{238}U$ isotope map (scale in Ma). Map B and C display a sharp divide between the left and right of the grain.

A single hematite grain containing up to 2,000 ppm U was first isotopically mapped by LA-ICP-MS to define homogeneous U-Pb domains (Fig. 1). The domains defined as U-rich, inclusions free and suitable to high precision dating were extracted for ID-TIMS analyses (Fig 2).

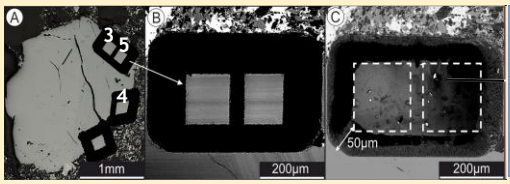


Figure 2. micro-sampling of grains *in-situ* for ID-TIMS. Ablation of trenches to form ~100 x 100 µm squares within polished blocks allows extraction of predefined areas. The white numbers in A match with data points in Figure 3.

U-Pb ID-TIMS dating was performed on 5 aliquots from two coarse grains from the same sample (Fig. 3). These yielded a $^{207}Pb/^{206}Pb$ age of 1589.91 ± 0.94 Ma, and an agreeable upper intercept age. Data points with the lowest uncertainties, which were pinpointed by isotope mapping, contain the highest U, up to 1,500 ppm. One point plots reversely discordant because off excess Pb. This may be due to diffusional processes. The data for the grain studied here is shown as points 3-5 corresponding to grain 2 on Figure 3.

In order to check the U-rich domains at the nanoscale a TEM foil was prepared using in situ FIB slicing across the zoning with highest U concentrations (Fig. 1A). HAADF STEM imaging across the foil shows faint banding and no discrete U- or Pb-inclusions (Fig. 4a). The specimen shows the same orientation throughout the foil when tilted on different zone axes. HAADF STEM imaging of hematite on [2-21] and [0-21] shows no lattice scale defects but satellite reflections are present in parts of the foils [Fig. 4b-d and Fast Fourier Transform (FFT) as insets]. These indicate doubling of distances on (012)* or (102*) lattice vectors (FFT in Fig. 4b). HAADF STEM images also show development of weak superstructuring in some areas (arrowed, Fig. 4d). Atom scale imaging shows the distribution of Fe in hematite on [2-21] and [0-21] zone axes is concordant with crystal structure models on these orientations (Fig. 4e, f).

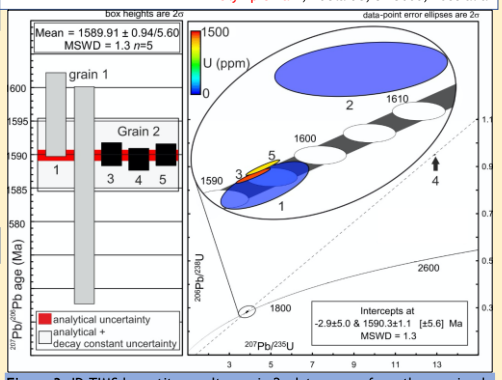


Figure 3. ID-TIMS hematite results; grain 2 data comes from the previously described grain in figures 1 and 2. The $^{207}Pb/^{206}Pb$ age of 1589.91 ± 0.94 Ma is calculated for the five aliquots from 2 large grains. Data points with the lowest uncertainties, as seen from the isotope map in Fig. 1 contain the highest U (up to 1500 ppm). One point (number 2) plots reversely discordant because off excess Pb and is attributed to diffusional processes.

We conclude that the sample is not affected by overprint as it is free of inclusions and shows crystallinity with no lattice damage induced by α-decay, all concordant with closed-system behavior with respect to U-Pb isotopes. The sample differs however with respect to development of long range superstructures as shown by [1] for oscillatory zoned hematite with U concentration an order of magnitude higher than the present sample.

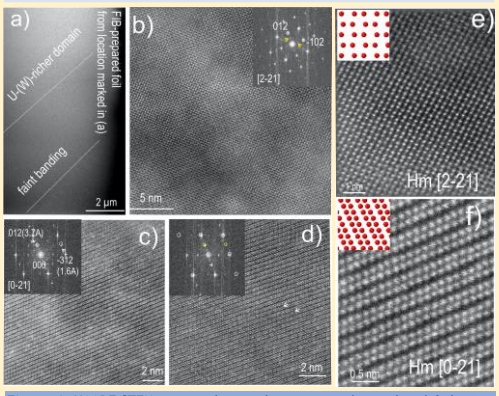


Figure 4. HAADF-STEM images showing hematite in the analysed foil (a) is clear of inclusions. (b-c) Hematite tilted on different zone axes as marked and shown by FFTs (insets) displays crystallinity and lacks lattice-scale defects. It shows however, superstructuring (arrowed on [d]. Satellite reflections are arrowed on (b) and marked as yellow circles on (d). The atomic structure shows Fe as bright atoms as seen from analogy with crystal structure models.

DISCUSSION AND CONCLUSIONS

Hematite has proven to be a remarkably robust mineral geochronometer when combining analytical techniques. The ages reported here are currently the best indicator for earliest hydrothermal activity at Olympic Dam with demonstrated reproducibility of results. It is likely that U-Pb hematite geochronology has far reaching application in many other ore deposits classes, including banded iron formations. However, integration of multiple analytical techniques should be considered when targeting accurate hematite ages.

REFERENCES

[1] Ciobanu, C.L. *et al.* (2013). Uranium-bearing hematite from the Olympic Dam Cu-U-Au deposit, South Australia: A geochemical tracer and reconnaissance Pb-Pb geochronometer. *Precambrian Research*. **238**,129-14

ACKNOWLEDGEMENTS

This is a contribution to "Trace elements in iron oxides: deportment, distribution and application in ore genesis, geochronology, exploration and mineral processing" (FOX project), supported by BHP Olympic Dam and the Government of South Australia Mining and Petroleum Services Centre of Excellence

ADDITIONAL MATERIAL T

CONFERENCE ABSTRACT AND POSTER:

U-PB GEOCHRONOLOGY OF FE-OXIDES: LA-ICP-MS AND SHRIMP ANALYSIS

Liam Courtney-Davies[1], Allen K. Kennedy[2], Cristiana L. Ciobanu[1], Nigel J. Cook[1], Kathy Ehrig[3], Benjamin P. Wade[4], , Daniel J. Condon[5], Simon R. Tapster[5]

[1]*School of Chemical Engineering and Advanced Materials, The University of Adelaide, Adelaide, SA 5005, Australia*

[2]*John de Laeter Centre, Curtin University of Technology, Bentley, WA 6102, Australia*

[3]*BHP Olympic Dam, Adelaide, SA 5000, Australia*

[4]*Adelaide Microscopy, The University of Adelaide, Adelaide, SA 5005, Australia*

[3]*NIGL, British Geological Survey, Keyworth, U.K.*

Conference abstract and poster, Goldschmidt 2016, Yokohama, Japan, 26th June – 1st July

U-Pb geochronology of Fe-oxides: LA-ICP-MS and SHRIMP analysis

L. COURTNEY-DAVIES[1*], A.K. KENNEDY[2], C.L. CIOBANU[1], N.J. COOK[1], K. EHRIG[3], B.P. WADE[4], D. CONDON[5] AND S. TAPSTER[5]

[1]School of Chemical Engineering, Univ. of Adelaide, Adelaide, SA 5005, Australia (*Correspondence: Liam.Courtney-Davies@adelaide.edu.au)
[2]John de Laeter Centre, Curtin University of Technology, Bentley, WA, Australia
[3]BHP Billiton Olympic Dam, Adelaide, SA 5000, Australia
[4]Adelaide Microscopy, Univ. of Adelaide, Adelaide, SA 5005, Australia
[5]NERC, British Geological Survey, Keyworth, UK

High U-bearing hematite (Hm; up to few wt.% U) from the Olympic Dam IOCG deposit (OD; South Australia) was used as a Pb-Pb geochronometer [1] to give ages of 1590±8 & 1577±5 Ma via LA-ICP-MS using GJ-1 zircon as a primary standard. An Fe-oxide matrix matched standard is required if the method is to be routinely applied to estimate the timing and duration of mineralising events. Here, we employ SHRIMP analysis to check isotopic homogeneity of dated Hm [1] as well as for low-U, high-W Hm (hundred ppm U; 1-2 wt.% W) with comparable oscillatory zonation patterns as those reported for the high-U type [1].

The first SHRIMP analysis here shows certain grains of both Hm types as isotopically homogeneous (e.g., Fig. 1), providing confidence that a natural standard can be identified from OD material. The next step is to measure absolute U/Pb isotopic values using ID-TIMS on homogeneous areas in grains assessed by SHRIMP and extracted using a micro-drill.

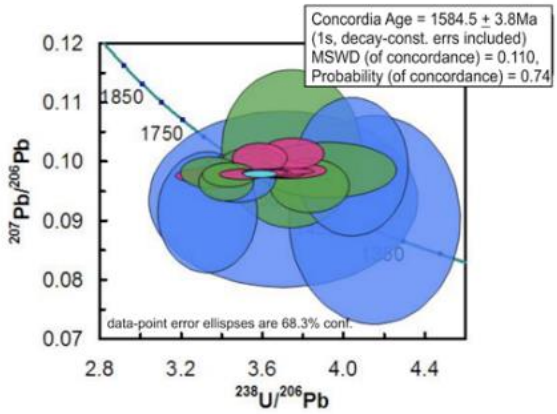


Fig. 1: SHRIMP U/Pb concordia plot for low-U hematite

[1] Ciobanu *et al.* (2013), *Precambr. Res.* **238**,129-147.

U-Pb Geochronology of Fe-Oxides: LA-ICP-MS and SHRIMP Analysis

L. Courtney-Davies[1*], A.K. Kennedy[2], C.L. Ciobanu[1], N.J. Cook[1], K. Ehrig[3], B.P. Wade[4]

[1]School of Chemical Engineering, The University of Adelaide, Adelaide, SA 5005, Australia
[2]John de Laerter Centre, Curtin University of Technology, Bentley, WA, Australia
[3]BHP Billiton Olympic Dam, Adelaide, SA 5000, Australia
[4]Adelaide Microscopy, Univ. of Adelaide, Adelaide, SA 5005, Australia *liam.courtney-davies@adelaide.edu.au

Abstract

High U-bearing hematite (Hm) (up to few wt.% U) from the Olympic Dam (OD) IOCG deposit, South Australia, was used as a Pb-Pb geochronometer (Ciobanu et al., 2013 [1]) to give ages of 1590±8 & 1577±5 Ma via LA-ICP-MS using GJ-1 zircon as a primary standard. An Fe-oxide matrix matched standard is required if the method is to be routinely applied to estimate the timing and duration of mineralising events. Here, we employ a new U-Pb LA-ICP-MS solution dating technique and SHRIMP analysis to check isotopic homogeneity of dated Hm [1] as well as for low-U, high-W Hm (hundred ppm U; 1-2 wt.% W) with comparable oscillatory zonation patterns as those reported for the high-U type [1]. The first SHRIMP analysis here shows certain grains of both Hm types as isotopically homogeneous, providing confidence that a natural standard can be identified from Olympic Province material. The next stage has been to measure absolute U/Pb isotopic values using ID-TIMS at the British Geological Survey.

U-Pb Methods

SHRIMP (Curtin)

- Ion microprobe analytical methods follow Compston et al. (1984) Claoue-Long et al. (1995) and Williams (1998).
- All isotopic measurements were reduced by off-line computer programs using standard techniques.
- U/Pb ages were normalized to a value of 1575 Ma assumed for the concordant hematite grain used as a standard.
- The given $^{207}Pb/^{206}Pb$ ages are independent of our standard analyses.
- Common-Pb was corrected using the ^{201}Pb or ^{238}Pb method discussed in Williams (1998), for the standards.

LA-ICP-MS Solution Dating (Adelaide)

- A homogeneous solution containing fixed U- and Pb-isotope ratios was prepared and the U/Pb ratio approximated to that of the unknown (e.g. 1ppb, 4ppb, 12ppb)
- U-Pb mixed solution and ablated material from pure synthetic hematite was mixed in the spray chamber and introduced to the ICP-MS
- Theoretically this should lessen matrix effects compared with non matrix-matched solid standard (GJ-1 Zircon) giving higher precision and accuracy

Samples

Samples studied derive primarily from the Olympic Cu-Au province **(Fig 1,2.)**. **(A-B Right)** BSE images of U-bearing zoned Hm displaying oscillatory and sectorial zoning expressed as high-U (bright zones). Note differences in size, coarser zones for the latter and the association with sulphides, bornite (Bn) and chalcopyrite (Cp), respectively.

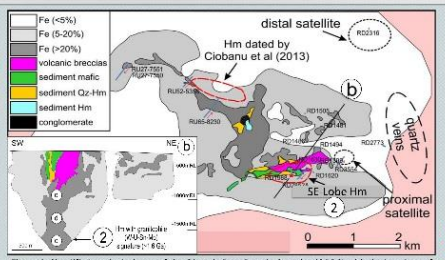
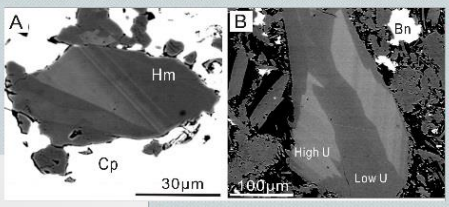


Figure 1. Simplified geological map of the Olympic Dam Breccia Complex (ODBC) with the locations of samples analysed by Ciobanu et al.,(2013) (also in this study) and samples from the SE Lobe. The bottom left is a cross section of the SE-Lobe showing sample depth. Modified from Ehrig et al. (2012).



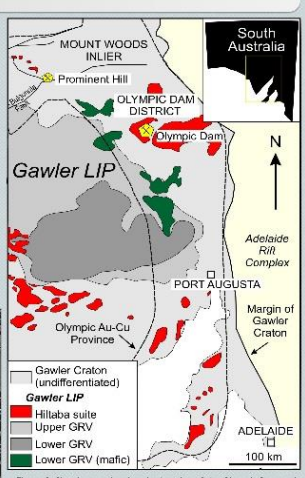


Figure 2. Sketch map showing the location of the Olympic Dam and Prominent Hill deposits (Olympic Cu-Au Province, South Australia)

SHRIMP

- Ion yields are acceptable with count rates in the 1000s of c/s for UO^+ and UO_2^+.
- The $^{238}U^+$ peak had unacceptably low counts and should not be measured.
- There was only minor variation of c/s of the molecular $Fe_2O_3^+$ reference peak, between and within analyses, suggesting that it is unlikely there is a crystallographic orientation effect on ion yields.
- ^{204}Pb is present in variable amounts and small corrections are needed

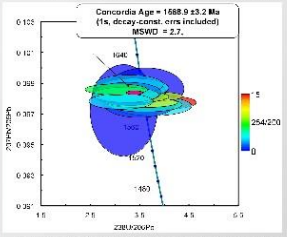


Figure 3. T-W Concordia diagram for hematite from 10.2 OD, a high-grade bornite rich ore sample previously used for LA-ICP-MS Pb-Pb dating in Ciobanu, et al., (2013). Colour-coding of the points uses the $^{238}U^{16}O/^{56}Fe_2^{16}O_3$ peak ratio (254/200) as a proxy for U concentration in hematite. The U decay constants used in calculations are those of Steiger and Jager (1977).

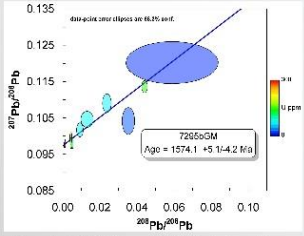
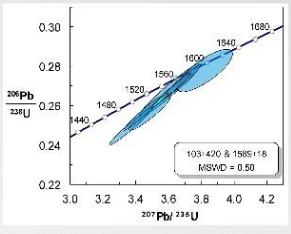


Figure 4. A $^{207}Pb/^{206}Pb$ vs $^{208}Pb/^{206}Pb$ isochron diagram for hematite from the SE Lobe of OD and the same sample as dated by LA-ICP-MS in **figure 6.**

Figure 5. 6 points within one grain from the SE-Lobe were isotopically homogeneous within the SHRIMP analytical uncertainty. This shows that some hematite grains in the OD samples are homogeneous, and that a Reference Material for Hematite may be identified. The discordance of this grain may be real, or reflect the assumed age of the adopted standard, or the U-Pb calibration used, matrix effects, or crystallographic orientation effects on secondary ion yields



Conclusion:

SHRIMP U-Pb and Pb-Pb dating of hematite produces excellent results, if BSE imaging is used to identify grains with hydrothermal oscillatoy or sector zoning, or homogeneous undisturbed cores and patches. Currently, we are searching for more homogeneous, high U hematite that will be characterised by ID-TIMS and used as a SIMS reference material.

LA-ICP-MS

- To further evaluate the potential of hematite as a U-Pb geochronometer;
- To assess the matrix effects when using the U-Pb solution compared to a non-matrix matched standard
- To test whether the method gives reliable ages for hematite with low U concentrations

Figure 6. The most concordant OD sample from the analyses, the T-W shows the system has remained closed with almost No common Pb. The 1595±6 date fits exactly with U/Pb zircon ages in the literature e.g. Johnson and Cross, (1995). Certain grains within this sample are now undergoing ID-TIMS for evaluation as standard material.

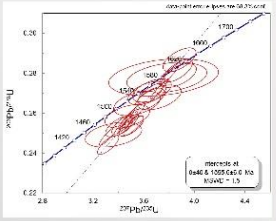
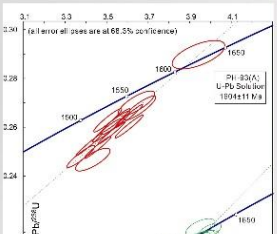


Figure 7. Sample PH-93 was dated at an upper intercept age of 1604±11 Ma and anchored to 0±40 Ma **(A)**, using a 27 µm spot size and a 12 ppb mixed solution. PH-93 plots very close to concordia but displays evidence of slight recent Pb loss. Sample PH-93 was also dated using GJ-1 Zircon as the primary standard, giving age of 1597.2±6.1 Ma **(B)**, utilizing 82 of a total of 95 points. Although the error is small, the range of discordance of points along the discordia is large when compared to the solution analysis in which spots plot close to or on concordia, potentially meaning a reduction in matrix effects from the solution method.



Conclusion:

The solution dating method does not take into account down hole fractionation, but nevertheless we have shown that 207Pb/206Pb ages are not greatly affected by matrix matching, and thus the GJ1-Zircon is reliable for dating Hm and further validates the 1590±8 & 1577±5 Ma Pb-Pb ages [1]. Further refinements of the method and analyses with magnetite will now take place.

References

Ciobanu et al. (2013). *Precambrian Research*, **238**,129-147.
Claoue-Long et al.,(1995). *Society for Sedimentary Geology-Special Publications*, **54**: 3-21.
Compston et al. (1984). Proceedings of the fourteenth Lunar and Planetary Science Conference, Par 2. *Journal of Geophysical Research*.
Ehrig et al. (2012). Special Publication Number 16 Geology and Genesis of Major Copper Deposits, *Society of Economic Geologists*, p. 237-267
Johnson & Cross. (1995). *Economic Geology*., **90**, 1046–1063.
Williams. (1998). *Reviews in Economic Geology*. M. A. McKibben, Shanks, W.C., Ridely, W.I. **7**: 1-35.

Acknowledgements: This is a contribution to the **FOX Project** (Trace elements in Fe-oxide) sponsored by BHP Billiton and the South Australian Government Department of State Development.

Implications

- Precise and accurate U-Pb dating of Fe-oxides allows for unparalleled constraints on the timing of mineralization in certain ore deposits.
- Constraining the timing of mineralization more accurately at Olympic Dam is particularly important as current genetic models are associated with structural and stratigraphic interpretations combined with dating of accessory minerals associated with the mineralization, but not necessarily formed during the metallogenic event.
- These initial experiments into Hm dating opens up much further scope for continued research within the field to refine techniques and add data from different instruments to allow movement towards finding a suitable hematite standard for routine high precision dating.

Ongoing work: Grain areas containing high U zonation have now been removed by micro drilling and lasering around these areas (then tweezed out under microscope) to be analysed by ID-TIMS at the British Geological Survey. Analyses will go towards further constraints on the timing of mineralisation and the validity of using other techniques.

ADDITIONAL MATERIAL U

CONFERENCE ABSTRACT:

THE U-PB SYSTEMATICS OF HYDROTHERMAL HEMATITE: INSIGHTS FROM THE IOCG SYSTEM AT OLYMPIC DAM, SOUTH AUSTRALIA

Liam Courtney-Davies[1], Cristiana L. Ciobanu[1], Simon R. Tapster[2], Nigel J. Cook[1], Kathy Ehrig[4], Allen K. Kennedy[3], Daniel J. Condon[2], Max Verdugo-Ihl[1], Benjamin P. Wade[5], Sarah E. Gilbert[5]

[1]*School of Chemical Engineering and Advanced Materials, The University of Adelaide, Adelaide, SA 5005, Australia*

[2]*NIGL, British Geological Survey, Keyworth, Nottingham, NG12 5GG, UK*

[3]*BHP Olympic Dam, Adelaide, SA 5000, Australia*

[4]*John de Laeter Centre, Curtin University of Technology, Bentley, WA 6102, Australia*

[5]*Adelaide Microscopy, The University of Adelaide, Adelaide, SA 5005, Australia*

Conference abstract and oral presentation, 15th Quadrennial IAGOD Symposium, Salta, Argentina, August 28th-31st. Symposium Volume, SEGEMAR, 171-172.

15th Quadrennial IAGOD International Association on the Genesis of Ore Deposits Symposium, Salta, Argentina.



THE U-Pb SYSTEMATICS OF HYDROTHERMAL HEMATITE: INSIGHTS FROM THE IOCG SYSTEM AT OLYMPIC DAM, SOUTH AUSTRALIA

Liam Courtney Davies[1], Cristiana L. Ciobanu, Simon R. Tapster, Nigel J. Cook, Kathy J. Ehrig, Allen K. Kennedy, Daniel J. Condon, Max R. Verdugo-Ihl, Benjamin S. Wade, Sarah E. Gilbert

[1]*The University of Adelaide - liam.courtney-davies@adelaide.edu.au*

BACKGROUND

Uranium-bearing minerals that have been isotopically closed since crystallization can be used to accurately constrain geologic events via the coupled U-Pb decay chain. However, the primary isotopic signature of a mineral can be easily modified, through multiple episodes of fluid exsolution, overprinting processes, regional metamorphism and protracted thermal events. Defining a chronology within complex environments such as Proterozoic ore deposits can therefore prove challenging.

The iron-oxide-Cu-Au (IOCG) deposit at Olympic Dam (OD), South Australia, is the largest publicly declared U resource. Located within the ~1.6 Ga Gawler Silicic Large Igneous Province, the deposit is entirely contained within the Olympic Dam Breccia Complex (ODBC); [1, 2], hosted and dominantly derived from the enclosing Roxby Downs Granite (RDG). The magmatic system at OD has been well constrained to ~1593 Ma, however, dating of hydrothermal mineralization has so far yielded low-resolution dates broadly coeval with the magmatism (e.g. uraninite and apatite from altered RDG and pene- contemporaneous volcanic units [3]). We aim to understand if the magmatic-hydrothermal transition can be accurately recorded in minerals that can have only a hydrothermal origin [4, 5], and are closely associated with the ores.

As has been shown at OD [6], hematite is a ubiquitous component of IOCG systems and can contain wt% levels of U, as well as elevated concentrations of W, Mo, Sn, and Pb. The occurrence of primary, often well-preserved oscillatory-zoned, U-W-Sn-Mo-bearing hematite throughout OD provides a mechanism for accurately constraining the timing of hydrothermal mineralization. This type of hematite is present throughout all ore zones and major lithologies at OD (e.g. breccias, sedimentary and volcanic rocks), occurring along the orebody's entire 6 km NW-SE strike [7] and depths of up to ~2 km. There is an intimate association between hematite-rich breccias and primary economic Cu-U-Au-Ag mineralization, which is manifested as concentric zonation with respect to sulphides [2]. Remobilisation of uranium is noted within the ODBC at scales from sub-micron upwards. Deposited as flooding, veinlets and pockets, remobilised uraninite accounts for local U enrichment and is clearly late relative to the widespread disseminations, inferring (probably multiple) processes of dissolution and re-precipitation. Therefore, understanding the principal sources and timing of metal introduction relative to the ~1.6 Ga primary magmatic-hydrothermal event is pivotal in understanding the genesis of OD, as remobilisation or isotopic resetting of minerals may be misinterpreted as new metal influxes and late mineralization events.

The potential of zoned hematite at OD for U-Pb geochronology was first recognised in a reconnaissance geochronological study [6]. Calibration with a non-matrix-matched reference material restricted full assessment of dating accuracy, however, 207Pb/206Pb weighted mean laser-ablation inductively-coupled-plasma mass-spectrometry (LA-ICP-MS) dates broadly tied hematite mineralization as coeval to the RDG. Further LA-ICP-MS studies [8], complemented previous work, but did not critically improve temporal constraints. The biggest obstacle for routine U-Pb hematite dating is the lack of homogeneous reference materials. We have therefore implemented isotope-dilution thermal-ionization-mass- spectrometry (ID-TIMS) to constrain robust ages at OD. Through combined U-Pb isotope- mapping (LA-ICP-MS) and ID-TIMS, targeted grain domains in Proterozoic samples can provide accurate ages down to ~0.05% precision. Data features such as common Pb, discordancy, and reverse discordance are assessed, their mechanisms proposed, and the analytical precision achievable at different resolutions at OD defined.

METHODS

Elevated concentrations of U in hematite can be directly imaged under backscattered electron imaging by scanning electron microscopy, which enables selective targeting of U- rich and inclusion-free domains within grains, ranging from tens of Mm to cm in size. The combination of LA-ICP-MS spot-analysis/mapping, sensitive high-resolution ion microprobe (SHRIMP) and ID-TIMS, allows investigation into the U-Pb systematics of hematite at different analytical and spatial resolutions. Isotopic measurements were collected at Adelaide Microscopy (LA-ICP-MS), Curtin University (SHRIMP) and the British Geological Survey (ID-TIMS). The developing, experimental approach to hematite isotope-dilution required micro-sampling of grains in-situ, by ablating trenches to form ~100 x 100 Mm squares within polished blocks which could be manually extracted under a microscope.

RESULTS AND DISCUSSION

Hematite 207Pb/206Pb weighted mean ID-TIMS ages can be used to interpret ore forming events to a precision of ~0.05%, compared to >1% for microbeam techniques (LA-ICP-MS and SHRIMP). However, as with any mineral, some are subject to chemical overprinting effects yielding lower resolution data. Isotope mapping demonstrates the susceptibility of zoned hematite to overprinting, with low-U, high-common Pb domains affected by fluid- mineral interactions. Potential Pb-diffusion from high- to low-U zones can also be imaged using LA-ICP-MS, where excess, unsupported radiogenic Pb produces reverse discordance.

Nevertheless, in the best-case scenarios, ID-TIMS yields a 207Pb/206Pb hematite weighted mean age of 1592.1 ± 0.88 Ma (MSWD=0.52, n=5), signifying pene-contemporaneous mineralization after RDG crystallization (1593.9 ± 0.4 Ma; [9]), while near-concordant ID- TIMS aliquots point towards negligible disturbance of the U-Pb system. Furthermore, the lifespan of the major mineralizing event is demonstrated to be short when using hematite as a proxy, as there is no robust divergence in age from ~1590 Ma. This does not however rule out mineralization post-dating the oscillatory-zoned hematite but is representative of the bulk of Cu-U mineralization. The ubiquitous presence of hematite within the orebody, and the fact that many subsequent hematite types at OD can be tied to replacement of the zoned type, clearly indicate that the U resource is associated with the magmatic-hydrothermal IOCG system at OD rather than other exotic sources. Dating of zoned hematite in sandstones from a depth of ~1.6 km yields ~1590 Ma dates. Such sediments may be older than the ODBC, and entrapped within the RDG during uplift and brecciation, supporting a deep, rather than shallow granite emplacement.

CONCLUSIONS

The key to robust temporal interpretations, particularly for deposits like OD, is a well- constrained magmatic U-Pb framework combined with a sufficiently large n sample set of hydrothermal grains. This enables interpretation of different, deposit-wide processes, which is rapidly achievable with hematite. Iron-oxide minerals, including magnetite, can become important tools for directly dating mineralization in ore deposits, particularly where other datable minerals are either absent, metamict or not representative of the ore-forming event. The ubiquitous presence of hematite in IOCG deposits, as well as banded iron formation deposits, suggests it has far reaching value in both old, and new, ore deposit research.

REFERENCES

Apukhtina O. B., Kamenetsky V. S., Ehrig, K., Kamenetsky, M. B., Maas, R., Thompson, J., McPhie, J., Ciobanu, C. L., Cook N. J., 2017. Early, deep magnetite-fluorapatite mineralization at the olympic dam cu-u-au-ag deposit, south australia. Economic Geology 112, 1531-1542.

Ciobanua C. L., Wadec B. P., Cook N. J., Schmidt M. A., Giles, D., 2013. Uranium-bearing hematite from the Olympic Dam Cu–U–Au deposit, South Australia: A geochemical tracer and reconnaissance Pb–Pb geochronometer. Precambrian Research, 238, 129-147.

Courtney-Davies, L., Zhu, Z., Ciobanu, C. L., Wade, B.P., Cook, N.J., Ehrig, K., 2016. Matrix-matched iron-oxide laser ablation ICP-MS U–Pb geochronology using mixed solution standards. Minerals, 6 (3), 85.

Ehrig, K., McPhie, J., Kamenetsky, V., 2012. Geology and mineralogical zonation of the Olympic Dam iron oxide Cu-U-Au-Ag deposit, South Australia, In: Hedenquist, J.W., Harris, M., F. Camus (Eds.), Geology and Genesis of Major Copper Deposits and Districts of the World. SEG Special Publication 16, 237-268.

Jagodzinski, E.A., 2016. http://minerals.statedevelopment.sa.gov.au/latest_ updates /mineral_ systems_ drilling_ program _ open_day_presentations.

Krneta, S., Ciobanu, C., Cook, N., Ehrig, K., Kontonikas Charos, A., 2017. Rare Earth Element Behaviour in Apatite from the Olympic Dam Cu–U–Au–Ag Deposit, South Australia. Minerals, 7, 135.

Macmillan, E., Ciobanu, C.L., Ehrig, K., Cook, N.J., and Pring, A., 2016. Chemical zoning and lattice distortion in uraninite from Olympic Dam, South Australia. American Mineralogist, 101, 2351–2354.

Reeve JS, Cross KC, Smith RN & Oreskes N. 1990. Olympic Dam copper-uranium-gold deposit. In: Hughes FE (ed), Geology of the Mineral Deposits of Australia and Papua New Guinea. The Australasian Institute of Mining and Metallurgy, 1009-1035.

Verdugo Ihl, M., Ciobanu, C., Cook, N., Ehrig, K., Courtney-Davies, L., Gilbert, S., 2017. Textures and U-W-Sn-Mo signatures in hematite from the Olympic Dam Cu-U-Au-Ag deposit, South Australia: Defining the archetype for IOCG deposits. Ore Geology Reviews, 10, 1016.

ADDITIONAL MATERIAL V

CONFERENCE ABSTRACT:

OSCILLATORY-ZONED HEMATITE: A RELIABLE U-PB MINERAL GEOCHRONOMETER

Liam Courtney-Davies[1], Cristiana L. Ciobanu[1], Nigel J. Cook[1], Max Verdugo-Ihl[1], Simon R. Tapster[2], Daniel J. Condon[2], Allen K. Kennedy[3], Kathy Ehrig[4], Benjamin P. Wade[5], Sarah E. Gilbert[5]

[1]*School of Chemical Engineering and Advanced Materials, The University of Adelaide, Adelaide, SA 5005, Australia*

[2]*NIGL, British Geological Survey, Keyworth, Nottingham, NG12 5GG, UK*

[3]*John de Laeter Centre, Curtin University of Technology, Bentley, WA 6102, Australia*

[4]*BHP Olympic Dam, Adelaide, SA 5000, Australia*

[5]*Adelaide Microscopy, The University of Adelaide, Adelaide, SA 5005, Australia*

Conference abstract and oral presentation, Goldschmidt 2017, Paris, France, August 13th-18[5h].

Goldschmidt2017 Abstract

Oscillatory-zoned hematite: a reliable U-Pb mineral geochronometer

L. COURTNEY-DAVIES[1*], C.L. CIOBANU[1], N.J. COOK[1], M. VERDUGO-IHL[1], S.R. TAPSTER[2], D.J. CONDON[2], A.K. KENNEDY[3], K. EHRIG[4], B.P. WADE[5], S.E. GILBERT[5]

[1]School of Chemical Engineering, Univ. of Adelaide, Adelaide, SA 5005, Australia (correspondence: Liam.Courtney-Davies@adelaide.edu.au; Cristiana.Ciobanu@adelaide.edu.au; Nigel.Cook @adelaide.edu.au; Max.VerdugoIhl@adelaide.edu.au)

[2]NERC, British Geological Survey, Keyworth, U.K. (simont@bgs.ac.uk; dcondon@bgs.ac.uk)

[3]John de Laeter Centre, Curtin University, Bentley, WA, Australia (A.Kennedy@exchange.curtin.edu.au)

[4]BHP Billiton Olympic Dam, Adelaide, SA 5000, Australia (Kathy.J.Ehrig@bhpbilliton.com)

[5]Adelaide Microscopy, Adelaide, SA 5005, (Benjamin.Wade@adelaide.edu.au; Sarah.Gilbert@adelaide.edu.au)

Uranium-bearing oscillatory-zoned hematite has previously been proposed as a U-Pb geochronometer [1,2]. The presence of lattice bound U-W-Sn-Mo-Pb bearing hematite featuring oscillatory zonation was shown across the 6 km strike and 2 km vertical extent of the Iron Oxide Copper Gold (IOCG) deposit at Olympic Dam, South Australia [3]. LA-ICP-MS dating of these U-W-Sn-Mo oscillatory-zoned hematites displays a common $^{207}Pb/^{206}Pb$ upper intercept age of ~1.6 Ga. However the reliability of LA-ICP-MS U-Pb data is difficult to assess without a matrix-matched standard and poorly constrained matrix-effects.

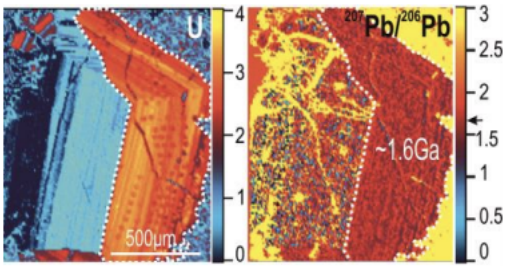


Fig. 1: LA-ICP-MS chemical maps of oscillatory-zoned hematite from Olympic Dam (U map in counts-per-second 10^n; Pb/Pb map in Ga).

LA-ICP-MS mapping of zoned grains show consistent ~1.6 Ga $^{207}Pb/^{206}Pb$ ages within the higher U domains (Fig. 1). Further asessment of the U-Pb sytematics has been conducted using SHRIMP and ID-TIMS micro-sampled domain analysis. The data confirm the presence of low common Pb, near-closed system crystals domains and zero-age open-system behaviour. Results show: (i) oscillatory zoning traps radiogenic daughter isotopes in hematite; and (ii) such hematite, confirmed in IOCGs worldwide [2], marks the onset of mineralisation.

[1] Ciobanu, C.L. et al. (2013), Precambr. Res. 238,129-147 [2] Courtney-Davies, L. et al. (2016), Minerals 6(3), 85 ; doi:10.3390/min6030085 [3] Verdugo-Ihl, M. et al. (2017) Extended abstract, SGA-2017, Quebec.

ADDITIONAL MATERIAL W

CONFERENCE ABSTRACT:

MATRIX-MATCHED FE-OXIDE LASER ABLATION ICP-MS U-PB GEOCHRONOLOGY USING MIXED SOLUTION STANDARDS

Liam Courtney-Davies[1], Zhi-Yong Zhu[1], Cristiana L. Ciobanu[1], Benjamin P. Wade[5], Nigel J. Cook[1], Kathy Ehrig[4]

[1]*School of Chemical Engineering and Advanced Materials, The University of Adelaide, Adelaide, SA 5005, Australia*

[2]*Adelaide Microscopy, The University of Adelaide, Adelaide, SA 5005, Australia*

[3] *BHP Olympic Dam, Adelaide, SA 5000, Australia*

Conference abstract and oral presentation. CHEMECA, Adelaide, Australia, 25-28 September, 2016.

Topic 2: crystallisation, particles and mineral processes

Matrix-matched Fe-oxide laser ablation ICP-MS U-Pb geochronology using mixed solution standards

Liam Courtney-Davies[1], Zhi-yong Zhu[1,2], Cristiana L. Ciobanu[1], Benjamin S. Wade[3], Nigel J. Cook[1], Kathy Ehrig[4]

[1]School of Chemical Engineering, The University of Adelaide, Adelaide, SA 5005, Australia (*Correspondence: liam.courtney-davies@adelaide.edu.au)
[2] School of Earth Sciences and Engineering, Nanjing University, Nanjing, Jiangsu, 210093, China
[3]Adelaide Microscopy, The University of Adelaide, Adelaide, SA 5005, Australia
[4]BHP Billiton Olympic Dam, Adelaide, SA 5000, Australia

U-Pb dating of the common iron-oxide, hematite (α-Fe_2O_3) by laser-ablation inductively-coupled plasma-mass spectrometry allows unparalleled insights into the genesis of mineral deposits. The full potential of the method has previously been negatively impacted by the lack of suitable matrix-matched standards. We report an approach in which a mixed U/Pb solution and laser-ablation aerosol was mixed in a nebulizer chamber and simultaneously introduced to the ICP. The method utilizes 99.99% hematite, blank and standard solutions (2% HNO_3). The standard solution contains fixed U- and Pb-isotope ratios calibrated independently. To achieve matrix-matching, pure hematite is ablated and mixed with the standard solution. When measuring unknowns, the blank solution is introduced into the ICP simultaneously to ensure matrix-matching. This matrix-matched standard is extremely homogeneous relative to other solid reference materials.

An advantage of the method is that the U-Pb concentration and isotope ratio of solution can be adjusted to approximate that in the unknown. The method is thus efficient for hematite containing U from low (~10 ppm), to high (>1 wt.%) concentrations - difficult to be achieved with solid standards. The ionization efficiency of U and Pb increased fourfold after introduction of the solution, inferring that the method is suitable for low-U samples. Using the solution method we obtain ages that overlap statistically with those obtained using the GJ-1 zircon standard for a variety of hematite samples from South Australia and elsewhere. The matrix-matched solution method is suitable for dating iron-oxide deposits worldwide.

Key words: U-Pb geochronology, hematite, matrix-matched standard.

ADDITIONAL MATERIAL X

CO-AUTHORED CONFERENCE ABSTRACT:

SHRIMP U-PB ANALYSIS OF HEMATITE

Allen K. Kennedy[1], **Liam Courtney-Davies**[2], Cristiana L. Ciobanu[2], Benjamin P. Wade3, Nigel J. Cook[1], Kathy Ehrig[4], C. Talavera[1], Daniel J. Condon[5], Simon R. Tapster[5]

[1]John de Laeter Centre, Curtin University of Technology, Bentley, WA 6102, Australia

[1]School of Chemical Engineering and Advanced Materials, The University of Adelaide, Adelaide, SA 5005, Australia

[3]Adelaide Microscopy, The University of Adelaide, Adelaide, SA 5005, Australia

[4]BHP Olympic Dam, Adelaide, SA 5000, Australia

[5]NIGL, British Geological Survey, Keyworth, Nottingham, NG12 5GG, UK

Conference abstract and oral presentation (presented by Allen K. Kennedy), VIII International SHRIMP Workshop, Granada, Spain, 6-10 September, 2016.

An extensive Tonian Oceanic Arc Super Terrane (TOAST) has been recognized in a so far poorly studied area in eastern Dronning Maud Land based on integrated geological-geophysical studies. The TOAST is sandwiched in between Kalahari and Rukerland and consists of a characteristic gabbro-trondhjemite-tonalite-granite suite SHRIMP-dated at ca. 1000-900 Ma. TOAST samples have normalised trace element patterns typical for subduction-related magmas, have mostly a positive initial epsilon Nd and lack significant inheritance, typical for juvenile crust. The TOAST underwent protracted Late Neoproterozoic/Early Palaeozoic crustal reworking, migmatisation and polyphase melt production as a result of accretion-collision tectonics from ca. 650-500 Ma. Airborne geophysics allows us to speculate that the TOAST has a significant southern extent until ca. 77°S, where it abuts against a cryptic craton. The western margin of the TOAST probably represents the Forster Magnetic Anomaly in central Dronning Maud Land, whilst the eastern margin is poorly surveyed at present. We have tested the validity of the southern extension of the TOAST with the help of a U-Pb zircon detrital moraine study from the southern side of the Sør Rondane Mts. One-thousand zircons from nine moraine samples from southernmost Sør Rondane, the Nansen ice field and Steingarden, were dated by LA-ICP-MS. The analyses fall into three major age groups at ca. 1080, 950 and 550 Ma; only very few older Palaeoproterozoic zircons were found. Apart from late-tectonic granites, another common lithology in the moraines is a grey gneiss with a U-Pb zircon age of ca. 1080 Ma, similar to the oldest major age peak found. Rocks of this age are not commonly exposed in Sør Rondane. Similar to TOAST samples, the grey gneisses have a subduction signature with negative Nb/Ta anomalies; however, they are more evolved than the proximate juvenile TOAST. Although rocks with ages of ca. 1080 Ma are common in the Maud and Rayner belts to the E and W, the grey gneisses in the moraines differ from the latter two in that they are much more juvenile. The grey gneisses probably rather represent an early, late Mesoproterozoic phase of the TOAST. A Late Mesoproterozoic/Tonian metamorphic overprint is neither recorded in rocks of the TOAST nor the grey gneisses, indicating that these oceanic arcs probably evolved outboard of Rodinia.

SHRIMP U-Pb analysis of Hematite

Kennedy, AK[1], Courtney-Davies, L[2], Ciobanu, CL[2], Wade, BS[3], Cook, NJ[2], Ehrig, K[4], Talavera, C[1], Condon, D[5] and Tapster, S[5]

1: John de Laeter Centre, Curtin University of Technology, Bentley, WA, Australia
2: School of Chemical Engineering, The University of Adelaide, Adelaide, SA 5005, Australia
3: Adelaide Microscopy, The University of Adelaide, Adelaide, SA 5005, Australia
4: BHP Billiton Olympic Dam, Adelaide, SA 5000, Australia
5: NERC, British Geological Survey, Keyworth, UK

Introduction

The common Fe oxides, hematite and magnetite, are abundant in Iron-Oxide-Copper Gold (IOCG) deposits, and also occur as accessory phases in a wide range of igneous and metamorphic rocks, and, they are the major components in Precambrian Banded Iron Formations. Hematite and magnetite can accommodate a broad range of trace elements within their structures via isostructural exchange mechanisms, and/or coupled substitution mechanisms that conserve overall charge balance (Ciobanu et al., 2013). U, W, Si, Al, can be at % levels, while Sn and Mo can reach 100s of ppm. These trace elements may allow tracking of the provenance of alluvial Fe oxides, and fingerprinting of different types of Fe oxide-bearing ore deposits. In addition, Pb-Pb and U-Pb geochronology of iron oxides (Ciobanu et al., 2013; Courtney-Davies et al., 2016a) will allow us to directly date ore formation, and any subsequent reworking and enrichment process.

Samples

Olympic Dam ore samples containing hematite were studied by optical imaging, and BSE imaging using a FEI Quanta 450 SEM at Adelaide Microscopy, the University of Adelaide. Hematite grains targeted for analysis were identified in a block mount of sample 7295bGM, a deep drillhole sample from the SE part of the Olympic Dam deposit (Ehrig et al., 2012). Figure 1 shows individual hematite grains that are enriched in U and W.

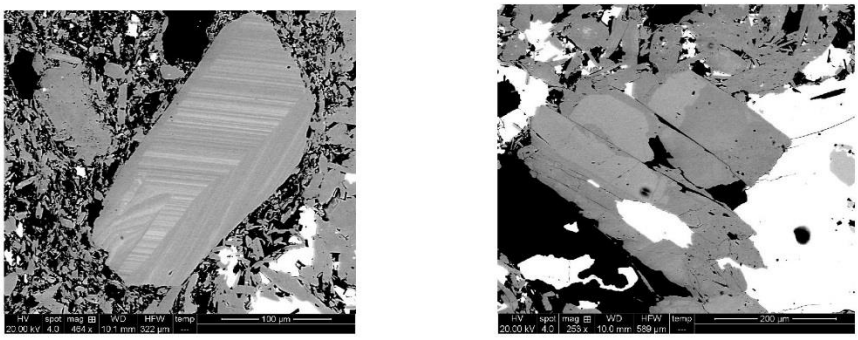


Figure 1. BSE images of hematite grains showing oscillatory zoning and homogeneous core patches from sample 7295bGM (drillhole 1988; 1808,8m; see Ehrig et al., 2012).

Analytical Details

Ion microprobe analytical methods follow those described by Compston et al., 1984; Claoue-Long et al., 1995 and Williams 1998. During initial testing we analysed two points in 7 grains, within a single block mount (7295bGM) of Olympic Dam ore. Data was collected during 6 cycles through nine magnetic field values, corresponding to $^{56}Fe_3{}^{16}O_2{}^+$, $^{204}Pb^-$, BKGD, $^{206}Pb^-$, $^{207}Pb^+$, $^{208}Pb^+$, $^{238}U^{16}O^+$, $^{232}Th^{16}O^+$, $^{238}U^{16}O_2{}^+$, with respective count intervals of 4, 10, 10, 30, 30, 20, 5, 5 and 5 seconds.

Results

Ion yields are acceptable with count rates in the 1000s of c/s for UO^+ and $UO_2{}^+$. The $^{238}U^+$ peak had unacceptably low counts and should not be measured. There was only minor variation of c/s of the molecular $Fe_3O_2{}^+$ reference peak, between and within analyses, suggesting that it is unlikely there is a crystallographic orientation effect on ion yields. Common Pb is present in variable amounts and small corrections are needed, but these are relatively minor corrections for many points, as the ^{204}Pb c/s are close to the background c/s. The distribution of uranium is highly variable between and within grains. For example, in the 4th grain analysed the UO^+ count rate varied from 116 to 4793 c/s. The consistently low Th content of the hematite means that the best correction for common lead is the ^{208}Pb method.

As a result of the observed wide range of U concentrations we decided to test the possibility of producing a $^{207}Pb/^{206}Pb$ vs $^{206}Pb/^{208}Pb$ isochron by treating all ^{208}Pb as common Pb. Figure 2 shows the $^{207}Pb/^{206}Pb$ vs $^{206}Pb/^{208}Pb$ isochron derived from the 11 highest U analytical points. The calculated age of 1574 +5.1/-4.2 Ma is typical of ages obtained in other geochronological studies of Olympic Dam ore (See Ciobanu et al., 2013, for references). This shows that the assumptions, of a single age and a single common Pb composition, are reasonable for the analysed hematite grains.

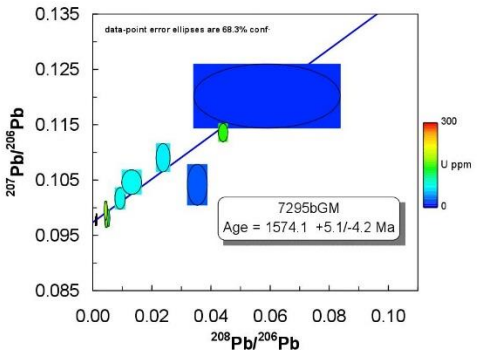


Figure 2. A $^{207}Pb/^{206}Pb$ vs $^{206}Pb/^{208}Pb$ isochron diagram for hematite from sample 7295bGM.

The U-Pb data from a second analytical session on Olympic Dam ore (10.2 OD) was reduced using a SQUID2 task. The $^{206}Pb/^{238}U$ ages for the grains in the 10.2 OD sample are calculated using the normal calibration approach, which assumes the same power law relationship exists between $^{206}Pb^*/^{238}U^{16}O$ and $^{238}U^{16}O_2/^{238}U^{16}O$ for both the Reference Material (RM) and unknown. Currently we have no RM, so we used the hematite grains from another block mount, as our RM, with an assumed age of 1584 Ma. Twenty seven analyses of hematite from our RM block were interspersed between the 10.2 OD hematite analyses in this analytical session. Our results are shown in Figure 3.

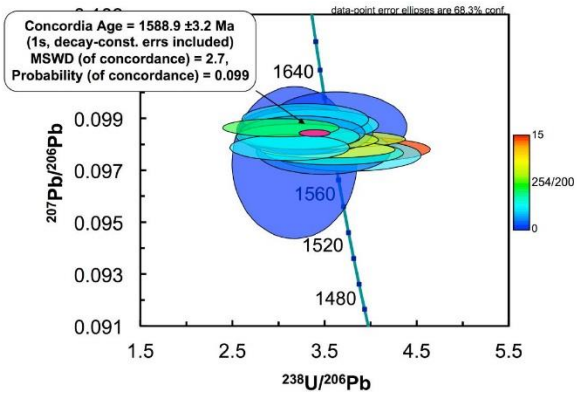


Figure 3. Tera-Wasserburg Concordia diagram for hematite from 10.2 OD, a high-grade bornite rich ore sample previously used for LA-ICP-MS Pb-Pb dating in Ciobanu, et al., (2013). Colour-coding of the points uses the $^{238}U^{16}O/^{56}Fe_3{}^{16}O_2$ peak ratio (254/200) as a proxy for U concentration in hematite. The U decay constants used in calculations are those of Steiger and Jager (1977).

Conclusion

From the above analytical sessions it was conclude that SHRIMP U-Pb and Pb-Pb dating of hematite produces excellent results, if BSE imaging is used to identify grains with hydrothermal oscillatory or sector zoning, or homogeneous undisturbed cores and patches. Currently, we are searching for homogeneous, high U hematite that can be characterised and used as a SIMS RM, and exploring alternate approaches for using iron oxides in geochronology (Courtney-Davies et al., 2016b, in review).

Acknowledgements

This is a contribution to the FOX project (Trace elements in Fe-oxide) sponsored by BHP Billiton and the South Australian Government Department of State Development.

References

Ciobanu, CL, Wade, BP, Cook, NJ, Schmidt Mumm, AS, Giles, D. (2013) Uranium-bearing hematite from the Olympic Dam Cu–U–Au deposit, South Australia: A geochemical tracer and reconnaissance Pb–Pb geochronometer. Precambrian Research 238 129–147.

Claoue-Long, JC, Compston, W, Roberts, J, Fanning, CM. (1995) Two Carboniferous ages: A comparison of SHRIMP zircon dating with conventional zircon ages and $^{40}Ar/^{39}Ar$ analysis. Geochronology, Timescales and Global Stratigraphic Correlation. W. A. Berggren, Kint, D.V., Aubry, M.P., Hardenbol, J., Society for Sedimentary Geology Special Publications. 54: 3-21.

Compston, W, Williams, IS, Meyer, CE. (1984). U-Pb geochronology of zircons from lunar breccia 73217 using a sensitive high-mass resolution ion microprobe. Proceedings of the fourteenth Lunar and Planetary Science Conference, Par 2. Journal of Geophysical Research.

Courtney-Davies, L, Ciobanu, CL, Wade BP, Cook, NJ, Ehrig, K, Cabral, AR, Kennedy, AK, Condon, D, Tapster, S. (2016a) U-Pb geochronology of Fe-oxides: LA-ICP-MS and SHRIMP analysis. 2016 Goldschmidt Conference Abstracts 551.

ADDITIONAL MATERIAL Y

CO-AUTHORED CONFERENCE ABSTRACT:

A MULTI-PLATFORM MICROANALYSIS APPROACH TO UNRAVELLING GEOLOGICAL PROBLEMS: A CASE STUDY FROM OLYMPIC DAM SOUTH AUSTRALIA

Angus K.O. Netting[1], Benjamin P. Wade[1], Max R. Verdugo-Ihl[2], Liam Courtney-Davies[2], Cristiana L. Ciobanu[2], Nigel. J Cook[2], Kathy Ehrig[3], Ashley Slattery[1], Sarah E. Gilbert[1], Ken Neubauer[1]

[1]Adelaide Microscopy, The University of Adelaide, Adelaide, SA 5005, Australia

[1]School of Chemical Engineering and Advanced Materials, The University of Adelaide, Adelaide, SA 5005, Australia

[3] BHP Olympic Dam, Adelaide, SA 5001, Australia

Conference abstract and oral presentation (presented by Angus K.O. Netting), Microscopy and Microanalysis 2019, Portland, U.S.A, 4th-8th August, 2019. 25(S2):2432-2433.

2432
doi:10.1017/S1431927619012893
Microsc. Microanal. 25 (Suppl 2), 2019
© Microscopy Society of America 2019

A Multi-platform Microanalysis Approach to Unravelling Geological Problems: a Case Study from Olympic Dam South Australia

Netting A.K.O.*[1], Wade, B.P.[1], Verdugo-Ihl, M.R.[2], Courtney-Davies, L.[2], Ciobanu, C.L.[2], Cook, N.[2], Ehrig, K.[3], Slattery, A.[1], Gilbert, S.[1], Neubauer, K.[1]

1. Adelaide Microscopy, University of Adelaide, Adelaide, Australia.
2. School of Chemical Engineering, University of Adelaide, Adelaide, Australia.
3. BHP Olympic Dam, Adelaide, Australia
* Corresponding author: angus.netting@adelaide.edu.au

The ca. 1.6 Ga iron-oxide-Cu-Au (IOCG) Olympic Dam (OD) deposit in South Australia is considered the archetypal example of IOCG formation. It is the largest known IOCG system on Earth, with a Cu-U-Au-Ag resource in excess of 10 Bt [1]). Like other IOCG systems worldwide, the OD ores record an extended complex formation history that is expressed in a diverse package of preserved mineral assemblages [2]. Pulling apart both the chemical and temporal complexity at the micro/nano scale is key to understanding the evolution of the deposit.

Iron-oxides (dominant hematite α-Fe_2O_3 and subordinate magnetite Fe_3O_4) are the most dominant minerals within the deposit, and the most visible expression of hydrothermal alteration of the host granite. These iron-oxides can be directly related to the mineralizing process thus information contained within them such as chemical composition, crystal structure, and age of formation, provides direct information on the processes responsible for the genesis of the OD IOCG deposit [3,4,5].

Imaging and microanalysis of hematite using complimentary techniques that bridge scales of observation from the millimetre to Angstrom scales, such as FIB-SEM, EPMA, LA-ICP-MS, and HR-TEM, have been used to better understand into the OD deposit. Distinct chemical signatures are found to be preserved at the micro and nanoscale, indicating that whereas some primary iron-oxides are well preserved, others have passed through replacement, reworking, and recrystallization events during multiple cycles of interaction with fluids [3-6].

An example of this complex relationship of preservation vs overprinting is displayed in Figure 1. Primary oscillatory zoned hematite displays embayments of hematite replacement as evidenced by the dark area on the grain in BSE. This overprinting is characterised by decoupling between the granitophile elements W and Sn evident in the LA-ICPMS maps. Selective removal of trace elements can be invoked by evolving redox conditions, resulting in disequilibrium of the fluid involved affecting elements with differences in the stability of cationic oxidation states (Sn^{4+} vs W^{6+}; [5]).

This is further evidenced in HR-TEM images of FIB-SEM foils of overprinted hematite (Figure 2). Overprinted areas display extensive inclusion trails comprising voids, silica bearing nanoparticles, and a range of metallic nanoparticles (W, Cu, As). In addition to this wispy splays of WO_3 (Ferberite) were present. Atomic resolution HAADF-STEM imaging of hematite immediately adjacent inclusion trails show nanodomains of dense twin sets, indicating localised reprecipitation of hematite. Combined with the diverse complex inclusion population, and gross scale elemental zonation in LA-ICPMS maps, a mechanism of *in-situ* combined dissolution reprecipitation reaction (CDRR [7]) is concluded as the primary replacement mechanism for hematite at Olympic Dam.

Microsc. Microanal. 25 (Suppl 2), 2019

References

[1] BHP Billiton, 2016. Annual Report 2016.
[2] Hitzman *et al.*, Precambrian Research 58 (1992), p. 241-287.
[3] Ciobanu et al., Precambrian Research 238 (2013), p. 129-147.
[4] Ciobanu et al., 13th SGA Biennial Meeting 2015. Miner. Resour. Sustainable World 3, 1071-1074.
[5] Verdugo-Ihl et al., Ore Geology Reviews 91 (2017), p. 173-195.
[6] Verdugo-Ihl et al., 15th Quadrennial IAGOD, 189-190.
[7] Putnis, Mineralogical Magazine 80 (2002), p. 689-708.

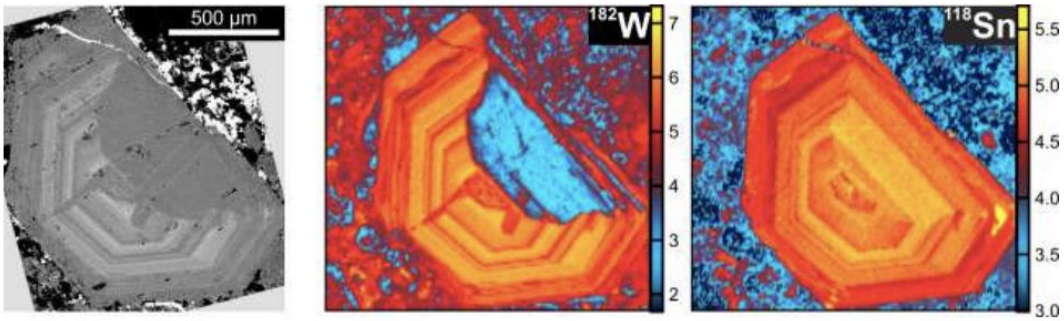


Figure 1. BSE image and LA-ICP-MS maps of zoned hematite grain. Scale in cps (log 10^n) [5]

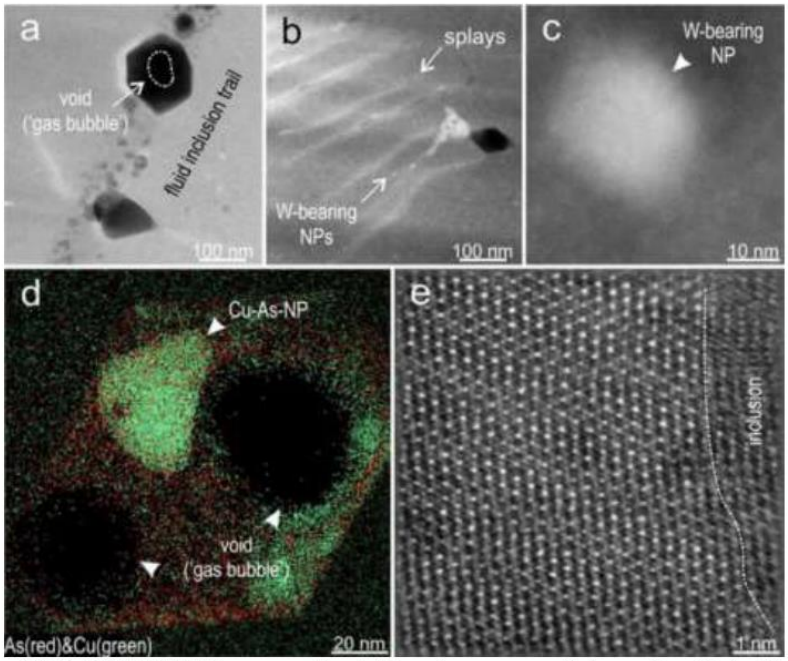


Figure 2. (a-c,e) HAADF-STEM images of metal bearing nanoparticles and voids inside hematite; (d) EDS-STEM map of metal bearing nanoparticle [6]

ADDITIONAL MATERIAL Z

CO-AUTHORED CONFERENCE ABSTRACT:

IRON OXIDES: A VERSATILE TOOL FOR GEOCHEMICAL FINGERPRINTING AND GEOCHRONOLOGY

Cristiana L. Ciobanu[1], Nigel J. Cook[1], Kathy Ehrig[2], William M. Keyser[1], **Liam Courtney-Davies[1]**, Benjamin P. Wade[3], Vadim S. Kamenetsky[4], Christian Maunders[5]

[1]School of Chemical Engineering and Advanced Materials, The University of Adelaide, Adelaide, SA 5005, Australia

[2] BHP Olympic Dam, Adelaide, SA 5001, Australia

[3]Adelaide Microscopy, The University of Adelaide, Adelaide, SA 5005, Australia

[4]School of Physical Sciences, University of Tasmania, Hobart, TAS 7001, Australia

[5]FEI Company, Achtseweg Noord 5, PO Box 80066, KA Eindhoven, The Netherlands

Conference presentation (Oral presentation given by Cristiana L. Ciobanu), 35th International Geological Congress 2016, Cape Town, South Africa, August 27th-September 4th.

Paper Number: 5127

Iron oxides: a versatile tool for geochemical fingerprinting and geochronology

Ciobanu, C.L.[1] Cook, N.J.[1], Ehrig, K.[2,] Keyser, W.M.[1], Courtney-Davies, L.[1], Wade, B.P.[3], Kamenetsky, V.S.[4] Maunders, C.[5].

[1]School of Chemical Engineering, University of Adelaide, SA 5005, Australia; cristiana.ciobanu@adelaide.edu.au
[2]BHP Billiton Olympic Dam, Adelaide, SA 5001, Australia
[3]Adelaide Microscopy, University of Adelaide, SA 5005, Australia
[4]School of Physical Sciences, University of Tasmania, Hobart, Tasmania 7001, Australia
[5]FEI Company, Achtseweg Noord 5, PO Box 80066, 5600 KA Eindhoven, The Netherlands

---

The common iron-oxides (magnetite and hematite) can incorporate >30 different trace elements into their crystal lattices at concentrations readily measurable by LA-ICP-MS. Coupled with their refractory character allowing preservation of primary signatures, this makes them attractive targets for systematic geochemical fingerprinting. The distinct trace element signatures in oxides of different provenance and age can be used to support development of genetic and space-time evolution models. South Australia (SA) hosts a broad variety of iron deposits (Archean to Neoproterozoic), including BIF-style and reworked, redeposited sub-types, in some instances overprinted during tectonothermal events. Iron oxides are also the dominant component of giant Mesoproterozoic iron oxide copper-gold (IOCG) systems such as Olympic Dam (OD). Anomalously high-concentrations of rare earth elements and Y (collectively, REY) and the elements U, W, Sn and Mo ('granitophile' elements), as well as distinct variation in chondrite-normalised REY-fractionation trends are measured in hematite from different parts of the OD orebody and immediately adjacent [1]. In combination with preliminary U-Pb dating of Fe-oxides, these trace element patterns help define space-time evolution of Fe-oxides, from deep (early; ~1.6 Ga) to shallow (late; ~1.4-1.2 Ga) parts of the OD breccia complex. Fe-oxide geochemistry also assists recognition of older (~1.8-1.75 Ga), inherited BIF-type protoliths on the margins of the deposit [2]. These older blocks are interpreted to have been encapsulated within the ~1.6 Ga Roxby Downs Granite, hosting OD mineralisation. Younger (~0.8 Ga) ages are obtained from dating accessory minerals in post-magmatic magnetite-apatite assemblages within mafic intrusions [3]. Data for BIF-style systems in SA show that Fe-oxides from different ore types have subtle differences in geochemical signatures in a given orefield and/or orebody (Keyser et al. this conference). In particular, an increase in ΣREY budget and changes in REY fractionation trends are associated with replacement processes between Fe-oxides or of Fe-oxides by Fe-hydroxides. Although hematite from some BIFs contains measurable U and W, hydrothermal Fe-oxides from IOCG systems show the highest content of 'granitophile' elements, e.g. hematite displaying oscillatory zonation where either U or W can reach concentrations up to few wt.% [1, 4].

High-U hematite from OD was used as a Pb-Pb geochronometer [4] to give ages of 1590±8 and 1577±5 Ma via LA-ICP-MS using GJ-1 zircon as a primary standard. An iron-oxide matrix-matched standard is required if the method is to be routinely applied to estimate the timing and duration of mineralising events. Such work is in progress and employs ID-TIMS analysis to measure absolute U/Pb isotopic values on homogeneous areas in grains pre-assessed by SHRIMP and extracted using a micro-drill. The reliability of Fe-oxides as a versatile tool for geochemical fingerprinting/ geochronology depends upon understanding the mechanisms of trace element incorporation/ release. Transmission Electron Microscopy (TEM) and scanning-TEM imaging using the ultra-high-resolution FEI Titan Themis TEM

(Adelaide Microscopy) to evaluate high-U and high-W hematites shows differences in their superstructure domains and nanoscale characteristics. This suggests W substitution into oxygen sites, which may be a more robust mechanism for trace element incorporation than direct metal-for-metal substitution previously proposed for high-U hematite [4].

References

[1] Ciobanu et al. (2015) Proceedings, 13th Biennial SGA Meeting, Nancy, France, p. 1071-1074.
[2] Ciobanu et al. (2015) Abstract, SEG Conference, Hobart.
[3] Apukthina et al. (2016) Contrib Mineral Petrol 171 (2): DOI 10.1007/s00410-015-1215-7.
[4] Ciobanu et al. (2013) Precambrian Research 238: 129-147.

ADDITIONAL MATERIAL AA

CO-AUTHORED CONFERENCE ABSTRACT:

TOWARDS A SUITABLE NATURAL STANDARD FOR ROUTINE U-PB DATING OF IRON OXIDES

Cristiana L. Ciobanu[1], Nigel J. Cook[1], Kathy Ehrig[2], **Liam Courtney-Davies[1]**, William M. Keyser[1], Benjamin P. Wade[3], Christian Maunders[4], Vadim S. Kamenetsky[5]

[1]School of Chemical Engineering and Advanced Materials, The University of Adelaide, Adelaide, SA 5005, Australia

[2]BHP Olympic Dam, Adelaide, SA 5000, Australia

[3]Adelaide Microscopy, The University of Adelaide, Adelaide, SA 5005, Australia

[4]FEI Company, Achtseweg Noord 5, PO Box 80066, 5600 KA Eindhoven, The Netherlands

[5]School of Physical Sciences, University of Tasmania, Hobart, TSA 7001, Australia

Conference presentation (Oral presentation given by Cristiana L. Ciobanu), Australian Earth Sciences Convention 2016, 'Uncover Earth's Past to Discover Our Future', Adelaide, SA, Australia, June 26-30th.

AESC 2016 – Australian Earth Sciences Convention
Uncover Earth's Past to Discover Our Future
26-30 June 2016, Adelaide Convention Centre
www.aesc2016.gsa.org.au

Towards a suitable natural standard for routine U-Pb dating of iron oxides

Ciobanu, Cristiana, L.[1*], Cook, Nigel J.[1], Ehrig, Kathy[2], Courtney-Davies, Liam.[1], Keyser, William M.[1], Wade, Benjamin P.[3], Maunders, Christian[4], Kamenetsky, Vadim S.[5]

[1]*School of Chemical Engineering, The University of Adelaide, Adelaide, SA 5005, Australia*
[2]*BHP Billiton Olympic Dam, Adelaide, SA 5000, Australia*
[3]*Adelaide Microscopy, The University of Adelaide, Adelaide, SA 5005, Australia*
[4]*FEI Company, Achtseweg Noord 5, PO Box 80066, 5600 KA Eindhoven, The Netherlands*
[5]*School of Physical Sciences, University of Tasmania, Hobart, Australia*

Hematite and magnetite are important components of Iron-Oxide Copper Gold (IOCG) and Banded Iron Formation (BIF)-style deposits, both of which are widespread throughout the crust of South Australia. Anomalously high-concentrations of rare earth elements and Y (collectively, REY) and the elements U, W, Sn and Mo ('granitophile elements'), as well as distinct variation in chondrite-normalised REY-fractionation trends, have been reported for Fe-oxides from different parts of the Olympic Dam (OD) IOCG deposit [1]. In combination with preliminary U-Pb dating of Fe-oxides, these trace element patterns help define differences between samples from deep (early; ~1.6 Ga) and shallow (late; ~1.4-1.2Ga) parts of the OD breccia complex. Fe-oxide geochemistry also assists recognition of older (~1.8-1.75Ga), inherited BIF-type protoliths [2] on the margins of the deposit, encapsulated within the ~1.6Ga Roxby Downs Granite, hosting OD mineralisation. The reliability of Fe-oxides as a versatile tool for geochemical fingerprinting, geochronology and genetic modelling depends upon understanding the mechanisms of trace element incorporation/release, as well as greater insight into the causes of compositional heterogeneity observed in Fe-oxides from OD. These factors impact significantly upon the identification of natural material suitable for use as a matrix-matched standard for U-Pb geochronology applications.

Here we show that, at OD, high-W hematite is more widespread than the high-U type (e.g. at deposit edges and upper, middle part of the orebody). Considering that the presence of W is always a good proxy for U, we provide insights into the nanoscale characteristics of such hematite.

Larger unit cells (superstructures) that assume metal vacancies were inferred from Transmission Electron Microscopy (TEM) study of high-U, oscillatory-zoned hematite [3]. TEM study of high-W hematite (up to 1-2 wt.% W) and of low-U (hundreds ppm U) from the deep, SE lobe of the deposit [1,2] instead shows domains with a simpler, 2-fold superstructure (Liu and Ciobanu, unpublished data). Understanding the distribution of these domains relative to W-rich zones requires High-Angular Annular Dark Field (HAADF) and Scanning-TEM imaging. This was performed using the ultra-high resolution FEI Titan Themis TEM (Adelaide Microscopy) on a foil prepared *in-situ* by Focused Ion Beam-SEM. The sampled hematite co-exists with high-U hematite in dated high-grade ore [3]. HAADF-STEM high-resolution imaging shows defect-free, compositionally homogenous hematite except the presence of darker areas, a few nm in width. The 2-fold superlattice, detected only by electron diffractions is restricted to such areas. HAADF-STEM imaging shows coherent lattice fringes across the boundary between hematite and inclusions of a W-bearing mineral, wolframite, 10-20 nm across. This suggests W substitution into oxygen sites, which may be a more robust mechanism for trace element incorporation than the direct metal-for-metal substitution suggested for high-U hematite [3]. Further work will be undertaken to better asses the dark areas attributable to O vacancies, and provide a key to understand how the crystal structure behaves during trace element incorporation/release.

References

[1] Ciobanu et al. (2015) Proceedings, 13th Biennial SGA Meeting, Nancy, France, p. 1071-1074
[2] Ciobanu et al. (2015) Abstract, SEG Conference, Hobart.
[3] Ciobanu et al. (2013) Precambrian Research 238: 129-147.

ADDITIONAL MATERIAL BB

CO-AUTHORED CONFERENCE ABSTRACT:

TRACE ELEMENT SIGNATURES OF IRON OXIDES IN BIF-STYLE IRON DEPOSITS OF THE MIDDLEBACK RANGES, SOUTH AUSTRALIA

William M. Keyser[1], Cristiana L. Ciobanu[1], Nigel J. Cook[1], Geoff Johnson[2], Holly Feltus[2], Steve Johnson[2], Kathy Ehrig[3], **Liam Courtney-Davies[1]**, Vadim S. Kamenetsky[4]

[1]School of Chemical Engineering and Advanced Materials, The University of Adelaide, Adelaide, SA 5005, Australia

[2]Arrium Mining, PO Box 21, Whyalla, SA 5600, Australia

[3]BHP Olympic Dam, Adelaide, SA 5001, Australia

[4]School of Physical Sciences, University of Tasmania, Hobart, TAS 7001, Australia

Conference presentation, 35th International Geological Congress 2016, Cape Town, South Africa, August 27th-September 4th.

Trace element signatures of iron oxides in BIF-style iron deposits of the Middleback Ranges, South Australia

Keyser, W.M.[1], Ciobanu, C.L.[1] Cook, N.J.[1], Feltus, H.[2], Johnson, S.[2], Johnson, G.[2], Ehrig, K.[3], Courtney-Davies, L.[1], Kamenetsky, V.S.[4]

[1]School of Chemical Engineering, University of Adelaide, Adelaide, SA 5005, Australia (correspondence: william.keyser@adelaide.edu.au)
[2]Arrium Mining, PO Box 21, Whyalla, SA 5600, Australia
[3]BHP Billiton Olympic Dam, Adelaide, SA 5001, Australia
[4]*School of Physical Sciences, University of Tasmania, Hobart, TAS 7001, Australia*

Banded iron formation (BIF)-style mineralization occurs in the Middleback Ranges deposits in the southeastern region of the Gawler Craton, South Australia. The >20 discrete deposits form a ~60 km-long N-S-striking belt which is characterized by the Lower Middleback Iron Formation (LMIF) and the Upper Middleback Iron Formation (UMIF). Tectonothermal events leading to formation and deformation of the Gawler Craton span the Archean to the Mesoproterozoic, and have impacted the iron formations (e.g. [1]). Such events may be recorded in the trace element signatures of iron oxides from these iron formations and related iron deposits. Here, we provide the first LA-ICM-MS trace element analyses of magnetite and hematite from a suite of samples representative of different deposits throughout the Middleback Ranges. The aim is to understand whether the distinct trace element signatures in oxides of different provenance and age can be used to support the development of genetic and space-time evolution models.

Iron deposits in the Middleback Ranges are hosted predominantly within the LMIF, which consists of a 'mixed' basal sequence, a lower iron carbonate unit, a middle iron talc unit and an upper iron silica unit, all grading up sequence and laterally [2]. Deposit sequences themselves can be complex, as exemplified in the Iron Magnet deposit. Magnetite mineralization is hydrothermal and occurs as layer replacement (from laminae to beds), matrix to breccias and clasts within breccias, and within veins and fractures [2]. At higher levels, hematite textures are varied, but pseudomorphic replacement of magnetite (martitisation) is a common feature throughout all deposits. In massive ores, hematite occurs as lamellar or anhedral, fine-grained aggregates with abundant vugs, often with dusty inclusions of gangue minerals. In more oxidized samples, iron hydroxides replace hematite.

LA-ICP-MS data for magnetite and hematite show measurable concentrations of a broad range of minor and/or trace elements. Of these, some are common in BIF-style ores (e.g. Al, Si, Mn and P) but others present here are sparsely reported in analogous ores. Examples include rare earth elements and yttrium (REY), Zn, Cu, As, Sb, Ti, Zr, and most interestingly, U (tens to hundred(s) ppm in samples from the central part of the belt). Moreover, chondrite-normalised REY fractionation trends can vary within individual samples and from one deposit to another, with changes in the sign of Ce-, Eu- and/or Y-anomalies, overall slope (from flat to LREE-enriched), and increase in ΣREY over 1-2 orders of magnitude. Such changes are observed in magnetite showing deformation, related to martitisation or transformation of hematite into Fe-hydroxides. Magnetite tends to be lower in ΣREY than hematite, which is enriched in LREE, and generally has positive Eu- and Y-anomalies. Intriguingly, Fe-hydroxides are still richer in the same trace elements than precursory hematite in any given sample.

Recognition of measurable U and Pb in Fe-oxides in Middleback Ranges raises the alluring possibility of applying U-Pb geochronology to date sedimentary iron ores. U-bearing hematite is suitable for Fe-oxide geochronology, and was found to be a robust tool that could be successfully applied to give Pb-Pb ages for U-bearing hematite in the Olympic Dam deposit [3]. Dating of U-bearing hematite from the present study would be critical in deciphering the geological evolution of the Middleback Ranges.

References:

[1] Szpunar et al. (2011) Precambrian Research 187: 99-126
[2] Leevers at al. (2005) Iron Ore Conference, Fremantle, WA, 19-21 Sept. 2005, AusIMM, Publ. Series 8, 85-97

ADDITIONAL MATERIAL CC

CO-AUTHORED CONFERENCE ABSTRACT:

BIF-STYLE IRON DEPOSITS OF THE MIDDLEBACK RANGES, SOUTH AUSTRALIA: TRACE ELEMENT SIGNATURES OF FE-OXIDES AND IMPLICATIONS FOR ORE FORMATION

William M. Keyser[1], Cristiana L. Ciobanu[1], Nigel J. Cook[1], Geoff Johnson[2], Holly Feltus[2], Steve Johnson[2], Kathy Ehrig[3], **Liam Courtney-Davies[1]**, Vadim S. Kamenetsky[4]

[1]School of Chemical Engineering and Advanced Materials, The University of Adelaide, Adelaide, SA 5005, Australia

[2]Arrium Mining, PO Box 21, Whyalla, SA 5600, Australia

[3]BHP Olympic Dam, Adelaide, SA 5001, Australia

[4]School of Physical Sciences, University of Tasmania, Hobart, TAS 7001, Australia

Conference presentation, Australian Earth Sciences Convention 2016, 'Uncover Earth's Past to Discover Our Future', Adelaide, SA, Australia, June 26-30th.



BIF-style iron deposits of the Middleback Ranges, South Australia: Trace element signatures of Fe-oxides and implications for ore formation

Keyser, W.M.[1], Ciobanu, C.L.[1], Cook, N.J.[1], Johnson, G.[2], Feltus, H.[2], Johnson, S.[2], Ehrig, K.[3], Courtney-Davies, L.[1], Kamenetsky, V.S.[4]

[1]*School of Chemical Engineering, University of Adelaide, Adelaide, Australia*
[2]*Arrium Mining, Whyalla, Australia*
[3]*BHP Billiton Olympic Dam, Adelaide, Australia*
[4]*School of Physical Sciences, University of Tasmania, Hobart, Australia*

Banded iron formation (BIF)-style mineralization of the Middleback Ranges (MR) forms a ~60 km-long N-S-striking belt in the southeastern part of the Gawler Craton. The iron deposits are predominantly hosted within the Lower Middleback Iron Formation (LMIF), which consists of a 'mixed' basal sequence, a lower iron carbonate unit, a middle iron talc unit and an upper iron silica unit, all grading up sequence and laterally [1]. Deposit sequences themselves can be complex, as exemplified in the Iron Magnet deposit. Magnetite occurs as layer replacement, matrix to breccias and clasts within breccias, and within veins [1]. At higher levels, hematite is dominant and varies in textures but pseudomorphic replacement of magnetite (martitisation) is common throughout all deposits. In massive ores, hematite occurs as lamellar or anhedral, fine-grained, vuggy aggregates, often with dusty inclusions of gangue minerals. Tectonothermal events spanning the Archean to Mesoproterozoic responsible for formation and deformation of the Gawler Craton have impacted the LMIF (e.g. [2]).

Trace element signatures of Fe-oxides from these deposits may record such events. Here, we discuss the first LA-ICP-MS trace element analyses of magnetite and hematite from samples representative of deposits along the belt with the aim to understand whether distinct trace element signatures in such minerals can be used to support genetic models.

LA-ICP-MS data for magnetite and hematite show measurable concentrations of a broad range of minor and/or trace elements. Of these, some are common in BIF-style ores (e.g. Al, Si, Mn and P) but others are sparsely reported in analogous ores. Examples include rare earth elements and yttrium (REY), Zn, Cu, As, Sb, Ti, Zr, and interestingly, U (tens to hundred(s) ppm and radiogenic Pb in samples from the central part of MR. Chondrite-normalised REY fractionation trends can vary within individual samples and between deposits, with changes in the sign of Ce-, Eu- and/or Y-anomalies, overall slope (from flat to LREE-enriched), and increase in ΣREY over 1-2 orders of magnitude. Such changes are observed in magnetite showing deformation, related to martitisation or transformation of hematite into Fe-hydroxides. Magnetite tends to be lower in ΣREY than hematite, which is enriched in LREE, and generally displays positive Eu- and Y-anomalies. Such signatures will be discussed with respect to host lithologies signatures, their role in identifying marker protoliths for stratigraphic reconstructions, as well as processes during which the BIF formation is upgraded to Fe-ores.

Importantly, recognition of measurable U in Fe-oxides from MR raises the possibility of applying U-Pb geochronology to date sedimentary iron ores. Iron-oxide geochronology, based on analysis of U-bearing hematite, was successfully applied to give Pb-Pb ages for U-bearing hematite in the Olympic Dam deposit [3]. Dating of U-bearing hematite from the present study would be critical in deciphering the geological evolution of the MR and the region.

ADDITIONAL MATERIAL DD

CO-AUTHORED CONFERENCE ABSTRACT:

LINKS BETWEEN SEDIMENTARY PROTOLITHS AND IOCG-SKARN ALTERATION, ISLAND DAM, SOUTH AUSTRALIA

William Keyser[1], Cristiana L. Ciobanu[1], Nigel J. Cook[1], **Liam Courtney-Davies[1]**,

Kathy Ehrig[2], Sarah Gilbert[3], Jocelyn McPhie[4]

[1]School of Chemical Engineering and Advanced Materials, The University of Adelaide, Adelaide, SA 5005, Australia

[2] BHP Olympic Dam, Adelaide, SA, 5000, Australia

[3] Adelaide Microscopy, The University of Adelaide, Adelaide, SA 5005, Australia

[4] School of Physical Sciences, University of Tasmania, Hobart, TAS 7001, Australia

Extended conference abstract and poster, Mineral Resources to Discover. Proceedings of the 14th SGA Biennial Meeting, Québec, Canada, August 20-23rd, 2017. ISBN: 978-2-9816898-0-1, Volume 3, 935-938.

Links between sedimentary protoliths and IOCG-skarn alteration, Island Dam, South Australia

William M. Keyser, Cristiana L. Ciobanu, Nigel J. Cook, Liam Courtney-Davies *University of Adelaide, Australia*

Kathy Ehrig
BHP Billiton Olympic Dam, Australia

Sarah Gilbert
University of Adelaide, Australia

Jocelyn McPhie
School of Physical Sciences, University of Tasmania, Hobart, Australia

Abstract. The Island Dam prospect is located within the Mesoproterozoic Olympic Cu-Au Province, South Australia. Banded iron formation (BIF)-style mineralization is overprinted by amphibole-magnetite alteration we refer to herein as 'skarns'. Iron oxides within BIF and skarn lithologies display textures and geochemical signatures defining the two contrasting mineralization styles. Iron oxide layers in BIF are composed of martite, which features relative enrichment in Ni, Co, Mn, As, Sb, U, Y and REE. Skarn lithologies contain cm-scale laths of hematite that are markedly enriched in W and Sn (thousands of ppm, and compositionally zoned with respect to these elements). Iron oxide-copper-gold (IOCG) mineralization is associated with skarn alteration in some parts of the Olympic Cu-Au Province and is linked to a ~1.6 Ga magmatic-hydrothermal event, which generated the World's largest concentration of iron oxide-copper-gold (IOCG) deposits. Skarn alteration at Island Dam can be attributed to the same event. Iron oxides are ideal tracers of alteration processes in iron oxide-bearing ore systems. At Island Dam, recognition of distinct signatures in iron oxides highlights their capacity to distinguish protolith from alteration products and trace hydrothermal history. Moreover, interpreting the evolution of iron oxide mineralogy may be an important step for understanding the spatial-temporal relationships between BIF and IOCG mineralization.

1 Introduction

The common iron oxides (hematite or magnetite) are the dominant components of both banded iron formations (BIF) and iron oxide-copper-gold (IOCG)-style mineralization. Both types are present in deposits and prospects in the Gawler Craton of South Australia (S.A.). Iron oxides can incorporate a wide variety of different minor/trace elements into their crystal lattices (e.g. Dupuis and Beaudoin 2011). This allows for their use as tracers of ore formation throughout time and space in different types of iron oxide-bearing systems (e.g. Ciobanu et al. 2013, 2015; Dare et al. 2014). Moreover, the presence of U and Pb in hematite (Ciobanu et al. 2013; Courtney-Davies et al. 2016) highlights the applicability of iron oxides as geochronometers to constrain the timing of hydrothermal ore formation. The common spatial association of metasedimentary units hosting BIF-style mineralization with giant IOCG deposits draws attention to possible genetic links between the two styles of mineralization in Precambrian terranes in S.A. and elsewhere, such as Carajas, Brazil. The present study is prompted by such a hypothesis. Iron oxides have been studied from lithologies in the Island Dam prospect, one of several IOCG-type prospects in S.A. hosted within older meta-sedimentary rocks inferred to include BIF horizons. The main question addressed is whether the trace element signatures can distinguish different generations of iron oxides if combined with mineralogical-petrographic studies.

2 Geological background

The Island Dam prospect is located in the eastern Gawler Craton, ~90 km southeast of the World-class Olympic Dam IOCG deposit within the Olympic Cu-Au Province (Fig. 1; see also Ehrig et al. this volume). Mineralization in the Olympic Cu-Au Province is spatially and temporally linked to volcanism and plutonism during generation of a ~1.6 Ga siliceous large igneous province. In contrast to the granite-hosted, hematite-breccia deposit at Olympic Dam, the Cu prospect at Island Dam is hosted within metasedimentary and volcanic rocks of the Wallaroo Group (WG). These were deposited, at 1765-1740 Ma, onto older (~1850 Ma) gneissic granites of the Donington Magmatic Suite (Cowley et al. 2003 and references therein). The WG sequences include impure limestone and dolostone horizons, as well as thin BIF-like layering, which is also observed/inferred, for example, in the northern part of the Olympic Dam district (Fig. 1). These clearly pre-date ~1600-1585 Ma Hiltaba Igneous Suite (HIS) equivalents.

The formation extends from the Mt. Woods Inlier in the northern Gawler Craton to the upper Yorke Peninsula in the south, but paleo-reconstruction and district correlation of WG sequences is hampered not only by younger cover sequences but also by superimposed alteration, including alkali-(calcic) + Fe metasomatism with regional expression in the Moonta area (Conor et al. 2010; Kontonikas-Charos et al. 2014), as well as calcic skarn formation in prospects such as the Groundhog Zn-Cu skarn in the Punt Hill area (Reid et al. 2011), or the Cu-Au skarn at Hillside, Yorke

Peninsula (Conor et al. 2010; Ismail et al. 2014). Thick (~500 m) sequences of interbedded garnet skarn and banded calc-silicate-feldspar rocks are intersected between the Gawler Range Volcanics and Donington Granite in drillholes (e.g. SAR9) west of the Punt Hill area, where meter-scale intervals rich in iron oxides with a BIF-like appearance also occur as horizons within the skarn in SAR9. Mineralization within prospects hosted by the WG are dated at ~1.6 Ma, e.g. Sm-Nd dating of pyroxene-garnet skarn at Groundhog (Reid et al. 2011), or accessory minerals elsewhere (Skirrow et al. 2007).

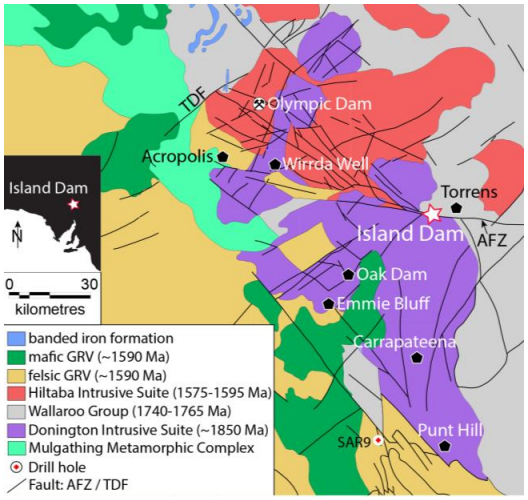


Figure 1. Basement geological map of the middle part of the Olympic Cu-Au Province, S.A., showing the location of the Island Dam Cu prospect, the Olympic Dam deposit and surrounding prospects (diamonds). AFZ-Andamooka Fault Zone; TDF-Todd Dams Fault. Inset location within S.A. (black) Map sourced from https://map.sarig.sa.gov.au/.

3 Approach and methodology

Samples were collected from 10 drillcores within and surrounding magnetically anomalous domains in the Island Dam area. While some cores contain recognizable BIF-like lithologies (e.g. Fig. 2a), others intersect granites underlying the metasedimentary rocks. In most cases the lithologies consist of rock packages that are either strongly altered (chloritized), or display banding with green and pink-reddish colors as for those mentioned above for WG rocks, with skarn alteration (Fig. 2b), and in which magnetite banding can also occur (Fig. 2c). A spectacular specimen displays coarse, cm- to dm-sized lamellar aggregates of specular hematite filling vugs or short veins in association with carbonates (calcite and/or siderite) (Fig. 2d). Development of cavities where mineral growth can reach coarse crystals is always a feature of skarns, either during prograde or retrograde stages. Chalcopyrite and pyrite occur as disseminations and small pockets throughout all lithologies, but are most abundant in the most intensely altered rocks (late carbonates + quartz).

This study focuses on a selection of ~25 samples containing iron oxides from lithologies with BIF and WG-like appearance, as well as several specimens of specular hematite. Polished blocks were analyzed using scanning electron microscopy in back-scatter electron mode (BSE), and laser ablation inductively-coupled plasma mass spectrometry (LA-ICP-MS) for trace elements using BHVO-2G, GSD-1G and NIST610 as reference standards. All instrumentation is housed at Adelaide Microscopy, The University of Adelaide.

4 Results

Distinct generations of iron oxides within the two main lithologies of interest here, BIFs and skarns, are recognized based on textural and compositional variations. Iron oxides within the BIFs are dominantly a martite, readily recognizable from granular shapes, inclusions of magnetite, and often the presence of acicular-shaped mineral relicts that are marked by fine-grained chlorite within the martite mass (Fig. 3a) and could represent original actinolite grains.

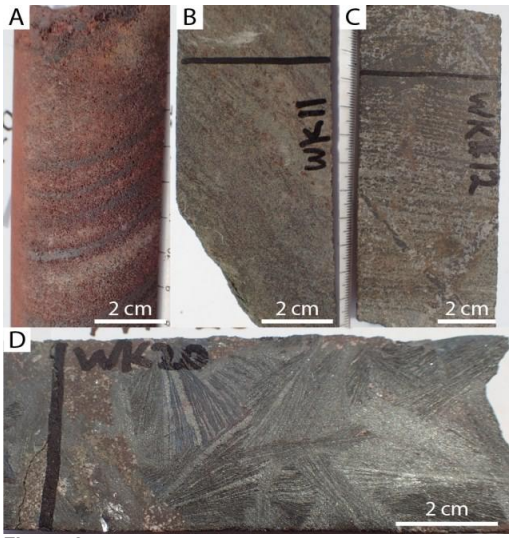


Figure 2. Hand specimen photographs showing characteristic BIF and skarn lithologies discussed in the text. **a** BIF (martite-carbonate-quartz banded rock). **b** Actinolite-magnetite skarn. **c** Rhythmic magnetite banding in altered skarn. **d** Coarse specular hematite in altered skarn.

Quartz, carbonates (mainly siderite) and chlorite are abundant gangue minerals in the BIFs. There is clear evidence for K-Fe alteration as 10-20 µm K-feldspar grains rimmed by film-like hematite within quartz (Fig. 3b).

What we refer here to as skarn is recognized by the presence of actinolite (Fig. 4a), phlogopite, magnetite, apatite, titanite, calcite, fluorite and tourmaline, lending the rocks a green color with patchy alteration domains that may display banding (Fig. 2b, c). Massive or banded actinolite skarn varieties are progressively altered,

particularly by pseudomorphic replacement during the retrograde skarn stage.

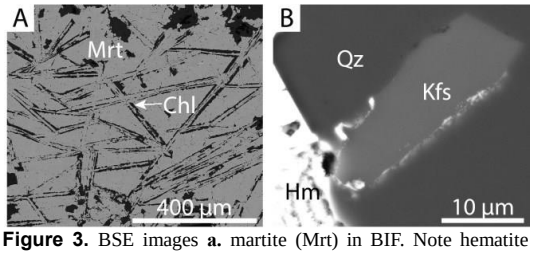


Figure 3. BSE images **a.** martite (Mrt) in BIF. Note hematite replacing a previous lath-shaped mineral with contours marked by chlorite (Chl). **b** K-feldspar (Kfs) with a film of hematite around the margin as inclusions within quartz (Qz).

In contrast to martite from the BIF, euhedral magnetite in the actinolite skarn displays oscillatory zoning with respect to Si and Ca, and may contain inclusions of quartz, calcite and chlorite (Fig. 4b). Thin lamellar aggregates of hematite are also noted. In the actinolite skarn there are numerous pseudomorphs of rutile + calcite after coarse, lozenge-shaped titanite. In detail, the rutile also shows tiny inclusions of scheelite at the boundaries between W-poor cores and W-richer rims.

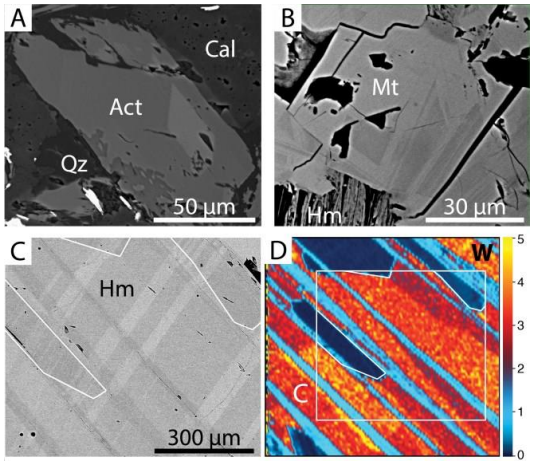


Figure 4. BSE images from amphibole-magnetite (skarn) lithologies showing **a** actinolite (Act) with Fe-rich (bright) domains. **b** Si- and Ca- (dark and bright) zoned magnetite (Mt). **c** and **d** BSE image and LA-ICP-MS element map showing W-zonation in coarse-grained Hm. Scale: parts per million (x10^3).

A close relationship between hematite and sulfides is seen in samples from altered skarn and/or of BIF affiliation. The majority of iron oxides are represented by aggregates comprising martite-magnetite intergrowths with irregular and/or scalloped mutual boundaries.

Sulfides, chalcopyrite, pyrite, and minor bornite occur as patches throughout carbonate + quartz + chlorite assemblages interstitial to the iron oxides, as well as hosted along the aforementioned magnetite margins. A distinct generation of hematite, occurring as small lamellae, occurs within areas of sulphides. This hematite also displays zonation with respect to W. The coarse-grained (as large as 4 cm) specular hematite (Fig. 2d), features polysynthetic twinning as well as strong zonation with respect to W. This is expressed as W-rich and -poor sectors along the lamellae as shown by the LA-ICP-MS map for W (Fig. 4c, d). There are also various overprinting aspects marked by W depletion, either along grain boundaries (as in Fig. 4d) or within brecciation domains in other samples.

The existing trace element dataset for magnetite is small and will not be discussed here; only that for hematite is presented. Martite, representing BIF mineralization, and the coarse lamellar hematite within amphibole-magnetite assemblages show distinct differences (Fig. 5).

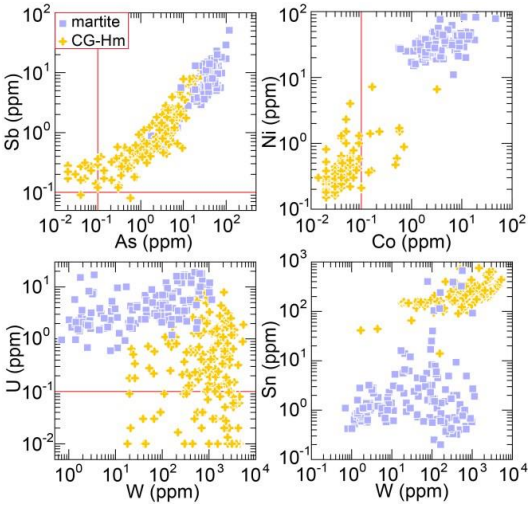


Figure 5. Binary plots of As vs. Sb (top left), Ni vs. Co (top right), U vs. W (lower left) and Sn vs. W (lower right) showing discriminant fields of hematite in Island Dam. CG-Hm - coarse-grained hematite.

Chalcophile elements, As and Sb, (average 39 and 9 ppm, respectively) and transition metals such as Ni, Co and Mn, are higher (tens of ppm) in martite than in coarse-grained hematite. Uranium concentrations in martite average 6 ppm. In contrast, coarse-grained hematite contains higher concentrations of high-field strength elements (HFSE), such as Sc and Nb, than martite. Most interestingly, coarse-grained hematite features a high Sn content (average 240 ppm), and still higher (several thousands of ppm) concentrations of W. In addition to its enrichment in hematite, W is also present in zoned rutile and as inclusions of scheelite, and sometimes in hematite. Martite contains higher ΣREE and Y (ΣREY) than coarse-grained hematite (means 2.6 and 0.38 ppm, respectively). Chondrite-normalized REY fractionation patterns for distinct hematite textures (Fig. 6) also differ. Martite is enriched in LREE relative to HREE whereas coarse-

grained hematite displays a relatively flat trend.

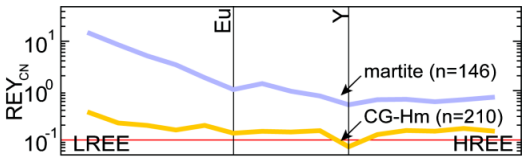


Figure 6. Chondrite-normalized REY fractionation trends of the two textural types of hematite as marked.

5 Discussion and implications

The distinct textural and compositional character of iron oxide populations suggests at least two generations of Fe-mineralization in the Island Dam area. The relative enrichment in transitional metals, chalcophile elements, U and ΣREY in the BIF lithologies, characterized by a martite texture, is most likely attributable to superimposed fluid-rock interaction from sedimentary deposition to supergene enrichment followed by interaction with hydrothermal fluids (IOCG event at ~1.6 Ga), a scenario comparable to that suggested by Ciobanu et al. (2015) for the deposit margins at Olympic Dam. In contrast, the younger skarn lithologies represented by the coarse-grained hematite are rich in HFSE and granitophile group elements and can be directly related to hydrothermal fluids affiliated with Hiltaba magmatism. The W-Sn-rich signatures are attributable to the major 1.6 Ga IOCG event since such signatures are recognized in most deposits and prospects across the region, either in iron oxides (Olympic Dam, Prominent Hill), or in garnet skarns when suitable protoliths are present (Hillside and Punt Hill,).

In contrast with other, potentially analogous terranes, such as the Great Bear Region, where alteration sequences can be directly mapped over large distances (Corriveau et al. 2016), at Island Dam, and in general in the Olympic Cu-Au province, this is not the case. Because of the cover, geological interpretation is almost entirely dependent on available drillcores. Moreover, the present work at Island Dam is carried on drillholes adjacent to the Andamooka fault system, likely with a multiple reactivation history.

Attempts to date the two hematite types from Island Dam via LA-ICP-MS using GJ-1 zircon as primary standard gave an indication of two age groups: (i) older than 1.6 (WG for BIFs); and (ii) ~1.6 Ga or younger (~1.2 Ga) for coarse-grained hematite. These data show, however, large errors either due to the high common Pb, or the low-U concentration. Future work targets alternative dating methods such as (U-Th)/He dating of hematite combined with dating of U-bearing accessory minerals (monazite, apatite, titanite and/or rutile). The pre-existing BIF mineralization is interpreted as a post-WG deposition (1765-1740 Ma), with martitization occurring during later oxidation. Martite signatures presented here are inferred to represent pre-skarn mineralization, as they lack HFSE and W + Sn element signatures of the coarse-grained, skarn-type hematite. This suggests that iron oxides retained primary signatures despite overprinting. The capacity to retain primary signatures shows the potential for iron oxides to not only distinguish protolith from alteration products, but also trace hydrothermal processes. If BIFs are found as protoliths in terranes where IOCGs also occur, then geochemical signatures should still be recognizable when, the textures, of the sedimentary protoliths are retained.

Acknowledgements

This is a contribution to the 'FOX' project, supported by BHP Billiton Olympic Dam and the South Australian Mining and Petroleum Services Centre of Excellence. Sasha Krneta kindly assisted with preparation of Figure 1. Two reviewers are thanked for their helpful suggestions.

References

Ciobanu CL, Wade B, Cook NJ, Schmidt Mumm A, Giles D (2013) Uranium-bearing hematite from the Olympic Dam Cu-U-Au deposit, South Australia; a geochemical tracer and reconnaissance Pb-Pb geochronometer. Precambrian Res 238:129–147

Ciobanu CL, Cook NJ, Ehrig K, Wade BP, Kamenetsky, VS (2015) Trace element signatures in iron oxides from the Olympic IOCG deposit, South Australia. Mineral Resources in a Sustainable World, 13th SGA Biennial Meeting 2015, Nancy, pp 1071–1074

Conor C, Raymond OL, Baker T, Teale G, Say P, Lowe G (2010) Alteration and mineralisation in the Moonta-Wallaroo Copper-Gold Mining Field Region, Olympic Domain, South Australia. In: Porter TM (ed.), Hydrothermal Iron Oxide Copper-Gold & Related Deposits, vol. 3-4. PGC Publishing, Adelaide, pp 1–24

Corriveau L, Montreuil J-F, Potter EG (2016) Alteration facies linkages among iron oxide copper-gold, iron oxide-apatite, and affiliated deposits in the Great Bear magmatic zone, Northwest Territories, Canada. Econ Geol 111, 2045–2072

Courtney-Davies L, Zhu Z, Ciobanu CL, Wade BP, Cook NJ, Ehrig K, Cabral AR, Kennedy A (2016) Matrix-matched iron-oxide laser ablation ICP-MS U-Pb geochronology using mixed solution standards. Minerals 6(3), 85; doi:10.3390/min6030085

Cowley W, Conor C, Zang W (2003) New and revised Proterozoic stratigraphic units on northern Yorke Peninsula. MESA J. 29:46-58

Dare S, Barnes S, Beaudoin G (2014) Trace elements in magnetite as petrogenetic indicators. Ore Geol Rev 49:785–796

Dupuis C, Beaudoin G (2011) Discriminant diagrams for iron oxide trace element fingerprinting of mineral deposit types. Miner Deposita 46:319–335

Ehrig K, Kamenetsky VS, McPhie J,Apukhtina A, Ciobanu CL, Cook NJ, Kontonikas-Charos A, Krneta S (2017) this volume. The IOCG-IOA ore system at Olympic Dam and nearby prospects, South Australia, South Australia. This volume

Ismail R, Ciobanu CL, Cook NJ, Teale GS, Giles D, Mumm AS, Wade B (2014) Rare earths and other trace elements in minerals from skarn assemblages, Hillside iron oxide-copper-gold deposit, Yorke Peninsula, South Australia. Lithos 184-187:456–477

Kontonikas-Charos A, Ciobanu CL, Cook NJ (2014) Albitization and redistribution of REE and Y in IOCG systems: Insights from Moonta-Wallaroo, Yorke Peninsula, South Australia. Lithos 208–209:178–201

Reid AJ, Swain G, Mason D, Maas R (2011) Nature and timing of Cu-Au-Zn-Pb mineralisation at Punt Hill, eastern Gawler Craton. MESA Journal 60:7–17

Skirrow RG, Bastrakov E, Evgeniy N, Barovich K, Fraser GL, Creaser RA, Fanning CM, Raymond OL, Davidson GJ (2007) Timing of iron oxide Cu-Au-(U) hydrothermal activity and Nd isotope constraints on metal sources in the Gawler craton, South Australia. Econ Geol 102:1441–1470

View publication stats

ADDITIONAL MATERIAL EE

CO-AUTHORED CONFERENCE ABSTRACT:

TRACE ELEMENT SIGNATURES IN U-W-SN-MO ZONED HEMATITE FROM THE IOCG DEPOSIT AT OLYMPIC DAM, SOUTH AUSTRALIA

Max R. Verdugo-Ihl[1], Cristiana L. Ciobanu[1], Nigel J. Cook[1], Kathy Ehrig[2], **Liam Courtney-Davies[1],** Sarah E. Gilbert[3]

[1]School of Chemical Engineering and Advanced Materials, The University of Adelaide, Adelaide, SA 5005, Australia

[2]BHP Olympic Dam, Adelaide, SA 5000, Australia

[2]Adelaide Microscopy, The University of Adelaide, Adelaide, SA 5005, Australia

Extended conference abstract and poster, Mineral Resources to Discover. Proceedings of the 14th SGA Biennial Meeting, Québec, Canada, August 20-23rd, 2017. ISBN: 978-2-9816898-0-1, Volume 3, 967-970.

Trace element signatures in U-W-Sn-Mo zoned hematite from the IOCG deposit at Olympic Dam, South Australia

Max R. Verdugo-Ihl, Cristiana L. Ciobanu, Nigel J. Cook, Liam Courtney-Davies
University of Adelaide, Australia

Kathy J. Ehrig
BHP Billiton Olympic Dam, Australia

Sarah Gilbert
University of Adelaide, Australia

Abstract. Hematite is the dominant gangue component of the Olympic Dam Cu-U-Au-Ag orebody, South Australia. A distinct oscillatory-zoned hematite, conspicuously rich in 'granitophile' elements (U, W, Sn, Mo) is recognized throughout the ~2 km vertical extent of deposit zonation, from deep pyrite-chalcopyrite to shallow bornite-chalcocite orezones, as well as throughout the entire NW-SE strike of the orebody. Concentrations of granitophile elements are retained, albeit at lower concentrations, in later replacement hematites. Comparison of trace element datasets for U-W-Sn-Mo-zoned hematite relative to replacement hematite provides evidence for localized fluid-mineral reaction and for the importance of reactions coupling dissolution with reprecipitation rates in driving element exchange. The oscillatory-zoned hematite is analogous to that previously dated by LA-ICP-MS, confirming that this generation of hematite was formed at ~1.6 Ga during the onset of the IOCG mineralising system. Such 'granitophile'-rich hematite may be common in other IOCG deposits, and typifies precipitation from fluids rich in these elements during the main hydrothermal stages. Lack of evidence for this type elsewhere is most likely attributable to advanced overprinting in which such signatures are largely obliterated.

1 Introduction

Inherent to all iron-oxide copper gold (IOCG) deposits is the abundance of Fe-oxides as hematite (α-Fe_2O_3) and/or magnetite (Fe_3O_4). The increasing volume of published trace/minor element data for minerals from hydrothermal ores (Cook et al. 2016 and references therein) include studies of Fe-oxides for fingerprinting mineral deposits of different types (e.g. Dupuis and Beaudoin 2011). Trace element signatures of magnetite from end-member IOCG deposits *sensu lato* such as Kiruna (Sweden) and El Laco (Chile) have been obtained to support debates around their magmatic versus hydrothermal origins (Dare et al. 2015; Knipping et al. 2015). In contrast, trace elements in Fe-oxides from *sensu stricto* IOCG-systems, and specifically hematite, have not been studied in detail despite being the main products of alteration closely associated with mineralising processes. Among the exceptions is hematite from the IOCG deposit at Olympic Dam (OD), South Australia (S.A.), which was found to incorporate a wide range of trace elements, including HFSE, REE+Y (REY) and is particularly rich in U, W, Sn, and Mo (hereafter 'granitophile' elements) (Ciobanu et al. 2013; 2015; Cook et al. 2016). Incorporation of U and its decay products within grains showing oscillatory zonation patterns facilitates its use as a mineral geochronometer for directly dating hydrothermal ore-forming processes in IOCG deposits from S.A. and elsewhere (Ciobanu et al. 2013; Courtney-Davies et al. 2016). Hematite from OD shows incredible textural diversity including pseudomorphic replacement of pre-existing minerals and/or rock fragments, overgrowths of hematite with distinct trace/minor element signatures, as well as cycles of (inter)conversion with magnetite, all of which is mirrored by a complexity of preserved trace element signatures (Ciobanu et al. 2013; 2015; Cook et al. 2016). Hence, studies of hematite signatures and their variation can offer insights into the processes responsible for the genesis and overprinting of IOCG-deposits, as well as providing a temporal context for regional metallogenic events.

2 Geological background

Olympic Dam is a giant, Cu-U-Au-Ag deposit (10,400 Mt @ 0.77 % Cu, 250 ppm U_3O_8, 1 ppm Ag and 0.32 ppm Au; BHP Billiton 2016) located on the eastern margin of the Gawler Craton. It belongs to the Olympic Cu-Au Province (e.g. Skirrow et al. 2007) in which IOCG mineralisation is associated with ~1.6 Ga magmatism (Hiltaba Intrusive Suite; HIS and Gawler Range Volcanics, GRV), although ongoing work at OD shows the importance of subsequent overprinting events to account for the spectacular metal endowment of the deposit. The deposit is hosted within the Olympic Dam Breccia Complex (ODBC), which is confined to the Roxby Downs Granite (RDG; Fig. 1), a HIS granitoid. Latest, high-precision U-Pb dating of magmatic and hydrothermal zircon in RDG and ODBC shows that brecciation and hydrothermal alteration (at least the early stage) is coeval with RDG crystallisation at ~1595 Ma (e.g. Jagodzinski 2005 and unpublished data). U-Pb geochronology of oscillatory-zoned hematite from two locations in the deposit shows overlaps with the zircon ages (Ciobanu et al. 2013; Courtney-Davies et al. 2016).

The RDG displays a gradational continuum from altered, through fractured to brecciated lithologies, associated with an increase in Fe-metasomatism and

multiple episodes of brecciation and displacement. OD is mineralogically zoned at the deposit scale, characterized by an inwards-, roughly concentric and quasi-continuous Cu(-Fe)-sulphide zonation that spans vertically and horizontally from pyrite-chalcopyrite (Py-Cp) through chalcopyrite-bornite (Cp-Bn) to bornite-chalcocite (Bn-Cc) dominated assemblages (Ehrig et al. 2012), a pattern considered to represent a primary feature of hypogene ore precipitation (Ciobanu et al. 2017). Hematite is the main Fe-oxide within the orebody, even though at depth and along the deposit margins magnetite is also present and shows various, complex replacement textures with hematite (Ehrig et al. 2012; Ciobanu et al. 2015).

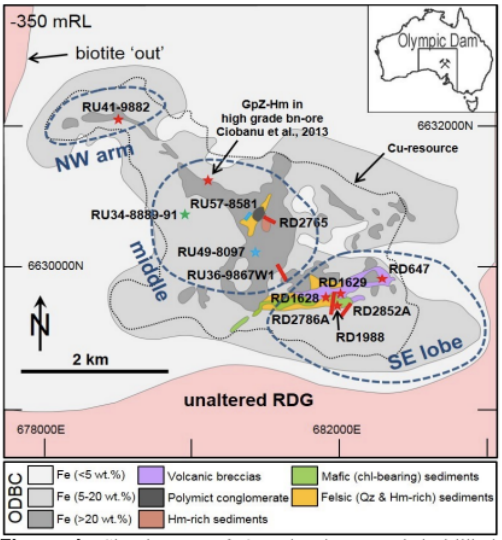


Figure 1. Sketch map of OD showing sampled drillholes. Different categories of hematite (Hm) as follows: red: oscillatory-zoned (GpZ-Hm); green: carbonate replacement (RC-Hm); blue: replacement, undifferentiated. After Ehrig et al. (2012).

3 Sampling approach and methodology

The present study is undertaken on ~50 samples collected from drillholes intersecting different parts of the OD orebody along its ~6 km strike and throughout the entire ~2 km vertical zonation in the SE lobe. These were selected to represent the lithological complexity, e.g. (i) presence of blocks of sediments and brecciated felsic volcanics in the SE lobe; (ii) sediments in the 'barren core' from the middle part of the deposit (>20 wt.% Fe); (iii) high-grade chalcocite and bornite ores from the middle (RU34-8889-8891) and NW arm (RU41-9882) of the deposit, respectively. Polished blocks were analysed using reflected light microscopy, scanning electron microscopy in back-scatter electron mode (BSE), electron probe microanalysis (EPMA) and laser ablation inductively-coupled plasma mass spectrometry (LA-ICP-MS) for trace elements using BHVO-2G and NIST610 as reference standards. All instrumentation is housed at Adelaide Microscopy, The University of Adelaide.

4 Results

Oscillatory zonation in hematite with respect to concentrations of U+W+Sn+Mo is recognised throughout most samples from across the deposit area, including from the shallow Bn-Cc orezone in the SE lobe, in hematite-richest breccias from the 'barren core', and in high-grade bornite ores from the NW arm of the deposit (Fig. 1). This type of hematite (GpZ-Hm; Fig. 2) occurs as single grains of variable size (tens to hundreds of µm), and more rarely as lamellar aggregates. Remarkable concentrations of granitophile elements, routinely measured by LA-ICP-MS (see below), are confirmed by EPMA analysis (e.g. up to wt.% levels of UO_3 and WO_3; Fig. 2a). Overprinting of such hematite is recognised, including marginal corrosion and replacement, brecciation, porosity, fields of discrete inclusions (U-, W-, or REE-minerals), as well as cross-cutting veinlets. In most cases, GpZ-Hm grains display varying degrees of pseudomorphic replacement, leading to overgrowths of hematite poor in granitophile elements (Fig. 2a). There are, however, also grains with a clast-like morphology, little apparent replacement, and excellent preservation of compositional zoning (Fig. 2b). These are specific to samples from the 'barren core', or from entrapped sediments from the SE lobe.

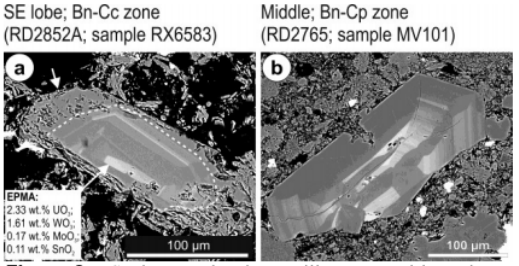


Figure 2. BSE images showing oscillatory-zoned hematite and styles of overprinting.

Although the abundance of GpZ-Hm is higher in samples analysed here from the SE lobe, this type of hematite is relatively minor on the deposit-scale (~10 vol.% within a given sample) relative to other hematite types. These include porous aggregates, and fine-grained hematite filling single grains of other minerals (feldspars in RDG or volcanic rocks), other rock fragments, or the dominant fine-grained hematite that makes up the matrix for breccias, notably in samples from the 'barren core' of the deposit. One type of replacement hematite is defined by fine aggregates of hematite filling coarser lamellae (mm-size) arranged within an overall rhombic outline (RC-Hm). The pre-existing mineral may have been a carbonate. Importantly, such aggregates host abundant chalcocite and define high-grade chalcocite-only ores in the middle part of the deposit.

Trace element data for zoned hematite show variation with respect to REY, HFSE (particularly Nb and V), as well as in the relative proportions of the granitophile elements, e.g. U vs. W+Sn+Mo (Fig. 3). Concentrations of U and W can both reach up to several wt.%; in some cases, hematite grains rich in U and W co-exist in the same sample (e.g. in the Cp-Py zone at depth in the SE lobe). Sn and Mo concentrations are generally subordinate: up to hundreds of ppm (exceptionally thousands of ppm Sn in samples from the SE lobe). Such variation is, however, neither systematic with respect to location within the deposit nor throughout its vertical extent. Replacement hematite, particularly in samples from the middle part of the deposit (included here for comparison) can also be relatively rich in granitophile elements, albeit 1-2 orders of magnitude lower than in GpZ-Hm (Fig. 3). There is an apparent decrease in the U content of hematite from SE to NW. GpZ-Hm in samples from the SE lobe and 'barren core' appear the poorest in HFSE relative to other types.

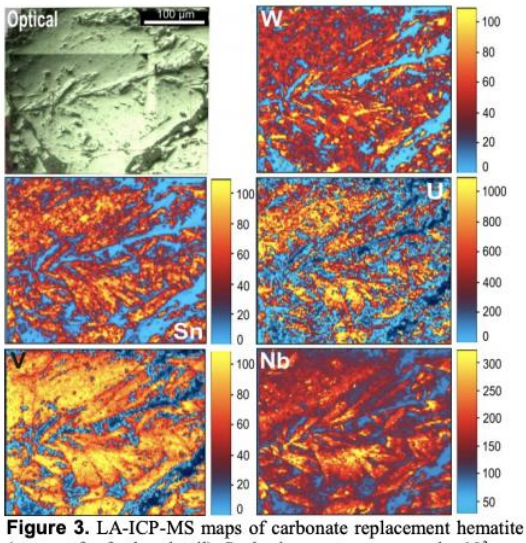


Figure 3. LA-ICP-MS maps of carbonate replacement hematite (see text for further detail). Scales in counts-per-second x 10^3.

The relatively homogenous distribution of granitophile elements and HFSE in the RC-Hm type (Fig. 3) seems to map out the coarse lamellae rather than fine-grained nature of the hematite filling. RC-Hm also stands out by having the highest, consistent Nb+V concentrations (Fig. 4c). In contrast, ΣREY concentrations display a relatively constant spread, with a wide range across several orders of magnitude, irrespective of hematite type (Fig. 4a).

Chondrite-normalised REY fractionation trends (Fig. 5) show that GpZ-Hm is, for the most part, poor in REY, but nevertheless displays a consistent pattern defined by relative LREE enrichment. Other REY trends, including flat to slightly concave profiles, are obtained from grains with higher-ΣREY throughout all categories of hematite. RC-Hm is an exception, however, and shows conspicuous, concave, HREE-enriched trends throughout all analyses.

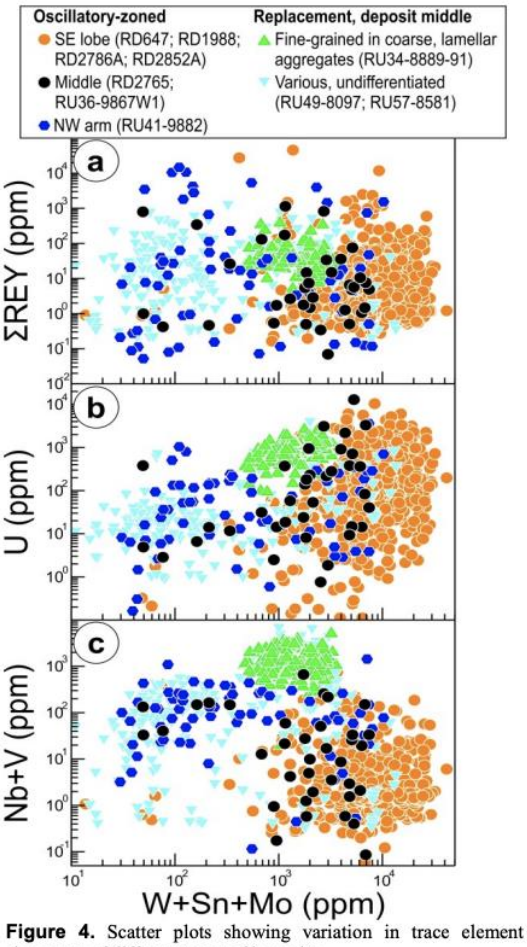


Figure 4. Scatter plots showing variation in trace element signatures of different types of hematite.

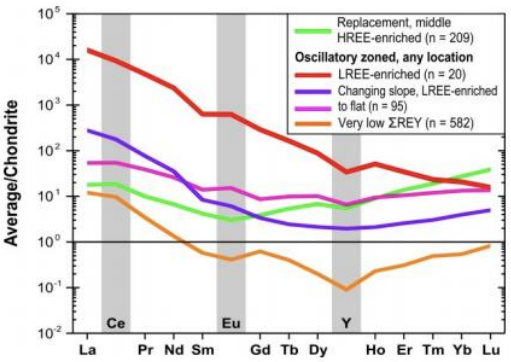


Figure 5. Chondrite normalized REY fractionation trends of different types of hematite.

5 Discussion and implications

'Granitophile'-rich, oscillatory-zoned hematite previously reported from a couple of locations in the OD deposit (Ciobanu et al. 2013; 2015) is now recognised as present throughout the ~2 km vertical extent of deposit zonation (from deep Py-Cp to shallow Bn-Cc orezones), as well as throughout the entire NW-SE strike of the orebody. Such hematite has been also dated by LA-ICP-MS, using GJ-1 zircon as primary standard, and shows the same ~1.6 Ga age (Courtney-Davies et al. unpublished data), firmly indicating that this generation of hematite was formed during the onset of the IOCG mineralising system.

GpZ-Hm is a poor host for REY; higher ΣREY are mostly attributable to discrete inclusions of REE-minerals. The change in REY fractionation trend from LREE, dominant throughout most hematite types, to HREE-enriched, as documented here for RC-Hm, can be related to pH variation, as this parameter can strongly impact on REE solubility (Midgisov et al. 2016 and references therein). This is concordant with the interpretation of replacement of a pre-existing carbonate, strongly reactive to the acidic fluids leading to hydrolytic (sericite-hematite) alteration, and could also account for the formation of high-grade chalcocite ore. One of the interesting findings is the potential that HFSE may have for understanding primary deposit zonation, or the importance of different protoliths relative to granitophile-rich hydrothermal fluids.

The fact that concentrations of U and other granitophile elements are retained throughout all replacement hematites, some of which are clearly formed on behalf of the oscillatory-zoned type, suggests the importance of reactions coupling dissolution with reprecipitation rates (CDRR) throughout the ODBC, retaining such elements close to the sites of fluid-mineral interaction. The data for U-W-Sn-Mo-zoned hematite can be considered as evidence for localised fluid-mineral reaction throughout the ODBC and the importance of CDRR in driving element exchange as was shown for OD uraninite (Macmillan et al. 2016a, b) and for feldspar alteration in the RDG outside the orebody (Kontonikas-Charos et al. 2017).

Comparable compositional zonation with respect to W+U was shown for hematite from other deposits in the Olympic Cu-Au Province and from Carajas, Brazil (Courtney-Davies et al. 2016), irrelevant of host lithologies (granitoid hosted or not). It is likely that 'granitophile'-rich hematite is one of the main types in IOCG deposits, and typifies precipitation from fluids rich in these elements during the main hydrothermal stages, assuming no other minerals that are normally good 'granitophile' carriers are formed at the same time (e.g. skarn calc-silicates). A lack of evidence for this type elsewhere is most likely attributable to advanced overprinting (obliteration of such signature), and/or poor mineralogical/petrological studies.

Acknowledgments

This is a contribution to the 'FOX' project, supported by BHP Billiton Olympic Dam and South Australian Mining and Petroleum Services Centre of Excellence.

References

BHP Billiton (2016) http://www.bhpbilliton.com/~/media/bhp/documents/investors/annual-reports/2016/bhpbillitonannualreport2016.pdf.

Ciobanu CL, Cook NJ, Ehrig K (2017) Ore minerals down to the nano-scale: Cu-(Fe)-sulphides from the Iron Oxide Copper Gold deposit at Olympic Dam, South Australia. Ore Geol Rev 81:1218-1235

Ciobanu CL, Cook NJ, Ehrig K, Wade BP, Kamenetsky VS (2015) Trace element signatures in iron oxides from the Olympic IOCG deposit, South Australia. Mineral Resources in a Sustainable World, 13th SGA Biennial Meeting 2015, Nancy:1071-1074

Ciobanu CL, Wade B, Cook NJ, Schmidt Mumm A, Giles D (2013) Uranium-bearing hematite from the Olympic Dam Cu-U-Au deposit, South Australia; a geochemical tracer and reconnaissance Pb-Pb geochronometer. Precambr Res 238:129-147

Cook NJ, Ciobanu CL, George L, Zhu Z-Y, Wade BP, Ehrig K (2016) Trace element analysis of minerals in magmatic-hydrothermal ores by laser ablation inductively-coupled plasma mass spectrometry: approaches and opportunities. Minerals 6(4), 111; doi:10.3390/min6040111

Courtney-Davies L, Zhu Z, Ciobanu CL, Wade BP, Cook NJ, Ehrig K, Cabral AR, Kennedy A (2016) Matrix-matched iron-oxide laser ablation ICP-MS U-Pb geochronology using mixed solution standards. Minerals 6(3), 85; doi:10.3390/min6030085

Dare SAS, Barnes S-J, Beaudoin G (2015) Did the massive magnetite "lava flows" of El Laco (Chile) form by magmatic or hydrothermal processes? New constraints from magnetite composition by LA-ICP-MS. Mineral Deposita 50:607-617

Dupuis C, Beaudoin G (2011) Discriminant diagrams for iron oxide trace element fingerprinting of mineral deposit types. Mineral Deposita 46:319–335

Ehrig K, McPhie J, Kamenetsky V (2012) Geology and mineralogical zonation of the Olympic Dam Iron Oxide Cu-U-Au-Ag deposit, South Australia. SEG Spec Publ 16:237-267

Jagodzinski EA (2005) Compilation of SHRIMP U–Pb Geochronological Data. Olympic Domain, Gawler Craton, South Australia, 2001–2003. Geoscience Australia, Record 2005/20

Knipping JL, Bilenker LD, Simon AC, Reich M, Barra F, Deditius AP, Lundstrom C, Bindeman I, Munizaga R (2015) Giant Kiruna-type deposits form by efficient flotation of magmatic magnetite suspensions. Geology 43:591-594

Kontonikas-Charos A, Ciobanu CL, Cook NJ, Ehrig K, Krneta S, Kamenetsky VS (2017) Feldspar evolution in the Roxby Downs Granite, host to Fe-oxide Cu-Au-(U) mineralisation at Olympic Dam, South Australia. Ore Geol Rev 80:838-859

Macmillan E, Ciobanu CL, Ehrig K, Cook NJ, Pring A (2016a) Chemical zoning and lattice distortion: Uraninite from Olympic Dam, South Australia. Amer Mineral 101:2351-2354

Macmillan E, Cook NJ, Ehrig E, Ciobanu CL, Pring A (2016b) Uraninite from the Olympic Dam IOCG-U-Ag deposit: linking textural and compositional variation to temporal evolution. Amer Mineral 101:1295-1320

Migdisov A, Williams-Jones A, Brugger J, Caporuscio F (2016) Hydrothermal transport, deposition, and fractionation of the REE: Experimental data and thermodynamic calculations. Chem Geol 439:13-42

Skirrow RG, Bastrakov E, Evgeniy N, Barovich K, Fraser GL, Creaser RA, Fanning CM, Raymond OL, Davidson GJ (2007) Timing of iron oxide Cu-Au-(U) hydrothermal activity and Nd isotope constraints on metal sources in the Gawler craton, South Australia. Econ Geol 102:1441-1470

ADDITIONAL MATERIAL FF

CO-AUTHORED CONFERENCE ABSTRACT:

WHY DETAILED MINERALOGY IS IMPORTANT: UNDERSTANDING EVOLUTION OF THE OLYMPIC DAM IRON-OXIDE-COPPER-GOLD SYSTEM, SOUTH AUSTRALIA

Nigel Cook[1], Kathy Ehrig[2], Cristiana Ciobanu[1], **Liam Courtney-Davies[1]**, Max Verdugo-Ihl[1], Mark Rollog[1], Danielle Schmandt[1], Nicholas Owen[1], Edeltraud Macmillan[2], Alkiviadis Kontonikas-Charos[1], Sasha Krneta[1], Marija Dmitrijeva[1]

[1]School of Chemical Engineering and Advanced Materials, The University of Adelaide, Adelaide, SA 5005, Australia

[2]BHP Olympic Dam, Adelaide, SA 5000, Australia

Conference presentation, 15th Quadrennial IAGOD Symposium, Salta, Argentina, August 28th-31st. Symposium Volume, SEGEMAR, 371-372.

15th Quadrennial IAGOD International Association on the Genesis of Ore Deposits Symposium, Salta, Argentina.



WHY DETAILED MINERALOGY IS IMPORTANT: UNDERSTANDING EVOLUTION OF THE OLYMPIC DAM IRON-OXIDE COPPER-GOLD SYSTEM, SOUTH AUSTRALIA

Nigel Cook[1], Kathy Ehrig, Cristiana Ciobanu, Liam Courtney-Davies, Max Verdugo-Ihl, Mark Rollog, Danielle Schmandt, Nicholas Owen, Edeltraud Macmillan, Alkiviadis Kontonikas-Charos, Sasha Krneta, Marija Dmitrijeva

[1]*School of Chemical Engineering, University of Adelaide, Australia - nigel.cook@adelaide.edu.au*

Olympic Dam is one of the largest deposits on Earth and a significant producer of copper, uranium, gold and silver (Ehrig, *et al.*, 2013). Uranium-Pb geochronology using undisturbed magmatic and hydrothermal minerals allows interpretation of the initial and major hydrothermal ore- forming event at ~1593 Ma, associated with emplacement of the Gawler Silicic Large Igneous Province. The >10 billion-tonne resource is heterogeneous and contained within a breccia complex, itself confined to the ~1593 Ma Roxby Downs Granite. Ore textures suggest multiple episodes of replacement, remobilization and recrystallization and are supported by (radio) isotope data yielding a range of younger ages. Conceptual models for ore formation, necessary for exploration in the region, and optimised processing of complex fine-grained ores characterised by enrichment in an extraordinarily wide variety of elements are dependent on an exceptionally thorough understanding of mineralogy and geochemistry underpinned by high-quality, high-resolution assay data, extensive MLA datasets, and deportment models for multiple elements.

Micron - to nanoscale studies of feldspars and accessory phases within the alteration envelope, and of Fe-oxides, Cu-(Fe)-sulphides, sulphates, U- and REE-bearing minerals within the deposit all point to common mechanisms involved in formation of the mineral assemblages as observed today, the prevailing Mm-scale mineral textures, and measured variations in mineral compositions. Detailed mineralogical investigation has proven pivotal in establishing a framework for ore evolution.

Each of the 100 minerals in the Olympic Dam deposit has a story to tell. The complex fine- grained, intergrown, heterogeneous assemblages necessitate ultra-careful investigation on multiple representative samples and with compositional data requiring verification by examination at the nanoscale. We therefore use a combination of whole rock assay, optical and scanning electron microscopy, electron probe microanalysis (EPMA), laser-ablation inductively-coupled plasma mass spectrometry, complemented by imaging and nanoscale compositional analysis by transmission electron microscopy (TEM) on foils extracted *in-situ* by focussed ion beam SEM methods.

Investigation of feldspars from within and outside the deposit allows an understanding of the magmatic to hydrothermal transition and early Fe-metasomatism (Kontonikas-Charos, *et al.*, 2017). Nanoscale characterization of feldspars undergoing transformation from early post-magmatic (deuteric) to hydrothermal stages in granites hosting the deposit reveals complex perthitic textures, anomalously Ba, Fe, or REE-rich compositions, and REE-fluorocarbonate+molybdenite assemblages that pseudomorph feldspars (Kontonikas-Charos, *et al.*, 2018). Epitaxial orientations between (igneous) cryptoperthite, (deuteric) patch and albite replacive within vein perthite support interface-mediated reactions between pre-existing alkali-feldspars and pervading fluid, irrespective of micron-scale crystal morphology. Such observations are consistent with coupled dissolution-replacement reactions (CDRR), indicating that albitization enhances rock permeability via the generation of transient pores which facilitate grain-scale element remobilization and trap elements as nanoscale inclusions. These inclusions represent the earliest stage of REE remobilization at the grain-scale, and reflect the significant role feldspar replacement reactions play in concentrating REE during hydrothermal alteration.

Hematite is by far the most abundant hydrothermal mineral and preserves oscillatory and sectorial zoning and incorporation of U, W, Mo, Sn and other trace elements, including REE (Verdugo-Ihl, *et al.*, 2017). The presence of U and Pb allows application of hematite U-Pb geochronology [e.g., Courtney-Davies, *et al.*, 2018]. These primary textures give way to repeated processes of brecciation, fluid-assisted reworking, element redistribution, recrystallization and overprinting. CDRR permits release of trace elements from the lattice to be trapped as nm- to Mm-scale inclusions (e.g., uraninite), or to form discrete minerals (e.g., scheelite molybdenite) in the near vicinity.

EPMA-scale compositional data combined with TEM investigation of chalcocite-group minerals, bornite and chalcopyrite has shown that Cu-Fe-sulphides from different ore zones feature nanoscale intergrowths, lattice defects, superstructure domains and antiphase boundary domains (Ciobanu, *et al.*, 2017). Such features can be interpreted as having originated via a combination of exsolution, coarsening, and phase transformation during cooling from high-T solid solutions (e"400°C) in the system Cu-Fe-S and sub-systems. A scenario of 'exsolution from primary solid-solution, corroborated by the consistency in phase relations within each zone across different scales of observation from deposit- to nanoscale, supports a model of primary hypogene ore precipitation rather than replacement, and

accounts for the observed zoning patterns at OD. Nonetheless, evidence for CDRR, replacement, phase transformation and local (Mm- to tens m-wide) remobilization is evident.

Uraninite, coffinite, brannerite and hematite are the dominant U hosts [Courtney-Davies, *et al.*, 2018, Macmillan, *et al.*, 2016, Macmillan, *et al.,* 2017). Although some uraninite and hematite retain U and daughter isotopes, breakdown and replacement can lead to release, remobilization and redistribution of radionuclides (RN) at scales from nm upwards. New minerals may be formed (late uraninite, coffinite) and U and Pb can also be incorporated into existing minerals (barite, svanbergite-woodhouseite). RN are, however, also concentrated as sub-microscopic particles within pores, microfractures and at grain boundaries in the near vicinity of altered or replaced U-bearing mineral grains (Rollog, *et al.*, 2018) attesting to fluid-mediated processes. Such redistribution carries implications for ore processing and, potentially also for the interpretation of geochronological data.

Three groups of REE-minerals are observed: REE-fluorocarbonates (bastnosite and subordinate synchysite (Schmandt, *et al.*, 2017), which appear paragenetically early; REE-phosphates (dominantly florencite of variable age and association but also minor xenotime, the main carrier of HREE); and Ca-, Sr-, REE-bearing phosphate-sulphates (svanbergite- woodhouseite], which are generally late and replace earlier-formed minerals (Owen, *et al.,* 2018). Minor REE are also contained in apatite, which displays evolving chondrite-normalized REE fractionation trends that can be explained in terms of changes in fluid parameters and speciation of REY in ore-forming fluids (Krneta, *et al.,* 2017). Under hydrothermal conditions typical of iron- oxide copper gold mineralization, a decrease in salinity, pH and temperature is associated with hematite-sericite alteration sufficient to produce a characteristic MREE-enriched apatite. However, anomalous high-pH (~7) fluids at 300 °C may account for high-grade Cu ores as modelled from apatite with strong positive Eu anomalies (Krneta, *et al.,* 2017).

Although primary assemblages are identified, a persistent narrative is offered by multiple episodes of fluid-assisted replacement, phase transition, remobilization, migration, and re- precipitation of all ore components. These processes played a major role in the modification of textural and geochemical patterns in many minerals. However, more refractory minerals, notably hematite, apatite, pyrite, some REE-minerals, and some sub-types of U-minerals, can preserve primary geochemical signatures and can also record and retain evidence of evolving and overprinting fluid signatures. Fluid regimes were likel heterogeneous given observations of texturally and geochemically distinct generations of the same mineral within single samples.

REFERENCES

Ehrig, K., McPhie, J., Kamenetsky, V., 2013. Geology and mineralogical zonation of the Olympic Dam iron oxide Cu-U-Au-Ag deposit, South Australia. In: Hedenquist, J.W., Harris, M., Camus, F. (Eds), Geology and Genesis of Major Copper Deposits and Districts of the World, a Tribute to Richard Sillitoe. SEG Special Publication 16, pp. 237-268.

Kontonikas-Charos, A., Ciobanu, C.L., Cook, N.J., Ehrig, K., Krneta, S., Kamenetsky, V.S., 2017. Feldspar evolution in the Roxby Downs Granite, host to Fe-oxide Cu-Au-(U) mineralization at Olympic Dam, South Australia. Ore Geology Reviews, 80, 838-859.

Kontonikas-Charos, A., Ciobanu, C.L., Cook, N.J., Ehrig, K., Ismail, R., Krneta, S., Basak, A., 2018. Feldspar mineralogy and rare earth element (re)mobilization in iron-oxide copper gold systems from South Australia: a nanoscale study. Mineralogical Magazine 82 (S1), S173–S197.

Verdugo-Ihl, M.R., Ciobanu, C.L., Cook, N.J., Ehrig, K., Courtney-Davies, L., Gilbert, S., 2017. Textures and U-W-Sn-Mo signatures in hematite from the Cu-U-Au-Ag orebody at Olympic Dam, South Australia: defining the archetype for IOCG deposits. Ore Geology Reviews 91, 173–195.

Courtney-Davies, L., Ciobanu, C.L., Tapster, S.R., Cook, N.J., Ehrig, K.J., Kennedy, A.K., Condon, D.J., Verdugo-Ihl, M.R., Wade, B.S., Gilbert, S.E., 2018. The U-Pb systematics of hydrothermal hematite; insights from the IOCG system at Olympic Dam, South Australia. IAGOD Symposium, Salta (this volume).

Ciobanu, C.L., Cook, N.J., Ehrig, K., 2017. Ore minerals down to the nanoscale: Cu-(Fe)- sulphides from the iron oxide copper gold deposit at Olympic Dam, South Australia. Ore Geology Reviews 81, 1218-1235.

Macmillan, E., Cook, N.J., Ciobanu, C.L., Ehrig, E., Pring, A., 2016. Uraninite from the Olympic Dam IOCG-U-Ag deposit: linking textural and compositional variation to temporal evolution. American Mineralogist 101, 1295–1320.

Macmillan, E., Cook, N.J., Ehrig, K., Pring, A., 2017. Chemical and textural interpretation of late-stage coffinite and brannerite from the Olympic Dam IOCG-Ag-U deposit. Mineralogical Magazine 81, 1323-1366.

Rollog, M., Cook, N.J., Gugliardo, P., Ehrig. K., Kilburn, M., 2018. In situ spatial distribution mapping of radionuclides in minerals by nanoSIMS. Geochemistry – Exploration, Environment, Analysis (in press).

Schmandt, D.S., Cook, N.J., Ciobanu, C.L., Ehrig, K., Wade, B.P., Gilbert, S., Kamenetsky, V.S., 2017. Rare earth element fluorocarbonate minerals from the Olympic Dam Cu-U-Au-Ag deposit, South Australia. Minerals 7(10), 202; doi: 10.3390/min7100202.

Owen, N.D., Ciobanu, C.L., Cook, N.J., Slattery, A., Basak, A., 2018. Nanoscale study of clausthalite-bearing symplectites in Cu-Au-(U) ores: Implications for ore genesis. Minerals, 8(2), 67; doi:10.3390/min8020067.

Krneta, S., Ciobanu, C.L., Cook, N.J., Ehrig, K., Kontonikas-Charos, A., 2017. Rare earth element behaviour in apatite from the Olympic Dam Cu-U-Au-Ag deposit, South Australia. Minerals 7(8), 135; doi:10.3390/min7080135.

ADDITIONAL MATERIAL GG

CO-AUTHORED CONFERENCE ABSTRACT:

NANOSCALE STUDY OF SILICIAN MAGNETITE FROM IOCG SYSTEMS: EXAMPLES FROM THE OLYMPIC DAM DISTRICT, SOUTH AUSTRALIA

Cristiana L. Ciobanu[1], Max R. Verdugo-Ihl[1], Ashley Slattery[2], Nigel J. Cook[1], Kathy Ehrig[3],

Liam Courtney-Davies[1]

[1]School of Chemical Engineering and Advanced Materials, The University of Adelaide, Adelaide, SA 5005, Australia

[2]Adelaide Microscopy, The University of Adelaide, Adelaide, SA 5005, Australia

[3]BHP Olympic Dam, Adelaide, SA 5000, Australia

Conference presentation, 15th Quadrennial IAGOD Symposium, Salta, Argentina, August 28th-31st. Symposium Volume, SEGEMAR, 185-186

15th Quadrennial IAGOD International Association on the Genesis of Ore Deposits Symposium, Salta, Argentina.



NANOSCALE STUDY OF SILICIAN MAGNETITE FROM IOCG SYSTEMS: EXAMPLES FROM THE OLYMPIC DAM DISTRICT. SOUTH AUSTRALIA

Cristiana L. Ciobanu[1], Max R. Verdugo-Ihl, Ashley Slattery, Nigel J. Cook, Kathy J. Ehrig, Liam Courtney- Davies

[1]*School of Chemical Engineering, University of Adelaide, Adelaide, Australia - cristiana.ciobanu@adelaide.edu.au*

BACKGROUND

'Silician magnetite' (Si-magnetite) refers to magnetite with variable Si (up to ~10 wt.% SiO_2) and occurs in deposits spanning the magmatic-hydrothermal spectrum, low-T metamorphosed BIF ores as well as in mafic and ultramafic rocks (Huberty *et al.*, 2012 and references therein). Definition of Si-magnetite nanoprecipitates as Si^{IV} $[(vacancy)_{0.5}Fe^{2+}_{0.5}]^{VI}$ $[Fe^{3+}]^{VI}$ O_4 with maghemite-type vacancy-ordering was only recently possible by using Z-contrast techniques for high-resolution Scanning Transmission Electron Microscopy (STEM) imaging (Xu *et al.*, 2014). Formation of Si-magnetite in hydrothermal systems can be considered as co- precipitation of aqueous silica and Fe-silicate complexes during crystal growth (Xu *et al.*, 2014). It is thus important in modelling deposits where regional/orefield zonation patterns result from fluid evolution. In Iron-Oxide Copper Gold (IOCG) systems, magnetite is associated with early, higher-T, alkali/calcic metasomatism, in turn associated with chalcopyrite-pyrite mineralization in the Olympic Dam District (ODD), South Australia, but not necessarily elsewhere. The Olympic Dam (OD) deposit is hosted within hematite-bearing breccias placed in the central, upper part of the Roxby Downs Granite (RDG) associated with ~1.6 Ga IOCG mineralization and magmatism.

Here we discuss Si-magnetite from 5 locations: 4 from the outer, weakly-mineralised shell of brecciated RDG at OD, and one from the older (~1.85 Ga) Donington granite hosting the Wirrda Well (WW) IOCG prospect, ~17 km SW from OD. These samples are representative of Si-magnetite found in concentrations varying from massive intervals with carbonate gangue at OD to cm-dm-sized nodules or irregular pockets in variably altered granite (OD, WW) and at depths from ~700 m to 2 km. We aim to: (i) characterise; and (ii) explore the petrogenetic significance of Si-magnetite in IOCG systems from terranes with protracted geological histories.

METHODS

Si-magnetite foils prepared for TEM using focused ion beam (FIB)-SEM methods were cut across zonation patterns. Seven foils were analysed using High Angle Annular Dark Field (HAADF) STEM imaging and energy dispersive X-ray spectrometry (EDX)-STEM mapping.

RESULTS

In all samples, magnetite features µm-scale zonation patterns (Fig. 1a) which consists of Si- magnetite nanoprecipitates (Fig. 1b). An eclectic range of other nanomineral inclusions comprising silicates, carbonates, rutile, and U-, and Y±As-bearing nanoparticles (NPs; Fig.1b) were identified using EDX-STEM spot analysis/mapping, and HR-HAADF STEM imaging. Calc-silicates (±rutile) are present in Si-magnetite on the eastern side of OD and at WW, whereas NPs were only identified from the carbonate-hosted Si-magnetite.

Si-magnetite nanoprecipitates occur as darker inclusions on HAADF STEM images (Fig. 1c), varying in size from few to tens of nm, shape and density. Narrower bands (1-2 unit cells wide) of still darker Si-magnetite are stacked along d111 magnetite within the coarser precipitates, or directly in magnetite (Fig. 1c, d). Minor Al and K are measured in Si-magnetite bands from the irregular patches at the location with Fe-oxide nodules in RDG. Although both magnetite and Si-magnetite have very similar crystal structures, intensity line profiles show variation attributable to Si substitution and vacancies comparable with the maghemite model (Xu *et al.*, 2014) (Fig. 1e). Satellite reflections on Fast Fourier Transform (FFT; inset Fig. 1c) are concordant with interpretation of maghemite superstructures.

The strongest overprint is recognised as: (i) abundant lattice-scale defects (twinning, faults), K- and Al-banding, SiO_2-rich inclusion subpopulation and replacement by fluorite in the magnetite from RDG with Fe-oxide nodules; and (ii) conspicuous U, Y and As-enrichment along trails cross-cutting zonation (Fig. 1b and inset), in the carbonate-hosted, massive magnetite occurrence. Calc-silicates are present within Si-magnetite from RDG on the eastern side at OD whereas Ca-Al-bearing amphibole (tschermakite - used as a proxy for the crystal structure model (Abdu and Hawthorne, 2009)) is identified by imaging (Fig. 1f) and mapping of inclusions in magnetite from WW.

DISCUSSION AND CONCLUSIONS

Formation of mineral inclusions in all samples analysed here is attributable to coarsening of Si-magnetite nanoprecipitates during interaction with fluids enriched in elements typical of that evolution stage, e.g., K-Al-

banding and calc-silicates are compatible with early alkali- calcic alteration in IOCGs. Some of these elements can be enriched during early-mineral replacement of granite (Ca, Al, Mg, Ti from plagioclase+mica in RDG). Higher-T for the Ca- Al-amphibole stability may be a response to post-Donington metamorphism. Carbonate- hosted magnetite could be inherited from pre-existing BIF horizons in sediments intruded by RDG but with an IOCG overprint as recognised from the U-Y-As signature. Si-magnetite in samples studied here is distinct from magmatic magnetite in RDG (Cook *et al.*, 2017), or vein-magnetite in volcanics from ODD, both typified by exsolutions of ilmenite±rutile+hercynite. It also differs from occurrences elsewhere studied at the nanoscale, e.g., kin IOCG deposits containing both Ti-spinel and calc-silicates (Deditius *et al.*, 2018), or low-T metamorphosed BIFs (Huberty *et al.*, 2012; Xu *et al.*, 2014). Si-magnetite represents a petrogenetic tool if used in a given context and with the complexity of crystal- chemical phenomena adequately characterised down to the nanoscale.

REFERENCES

Abdu Y.A., Hawthorne F.C., 2009. Crystal structure and Mössbauer spectroscopy of tschermakite from the ruby locality at Fisknaesset, Greenland. Canadian Mineralogist 47, 917-926.

Cook, N.J., Ciobanu, C.L., Ehrig, K., Slattery, A., Verdugo-Ihl, M.R., Courtney-Davies, L. and Gao, W., 2017. Advances and opportunities in ore mineralogy. Minerals 7(12), 233; doi:10.3390/min7120233.

Deditius A.P., Reich, M., Simon, A.C., Suvorova, A., Knipping, J., Roberts, M.R., Rubanov, S., Dodd, A., Saunders, M., 2018. Nanogeochemistry of hydrothermal magnetite. Contributions to Mineralogy and Petrology, 173, 46; https://doi.org/10.1007/s00410-018-1474-1.

Huberty, J.M., Konishi, H., Heck, P.R., Fournette, J.H., Valley, J.W., Xu, H.F., 2012. Silician magnetite from the Dales Gorge Member of the Broc kman Iron Formation, Hamersley Group, Western Australia. American Mineralogist 97, 26–37.

Xu, H., Shen, Z., Konishi, H., 2014. Si-magnetite nano-precipitates in silician magnetite from banded iron formation: Z-contrast imaging and ab initio study. American Mineralogist 99, 2196–2202.

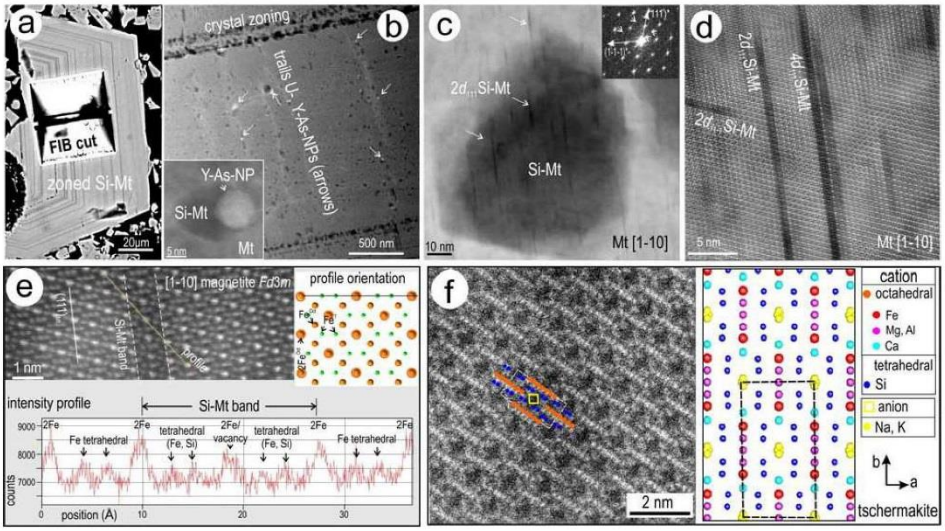


Fig. 1 (a) Back-scatter electron image showing location of FIB-cut across zoning in Si- magnetite. HAADF STEM images of Si-magnetite (b-e) and amphibole (f). Satellite reflections arrowed on FFT (inset) obtained from image in (c). Intensity profile (e) and crystal-structure models (e,f). Tschermakite (Abdu and Hawthorne, 2009) is used as a proxy for the Ca-Al-amphibole. The (Na,K) position has the best fit for the image compared to other potential Ca- amphiboles (e.g., actinolite). Imaging and EDX-STEM at 200 kV (Titan Themis; Adelaide Microscopy).

ADDITIONAL MATERIAL HH

CO-AUTHORED CONFERENCE ABSTRACT:

METAL-BEARING NANOPARTICLES IN HEMATITE

Max R. Verdugo-Ihl[1], Cristiana L. Ciobanu[1], Nigel J. Cook[1], Ashley Slattery[2], Kathy Ehrig[3],

Liam Courtney-Davies[1]

[1]*School of Chemical Engineering and Advanced Materials, The University of Adelaide, Adelaide, SA 5005, Australia*

[2]*Adelaide Microscopy, The University of Adelaide, Adelaide, SA 5005, Australia*

[3]*BHP Olympic Dam, Adelaide, SA 5000, Australia*

Conference presentation, 15th Quadrennial IAGOD Symposium, Salta, Argentina, August 28th-31st. Symposium Volume, SEGEMAR, 189-190.

15th Quadrennial IAGOD International Association on the Genesis of Ore Deposits Symposium, Salta, Argentina.



METAL-BEARING NANOPARTICLES IN HEMATITE

Max R. Verdugo-Ihl, Cristiana L. Ciobanu[1], Nigel J. Cook, Ashley Slattery, Kathy J. Ehrig, Liam Courtney-Davies

[1]*School of Chemical Engineering, The University of Adelaide - max.verdugoihl@adelaide.edu.au*

BACKGROUND

Interaction between minerals and hydrothermal fluids can result in pseudomorphic replacements if dissolution- and (re-)precipitation rates are coupled with one another (CDRR). Such processes are mediated by reaction interfaces along which transient porosity is generated, in which mineral inclusions as products of fluid-mineral interactions can precipitate (Tooth *et al.,* 2011). Hydrothermal hematite from the granite-hosted, iron-oxide-copper-gold deposit at Olympic Dam, South Australia, displays a distinct enrichment in granitophile elements (U-Pb-W-Sn-Mo) (Verdugo-Ihl *et al.*, 2017). These geochemical signatures can be modified within grains featuring partial to complete pseudomorphic replacement of hematite that results in a newly-formed hematite featuring new sets of zonation, porosity, and/or micron-scale inclusion-attached pores. Commonly, the composition of the new hematite differs markedly from that of its precursor.

Among the products of hematite replacement via CDRR discussed in (Verdugo-Ihl *et al.,* 2017), samples from bornite-chalcocite and sulphide-poor intervals represent two unusual cases. These samples, studied here at the nanoscale, originate from the upper mineralised level in the SE-part of the orebody, ~170 m apart from one another. In the first case, a mm-sized hematite grain is partially replaced by hematite depleted in W but preserves some of the other primary elements (e.g., Sn). In the second case, newly-formed oscillatory zonation patterns in hematite are defined by As and Cu-rich bands. Such patterns form overgrowths on the more common U-Pb-W-Sn-Mo oscillatory zoning.

Here, we present evidence for metal-bearing nanoparticles (NPs) occurring along trails of inclusions in such hematites and for the re-precipitation of the host hematite. These observations assist in understanding the behaviour of trace elements during CDRR and, thus, constrain mechanisms of metal remobilisation during superimposed fluid percolation.

METHODS

Foils were prepared for transmission electron microscopy (TEM) by focused ion beam (FIB)- SEM, cut across: (I) a relict U-Pb-W-Sn-Mo zonation pattern showing microfractures/pores, and (II) the unusual Cu-As-rich overgrowths. The foils were analysed using High Angle Annular Dark Field (HAADF) scanning-TEM (STEM) imaging and energy dispersive X-ray spectrometry (EDX)-STEM mapping (Titan Themis instrument operated at 200 kV).

RESULTS

Case-I hematite displays nm-sized inclusions along densely populated, longer trails (Fig. 1a) and shorter sets of splays (Fig. 1b) branching from the main trails. Up to ~200-300 nm sized inclusions occur sporadically along swarms of smaller NPs (1-5 nm). All inclusions along the main trails have comparable contents of Si, Cl, K, Na, and occasionally As (EDX-STEM spot- analysis/mapping). Metal-bearing NPs, mostly W-bearing phases (ferberite and/or WO_3; Fig. 1c) occur attached to silica-bearing inclusions (Fig. 1b).

Case-II hematite displays inclusion trails comparable to *case-I* but also shows As-rich bands of different orientation to the trails, which host As(±Pb)-bearing NPs. As in *case-I*, the trails feature inclusion populations of variable size (from ~5 up to hundreds of nm). However, the coarsest inclusions are multicomponent and often comprise metal-bearing NPs (Cu, As, Mo, W, and Sn; Fig. 1d). As in *case-I*, elements such as K, Na, and Cl are measurable throughout the composite inclusions. The presence of such elements, as well as rounded voids (Fig. 1a, d), suggest that coarser inclusions correspond to fluid inclusions containing a volatile phase that were opened during FIB-milling. The occurrence of clustered Cu-NPs (5-10 nm) is also noted on the walls of voids. High-resolution HAADF-STEM imaging of hematite along the trails displays nanodomains of variable orientation, defects and sets of twinning (Fig. 1e), which differs from the host hematite that consists of a single grain almost devoid of defects. This is evidence that the hematite along the inclusion trails is a fine-grained precipitate formed during interaction between precursor hematite and pervading fluids.

DISCUSSION AND CONCLUSIONS

Metal-bearing NPs along splays branching with fluid inclusion trails are sourced by the release of W and other elements from primarily-zoned domains in host hematite. Evolution of this process led to precipitation of W-depleted

domains adjacent to areas studied here. The antipathetic behaviour of W relative to other granitophile elements (e.g., Sn) may be attributed to their different complexation behaviour during interaction with the pervading fluid at the reaction front. Given the close association between W- and silica-bearing NPs along the splays, we speculate about the reaction of silica-bearing fluids interactive with W but not with other elements.

Results indicate 'open system behaviour' of granitophile elements, including U, in domains that may otherwise be considered reliable for high-precision U-Pb dating (see Courtney-Davies *et al.*, 2018). The presence of metal-bearing fluid inclusions also shows the role played by CDRR in trapping metals released during interaction with fluids. In this case, S-depleted fluids can be invoked to explain precipitation of native elements as NPs, correlating with the presence of Cu-Au alloys, and indeed coarser particles of native copper (Verdugo-Ihl *et al.*, 2017).

REFERENCES

Courtney-Davies, L., Ciobanu, C.L., Tapster, S.R., Cook, N.J., Ehrig, K.J., Kennedy, A.K., Condon, D.J., Verdugo-Ihl, M.R., Wade, B.S., Gilbert, S.E., 2018. The U-Pb systematics of hydrothermal hematite; Insights from the IOCG system at Olympic Dam, South Australia, 15th Quadrennial Symposium of the International Association on the Genesis of Ore Deposits (IAGOD) this volume.

Tooth, B., Ciobanu, C.L., Green, L., O'Neil, B., Brugger, J., 2011. Bi-melt formation and gold scavenging from hydrothermal fluids: An experimental study, Geochimica et Cosmochimica Acta, 75, 5423-5443. doi: 10.1016/j.gca.2011.07.020.

Verdugo-Ihl, M.R., Ciobanu, C.L., Cook, N.J., Ehrig, K.J., Courtney-Davies, L., Gilbert, S., 2017. Textures and U-W-Sn-Mo signatures in hematite from the Olympic Dam Cu-U-Au-Ag deposit, South Australia: Defining the archetype for IOCG deposits, Ore Geology Reviews, 91, 173-195. doi: 10.1016/j.oregeorev.2017.10.007.

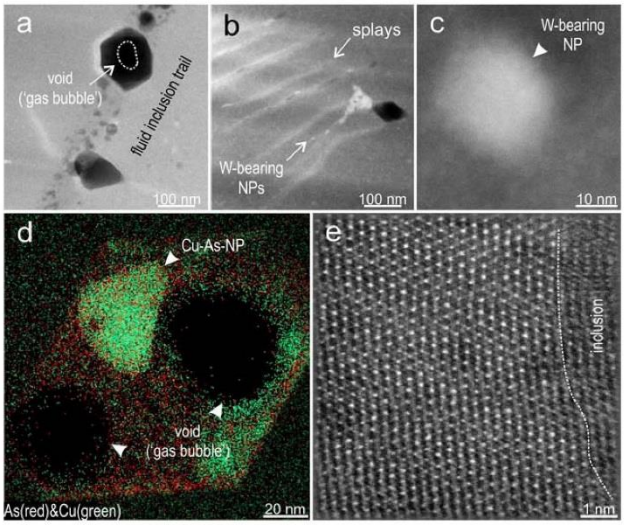


Fig. 1. HAADF-STEM images (a-c, e) and EDX-STEM map (d) showing aspects of inclusions and metal-bearing NPs in recrystallised hematite. See text for further explanations.

ADDITIONAL MATERIAL II

CO-AUTHORED CONFERENCE ABSTRACT:

GEOLOGICAL SETTING OF BIF ORES, MIDDLEBACK RANGES, SOUTH AUSTRALIA

William M. Keyser[1], Cristiana L. Ciobanu[1], Nigel J. Cook[1], **Liam Courtney-Davies[1]**, Holly Feltus[2], Geoff Johnson[2], Allen Kennedy[3], Kathy Ehrig[4]

[1]School of Chemical Engineering and Advanced Materials, The University of Adelaide, Adelaide, SA 5005, Australia

[2]SIMEC Mining, Level 2, 169 Fullarton Road, Dulwich, SA 5065, Australia

[3]John de Laeter Centre, Curtin University of Technology, Bentley, WA 6102, Australia

[4]BHP Olympic Dam, Adelaide, SA 5000, Australia

Conference presentation, 15th Quadrennial IAGOD Symposium, Salta, Argentina, August 28th-31st. Symposium Volume, SEGEMAR, 191-192.

15th Quadrennial IAGOD International Association on the Genesis of Ore Deposits Symposium, Salta, Argentina.



GEOLOGICAL SETTING OF BIF ORES, MIDDLEBACK RANGES, SOUTH AUSTRALIA

William Keyser[1], Cristiana L. Ciobanu, Nigel J. Cook, Liam Courtney-Davies, Holly Feltus, Geoff Johnson, Allen Kennedy, Kathy Ehrig

[1]*School of Chemical Engineering, The University of Adelaide - william.keyser@adelaide.edu.au*

INTRODUCTION

The Middleback Ranges form a 60 km-long, N-S striking BIF-hosted iron ore belt in the northeastern Eyre Peninsula, Gawler Craton, South Australia, comprising >20 discrete deposits and prospects (Fig. 1A). The belt is hosted within a granite-gneissic basement terrane considered of Archean to Paleoproterozoic age (Szpunar *et al.,* 2011). Various mafic rocks of debated age are found concordant or discordant to the BIFs along the belt. Iron-oxides from BIFs and ores throughout the belt exhibit textural variation and modification of geochemical signature resulting from overprinting event(s), e.g., interaction with base-metal bearing fluids (As, Sb), or elements attributable to granitic affiliation (Sn, Mo, W, U, REE+Y) (Dmitrijeva *et al.,* 2018, Keyser *et al.,* 2018). The variation of iron-oxide chemistry seen throughout the belt emphasises the need to investigate local deposit settings. One such example is recognized at Iron Count (Fig. 1A) where hematite mineralization shows evidence for interaction with fluids derived from granitic/volcanic rocks emplaced during a ~1790 Ma intracontinental rifting event (Fig. 1B).

Here, we present petrographic and geochronological data for mafic rocks and granitoids associated with several orebodies from the Middleback Ranges with the purpose of better constraining environments of BIF deposition and subsequent tectonomagmatic events that may have impacted on iron-oxide geochemistry.

METHODS

The sample suite for the present study comprises amphibole-bearing mafic rock types and granites. Sensitive high-resolution ion microprobe (SHRIMP) data for zircons separated and concentrated from the samples was obtained using a SHRIMP II at the John De Laeter Centre, (Perth, Western Australia). Uranium-bearing hematite from one deposit was dated by Laser-Ablation Inductively-Coupled Plasma-Mass Spectrometry (LA-ICP-MS) using GJ zircon as internal standard (Adelaide Microscopy).

RESULTS

Granites preserve magmatic alkali-feldspars but display varying degree of alteration whereby magmatic plagioclase (oligoclase) and biotite are rarely observed. Hydrothermal alteration is recognized as calcic (garnet-titanite-calcite-apatite) and potassic (Ba-bearing K- feldspar) in the northern (Iron Monarch) and central (Iron Baron) parts of the belt, respectively. In the south (Iron Magnet), syn-deformational alteration of the granitic basement, thrust onto BIF sequences, is expressed as shears affecting feldspar phenocrysts and comprising new micas, albite and a variety of REE-minerals.

Mafic rocks concordant with BIF sequences at Iron Magnet display a marked schistosity and preserve assemblages recording amphibolite-facies metamorphism (Mg-Fe- and Ca- amphiboles, almandine, biotite, corundum), as well as accessories attributable to an igneous origin (magnetite with trellis-like exsolution of ilmenite). These are nonetheless retrogressed to chlorite facies and locally affected by metasomatism (tourmalinization). In contrast to such lithologies, NW-SE trending mafic dikes crosscutting BIFs are more common throughout the belt. These display doleritic textures consisting of Ca-amphibole and plagioclase and contain Fe-Ti oxides, apatite and baddeleyite as accessories.

SHRIMP U-Pb zircon ages (207Pb/206Pb weighted means) at ~3.1 Ga from granites across the belt are interpreted as the timing of magmatic crystallization (Fig. 1B), whereas the amphibolite at Iron Magnet yields an age of 2670±18 Ma, interpreted as the emplacement age. Zircon from dikes in the central part of the belt produced a spread of ages pointing towards younger emplacement <1.0 Ga. U-Pb dating of hematite from ores from the Iron Knight deposit also yielded young (~650 Ma) ages (Fig. 1B).

DISCUSSION AND CONCLUSIONS

The consistent ages of ~3.1 Ga for the studied granites suggest a more extensive distribution of the ~3.15 Ga Cooyerdoo Granite suite (and other granites ~100 Ma older still, e.g., Sultan) than previously recognised, and support the existence of an Archean basement beneath the entire Middleback Ranges BIF sequence. Although no granite ages attributable to the regionally expansive Donington Magmatic Suite (~1850 Ma) or Hiltaba Suite (~1590 Ma) were found, overprints during post-Archean metamorphism and/or magmatic events (Fig. 1B) are recognizable

from retrograde metamorphism and hydrothermal alteration affecting both granites and amphibolites. These correlate with zircon domains of variable Pb-loss yielding discordant data.

The distribution of mafic rocks throughout the belt suggests intervals of magmatism contemporaneous with BIF deposition, which extended until <1.0 Ga. However, a firm age for dikes requires further constraints. Nonetheless, the present study confirms that dikes were emplaced throughout the belt during younger, tectonothermal events and likely affected BIFs and related ores, e.g. the younger ~650 Ma U-Pb age (Fig. 1B) obtained for Iron Count hematite. Importantly, the 2670±18 Ma age obtained from the dated amphibolite concordant with BIF supports their deposition during the Archean.

REFERENCES

Dmitrijeva, M., Metcalfe, A.V., Ciobanu, C.L., Cook, N.J., Frenzel, M., Keyser, W.M., Johnson, G., Ehrig, K., 2018. Discrimination and variance structure of trace element signatures in hematite: a case study of BIF-mineralization from the Middleback Ranges, South Australia. Mathematical Geosciences (in press). https://doi.org/10.1007/s11004-018-9734-1.

Keyser, W.M., Ciobanu, C.L., Cook, N.J., Johnson, G., Feltus, F., Johnson, S., Dmitrijeva, M., Ehrig, K., Nguyen, P., 2018. Petrography and trace element signatures of iron-oxides in deposits from the Middleback Ranges, South Australia: from banded iron formation to ore. Ore Geology Reviews 93, 337-360.

Szpunar, M., Hand, M., Barovich, K., Jagodzinski, E., Belousova, E., 2011. Isotopic and geochemical constraints on the Paleoproterozoic Hutchison Group, southern Australia: Implications for Paleoproterozoic continental reconstructions. Precambrian Research 187, 99-126.

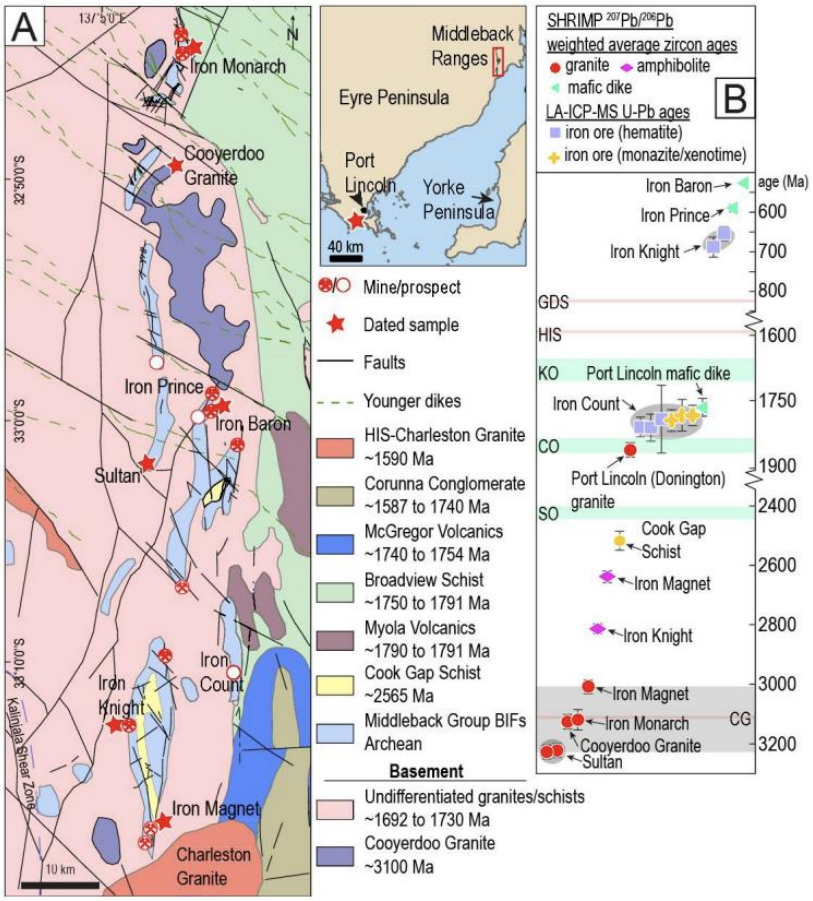


Figure 1. A) Geological map of the Middleback Ranges. B) U-Pb ages for rocks and hematite ores (as marked) in the context of the tectonomagmatic events affecting the eastern Eyre Peninsula. CG-Cooyerdoo Granite; CO-Cornian Orogeny; GSD-

ADDITIONAL MATERIAL JJ

CO-AUTHORED CONFERENCE ABSTRACT:

A MULTIPLATFORM APPROACH TO ORE MINERALOGY: ADVANCES AND FUTURE PROSPECTS

Angus K.O. Netting[1], Cristiana. L. Ciobanu[2], Nigel J. Cook[2], Ben P. Wade[1], Ashley Slattery[1], Max R. Verdugo-Ihl[2], Liam Courtney-Davies[2], Kathy Ehrig[3]

[1] *Adelaide Microscopy, The University of Adelaide, Adelaide, SA 5000, Australia;*

[2]*School of Chemical Engineering and Advanced Materials, The University of Adelaide, Adelaide, SA 5005, Australia*

[3] *BHP Olympic Dam, Adelaide, SA 5000, Australia*

Conference presentation. 16th European Workshop on Modern Developments and Applications in Microbeam Analysis (EMAS 2019), Norwegian University of Technology and Science, Trondheim, Norway, 19-23 May 2019

Abstract

In the last decade, the rapid technological advancement of micro- and nano-imaging and analytical techniques has transformed the field of ore mineralogy. The increasing spatial resolution and limit of detection of these techniques has allowed the physical and chemical signature of the minerals to be determined that would otherwise have been impossible in the not too distant past. The technological advancement of these techniques has met with a concurrent change to the way we approach analytical mineralogy. Increases in the sensitivity of analytical instruments now allows critical petrogenetic trace chemical data to be obtained from minerals that were otherwise impossible to analyse quantitatively with microbeam techniques. *In-situ* nanoscale imaging and analytical characterisation is becoming an increasingly important field for understanding how the chemical signatures we measure at the micron-scale are distributed at the atomic level within the mineral. A complementary and crucial aspect of these imaging and analytical techniques has been the development of new geochronometers such as the U-Pb hematite geochronometer, allowing for important temporal information to be assigned to observable chemical changes. As a result, there is an increasing recognition that a holistic approach, encompassing both ore minerals and gangue, and across all spatial scales, is necessary. In the context of the ore deposit that hosts them, the chemical and structural characterisation of mineral assemblages can give important insights on fundamental questions of solid-state chemistry and ore-forming processes. It follows that broad regional- or deposit-scale genetic models can be tested and validated via observation and analysis of minerals down to the smallest scale, thus enabling improved exploration models. Increased volumes of data generated at different scales of observation on the same samples will in turn generate additional fundamental questions and catalyse further technological advancements. Fields likely to be the focus of future advancement include the atomic-scale distribution of metals within ore minerals, and the roles played by nanoparticles in that distribution. This includes observation of lattice-scale structural changes to minerals as they incorporate these metals as a response to changing physiochemical conditions.

1. Introduction

The present-day ore mineralogist is tremendously fortunate to have a large number of advanced analytical methods at hand, which can, particularly when used in combination, *in-situ*, on the same material, and bridging different scales of observation, provide extraordinary levels of information impossible a generation ago (Cook et al. 2017). Although the generation of large

volumes of data can at times present its own problems regarding the necessity of rigorous, time-consuming data quality control, and increased resolution of ever smaller features may often expose unexplained complexities, it is nevertheless an extraordinarily exciting time to be working in the field.

Using examples from published work carried out in the laboratories of Adelaide Microscopy, we show how increased analytical capabilities offer the potential to resolve outstanding questions in ore mineralogy. Analytical techniques and methodologies reviewed here include laser ablation inductively coupled plasma mass spectrometry (LA-ICP-MS); recent developments in U-Pb hematite geochronology and associated preparation of a matrix-matched hematite standard for microbeam analysis; and high-angle annular dark field scanning transmission electron microscopy (HAADF STEM) applied to mixed-layer minerals, nanoparticle mapping and other problems in ore mineralogy.

2. LA-ICP-MS; imaging of trace elements and temporal constraints

The ability to both accurately and precisely measure trace chemical variations of minerals *in-situ* has led to a prolific increase of this tool being applied to mineralogical problems over the last two decades (Sylvester 2008, Cook et al. 2016 and references therein). Coupled with more traditional "spot" analysis, more recent development of this technique as an imaging tool to map the distribution of trace elements at the grain scale has helped validate models of ore formation at the deposit scale. The rapid and relatively inexpensive nature of the technique coupled with its excellent detection limits, complements other traditional microanalytical techniques commonly used, such as scanning electron microscopy (SEM) and electron probe microanalysis (EPMA).

The combination of all these techniques – *in-situ* on the same sample – allow for generation of large, representative datasets informing about elemental deportment in ore or gangue minerals that can aid in the development of models for ore genesis, underpin geochemical vectors for mineral exploration, and help guide optimization of mineral processing strategies (Cook et al. 2016) The LA-ICP-MS platform also offers the capability for rapid *in-situ* geochronology, providing important temporal constraints on ore-forming processes (Woodhead et al. 2016). Commonly, U-Pb dating is applied to minerals such as zircon and monazite but is rapidly being extended to other dateable minerals more readily relatable to mineralising and alteration events, including hematite, apatite, cassiterite and epidote-group minerals.

2.1. Spot analysis vs. elemental maps

Traditional LA-ICP-MS analysis consists of focussing a beam of pulsed UV light at a fixed position on the surface of a sample at which ablation will occur. The energy of the laser beam is transferred to the material and if above the ablation threshold volatilisation of the sample will occur. This volatilisation involves the formation of nanoparticles composed of the ablated material, which are transported via gas flow (usually He+Ar mix) from the ablation site into an ICP-MS where the elements of interest are measured. Many analytical aspects in both the laser and analysis mass spectrometer need to be considered for quality analyses, including, but certainly not limited to, factors such as downhole fractionation at the site of ablation (e.g. Gilbert et al. 2014, Zhu et al. 2017), mass bias within the spectrometer (Günther and Koch 2008), standards used for quantitative analysis (e.g. Danyushevsky et al. 2011) and isobaric interferences.

The spatial resolution of analysis is inherently tied to the size of the laser beam used for analysis, and can be varied within each manufacturers software, usually anywhere from a few micron up to 100's of micron in diameter. However as elemental detection in ICP-MS is a physical transport process of ablated particles into a mass spectrometer, larger diameter laser spots give better detection limits due to the greater volume of ablated material and thus larger quantities of nanoparticles produced. As such typical quantitative laser ablation of minerals use spots sizes ranging from tens of microns to ~100 µm. As such, LA-ICP-MS will never approach the spatial resolution offered by e-beam techniques such as EPMA, however it provides superior detection limits, usually in the ppb range, at least for most heavy elements, with elements traditionally difficult to measure such as REE (due to interference issues) becoming relatively straightforward in a variety of matrices such as feldspars (Kontonikas-Charos et al. 2017), apatite (Krneta et al. 2017), or hematite (Verdugo-Ihl et al. 2017; Keyser et al. 2018).

During spot analysis, traditionally the laser beam is kept firing at a single location for on average ~0.5-1 minute depending on the purpose of analysis. During this period we are measuring the elements of interest repeatedly to give us time-resolved analysis. Due to the nature of laser ablation, we are continuously drilling down into our mineral of interest, and as such the time-resolved signal acquired relates to how each of the measured masses are changing subsurface. The depth of the ablation pit over the course of each analysis is highly dependent on the laser energy utilised and nature of the mineral matrix being ablated and can range anywhere from a few microns to tens of microns deep in the case of soft sulphides like galena or chalcopyrite (George et al. 2015, 2018). Figure 1 displays some typical downhole spot

analysis profiles from the mineral hematite (α-Fe_2O_3). The elemental trends downhole reflects a combination of the homogeneity of the mineral being ablated (i.e. does the mineral contain any inherent chemical zonation?), in addition to the presence of other minerals as micro-/nanoscale inclusions within the primary mineral (seen as "spikes" in certain elements, at least in case when those inclusions are of sufficient size).

This measurement volume differs to normal e-beam methods of measurement such as EPMA, where at operating conditions of 15 kV interaction volumes in hematite are on the order of one micron (ignoring secondary fluorescence effects).

The more recent development of utilising LA-ICP-MS as a trace element mapping tool has allowed visualisation of elemental distributions that would require extreme analytical conditions, or otherwise impossible to detect via traditional e-beam methods. The process involves setting up a series of parallel laser rasters over the area of interest, along which the laser beam travels at a speed set by the user. In this way time resolved intensity data is collected, which can be stitched together into a 2-D images with commercial software and quantified if the appropriate microanalytical standards are available. Figure 2 displays an example of LA-ICP-MS maps of an aggregate of pyrite grains.

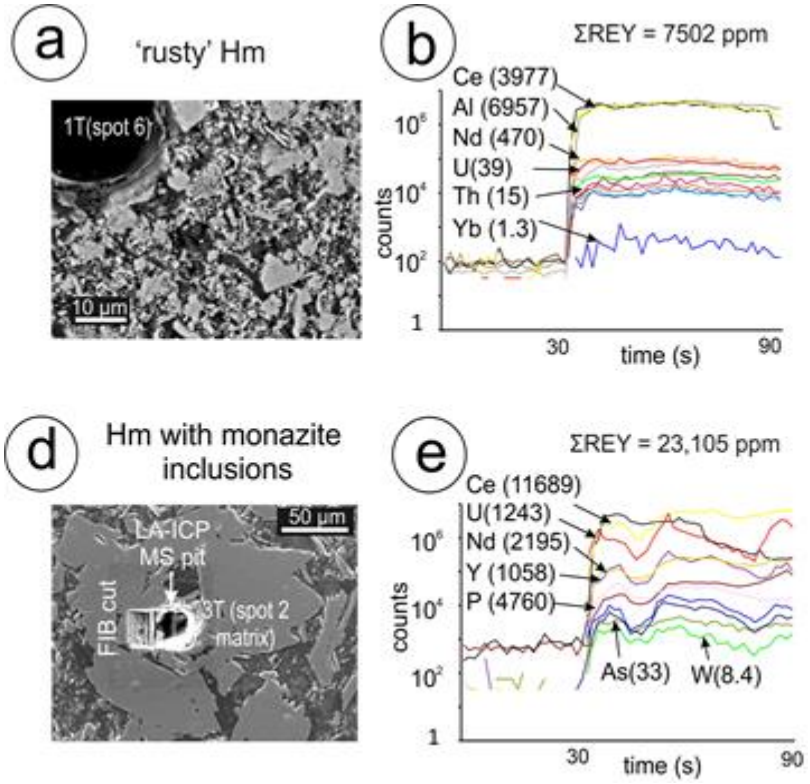


Figure 1. (a) and (d) Secondary electron (SE) images of hematite from Olympic Dam, South Australia; (b) time-resolved downhole elemental intensities of laser pit shown in (a). Note consistent flat elemental profiles indicating either homogeneous material is being ablated or that these elements occur as evenly distributed nanoscale inclusions within hematite; (e) time

resolved downhole profile of laser pit shown in (d). Note uneven nature of signals for P and REE, suggesting the presence of subsurface micron-sized monazite inclusions. FIB-SEM extraction of a foil taken adjacent to ablation pit, and subsequent analysis by TEM confirmed the presence of monazite inclusions. Figure reproduced from Cook et al. (2016).

Immediately obvious in the figure is the oscillatory zoning in As, Co, and Ni, which represent minor element concentrations (1000's of ppm) that would otherwise be measurable by X-ray mapping techniques such as EPMA, albeit at a worse signal/noise ratio. These three elements occur within solid solution in pyrite, often displaying oscillatory zoning patterns. The remaining mapped elements illustrated (Ga, Ag, Bi, and W) are present in much lower concentrations (maximum of a few hundred ppm), and display a drastically different elemental distribution. Silver and bismuth in particular display elevated concentrations of these elements along both fractures and cleavage planes within the pyrite grains, the latter usually invisible in typical back-scattered electron (BSE) SEM imaging. The concentration levels of these elements would make them undetectable by normal e-beam techniques. LA-ICP-MS mapping allows heterogeneous distributions of trace elements present at concentrations of just a few ppm to be seen clearly (e.g. the fine-scale Te and Se zoning in arsenopyrite; Cook et al. 2013).

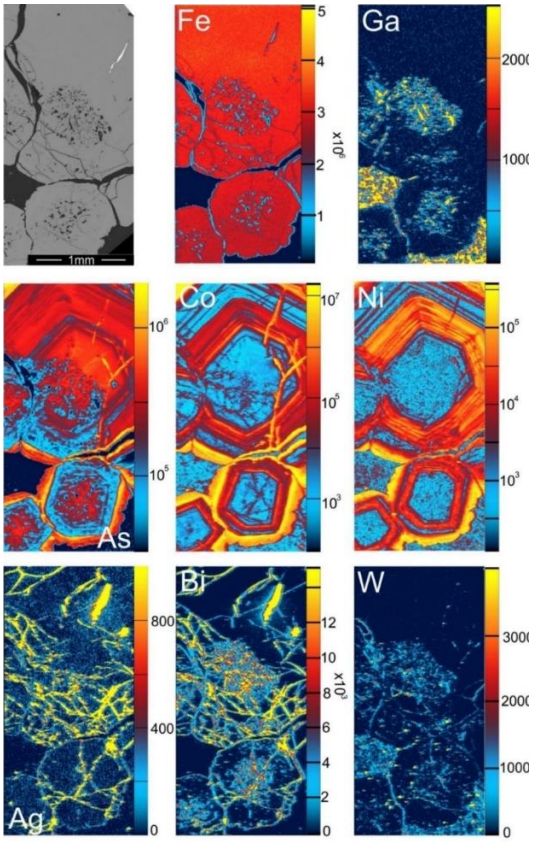


Figure 2. Laser ablation maps of pyrite grains. Intensity colour scale in CPS. Note oscillatory zoning of As, Co, and Ni, indicating solid solution lattice bound elements within pyrite. Ga, Ag, Bi, W display elevated concentration along microfractures and cleavage planes. Figure reproduced from Cook et al. (2016).

LA-ICP-MS mapping removes the inherently biased nature of the alternate option of a spot traverse over the mineral in question, and often reveals elemental distributions that would have otherwise been missed. Experience with different mineral matrices, including those for which only limited trace element data was hitherto available, e.g. baryte (Schmandt et al. 2019), indicates that a majority of minerals are chemically zoned, and thus spot analysis alone will not provide adequate characterisation of trace element concentrations. The sensitive nature of the LA-ICP-MS mapping technique makes it very powerful when used in combination with other e-beam mapping techniques such as EPMA, or if complemented by other methods affording visualisation of distribution patterns at sub-micron (e.g. nanoSIMS) or nm-scale (e.g. TEM-EDS element mapping).

LA-ICP-MS mapping has two additional advantages over conventional spot analysis: Firstly, it allows a direct visualisation of the systematic preferential partitioning of trace elements between co-existing mineral phases, e.g. co-existing base metal sulphides (George et al. 2016) or common Cu-Pb-Sb-sulphosalts (Li et al. 2019a). Secondly, the method allows for ready recognition of non-traditional mineral hosts for elements of interest (e.g. the occurrence of significant concentrations of U, Sn, Mo, and W within skarn garnet; Xu et al. 2017).

2.2. New geochronological tools: microanalysis and standard development

Accurate determination of the timing of a mineralisation event can be challenging. This is often primarily due to the ambiguity of linking growth of the dated (gangue) mineral with the associated minerals hosting the metals of interest. In addition, these complex ore mineral systems may involve multiple phases of mineral growth and fluid flow events that can overprint textures and reset geochronological clocks, making unequivocal interpretation difficult. Whenever possible, it is desirable to directly date the ore minerals themselves – and successful attempts with minerals such as molybdenite, cassiterite, columbite-tantalite, and uraninite are well reported in the literature. Often, however, these datable minerals are absent or only found in very specific mineral deposits, and as such the geologist is usually bound to analysis of more traditional U-Pb geochronometers such as zircon, monazite, and rutile. However, the accessory refractory nature of these minerals and their propensity for age “inheritance” can make it difficult to directly relate the calculated age of these minerals to a mineralising event.

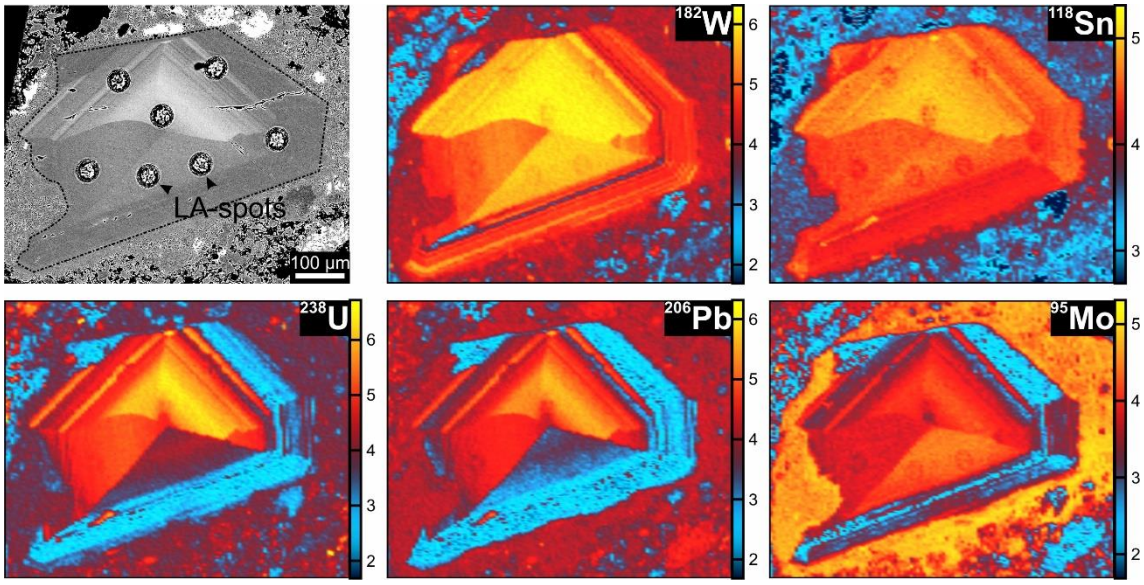


Figure 3. Laser ablation elemental maps of hematite grains. Note elevated levels of U and Pb in the oscillatory-zoned core domain (up to 1000 ppm), and 100's to 1000's ppm of W, Sn, and Mo. Scales in cps (x 10^n). Figure adapted from Verdugo-Ihl et al. (2017).

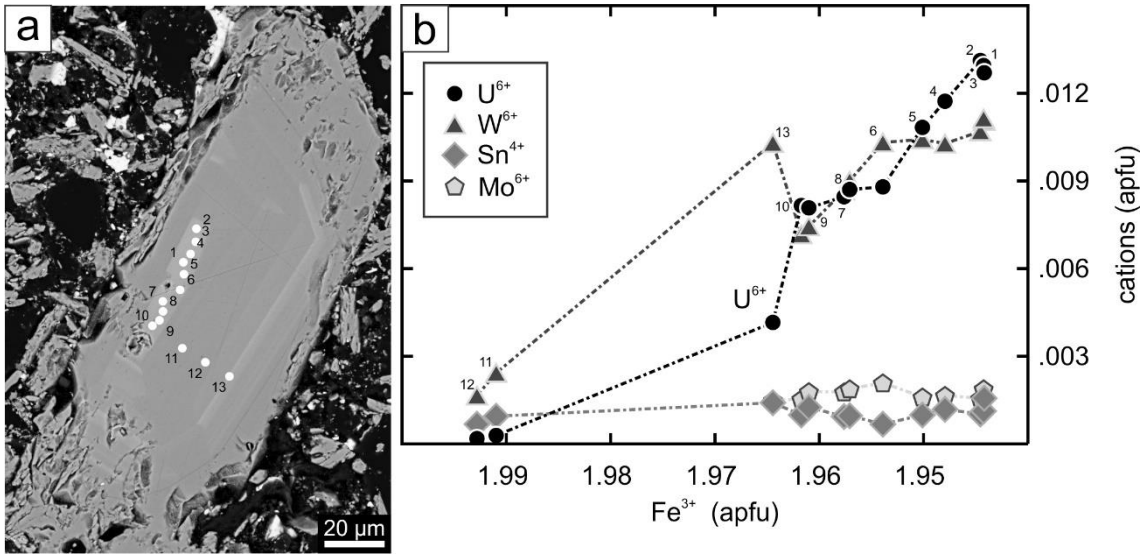


Figure 4. (a) BSE image of a typical hematite grain displaying zonation as bright zones. Spots represent EPMA analytical locations. (b) EPMA compositional spot data of grain displayed in (a). Note increasingly elevated U and W values corresponding with bright zones in BSE. Figure adapted from Verdugo-Ihl et al. (2017).

As such, effort has been made to identify potential new U-Pb mineral geochronometers. Hematite, a common Fe-oxide in many types of ore deposits, and the most abundant minerals in many Iron Oxide Copper Gold (IOCG) deposits. The presence of U- and Pb-bearing hematite at Olympic Dam (Oreskes 1990), the world's largest IOCG-type deposit (Ehrig et al. 2012) therefore raised the question of whether the mineral could be accurately and precisely dated. Textural evidence for crystallization of hematite at the same time as Cu mineralization allows

age relationships to established with confidence. The high levels, and grain-scale distribution of U endowment in Olympic Dam hematite were first quantified by Ciobanu et al. (2013); additional data and LA-ICP-MS maps are given by Verdugo-Ihl et al. (2017). These studies showed that hematite readily accepts up to wt% levels U and radiogenic Pb into its crystal structure without major structural modification or radiogenic damage to its lattice due to α-decay (Figures 3 and 4).

Ciobanu et al. (2013) attempted to date these grains via LA-ICP-MS and since then, additional efforts have been made to date Olympic Dam hematite with similar results (Courtney-Davies et al. 2016, 2019a). Courtney-Davies et al. (2016) also provided U-Pb hematite age for mineralization from Carajas, Brazil. Recently, Keyser et al. (2019) gave a U-Pb hematite age for upgrading of banded iron formation iron ores from the Middleback Ranges, South Australia, using hematite that contained just 7-24 ppm U. This demonstrates both the versatility and huge potential of the new method.

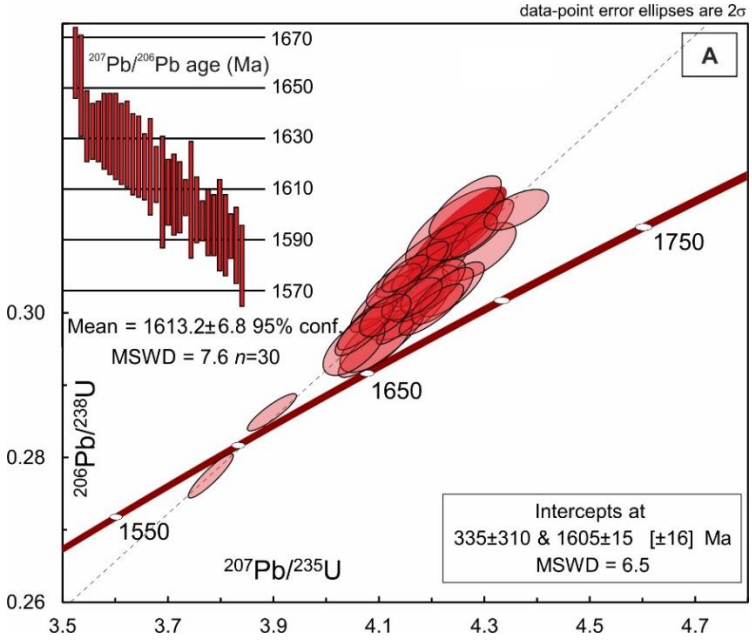


Figure 5. U-Pb concordia diagram adapted from Courtney-Davies et al. (2019a) displaying weighted mean and intercept ages of ~1600 Ma. Note "reverse discordance" of data ellipses sitting above concordia line. This is predominantly an analytical artefact induced by correcting U-Pb ratios in analysed hematite against a zircon reference material.

In the absence of U-Pb hematite reference material, both studies utilised a zircon reference material to correct U-Pb data. As discussed in previous sections, the process of laser ablation is a physical process in which the sample is volatilized, and ablated material is transported to the ICP-MS as nanoparticles. As such different minerals ablate differently dependant on their composition, resulting in a different downhole U-Pb ratio profile between hematite and zircon.

This results in inaccuracies in determination of U-Pb ratios of hematite when using zircon as a standard.

To circumvent this problem, suitable samples have been sent for U-Pb analysis via "standardless" Isotope Dilution Thermal Ionisation Mass Spectrometry (ID-TIMS) and begun development of a synthetic hematite U-Pb microanalytical standard. Initial ID-TIMS results give excellent accuracy and precision with expected age of the mineralization event (Figure 5; Courtney-Davies et al. 2019a). Although accepted as the "gold standard" of U-Pb analysis, ID-TIMS is a time-consuming and costly process and a need was recognised for more routine fast U-Pb analysis of hematite grains via microbeam techniques such as LA-ICP-MS or SHRIMP. To achieve this hydrated ferric oxide (HFO) has been doped with a U and Pb solution, homogenised, dried, and then converted to hematite via heating to ~700 °C (Figure 6; Courtney-Davies et al. 2019b). The resultant hematite chips display encouraging homogeneity in U-Pb ratio and concentration and are currently being further refined and analysed via ID-TIMS for certification.

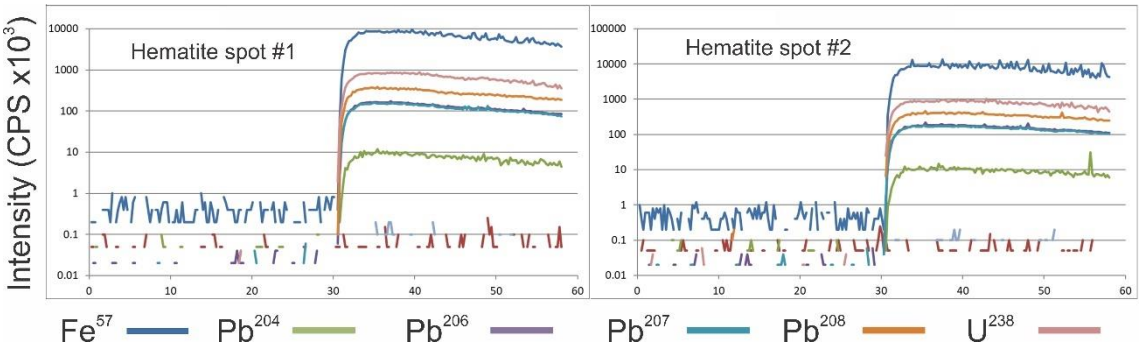


Figure 6. Representative time-resolved analysis of two separate chips. Note inhomogeneous downhole signal ^{204}Pb in spot #2, indicating some subsurface heterogeneity. Figure adapted from Courtney-Davies et al. (2019b).

3. High-resolution transmission electron microscopy

The range of techniques discussed here represent a broad spectrum in spatial resolution, ranging from exceptional elemental detection limits at scales of several to a few tens of microns, to higher resolution imaging and elemental analysis of features on polished block surfaces that may only be a few nanometres in size. Transmission electron microscopy (TEM) extends this range substantially, enabling imaging and powerful analytical techniques ranging from the micron scale down to the scale of individual atoms.

3.1 Sample preparation - Focused Ion Beam milling

Samples for TEM analysis must be thinned to electron transparency, well below 200 nm, ideally ~60 nm. An important aspect of using a multiplatform approach is the ability to link

regions of interest between techniques, which can make the precise extraction of a suitable TEM sample challenging. In order to study a specific feature within a mineral using TEM (such as a grain boundary, or compositionally-zoned domain within a specific grain), a precise method is required to extract an extremely thin section at the required location. This section must also be extracted at an exact orientation, in order to ultimately visualise the crystal lattice at the desired orientation, allowing the observation of specific grain boundaries and defects. This process is shown in Figure 7.

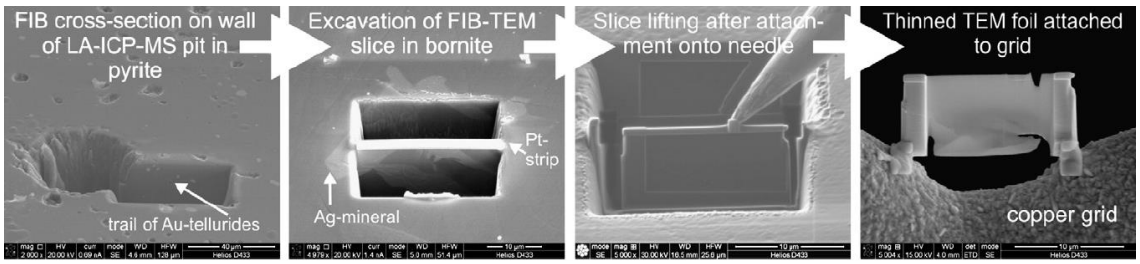


Figure 7. Sequence of analytical procedures for FIB–TEM foil preparation. Figure adapted from Ciobanu et al. (2011).

Dualbeam instruments have proven invaluable for *in-situ* preparation of TEM samples in a range of fields, including materials science, metallurgy, earth science and the semiconductor industry. These focused ion beam – scanning electron microscopes (FIB-SEM) incorporate a traditional SEM column for non-destructive imaging, and an ion column utilising heavy ions (e.g. Ga, Xe, Ar) for imaging and precise milling of the sample. The imaging/milling capability allows regions in a mineral to be precisely identified, which can be of significant advantage when that mineral has been comprehensively characterised prior to FIB-SEM work (by SEM, EPMA and LA-ICP-MS). A thin TEM cross-section (or foil), is milled and lifted from the sample. A range of artefacts that can result from milling and thinning of ore mineral, e.g. via interaction with the Ga^+ source, melting, etc., have been highlighted in Ciobanu et al. (2011).

3.2 Scanning transmission electron microscopy

Scanning transmission electron microscopy (STEM), in particular high angle annular dark-field (HAADF STEM) is proving to be an exceptional technique for the characterisation of minerals from ores. In STEM mode, the incident electron beam is focused into a small probe and raster-scanned across the sample surface, in a similar manner to the SEM. The difference between these techniques lies in the transmission of the beam through the sample, where post-sample detectors collect the electrons from different interaction events with the specimen. Although many signals are accessible simultaneously, of particular relevance is the HAADF detector. This detector is an annular type which allows electrons with little or no scattering to

pass through, while collecting the electrons scattered at high angles due to strong interactions with the atomic nuclei. The HAADF signal, importantly, is incoherent and monotonic, scaling with the thickness of the sample by $I=t$ and the elemental mass by $I=Z\sim^{2}$.

The Z-contrast observed by HAADF STEM positions the technique as exceptional for characterising minerals of direct relevance to ore deposit studies, allowing the rapid identification of fine particles (100-2500 nm) and ultrafine nanoparticles (1-100 nm) as inclusions, layer stacking in mixed layer compounds, crystal-structural motifs in large structures such as Pb-Bi-sulfosalts, as well as atom-scale defects. In addition to this, the incoherent nature of the signal results in atomic resolution images which are readily interpretable, showing the location of atoms in the lattice directly and, in simple cases, suggesting the atomic species based on observed Z contrast. Experience has shown that HAADF STEM imaging is particularly well-suited to modular minerals composed of atomic layers that differ markedly in composition and thus contrast on the images.

The ability to directly visualise these crystal structures is valuable for several reasons. Firstly, modular minerals (notably Pb-Bi-sulphosalts) may belong to structurally-defined homologous series in which changes in chemistry are accommodated by incremental changes in homology (Ciobanu et al. 2016; Li et al. 2019b). Secondly, there may exist multiple polytypes, and potentially, new mineral species, that occupy compositional space between end-members, and which can be built by combinations of two or more building blocks. For example, there exist at least 11 distinct polytypes in the bastnäsite-synchysite group of rare earth element fluorocarbonates that can be directly imaged in terms of combinations of bastnäsite (B) and synchysite (S) layers, B_2S, BS, BS_2 etc. (Figure 8; Ciobanu et al. 2017a). Thirdly, layered minerals commonly display non-stoichiometry at the scale of the electron microprobe, a phenomenon readily explained by irregular, or semi-regular intergrowths (of various amplitude) of layers at the lattice scale, as for example in Bi-chalcogenides of the tetradymite group (Ciobanu et al. 2009) – minerals commonly found in gold deposits (e.g. Ciobanu et al. 2012) and the natural equivalents of some of the best semi-conductors known. The capabilities of HAADF STEM imaging are clearly observed for the mineral tellurobismuthite, Bi_2Te_3, which displays distinct Z contrast for the bismuth and tellurium atoms as shown in Figure 9.

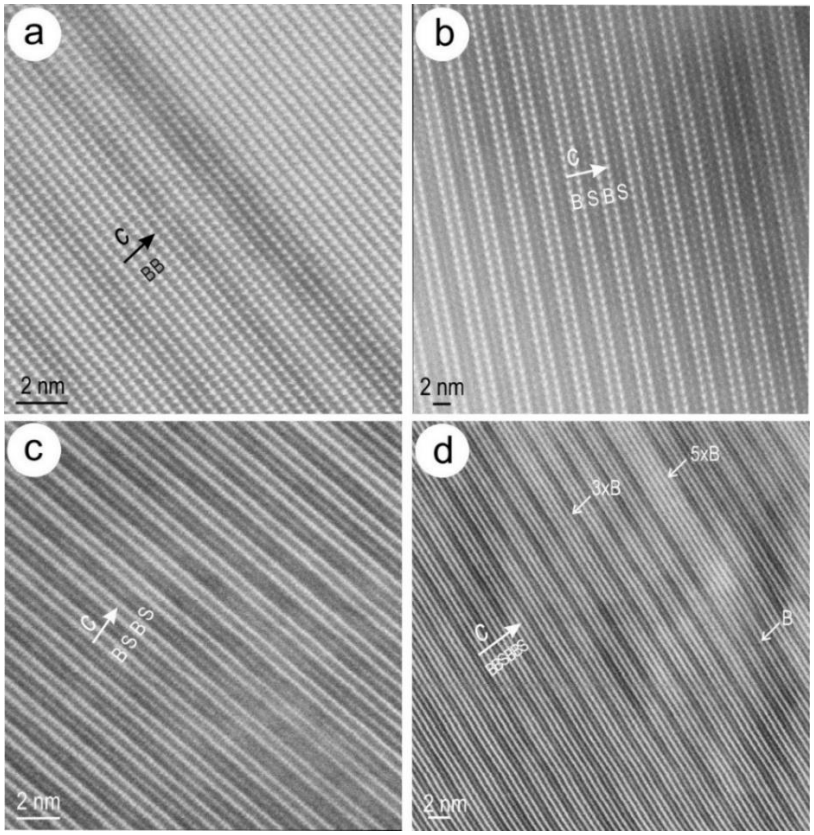


Figure 8. HAADF STEM images showing the typical stacking sequences in (a) bastnäsite down to [−1100]; (b and c) parisite down to [−1100] and [10–10] zone axis, respectively. The sequence is characterised by two rows of bright atoms (B slab) and one row of slightly darker atoms ('f' layer in the middle of the S slab); and (d) B_2S imaged down to [10–10] zone axis. Figure reproduced from Ciobanu et al. (2017).

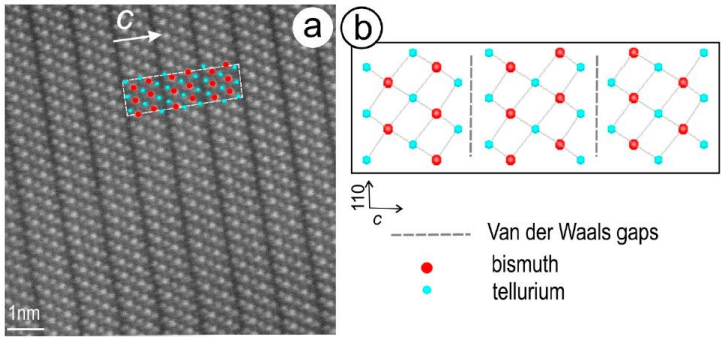


Figure 9. (a) High-resolution HAADF STEM image of tellurobismuthite (Bi_2Te_3), and (b) crystal structure model for the mineral, showing the positions of the atoms and the Van der Waals gaps between the layers. Figure reproduced from Cook et al. (2017).

3.3. Incorporation and release of trace elements in ore minerals

The high resolution and Z contrast achievable by HAADF STEM make the technique ideal for study of lattice-scale incorporation and release of heavy elements into and from mineral matrices. One good example is uranium within the crystal lattice of hematite. Studies of U-being hematite are important for development of U-Pb geochronology, as documented above, and also for mineral processing. In U-W-Sn-Mo oscillatory-zoned hematite from Olympic Dam

that experienced overprinting (Verdugo-Ihl et al. 2017), uraninite nanoparticles were identified (Figure 10) from domains where fluid percolation assisted U release from the crystal lattice of hematite and led to crystal zoning re-shaping.

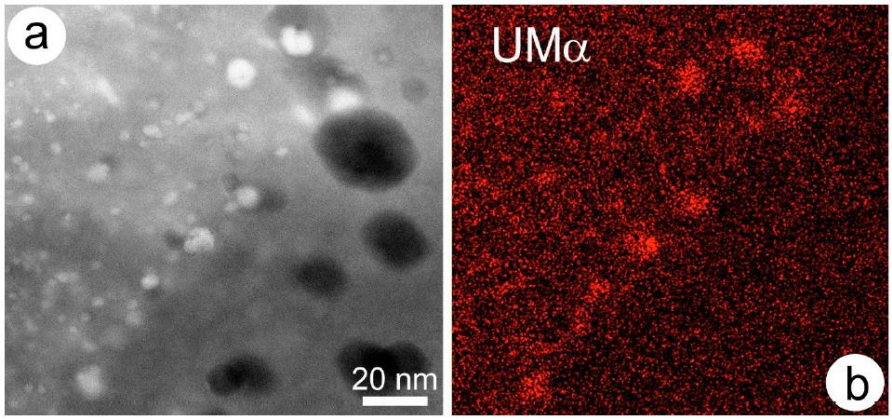


Figure 10. Hematite mineral from the Olympic Dam orebody, showing (a) HAADF STEM image of uraninite nanoparticles and (b) EDX map of the imaged area, confirming the distribution of uranium. Figure reproduced from Cook et al. (2017).

HAADF STEM study of FIB-prepared foils extracted from across zoning in hematite containing some of the most U (up to 2-3 wt.% UO_2) from Olympic Dam shows instead presence U-free nm-scale needles of magnetite (Fe_3O_4) (Ciobanu et al. 2018; Figure 11). Lattice scale faults assist transformation of the rhombohedral hematite$_{[1\text{-}10]}$ into the cubic magnetite$_{[1\text{-}10]}$ lattice (Figure 11a). The epitaxial relationships between the two Fe-oxides are preserved in the widest needles (10-20 nm wide; Figure 11b). Identification of magnetite against other phases such as cubic (β-, or γ-) Fe_2O_3 polymorphs is based upon EDS-STEM mapping showing higher-Fe and lower-O composition of the needle relative to host hematite as well, as by STEM simulation of the images (Figure 11c). Such needles are not found in domains of high-W (up to several wt% WO_3) or low-U (up to thousands of ppm U) hematite. Results suggest that such magnetite needles only occur at the upper U solubility limit in the U-bearing hematite lattice. This is most significant for understanding reliability of such grains for high-precision U-Pb dating.

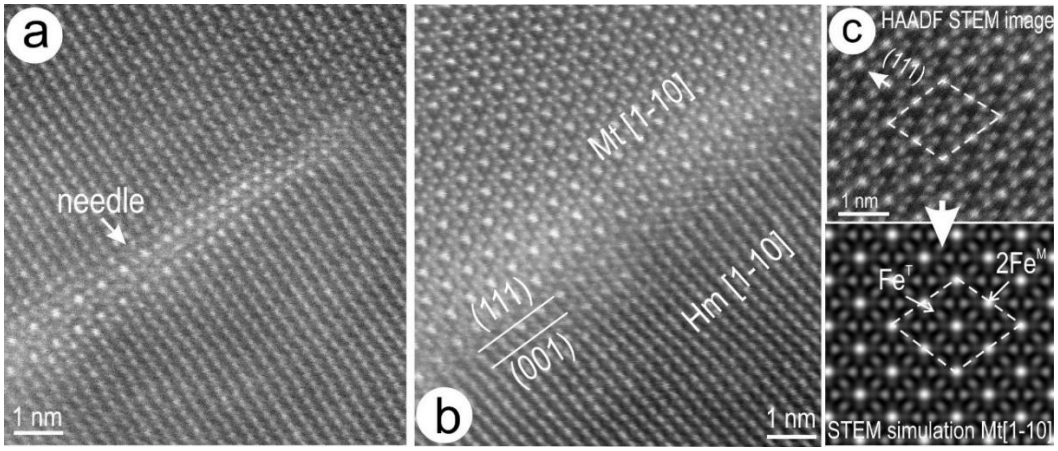


Figure 11. HAADF STEM images showing needles of magnetite (Mt) in U-rich hematite (Hm): a few atoms in width (a) and some tens of nm-wide (b). (c) Image and STEM simulation of Mt on [1-10] zone axis. T=tetrahedral site; M=octahedral site. Images obtained at 200 kV. STEM simulation using WinHREM^{TM} version 4.1 software. Figure adapted from Ciobanu et al. (2018).

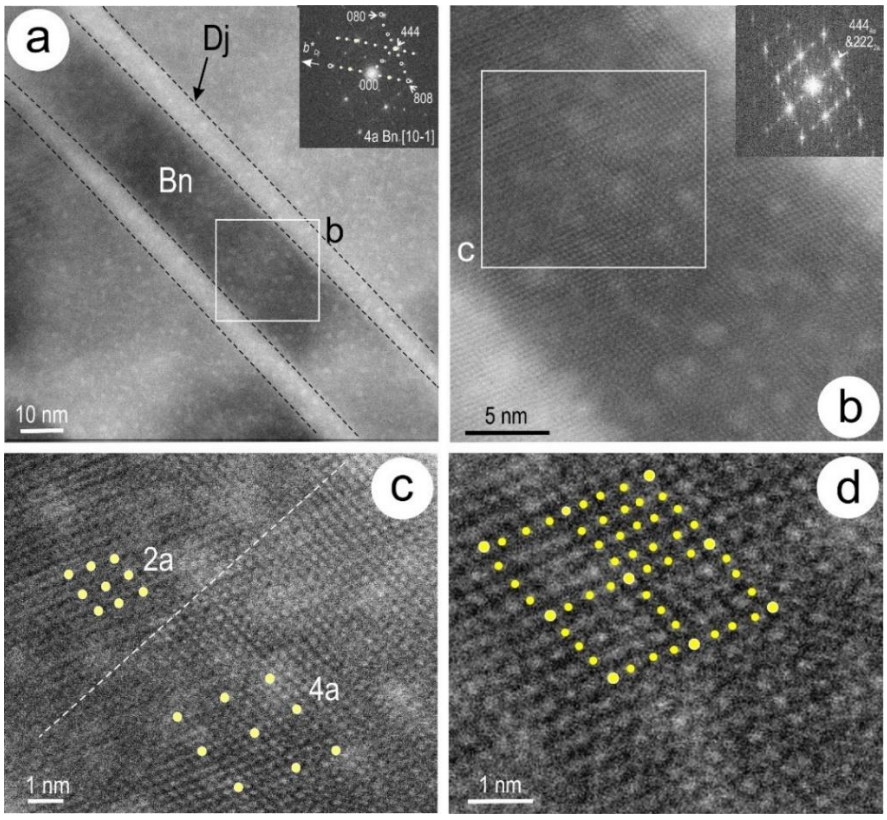


Figure 12. Atomic-scale HAADF STEM images of bornite superstructures down to the [101] zone axis. (a) Bornite with marginal djurleite. FFT (inset) shows coherent intergrowths between 4*a* bornite and djurleite. (b) Close-up of the area marked in (a) showing domain heterogeneity throughout the bornite. Satellite reflections (FFT in inset) shows four-fold periodicity but with variation in intensity indicating the co-existence of 2*a* and 4*a* superstructures. (c) 2*a* and 4*a* superstructure domains in the area marked in (b). Yellow dots highlight structural motifs for the two species. (d) Detail of 4*a* superstructure showing atom distribution throughout the superlattice as marked by the yellow dots. Note faint variation in grey-scale intensity of the atoms that make the superstructure unit cell. Bn—bornite; Dj—djurleite. Figure adapted from Owen et al. (2018).

3.4. Other crystal structural modifications: superstructures

Phase transitions and crystal structural modifications can occur in mineral that crystallise from high temperature solid-solutions; Cu-Fe-sulphides are a typical example. Cu-Fe-sulphides from different ore zones at Olympic Dam feature nanoscale intergrowths, superstructure domains (larger structures built from a simpler crystal structure in which mixed sites, vacancies, or impurities are ordered over *'n'* unit cells) and antiphase boundary domains that can be interpreted as exsolution, coarsening and phase transformation during cooling from high-T solid solutions in the system Cu-Fe-S and sub-systems according to published phase diagrams (Ciobanu et al. 2017b). Bornite (Cu_5FeS_4) superstructures are formed by Fe vacancy ordering (Ding et al. 2005). These (Figure 12) are documented for the first time by HAADF STEM imaging of Cu-ores from South Australia (Owen et al. 2018).

4. Concluding remarks

Using different techniques on the same sample material, bridging scales of observation from that of mm down to Ångstroms, and proceeding from least- to most-destructive, has facilitated significant advances in the research field. In particular, samples extracted *in-situ* by FIB-SEM after micron-scale characterisation possess extraordinary versatility. Not only can HAADF STEM imaging provide insights down to the nanoscale but FIB-prepared foils can be readily examined by electron back-scatter diffraction (EBSD) to understand crystal orientations and modification thereof (as applied to uraninite; Macmillan et al. 2016), or synchrotron X-ray studies to determine the speciation of component ions (as applied to Cu in sphalerite; Cook et al. 2015).

Acknowledgements

Much of the research reported here was funded from the ARC Research Hub for Australian Copper-Uranium (Grant IH130200033) and the 'FOX' project, supported by BHP Olympic Dam and the South Australian Government Mining and Petroleum Services Centre of Excellence.

References

Ciobanu, C.L., Pring, A., Cook, N.J., Self, P., Jefferson, D., Dima, G., Melnikov, V., 2009. Chemical-structural modularity in the tetradymite group: a HRTEM study. *Am. Mineral.* 94, 517–534.

Ciobanu, C.L., Birch, W.D., Cook, N.J., Pring, A., Grundler, P.V., 2010. Petrogenetic significance of Au-Bi-Te-S associations: the example of Maldon, Central Victorian gold province, Australia. *Lithos* 116, 1-17.

Ciobanu, C.L., Cook, N.J., Utsunomiya, S., Pring, A., Green, L., 2011. Focussed ion beam - transmission electron microscopy applications in ore mineralogy: bridging micron- and

nanoscale observations. *Ore Geol. Rev.* 42, 6-31.

Ciobanu, C.L., Wade, B., Cook, N.J., Schmidt Mumm, A., Giles, D., 2013. Uranium-bearing hematite from the Olympic Dam Cu-U-Au deposit, South Australia; a geochemical tracer and reconnaissance Pb-Pb geochronometer. *Precambr. Res.* 238, 129-147.

Ciobanu, C.L., Cook, N.J., Maunders, C., Wade, B.P., Ehrig, K., 2016. Focused Ion Beam and Advanced Electron Microscopy for Minerals: Insights and Outlook from Bismuth Sulphosalts. *Minerals* 6, 112.

Ciobanu, C.L., Kontonikas-Charos, A., Slattery, A., Cook, N.J., Ehrig, K., Wade, B.P., 2017a. Short-range stacking disorder in mixed-layer compounds: A HAADF STEM study of bastnäsite-parisite intergrowths. *Minerals* 7, 227.

Ciobanu, C.L., Cook, N.J., Ehrig, K., 2017b. Ore minerals down to the nanoscale: Cu-(Fe)-sulphides from the iron oxide copper gold deposit at Olympic Dam, South Australia. *Ore Geol. Rev.* 81, 1218–1235.

Ciobanu, C.L., Slattery, A., Verdugo-Ihl, M., Courtney-Davies, L., Cook, N.J., Ehrig, K., 2018. Crystal structural modifications in U-rich, oscillatory-zoned hematite. Abstract, Goldschmidt-2018, Boston, MA, USA, 12-17 August 2018.

Cook, N.J., Ciobanu, C.L., Meria, D., Silcock, D., Wade, B., 2013. Arsenopyrite-pyrite association in an orogenic gold ore: tracing mineralization history from textures and trace elements. *Econ. Geol.* 108, 1273–1283.

Cook, N.J., Etschmann, B., Ciobanu, C.L., Howard, D., Williams, T., Rae, N., Pring, A., Geraki, K., Chen, G.R., Brugger, J., 2015. Synchrotron XANES study of a Ge-(Fe)-bearing sphalerite. *Minerals* 5, 117-132.

Cook, N.J., Ciobanu, C.L., George L., Ehrig, K., 2016. Trace Element Analysis of Minerals in Magmatic-Hydrothermal Ores by Laser Ablation Inductively-Coupled Plasma Mass Spectrometry: Approaches and Opportunities. *Minerals*, 6, 111.

Cook, N.J., Ciobanu, C.L., Ehrig, K., Slattery, A., Verdugo-Ihl, M.R., Courtney-Davies, L., Gao, W., 2017. Advances and opportunities in ore mineralogy. *Minerals*. 7, 233.

Courtney-Davies, L., Zhu, Z., Ciobanu, C.L., Wade, B.P., Cook, N.J., Ehrig, K., Cabral, A.R., Kennedy, A., 2016. Matrix-matched iron-oxide laser ablation ICP-MS U-Pb geochronology using mixed solution standards. *Minerals* 6, 85.

Courtney-Davies, L., Tapster, S.R., Ciobanu, C.L., Cook, N.J., Verdugo-Ihl, M.R., Ehrig, K.J., Kennedy, A.K., Gilbert, S.E., Condon, D.J., Wade, B.P., 2019a. A multi-technique evaluation of hydrothermal hematite U-Pb isotope systematics: Implications for ore deposit geochronology. *Chem. Geol.*, in press, https://doi.org/10.1016/j.chemgeo.2019.03.005

Courtney-Davies, L., Ciobanu, C.L., Richardson, M.W., Prosser, N., Verdugo-Ihl, M., Wade, B.P., Gilbert, S.E., Ehrig, K.J., Cook, N.J., 2019b. Synthesis of U-Pb doped hematite using a hydrated ferric oxide approach. *J. Crystal Growth*, in press, https://doi.org/10.1016/j.jcrysgro.2019.02.053

Danyushevsky, L., Robinson, P., Gilbert, S., Norman, M., Large, R., McGoldrick, P., Shelley, M., 2011. Routine quantitative multi-element analysis of sulphide minerals by laser ablation ICP-MS: Standard development and consideration of matrix effects. *Geochem. Explor. Environ. Anal.* 11, 51–60.

Ding, Y., Veblen, D.R., Prewitt, C.T., 2005. High-resolution transmission electron microscopy (HRTEM) study of 4*a* and 6*a* superstructure of bornite Cu_5FeS_4. *Am. Mineral.* 90, 1256–1264.

Ehrig, K., McPhie, J., Kamenetsky, V., 2012. Geology and Mineralogical Zonation of the Olympic Dam Iron Oxide Cu-U-Au-Ag Deposit, South Australia, in: Hedenquist, J.W., Harris, M., Camus, F. (Eds.), Geology and Genesis of Major Copper Deposits and Districts of the World: A Tribute to Richard H. Sillitoe. *Soc. Econ. Geol., Spec. Publ.* 16, p. 237–267.

George, L., Cook, N.J., Ciobanu, C.L., Wade, B.P., 2015. Trace and minor elements in galena: A reconnaissance LA-ICP-MS study. *Am. Mineral.* 100, 548-569.

George, L.L., Cook, N.J., Ciobanu, C.L., 2016. Partitioning of trace elements in co-crystallized sphalerite-galena–chalcopyrite hydrothermal ores. *Ore Geol. Rev.* 77, 97-116.

George, L.L., Cook, N.J., Crowe, B.B.P., Ciobanu, C.L., 2018. Trace elements in hydrothermal chalcopyrite. *Mineral. Mag.* 82, 59-88.

Gilbert, S.E., Danyushevsky, L.V., Goemann, K., Death, D., 2014. Fractionation of sulphur relative to iron during laser ablation-ICP-MS analyses of sulphide minerals: Implications for quantification. *J. Anal. Atom. Spectrom.* 29, 1024–1033.

Günther, D., Koch, J., 2008. Formation of aerosols generated by laser ablation and their impact on elemental fractionation in LA-ICP-MS. In: Laser Ablation ICP-MS in the Earth Sciences: Current Practices and Outstanding Issues (P. Sylvester, ed.), Mineral. Assoc, Canada Short Course Volume 40, pp. 19–34.

Keyser, W.M., Ciobanu, C.L., Cook, N.J., Johnson, G., Feltus, F., Johnson, S., Dmitrijeva, M., Ehrig, K., Nguyen, P., 2018. Petrography and trace element signatures of iron-oxides in deposits from the Middleback Ranges, South Australia: from banded iron formation to ore. *Ore Geol. Rev.* 93, 337-360.

Keyser, W., Ciobanu, C.L., Cook, N.J., Dmitrijeva, M., Courtney-Davies, L., Feltus, H., Gilbert, S., Johnson., G, Ehrig, K., 2019. Iron-oxides constrain BIF evolution in terranes with protracted geological histories: The Iron Count prospect, Middleback Ranges, South Australia. *Lithos* 324, 20-38.

Kontonikas-Charos, A., Ciobanu, C.L., Cook, N.J., Ehrig, K., Krneta, S., Kamenetsky, V.S., 2017. Feldspar evolution in the Roxby Downs Granite, host to Fe-oxide Cu-Au-(U) mineralisation at Olympic Dam, South Australia. *Ore Geol. Rev.* 80, 838–859.

Krneta, S., Ciobanu, C.L., Cook, N.J., Ehrig, K., Kontonikas-Charos, A., 2017. Rare earth element behaviour in apatite from the Olympic Dam Cu-U-Au-Ag deposit, South Australia. *Minerals* 7, 135.

Li, W., Cook, N.J., Ciobanu, C.L., Xie, G.Q., Wade, B.P., Gilbert, S.E., 2019a. Trace element distributions in (Cu)-Pb-Sb sulfosalts from the Gutaishan Au-Sb deposit, South China: Implications for formation of high fineness native gold. *Am. Mineral.* 104, 425–437.

Li, W., Ciobanu, C.L., Slattery, A., Cook, N.J., Liu, W., Wade, B.P., Xie, G.Q., 2019b. Chessboard structures: atom-scale imaging of homologues from the kobellite series. *Am. Mineral.* 104, 459–462.

Macmillan, E., Ciobanu, C.L., Ehrig, K., Cook, N.J., Pring, A., 2016. Replacement of uraninite by bornite via coupled dissolution-reprecipitation: Evidence from texture and microstructure. *Can. Mineral.* 54, 1369-1383.

Owen, N.D., Ciobanu, C.L., Cook, N.J., Slattery, A., Basak, A. 2018. Nanoscale Study of Clausthalite-Bearing Symplectites in Cu-Au-(U) Ores: Implications for Ore Genesis. *Minerals* 8, 67.

Oreskes, N., 1990. Uranium content of Olympic Dam hematite: Implications for fluid chemistry and ore depositional mechanisms. Program with Abstracts, 8th Quadrennial IAGOD Conference, Ottawa, Canada, p. A137.

Schmandt, D.S., Cook, N.J., Ehrig, K., Gilbert, S., Wade, B.P., Rollog, M., Ciobanu, C.L., Kamenetsky, V.S., 2019. Uptake of trace elements by baryte during copper ore processing: A case study from Olympic Dam, South Australia. *Minerals Eng.* 135, 83-94.

Sylvester, P. Laser Ablation ICP-MS in the Earth Sciences: Current Practices and Outstanding Issues. Mineralogical Association of Canada: Québec, QC, Canada, 2008, Vol. 40.

Verdugo-Ihl, M.R., Ciobanu, C.L., Cook, N.J., Ehrig, K.J., Courtney-Davies, L., Gilbert, S., 2017. Textures and U-W-Sn-Mo signatures in hematite from the Olympic Dam Cu- U-Au-Ag deposit, South Australia: Defining the archetype for IOCG deposits. *Ore Geol. Rev.* 91, 173–195.

Woodhead, J.D., Horstwood, M.S.A., Cottle, J.M., 2016. Advances in isotope ratio determination by LA–ICP–MS. *Elements* 12, 317–322.

Xu, J., Ciobanu, C.L., Cook, N.J., Zheng, Y., Sun, X., Wade, B.P., 2016. Skarn formation and trace elements in garnet and associated minerals from Zhibula copper deposit, Gangdese Belt, southern Tibet. *Lithos* 262, 213–231.

Zhu, Z.Y., Jiang, S.Y., Yang, T., Ciobanu, C.L., Cook, N.J., 2016. Sulfur isotope fractionation in pyrite during laser ablation: Implications for laser ablation multiple collector inductively coupled plasma mass spectrometry mapping. *Chem. Geol.* 450, 223-234,

ADDITIONAL MATERIAL KK

CO-AUTHORED CONFERENCE ABSTRACT:

TUNGSTEN-BEARING NANOPARTICLES IN HEMATITE: INSIGHTS INTO OPEN SYSTEM BEHAVIOUR OF MINERAL GEOCHRONOMETERS

Max R. Verdugo-Ihl[1], Cristiana L. Ciobanu[1], Nigel J. Cook[1], **Liam Courtney- Davies**[1], Kathy Ehrig[3], Ashley Slattery[2]

[1]*School of Chemical Engineering and Advanced Materials, The University of Adelaide, Adelaide, SA 5005, Australia*

[2]*Adelaide Microscopy, The University of Adelaide, Adelaide, SA 5005, Australia*

[3]*BHP Olympic Dam, Adelaide, SA 5000, Australia*

Poster presentation at TIGeR 2019, Perth, Australia, September 11th-13th.

Tungsten-bearing nanoparticles in hematite: insights into open system behaviour of mineral geochronometers

Max R. Verdugo-Ihl[1,], Cristiana L. Ciobanu[1], Nigel J. Cook[1], Liam Courtney-Davies[1], Kathy Ehrig[2], Ashley Slattery[3]*

[1] School of Chemical Engineering and Advanced Materials, The University of Adelaide, Adelaide, SA, 5005, Australia;*max.verdugoihl@adelaide.edu.au; cristiana.ciobanu@adelaide.edu.au; nigel.cook@adelaide.edu.au; liam.courtney-davies@adelaide.edu.au

[2] BHP Olympic Dam, Adelaide, SA 5000, Australia; kathy.ehrig@bhp.com

[3] Adelaide Microscopy, The University of Adelaide, Adelaide, SA, 5005, Australia; ashley.slattery@adelaide.edu.au

Formation of metal-bearing nanoparticles (NPs) in minerals can fingerprint replacement processes at the atomic scale, at which element exchange occurs. Advanced transmission electron microscopy, particularly Z-contrast imaging using high-angle annular dark field scanning transmission electron microscopy (HAADF STEM), on a sample extracted *in-situ* from locations of petrogenetic interest is a powerful approach for understanding trace element incorporation in and their release from a host mineral (Ciobanu et al. 2016). Copper-As NPs were documented from oscillatory-zoned U-W-Sn-Mo-bearing hematite that also shows atypical Cu-As-zoning and weave-twinning patterns (Verdugo-Ihl et al. 2017, 2019). These NPs occur either along (i) trails of inclusions interpreted as inclusions opened during sample preparation, or (ii) within Si-Al-K-bearing planes that also host sericite. Formation of the two types of NPs was interpreted as due to interaction between hematite and hydrolytic fluids whereby fluid supersaturation and phase separation during depressurisation account for different regimes of fluid-rate infiltration along pre-existing twin planes. Uranium-Pb systematics in the same type of hematite have been addressed by various microbeam techniques and high-precision U-Pb ID TIMS on material microsampled from U-rich domains (Courtney-Davies et al. 2019), which showed both closed and open system behaviour for U-Pb isotopes.

Here we address the issue of nanoscale manifestation of open system behaviour in hematite from samples that display compositional zoning affected by preferential removal of some elements, in this case W. Selective removal of different elements from the zonation patterns was previously interpreted as replacement reactions coupling dissolution with reprecipitation rates (CDRR; Verdugo-Ihl et al. 2017). The sample was collected from ~170 m below the hematite hosting Cu-As-NPs from a downwards-plunged block in the SE part of the Olympic Dam deposit, South Australia. The TEM foil was obtained by focused ion beam SEM by cutting across microfractures occurring along the boundary between preserved U-W-Sn-Mo zonation (microsampled for ID TIMS U-Pb geochronology) and a W-depleted domain (Verdugo-Ihl et al. 2017). Bright field (BF) and HAADF STEM imaging, as well as STEM energy-dispersive X-ray spectrometry (EDX) mapping and spot analysis, were performed using a high-resolution, probe-corrected FEI Titan Themis S/TEM at 200 kV (all instruments are housed at Adelaide Microscopy). Imaging of the foil shows domains with fractures and splays adjacent to twin planes in hematite which all display W and Pb enrichment on STEM EDX maps (Fig. 1a, b). In addition, W-bearing NPs occur along trails proximal to such structures (Fig. 1c). High-resolution HAADF STEM imaging shows the twin planes have nm-wide crests with defects showing swelling and displacement (Fig. 1d). The hematite on each of the twin planes shows sets of misorientation directions, in addition to superstructuring. In detail, arrangements of the Fe atoms in the dumbbell motif typical of $[12\bar{1}]_{\text{hematite}}$ show alternating brighter and darker units indicative of a 2-fold superstructure (Fig. 1e), and also indicated by Fast Fourier Transforms displaying satellite reflections.

The results allow for the following interpretation. Micron-scale fracturing of the oscillatory zoned hematite results in mechanical twinning and these provide nm-wide channels for fluid infiltration resulting in removal of W and Pb from primary zoning. The twin directions are marked by measurable W and Pb inferring these structures are effective traps for them. In contrast, the W-bearing NPs do not concentrate Pb, implying that this element is lost from the

system during fluid channeling. Defects and structural modifications of hematite are evidence for strain-induced effects in the crystal lattice during fluid percolation. As in the case of the Cu-As-NPs, we show that nanoscale studies can fingerprint fluid-mineral interaction. Additionally, the data demonstrates open system behaviour of U-Pb systematics in hematite. This is concordant with ID TIMS data recording high common Pb in the aliquots prepared from this grain (Courtney-Davies et al. 2019).

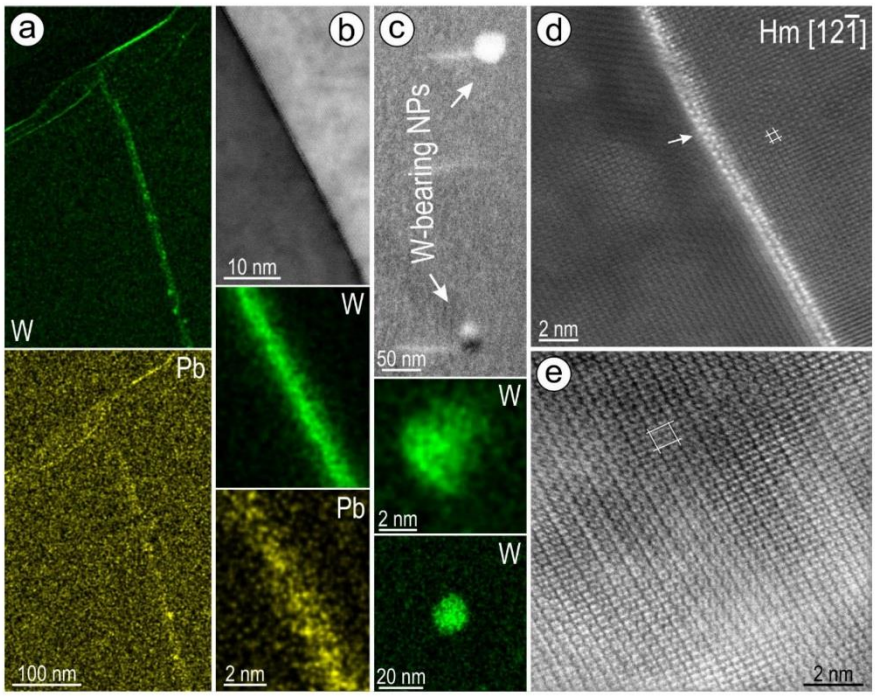


Figure 1. (a) STEM EDX maps of hematite (Hm) domain with fractures and splays adjacent to a twin plane featuring W- and Pb-enrichment. (b) BF STEM and STEM EDX maps of W- and Pb-enrichment along twin boundary. (c) HAADF STEM image and TEM EDX maps of W-bearing NPs along a trail; note that no Pb is detected within such NPs. (d) HAADF STEM image of Hm with a twin crest (arrowed) enriched in W-Pb, and featuring defects (swelling and displacement). (e) HAADF STEM image of Hm adjacent to the twin plane displaying 2-fold superstructuring (white lines) of the basic dumbbell motif on the [12$\bar{1}$] zone axis.

Overall, these results attest to the importance of CDRR in the formation of NPs and domains that are relatively enriched in certain trace elements, and how these impact on trace element signatures measured by microbeam techniques (LA-ICP-MS and/or EPMA). If characterized at appropriate scales of observation, such features can provide evidence for open system behaviour in hematite and other minerals. This, in turn, carries implications for the separation of daughter radionuclides from parent isotopes (Rollog et al. 2019) and the modification of isotopic systematics, both impacting on the accuracy and precision of geochronometers (e.g. U-Pb system in hematite; Courtney-Davies et al. 2019).

References

Ciobanu CL, Cook NJ, Maunders C, Wade BP, Ehrig, K (2016). Minerals 6, 112; doi:10.3390/min6040112.

Courtney-Davies L, Tapster S, Ciobanu CL, Cook NJ, Verdugo-Ihl MR, Ehrig KJ, Kennedy AK, Gilbert SE, Condon DJ, Wade BP (2019). Chem. Geol. 513, 54–72. doi:10.1016/j.chemgeo.2019.03.005.

Rollog M, Cook NJ, Guagliardo P, Ehrig KJ, Kilburn M (2019) Geochem.: Explor. Environm. Analysis. doi:10.1144/geochem2018-038.

Verdugo-Ihl MR, Ciobanu CL, Slattery A, Cook NJ, Ehrig K, Courtney-Davies L (2019) Minerals 9, doi:10.3390/min9070388.

Verdugo-Ihl MR, Ciobanu CL, Cook NJ, Ehrig KJ, Courtney-Davies L, Gilbert S (2017) Ore Geol. Rev. 91, 173–195. doi:10.1016/j.oregeorev.2017.10.007.

CHAPTER 12

REFERENCES

Allen, S., McPhie, J., Ferris, G., Simpson, C., 2008. Evolution and architecture of a large felsic igneous province in western Laurentia: the 1.6 Ga Gawler Range Volcanics, South Australia. Journal of Volcanology and Geothermal Research 172, 132-147.

Anderson, T., 2002. Correction of common lead in U–Pb analyses that do not report ^{204}Pb. Chemical Geology 192, 59–79.

Apukhtina, O.B., Kamenetsky, V.S., Ehrig, K., Kamenetsky, M.B., Maas, R., Thompson, J., McPhie, J., Ciobanu, C.L., Cook, N.J., 2017. Early, deep magnetite-fluorapatite mineralization at the Olympic Dam Cu-U-Au-Ag deposit, South Australia. Economic Geology 112, 1531–1542.

Apukhtina, O.B., Kamenetsky, V.S., Ehrig, K., Kamenetsky, M.B., McPhie, J., Maas, R., Meffre, S., Goemann, K., Rodemann, T., Cook, N.J., Ciobanu, C.L., 2016. Postmagmatic magnetite–apatite assemblage in mafic intrusions: a case study of dolerite at Olympic Dam, South Australia. Contributions to Mineralogy and Petrology 171, 15.

Bai, T., Koster van Groos, A., 1999. The distribution of Na, K, Rb, Sr, Al, Ge, Cu, W, Mo, La, and Ce between granitic melts and coexisting aqueous fluids. Geochimica et Cosmochimica Acta 63, 1117–1131.

Barkov, A.Y., Martin, R.F., Shi, L., LeBarge, W., Fedortchouk, Y., 2008. Oscillatory zoning in stanniferous hematite and associated W- and Bi-rich minerals from Canadian Creek, Yukon, Canada. Canadian Mineralogist 46, 59-72.

Barton, M.D., 2014. Iron oxide (-Cu-Au-REE-P-Ag-U-Co) systems. In Treatise on Geochemistry, 2nd ed.; Elsevier: Amsterdam, the Netherlands, 13, 515–541.

Bastrakov, E.N., Skirrow, R.G., Davidson, G.J., 2007. Fluid Evolution and Origins of Iron Oxide Cu-Au Prospects in the Olympic Dam District, Gawler Craton, South Australia. Economic Geology 102, 1415–1440.

Becker, J.S., 2002. State-of-the-art and progress in precise and accurate isotope ratio measurements by ICP-MS and LA-ICP-MS. Journal of Analytical Atomic Spectrometry 17, 1172-1185.

Belousova, E.A., Griffin, W.L., O'Reilly, S.Y., Fisher, N.I., 2002. Igneous zircon: trace element composition as an indicator of source rock type. Contributions to Mineralogy and Petrology 143, 602–622.

BHP, 2019. BHP Annual report 2019. 316, https://www.bhp.com/investor-centre/annual-report-2019/.

Black, L.P., Kamo, S.L., Williams, I.S., Mundil, R., Davis, D.W., Korsch, R.J., Foudoulis, C., 2003. The application of SHRIMP to Phanerozoic geochronology; a critical appraisal of four zircon standards. Chemical Geology 200 (1–2), 171–188.

Blissett, A.H., Creaser, R.A., Daly, S.J, Flint, D.J., Parker, A.J., 1993. Gawler Range Volcanics. In: Drexel, J.F., Preiss, W.V., Parker, A.J. (eds.), The Geology of South Australia. Volume 1, The Precambrian: Adelaide, Geological Survey of South Australia, Bulletin 54, 107–131.

Bowden, B., Fraser, G., Davidson, G.J., Meffre, S., Skirrow, R.G., Bull, S., Thompson, J., 2017. Age constraints on the hydrothermal history of the Prominent Hill iron oxide copper-gold deposit, South Australia. Mineralium Deposita 52, 863–881.

Bowring, J. F., McLean, N.M., Bowring, S.A., 2011. Engineering cyber infrastructure for U-geochronology. Tripoli and U-Pb Redux. Geochemistry Geophysics Geosystems 12, Q0AA19, doi: 10.1029/2010GC003479.

Bowring, J.F., McLean, N.M., and Bowring, S.A., 2011, Engineering cyber infrastructure for U-geochronology: Tripoli and U-Pb Redux: Geochemistry, Geophysics, Geosystems 12, Q0AA19.

Buddington, A.F., Lindsley, D.H., 1964. Iron-titanium oxide minerals and synthetic equivalents. Journal of Petrology 5, 310–357.

Candela, P.A., 1991. Physics of aqueous phase evolution in plutonic environment. American Mineralogist, 76, 1081-1091.

Candela, P.A., Blevin, P.L., 1995. Do some miarolitic granites preserve evidence of magmatic volatile phase permeability. Economic Geology, 90 (8), 2310–2316.

Carr, L.K., Korsch, R.J., Holzschuh, J., Costelloe, R.D., Meixner, A.J., Matthews, C., Godsmark, B., 2010. Geological interpretation of seismic reflection lines 08GA-C1 and 09TE-01: Arrowie Basin, South Australia. In: Korsch, R.J., Kositcin, N., South Australian Seismic and MT Workshop 2010, Extended Abstracts. Geoscience Australia Record 2010/10, 54–65.

Cherniak, D., Watson, E.B., Grove, M., Harrison, T.M., 2004. Pb diffusion in monazite: a combined RBS/SIMS study. Geochimica et Cosmochimica Acta 68, 829–840.

Cherry, A., Ehrig, K., Kamenetsky, V., McPhie, J., Crowley, J., and Kamenetsky, M., 2018, Precise geochronological constraints on the origin, setting and incorporation of ca. 1.59 Ga surficial facies into the Olympic Dam Breccia Complex, South Australia. Precambrian Research, 315, 162-178.

Cherry, A.R., Kamenetsky, V.S., McPhie, J., Kamenetsky, M., Ehrig, K., Keeling, J.L., 2017. Post-1590 Ma modification of the supergiant Olympic Dam deposit: links with regional tectonothermal events. Proceedings, 14th SGA Biennial Meeting 'Mineral Resources to Discover', Québec City, QC, Canada, 20–23 August 2017, 847-850.

Cherry, A.R., Kamenetsky, V.S., McPhie, J., Thompson, J.M., Ehrig, K., Meffre, S., Kamenetsky, M.B., Krneta, S., 2018. Tectonothermal events in the Olympic IOCG Province constrained by apatite and REE-phosphate geochronology. Australian Journal of Earth Sciences 65, 643–659.

Cherry, A.R., McPhie, J., Kamenetsky, V.S., Ehrig, K., Keeling, J.L., Kamenetsky, M.B., Meffre, S., Apukhtina, O.B., 2017. Linking Olympic Dam and the Cariewerloo Basin: Was a sedimentary basin involved in formation of the world's largest uranium deposit?. Precambrian Research 300, 168-180.

Chew, P.J., Sylvester, M.N., Tubrett, M.N., 2011. U-Pb and Th-Pb dating of apatite by LAICPMS. Chemical Geology 280, 200–216.

Chiaradia, M., Caricchi, L., 2017. Stochastic modelling of deep magmatic controls on porphyry copper deposit endowment. Scientific Repots, 7, 44523.

Chiaradia, M., Schaltegger, U., Spikings, R.A., 2014. Time scales of mineral systems – advances in understanding over the past decade. Society of Economic Geologists, Special Publication, 18, 37–58.

Chiaradia, M., Schaltegger, U., Spikings, R.A., Wotzlaw, J.F., Ovtcharova, M., 2013. How accurately can we date the duration of magmatic-hydrothermal events in porphyry systems? Economic Geology, 108, 565–584.

Ciobanu C.L., Cook, N.J., Ehrig, K., 2017, Ore minerals down to the nanoscale: Cu-(Fe)-sulphides from the iron oxide copper gold deposit at Olympic Dam, South Australia. Ore Geology Reviews, 81, 1218–1235.

Ciobanu, C.L., Cook, N.J., Wade, B.P., Ehrig, K., 2014. Ore Minerals Down to Nanoscale: Petrogenetic Implications. Acta Geologica Sinica 88, 1441–1443.

Ciobanu, C.L., Slattery, A., Verdugo-Ihl, M., Courtney-Davies, L., Cook, N.J., Ehrig, K., 2018. Crystal structural modifications in U-rich, oscillatory-zoned hematite. Abstract, Goldschmidt Conference, Boston, MA, USA, 12-17 August 2018.

Ciobanu, C.L., Verdugo-Ihl, M.R., Slattery, A., Cook, N.J., Ehrig, K., Courtney-Davies, L., Wade, B.P., 2019. Silician Magnetite: Si–Fe-Nanoprecipitates and Other Mineral Inclusions

in Magnetite from the Olympic Dam Deposit, South Australia. Minerals 9(5), 311; https://doi.org/10.3390/min9050311.

Ciobanu, C.L., Verdugo-Ihl, M.R., Slattery, A., Cook, N.J., Ehrig, K.J., Courtney-Davies, L., 2018. Nanoscale study of silician magnetite from IOCG systems: Examples from the Olympic Dam District (South Australia). In: Proceedings of the 15th Quadrennial IAGOD Symposium, Salta, Argentina. 185-186.

Ciobanu, C.L., Wade, B.P., Cook, N.J., Mumm, A.S. Giles, D., 2013. Uranium-bearing hematite from the Olympic Dam Cu–U–Au deposit, South Australia: A geochemical tracer and reconnaissance Pb–Pb geochronometer. Precambrian Research 238, 129-147.

Ciobanu, C.L., Cook, N.J., Maunders, C., Wade, B.P., Ehrig, K. 2016. Focused Ion Beam and Advanced Electron Microscopy for Minerals: Insights and Outlook from Bismuth Sulphosalts. Minerals 6, 112.

Claoué-Long, J.C., Compston, W., Roberts, J., Fanning, C.M., 1995. Two Carboniferous ages: a comparison of SHRIMP zircon dating with conventional zircon ages and $^{40}Ar/^{39}Ar$ analysis. Geochronology time scales and global stratigraphic correlation. SEPM Special Publication 54, 3-21.

Clark, J.M., Poznik, N., Ehrig, K., Cherry, A., McPhie, J., Kamenetsky, V.S., 2018. Syn- to Post-mineralization Structural Dismemberment of the Olympic Dam Fe-Cu-U-Au-Ag Deposit, Gawler Craton. SEG 2018 Conference Abstract, Keystone, Colorado, USA.

Clemens, J.D., 1984. Water contents of silicic to intermediate magmas. Lithos, 17, 273–287.

Cline, J.S., and Bodnar, R.J., 1991. Can economic porphyry copper mineralization be generated by a typical calc-alkaline melt?. Journal of Geophysical Research, 96, 8113.

Compston, W., Williams, I.S., Meyer, C.E., 1984. U-Pb geochronology of zircons from lunar breccia 73217 using a sensitive high-mass resolution ion microprobe, Proceedings of the

fourteenth Lunar and Planetary Science Conference, Part 2: Journal of Geophysical Research 89, B525 B534.

Condon, D.J.; Schmitz, M.D., 2013. One hundred years of geochronology. Elements 9, 3–80.

Conor, C., Raymond, O., Baker, T., Teale, G., Say, P., Lowe, G., 2010. Alteration and Mineralisation in the Moonta-Wallaroo Cu-Au Mining Field Region, Olympic Domain, South Australia. In: Porter, T.M. (ed), Hydrothermal Iron Oxide Copper-Gold and Related Deposits: A Global Perspective 3, PGC Publishing, Adelaide, 1-24.

Cook, N.J., Ciobanu, C.L., George, L. Zhu, Z.Y., Wade, B., Ehrig, K., 2016. Trace element analysis of minerals in magmatic-hydrothermal ores by laser ablation inductively-coupled plasma mass spectrometry: Approaches and opportunities. Minerals 6(4), 111, doi:10.3390/min6040111.

Courtney-Davies, L., Zhu, Z., Ciobanu, C.L., Wade, B.P., Cook, N.J., Ehrig, K., Cabral, A.R., Kennedy, A., 2016. Matrix-matched iron-oxide laser ablation ICP-MS U-Pb geochronology using mixed solution standards. Minerals 6, 85.

Courtney-Davies, L., Ciobanu, C.L., Richardson, M.W., Prosser, N., Verdugo-Ihl, M.R., Wade, B.P., Gilbert, S.E., Ehrig, K., Cook., N.J., 2019. Synthesis of U-Pb doped hematite using a hydrated ferric oxide approach. Journal of Crystal Growth. 513, 48-57.

Courtney-Davies, L., Ciobanu, C.L., Tapster, S.R., Cook, N.J., Ehrig, K., Crowley, J.L., Verdugo-Ihl, M.R., Condon, D.J., in review. Opening the Magmatic-Hydrothermal Window: High-Resolution Geochronology of the Olympic Dam Iron Oxide-Cu-U-Au-Ag Deposit, South Australia. Economic Geology.

Courtney-Davies, L., Ciobanu, C.L., Verdudo-Ihl, M.R., Slattery, A., Cook, N.J., Dmitrijeva, M., Keyser, W., Wade, B.P., Domnick, U.I., Ehrig, K., Xu, J., Kontonikas-Charos, A., 2019. Zircon at the nanoscale records metasomatic processes leading to large magmatic-hydrothermal ore systems. Minerals 9, 364; doi:10.3390/min9060364.

Courtney-Davies, L., Ciobanu, C.L., Verdugo-Ihl, M.R., Cook, N.J., Ehrig, K., Benjamin P. Wade, Z.-Y. Zhu., in review. ~1760 Ma magnetite-bearing protoliths in the Olympic Dam deposit, South Australia: Implications for ore genesis and regional metallogeny. Ore Geology Reviews, 118, 103337.

Courtney-Davies, L., Ciobanu, C.L., Verdugo-Ihl, M.R., Dmitrijeva, M., Cook, N.J., Ehrig, K., Wade, B.P., 2019. Hematite geochemistry and geochronology resolve genetic and temporal links among iron-oxide copper gold systems, Olympic Dam district, South Australia. Precambrian Research 335, 105480.

Courtney-Davies, L., Richardson, M., Gilbert, S.E., Ciobanu, C.L., Verdugo-Ihl, M.R., Cook, N.J., Ehrig, K., Wade, B.P., 2018. U-Pb doped synthetic reference material for in-situ hematite geochronology. Geoanalysis 2018, Sydney, Conference Abstract.

Courtney-Davies, L., Tapster, S.R., Ciobanu, C.L., Cook, N.J., Verdugo-Ihl, M.R., Ehrig, K.J., Kennedy, A.K., Gilbert, S.E., Condon, D.J., Wade, B.P., 2019. A multi-technique evaluation of hydrothermal hematite U-Pb isotope systematics: Implications for ore deposit geochronology. Chemical Geology 513, 54-72.

Cowley, W., Conor, C., Zang, W., 2003. New and revised Proterozoic stratigraphic units on northern Yorke Peninsula. MESA Journal 29, 46-58.

Creaser, R.A., 1989. The geology and petrology of Middle Proterozoic felsic magmatism of the Stuart shelf, South Australia. Unpublished Ph.D. thesis, La Trobe University.

Creaser, R.A., 1996, Petrogenesis of a Mesoproterozoic quartz latite-granitoid suite from the Roxby Downs area, South Australia. Precambrian Research, 79, 371–394.

Creaser, R.A., and Cooper, J.A., 1993. U-Pb geochronology of Middle Proterozoic felsic magmatism surrounding the Olympic Dam Cu-U-Au-Ag and Moonta Cu-Au-Ag deposits, South Australia. Economic Geology 88, 186-197.

Creaser, R.A., Fanning, C.M., 1993. A U-Pb zircon study of the Mesoproterozoic Charleston Granite, Gawler Craton, South Australia. Australian Journal of Earth Science 40, 519–526.

Cross, K.C., 1993. Acropolis and Wirrda Well. In: Drexel, J.F., Preiss, W.V., Parker, A.J., (eds.), The geology of South Australia. vol. 1, The Precambrian. Geological Survey of South Australia, South Australia 54, 138.

Davidson, G.J., Paterson, H.L., Meffre, S., Berry, R.F., 2007. Characteristics and origin of the Oak Dam East breccia-hosted, iron oxide Cu-U-(Au) deposit: Olympic Dam region, Gawler Craton, South Australia. Economic Geology 102, 1471–1498.

Deer, W.A., Howie, R.A., Zussman, J., 2013. An Introduction to the Rock-Forming Minerals. Mineralogical Society of Great Britain and Ireland. https://doi.org/10.1180/DHZ.

Dmitrijeva, M., Ciobanu, C.L., Ehrig, K., Cook, N.J., Metcalfe, A., Verdugo-Ihl, M.R., and McPhie, J., 2019. Defining IOCG signatures through compositional data analysis: A case study of lithogeochemical zoning from the Olympic Dam deposit, South Australia. Ore Geology Reviews 105, 86–101.

Dmitrijeva, M., Ciobanu, C.L., Ehrig, K.J., Cook, N.J., Metcalfe, A., Verdugo-Ihl, M.R., McPhie, J., 2019. Mineralization-alteration footprints in the Olympic Dam IOCG district, South Australia: The Acropolis prospect. Journal of Geochemical Exploration 205, 106333.

Dmitrijeva, M., Metcalfe, A.V., Ciobanu, C.L., Cook, N.J., Frenzel, M., Keyser, W.M., Johnson, G., Ehrig, K., 2018. Discrimination and variance structure of trace element signatures in hematite: a case study of BIF-mineralization from the Middleback Ranges, South Australia. Mathematical Geosciences 50, 381-415.

Dmitrijeva, M. Ciobanu, C.L., Ehrig, K.J., Cook, N.J., Verdugo-Ihl, M.R., Metcalfe, A.V., in review. Geochemical data analysis and 3D models for Wirrda Well prospect, South Australia: structural control on iron-oxide copper gold mineralisation. Economic Geology.

Domnick, U., Cook, N.J., Bluck, R., Brown, C., Ciobanu, C.L., 2018. Petrography of granitoids from the Samphire Pluton, South Australia: implications for uranium mineralization in overlying sediments. Lithos 300–301, 1–19.

Donovan, J.J., Singer, J.W., Armstrong, J.T., 2016. A new EPMA method for fast trace element analysis in simple matrices. American Mineralogist 101, 1839–1853.

Drexel, J.F., Preiss, W.V., Parker, A.J., 1993. The Geology of South Australia. Vol. 1, the Precambrian. Geological Survey of South Australia Bulletin 54.

Duff, M.C., Coughlin, J.U., Hunter, D.B., 2002. Uranium co-precipitation with iron oxide minerals. Geochimica et Cosmochimica Acta 66, 3533–3547.

Edwards, R.L., Chen, J.H., Wasserburg, G.J., 1986. ^{238}U-^{234}U-^{230}Th-^{232}Th systematics and the precise measurement of time over the past 500,000 years. Earth and Planetary Science Letters 81, 175–192.

Eggins, S.M., Kinsley, L.P.J., Shelley, J.M.G., 1998. Deposition and element fractionation processes during atmospheric pressure laser sampling for analysis by ICP-MS. Applied Surface Science 127-129, 278-286.

Ehrig, K., 2013. Geology of the Wirrda Well IOCG Deposit. 10th Annual SA Exploration and Mining Conference. http://www.saexplorers.com.au/archive/2013/.

Ehrig, K., Kamenetsky, V.S., McPhie, J., Apukhtina, O., Ciobanu, C., Cook, N., Kontonikas-Charos, A., Krneta, S., 2017. The IOCG-IOA Olympic Dam Cu-U-Au-Ag deposit and nearby prospects, South Australia. Proceedings, 14th Biennial SGA Meeting 'Mineral Resources to Discover' Québec City, Canada. 3, 823-826.

Ehrig, K., McPhie, J., Kamenetsky, V., 2012. Geology and mineralogical zonation of the Olympic Dam iron oxide Cu-U-Au-Ag deposit, South Australia. In: Hedenquist, J.W., Harris, M., Camus, F. (Eds), Geology and Genesis of Major Copper Deposits and Districts of the World, a Tribute to Richard Sillitoe. SEG Special Publication 16, 237-268.

Erel Y., Harlavan Y., Stein M., Blum J.D., 1997. U-Pb dating of Fe-rich phases using a sequential leaching method. Geochimica et Cosmochimica Acta 61, 1697–1703.

Ernst, R., 2014. Large Igneous Provinces. Cambridge University Press, Cambridge.

Ewing, R.C., Meldrum, A., Wang, L., Weber, W.J., Corrales, L.R., 2003.Radiation effects in zircon. In: J.M. Hanchar, P.W.O. Hoskin (eds.) Zircon. Mineralogical Society of America. Reviews in Mineral Geochemistry 53, 387-425.

Ewing, R.C., Chakoumakos, B.C., Lumpkin, G.R., Murakami, T., Greegor, R.B., Lytle, F.W., 1988. Metamict minerals: Natural analogues for radiation damage effects in ceramic nuclear waste forms. Nuclear Instrument Methods Physical Research Section B 32, 487–497.

Ewing, R.C., Lutze, W., Weber, W.J., 1995. Zircon—a Host-Phase for the Disposal of Weapons Plutonium. Journal of Material Research 10, 243–246.

Fanning, C.M., Flint, R.B., Parker, A.J., Ludwig, K.R., Blisset, A.H., 1988. Refined Proterozoic evolution of the Gawler craton, South Australia, through U-Pb zircon geochronology. Precambrian Research 40, 363-386.

Fanning, C.M., Reid, A.J., Teale, G.S., 2007. A geochronological framework for the Gawler Craton, South Australia: Geological Survey of South Australia. Geological Society of South Australia Bulletin 55, 258.

Fraser, G.L., Neumann, N., 2010. New SHRIMP U-Pb zircon ages from the Gawler craton and Curnamona province, South Australia, 2008–2010. Geoscience Australia Record 2010/16, 256.

Frei R., Bridgwater D., Rosing M., Sletcher O., 1999. Controversial Pb-Pb and Sm-Nd isotope results in the early Archean Isua (West Greenland) oxide iron formation: Preservation of primary signatures versus secondary disturbances. Geochimica et Cosmochimica Acta 63, 476–488.

Geisler, T., Rashwan, A.A., Rahn, M.K.W., Poller, U., Zwingmann, H., Pidgeon, R.T., Schleicher, H., Tomaschek, F., 2003. Low temperature hydrothermal alteration of natural metamict zircons from the Eastern Desert, Egypt. Mineralogical Magazine 67, 485–508.

Geisler, T., Schaltegger, U., Tomaschek, F., 2007. Re-equilibration of zircon in aqueous fluids and melts. Elements 3, 43–50.

Geological Survey of South Australia, 2019. SARIG Database. https://map.sarig.sa.gov.au/.

Gerstenberger, H., Haase, G., 1997. A highly effective emitter substance for mass spectrometric Pb isotope ratio determinations. Chemical Geology 136, 309–312.

Goldfarb, R.J., Bradley, D., Leach, D.L., 2010. Secular variation in economic geology. Economic Geology 105, 459–465.

Grainger, C.J., Groves, D.I., Tallarico, F.H.B., Fletcher, I.R., 2008. Metallogenesis of the Carajás mineral province, southern amazon craton, Brazil: Varying styles of Archean through Paleoproterozoic to Neoproterozoic base and precious-metal mineralisation. Ore Geology Reviews 33, 451–489.

Groves, D.I., Bierlein, F.P., Meinert, L.D., Hitzman, M.W., 2010. Iron oxide copper-gold (IOCG) deposits through Earth history: Implications for origin, lithospheric setting, and distinction from other epigenetic iron oxide deposits. Economic Geology 105, 641–654.

Groves, D.I., Zhang, L., and Santosh, M., in press, Subduction, mantle metasomatism, and gold: A dynamic and genetic conjunction. Geological Society of America Bulletin, https://doi.org/10.1130/B35379.1

Gualtieri, A.F., Venturelli, P., 1999. In situ study of the goethite-hematite phase transformation by real time synchrotron powder diffraction. American Mineralogist 84, 895-904.

Günther, D., 2002. Laser Ablation-Inductively Coupled Plasma Mass Spectrometry Trends. Journal of Analytical and Bioanalytical Chemistry 372, 31-32.

Günther, D., Heinrich, C.A., 1999. Enhanced sensitivity in laser ablation-ICP mass spectrometry using helium-argon mixtures as aerosol carrier. Journal of Analytical Atomic Spectrometry 14, 1363-1368.

Harley, S.L., Kelly, N.M., 2007. Zircon Tiny but Timely. Elements 3, 13-18.

Hawkins, D., Bowring, S., 1997. U-Pb systematics of monazite and xenotime: case studies from the Paleoproterozoic of the Grand Canyon, Arizona. Contributions to Mineralogy and Petrology 127, 87-103.

Haynes, D.W., Cross, K.C., Bills, R.T., Reed, M.H., 1995. Olympic Dam ore genesis: a fluid-mixing model. Economic Geology, 90, 281–307.

Hayward, N., Skirrow, R.G., 2010. Geodynamic setting and controls on iron oxide Cu-Au (±U) ore in the Gawler Craton, South Australia. In: Porter, T.M (ed.). Hydrothermal Iron Oxide Copper-Gold & Related Deposits: A Global Perspective, PGC Publishing, Adelaide, 3, 1-27.

Hiess, J., Condon, D.J., McLean, N., Noble, S.R., 2012. $^{238}U/^{235}U$ Systematics in Terrestrial Uranium-Bearing Minerals. Science 335, 1610-1614.

Holland, H.D., Gottfried, D., 1955. The effect of nuclear radiation on the structure of zircon. Acta Crystallographica 8, 291-300.

Holtz, F., Johannes, W., Tamic, N., Behrens, H., 2001. Maximum and minimum water contents of granitic melts generated in the crust: a reevaluation and implications. Lithos, 56, 1–14.

Horn, I, Rudnick, R.L., McDonough, W.F., 2000. Precise elemental and isotope ratio determination by simultaneous solution nebulization and laser ablation-ICP-MS: application to U–Pb geochronology. Chemical Geology 164, 281–301.

Horstwood, M., 2008. Data reduction strategies, uncertainty assessment and resolution of LA-(MC-) ICP-MS isotope data. In: P. Sylvester (ed.), Laser Ablation ICP–MS in the Earth Sciences, Mineralogical Association of Canada Short Course vol. 40, 283-303.

Horstwood, M.S., Košler, J., Gehrels, G., Jackson, S.E., McLean, N.M., Paton, C., Pearson, N.J., Sircombe, K., Sylvester, P., Vermeesch, P., Bowring, J.F., Condon, D.J., Schoene, B., 2016. Community-Derived Standards for LA-ICP-MS U-(Th)-Pb Geochronology–Uncertainty Propagation, Age Interpretation and Data Reporting. Geostandards and Geoanalytical Research 40, 311–332.

Hoskin, P.W.O., Schaltegger, U., 2003. The composition of zircon and igneous and metamorphic petrogenesis. In Zircon (J.M. Hanchar, P.W.O. Hoskin, eds.). Reviews in Mineralogy and Geochemistry 53, 27-62.

Huang, Q., Kamenetsky, V.S., Ehrig, K., McPhie, J., Kamenetsky, M., Cross, K., Meffre, S., Agangi, A., Chambefort, I., Direen, N.G., Maas, R., Apukhtina, O., 2016. Olivine-phyric basalt in the Mesoproterozoic Gawler silicic large igneous province, South Australia: Examples at the Olympic Dam Iron Oxide Cu–U–Au–Ag deposit and other localities. Precambrian Research 281, 185–199.

Huang, Q., Kamenetsky, V.S., McPhie, J., Ehrig, K., Meffre, S., Maas, R., Thompson, J., Kamenetsky, M., Chambefort, I., Apukhtina, O., Hu, Y., 2015. Neoproterozoic (ca. 820–830 Ma) mafic dykes at Olympic Dam, South Australia: Links with the Gairdner Large Igneous Province. Precambrian Research 271, 160-172.

Huberty, J.M., Konish, H., Heck, P.R., Fournelle, J.H., Valley, J.W., Xu, H., 2012. Silician magnetite from the Dales Gorge member of the Brockman iron formation, Hamersley Group, Western Australia. American Mineralogist 97, 26–37.

Ismail, R., Ciobanu, C.L., Cook, N.J., Teale, G.S., Giles, D., Mumm, A.S., Wade, B., 2014. Rare earths and other trace elements in minerals from skarn assemblages, Hillside iron oxide-copper-gold deposit, Yorke Peninsula, South Australia. Lithos 184-187, 456-477.

Jackson, S.E., Pearson, N.J., Belousova, E.A., Griffin, W.L., 2004. The application of laser ablation-inductively coupled plasma-mass spectrometry (LA-ICP-MS) to in situ U-Pb geochronology. Chemical Geology 211, 47–69.

Jaffey, A.H., Flynn, K.F., Glendenin, L.E., Bentley, W.C., Essling, A.M., 1971. Precision measurement of half-lives and specific activities of ^{235}U and ^{238}U. Physical Reviews C, Nuclear Physics 4, 1889–1906.

Jagodzinski, E.A., 2005. Compilation of SHRIMP U-Pb geochronological data Olympic Domain, Gawler Craton, South Australia, 2001-2003. Geoscience Australia Record 2005.

Jagodzinski, E.A., 2004. The age of magmatic and hydrothermal zircon at Olympic Dam. In: Proceedings of the 2014 Australian Earth Sciences Convention, Sustainable Australia, Newcastle, Australia. 110, 260.

Jagodzinski, E.A., 2016. Dating of the Hiltaba-GRV event and associated mineral systems. Presentation, Mineral Systems Drilling Program Open Day, 11th August 2016, http://minerals.statedevelopment.sa.govau/latest_updates/mineral_systems_drilling_program_open_day_presentations.

Johnson, J.P., 1993. The geochronology and radiogenic isotope systematics of the Olympic Dam copper-uranium-gold-silver deposit, South Australia: Unpublished Ph.D. thesis, Canberra, Australia, The Australian National University.

Johnson, J.P., Cross, K.C., 1995. U-Pb geochronological constraints on the genesis of the Olympic Dam Cu-U-Au-Ag deposit, South Australia: Economic Geology 90, 1046–1063.

Keppler, H., Wyllie, P.J., 1991. Partitioning of Cu, Sn, Mo, W, U, and Th between melt and aqueous fluid in the systems haplogranite-H_2O-HCl and haplogranite-H_2O-HF: Contributions to Mineralogy and Petrology, 109, 139–150.

Keyser, W., Ciobanu, C.L., Cook, N.J., Courtney-Davies, L., Kennedy, A., Wade, B.P., Ehrig, K., Dmitrijeva, M., Kontonikas-Charos, A., Feltus, H., Johnson, G., 2019. Petrographic and

geochronological constraints on the granitic basement to the Middleback Ranges, South Australia. Precambrian Research 324, 170-193.

Keyser, W., Ciobanu, C.L., Cook, N.J., Feltus, H., Johnson, G., Slattery, A., Wade, B.P., Ehrig, K., 2019. Mineralogy of zirconium in iron-oxides: A micron- to nanoscale study of hematite ore from Peculiar Knob. Minerals 9, 244.

Keyser, W., Ciobanu, C.L., Cook, N.J., Johnson, G., Dmitrijeva, M., Courtney-Davies, L., Feltus, H., Gilbert, S., Johnson, G., Ehrig, K., 2019. Iron-oxides constrain BIF evolution in terranes with protracted geological histories: the Iron Count prospect, Middleback Ranges, South Australia. Lithos 324-325, 20-38.

Keyser, W., Ciobanu, C.L., Cook, N.J., Wade, B.P., Wade, B.P., Kennedy, A., Kontonikas-Charos, A., Ehrig, K., Feltus, H., Johnson, G., 2020. Episodic mafic magmatism in the Eyre Peninsula: defining syn- and post-depositional BIF environments for iron deposits in the Middleback Ranges, South Australia. Precambrian Research. 337, 105535.

Keyser, W.M., Ciobanu, C.L., Cook, N.J., Courtney-Davies, L., Ehrig, K., Gilbert, S., McPhie, J., 2017. Links between sedimentary protoliths and IOCG-skarn alteration, Island Dam, South Australia, Extended abstract, 14th Biennial SGA Conference, Québec, Canada, 3, 935-938.

Keyser, W.M., Ciobanu, C.L., Cook, N.J., Johnson, G., Feltus, F., Johnson, S., Dmitrijeva, M., Ehrig, K., Nguyen, P., 2018. Petrography and trace element signatures of iron-oxides in deposits from the Middleback Ranges, South Australia: from banded iron formation to ore. Ore Geology Reviews 93, 337-360.

Kirchenbaur, M., Maas, R., Ehrig, K., Kamenetsky, V.S., Strub, E., Ballhaus, C., Münker, C., 2016. Uranium and Sm isotope studies of the supergiant Olympic Dam Cu–Au–U–Ag deposit, South Australia. Geochimica et Cosmochimica Acta 180, 15–32.

Kontonikas-Charos, A., Ciobanu, C.L., Cook, N.J., Ehrig, K., Krneta, S., Kamenetsky, V.S., 2017. Feldspar evolution in the Roxby Downs Granite, host to Fe-oxide Cu-Au-(U) mineralisation at Olympic Dam, South Australia. Ore Geology Reviews 80, 838–859.

Kontonikas-Charos, A., Ciobanu, C.L., Cook, N.J., Ehrig, K., Krneta, S., Kamenetsky, V.S., 2018. Rare earth element geochemistry of feldspars: Examples from Fe-oxide Cu-Au systems in the Olympic Cu-Au Province, South Australia. Mineralogy and Petrology 112, 145-172.

Kontonikas-Charos, A., Ciobanu, C.L., Cook, N.J., Ehrig, K., Ismail, R., Krneta, S., Basak, A., 2018. Feldspar mineralogy and rare earth element (re)mobilization in iron-oxide copper gold systems from South Australia: a nanoscale study. Mineralogical Magazine 82, S173–S197.

Košler, J., Fonneland, H., Sylvester, P., Tubrett, M., Pedersen., 2002. R-B. U–Pb dating of detrital zircons for sediment provenance studies—a comparison of laser ablation ICPMS and SIMS techniques. Chemical Geology 182, 2–4, 605–618.

Kozlov, V.D., 2011. Trace-element composition and origin of granitoids from the Shakhtama complex and Kukul'bei rare-metal complex (Aga zone, Transbaikalia). Russian Geology and Geophysics, 52(5), 526–536

Krneta, S., Ciobanu, C., Cook, N., Ehrig, K., 2018. Numerical modeling of REE fractionation patterns in fluorapatite from the Olympic Dam deposit (South Australia). Minerals 8, 342, https://doi.org/10.3390/ min8080342.

Krneta, S., Ciobanu, C.L., Cook, N.J., Ehrig, K., Kontonikas-Charos, A., 2016. Apatite at Olympic Dam, South Australia: a petrogenetic tool. Lithos, 262, 470–485

Krneta, S., Ciobanu, C.L., Cook, N.J., Ehrig, K., Kontonikas-Charos, A., 2017. Rare earth element behaviour in apatite from the Olympic Dam Cu–U–Au–Ag deposit, South Australia. Minerals 7, 135, https://doi.org/10.3390/min7080135.

Krneta, S., Ciobanu, C.L., Cook, N.J., Ehrig, K., Kontonikas-Charos, A., 2017. The Wirrda Well and Acropolis prospects Gawler Craton, South Australia: insights into evolving fluid conditions through apatite chemistry. Journal of Geochemical Exploration 181, 276-291.

Kuhn, B.K., Birbaum, K., Luoc, Y., Günther, D., 2009. Fundamental studies on the ablation behaviour of Pb/U in NIST 610 and zircon 91500 using laser ablation inductively coupled plasma mass spectrometry with respect to geochronology. Journal of Analytical Atomic Spectrometry 25, 21–27.

Kusiak, M.A., Dunkley, D.J., Wirth, R., Whitehouse, M.J., Wilde, S.A., Marquardtd, K., 2015. Metallic lead nanospheres discovered in ancient zircons. Proceedings of the National Academy of Sciences 112, 4958–4963.

Langmuir, D., 1997. Aqueous Environmental Geochemistry, Prentice Hall, Pearson, ISBN: 0-02-367412-1.

Leach, J.J, Allen, L.A., Aeschliman, D.B., Houk, R.S., 1999. Calibration of Laser Ablation ICP-MS Using Standard Additions with Dried Solution Aerosols. Journal of Analytical Chemistry 71, 440-445.

Li, Y., Selby, D., Condon, D., Tapster, S., 2017. Cyclic Magmatic-Hydrothermal Evolution in Porphyry Systems: High-Precision U-Pb and Re-Os Geochronology Constraints on the Tibetan Qulong Porphyry Cu-Mo Deposit. Economic Geology 112, 1419-1440.

Lu, Y.J., Loucks, R.R., Fiorentini, M.L., McCuaig, T.C., Evans, N.J., Yang, Z.M., Hou, Z.Q., Kirkland, C.L., Parra-Avila, L.A., Kobussen, A., 2016. Zircon compositions as a pathfinder for porphyry Cu ± Mo ± Au deposits. Economic Geology 19, 329–347.

Ludwig, K.R., 2012. A User's Manual for Isoplot 3.75: A Geochronological Toolkit for Microsoft Excel. Berkeley Geochronology Centre Special Publication 5.

Ludwig, K.R.A., 2012. Isoplot/Ex rev. 4.1: A Geochronological Toolkit for Microsoft Excel; Berkeley Geochronology Centre Special Publication; Berkeley Geochronology Centre: Berkeley, CA. 5, 75.

Ludwig, K.R.A., 2009. SQUID 2.50: A User's manual: Berkeley Geochronology Center, Special Publication No. 5, 110, Berkeley, California.

Lugmair, G.W., Galer, S.J.G., 1992. Age and isotopic relationships among the angrites Lewis Cliff 86010 and Angra dos Reis. Geochimica et Cosmochimica Acta 56, 1673-1694.

Maas, R., Kamenetsky, V.S., Ehrig, K., Meffre, S., McPhie, J., Diemar, G., 2011. Olympic Dam U-Cu-Au deposit, Australia: New age constraints. Mineralogical Magazine 75, 1375.

Machado, N., Lindenmayer, Z., Krogh, T.E., Lindenmayer, D., 1991. U-Pb geochronology of Archean magmatism and basement reactivation in the Carajás area, Amazon Shield, Brazil, Precambrian Research 49, 329–354.

Macmillan, E., Ciobanu, C.L., Ehrig, K., Cook, N.J., Pring, A., 2016. Replacement of uraninite by bornite via coupled dissolution-reprecipitation: evidence from texture and microstructure. Canadian Mineralogist 54, 1369–1383.

Macmillan, E., Cook, N.J., Ehrig, K., Ciobanu, C.L., Pring, A., 2016. Uraninite from the Olympic Dam IOCG-U-Ag deposit: linking textural and compositional variation to temporal evolution. American Mineralogist 101, 1295–1320.

Marshall, T.A., Morris, K., Law, G.T.W., Livens, F.R., Mosselmans, F.W.J., Bots, P., Shaw, S., 2014. Incorporation of Uranium into Hematite during Crystallization from Ferrihydrite, Environmental Science Technology 48, 3724–3731.

Maslen, E.N., Streltsov, V.A., Streltsova, N.R., Ishizawa, N., 1994. Synchrotron X-ray study of the electron density in α-Fe_2O_3. Acta Crystallographica 50, 435–441.

Mattinson, J.M., 2005. Zircon U–Pb chemical abrasion ("CA-TIMS") method: Combined annealing and multi-step partial dissolution analysis for improved precision and accuracy of zircon ages. Chemical Geology 220, 47-66.

Mattinson, J.M., Graubard, C.M., Parkinson, D.L., McClelland, W.C., 1996. U-Pb reverse discordance in zircons: the role of fine-scale oscillatory zoning and sub-micron transport of Pb: in A.R. Basu, S.R. Hart, eds., Earth Processes: Reading the Isotopic Code, Geophysical Monograph Series 95, American Geophysics Union 355-370.

Mauger, A.J., Ehrig, K., Kontonikas-Charos, A., Ciobanu, C.L., Cook, N.J., Kamenetsky, V.S., 2016. Alteration at the Olympic Dam IOCG–U deposit: insights into distal to proximal feldspar and phyllosilicate chemistry from infrared reflectance spectroscopy. Australian Journal of Earth Sciences 63, 959-972.

McFarlane, C.R.M., Yan, L., 2012. U-Pb Geochronology Using 193 nm Excimer LA-ICP-MS Optimized for In-Situ Accessory Mineral Dating in Thin Sections. Geoscience Canada: Analytical Techniques Series 39, 158-172.

McInnes, B.I.A., Keays, R.R., Lambert, D.D., Hellstrom, J., Allwood, J.S., 2008. Re-Os geochronology and isotope systematics of the Tanami, Tennant Creek and Olympic Dam Cu-Au deposits. Australian Journal of Earth Sciences 55, 967–981.

McPhie, J., 2016. Acropolis Report. BHP Olympic Dam (unpublished).

McPhie, J., Orth, K., Kamenetsky, V., Kamenetsky, M., Ehrig, K., 2016. Characteristics, origin and significance of Mesoproterozoic bedded clastic facies at the Olympic Dam Cu-U-Au-Ag deposit, South Australia. Precambrian Research 276, 85-100.

Meffre, S., Ehrig, K., Kamenetsky, V.S., Chambefort, I., Maas, R., McPhie, J., 2010. Pb isotopes at Olympic Dam: Constraining sulphide growth: Giant ore deposits down under: Proceedings of 13th Quadrennial International Association on the Genesis of Ore Deposits (IAGOD) Symposium, Adelaide, South Australia, 78–79.

Meldrum, A., Boatner, L.A., Weber, W.J., Ewing, R.C., 1988. Radiation damage in zircon and monazite. Geochimica et Cosmochimica Acta 62, 2509-2520.

Mortimer, G.E., Cooper, J.A., Paterson, H.L., Cross, K., Hudson, G.R.T., Uppill, R.K., 1988. Zircon U–Pb Dating in the Vicinity of the Olympic Dam Cu–U–Au Deposit, Roxby Downs, South-Australia. Economic Geology 83, 694–709.

Murakami, H., Seo, J.H., Heinrich, C.A., 2010. The relation between Cu/Au ratio and formation depth of porphyry-style Cu–Au ± Mo deposits. Mineralium Deposita 45, 11–21.

Nasdala, L., Corfu, F., Schoene, B., Tapster, S.R., Wall, C.J., Schmitz, M.D., Ovtcharova, M., Schaltegger, U., Kennedy, A.K., Kronz, A., Reiners, P.W., Yang, Y., Wu, F., Gain, S.E., Griffin, W.L., Szymanowski, D., Chanmuang N.,C., Ende, M., Valley, J.W., Spicuzza, M.J., Wanthanachaisaeng, B. Giester, G., 2018. GZ7 and GZ8 – Two Zircon Reference Materials for SIMS U-Pb Geochronology. Geostandards and Geoanalytical Research 42, 431-457.

Nasdala, L., Kronz, A., Wirth, R., Váczi, T., Pérez-Soba, C., Willner, A., Kennedy, A.K., 2009. Alteration of radiation-damaged zircon and the related phenomenon of deficient electron microprobe totals. Geochimica et Cosmochimica Acta 73, 1637–1650.

Oreskes, N., 1990. Uranium content of Olympic Dam hematite: Implications for fluid chemistry and ore depositional mechanisms. Program with Abstracts, 8th Quadrennial IAGOD Conference, Ottawa, Canada, p. A137.

Oreskes, N., Einaudi, M.T., 1990. Origin of rare earth element-enriched hematite breccias at the Olympic Dam Cu-U-Au-Ag deposit, Roxby Downs, South Australia. Economic Geology, 85, 1–28.

Ovalle, J.T., La Cruz, N.L., Reich, M., Barra, F., Simon, A.C., Konecke, B.A., Rodriguez-Mustafa, M.A., Deditius, A.P., Childress, T.M., Morata, D. Formation of massive iron deposits linked to explosive volcanic eruptions. Scientific Reports 8, 14855.

Owen, N.D., Ciobanu, C.L., Cook, N.J., Slattery, A., Basak, A., 2018. Nanoscale study of clausthalite-bearing symplectites in Cu-Au-(U) ores: Implications for ore genesis. Minerals, 8, 67, DOI: 10.3390/min8020067.

Paton, C., Hellstrom, J., Paul, P., Woodhead, J., Hergt, J., 2011. Iolite: Freeware for the visualisation and processing of mass spectrometric data. Journal of Analytical Atomic Spectrometry, 26, 2508.

Pérez-Soba, C., Villaseca, C., Gonzáles del Tánago, J., Nasdala, L., 2007. The composition of zircon in the peraluminous Hercynian granites of the Spanish Central System batholith. Canadian Mineralogist 45, 509–527.

Peterman, E.M., Reddy, S.M., Saxey, D.W., Snoeyenbos, D.R., Rickard, W.D., Fougerouse, D., Kylander-Clark. A.R., 2016. Nanogeochronology of discordant zircon measured by atom probe microscopy of Pb enriched dislocation loops. Science Advances 2, e1601318.

Petrus, J., Kamber, B., 2012. VizualAge: A Novel Approach to Laser Ablation ICP-MS U-Pb Geochronology Data Reduction. Geostandards and Geoanalytical Research 36, 247-270.

Petrus, J., Chew, D., Leybourne, M., Kamber, B., 2017. A new approach to laser-ablation inductively-coupled-plasma mass-spectrometry (LA-ICP-MS) using the flexible map interrogation tool 'Monocle'. Chemical Geology 463, 76-93.

Pickhardt, C., Becker, J.S., Dietze, H.J., 2000. A new strategy of solution calibration in laser ablation inductively coupled plasma mass spectrometry for multi element trace analysis of geological samples. Journal of Analytical Chemistry 368, 173–181.

Pimentel, M.M., Heaman, L., Fuck, R.A., Marini, O.J., 1992. U-Pb zircon geochronology of Precambrian tin-bearing continental-type acid magmatism in central Brazil. Precambrian Research 52, 321-335.

Pinheiro, R.V.L., Holdsworth, R.E., 1997. Reactivation of Archaean strike-slip fault systems, Amazon region, Brazil. Journal of the Geological Society 154, 99-103.

Reeve, J.S., Cross, K.C., Smith, R.N., Oreskes, N., 1990. Olympic Dam copper-uranium-gold-silver deposit: in Hughes, F.E., ed., Geology of the Mineral Deposits of Australia and Papua New Guinea: Melbourne, Australia, Australian Institute of Mining and Metallurgy, 1009-1035.

Reid, A., 2019. The Olympic Cu-Au Province, Gawler Craton: A Review of the Lithospheric Architecture, Geodynamic Setting, Alteration Systems, Cover Successions and Prospectivity. Minerals 9, 371, doi:10.3390/min9060371.

Reid, A., Smith, R.N., Baker, T., Jagodzinski, E.A., Selby, D., Gregory, C.J., Skirrow, R.G., 2013. Re-Os dating of molybdenite within hematite breccias from the Vulcan Cu-Au prospect, Olympic Cu-Au province, South Australia. Economic Geology 108, 883–894.

Reid, A.J., Swain, G.S., Mason, D., Maas, R., 2011. Nature and timing of Cu-Au-Zn-Pb mineralisation at Punt Hill, eastern Gawler Craton. MESA Journal 60, 7–17.

Reiners, P.W., Renne, R.W., Carlson, K.M., Cooper, D.E., Granger, N.M., McLean, B. Schoene, B., 2017. Geochronology and Thermochronology, John Wiley & Sons.

Richards, J.P., 2018. A Shake-Up in the Porphyry World?. Economic Geology, 113 (6), 1225–1233.

Ríos, S., Malcherek, T., Salje, E.K.H., Domeneghetti, C., 2000. Localized defects in radiation-damaged zircon. Acta Crystallographica 56, 947-952.

Rollog, M., Cook, N.J., Guagliardo, P., Ehrig, K., Kilburn, M., 2019. In situ spatial distribution mapping of radionuclides in minerals by nanoSIMS. Geochemistry. Exploration, Environment, Analysis 19, 245-254.

Routhier, P., 1967. Le modèle de la genèse. Quelques concepts fondamentaux en pétrologie et en métallogénie. Modèles des théories métallogénétiques. Chron Min 363, 177–190

Rubatto, D.; Hermann, J., 2007. Zircon behaviour in deeply subducted rocks. Elements 3, 31-35.

Salje, E.K.H., Chrosch, J., Ewing, R.C., 1999. Is "metamictization" of zircon a phase transition?. American Mineralogist 84, 1107-1116.

Saxey D.W., Moser D.E., Piazolo S., Reddy S.M., Valley J.W., 2018. Atomic worlds: Current state and future of atom probe tomography in geoscience. Scripta Materialia 148, 115-121.

Schaltegger, U., Schmitt, A., Horstwood, M., 2015. U–Th–Pb zircon geochronology by ID-TIMS, SIMS, and laser ablation ICP-MS: Recipes, interpretations, and opportunities. Chemical Geology 402, 89-110.

Schaltegger, U., Schmitt, A.K., Horstwood, M.S.A., 2015. U–Th–Pb zircon geochronology by ID-TIMS, SIMS, and laser ablation ICP-MS: Recipes, interpretations, and opportunities. Chemical Geology 402 89-110.

Scherer, E.E., Whitehouse, M.J., Munker, C., 2007. Zircon as a Monitor of Crustal Growth. Elements 3, 19-24.

Schlegel, T.U., Wagner, T., Boyce, A., Heinrich, C.A., 2017. A magmatic source of hydrothermal sulfur for the Prominent Hill deposit and associated prospects in the Olympic iron oxide copper-gold (IOCG) province of South Australia. Ore Geology Reviews 89, 1058–1090.

Schmandt, D.S., Cook, N.J., Ciobanu, C.L., Ehrig, K., Wade, B.P., Gilbert, S., Kametetsky, V.S., 2019. Rare earth element phosphate minerals from the Olympic Dam Cu-U-Au-Ag deposit, South Australia: Recognizing temporal-spatial controls on REE mineralogy in an evolved IOCG systems. Canadian Mineralogist 57, 3–24.

Schmitz, M.D., Schoene, B., 2007. Derivation of isotope ratios, errors, and error correlations for U-Pb geochronology using ^{205}Pb-^{235}U-(^{233}U)-spiked isotope dilution thermal ionization mass spectrometric data. Geochemistry, Geophysics, Geosystems 8, Q08006, doi:10.1029/2006GC001492.

Schoene, B., Bowring, S.A., 2007. Determining accurate temperature–time paths from U–Pb thermochronology: an example from the Kaapvaal craton, southern Africa. Geochimica etCosmochimica Acta 71, 165-185

Schoene, B., Condon, D.J., Morgan, L.N., McLean, N., 2013. Precision and Accuracy in Geochronology. Elements 9, 19-24.

Seydoux-Guillaume, A.M., Bingen, B., Paquette, J.L., Bosse, V., 2015. Nanoscale evidence for uranium mobility in zircon and the discordance of U-Pb chronometers. Earth and Planetary Science Letters 409, 43-48.

Sillitoe, R.H., Mortensen, J.K., 2010. Longevity of porphyry copper formation at Quellaveco, Peru. Economic Geology 105, 1157–1162.

Simonetti, A., Heaman, L.M., Hartlaub, R.P., Creaser, R.A., MacHattie, T.G., Böhm, C., 2005. U-Pb zircon dating by laser ablation MC-ICP-MS using a new multiple ion counting Faraday collector array. Journal of Analytical Atomic Spectrometry 20, 677-686.

Skirrow, R., Bastrakov, E., Davidson, G., Raymond, O., Heithersay, P., 2002. The geological framework, distribution and controls of Fe-oxide Cu-Au mineralisation in the Gawler Craton, South Australia. Part II-alteration and mineralisation. In Porter, T.M. (Ed.), Hydrothermal Iron Oxide Copper-Gold and Related Deposits: A Global Perspective, PGC Publishing, Adelaide, 33-47.

Skirrow, R.G., Bastrakov, E.N., Baroncii, K., Fraser, G.L., Creaser, R.A., Fanning, C.M., Raymond, and O.L., Davidson, G.J., 2007. Timing of iron oxide Cu-Au-(U) hydrothermal activity and Nd isotope constraints on metal sources in the Gawler craton, South Australia. Economic Geology, 102, 1441–1470.

Skirrow, R.G., Van Der Wielen, S.E., Champion, D.C., Czarnota, K., Thiel, S., 2018. Lithospheric architecture and mantle metasomatism linked to iron oxide Cu-Au ore

formation: Multidisciplinary evidence from the Olympic Dam Region, South Australia. Geochemistry, Geophysics, Geosystems 19, 2673–2705.

Sláma, J., Košler, J., Condon, D.J., Crowley, J.L., Gerdes, A., Hanchar, J.M., Horstwood, M.S.A., Morris, G.A., Nasdala, L., Norberg, N., Schaltegger, U., Schoene, B., Tubrett, M.N., Whitehouse, M.J., 2008. Plešovice zircon - a new natural reference material for U–Pb and Hf isotopic microanalysis. Chemical Geology 249, 1–35.

Stacey, J.S., Kramers, J.D., 1975. Approximation of Terrestrial Lead Isotope Evolution by a 2-Stage Model. Earth and Planetary Science Letters 26, 207-221.

Steiger, R.H., Jäger, E., 1977. Subcommission on geochronology: Convention on the use of decay constants in geo- and cosmochronology. Earth and Planetary Science Letters 36, 359-362.

Stern, T.W., Bateman, P.C., Morgan, B.A., Newell, M.F., Peck, D.L., 1981. Isotopic U-Pb ages of zircon from the granitoids of the central Sierra Nevada, California. U.S. Geological Survey Professional Paper 1185, 17.

Stirling, C.H., Andersen, M.B., Potter, E.K., Halliday, A.N., 2007. Low-temperature isotopic fractionation of uranium. Earth and Planetary Science Letters 264, 208-225.

Szpunar, M., Hand, M., Barovich, K., Schwarz, M., Jagodzinski, E., Belousova, E., 2011. Isotopic and geochemical constraints on the Paleoproterozoic Hutchison Group, southern Australia: Implications for Paleoproterozoic continental reconstructions. Precambrian Research 187, 99-126.

Tang, F., Taylor, J.M., Einsle, J.F., Borlina, C.S., Fu, R.R., Weiss, B.P., Williams, H.M., Williams, W., Nagy, L., Midgley, P., Lima, E.A., Bell, E.A., Harrison, T.M., Alexander, E., Harrison, R.J., 2019. Secondary magnetite in ancient zircon precludes analysis of a Hadean geodynamo. Proceedings of the National Academy of Science 116, 407-412.

Tapster, S., Condon, D.J., Naden, J., Noble, S.R., Petterson, M.G., Roberts, N.M.W., Saunders, A.D., Smith, D.J., 2016. Rapid thermal rejuvenation of high-crystallinity magma linked to porphyry copper deposit formation; evidence from the Koloula porphyry prospect, Solomon Islands. Earth and Planetary Science Letters 442, 206–217.

Thompson, J., Meffre, S., Maas, R., Kamenetsky, V., Kamenetsky, M., Goemann, K., Danyushevsky, L., 2016. Matrix effects in Pb/U measurements during LA-ICP-MS analysis of the mineral apatite. Journal of Analytical Atomic Spectrometry 31, 1206–1215.

Tooth, B., Ciobanu, C.L., Green, L., O'Neill, B., Brugger, J., 2011. Bi-melt formation and gold scavenging from hydrothermal fluids: An experimental study. Geochimica et Cosmochimica Acta 75, 5423-5443.

Troll, V.R., Weis, F.A., Jonsson, E., Andresson, U.B., Majidi, S.A., Högdahl, K., Harris, C., Millet, M.-A., Chinnasamy, S.S., Kooijman, E., Nilsson, K.P., 2019. Global Fe–O isotope correlation reveals magmatic origin of Kiruna-type apatite-iron-oxide ores. Nature Communications, https://doi.org/10.1038/s41467-019-09244-4

Trueman, N.A., Long, J.V.P., Reed, S.J.B., Chinner, G.A., 1988. The lead-uranium systematics, and rare earth element distributions of some Olympic Dam and Stuart shelf mineralisation: Adelaide, Australia, Western Mining Corporation, unpublished report, K/3143, 46.

Utsunomiya S., Ewing R.C., 2003. Application of high-angle annular dark field scanning transmission electron microscopy—energy dispersive X-ray spectrometry, and energy-filtered transmission electron microscopy to the characterization of nanoparticles in the environment. Environmental Science Technology 37, 786–791.

Utsunomiya, S., Palenik, C.S., Valley, J.W., Cavosie, A.J., Wilde, S.A., Ewing, R.C., 2004. Nanoscale occurrence of Pb in an Archean zircon. Geochimica et Cosmochimica Acta 68, 4679–4686.

Utsunomiya, S., Valley, J.W., Cavosie, A.J., Wilde, S.A., Ewing, R.C., 2007. Radiation damage and alteration of zircon from a 3.3 Ga porphyritic granite from the Jack Hills, Western Australia. Chemical Geology 236, 92–111.

Valley, J.W., Reinhard, D.A., Cavosie, A.J., Ushikubo, T., Lawrence, D.F., Larson, D.J., Kelly, T.F., Snoeyenbos, D.R., Strickland, A., 2015. Nano- and micro-geochronology in Hadean and Archean zircons by atom-probe tomography and SIMS: New tools for old minerals. American Mineralogist 100, 1355–1377.

Van Achterbergh, E., Ryan, C., Jackson, S., Griffin, W., 2001. Appendix 3 Data reduction software for LA-ICP-MS. In: Laser-Ablation-ICPMS in the Earth Sciences (Sylvester, P., Ed.), Short Course Volume, Mineralogical Association of Canada: Quebec City, QC, 29, 239–243.

Verdugo-Ihl, M.R., Ciobanu, C.L., Cook, N.J., Ehrig, K., Courtney-Davies, L., 2020. Defining early stages of IOCG systems: Evidence from iron-oxides in the outer shell of the Olympic Dam deposit, South Australia. Mineralium Deposita, in press, http/doi:10.1007/s00126-019-00896-2.

Verdugo-Ihl, M.R., Ciobanu, C.L., Cook, N.J., Ehrig, K., Courtney-Davies, L., Gilbert, S., 2017. Textures and U-W-Sn-Mo signatures in hematite from the Olympic Dam Cu-U-Au-Ag deposit, South Australia: Defining the archetype for IOCG deposits. Ore Geology Reviews, 91, 173-195.

Verdugo-Ihl, M.R., Ciobanu, C.L., Slattery, A., Cook, N.J., Ehrig, K., Courtney-Davies, L., 2019. Copper-Arsenic Nanoparticles in Hematite: Fingerprinting Fluid-Mineral Interaction. Minerals 9(7), 388, https://doi.org/10.3390/min9070388.

Vigneresse, J.L., 2007. The role of discontinuous magma inputs in felsic magma and ore generation. Ore Geology Reviews 30, 181–216.

Von Quadt, A., Erni, M., Martinek, K., Moll, M., Peytcheva, Heinrich, C.A., 2011, Zircon crystallization and the lifetimes of ore-forming magmatic-hydrothermal systems. Geology 39, 731−734.

Vu, H.P.S., Shaw, L., Brinza, L.G., 2010. Benning, Crystallization of hematite (α-Fe2O3) under alkaline condition: The effects of Pb. Crystal Growth and Design 10, 1544-1551.

Wade C.E., Payne, J.L., Barovich, K.M., Reid, A.J., 2019. Heterogeneity of the sub-continental lithospheric mantle and 'non-juvenile' mantle additions to a Proterozoic silicic large igneous. Lithos 340–341, 87-107.

Walter, B.F., Gerdes, A., Kleinhanns, I.C., Dunkl, I., Von, H., Kreissl, S., Markl, G., 2018. The connection between hydrothermal fluids, mineralization, tectonics and magmatism in a continental rift setting: fluorite Sm-Nd and hematite and carbonates U-Pb geochronology from the Rhine graben in SW Germany. Geochimica et Cosmochimica Acta 240, 11-42

Weatherley, D.K., Henley, R.W., 2013. Flash vaporization during earthquakes evidenced by gold deposits. Nature Geoscience 6, p. 294–298.

Wendt, I., Carl, C., 1991. The Statistical Distribution of the Mean Squared Weighted Deviation. Chemical Geology 86, 275-285.

Wetherill, G.W., 1956. Discordant U-Pb ages, Transactions of the American Geophysics Union 37, 3.

Weyer, S., Anbar, A.D., Gerdes, A., Gordon, G.W., Algeo, T.J., Boyle, E.A., 2008. Natural fractionation of $^{238}U/^{235}U$. Geochimica et Cosmochimica Acta 72 345-359.

White, W.M., Albarède, F., Télouk, P., 2000. High-precision analysis of Pb isotope ratios by multi-collector ICP-MS. Chemical Geology 167, 257–270.

Wiedenbeck, M., Alle, P., Corfu, F., Griffin W.L., Meier M., Oberli F., von Quadt A., Roddick J.C., Spiegel W., 1995. 3 natural zircon standards for U-Th-Pb, Lu-Hf, trace-element and REE analyses. Geostandards Newsletter 19, 1–23.

Williams, I.S., 1998. U-Th-Pb geochronology by ion microprobe. Applications of microanalytical techniques to understanding mineralizing processes. Reviews in Economic Geology 7, 1-35

Wingate, M.T.D., Campbell, I.H., Compston, W., Gibson, G.M., 1998. Ion microprobe U–Pb ages for Neoproterozoic basaltic magmatism in south-central Australia and implications for the breakup of Rodinia. Precambrian Research 87, 135–159.

Wise, T., 2019. Prospectivity modelling of the Olympic Cu–Au Province. MESA Journal 90, 36-41.

Xu, H., Shen, Z., Konishi, H., 2014. Si-magnetite nano-precipitates in silician magnetite from banded iron formation: Z-contrast imaging and ab initio study. American Mineralogist 99, 2196-2202.

York, D. Least-squares fitting of a straight line with correlated errors. Earth and Planetary Science Letters 5, 320-324.

Zhou, H., Sun, X., Wu, Z., Liao, J., Fu, Y., Li, D., Hollings, P., Liu, Y., Lin, H., Lin, Z., 2017. Hematite U-Pb geochronometer: insights from monazite and hematite integrated chronology of the Yaoan gold deposit, Southwest China. Economic Geology 112, 2023–2039.

Zimmerman, A., Stein, H.J., Morgan, J.W., Markey, R.J., Watanabe, Y., 2014. Re-Os geochronology of the El Salvador porphyry Cu-Mo deposit, Chile: Tracking analytical improvements in accuracy and precision over the past decade. Geochimica et Cosmochimica Acta 131, 13–32.